Yutaka Yoshida · Ko Mibu *Editors*

ICAME 2011

Proceedings of the 65th Yamada Conference and the 31st International Conference on the Applications of the Mössbauer Effect (ICAME 2011) held in Kobe, Japan, 25-30 September 2011

Springer

Hyperfine Interact (2012) 204:1–2
DOI 10.1007/s10751-012-0592-9

OBITUARY

In memoriam Rudolf L. Mößbauer

Published online: 30 March 2012

It is with deepest sadness that the International Board on the Applications of the Mössbauer Effect (IBAME) announces the passing of its Honorary Member, the father of our method,

Professor Rudolf L. Mößbauer
Technical University of Munich, Munich, Germany
who died on 14 September 2011

Rudolf Mößbauer was born in Munich. He graduated from the Technical University of Munich (TUM) in 1955 and prepared his PhD thesis in 1957–58 at the same university under the auspices of Heinz Maier-Leibnitz the latter work has been performed in Heidelberg, at the Max Planck Institute for Medical Research, though.

In his PhD work, he described and explained the recoilless nuclear fluorescence of gamma rays in ^{191}Ir, i.e. the Mössbauer effect. For this discovery, he was awarded the Nobel Prize in Physics in 1961.

In 1960, Rudolf Mössbauer was invited to Caltech where he became a full professor in 1962. In 1964, he returned to TUM Munich where he was a full professor until 1997 when he became professor emeritus. From 1972 to 1977 he was the director of the Institut Laue–Langevin (ILL) in Grenoble, France and played an important role in introducing the user regime at the ILL high-flux reactor.

Although, since the mid-seventies, Mößbauer's interest has gradually shifted towards neutrino physics, he has never lost either scientific or personal contact to the Mössbauer effect and the international Mössbauer community, respectively. Even in the nineties he published papers on nuclear diffraction of Mössbauer radiation. He was a distinguished speaker of many Mössbauer conferences the last ICAME conferences with his participation being 1999 in Garmisch-Partenkirchen, Germany and 2003 in Muscat, Oman.

Rudolf Mößbauer's role in Mössbauer spectroscopy, both with the discovery of the Mössbauer effect and also with his continuing interest, can hardly be overstated. The Mössbauer Community thanked him for his unsurpassable services by having elected him the first Honorary Member of IBAME.

We shall miss him. Our thoughts are with his family. The funeral services took place on Tuesday, 20 September 2011.

D.L. Nagy
Chair, IBAME

Hyperfine Interact (2012) 204:3–6
DOI 10.1007/s10751-012-0597-4

Preface

Yutaka Yoshida

Published online: 20 March 2012

The 65th Yamada Conference / the 31st International Conference on the Applications of Mössbauer Effect (ICAME) was held on 25–30 September 2011 in Kobe under the sponsorship of Yamada Science Foundation. The number of participants registered was 183 from 25 different countries: 183 registered (118 regular, 33 invited, 32 students) and in addition, 13 accompanied. The numbers of the papers presented as invited talks, oral talks, and posters were 21, 33, and 201, respectively. In addition, we had 5 invited talks for the evening session, and 18 posters were selected for short oral presentations. In this proceeding volume, 120 papers are accepted for publication in the Hyperfine Interactions journal from 129 papers submitted through the website-based editorial management system newly provided by the publisher, Springer.

We started five years ago preparing this conference, before ICAME2007 in Kanpur, India, and proposed our main plan in the IBAME meeting there. We were nearly ready for the conference before 11 March 2011, when the earthquake attacked the Tohoku region, the north part of Japan, resulting in the heavy accidents in the Fukushima Nuclear Power Plants. Since this news was so shocking and triggering an unusual situation in the whole country, we felt forced to decide to move the conference venue from Tokyo to Kobe at the beginning of April. After one half year there was no danger in Tokyo, but it was inevitable for us to change the venue. To explain the whole situation, we organized a special lecture on "FUKUSHIMA ACCIDENT: WHAT HAPPENED?" by Prof. M. Baba, Cyclotron and Radioisotope Center, Tohoku University, on Tuesday night. We hoped that the decision we made affected positively to motivate people to come to Kobe, although the worldwide economic crisis also negatively influenced on the organization.

Y. Yoshida (✉)
Chair ICAME2011_Kobe, Shizuoka Institute of Science and Technology, Shizuoka, Japan
e-mail: yoshida@ms.sist.ac.jp

Professor Rudolf L. Mössbauer passed away just before this conference, on 14 September 2011. At the Opening Ceremony by Dénes Nagy, Chairperson of IBAME, with Yutaka Yoshida, Chairperson of the Organizing Committee, dedicated the conference to the memory of Professor Mössbauer. At this moment in the history of Mössbauer community, we have to overcome the generation change, since many leading scientists are retiring also from the community. One of the main purposes of ICAME2011 was to create the new generation of Mössbauer spectroscopists, and therefore, "Tutorial session", "Evening Session", "Short oral presentations", and "poster prices" were specially organized to encourage young scientists.

On Sunday at Sourakuen kaikan, we arranged the tutorial lectures "General Introduction to Mössbauer Spectroscopy" by Saburo Nasu, "Chemical Applications" by Philipp Gütlich, "Earth Sciences" by Robert E. Vandenberghe, "Fe-based Nanostructures" by Jean-Marc Greneche, "Magnetic Multilayers and Interfaces" by Teruya Shinjo, "Ion Implantation" by Guido Langouche. Unfortunately professors Gütlich could not attend the conference, but the lecture on chemical applications was given by Yann Garcia. The manuscripts of all tutorials will be published by Springer.

Furthermore, on Tuesday we had an evening session, where the following lectures were given: "Fifty Years of Mössbauer Spectroscopy: What now?" by C.E. Johnson, "Personal Recollections of 52 Years of Mössbauer Spectroscopy Research" I. Nowik who could not come to Kobe regrettably, but his manuscript appears in the proceedings, "A personal View on the Future of Diffusion Studies with the New X-ray Sources" by G. Vogl, "Redox Topotactic Reactions in FeII-III Oxyhydroxycarbonate New Minerals related to Fougèrite in Gleysols: Trébeurdenite and Mössbauerite" by J.M. Genin, "Rudolf Mössbauer and the Development of the Garching Research Site" by F. E. Wagner, "45 Years: From Antimony Mössbauer Spectroscopy to Nano Systems", J. Stevens.

In the scientific programme, we shed light on the materials research for the global environment among the usual topics which have been discussed in this long-standing conference series: T1 Material Research for the Environment; T2 Advances in Experimental techniques and Methodology; T3 Theories of Hyperfine Interactions; T4 Dynamics; T5 Biological and Medical Applications; T6 Chemical Applications; T7 Nanomaterials; T8 Solid State Physics; T9 Earth Science, Mineralogy and Archaeology; T10 Materials Science and Industrial Applications. After the opening ceremony on Monday, Prof. W. Keune gave us a keynote lecture on the applications of Mössbauer Spectroscopy in Magnetism. In addition, there were both a special session on the Database and the hot topics session on Iron based superconductors. In the final session on Friday, Prof. S. Campbell made concluding remarks. More details can be found in the proceedings in Hyperfine Interactions.

We promised that the proceedings would be quickly published in Hyperfine Interactions two months after the conference. "Color figures" can be used for the first time not only in the open access version, but also in the final printed version. The organizers were expecting that both the quick publication schedule, i.e. two months after the conference, and the color pages, would be attractive for the participants who considered publishing their research works in the proceedings. The complete publication procedure was performed through a special website provided by Springer, publisher of Hyperfine Interactions. The access to Hyperfine Interactions through this Editorial Manager was triggered by the ICAME 2011. Two months after the conference, most papers are published on-line already.

On behalf of the organizing committee, finally, we would like to express sincere thanks to all the participants and the international committee of the ICAME2011 for coming to Kobe, Japan, despite the fact that the period to visit Japan was not fully appreciated after the disasters triggered by the huge earthquake on 11 March 2011. We could feel always your solidarity and warmness to the Japanese. We hope the ICAME2011_Kobe has created a strong Kizuna (絆) – a strong bond - in our community, which will keep our research fields active and fruitful using Mössbauer spectroscopy.

Finally, I would like to mention that ICAME2011 was kindly sponsored by the Yamada Science Foundation as the 65th Yamada Conference. I sincerely thank the Foundation, especially Prof. J. Kanamori. Furthermore, to change the conference city from Tokyo to Kobe, many warm supports have been provided by the Kobe International Conference Center. During the whole period for the preparation, I had always a feeling that we are warmly supported from the ICAME family and the international programme committee. I am extremely grateful to Profs. Guido Langouche, Denes Nagy, Michael Reissner, Jean-Marc Greneche, Teruya Shinjo, Saburo Nasu and the local organizing committee for their kind support in the organization. This conference was supported by Japan Conference services, and I appreciate their warm and professional support.

31 January 2012

Acknowledgements
Yamada Science Foundations
Meet in Kobe 21
Nakauchi Tsutom Convention Foundation

Technical Presentations
SHIMADZU CORPORATION
APCO
PHOTON Design Corporation
NIKI GLASS CO., LTD
RITVERC GmbH
MIMOS, Univ.Mainz


The 65th Yamada Conference
The 31st
International Conference on the Applications of the Mössbauer Effect
ICAME 2011
25-30 September
Kobe, JAPAN

Hyperfine Interact (2012) 204:7–9
DOI 10.1007/s10751-012-0598-3

Chairs and Committees

Published online: 21 March 2012

Organizing Committee

Yutaka Yoshida, Shizuoka Institute of Science and Technology (Chair)
Tetsuaki Nishida, Kinki Univ. (Co-chair)
Norimichi Kojima, Univ. of Tokyo (Director)
Makoto Seto, Kyoto Univ. (Programme)
Ko Mibu, Nagoya Institute of Technology (Proceedings Editor)
Hisazumi Akai, Osaka Univ.
Yoshio Kobayashi, RIKEN
Motoyuki Matsuo, Univ. of Tokyo
Satoru Nakashima, Hiroshima Univ.
Kiyoshi Nomura, Univ. of Tokyo
Satoshi Tsutsui, JASRI/SPring-8
Yasuhiro Yamada, Tokyo Univ. of Science
Tomoyuki Mochida, Kobe Univ.

Honorary Members

Teruya Shinjo and Saburo Nasu

International Programme Committee

E. E. Alp (USA)
E. M. Baggio Saitovitch (Brazil)
F. Berry (UK)
S. Campbell (Australia)
M. Carbucicchio (Italy)
J. M. Greneche (France)
P. Gutlich (Germany)
G. Langouche (Belgium)
I. S. Lyubutin (Russia)
J. F. Marco (Spain)
M. Miglierini (Slovakia)

Yamada Science Foundation and the Scope of Yamada Conference

Yamada Science Foundation was established in February 1977 in Osaka through the generosity of Mr. Kiro Yamada. Mr. Yamada was President of Rohto Pharmaceutical Company Limited, a well-known manufacturer of medicines in Japan. He recognized that creative, unconstrained, basic research is indispensable for the future welfare and prosperity of mankind and he has been deeply concerned with its promotion. Therefore, funds for this Foundation were donated from his private holdings.

The principal activity of the Yamada Science Foundation is to offer financial assistance to creative research in the basic natural sciences, particularly in interdisciplinary domains that bridge established fields. Projects which promote international cooperation are also favored. By assisting in the exchange of visiting scientists and encouraging international meetings, this Foundation intends to greatly further the progress of science in the global environment.

In this context, Yamada Science Foundation sponsors international Yamada Conferences once or twice a year in Japan. Subjects to be selected by the Foundation should be most timely and stimulating. These conferences are expected to be of the highest international standard so as to significantly foster advances in their respective fields.

Hyperfine Interact (2012) 204:11
DOI 10.1007/s10751-012-0599-2

Welcome address of the President of the Yamada Science Foundation, Professor Emeritus of Osaka University, Prof. Junjiro Kanamori

Published online: 20 March 2012

On behalf of the Yamada Science Foundation, I would like to extend our heartfelt welcome to all participants of the 31st International Conference on the Applications of the Mössbauer Effect (ICME2011). I thank all of you for participating in this conference, overcoming various difficulties caused by the big earthquake of last March. I would like to express also our sincere thanks to Professor Yoshida and other organizers for their extraordinary efforts to prepare and work out this conference.

This conference is supported by the Yamada Science Foundation as the 65th Yamada Conference. I would like to describe briefly the Yamada Science Foundation (YSF), summarizing the outline given in the homepage of the Foundation (http://www.yamadazaidan.jp). The Foundation was established in 1977 with the donation of about 30 million dollars made by late Mr. Kiro Yamada, President of the Rohto Pharmaceutical Company Limited at that time where he worked for more than fifty years. Concerned with the lack of innovative works in Japan's science and technology, he intended to help assist creative basic research in the fields of physics, chemistry and life sciences in Japan. YSF puts emphasis on original and pure science programs by individual scientists that are not always well funded by government and industry. Science has its own intrinsic motivation of development irrespective of whether it is of practical use or not. YSF support is made to promote pure science based on its intrinsic motivation. YSF supports domestic individual research and international conferences and symposia to this purpose. In the selection of support items, an emphasis is laid on interdisciplinary projects. As is described in the objective of this conference, the Mössbauer Spectroscopy is an experimental method which is used in a wide range of research fields of basic sciences, providing with deep insight into the atomistic nature of materials. Thus this conference fits well the objective of the foundation.

Let me introduce myself briefly. I was a professor of theoretical solid state physics at Osaka University from 1965 to 1991 and engaged mainly in the research of magnetism. The Mössbauer effect is naturally one of the subjects which I am interested deeply in. Thus both officially and personally I hope sincerely that this Yamada Conference will become a fruitful event which benefits all participants and will be remembered for a long time. Hoping also that all participants will enjoy the conference and foster friendship, I conclude this welcome address.

Hyperfine Interact (2012) 204:13–45
DOI 10.1007/s10751-012-0570-2

Application of Mössbauer spectroscopy in magnetism

Werner Keune

Published online: 9 February 2012

Abstract An overview is provided on our recent work that applies ^{57}Fe Mössbauer spectroscopy to specific problems in nanomagnetism. ^{57}Fe conversion electron Mössbauer spectroscopy (CEMS) in conjunction with the ^{57}Fe probe layer technique as well as ^{57}Fe nuclear resonant scattering (NRS) were employed for the study of various nanoscale layered systems: (i) metastable fct-Fe; a strongly enhanced hyperfine magnetic field B_{hf} of ∼39 T at 25 K was observed in ultrahigh vacuum (UHV) on uncoated three-monolayers thick epitaxial face-centered tetragonal (fct) ^{57}Fe(110) ultrathin films grown by molecular-beam epitaxy (MBE) on vicinal Pd(110) substrates; this indicates the presence of enhanced Fe local moments, μ_{Fe}, as predicted theoretically; (ii) Fe spin structure; by applying magnetic fields, the Fe spin structure during magnetization reversal in layered (Sm–Co)/Fe exchange spring magnets and in exchange-biased Fe/MnF_2 bilayers was proven to be non-collinear and depth-dependent; (iii) ferromagnet/semiconductor interfaces for electrical spin injection; CEMS was used as a diagnostic tool for the investigation of magnetism at the buried interface of Fe electrical contacts on the clean surface of GaAs(001) and GaAs(001)-based spin light-emitting diodes (spin LED) with in-plane or out-of-plane Fe spin orientation; the measured rather large average hyperfine field of ∼27 T at 295 K and the distribution of hyperfine magnetic fields, $P(B_{hf})$, provide evidence for the absence of magnetically "dead" layers and the existence of relatively large Fe moments ($\mu_{Fe} \sim 1.8\ \mu_B$) at the ferromagnet/semiconductor interface. - Finally, a short outlook is given for potential applications of Mössbauer spectroscopy on topical subjects of nanomagnetism/spintronics.

W. Keune (✉)
Fakultät für Physik, Universität Duisburg-Essen, 47048 Duisburg, Germany
e-mail: wernerkeune@web.de

W. Keune
Max-Planck-Institut für Mikrostrukturphysik, Weinberg 2, 06120 Halle, Deutschland

Keywords Mössbauer spectroscopy · CEMS · Nuclear resonance scattering (NRS) · Magnetism · Interfaces · Thin films · Multilayers · Hyperfine field · Spin structure · Exchange spring magnets · Exchanged bias · Iron/gallium arsenide

1 Introduction

Solid state magnetism is a cooperative phenomenon and results from the interaction of atomic magnetic moments that experience magnetic exchange forces, magneto-crystalline anisotropy forces and magnetic dipolar-field forces [1]. Figure 1 displays a schematic listing of some interesting phenomena of solid state magnetism. These encompass the spatial arrangement of magnetic moments (spin structures, such as, e.g., ferromagnetic (F), antiferromagnetic (AF), spin-density-wave (SDW) or spin-glass-type structures), external-field induced magnetic phase transitions [2] and the temperature dependence of the magnetization M(T) or of the hyperfine magnetic field B_{hf}(T) (where the dimensionality of the magnetic system plays a crucial role in the vicinity of the magnetic ordering temperatures [3, 4], T_C or T_N), spin waves and Stoner excitations in metals, magnetization hysteresis loops (along magnetic easy or hard axes, determining magnetic anisotropy), spin-orbit coupling and spin orientations at surfaces/interfaces, and magnetic domain structures. The latter are of crucial important for technological applications, e.g., in magnetic data storage. Magnetically ordered metals are described by a spin-dependent electronic band structure, which shows two bands, the majority (or "spin-up") band and the minority (or "spin down") band. Both bands are shifted in energy relative to each other by the exchange splitting E_{ex}, leading to different electronic density-of-states ($N_\uparrow$ and $N_\downarrow$) at the Fermi energy E_F and, therefore, to an electronic spin polarization P of conduction electrons at E_F. For bcc Fe, the spin polarization at the Fermi energy is P = 44% [5]. Recently, Heusler compounds with the $L2_1$ crystallographic structure, such as Co_2FeSi, which are potential "half-metallic" ferromagnets with a theoretical spin polarization of 100%, attract high interest because of potential spintronics applications [6].

Two breathtaking discoveries triggered a tremendous upswing of new branches of solid state magnetism, namely nanomagnetism, magnetoelectronics and spintronics [7–11]: the observation of (i) oscillatory interlayer exchange coupling (IEC) by P. Grünberg and coworkers [12], and (ii) giant magnetoresistance (GMR) by A. Fert and coworkers [13] and by P. Grünberg and coworkers [14]. For their findings, A. Fert and P. Grünberg were awarded the Nobel prize in physics in 2007. Figure 2 (top) shows schematically the oscillatory IEC between two ferromagnetic metallic layers separated by a non-magnetic metallic spacer layer [10]. The interlayer exchange-interaction parameter J oscillates as a function of the spacer layer thickness t between ferromagnetic (F) coupling and antiferromagnetic (AF) coupling due to the long-range Ruderman–Kittel–Kasuya–Yoshida (RKKY) interaction mediated by conduction electrons [15]. Figure 2 (bottom) displays the GMR effect: a higher electrical resistance R_{AP} at antiparallel magnetization orientation in the remanent state (at applied field $B_0 = 0$ T) and a lower resistance R_P at parallel orientation at magnetic saturation [10]. The GMR ratio is defined as $(R_{AP} - R_P)/R_P = \Delta R/R_P$. The effect is caused by spin-dependent scattering of conduction electrons at the

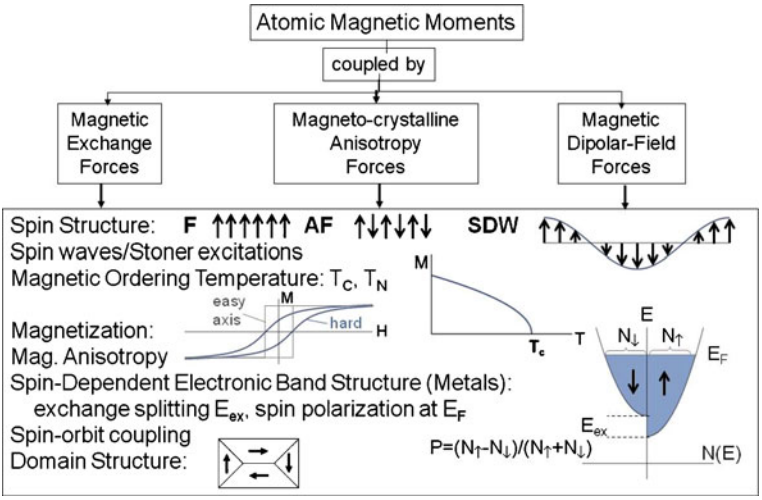

Fig. 1 Schematic representation of some phenomena and topics of interest in solid state magnetism

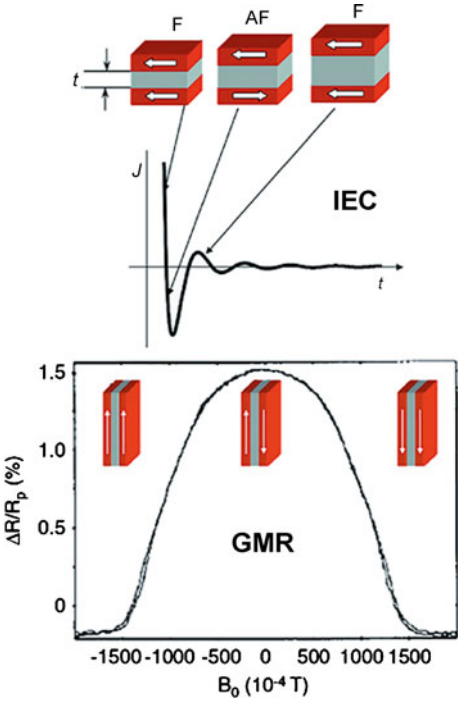

Fig. 2 *Top*: schematics of the indirect oscillatory interlayer exchange coupling J between two ferromagnetic metallic layers separated by a non-magnetic metallic spacer layer of varying thickness t; *bottom*: giant magnetoresistance (GMR) effect $(R_{AP} - R_P)\,R_P = \Delta R/R_p$ versus applied field B_0 (according to Ref. [14]). At remanence, the magnetizations of the two ferromagnetic layers are antiparallel (AP), whereas they are parallel (P) at magnetic saturation. (Adapted from Ref. [10])

Fermi energy [16]. If the non-metallic spacer layer is replaced by an insulating tunnelling layer, one talks about tunnelling magnetoresistance (TMR).

The impact of the Mössbauer effect on solid state magnetism was described in an excellent review article by J. Chappert in 1983 [17]. Since then, applications of

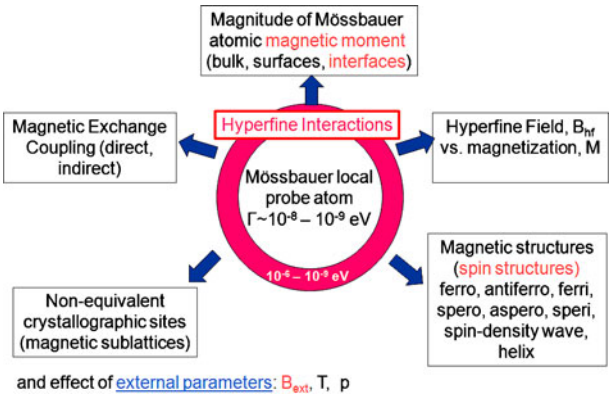

Fig. 3 Schematic representation of some magnetic phenomena that can be studied via magnetic hyperfine interaction by Mössbauer spectroscopy

Mössbauer spectroscopy in magnetism have developed tremendously, partially due to the use of conversion electron Mössbauer spectroscopy (CEMS) for the study of surface/interface magnetism [18–20] and the development of nuclear resonant scattering (NRS) of synchrotron radiation [21]. It is impossible to present a comprehensive review of the impact of Mössbauer spectroscopy on the field of magnetism in a short article. Instead, some representative applications, selected from our own work, will be presented and discussed here.

The Mössbauer nucleus with its nuclear magnetic moment acts as a local probe in the solid. The nuclear and atomic (electronic) magnetic moments are coupled by the magnetic hyperfine interaction (Fig. 3). This means that the nuclear magnetic moment senses a local magnetic field (the hyperfine field B_{hf}) produced by the electrons. The unique feature of the Mössbauer effect is its fantastic energy resolution, which enables to detect the effects of hyperfine interactions on the nuclear energy levels (Fig. 4), which are of the order of 10^{-6} to 10^{-9} eV. The magnitude of the hyperfine field B_{hf} is a rough and indirect measure of the magnitude of the Mössbauer atomic magnetic moment. In this respect, the Mössbauer effect is complementary to other powerful methods, like X-ray magnetic circular dichroism (XMCD) [22], which, however, provides the local atomic magnetic moment directly with high precision, and often enables to distinguish atomic orbital and spin magnetic moments of the electrons. On the other hand, magnetic properties of non-equivalent crystallographic sites (magnetic sublattices) in metallic *alloys*, as revealed by their different hyperfine fields, may be observed by Mössbauer spectroscopy [6, 23, 24], whereas such magnetic sublattices cannot be resolved by XMCD, and only the average atomic magnetic moment is measured by the latter technique [24]. It is well known that the hyperfine field and the Mössbauer isomer shift (chemical shift) both correlate with the chemical charge state of the Mössbauer atom. The best example are high-spin Fe^{2+} and Fe^{3+} valence states, e.g., in magnetite (Fe_3O_4) nanoparticles [25]. X-ray absorption spectroscopy (XAS) is an alternative method, which has been employed successfully to distinguish Fe^{2+} and Fe^{3+} states in Fe_3O_4 nanoparticles even in a liquid matrix (Warland et al., unpublished).

Other important magnetic phenomena that can be investigated by Mössbauer spectroscopy are magnetic exchange coupling (e.g., via modelling the T-dependence of B_{hf}), magnetic moment arrangements (spin structures), and the relation between the hyperfine field and the macroscopic magnetization M. These properties are

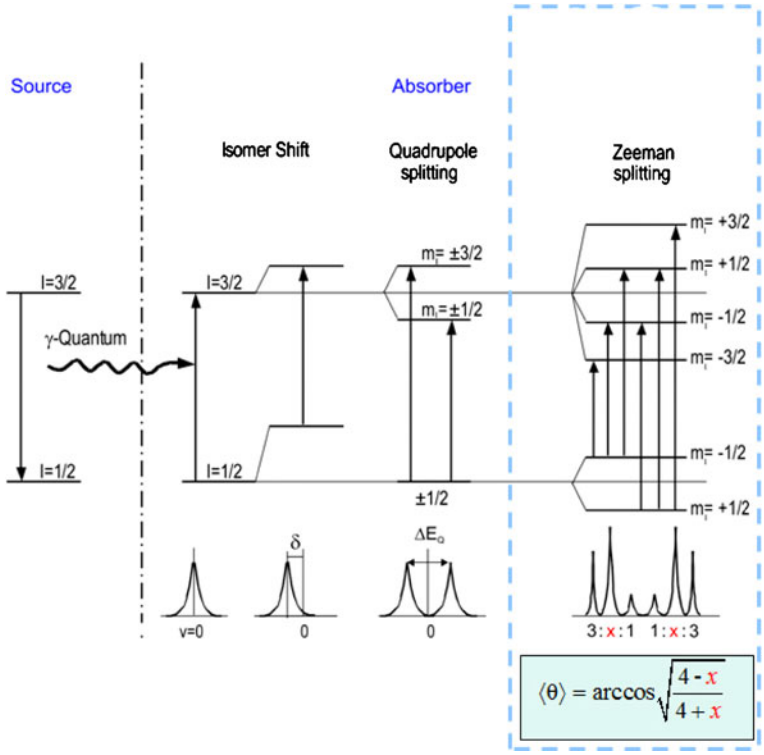

Fig. 4 Effect of different hyperfine interactions (electric monopole, pure electric quadrupole and pure magnetic dipole) on the ^{57}Fe nuclear levels. The relative intensity x (or R_{23}) of lines #2 and 5 of the Zeeman sextet depends on the angle θ between the Fe spin direction (or hyperfine field direction) and the direction of the 14.4-keV γ-ray from the Mössbauer source

often of interest as a function of external parameters (e.g., external field B_{ext}, temperature T or pressure p). For example, the local Fe-selective magnetic hysteresis loop was measured by ^{57}Fe Mössbauer spectroscopy in a strong external magnetic field on nanoscale Fe/Tb multilayers at 5 K, where these samples exhibit hard magnetic properties with a huge coercive field H_c and out-of-plane average Fe spin orientation forming a cone state [26]. The Fe-projected hysteresis loop measured by the Mössbauer effect was found to be remarkably different from the loop obtained by SQUID (superconducting quantum interference device) magnetometry, the latter measuring the macroscopic magnetization of the whole sample [26]. Figure 3 gives a schematic overview of some magnetic phenomena that can be investigated by Mössbauer spectroscopy.

The Mössbauer isotope ^{57}Fe (of ∼2% in natural abundance) has found widespread use in the field of magnetism, although ^{119}Sn is a convenient non-magnetic probe for the study of the transferred hyperfine field arising from spin-polarized conduction electrons, e.g., in Cr/Fe multilayers [27] or in Co_2MnSn Heusler alloy films [28, 29]. Figure 4 displays the well-known nuclear level scheme of ^{57}Fe for the different types of hyperfine interactions. They lead to the isomer shift (due to electric monopole interaction), quadrupole splitting (due to electric quadrupole interaction) and Zeeman

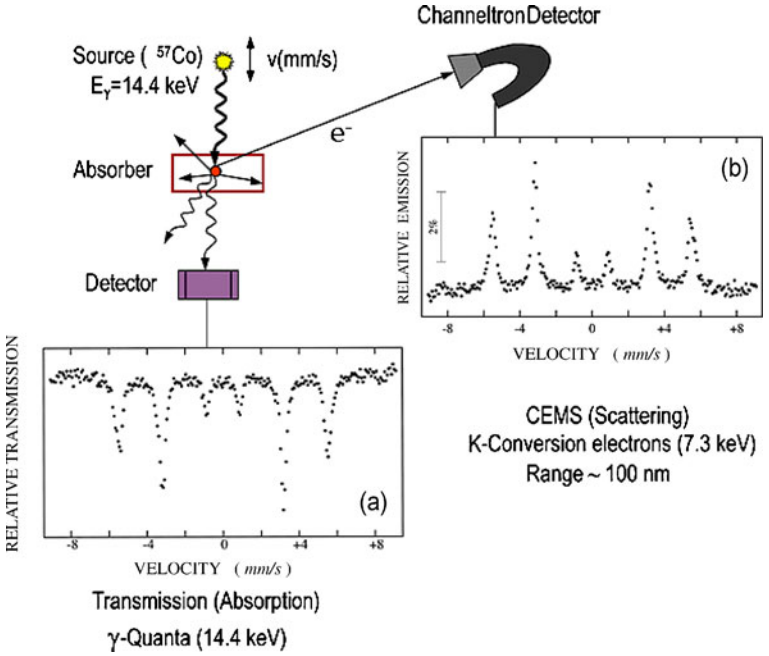

Fig. 5 Schematic setup for ^{57}Fe Mössbauer experiments in **a** transmission geometry or **b** backscattering geometry detecting conversion electrons by use of a channeltron electron detector (CEMS)

splitting (due to Fermi-contact and magnetic dipolar interaction). The latter results in the well-known sextet spectrum, with a line intensity ratio of 3 : x : 1 : 1 : x : 3. From a measurement of the relative line intensity x of the Mössbauer lines number 2 and 5, the average angle $< \theta >$ between the γ-ray direction and the hyperfine-field direction (or Fe spin direction) in the sample can be deduced by use of the expression $< \theta >= \arccos\left[(4-x)/(4+x)\right]^{1/2}$. This gives the possibility to provide information on the arrangement of Fe magnetic moments (Fe spin structure) in the sample, in the bulk and thin films as well as at surfaces and buried interfaces. For bulk bcc Fe, the magnitude of the ^{57}Fe hyperfine field is well-known to be 33.0 T at room temperature (RT) or 33.8 T at 4 K [30]. In some bulk Fe alloys, like Y_xFe_{1-x}, the ratio B_{hf}/μ_{Fe} is practically constant at a value of ~15 T/μ_B [31]. This conversion factor can be used in some cases to estimate the atomic magnetic moment of the Mössbauer atom, μ_{Fe}, from the measured B_{hf} value. This works reasonably well in those cases where the core-polarization contribution, B_{core}, to the total hyperfine magnetic field, B_{hf}, dominates over other contributions, as, for instance, the contribution from spin-polarized conduction electrons, B_{ce}, (spin-polarized by magnetic atoms). As an example, let us consider the chemically ordered quasi-Heusler compound Fe_3Si with the $D0_3$ structure, where two inequivalent Fe lattice sites exist [23, 24]: Fe(D) sites with $B_{hf}(D) = 30.8$ T and Fe(A) sites with $B_{hf}(A) = 20$ T, and corresponding Fe atomic moments of $\mu_{Fe}(D) = 2.2\ \mu_B$ and $\mu_{Fe}(A) = 1.35\ \mu_B$, as determined by magnetic neutron scattering [32]. This results in a ratio of 14.0 T/μ_B for the D site and 14.8 T/μ_B for the A site, i.e., in a deviation of ~6%.

The Mössbauer effect can be measured in transmission or backscattering geometry, as shown schematically in Fig. 5. Mössbauer spectra from surfaces, thin films and multilayers are measured effectively by detection of the 7.3-keV conversion electrons which have a mean escape depth from below the Fe surface of ∼100 nm [33]. For thin-film preparation in ultrahigh vacuum (UHV) and *in situ* CEMS, a channeltron electron detector can be used, and the sample may be studied *in situ* from low temperature to RT or higher [34]. Due to the small angle of acceptance and low detection efficiency of the channeltron, ^{57}Co Mössbauer sources of high activity (of the order of ∼100 mCi or 3.7 GBq) are required for investigations of ultrathin ^{57}Fe films in UHV, occasionally with long measurement times of up to ten days per spectrum.

In the following, selected applications of CEMS and NRS in the field of interface magnetism and thin-film magnetism will be presented.

2 Enhanced hyperfine magnetic field in fct Fe(110) ultrathin films on a vicinal Pd(110) substrate

The structural and hyperfine magnetic properties of epitaxial Fe ultrathin films on the vicinal Pd(110) surface were investigated by means of LEED (low-energy electron diffraction), RHEED (reflection high-energy electron diffraction) and ^{57}Fe CEMS [35].

Earlier experimental work demonstrated that Pd becomes ferromagnetic when in proximity to Fe [36, 37] and carries a magnetic moment [38]. These results were supported by theoretical studies [39, 40]. For interfacial Fe in Fe/Pd multilayers, increased hyperfine fields were discovered by Li et al. [41] using Mössbauer spectroscopy. Cheng et al. [42] measured a strong (14%) enhancement in the magnitude of the hyperfine field, $|B_{hf}|$, of the 2-ML thick interfacial Fe region in magnetron-sputtered Fe/Pd multilayers by extrapolation to low T. By considering only the core polarization of the Fe atomic shell, these authors deduced an Fe atomic moment of 2.8 μ_B from $|B_{hf}|$, being in agreement with theoretical results on Fe/Pd(001) superlattices by Stoeffler et al. [40]. Fe on Pd(001) is the most studied system, experimentally [43, 44] and theoretically [45, 46]. Other substrate orientations, such as Pd(110), have attracted less attention [47].

Our choice of the Fe/vicinal-Pd(110) system was motivated by the fact that the vicinal Pd(110) surface exhibits a large atomic step density and, consequently, shows a strong step-induced in-plane magnetic anisotropy in the Fe overlayer [47]. Knowing that the Fe magnetic moments are oriented in-plane makes the Mössbauer data analysis easier. Furthermore, the induced ferromagnetic moment extends up to ∼5 ML into the (110) surface of Pd [48].

Our experiments were performed in an UHV chamber (base pressure $<6 \times 10^{-11}$ mbar) equipped with facilities for LEED, RHEED, Auger spectroscopy, Ar^+ sputtering for surface cleaning and *in situ* CEMS. The Pd(110) substrate had a vicinal angle of 5°. The ^{57}Fe ultrathin films (of 95.5% isotopic enrichment) were deposited on the clean Pd(110) surface at a substrate temperature of 70°C. The film thickness and deposition rate (0.25 Å/min) were controlled by a calibrated quartz-crystal microbalance. Further details on the sample preparation are given in Ref. [35]. After ^{57}Fe film preparation and LEED/RHEED studies the sample was transferred

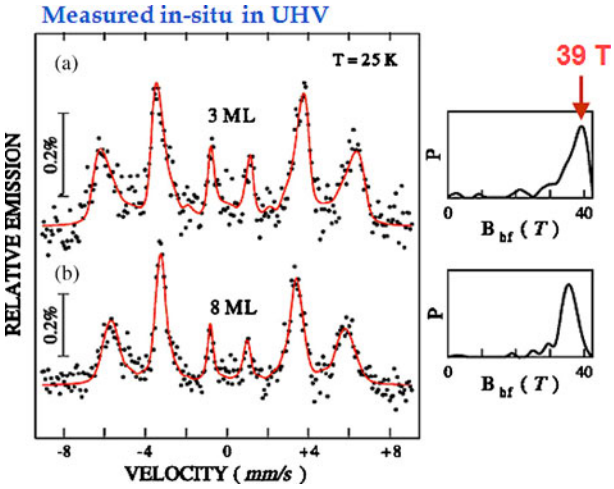

Fig. 6 Mössbauer spectra (CEMS) of **a** 3-ML thick and **b** 8-ML thick epitaxial fct ^{57}Fe(110) ultrathin films on vicinal Pd(110) measured *in situ* in UHV at T = 25 K. The corresponding distribution of hyperfine magnetic fields, $P(B_{hf})$, is shown on the right-hand side. The incident γ-ray was perpendicular to the film surface. (Adapted from Ref. [35])

and fixed in the same UHV system to the cold finger of a liquid-helium flow cryostat. CEMS spectra were taken *in situ* in UHV in zero external field at 25 K (i.e., near thermal magnetic saturation of Fe) using a channeltron electron detector. In order to improve the efficiency of the channeltron, we placed a rectangular-shaped Al tube (with its inner walls coated by a thin MgO film) in front of the channeltron aperture [49]. The MgO layer converts part of the high-energy (7.3 keV) conversion electrons from the sample into low-energy secondary electrons entering the detector. The ^{57}Co(Rh) source of ~40 mCi (or ~1.5 GBq) activity was outside of the UHV system, and the 14.4-keV γ-radiation was transmitted through a UHV-tight Be window in normal incidence to the film plane. LEED and RHEED provided evidence for initial epitaxial (pseudomorphic) ^{57}Fe film growth on Pd(110). The relative in-plane Fe atomic distance (relative to the Pd(110)-substrate atomic distance) perpendicular to the scattering plane has been determined as a function of the ^{57}Fe film thickness from the distance of the RHEED streaks in reciprocal space. This demonstrated the stabilization of the metastable face-centered tetragonal (fct) Fe structure on Pd(110) at small Fe film thickness ($\leq$~3 ML Fe) due to the in-plane Fe lattice expansion by the Pd substrate [35]. This lattice expansion was found to be reduced with increasing Fe film thickness. Tetragonal Fe lattice distortions were previously observed by Boeglin et al. [50] during epitaxial growth of Fe on Pd(001) at RT.

The CEM spectra from epitaxial 3 and 8 ML Fe on vicinal Pd(110) recorded at 25 K are shown in Fig. 6a and b, respectively. The spectra were least-squares fitted with a distribution of hyperfine fields $P(B_{hf})$ (right-hand side in Fig. 6), including a small mean electric-quadrupole nuclear level shift ε [51]. This fitting resulted in the following Mössbauer parameters at 25 K: (i) for 3 ML Fe: average hyperfine field $< B_{hf} >= 34.5 \pm 0.4$T, peak in the $P(B_{hf})$ distribution $B_{hf}^{peak} = 39.2 \pm 0.5$T, $2\varepsilon = -0.09 \pm 0.03$mm/s and average angle $< \theta >= 75° \pm 4°$ (relative to the film normal direction); (ii) for 8ML Fe: $< B_{hf} >= 34.2 \pm 0.4$T, $B_{hf}^{peak} = 35.2 \pm 0.5$T, $2\varepsilon = -0.01 \pm 0.02$mm/s and $< \theta >= 90° \pm 5°$. The $< \theta >$ values indicate a preferred in-plane Fe spin orientation, as expected. The other Mössbauer parameters are significantly

different from those of bulk bcc Fe (also at 25 K : $B_{hf} = 33.8 \pm 0.2$T, $2\varepsilon = 0$mm/s). In both Fe/Pd(110) films, the magnitude of the hyperfine field is clearly enhanced relative to that of bulk bcc Fe. For 3 ML Fe/Pd(110), the value of $B_{hf}^{peak} = 39.2$T is the largest hyperfine field ever observed for Fe films on metallic substrates. The 8-ML Fe/Pd(110) film also exhibits an enhanced hyperfine field (with $B_{hf}^{peak} = 35.2$T), but the enhancement is smaller than that of the 3-ML film.

The electric quadrupole interaction, i.e., the observed nuclear level shift ε, arises from a non-zero electric field gradient (EFG) at the ^{57}Fe nucleus due to an asymmetric (non-spherical) electronic charge distribution around the nucleus. Therefore, the observed (negative) quadrupole level shift 2ε of -0.09 mm/s for the 3-ML Fe/Pd(110) film provides a model-independent proof for a locally non-cubic structure (lattice distortion) of the 3 ML Fe film, in qualitative agreement with our RHEED result [35]. 2ε obtained for the 8 ML Fe film is negligible within error bars, pointing to a much less distorted lattice of this thicker Fe film. One may infer that the change of B_{hf} with changing Fe thickness is the result of the associated structural modification (lattice distortion). This conclusion is supported by the result of Mühlbauer et al. [52], who observed an enhanced Fe atomic moment of 2.7 μ_B by magnetometry, correlated with the fcc Fe structure in polycrystalline Fe/Pd multilayers. A large Fe atomic moment of 2.67 μ_B was also inferred from XMCD measurements on 3 ML Fe/Pd(001) [53].

In this context it is interesting to mention the pioneering depth-selective CEMS studies by Kisters et al. [54], who investigated the interfacial region of Pd-coated epitaxial bcc-Fe(001) film structures using ^{57}Fe probe layers in bcc Fe(001) at different distances from the Pd/bcc-Fe(001) interface. Even at RT B_{hf} was observed to oscillate and to be enhanced to a value of ~37.8 T in the second Fe monolayer below the interface, but approached the bcc-Fe bulk value within 8–10 Fe monolayers. This oscillating behaviour was explained by a superposition of two effects: first, an exponential short-range exchange interaction (mainly due to 3 d–4 d hybridization) within the first three Fe monolayers from the interface, and second an oscillating RKKY-type long-range interaction via conduction electrons in deeper Fe layers. A similar hybridization effect at the fct-Fe/Pd(110) interface may contribute to the strongly enhanced B_{hf} value observed in our work [35].

Is the Fe atomic moment, μ_{Fe}, proportional to the measured hyperfine field B_{hf} at and near the fct-Fe/Pd(110) interface ? In order to address this question we recall that the measured (negative) total hyperfine magnetic field B_{hf} at the ^{57}Fe nucleus in a metal is essentially the sum of several contributions:

$$B_{hf} = B_{int} + B_{dem} = B_{core} + B_{val,core} + B_{val,tr} + B_{dem} = B_{hf,loc} + B_{hf,tr} + B_{dem} \quad (1)$$

The (positive) demagnetizing field B_{dem} is negligible in our case of an in-plane magnetization direction. B_{core} and $B_{val,core}$ are the contributions caused via intra-atomic spin polarization of (1 s, 2 s, 3 s) Fe core electrons and 4 s electrons, respectively, by the local 3 d moment of the Fe Mössbauer atom. $B_{val,tr}$ is the transferred hyperfine field due to inter-atomic polarization of valence 4 s electrons by d electrons of neighboring Fe (and Pd) atoms. According to theory, $B_{hf,loc} = B_{core} + B_{val,core}$ is proportional to the local 3 d moment of Fe [55, 56] ($\mu_{3d} \sim \mu_{Fe}$), whereas $B_{val,tr}$ depends on the degree of hybridization of valence 4 s electrons with d electrons of neighboring atoms surrounding the Mössbauer atom, and on

their magnetic moments. Therefore, $B_{val,tr}$ is of nonlocal nature. For the Pd/bcc-Fe(001) system, assuming ideally flat interfaces, S. Handschuh and S. Blügel (private communication) have obtained the monolayer-resolved ground state Fe magnetic moments, μ_{Fe}, and ^{57}Fe hyperfine fields from ab initio full-potential linearized augmented plane wave (FLAPW) calculations. Within an interfacial region of about four atomic layers (layers S, S-1, S-2 and S-3) μ_{Fe} was found to decrease monotonically from an enhanced value of ~2.75 μ_B (at the Fe "surface" layer S) to ~2.3 μ_B (at subsurface layer S-1) to the bulk value of ~2.12 μ_B (at layer S-3). Simultaneously, the magnitude $|B_{hf}|$ behaves nonmonotonically with depth, exhibiting an enhanced value of ~35.8 T directly at the Pd/bcc-Fe(001) interface (layer S), an even stronger enhancement to ~38.5 T at the first subinterface layer (S-1), followed by a rapid drop to the bulk bcc-Fe value. The computed maximum $|B_{hf}|$ of 38.5 T is in good agreement with our experimental value of $B_{hf}^{peak} = 39.2(5)$ T for 3 ML Fe/Pd(110). The theoretical result (Handschuh and Blügel, private communication) demonstrates that there is no monolayer-resolved proportionality between $|B_{hf}|$ and μ_{Fe}. However, it is remarkable that the theoretical average hyperfine field $<B_{hf}>_{3ML}= 36.2$ T and the theoretical average Fe atomic moment $<\mu_{Fe}>_{3ML}= 2.4\ \mu_B$, both averaged over a 3-ML thick Fe interface region, yield a conversion factor of 15.1 T/μ_B, which agrees surprisingly well with the usual experimental conversion factor of 15 T/μ_B for bulk bcc-Fe alloys [31]. This observation justifies our conclusion that our measured enhanced hyperfine field $<B_{hf}>= 34.5$ T (averaged over our 3-ML-thick fct-Fe film) corresponds to an enhanced average moment of $<\mu_{Fe}>$ of ~2.3 μ_B. These values of $<B_{hf}>= 34.5$ T and $<\mu_{Fe}>= 2.3\ \mu_B$ should be considered as lower limits, because $P(B_{hf})$ in Fig. 6 shows a low-field tail, which reduces $<B_{hf}>$ and which might be caused by a small fraction of thermally rapidly relaxing Fe spins in the ultrathin films even at 25 K. Finally we like to mention that the bcc structure and the fct structure are related via the so-called Bain transformation [57]. A detailed description of the work presented here is given in Ref. [35].

As mentioned above, $<\theta>= 90°$ for the 8-ML film indicates full in-plane Fe spin orientation. On the other hand, $<\theta>= 75°$ for the 3-ML film reveals a small out of plane Fe spin component. We can speculate about the origin of this perpendicular spin component. It could possibly be induced by the tetragonal lattice distortion of the 3-ML Fe film, resulting in an incomplete quenching of the orbital Fe magnetic moment (as compared to complete quenching in cubic symmetry). Then, the small out-of-plane Fe spin component is induced by spin-orbit interaction. The orbital Fe magnetic moment is expected to be also small. The out-of-plane magnetization component induces a small demagnetizing field along the film normal direction. Assuming a full demagnetizing field B_{dem} of 2 T for Fe, its component along the film-normal direction, $B\perp_{dem} = B_{dem}\cos(75°)$, is 0.5 T only, which is much too small to explain in any way the large B_{hf} enhancement observed here for the 3-ML Fe film.

3 The Fe spin structure in layered systems

As mentioned in the introduction and in Fig. 4, the relative intensity of the sextet lines #2 and 5 depends on the angle θ between the Fe-spin direction (or hyperfine field direction) and the direction of the incoming γ-ray. This offers the exciting

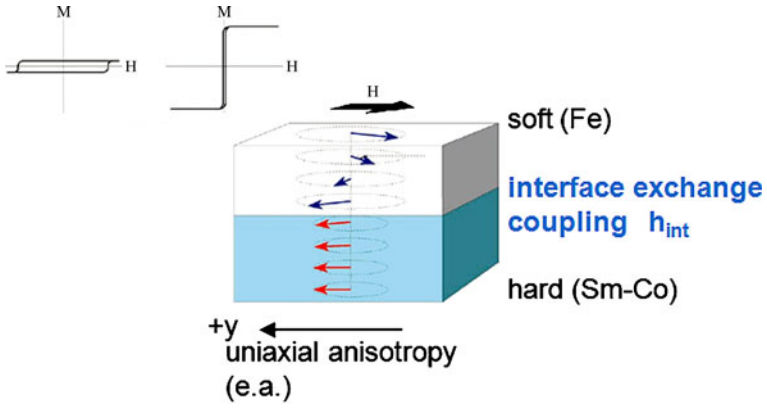

Fig. 7 Schematic representation of a nanoscale exchange-spring magnet, consisting of a magnetically hard ferromagnetic (*bottom*) layer (here: Sm-Co alloy) in contact with a magnetically soft ferromagnetic (*top*) layer (here: bcc Fe). Both layer magnetizations are mutually exchange-coupled at the hard/soft interface. If the soft layer exceeds a certain thickness (the magnetic domain wall thickness), an applied magnetic field H may reversibly induce a helical spin structure in the soft Fe layer during magnetization reversal. (Adapted from Ref. [58])

possibility to determine the Fe spin structure (or Fe spin texture) in the sample by the Mössbauer effect, with or without applying a magnetic field. We have employed ^{57}Fe CEMS with the sample exposed to an in-plane external field H in order to observe changes in the Fe spin structure of layered systems.

3.1 (Sm-Co)/Fe exchange-spring magnets

The first example is the case of a nanoscale (Sm-Co)/Fe exchange spring magnet. The principle of a layered nanoscale exchange spring magnet is illustrated in Fig. 7 [58]. It is a magnetic heterostructure, consisting of a magnetically hard ferromagnetic (bottom) layer (here: Sm-Co alloy) in contact with a magnetically soft ferromagnetic (top) layer (here: bcc Fe). The hard layer is characterized by a low saturation magnetization and a wide hysteresis loop (implying a large coercive field) and possesses a huge in-plane magnetic anisotropy with the easy axis (e.a.) oriented in-plane along the y-axis. The soft layer has a high but narrow hysteresis loop (very small coercive field) and a very small magnetic anisotropy. Both layer magnetizations are mutually exchange coupled at the hard/soft interface, with the interfacial Fe spins strongly pinned to the hard magnet spins. If the soft layer exceeds a certain thickness (the magnetic domain wall thickness, being of the order of a few nanometers), an applied magnetic field H may reversibly induce a helical spin structure in the soft Fe layer. This may occur during magnetization reversal from the magnetically saturated state (originally saturated along the +y-direction) by reversing H along the -y-direction. The resulting helical (sometimes called “twisted”) Fe spin structure resembles the spin configuration in a magnetic domain wall. It can be controlled by an external magnetic field. Such magnetic-field controlled non-collinear spin structures are of relevance in the field of nanomagnetism/spintronics. For example, domain wall motion induced by electrical currents [11, 59] in ferromagnetic nanowires is connected with the movement of non-collinear spin structures along a nanowire.

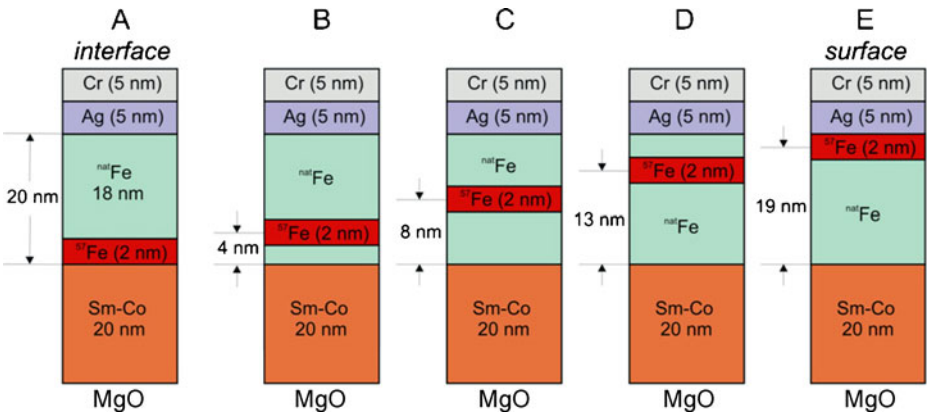

Fig. 8 Schematic representation (cross-sections) of the five different layered (Sm-Co)/Fe exchange-spring samples studied by CEMS. The total thickness of the Sm-Co layer and the Fe layer is 20 nm each. 2-nm thick ^{57}Fe probe layers are placed at different distances d from the (Sm-Co)/Fe interface in the Fe layers. Sample A (interface sample): directly at the interface, d = 1 nm; sample B: d = 4 nm; sample C: d = 8 nm; sample D: d = 13 nm; and sample E (surface sample): d = 19 nm [65]

In the future, this effect may lead to a new type of magnetic memory ("racetrack memory" [11]).

Although ^{57}Fe nuclear resonant scattering [60, 61] and CEMS [62] have been used in the past to elucidate the helical spin structure in exchange spring systems, its determination at the atomic scale is still a challenging problem. For example, in Ref. [62] it was assumed in the model used that the pitch of the Fe spin helix is uniform along the film normal direction, which, very likely, is only a rough approximation. Here, the results of CEMS measurements on (Sm-Co)/Fe bilayers performed at RT in an in-plane external magnetic field will be described. Thin ^{57}Fe probe layers were placed in the Fe layer at different distances from the (Sm-Co)/Fe interface to obtain site-selective (isotope-selective) data during the magnetization reversal process.

Five different (Sm-Co)/Fe bilayer samples with in-plane uniaxial magnetic anisotropy were prepared using dc magnetron sputtering. Details of the preparation are described in Refs. [63] and [64]. Epitaxial Sm-Co layers (20 nm thick) with a nominal composition of Sm_2Co_7 were grown at 600°C on MgO(110) substrates with an epitaxial Cr(211) buffer layer. The epitaxial relationship for the magnetically hard (Sm-Co)(1–100) layer is (Sm-Co)[0001]//Cr[01-1]//MgO[001]. This induces a uniaxial in-plane easy axis parallel to the (in-plane) hexagonal Sm-Co c-axis. In all samples the polycrystalline bcc Fe layer (20 nm in total thickness, of 2.14% in natural isotopic ^{57}Fe abundance) was deposited onto the Sm-Co layer by sputtering at a substrate temperature T_s of 300–400°C. The Fe layer was coated by 5 nm of Ag followed by 5 nm of Cr for protection. Within every Fe layer, a 2-nm thick isotopically enriched ^{57}Fe probe layer (enriched to 95% in ^{57}Fe) was placed by sputter deposition at different distances from the hard/soft interface in order to probe the depth-dependence of the Fe spin structure. This resulted in five different samples labeled samples A (interface sample), B, C, D and E (surface sample) (Fig. 8). The macroscopic magnetic properties of the samples at RT were measured by alternating-gradient magnetometry (AGM). The hysteresis loop shapes observed (not shown)

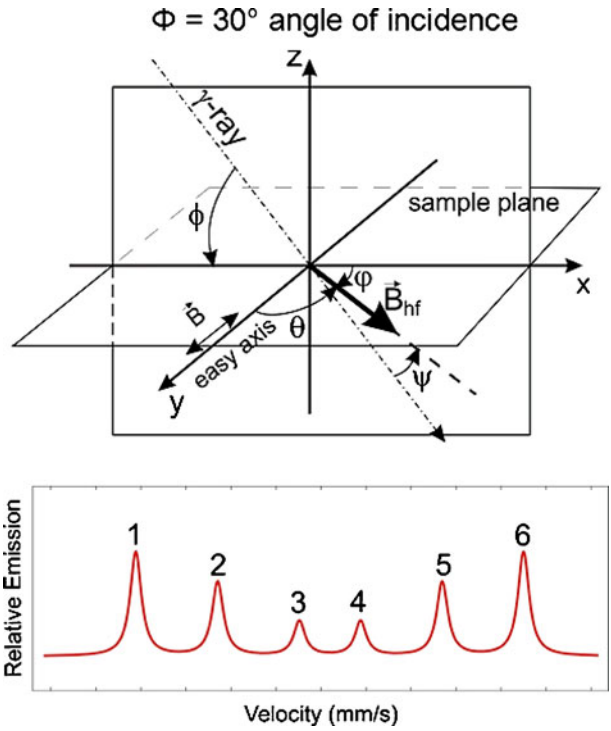

Fig. 9 *Top*: schematic geometrical arrangement of the CEMS measurement at inclined incidence of the γ-ray relative to the sample plane (xy plane). The angle of incidence is $\Phi = 30°$. The external magnetic field H is applied along the Sm-Co easy-axis direction (the y axis). The hyperfine field B_{hf} and Fe atomic magnetic moment μ_{Fe} lie in the sample plane. Ψ is the angle between the γ-ray direction and the direction of B_{hf}. (The angle Ψ is identical to the angle θ in Section 1 and in Fig. 4). The x axis is defined by the projection of the γ-ray direction onto the sample plane. *Bottom*: schematic Zeeman sextet of ^{57}Fe with numbers labelling the six Mössbauer lines

displayed a double step typical for layered exchange-spring magnetic systems [66–68]. Separate switching transitions were observed for the soft Fe and hard Sm-Co layers upon magnetization reversal. As expected, the shape of the hysteresis loops was found to be similar for all five samples in the low- and medium-field range (~ -350 mT $\leq \mu_0 H \leq \sim +350$ mT), where the Fe magnetization reverses, since chemically and magnetically the Fe layers have the same total thickness of 20 nm in all samples.

For detection of conversion electrons, each sample was mounted inside of a small self-built He-4% CH_4 proportional counter. The counter was placed between the poles of an electromagnet with its field H oriented in the sample plane along the easy axis direction (y-direction) of the magnetically hard Sm-Co film. The Fe spin configuration in the ^{57}Fe probe layers during the magnetization reversal process was studied at RT by CEMS in decreasing magnetic fields H, ranging from +1150 mT (+y direction, start) to −1150 mT (−y direction, stop). If the direction of the hyperfine magnetic field at the ^{57}Fe nucleus B_{hf} (which is antiparallel to the direction of the Fe atomic moment, μ_{Fe}) forms an angle Ψ with the incident Mössbauer γ-ray direction (Fig. 9), then the intensity ratio $R_{23} = I_2/I_3 = I_5/I_4$ of lines #2 and 3 (or lines #5 and 4) is given by [69, 70] $R_{23} = 4\left\langle \sin^2(\Psi) \right\rangle / \left[1 + \left\langle \cos^2(\Psi) \right\rangle\right]$, where the brackets <...> indicate averaging over the angular Fe spin distribution in the sample. (The angle Ψ used here is identical to the angle θ used in Section 1 and in Fig. 4). For the case of in-plane distributed Fe magnetic moments and perpendicular γ-ray incidence, i.e., for $\Psi = \Phi = 90°$ in Fig. 9, the intensity ratio is $R_{23} = 4$ and is insensitive to the in-plane

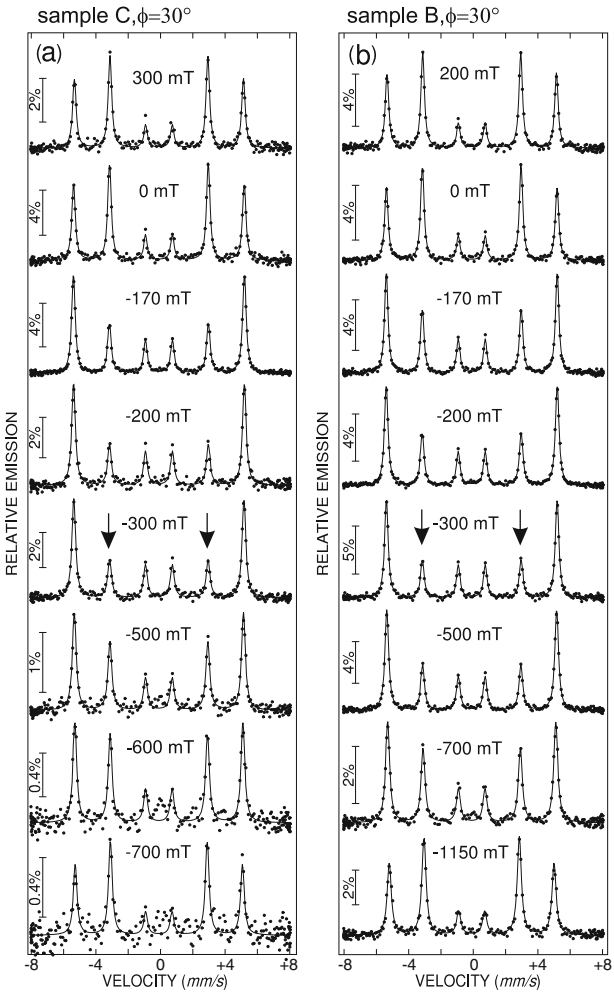

Fig. 10 RT CEM spectra of **a** sample C and **b** sample B, taken at inclined incidence of the γ-radiation (at $\Phi = 30°$) and in different in-plane magnetic fields $\mu_0 H$ applied along the easy axis direction of the Sm-Co film (along the y direction). For each sample, the sequence of measurements started with the highest (positive) field and finished with the lowest (negative) field. The least-squares fitted curves are explained in the text (Khrenov 2005, unpublished)

spin direction. (This is valid for unpolarized γ-radiation and is applicable here, since we use a ~50 mCi unpolarized ^{57}Co(Rh) source in our experiments). Therefore, the in-plane Fe spin configuration in our sample can be studied only at inclined incidence of the γ-radiation. In our present experiments we have chosen $\Phi = 30° \pm 5°$ as the angle of incidence. From the equation above, the model-independent average quantity

$$\left\langle \cos^2(\Psi) \right\rangle = (4 - R_{23}) / (4 + R_{23}) \tag{2}$$

that characterizes the angular distribution of the Fe spins can be obtained from a measurement of the intensity ratio R_{23}.

Typical RT CEM spectra taken under $\Phi = 30°$ and in different applied fields are shown in Fig. 10a and b for sample C and B respectively. The spectra of the other samples (not shown) are of similar quality. For every sample the spectra were measured in the sequence from the highest (positive) field to the lowest (negative)

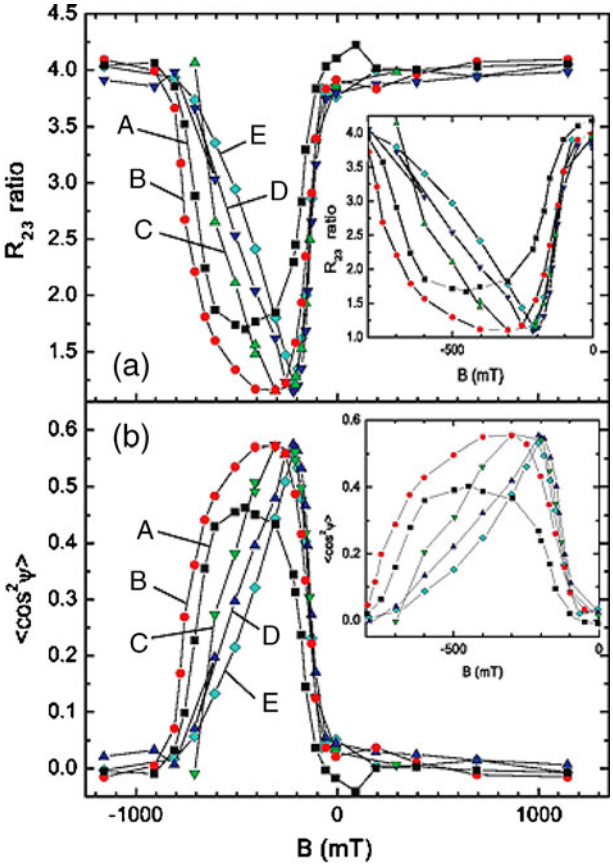

Fig. 11 **a** Measured Mössbauer line intensity ratio R_{23} versus the external field $\mu_0 H = B$ applied along the easy axis direction and following the decreasing field branch of the hysteresis loop, obtained from least-squares fitting of the CEM spectra of samples A to E. *Black squares*: sample A(interface); *red circles*: sample B; *green triangles tip up*: sample C; *dark-blue triangles tip down*: sample D; *light-blue diamonds*: sample E (surface). Insert: zoom of the *left curves*. **b** The model independent average angular quantity $<\cos^2(\Psi)>$ versus the external field $\mu_0 H = B$ obtained from **a**. Symbols in the same color as in **a** are used in **b**. Insert: zoom of the *left curves*. (The lines are a guide for the eye) (Khrenov 2005, unpublished)

field, as indicated in Fig. 10. All spectra in Fig. 10 are simple Zeeman sextets typical for α-Fe, as expected for the ^{57}Fe probe layers sandwiched with natural α-Fe layers on both sides. These spectra were least-squares fitted by one sextet with narrow Lorentzian lines using the program NORMOS by Brand [71]. The magnitude of the hyperfine field B_{hf} obtained for the spectra at remanence (i.e., at $\mu_0 H = 0$ T) is in good agreement with the value of 33.0 T of bulk α-Fe at RT. Obviously, our Fe films consist of the α-Fe phase, as expected. The interesting effect in Fig. 10 is the systematic intensity variation of the lines #2 and 5 (marked by arrows) versus the applied field H. This observation is an atomistic manifestation of the Fe spin reversal process.

The measured line intensity ratio R_{23} and the corresponding angular quantity $<\cos^2(\Psi)>$ versus the in-plane external field $\mu_0 H$ is shown in Fig. 11a and b, respectively, for samples A to E. At magnetic saturation, i.e., for the strongest positive (+1150 mT) and negative (−1150 mT) fields, $R_{23} \sim 4$ and $<\cos^2(\Psi)> \sim 0$, indicating that, for all samples, all the Fe spins point along the applied field direction (along the +y or −y direction, respectively), forming an angle $\Psi = 90°$ with the incident γ-ray. Moreover, the data in Fig. 11 show a nonmonotonic behaviour, i.e., for all samples they show a minimum in $R_{23}(H)$ at (R_{min}, $\mu_0 H_{min}$) and a maximum

in $<\cos^2(\Psi)>$ versus $\mu_0 H$. When R_{min} (or the maximum, $<\cos^2(\Psi)>_{max}$) is reached at $\mu_0 H_{min}$, the Fe spins in the ^{57}Fe probe layer have acquired such a particular in-plane angular spin distribution or Fe spin texture that, in the average, they have a maximum component along the direction of the in-plane projection of the incoming γ-ray, i.e., along the x axis (Fig. 9). This is that particular field where the average Fe spin direction reverses its y-component from positive to negative.

The striking effect in Fig. 11 is that the H-dependences of R_{23} and of $<\cos^2(\Psi)>$ have a different functional behaviour for the different samples A to E, which is a manifestation of the depth-dependence of the Fe spin structure. For example, for sample E (where the ^{57}Fe probe layer is at the "surface" of the natural Fe layer) the field $\mu_0 H_{min}$ is at a smaller negative $\mu_0 H$ value than for the interface-sample A (where the probe layer is directly at the hard/soft interface). This tells us that, upon increasing the negative field, the "surface" Fe spins (sample E) switch first, and the interface Fe spins (sample A) switch later due to the stronger coupling of interface Fe spins with the spins of the hard layer. It is also interesting to see that the value of R_{min} (and also of $<\cos^2(\Psi)>_{max}$) is different for the interface sample A (with $R_{min} = 1.7$) and for the off-interface samples B - E (with $R_{min} = 1.2$). This proves that the Fe spin texture upon switching is different for the interface and off-interface samples. It turns out that the depth-dependent Fe spin structure in these samples is rather complex. Presently, efforts are undertaken to determine the Fe spin structure in our samples by simulations using the electronic band-structure theory by Uzdin and Vega [72, 73] with a minimum of assumptions.

3.2 Exchange-biased Fe/MnF_2 bilayers

Exchange coupling at the interface between films of a ferromagnet (F) and an antiferromagnet (AF) is often manifested by a center shift of the magnetic hysteresis loop away from the zero-field axis [74]. This is called the exchange-bias (EB) effect. It is generally conceived that the EB effect originates from the exchange interaction of interfacial F spins and a fraction of interfacial AF spins that are rigidly frozen after field cooling (or after cooling in the remanent state) from a temperature $T > T_N$ (T_N = Néel temperature) to a sufficiently low temperature $T < T_N$. In a simplified picture, if the EB state is induced, for instance, by a positive cooling field, an excess negative applied field is required upon magnetization reversal in order to overcome the pinning of F spins by the interfacial exchange coupling to the frozen AF spins. This then leads to a hysteresis loop shifted towards negative applied fields.

An example of a shifted hysteresis loop is shown in Fig. 12 for an exchange-biased Fe/$FeSn_2$(001) bilayer, measured by SQUID (superconducting quantum interference device) magnetometry at T = 10 K after cooling the sample in a field of 0.5 T [75]. The sample was essentially a Fe/$FeSn_2$(001) bilayer on a clean InSb(001) substrate, where Fe is the F layer and $FeSn_2$ is the AF layer (T_N = 378 K). The exact sample composition was

$$\mathrm{Sn(2nm)/Fe(6nm)/^{57}FeSn_2(5nm)/FeSn_2(15nm)/InSb(001)},$$

with the sample coated by 2 nm of Sn for protection. The $FeSn_2$(001) film was epitaxially grown in UHV at $T_s = 150°C$ by co-deposition of natural Fe and Sn, followed by $^{57}FeSn_2$(001) (95% enriched in ^{57}Fe). The subsequent polycrystalline natural Fe film and the Sn film (coating) were grown at RT. Details of Fe/$FeSn_2$

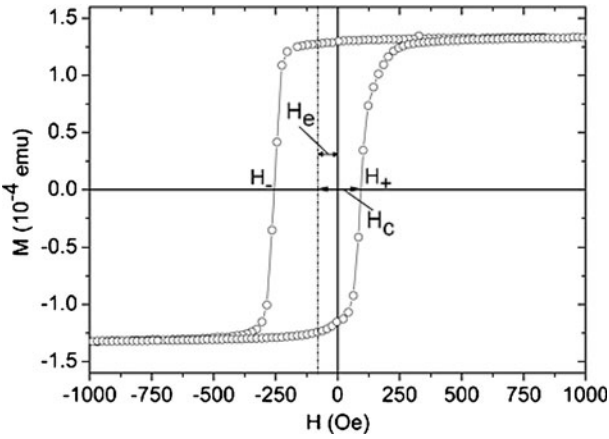

Fig. 12 Magnetic hysteresis loop of an exchange-biased $Fe/FeSn_2(001)$ bilayer measured at 10 K after cooling in a field of $\mu_0 H = 0.5$ T. The center of the loop shows a shift by $H_e = -82$ Oe relative to the vertical $H = 0$ axis. H_e is the exchange-bias field. The cooling field and the measurement field were oriented in the film plane along the [108] direction of the epitaxial $FeSn_2(001)$ film [75]

sample preparation are described elsewhere [76–78]. After field-cooling, the center of the hysteresis loop in Fig. 12 shows a clear shift by $H_e = -82$ Oe towards negative fields. The exchange field H_e is a measure of the exchange coupling at the F/AF interface.

The EB effect has found important applications in spin-valve-type devices [79]. Although the EB effect has led to great technological advancement and intense research efforts, investigation of the magnetic structure at the F/AF interface and its depth dependence perpendicular to the film plane (z direction) is a challenging task. For example, some theoretical models predict a helical AF spin structure along the z direction in the F/AF interfacial region upon magnetization reversal [80–82]. Non-collinear spin structures in the F layer (partial domain walls) near the F/AF interface were also theoretically predicted [83, 84] and rarely investigated experimentally [85]. Earlier CEMS studies using ^{57}Fe probe layers at different depths in the Fe layer of exchange-biased Fe/MnF_2 bilayers did not reveal a depth-dependent Fe spin structure in Fe [86, 87]. However, these CEMS measurements were performed at remanence due to the difficulties with electron detection in strong applied fields.

A particular promising technique for the direct measurement of Fe spin structures at surfaces and buried interfaces at low T and in strong external fields is ^{57}Fe nuclear resonant scattering (NRS) of synchrotron radiation, in combination with ^{57}Fe probe layers (a few Ångstroms thick). Using this technique, the depth-dependent Fe spin rotation upon magnetization reversal was measured in exchange-coupled $Fe/MnF_2(110)$ bilayers with an ^{57}Fe probe layer placed at different depths within an ^{56}Fe film (depleted in ^{57}Fe) [88]. MnF_2 is an AF with $T_N = 67$ K. Kiwi et al. [84] proposed a model for exchange-biased $Fe/FeF_2(110)$, where the AF FeF_2 is isostructural with MnF_2. This model predicted that upon magnetization reversal by an applied field, EB energy is reversibly stored in the Fe layer like in an exchange-spring magnet, forming an incomplete magnetic domain wall in the Fe layer [84]. As a consequence of the interfacial F/AF exchange coupling strength $J_{F/AF}$ (being the only adjustable parameter in the calculations), two features in the calculated M-versus-H plot (Fig. 13b) can be noticed: a negative EB field H_e and an asymmetric shape of the M-versus-H plot, marked by "offset" in Fig. 13b. Both features have been confirmed experimentally for Fe/MnF_2, as will be shown below.

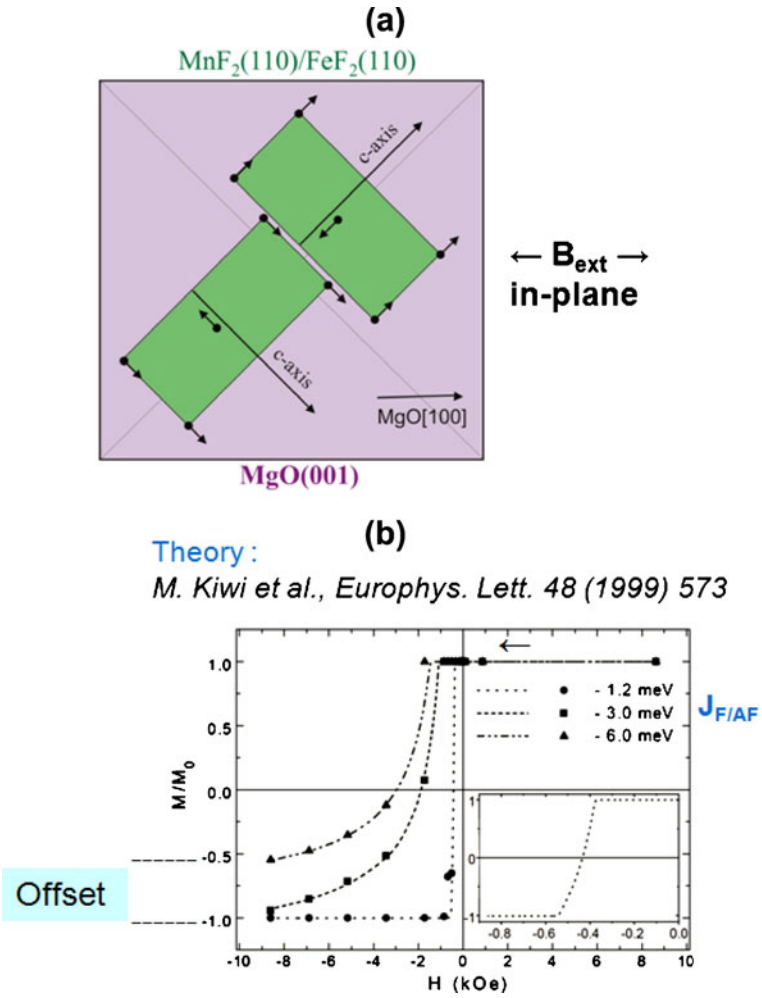

Fig. 13 **a** schematic representation of the AF spin structure in crystallographically twinned $MnF_2(110)$ and $FeF_2(110)$ thin films; the AF easy axes (c axes) are at ±45° relative to the MgO[98] direction (or x axis), along which the magnetic field H and the x-ray beam were aligned. **b** Magnetization M versus applied field H upon magnetization reversal in the exchange-biased state of a Fe/FeF_2 bilayer, computed by Kiwi et al. [84] as a function of the interfacial exchange coupling strength $J_{F/AF}$. The exchange-bias field H_e and the asymmetric shape of the plot depend strongly on $J_{F/AF}$. The asymmetric shape (indicated by "offset") is due to the formation of a non-collinear spin structure (an incomplete domain wall) in the Fe layer. Insert: zoom of the stepped curve near H = 0 kOe. (Adapted from Ref. [84])

The Fe/MnF_2(110) sample structure is shown in Fig. 14a. First an epitaxial 52-nm-thick MnF_2(110) layer was grown by MBE on a MgO(001) substrate carrying a 16-nm-thick ZnF_2(110) buffer layer. The MnF_2 film grows as a (110)-oriented pseudo-twinned quasiepitaxial layer (Fig. 13a) and exhibits a nominally "compensated" AF surface with the Mn spins in the surface plane. Figure 13a also illustrates that the AF easy axes directions (or c-axes directions) of the MnF_2(110) twin domains

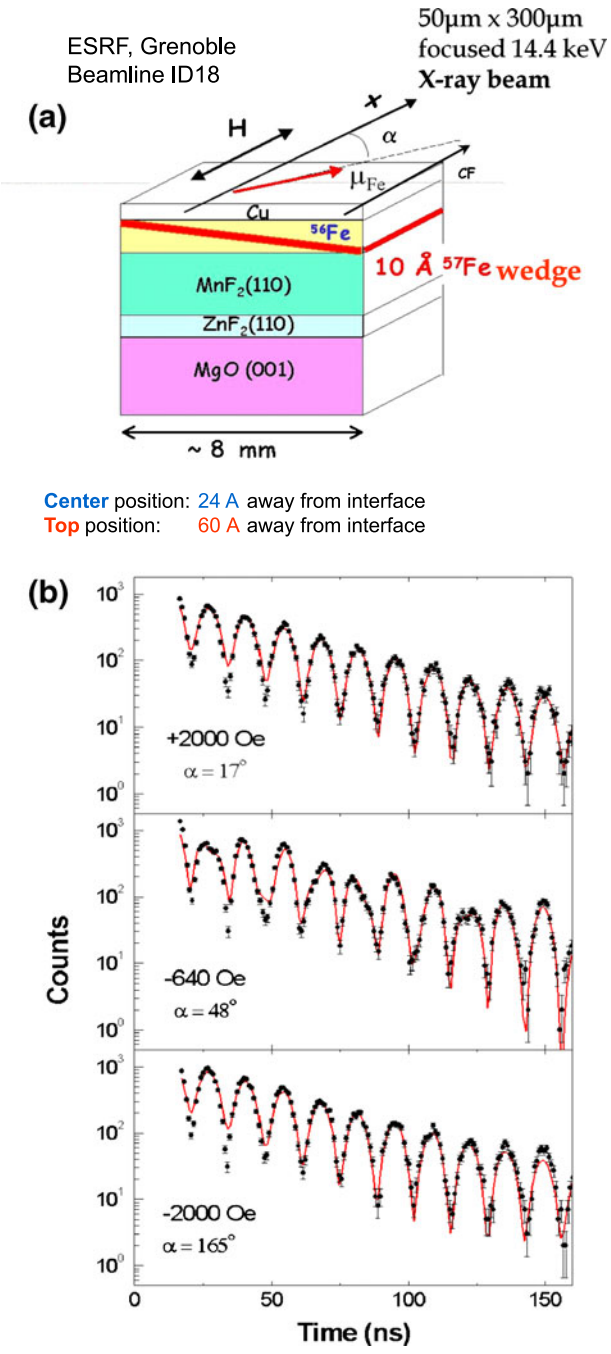

Fig. 14 **a** Schematic diagram of the wedge sample and the NRS experimental geometry: the incident x-ray beam, reflected at an angle of 4 mrad relative to the surface, is oriented along the x direction (the MgO[98] direction), together with the applied field H; (all the arrows are in the sample plane). **b** Typical NRS time spectra measured at 10 K in decreasing magnetic fields, with the x-ray beam probing the ^{57}Fe center position of the wedge. The red solid lines are least-squares fits to the experimental data. α is the angle between the in-plane Fe spin direction and the +x direction (Adapted from Ref. [88])

are oriented at ±45° with respect to the (horizontal) MgO [98] direction (or x axis direction), along which the in-plane magnetic field $B_{ext} = \mu_0 H$ was applied. The 1-nm-thick ^{57}Fe probe layer (95.5% enriched) was inserted diagonally, i.e., between

two inverted wedge-shaped ^{56}Fe layers (depleted in ^{57}Fe), providing a polycrystalline Fe layer of 7 nm in total thickness. The sample was capped by 4 nm of Cu.

The NRS experiments were performed at beamline ID18 of the European Synchrotron Radiation Facility (ESRF) in Grenoble, France. The photon beam, at grazing incidence of 4 mrad, was oriented along the MgO [001] direction (or x direction, Fig. 14a) and parallel to the applied field. The experimental arrangement (cryomagnet cryostat) allowed the precise scanning of the photon beam (of 50 μm × 300 μm cross section) over the sample surface. This provides the depth selectivity along the wedge with the ^{57}Fe probe layer at different distances from the F/AF interface. Two beam positions were selected for the NRS measurements: the "center position (2.4 nm away from the F/AF interface) and the "top" position (6.0 nm away from the interface).

In NRS, the time response of the forward scattered intensity reflected from the ultrathin ^{57}Fe probe layer is measured. Some typical time spectra, when the photon beam hits the center position of the wedge, are shown in Fig. 14b. Spectra of similar quality were obtained with the beam at the top position of the wedge. The spectra were taken at 10 K along the decreasing-field branch of the hysteresis loop after field cooling from 150 K in a field of 2 kOe. The measured data were least-squares fitted using the CONUSS program [89] (red solid lines in Fig. 14b). The orientation of the in-plane Fe magnetic moments, μ_{Fe}, with respect to the incident photon-beam direction (x axis), characterized by the in-plane angle α, was determined from the fittings. This provides similar information as obtained from the line intensity ratio R_{23} in conventional Mössbauer spectroscopy, but with higher angular accuracy. A hyperfine field of $B_{hf} = 34.1 \pm 0.2$ T at 10 K was obtained for all time spectra at the center and top positions in the entire external field range. Within error bars, this is the expected B_{hf} value for bcc Fe at 10 K. Under the assumption of a unidirectional collinear Fe spin structure within the thin ^{57}Fe probe layer depth sensed by the photon beam, the in-plane angle α was determined as a function of the applied field H. Since NRS of the linearly polarized x-rays used here are unable to distinguish μ_{Fe} components along positive (along + x) or negative (along −x) H directions, respectively, the sign of the SQUID magnetization loop (not shown) was used to determine the magnetization reversal points from the +x to the −x direction.

Following this procedure, a NRS angular hysteresis loop with α versus H can be deduced from the measured data. Figure 15a shows the full 10-K angular hysteresis loop for the ^{57}Fe "center" position of the wedge (2.4 nm away from the interface, full blue circles) and the 10-K descending field branch for the ^{57}Fe "top" position of the wedge (6.0 nm away from the interface, full red squares). For the top position, we notice that the (in-plane) ^{57}Fe spins first rotate continuously and only weakly from full alignment ($\alpha = 0°$) along H = +2000 Oe to an off-field direction with $\alpha = 42°$, and subsequently "jump" unexpectedly to $\alpha = 138°$ followed by a gradual rotation to $\alpha = 180°$ (full alignment) at H = −2000 Oe. The corresponding model Fe spin configuration within the top ^{57}Fe probe layer (angle α) and the directional spin "jump" are sketched in Fig. 15b (based also on earlier CEMS studies on similar samples [86]). Similarly, a jump of the ^{57}Fe spin direction is observed during the descending-field branch as well as during the increasing-field branch for the ^{57}Fe center position (full blue circles, Fig. 15a). It is remarkable that NRS was able to identify the α values between which the ^{57}Fe atomic magnetic moments, μ_{Fe}, jump upon magnetization reversal ! It is striking that the α values observed near the

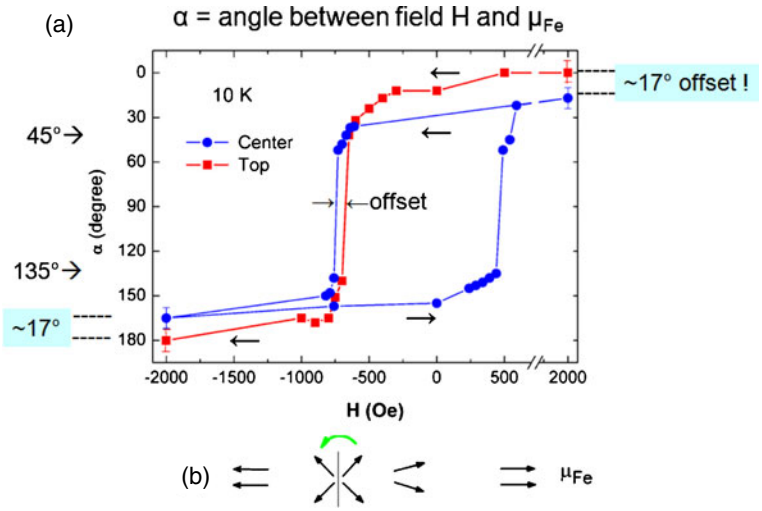

Fig. 15 *Top*: NRS angular hysteresis loop of α versus H measured at 10 K at the ^{57}Fe center position of the wedge (2.4 nm away from the Fe/MnF_2 interface, *blue full circles*) and the descending-field branch of α versus H (at 10 K) at the ^{57}Fe *top position* of the wedge (6.0 nm away from the Fe/MnF_2 interface, *red full squares*). The *center* and *top* data were measured in two independent NRS runs after field-cooling in +2000 Oe from 150 to 10 K. The error bars of α near the reversal are $\pm 3°$. *Bottom* or **b**: Schematical model of the Fe spin configuration within the *top* ^{57}Fe probe layer, indicating the directional Fe spin "jump" from $\alpha = 45°$ to $\alpha = 135°$ upon magnetization reversal. (Adapted from Ref. [88])

magnetization reversals are close to the AF easy axes directions (45° and 135°) of the MnF_2 twin domains (Fig. 13a). Thus, the jumps occur from one of the twinned MnF_2 easy axis ($\pm 45°$) to the other ($\pm 135°$). This is the result of the strong interfacial exchange coupling, enforcing the Fe spin directions along (or maybe perpendicular to) the AF easy axes. The Fe spins revers by jumps of $\Delta\alpha = 90°$, indicating an angular instability range for the Fe spins exchange coupled to Mn spins of the twinned MnF_2 domains. This is also a direct observation of the four-fold magnetic anisotropy induced by the exchange interaction between the Fe and MnF_2(110) layers.

Figure 15a provides a proof of depth-dependent magnetization reversal at 10 K. This manufests itself in two features: (i) The top-position ^{57}Fe spins of the wedge (6.0 nm away from the F/AF interface) revert earlier (by ~40 Oe) than the ^{57}Fe spins at the center position of the wedge (2.4 nm away from the interface), implying stronger pinning of Fe spins closer to the exchange-biased Fe/MnF_2 interface and, consequently, a depth-dependence of the induced four-fold magnetic anisotropy; (ii) at H = +2000 Oe, the top-position ^{57}Fe spins are fully aligned along the field H ($\alpha = 0°$), whereas the ^{57}Fe spins at the center position are misaligned with respect to the H direction by $\delta\alpha \sim 17°$ (offset). The same tendency is observed at H = −2000 Oe. Thus, the reversal and the saturation are easier to achieve at 6.0 nm that at 2.4 nm from the F/AF interface. Both observations imply that the Fe spin rotation in an exchange-biased system occurs like in a spring magnet, forming a non-collinear spin structure (or partial domain wall), as predicted by Kiwi et al. [84] (Fig. 13b). A more detailed presentation of the work described here can be found in Ref. [88].

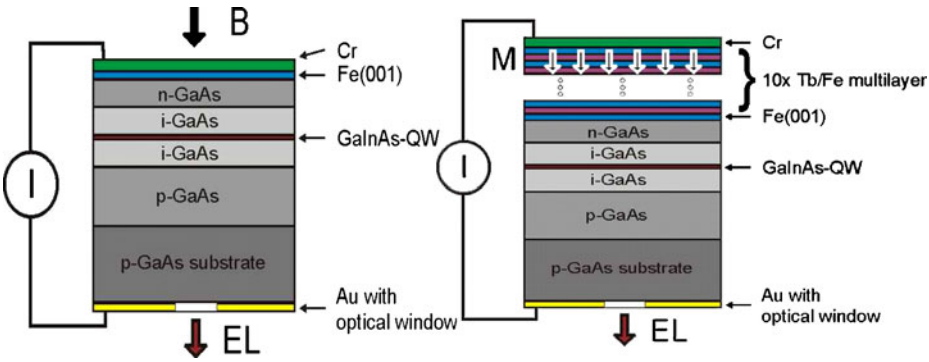

Fig. 16 *Left*: Schematic sketch of the structure of a spin LED with an epitaxial ferromagnetic Fe(001) electrical contact on top and a Au contact at the bottom. The *vertical direction* of the strong magnetic field B and the circular-polarized electroluminescent light (EL) is also indicated. The EL light is emitted from the GaInAs quantum-well after recombination of spin-polarized electrons and unpolarized holes. *Right*: Same as on left-hand side, but with a Tb/Fe multilayer-contact with perpendicular (*vertical*) magnetization at remanence (at B = 0 T) on top. (Adapted from Ref. [97])

4 Ferromagnet/semiconductor heterostructures: Fe on GaAs(001)

Fe/GaAs-based hybrid systems are interesting candidates among metallic ferromagnet (F)/semiconductor (SC) heterostructures that open possible future spintronics applications [90–93], including electrical electron spin injection into the semiconductor [94–98]. A new branch of spintronics, so-called spin-optoelectronics, is developing rapidly [93, 99, 100]. Detection of electrical spin injection into semiconductors has been achieved by exploiting the circular polarization of the electroluminescence (EL) light (of wavelength 855 nm) that is emitted from so-called spin light-emitting diodes (spin LEDs), which are GaAs-based semiconductor heterostructures carrying an electrical ferromagnetic thin-film metal contact (e.g., an epitaxial Fe(001) thin film, the top electrode in Fig. 16 (left)). The EL circular-polarized light is emitted after applying a bias voltage between the top (e.g., Fe) electrode and the bottom (e.g., Au) electrode. The spin-polarized electrons are injected from the ferromagnetic (top) electrode into the semiconductor and move to the quantum-well (QW) of the LED, where they recombine with unpolarized holes under EL light emission [97]. The condition for purely circular-polarized light emission is that the spins of the injected electrons are perpendicular to the QW plane. This follows from optical selection rules [101] based on angular momentum conservation, and from the existence of an orbital angular momentum oriented perpendicular to the quantum well due to electron confinement. Since simple conventional ferromagnetic thin films (like Fe) exhibit in-plane magnetization due to their magnetic shape anisotropy, strong external fields of up to a few Tesla are required to rotate the film magnetization into the perpendicular (vertical) direction. Such high fields are hardly acceptable for future spin-optoelectronics devices, such as spin vertical-cavity surface emitting lasers (VCSELs) [102, 103]. Therefore, the development of more complex ferromagnetic spin-injector contacts with spontaneous out-of-plane magnetization is a key issue for the development of spin-optoelectronic devices. This issue will be discussed later.

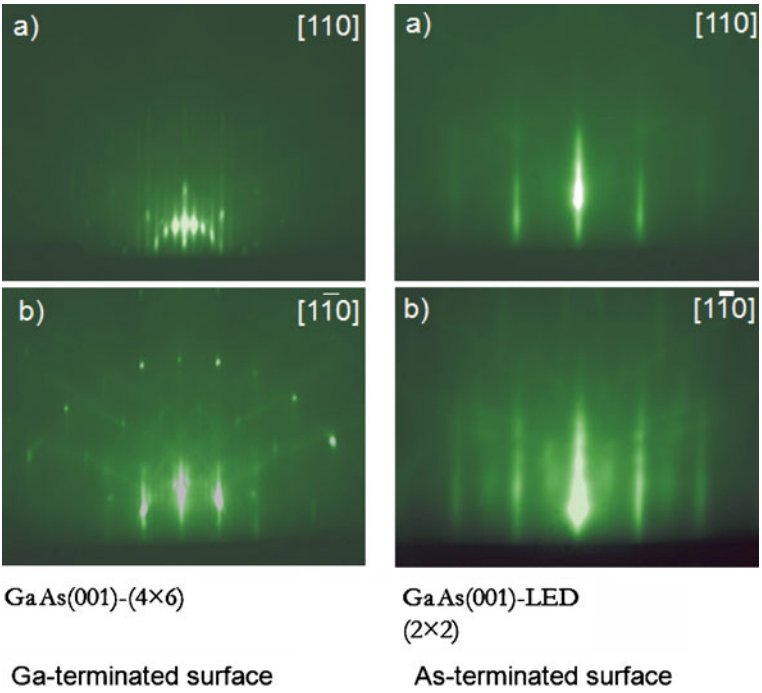

Fig. 17 (*Left*) RHEED images from a clean Ga-terminated GaAs(001) surface showing pseudo-(4 × 6) superstructure reflections. The RHEED beam was along the azimuthal [108] direction of GaAs(001) in **a** and along [1–10] in **b**. (*Right*) RHEED images from a clean As-terminated GaAs(001) surface of a LED structure after desorption of an As-cap layer at 400°C in UHV, showing (2 × 2) superstructure reflections. The RHEED beam was along the azimuthal [108] direction of GaAs(001) in **a** and along [1–10] in **b**. (Electron energy: 15 keV) [112]

The system Fe/GaAs(001) has been widely investigated in literature reports. For instance, magnetic anisotropy is discussed in a recent paper [104], and an extensive review up to the year 2005 is given in Ref. [105]. The advantage of bcc-Fe(001) contacts on GaAs(001) is the high Curie temperature of 1043 K, the high Fe atomic moment of 2.2 μ_B, the high electronic spin polarization at the Fermi energy of 44%, and the favourable lattice parameter which corresponds to a lattice misfit $2a_{Fe}/a_{GaAs}$ of only 1.4%. Another advantage for spin injection is the formation of a natural Schottky barrier at the Fe/GaAs interface, which acts as a natural tunnel barrier and is favourable for electrical spin injection.

However, a problem with Fe/GaAs is the high chemical reactivity of the GaAs surface with respect to Fe. In order to achieve effective spin injection, it is crucial to prepare an optimum crystallographic and magnetic interface structure, because strongly interdiffused, weakly magnetic or non-magnetic Fe-As phases/compounds ("magnetic dead layers") are detrimental for spin injection. High quality epitaxial growth of Fe(001) on the GaAs(001) surface is another crucial condition for spin injection. Our earlier *in situ* CEMS measurements in UHV have demonstrated that epitaxial Fe(001) island growth on GaAs(001) occurs below a critical percolation thickness of ~4 ML Fe, combined with superparamagnetism, while smooth closed Fe(001) films are formed above that critical thickness [106].

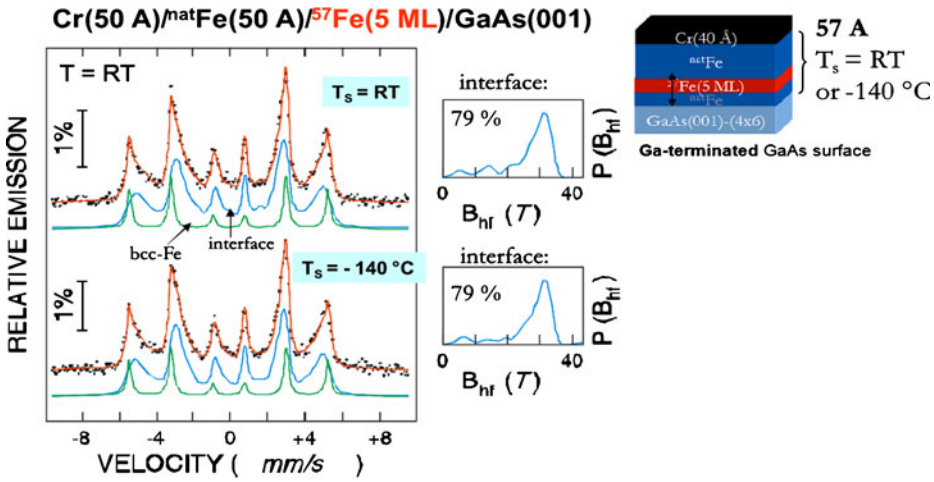

Fig. 18 RT-CEM spectra and corresponding hyperfine-field distributions $P(B_{hf})$ (*right-hand side*) taken from an epitaxial buried 5-ML-thick $^{57}Fe(001)$ probe layer placed directly at the Ga-terminated GaAs(001)-(4 × 6) surface. The sample structure was Cr(4 nm)-cap/Fe(5 nm)/^{57}Fe(5 ML)/GaAs(001)-(4 × 6). The natural Fe and ^{57}Fe layers (total thickness: 5.7 nm) were grown on GaAs(001) at room temperature (*top*) and at −140°C (*bottom*), respectively. The incident γ-ray was perpendicular to the film surface [112]

We have employed CEMS and ^{57}Fe probe layers at the Fe/GaAs and Fe/GaAs(001)-LED interface as a standard diagnostic tool for the characterization of the structural and magnetic state of the interface region [107–110]. The substrate surfaces were Ga-terminated in the case of GaAs(001)-(4 × 6) substrates and cleaned in UHV by cycles of Ar^+ sputtering and annealing, following Ref. [111]. Clean As-terminated GaAs(001)-(2 × 2)-LED surfaces were obtained by desorption of a protective As coating layer at 400°C in UHV. Figure 17 shows RHEED patterns of the Ga-terminated (left) and As-terminated (right) surfaces, respectively, indicating clean, well-ordered and atomically smooth surfaces.

Figure 18 shows typical CEM spectra obtained from a 5-ML- (or 0.72-nm-) thick epitaxial $^{57}Fe(001)$ probe layer (95.5% enriched) placed directly on the Ga-terminated GaAs(001)-(4 × 6) surface, followed by a 5-nm-thick natural Fe(001) layer and a 5-nm Cr(001) cap [112]. The films were grown with the substrate at RT (top spectrum) or at −140°C (bottom spectrum). RHEED indicated epitaxial film growth for both types of samples (not shown). The top spectrum (T_s = RT) was least-squares fitted with two subspectra: (i) a Zeeman sextet with sharp Lorentzian lines, a hyperfine field of 33.0 ± 0.01 T, a quadrupole level shift $2\varepsilon = 0$ mm/s and an isomer shift $\delta = 0$ mm/s, originating predominantly from probe-layer ^{57}Fe atoms in the bcc-Fe phase; (ii) a subspectrum with a hyperfine-field distribution $P(B_{hf})$, implying an average hyperfine field $B_{hf} = 26.8 \pm 0.2$ T, average $2\varepsilon = -0.03 \pm 0.01$ mm/s and average isomer shift $< \delta >= 0.15 \pm 0.04$ mm/s, which is attributed to ^{57}Fe probe layer atoms affected by the GaAs interface (interface Fe alloy). In-plane Fe spin orientation, i.e. an intensity ratio of $R_{23} = x = 4$ was assumed for the fitting. The relative spectral area of the sharp bcc-Fe sextet is 21% (and 79% for the $P(B_{hf})$-interface component), as obtained from the fitting. Very similar Mössbauer parameters were

obtained from the fitting of the bottom spectrum in Fig. 18 for the sample grown at $T_s = -140°C$. This demonstrates that low-temperature epitaxial Fe(001) growth at −140°C on GaAs(001) leads to the same interface state as Fe film growth at RT. This conclusion is also supported by the similar shape of the $P(B_{hf})$ distributions for film growth at RT and −140°C, Fig. 18 (right-hand side).

The value of the average isomer shift $< \delta >= 0.15 \pm 0.04$ mm/s of the $P(B_{hf})$ spectral component for the film grown at RT (and $< \delta >= 0.11 \pm 0.04$ mm/s for the film grown at −140°C) is found to be slightly positive relative to the value of $\delta = 0$ mm/s of pure bulk α-Fe at RT (our reference absorber). This indicates a decrease of the s-electron density at the ^{57}Fe nucleus at the Fe/GaAs interface. This effect can be explained by interdiffused Ga and/or As neighboring atoms of ^{57}Fe in the bcc-Fe lattice, since positive isomer shifts are typically observed for $Fe_{1-x}Ga_x$ and $Fe_{1-x}As_x$ solid solutions [113, 114].

It is obvious that a minor amount (nominally ∼14%) of the total Mössbauer signal (total spectral area) originates also from ^{57}Fe atoms in the 5-nm-thick natural bcc-Fe(001) layer (of ∼2% in ^{57}Fe isotopic abundance), while 79% of the total signal (the interfacial $P(B_{hf})$ spectral component) can be attributed to an interface alloy in the ^{57}Fe probe layer. The small rest (∼7%) of the signal intensity arises from ^{57}Fe atoms in the bcc-Fe phase existing in the probe layer. A simple calculation shows that effectively a thickness of 0.66 nm (or 4.6 ML) of the ^{57}Fe probe layer is affected by Fe/GaAs interface alloying, and only 0.06 nm (or 0.4 ML) of the probe layer exists in the bcc-Fe phase. This result demonstrates that nearly the entire 5-ML-thick ^{57}Fe probe layer is affected by alloying with Ga and/or As atoms from the substrate. Since also the RT-CEM spectrum of the films deposited at $T_s = -140°C$ (Fig. 18, bottom) exhibits a spectral area of 79% for the interfacial $P(B_{hf})$ component, the effective thickness of the interdiffused interface region apparently is independent of Fe film growth at RT or at −140°C on GaAs(001).

One of the most important results of our study follows from the hyperfine-field distributions $P(B_{hf})$ in Fig. 18. The fact that no significant contribution at $B_{hf} = 0$ T in $P(B_{hf})$ exists proves the absence of a "magnetic dead layer" in the interfacial region of both samples. The average hyperfine field $<B_{hf}>$ at RT in the interfacial region (obtained from $P(B_{hf})$) is 26.8 T for T_s = RT and 27.4 T for $T_s = -140°C$, i.e., about 27 T. Assuming proportionality of hyperfine field and Fe atomic magnetic moment, μ_{Fe}, and the validity of the conversion factor of 15 T/μ_B for Fe alloys [31], we obtain a rather high value μ_{Fe} of ∼1.8 μ_B for the alloyed Fe/GaAs(001) interface region. The peak field B_{hf}^{peak} at the maximum of $P(B_{hf})$ is found to be at 31.2 T for both samples (Fig. 18), corresponding to a calculated Fe atomic moment of 2.1 μ_B. Our μ_{Fe} values, calculated from the measured hyperfine fields, are in good agreement with Fe atomic moments of 1.84–1.96 μ_B measured directly by XMCD on Fe(001) sub-monolayers on GaAs(001) [115]. Such bulk-like high Fe magnetic moments are a crucial condition for spintronics applications via electron spin injection.

Now we come back to the topic of the spin LED. As discussed above, the disadvantage of many published approaches is the requirement of a strong external field of more than 2 T counterbalancing the shape anisotropy of the ferromagnetic thin film contact in order to achieve a perpendicular (vertical) magnetization direction along the optical quantization axis in the so-called Faraday geometry. Therefore, ferromagnetic contacts with spontaneous perpendicular magnetization direction (perpendicular magnetic anisotropy, PMA) are highly desirable, since they

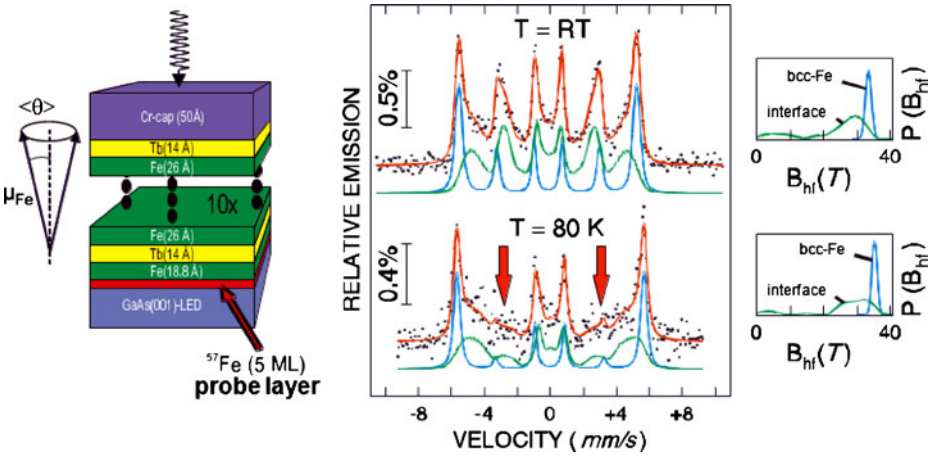

Fig. 19 CEM spectra taken at RT (*top*) and 80 K (*bottom*) from an epitaxial buried 5-ML-thick ^{57}Fe(001) probe layer placed directly at the As- terminated GaAs(001)-(2 × 2) surface of a LED and covered by a Tb/Fe multilayer. The corresponding hyperfine-field distributions $P(B_{hf})$ are shown on the right-hand side. The sample structure is schematically shown on the left-hand side. The arrows emphasize the nearly disappearance of the lines #2 and 5 at 80 K, indicating perpendicular Fe spin texture in the ^{57}Fe interfacial probe layer. The incident γ-ray was perpendicular to the film plane [112]

allow optical detection of electron spin injection in the remanent state (i.e. at zero external magnetic field). The principle is sketched schematically in Fig. 16 (right).

The successful fabrication and CEMS-characterization of ferromagnetic Fe/Tb multilayer contacts with PMA on the clean As-terminated GaAs(001)–(2 × 2) surface of a GaAs-based LED heterostructure are described in Refs. [109, 110]. It is well known that bcc-Fe layers in nanoscale Fe/Tb multilayers exibit PMA [26, 116–125] due to interface anisotropy. The PMA is conceived to be caused by antiferromagnetically exchange-coupled Fe-Tb atomic pairs combined with single-ion anisotropy and the large orbital moment of the Tb ion [123–125]. An ultrathin amorphous Fe-Tb alloy phase at the Fe/Tb interface (a few atomic layers thick), as observed by Mössbauer spectroscopy [116–121], is also involved in creating PMA. Figure 19 shows CEM spectra taken at RT (top) and 80 K (bottom) from a GaAs(001)-based LED (with an InGaAs quantum well) carrying a Tb/Fe-multilayer electrode and a 5-ML-thick ^{57}Fe(001) probe layer at the interface . The exact composition of the sample is:

$$\left[\text{Fe (2.6nm) /Tb (1.4nm)}\right]_{10} \text{/Fe (1.88nm) /}^{57}\text{Fe (5ML) /GaAs-LED.}$$

The metal contact was grown at RT by MBE on the clean As-terminated GaAs(001)-(2 × 2) surface of the LED (Fig. 16, right panel). The epitaxial 5-ML- (or 0.72-nm-) thick ^{57}Fe(001) probe layer was grown first, followed by 1.88 nm of epitaxial natural Fe(001). Thus, the total Fe(001) thickness is 2.6 nm. Subsequently, a $[\text{Fe(2.6 nm)/Tb(1.4 nm)}]_{10}$ multilayer (containing natural Fe) was grown, coated by Cr(5 nm) for protection. The 5-ML ^{57}Fe layer probes the Fe- magnetic state/Fe-spin structure directly at the Fe/GaAs-LED interface. A schematic drawing

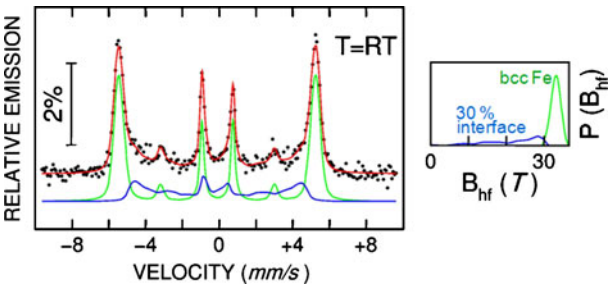

Fig. 20 RT-CEM spectrum and corresponding hyperfine-field distribution $P(B_{hf})$ (*right-hand side*) from an epitaxial buried 10-ML-thick ^{57}Fe probe layer placed directly at the surface of an epitaxial MgO(001) tunnel barrier on GaAs(001)-(2 × 2)-LED and covered by a [natural-Fe(2.6 nm)/Tb(1.4 nm)] multilayer with perpendicular magnetic anisotropy and a Au cap. The nearly disappearance of the lines #2 and 5 indicates strong perpendicular Fe spin texture in the ^{57}Fe probe layer in contact with MgO(001). The incident γ-ray was perpendicular to the film plane [126]

of the sample structure is shown in Fig. 19 (left-hand side). The CEM spectra in Fig. 19 were again least-squares fitted with two spectral components: (i) a sextet component with a sharp distribution of hyperfine fields $P(B_{hf})$ (right-hand side) assigned to the bcc-Fe phase, and (ii) a second component with a broad distribution of hyperfine fields, $P(B_{hf})$, originating from the interfaces in the sample.

The first important observation is that the average hyperfine fields for the bcc-Fe phase obtained from the corresponding distributions in Fig. 19 are $\langle B_{hf}\rangle_{bcc-Fe} = 33.5 \pm 0.1$ T at RT and 35.3 ± 0.4 T at 80 K. These values are slightly enhanced with respect to the bulk α-Fe values because the perpendicular component of the demagnetization field adds to the intrinsic bcc-Fe hyperfine field [118] in the case of PMA. The average hyperfine fields of the interface component deduced from the corresponding distributions are $\langle B_{hf}\rangle_{interface} = 23.8 \pm 0.3$ T at RT and 26.8 ± 1.0 T at 80 K. These values are relatively large, and no indication of a significant "magnetic dead layer" is observed in the distributions $P(B_{hf})$ of Fig. 19, similar to the case of Fe grown on the Ga-terminated GaAs(001) surface, as described above. However, the present RT value of $<B_{hf}>_{interface} = 23.8$ T is smaller than the corresponding value of $<B_{hf}>_{interface} = 27$ T for the Ga-terminated Fe/GaAs(001) interface at RT. Here, $P(B_{hf})$ in Fig. 19 should be attributed to the spectral contributions from the alloyed ^{57}Fe/GaAs interface (nominally ~55% contribution) and the alloyed natural-Fe/Tb interfaces (nominally ~45% contribution), which are difficult to distinguish spectroscopically. Using the conversion factor of 15 T/μ_B, an average Fe atomic moment of ~1.6 μ_B can be estimated from the average hyperfine field, averaged over all interfaces involved.

As decribed in Section 3.1, the measured line-intensity ratio R_{23} (=x) in the CEM spectra of Fig. 19 provides information on the canting angle θ (identical to the angle Ψ in Section 3.1) of the Fe magnetic moments μ_{Fe} relative to the film normal direction (Figs. 4 and 19). We use $\langle\cos^2(\theta)\rangle = (4 - R_{23}) / (4 + R_{23})$ in order to calculate the average canting angle $\langle\theta\rangle = \arccos\left[(4 - R_{23}) / (4 + R_{23})\right]^{1/2}$. It is found that at RT $< \theta >_{bcc-Fe} = 39°$ for the bcc-Fe phase and $< \theta >_{interface} = 66°$ for the interface regions. Both values indicate already out-of-plane Fe spin components. The

perpendicular components increase at 80 K, where $< \theta >_{\mathrm{bcc-Fe}} = 22°$ for the bcc-Fe phase and $< \theta >_{\mathrm{interface}} = 33°$ for the interface region. However, since the nominal Mössbauer signal (relative spectral area) from this sample originates to only ~55% from the 5-ML-thick ^{57}Fe probe layer and the rest of 45% from ^{57}Fe in the natural Fe/Tb multilayer, we cannot claim that these canting angles are typical for the 5-ML ^{57}Fe probe layer, because the measurement averages over the whole sample. However, we can give an approximation for the angle $< \theta >_{\mathrm{Fe}}$ of the bcc-Fe phase in the probe layer, since we have measured the canting angle $< \theta >_{\mathrm{Fe/Tb}}$ for the bcc-Fe phase in a reference sample with the same structure as the probe-layer sample, except that all Fe layers were isotopically enriched to 95% in ^{57}Fe. This fully enriched sample showed values of $< \theta >_{\mathrm{Fe/Tb}} = 32°$ at RT and 24° at 80 K, averaged over all the polycrystalline bcc-^{57}Fe layers in the reference sample. Using the relation $\langle \cos^2 \theta \rangle_{\mathrm{bcc-Fe}} = 0.55 \langle \cos^2 \theta \rangle_{\mathrm{Fe}} + 0.45 \langle \cos^2 \theta \rangle_{\mathrm{Fe/Tb}}$, we calculate values of $< \theta >_{\mathrm{Fe}} = 44°$ at RT and $< \theta >_{\mathrm{Fe}} = 20°$ at 80 K for the bcc-Fe phase in the 5-ML ^{57}Fe probe layer [112]. This supports the above conclusion that spontaneous perpendicular Fe spin components exist in the ^{57}Fe probe layer at the Fe/GaAs-LED interface. Recently, a spin LED with an inserted MgO(001) tunnel barrier was developed, which exhibits strong perpendicular Fe spin components even at RT. The CEM spectrum of such a spin LED [126] is displayed in Fig. 20. The 10-ML-thick ^{57}Fe(001) probe layer, deposited onto the MgO(001)/GaAs(001)-LED surface and covered by a Fe/Tb multilayer with PMA, shows a small canting angle $< \theta >$ of only 21° at RT and a large bcc-Fe spectral contribution of ~70%, while the contribution from interface alloying (~30%) is rather small. It was shown by in-field Mössbauer spectroscopy in Ref. [26] that the Fe spins in such Fe/Tb multilayers form a "cone state", with the Fe spins lying on a cone of half-angle $< \theta >$ relative to the film normal direction (or cone symmetry axis).

Therefore, such ferromagnetic Fe/Tb multilayer contacts on LED surfaces are useful for electron spin injection and optical detection of spin injection in the Faraday geometry in zero external field. This has been proven in several reports, in which CEMS was an indispensible tool for characterizing the interfacial perpendicular Fe spin structure in these spin-optoelectronic devices [97, 127–129]. The degree of optical circular polarization achieved at RT was 1.5% at remanence and 4.4% at $\mu_o H = 2$ T [129]. Recently, the concept of using Fe/Tb-multilayer contacts with strong PMA at RT was applied to a new type of GaAs(001)-based LED containing light-emitting InAs quantum dots [130, 131]. Combined measurements at RT of the canting angle $< \theta >$ at the Fe/GaAs-LED interface by ^{57}Fe-probe layer CEMS and of the degree of circular polarization of the EL light in remanence allowed to determine the spin relaxation depth of the injected electrons in the semiconductor [131]. Moreover, the successful fabrication and CEMS characterization of ferromagnetic Fe/Tb multilayer contacts with PMA was also reported for the semiconductor InAs(001) [132].

5 Outlook

50 years after R. L. Mössbauer has been awarded the Nobel prize in physics, the Mössbauer effect continues to be a valuable and often unique method in the field of solid state magnetism. "A Mössbauer spectrum does not lie." A simple Mössbauer

measurement can often prove whether a model inferred from macroscopic magnetic measurement is correct or not.

Figure 1 in Ref. [11] gives a schematic overview of topical subjects in the rapidly evolving fields of spintronics and magnetoelectronics [8, 11]. Besides the familiar control of magnetic devices by external magnetic fields, new and exciting phenomena have been discovered recently, including control by a spin polarized current [133], by electric fields [134–137] or by photonic fields in ultrafast light pulses [11]. Most of these phenomena are observed in nanoscale magnetic systems. The influence of a strong electric field at the interface between a ferromagnetic and a ferroelectric (or insulating) material on the interfacial electronic band structure in the ferromagnet [134–136] might be revealed in the Mössbauer isomer shift and/or hyperfine magnetic field, because both quantities are related to the s-electron density at the ^{57}Fe nucleus. One important aspect of Mössbauer spectroscopy is its sensitivity to chemical ordering processes at the atomic scale in magnetic alloys. Mössbauer spectroscopy can contribute to the characterization and development of Mössbauer-isotope containing chemically ordered thin-film Heusler alloys [6, 23, 24, 28, 29], which are important electron spin injectors, e.g. for GMR, TMR or spin-optoelectronics devices, due to their anticipated huge electronic spin polarization at the Fermi energy. Due to their sensitivity to buried interfaces, CEMS and in particular NRS may contribute to the understanding of electric-field controlled effects in magnetism [134–137]. With the advent of new intense synchrotron light sources with micron or submicron focusing (e.g., PETRA III at DESY), one can conceive novel NRS experiments with spatial resolution for the study of nanomagnetism, and even NRS measurements on monolayers of paramagnetic biomolecules (e.g., Fe-porphyrin molecules) magnetically coupled to ferromagnetic surfaces [138, 139] may become feasible. Such experiments are demanding, because mostly they would require *in situ* NRS measurements under ultrahigh-vacuum (UHV) conditions. Moreover, the method of nuclear resonant inelastic x-ray scattering (NRIXS) of synchrotron radiation, which allows to directly measure the phonon density of states, so far has been seldom used in relation to magnetic phenomena, although changes in the phonon spectrum of FeO (an antiferromagnetic material with a large Fe orbital moment) have been observed and interpreted by magneto-elastic coupling [140]. In the future, it is expected that Mössbauer spectroscopy will participate vigorously in the discovery and understanding of novel phenomena in magnetism at the nanoscale.

Acknowledgements This paper could not have been accomplished without significant contributions by the author's former graduate students in Duisburg: A. Khrenov, R. Peters, B. Roldan Cuenya, B. Sahoo, E. Schuster and F. Stromberg. The author is particularly grateful to U. von Hörsten for his expertise technical and computational support and to C. Antoniak, R. A. Brand, B. Krumme, S. Makarov, A. Warland and C. Weis (all Duisburg) for enlightening discussions. The continuous cooperation and valuable discussions with H. Wende (Duisburg) and J. Kirschner (Halle) are highly appreciated. The author thanks G. Bayreuther (Regensburg and Halle) for critically reading the manuscript and for valuable comments. This work was financially supported by the Deutsche Forschungsgemeinschaft (Sonderforschungsbereich 491 Bochum-Duisburg).

References

1. Blundell, S.: Magnetism in Condensed Matter. Oxford Master Series in Condensed Matter Physics. Oxford University Press, Oxford, New York (2003)
2. Reiff, W.M., Wong, H., Frankel, R.B., Foner, S.: Inorg. Chem. **16**, 1036 (1977)

3. Eibschütz, M., Davidson, G.R., Guggenheim, H.J.: Phys. Rev. B **9**, 3885 (1974)
4. Ito, A., Horiike, M.: J. Phys. (Paris) Colloq. **40**, C2–C290 (1979)
5. Moodera, J.S., Nassar, J., Mathon, G.: Annu. Rev. Mater. Sci. **29**, 381 (1999)
6. Ksenofontov, V., Wojcik, M., Wurmehl, S., Schneider, H., Balke, B., Jakob, G., Felser, C.: J. Appl. Phys. **107**, 09B106 (2010)
7. Zutic, I., Fabian, J., Das Sarma, S.: Rev. Mod. Phys. **76**, 323 (2004)
8. Bader, S.D.: Rev. Mod. Phys. **78**, 1 (2006)
9. Bader, S.D., Buchanan, K.S., Chung, S.-H., Guslienko, K.Y., Hoffmann, A., Li, Y., Novisad, V.: Superlattices Microstruct. **41**, 72 (2007)
10. Zabel, H.: Superlattices Microstruct. **46**, 541 (2009)
11. Bader, S.D., Parkin, S.S.P.: Annu. Rev. Condens. Matter Phys. **1**, 71 (2010)
12. Grünberg, P., Schreiber, R., Pang, Y., Brodsky, M.B., Sowers, H.: Phys. Rev. Lett. **57**, 2442 (1986)
13. Baibich, M.N., Broto, J.M., Fert, A., Nguyen van Dau, F., Petroff, F., Etienne, P., Creuzet, G., Friederich, A., Chazelas, J.: Phys. Rev. Lett. **61**, 2472 (1988)
14. Binasch, G., Grünberg, P., Saurenbach, F., Zinn, W.: Phys. Rev. B **39**, 4828 (1989)
15. Bruno, P.: Phys. Rev. B **49**, 13231 (1994)
16. Zahn, P., Mertig, I., Richter, M., Eschrig, H.: Phys. Rev. Lett. **75**, 2996 (1995)
17. Chappert, J.: Hyperfine Interact. **13**, 25 (1983)
18. Sauer, Ch., Zinn, W.: In: Bennett, L.H., Watson, R.E. (eds.) Magnetic Multilayers. World Scientific, Singapore (1993)
19. Przybylski, M.: Hyperfine Interact. **113**, 135 (1998)
20. Shinjo, T., Keune, W.: J. Magn. Magn. Mater. **200**, 598 (1999)
21. Gerdau, E., de Waard, H. (eds.): Nuclear Resonant Scattering of Synchrotron Radiation. Baltzer Science Publishers, Amsterdam (1999/2000)
22. Dürr, H.A., et al.: IEEE Trans. Magn. **45**, 15 (2009)
23. Makarov, S., Krumme, B., Stromberg, F., Weis, C., Keune, W., Wende, H.: Appl. Phys. Lett. **99**, 141910 (2011)
24. Krumme, B., Weis, C., Herper, H.C., Stromberg, F., Antoniak, C., Warland, A., Schuster, E., Srivastava, P., Walterfang, M., Fauth, K., Minár, J., Ebert, H., Entel, P., Keune, W., Wende, H.: Phys. Rev. B **80**, 144403 (2009)
25. Schmidbauer, E., Keller, M.: J. Magn. Magn. Mater. **297**, 107 (2006)
26. Tappert, J., Neumann, S., Brand, R.A., Keune, W., Klose, F., Maletta, H.: Europhys. Lett. **46**, 238 (1999)
27. Mibu, K., Tanaka, S., Shinjo, T.: J. Phys. Soc. Jpn. **67**, 2633 (1998)
28. Mibu, K., Gondo, D., Hori, T., Tanaka, M.A., Kondou, K., Kasai, S., Ono, T.: J. Phys.: Conf. Ser. **200**, 062012 (2010)
29. Mibu, K., Gondo, D., Hori, T., Ishikawa, Y., Tanaka, M.A.: J. Phys.: Conf. Ser. **217**, 012094 (2010)
30. Preston, R.S., Hanna, S.S., Heberle, J.: Phys. Rev. **128**, 2207 (1962)
31. Gubbens, P.C.M., Buschow, K.H.J.: J. Phys. F **4**, 921 (1974)
32. Hines, W.A., Menotti, A.H., Budnick, J.I., Burch, T.J., Litrenta, T., Niculescu, V., Raj, K.: Phys. Rev. B **13**, 4060 (1976)
33. Liljequist, D., Ekdahl, T., Bäverstam, U.: Nucl. Instrum. Methods **155**, 529 (1978)
34. Keune, W., Schatz, A., Ellerbrock, R.D., Fuest, A., Wilmers, K., Brand, R.A.: J. Appl. Phys. **79**, 4265 (1996)
35. Roldan Cuenya, B., Keune, W., Li, D., Bader, S.D.: Phys. Rev. B **71**, 064409 (2005)
36. Rader, O., Carbone, C., Clemens, W., Vescovo, E., Blügel, S., Eberhardt, W., Gudat, W.: Phys. Rev. B **45**, 13823 (1992)
37. Rader, O., Vescovo, E., Redinger, J., Blügel, S., Carbone, C., Eberhardt, W., Gudat, W.: Phys. Rev. Lett. **72**, 2247 (1994)
38. Vogel, J., Fontaine, A., Cros, V., Petroff, F., Kappler, J.-P., Krill, G., Rogalev, A., Goulon, J.: Phys. Rev. B **55**, 3663 (1997)
39. Klautau, A.B., Peduto, P.R., Frota-Pessoa, S.: J. Magn. Magn. Mater. **186**, 223 (1998)
40. Stoeffler, D., Ounadjela, K., Sticht, J., Gautier, F.: Phys. Rev. B **49**, 299 (1994)
41. Li, M., et al.: J. Phys.: Condens. Matter **6**, L785 (1994)
42. Cheng, L., Altounian, Z., Ryan, D.H., Ström-Olsen, J.O.: J. Appl. Phys. **91**, 7188 (2002)
43. Liu, C., Bader, S.D.: J. Vac. Sci. Technol. A **8**, 2727 (1990)
44. Jin, X.F., Barthel, J., Shen, J., Manoharan, S.S., Kirschner, J.: Phys. Rev. B **60**, 11809 (1999)
45. Li, C., Freeman, A.J., Jansen, H.J.F., Fu, C.L.: Phys. Rev. B **42**, 5433 (1990)

46. Blügel, S., Drittler, B., Zeller, R., Dederichs, P.H.: Appl. Phys. Solid Surf. **49**, 547 (1989)
47. Li, D., Roldan Cuenya, B., Pearson, J., Bader, S.D., Keune, W.: Phys. Rev. B **64**, 144410 (2001)
48. Weber, W., Wesner, D.A., Hartmann, D., Güntherodt, G.: Phys. Rev. B **46**, 6199 (1992)
49. Kiauka, W., van Cuyck, C., Keune, W.: Mater. Sci. Eng. B **12**, 273 (1992)
50. Boeglin, C., Bulou, H., Hommet, J., Le Cann, X., Magnan, H., Le Fevre, P., Chandesris, D.: Phys. Rev. B **60**, 4220 (1999)
51. Wertheim, G.K.: Mössbauer Effect: Principles and Applications. Academic Press, New York (1964)
52. Mühlbauer, H., Müller, Ch, Dumpich, G.: J. Magn. Magn. Mater. **192**, 423 (1999)
53. Le Cann, X., Boeglin, C., Carriere, B., Hricovini, K.: Phys. Rev. B **54**, 373 (1996)
54. Kisters, G., Sauer, Ch., Tsymbal, E., Zinn, W.: Hyperfine Interact. **92**, 1285 (1994)
55. Ohnishi, S., Freeman, A.J., Weinert, M.: Phys. Rev. B **28**, 6741 (1983)
56. Ohnishi, S., Weinert, M., Freeman, A.J.: Phys. Rev. B **30**, 36 (1984)
57. Roldan Cuenya, B., Doi, M., Löbus, S., Courths, R., Keune, W.: Surf. Sci. **493**, 338 (2001)
58. Bader, S.D.: Rev. Mod. Phys. **78**, 1 (2006)
59. Parkin, S.S.P., Hayashi, M., Thomas, L.: Science **320**, 190 (2008)
60. Röhlsberger, R., Thomas, H., Schlage, K., Burkel, E., Leupold, O., Rüffer, R.: Phys. Rev. Lett. **89**, 237201 (2002)
61. Klein, T., Röhlsberger, R., Crisan, O., Schlage, K., Burkel, E.: Thin Solid Films **51**, 52531 (2006)
62. Kuncser, V.E., Doi, M., Keune, W., Askin, M., Spies, H., Jiang, J.S., Inomata, A., Bader, S.D.: Phys. Rev. B **68**, 064416 (2003)
63. Fullerton, E.E., Jiang, J.S., Bader, S.D.: J. Magn. Magn. Mater. **200**, 392 (1999)
64. Choi, Y., Jiang, J.S., Ding, Y., Rosenberg, R.A., Pearson, J.E., Bader, S.D., Zambano, A., Murakami, M., Takeuchi, I., Wang, Z.L., Liu, J.P.: Phys. Rev. B **75**, 104432 (2007)
65. The (Sm-Co)/Fe samples were prepared by J. S. Jiang, Materials Science Division, Argonne National Laboratory, Argonne, IL 60439, U.S.A.
66. Fullerton, E.E., Jiang, J.S., Grimsditch, M., Sowers, C.H., Bader, S.D.: Phys. Rev. B **58**, 12193 (1998)
67. Mibu, K., Nagahama, T., Shinjo, T.: J. Magn. Magn. Mater. **163**, 75 (1996)
68. Chumakov, D., Schäfer, R., Elefant, D., Eckert, D., Schultz, L., Yan, S.S., Barnard, J.A.: Phys. Rev. B **66**, 134409 (2002)
69. Kuncser, V., Keune, W., Vopsaroiu, M., Bissell, P.R.: Nucl. Instrum. Methods Phys. Res. B **245**, 539 (2006)
70. Kuncser, V., Keune, W.: J. Magn. Magn. Mater. **323**, 2196 (2011)
71. Brand, R.A.: Nucl. Instrum. Methods Phys. Res. **28**, 417 (1987)
72. Uzdin, V.M., Vega, A.: Nanotechnology **19**, 315401 (2008); Phys. Rev. B **77**, 134446 (2008)
73. Uzdin, V.M., Vega, A., Khrenov, A., Keune, W., Kuncser, V.E., Jiang, J.S., Bader, S.D.: Phys. Rev. B **85**, 024409 (2012)
74. Nogués, J., Schuller, I.K.: J. Magn. Magn. Mater. **192**, 203 (1999)
75. Stromberg, F.: Dissertation, Universität Duisburg-Essen (2009, in German)
76. Kuncser, V., Doi, M., Sahoo, B., Stromberg, F., Keune, W.: J. Appl. Phys. **94**, 3573 (2003)
77. Kuncser, V.E., Stromberg, F., Acet, M., Keune, W.: J. Appl. Phys. **97**, 063513 (2005)
78. Stromberg, F., Keune, W., Kuncser, V., Westerholt, K.: Phys. Rev. B **72**, 064440 (2005)
79. Radu, F., Zabel, H.: In: Bader, S.D., Zabel, H. (eds.) Magnetic Heterostructures, Advances and Perspectives in Spinstructures and Spintransport. Springer, Berlin (2007)
80. Schulthess, T.C., Butler, W.H.: Phys. Rev. Lett. **81**, 4516 (1998); J. Appl. Phys. **85**, 5510 (1999)
81. Stamps, R.L.: J. Phys. D **33**, R247 (2000)
82. Krivorotov, I.N., Leighton, C., Nogués, J., Schuller, I.K., Dahlberg, E.D.: Phys. Rev. B **68**, 054430 (2003)
83. Kiwi, M.: J. Magn. Magn. Mater. **234**, 584 (2001)
84. Kiwi, M., Mejia-Lopez, J., Portugal, R.D., Ramirez, R.: Europhys. Lett. **48**, 573 (1999)
85. Morales, R., Li, Z.-P., Petracic, O., Batlle, X., Schuller, I.K., Olamit, J., Liu, K.: Appl. Phys. Lett. **89**, 072504 (2006)
86. Macedo, W.A.A., Sahoo, B., Kuncser, V., Eisenmenger, J., Felner, I., Nogués, J., Liu, K., Keune, W., Schuller, I.K.: Phys. Rev. B **70**, 224414 (2004)
87. Sahoo, B., Macedo, W.A.A., Keune, W., Kuncser, V., Eisenmenger, J., Nogués, J., Schuller, I.K., Felner, I., Liu, K., Röhlsberger, R.: Hyperfine Interact. **169**, 1371 (2006)

88. Macedo, W.A.A., Sahoo, B., Eisenmenger, J., Martins, M.D., Keune, W., Kuncser, V., Röhlsberger, R., Leupold, O., Rüffer, R., Nogués, J., Liu, K., Schlage, K., Schuller, I.K.: Phys. Rev. B **78**, 224401 (2008)
89. Sturhahn, W.: Hyperfine Interact. **125**, 149 (2000)
90. Prinz, G.A.: Science **250**, 1092 (1990)
91. Fiederling, R., Keim, M., Reuscher, G., Ossau, W., Schmidt, G., Waag, A., Molenkamp, L.W.: Nature (London) **402**, 787 (1999)
92. Wolf, S.A., Awschalom, D.D., Buhrman, R.A., Daughton, J.M., von Molnar, S., Roukes, M.L., Chtchelkanova, A.Y., Treger, D.M.: Science **294**, 1488 (2001)
93. Žutić, I., Fabian, J., das Sarma, S.: Rev. Mod. Phys. **76**, 323 (2004)
94. Hanbicki, A.T., Jonker, B.T., Itskos, G., Kioseoglou, G., Petrou, A.: Appl. Phys. Lett. **80**, 1240 (2002)
95. Zhu, H.J., Ramsteiner, M., Kostial, H., Wassermeier, M., Schönherr, H.-P., Ploog, K.H.: Phys. Rev. Lett. **87**, 016601 (2001)
96. Jiang, X., Wang, R., Shelby, R.M., MacFarlane, R.M., Bank, S.R., Harris, J.S., Parkin, S.S.P.: Phys. Rev. Lett. **94**, 056601 (2005)
97. Gerhardt, N.C., Hövel, S., Brenner, C., Hofmann, R.M., Lo, F.-Y., Reuter, D., Wieck, A.D., Schuster, E., Keune, W., Westerholt, K.: Appl. Phys. Lett. **87**, 032502 (2005)
98. Kioseoglou, G., Yasar, M., Li, C.H., Korkusinski, M., Diaz-Avila, M., Hanbicki, A.T., Hawrylak, P., Petrou, A., Jonker, B.T.: Phys. Rev. Lett. **101**, 227203 (2008)
99. Wu, M.W., Jiang, J.H., Weng, M.Q.: Phys. Rep. **493**, 61 (2010)
100. Li, M.Y., Jähme, H., Soldat, H., Gerhardt, N.C., Hofmann, M.R., Ackemann, T.: Appl. Phys. Lett. **97**, 191114 (2010)
101. Meier, F., Zakharchenya, B.P. (eds.): Optical Orientation. North-Holland, New York (1984)
102. Holub, M., Shin, J., Saha, D., Bhattacharya, P.: Phys. Rev. Lett. **98**, 146603 (2007)
103. Hövel, S., Bischoff, A., Gerhardt, N.C., Hofmann, M.R., Ackemann, T., Kroner, A., Michalzik, R.: Appl. Phys. Lett. **92**, 041118 (2008)
104. Kardasz, B., Mosendz, O., Heinrich, B., Przybylski, M., Kirschner, J.: J. Phys.: Conf. Ser. **200**, 072046 (2010)
105. Wastlbauer, G., Bland, J.A.C.: Adv. Phys. **54** (2005)
106. Roldan Cuenya, B., Naitabdi, A., Schuster, E., Peters, R., Doi, M., Keune, W.: Phys. Rev. B **76**, 094403 (2007)
107. Doi, M., Roldan Cuenya, B., Keune, W., Schmitte, T., Nefedov, A., Zabel, H., Spoddig, D., Meckenstock, R., Pelzl, J.: J. Magn. Magn. Mater. **240**, 407 (2002)
108. Roldan Cuenya, B., Doi, M., Keune, W., Hoch, S., Reuter, D., Wieck, A., Schmitte, T., Zabel, H.: Appl. Phys. Lett. **82**, 1072 (2003)
109. Schuster, E., Keune, W., Lo, F.-Y., Reuter, D., Wieck, A., Westerholt, K.: Superlattices Microstruct. **37**, 313 (2005)
110. Schuster, E., Brand, R.A., Stromberg, F., Lo, F.-Y., Ludwig, A., Reuter, D., Wieck, A.D., Hövel, S., Gerhardt, N.C., Hofmann, M.R., Wende, H., Keune, W.: J. Appl. Phys. **108**, 063902 (2010)
111. Zölfl, M., Brockmann, M., Köhler, M., Keuzer, S., Schweinböck, T., Miethaner, S., Bensch, F., Bayreuther, G.: J. Magn. Magn. Mater. **175**, 16 (1997)
112. Schuster, E.: Dissertation, Universität Duisburg-Essen (2007, in German)
113. Newkirk, L.R., Tsuei, C.C.: Phys. Rev. B **4**, 4046 (1971)
114. Vincze, I., Aldred, A.T.: Phys. Rev. B **9**, 3845 (1974)
115. Claydon, J.S., Xu, Y.B., Tselepi, M., Bland, J.A.C., van der Laan, G.: Phys. Rev. Lett. **93**, 037206 (2004)
116. Cherifi, K., Dufour, C., Piecuch, M., Bruson, A., Bauer, Ph., Marchal, G., Mangin, Ph.: J. Magn. Magn. Mater. **93**, 609 (1991)
117. Mibu, K., Hosoito, N., Shinjo, T.: Hyperfine Interact. **68**, 341 (1991)
118. Scholz, B., Brand, R.A., Keune, W.: Phys. Rev. B **50**, 2537 (1994)
119. Kim, W.S., Kleemann, W., Brand, R.A., Keune, W.: J. Phys., Condens. Matter **11**, 4317 (1999)
120. Tappert, J., Neumann, S., Jungermann, J., Kim, W.S., Ruckert, T., Brand, R.A., Keune, W., Kleemann, W., Richomme, F., Teillet, J., Klose, F., Maletta, H.: Philos. Mag. **80**, 257 (2000)
121. Richomme, F., Teillet, J., Fnidiki, A., Keune, W.: Phys. Rev. B **64**, 094415 (2001)
122. Honda, S., Nawate, M.: J. Magn. Magn. Mater. **136**, 163 (1994)
123. Sato, N.: J. Appl. Phys. **59**, 2514 (1986)
124. Baczewski, L.T., Piecuch, M., Durand, J., Marchal, G., Delcroix, P.: Phys. Rev. B **40**, 11237 (1989)

125. Shan, Z.S., Sellmyer, D.J.: In: Gschneider, K.A., Eyring, L. (eds.) Handbook on the Physics and Chemistry of Rare Earths. Elsevier Science, Amsterdam (1996)
126. The Au/[Fe/Tb]$_4$/^{57}Fe(10ML)/Mg0(001) multilayer was grown on a GaAs(001)-LED and the CEM spectrum was taken by F. Stromberg, University of Duisburg - Essen
127. Gerhardt, N.C., Hövel, S., Brenner, C., Hofmann, M.R., Lo, F.-Y., Reuter, D., Wieck, A.D., Schuster, E., Keune, W., Halm, S., Bacher, G., Westerholt, K.: J. Appl. Phys. **99**, 073907 (2006)
128. Hövel, S., Gerhardt, N.C., Hofmann, M.R., Lo, F.-Y., Reuter, D., Wieck, A.D., Schuster, E., Keune, W., Wende, H., Petracic, O., Westerholt, K.: Appl. Phys. Lett. **92**, 242102 (2008)
129. Hövel, S., Gerhardt, N.C., Hofmann, M.R., Lo, F.-Y., Ludwig, A., Reuter, D., Wieck, A.D., Schuster, E., Wende, H., Keune, W., Petracic, O., Westerholt, K.: Appl. Phys. Lett. **93**, 021117 (2008)
130. Ludwig, A., Roescu, R., Rai, A.K., Trunov, K., Stromberg, F., Li, M., Soldat, H., Ebbing, A., Gerhardt, N.C., Hofmann, M.R., Wende, H., Keune, W., Reuter, D., Wieck, A.D.: J. Cryst. Growth **323**, 376 (2011)
131. Soldat, H., Li, M., Gerhardt, N.C., Hofmann, M.R., Ludwig, A., Ebbing, A., Reuter, D., Wieck, A.D., Stromberg, F., Keune, W., Wende, H.: Appl. Phys. Lett. **99**, 051102 (2011)
132. Peters, R., Keune, W., Schuster, E., Kashiwada, S., Ferhat, M., Yoh, K.: Superlattice. Microstruct. **41**, 81 (2007)
133. Sbiaa, R., Law, R., Lua, S.Y.H., Tan, E.L., Tahmasebi, T., Wang, C.C., Piramanayagam, S.N.: Appl. Phys. Lett. **99**, 092506 (2011)
134. Duan, C.-G., Jaswal, S.S., Tsymbal, E.Y.: Phys. Rev. Lett. **97**, 047201 (2006)
135. Maruyama, T., Shiota, Y., Nozaki, T., Ohta, K., Toda, N., Mizuguchi, M., Tulapurka, A.A., Shinjo, T., Shiraishi, M., Mizukami, S., Ando, Y., Suzuki, Y.: Nature Nanotechnology **4**, 158 (2009)
136. Nozaki, T., Shiota, Y., Shiraishi, M., Shinjo, T., Suzuki, Y.: Appl. Phys. Lett. **96**, 022506 (2010)
137. Kleemann, W.: Physics **2**, 105 (2009)
138. Bernien, M., Miguel, J., Weis, C., Ali, Md.E., Kurde, J., Krumme, B., Panchmatia, P.M., Sanyal, B., Piantek, M., Srivastava, P., Baberschke, K., Oppeneer, P.M., Eriksson, O., Kuch, W., Wende, H.: Phys. Rev. Lett. **102**, 047202 (2009)
139. Wende, H.: Adv. Solid State Phys. **48**, 199 (2009)
140. Struzhkin, V.V., Mao, H.-K., Hu, J., Schwoerer-Böhning, M., Shu, J., Hemley, R.J., Sturhahn, W., Hu, M., Alp, E.E.: Phys. Rev. Lett. **25**, 255501 (2001)

Hyperfine Interact (2012) 204:47–55
DOI 10.1007/s10751-011-0510-6

Fifty years of Mössbauer spectroscopy: from alloys and oxides to glasses and nanoparticles

C. E. Johnson · J. A. Johnson

Published online: 20 December 2011

Abstract The Mössbauer Effect was discovered in 1957. In 1960 Mössbauer spectroscopy was born when two important papers appeared on (i) the magnetic hyperfine interaction and (ii) the electric monopole (isomer shift) and quadrupole interactions. These transformed an interesting phenomenon into a method for probing solids. Applications to magnetism, metals and alloys, chemical compounds, biological molecules, geology, archaeology and other sciences followed and are still of current interest. Two areas of research where Mössbauer spectroscopy is making unique contributions are in determining oxidation states in (i) glasses and (ii) nanoparticles. Some recent measurements are described.

Keywords Magnetism · Nanoparticles · Glasses · Mössbauer spectroscopy

1 Introduction

Mössbauer spectroscopy began with two important papers which were published in 1960, one by Hanna et al. [1] on the magnetic hyperfine interaction in ferromagnetic metallic iron, and the other by Kistner and Sunyar [2] on the electric monopole (isomer or chemical shift) and quadrupole interactions in the antiferromagnet Fe_2O_3. These transformed an interesting phenomenon into a method for probing solids. Applications to the magnetism of iron alloys (Fig. 1) and oxides (Figs. 2 and 3) followed quickly, and were extended to studies of chemical compounds and biological molecules. In addition to iron, about 20 other elements including tin, europium and

C. E. Johnson (✉)
Center for Laser Applications, University of Tennessee Space Institute,
Tullahoma, TN 37388, USA
e-mail: cjohnson@utsi.edu

J. A. Johnson
Department of Mechanical, Aerospace and Biomedical Engineering,
University of Tennessee Space Institute, Tullahoma, TN 37388, USA

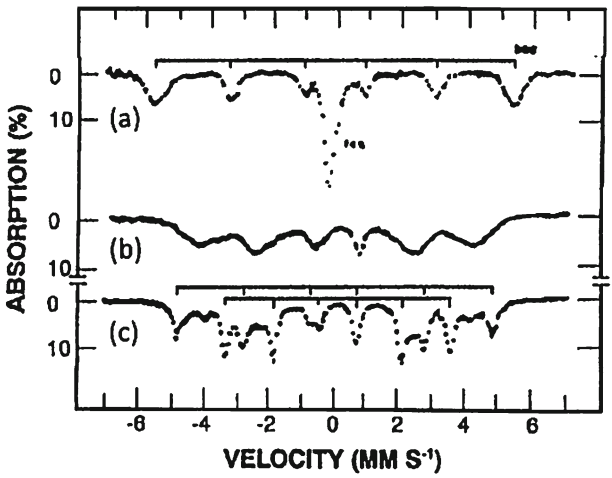

Fig. 1 Iron alloys (**a**) 32% Ni, showing bcc and fcc phases (**b**) 25% Al (**c**) ordered Fe_3Al showing two iron sites

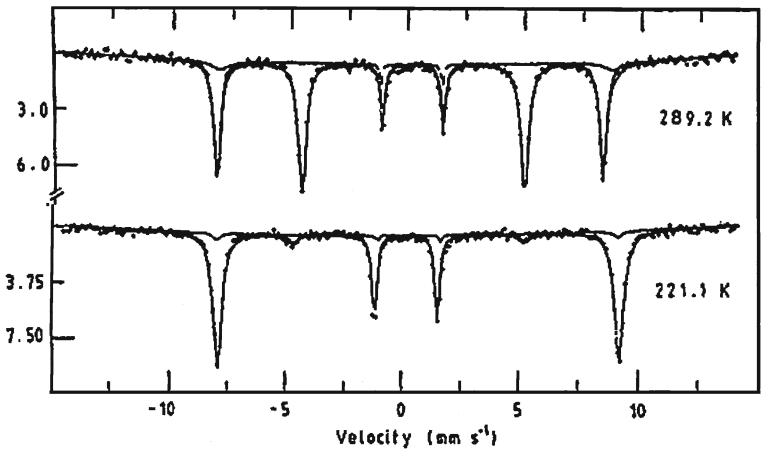

Fig. 2 α-Fe_2O_3: Morin transition. The γ-rays are parallel to the *c*-axis. At 260 K the spins re-orient from parallel to perpendicular to *c* and the electric field gradient changes sign

antimony showed the Mössbauer effect. Its use in other sciences, such as geology and archaeology, became quickly established and are of continuing interest and activity.

Although the Mössbauer effect is limited to only a few elements in the periodic table, they are important elements and unlike x-ray diffraction, which requires the periodic lattice of a crystal, the measurements do not require crystals. It is powerful in selecting the resonant isotope (e.g. ^{57}Fe) in the presence of other atoms in a sample. Furthermore through the isomer (chemical) shift it is sensitive to the charge state of the atom and so can distinguish between different oxidation states.

Mössbauer spectra, like x-ray diffraction patterns, can be used to provide fingerprints for identifying compounds or alloy phases and mixtures of them. They have been used to analyze soil and rocks from the surface of the moon and on Mars. In biochemistry some new proteins have been discovered. One of the most striking

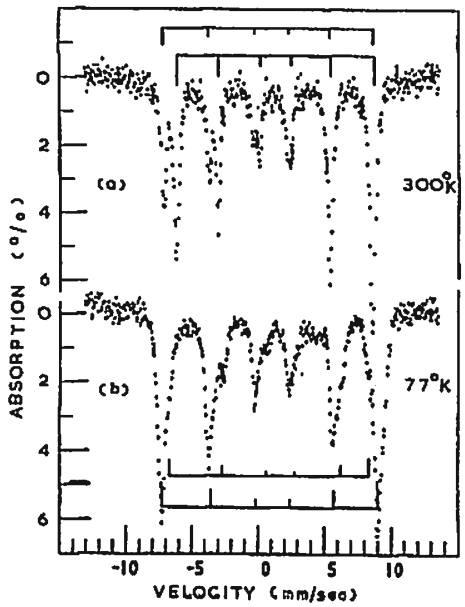

Fig. 3 Fe_3O_4: Verwey transition. At 110 K the structure changes from normal to inverted spinel

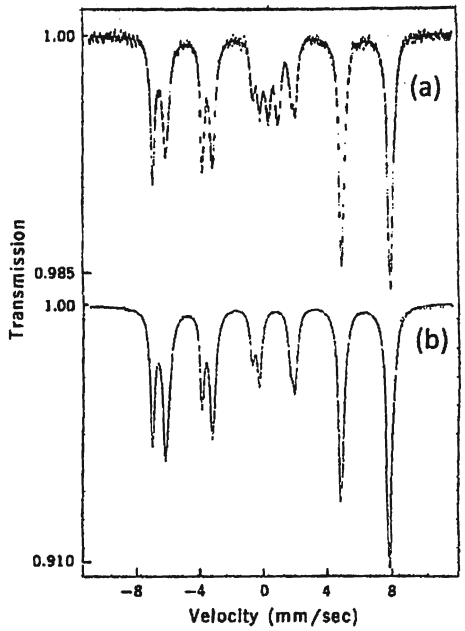

Fig. 4 ^{57}Fe spectrum at room temperature of (**a**) magnetic cells from magnetotactic bacteria *spirillum* (**b**) Fe_3O_4 [3]

examples of its use in biology was by Frankel et al. [3] who identified Fe_3O_4 in the brain of pigeons and in magnetotactic bacteria, thereby establishing that birds and bacteria navigate by sensing the earth's magnetic field. Figure 4a shows the spectrum of cells from magnetotactic *spirillum* which is seen to be similar to that of magnetite Fe_3O_4 in Fig. 4b. Subsequent electron micrographs revealed a string

of Fe_3O_4 nanocrystals in the cells [3]. Among other examples of fingerprinting have been studies of magnetic phase changes [4].

Hence two areas of research where Mössbauer spectroscopy can make a unique contribution in complementing x-ray diffraction methods are (i) glasses, which only scatter x-rays incoherently, and (ii) nanoparticles, which are prone to oxidation because a large fraction of the atoms are on their surface. The ability of the Mössbauer effect to distinguish different oxidation states offers an important way of characterizing nanoparticles

Magnetic nanoparticles exhibit superparamagnetism, i.e. they are single domain and below their ordering temperature T_c their magnetic moments fluctuate rapidly so that they have a reduced net magnetization. Their Mössbauer spectra then show broadened magnetic hyperfine lines. When they are cooled below the so-called blocking temperature, T_B, given approximately by,

$$kT_B \approx aKV,$$

the fluctuations slow down and the full magnetic splitting is observed. Here V is the volume of the particles and K their magnetic anisotropy constant and a is a constant of the order of 0.04.

2 Silicate glasses

Tin and iron are both important constituents of industrial silicate glasses. Tin is involved in the float glass process which is used almost universally in flat glass manufacture nowadays. Iron is an impurity in the raw sand from which the glass is produced and is sometimes added (as also is tin) to produce glass with certain optical properties. Both these atoms can exist in different valence states and Mössbauer spectroscopy has been used to determine them.

Float glass is made, as the name suggests, by floating a moving ribbon of molten glass on liquid tin. Some of the tin diffuses into the surface and it is important to know the chemistry involved. Figure 5 shows data of Williams et al. [5] who measured ^{119}Sn spectra of slices at different average depths from the surface. It is seen that at the surface the tin is predominantly Sn^{2+} and with increasing depth the concentration of Sn^{4+} increases.

3 Iron phosphate glasses

Iron is not a glass former, but with other oxides can form glasses and usually exists in more than one valence state. For example iron phosphate glasses, a possible candidate for storing nuclear wastes, is produced by melting Fe_2O_3 and P_2O_5 and always contains some Fe^{2+}. Ray et al. [6] investigated the effect of temperature and time on the composition of these glasses. Some more recent spectra (Smith et al., private communication) are shown in Fig. 6. Both Fe^{2+} (shift 1.4 mm/s) and Fe^{3+} (shift 0.3 mm/s) are present, with the amount of Fe^{2+} increasing with increasing temperature and time of melting.

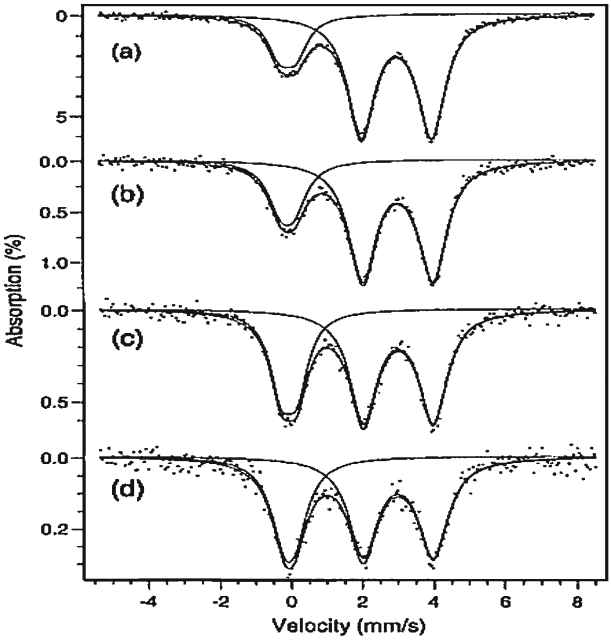

Fig. 5 ^{119}Sn spectra at room temperature of float glass slices of thickness t and average depth d below the surface (**a**) d = 8.5 μm, t = 17 μm (**b**) d = 9.25 μm, t = 15.5 (**c**) t = 11.0 μm, t = 12 μm and (**d**) d = 14.75 μm, t = 4.5 μm. At the surface the tin is mostly Sn^{2+}, becoming increasingly Sn^{4+} with increasing depth [5]

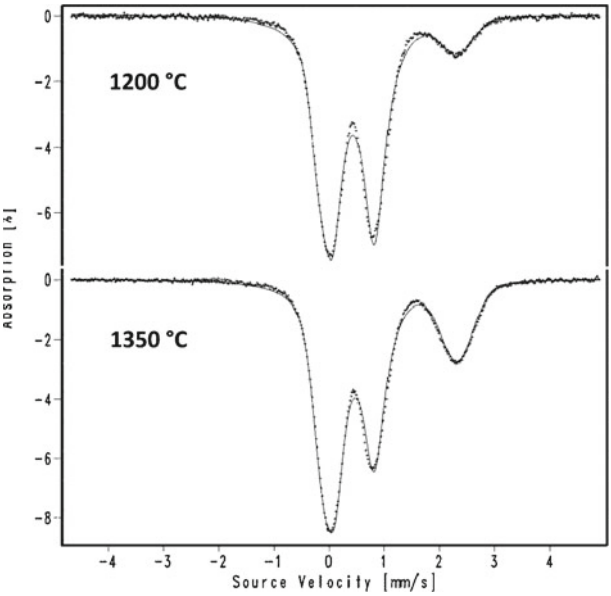

Fig. 6 ^{57}Fe spectra at 23°C of 33%Fe_2O_3-67%P_2O_5 glasses melted at (**a**) 1200°C and (**b**) 1350°C. The fraction of Fe^{2+} increases with increasing temperature and time of melting (Smith et al., private communication)

4 Nanoparticles of iron and iron alloys

Nanoparticles of iron and its alloys are interesting because of the possibility that high temperature phases not normally stable at room temperature may be frozen in by the rapid quenching rate. They also have practical importance as they are

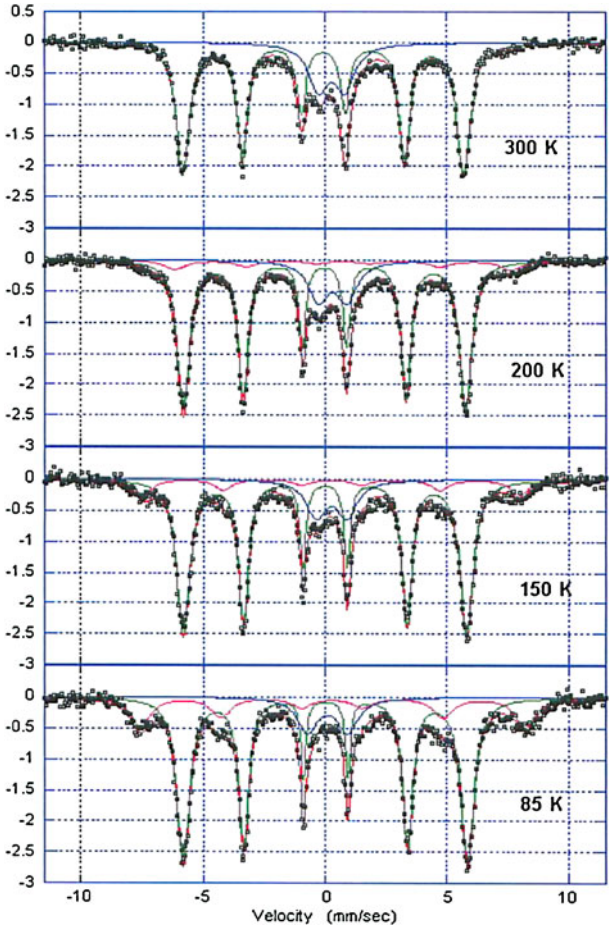

Fig. 7 ^{57}Fe spectra of 20 nm nanoparticles of $Fe_{0.5}Co_{0.5}$. The superparamagnetic oxide film on the surface becomes more apparent at low temperatures [7]

promising candidates for high density magnetic recording owing to their high saturation magnetization and coercivity. Their use may be limited by superparamagnetic fluctuations when the particle size is very small. The inevitable oxidation has a useful effect as it provides a passivating shell which protects the iron from further oxidation [7]. By reducing the interactions between the iron particles this shell can reduce the superparamagnetic fluctuations.

Mössbauer spectra (Shafranovsky et al., private communication) of 20 nm particles of $Fe_{0.5}Co_{0.5}$ at different temperatures are shown in Fig. 7. At 300 K the six lines of iron with a hyperfine field of about 34 T are seen together with a doublet arising from the superparamagnetic oxide coating where the magnetic hyperfine interactions are destroyed by the fluctuations. As the temperature is lowered the fluctuations slow down and the hyperfine lines of the oxide appear outside the iron lines with a field of about 50 T. The coating appears to contain amorphous Fe_3O_4 together with other oxides.

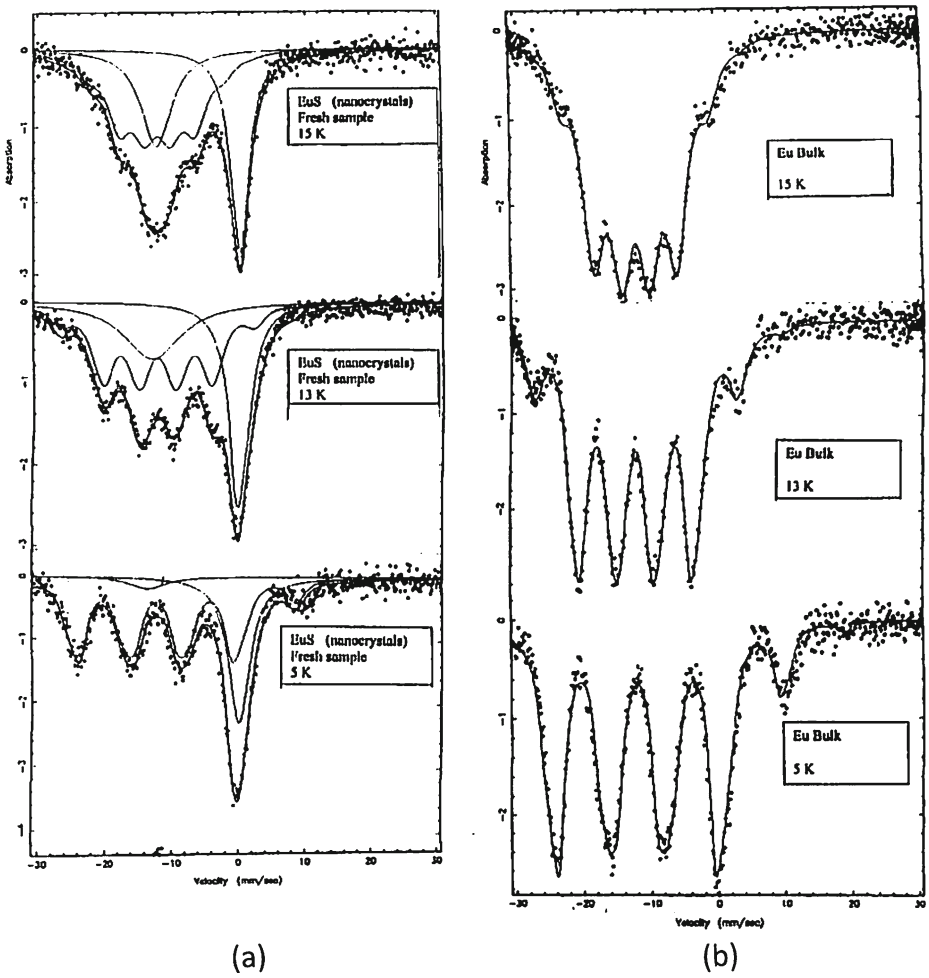

Fig. 8 ^{151}Eu spectra at 5, 13 and 15 K of (**a**) 20 nm EuS nanoparticles (note the Eu^{3+} surface impurity) compared to (**b**) bulk EuS crystals [10]

5 Nanoparticles of Europium (II) sulfide

EuS is a non-metallic ferromagnet with a Curie point $T_c \approx 18$ K. Mössbauer spectra (Dickerson et al. 2011, to be published) of EuS nanoparticles at different temperatures are shown in Fig. 8a, and may be compared with bulk EuS at the same temperatures in Fig. 8b. The spectra of the nanoparticles (Fig. 8a show that a large fraction of the europium has been oxidized to Eu^{3+}, presumably on the surface, with an isomer shift of 0 mm/s relative to the EuF_3 source. The Eu^{2+} line with a shift of −12.9 mm/s initially broadens as the temperature is reduced, characteristic of a superparamagnet, and eventually shows magnetic (Zeeman-like) splitting when the fluctuations have become sufficiently slow. The spectra then are similar to those of a

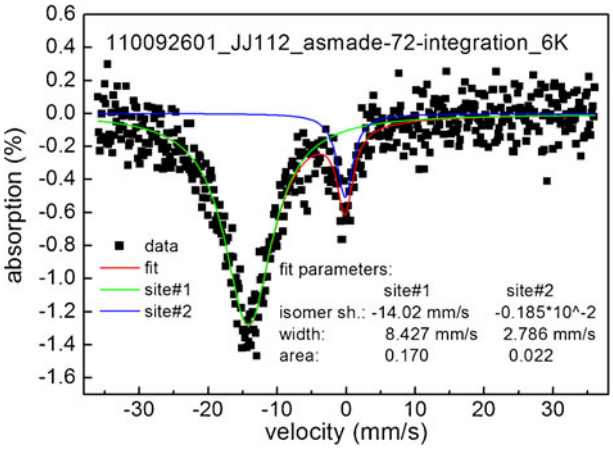

Fig. 9 ^{151}Eu spectra of Eu-doped nanocrystals of $BaCl_2$ in a matrix of a fluorozirconate glass (ZBLAN). About 90% of the Eu is in the Eu^{2+} state (Johnson et al. 2011, to be published)

ferromagnet (Fig. 8b) where the hyperfine splitting increases steadily with decreasing temperature to a saturated value (29 T) at the lowest temperature.

6 Nanocrystals of $BaCl_2$:Eu^{2+} in fluorozirconate glass

Fluorozirconate glasses based on a modified ZBLAN composition show promise as an x-ray image plate for mammography due to the extremely high spatial resolution. Upon heat treatment, these glasses precipitate $BaCl_2$ nanoparticles, which contain divalent europium. Upon x-ray irradiation electron-hole pairs are produced, which are stored until scanned by a laser. The light output is maximized by maintaining europium in the 2+ state therefore it is important to monitor the valence state of the Eu. For several years, the synthesis process has led to a roughly 50% conversion of Eu^{2+} to Eu^{3+}. However, very recent results have enabled us to document the success of maintaining 90% Eu^{2+}. Without Mossbauer spectroscopy this would have been impossible. Figure 9 is the spectrum of a sample showing this result.

7 Conclusion

It would be impossible to do justice to the wide variety of applications of Mössbauer spectroscopy in a short paper, and this is a personal, incomplete and highly selective account of some current work.

Acknowledgements This research is funded by the National Institutes of Health, National Institute Biomedical Imaging and Bioengineering, Award No, RO1 EB 0061145 and the National Science Foundation Award # DMR 1001381.

We thank our collaborators : L. Costa, M. Vu (University of Tennessee Space Institute), D.E. Brown (Northern Illinois University), R.K. Brow, M. Schmitt (University of Missouri, Rolla), E.A. Shafranovsky (Russian Academy of Sciences, Moscow), J.H. Dickerson, S. Somarajan (Vanderbilt University), S. Schweizer, C. Pfau, C Paßlick (University of Halle-Wittenberg, Halle, Germany).

References

1. Hanna, S.S., Heberle, J., Littlejohn, C., Perlow, G.J., Preston, R.S., Vincent, D.H.: Phys. Rev. Lett. **4**, 177 (1960)
2. Kistner, O.C., Sunyar, A.W.: Phys. Rev. Lett. **4**, 412 (1960)
3. Frankel, R.B., Blakemore, R.P., Wolfe, R.S.: Science **203**, 1355 (1979)
4. Johnson, C.E.: Hyp. Int. **49**, 19 (1989)
5. Williams, K.F.E., Johnson, C.E., Greengrass, J., Tilley, B.P., Gelder, D., Johnson, J.A.: J. Non-Cryst. Solids **211**, 164 (1997)
6. Ray, C.S., Fang, X., Karabulut, M., Marasinghe, G.K., Day, D.E.: J. Non-Cryst. Solids **249**, 1 (1999)
7. Shafranovsky, E.A., Petrov, Y.I.: J. Nanopart. Res. **6**, 71 (2004)

Hyperfine Interact (2012) 204:57–64
DOI 10.1007/s10751-011-0512-4

Personal recollections of 52 years of Mössbauer spectroscopy research

Israel Nowik

Published online: 20 December 2011

Abstract The history of the scientific developments of the Mössbauer effect, through 52 years, is discussed in terms of personal observations and participation.

Keywords Paramagnetic relaxation · Intermediate valence · Bound diffusion · Superconductivity · Relativity

1 Introduction

I was exposed to Mössbauer spectroscopy (MES) early in 1959 when Solly Cohen and Shimon Ofer returned from the US to Jerusalem with the great promise for a new method of research, for low energy nuclear physics and hyperfine interactions in solids. I became the first MES student in Jerusalem. Two years later, immediately after accepting the Nobel Prize, Mössbauer the person, arrived directly from Stockholm to Jerusalem to present us, his Nobel Prize lecture. In the summer of 1970 I spent 4 months in Garching doing research with Mössbauer's group. Mössbauer visited Jerusalem several times. In one of his early visits he posed for a picture together with his hosts and Professor Felix Bloch (Bloch waves and NMR) who was also present (Fig. 1).

In the first few years MES served the nuclear physicists in their pursuit for new MES isotopes, their nuclear moments and radii. The isotopes ^{161}Dy and ^{160}Dy were discovered in Jerusalem [1].

Only a few experiments were devoted to general physics, like relativity [2, 3] interference, γ-ray optics [4], start time dependent MES [5] (all of great interest today with Synchrotron MES). The state of the art in the first four years was well documented in Frauenfelder's book [6].

I. Nowik (✉)
Racah Institute of Physics, The Hebrew University, Jerusalem 91904, Israel
e-mail: nowik@vms.huji.ac.il

Fig. 1 From right to left: The Professors R. L. Mössbauer, S. Ofer, S. G. Cohen and Felix Bloch

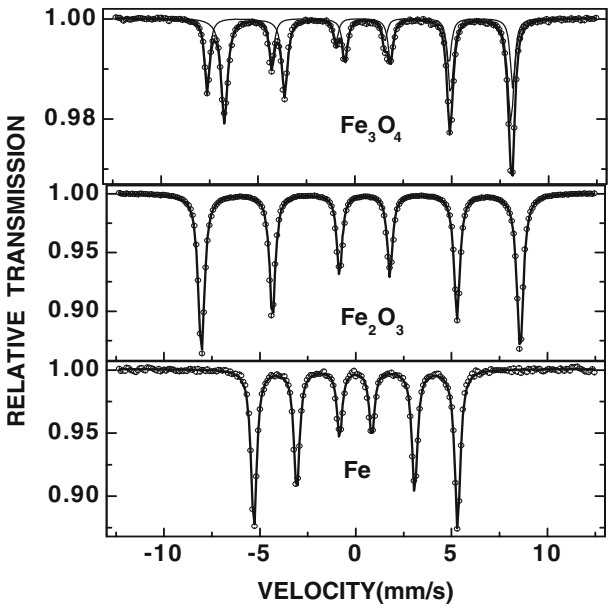

Fig. 2 Room temperature Mössbauer spectra of the most common magnetic materials

Very soon Physicists and Chemists joined with extensive studies of solid-state properties. All branches of Chemistry were investigated. The largest number of publications and books [7] are devoted to these subjects. All thermodynamic phase transitions were studied. New unexpected dynamic phenomena, directly observable in the spectrum like: spin relaxation [8, 9] in iron, and in all rare earths and actinides, spin crossover and transitions in iron compounds [10], intermediate valence and valence changes [11] in iron, europium, samarium and even neptunium, and bound diffusion [12], were all discovered in a very wide range of compounds.

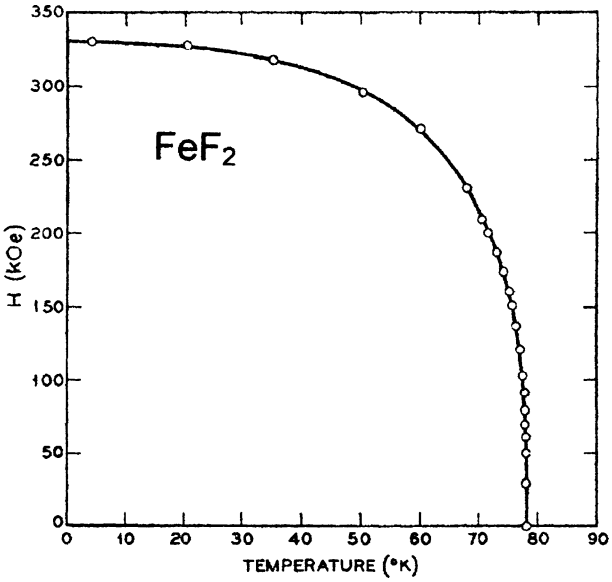

Fig. 3 The temperature dependence of the internal magnetic field acting on Fe in FeF_2 [21]

Researchers interested in biological compounds, found in MES a very useful tool. They found that live biological systems are, in many characteristics, a unique phase of matter, in between solid and liquid. The associated theory explained well the observed phenomena [13, 14].

Superconductivity was always of interest for MES researchers. But only the discoveries of magneto-superconductors, in particular those with high T_c, made the MES research contribution significant [15, 16]. Coexistence of magnetic order and superconductivity is now well established.

During the last 52 years I was involved in some of the research projects mentioned above, performed in Jerusalem (with S. G. Cohen, S. Ofer, E. R. Bauminger, I. Felner and R. H. Herber), Bell Telephone Laboratories (with H. H. Wickman and R. L. Cohen), Argonne National Laboratory (with B. D. Dunlap), Technical University of Munich (with G. M. Kalvius) and the Free University of Berlin (with G. Kaindl and G. Wortmann)

In the present short review, the historical aspects and the scientists involved in the most interesting of the subjects mentioned above will be given. The recent studies of magneto-superconductors (with FeAs and FeSe) and the experiment for the discovery of a possible existence of a maximum acceleration in General Relativity [17] will be presented.

2 Detailed discussion

One of the early prominent studies concerned the subject of magnetism in solids. Just the discovery that one can measure so easily the magnetic Zeeman splitting of nuclear levels (magnetic hyperfine structure) was unbelievable earlier. The most

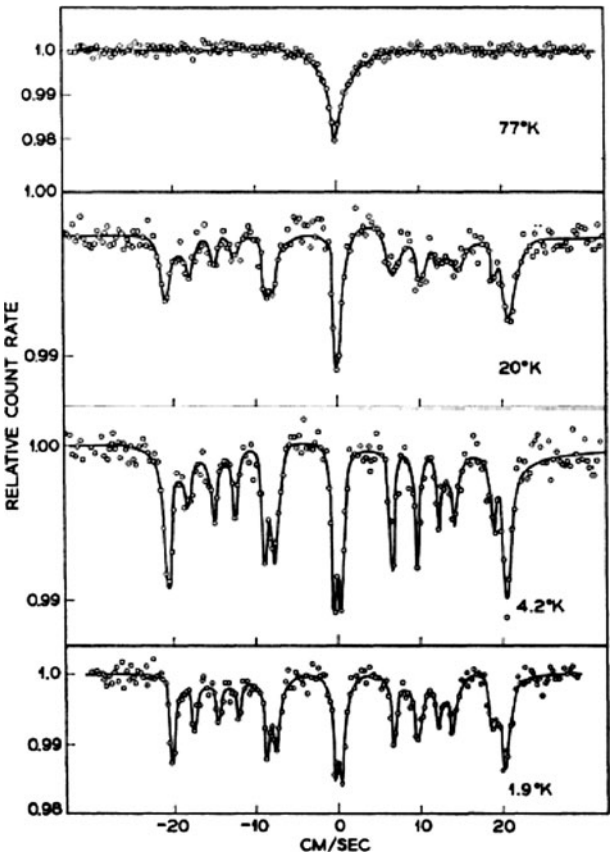

Fig. 4 The 26 keV Mössbauer spectra of ^{161}Dy in dysprosium aluminum garnet ($Dy_3Al_5O_{12}$) [22]

common magnetic iron compounds were immediately studied, Fig. 2. The discovery of many rare earth Mössbauer isotopes prompted studies of magnetic compounds of rare earths (this was the subject of my PhD thesis).

The high resolution of the ^{57}Fe Mössbauer 14.4 keV urged scientists to try to test General relativity in their laboratory. The successful measurement of the "gravitational weight" of a photon was sensational [2]. The story tells that another group made the same experiment. In an internal seminar the experiment was displayed, and an undergraduate student asked about the source and absorber temperature, when answered "why is it important?" he explained the importance, and published it [18]. He has discovered what is known today as the thermal shift, which is also the relativistic second order Doppler shift. The student was B. D. Josephson, who won later the Nobel Prize for much more important discoveries. W. Kündig performed an experiment [3] in which he tried to measure directly the second order Doppler shift, with an absorber moving perpendicular to the direction of the γ-ray. Quantum beats due to interference phenomena, were discovered by G. J. Perlow [19, 20].

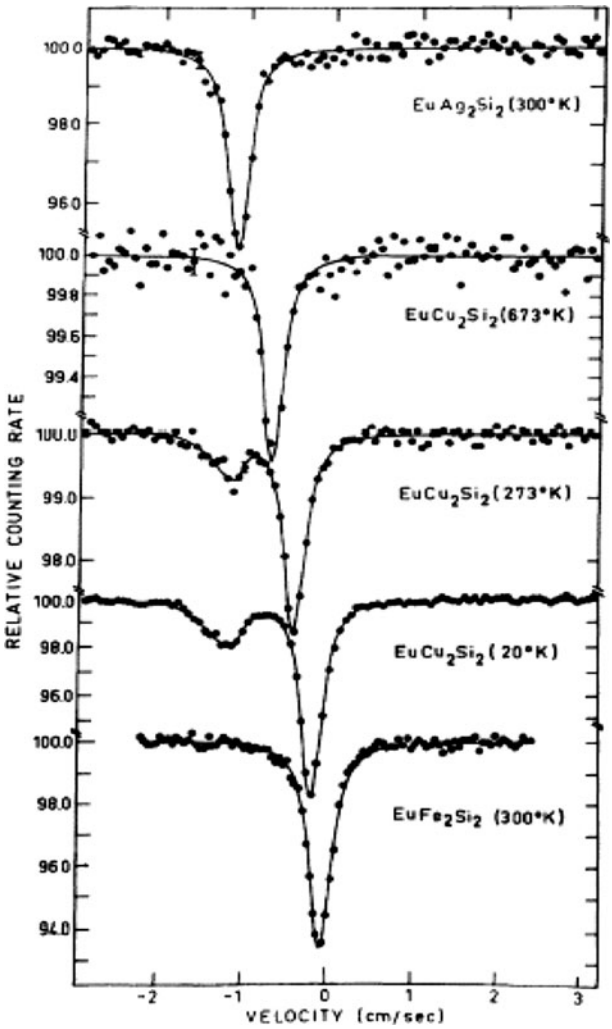

Fig. 5 ^{151}Eu Mössbauer spectra of temperature dependent valence in $EuCu_2Si_2$ [11]

Among the various phase transitions the most investigated were the magnetic transitions, studied by recording the temperature dependence of the hyperfine field. One of the first was that by G.K. Wertheim [21] shown in Fig. 3.

The dynamic phenomenon of spin relaxation in paramagnetic compounds was discovered for iron and then also for many rare earth isotopes [9]. The phenomenon in magnetically ordered systems was very shortly also observed [8]. Typical relaxation spectra in paramagnetic $Dy_3Al_5O_{12}$ are shown in Fig. 4.

The phenomenon of intermediate valence in rare earth compounds [23] started with $EuCu_2Si_2$ [11], shown in Fig. 5.

The phenomenon of bound diffusion in biological systems [12], has been studied by P. Parak's group [14], by R. L. Mössbauer [24], and by our group. The theoretical

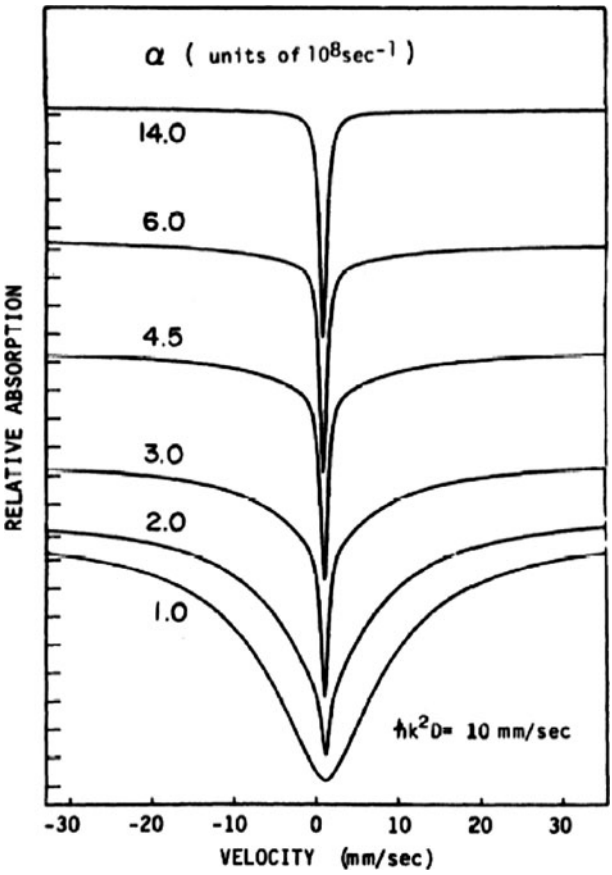

Fig. 6 Theoretical curves demonstrating how bound diffusion, with the decay rate (α) of a local deviation of a Mössbauer nucleus, to it's average position increases with temperature, leads from a narrow solid like absorption line to a very broad liquid like absorption line [13]

curves showing how a solid-like biological system, undergoing bound diffusion (relaxation rate increases with temperature), becomes liquid like, is shown in Fig. 6.

Mössbauer studies of magnetism in superconducting materials are very popular these days, due to the discovery of the FeAs [16] and lately the FeSe systems. From our studies we conclude that when the iron magnetic order is of spin density wave type, like in $EuFe_2(As_{1-x}P_x)_2$ [25], the appearance of superconductivity for certain x values destroys the spin density magnetism. However in the temperature rang in which the europium is magnetically ordered a transferred hyperfine field is observed even when the material is superconducting [25], Fig. 7. In the FeSe materials [26], the iron has a local moment and a large hyperfine field even at room temperature, and orders magnetically around 500 K. In this case the superconductivity and the magnetic order seem not affect each other.

Y. Friedman predicts [17] that General Relativity requires not only an absolute maximal velocity c, but also a maximal acceleration a_m. According to Friedman the second order Doppler shift for an absorber moving with velocity v and acceleration "a" in a direction perpendicular to the γ-ray is given by the formula: $-{}^1/_2 v^2/c^2 - {}^1/_2 a/a_m$. He argues that a correct analysis of the Kündig experiment [3] does not

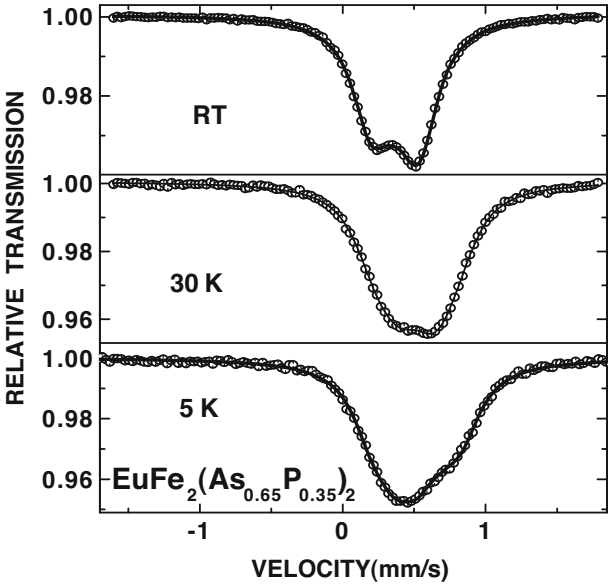

Fig. 7 ^{57}Fe spectra of $EuFe_2(As_{0.65}P_{0.35})_2$ at 5.0 K, in the superconducting state of the FeAs layers, at 30 K above T_M ~27 K of Eu, and at 297 K [25]

agree with the simple relativity formula and suggested an experiment in which the shift due to mechanical rotation will depend only on the centripetal acceleration. We are in the process of carrying out this experiment.

References

1. Bauminger, E.R., Cohen, S.G., Marinov, A., Ofer S.: Phys. Rev. Lett. **6**, 467 (1961)
2. Pound, R.V., Rebka G.A.: Phys. Rev. Lett. **4**, 337 (1960)
3. Kündig, W.: Phys. Rev. **129**, 2371 (1963)
4. Nowik, I.: Phys. Rev. **126**, 1878 (1962)
5. Lynch, F.J., Holland, R.E., Hamermesh, M.: Phys. Rev. **120**, 513 (1960)
6. Frauenfelder, H.: The Mössbauer Effect: A Review – with a Collection of Reprints (Frontiers in Physics Series), W. A. Benjamin (1962)
7. List of Mössbauer books is given in the web site www.mossbauer.org (2011). Accessed 15 Dec 2011
8. Nowik, I., Wickman, H.H.: Phys. Rev. Lett. **17**, 949 (1966)
9. Wichman, H.H., Wertheim, G.K.: Chap. 11 In: V.I. Goldanskii, R.H. Herber (eds.) Chemical Applications of Mössbauer Spectroscopy. Academic Press (1968)
10. Gutlich, P.: Struct. Bond. **44**, 83 (1981)
11. Bauminger, E.R., Froindlich, D., Nowik, I., Ofer, S., Felner, I., Mayer, I.: Phys. Rev. Lett. **30**, 1053 (1973)
12. Cohen, S.G., Bauminger, E.R., Nowik, I., Ofer, S.: Phys. Rev. Lett. **46**, 124 (1981)
13. Nowik, I., Cohen, S.G., Bauminger, E.R., Ofer, S.: Phys. Rev. Letters **50**, 1528 (1983)
14. Parak, P., Knapp, E.W.: Proc. Natl. Acad. Sci. Biophys. **81**, 7088 (1984)
15. Felner, I., Nowik, I.: Supercond. Sci. Technol. **8**, 121 (1995)
16. Nowik, I., Felner, I.: Phys. C –Supercond. Appl. **469**, 485 (2009)
17. Friedman, Y.: Ann. Phys. **523**, 408 (2011)
18. Josephson, B.D.: Phys. Rev. Lett. **4**, 341 (1960)
19. Perlow, G.J.: Phys. Rev. Lett. **40**, 896 (1978)
20. Monahan, J.E., Perlow, G.J.: Phys. Rev. A **20**, 1499 (1979)
21. Wertheim, G.K.: Phys. Rev. **161**, 478 (1967)

22. Nowik, I., Wickman, H.H.: Phys. Rev. **140**, 860 (1965)
23. Nowik, I.: Hyperfine Interact. **13**, 89 (1983)
24. Mössbauer, R.L.: Hyperfine Interact. **33**, 199 (1987)
25. Nowik, I., Felner, I., Ren, Z., Cao, G.H., Xu, Z.A.: J. Phys. Condens. Matter **23**, 065701 (2011)
26. Nowik, I., Felner, I., Zhang, M., Wang, A.F., Chen, K.H.: Supercond. Sci. Technol. **24**, 095015 (2011)

Hyperfine Interact (2012) 204:65–70
DOI 10.1007/s10751-011-0513-3

Future diffusion studies with new X-ray sources

G. Vogl

Published online: 13 December 2011

Abstract I report on two rather new applications of highly brilliant synchrotron X-radiation for studying diffusion in solids, and try to give hints on further exploitation of these achievements.

Keywords Diffusion · Nuclear resonance scattering · Mössbauer effect · XPCS · Correlation spectroscopy · Surface diffusion · Scattering

1 Surface diffusion with nuclear resonant scattering (NRS) of ^{57}Fe synchrotron radiation

The intensity of synchrotron radiation re-emitted from a "Mössbauer level" in forward direction after nuclear resonance absorption (Mössbauer effect) decays exponentially, if the scattering sample is sufficiently thin and hyperfine interactions are absent (Fig. 1). If, however, the re-emitting nuclei are diffusing with characteristic jump times τ of the order of the Mössbauer level's life time τ_0 or faster, then the coherence of the re-emitted radiation will be disturbed and the decay will apparently be accelerated.

According to Smirnov and Kohn [1, 2], the forward scattered intensity is essentially the square of the momentum-time scattering function

$$S(\mathbf{Q}, t) = \exp\left[(-t/\tau)\left(1 - \sum\nolimits_i p_i \cos(\mathbf{s}_i \mathbf{Q})\right)\right]$$

with p_i the probabilities for jumps, $\mathbf{s}_i$ the jump vectors, $\mathbf{Q}$ the scattering vector.

It is evident that the faster the atom jumps (the shorter τ), the steeper will be the decay of the forward scattered intensity.

G. Vogl (✉)
Dynamics of Condensed Systems, Fakultät für Physik der Universität Wien, Strudlhofgasse 4, 1090 Wien, Austria
e-mail: gero.vogl@univie.ac.at

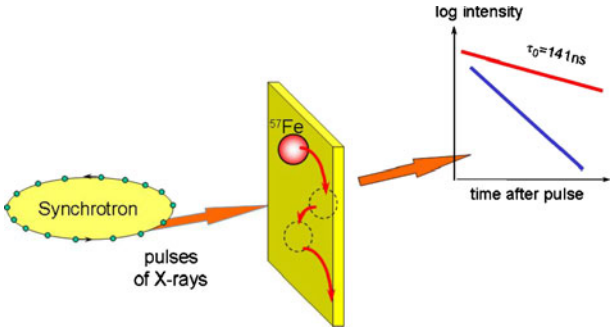

Fig. 1 The logarithm of the intensity of NRS from ^{57}Fe in forward direction decays linearly with characteristic time of 141 ns in absence of diffusion (*red line*). When the scattering atoms diffuse, the coherence of the forward scattered beam is lost and the decay is accelerated (*blue line*)

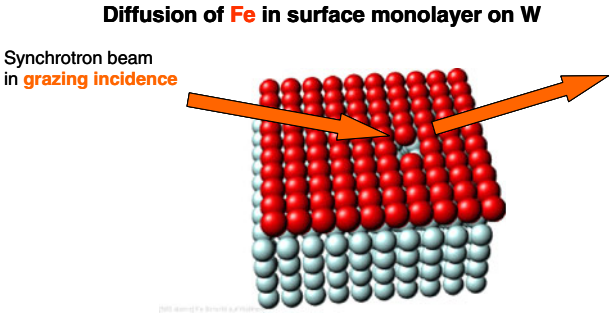

Fig. 2 Diffusion of iron atom by help of a vacancy in surface monolayer on tungsten. The arrows symbolize synchrotron X-radiation incoming and scattered in grazing incidence geometry

This has been experimentally proven by Sepiol et al. [3, 4] in 1999. The results for diffusion of iron in intermetallic alloys agreed essentially with the results from conventional Mössbauer spectroscopy [5]. It therefore appeared as a necessary challenge to apply the method of nuclear resonant forward scattering to systems not accessible to conventional Mössbauer spectroscopy.

Two dimensional systems represent such case. Whereas the intensity achievable with radioactive Mössbauer sources is not sufficiently high for receiving spectra of 10^{15} nuclei or less (the number of atoms in an iron monolayer with a diameter of several millimeters) within reasonable measurement times, the brilliance of synchrotrons of third generation enables such research. The monolayer has to be hit by the synchrotron beam in grazing incidence. For scattering in forward direction we may expect diffusional acceleration of the nuclear decay and a change of the quadrupole interaction when the Mössbauer atom starts jumping (Fig. 2).

The experiment was carried out at the nuclear resonance beamline ID18 [6] at the European Synchrotron Radiation Facility using a recently constructed multifunctional ultrahigh-vacuum system [7].

The experiment (Fig. 3) gives indeed the expected information.

At room temperature the intensity decays essentially with the nuclear life time (141 ns) of the 14.4 keV first excited level of ^{57}Fe. At 723 K, on the contrary, the decay appears to be much faster. In addition there is a beat with its maximum at about 80 ns. After cooling the sample down again to room temperature the decay is nearly the same as before the heating procedure, i.e. almost a straight line on a logarithmic scale.

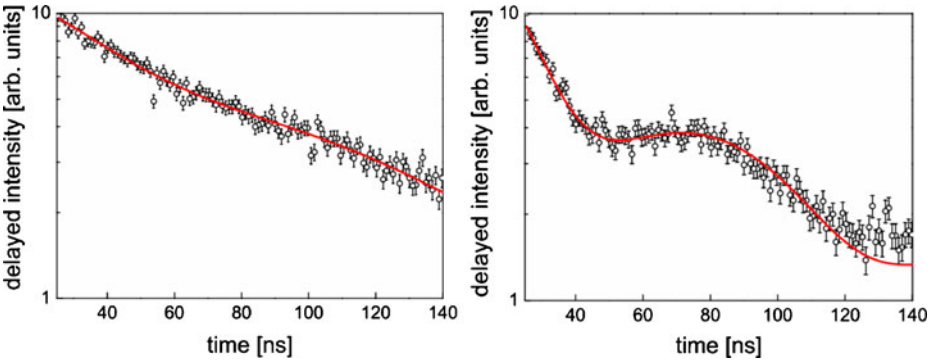

Fig. 3 Forward scattering from ^{57}Fe jumping in an iron monolayer on tungsten. Left: data taken at room temperature, right: data at 723 K. From [8]

Assuming that the change in the spectrum is caused by defects jumping in the surface, from the temperature dependence of the size of the beat and the steepness of the temporal decay, activation energies of formation and migration of the defects can be estimated.

This investigation [8] is meant as a demonstration of what could be achieved in the field of diffusion in and on surfaces and in monolayers by using highly brilliant synchrotron X-radiation. For determining the angular dependence of the diffusionally accelerated decay of forward scattering – and so the elementary diffusion jump as has been achieved in bulk iron alloys – further studies are necessary. To follow the diffusion of ad-atoms, i.e. of atoms diffusing *on* surfaces, a longer way remains to be gone. Such studies would be highly rewarding since they could contribute to our understanding of the dynamics of physical and chemical adsorption at surfaces [9]. X-ray sources with higher brightness are desirable for pursuing that goal.

2 X-ray photon correlation spectroscopy (XPCS)

Nearly a decade ago the question arose whether it would be possible to study the diffusion jump in a time regime inaccessible to the nuclear methods like Mössbauer and neutron scattering by using XPCS [10]. XPCS is a daughter of PCS which makes use of the coherence of laser light. What is registered in PCS and XPCS is the loss in correlation of a pattern of intensities, called "speckles" because of the interchange of brighter (constructive interference of the coherent light) and darker (destructive interference) scattered into a manifold of directions, i.e. for a segment of k-space, due to dynamics in the specimen.

Beginning from 1990 XPCS had be developed to a level where it had been possible to follow the diffusion of larger particles by way of small-angle XPCS [11–13], i.e. scattering in the neighbourhood of Bragg reflections. For taking subsequent "frames" (speckle patterns of sections of k-space, Fig. 4 shows how a speckle pattern looks like) because of time needed for counting and managing the counts, times of seconds to minutes are needed. Therefore characteristic diffusion times accessible to investigation are of that order.

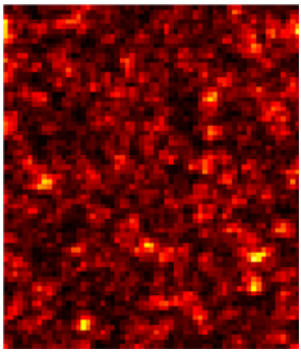

Fig. 4 False colour pattern of constructive and destructive interferences (brighter and darker pixels, called "speckle pattern") of partially coherent X-ray light in k-space. Segment of picture taken with CCD pixel detector, pixel size $20 \times 20\ \mu m^2$. 8 keV X-rays

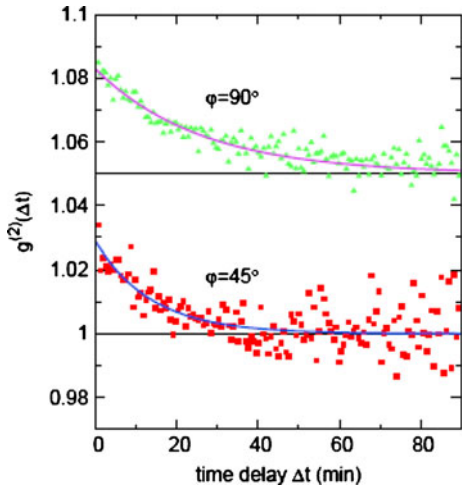

Fig. 5 Temporal intensity-autocorrelations, variation with position in reciprocal space. Temperature 270°C, scattering angle 25°, two different azimutal angles. The top plot is shifted by 0.05 for better clarity. From [14]

Now the challenge arose that the regime for the diffusion *of single atoms* is in k-space far outside the Bragg reflections, i.e. in the range of diffuse scattering. There the intensity is extremely small and it appeared most improbable that with present synchrotrons sufficient coherent intensity would be available.

Yet in 2009 choosing a binary alloy with large differences in electronic scattering of the components and making use of improved 1340×1300 pixel detectors, first results of correlation relaxation in the diffuse scattering regime were achieved, and from measurements on single crystals of CuAu it became possible to deduce frequency and vector of the diffusion jump [14]. To this aim the primary synchrotron beam had to be severely reduced, eventually by a beam hole of about 10 μm in diameter, in order to guarantee a sufficiently high fraction of coherent intensity which even then remained only in the order of ten percent. Figure 5 shows first results. Here $g^{(2)}(\Delta t)$ is the intensity correlation, it is plotted a function of the delay time between two frames. $g^{(2)}(\Delta t)$ is intimately related to the momentum-time correlation function $S(\mathbf{Q},\omega)$ as measured by nuclear resonance scattering (paragraph 1). As an intensity it is essentially proportional to the square of $S(\mathbf{Q},\omega)$. Experience with Mössbauer effect therefore paved the way to proving the feasibility of XPCS for studies of the elementary diffusion jump.

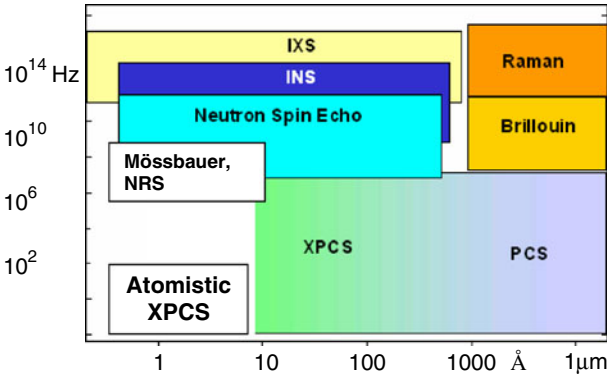

Fig. 6 Resolution of methods probing dynamics on length and time scale

Figure 5 proves that the decay times of correlation differ significantly for data taken at azimutal angles of 45 and 90°. From the correlation decay the jump frequency and from its angular or **Q**–dependence the jump vector were deduced for the case of diffusion in short-range ordered Cu-10at.%Fe. [14].

It appears from Fig. 6 that now the whole length and time range of diffusion is accessible to investigation, including very slow diffusion, even though faster XPCS would be desirable in order to fill the time range between "Atomistic XPCS" and Mössbauer/NRS/neutron scattering. This should be progressively possible with the upcoming of X-ray sources with higher brilliance. Already now, Petra 3 promises to improve the brilliance significantly. Whether the free electron lasers sprouting in various places of the world will further improve the possibilities of diffusion studies, has still to be seen. However, already now we can state that the future in the field of diffusion remains exciting.

Acknowledgements This is of course only very marginally my own work, I have essentially been the person giving ideas and demanding experimental solutions.

The NRS work on surface diffusion is broadly the work of Eva Partyka-Jankowska, and many other colleagues have contributed. From the ESRF side that were Sascha Chumakov and Rudolf Rüffer of ID 18, and the ultrahigh-vaccuum facilities (but not only these) were set up by Svetli Stankov. All the experience of the Cracow group of Jozef Korecki has flown in, members of that group, particularly Marcin Zajac, having contributed to the experiments, and of course the experience of my Vienna group led by Bogdan Sepiol.

The XPCS work resulted in discussions I had ten years ago with Gerhard Grübel who supported us also further on. From the ESRF it has been the team of ID 10, in particular Anders Madsen. From my Vienna group Lorenz Stadler conducted the first path-breaking experiments, and later on it was in particular Michael Leitner who showed how to succeed. And again always Bogdan Sepiol with his great experience and broad knowledge experimentally and theoretically as well.

A number of projects financed by the Austrian Fonds zu Förderung der Wissenschaftlichen Forschung furnished the financial basis for our research, among others P-20713-N20 and P-17775. Not to forget the Austrian Ministerium für Wissenschaft und Forschung (MR Dr. Daniel Weselka et al.) which guaranteed the Austrian membership to the ESRF.

References

1. Smirnov, G.V., Kohn,V.G.: Phys. Rev. B **52**, 3356 (1995)
2. Kohn, V.G., Smirnov, G.V.: Phys. Rev. **57**, 5788 (1998)

3. Sepiol, B., Meyer, A., Vogl, G., Rüffer , R., Chumakov, A.I., Baron, A.Q.R.: Phys. Rev. Lett. **76**, 3220 (1996)
4. Sepiol, B., et al.: Phys.Rev. B **57**, 10433 (1998)
5. Sepiol, B., Vogl, G.: Phys. Rev. Lett. **71**, 731 (1993)
6. Rüffer, R., Chumakov, A.I.: Hyperfine Interact. **97**, 589 (1996)
7. Stankov, S., et al.: Phys. Sci. Instr. **79**, 045108 (2008)
8. Vogl, G., Partyka-Jankowska, E., Zając, M., Chumakov, A.I.: Phys. Rev. B **80**, 115406 (2009)
9. Ertl, G.: Angew. Chem. Int. Ed. **47**, 3524 (2008)
10. Grübel, G., Vogl, G.: Synchrotron Radiat. News **15**, 14 (2002)
11. Brauer, S., et al.: Phys. Rev. Lett. **74**, 2010 (1995)
12. Stadler, L.-M., et al.: Phys. Rev. B **68**, 189101(R) (2003)
13. Stadler, L.-M., et al.: Phys.Rev. E **74**, 041107 (2006)
14. Leitner, M., Sepiol, B., Stadler, L.-M., Pfau, B., Vogl, G.: Nature Mater. **8**, 717 (2009)

Hyperfine Interact (2012) 204:71–81
DOI 10.1007/s10751-011-0500-8

Redox topotactic reactions in Fe^{II-III} (oxy)hydroxycarbonate new minerals related to fougèrite in gleysols: "trébeurdenite and mössbauerite"

Jean-Marie R. Génin · O. Guérin · A. J. Herbillon · E. Kuzmann · S. J. Mills · G. Morin · G. Ona-Nguema · C. Ruby · C. Upadhyay

Published online: 13 January 2012

Abstract Fougèrite mineral responsible for the bluish-green shade of gleysols in aquifers was identified as Fe^{II-III} oxyhydroxycarbonate, $[Fe^{II}_{6(1-x)}Fe^{III}_{6x}O_{12}H_{2(7-3x)}]^{2+} \cdot [CO_3^{2-} \cdot 3H_2O]^{2-}$ where the average ferric molar fraction $x = [Fe^{III}/Fe_{total}]$ was restricted to the [1/3–2/3] range, up till now. In this paper, Mössbauer spectra of gleys extracted from the schorre of maritime marshes have values of x in the [2/3–1] range. Magnetic properties of homologous chemical compounds studied by Mössbauer

J.-M. R. Génin (✉) · C. Ruby
Institut Jean Barriol FR2843 CNRS-Université de Lorraine, ESSTIN, 2 rue Jean Lamour, 54500 Vandoeuvre-Lès-Nancy, France
e-mail: jean-marie.genin@esstin.uhp-nancy.fr

O. Guérin
Laboratoire de Géomorphologie, Ecole Pratique des Hautes Etudes, 15 bd de la mer, 35800 Dinard, France

A. J. Herbillon
Unité des Sciences du Sol, Université Catholique de Louvain, 1348 Louvain-la-Neuve, Belgium

E. Kuzmann
Chemistry Department, Eötvös Lorand Univ., Pazmany Peter setany, 1117, Budapest, Hungary

S. J. Mills
Geosciences Museum Victoria, GPO Box 666, Melbourne 3001, Australia

G. Morin · G. Ona-Nguema
Institut Minéralogie & Phys. Milieux Condensés, Univ. P. & M. Curie, 75252 Paris, France

C. Upadhyay
School of Materials Science & Technology, IT-Banaras Hindu Univ., 221005 Varanasi, India

spectroscopy are explained with long range order of Fe^{III} ions within Fe cation layers for $x = 1/3$, 2/3 and 1. Observed values are mixtures of topotactic domains that are in fact minerals with names proposed to IMA: fougèrite for $x = 1/3$, trébeurdenite for $x = 2/3$ and mössbauerite for $x = 1$.

Keywords Fe^{II-III} (oxy)hydroxycarbonate · Green rust · Mössbauer spectroscopy · Fougèrite · Trébeurdenite · Mössbauerite · Topotaxy

1 Introduction

Redox reactions in soils are of utmost importance for understanding their genesis but also the mechanisms of their remediation in view of sustainable development. For instance, we are involved in programs of denitrification in Brittany (France) where a proliferation of green algae is due to intensive agricultural practice and Fe^{II-III} green rusts which are able to reduce nitrates are forwarded [1, 2]. In parallel, the same type of compounds was found in natural "gleysols" [3, 4]. Thus, in this paper, we intend to compare gleysols found in continental aquifers with those in maritime marshes.

Gleys are ubiquitous, wherever water lies in soils; their shade goes from bluish-green to ocher through olive green. Mössbauer spectra allowed us to show that this phenomenon was due to the presence of iron containing compounds strongly resembling Fe^{II-III} hydroxycarbonate green rust, $GR(CO_3^{2-})$, that was studied for its intermediate role during the corrosion of iron-based materials [5–7]. $GR(CO_3^{2-})$ belongs to the layered double hydroxide family; it consists in stacking brucite-like $[Fe^{II}_4Fe^{III}_2(OH)_{12}]^{2+}$ layers that alternate with $[CO_3 \cdot 3\ H_2O]^{2-}$ interlayers within $R\bar{3}\,m$ space group [8–10]. $GR(CO_3^{2-})$ usually gets oxidised into ferrihydrite that evolves to goethite by aerial oxidation [11, 12]; this process is responsible for the corrosion of iron since $GR(CO_3^{2-})$ is dissolved by rejecting the anions into solution and Fe^{III} ions, that form, precipitate as a ferric solid. In contrast, it was demonstrated recently that it could also follow another route by *in situ* oxidation into a "ferric green rust" $GR(CO_3^{2-})$*, $[Fe^{III}_6O_4(OH)_8]^{2+} \cdot [CO_3 \cdot 3H_2O]^{2-}$, where some OH^- ions get deprotonated [12, 13]. For instance, any intermediate value of ferric molar fraction $x = [Fe^{III}/Fe_{total}]$ from 0.33 to 1 can be reached by oxidising a synthetic $GR(CO_3^{2-})$, if one uses an appropriate amount of H_2O_2 solution that leads to Fe^{II-III} (oxy)hydroxycarbonate, $[Fe^{II}_{6(1-x)}Fe^{III}_{6x}O_{12}H_{2(7-3x)}]^{2+} \cdot [CO_3^{2-} \cdot 3H_2O]^{2-}$, where $x \in [0.33,1]$ [13, 14].

The identification of a green rust in a "gleysol" was first accomplished in 1996 with samples extracted from the aquifer of the State owned forest of Fougères (Brittany-France) and the mineral was thus christened fougèrite (IMA2003–057) [3, 4]. Up till now, samples were taken out of permanently waterlogged gleys that lie in water tables and measurements accomplished by Mössbauer spectroscopy showed that the value of x was restricted to the [1/3–2/3] range [15, 16]. In this paper, samples that are extracted from gleys lying in maritime marshes display values of x in the [2/3–1] range and, consequently, the definition of fougèrite must be revisited whereas the existence of two new minerals related to $GR(CO_3^{2-})$ must be forwarded, the names of which, trébeurdenite and mössbauerite, are proposed.

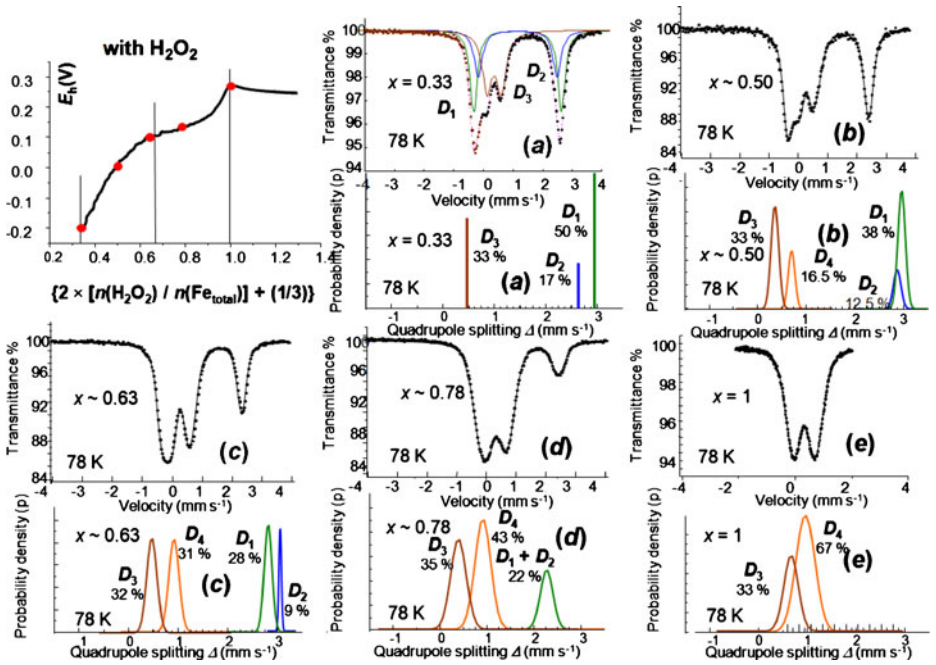

Fig. 1 Mössbauer spectra measured at 78 K of a set of Fe^{II-III}oxyhydroxycarbonate green rust samples during depronation as followed by the electrode potential E_h of the solution vs the amount of H_2O_2 poured into solution for values of $x = [Fe^{III}]/[Fe_{total}]$ ranging from 0.33 to 1. The experimental values that are obtained are 0.33, 0.50, 0.63, 0.78 and 1. Under each spectrum, Gaussian distributions of quadrupole splitting by fitting Voigt profile doublets (from [8, 12, 14])

2 Experimental

Almost all beaches of Northern Brittany and of the bay of Mont Saint Michel present levels of clayey sediments, sometimes developed on several meters. These fine sediments display a characteristic blue color, corresponding to ancient salt marshes in which halophyte roots are easily recognized. These marshes have developed behind foredunes or shingle bars and were filled with sediments of marine origin or coastal river input, mainly between 4000 and 3000 years BP at a time when the sea level was low. In Northern Brittany, the erosion of quaternary cliffs provides silky sediments into these old salt marshes, which locally take advantage of three factors for their settlement and conservation, namely fine sediment supplies, appropriate tidal range and level, and finally, sheltered location.

In the bay of Mont Saint Michel, a high proportion of carbonate fraction indicates an important or even prevailing supply of shelly bioclasts. Most of the present salt marshes have resulted in an active filling with sedimentary supply of about one million m^3 per year. The more or less carbonated sediments are saturated with water and rich biological substances (diatoms) and their colors vary most of the time from grey to black. Blue "marls" are only found in some few places where sediments are compacted; this would suggest that the gley we have sampled in these old fossil salt marshes at many scattered locations in the bay contains minerals in the course of

Table 1 Hyperfine parameters of GR(CO_3^{2-})* for $x = [Fe^{III}]/[Fe_{total}] \in [(1/3)\text{-}1]$ (from [14])

	Quadrupole doublets	δ(mm s^{-1})	$<\Delta>$(mm s^{-1})	$<\delta\Delta>$ (mm s^{-1})	*RA* (%)
$x = 0.33$					
Fe^{II}	D_1	1.25	2.92	0	50
	D_2	1.25	2.63	0	17
Fe^{III}	D_3	0.48	0.47	0	33
$x \sim 0.50$					
Fe^{II}	D_1	1.21	2.98	0.14	38
	D_2	1.21	2.72	0.16	12.5
Fe^{III}	D_3	0.49	0.40	0.15	33
	D_4	0.49	0.70	0.28	16.5
$x \sim 0.63$					
Fe^{II}	D_1	1.24	2.80	0.15	28
	D_2	1.24	3.05	0.05	9
Fe^{III}	D_3	0.48	0.49	0.20	32
	D_4	0.48	0.90	0.21	31
$x \sim 0.78$					
Fe^{II}	$D_1 + D_2$	1.21	2.89	0.31	22
Fe^{III}	D_3	0.47	0.45	0.32	35
	D_4	0.47	0.95	0.34	43
$x = 1$					
Fe^{III}	D_3	0.47	0.60	0.30	33
	D_4	0.47	0.88	0.41	67

Values of x experimentally obtained are approximately 0.50, 0.63 and 0.78 and precisely 0.33 and 1. Spectra are measured at 78 K (Fig. 2) and fitting uses a Voigt profile. δ : isomer shift in mm s^{-1} (reference is α-iron at ambient), $<\Delta>$: mean value of quadrupole splitting in mm s^{-1} and $<\delta\Delta>$: its standard deviation; *RA*(%): relative area

diagenesis. The samples were extracted from the beaches at low tide at a reasonable depth (less than one meter) and no particular precautions were taken for conservation once they are completely dry. Mössbauer spectra were done by transmission and computed with a classical least-square fit procedure using Lorentzian shape lines. Displayed spectra are examples of many others intended to study the diagenesis of maritime gleys and sediments out of the scope of this paper.

Since Mössbauer spectra of the natural samples must be compared to those of the corresponding synthetic compounds measured at 78 K, let us recall the procedure for preparing the synthetic samples [8, 12, 14]: (i) GR(CO_3^{2-}) was coprecipitated by mixing ferrous and ferric sulphates in a 2:1 [Fe^{II}]/[Fe^{III}] ratio in the presence of HCO_3Na, (ii) hydrogen peroxide was introduced with a peristaltic pump into the GR(CO_3^{2-}) solution while the electrode potential E_h was followed versus the amount of H_2O_2 (Fig. 1). Four samples were measured at 78 K by transmission Mössbauer spectroscopy besides the initial GR(CO_3^{2-}) at values of $x = 0.50, 0.63, 0.78$, and 1 (Fig. 1, Table 1).

3 Results and discussion

Spectra were fitted by a deconvolution procedure with Voigt profile (Fig. 1) and results yielded values of isomer shift δ and quadrupole splitting Δ with the standard

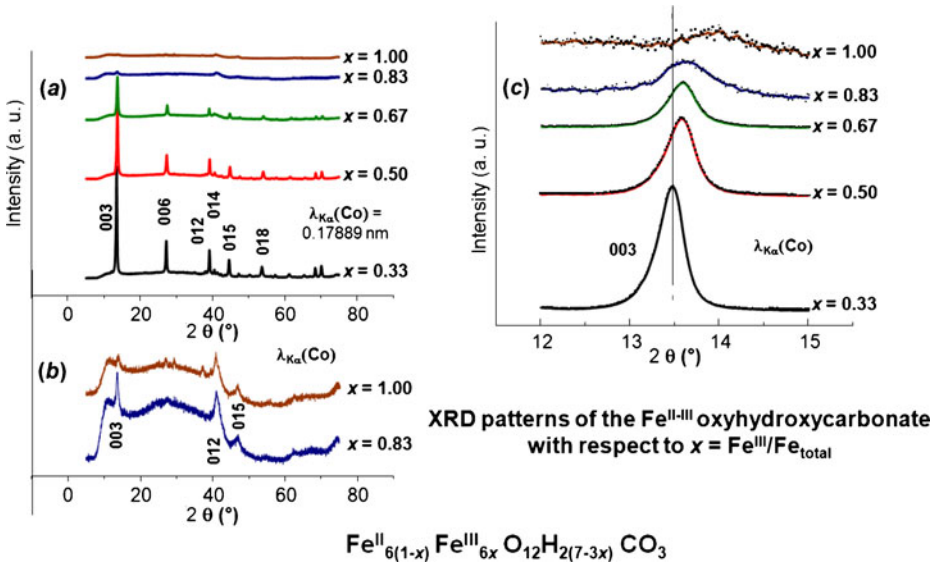

Fig. 2 X-ray diffraction patterns (XRD) of a set of hydroxycarbonate green rust samples during deprotonation for values of $x = [Fe^{III}]/[Fe_{total}]$ ranging from 0.33 to 1. (**a**) all patterns using the same scale for intensity, (**b**) details for $x = 0.83$ and 1, (**c**) the (003) lines demonstrating the contraction of the lattice with x and the resulting strain due to the progressive deprotonation (from [17])

Table 2 Interplanar distances d_{hkl} and cell parameters of $R\bar{3}\,m$ space group $GR[CO_3^{2-}(x)]$ computed from XRD data versus average ferric molar fraction $x = [Fe^{III}]/[Fe_{total}] \in [(1/3)\text{-}1]$ (from [17])

x	0.33	0.50	0.67	0.83	1
d_{003} (Å)	7.632	7.569	7.565	7.54	~ 7.34
d_{012} (Å)	2.679	2.669	2.672	–	–
c (Å)	22.896	22.707	22.695		
a (Å)	3.182	3.168	3.173		

deviation of gaussian distributions (Table 1) [8, 14]. Four quadrupole doublets were displayed, where D_1 and D_2 with large splitting were attributed to Fe^{II} state and D_3 and D_4 with small splitting to Fe^{III} state. The ferrous D_1 and D_2 were always in a 3:1 abundance ratio as due to Fe^{II} in register to water molecules or to a carbonate ion in the neighbouring interlayer. D_3 had always an abundance of 33% corresponding to the Fe^{III} cations that balanced the carbonate anions as in $GR(CO_3^{2-})$ whereas D_4, which did not exist initially in $GR(CO_3^{2-})$ (Fig. 1a), appeared with the deprotonation of OH^- ions at the vertices of the octahedrons that surrounded the Fe^{II} cations getting oxidised.

The structure keeps essentially that of $GR(CO_3^{2-})$ as testified by X-ray diffraction patterns (Fig. 2) [17] meaning that the long range order of anions is conserved within the interlayers and that Fe^{III} ions in layers are also ordered leading to diversified magnetic properties [18]. When x increases, OH^- ions at the vertices of the octahedrons surrounding Fe cations get deprotonated, and consequently, the lattice contraction shifts the diffraction lines towards higher angles that results in a strain

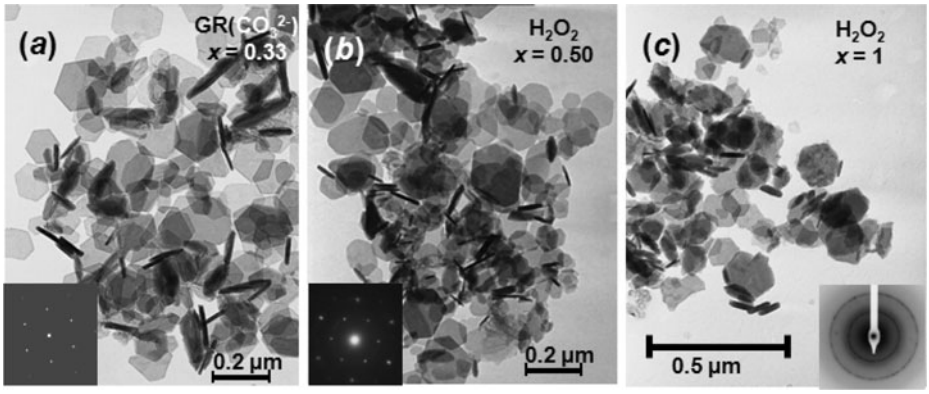

Fig. 3 Transmission electron micrographs of synthetic samples (**a**) GR(CO_3^{2-}) green rust with $x = 1/3$, (**b**) $x = 0.50$ and (**c**) GR(CO_3^{2-})* "ferric green rust" with $x = 1$. The shape of the crystals is identical since the reaction is topotactic (from [12])

since the octahedrons are no longer regular in shape (Fig. 2, Table 2) [17]; this fact is well illustrated by following the main (003) line while x increases and which becomes very hard to distinguish with ferric GR(CO_3^{2-})*. In contrast, no change occurs in the hexagonal shape of the crystals as observed by transmission electron microscopy (Fig. 3) [12].

Long range orders appear when x increases. At $x = 1/3$, for initial GR(CO_3^{2-}), each Fe^{III} ion is surrounded by 6 Fe^{II} ions; in contrast, at $x = 2/3$, each Fe^{II} ion is surrounded by 6 Fe^{III} ions and at $x = 1$, all cations are ferric (Fig. 5b–d). These ordered domains are topotaxically mixed and enable to reach any intermediate value of x as it is observed from Mössbauer spectra. Magnetic properties reflect the long range ordering of Fe^{III} cations for the definite values of x at 1/3, 2/3 and 1 [18]. The two sublattices of Fe^{II} and Fe^{III} ions in the hexagonal layer display an antiparallel coupling for $x = 1/3$ and 2/3 showing a ferrimagnetic behaviour with Néel temperatures of 5 K and about 20 K, respectively. In contrast, the "ferric green rust" at $x = 1$ is obviously ferromagnetic with a Curie temperature around 80 K with a broad range of transition.

Now, let us look at the Mössbauer spectra obtained with the samples extracted from the gleys (Fig. 4). Their fitting is classically done by using Lorentzian shape lines (Table 3). Firstly, the spectrum of the synthetic sample at $x = 0.50$ and that of the first sample extracted from the water table of the forest of Fougères can be compared (Fig. 4a & b); only two quadrupole doublets, one ferrous, in fact the superimposition of D_1 and D_2, and one ferric, the superimposition of D_3 and D_4 were considered [3, 4]. Then, the spectra of four samples extracted from the maritime marshes are displayed (Fig. 4c–f); the first one was extracted at Trébeurden and measured at room temperature (Fig. 4c) and the three others were extracted from the bay of Mont saint Michel and measured at 78 K (Fig. 4d–f). These spectra are fitted with three quadrupole doublets, one ferrous and two ferric, D_{1+2}, D_{3+4} and D'_{3+4}. When looking at the first one (Fig. 4c), we were very surprised since we were expecting to find a spectrum resembling all those previously extracted from the gley within water tables

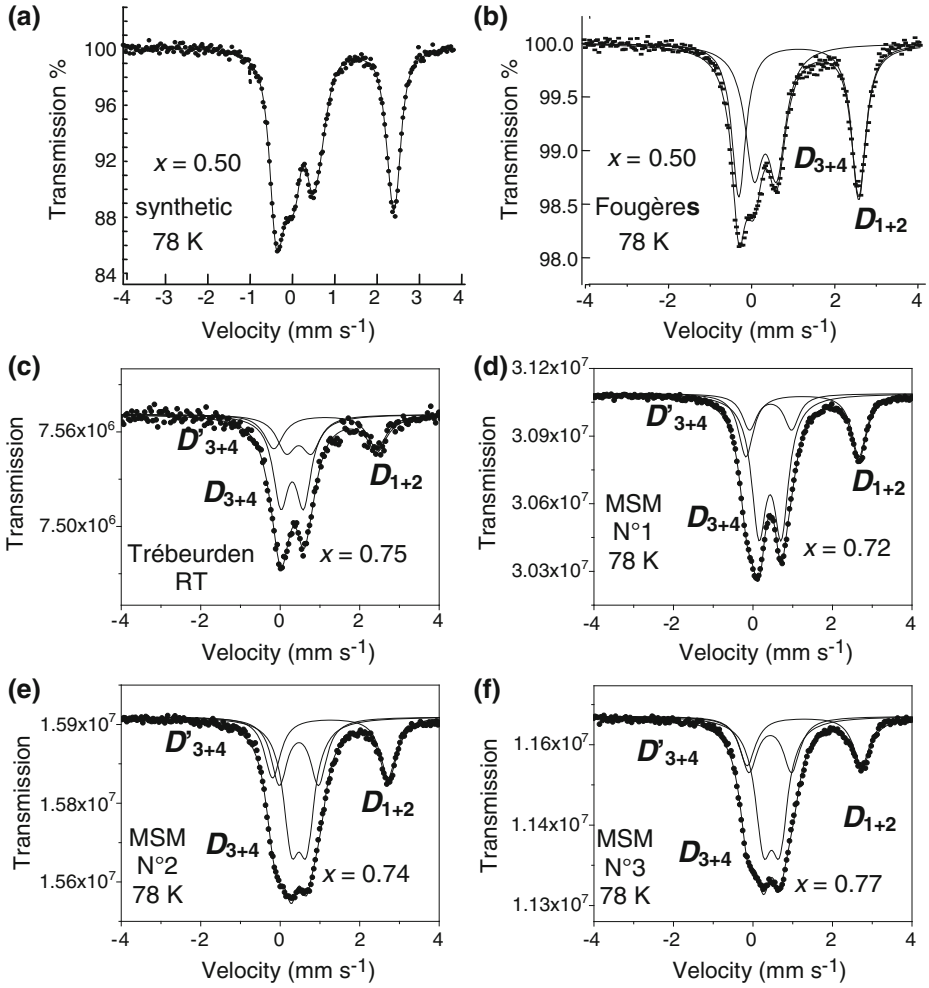

Fig. 4 Transmission Mössbauer spectra measured at 78 K of (**a**) a synthetic sample of $GR(CO_3^{2-})$* at $x = 0.50$ [8, 14], (**b**) the first sample of gley extracted from the aquifer of the forest of Fougères [4], (**c**) the first spectrum measured at room temperature of a gley sample extracted from the schorre of a maritime marsh in Trébeurden (Brittany), (**d–f**) spectra measured at 78 K of samples extracted from widely scattered locations in the bay of Mont Saint Michel (Normandy)

(Fig. 4b) where x belonged to the [1/3–2/3] range. Obviously, this assertion must be revisited since x belongs to the [2/3–1] range and we do know now that gleys from maritime marshes are different of those from continental aquifers. The first difference we can think of is that the schorre of marshes is most of the time dry and covered of water only at high tide (above tidal level 70); therefore the gley gets partially oxidized and a steady state is reached at an x value higher than for permanently waterlogged aquifers. All samples extracted from the bay of Mont Saint Michel do confirm this observation (Fig. 4d–f).

Table 3 Hyperfine parameters of quadrupole doublets in gley samples extracted from maritime marshes

Quadrupole doublet		D_{1+2} Fe^{II}(T)	D_{3+4} Fe^{III}(T)	D'_{3+4} Fe^{III}(M)
Trébeurden room temperature				
$x = 0.75$	δ(mms^{-1})	1.294 ± 0.000	0.301 ± 0.000	0.307 ± 0.000
	Δ(mm s^{-1})	2.66 ± 0.001	0.549 ± 0.000	0.972 ± 0.000
	RA (%)	25	50	25
	Γ(mm s^{-1})	0.56	0.45	0.49
Mont Saint Michel bay 78 K				
N°1	δ(mm s^{-1})	1.245	0.429	0.441
$x = 0.72$	Δ(mm s^{-1})	2.842	0.560	1.059
	RA(%)	28	56	16
	Γ(mm s^{-1})	0.45	0.49	0.50
N°2	δ(mm s^{-1})	1.263	0.471	0.470
$x = 0.74$	Δ(mm s^{-1})	2.908	0.381	0.986
	RA(%)	26	52	22
	Γ(mm s^{-1})	0.45	0.49	0.50
N°3	δ(mm s^{-1})	1.292	0.466	0.434
$x = 0.77$	Δ(mm s^{-1})	2.877	0.405	1.073
	RA (%)	23	46	31
	Γ(mm s^{-1})	0.45	0.49	0.50

Spectra are measured at room temperature or 78 K (Fig. 3) and fitting uses Lorentzian shape lines. δ: isomer shift in mm s^{-1} (reference is α-iron at ambient), Δ: quadrupole splitting in mm s^{-1}, *RA* (%): relative area and Γ: half width at half maximum in mm s^{-1}

In order to stress the long range orders that define the three distinct compounds corresponding to x values, 1/3, 2/3 and 1, and which are mixed, computer fittings used here with the samples extracted from the maritime marshes (Fig. 4c–f, Table 3) display doublets attributed to the ordered compound at $x = 2/3$, i.e. D_{1+2} and D_{3+4} in a 1:2 intensity ratio, and one other ferric doublet D'_{3+4} attributed to the ferric compound at $x = 1$. Note that the quadrupole splitting is much larger for D'_{3+4} (around 1 mm s^{-1}) than for D_{3+4} (around 0.5 mm s^{-1}) as it was also the case with synthetic samples.

Three minerals must correspond to the three compounds that are topotaxically mixed. We propose (i) to redefine and limit to $x = 1/3$ "fougèrite" $\boldsymbol{F}$, the Fe^{II-III} hydroxycarbonate green rust GR(CO_3^{2-}), i.e. $Fe^{II}_4Fe^{III}_2(OH)_{12}CO_3 \cdot 3H_2O$, (ii) to name "trébeurdenite" $\boldsymbol{T}$, the Fe^{II-III} oxyhydroxycarbonate, i.e. $Fe^{II}_2Fe^{III}_4(OH)_{10}O_2CO_3 \cdot 3H_2O$ with $x = 2/3$, and finally (iii) to name "mössbauerite" $\boldsymbol{M}$, the "ferric green rust" GR(CO_3^{2-})*, i.e. $Fe^{III}_6(OH)_8O_4CO_3 \cdot 3H_2O$ ferric oxyhydroxycarbonate, with $x = 1$. The three dimensional structure of these minerals is drawn (Fig. 5).

An average formula $Fe^{II}_{6(1-x)}Fe^{III}_{6x}O_{12}H_{2(7-3x)}CO_3 \cdot 3H_2O$ can be obtained by mixing these minerals and, in fact, any sample in the range [1/3, 2/3] is a mixture of $\boldsymbol{F}$ and $\boldsymbol{T}$ and their proportions are obtained by the lever rule: $\left[(2-3x)\,\boldsymbol{F} + (3x-1)\,\boldsymbol{T}\right]$, whereas, in the range [2/3, 1], it is a mixture of $\boldsymbol{T}$ and $\boldsymbol{M}$ with proportions of $\left[3\,(1-x)\,\boldsymbol{T} + (3x-2)\,\boldsymbol{M}\right]$. Up till now, occurrences of gleys extracted from continental aquifers as in Fougères [3, 4, 15, 16] and Denmark [12], or from maritime marshes as in Trébeurden and Mont Saint Michel display values of $x \in [0.33, 0.67]$ or [0.67, 1], respectively.

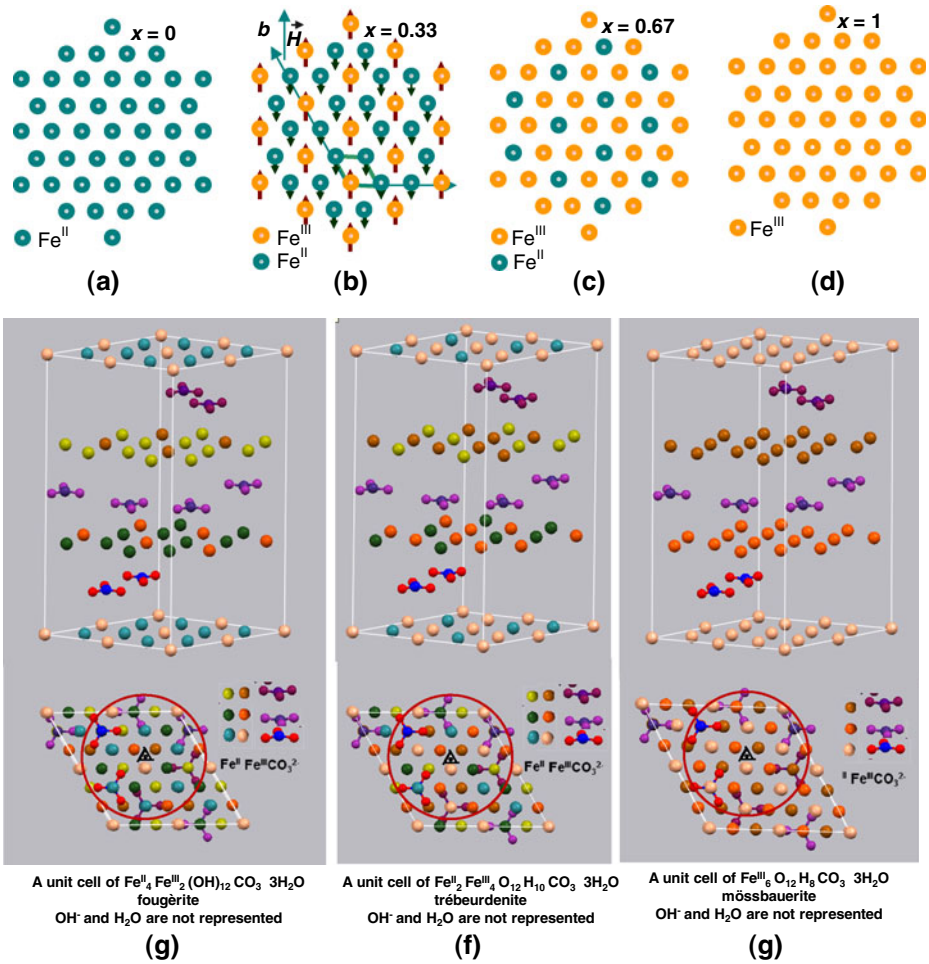

Fig. 5 Ordering of Fe^{III} ions within an hexagonal layer of Fe cations leading to various magnetic properties [18]: (**a**) $Fe^{II}_6(OH)_{10}(H_2O)_2\ CO_3 \cdot 3H_2O$; (**b**) $Fe^{II}_4Fe^{III}_2(OH)_{12}CO_3 \cdot 3H_2O$; (**c**) $Fe^{II}_2Fe^{III}_4(OH)_{10}O_2CO_3 \cdot 3H_2O$ (**d**) $Fe^{III}_6(OH)_8O_4CO_3 \cdot 3H_2O$. Three dimensional views of (**e**) fougèrite ***F***, (**f**) trébeurdenite ***T***, and (**g**) mössbauerite ***M***

4 Conclusion

Several occurrences of "gleys" extracted from maritime marshes reveal that the iron containing minerals which are responsible for their bluish-green or grey shade are topotaxically related with an average ferric molar fraction $x = [Fe^{III}/Fe_{total}]$ belonging to the [2/3–1] range whereas "gleys" that were extracted from continental aquifers displayed, up till now, x values within the [1/3–2/3] range. By comparing the Mössbauer spectra with those of synthetic samples, one concludes that there exist three definite minerals we propose to call (i) "fougèrite", ***F***: $Fe^{II}_4Fe^{III}_2(OH)_{12}CO_3 \cdot 3H_2O$ where $x = 1/3$, (ii) "trébeurdenite", ***T***: $Fe^{II}_2Fe^{III}_4(OH)_{10}O_2CO_3 \cdot 3H_2O$ where

$x = 2/3$ and (iii) "mössbauerite", ***M***: $Fe_6^{III}(OH)_8O_4CO_3 \cdot 3H_2O$ where $x = 1$. Any average formula, i.e. $Fe^{II}_{6(1-x)}Fe^{III}_{6x}\ O_{12}H_{2(7-3x)}\ CO_3 \cdot 3H_2O$ can be obtained by topotactic mixture of these minerals, ***F*** and ***T*** in the [1/3, 2/3] range (continental aquifers) and ***T*** and ***M*** in the [2/3, 1] range (maritime marshes). We shall use these findings for studying the diagenesis of littoral sediments into thalassasoils.

Acknowledgement We thank Dr. M. Abdelmoula for experimental help.

References

1. Hansen, H.B., Koch, C.B., Nancke, K.H., Borggard, O.K., Sorensen, J.: Abiotic nitrate reduction to ammonium: key role of green rust. Environ. Sci. Technol. **30**, 2053 (1996)
2. Génin, J.M.R., Renard, A., Ruby, C.: Fougerite Fe^{II-III} oxyhydroxycarbonate in environmental chemistry and nitrate reduction. Hyperfine Interact. **186**, 913 (2008)
3. Trolard, F., Génin, J.M.R., Abdelmoula, M., Bourrié, G., Humbert, B., Herbillon, A.J.: Identification of a green rust mineral in a reductomorphic soil by Mössbauer and Raman spectroscopies. Geochim. Cosmochim. Acta **61**, 1107 (1997)
4. Génin, J.M.R., Bourrié, G., Trolard, F., Abdelmoula, M., Jaffrezic, A., Refait, Ph.: Thermodynamic equilibria in aqueous suspensions of synthetic and natural Fe^{II}-Fe^{III} green rusts: occurrences of the mineral in hydromorphic soils. Environ. Sci. Technol. **32**, 1058 (1998)
5. Génin, J.M.R., Bauer, Ph., Olowe, A.A., Rézel, D.: Mössbauer study of the kinetics of simulated corrosion process of iron in chlorinated aqueous solution around room temperature: the hyperfine structure of ferrous hydroxides and green rust I. Hyperfine Interact. **29**, 1355 (1986)
6. Génin, J.M.R., Olowe, A.A., Refait, Ph., Simon, L.: On the stoichiometry and Pourbaix diagram of Fe(II)-Fe(III) hydroxysulphate or sulphate-containing green rust 2: An electrochemical and Mössbauer spectroscopy study. Corros. Sci. **38**, 1751 (1996)
7. Drissi, S.H., Refait, Ph., Abdelmoula, M., Génin, J.M.R.: The preparation and thermodynamic properties of Fe(II)-Fe(III) hydroxycarbonate (green rust 1); Pourbaix diagram of iron in carbonate-containing aqueous media. Corros. Sci. **37**, 2025 (1995)
8. Génin, J.M.R., Abdelmoula, M., Ruby, C., Upadhyay, C.: Speciation of iron; characterisation and structure of green rusts and Fe^{II-III} hydroxycarbonate fougerite. C.R. Geosciences **338**, 402 (2006)
9. Aïssa, R., François, M., Ruby, C., Fauth, F., Medjahdi, G., Abdelmoula, M., Génin, J.M.R.: Formation and crystallographical structure of hydroxysulphate and hydroxycarbonate green rusts synthesized by coprecipitation. J. Phys. Chem. Solids **67**, 1016 (2006)
10. Génin, J.M.R., Ruby, C.: Structure of some Fe^{II-III} hydroxysalt green rusts (carbonate, oxalate, methanoate) from Mössbauer spectroscopy. Hyperfine Interact. **185**, 871 (2008)
11. Benali, O., Abdelmoula, M., Refait, Ph., Génin, J.M.R.: Effect of orthophosphate on the oxidation products of Fe(II)-Fe(III) hydroxycarbonate: the transformation of green rust to ferrihydrite. Geochim. Cosmochim. Acta **65**, 1715 (2001)
12. Génin, J.M.R., Aïssa, R. Géhin, A., Abdelmoula, M., Benali, O., Ernstsen, V., Ona-Nguema, G., Upadhyay, C., Ruby, C.: Fougerite and Fe^{II-III} hydroxycarbonate green rust; ordering, deprotonation and/or cation substitution; structure of hydrotalcite-like compounds and mythic ferrosic hydroxide $Fe(OH)_{(2+x)}$. Solid State Sci. **7**, 545 (2005)
13. Génin, J.M.R., Ruby, C., Géhin, A., Refait, Ph.: Synthesis of green rusts by oxidation of $Fe(OH)_2$, their products of oxidation and reduction of ferric oxyhydroxides; E_h–pH Pourbaix diagrams. C.R. Geosciences **338**, 433 (2006)
14. Ruby, C., Upadhyay, C., Géhin, A., Ona-Nguema, G., Génin, J.M.R.: In situ redox flexibility of Fe^{II-III} oxyhydroxycarbonate green rust and fougerite. Environ. Sci. Technol. **40**, 4696 (2006)
15. Féder, F., Trolard, F., Klingelhöfer, G., Bourrié, G.: In situ Mössbauer spectroscopy evidence for green rust (fougerite) in a gleysol and its mineralogical transformations with time and depth. Geochim. Cosmochim. Acta **69**, 4463 (2005)
16. Rodionov, D., Klingelhöfer, G., Bernhardt, B., Schroder, C., Blumers, M., Kane, S., Trolard, F., Bourrié, G., Génin, J.M.R.: Automated Mössbauer spectroscopy in the field and monitoring of fougerite. Hyperfine Interact. **167**, 869 (2006)

17. Ruby, C., Abdelmoula, M., Naille, S., Renard, A., Khare, V., Ona-Nguema, G., Morin, G., Génin, J.M.R.: Oxidation modes and thermodynamics of Fe^{II-III} oxyhydroxycarbonate green rust: dissolution-precipitation versus in-situ deprotonation. Geochim. Cosmochim. Acta **74**, 953 (2010)
18. Rusch, B., Génin, J.M.R., Ruby, C., Abdelmoula, M., Bonville, P.: Ferrimagnetic properties of $Fe^{(II-III)}$ (oxy)hydoxycarbonate green rust. Solid State Sci. **10**, 40 (2008)

Hyperfine Interact (2012) 204:83–88
DOI 10.1007/s10751-012-0567-x

Rudolf Mössbauer and the development of the Garching research site

Friedrich E. Wagner

Published online: 22 February 2012

Abstract The scientific career of Rudolf Mössbauer is intricately interwoven with the development of the Garching research site and the present day Garching campus of the Technical University of Munich. A brief description of this development will be given.

Keywords Rudolf Mössbauer · Garching · Technical University of Munich

1 The early days

In 1956 the construction of the first research reactor in Germany began. The reactor, a commercial swimming pool reactor made by the US company AMF, became critical on October 30, 1957, at a time when Mössbauer had already discovered recoilless nuclear gamma resonance, but had not yet published his results. The reactor was built in a remote area about 10 miles north of the city of Munich, on the diluvial gravel plain west of the river Isar, and about 2 miles from the nearest settlement, a small village named Garching. At that time nobody would have predicted the stupendous development this patch of land was to undergo in the 50 years to come. Figure 1 shows the reactor site in about 1960. The egg-shaped building houses the reactor, and the barracks next to it is where the handful of researchers worked. The scientific director of the reactor was Professor Heinz Maier-Leibnitz, the PhD supervisor of Rudolf Mössbauer at the Technical University of Munich (TUM).

The construction of the Garching reactor and the discovery of the Mössbauer effect roughly coincide in time, but on Maier-Leibnitz's recommendation Mössbauer performed the experiments which resulted in the discovery of recoilless nuclear gamma resonance absorption at the Max Planck Institute of Medical Research in Heidelberg, where the experimental conditions were by far superior to those

F. E. Wagner (✉)
Physics Department E15, Technical University of Munich, 85747 Garching, Germany
e-mail: friedrich.wagner@ph.tum.de

Fig. 1 The site of the Garching research reactor (the egg-shaped building) in about 1960. Mössbauer had set up his laboratory in the left of the two low barracks facing the reactor

at Maier-Leibnitz's crowded Munich institute. The radioactive ^{191}Os sources Mössbauer needed for his experiments with the 129 keV transition in ^{191}Ir were produced at Harwell, England, and—according to what Mössbauer told occasionally—carried to Heidelberg in his suitcase. Mössbauer published his results in 1958 [1, 2], and only after that did he construct a Mössbauer spectrometer in one of the barracks next to the Garching reactor. This spectrometer [3] was about a meter high and 2 m long and consisted of two cryostats cooled with liquid hydrogen, one for the source and the other for the absbsorber. The absorber cryostat sat on a trolly running on rails and moving back and forth by about 20 cm, driven by a chain running over sprocket wheels. The cryostats were designed by Werner Wiedemann, a collaborator of Walter Meissner and expert in low temperature techniques. It was first used to study the broad 134 keV resonance in ^{187}Re [3]. In fact, Mössbauer was not the only researcher working in Mössbauer spectroscopy in Munich and at Garching in the early days. Others were, to name just a few, Egbert Kankeleit, who developed the double-loudspeaker type velocity drive, Mike Kalvius, who studied the 8.4 KeV resonance in ^{169}Tm and Paul Kienle, who became interested mainly in nuclear physics aspects of the Mössbauer method. The author started doing a diploma thesis under Mössbauer's supervision in the fall of 1960, but Mössbauer left soon afterwards for the United States, having accepted an offer to work at the California Institute of Technology (Caltech, Pasadena). He was awarded the Nobel Prize for his discovery of recoilless nuclear resonance absorption in 1961, when he was already working at Caltech. Notwithstanding, after his departure a lively Mössbauer group remained active at Garching, mainly under the supervision of Paul Kienle and, as far as his limited time permitted, Maier-Leibnitz himself. In the course of time a number of new buildings were erected at the Garching site, for instance the administrative building for the reactor shown in the left middle of Fig. 2, which shows the place in about 1965. Not all of the building activity was for the Technical University, though. For instance, the newly founded Max-Planck-Institute for Plasma Physics was established just south of the reactor site.

Fig. 2 The reactor site in about 1965. On his return to Munich, Mössbauer had his office in the right front corner of the two-storey administrative building at the left margin of the picture and his laboratories were in the two flat barracks from the early days of the reactor. The radiochemistry laboratory needed to make Mössbauer sources was in the ring-shaped building surrounding the reactor

2 The second Mössbauer effect

For the Garching site, a major step forward was taken in 1964, when Mössbauer agreed to return from the United States to become full professor at the Technical University of Munich. In his negotiations with the Bavarian State Government he was in a rather strong position. One of the conditions for his return was the that a proposal made several years earlier by the physics professors of TUM for the foundation of a big physics faculty with many new positions for physics professors and scientific and other staff be finally accepted by politics and that a big new building was to be built at the Garching site. Mössbauer got what he asked for, and this miracle of sorts became known as "The Second Mössbauer Effect". In the United States Mössbauer had seen the department system with a many professors on an equal footing, and this was to become the structure for the new institute, which was duly called the Physics Department.

Figure 2 shows the Garching site at about the time of Mössbauer's return. He moved into an office in the recently added administrative building and had his laboratories in the two flat barracks, in one of which he had set up his first Garching spectrometer 5 years previously. Mössbauer brought Richard Cohen to Munich, who had done his PhD thesis with him at Caltec. Richard helped him to set up his research group. The Mössbauer spectroscopy group that had been working at Garching during Mössbauer's absence continued under the direction of Paul Kienle. In fact, the two groups worked side by side in the same laboratories rather peacefully, except for some occasional mutual accusations of pinching equipment, which was always a bottleneck in our research efforts. Meanwhile, the new Physics Department building was being constructed (Fig. 3) north of the reactor site and during the years 1969 and

Fig. 3 The Garching research campus in about 2005, with the now sizeable town of Garching behind, the city of Munich in the rear and the Alps in the haze on the horizon. The new high flux reactor, officially called the Heinz Maier-Leibnitz neutron source, is the big building left of the egg-shaped building of the 1957 Garching research reactor. The building of the Physics Department is in the foreground next to the two reactors

1970 everybody moved into it, including most of those who had still been working on the city campus of the Technical University.

The Garching campus continued to grow. Chemistry was the first faculty after physics to move from downtown Munich to Garching. Eventually, the faculties of mechanical engineering, and of mathematics and computer science followed. Several more Max Planck institutes—for extraterrestrial physics, for astrophysics and for quantum optics—as well as the European Southern Observatory are now situated on the Garching research site. In the late 1960s a tandem Van de Graaff accelerator was built jointly by the Technical University and the Ludwig Maximilian University of Munich, and, last but not least and after considerable political squabble, the new high flux research reactor of the Technical University became operational in 2005, five years after the old 1957 reactor whose construction had laid the foundation of the Garching research site had been closed down in the summer of 2000. A present day view of the Garching campus is shown in Fig. 3. The startling development of the Garching research campus is certainly not all due to Rudolf Mössbauer, but the Nobel Prize laureate of 1961 certainly contributed much to what the Garching Campus is today.

In 1971 Mössbauer was offered the directorship of the Institute Laue-Langevin in Genoble, France, the high flux reactor that had been built in the late 1960s. To run his research group in Munich during his absence, Mike Kalvius came back from Argonne National Laboratory and became full professor at the Physics Department. Paul Kienle lost his interest in Mössbauer spectroscopy and eventually all Mössbauer spectroscopy work concentrated in the Klavius group.

Fig. 4 Rudolf Mössbauer and his friend Vitalii Goldanskii at a party in Fritz Parak's house during one of the joint Russian-German seminars

Fig. 5 Yuri Kagan, the Russian theoretician, and Rudolf Mössbauer in Fritz Parak's garden during the same joint Russian-German seminar

3 Mössbauer turns to neutrino physics

In the three decades to come, Mössbauer spectroscopy continued to flourish at Garching. In fact, the scope of hyperfine interaction studies was expanded by additional methods like time differential perturbed $\gamma - \gamma$ angular correlations (TDPAC) and muon spin resonance (μSR). Mössbauer himself, however, had largely lost his interest in nuclear gamma resonance when he returned from Grenoble to Munich in 1976. In Grenoble he had seen a group of researchers from Munich do experiments at the high flux reactor to study neutrino oscillations, and this field had fascinated him so much that he turned his interest to neutrino physics, mainly to neutrino oscillations. Some aspects of nuclear gamma resonance, however, continued to interest him, mainly the Bragg scattering of resonant gamma radiation from ideal crystals and the phase problem in x-ray structure determination of biological materials. The actual work in these fields was mainly done by Uwe van Bürck, who later became engaged in experiments with synchrotron radiation, and Fritz Parak, who eventually turned to biological applications of Mössbauer spectroscopy like the dynamics proteins. Mössbauer showed continued interest in these fields and gave support to them. Mössbauer also continued to support the collaboration with

physicists from countries behind the Iron Curtain, mainly the Soviet Union, which he had initiated already on his return from the United States. This collaboration largely sprang from his personal friendship with Vitalii Goldanskii of the Soviet (later Russian) Academy of Sciences. The lively exchange of scientists and a number of joint seminars held alternatingly in Germany and Russia was certainly a major feat during the years of the Cold War. To achieve this both Mössbauer and Goldanskii had to use all the influence on politics they could muster. Mössbauer used to enjoy this collaboration and the joint seminars, and also the parties going along with the latter. Figures 4 and 5 show him during a party held in Fritz Parak's home during one of these seminars. Mössbauer also still attended ICAME conferences, like the one at Garmisch in 1999, where he gave a talk on the discovery of the "M-effect", as he used to call it [4], or the one in Muscat, Oman in 2003. Mössbauer was not always happy with the development that the Physics Department eventually took, but his contribution to its foundation will always be remembered.

The eventual slow decline of Mössbauer spectroscopy at Garching began in the 1990s, when the Physics Faculty decided to put all its efforts into neutron physics and the use of the new high-flux research reactor and thus to eventually phase out the application of hyperfine methods in solid state science by not replacing researchers who either left or retired. The neutrino side of Mössbauer's activites, however, continues to flourish, now being part of the larger field of astroparticle physics. After his retirement in 1997, Franz von Feilitzsch became his successor and the group now is engaged in many experiments in neutrino physics and dark matter studies and is part of a larger research initiative for studying the origin and structure of the universe.

References

1. Mössbauer, R. L. : Z. Physik **151**, 124 (1958)
2. Mössbauer, R. L. : Naturwiss. **45**, 538 (1958)
3. Mössbauer, R. L.: Wiedemann, W.: Z. Physik **159**, 33 (1960)
4. Mössbauer, R. L.: Hyp. Interact. **126**, 1 (2000)

Hyperfine Interact (2012) 204:89–96
DOI 10.1007/s10751-011-0535-x

The collective Lamb shift in nuclear γ-ray superradiance

Ralf Röhlsberger

Published online: 7 January 2012

Abstract The electromagnetic transitions of Mössbauer nuclei provide almost ideal two-level systems to transfer quantum optical concepts into the regime of hard x-rays. If many identical atoms collectively interact with a resonant radiation field, one observes (quantum) optical properties that are strongly different from those of a single atom. The most prominent effect is the broadening of the resonance line known as collective enhancement, resulting from multiple scattering of *real* photons within the atomic ensemble. On the other hand, the exchange of *virtual* photons within the ensemble leads to a tiny energy shift of the resonance line, the collective Lamb shift, that remained experimentally elusive for a long time after its prediction. Here we illustrate how highly brilliant synchrotron radiation allows one to prepare superradiant states of excited Mössbauer nuclei, an important condition for observation of the collective Lamb shift.

Keywords Collective Lamb shift · Superradiance · Mössbauer effect · Synchrotron radiation

1 Introduction

A multitude of collective optical phenomena have been studied in the regime of visible light, particularly after the development of pulsed laser systems to promote ensembles of atoms into well-defined excited states. This research area gained momentum when it became possible to capture and control ensembles of cold atoms in electromagnetic traps. In recent years it also became possible to prepare excitonic states as 'artificial atoms' in condensed matter systems like quantum wells and quantum dots. As a result, cooperative effects between light and matter like superradiance

R. Röhlsberger (✉)
Deutsches Elektronen Synchrotron DESY, Notkestr. 85, 22607 Hamburg, Germany
e-mail: ralf.roehlsberger@desy.de

can now be studied in solid state systems as well [1–3]. Ultimately, the precise control of the spatial arrangement of atomic ensembles could allow one to control the superradiant energy transfer between the photon field and the system, rendering this area very attractive for applications. Examples are the superradiant light-matter interaction of molecular aggregates [4], e.g, in light-harvesting molecules and the collective radiance of quantum well superlattices [1] with potential applications in optical data processing devices.

The phenomenon of superradiance was first described by Dicke in 1954 [5]. It took almost 20 years for its experimental confirmation when laser techniques became available to create fully inverted ensembles of excited atoms [6]. About at the same time it was realized that the enhanced decay width of the collective emission goes along with a shift of the transition energy, the collective Lamb shift (CLS) [7]. It then took again nearly 20 years until the first measurement of the CLS, reported for a multiphoton excitation scheme in a noble gas [8, 9]. For transitions from the ground state, especially in solid-state samples, the CLS has not been reported as of yet due to intrinsic difficulties to be discussed below. In this contribution I will describe how the CLS can be observed in the x-ray regime for spontaneous emission from an ensemble of Mössbauer atoms that are resonantly excited by synchrotron radiation pulses.

2 Superradiance and the collective Lamb shift

The single-atom Lamb shift results from the emission and reabsorption of virtual photons by the same atom, leading to a self-energy correction of the electronic binding energy, first observed for atomic levels in Hydrogen by Lamb and Retherford in 1947 [10]. The proper theoretical description of this effect was the starting point for the development of the theory of quantum electrodynamics. The collective Lamb shift is an analog of the single-atom Lamb shift where the virtual photon emitted by one atom is reabsorbed by another atom within the same ensemble, illustrated in a diagrammatical fashion in Fig. 1. Thus, the ensemble of identical atoms acts as a 'superatom' that similarly experiences a self-energy correction of its energy levels. Due to the long-range nature of the photon exchange, the CLS is strongly depending on the geometry of the sample and has been discussed in several reviews, of which we refer to two of the most recent ones and references therein [11, 12].

The collective Lamb shift is closely related to superradiance, i.e., the phenomenon of collective spontaneous emission. Dicke originally proposed two methods to create a superradiant state [5]. The first variant starts with a fully inverted ensemble of N atoms that evolves into a superradiant state via spontaneous radiative coupling of the emitters. The maximum intensity of the radiated light scales with the square of the number of atoms in the ensemble, N^2. The observation of this effect constituted the first experimental confirmation of superradiant emission [6] and was later referred to as 'superfluorescence' [13, 14].

In the second variant described by Dicke, a coherent radiation pulse directly excites the ensemble of two-level atoms from the ground state into a superradiant state. This is the case that shall be considered in the following. Particularly interesting is the situation where only one atom in the ensemble is excited. For the case that the

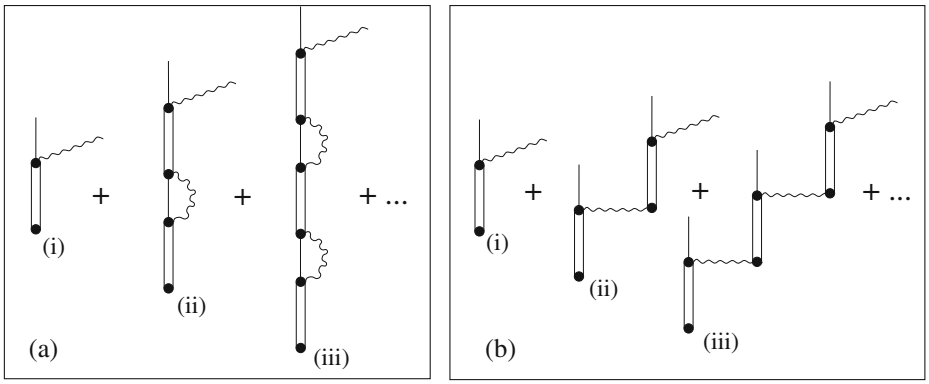

Fig. 1 *Left* (i) Emission of a real photon from an excited atom (*double line*) (ii), (iii) higher-order diagrams that contribute to the emission process, originating from emission and reabsorption of virtual photons by the same atom, leading to (self-energy) corrections of the single-atom transition energy that result in the Lamb shift. *Right* Photon emission after exchange of virtual photons with other atoms within the ensemble, leading to the collective Lamb shift

sample extension R is much smaller than the wavelength of the radiation, $k_0 R \ll 1$, the state is written as

$$|\Psi_+\rangle = \frac{1}{\sqrt{N}} \sum_j |\downarrow_1 \downarrow_2 \ldots \uparrow_j \ldots \downarrow_N\rangle, \tag{1}$$

where $|\downarrow_1 \downarrow_2 \ldots \uparrow_j \ldots \downarrow_N\rangle$ is a Fock state with atom j being in the excited state $\uparrow$ and all other atoms being in the ground state $\downarrow$. In most cases of quantum optics, laser physics or x-ray physics, however, the opposite limit is encountered where $k_0 R \gg 1$, so that the spatial position of the atoms within the ensemble has to be taken into account:

$$|\Psi_+\rangle_{k_0} = \frac{1}{\sqrt{N}} \sum_j e^{i\vec{k}_0 \cdot \vec{r}_j} |\downarrow_1 \downarrow_2 \ldots \uparrow_j \ldots \downarrow_N\rangle, \tag{2}$$

where $\vec{k}_0$ is the wave vector of the incident photon and $\vec{r}_j$ denotes the position of the j^{th} atom. This state is fully symmetric with respect to exchange of any two atoms. Due to the phasing, the emission proceeds into the direction of the incident photon wave vector [15, 16] with a temporal evolution given by [7, 17–20]:

$$\beta(t) \approx \beta_0 \, e^{-\Gamma_C t} \quad \text{with} \quad \Gamma_C = \Gamma_N \left(1 - \frac{i\,S}{k_0 R}\right) \tag{3}$$

valid for single-photon superradiant emission from an extended spherical cloud (radius R, containing N atoms) in the limit $k_0 R \gg 1$. $\Gamma_N = (\rho \lambda^2 R/2\pi)\,\Gamma_0$ is the collective decay width. In this notation the decay width Γ_C appears to exhibit an imaginary part that describes an energetic shift, the collective Lamb shift $L_N = -(S/k_0 R)\,\Gamma_N$. S is a factor that contains corrections to Γ_C that depend on the kind of model used for the electromagnetic field (scalar/vector) and on specific approximations made during the calculation [21]. The leading term in all these models, however, is of the form

given in (3). This means that the CLS scales as $L_N \sim \rho\,\lambda^3\,\Gamma_0$. Thus, for the CLS to be observable, the optical density $\rho\,\lambda^3$ has to be sufficiently high. In gaseous samples, however, an increase of the density goes along with the increase of interactions between atoms and the wall of the container, leading to collisional broadening of the resonance line. As a result, the inhomogeneous linewidth becomes much larger than the collective decay width, leading to a quenching of the superradiant dynamics. In condensed matter systems the corresponding effect is inhomogeneous broadening of the resonance line that poses a challenge for the preparation of ensembles of identical emitters like quantum dots, for example. Moving from the optical into the x-ray regime, the nuclear resonances of Mössbauer nuclei provide almost ideal two-level systems, provided that the inhomogeneous broadening induced by residual hyperfine interactions can be sufficiently well controlled.

The most widely used isotope in this field is ^{57}Fe with a transition energy of $E_0 = 14.4$ keV, a natural linewidth of $\Gamma_0 = 4.7$ neV, corresponding to a lifetime of $\tau_0 = 141$ ns. Beamlines at present-day 3rd generation synchrotron radiation sources like ESRF, APS, SPring8 and PETRA III deliver a spectral flux of about 10^4 photons/s/Γ_0. The radiation comes typically in pulses with a duration of a few 10 ps, so that excitation and subsequent emission can be treated as independent processes. For typical electron beam currents in the range of 100 mA one obtains about 0.01–0.1 resonant photons per pulse. This means that at a given time either one or no nucleus within the ensemble can be excited, so that the limit of *single-photon* superradiance is ensured that originates from the symmetric state in (2). The preparation of this state, however is not trivial because the excitation probability for all atoms in the sample has to be the same. This condition, however, is not fulfilled for optically thick samples. In this case the superradiant dynamics is seriously affected by propagation effects of the emitted radiation in the sample. For example, the radiation from atoms at the entrance front of the sample interferes with radiation from atoms deeper in the sample [15]. During the emission process this interference alternates between being destructive and constructive, thus leading to periodic changes between superradiant and subradiant emission as function of time. In other words, in conventional forward scattering the excited state of atoms is not an oscillatory eigenstate of the system, mainly because the ensemble of atoms does not remain uniformly excited during the emission process as a result of the interference processes mentioned above. Only for a system with perfect permutational symmetry the coupling between the superradiant and the subradiant modes is ruled out. However, any type of symmetry breaking allows the coexistence of superradiance and subradiance in the sense that a system initially prepared in a superradiant mode will partially evolve into less symmetric, subradiant modes. The energies of the participating normal modes (eigenstates) are distributed around the single-atom resonance energy [15], so that the total CLS for an extended sample eventually vanishes. In the time domain, the interference of these contributions results in the so-called dynamical beats or propagation quantum beats [22] that obstruct the strictly exponential time evolution of the superradiant state.

Summarizing this section, the perspectives to observe the CLS for nuclear resonant emission do not look too promising, especially if one tries to estimate the magnitude of the CLS: For the 14.4 keV resonance we have $\lambda = 0.086$ nm and the maximum number density is $\rho \approx 7.5 \cdot 10^{28}\,\mathrm{m}^{-3}$ (Fe metal), so that $\rho\,\lambda^3 \approx 0.05$. We will see below that this is not a valid measure here, and we will present an approach

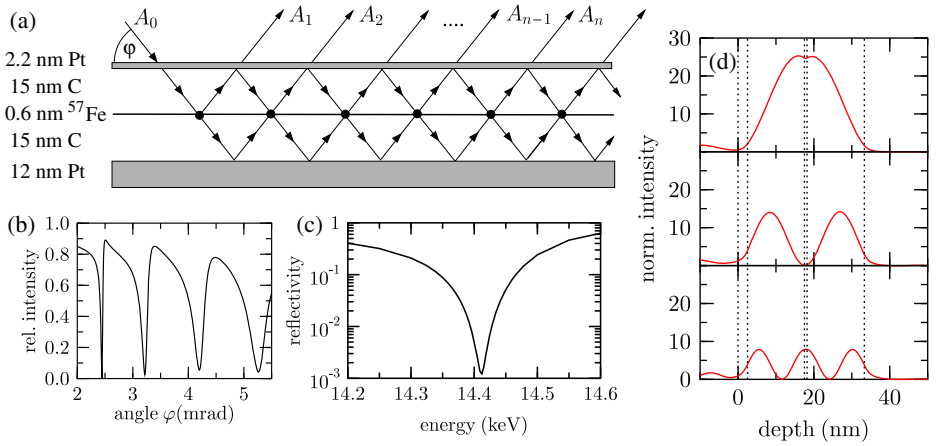

Fig. 2 **a** Structure of the planar cavity and scattering geometry used for calculation of the CLS for an ensemble of resonant ^{57}Fe nuclei embedded in its center. **b** Calculated non-resonant x-ray reflectivity at 14.4 keV of the cavity consisting of (2.2 nm Pt)/(15 nm C)/(0.6 nm ^{57}Fe)/(15 nm C)/(20 nm Pt)/Si. Guided modes are excited at the angular positions of the minima. **c** Energy dependence of the reflectivity in the first-order mode, indicating the spectral width of about 100 eV of the mode. **d** Depth dependence of the normalized field intensity $|a(z)|^2$ for the first three guided modes of the cavity. The maximum value of 25 reached at the center of the guiding layer in the first-order mode equals approximately the finesse of the cavity

to overcome the obstacles mentioned above so that relatively large values for the CLS can be obtained.

3 Nuclear γ-ray superradiance in a cavity

In order to prepare a state that stays symmetric during its time evolution one has to ensure that the sample appears optically thin upon excitation but optically thick upon emission. We will show in the following that this can be achieved by embedding the ensemble of atoms in a planar cavity.

The cavity geometry is sketched in Fig. 2 where the resonant isotope ^{57}Fe is located in the center of the cavity that consists of a material of low electron density (C, 32 nm thick) which is sandwiched between two layers of high electron density (Pt). The propagation of electromagnetic waves in stratified media can be described within an optical transfer matrix formalism [23]. Due to the high energies of x-rays compared to electronic binding energies in atoms, the refractive index n of any material is slightly below unity. Thus, n is commonly written as:

$$n(E) = 1 + \frac{2\pi\rho}{k_0^2}(f_e + f_n(x)) = 1 + \frac{2\pi\rho}{k_0^2}\left[\left(-Z\,r_e + \frac{\sigma}{2\lambda}\right) + \frac{f_0}{x - i}\right] \qquad (4)$$

where ρ is the number density of scatterers, f_e and f_n are the electronic and nuclear scattering amplitudes, respectively. r_e is the classical electron radius, σ the photoelectric absorption cross section and f_0 the nuclear scattering amplitude

at resonance. $x = \Delta/\Gamma_0$ denotes the detuning Δ of the photon energy from the resonance in units of the natural linewidth Γ_0.

According to (4) in the x-ray regime every material is optically thinner than vacuum, thus total reflection occurs for angles of incidence φ (measured relative to the surface) below the critical angle $\varphi_c = \sqrt{2\delta}$. Since $\delta \approx 10^{-6}...10^{-5}$ for hard x-rays with energies between about 10 and 20 keV, the critical angle φ_c is typically a few mrad. In the regime of total reflection, the radiation penetrates only a few nm into the material via the evanescent wave. Thus, x-rays can be evanescently coupled into a waveguide through a layer of a few nm thickness as sketched in Fig. 2. If the z-component of the wavevector in the guiding layer of thickness D is an integer multiple of π/D, the radiation forms a standing wave within the guiding layer. As a result, one obtains a strong enhancement of the normalized field intensity inside the layer (see Fig. 2d), corresponding to an amplification of the photonic density of states.

In the example shown in Fig. 2 the top Pt layer is thin enough (2.2 nm) that x-rays impinging under grazing angles can evanescently couple into the cavity. Guided modes are excited at angles of incidence where deep minima in the x-ray reflectivity appear, see Fig. 2b. In the first-order mode at about 2.49 mrad one obtains a 25-fold enhancement of the normalized intensity in the center of the cavity, as shown in Fig. 2d. The absorption due to the presence of the ^{57}Fe layer shows up as a little dip in the curve, indicating that the influence of this layer on the wavefield inside the cavity can be taken as small perturbation.

In the following we calculate the spectral response of this system around the nuclear resonance energy to determine the collective decay width as well as the collective Lamb shift. This will be accomplished via a perturbation expansion of the resonant reflectivity R of the cavity in powers of f_n at the angular position $\varphi = \varphi_1$ of the first-order mode. It can be represented in a diagrammatical fashion, as illustrated in Fig. 2. Each order of the perturbation series of R corresponds to one of the outgoing partial waves A_i that are emitted from the nuclear ensemble at the 'vertices' (denoted by the black dots) in the diagram. In order to sum up all the diagrams in Fig. 2, we note that the scattered amplitude in the nth outgoing wave is related to the $(n-1)$th amplitude via $A_n = (i\,d\,f_N)\,p\,q\,A_{n-1}$. Here d is the thickness of the ^{57}Fe layer and p and q are the amplitudes of the wavefields (at the position of the resonant nuclei) propagating in the directions of the incident and the reflected beams, respectively [24]. For the first vertex we have $A_1 = (i\,d\,f_N)\,p^2\,A_0$ that also includes the coupling of the radiation into the cavity. Finally, the sum over all orders results in

$$R = i\,d\,f_N p^2 \sum_{k=0}^{\infty} (i\,d\,p\,q\,f_N)^k = \frac{i\,dp^2\,f_N}{1 - i\,d\,p\,q\,f_N}. \tag{5}$$

Inserting f_n from (4) we obtain a spectral response that is again a Lorentzian resonance line

$$R(E) = \frac{C\,d\,p^2\,(\Gamma_0/2)}{E - E_0 + L_N + i\,(\Gamma_0 + \Gamma_N)/2} \tag{6}$$

that exhibits a decay width of $\Gamma_N = C\,d\,|\mathrm{Re}(p\,q)|\,\Gamma_0$ and an energy shift of $L_N = -C\,d\,\mathrm{Im}(p\,q)\,\Gamma_0/2$. The factor $\chi = \Gamma_N/\Gamma_0 = C\,d\,|\mathrm{Re}(p\,q)|$ describes the speedup of

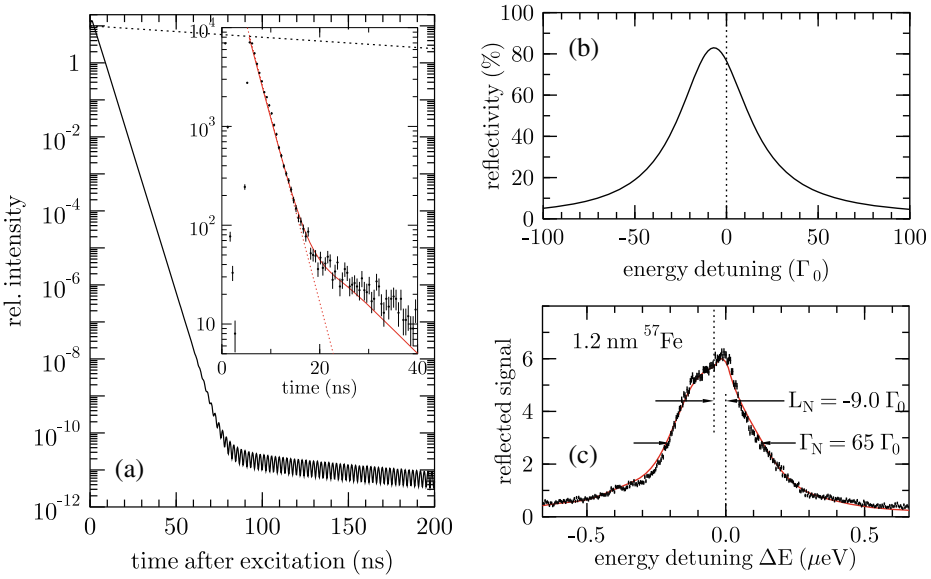

Fig. 3 **a** Calculated time response of a 1.2 nm layer of ^{57}Fe atoms embedded in the center of the planar cavity sketched in Fig. 2, excited in the first-order guided mode at an angle of φ = 2.49 mrad. The decay proceeds strictly exponential over 12 orders of magnitude with a speedup of $\chi = 60$ compared to the natural decay (*dashed line*). The *inset* shows the measured time spectrum from the sample discussed in the text. **b** The corresponding energy spectrum of the reflectivity exhibits a negative shift of about $-9\,\Gamma_0$ which is the collective Lamb shift for this sample. **c** Measured energy spectrum of the reflectivity [24]. *Red solid line* is the theoretical calculation. The asymmetry of the curve results from the residual hyperfine interaction of the ^{57}Fe nuclei in the C matrix

the decay $I(t) = I_0 \exp[-(1+\chi)\Gamma_0 t/\hbar]$ relative to the natural decay. Combining these results into one expression for the complex-valued decay width Γ_C, we obtain

$$\Gamma_C = \Gamma_N \left(1 - i\,\frac{\mathrm{Im}(p\,q)}{|\mathrm{Re}(p\,q)|}\right) \tag{7}$$

While for a spherical atomic cloud the ratio between the collective shift and the collective decay width decreases with increasing size R of the sample, as described by (3), for the planar cavity geometry this ratio is given by $\mathrm{Im}(p\,q)/|\mathrm{Re}(p\,q)|$ thus being independent of the size R of the nuclear ensemble. The reason for this difference is the fact that due to the grazing incidence geometry the phase incursion of the wavefield over the sample thickness is given by $k_{0z}R$ instead of $k_0 R$, where $k_{0z} = \varphi k_0$ is the component of the wavevector normal to the sample plane. This means, that the cooperative emission from the nuclei in the cavity takes place in the limit $k_{0z}R \ll 1$, where (3) apparently is not valid anymore.

Explicitely, the collective Lamb shift derived here is written as:

$$L_N = -\frac{1}{2}\left[\frac{2\pi c_N \rho_N}{k_0^2}\,\frac{d}{\varphi}\,\Gamma_0\right]\mathrm{Im}(p\,q) \tag{8}$$

In the first-order mode $\mathrm{Im}(p\,q)$ is maximum in the center of the guiding layer. For the cavity shown in Fig. 2a one can expect a radiative level shift up to $-13\Gamma_0$, reached for

a ^{57}Fe layer thickness above 2 nm. This value is eventually limited by the electronic photoabsorption of the Fe atoms that disturbs the wavefield in the cavity.

The collective Lamb shift as described here could be experimentally verified recently [24], as illustrated in Fig. 3. For that purpose a 1.2 nm thin layer of ^{57}Fe was embedded in the center of a planar cavity consisiting of (2 nm Pt)/(30 nm C)/(20 nm Pt)/Si. Embedded in the C matrix the ^{57}Fe layer exhibited almost a single resonance line with a residual broadening and quadrupole splitting well below the homogeneous superradiant decay width Γ_N. The measured data, taken at the Nuclear Resonance Beamline ID18 of the ESRF and displayed in Fig. 3, clearly show the collective Lamb shift in excellent agreement with theoretical calculations.

4 Conclusion

We have shown how a planar cavity can be employed to create superradiant states of ensembles of Mössbauer nuclei. In this geometry the small-sample limit $k_0 R \ll 1$ of Dicke superradiance is realized where large values for the collective Lamb shift are encountered. The experimental approach described here provides an ideal playground to explore further properties of cooperative emission by employing nuclear resonances as two-level systems.

References

1. Hübner, M., Kuhl, J., Stroucken, T., Knorr, A., Koch, S.W., Hey, R., Ploog, K.: Phys. Rev. Lett. **76**, 4199 (1996)
2. Scheibner, M., Schmidt, T., Worschech, L., Forchel, A., Bacher, G., Passow, T., Hommel, D.: Nature Phys. **3**, 106 (2007)
3. Brandes, T.: Phys. Rep. **408**, 315 (2005)
4. Potma, E.O., Wiersma, D.A.: J. Chem. Phys. **108**, 4894 (1998)
5. Dicke, R.H.: Phys. Rev. **93**, 99 (1954)
6. Skribanowitz, N., Herman, I.P., Mac Gillivray, J.C., Feld, M.S.: Phys. Rev. Lett. **30**, 309 (1973)
7. Friedberg, R., Hartmann, S.R., Manassah, J.T.: Phys. Rep. C **7**, 101 (1973)
8. Garrett, W.R., Hart, R.C., Wray, J.E., Datskou, I., Payne, M.G.: Phys. Rev. Lett. **64**, 1717 (1990)
9. Friedberg, R., Hartmann, S.R., Manassah, J.T.: Phys. Rev. A **39**, 93 (1989)
10. Lamb, Jr., W.E., Retherford, R.C.: Phys. Rev. **72** 241 (1947)
11. Svidzinsky, A.A., Chang, J.-T., Scully, M.O.: Phys. Rev. A **81**, 053821 (2010)
12. Friedberg, R., Manassah, J.T.: Phys. Rev. A **84**, 023839 (2011)
13. Bonifacio, R., Lugiato, L.A.: Phys. Rev. A **11**, 1507 (1975a)
14. Bonifacio, R., Lugiato, L.A.: Phys. Rev. A **12**, 587 (1975b)
15. Hannon, J.P., Trammell, G.T.: Hyperfine Interact. **123–124**, 127 (1999)
16. Scully, M.O., Fry, E., Ooi, C.H.R., Wodkiewicz, K.: Phys. Rev. Lett. **96**, 010501 (2006)
17. Svidzinsky, A.A., Chang, J.-T.: Phys. Rev. A **77**, 043833 (2008)
18. Scully, M.O.: Phys. Rev. Lett. **102**, 143601 (2009)
19. Friedberg, R., Manassah, J.T.: Phys. Lett. A **373**, 3423 (2009)
20. Manassah, J.T.: Laser Phys. **20**, 259 (2010)
21. Friedberg, R., Manassah, J.T.: Phys. Lett. A **374**, 1648 (2010)
22. van Bürck, U.: Hyperfine Interact. **123/124**, 483 (1999)
23. Röhlsberger, R.: Hyperfine Interact. **123/124**, 301 (1999)
24. Röhlsberger, R., Schlage, K., Sahoo, B., Couet, S., Rüffer, R.: Science **328**, 1248 (2010)

Hyperfine Interact (2012) 204:97–100
DOI 10.1007/s10751-011-0488-0

Synchrotron radiation ^{57}Fe-Mössbauer spectroscopy using nuclear monochromator

Takaya Mitsui · Ryo Masuda · Naohisa Hirao · Ko Mibu · Makoto Seto

Published online: 7 December 2011

Abstract A synchrotron radiation (SR) Mössbauer spectrometer has been developed by using a nuclear Bragg monochromator (NBM). It enables energy-domain ^{57}Fe SR-Mössbauer spectroscopy (SRMS). Doppler-shifted SR-Mössbauer radiation is produced by pure nuclear Bragg reflection (PNBR) from an oscillating $^{57}FeBO_3$ crystal near the Néel point. In this paper, we describe the optics and its applications, including high-pressure SRMS, grazing incidence SRMS and γ-ray diffraction studies with the Rayleigh scattering of Mössbauer radiation (RSMR) method.

Keywords Synchrotron radiation · Mössbauer effect · Nuclear resonant scattering · Bragg scattering

1 Introduction

To bring a marked progress in Mössbauer spectroscopy (MS), we have successfully developed a SR-^{57}Fe-Mössbauer spectrometer with a NBM, which yields high-brilliant SR-^{57}Fe-Mössbauer radiation of about three natural linewidths (See Fig. 1) [1–3]. This paper reports on the optics and applications.

T. Mitsui (✉) · R. Masuda · M. Seto
Japan Atomic Energy Agency, Sayo-cho, Sayo-gun, Hyogo 679–5148, Japan
e-mail: taka@spring8.or.jp

N. Hirao
Japan Synchrotron Radiation Research Institute, 1–1–1 Kouto, Sayo-cho, Sayo-gun, Hyogo 679–5198, Japan

K. Mibu
Nagoya Institute of Technology, Gokiso-cho, Showa-ku, Nagoya, Aichi 466–8555, Japan

Makoto Seto
Research Reactor Institute, Kyoto University, Kumatori, Osaka 590–0494, Japan

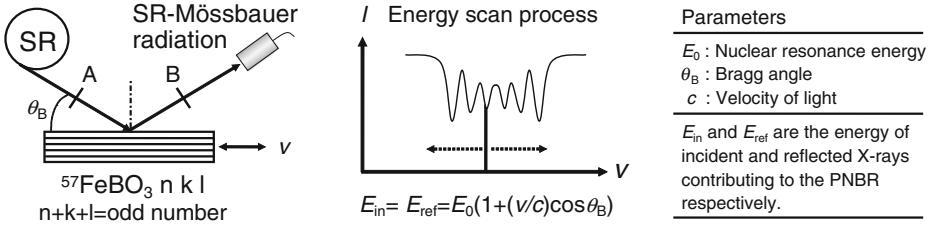

Fig. 1 Experimental scheme of ^{57}Fe-SRMS with single-line pure nuclear Bragg reflection. A PNBR from $^{57}FeBO_3$ (95% ^{57}Fe), oscillating parallel to the reflection plane, filters a Doppler-shifted ^{57}Fe-Mössbauer radiation from SR X-rays and emits at a fixed beam position. An extremely narrow-bandwidth (∼neV) is achieved by PNBR near the Néel point. Then, if a sample is placed at position A or B, the Mössbauer spectrum is measured by counting the reflected radiation as a function of velocity (v)

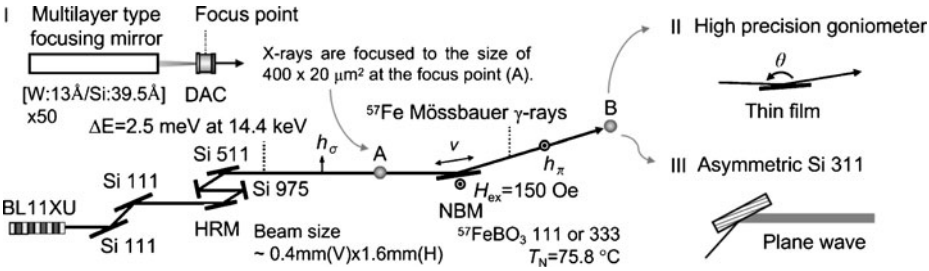

Fig. 2 Optical system for SR-^{57}Fe-Mössbauer spectrometer at SPring-8 (BL11XU). Optical devices (I, II and III) are used for high-pressure study with a diamond anvil cell (DAC), grazing incidence MS (GIMS) and γ-ray diffraction study, respectively. In this optics, NBM converts the σ-polarized SR X-rays into the π-polarized γ-rays

2 Optics and applications

Figure 2 shows the optics of the ^{57}Fe-SRMS spectrometer at SPring-8 (BL11XU) [3]. X-rays with a bandwidth of 2.5 meV at 14.4 keV, produced by a high resolution monochromator (HRM), are ultrafinely monochromatized to a 15.4 neV bandwidth by PNBR from a heated $^{57}FeBO_3$ crystal in $H_{ex} = 150$ Oe. The resonance energy is varied as shown in Fig. 1. The counting rate is $\sim 2.0 \times 10^4$ Hz for $^{57}FeBO_3$ 111 ($\sim 1.2 \times 10^4$ Hz for $^{57}FeBO_3$ 333).

As a transmission experiment, the SRMS of FeH was studied under high pressures up to 65 GPa at 300 K [4]. A tiny polycrystalline iron metal (^{57}Fe 95%, ϕ <50 μm) and ruby pressure markers were enclosed in a DAC filled with liq. H_2. By using a focusing optics (Fig. 2), a good quality spectrum was obtained in a rather short time (2–5 h), whose results proved a great advantage in high pressure SRMS using a NBM in comparison with conventional MS using a ^{57}Co source (See Fig. 3). The spectra show that ferromagnetic dhcp-FeH, formed at $P > 3.5$ GPa, changes into a non-magnetic high-pressure phase ($P > 32.0$ GPa). The origin is the pressure-induced 3d band broadening; it reduces the density of states at the Fermi level $D(E_f)$ so that the Stoner criterion for ferromagnetism is unsatisfied.

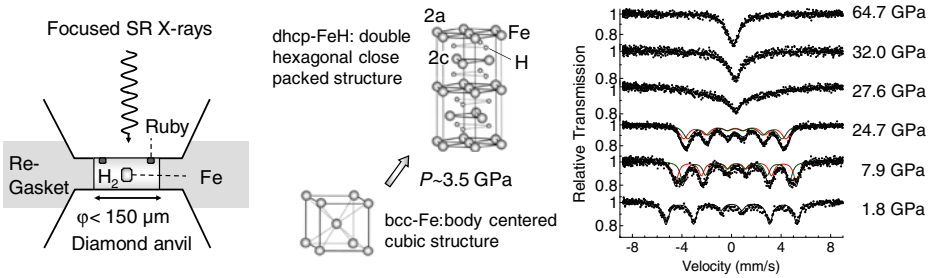

Fig. 3 Hydrogenation of Fe in a DAC and the MS spectra of FeH at high pressures up to 65 GPa. At $P = 7.9$ GPa, the spectrum shows two magnetic sextets due to two different Fe sites (2a, 2c) in a dhcp-FeH. The origin of the ferromagnetic state is the volume expansion and increase in $3d$ electron occupation due to the H_2 absorption, leading to the increase in $D(E_f)$ to satisfy the Stoner criterion. In contrast, at $P > 32.0$ GPa, a ferromagnetic-nonmagnetic transition is caused by the volume reduction, leading to the decrease in $D(E_f)$

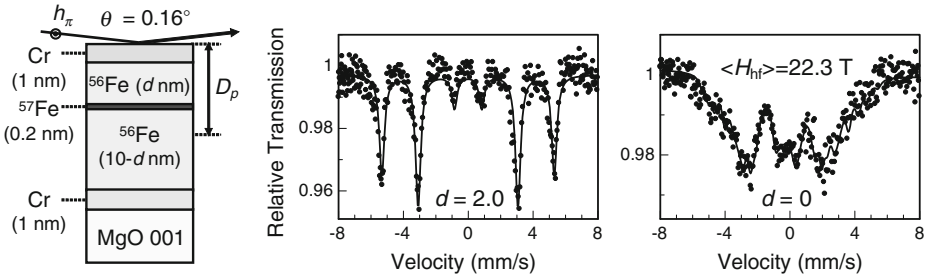

Fig. 4 A principal structure of the prepared Cr/Fe thin films and the observed GIMS spectra. Under the conditions of electronic total external reflection, the penetration depth D_p of X-rays is a few nm, which is deeper than the ^{57}Fe probe layer position in the films. Then, the reflectivity is dominated by the contribution of much larger electronic scattering; the nuclear scattering contribution becomes negligible due to the relatively low ^{57}Fe content. As the result, the GIMS spectrum shows a MS absorption profile

In a grazing-incidence experiment, SRMS of a Cr/Fe film, with 1 monolayer (ML) ^{57}Fe probe atoms, was performed at 300 K without external field. Figure 4 shows the prepared Cr/Fe multilayer structures. The spectra of two different probe layer depths d (2.0 and 0.0 nm) were measured with a data acquisition time of 4.0 h. The probe beam was incident on the films at an angle $\theta = 0.16°$, below the critical angle of electronic total reflection. Then, the GIMS spectrum gives a usual absorption profile as explained in Fig. 4. In fact, the spectrum for $d = 2.0$ nm shows a magnetic sextet of bulk α-Fe (H_{hf} ~33T). In contrast, the result for $d = 0$ nm shows a broad hyperfine field distribution, whose average value $< H_{hf} >$ is less than that of $d = 2.0$ nm; the Cr/Fe interface is composed of flat regions separated by step sites on a scale of a few ML so that the magnetic hyperfine field at the ^{57}Fe nuclei is reduced upon an increase of neighboring Cr atoms [5]. The result verifies that the GIMS, combined with the probe layer method, is a useful tool for thin film study with atomic-scale resolution.

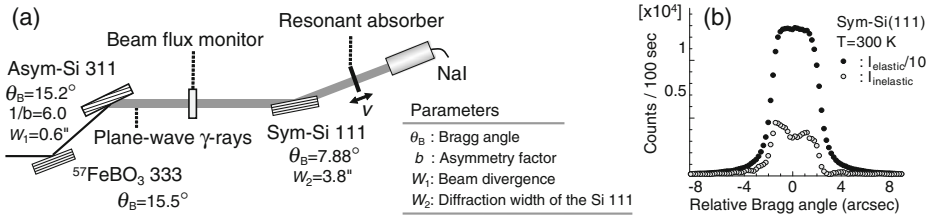

Fig. 5 **a** Experimental setup. **b** Elastic and inelastic scattering at a Si 111 reflection. The beam flux is monitored by a transparent type avalanche photo diode detector (transmittance ~90%). The resonant absorber of a mixture of fluoferrates exhibits a wide line of about 50 neV

As a γ-ray diffraction study, the thermal diffuse scattering (TDS) was measured at a Si Bragg reflection. The plane-wave γ-rays were produced by asymmetric Si 311, forming a parallel ($\pm$) setting with $^{57}FeBO_3$ 333. The beam divergence $W_1 = 0.6''$ was much smaller than the diffraction width $W_2 = 3.8''$ of symmetric Si 111. In Fig. 5a, the Si 111 rocking curves were measured with on and off resonant conditions by a "Black" resonant absorber with a line width of ~50 neV. The elastic and inelastic (TDS) parts were determined according to ref. [6]. In Fig. 5b, the TDS curve, increasing near the Bragg angle, shows a small dip in the total reflection region for dynamical Bragg diffraction. The dip is a result of energy conservation; the reflected beam is quite strong and consequently little energy enters the crystal to produce TDS [7]. The result proves that the SR-based RSMR enables the TDS study at the Bragg peaks in a high angular resolution ($\sim 10^{-6}$ rad).

3 Conclusion

Today high-brilliant ^{57}Fe γ-rays are available at any bunch-mode of SR. This contrasts with time domain ^{57}Fe-SRMS, requiring a bunch-period over 100 ns. Energy domain ^{57}Fe-SRMS enters a new stage in both basic and practical studies.

Acknowledgements This work was supported by JST/CREST and partially by NEDO (Hydro-Star).

References

1. Chumakov, A.I., Zelepukhin, M. V. , Smirnov, G. V. , van Bürck, U., Rüffer, R., Hollatz, R., Rüter, H.D., Gerdau, E.: Phys. Rev. B **41**, 9545–1547 (1990)
2. Smirnov, G.V., van Bürck, U., Chumakov, A.I., Baron, A.Q.R., Rüffer, R.: Phys. Rev. B **55**, 5811–5815 (1997)
3. Mitsui, T., Hirao, N., Ohishi, Y., Masuda, R., Nakamura, Y., Enoki, H., Sakaki, K., Seto, M.: J. Synchrotron Radiat. **16**, 723–729 (2009)
4. Mitsui, T., Hirao, N.: Mater. Res. Soc. Symp. Proc. **1262**, W06–09 (2010)
5. Landes, J., Sauer, Ch., Brand, R.A., Zinn, W., Mantl, S., Kajcsos, Zs.: J. Magn. Magn. Mater. **86**, 71–77 (1990)
6. O'Connor, D.A., Butt, N.M.: Phys. Lett. **7**, 233–235 (1963)
7. Annaka, S., Kikuta, S., Kohra, K.: J. Phys. Soc. Jpn. **21**, 1559–1564 (1966)

Hyperfine Interact (2012) 204:101–110
DOI 10.1007/s10751-011-0543-x

Fast scintillation detectors for high-energy X-ray region

Shunji Kishimoto · Fumihiko Nishikido · Rie Haruki · Kengo Shibuya · Masanori Koshimizu

Received: 22 September 2011 / Accepted: 16 December 2011 / Published online: 3 January 2012

Abstract We have developed fast scintillation detectors for nuclear resonant scattering experiments using synchrotron radiation and a nuclear excited level existing in >30 keV. A fast x-ray detector using an organic-inorganic perovskite scintillator of phenethylamine lead bromide ($PhE\text{-}PbBr_4$) had a dominant light emission with a fast decay time of 9.9 ns. An x-ray detector equipped with a 0.9-mm-thick $PhE\text{-}PbBr_4$ crystal (size: $\sim 8 \times 7$ mm^2) was used to detect nuclear resonant scattering in ^{61}Ni (the first excited level: 67.41 keV; half-life: 5.3 ns). We could successfully record the decaying gamma rays emitted from ^{61}Ni with a relatively high detection efficiency of 24%. A lead-doped plastic scintillator (NE142, Pb ∼5 wt% doped) had been known to have a faster decay time of 1.7 ns. Following a test of a single NE142 detector, a four-channel NE142 detector was fabricated and successfully applied to the synchrotron-radiation based Mössbauer spectroscopy experiment on ^{61}Ni.

Keywords Synchrotron Radiation · Nuclear resonant scattering · Scintillation detector · Scintillator

S. Kishimoto (✉)
High Energy Accelerator Research Organization, 1-1 Oho, Tsukuba, Ibaraki, 305-0801, Japan
e-mail: syunji.kishimoto@kek.jp

F. Nishikido
National Institute of Radiological Science, 4-9-1 Anagawa, Inage-ku, Chiba, 263-8555, Japan

R. Haruki
Japan Atomic Energy Agency, 2-4 Shirakata Shirane, Tokai, Naka, Ibaraki, 319-1195, Japan

K. Shibuya
University of Tokyo, 3-8-1 Komaba, Meguro-ku, Tokyo, 153-8902, Japan

M. Koshimizu
Tohoku University, 6-6 Aramaki Aza Aoba, Aoba-ku, Sendai, Miyagi, 980-8579, Japan

1 Introduction

Fast detectors have been developed for nuclear resonant scattering (NRS) using synchrotron radiation. A silicon avalanche photodiode (Si-APD) can be used as a photon sensor by direct absorption of γ-rays in a depletion region of silicon. A Si-APD detector of direct detection for X-rays has been a standard detector in this field [1]. The reasons why the Si-APD is suitable for the NRS experiments exist in a wide dynamic rage of outputs from 10^{-2} to 10^{8} s^{-1} and in a sub-nanosecond time resolution for X-ray photons. The properties are extremely useful for separating nuclear radiation from an intense atomic scattering generated when nuclei are excited by an X-ray beam of synchrotron radiation. However, since one device of Si-APD has a thin sensitive layer of 10–150 μm thick and silicon itself has a small atomic number of 14, the intrinsic efficiency is limited to be low of several % for the photon energy of >30 keV. Since the third generation synchrotron rings have recently supplied high-energy X-ray beams of $>10^{10}$ photons s^{-1}, a lot of nuclei whose excited levels exist in >30 keV have been offered to the NRS experiments. With a stack of the APD devices, we can obtain a larger efficiency, for example, 10% even at energy of 67.4 keV [2]. In this case, a beam acceptance of the detector was limited to be a small area of 2×0.03 mm^2, less than 1 mm^2. A larger solid angle of a detector is generally needed except for nuclear forward scattering.

Before the Si-APD detectors were widely used, scintillation detectors had been tested for the NRS experiments. A scintillation detector mounting a plastic scintillator was reported as a fast detector in the year of 1990 [3, 4]. The performance was evaluated at energies of < 20 keV, at that time. The maximum count-rate of the detector was high, up to 10^7, but the detector suffered from a noise of several tens s^{-1} from a photomultiplier tube. No new scintillator suitable for the NRS experiments using high-energy X-rays had been known for these two decades. If using with a new scintillator and with a new experimental method, a scintillation detector will again give us some benefits, covering a low detection-efficiency for high energy photons when using a Si-APD detector. Here, we report on our scintillation detectors newly developed for the NRS experiments in high energy X-ray region.

2 New scintillation detectors

Our new scintillation detectors are listed in Table 1. Properties as a fast detector were investigated by using synchrotron X-rays at beamline BL-14A at the Photon Factory. Figure 1 shows measurement setups for the detectors. In (a) of Fig. 1, X-ray beam directly impinges on the detector window for measurements of energy and time spectra and (b) shows a setup for measuring a time spectrum of scintillation lights. System E is an energy spectroscopy system using a charge-sensitive preamplifier, a main amplifier and a multichannel analyzer (MCA). System T is a time spectroscopy system using a wide-band high-frequency amplifier, a constant-fraction discriminator (CFD), and a time-to-amplitude converter (TAC). In the setup of (b), scintillation light was detected by a photomultiplier tube (PMT, Hamamatsu R7400P) with a probability of less than single photon detection, provided by a distance of several tens mm, between the scintillator and the PMT having an effective entrance window of 8 mm in diameter.

Table 1 Fast scintillation detectors for nuclear resonant scattering

Detector	Scintillator	PMT	Experiment
A	PhE-$PbBr_4$ 8 × 7 mm × 0.9 mm thick	R7400P	Ni-61
B	NE142 9 mm dia. × 5 mm thick	R7400P	I-127
C	NE142 17 mm dia. × 10 mm thick 4 elements	R7400P 4 channels	Ni-61

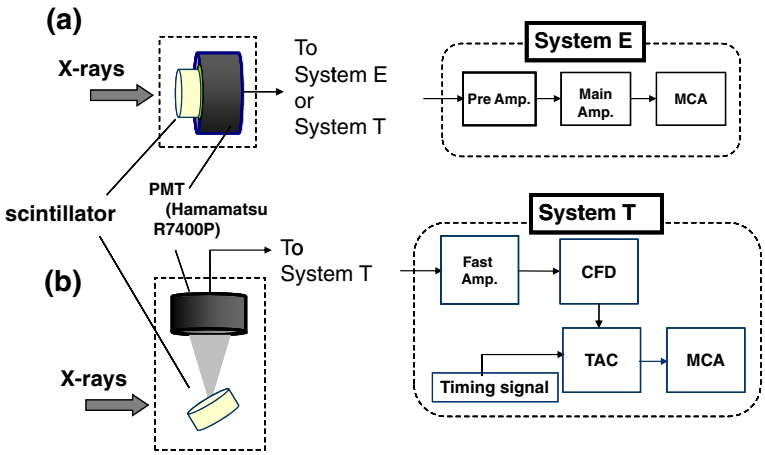

Fig. 1 Experimental setups: (**a**) for direct detection of X-rays and (**b**) for scintillation detection with a single-photon probability. System (E) is used for measuring an energy spectrum and System (T) is for time spectrum

2.1 The PhE-$PbBr_4$ detector

A fast X-ray detector using an organic-inorganic perovskite scintillator of phenethylamine lead bromide (PhE-$PbBr_4$) (Detector A in Table 1) was recently reported [5, 6]. The name of PhE-$PbBr_4$ is abbreviation of $(C_6H_5C_2H_4NH_3)_2PbBr_4$ crystal (bis-(phenethylammonium) tetrabromoplumbate (II). The crystal has the low-dimensional structure consisting of metal-halide layers. This structure causes relatively high efficiency of a fast light emission by exciton, even at room temperature owing to the quantum confinement effect [7]. We produced single crystals of PhE-$PbBr_4$ (area: 10–100 mm^2; thickness: up to 1.7 mm). Although sub-nanosecond light was not observed, the scintillator had a dominant light emission with a fast decay time of 9.9 ± 0.2 ns (72 ± 1% of the total light yield). Other components were estimated by 23 ± 1 ns (25 ± 2%), and 94 ± 3 ns (2.3 ± 0.1%) ns. An X-ray detector equipped with the PhE-$PbBr_4$ crystal was used to detect NRS in ^{61}Ni (the first excited level: 67.41 keV; half-life: 5.34 ns [8]). The Ni-61 NRS measurement was carried out at beamline BL09XU of the SPring-8. Figure 2 shows the PhE-$PbBr_4$ crystal (size: ∼8 × 7 mm^2, thickness: 0.9 mm) and a photomultiplier tube (PMT, Hamamatsu R7400P) of the detector used for the Ni-61 experiment. A sample of

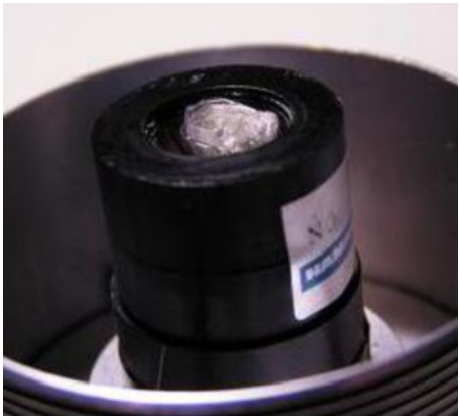

Fig. 2 Photograph of a PhE-$PbBr_4$ crystal and a photomultiplier tube (Hamamatsu R7400P)

Ni metal foil (thickness: 0.38 mm; ^{61}Ni: 95% enriched) was attached to a 3-mm-thick aluminum plate in order to absorb fluorescent X-rays from the Ni foil. We could successfully record the decaying gamma rays emitted from ^{61}Ni with a time resolution of 0.71 $\pm$ 0.05 ns (FWHM) and a relatively high detection-efficiency of 23.7 $\pm$ 0.1%. Although the scintillator had a good efficiency for high-energy X-rays and relatively fast scintillation light, the slow components prolonged the tail of output pulse, unfortunately.

2.2 The NE142 detectors

2.2.1 The single-channel detector

Detector B in Table 1 was fabricated, expecting the time response faster than that of Detector A. A lead-doped plastic scintillator of NE142 (Pb ~5 wt% doped; equivalent to Saint Gobain BC-452) was equipped to the detector and applied to nuclear quasi-elastic scattering on ^{127}I (the first excited level: 57.60 keV; half-life: 1.9 ns [9]). A cylindrical scintillator of 9 mm in dia. and 5 mm thick was mounted on a small metal-package PMT (Hamamatsu R7400P), which was the same as that of the PhE-$PbBr_4$ detector. By containing lead in plastic base of the scintillator, absorption of X-rays increased to a relatively high value. The intrinsic efficiency was measured in the arrangement of direct beam incident, which was a setup of (a) in Fig. 1, using the system E with a charge-sensitive preamplifier of Canberra 2005 and the PMT voltage of $-$650 V. The obtained result was 15.3% at 57.6 keV. A simulation result by Geant4 (http://geant4.cern.ch/) indicated that a lead component of 4.2 wt% best fitted to the experimental energy spectrum of Fig. 3. Prepared for an experiment of nuclear inelastic or quasi-elastic scattering, the detection efficiency was estimated to be 3.4% by the simulation, considering with its solid angle of 30%, when X-rays were isotropically emitted from a point 1.9 mm apart from the center of the scintillator's surface. Using the system T in Fig. 1, an output pulse from the 300 MHz-bandwidth fast amplifier ORTEC VT120A was recorded, as shown in Fig. 4. The pulse width (FWHM) was 3 ns at the PMT voltage of $-$500 V. Count-rate property of the detector was measured at 57.6 keV with the fast counting system using a 500 MHz counter,

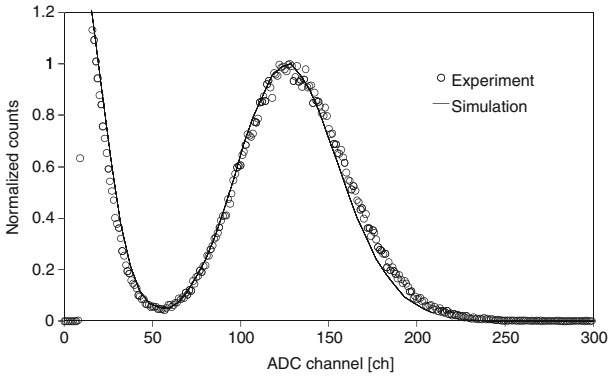

Fig. 3 Energy spectra of the single NE 142 detector: ○ measured at 57.6 keV and − calculated by Geant4

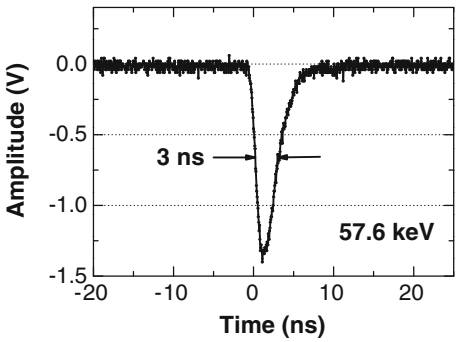

Fig. 4 An output pulse of the single NE142 detector, observed at 57.6 keV

instead of the TAC in System T of Fig. 1. Figure 5 shows the result of the output rates vs. the input photon rates. The input photon rate was controlled with filters of tungsten foil. A detector mounted with a 5-mm thick NaI(Tl) scintillator and the tungsten filters were used to convert a low-rate count less than 10^3 s^{-1} into the input photon rate. The threshold level of the CFD (ORTEC 935) was set to be −0.11 V. In Fig. 5, open circles indicate the output rate and a solid curve means the paralyzable model which has an output width of 26 ns [10]. The observed output rate was saturated at 1.39×10^7 s^{-1}, which was similar to the maximum of the paralyzable model of 26-ns pulse width. Since the pulse width was 7–8 ns on the 0-V baseline, the count limit was caused not only by the output width, also maybe by a PMT current. The time property of the detector was measured at a single-bunch operation of the PF ring, which mode had an X-ray pulse-interval of 624 ns. The scintillation light from the plastic scintillator had a fast decay time of 1.7 ns (96% of the total light yield), and others of 6.4 ns (3.3%) and 41 ns (0.3%), from the fitted result shown in Fig. 6. Each uncertainty given by one standard deviation was at most 7% on both the decay constant and the light yield. This spectrum was measured with the setup of (b) in Fig. 1 and a faster 1.5 GHz amplifier of Phillips Scientific 6954, instead of VT120A. Time resolution of 0.54 ± 0.01 ns (FWHM) was obtained from a peak profile at the setup (a) in Fig. 1, by setting a threshold level of −0.2 V and the PMT voltage of −500 V, as shown in Fig. 7. The single NE142 detector was thus applied

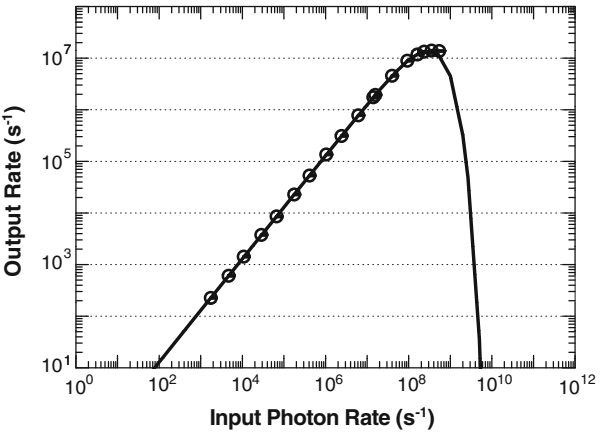

Fig. 5 Output count-rates vs. input photon rates, measured with the single NE142 detector at 57.6 keV

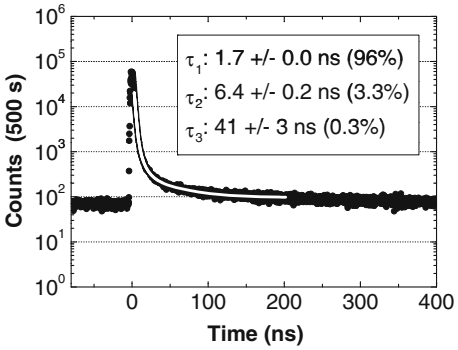

Fig. 6 Scintillation decay of NE142, recorded at 57.6 keV using a single-bunch mode of the PF ring

to the nuclear quasi-elastic scattering experiment on a potassium iodide solution, carried out at BL09XU of the SPring-8 (proposal No. 2009B1070). This fast response could separate delayed nuclear events from huge electronic scattering in a shorter period of ∼5 ns. The result in detail will be reported in another place.

2.2.2 The four-channel detector

For the Synchrotron Radiation (SR) based Mössbauer spectroscopy experiment [11], a multiple detector mounted with four plastic scintillators of NE142 (Detector C in Table 1) was developed. The scintillator size of one element was 17 mm in diameter and 10 mm thick. In order to obtain a larger solid angle, the scintillator size increased by a factor of about 14.3 in total area, compared with that of the Detector B. The thickness of the one element scintillator was also two times as large as that of the Detector B, to be more sensitive for high-energy X-rays. Figure 8 shows the arrangement of the detector elements and its measurement system. An aluminum window of 25 μm thick and 50 mm in diameter was put at the front of the brass cylindrical case.

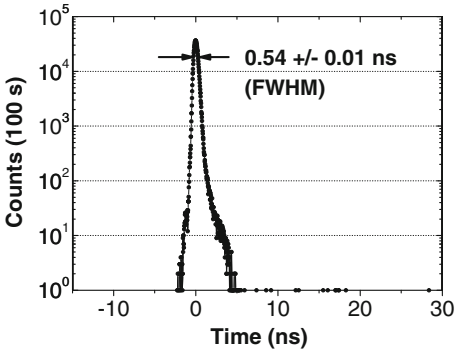

Fig. 7 Time spectrum of 57.6-keV X-ray beam profile, measured with the single NE142 detector. A time resolution (FWHM) was 0.54 ± 0.01 ns

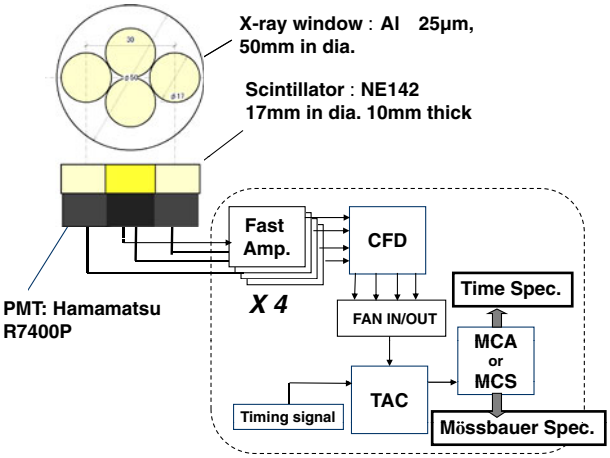

Fig. 8 Scintillator arrangement of the four-channel NE142 detector and its measurement system

The four-channel detector was applied to the Ni-61 SR based Mössbauer experiment on iron pnictide [12] at beamline BL09XU of the SPring-8 (Proposal No. 2010B1369). An enriched Ni doped iron pnictide of $Ba(Fe_{1-x}Ni_x)As_2$, x = 3% and 5% was a sample for our experiment. Coexistence of magnetism and superconductivity was reported on this compound [13]. Non-doped $BaFe_2As_2$ show antiferromagnetism below 130 K. The Neel temperature decreased with Ni doping, and superconductivity was appeared. At 5% Ni doping, the antiferromagnetism was disappeared and then only superconductivity was observed. The microscopic state of Fe and Ni atoms on this coexistence of magnetism and superconductivity is very interesting to elucidate the mechanism of the superconductivity.

Each of the samples x = 3% (150 mg) and 5% (107.5 mg), shaped with 7 mm in diameter, was set to a cryostat for liquid-helium flow cooling, as a transmitter. A piece of $Ni_{84}V_{16}$ alloy, 3.8 μm thick was used as a scatterer because the alloy show a single absorption peak at Mössbauer measurement. The scatterer was mounted on a copper block 30° inclined to the horizontal plane in the cryostat and was moved in the constant-acceleration mode using a transducer for Mössbauer spectroscopy. 86.2%-enriched Ni-61 was doped to all the samples.

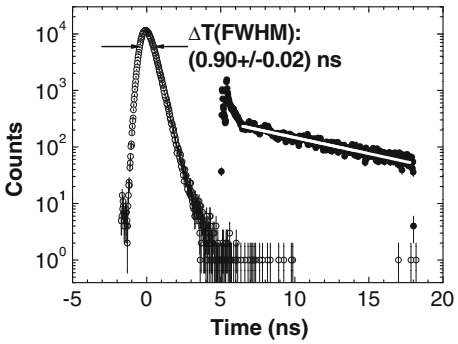

Fig. 9 Time spectra measured on the resonance with the prompt peak (open circles) and without the prompt peak (closed circles). The white line indicates a 7.7-ns decay curve fitted to the data

Table 2 A comparison of the Si-APD detector and the four-channel NE142 detector

	[A]Efficiency ([B]Int. eff.)	Delayed signals (cps), Time region (ns)
Si-APD (1 × 2 mm^2, 0.03 mm thick, 8 pixels)	[C]1.8% (42.1%)	13 cps, 5–18 ns
NE142 (17 mm dia., 10 mm thick, 4 elements)	9.3% (29%)	60 cps, 6.5–18 ns

[A]Considering each solid angle (4.3% for Si-APD, 35% for NE142).

[B]Absorption by an X-ray beam of 1 mm in diameter.

[C]This is given by Ni-K X-ray Absorption.

Time spectra on the resonance without the prompt peak (closed circles) and with the prompt peak (open circles) were recorded by radiation from the scatterer, as shown in Fig. 9. By using the timing system, detector counts were inhibited for the period of the prompt scattering, before 5 ns, as the spectrum of closed circles. A time resolution (FWHM) of the detector was known to be 0.90 ± 0.02 ns from the prompt peak in Fig. 9. A decay structure by nuclear radiation from the Ni-61 excited state was well observed without the intense prompt peak. A decay curve of 7.7-ns time constant, the white line in Fig. 9, well fitted to the measured data after 6.5 ns. Using the counts after 6.5 – 18 ns, a peak profile of the Ni-61 nuclear radiation around 67.4 keV was measured, while scanning energy of the incident X-ray beam. An FWHM of 7.6 ± 0.3 eV was observed for the peak profile, as shown in Fig. 10. This value means an energy width of the selected nuclear radiation, determined mainly by optics of the beamline. The net count-rate of the delayed nuclear radiation reached more than 50 s^{-1}, four times than that for a Si-APD detector (1 × 2 mm^2, 30 μm; 8 pixels) at almost the same experimental condition. Detection efficiency was calculated for the Si-APD and the present four-channel detectors by the simulation code of Geant4. The results are listed in Table 2. The distance between the center of detector window and the scattering point was assumed to be 5 mm in the calculation. The efficiency including geometry, of the NE142 detector was obtained to be 9.2% for 67.4-keV γ rays, while that of the APD detector was 1.8% for Ni KX-rays. These values well explained the higher count-rate for the delayed nuclear radiation with the detector C. With the multi-channel scaling of the delayed counts, we observed a Mössbauer absorption spectrum in Fig. 11, where open circles indicate the resonant absorption by the sample of x = 3%. The measured temperature was 12 ± 0.1 K

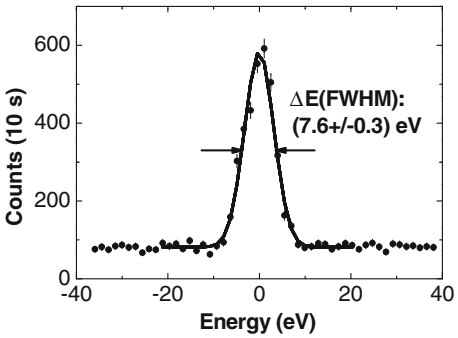

Fig. 10 Peak profile of nuclear resonant scattering, measured with scanning the incident photon energy around 67.4 keV. An energy width (FWHM) was observed to be 7.6 ± 0.3 eV

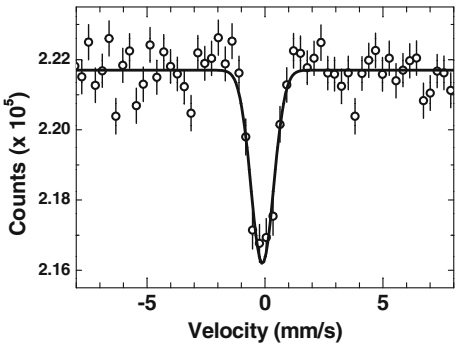

Fig. 11 Observed Mössbauer absorption spectra on a sample of $Ba(Fe_{1-x}Ni_x)As_2$, x = 3%

for the samples as the transmitter and 20.5 ± 0.6 K for the scatterer. The measuring time was about 52 hours. From Gaussian fitting to the absorption peak, drawn by the solid curve in Fig. 11, the peak width (FWHM) was obtained to be 1.1 ± 0.1 mm/s. Comparison with the result for the sample of x = 5% and the discussion will be presented in a future article by Y. Kobayashi et al..

3 Conclusions

Performances of our scintillation detectors have been reviewed and discussed for the NRS experiments. Fast decay time of the scintillation light is possible to select nuclear radiation from a sample to analyze with the time spectroscopy using synchrotron X-ray pulse. Compared with silicon avalanche photodiodes, scintillation detectors are useful for high-energy X-rays, especially in the measurements which need a larger solid angle and detection efficiency. The multi-element NE142 detector actually proved successful in the Ni-61 experiment with the SR-based Mössbauer spectroscopy. Further we are studying to obtain a scintillator with both a fast decay time and a larger absorption of X-rays. Simulation by Geant4 is quite effective for expectation of the detector performance and also for its evaluation. For improving noise rate from the existing photomultiplier tube, new development for a photosensor will also be important.

Acknowledgements The work was partly supported by the Japan Science and Technology Agency, CREST. The study for the NE142 detectors was performed with the approval of Japan Synchrotron Radiation Research Institute (JASRI) (Proposal No. 2009B1070 and 2010B1369) and of the Photon Factory Advisory Committee (Proposal No. 2008G104 and 2010G179).

References

1. Baron, A.Q.R.: Hyperfine Interact. **125**, 29–42 (2000)
2. Sergueev, I., Chumakov, A.I., Deschaux Beaume-Dang, T.H., Rüffer, R., Strohm, C., van Bürck, U.: Phys. Rev. Lett. **99**, 097601 (2007)
3. Radtke, J.L.: IEEE Trans. Nucl. Sci. **37**, 129–133 (1990)
4. Metge, J., Rüffer, R., Gerdau, E.: Nucl. Instr. and Meth. **A292**, 187–190 (1990)
5. Kishimoto, S., Shibuya, K., Nishikido, F., Koshimizu, M., Haruki, R., Yoda, Y.: Appl. Phys. Lett. **93**, 261901 (2008)
6. Shibuya, K., Koshimizu, M., Nishikido, F., Saito, H., Kishimoto, S.: Acta Cryst. **E65**, m1323–m1324 (2009)
7. Shibuya, K., Koshimizu, M., Asai, K., Shibata, H.: Appl. Phys. Lett. **84**, 4370–4372 (2004)
8. Bhat, M.R.: Nucl. Data Sheets **88**, 417–532 (1999)
9. Hashizume, A.: Nucl. Data Sheets **112**, 1647–1831 (2011)
10. Kishimoto, S.: Nucl. Instr. Meth. **A397**, 343–353 (1997)
11. Seto, M., Masuda, R., Higashitaniguchi, S., Kitao, S., Kobayashi, Y., Inaba, C., Mitsui, T., Yoda, Y.: Phys. Rev. Lett. **102**, 217602 (2009)
12. Kamihara, Y., Hiramatsu, H., Hirano, M., Kawamura, R., Yanagi, H., Kamiya, T., Hosono, H.: J. Am. Chem. Soc. **128**, 10 012 (2006)
13. Canfield, P.C., Bud'ko, S.L., Ni, Ni, Yan, J.Q., Kracher, A.: Phys. Rev. **B80**, 060501(R) (2009)

Hyperfine Interact (2012) 204:111–117
DOI 10.1007/s10751-012-0564-0

Mössbauer spectroscopy database: past, present, future

Junhu Wang · Chang Zi Jin · Xin Liu · D. R. Liu · Hui Sun · Fang Fang Wei · Tao Zhang · J. G. Stevens · A. Khasanov · I. Khasanova

Published online: 25 January 2012

Abstract Mössbauer Spectroscopy is a useful tool for scientific research in many fields, lots of researchers benefited from this technology which discovered by Rudolf Mössbauer. Up to now, there are more than one million Mössbauer data records present in public papers and books, and the number is increasing. Most of these data records have been collected by Mössbauer Effect Data Center (MEDC) since 40 years ago, and now all these data records can be seen on the web of database. MEDC, as a part of Mössbauer community, is and always will be offering better service with the help of the entire community.

Keywords Mössbauer effect data center · Isomer shift · Quadrupole splitting · Mössbauer database

Mössbauer Spectroscopy is a research tool successfully utilized by scientists in various fields—physics, chemistry, geology, biology and others. More than 53,000 papers related to the subject were published since the famous discovery by Rudolf Mössbauer in 1958. During past 50 years, more than 50,000 scientists contributed to

J. Wang (✉) · C. Z. Jin · X. Liu · D. R. Liu · H. Sun · F. F. Wei · T. Zhang
Mössbauer Effect Data Center, Dalian Institute of Chemical Physics,
Chinese Academy of Sciences, 457 Zhongshan Road,
Dalian 116023, China
e-mail: wangjh@dicp.ac.cn

T. Zhang
e-mail: taozhang@dicp.ac.cn

J. G. Stevens · A. Khasanov · I. Khasanova
Department of Chemistry, University of North Carolina at Asheville,
One University Heights, CPO 2311, Asheville,
NC 28804-8511, USA

the development and application of the method. Currently, more than 3,000 scientists from about 1,000 institutions in more than 70 countries around the world benefit in their research activities from the use of Mössbauer spectroscopy [1–3]. Among them, one can identify 2,182 individuals from 756 institutions who are strongly connected to the application of the method [4]. Closer look helps to select a core group of the best specialists in the field of Mössbauer Spectroscopy – 875 scientists from 385 institutions [5]. All these researchers are known informally as Mössbauer Research Community, which is organized under the International Board on Application of Mössbauer Effect (IBAME).

Members of the Mössbauer Community are involved in various kinds of scientific work and publish their results in 910 different scientific periodicals and 144 books [6]. An enormous amount of research data was collected during the past 50 years. An acute demand for systematization of results, facilitating information dissemination, strengthening contacts between researchers was served for many years by the Mössbauer Effect Data Center (MEDC). Mössbauer spectroscopy is rather time-consuming type of scientific study. MEDC using the database can help to coordinate the research in the world to avoid unnecessary and expensive duplication. For example, 458 data records registered in the database under the absorber name Fe_2O_3, a-Fe_2O_3 and hematite, all extracted from various publications indicate certain redundancy in experimental activity.

MEDC, which had operated for 40 years in Asheville (USA), recently has been moved to Dalian (China). One of the activities of the Center is maintaining the Mössbauer Spectroscopy Database.

The idea of Mössbauer Spectroscopy Database goes back to Mössbauer Spectroscopy Index compiled by Muir and colleagues [7]. Further development of the concept was undertaken by the team of Mössbauer Effect Data Center led by John Stevens. The first generation of the Mössbauer Spectroscopy Database was established in 1979. It was created using RDB-VMS software and was running on DEC-VAX computers. The true innovation at the time was the concept of the spectral parameters—isomer shift and quadrupole splitting values along with other information being entered in the database. This information was extracted from the scientific publications by trained Mössbauer spectroscopists, who were digesting a vast volume of articles published in journals all over the world. A group of associate editors of the Mössbauer Effect Reference and Data Journal were contributing considerably to this process.

Technological advancements of the 1990's in computer hardware made possible a transfer of the database from mainframe computers to desktop machines. The whole database was moved to a desktop PowerPC Macintosh computer. The new 4D database software had been chosen for implementation of the new database design. At that time Mössbauer Effect Data Center made its first presence on the web and the database was made accessible worldwide.

Now the international Mössbauer Community has reached the new level of development and needs new services based on the web access database. Following the best achievements of the web development, it seems reasonable to accept the model of the database implemented on the platform of the open source products like Apache web server, MySQL database and PHP-based interface. This choice allows hardware platform independence of the solution allowing deployment of the system on Windows, Linux and Macintosh OS machines. This solution also opens

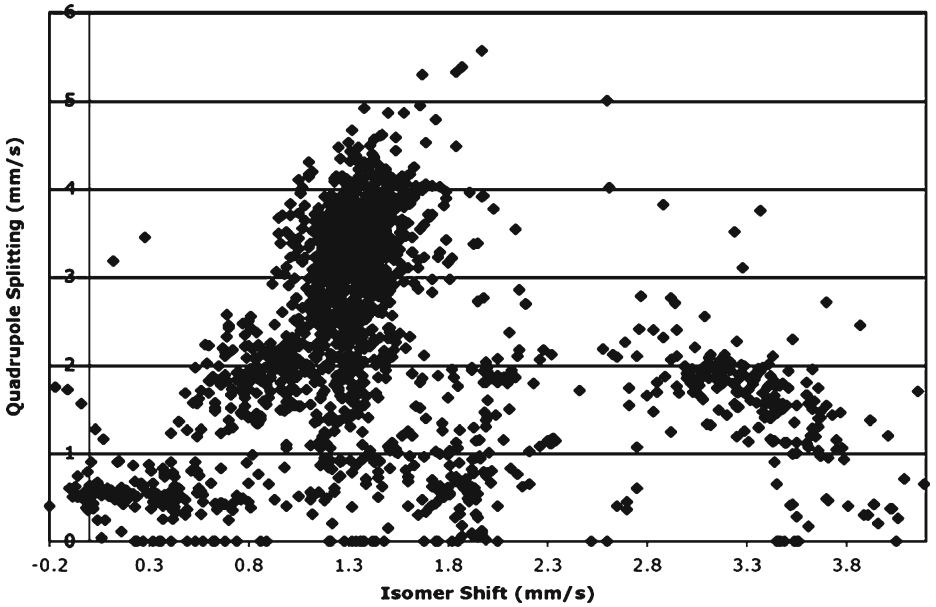

Fig. 1 ^{119}Sn Mössbauer spectral parameters from the MEDC database plotted on Isomer Shift – Quadrupole Splitting graph

the opportunity for making the future Mössbauer information system open source type one, allowing all members of the community to participate in development and improvement of the software.

Let's check out a possible database used by a researcher interested in ^{119}Sn isotope. Since the discovery of the Mössbauer effect, chemists appreciated the information obtained from the main spectral parameters—isomer shift (IS) and quadrupole splitting (QS). These values proved to be very sensitive to electron density and charge distribution in the atoms with resonant nuclei. For the past fifty years, thousands various substances were studied by using Mössbauer spectroscopy and a vast amount of experimental information was collected. For example, the observed values for ^{119}Sn isomer shift stretch over the span of more than 4 mm/s and the absolute value of quadrupole splitting values covers a 6 mm/s of Doppler velocity range. The distribution of the observed values shows some characteristic congregations (Fig. 1). If the results are plotted as distribution of observed isomer shift values, then a clear maximum is observed around 1.3 mm/s value (Fig. 2). One could inquire if the collected IS/QS data could be used for substance identification at least in the case of ^{119}Sn Mössbauer spectroscopy. The data plotted on Fig. 3 shed light on this question showing the distribution of quadrupole splitting values reported in publications having the isomer shift restricted to the mostly represented region around 1.3 mm/s. The distribution clearly shows that the number of observed results for a selected pair IS/QS stays below 1 for the all QS values except the region around 3.4 mm/s, were it does not exceed 2. This means that using a pair of values IS and QS, an inquisitive researcher will have no trouble of identifying the measured sample using the database of Mössbauer spectroscopic parameters.

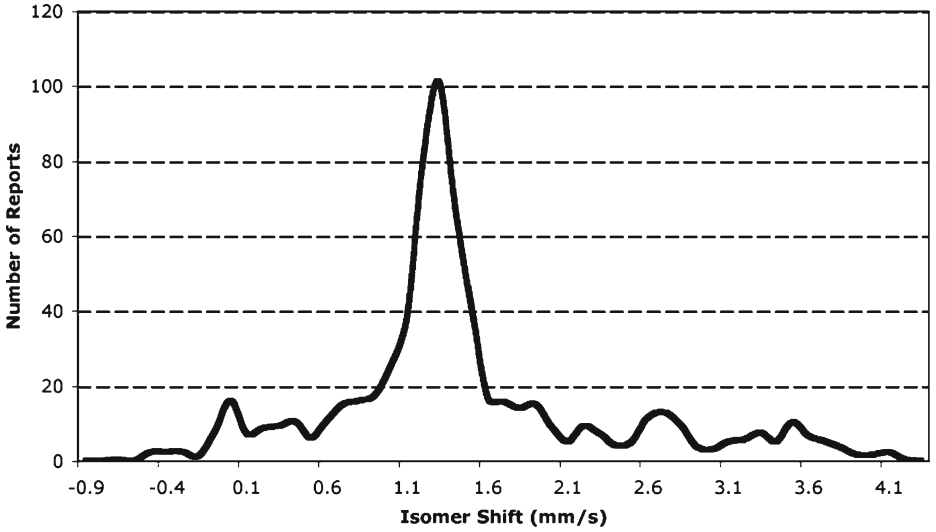

Fig. 2 Distribution of reported values of Isomer Shift for ^{119}Sn

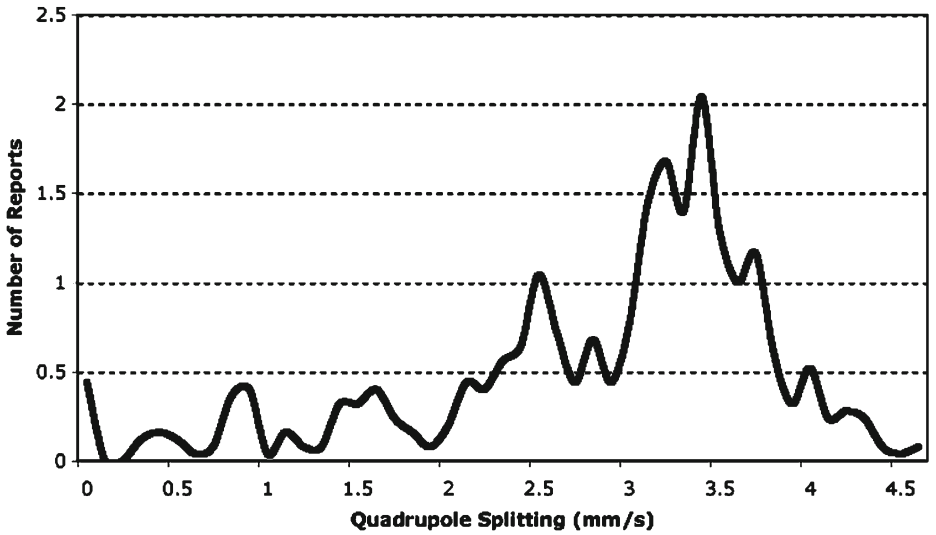

Fig. 3 Distribution of reported Quadrupole Splitting values for ^{119}Sn with Isomer Shift values between 1.3 mm/s and 1.4 mm/s

Mössbauer spectroscopists know how important is visual assessment of the spectrum. That is why it would be very helpful to create a tool that would allow visual comparison of a spectrum collected by anybody to as many appropriate results available. Currently, no such tool does exist. Popular fitting tools offer very limited capability of such kind even for a collection of spectra on one machine. Second feature any researcher would appreciate if the fitting tool equipped with a set of different models including dynamic effects, distribution of parameters etc. in addition

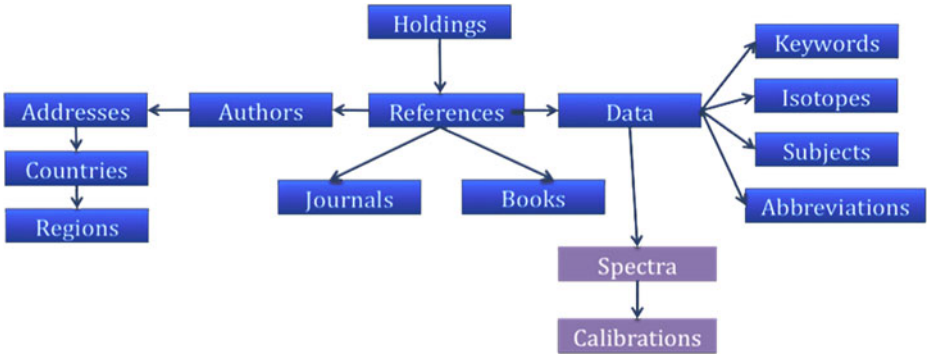

Fig. 4 Spectra and Calibrations tables added to the relational scheme of MEDC database

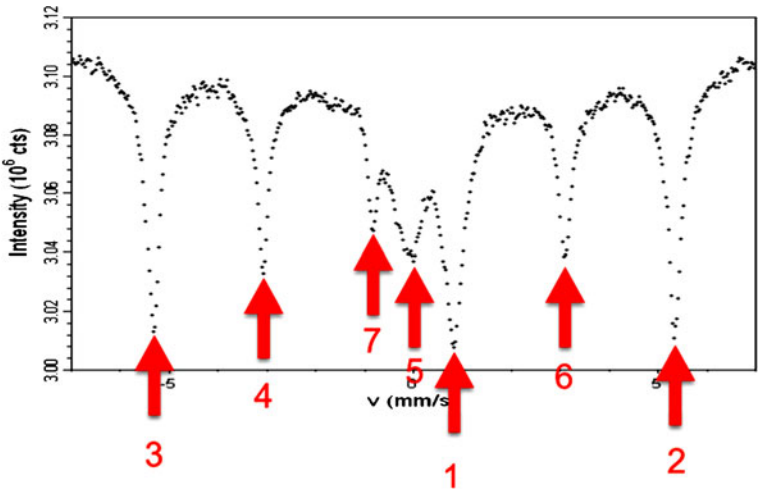

Fig. 5 Suggested scheme of indexing of the Mössbauer spectra for faster search in the table "Spectra"

to a regular lorentzian lineshape. These models can vary substantially and it is very difficult to expect them in the fitting package from one vendor. The modular solution based on open source ideology looks like a better solution, especially having in mind the problem of software support pertinent to any small company. Finally, only a fraction of MS measurements reach the stage of being published in a reviewed journal. It seems that the Mössbauer community could gain a lot by establishing a professional online publishing medium were any measured spectrum could be published and viewed by interested researchers.

We see the need of development of the next generation MS database capable of storing and managing not only spectral parameters, but also the whole original spectrum. This capability will open possibility for better use of the information collected in the measurement. Possibility for reevaluation of the spectra using different fitting models is also very helpful. The intrinsic digital nature of the Mössbauer spectra suggested this advancement long time ago, but only recently the development of

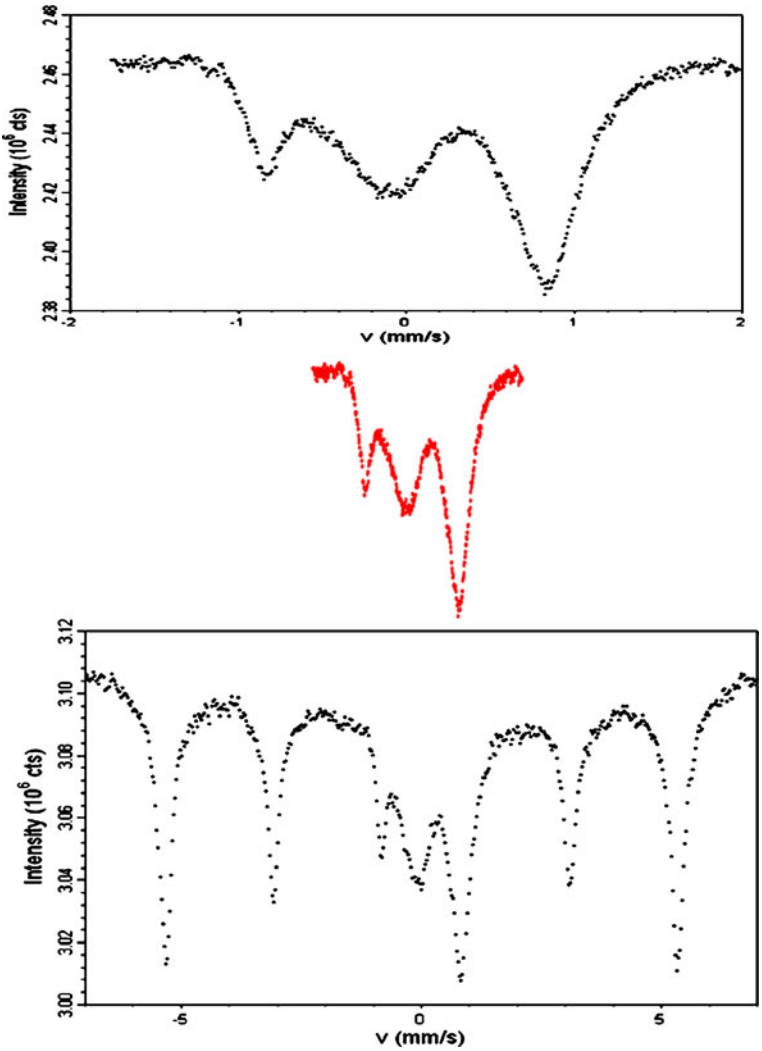

Fig. 6 The visual overlap comparison tool must perform absolute rescale of the velocity axis and relative rescale of the intensity axis

computer technology made it possible. The spectrum table of the database will fit naturally into the existing relational design of MEDC database (Fig. 4).

Each measurement is worthy only with proper calibration provided. That is why each stored spectrum must be linked to a file of calibration measurement, absolute or relative. An additional set of absolute calibration values for selected standard materials used for relative calibration must be provided in the system.

An additional methodology for fast searches in the database of raw spectra must be developed. A system of indexing based on positions and relative intensities of major resolved absorption (emission) peaks could be a solution that will allow fast

selection of relatively small set of spectra, which are presented for a human analysis or subjected to more detailed artificial intelligence analysis (Fig. 5).

Online graphical tool for comparison of two spectra will allow user to upload a spectrum with calibration, will perform calibration and scaling of the plot long x and y axis. The spectrum from the database will be overlaid for comparison using the same velocity scale. The relative intensity must be scaled as well to eliminate irrelevant difference in absolute statistics (Fig. 6).

A proper statistical criterion for comparison of two spectra must be developed so that in addition to subjective impression the user is provided with an objective criterion of similarity of two spectra under consideration.

The current stage of development of the Mössbauer database was achieved by MEDC staff and dedicated group of associate editors. More than 54,000 publications are entered in the MEDC database. More than 107,000 data records are created by processing the information published in these publications. About 1,300,000 keywords generated to facilitate searches in the database.

The realization of the next stage of development is possible only with the help, support and contribution from the entire Mössbauer community.

References

1. Number of authors in Mössbauer related papers in 2005 – 3,684; in 2006 – 2,450; in 2007 – 3,310; in 2008 – 3,132. (From MEDC database analysis)
2. Number of affiliation institutions in 2005 – 1,093; in 2006 – 1,045; in 2007 – 965; in 2008 – 940. (From MEDC database analysis)
3. Number of countries in connection to publications in 2005 -73 countries, in 2006 – 78, in 2007 – 79, in 2008 – 75. (From MEDC database analysis)
4. Criterion used for strong connection is 5 or more papers published in the last 10 years
5. Criterion used for a specialist is 10 or more papers published in the last 10 years
6. Papers published in 910 different journals and 144 books in the last 10 years, total number of journals – 3,413 books – 1,520
7. Muir, A.H., Ando, K.J., Coogan, H.M.: Mössbauer effect data index (1966)

Hyperfine Interact (2012) 204:119–123
DOI 10.1007/s10751-011-0422-5

Coordination preference and magnetic properties of Fe^{II} assemblies with a bis-azole bearing 1,2,4-triazole and tetrazole

Anil D. Naik · Antoine P. Railliet · Marinela M. Dîrtu · Yann Garcia

Published online: 1 November 2011

Abstract With a new bis-azole molecular fragment (**Htt**) bearing 1,2,4-triazole and tetrazole, a mononuclear complex $[Fe(tt)_2(H_2O)_4]\cdot 2H_2O$ (**1**), a trinuclear complex $[Fe_3(tt)_6(H_2O)_6]\cdot 2H_2O$ (**2**) and a 1D coordination polymer $[Fe(tt)(Htt)_2]BF_4\cdot 2CH_3OH$ (**3**) were obtained by varying reaction conditions. **Htt** acts either as an anionic or neutral ligand depending upon the reaction medium and pH. Thermal variation of spin states of **1**–**3** were investigated in the range 77–300 K by ^{57}Fe Mössbauer spectroscopy. **1** totally remains in high-spin state over the entire temperature range whereas no spin crossover was evidenced in **2**. Nearly 1:1 high-spin and low-spin population ratio is found in **3**, which remains constant over the entire temperature range investigated.

Keywords ^{57}Fe Mössbauer spectroscopy · Coordination polymers · Spin-transition, 1,2,4-triazole

1 Introduction

Spin crossover (SCO) area continues to proliferate with the advent of new SCO materials, associated theories, and prospective applications [1–5]. In Fe^{II} SCO materials synthesized with suitably designed ligand system, the spin state of iron can be switched between high-spin (HS) and low-spin (LS) with the aid of external addressing parameters like temperature, pressure and light irradiation with an elegant readout signal [1–5]. The phenomenal properties associated with such transition have high technological relevance that is proposed for the memory and display devices and as temperature/optical alerts in molecular sensors [1, 2]. The very basic requirement to fabricate SCO materials is the design of suitable ligand with appropriate ligand

A. D. Naik · A. P. Railliet · M. M. Dîrtu · Y. Garcia (✉)
Institute of Condensed Matter and Nanosciences, MOST–Inorganic Chemistry,
Université Catholique de Louvain, Place L. Pasteur 1, 1348 Louvain-la-Neuve, Belgium
e-mail: yann.garcia@uclouvain.be

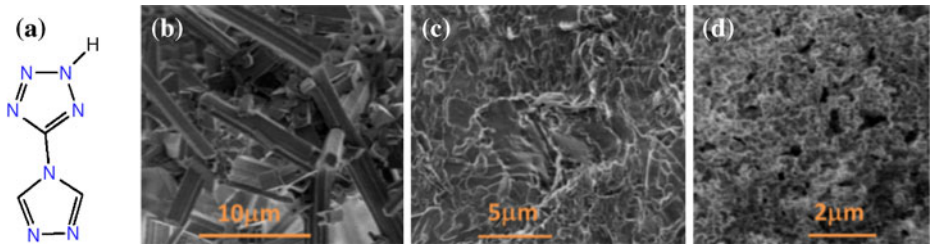

Fig. 1 **a** Molecular structure of **Htt**. **b–d** SEM images depicting morphologies on bulk samples of **1**, **2**, and **3**, respectively

field strength. An ideal ligand should also enhance the cooperativity among iron centers through its rigid framework and further through lattice by supramolecular interactions [4, 6]. In this context, we introduced a new nitrogen donor rich molecular fragment bearing two flagged motifs of 1,2,4-triazole and tetrazole (**Htt**) attached on a common platform. Both these precursors are independently very well recognized as excellent precursors in SCO area by demonstrating a wide range of coordinating capabilities, diverse topologies ranging from mononuclear complexes to high dimensional networks and exceptional SCO properties [1, 4, 6]. In the present work three new Fe^{II} assemblies with structural diversities are reported together with their magnetic properties investigated by ^{57}Fe Mössbauer spectroscopy.

2 Experimental

Synthesis of ligand (**Htt**) and complexes **1–3** (Fig. 1a) was carried out according to the reported procedure [7]. Reaction of **Htt** (100 mg) with $[Fe(H_2O)_6](BF_4)_2$ (82 mg) in water (30 mL, pH = 1) yielded colorless micro-crystals (**1**) within a week. Under similar experimental condition but with a minimum quantity of water (15 mL) a pink solid (**2**) was isolated within a day. If the same reaction is carried out in MeOH (pH = 3), immediately a pale pink solid is obtained (**3**).

3 Results and discussion

Elemental analysis, thermogravimetric (TGA) analysis, FT-IR supported the following compositions: a mononuclear complex $[Fe(tt)_2(H_2O)_4]\cdot 2H_2O$ (**1**), a trinuclear complex $[Fe_3(tt)_6(H_2O)_6]\cdot 2H_2O$ (**2**), and a 1D coordination polymer (CP) $[Fe(tt)(Htt)_2]BF_4\cdot 2MeOH$ (**3**). The lability of proton attached to the tetrazole part in **Htt** is found to be sensitive to the reaction medium and significantly affects the structure and magnetic properties in **1–3**. Presence of coordinated and non-coordinated solvent molecules in **1–3** was deduced and quantified from TGA. In **1** and **2** coordinated water molecules are lost around 100°C and 120°C, respectively, whereas in **3**, non-coordinated methanol molecules are lost between 40–70°C. FT-IR spectra of **1** and **2** indicate absence of characteristic BF_4^- anion thus confirming that ligand acts as mono-anionic whereas **3** shows strong overlapped bands around 1080 cm^{-1} which proves the presence of BF_4^- anion. SEM images on bulk samples

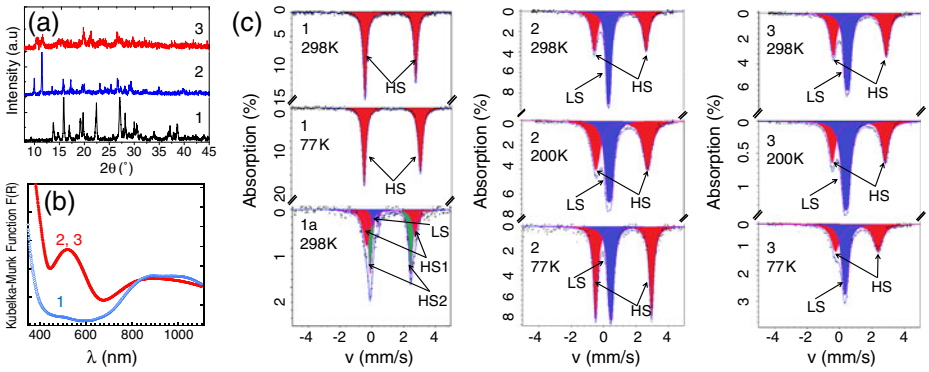

Fig. 2 **a** XRPD pattern for **1–3**. **b** DRS for **1** and **2**. **c** Mössbauer spectra of **1–3** at selected temperatures

shows 10 × 1 μm rods (Fig. 1b) for **1**, randomly oriented blocks for **2** (Fig. 1c) and 100–150 nm diameter granules (Fig. 1d) for **3**. Signals in X-ray powder diffraction (XRPD) (Fig. 2a) are quite strong for **1** whereas it is weak but distinct in **2**. The poor diffractogram of **3** confirms amorphous nature found from SEM (Fig. 1d).

3.1 Spectroscopic studies

Diffuse reflectance spectrum (DRS) (Fig. 2b) of **1**, shows a broad band around 900 nm which corresponds to $^5T_{2g} \rightarrow {}^5E_g$ transition of HS Fe^{II} species. In addition, an additional band is found around 520 nm in **2** and **3** that correspond to $^1A_{1g} \rightarrow {}^1T_{1g}$ transition of LS Fe^{II} species thus proving the co-existence of both HS and LS species [2]. Colorless crystals of **1** and pink solid of **3** does not show thermochromism when quenched in $N_{2(l)}$. The pink color of **2** turns to off-white when warmed to around 423 K, most presumably as a consequence of water release and stabilization of the HS state. CP **3** is highly sensitive and decomposes to brown solid upon warming. ^{57}Fe Mössbauer spectral study was undertaken over the temperature range 77–300 K to deduce the electronic and structural aspects of **1–3**. Selected spectra are displayed in Fig. 2 and parameters are grouped in Table 1.

At 298 K, the spectrum of **1** consists of a quadrupole split doublet with $\delta = 1.17(2)$ mm/s and $\Delta E_Q = 3.18(3)$ mm/s corresponding to HS state of Fe^{II}. Situation is similar at 77 K thus confirming absence of any spin state crossover. The asymmetry of the lines observed in the HS state is attributed to a texture effect. As expected, with water as weak coordinating ligand the situation is not favorable for a spin state switching. In air or under vacuum, **1** loses non-coordinated water molecules to give $[Fe(tt)_2(H_2O)_4]$, **1a**. The appearance of a new HS signal along with a few LS species in Mössbauer spectrum (Fig. 2c) of desolvated complex (**1a**) suggests disruption of supramolecular network that leads to non-equivalent HS iron sites. Trinuclear complex **2** appears pink at 298 K but Mössbauer and DRS spectra at 298 K shows existence of both HS and LS species. In fact, **Htt** acts as an anionic ligand by deprotonation from its tetrazole part and bridges iron centers by its triazole counterpart. Thus, two types of iron centers are created, one with a central FeN_6 octahedron and two terminal FeN_3O_3 coordination spheres which are supported by

Table 1 ^{57}Fe Mössbauer parameters for **1–3**

Compound	T (K)	δ (mm/s)	ΔE_Q (mm/s)	$\Gamma/2$ (mm/s)	Species, %
1	298	1.17(2)	3.18(3)	0.18(2)	HS, 100
	77	1.25(2)	3.35(2)	0.19(2)	HS, 100
1a	298	1.18(3)	2.5(3)	0.17(2)	HS1, 50(2)
		1.21(3)	3.0(3)	0.18(2)	HS2, 42(2)
		0.23(3)	0.33(3)	0.19(2)	LS[a], 8(3)
2	298	0.40(3)	0.15(4)	0.2(6)	LS, 55(4)
		1.14(5)	3.13(2)	0.22(2)	HS, 45(3)
	200	0.39(3)	0.26(2)	0.21(2)	LS, 43(4)
		1.16(4)	3.16(3)	0.25(2)	HS, 57(4)
	77	0.45(4)	0.19(2)	0.16(2)	LS, 36(3)
		1.24(5)	3.44(2)	0.17(2)	HS, 64(4)
3	298	0.35(2)	0.18(2)	0.19(2)	LS, 48(2)
		1.07(2)	2.62(2)	0.22(2)	HS, 52(4)
	200	0.37(3)	0.26(2)	0.25(3)	LS, 52(3)
		1.17(2)	3.28(2)	0.25(3)	HS, 48(2)
	77	0.43(4)	0.23(3)	0.17(3)	LS, 48(4)
		1.19(3)	3.23(2)	0.24(3)	HS, 52(4)

δ: isomer shift (with respect to α-Fe at 298 K); ΔE_Q: quadrupole splitting; $\Gamma/2$: half width at half maximum
[a]Diamagnetic species adsorbed on surface

coordinated water molecules [6, 8]. At 77 K the major quadrupole doublet with $\delta = 0.45(4)$ mm/s and $\Delta E_Q = 0.19(2)$ mm/s corresponds to the LS state of central Fe^{II} ions and $\delta = 1.24(5)$ mm/s and $\Delta E_Q = 3.44(2)$ mm/s that corresponds to the HS state of terminal Fe^{II} ions are found with a relative intensity of 1:2. The presence of a small quadrupole splitting in the LS signal stems from a lattice contribution to the electric field gradient and therefore reveals a distorted character for the central LS octahedron. Subsequent warming at an interval of 50 K shows only slight changes in Mössbauer parameters. On warming to 298 K, the spectrum remains essentially the same, with the difference observed in the intensities of lines which can be attributed to the known difference in the Debye-Waller factors for the LS and HS states due to which the area fraction of both spin states do not reflect the actual concentration of the two species [6]. Spectrum above room temperature was not recorded due to risk of explosion from energetic tetrazole moiety. The spectrum of **3**, at 77 K corresponds to co-existence of HS and LS species roughly in 1:1 ratio and essentially remains constant upon warming to 298 K. The observed decrease in δ (Table 1) on warming from 77 K is due to relativistic second order Doppler shift [8].

Acknowledgements We acknowledge financial support from IAP-VI (P6/17) INANOMAT, the Fonds National de la Recherche Scientifique (FNRS) (FRFC 2.4508.08, IISN 4.4507.10), ARC Louvain and from the Groupe Francophone de Spectrométrie Mössbauer (GFSM) for partially supporting A.D.N and A.P.R to attend ICAME 2011 (Kobe) and GFSM 2011 (Strasbourg).

References

1. Kahn, O., Kröber, J., Jay, C.: Spin transition molecular materials for displays and data recording. Adv. Mater. **4**, 718 (1992)
2. Gütlich, P., Garcia, Y., Goodwin, H.A.: Spin crossover phenomena in Fe(II) complexes. Chem. Soc. Rev. **29**, 419 (2000)
3. Bousseksou, A., Molnár, G., Salmon, L., Nicolazzi, W.: Molecular spin crossover phenomenon: recent achievements and prospects. Chem. Soc. Rev. **40**, 3313 (2011)

4. Garcia, Y., Niel, V., Muñoz, M.C., Real, J.A.: Spin crossover in 1D, 2D and 3D polymeric Fe(II) networks; spin crossover in transition metal compounds. Top. Curr. Chem. **233**, 229 (2004)
5. Prins, F., Monrabal-Capilla, M., Osorio, E.A., Coronado, E., van der Zant, H.S.J.: Room-temperature electrical addressing of a bistable spin-crossover molecular system. Adv. Mater. **23**, 1545 (2011)
6. Garcia, Y., Guionneau, P., Bravic, G., Chasseau, D., Howard, J.A.K., Kahn, O., Ksenofontov, V., Reiman, S., Gütlich, P.: Synthesis, crystal structure, magnetic properties and ^{57}Fe Mössbauer spectroscopy of the new trinuclear $[Fe_3(4\text{-}(2'\text{-hydroxy-ethyl})\text{-}1,2,4\text{-triazole})_6(H_2O)_6](CF_3SO_3)_6$ spin crossover compound. Eur. J. Inorg. Chem. 1531 (2000)
7. Naik, A.D., Marchand-Brynaert, J., Garcia, Y.: A simplified approach to N- and N,N′-linked 1,2,4-triazoles by transamination. Synthesis **1**, 149 (2008)
8. Robert, F., Naik, A.D., Garcia, Y.: Influence of a thermochromic anion on the spin crossover of iron(II) trinuclear complexes probed by Mössbauer spectroscopy. J. Phys. Conf. Ser. **217**, 012031 (2010)

Hyperfine Interact (2012) 204:125–128
DOI 10.1007/s10751-011-0487-1

In-beam Mössbauer spectroscopy of ^{57}Mn implanted into lithium hydride

Takashi Nagatomo · Yoshio Kobayashi · Michael K. Kubo · Yasuhiro Yamada · Mototsugu Mihara · Wataru Sato · Jun Miyazaki · Kazuya Mae · Shinji Sato · Atsushi Kitagawa

Published online: 30 November 2011

Abstract We measured the temperature dependence of ^{57}Fe Mössbauer spectra obtained after ^{57}Mn implantation into polycrystalline LiH with an extremely low implantation dose. Density functional calculations suggested that the Fe atoms were predominantly implanted into both Li and H substitutional sites of the LiH crystal.

Keywords ^{57}Fe Mössbauer spectroscopy · Radioactive ^{57}Mn beam · LiH

1 Introduction

In-beam Mössbauer spectroscopy based on ^{57}Fe arising from short-lived ^{57}Mn ($T_{1/2} = 87.2$ s) can provide direct information on the electromagnetic properties

T. Nagatomo (✉) · M. K. Kubo · K. Mae
International Christian University, Osawa 3-10-2, Mitaka, Tokyo 181-8585, Japan
e-mail: nagatomo@riken.jp

Y. Kobayashi
RIKEN Nishina Center, Hirosawa 2-1, Wako, Saitama 351-0198, Japan

Y. Yamada
Tokyo University of Science, Kagurazaka 1-3, Shinjuku-ku, Tokyo 162-8601, Japan

M. Mihara
Osaka University, Machikaneyama 1-1, Toyonaka, Osaka 560-0043, Japan

W. Sato
Kanazawa University, Kakuma, Kanazawa, Ishikawa 920-1192, Japan

J. Miyazaki
Nihon University, Shin-ei 2-11-1, Narashino, Chiba 275-8576, Japan

S. Sato · A. Kitagawa
National Institute of Radiological Sciences, Anagawa 4-9-1, Inage-ku, Chiba 263-8555, Japan

of the surrounding environment and on exotic oxidation states and novel chemical bondings of unstable nuclear probes such as ^{57}Mn/^{57}Fe implanted into $KMnO_4$ [1] and O_2 solids [2]. Recently, our detection system was successfully improved to obtain ^{57}Mn/^{57}Fe in-beam Mössbauer spectra with a very high signal/noise ratio at the Heavy Ion Medical Accelerator in Chiba (HIMAC) facility of the National Institute of Radiological Sciences NIRS [3]. We applied this improved detection system to investigations of ^{57}Mn/^{57}Fe in metal oxides [4] and rock salt type crystals, e.g. alkali halides and lithium hydride (LiH). The crystal structure of LiH contains one Li^+ cation surrounded by six H^- anions. A stable ternary compound Mg_2FeH_6 consisting of $[FeH_6]^{4-}$ complex anion has been reported [5], but binary compounds of hydrogen and iron or manganese have not been synthesized. In the present work, we investigated the chemical and physical behaviors of ^{57}Fe arising from ^{57}Mn in LiH.

2 Experiment

The experiment was carried out at the heavy ion synchrotron facility HIMAC of NIRS [6]. The basic experimental setup was described previously [3, 4]. Radioactive ^{57}Mn ions were used as a highly energetic secondary beam ($E = \sim 260A$ MeV) which was produced from the projectile fragmentation process of nuclear collisions between ^{58}Fe ions ($500A$ MeV, $\sim 1 \times 10^8$ particles per beam) and ^{9}Be nuclei in a 27-mm-thick production target. The ^{57}Mn beam was purified by a fragment separator installed in the secondary beam line SB2 of the HIMAC facility, and the purity was higher than 80%. The typical implantation dose of ^{57}Mn was about 1×10^6 particles per beam. The period of the ^{57}Mn secondary beam was active for $\sim$ 300 ms every 3.3 s. The implantation depth of the ^{57}Mn ions was controlled by passing the ion beam through an appropriate combination of energy degraders. LiH powder, purchased from Wako Pure Chemical Industries, was used to cover a 33×33 mm area to a depth of about 3 mm, which was sufficient to stop all of the ^{57}Mn ions within the sample. The LiH sample was mounted on a boron nitride heater in a vacuum chamber in order to control the sample temperature in the range from room temperature to over 800 K. After β decay of the implanted ^{57}Mn, the 14.4-keV γ rays emitted from ^{57}Fe were selectively detected by a combination of a Mössbauer resonance counter (parallel plate avalanche counter—PPAC) [7] and an anti-coincidence method to reject the β rays [3]. The PPAC was mounted on the Mössbauer driving unit to apply the Doppler velocity. Using this new detection system, we were able to obtain emission Mössbauer spectra of high quality using a very small number of implanted ^{57}Mn ions, realizing an environment in which each implanted ^{57}Fe atom is completely isolated from the other ^{57}Fe atoms in the sample.

3 Results and discussion

Mössbauer spectra of ^{57}Mn/^{57}Fe in LiH at room temperature and at 623 K were obtained, as shown in Fig. 1 together with several best-fit singlet and doublet curves, assuming a Lorentzian shape. Figure 1 suggests that with increasing sample temperature, the symmetrical crystalline structure surrounding the Fe atom was recovered

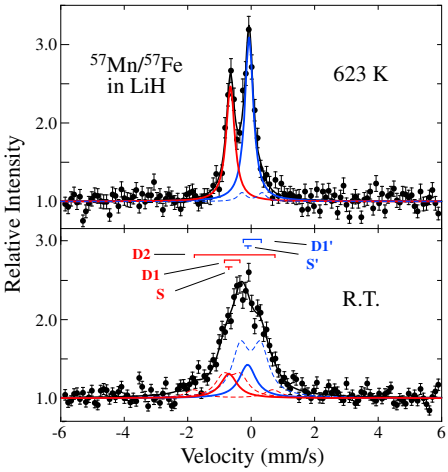

Fig. 1 Obtained emission Mössbauer spectra of ^{57}Fe after β decay of ^{57}Mn implanted into LiH along with best-fit curves. The *red* and *blue lines* correspond to Fe atoms that substitute Li and H sites, respectively, according to estimations based on density functional calculations. For more details, see the text

Table 1 Emission Mössbauer parameters of ^{57}Mn implanted into LiH

	^{57}Fe at Li substitutional site				
	Experimental		Theoretical		
	I.S. (mm/s)	$\lvert\Delta E_Q\rvert$ (mm/s)	*I.S.* (mm/s)	ΔE_Q (mm/s)	
S	−0.76(6)	–	−0.558	–	
D1	−0.63(9)	0.56(6)	−0.577	0.463	(with a Li defect)
D2	−0.60(28)	2.41(54)	−0.705	−2.091	(with a H defect)
	^{57}Fe at H substitutional site				
	Experimental		Theoretical		
	I.S. (mm/s)	$\lvert\Delta E_Q\rvert$ (mm/s)	*I.S.* (mm/s)	ΔE_Q (mm/s)	
S’	−0.19(5)	–	−0.015	–	
D1’	−0.04(5)	0.69(11)	−0.105	−0.534	(with a Li defect)
			−0.105	−0.533	(with a H defect)

The sign of isomer shift *I.S.* in the obtained emission Mössbauer spectrum was opposite to that of conventional absorption Mössbauer spectrum

by an annealing effect. The Mössbauer spectrum obtained at 623 K indicated that two singlets S and S’ were dominant, and the isomer shifts (*I.S.*) were determined to be −0.76(6) mm/s and −0.19(5) mm/s, respectively, relative to Fe metal at room temperature.

Density functional calculations were performed for an Fe atom surrounded by a Li_mH_n lattice with an additional 412 point charges (±1) to predict the Mössbauer parameters. For the Li substitutional site ($m = 42$ and $n = 38$), the isomer shift was estimated to be $I.S. = -0.588$ mm/s, and $I.S. = -0.015$ mm/s for the H substitutional site ($m = 38$ and $n = 42$). Comparing the observed spectra to these predictions suggests that the Fe atom was located at a Li substitutional site for the singlet S and at an H substitutional site for the singlet S’. The doublet D1 (D2) in Fig. 1 corresponds to an Fe atom at a Li substitutional site with a missing nearest Li(H)

atom. D1' corresponded to an Fe atom located at an H substitutional site with a neighboring Li or H defect. These Mössbauer parameters are summarized in Table 1. To confirm the implantation sites and to discuss the more detailed chemical states, systematic measurements at the temperature range from 10 to 800 K and additional numerical analysis are underway.

Acknowledgements We are thankful to Dr. N. Suzuki and Dr. S. Kamiguchi of the Chemical Analysis Team at RIKEN for the production of ^{58}Fe-enriched ferrocene as an ion source. This work was carried out as a part of the Research Project with Heavy Ions at NIRS-HIMAC with partial support from the Support Program for Private Universities (S0801012) of the Ministry of Education, Culture, Sports, Science and Technology, Japan.

References

1. Kobayashi, Y., et al.: J. Radioanal. Nucl. Chem. **255**, 403 (2003)
2. Kobayashi, Y., et al.: Hyperfine Interact. **166**, 357 (2006)
3. Nagatomo, T., et al.: Nucl. Instrum. Methods B **269**, 455 (2011)
4. Kobayashi, Y., et al.: Hyperfine Interact. **198**, 173 (2010)
5. Didisheim, J.-J., et al.: Inorg. Chem. **23**, 1953 (1984)
6. Hirao, Y., et al.: Nucl. Phys. A **538** 541 (1992)
7. Saito, T., et al.: Nucl. Chem. **255**, 519 (2003)

Hyperfine Interact (2012) 204:129–132
DOI 10.1007/s10751-011-0446-x

Nuclear inelastic scattering of 1D polymeric Fe(II) complexes of 1,2,4-aminotriazole in their high-spin and low-spin state

Juliusz A. Wolny · Sergej Rackwitz · Klaus Achterhold · Kai Muffler · Volker Schünemann

Published online: 15 November 2011

Abstract The vibrational properties of Fe(II) 1D spin crossover polymers have been characterized by nuclear inelastic scattering (NIS). The complexes under study were the tosylate and perchlorate salts of $([Fe(4\text{-amino-}1,2,4\text{-triazole})_3]^{+2})_n$ complexes. The complexes have LS (S = 0) marker bands in the range of 300–500 cm^{-1}, while the marker bands corresponding to the HS (S = 2) state are detected between 200 cm^{-1} and 300 cm^{-1}, in line with the decreasing Fe-N bond strengths during the transition from LS to HS. Accompanying DFT calculations using the functional B3LYP and the basis set CEP-31G confirm these assignments.

Keywords Nuclear inelastic scattering · Spin crossover · Molecular magnetism · Density functional theory

1 Introduction

The design of new spin crossover (SCO) materials [1, 2] requires a better understanding of the nature and origin of the co-operative behavior and resulting bistability of this class of compounds. Vibrational spectroscopy combined with quantum chemical calculations may provide a better understanding of the SCO effects by clarifying the

Electronic supplementary material The online version of this article (doi:10.1007/s10751-011-0446-x) contains supplementary material, which is available to authorized users.

J. A. Wolny (✉) · S. Rackwitz · K. Muffler · V. Schünemann
Department of Physics, University of Kaiserslautern, Erwin-Schrödinger-Str. 46, 67663 Kaiserslautern, Germany
e-mail: wolny@physik.uni-kl.de

K. Achterhold
Department of Physics, Technische Universität München, 87548 Garching, Germany

relationships between microscopic effects of vibrations, energy and molecular strain and the terms derived from phenomenological models [3]. Among them, nuclear inelastic scattering (NIS), also called nuclear resonant vibrational spectroscopy (NRVS) is of special interest because it gives much more details on the vibrational properties of Mössbauer nuclei, as compared to Raman and IR spectroscopy [4]. We have previously reported the results of NIS studies for the linear trimeric SCO $[Fe_3(4\text{-}(2'\text{–hydroxy-ethyl})\text{-}1,2,4\text{-triazole})_6(H_2O)_6]^{+6}$ system [5]. Here we report the first NIS study of a one-dimensional polymeric material, based on 4-amino-1,2,4-triazole (ATZ) complexes. This class of complexes has been widely studied by other methods [6] because of the strong dependence of transition temperature and hysteretic behavior on the nature of the anion. Therefore we performed NIS measurements for two systems with different counterions: the low-spin isomer of the tosylate salt of $([Fe(4\text{-amino-}1,2,4\text{-triazole})_3]^{+2})_n$ (**1**) and its perchlorate analogue (**2**). The tosylate salt (**1**) is low-spin at room temperature [7]. For the perchlorate salt (**2**) the transition temperatures of 210 K [8] and 130 K [9] were reported independently.

2 Materials and methods

The complexes were obtained by a slightly modified literature method [8], i.e. by mixing the ethanolic solution of the 4-amino-1,2,4-triazole ligand with a water solution of the corresponding salt containing 99% enriched ^{57}Fe. The latter were obtained from $^{57}Fe(SO_4)*7H_2O$ and the corresponding barium salts. Nuclear inelastic scattering (NIS) was performed at the Nuclear Resonance Beamline ID 18 of the European Synchrotron Radiation Facility (ESRF) in Grenoble, France, under experiment No. CH 2839. During the experiments the 6 GeV electron storage ring was operated in 16 bunch mode. The incident beam was monochromatized by a Si(111) double-crystal premonochromator to a bandwidth of 2.1 eV. A further decrease of bandwidth down to 1 meV was obtained with a refractive beryllium collimator and a high-resolution monochromator.

DFT calculations were performed as described in [5], using a pentanuclear model system with full charge compensation.

3 Results and discussion

The NIS spectrum of (**1**) obtained at 100 K reveals a number of bands in the 300–500 cm^{-1} region. On the other hand the system (**2**) displays two broad bands at 200–270 cm^{-1}. On cooling (**2**) to 100 K these are retained, but also new bands appear in the 300–500 cm^{-1} region (Fig. 1). The above results imply that the observed changes are due to a spin transition from HS to LS state on cooling. Consequently, the LS marker bands occur in the range of 300–500 cm^{-1}, while those corresponding to the HS state are seen between 200 cm^{-1} and 300 cm^{-1}, in line with the decreasing Fe-N bond strengths during the transition from LS to HS [1]. This assumption has been corroborated by the DFT calculations on a pentameric model molecule $[Fe_5(ATZ)_{12}(H_2O)_6]_2Cl_{10}$, using the B3LYP functional and the CEP-31G basis set (Fig. 2). The comparison of the experimental and theoretically derived spectra

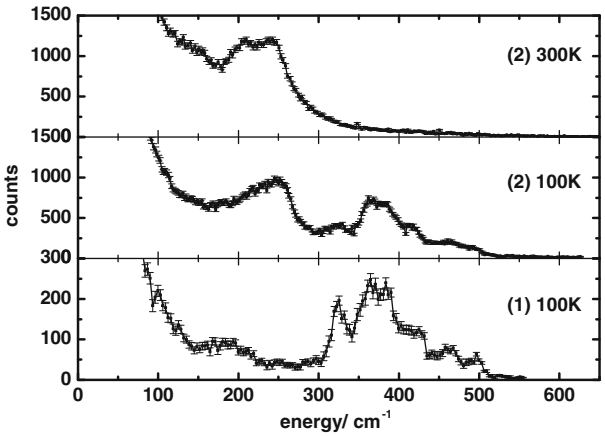

Fig. 1 NIS spectra of (**1**) at 100 K (*bottom*) and of (**2**) at 300 K (*top*) and 100 K (*middle*)

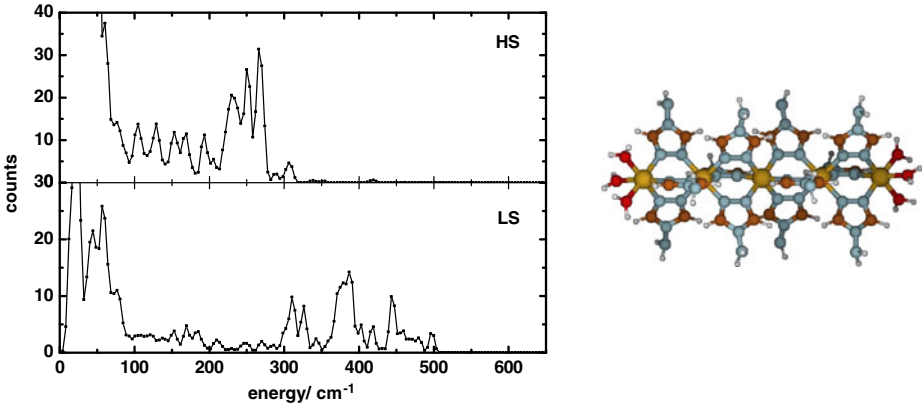

Fig. 2 *Left* simulated NIS spectra for the LS (*bottom*) and HS (*top*) based on DFT calculations for the pentameric model molecule $[Fe_5(ATZ)_{12}(H_2O)_6]_2Cl_{10}$. *Right* graphic representation of the model. Chlorine anions were removed for clarity. Movies of the representative HS marker bands (233 cm^{-1}) and of LS-marker bands (326 cm^{-1}) are given as supplementary material

shows that the NIS spectra of the Fe(II) polymers under study can be reliably reproduced using a pentameric model molecule. The calculations predict the iron-ligand stretching modes in the 320–500 cm^{-1} and 200–300 cm^{-1} regions, for LS and HS systems, respectively (Fig. 2). We previously reported that the only Raman LS marker bands for the polymers under study occur at ca. 260 cm^{-1}. According to the DFT calculations presented there this band corresponds to Fe-N bending, rather than stretching modes [10]. The comparison of the overall spectral pattern of the NIS spectra of both spin isomers of the systems point out to a negligible influence of the anion.

Acknowledgements This work has been supported by the Federal Ministry of Education and Research under contract number 05 K10UKA

References

1. Gütlich, P., Goodwin, H.A. (eds.): Spin Crossover in Transition Metal Compounds I-III. Springer, Berlin Heidelberg New York (2004)
2. Bodenthin, Y., Kurth, D.G., Schwarz, G.: Chem. Unserer Zeit **42**, 256 (2008)
3. Spiering, H.: Top. Curr. Chem. **235**, 171 (2004)
4. Wolny, J.A., Paulsen, H., Schünemann, V., Trautwein, A.X.: Coord. Chem. Rev. **253**, 2423 (2009)
5. Wolny, J.A., Rackwitz, S., Achterhold, K., Garcia, Y., Muffler, K., Naik, A.D., Schünemann, V.: Phys. Chem. Chem. Phys. **12**, 14782 (2010)
6. Dîrtu, M.M., Neuhausen, C., Naik, A.D., Rotaru, A., Spinu, L., Garcia, Y.: Inorg. Chem. **49**, 5723 (2010) and references therein
7. Codjovi, E., Sommier, L., Kahn, O., Jay, C.: New J. Chem. **20**, 503 (1996)
8. Lavrenova, L.G., Shakirova, O.G., Varnek, V.A., Sheludyakova, L.A., Larionov, S.V.: Koord. Chim. **29**, 22 (2003)
9. Kröber, J., Codjovi, E., Kahn, O., Grolière, F., Jay, C.: J. Am. Chem. Soc. **115**, 9810 (2003)
10. Ahrens-Botzong, A., Muffler, K., Stuppy, S.M., Rackwitz, S., Rüffer, R., Schünemann, V., Wolny, J.A.: J. Phys.: Conf. Series **217**, 012033 (2010)

Hyperfine Interact (2012) 204:133–137
DOI 10.1007/s10751-011-0424-3

^{57}Fe charge states in MC-Si solar cells under light illumination after GeV-implantation of ^{57}Mn

Yutaka Yoshida · Kunifumi Suzuki · Yoshio Kobayashi · Takashi Nagatomo · Yuki Akiyama · Kenichi Yukihira · Kazuo Hayakawa · Hideki Ueno · Akihiro Yoshimi · Daisuke Nagae · Koichiro Asahi · Guido Langouche

Published online: 26 October 2011

Abstract Immediately after the GeV-implantation of ^{57}Mn nuclei produced by the RIKEN-RIBF facility, ^{57}Mn/^{57}Fe Mössbauer spectra in Si-solar cells are measured under light illumination. Comparing with the spectrum of p-type multi-crystalline-Si, the broad spectra of the solar cell under operation can be analyzed as a superposition of interstitial and substitutional Fe components with different charge states. The charge states of Fe impurities are created by the excess carrier injection followed by a directional carrier flow in the p-n junction. The present results provide us a possibility to clarify the carrier trapping process at the Fe impurities in Si-solar cells.

Keywords ^{57}Mn/^{57}Fe implantation Mössbauer spectroscopy · Si solar cell · Fe impurity · Carrier trapping · Energy conversion efficiency

1 Introduction

Iron impurities in Si have been intensively investigated for more than 50 years by different experimental techniques [1] including ^{57}Fe Mössbauer spectroscopy [2–9], because Fe impurities can be easily incorporated into the Si matrix during

Y. Yoshida (✉) · Y. Akiyama · K. Yukihira · K. Hayakawa
Shizuoka Institute of Science and Technology, Toyosawa 2200-2,
Fukuroi-city, Shizuoka 437-8555, Japan
e-mail: yoshida@ms.sist.ac.jp

Y. Kobayashi · T. Nagatomo · H. Ueno · A. Yoshimi
RIKEN Nishina Center, Wakō, Japan

K. Suzuki · D. Nagae · K. Asahi
Department of Physics, Tokyo Institute of Technology, Tokyo, Japan

G. Langouche
Institute for Nuclear and Radiation Physics, Physics Department, Leuven University,
Leuven, Belgium

the processes, and even an extremely low Fe concentration of $10^{11}/cm^3$ can degrade seriously the electronic properties of silicon-based devices and solar cells. This is due to the deep levels formed in the Si band gap, producing strong trapping centres for the carriers in the devices. Interstitial Fe_i is well known to form an acceptor level at 0.39 eV from the valence band edge, while substitutional Fe_s is expected to form a donor level of 0.69 eV from the first principle calculation [10]. Although interstitial and substitutional Fe appeared as spectral components in ^{57}Fe Mössbauer experiments [2–9], the charge states could not be identified in terms of different isomer shifts of Mössbauer spectrum experimentally in comparison with the values calculated theoretically.

The present investigation is carried out to observe directly the charge states of Fe atoms in multi-crystalline Si solar cells under light illumination, which will shift the Fermi level by injecting excess carriers, and consequently the different charge states of interstitial and substitutional Fe are expected to appear in the spectrum. In order to study Fe impurities existing inside of a Si solar cell, however, we have to realize a well isolated ^{57}Fe probe with an extremely low concentration, and the probes must be introduced into a region where the carrier trapping processes are occurring during solar cell operation, i.e. light illumination. At the RI-beam facility in RIKEN we have been developing a novel technique of projectile fragmentation combined with ^{57}Mn/^{57}Fe implantation Mössbauer spectroscopy. The probes are deeply implanted into mc-Si solar cell, and Mössbauer spectra can be measured under operation immediately after each implantation of ^{57}Mn. This is possible because of the extremely high implantation energy of GeV, providing an implantation depth of 100 μm with a straggling of 50 μm.

In the present paper the first Mössbauer spectra of ^{57}Fe in mc-Si solar cell are reported in different conditions for excess carrier injection and subsequent carrier flow by light illumination. The results are compared with the spectrum measured in the same p-type mc-Si wafer.

2 Experimental procedure

Radioactive isotopes of ^{57}Mn ($\tau_{1/2} = 1.45$ m) were produced by the nuclear projectile fragmentation of $^{58}Fe^{21+}$ primary beam (E = 63 MeV/nucleon) with a Be target, and were subsequently separated as a secondary beam by an on-line isotope separator, RIPS at the RIKEN RI-beam facility. Mössbauer spectra of ^{57}Mn/^{57}Fe in p-type multi-crystalline-Si as well as in Si-solar cells were measured at 300 K and 400 K under Xe lamp illumination immediately after the implantation of ^{57}Mn with energy of GeV. The implantation was performed through an aluminum foil degrader with a thickness of 200 μm, so that the ^{57}Mn probes stopped at approximately 100 μm from the surface of the sample. The total fluence of ^{57}Mn was 2×10^{12} ^{57}Mn/cm^2 typically for one spectrum, requiring a measurement time for 4 h per spectrum.

3 Results and discussions

The mc-Si solar cell is covered with Ag electrode lines and a Si-N layer on the top, and Ag electrode layer at the bottom. The ^{57}Mn implantation was performed through

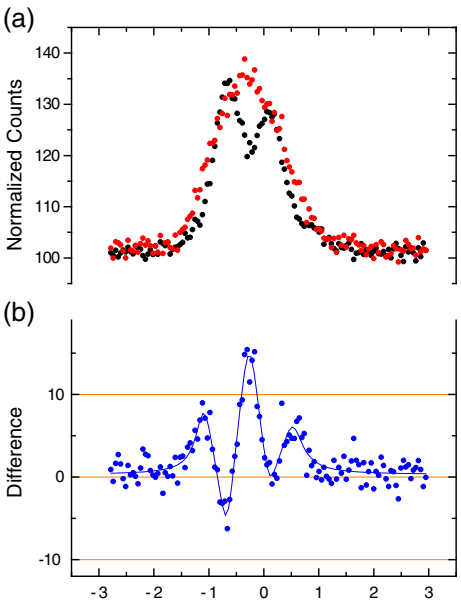

Fig. 1 (**a**) Mössbauer spectra of ^{57}Mn/^{57}Fe in p-type multi-crystalline-Si (*black points*) as well as in Si-solar cells (*red points*) were measured at 400 K under Xe lamp illumination. The difference of the two spectra is shown with blue points in Fig. 1 (b)

this top surface. During a Mössbauer spectral measurement under dark condition, an I–V characteristic of the p-n junction was measured after every hour. The value of the highest current at a forward voltage of 0.7 V increases substantially after 1 h in comparison with that obtained before the spectral measurement, but does not further increase at later times during the measurements. Accordingly, we may ignore the defect accumulation due to ^{57}Mn implantation, because the I–V characteristic does not further change with increasing implantation dose.

The spectra of ^{57}Fe in p-type multi-crystalline (mc)-Si and in the p-region of the p-n junction Solar cell are measured at 400 K under light illumination. The spectra are shown in Fig. 1(a) with red and black points, respectively. The "black spectrum" consists of two components, as is shown in Fig. 2(a), which can be assigned to interstitial and substitutional Fe in Si matrix with the isomer shifts of 0.8 and -0.06 mms^{-1}, respectively. On the other hand, the "red spectrum" of the solar cell appears to be very broad, and therefore, to be difficult to analyze by a superposition of singlets. To understand such broad spectrum, we subtract the "black spectrum" from the "red spectrum", obtaining the difference, which is shown in Fig. 1(b). The difference spectrum can be fitted by three appearing components (pink, yellow, and light blue) and two disappearing ones (red and green), as are shown in Fig. 2(b).

These singlets can be assigned to different charge states of ^{57}Fe atoms on interstitial Fe$_i$ sites and substitutional Fe$_s$ sites: Fe_i^{2+}, Fe_i^{1+}, Fe_i^{0}, Fe_s^{0}, and Fe_s^{-1} and are colored by pink, red, yellow, green and light blue, respectively in Fig. 2(b). The isomer shift values are in good agreement with those of previous absorber experiments obtained in ^{57}Fe deposited mc-Si [8]. Notice that the ^{57}Mn probes were implanted into the p-type region of mc-Si solar cell, which is the same material as the p-type mc-Si wafer.

The present results indicate that the light illumination changes not only the Fermi level (quasi-Fermi level) by the excess carrier injection, but also the carrier trapping

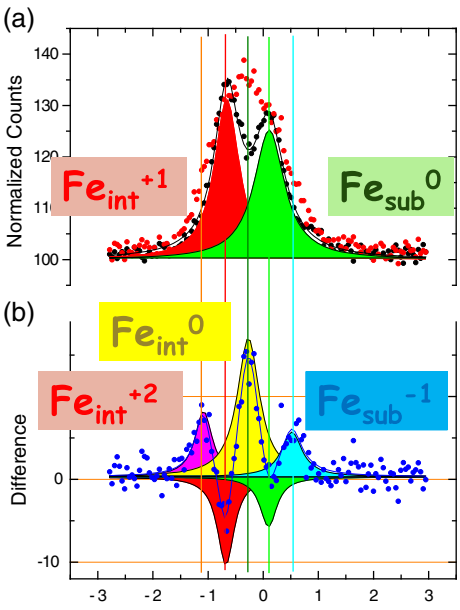

Fig. 2 (**a**) and (**b**) The difference spectrum can be analyzed by the appearing three singlets (pink, yellow, and light blue components in Fig. 2 (b)) and the two disappearing singlets (red and green components in Fig. 2 (b)). The colored lines are eye guides, showing the positions of the singlets which correspond to different charge and lattice states of Fe in Si

processes. The latter must be due to the directional excess carrier flow through the p-n junction, which affects the carrier trapping kinetics with electrons and holes at the Fe impurities, leading to the different charge states on both Fe substitutional and interstitial sites in the p-region in mc-Si solar cell. This is, in fact, the first in-situ observation of the carrier trapping processes at Fe impurities in mc-Si solar cell, which degrades the energy conversion efficiency.

4 Summary

For more than half a century the carrier trapping process at Fe impurities in Si has been one of the central problems in defect solid state physics and also in semiconductor industry, because Fe impurities are thought to degrade strongly LSI devices and Si solar cell performance. Fe gettering techniques have been successfully developed for LSI devices to remove Fe impurities from the device active zone, while for multi-crystalline Si-solar cells, i.e., the dominant production of the solar cell market, the complicated defect distributions have prohibited one from achieving Fe gettering. The present Mössbauer study clearly shows for the first time the Fe interstitial and substitutional impurities with different charge states in mc-Si solar cell, which are created through the carrier trapping process during the solar cell operation.

Acknowledgements Drs. M.Yamatani, K. Niira, and K. Shirasawa, KYOCERA Corporation, are greatly acknowledged for providing us the Si solar cells specially made for the present investigation. The RIBF facility members at RIKEN have intensively supported to provide us the excellent stable and highly intensive beam of ^{58}Fe for the projectile fragmentations. Dr. Atsushi Yoshida is appreciated for his kind supports and valuable advices for the RIPS operations since more than 10 years.

References

1. Istratov, A.A., Hieslmair, H., Weber, E.R.: Appl. Phys. **A69**, 13 (1999)
2. Schwalbach, P., Laubach, S., Hartick, M., Kankeleit, E., Keck, B., Menningen, M., Sielemann, R.: Phys. Rev. Lett. **64**, 1274 (1990)
3. Gunnlaugsson, H.P., Weyer, G., et al.: Appl. Phys. Lett. **80**, 2657 (2002)
4. Yoshida, Y.: In: ALTECH 2003 analytical and diagonistic techniques for semiconductor materials, devices, and processes, vol. 479 (2003)
5. Kobayashi, Y., Yoshida, Y., et al.: Hyperfine Interact. **126**, 417 (2000)
6. Yoshida, Y., Kobayashi, K., et al.: Defect Diffus. Forum **194–199**, 611 (2001)
7. Yoshida, Y., Kobayashi, Y., Hayakawa, K., Yukihira, K., Yoshida, A., Ueno, H., Shimura, F., Ambe, F.: Physica B **376–377**, 69 (2006)
8. Yoshida, Y., Ogawa, S., Arikawa, K.: Physica B **340–342**, 605 (2003)
9. Yoshida, Y., Horie, S., Niira, K., Fukui, K., Shirasawa, K.: Physica B **376–377**, 227 (2006)
10. Estreicher, S.K., Sanati, M., Gonzalez Szwacki, N.: Phys. Rev. B **77**, 125214 (2008)

Hyperfine Interact (2012) 204:139–142
DOI 10.1007/s10751-011-0470-x

An in situ Mössbauer study using synchrotron radiation

Ryo Masuda · Takaya Mitsui · Keiji Itoh · Kouji Sakaki · Hirotoshi Enoki · Yumiko Nakamura · Makoto Seto

Published online: 3 January 2012

Abstract We have been developing a system for in situ Mössbauer studies using synchrotron radiation (SR) to elucidate the mechanism of hydrogenation processes. In the system, samples reacts in a pressure-temperature chamber and SR-based Mössbauer spectra using variable-frequency nuclear monochromator and energy spectra of inelastic nuclear resonant scattering (NRS) of SR are measured. As a feasibility study, the temperature dependence of the Mössbauer and inelastic NRS spectra of ^{57}Fe in *c*-$GdFe_2H_3$ under vacuum were measured. In both spectra, clear differences were observed between 373 K and 573 K. These differences can be interpreted by the change of microscopic environment around Fe at the dehydrogenation. Thus, it is confirmed that this system works well enough to perform the in-situ Mössbauer study on the dehydrogenation of *c*-$GdFe_2H_3$.

Keywords Hydrogen desorption · In situ Mössbauer study · Synchrotron radiation · $GdFe_2$ · Nuclear monochromator · Inelastic nuclear resonant scattering

R. Masuda (✉) · T. Mitsui · M. Seto
Condensed Matter Science Division, Japan Atomic Energy Agency,
Sayo-cho, Sayo-gun, Hyogo 679-5148, Japan
e-mail: masudar@spring8.or.jp

K. Itoh
Faculty of Education, Okayama University, Tsushima-Naka, Kita-ku,
Okayama 700-8530, Japan

K. Sakaki · H. Enoki · Y. Nakamura
Energy Technology Research Institute, National Institute of Advanced Industrial
Science and Technology, AIST Tsukuba Central 5, Tsukuba, Ibaraki 305-8565, Japan

M. Seto
Research Reactor Institute, Kyoto University, Kumatori-cho,
Sennan-gun, Osaka 590-0494, Japan

T. Mitsui · M. Seto
CREST, Japan Science and Technology Agency, Honcho, Kawaguchi, Saitama 332-0012, Japan

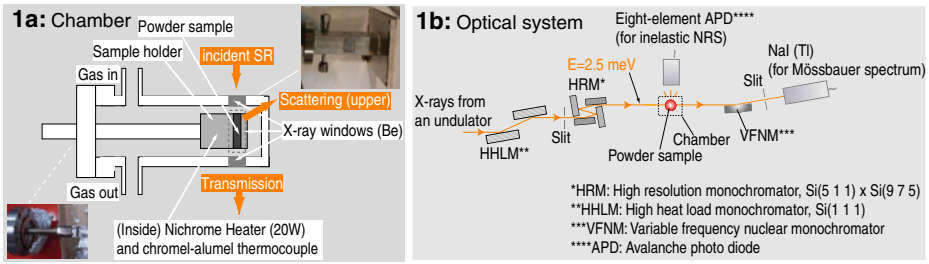

Fig. 1 Schematic drawings; **1a**: the developed chamber for in situ Mössbauer study. **1b**: the optical system at the experiment in BL11XU. The orange bold arrows mean the path of the beam. The upper right and the lower left at Fig. 1a is the photograph of the chamber

1 Introduction

Hydrogen absorption to materials and desorption from them have been studied by many researchers. These processes are affected by the diffusion of H and the constituent atoms as well as the bonding between them [1]. Thus, their local electronic and vibrational states are important. To study them, we have been developing a system for in situ Mössbauer studies using synchrotron radiation (SR); a sample in a newly developed pressure-temperature chamber is studied by SR-based ^{57}Fe Mössbauer spectra using the variable-frequency nuclear monochromator (VFNM) and energy spectra of the inelastic nuclear resonant scattering (NRS) of SR by ^{57}Fe. Here, we report the system and the feasibility study, in which we observed the dehydrogenation of *c*-$GdFe_2H_3$ in both spectra.

2 Experiments

The developed chamber is shown in Fig. 1a. All parts with no mention are made of stainless steel to resist H_2 gas. The sample holder of an Al alloy has a cavity to form an edge in the sample cluster; SR transmits the edge and is scattered by the surface of the cluster. The distance between the surface and the outside of the upper X-ray window is typically 7 mm, to detect the isotropic inelastic scattering efficiently.

With this chamber, the SR-based Mössbauer and inelastic NRS spectra of ^{57}Fe were measured at BL11XU of SPring-8. The experimental setup is shown in Fig. 1b. SR monochromatized to 2.5 meV around the energy of ^{57}Fe nuclear resonance was incident on the powder sample of *c*-$GdFe_2H_3$ (47% enrichment of ^{57}Fe). The chamber was kept in the vacuum of 1 Pa and the temperature of the sample was tuned by the heater in the chamber. The transmitted radiation from the sample was diffracted by VFNM and detected by a NaI(Tl) detector to observe the Mössbauer spectra; the details of the setup are written in [2]. The inelastic NRS from the sample is detected by an eight-element avalanche photo diode detector; the details of the setup are written in [3].

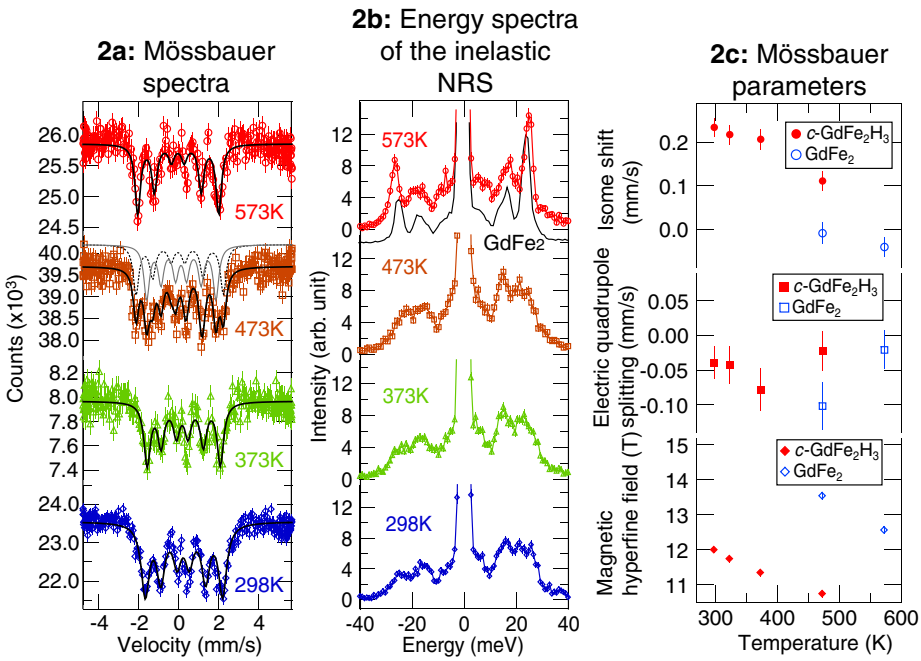

Note:
At 473 K, the hydrogen desorbed from the sample and thus the Mössbauer spectrum at 473 K shows the two sextets corresponding to GdFe2 and c-GdFe2H3. However, the inelastic spectrum at 473 K looks similar to those of *c*-GdFe2H3 below 373 K. This must be due to the relation between the measuring time and the time scale of the dehydrogenation. Because the sample desorbed the hydrogen slowly at 473 K, GdFe2 had formed little in the earlier measurement of inelastic spectra (typically 2 hours measuring time), although GdFe2 was no longer little in the later measurement of Mössbauer spectrum (typically 4 hours).

Fig. 2 Experimental results; **2a**: the SR-based Mössbauer spectra with VFNM (measuring time: typically 4 h per spectrum). **2b**: the energy spectra of the inelastic NRS of SR (typically 2 h per spectrum). **2c**: the Mössbauer parameters from Fig. 2a. The velocity scale of Fig. 2a is calibrated by α-Fe at 298 K. The black bold lines in Fig. 2a show fitting lines. The gray line and the dashed black line above the spectra at 473 K in Fig. 2a are the components of the fitting for the spectrum at 473 K. The lines in Fig. 2b are only eye guides except the black line just below the spectrum at 573 K, which is the inelastic NRS spectrum of $GdFe_2$ at 298 K

3 Results and discussion

The Mössbauer spectra at the temperatures from 298 K to 573 K are shown in Fig. 2a. Although the Mössbauer spectra except at 473 K can be approximately fitted with one Lorentz sextet, the spectrum at 473 K needs two sextets. The obtained Mössbauer parameters are shown in Fig. 2c. The gradual decrease of the isomer shift (IS) on heating below 473 K is well interpreted by the second order Doppler shift, but the abrupt emergence of another site with smaller IS value at 473 K indicates the dehydrogenation at this temperature because the decrease of surrounding H atoms reduces IS value. As for electric quadrupole splitting, there is little change because both *c*-$GdFe_2H_3$ and (dehydrogenated) $GdFe_2$ is C15 Laves structure. The gradual

decrease of the magnetic hyperfine field on heating is due to the thermal disturbance of the Fe magnetic moment and its steep increase at 473 K is due to the increase of the Fe magnetic moment caused by the lattice contraction in dehydrogenation. Thus, all changes in the Mössbauer spectra can be interpreted by the effects of the heating or the dehydrogenation.

The inelastic NRS spectra at the temperatures from 298 K to 573 K are shown in Fig. 2b. Below 473 K, the spectra show two broad peaks around 15 and 21 meV. In contrast, the spectrum at 573 K clearly differs from the others and shows two sharp peaks at 18 and 25 meV. This spectrum agrees with the inelastic NRS spectra of $GdFe_2$, as shown in Fig. 2b. In addition, the two sharp peaks of $GdFe_2$ correspond to the Gd-Fe bonding, according to the study on $DyFe_2$[4]. Thus, the broadening of these peaks in the spectra of *c*-$GdFe_2H_3$ below 473 K can be understood by the variation of the Gd-Fe bonding owing to the hydrogen insertion.

From these results, the dehydrogenation of *c*-$GdFe_2H_3$ was successfully observed in situ by both Mössbauer and inelastic NRS spectra. Hence, this system is expected to be applied to the detailed in situ study on hydrogenation processes, such as hydrogen induced amorphization. In fact, a H_2 gas transfer system is ready to connect in BL11XU now. It is noted that the in situ Mössbauer study with various nuclides using this chamber is available by the forward NRS method and the SR-based Mössbauer spectroscopy [5].

4 Summary

We have been developing a system for in situ Mössbauer study, including the newly developed pressure-temperature chamber. It enables us to observe the SR-based ^{57}Fe Mössbauer spectra with VFNM and the energy spectra of inelastic NRS of SR by ^{57}Fe in situ. As a feasibility study, the temperature dependence of *c*-$GdFe_2H_3$ was measured by both spectra and its dehydrogenation was clearly observed. The detailed Mössbauer study with this system would give further comprehension on the microscopic picture of the hydrogenation processes.

Acknowledgements This work has been supported by New Energy and Industrial Technology Development Organization (NEDO) under "Advanced Fundamental Research Project on Hydrogen Storage Materials".

References

1. Fukai, Y.: The Metal-Hydrogen System, Basic Bulk Properties, 2nd edn. Springer, Berlin (2010)
2. Mitsui, T., Hirao, N., Ohishi, Y., Masuda, R., Nakamura, Y., Enoki, H., Sakaki, K., Seto, M.: J. Synchrotron Radiat. **16**, 723–729 (2009)
3. Higashitaniguchi, S., Seto, M., Kitao, S., Kobayashi, Y., Saito, M., Masuda, R., Mitsui, T., Yoda, Y., Kamihara, Y., Hirano, M., Hosono, H.: Phys. Rev. B **78**, 174507 (2008)
4. Brwon, D.E., Toellner, T.S., Sturhahn, W., Alp, E.E., Hu, M., Kruk, R., Rogackt, K., Canfield, P.C.: Hyperfine Interact. **153**, 17–24 (2004)
5. Seto, M., Masuda, R., Higashitaniguchi, S., Kitao, S., Kobayashi, Y., Inaba, C., Mitsui, T., Yoda, Y.: Phys. Rev. Lett. **102**, 217602 (2009)

Hyperfine Interact (2012) 204:143–147
DOI 10.1007/s10751-011-0466-6

CEMS study of corrosion products formed by NaCl aqueous solution

A. Nakanishi

Published online: 29 November 2011

Abstract Conversion electron Mössbauer spectroscopy was used to study corrosion products by NaCl aqueous solution. A drop of the solution is put on an iron foil and the foil is left at RT. During the evaporation of the solution, corrosion products are formed. Conversion electron Mössbauer spectra were taken at temperatures between 15 K and room temperature (RT). In the Mössbauer spectra a ferric doublet is observed at RT, but sextets are found at 15 K. These results show that the corrosion product mainly consists of γ - FeOOH and a small amount of β - FeOOH is noticed. As NaCl concentration increases, the corrosion layer becomes thick and β-FeOOH / γ - FeOOH ratio increases slightly. Consequently, it has been concluded that the produced amount of β- FeOOH increases more rapidly than that of γ - FeOOH with increasing NaCl concentration.

1 Introduction

Conversion electron Mössbauer spectroscopy (CEMS) is a powerful tool for characterizing corrosion products because the Mössbauer spectrum can be observed without separating the corrosion products from the substrate materials. Corrosion products formed on an iron foil by the sulfuric acid water have been investigated with CEMS at low temperatures [1, 2]. From the results of previous studies, the corrosion products mainly consist of α-FeOOH, γ-FeOOH and γ-Fe_2O_3. But in a marine environment β-FeOOH is observed in the corrosion products [3], where chlorine ions exist. Though the Néel temperature of β-FeOOH is reported to be 299 K, a reduction of Néel temperature is often observed due to the existence of interstitial water molecules [4]. Thus, its Mössbauer spectrum measured at room temperature (RT) shows a ferric doublet which can not distinguish from that of

A. Nakanishi (✉)
Department of Physics, Shiga University of Medical Science, Seta, Otsu,
Shiga 520-2192, Japan
e-mail: nakanisi@belle.shiga-med.ac.jp

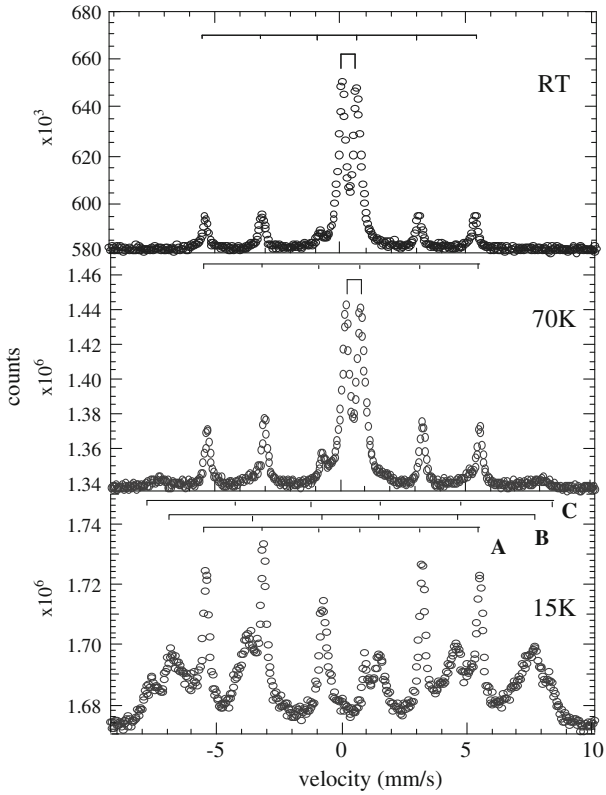

Fig. 1 CEM spectra of corrosion products by 0.01 M NaCl solution. Sextets A-C are due to iron foil, γ-FeOOH and β-FeOOH, respectively

γ-FeOOH. Furthermore the corrosion products consist of a lot of small particles, so that ferric doublets are mostly observed in a Mössbauer spectrum at RT due to their superparamagnetism. Therefore, in order to investigate the properties of corrosion products in detail, it is necessary to measure a Mössbauer spectrum at low temperatures.

Mössbauer spectroscopic studies of corrosion products by NaCl aqueous solution have been made extensively [5–7]. From these studies corrosion layer can be divided into two groups, the adherent rust and the non-adherent rust. The Mössbauer spectra of the adherent rust were recorded in transmission geometry, where corrosion products were removed from the substrate material by scraping or hitting. But there is possibility to vary the size distribution of corrosion products, which affects the Mössbauer spectrum. In this study in order to characterize the corrosion products formed in the marine environment, a dilute NaCl aqueous solution (0.01–1.0 M) was prepared and corrosion products formed by this solution were investigated with CEMS at low temperatures.

2 Experimental

Natural iron foil washed by acetone was used and NaCl aqueous solution (0.01–1.0 M) was prepared. Samples were prepared in two methods. One is that a drop of the aqueous solution is put on the surface of an iron foil and the foil is left at RT.

Fig. 2 Area ratio at 15 K

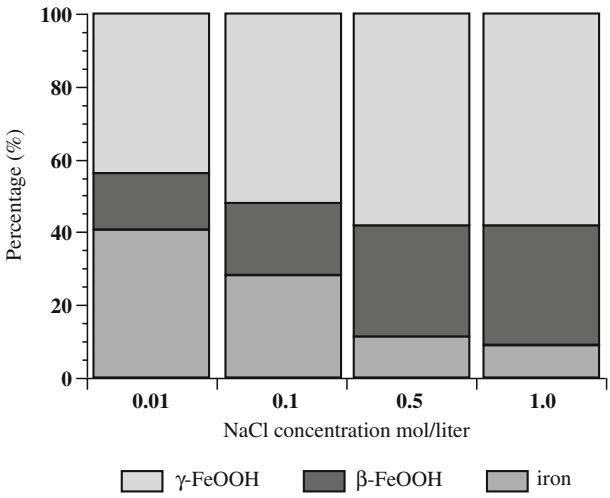

During the evaporation of aqueous solution, corrosion products are formed on the foil surface. Another method is that an iron foil is immersed in the NaCl aqueous solution for several days and dried at RT. During the immersion, corrosion products are formed on the surface.

Conversion electron Mössbauer (CEM) spectra were taken at temperatures between 15 K and RT, with the gas filled proportional counter described elsewhere [8–10]. Hydrogen gas and the 98% He – 2% CH4 gas mixture were used as the counter gas at low temperatures and RT, respectively. The velocity calibration was carried out with a natural iron foil. X-ray diffraction analyses were also performed using a Philips diffractometer (PW1710) with Co Kα radiation.

3 Results and discussion

CEM spectra of the corrosion products formed during the evaporation of 0.01 M NaCl solution in air are shown in Fig. 1. Similar spectra were observed for the corrosion products formed by higher concentration of NaCl aqueous solution. A weak sextet of the iron foil and a ferric doublet are observed at RT. In the spectrum at 70 K the doublet still remains, but at 15 K no doublet is observed and two sextets in addition to that of the iron foil are noticed. The value of hyperfine field suggests that the large sextet is assigned to γ-FeOOH and the small one to β-FeOOH, which is also confirmed by the XRD pattern. Magnetite and α- FeOOH were observed as traces in XRD pattern. Thus, sextets of magnetite and α- FeOOH are small and can not be separated from that of β-FeOOH. The relative area of these sextets are given if Fig. 2. From this figure, it is found that the corrosion layer becomes thicker as the NaCl concentration increases. Assuming that the recoilless fractions of these chemical species are same, a ratio of β-FeOOH to γ-FeOOH is calculated. A plot of the ratio as a function of NaCl concentration is give in Fig. 3. This plot shows that the β-FeOOH / γ - FeOOH ratio increases slightly with increasing of NaCl concentration.

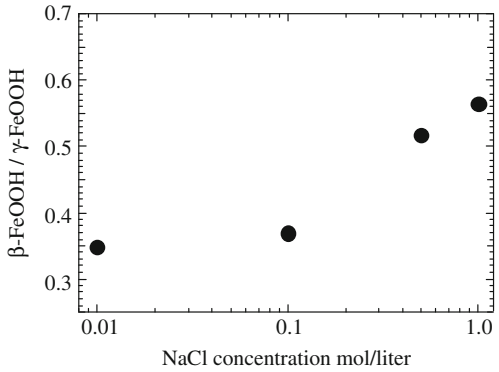

Fig. 3 β-FeOOH / γ-FeOOH ratio as a function of NaCl concentration

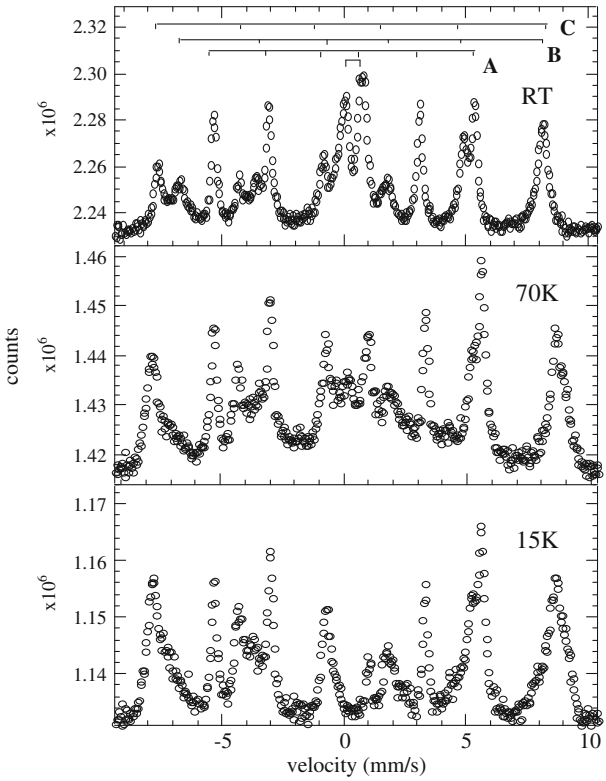

Fig. 4 CEM spectra of adherent layer on the iron foil. Sextet A is due to iron foil and sextets B, C are due to magnetite

In the case of immersion samples, corrosion products can be divided into two layers. The colour of the outer layer is light brown and that of the inner layer is black. The outer layer is not adherent and easy to remove from the substrate material in the solution. The inner layer is adherent and its CEM spectra are shown in Fig 3, where the iron foil was immersed in 0.01 M NaCl for two weeks. In RT spectrum, one doublet and two sextets in addition to that of the iron foil are observed. Hyperfine fields and isomer shifts of these sextets suggest that they are

due to magnetite, corresponding to iron atoms in A and B sites respectively. The isomer shift of the doublet is 0.35 mm/s, which indicates this doublet is ferric. But its quadrupole splitting is 0.7 mm/s which is larger than that of γ-FeOOH. In the XRD pattern of this sample, the peaks of magnetite are found and γ-FeOOH is observed as trace. In 70 K spectrum, the intensity of the doublet becomes much smaller than that in RT spectrum, and in 15 K the doublet disappears. If this doublet is due to γ-FeOOH, the intensity of doublet in 70 K must be similar to that in RT [1]. Therefore this doublet can not assign to γ-FeOOH. Since the fine powder of magnetite shows superparamagnetic relaxation [11], this doublet assigns to superparamagnetic magnetite (Fig. 4).

4 Conclusions

In the case of corrosion products formed by the evaporation of NaCl aqueous solution, corrosion products consist of γ-FeOOH and β-FeOOH. The β-FeOOH / γ-FeOOH ratio becomes large as NaCl concentration increase, which indicates that the produced amount of β- FeOOH increases more rapidly than that of γ - FeOOH with increasing NaCl concentration. In the case of immersion sample, the adherent layer on the foil consists magnetite including the superparamagnetic small particles.

References

1. Nakanishi, A., et al.: In: Ortalli, I. (ed.) Conf. Proc. SIF, Bologna **50**, 669 (1996)
2. Nakanishi, A., et al.: Hyperf. Interact. **112**, 43 (1998)
3. Murad, E., Johnston, J.H.: In: Long G.J. (ed.) Mössbauer spectroscopy applied to inorganic chemistry, vol. 2, p. 507. Plenum Press, New York (1987)
4. Chambaere, D., De Grave, E.: J. Mag. Mag. Mater. **42**, 263 (1984)
5. Garcia, K.E., et al.: Hyperf. Interact. **161**, 127 (2005)
6. Garcia, K.E., et al.: Corros. Sci. **48**, 2813 (2006)
7. Garcia, K.E. et al.: Corros. Sci. **50**, 763 (2008)
8. Fukumura, K., et al.: Nucl. Instr. Meth. **A301**, 871 (1991)
9. Fukumura, K., et al.: Nucl. Instr. Meth. **B86**, 387 (1994)
10. Kobayashi, T., et al.: Conf. Proc. In: Ortalli, I. (ed.) SIF, Bologna **50**, 899 (1996)
11. Harteidge, A. et al.: J. Mag. Mag. Mater. **176**, L89 (1997)

Hyperfine Interact (2012) 205:1–5
DOI 10.1007/s10751-011-0505-3

Mössbauer spectroscopic study on valence-detrapping and trapping of mixed-valence trinuclear iron(III, III, II) fluorine-substituted benzoate complexes

Yoichi Sakai · Satoru Onaka · Masashi Takahashi · Ryo Ogiso · Tsutomu Takayama · Tadahiro Nakamoto

Published online: 9 December 2011

Abstract Four mixed-valence trinuclear iron(III, III, II) fluorine-substituted benzoate complexes were synthesized; $Fe_3O(C_6F_5COO)_6(C_5H_5N)_3{\cdot}CH_2Cl_2$ (**1**), $Fe_3O(C_6F_5COO)_6(C_5H_5N)_3$ (**2**), $Fe_3O(2H\text{-}C_6F_4COO)_6(C_5H_5N)_3$ (**3**), and $Fe_3O(4H\text{-}C_6F_4COO)_6(C_5H_5N)_3$ (**4**), in which valence-detrapping and trapping phenomena have been investigated by ^{57}Fe- Mössbauer spectroscopy. The valence state of the three iron ions is trapped at lower temperatures while it is fully detrapped at higher temperatures for 1. Valence detrapping is not observed for **2, 3**, and **4** even at room temperature, although Mössbauer spectra for **3** and **4** show complicated temperature dependence.

Keywords ^{57}Fe-Mössbauer spectroscopy · Valence-detrapping and trapping · Mixed-valence trinuclear iron fluorine-substituted benzoate complexes

1 Introduction

Mixed-valence trinuclear iron(III, III, II) carboxylate complexes have attracted intensive attention from many chemists in the field of Mössbauer spectroscopy, where two Fe^{3+} ions and one Fe^{2+} ion exist in three chemically similar sites in the crystal. The extent of such site similarity being dependent on various conditions, it is a subtle and interesting problem whether the valence states of the

Y. Sakai (✉) · S. Onaka · R. Ogiso · T. Takayama
Daido University, Nagoya 457–8530, Japan
e-mail: yocsakai@daido-it.ac.jp

M. Takahashi
Toho University, Funabashi 274–8510, Japan

T. Nakamoto
Toray Research Center, Ohtsu 520–8567, Japan

three iron ions are in a detrapped (averaged) state or in a trapped state. Although many Mössbauer studies have been reported so far for such trinuclear iron carboxylates, only few papers have been published for benzoate complexes and benzoate-derivatives probably because of synthetic difficulties. In 2003, mixed-valence $Mn_3O(C_6F_5COO)_6(C_5H_5N)_3{\cdot}CH_2Cl_2$ was synthesized and single crystal ESR spectra were analyzed on the basis of X-ray structure analysis by Ito et al. [1]. We have succeeded in the synthesis of the mixed-valence trinuclear iron(III, III, II) fluorine-substituted benzoate by a similar method, and studied the valence states of iron ions by the Mössbauer technique.

2 Experimental

2.1 Materials

Four mixed valence trinuclear iron pentafluorobenzoate or tetrafluorobenzoate complexes were synthesized for the first time. The new products were identified by elemental analysis, TG-MS, FTIR spectroscopy, and Mössbauer spectroscopy.

***$Fe_3O(C_6F_5COO)_6(C_5H_5N)_3 \cdot CH_2Cl_2$* (1)** $FeCl_3{\cdot}6H_2O$ and $FeCl_2{\cdot}4H_2O$ were dissolved in ethanol. To this was added an excess amount of pyridine and the mixture was stirred for 30 min. C_6F_5COONa (prepared with pentafluorobenzoic acid and sodium hydroxide) was added and the mixture was stirred for a few hours. The resulting precipitates were collected and subsequently dissolved in dichloromethane. After adding ethanol and hexane, the mixture was stirred in a refrigerator for several days to afford dark-brown needle-like crystals (yield 30.0%) to grow.

Anal. Calcd (%) for $Fe_3O(C_6F_5COO)_6(C_5H_5N)_3{\cdot}CH_2Cl_2$: C, 39.31; Cl, 4.00; F, 32.16; H, 0.97; N, 2.37. Found (%): C, 39.81; Cl, 3.09; F, 32.41; H, 1.04; N, 2.43.

IR (Nujol, cm^{-1}, selected): $\nu(OCO)_{asym}$; 1654 (s), 1637 (m), and 1608 (w).

A satisfactory analytical result for the Cl content has not yet obtained. However, TG-MS results for complex **1** showed that the ratio of Fe_3O cluster/solvate molecule CH_2Cl_2 is close to 1.0. The ratio has been also confirmed by our preliminary single-crystal X-ray structural determination, which will be reported elsewhere soon.

***$Fe_3O(C_6F_5COO)_6(C_5H_5N)_3$* (2)** Polycrystalline solvate complex **1** was heated for 2 hours at 135°C under a reduced pressure of 0.1 Torr, to remove solvate CH_2Cl_2, on the basis of our TG-MS data for **1**.

Anal. Calcd (%) for $Fe_3O(C_6F_5COO)_6(C_5H_5N)_3$: C, 40.57; F, 33.78; H, 0.90; N, 2.49. Found(%): C, 39.66; F, 34.11; H, 0.92; N, 2.17.

IR (Nujol, cm^{-1}, selected): $\nu(OCO)_{asym}$; 1654 (m), 1637 (m), and 1605 (w).

The elemental analysis suggested that there might be a little thermal decomposition.

***$Fe_3O(2H-C_6F_4COO)_6(C_5H_5N)_3$* (3) *and* *$Fe_3O(4H\text{-}C_6F_4COO)_6(C_5H_5N)_3$* (4)** These two complexes were synthesized by a similar method to that of **1** described above, using sodium 2,3,4,5-tetrafluorobenzoate and sodium 2,3,5,6-tetrafluorobenzoate, and the yield was 25.0 and 36.6% for **3** and **4**, respectively.

Anal. Calcd (%) for $Fe_3O(2H\text{-}C_6F_4COO)_6(C_5H_5N)_3$: C, 43.35; F, 28.87; H, 1.34; N, 2.65. Found (%): C, 43.27; F, 28.87; H, 1.44; N, 2.63.

IR (Nujol, cm^{-1}, selected): $\nu(OCO)_{asym}$; 1652 (m), 1636 (m), and 1604 (w).

Anal. Calcd (%) for $Fe_3O(4H\text{-}C_6F_4COO)_6(C_5H_5N)_3$: C, 43.35; F, 28.87; H, 1.34; N, 2.65. Found (%): C, 42.72; F, 28.71; H, 1.39; N, 2.69.

IR (Nujol, cm^{-1}, selected): $\nu(OCO)_{asym}$; 1637 (s), and 1605 (m).

2.2 ^{57}Fe-Mössbauer measurements

Mössbauer measurements were performed in an ordinary mode with a Mössbauer spectrometer with a ^{57}Co(Rh) source. The measurement temperature was ranged from 5 K to 300 K. The spectral curve fitting was carried out by using MossWinn 4.0Pre software. The isomer shift and Doppler velocity scale were calibrated with respect to metallic iron at room temperature.

3 Results and discussion

The temperature-dependent Mössbauer spectra are shown in Figs. 1 and 2 for trinuclear iron pentafluorobenzoate complexes (**1** and **2**) and tetrafluorobenzoate complexes (**3** and **4**), respectively.

As shown in the upper part of Fig. 1, the spectral line-shapes of **1**, which contains CH_2Cl_2 as a solvate molecule in the crystalline solid, are quite sensitive to temperature. Two pairs of the absorption doublet are separately observed with an area ratio of about 2:1 at 5 K. The isomer shift and the quadrupole splitting are estimated as follows: 0.54 mm/s and 1.21 mm/s for the higher intense doublet, and 1.23 mm/s and 2.19 mm/s for the lower one. The intensity ratio and Mössbauer parameters reveal that the valence state of the three iron ions should be trapped in two Fe^{3+} and one Fe^{2+}. Only one doublet was observed at 300 K with an isomer shift of 0.64 mm/s and a quadrupole splitting of 0.40 mm/s, implying that all iron ions should be in a fully detrapped valence state of +2.7, calculated as $[(+3) \times 2 + (+2)]/3 = 2.7$. Unfortunately it has not yet been successful to decompose the possible components at transient temperatures in the present analysis because of the complicated line-shapes. However, it is possible to estimate the transition temperature from the trapped to the detrapped state, ranging from 70 K to 100 K.

Complex **2** does not show an essential transformation from the trapped iron valence type to the detrapped type judging from the temperature dependence of the Mössbauer spectral line-shapes (the lower part of Fig. 1). This indicates that the valence-trapped state survives over the whole temperature range scanned in the present work. Hendrickson's group reported for the first time that the Mössbauer spectra of the mixed-valence trinuclear iron acetate complex at room temperature showed the detrapped type when it possessed one or more solvate molecules, $Fe_3O(CH_3COO)_6(C_5H_5N)_3 \cdot C_5H_5N$, while the trapped type spectra were observed upon the loss of solvate molecules at room temperature [2, 3]. Sorai's group have interpreted such phenomena from their molecular thermodynamic experiments and theoretical considerations [4]; they demonstrated that the phase transition of the mixed-valence complex should be associated with the intramolecular electron-transfer leading to valence detrapping, the rate of which might be accelerated by the

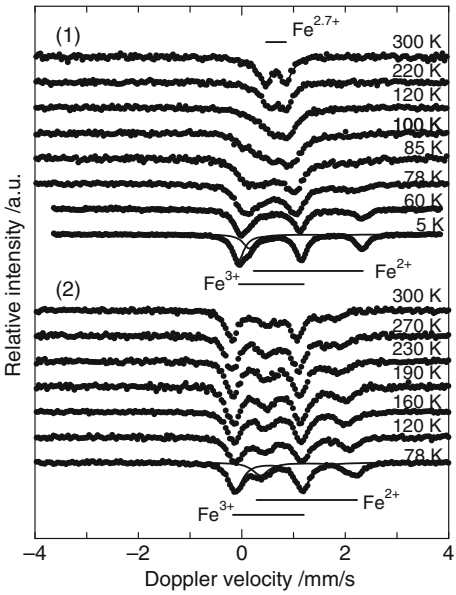

Fig. 1 Temperature dependence of ^{57}Fe-Mössbauer spectra of $Fe_3O(C_6F_5COO)_6(C_5H_5N)_3 \cdot CH_2Cl_2$ **1** and $Fe_3O(C_6F_5COO)_6(C_5H_5N)_3$ **2**

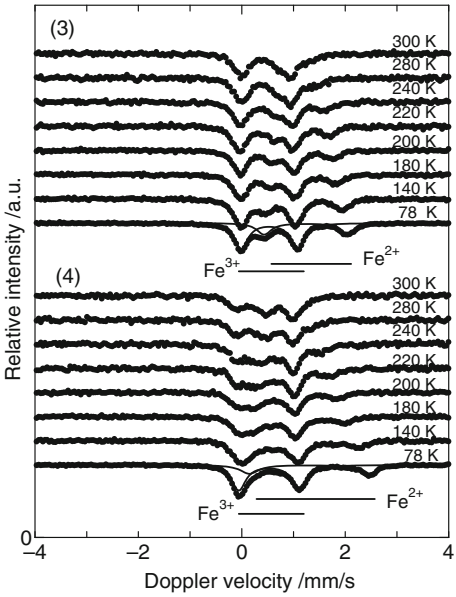

Fig. 2 Temperature dependence of ^{57}Fe-Mössbauer spectra of $Fe_3O(2H\text{-}C_6F_4COO)_6(C_5H_5N)_3$ **3** and $Fe_3O(4H\text{-}C_6F_4COO)_6(C_5H_5N)_3$**4**

presence of solvate molecules in the crystalline state. The mechanism was proven in terms of an unusually large transition entropy estimated from the heat capacity data, being due to a number of the rotational orientations of solvate molecules immediately after the transformation.

The variable-temperature Mössbauer spectra for **3** and **4** are exhibited in the upper part and the lower part of Fig. 2, respectively. The spectral-line shapes depend

significantly on the temperature for both complexes. The isomer shift is evaluated to be 0.46 mm/s by curve fitting of the spectrum at 300 K for **3** assuming one doublet although a little asymmetry is being observed. This value is not close to the isomer shift value ranging 0.65 to 0.75 mm/s at room temperature for the tri-iron carboxylate complexes in a fully valence-detrapped state [3, 5, 6], and also far from that (0.64 mm/s) for **1** described above. The spectra should rather be considered to be trapped one. As shown in Fig. 2, only a small change is observed in the peak positions of the doublet for the Fe^{3+} component while those for Fe^{2+} move to a much higher extent. Similar temperature dependence was reported for mixed-valence $Fe_3O(CH_3COO)_6(3\text{-}CH_3\text{-}C_5H_4N)_3\cdot CH_3CN$ by Oh et al. [5]; they explained that the quadrupole splitting of Fe^{2+} decreased greatly with the rise of temperature, because the electron population of each 3d-orbital in the low-lying electronic states (t_{2g}) becomes close by thermal activation, which results in a decrease of the electric field gradient by the valence electrons, for some high-spin Fe^{2+} compounds such as binuclear iron complexes of the binucleating clathrochelate ligand [7] and $Fe(C_5H_5N)_2I_2$ [8]. The quadrupole splitting for octahedral high-spin Fe^{3+} species with five 3d electrons is not expected to vary with the increase of temperature, because five electrons are equally populated in the five orbitals $(e_g)^2(t_{2g})^3$. We are tempted to interpret our observations that the Mössbauer spectral line shapes vary in a complicated manner with temperature for **3** and **4** in terms of the aforementioned mechanisms. Therefore, we conclude at this moment that the valence of three iron ions should be trapped even at 300 K for **3** and **4**.

References

1. Ito, M., et al.: Inorg. Chim. Acta. **353**, 51 (2003)
2. Oh, S.M., et al.: J. Am. Chem. Soc. **106**, 7984 (1984)
3. Woehler, S.E., et al.: J. Am. Chem. Soc. **109**, 1063 (1987)
4. Sorai, M., et al.: J. Am. Chem. Soc. **108**, 702 (1986)
5. Oh, S.M., et al.: J. Am. Chem. Soc. **109**, 1073 (1987)
6. Nakamoto, T., et al.: Inorg. Chem. **36**, 4347 (1997)
7. Temken, M.D., et al.: Inorg. Chem. **24**, 4202 (1985)
8. Merrithew, P.B., et al.: Inorg. Chem. **10**, 1401 (1971)

Hyperfine Interact (2012) 205:7–11
DOI 10.1007/s10751-012-0558-y

Mössbauer and NMR study of novel Tin(IV)-lactames

Erno Kuzmann · Roland Szalay · Zoltan Homonnay · Sandor Nagy

Published online: 18 January 2012

Abstract N-tributylstannylated 2-pyrrolidinone was reacted with tributyltin triflate in different molar ratios and the complex formation monitored using ^{1}H-NMR, ^{13}C-NMR and ^{119}Sn Mössbauer spectroscopy. Comparing the carbon NMR and tin Mössbauer results, a reaction scheme is suggested for the complexation which assumes the formation of a simultaneously O- and N-tributylstannylated pyrrolidinone cation. The formation of the only O-stannylated pyrrolidinone is also assumed to account for the non-constant Mössbauer parameters of the two tin environments in the distannylated pyrrolidinone cation when the ratio of tributyltin triflate is increased in the reaction.

Keywords Tin(IV) lactames · ^{119}Sn Mössbauer spectroscopy · NMR

1 Introduction

In a previous work we studied some cyclic N-trimethylsilylated carboxylic amide derivatives (ureas, lactames) [1] related to the recent interest in this field of coordination chemistry [2–4]. As an extension of that work here we have focused on tin as a heavier congener of silicon. N-tributylstannylated 2-pyrrolidinone was chosen as a model compound and its complexation with tributyltin triflate in different molar ratios was monitored.

The aim of this work was to prepare novel stannylated pyrrolidinone and characterize it by ^{119}Sn Mössbauer spectroscopy and NMR technique.

E. Kuzmann · R. Szalay · Z. Homonnay (✉) · S. Nagy
Institute of Chemistry, Eötvös Loránd University, Budapest, Hungary
e-mail: homonnay@ludens.elte.hu

2 Experimental

The model compound was prepared according to the common dehydration method starting from tributyltin oxide and pyrrolidinone [2]. After recrystallization from hexane, the pure substrate was dissolved in NMR-grade deuterochloroform containing TMS (tetramethylsilane) as internal standard and mixed with stannyl triflate also dissolved in $CDCl_3$, at triflate/substrate molar ratios of 0.3, 0.6, 1.2, 2.4 and 4.8. ^{1}H- and ^{13}C-NMR spectra of the solutions were taken at room temperature using Bruker Avance 250 MHz NMR spectrometer.

^{119}Sn Mössbauer spectra of frozen solution samples were recorded in transmission geometry with a conventional Mössbauer spectrometer (WISSEL) working in constant acceleration mode. The γ-rays were provided by a 10^9 Bq ^{119}Sn/$CaSnO_3$ source. The measurements were performed at 78 K in a temperature-controlled through-flow type liquid nitrogen cryostat (Leybold). Isomer shifts are given relative to $CaSnO_3$. The Mössbauer spectra were analyzed by least-square fitting of Lorentzian lines by the help of the MOSSWINN code [5].

3 Results and discussion

All peaks, even those derived from impurities (e.g. $(Bu_3Sn)_2O$ and free pyrrolidinone with N-H group) present in the samples, could be assigned in the ^{13}C-NMR spectra. Furthermore, in the 'non-triflated' solution of the N-tributyltin pyrrolidinone, the coupling constant values of the $^{1}J_{SnC}$ and $^{2}J_{SnCC}$ were found to be 353.4 Hz (for ^{117}Sn) / 369.8 Hz (^{119}Sn) and 62.8 Hz (^{117}Sn) / 65.1 Hz (^{119}Sn), respectively.

Upon varying triflate/substrate molar ratios from 0.3, 0.6, 1.2, 2.4 to 4.8, the ^{1}H- and ^{13}C-NMR spectra exhibited a systematic and significant change of the chemical shifts (Fig. 1). The medium effect on the shift values could be neglected since solutions containing both the pyrrolidinone and triflate at different absolute concentrations but with identical molar ratio gave virtually the same spectra.

The well-separated shifts of the ring carbon atom directly attached to the nitrogen (near at 48 ppm) together with those of the carbonyl (~184 ppm, not shown) and the ring C atom next to the carbonyl (~31 ppm) and the Sn bonded α carbon (~13 ppm), all exhibit a saturation-type increase with increasing amount of triflate. However, butyl carbons at the β, γ (CH_2) and δ (CH_3) positions relative to the Sn atom, being rather insensitive to the nature of the tin-bounded ligand and to the chemical environment anyway, experience much less change in their shift values (near at 27, 28 and 14 ppm, respectively). In the region of the ring carbon shifts, new peaks are not observed, and this indicates a rapid equilibrium between the triflated and the non-triflated forms on the NMR time scale. In the butyl carbon region, the signals belonging to the hexabutyl distannoxane present as an impurity in some percents, tend to shift and grow into those of the tributyltin triflate, however, even at the molar ratio of 4.8 the ppm values markedly differ by a few tenths from those of the pure triflate. The chemically very sensitive Sn-C carbon peak characteristic to a more or less bound tributyltin triflate gives only a very weak signal at triflate to pyrrolidinone ratio 0.6.

On the basis of the NMR results, we can conclude that there is an equilibrium between the stannyl pyrrolidinone and the distannylated adduct, however, the

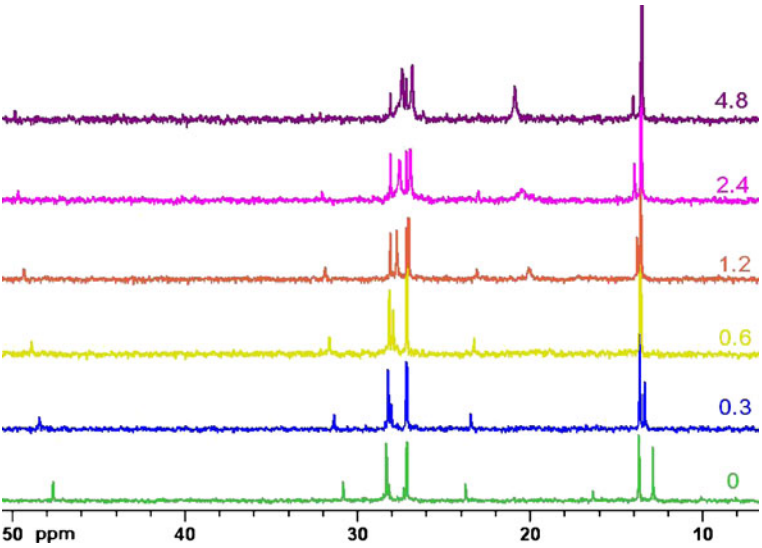

Fig. 1 A section of the ^{13}C NMR spectra for the tributylstannylated triflate-pyrrolidinone mixtures with different molar ratio of the triflate to pyrrolidinone indicated

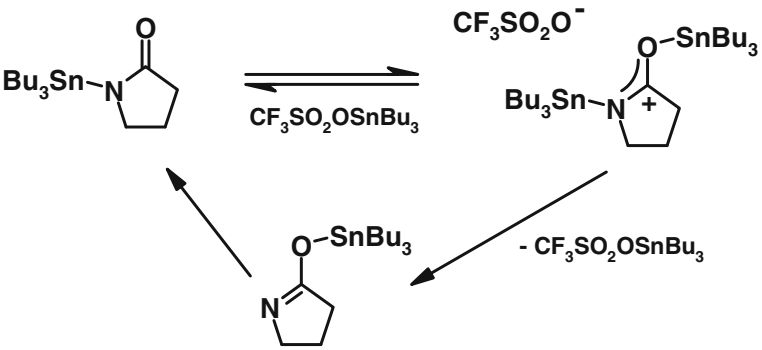

Fig. 2 A plausible mechanism of the reaction between N-tributyltin 2-pyrrolidinone and tributyltin triflate

equilibrium is pushed forward by an excess of triflate much higher than the stoichiometric amount (Fig. 2). On the NMR time scale the exchange rate of the tributylstannyl group is fast. A subordinate alternative decomposition route via the neutral O-stannylated pyrrolidinone isomer can not be completely excluded.

The ^{119}Sn Mössbauer spectra of tributyltin(IV) pyrrolidinone and tributyltin(IV) triflate and their mixture with different molar ratios are shown in Fig. 3. The Mössbauer spectra of tributyltin pyrrolidinone and that of stannyl triflate were decomposed into doublets with quadrupole splitting 2.10 mm/s and 4.84 mm/s, respectively, while all other spectra were evaluated as a superposition of 4 doublets. The isomer shift of all subspectra ($\delta = 1.36$–1.71 mm/s) reflects solely Sn^{IV} in these compounds. The relative occurrence of the components changes gradually with

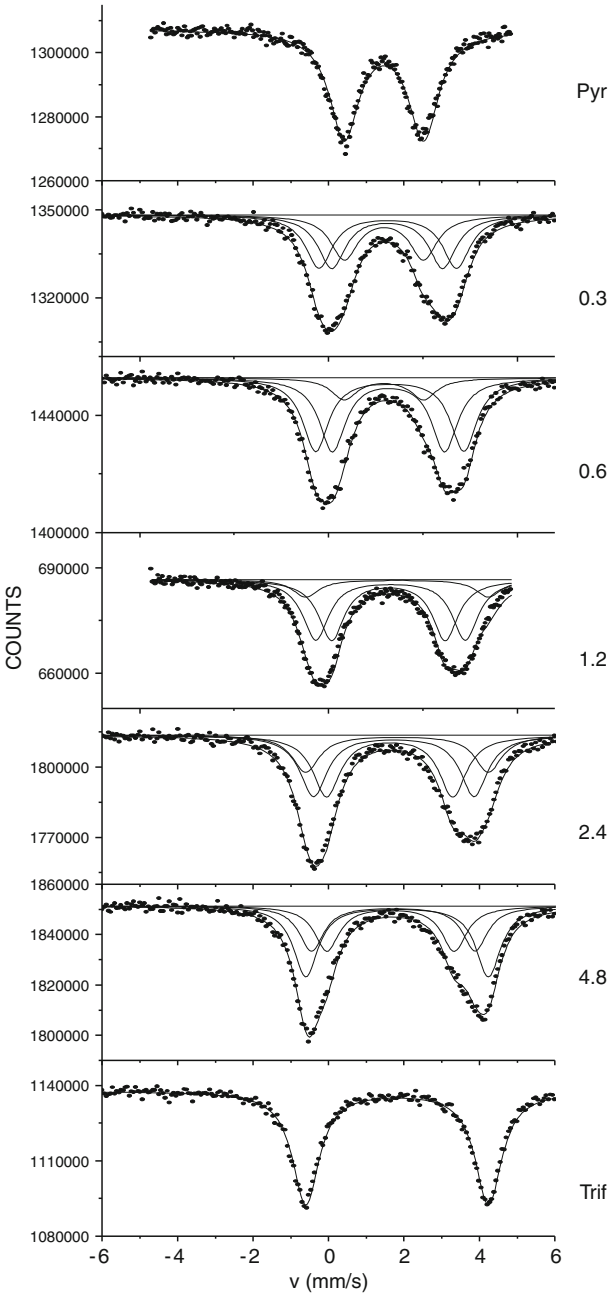

Fig. 3 78 K ^{119}Sn Mössbauer spectra of N-tributyltin 2-pyrrolidinone (Pyr) and tributyltin triflate (Trif) and their solutions with molar ratios (Trif/Pyr) indicated

increasing molar ratio of the tributyltin triflate component in the solution, however, the relative spectral areas do not correspond well to the estimated equilibrium values taking into consideration usual relative f-factors for the components. Furthermore, the isomer shift and quadrupole splitting values of the doublets tentatively attributed

to the new Sn-microenvironments expected to form in the mixture varied gradually with increasing ratio of the tin triflate.

4 Conclusions

Comparing the carbon NMR and tin Mössbauer results, one can conclude that each of the two new doublets in the Mössbauer spectra represents the Mössbauer signal of tributylstannylated pyrrolidinone in the distannylated cationic form. One doublet is assigned to the O-stannyl moiety, the other one to the N-stannyl moiety.

Taking into consideration the Mössbauer spectra of tributylstannylated pyrrolidinone (N-stannylate) and tributyltin triflate (O-stannylate), the quadrupole doublet with lower quadrupole splitting ($\Delta = 2.94$–3.38 mm/s) can be tentatively assigned to the N-stannyl form and the other doublet ($\Delta = 3.65$–4.34 mm/s) to the O-stannyl form.

The shifting of the parameters of these doublets with increasing ratio of tributyltin triflate may be due to the presence of O-tributylstannylated pyrrolidinone (according to the mechanism shown in Fig. 2) which could not be resolved in the Mössbauer spectra and the amount of which obviously depends on the amount of tributyltin triflate.

Acknowledgements The research was supported by grants of the Hungarian Science Foundation (OTKA K68135, K100424 and NN84307).

References

1. Kárpáti, Sz., Szalay, R., Császár, A.G., Süvegh, K., Nagy, S.: J. Phys. Chem. **A111**, 13172–13181 (2007)
2. Milios, C.J., Stamatatos, T.C., Perlepes, S.P.: Polyhedron **25**, 134–194 (2006)
3. Boshra, R, Doshi, A., Venkatasubbaiah, K., Jäkle, F.: Inorg. Chim. Acta **364**, 162–166 (2010)
4. Perry, H., Zon, J., Law, J., Clearfield, A.: J. Solid State Chem. **183**, 1165–1173 (2010)
5. Klencsár, Z., Kuzmann, E., Vértes, A.: J. Radioanal. Nucl. Chem. **210**, 105 (1996)

Hyperfine Interact (2012) 205:13–16
DOI 10.1007/s10751-011-0473-7

Mössbauer study of iron nitride films produced by pulsed laser deposition

Ryo Usui · Yasuhiro Yamada · Yoshio Kobayashi

Published online: 18 November 2011

Abstract Iron nitride films were produced by pulsed laser deposition of Fe onto an Al substrate in an N_2 atmosphere and their Mössbauer spectra and powder X-ray diffraction patterns were measured. The nitrogen content of the iron nitride films varied depending on the N_2 pressure. Under high N_2 pressures, γ"-FeN (ZnS structure) and γ"'-FeN (NaCl structure) were obtained. The yields of these two phases could be controlled by varying the Al substrate temperature. γ"-FeN and γ"'-FeN were found to be paramagnetic and antiferromagnetic, respectively, at 5 K.

Keywords Iron nitride film · γ-FeN · Pulsed laser deposition · Mössbauer spectroscopy · XRD

1 Introduction

Pulsed laser deposition (PLD) is a useful technique for preparing multielement films and it has been applied in industry. The composition and morphology of films produced by PLD can be controlled by varying the experimental conditions such as the substrate temperature during deposition, the ambient gas pressure, the laser power, and the laser wavelength. We have produced iron oxide [1] and iron carbide [2, 3] films by PLD.

Iron nitride has many phases and each phase has different magnetic characteristics. Iron nitride films or particles have been prepared by various methods [4–9]. Iron nitrides with low nitrogen contents have been extensively studied, whereas iron nitrides with high nitrogen contents have not been well investigated. FeN has been

R. Usui (✉) · Y. Yamada
Tokyo University of Science, 1-3 Kagurazaka, Shinjuku, Tokyo 162-8601, Japan
e-mail: jb110629@ed.kagu.tus.ac.jp

Y. Kobayashi
RIKEN, 2-1 Hirosawa, Wako, Saitama 351-0198, Japan

reported to have two phases, γ"-FeN (ZnS structure) and γ"'-FeN (NaCl structure), which generally form simultaneously so that it is difficult to produce a single phase [4–8]. In this study, we report the production of iron nitride films using PLD. These films were investigated by Mössbauer spectroscopy and powder X-ray diffraction (XRD).

2 Experimental

PLD of Fe on Al substrate was performed using a Nd:YAG laser (wavelength: 532 nm, pulse energy: 85 mJ, repetition rate: 10 Hz) while varying the N_2 pressure and Al substrate temperature. A Fe metal sheet was employed as the target material. The focal point of the laser light was continually scanned across the flat surface of the Fe metal target to prevent droplets from forming. The vapor was deposited on an Al substrate and 1.1×10^5 pulses were applied for the irradiation. The pressure of the N_2 atmosphere was maintained at the desired pressure between 1 and 1300 Pa. The Al substrate was maintained at the desired temperature between 100 and 520 K. The film samples were measured by Mössbauer spectroscopy (WISSEL, MDU1200) at 5 and 300 K and XRD (RINT2500, Rigaku; Cu-Kα) patterns were measured to confirm the assignments.

3 Results and discussion

According to Mössbauer spectra and XRD results, various iron nitride films were produced. γ" and γ"'-FeN were dominant in the films produced at N_2 pressures higher than 70 Pa, whereas ε-Fe$_x$N was produced at low N_2 pressures (1.2 Pa). As surface reactions with N_2 gas and thermal reactions of the films are strongly influenced by the substrate temperature, we performed PLD at various substrate temperatures. Films were produced at an N_2 pressure of 70 Pa at various substrate temperatures between 100 and 520 K and Mössbauer spectra were measured at room temperature (Fig. 1). We fitted these spectra by a combination of two components: γ"-FeN (a singlet: S2) [4, 5] and γ"'-FeN (a combination of a singlet S1 and a doublet D1). The absorption of γ"-FeN was dominant at low substrate temperatures (100 K; Fig. 1a), whereas γ"'-FeN was dominant at high substrate temperatures (520 K, Fig. 1c). Table 1 summarizes the Mössbauer parameters.

Mössbauer spectra of the same samples were measured at 5 K (Fig. 2). The spectrum of the film produced at 100 K (Fig. 2a) exhibited a singlet of γ"-FeN as the major absorption, which is similar to the spectrum obtained at room temperature (Fig. 1a). The spectra of the films produced at 300 and 520 K showed two sets of sextets. Since the sextets had broad half widths, the spectra were fitted by assuming distributions of hyperfine magnetic fields. Their Mössbauer parameters agreed with parameters reported in previous studies [4, 5]. The film produced at 520 K (Fig. 2c) was considered to be pure γ"'-FeN. Comparison of the area intensities of the spectra observed at 300 and 5 K (Table 1) reveals that the doublet D1 corresponds to the component with H = 300 kOe and the singlet S1 corresponds to the component with H = 500 kOe. The origin of the two Fe sites is not known. However, it is clear that γ"'-FeN has a crystal structure with two Fe sites. XRD patterns of the

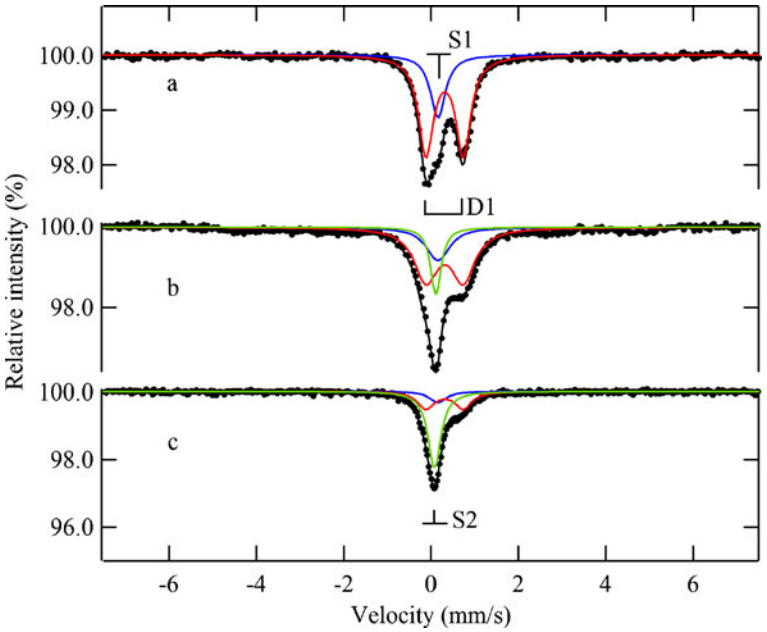

Fig. 1 Room-temperature Mössbauer spectra of films produced by PLD of Fe onto an Al substrate in 70 Pa N_2 for substrate temperatures during PLD of **a** 520, **b** 300, and **c** 100 K

Table 1 Mössbauer parameters of the films in Figs. 1 and 2

Sample	Substrate temp. while deposition (K)		Measured at 300 K			Measured at 5 K		
			δ (mm/s)	ΔEq (mm/s)	Yields (%)	δ (mm/s)	H* (kOe)	Yields (%)
a	520	D1	0.31	0.85	75.5	0.45	299	71.2
		S1	0.16	–	24.5	0.31	504	28.8
b	300	D1	0.31	0.85	61.3	0.45	306	54.6
		S1	0.16	–	20.1	0.32	509	22.5
		S2	0.11	–	18.6	0.22	–	22.9
c	100	D1	0.31	0.85	32.4	0.45	300	31.3
		S1	0.16	–	10.4	0.26	490	9.2
		S2	0.08	–	57.2	0.21	–	59.5

*Hyperfine magnetic field having the maximum population in the distribution

films were measured, and the intensity ratio of the peaks of γ"-FeN [6] and γ"'-FeN changed varying the Al substrate temperature, which were in good agreement with the Mössbauer results.

In previous studies, γ"-FeN and γ"'-FeN always formed simultaneously and no method for preparing a single phase of γ"-FeN or γ"'-FeN has been reported. However, in this study, the yields of the two phases could be varied and pure γ"-FeN and γ"'-FeN could be obtained by varying the substrate temperature during PLD. We are currently performing density functional calculations to help clarify the structure of γ"'-FeN.

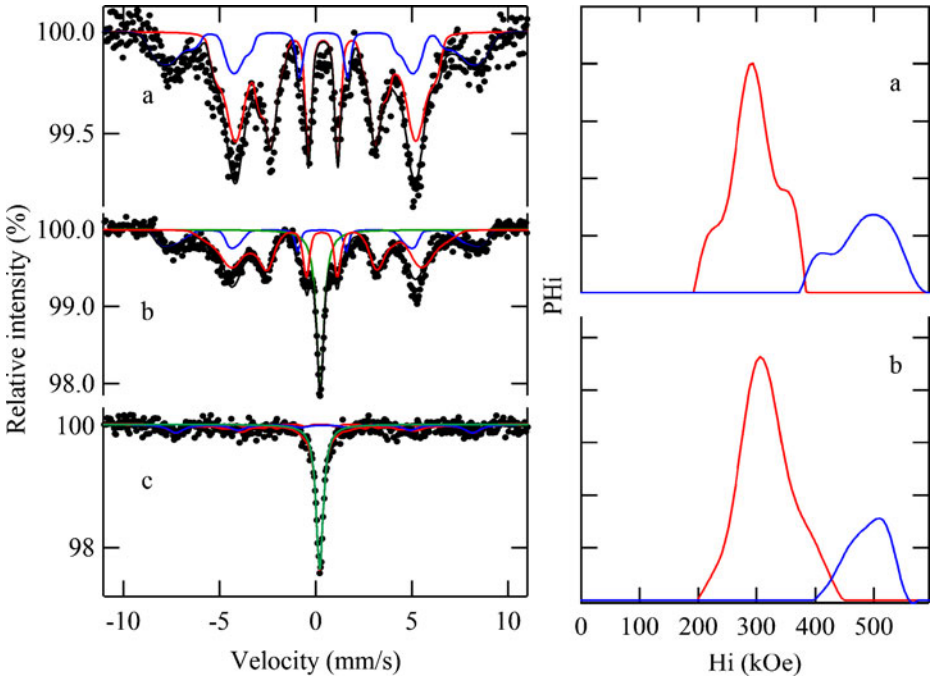

Fig. 2 Mössbauer spectra measured at 5 K of the films produced by PLD of Fe onto an Al substrate in 70 Pa N_2. Substrate temperatures during PLD were **a** 520, **b** 300, and **c** 100 K. The hyperfine magnetic field distributions are indicated on the right-hand side

4 Conclusion

PLD in N_2 ambient gas produced iron nitride films whose compositions could be controlled by varying the ambient N_2 gas pressure and the Al substrate temperature. Films produced at a high N_2 pressure (> 70 Pa) consisted of γ"-FeN and γ"'-FeN. The γ"-FeN and γ"'-FeN yields could be controlled by controlling the substrate temperature during deposition. Pure γ"-FeN and γ"'-FeN were obtained and their Mössbauer spectra and XRD patterns were observed.

References

1. Yokoyama, D., Namiki, K., Fukasawa, H., Miyazaki, J., Nomura, K., Yamada, Y.: J. Radioanal. Nucl. Chem. **272**, 631 (2007)
2. Yamada, Y., Yoshida, H., Kouno, K.: J. Phys.: Conf. Ser. **217**, 012096 (2010)
3. Yamada, Y., Yoshida, H., Kobayashi, Y.: Hyp. Int. **198**, 55 (2010)
4. Hinomura, T., Nasu, S.: Physica B **237–238**, 557–558 (1997)
5. Nakagawa, H., Nasu, S., Fujii, H., Takahashi, M., Kanamura, F.: Hyp. Int. **69**, 455–458 (1991)
6. Suzuki, K., Morita, H, Kaneko, T., Yoshida, H., Fujimori, H.: J. Alloys Compd. **201**, 11–16 (1993)
7. Schaaf, P., Illgner, C., Niederdrenk, M., Lieb, K.P.: Hyp. Int. **95**, 199–225 (1995)
8. Prieto, P., Macro, J.F., Sanz, J.M.: Surf. Interface Anal. **40**, 781–785 (2008)
9. Jirásková, Y., Hvlíek, S., Shneeweiss, O., Peřina, V., Blawert, C.: J. Magn. Magn. Mater. **234**, 477–488 (2001)

Hyperfine Interact (2012) 205:17–21
DOI 10.1007/s10751-011-0441-2

Mössbauer study of peroxynitrito complex formation with Fe^{III}-chelates

Zoltan Homonnay · Peter Buszlai · Judit Nádor · Virender K. Sharma · Erno Kuzmann · Attila Vértes

Published online: 1 November 2011

Abstract The reaction of the μ-oxo-diiron(III)-L complex (L = EDTA, ethylene diamine tetraacetate, HEDTA, hydroxyethyl ethylene diamine triacetate, and CyDTA, cyclohexane diamine tetraacetate) with peroxynitrite in alkaline solution was studied by Mössbauer spectroscopy using rapid-freezing technique. These complexes yield an $(L)Fe^{III}(\eta^2\text{-}O_2)^{3-}$ complex ion when they react with hydrogen peroxide and the formation of the peroxide adduct results in a deep purple coloration of the solution. The same color appears when the reaction occurs with peroxinitrite. Although spectrophotometry indicated some difference between the molar extinction coefficients of the peroxo and the peroxinitrito adducts, the Mössbauer parameters proved to be the same within experimental error. It is concluded that the peroxynitrite ion decomposes when reacting with $Fe^{III}(L)$ and the peroxo adduct forms.

Keywords Mössbauer spectroscopy · Iron chelates · Peroxo adduct · Frozen solution

1 Introduction

The reaction of the μ-oxo-diiron(III)-EDTA complex (EDTA = ethylene diamine tetraacetate) with H_2O_2 in alkaline solution has been studied earlier [1] by Mössbauer spectroscopy through rapid-freezing of the reaction medium in order to identify possible intermediate species during the formation and decomposition of the purple $(EDTA)Fe^{III}(\eta^2\text{-}O_2)^{3-}$ complex ion (Fig. 1).

Z. Homonnay (✉) · P. Buszlai · J. Nádor · E. Kuzmann · A. Vértes
Institute of Chemistry, Eötvös University, Budapest, Hungary
e-mail: homonnay@ludens.elte.hu

V. K. Sharma
Florida Institute of Technology, Melbourne, FL, USA

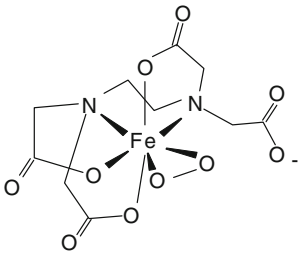

Fig. 1 Schematic structure of the (EDTA)$Fe^{III}(\eta^2\text{–}O_2)^{3-}$ complex ion.

This reaction has significance in environmental chemistry because photochemically formed peroxide in natural waters may be activated by this process and this facilitates decomposition of organic pollutants.

Nitrate is also an important industrial pollutant, and can interfere this reaction by forming peroxynitrite:

$$NO_3^- \xrightarrow{h\nu} ONOO^-$$

It is observed that when the dimer

$[(EDTA)Fe^{III}\text{–}O\text{–}Fe^{III}(EDTA)]^{4-}$ (which is stable at high pH) is reacted with peroxynitrite, the same color appears as that found in the reaction with hydrogen peroxide. It was observed that the UV-visible spectrum of this reaction product is the same as that of the *dihapto*-peroxo complex $[(EDTA)Fe^{III}(\eta^2\text{-}O_2)]^{3-}$, while the molar extinction coefficients significantly differ [2].

We have measured the Mössbauer spectra of the assumed peroxynitrito complexes in order to characterize them and to get information on their structure. In addition to EDTA, HEDTA, hydroxyethyl ethylene diamine triacetate, and CyDTA, cyclohexane diamine tetraacetate were also studied.

2 Experimental

Mössbauer Spectroscopy experiments were carried out in frozen solutions after mixing the solution of the $Fe^{III}(L)$ complex with peroxynitrite. The cooling rate was higher than 50 K/s which preserves the structure of the complexes [3]. The stock solution of peroxynitrite was purchased from Cayman Chemicals, and delievered in 0.3 M NaOH solution (required for its stability) with proper cooling. The maximum available concentration was 0.042 M and this set a limit of the maximum iron concentration (in the form of ^{57}Fe) used in the Mössbauer measurements. Peroxynitrite was applied in 3-fold excess relative to Fe^{III}. The final pH was set by the initial pH of the $Fe^{III}(L)$ solution.

The Mössbauer spectra were recorded in constant acceleration mode using a Ranger spectrometer with a $^{57}Co(Rh)$ source of about 10^9 Bq activity. The samples were kept frozen at 80 K in a tank type liquid nitrogen cryostat. The spectrum analyses were performed with help of the Mosswinn code. All isomer shifts are given relative to alpha iron at room temperature.

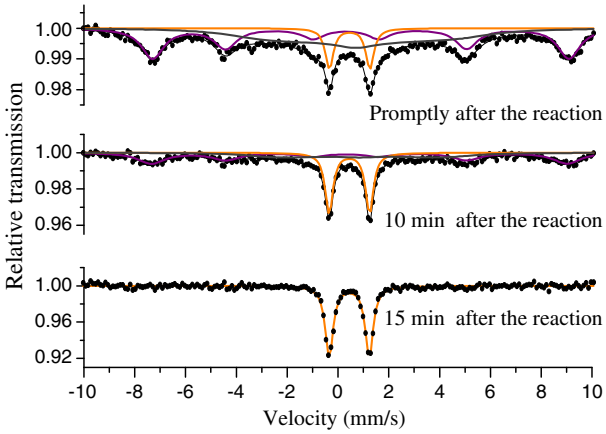

Fig. 2 Mössbauer spectra of the Fe^{III}-EDTA-peroxynitrite system at pH = 11

3 Results and discussion

As an example, selected Mössbauer spectra of the Fe—EDTA—peroxynitrite system can be seen in Fig. 2. The first spectrum was recorded right after mixing the Fe^{III}(L) solution with peroxynitrite, and then the frozen sample was let melt and, depending on how fast the purple color began to fade away, it was rapidly frozen again. The aim of this process was to identify intermediate iron species as many as possible during the decomposition of the purple species. These details will be published elsewhere.

Here we concentrate on the first major sextet observed in the spectra, which is a signature of the peroxo adduct. This assignment was also proved by the parallel disappearance of the color of the reaction mixture and the sextet from the Mössbauer spectra. The final stage of the reactions is always the formation of the [(L)Fe^{III}–O–Fe^{III}(L)] type dimer with very characteristic Mössbauer parameters (a doublet with $\delta = 0.45$ mm/s, $\Delta = 1.59$ mm/s).

Let us note that magnetic splitting of the monomeric [(L)Fe^{III}(η^2–O_2)] species is of paramagnetic spin relaxation origin and therefore it always appears with rather broad lines. In addition to this sextet, a relaxational component also shows up in most of the spectra which may be assigned to a so far unidentified intermediate species or simply due to random distance of the paramagnetic Fe^{III} species in the frozen solution resulting in variable relaxation distortion of the sextets. However, at least a significant part of the Fe^{III} species has relaxation slow enough to give rise to a well developed sextet, and this gives chance to determine the key parameters of this species. It is also noteworthy that monomeric species other than the peroxo adduct shows up only in the CyDTA system.

The well reproduced doublet of [(L)Fe^{III}–O–Fe^{III}(L)] is a result of fast relaxation due to the close proximity of the Fe^{III} centers in the dimeric structure.

Table 1 shows the Mössbauer parameters of the purple species formed with peroxynitrite in comparison with those obtained in reaction with hydrogen peroxide.

It can be seen that the isomer shifts are very close to each other disregarding the type of the chelating ligand or the choice of hydrogen peroxide *vs*. peroxynitrite. The value is somewhat lower in the case of CyDTA with peroxynitrite but it is still within experimental error. The same is true for the quadrupole shifts even if here the differences are larger.

Table 1 Mössbauer parameters of the assumed [(L)$Fe^{III}(ONO_2)$] species in comparison with those of [(L)$Fe^{III}(\eta^2—O_2)$], L = EDTA, HEDTA and CyDTA

	Peroxynitrite experiment			Hydrogen peroxide experiment		
	δ(mm/s)±0.02	εQ(mm/s)±0.15	B(T)±0.5	δ(mm/s)±0.03	εQ(mm/s)±0.18	B(T)±0.5
EDTA	0.60	+0.54	51.0	0.62[1]	+0.53[1]	51.5[1]
HEDTA	0.63	+0.55	50.8	0.54[5]	+0.87[5]	50.5[5]
CyDTA	0.60	+0.71	50.7	0.61[4]	+0.80[4]	50.2[4]

The hyperfine magnetic fields can also be considered identical.

There are two possible scenarios to explain this. Peroxynitrite has a peroxo moiety which may behave like peroxide and gets bound to the iron center via side-on configuration (dihapto binding). In this case it is difficult to judge to what extent the presence of NO group on the OO unit would change the isomer shift and the quadrupole shift compared to the peroxo adduct but, very likely, the effect would be larger than the experimental error.

On the other hand, it is also possible that peroxynitrite decomposes into NO and H_2O_2 as follows: $2HONOO+2H_2O \rightarrow 3H_2O_2+2NO$. This can provide conditions to the regular reaction between hydrogen peroxide and Fe^{III}(L). Here the question arises wether the limited amount of hydrogen peroxide that forms from decomposing peroxynitrite is enough to form the purple species? As can be seen from the equation of the chemical reaction, the applied 3-fold excess peroxynitrite provides 4.5-fold excess H_2O_2 if the decomposition is complete. Since in the hydrogen peroxide experiments we used 30-fold excess or even more, we ran an experiment with an amount of H_2O_2 stoichiometrically just equivalent with peroxynitrite. The purple species readily formed and the Mössbauer parameters were well reproduced.

4 Conclusion

We can now conclude that when peroxynitrite reacts with Fe^{III}(L) where L = EDTA, HEDTA or CyDTA, at high pH, the dihapto peroxo complex [(L)$Fe^{III}(\eta^2–O_2)$] readily forms. This assumes that peroxynitrite decomposes just before the reaction. This pre-decomposition may be initiated by the sudden drop of the pH from over 13 to about 10.5 to 11.

It is also possible that peroxynitrite gets bound to the iron center through its OO moiety which is followed by fast release of NO by a possibly multistep mechanism.

Acknowledgements This research was supported by the Hungarian National Research Fund (OTKA, grant number 67835) and Center of Ferrate Excellence, Florida Institute of Technology, USA.

References

1. Sharma, V.K., Szilágyi, P.A., Homonnay, Z., Kuzmann, E., Vértes, A.: Eur. J. Inorg. Chem. **2005**, 4393–4400 (2005)
2. Sharma, V.K., Yngard, R.A., Homonnay, Z., Dey, A., He, C.: Aquat. Geochem. **16**, 483–490 (2010)

3. Vértes, A., Nagy, D. L. : Mössbauer spectroscopy of frozen solutions.—Akadémiai Kiadó, Budapest, (1990)
4. Brausam, A., Maigut, J., Meier, R., Szilágyi, P.Á., Buschmann, H.-J., Massa, W., Homonnay, Z., van Eldik, R.: Inorg. Chem. **48**, 7864–7884 (2009)
5. Master Theses, Nóra Csuvár, Eötvös Loránd University (2009)

Hyperfine Interact (2012) 205:23–26
DOI 10.1007/s10751-011-0498-y

Orientation of hyperfine magnetic fields of α-iron films produced by laser deposition

Mamoru Yasuike · Ryo Usui · Yasuhiro Yamada · Yoshio Kobayashi

Published online: 7 December 2011

Abstract Iron films were produced by pulsed laser deposition (PLD) of iron in Ar gas and Mössbauer spectra of these films were obtained at room temperature. The orientation of the hyperfine magnetic field was found to vary depending on the pressure of the Ar gas. Iron films produced at low Ar pressures exhibited magnetic fields parallel to the substrate surface. The magnetic field became increasingly perpendicular to the substrate with increasing Ar pressure. Collisions with Ar gas molecules reduced the translational energies of laser-evaporated iron atoms and thus the orientation of crystals formed on the substrate varied depending on the Ar pressure.

Keywords Iron films · Pulsed laser deposition · Magnetic field orientation · Ar ambient gas

1 Introduction

The magnetic properties of thin films have been extensively studied, especially the magnetic field orientation dependence on the thin film shape. Mössbauer spectroscopy is a very useful technique for investigating magnetic properties and for determining the orientation of magnetic fields of iron-based materials. The intensity ratio ($I_{2,5}/I_{3,4}$) of sextet absorption in Mössbauer spectra varies depending on the angle between a γ-ray and the nuclear spin.

$$\frac{I_{2,5}}{I_{3,4}} = \frac{4\sin^2\theta}{1+\cos^2\theta}$$

M. Yasuike (✉) · R. Usui · Y. Yamada
Tokyo University of Science, 1-3 Kagurazaka, Shinjuku, Tokyo 162-8601, Japan
e-mail: yyasu@rs.kagu.tus.ac.jp

Y. Kobayashi
RIKEN, 2-1 Hirosawa, Wako, Saitama 351-0198, Japan

We have previously reported that the orientation of magnetic fields of iron films can be controlled by employing different deposition methods. Pulsed laser deposition (PLD) of Fe in a vacuum produces an iron film with a magnetic field parallel to the substrate surface [1], while deposition of Fe vaporized by resistive heating produces a film with a magnetic field perpendicular to the substrate surface [2]. Deposition of Fe atoms or ions vaporized by an arc plasma gun produces a film with a magnetic field aligned with the grooves on the substrate [3]. The magnetic field orientation is strongly influenced by the Fe vapor density and the translational energy; Fe vapors produced by laser evaporation have energies higher than 100 eV, Fe atoms vaporized by resistive heating have energies of several eV, and Fe atoms vaporized by an arc plasma gun have energies lower than 100 eV. We have previously reported PLD in ambient gases (O_2, N_2, and C_2H_2) to produce films of iron-based compounds (oxides, nitrides, and carbides) [4, 5]. In this study, we produced films on Al substrates by PLD of Fe in an Ar atmosphere while controlling the energy of the Fe atoms.

2 Experimental

A block of Fe metal in a vessel filled with Ar gas was laser evaporated using a Nd:YAG laser (NewWave, Tempest 10; wavelength: 523 nm; pulse energy: 85 mJ; repetition rate: 10 Hz). The Ar pressure was maintained at the target pressure between 10^{-7} and 20 Torr using a pressure controller. An Al substrate (thickness: 40 μm) was placed 10 mm from the Fe target. The film thickness was estimated by measuring the difference between the masses of the substrate before and after PLD. Mössbauer spectra of the Fe films were obtained at room temperature and their surface morphologies were observed by scanning electron microscopy (SEM).

3 Results and discussion

Fe films were produced by PLD on Al substrates for various Ar pressures in the range 10^{-7} to 10 Torr and their Mössbauer spectra were measured at room temperature (Fig. 1). The films were less than 1 μm thick. The film produced at the lowest Ar pressure (10^{-7} Torr) exhibited sextet absorption with an area intensity ratio $I_{2,5}/I_{3,4}$ of 3.5/1, indicating that the magnetic field was almost parallel to the substrate surface; the mean angle between the magnetic field and the Mössbauer γ-rays (perpendicular to the substrate) was calculated to be 75°. The intensity ratio $I_{2,5}/I_{3,4}$ decreased with increasing Ar pressure. The angles between the magnetic field and the Mössbauer γ-rays were calculated to be 60°, 49°, 39°, 34°, and 28° for the films produced at 0.1, 0.5, 1, 3, and 10 Torr Ar pressures, respectively. This indicates that the magnetic field tends to become increasingly perpendicular to the substrate surface with increasing Ar pressure. Collisions of Fe atoms with Ar gas molecules reduce the translational energies of the laser-evaporated Fe atoms. When the Fe atoms have high energies, the Fe atoms migrate on the film surface to form α-Fe crystals parallel to the surface. In contrast, Fe atoms with low energies do not migrate on the surface, so that α-Fe crystals grow perpendicular to the surface plane. Consequently, the orientation of the magnetic field of an α-Fe film can be controlled by the Ar pressure.

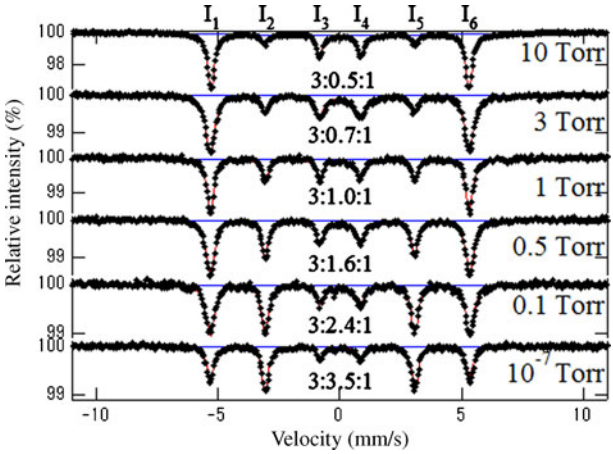

Fig. 1 Mössbauer spectra of α-iron thin films produced by PLD in Ar atmosphere at room temperature. The Ar pressure during PLD and the area intensity ratio $I_{1,6}$:$I_{2,5}$:$I_{3,4}$ are indicated in the figure

The surface morphology of the films was observed by SEM (Fig. 2). The film produced at an Ar pressure of 10^{-7} Torr had a smooth surface (Fig. 2a), whereas the film produced at an Ar pressure of 20 Torr had a rough surface (Fig. 2b). In addition, the cross section of the film produced at 20 Torr was observed through a crack (Fig. 2c). It shows column-shaped crystals aligned perpendicular to the substrate surface, indicating that the crystals mainly grew perpendicular to the surface. This finding is consistent with the Mössbauer spectroscopy results and thus the shape anisotropy of the α-Fe crystal is considered to be the origin of the magnetic orientation.

To estimate the energy of Fe atoms on the substrate, we performed Monte Carlo calculations [6] assuming a low-density Fe vapor. However, the calculation underestimated the Fe atom energy and the calculated energy was almost the same as that above 0.5 Torr, which does not agree with the present experimental results. Therefore, we recalculated using simple thermal equilibrium assuming a high-density Fe vapor; high-temperature Fe vapors and room-temperature Ar gas were mixed and reached the equilibrium temperature in a plume produced by a laser shot. The equilibrium temperature T_{eq} is calculated using

$$T_{eq} = \frac{T_{iniFe} M_{Fe} C_{V_{Fe}} + T_{iniAr} M_{Ar} C_{V_{Ar}}}{M_{Fe} C_{V_{Fe}} + M_{Ar} C_{V_{Ar}}},$$

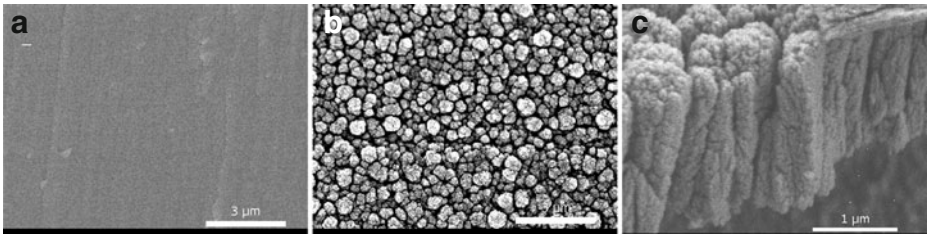

Fig. 2 SEM image of the films produced at Ar pressures of (**a**) 10^{-7} and (**b**) 20 Torr and (**c**) the cross section of a film produced at 20 Torr

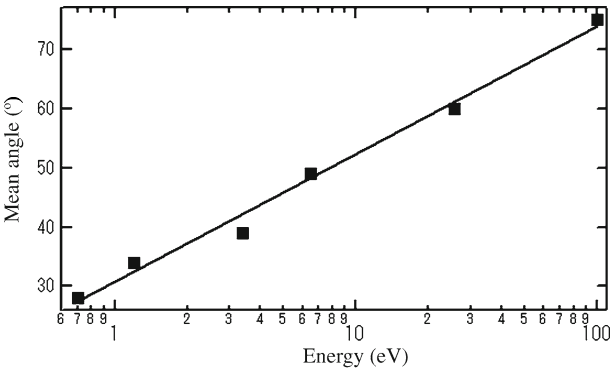

Fig. 3 Single logarithmic plot of the mean angle at each pressure and the energy of Fe atoms calculated by assuming thermal equilibrium

where M_{Ar} and M_{Fe} are respectively the amounts of Fe vapor and Ar gas in the plume, C_{VAr} andC_{VFe} are respectively the specific heats at constant volume of Ar and Fe, and T_{iniAr} andT_{iniFe} are respectively the initial temperatures of the Fe vapor and Ar gas (293 K). Assuming that the Fe atoms have an initial energy of 100 eV, the Fe atoms were estimated to have an energy in the range 0.7 and 100 eV. Figure 3 shows the correlation between the estimated energy of the Fe atoms and the angle of the hyperfine magnetic field. It shows that the magnetic field orientation at each pressure is correlated with the energy.

4 Conclusion

The orientation of hyperfine magnetic field of α-Fe films could be controlled by PLD in an Ar atmosphere. Mössbauer spectra and SEM images indicated that the orientation of magnetic fields was governed by the magnetic shape anisotropy. At high Ar pressures, the Fe atoms had low energies and the hyperfine magnetic fields of the α-Fe films were perpendicular to the substrate surface. At lower Ar pressures, the hyperfine magnetic field of the α-Fe films was parallel to the substrate surface.

References

1. Yamada Y., Namiki K.: Chem. Lett. **36**, 294–295 (2007)
2. Yokoyama D., Namiki K., Yamada Y.: J. Radioanal. Nucl. Chem. **268**, 283–288 (2006)
3. Yamada Y., Kato H., Kouno K., Yoshida H., Kobayashi Y.: Hyper. Inter. **191**, 121–127 (2009)
4. Yokoyama D., Namiki K., Fukasawa H., Miyazaki J., Nomura K., Yamada Y.: J. Radioanal. Nucl. Chem. **272**, 631–638 (2007)
5. Yamada Y., Yoshida H., Kouno K.: J. Phys.: Conf. Ser. **217**, 012096 (2010)
6. Motohiro T., Taga Y.: Thin Solid Films **112**, 161–173 (1984)

Hyperfine Interact (2012) 205:27–30
DOI 10.1007/s10751-012-0562-2

Crystal structure and spin state of mixed-crystals of iron with zinc and cobalt for the assembled complexes bridged by 1,3-bis(4-pyridyl)propanes

Haruka Dote · Satoru Nakashima

Published online: 17 January 2012

Abstract Mixed crystals of cobalt and zinc were synthesized using 1,3–bis(4–pyridyl)propane (bpp) as bridging ligand and NCS^- as anion. Red crystals and blue crystals were obtained. Powder X-ray diffraction patterns showed that the former is in 2D interpenetrated structure, while the latter has the same structure with $Zn(NCS)_2$(bpp). Iron ion was introduced both into the red crystals and blue crystals of the mixed crystals of cobalt with zinc. ^{57}Fe Mössbauer spectrum of the red crystals showed a main doublet of Fe^{II} high-spin state at 78 K, while the spectrum of blue crystals did not show Fe^{II} high-spin state at 78 K.

Keywords Assembled complexes · Mixed crystals · Mössbauer spectroscopy · Spin state

1 Introduction

Self-assembled coordination polymers containing transition metal ions and organic bridging ligands have attracted intensive interests because of their potential abilities for selective inclusion and transformation of ions and molecules [1]. It is possible to construct various structures for porous assembled iron complexes bridged by bis(4–pyridyl) type ligand. We have studied iron complexes bridged by 1,2–bis(4–pyridyl)ethane (bpa), and revealed the relation between the *anti*/*gauche* conformer for coordinated bpa and the assembled structure, and the relation between the

H. Dote
Graduate School of Science, Hiroshima University, Kagamiyama, Higashi-Hiroshima, 739–8526, Japan

S. Nakashima (✉)
Natural Science Center for Basic Research and Development, Hiroshima University, Kagamiyama, Higashi-Hiroshima, 739–8526, Japan
e-mail: snaka@hiroshima-u.ac.jp

guest molecule and the spin state of iron [2–5]. We have also studied the magnetic behaviors and structural properties for some assembled complexes with more flexible ligand, 1,3–bis(4–pyridyl)propane (bpp), which has three methylenes, by using single–crystal X–ray diffraction analysis, Mössbauer spectroscopy, and SQUID measurements [6, 7]. $Fe(NCX)_2(bpp)_2$ (X = S, Se, and BH_3) had a 2D interpenetrated structure and the $NCBH_3$ complex showed a spin–crossover phenomenon. We also synthesized $Fe(NCX)_2(bpp)_2{\cdot}2(benzene)$ (X = S, Se, and BH_3). They had a 1D structure and were in temperature-independent Fe^{II} high-spin state. Both 2D interpenetrated and 1D structures were converted to each other by desorption and adsorption of benzene molecules [7]. Recently, we discussed the spin state of the mixed crystals with zinc or cobalt ion both in the 2D interpenetrated and 1D structures for the assembled complexes bridged by bpp [8]. In the present study, we discussed the structure of the mixed crystals of zinc and cobalt ions for the assembled complexes bridged by bpp, and then we discussed the spin state of the mixed crystals of iron ion with zinc and cobalt ions for the assembled complexes bridged by bpp.

2 Experimental

Mixed crystals were obtained by diffusion method. Bottom layer; metals, NCS^-, and ascorbic acid in H_2O. Middle layer; H_2O and cyclohexane. Upper layer; bpp in EtOH and cyclohexane. Found for Zn complex: C, 47.28; H, 3.89; N, 14.90; S, 16.98%. Calcd for $Zn(NCS)_2bpp$: C, 47.43; H, 3.72; N, 14.75; S, 16.89%. Found for red crystals of $Fe_{0.14}Zn_{0.17}Co_{0.69}(NCS)_2bpp_2$: C, 58.78; H, 4.66; N, 14.74; S,11.19%. Calcd for $Fe_{0.14}Zn_{0.17}Co_{0.69}(NCS)_2bpp_2$: C, 58.76; H, 4.93; N, 14.69; S, 11.21%. Found for blue crystals of $Fe_{0.20}Zn_{0.63}Co_{0.17}(NCS)_2bpp$: C, 45.18; H, 3.45; N, 16.06; S, 17.43%. Calcd for $Fe_{0.20}Zn_{0.63}Co_{0.17}$ $(NCS)_2bpp$: C, 47.80; H, 3.75; N, 14.87; S, 17.02%. The relative contents of metals were determined by ICP-OES.

A $^{57}Co(Rh)$ source in a constant acceleration mode was used for ^{57}Fe Mössbauer spectroscopic measurements. ^{57}Fe Mössbauer spectra were measured at 78 K by using a Wissel Mössbauer spectrometer and a proportional counter. The isomer shift was referred to metallic iron foil. The Mössbauer parameters were obtained by a least-squares fitting to Lorentzian peaks.

3 Results and discussions

3.1 Mixed crystals of zinc and cobalt complexes

Zinc and cobalt ions were mixed in the synthetic process. From the solution, red crystals and blue crystals were obtained. The relative contents of metals were determined by ICP-OES, which revealed that red crystals have relatively larger cobalt content, while blue crystals have larger zinc content. Powder X-ray diffraction patterns (Fig. 1) showed that the red crystals are in the 2D interpenetrated structure like $Fe(NCS)_2bpp_2$ [6]. The patterns for red crystals and $Fe(NCS)_2bpp_2$ revealed a preferred orientation. On the other hand, the structure of blue crystals is similar to that of $Zn(NCS)_2bpp$. Although the structure of $Zn(NCS)_2bpp$ is unknown, there are two possibilities from the results of elemental analysis and powder X-ray diffraction

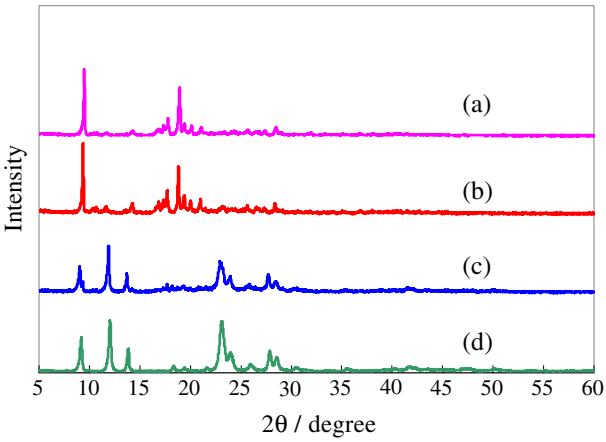

Fig. 1 Powder X-ray diffraction patterns of **a** $Fe(NCS)_2bpp_2$, **b** $Zn_{0.29}Co_{0.71}(NCS)_2bpp_2$ (*red crystals*), **c** $Zn_{0.89}Co_{0.11}(NCS)_2bpp$ (*blue crystals*), and **d** $Zn(NCS)_2bpp$

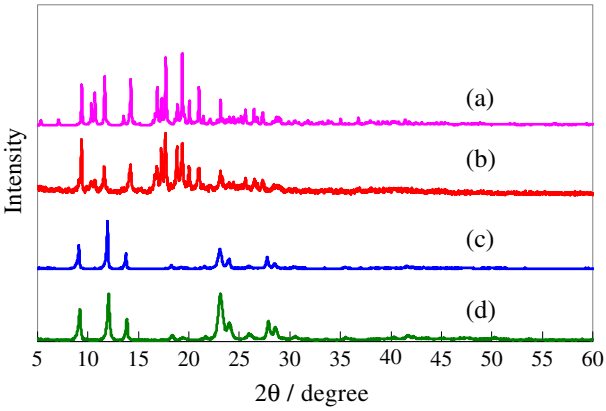

Fig. 2 Powder X-ray diffraction patterns of **a** $Fe(NCS)_2bpp_2$ (simulation), **b** $Fe_{0.14}Zn_{0.17}Co_{0.69}(NCS)_2bpp_2$ (*red crystals*), **c** $Fe_{0.20}Zn_{0.63}Co_{0.17}(NCS)_2bpp$ (*blue crystals*), and **d** $Zn(NCS)_2bpp$

patterns (Fig. 1). One is tetrahedral coordination around metals, and the other is octahedral coordination around metals whose NCS^- is used as bridging ligand.

3.2 Iron in mixed crystals of zinc and cobalt complexes

Iron, zinc, and cobalt ions were mixed in the synthetic process. From the solution, red crystals and blue crystals were obtained. Elemental analysis showed that red crystals have two bpp in their molecule, while blue crystals have one bpp in their molecule. Powder X-ray diffraction patterns (Fig. 2) showed that the red crystals are in the 2D interpenetrated structure like $Fe(NCS)_2bpp_2$ [6]. The pattern of red crystals did not reveal a preferred orientation. Therefore, the pattern is compared with a simulation pattern of $Fe(NCS)_2bpp_2$ from a result of single-crystal X-ray diffraction analysis. On the other hand, the structure of blue crystals is similar to that of $Zn(NCS)_2bpp$. In this case also, the structure of $Zn(NCS)_2bpp$ is unknown, and there are two possibilities of tetrahedral coordination around metals and octahedral coordination around metals whose NCS^- is used as bridging ligand. ICP-OES revealed that red

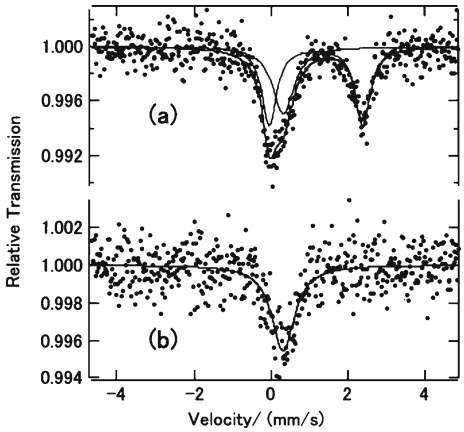

Fig. 3 ^{57}Fe Mössbauer spectra at 78 K of **a** $Fe_{0.14}Zn_{0.17}Co_{0.69}(NCS)_2bpp_2$ (*red crystals*) and **b** $Fe_{0.20}Zn_{0.63}Co_{0.17}(NCS)_2bpp$ (*blue crystals*)

crystals have larger cobalt content, while blue crystals have larger zinc content. And ICP-OES also revealed that the content of iron is relatively low both in red and blue crystals.

Figure 3 shows the ^{57}Fe Mössbauer spectrum of the red crystals of $Fe_{0.14}Zn_{0.17}Co_{0.69}(NCS)_2bpp_2$ at 78 K and the ^{57}Fe Mössbauer spectrum of the blue crystals of $Fe_{0.20}Zn_{0.63}Co_{0.17}(NCS)_2bpp$ at 78 K. There are two components in the spectrum of red crystals. Main component (IS = 1.16 mm/s, QS = 2.43 mm/s) is Fe^{II} high-spin state and minor component is singlet (IS = 0.31 mm/s). On the other hand, Fe^{II} high-spin state is not observed for blue crystals. Instead of Fe^{II} high-spin doublet, singlet (IS = 0.23 mm/s) is observed, which has a similar parameter with the minor component in the red crystals.

4 Conclusion

Different colored complexes were obtained by using zinc and cobalt ions (and iron ion) with NCS^- and bpp. It was shown from powder X-ray diffraction patterns that blue complexes have the same structure with pure zinc complex, while red crystals are in the 2D interpenetrated structure. The difference in structure affected the spin state of iron ion in the mixed crystals with zinc and cobalt.

References

1. Moulton, B., Zaworotko, M.J.: Chem. Rev. **101**, 1629 (2001)
2. Nakashima, S., Morita, T., Yamada, K., Inoue, K.: Hyperfine Interact. **166**, 469 (2005)
3. Morita, T., Asada, Y., Okuda, T., Nakashima, S.: Bull. Chem. Soc. Jpn. **79**, 738 (2006)
4. Morita, T., Nakashima, S., Yamada, K., Inoue, K.: Chem. Lett. **35**, 1042 (2006)
5. Nakashima, S., Morita, T., Inoue, K.: Hyperfine Interact. **188**, 107 (2009)
6. Atsuchi, M., Higashikawa, H., Yoshida, Y., Nakashima, S., Inoue, K.: Chem. Lett. **36**, 1064 (2007)
7. Atsuchi, M., Inoue, K., Nakashima, S.: Inorg. Chim. Acta **370**, 82 (2011)
8. Nakashima, S., Dote, H., Atsuchi, M., Inoue, K.: J. Phys. **C217**, 012035 (2010)

Hyperfine Interact (2012) 205:31–35
DOI 10.1007/s10751-011-0452-z

Iron carbide nanoparticles produced by laser ablation in organic solvent

T. Matsue · Y. Yamada · Y. Kobayashi

Published online: 23 November 2011

Abstract Laser ablation of iron in an organic solvent (pentane, hexane, or decane) was performed using an air-tight cell to produce iron carbide nanoparticles. Mössbauer spectra of the nanoparticles were obtained at room temperature. They revealed that the nanoparticles consisted of two paramagnetic components and magnetic components. The two paramagnetic components were a high-spin Fe(II) species and an amorphous iron carbide containing a large amount of carbon. Whereas the magnetic components measured at room temperature exhibited superparamagnetism, those measured at low temperature were fitted by a combination of four sextets, which were assigned to Fe_7C_3. The Fe_7C_3 yield was higher in higher molecular weight solvents. Transmission electron microscopy (TEM) images of the samples showed that the nanoparticles were spherical with diameters in the range 10–100 nm.

Keywords Laser ablation in solvent · Iron carbide · Nanoparticles · Mössbauer spectroscopy · Transmission electron microscopy

1 Introduction

Iron carbides have been extensively investigated because of their various useful industrial applications. Whereas iron-based materials such as ferrite, austenite, martensite, and cementite (Fe_3C) are well understood, Hägg (Fe_5C_2) and Eckstrom–Adcock (Fe_7C_3) carbides, which are metastable iron carbides, are less well understood. Fe–C compounds have recently attracted renewed interest because Fe was

T. Matsue (✉) · Y. Yamada
Graduate School of Chemical Science and Technology,
Tokyo University of Science, Tokyo, Japan
e-mail: ta_matue@yahoo.co.jp

Y. Kobayashi
RIKEN, Tokyo, Japan

found to catalyze the synthesis of carbon nanotubes [1, 2]. Fe-C core–shell structured nanoparticles were also investigated [3, 4]. Fe_3C and Fe_7C_3 nanoparticles have been produced by CO_2 laser pyrolysis of a vapor mixture of $Fe(CO)_5$ and C_2H_4 [5]. Iron carbides with high carbon contents were synthesized by mechanical alloying of iron and graphite powders; Mössbauer measurements revealed that Fe_3C and Fe_7C_3 were produced [6].

Nanoparticles produced by laser ablation of a solid metal in a liquid are expected to exhibit unique physical and chemical properties due to size effects. Noble metal nanoparticles such as gold nanoparticles have been extensively investigated [7, 8]. Laser ablation of Cu metal in water produced a mixture of amorphous and crystalline Cu_4O_3 nanoparticles [9]. The conventional method for producing metal or metal compound nanoparticles is laser ablation of a metal in a solvent. In this study, we produced iron carbide nanoparticles by laser ablation of Fe metal in organic solvents.

Most experiments involving laser ablation in solvents employ open-air conditions in which the target material is placed at the bottom of a vial filled with a solvent and the surface of the solvent is in contact with air. When laser light is irradiated through the surface of the solvent to the Fe metal sample at the bottom of the glass vial, bubbles produced by laser ablation disturb the surface, destabilizing the focal point and causing iron oxide to be produced because of dissolved air in the solvent. Therefore, we designed an air-tight cell to perform laser ablation under stationary conditions in inert gas atmosphere and to prevent the nanoparticles from being oxidized. A convex lens was directly attached to the side of the cell contacting the liquid and Ar gas was used to fill the space at the top of the cell.

2 Experiment

100 mL of an organic solvent (hexane, pentane, or decane), which had been degassed prior to use, was placed in the cell and a metal iron sample was placed in it. Ar gas was used to fill the space above the liquid surface to prevent oxidation. Laser ablation was performed for 18 h using a Nd:YAG laser (Continuum, Surelite I-10; wavelength: 532 nm; pulse repetition rate: 10 Hz; pulse energy: 190 mJ). The laser light was introduced through the convex lens attached to the cell. The produced nanoparticles were collected after removing the solvent and they were analyzed by Mössbauer spectroscopy. Transmission electron microscopy (TEM) images were obtained (Hitachi, H-9500 operated at 200 kV) from a sample prepared by placing a drop containing nanoparticles onto a 200-mesh copper grid coated with a collodion film.

3 Results and discussion

Iron carbide nanoparticles were produced by laser ablation of a Fe metal block in an organic solvent (pentane, hexane, or decane) and their Mössbauer spectra were measured (Fig. 1). The Mössbauer spectrum of the nanoparticles produced in pentane measured at 293 K (Fig. 1a) had a paramagnetic doublet as the dominant absorption. The spectrum was fitted by two doublets and a broad absorption. One of the paramagnetic doublets (D1: $\delta = 0.35$ mm/s and $\Delta E\mathrm{q} = 0.96$ mm/s) was assigned to

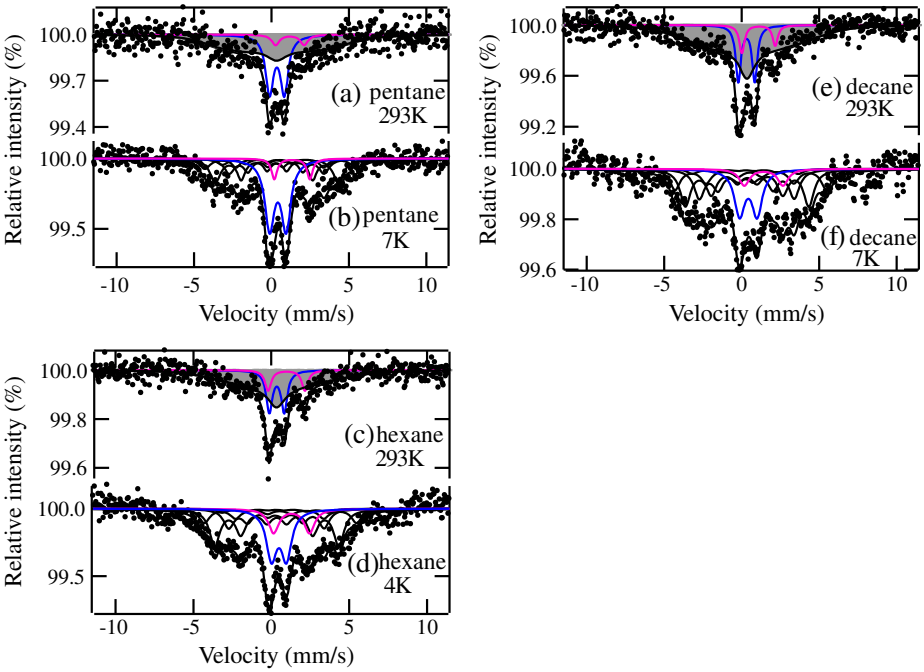

Fig. 1 Mossbauer spectra of nanoparticles produced (**a**) in pentane measured at 293 K, (**b**) in pentane measured at 7 K, (**c**) in hexane measured at 293 K, (**d**) in hexane measured at 4 K, (**e**) in decane measured at 293 K, and (**f**) in decane measured at 7 K

amorphous iron carbides containing a large amount of carbon. Species with similar Mössbauer parameters were also found in previous studies of laser deposition of iron carbides [10] and ball milling [6]. The other doublet (D2: $\delta = 1.19$ mm/s and $\Delta Eq = 1.84$ mm/s) was a high-spin Fe(II) species and has not been reported in other studies. This species has not been assigned yet; it may be an organometallic compound containing Fe^{II}–C chemical bonds. The broad absorption was attributed to a magnetic component exhibiting superparamagnetism, which was fitted by assuming it has a single relaxation time using Wickman's formula [11]. The same sample was measured at a low temperature of 7 K (Fig. 1b); the two paramagnetic doublets were almost the same in the spectra obtained at 7 and 293 K, whereas the magnetic components became sharper at the lower temperature. The absorption of the magnetic component was fitted assuming a distribution of hyperfine magnetic fields in the range of 100 to 310 kOe, and the distribution coincided with the combination of four sets of sextets of Fe_7C_3 [5]. Therefore, the absorption of the magnetic component was fitted by the combination of four sets of sextets, in which absorption peaks had relatively large half width because of the defects in Fe_7C_3. Iron oxides were not produced in the present study as we employed an air-tight cell. Similar experiments were performed using organic solvents of hexane (Figs. 1c and d) and decane (Figs. 1e and f). The obtained particles were almost independent of the solvent used. However, the yields of the species varied slightly with the solvent.

Table 1 Mössbauer parameters of nanoparticles produced in organic Solvents

Solvents		Measured at 293 K				Measured at low temperature (7 K, 4 K)		
		δ (mm/s)	ΔEq (mm/s)	τ (ns)	Yields (%)	δ (mm/s)	ΔEq (mm/s)	Yields (%)
Pentane	D1	0.35(2)	0.96(3)		34	0.41(2)	1.06(3)	34
	D2	1.19(9)	1.84(18)		6	1.33(3)	2.29(7)	6
	$Fe_7C_3^*$			7.8	60			60
Hexane	D1	0.34(4)	0.95(8)		22	0.41(2)	1.14(4)	22
	D2	0.98(23)	2.30(43)		11	1.16(5)	2.12(9)	11
	$Fe_7C_3^*$			4.2	67			67
Decane	D1	0.31(1)	1.06(2)		19	0.43(5)	1.13(8)	19
	D2	1.09(2)	2.15(5)		7	1.42(9)	2.50(20)	7
	$Fe_7C_3^*$			5.0	74			74

* Mössbauer parameters of Fe_3C_3 are fixed according to the literature [5]. site I: $\delta = 0.56$ mm/s, $\Delta Eq = 0.05$ mm/s, $H = 303$ kOe; site II: $\delta = 0.27$ mm/s, $\Delta Eq = -0.05$ mm/s, $H = 212$ kOe; site III: $\delta = 0.29$ mm/s, $\Delta Eq = 0.08$ mm/s, $H = 190$ kOe; site IV: $\delta = 0.35$ mm/s, $\Delta Eq = 0.00$ mm/s, $H = 247$ kOe

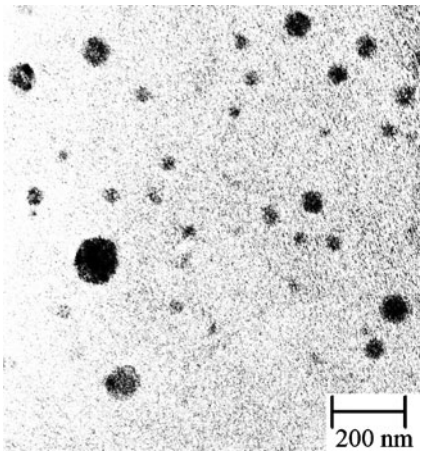

Fig. 2 TEM image of nanoparticles produced by laser ablation of Fe in decane

Nanoparticles produced in larger molecular weight solvents had higher Fe_7C_3 yields (Table 1). TEM images of the nanoparticles produced in the organic solvents were obtained. Figure 2 shows a TEM image of the nanoparticles produced in decane. Spherical nanoparticles were produced with diameters in the range 10–100 nm.

4 Conclusions

Iron carbide nanoparticles were produced by laser ablation in organic solvents in stationary condition in inert gas atmosphere using a newly designed cell. The products were assigned to amorphous iron carbides containing a large amount of

carbon: the high-spin Fe(II) species and metastable Fe_7C_3. Iron oxide was not found in the nanoparticles. The nanoparticles exhibited superparamagnetism at room temperature due to their small size (10–100 nm). A high-spin Fe(II) species was found that had not been reported in previous studies.

References

1. Pérez-Cabero, M., Taboada, J.B., Guerrero-Ruiz, A., Overweg A.R., Rodríguez-Ramos, I.: Phys. Chem. Chem. Phys. **8**, 1230 (2006)
2. de Resende, V., De Grave, E., Peigney A., Laurent, C.: J. Phys. Chem. C **112**, 5756 (2008)
3. Kopelev, N., Chechersky, V., Nath, A., Wang, Z.L., Kuzmann, E., Zhang, B., Via, G.H.: Chem. Mater. **7**, 1419–1421 (1995)
4. David, B., Pizúrová, N., Schneeweiss, O., Bezdička, P., Morjan, I., Alexandrescu, R.: J. Alloys Compd. **378**, 112–116 (2004)
5. Bi, X.-X., Ganguly, B., Huffman, G., Huggins F., Endo, M.: Mater J. Res. **8**, 1666 (1993)
6. Tanaka, T., Nasu, S., Ishihara, K.N., Shingu, P.H.: J. Less Common Met. **171**, 237 (1991)
7. Mafune, F., Kondow, T.: Chem. Phys. Lett. **372**, 199 (2003)
8. Tarasenko, N.V., Butsun, A.V., Nevar, E.A., Savastenko, N.A.: Appl. Surf. Sci. **252**, 4439 (2006)
9. Yeh, Y., Yeh, M., Lee, Y., Yeh, C.: Chem. Lett. **1998**, 1183 (1998)
10. Yamada, Y., Yoshida, H., Kouno, K.: J. Phys. Conf. Ser. **217**, 012096 (2010)
11. Wickman H.H., Wertheim, G.K.: In: Goldanski V.I., Herber, R.H. (eds.) Chemical applications of Mössbauer spectroscopy, chapter 11. Academic Press Inc., New York (1968)

Hyperfine Interact (2012) 205:37–40
DOI 10.1007/s10751-011-0459-5

Mössbauer spectra of Eu(III) and Gd(III) complexes of phosphine oxides with chelating perchlorate

Masashi Takahashi · Yuya Hirai

Published online: 22 November 2011

Abstract The reaction of $Ln(ClO_4)_3 \cdot nH_2O$ with triphenylphosphine oxide (TPPO) in methanol has led to the formation of $[Ln(ClO_4)_2(tppo)_4]ClO_4 \cdot MeOH$ (Ln = Nd, Eu, Gd, Dy, Yb), in which the perchlorate anion acts as a symmetric bidentate. The emission spectra of Eu(III)-TPPO complexes, showing enhancement in the intensity due to the phenyl group, indicate an isotropic electron distribution for the nitrato complex $[Eu(NO_3)_3(tppo)_2(EtOH)]$. ^{151}Eu and ^{155}Gd Mössbauer spectra of the TPPO complexes also lead to the same conclusion.

Keywords Lanthanide complex · Phosphine oxide · Perclorato complex · Emission spectra · Mössbauer spectra

1 Introduction

Phosphine oxides and organophosphates have been known as excellent synergistic coextractants for lanthanide and actinide ions. The coordination behavior of weakly coordinating anions is interesting in connection with the solvent extraction. Recently some actinide pertechnetato and perrehenato complexes have been obtained in the presence of phosphine oxides or organophosphate, an analogous condition to the PUREX process [1, 2]. Interestingly the coordination of triflate anion is also reported in the presence of phosphine oxide [3]. In this paper we have characterized the lanthanide perchlorato complexes carrying phosphine oxides using x-ray crystallography, emission spectra and ^{151}Eu and ^{155}Gd Mössbauer spectroscopy.

M. Takahashi (✉) · Y. Hirai
Toho University, Funabashi, Chiba 274-8510, Japan
e-mail: takahasi@chem.sci.toho-u.ac.jp

2 Experimental

2.1 Preparation

$Ln(ClO_4)_3(tppo)_4MeOH$ $Ln(ClO_4)_3 \cdot nH_2O$ (0.125 mmol) and TPPO (triphenylphosphine oxide; 139 mg, 0.500 mmol) were stirred in methanol (30 mL) for 1 h at room temperature. Ethanol (5 mL) was added and the solution was concentrated gently to yield a white crystalline powder. Eu complex: yield 125 mg, 63%. FAB-MS: $m/z = 1463$ $[M - ClO_4 - MeOH]^+$. Gd complex: yield:156 mg,79%. FAB-MS: $m/z = 1468$ $[M - ClO_4 - MeOH]^+$.

$Ln(NO_3)_3(tppo)_2EtOH$ These complexes were prepared similarly starting from $Ln(NO_3)_3 \cdot nH_2O$ [4].

2.2 Measurements

Emission and excitation spectra of CH_2Cl_2 solutions were recorded on a SPEX Fluorolog-3 (Horiba Jobin Yvon) at room temperature. X-ray diffraction data were collected on a SMART APEX (Bruker) fitted with monochromated Mo Kα X-ray radiation at 173 K. The data were processed as routine.

^{151}Eu Mössbauer spectra were measured on a Wissel Mössbauer system (DFG-1200 and MDU-1200H) at 77 K using a $^{151}Sm/SmF_3$ source. ^{155}Gd Mössbauer spectra were measured using Wissel 1200 Mössbauer system (MDU-1200, DFG-1200, MVC-1200). Both the absorber (100 mgGd cm^{-2}) and the source ($^{155}Sm/Pd_3^{154}Sm$) were kept at 12 K [5].

3 Results and discussion

X-ray structural determinations show that $Ln(ClO_4)_3(tppo)_4 \cdot MeOH$ with Ln = Nd, Eu, Gd, Dy, Yb are isostructural, indicating no change in coordination number across the 4f block. The crystal consists of $[Ln(ClO_4)_2(tppo)_4]^+$, counter anion and solvated MeOH. $[Gd(ClO_4)_2(tppo)_4]^+$ has a distorted dodecahedron configuration. Two perchlorate anions coordinate to Gd^{3+} symmetrically as a bidentate, and Gd–O bond lengths (253.4 pm in average) are longer than those of Gd–O_{tppo} (227.5 pm). Two GdO_2Cl chelate planes are almost orthogonal (dihedral angle = 88.4°). The electrospray mass spectra of the methanol solutions of the complexes suggest retention of coordinated ClO_4^-. The nine-coordinate complex $Gd(NO_3)_3(tppo)_2 \cdot EtOH$ is isostructural to the Eu(III) complex [6].

Figure 1 shows the excitation and emission spectra of Eu complexes in CH_2Cl_2 at room temperature. Hereafter we use the abbreviation Ln-L-X showing lanthanide centre (Ln), phosphine oxide (L), and coordinating anion (X). In the excitation spectra monitored at $\lambda = 614$ (nitrato complex) and 617 nm (perchlorato complexes), maxima are observed at 248 and 280 nm (Eu-tppo-ClO_4), 248 and 278 (Eu-tppo-NO_3) , and 243 nm (Eu-tbpo-ClO_4; tbpo = tributylphosphine oxide). The λ_{max} around 243–248 and 278–280 nm are assigned to n–π^* and $\pi - \pi^*$, respectively, which are in good agreement with λ_{max} of absorption spectra of these complexes. In the emission spectra, a strong antenna effect of phenyl group was observed while

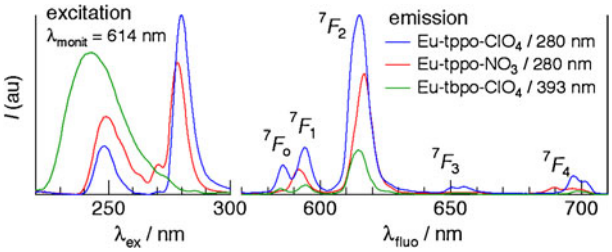

Fig. 1 Excitation and emission spectra of Eu-tppo-ClO_4, Eu-tppo-NO_3 and Eu-tbpo-ClO_4 in CH_2Cl_2 solution at room temperature

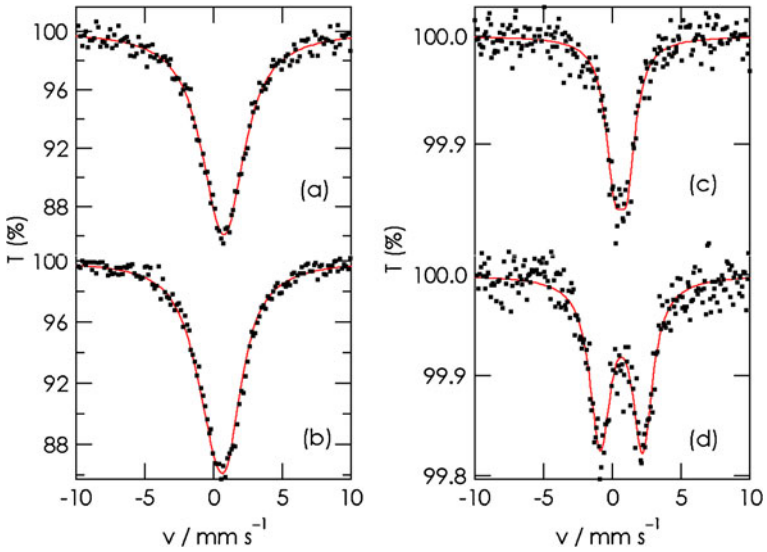

Fig. 2 ^{151}Eu (*left*) and ^{155}Gd Mössbauer spectra (*right*) of Ln-tppo-ClO_4 and Ln-tppo-NO_3. **a** Eu-tppo-NO_3, **b** Eu-tppo-ClO_4, **c** Gd-tppo-NO_3, **d** Gd-tppo-ClO_4

that of P=O group was not so effective. The red emissions are the transitions of $^5D_0 \rightarrow {}^7F_j$ of Eu^{3+} centre. The spectrum of Eu-tppo-NO_3 is slightly different from those of Eu-tppo-ClO_4 and Eu-tbpo-ClO_4. The emission to $^7F_0$ almost disappears in Eu-tppo-NO_3, suggesting high symmetry at the Eu(III) centre. The emission spectrum of solid state Eu-tppo-NO_3 does not show $^5D_0 \rightarrow {}^7F_0$ transition either.

Figure 2 shows the ^{151}Eu Mössbauer spectra of Eu complexes at 77 K. The parameters are summarized in Table 1. Both the spectra are slightly asymmetric. The quadrupole coupling constant (e^2qQ) values are 5.36 and 3.68 mm s^{-1} for Eu-tppo-ClO_4 and Eu-tppo-NO_3, respectively, suggesting higher symmetry in the nitrato complex. ^{155}Gd Mössbauer spectroscopy is more informative. The isomer shift values (δ) are those of eight or nine oxygen-coordinated Gd(III) complexes [7]. Gd-tppo-NO_3 shows a quite small e^2qQ value. Since Gd^{3+} has a half-filled 4f subshell, we may expect a large contribution of a lattice term to the electric field gradient V_{zz}. A quite small e^2qQ value of 1.99 mm s^{-1} clearly indicates that the electron distribution around the Gd^{3+} atom is much isotropic in Gd-tppo-NO_3. This observation agrees with the results of emission spectra of the Eu(III) complexes.

Table 1 ^{151}Eu and ^{155}Gd Mössbauer parameters. Asymmetric parameter is fixed to be zero

	^{151}Eu parameters at 77 K				^{155}Gd parameters at 12 K			
	δ^a	e^2qQ	Γ_{exp}	V_{zz}	δ^b	e^2qQ	Γ_{exp}	V_{zz}
	mm s^{-1}	mm s^{-1}	mm s^{-1}	10^{21}V m^{-2}	mm s^{-1}	mm s^{-1}	mm s^{-1}	10^{21}V m^{-2}
Ln-tppo-ClO_4	0.20	5.36	2.19	3.37	0.67	6.63	1.76	3.66
Ln-tppo-NO_3	0.30	3.68	2.59	2.32	0.61	1.99	1.50	1.10

[a]relative to EuF_3 at room temperature, [b]relative to ^{155}Sm/$SmPd_3$ source

Since Gd(III) and Eu(III) complexes are isostructural, we may compare the V_{zz} values directly. The V_{zz} value of Gd-tppo-ClO_4 agrees very well with that of Eu-tppo-ClO_4. However that of Eu-tppo-NO_3 (2.32×10^{21} V m^{-2}) is obviously larger than that of Gd-tppo-NO_3 (1.10×10^{21} V m^{-2}). This difference may arise from a small unignorable orbital contribution of Eu(III) atom having a hole in the 4f subshell.

Acknowledgement A part of this study is supported by an Interuniversity Joint Research Program Using JAEA Facilities.

References

1. Sarsfield, M. J. , Sutton, A. D., May, I., John, G. H. , Sharrad, C., Helliwell, M.: Chem. Commun. 2320–2321 (2004)
2. Sutton, A. D., May, I. Sharrad, C. A., Sarsfield, M. J., Helliwell, M.: Dalton Trans. 5734–5742 (2006)
3. Berthet, J. C., Lance, M., Nierlich, M., Ephritikhine, M.: Eur. J. Inorg. Chem. 2005–2007 (1999)
4. Cousins, D. R., Hart, F. A.: J. Inorg. Nucl. Chem. **29**, 1745–1757 (1967)
5. Wang, J., Abe, J., Kitazawa, T., Takahashi, M., Takeda, M.: Z. Naturforsch. **57a**, 581–585 (2002)
6. Valle, G., Casotto, G., Zanonato, P. L., Zarli, B.: Polyhedron **5**, 2093–2096 (1986)
7. Takeda, M., Wang, J., Nishimura, T., Suzuki, K., Kitazawa, T., Takahashi, M.: Hyperfine Interact. **156/157**, 359–364 (2004)

Hyperfine Interact (2012) 205:41–45
DOI 10.1007/s10751-011-0477-3

Study on the spin crossover transition and glass transition for Fe(II) complex film, [Fe(II)(H-triazole)$_3$]@Nafion, by means of Mössbauer spectroscopy

Akio Nakamoto · Hajime Kamebuchi · Masaya Enomoto · Norimichi Kojima

Published online: 29 November 2011

Abstract [Fe(II)(H-trz)$_3$]@Nafion (trz = triazole) is a transparent spin crossover complex film, where the spin crossover transition between the low-spin (S = 0) and the high-spin (S = 2) states takes place between 225 K and 300 K. In this film, two doublets corresponding to the low-spin and high-spin states were observed in the ^{57}Fe Mössbauer spectra, reflecting the spin crossover transition. From the analysis of ^{57}Fe Mössbauer spectra, the Debye temperatures of the low-spin and high-spin sites were estimated at 185 K and 176 K, respectively, in the temperature range between 10 K and 150 K. In this film, the total intensity of the Mössbauer spectra corresponding to the low-spin and high-spin sites drastically decreases above 200 K, reflecting the glass transition of Nafion, where the lattice vibration of $[Fe(H\text{-}trz)_3]_n^{2n+}$ is softened just as in solution due to micro-Brown motion of the segment of Nafion polymer membrane.

Keywords Spin crossover · Nafion · Glass transition · Mössbauer spectroscopy

1 Introduction

Transition metal complexes with d^4-d^7 configuration in an octahedral field have a possibility of spin transition between the low-spin (LS) and the high-spin (HS)

Electronic supplementary material The online version of this article (doi:10.1007/s10751-011-0477-3) contains supplementary material, which is available to authorized users.

A. Nakamoto · H. Kamebuchi (✉) · N. Kojima
Graduate School of Arts and Sciences, The University of Tokyo,
Komaba 3-8-1, Meguro-ku, Tokyo 153-8902, Japan
e-mail: cc106909@mail.ecc.u-tokyo.ac.jp

M. Enomoto
Department of Chemistry, Faculty of Science Division I, Tokyo University of Science,
Kagurazaka 1-3, Shinjuku-ku, Tokyo 162-8601, Japan

states. The spin crossover phenomenon has attracted much attention since the discovery of the photo-induced spin transition (light induced excited spin state trapping (LIESST)) for $[Fe(ptz)_6](BF_4)_2$ (ptz = 1-propyltetrazole) [1], and the thermally-induced spin transition with large thermal hysteresis around room temperature for 1,2,4-triazole (= H-trz) bridged Fe(II) complexes, $[Fe(H\text{-}trz)_{2.85}(NH_2\text{-}trz)_{0.15})](ClO_4)_2 \cdot H_2O$ [2]. In particular, the triazole bridged polymeric Fe(II) chain system has a possibility of molecular device such as display or memory at room temperature. However, these triazole-bridged complexes have been obtained as only powdered sample due to their rapid precipitation.

We have synthesized a transparent film, $[Fe(II)(H\text{-}trz)_3]$@Nafion, in which Nafion (an ion-exchange resin having side chain terminated by sulfonic acid group) behaves as a counter anion as well as a transparent substrate (see Fig. S1 in Electronic Supplementary Materials) and investigated the detailed LIESST effect [3]. Nafion, which was developed by DuPont Company in 1960s, is composed of a linear polymer of fluorocarbon and sulfonic acid groups and has been applied as fuel cell, sensor and catalyst due to its durability, chemical and thermal stability, and permselectivity. In the case of Nafion 117, reverse micelle consisted of perfluoroalkylether groups with hydrophilic SO_3H groups forms clusters of ca. 4 nm diameter separated by a distance of ca. 5 nm and interconnected through channels of ca. 1 nm when they are swollen with water [4]. In this paper, we report the spin transition and glass transition for the transparent spin crossover complex film, $[Fe(II)(H\text{-}trz)_3]$@Nafion, by means of ^{57}Fe Mössbauer spectroscopy.

2 Experimental

$[Fe(II)(H\text{-}trz)_3]$@Nafion was obtained according to the previous literature [3]. For ^{57}Fe Mössbauer spectroscopic measurement, ^{57}Co in Rh was used as a Mössbauer source. The Mössbauer spectra were calibrated by using the six lines of a body-centered cubic iron foil (α-Fe), the center of which was taken as zero isomer shift.

3 Results and discussions

3.1 Spin crossover transition

Figure 1a shows the temperature dependence of ^{57}Fe Mössbauer spectra for $[Fe(II)(H\text{-}trz)_3]$@Nafion, whose Mössbauer parameters are summarized in Table S1. In the spectra, two doublets corresponding to the LS and HS states coexist between 10 K and 258 K, which is consistent with the temperature dependence of magnetic susceptibility. As shown in Fig. 1b, the absorption intensity ratio of HS to LS states abruptly increases at about 200 K, reflecting the spin crossover transition.

In connection with the isomer shift for $[Fe(II)(H\text{-}trz)_3]$@Nafion, Lavrenova et al. reported the correlation between the isomer shift in the LS state (δ_{LS}) at 77 K and the spin transition temperature T_c for triazole-bridged Fe(II) compounds [5]. In general, a ligand having high π acceptability would withdraw electrons from d orbital to low-lying π^* orbital, so called π back donation, causing a reduction in the screening of the *s*-electrons of the iron and the decrease in the isomer shift. Through the hybridization

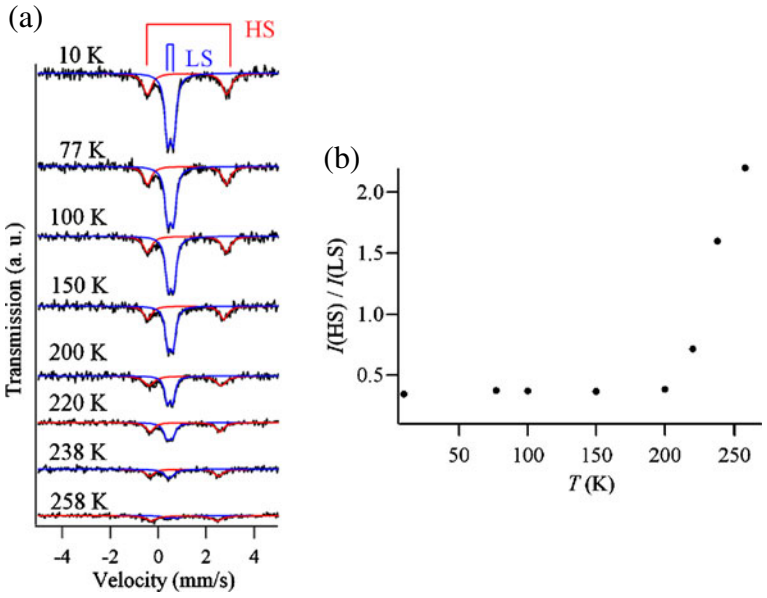

Fig. 1 **a** ^{57}Fe Mössbauer spectra for [Fe(II)(H-trz)$_3$]@Nafion at various temperatures. **b** Temperature dependence of the absorption intensity ratio of HS to LS states

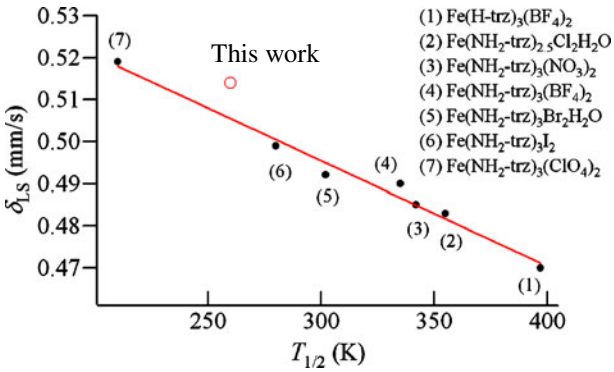

Fig. 2 Correlation between the isomer shift in the LS state at 77 K (δ_{LS}) and the spin transition temperature $T_{1/2}$ quoted from ref. [5]. The *red line* is the linear approximation by the least square method, and the *red open circle* corresponds to [Fe(II)(H-trz)$_3$]@Nafion

of the t_{2g} orbital and the π^* orbital, the ligand field splitting increases, leading to the increment of spin transition temperature. Figure 2 shows δ_{LS} versus T_c plots at 77 K and the linear approximation by the least square method. Since the δ_{LS} for [Fe(II)(H-trz)$_3$]@Nafion at 77 K is 0.514 (mm/s), its spin transition temperature is estimated at ca. 226 K by the extrapolation from the linear correlation between δ_{LS} and $T_{1/2}$. This value is lower than $T_{1/2} = 260$ K obtained from the magnetic susceptibility measurement.

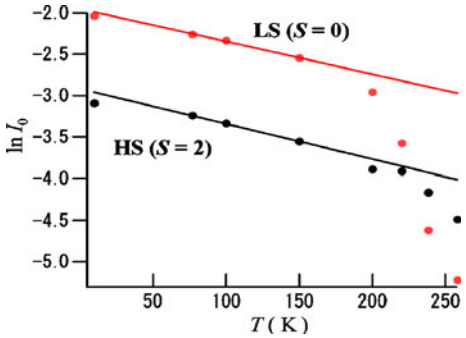

Fig. 3 Intensity of the Mössbauer spectra of the LS and HS states as a function of temperature for [Fe(II)(H-trz)$_3$]@Nafion

3.2 Glass transition of Nafion

The intensities of the ^{57}Fe Mössbauer spectra corresponding to the LS and HS states gradually become weak with increasing temperature above 150 K, and the signals almost vanish at 258 K. To investigate the hardness of lattice in the oligomer of $[Fe(H\text{-}trz)_3]_n^{2n+}$, Debye temperatures Θ_D of LS and HS states were estimated between 10 K and 150 K, where the ratio of HS to LS states is constant as shown in Fig. 1b. From the temperature dependence of the intensity of Mössbauer spectra, Θ_D of the HS and LS states can be determined using the following equation:

$$\ln\ I_0 = \ln\left(\frac{f_s n_A \sigma_0}{2}\right) - \frac{6E_R}{k\Theta_D^2}T$$

where I_0 is the absorption intensity, f_s the recoilless fraction of the Mössbauer source, n_A the area concentration of the Mössbauer nuclear, σ_0 the Mössbauer absorption cross section, E_R the recoil energy and k is the Boltzmann constant. Figure 3 shows $\ln I_0$ versus T plots, from which we can determine Θ_D to be 185 K (LS state) and 176 K (HS state), respectively, between 10 K and 150 K. Above 150 K, the plots exhibits the deviation from the linear approximation, and the values of Θ_D become small. These results show that the lattice vibration of $[Fe(H\text{-}trz)_3]_n^{2n+}$ in Nafion is softened above 150 K, and this behavior is derived from the micro-Brown motion of polymer chain segment. Nafion is known to exhibit the glass transition at 180 K, as a result, the motion in the oligomer of $[Fe(H\text{-}trz)_3]_n^{2n+}$ is softened just as in solution (see Fig. S2). Above 180 K, the recoilless fraction decreases with increasing temperature, and Mössbauer spectra of [Fe(II)(H-trz)$_3$]@Nafion cannot be observed around room temperature. Bauminger et al. reported the similar result with respect to $[Fe(II)(H_2O)_6]$ in Nafion [6]. Unfortunately, individual Θ_D of LS and HS states cannot be determined due to the spin transition above 200 K, but nonetheless we determined the average Θ_D to be 51 K from the analysis of $\{\ln I_0(LS) + \ln I_0(HS)\}$ versus T plots above 200 K (see Fig. S3).

4 Conclusion

We observed the spin crossover transition for [Fe(II)(H-trz)$_3$]@Nafion and estimated its spin transition temperature by means of ^{57}Fe Mössbauer spectroscopy. In addition, we also estimated the Debye temperature for the LS and HS sites between 10 K

and 150 K. Above 150 K, the Debye temperature remarkably decreased, suggesting that the lattice vibration of $[Fe(H\text{-}trz)_3]_n^{2n+}$ is softened due to the glass transition of Nafion.

References

1. Decurtins, S., Gütlich, P., Köhler, C.P., Spiering, H., Hauser, A.: Chem. Phys. Lett. **105**, 1 (1984)
2. Kröber, J., Codjovi, E., Kahn, O., Grolière, F., Jay, C.: J. Am. Chem. Soc. **115**, 9810 (1993)
3. Nakamoto, A., Ono, Y., Kojima, N., Matsumura, D., Yokoyama, T.: Chem. Lett. **32**, 336 (2003)
4. Gierke, T.D., Munn, G.E., Wilson, F.C.: J. Polym. Sci. **19**, 1687 (1981)
5. Varnek, V.A., Lavrenova, L.G.: J. Struct. Chem. **36**, 104 (1995)
6. Bauminger, E.R., Nowik, I., Ofer, S.: Polymer **26**, 1829 (1985)

Hyperfine Interact (2012) 205:47–50
DOI 10.1007/s10751-011-0468-4

Crystal structure and spin state of $Fe_{0.5}Co_{0.5}(NCS)_2(bpa)_2$

Satoru Nakashima · Takaki Morita · Katsuya Inoue

Published online: 1 December 2011

Abstract $Fe(NCS)_2(bpa)_2$, $Co(NCS)_2(bpa)_2$, and $Fe_{0.5}Co_{0.5}(NCS)_2(bpa)_2$ were synthesized. X-ray structural analysis revealed that the structure was the same among the three complexes. Although the metal-ligand distance in the mixed crystals was shorter than the distance in $Fe(NCS)_2(bpa)_2$ and was similar to that in $Co(NCS)_2(bpa)_2$, the spin state remained temperature-independent Fe^{II} high-spin state in ^{57}Fe Mössbauer spectra.

Keywords Assembled complexes · Mixed crystals · X-ray structure · Mössbauer spectroscopy · Spin state

1 Introduction

Self-assembled coordination polymers containing transition metal ions and organic bridging ligands have attracted intensive interests because of their potential abilities for selective inclusion and transformation of ions and molecules [1]. It is possible to construct various structures for porous assembled iron complexes bridged by bis(4–pyridyl) type ligand. We have studied iron complexes bridged by 1,2–bis(4–pyridyl)ethane (bpa), and revealed the relation between the *anti*/*gauche* conformer for coordinated bpa and the assembled structure, and the relation between the guest molecule and the spin state of iron [2–5]. We have also studied the magnetic behaviors and structural properties for some assembled complexes with more flexible ligand, 1,3–bis(4–pyridyl)propane (bpp), which has three methylenes, by using single

S. Nakashima (✉)
Natural Science Center for Basic Research and Development, Hiroshima University, Kagamiyama, Higashi-Hiroshima 739-8526, Japan
e-mail: snaka@hiroshima-u.ac.jp

T. Morita · K. Inoue
Graduate School of Science, Hiroshima University, Kagamiyama, Higashi-Hiroshima 739-8526, Japan

Table 1 Crystal data

Sample	FeY^1	$Fe_{0.5}Co_{0.5}Y^1$	CoY^1
a/ Å	19.7890(5)	19.775(6)	19.746(4)
b/ Å	9.9620(2)	9.948(2)	9.9444(19)
c/ Å	14.4810(5)	14.591(3)	14.571(3)
β/ °	110.156(1)	110.381(7)	110.403(3)
V/ Å^3	2679.9(1)	2690.6(11)	2681.7(9)

$^1Y=(NCS)_2(bpa)_2$

crystal X–ray diffraction analyses, Mössbauer spectroscopy, and SQUID measurements [6, 7]. Recently, we discussed the spin state of the mixed crystals with zinc or cobalt ion both in the 2D interpenetrated and 1D chain structures for the assembled complexes bridged by bpp [8]. The chemical pressure effect was observed in NCSe complex, while the effect was not observed in NCS complex. In the present study, we obtained single crystals of $Fe(NCS)_2(bpa)_2$, $Co(NCS)_2(bpa)_2$, and $Fe_{0.5}Co_{0.5}(NCS)_2(bpa)_2$, and discussed the structure and spin state of mixed crystals.

2 Experimental

$Fe(NCS)_2(bpa)_2$, $Co(NCS)_2(bpa)_2$, and $Fe_{0.5}Co_{0.5}(NCS)_2(bpa)_2$ were obtained by diffusion method. Iron and cobalt ions (1:1) were mixed in the synthetic process to obtain mixed crystals. The structures were determined by using single-crystal X-ray diffraction analysis.

A $^{57}Co(Rh)$ source in a constant acceleration mode was used for ^{57}Fe Mössbauer spectroscopic measurements. ^{57}Fe Mössbauer spectra were measured at 78 K and room temperature by using a Wissel Mössbauer spectrometer and a proportional counter. The isomer shift was referred to metallic iron foil. The Mössbauer parameters were obtained by a least-squares fitting to Lorentzian peaks.

3 Results and discussion

We obtained single crystals of $Fe(NCS)_2(bpa)_2$, $Co(NCS)_2(bpa)_2$, and $Fe_{0.5}Co_{0.5}(NCS)_2(bpa)_2$. The X-ray structural analyses revealed that all the samples had 1D chain structure, although the several types of crystal structure were expected. The color of the mixed crystals is orange, which is intermediate between yellow of iron complex and red of cobalt complex. The crystal data are summarized in Table 1. The crystal parameters are similar to each other. The unit-cell volume of iron complex is slightly smaller than that of cobalt complex, although the ion radius of Fe^{2+}(HS, 92 pm) is slightly larger than that of Co^{2+}(HS, 88.5 pm), suggesting a good packing of iron complex. The unit-cell volume of mixed crystals is largest among the three complexes. This suggests a relatively bad packing of 1D chains in mixed crystals maybe due to the coexistence of iron and cobalt ions in the crystal.

Figure 1 shows the crystal structure of $Fe_{0.5}Co_{0.5}(NCS)_2(bpa)_2$. It can be seen that the structure is 1D chain one. Metal ion showed a distorted octahedral geometry by coordination of four N atoms of bpa and two N atoms of NCS in the *trans* position. The bpa ligand is in *gauche* conformer. The average distance between metal and nitrogen atoms of ligand is 2.192(1), 2.161(3), and 2.165(1) Å for $Fe(NCS)_2(bpa)_2$, $Co(NCS)_2(bpa)_2$, and $Fe_xCo_{1-x}(NCS)_2(bpa)_2$, respectively. The distance in cobalt

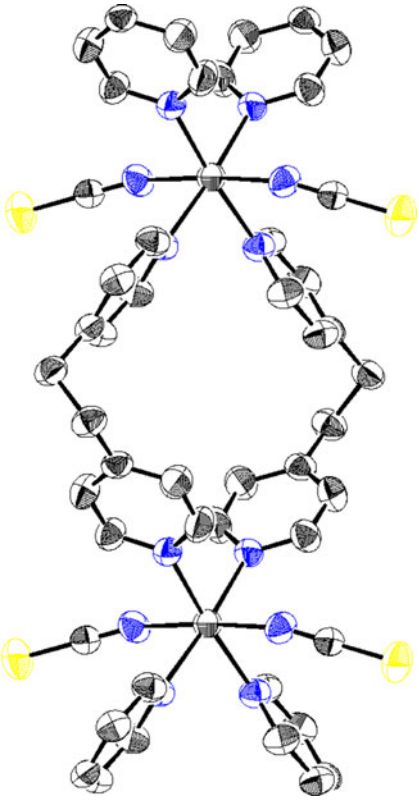

Fig. 1 Crystal structure of $Fe_{0.5}Co_{0.5}(NCS)_2(bpa)_2$

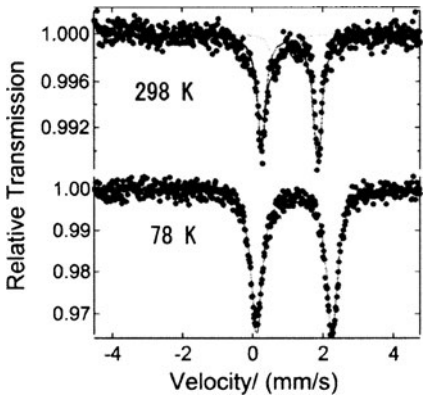

Fig. 2 ^{57}Fe Mössbauer spectra of $Fe_{0.5}Co_{0.5}(NCS)_2(bpa)_2$

complex is shorter than that of iron complex, because the ion radius for Co^{2+}(HS, 88.5 pm) is shorter than that of Fe^{2+}(HS, 92 pm), which shows the opposite trend observed in the unit-cell volume. The distance in mixed crystals is similar to that of cobalt complex. One of the explanations is that the chemical pressure effect worked on the iron ion by making the mixed crystals with the ion having smaller ion radius than Fe^{2+}.

Figure 2 shows the Mössbauer spectra of $Fe_{0.5}Co_{0.5}(NCS)_2(bpa)_2$ at 78 and 298 K. Mössbauer parameters (IS = 1.05 mm s^{-1}, QS = 1.60 mm s^{-1} at 298 K and IS = 1.18 mm s^{-1}, QS = 2.14 mm s^{-1} at 78 K) reveal a temperature-independent Fe^{II} high-spin state. Mixed crystals showed almost the same Mössbauer spectra with the corresponding pure iron complex in the 1D structure. No significant differences in Mössbauer parameters were observed between the pure iron complex [3] and mixed crystals. Line width, however, is somewhat larger at 78 K. One of the possibilities is that the coordination circumstances around iron ion have distribution because the coexisting cobalt ions affect the coordination circumstances around iron ion. The distribution will be averaged by the thermal vibration at room temperature, which results in the narrow line width at 298 K. The present spectra mean that the spin state of the mixed crystals is the same with $Fe(NCS)_2(bpa)_2$, although the chemical pressure effect was expected from the results of X-ray structural analyses.

In conclusion, the average distance between metal and nitrogen atoms in mixed crystals approached the distance in $Co(NCS)_2(bpa)_2$. The spin state, however, remained the temperature-independent high-spin type.

References

1. Moulton, B., Zaworotko, M.J.: Chem. Rev. **101**, 1629 (2001)
2. Nakashima, S., Morita, T., Yamada, K., Inoue, K.: Hyperfine Interact. **166**, 469 (2005)
3. Morita, T., Asada, Y., Okuda, T., Nakashima, S.: Bull. Chem. Soc. Jpn. **79**, 738 (2006)
4. Morita, T., Nakashima, S., Yamada, K., Inoue, K.: Chem. Lett. **35**, 1042 (2006)
5. Nakashima, S., Morita, T., Inoue, K.: Hyperfine Interact. **188**, 107 (2009)
6. Atsuchi, M., Higashikawa, H., Yoshida, Y., Nakashima, S., Inoue, K.: Chem. Lett. **36**, 1064 (2007)
7. Atsuchi, M., Inoue, K., Nakashima, S.: Inorg. Chim. Acta **370**, 82 (2011)
8. Nakashima, S., Dote, T., Atsuchi, M., Inoue, K.: J. Phys. **C217**, 012035 (2010)

Hyperfine Interact (2012) 205:51–55
DOI 10.1007/s10751-011-0413-6

1D iron(II) spin crossover complexes with 1,2,4-triazol-4-yl-propanoic acid

Antoine P. Railliet · Anil D. Naik · Aurelian Rotaru · Jacqueline Marchand-Brynaert · Yann Garcia

Published online: 8 November 2011

Abstract A series of 1D coordination polymers $[Fe(patrz)_3]X_2 \cdot solv$, (*patrz* = 1,2,4-triazol-4-yl-propanoic acid; X = BF_4^-, ClO_4^-, Cl^-, NO_3^- and solv = MeOH or H_2O) were precipitated from methanol. Their spin crossover properties were studied by temperature dependent SQUID magnetometry and ^{57}Fe Mössbauer spectroscopy, both for solvated and desolvated complexes. Compounds show gradual incomplete spin crossover with distinct thermochromism, in particular $[Fe(patrz)_3](BF_4)_2 \cdot MeOH$, for which only 27% of Fe^{II} ions are switched to the low-spin state at 77 K, as determined by a detailed ^{57}Fe Mössbauer study. Other prominent features of this work are the interesting self assembly of 1D chain with exclusively triazole coordination from patrz ligand despite its ditopic nature and a hysteretic room temperature spin crossover in $[Fe(patrz)_3]Cl_2$.

Keywords ^{57}Fe Mössbauer spectroscopy · Coordination polymers · Spin-transition · 1,2,4-Triazole

1 Introduction

Iron(II) spin crossover (SCO) materials exhibit the remarkable property of molecular bistability with rapid optical and magnetic feedback to external perturbations that could offer an attractive prospect for future molecular based information storage

A. P. Railliet · A. D. Naik · J. Marchand-Brynaert · Y. Garcia (✉)
Institute of Condensed Matter and Nanosciences, Université Catholique de Louvain,
Place L. Pasteur 1, 1348 Louvain-la-Neuve, Belgium
e-mail: yann.garcia@uclouvain.be

A. Rotaru
Department of Electrical Engineering and Computer Science,
"Stefan cel Mare" University, University Street, No. 13, Suceava 720229, Romania

devices [1, 2]. Among several factors that influence SCO, ligand design plays a crucial role. In this context, 1,2,4-triazole derivatives represent privileged candidates to prepare well-organized coordination polymers [3] which should leads to abrupt SCO with hysteresis loops ranging over a wide temperature domain. Recently β-amino acid derivatives have been successfully introduced as suitable precursors to build 1D coordination polymers exhibiting abrupt, hysteretic SCO around room temperature [4, 5]. This prompted us to employ a new analogous ligand derived from β-amino acid series. We report herein on the spin state properties of a series of 1D iron(II) complexes of formula $[Fe(patrz)_3](anion)_2 \cdot solv$, with patrz = 1,2,4-triazol-4-yl-propanoic acid.

2 Experimental

The patrz molecule was obtained following the reported procedure [6]. Iron complexes were prepared by mixing 1 eq. of iron salts with 3 eq. of patrz in methanolic solutions affording white or pink/purple powders that were isolated at room temperature and dried in air. Based on elemental analysis and thermogravimetric analyses, complexes were formulated as $[Fe(patrz)_3](BF_4)_2 \cdot MeOH$ (**1**·MeOH, white solid), $[Fe(patrz)_3](ClO_4)_2 \cdot MeOH$ (**2**·MeOH, white solid), $[Fe(patrz)_3]Cl_2 \cdot 2H_2O$ (**3**·$2H_2O$, purple solid) and $[Fe(patrz)_3](NO_3)_2 \cdot MeOH$ (**4**·MeOH, pink solid).

3 Results and discussion

Infrared spectral analysis of complexes shows prominent bands around 1060 cm^{-1} (**1**·MeOH), 1090 cm^{-1} (**2**·MeOH), 1385 cm^{-1} (**4**·MeOH), which confirms the presence of non-coordinated anions BF_4^-, ClO_4^- and NO_3^-, respectively. The neat $\nu_{(C=O)}$ observed at 1730 cm^{-1} in patrz is seen around the same value for all complexes. Both observations prove the non-involvement of carboxylic moiety suggesting the neutral nature of the ligand. Thus the coordination is assumed to occur exclusively from the bridging 1,2,4-triazole. Bulk samples were all analyzed by Scanning Electron Microscopy (SEM) revealing diversity in texture (Fig. 1), as well as an amorphous nature, the later was also confirmed by poor X-ray powder diffraction patterns.

Magnetic data of all solvated complexes were recorded over the temperature range 4–300 K. In addition, the samples were warmed up to 400 K (except for **2**·MeOH due to risk of explosion from perchlorate anion) and maintained at this temperature for 10 min so as to remove non-coordinated solvent molecules and measurements were repeated (Fig. 2a, b). A gradual decrease of the $\chi_M T$ product of 3.47 cm^3 K mol^{-1} is observed on cooling from room temperature for **1**·MeOH with $T_{1/2}$ = 128 K (Fig. 2a). The profile is slightly altered for **1**, with $T_{1/2}$ = 112 K after solvent removal (Fig. 2a). This magnetic behavior corresponds to a gradual incomplete spin conversion. Profile is similar in **2**·MeOH with $T_{1/2}$ = 138 K. The drop below 50 K is presumably due to the zero-field splitting for remaining high-spin (HS) Fe^{II} ions (Fig. 2a) [7]. Magnetic properties, recorded over the temperature range 4–300 K, for **3**·$2H_2O$ and **4**·MeOH are typical for low-spin (LS) complexes. A few iron ions remain however in the HS state, with a slightly higher proportion in **4**·MeOH

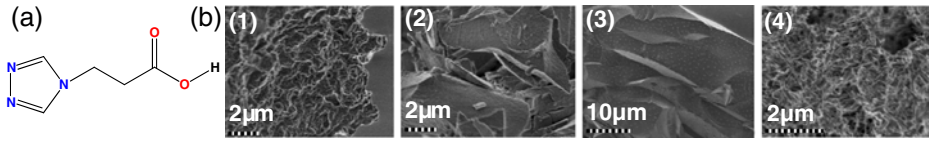

Fig. 1 **a** Molecular structure of patrz. **b** SEM images on **1**–**4**: highly aggregated particle of ∼200 nm (**1**·MeOH), amorphous solids (**2**·MeOH and **3**·2H_2O) and needles of ∼100 nm length (**4**·MeOH)

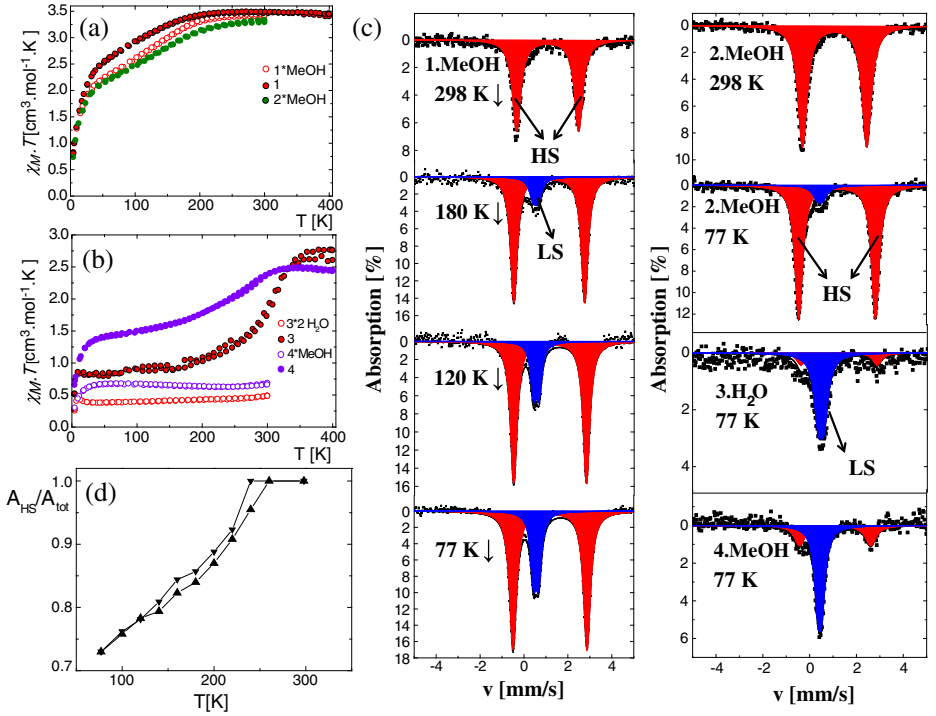

Fig. 2 $\chi_M T$ *vs.* T plot for the [Fe(patrz)$_3$](anion)$_2$ solvated (**a**) and desolvated series (**b**). (**c**) ^{57}Fe Mössbauer spectra for [Fe(patrz)$_3$](anion)$_2$·solv complexes at selected temperatures. (**d**) A_{HS}/A_{tot} *vs*. T for **1**·MeOH

(Fig. 2b). After solvent removal, there is a dramatic change in the magnetic behavior with significant increase of $\chi_M T$(2.77 cm^3 K mol^{-1} for **3** and 2.5 cm^3 K mol^{-1} for **4**) at 300 K. These desolvated complexes display on cooling a clear SCO to the LS state with $T_{1/2} = 294$ K for **3** and a gradual SCO behavior with $T_{1/2} = 233$ K for **4** (Fig. 2b). Remarkably the spin conversion curve is centered at room temperature for **3**, which has been rarely encountered [8], and is not complete in both HS and LS states. Such a room temperature SCO is highly sought for potential applications in molecular display and data storage devices [1, 2]. Indeed, insertion of more voluminous anions such as BF_4^- or ClO_4^- leads to the occurrence of SCO behavior at lower temperature (112–138 K) whereas smallest anions such as Cl^- or planar NO_3^- tends to stabilize the LS state and shifts the SCO behavior upwards (233–294 K) [9, 10].

Table 1 ^{57}Fe Mössbauer parameters for [Fe(patrz)$_3$](anion)$_2$·solv complexes

	T [K]	$\mathbf{A_{HS}/A_{tot}}$ [%]	HS [mm/s]			LS [mm/s]		
			δ	ΔE_Q	$\Gamma/2$	δ	ΔE_Q	$\Gamma/2$
1·MeOH	77	73(1)	1.18(1)	3.36(1)	0.19(1)	0.55(1)	0.24(1)	0.16(1)
	120↑	78(1)	1.17(1)	3.34(1)	0.19(1)	0.54(1)	0.24(1)	0.15(1)
	140↑	79(2)	1.16(1)	3.31(1)	0.19(1)	0.54(1)	0.24(2)	0.15(2)
	160↑	82(2)	1.15(1)	3.27(1)	0.19(1)	0.53(1)	0.22(3)	0.16(2)
	180↑	84(2)	1.14(1)	3.24(1)	0.19(1)	0.51(2)	0.20(4)	0.16(3)
	200↑	87(2)	1.13(1)	3.19(1)	0.19(1)	0.50(2)	0.24(4)	0.15(3)
	220↑	91(2)	1.11(1)	3.12(1)	0.19(1)	0.46(3)	0.2(1)	0.18(8)
	240↑	95(3)	1.10(1)	3.06(1)	0.21(1)	0.5(1)	0.2(4)	0.2(3)
	260↑	100	1.10(1)	2.99(1)	0.23(1)	–	–	–
	298	100	1.07(1)	2.83(1)	0.23(1)	–	–	–
	240↓	100	1.11(1)	3.05(1)	0.20(1)	–	–	–
	220↓	92(2)	1.11(1)	3.11(1)	0.19(1)	0.47(4)	0.23(8)	0.16(7)
	200↓	89(2)	1.13(1)	3.17(1)	0.19(1)	0.48(3)	0.20(9)	0.18(7)
	180↓	86(2)	1.14(1)	3.22(1)	0.19(1)	0.52(3)	0.23(9)	0.21(6)
	160↓	84(2)	1.15(1)	3.25(1)	0.18(1)	0.53(1)	0.23(3)	0.15(2)
	140↓	81(2)	1.16(1)	3.28(1)	0.19(1)	0.54(1)	0.25(2)	0.15(2)
	120↓	78(2)	1.17(1)	3.31(1)	0.19(1)	0.54(1)	0.25(2)	0.16(2)
	100↓	76(2)	1.17(1)	3.33(1)	0.19(1)	0.56(1)	0.25(1)	0.14(1)
2·MeOH	77(1)	91(2)	1.18(1)	3.28(1)	0.20(1)	0.45(4)	0.2(2)	0.2(1)
	298	100	1.07(1)	2.74(1)	0.24(1)	–	–	–
3·2H$_2$O	77(1)	15(8)	1.15(9)	3.5(2)	0.2(1)	0.52(2)	0.24(3)	0.16(3)
4·MeOH	77(1)	30(3)	1.17(2)	3.44(3)	0.20(3)	0.50(1)	0.21(2)	0.17(1)

δ: isomer shift (with respect to α-Fe at 298 K); ΔE_Q: quadrupole splitting; $\Gamma/2$: half width at half maximum

^{57}Fe Mössbauer spectra were recorded between 77 and 300 K for all solvated complexes. Selected spectra, shown in Fig. 2c, are consistent with the magnetic properties described above. At 298 K, the spectra of **1**.MeOH ($\delta^{HS} = 1.07(1)$ mm/s and $\Delta E_Q^{HS} = 2.83$ mm/s) and **2**.MeOH ($\delta^{HS} = 1.07(1)$ mm/s and ΔE_Q^{HS} 2.74(1) mm/s) are similar. On cooling to 77 K, a spin state conversion is confirmed with the growing of a LS doublet (in blue) with $\delta^{LS} = 0.55(4)$ mm/s and 0.45(4) mm/s for **1**·MeOH and **2**·MeOH, respectively. The HS doublet at 77 K (in red) indicates that a major fraction of Fe^{II} ions are not switched to the LS state. An incomplete spin conversion (only 27%) is thus detected as confirmed by the temperature dependence of A_{HS}/A_{tot} shown in Fig. 2c for **1**·MeOH. This curve also confirms the gradual nature of the spin conversion that was suggested by SQUID measurements and which could be related to steric constraints in this system. This unusual situation prevents to undergo any reliable determination of Debye temperatures in both spin states [11].

The diamagnetic character of **3**·2H$_2$O and **4**·MeOH is confirmed by a major LS doublet (in blue), a few HS Fe^{II} ions (in red) being also detected by Mössbauer spectroscopy (Fig. 2c). These hyperfine parameters are consistent with HS and LS Fe^{II} complexes with a distorted pseudo-octahedral coordination geometry, and fall in the range of parameters described for analogous 1D chain complexes [4, 5, 10, 11]. These Mössbauer parameters are also in a good agreement with computed values derived from similar family of materials [12] (Table 1).

A novel series of 1D Fe^{II} complexes has been prepared using a ditopic 1,2,4-triazole ligand and their magnetic properties studied by SQUID magnetometry and

^{57}Fe Mössbauer spectroscopy. $[Fe(patrz)_3]Cl_2$ display an hysteretic room temperature spin conversion whereas $[Fe(patrz)_3](BF_4)_2 \cdot MeOH$ show a gradual and incomplete spin conversion on cooling. Nanostructuration of these functional materials towards their future implementation in next generation devices are continuing.

Acknowledgements We gratefully acknowledge support from IAP INANOMAT, the FNRS (2.4508.08, 4.4507.10), a ARC grant allotted by the Académie Universitaire Louvain, the European Social Fund through Sectorial Operational Program Human Resources: PRiDE (POSDRU/89/1.5/S/57083) and from the Groupe Francophone de Spectrométrie Mössbauer for A. D. N. and A. P. R. to attend GFSM 2011 (Strasbourg) and ICAME 2011 (Kobe). J. M. B. is a senior research associate of the F.R.S.-FNRS. We thank Prof. J. Linares (Versailles) and M. M. Dîrtu for useful discussions.

References

1. Kahn, O., Kröber, J., Jay, C.: Spin transition molecular materials for displays and data recording. Adv. Mater. **4**, 718 (1992)
2. Garcia, Y., Ksenofontov, V., Gütlich, P.: Spin transition molecular materials: new sensors. Hyperfine Interact. **139/140**, 543 (2002)
3. Garcia, Y., Niel, V., Muñoz, M.C., Real, J.A.: Spin crossover in 1D, 2D and 3D polymeric Fe(II) networks; spin crossover in transition metal compounds I. Top. Curr. Chem. **233**, 229 (2004)
4. Dîrtu, M.M., Schmit, F., Naik, A.D., Rotaru, A., Marchand-Brynaert, J., Garcia, Y.: Spin transition sensors based on β-amino-acid 1,2,4-triazole derivative. Int. J. Mol. Sci. **12**, 5339 (2011)
5. Dîrtu, M.M., Naik, A.D., Marchand-Brynaert, J., Garcia, Y.: Room temperature hysteretic spin transition in 1D iron(II) coordination polymers. J. Phys. Conf. Ser. **217**, 012085 (2010)
6. Naik, A.D., Marchand-Brynaert, J., Garcia, Y.: A simplified approach to N- and N,N'-linked 1,2,4-triazoles by transamination. Synthesis **1**, 149 (2008)
7. Garcia, Y., Grunert, M., Reiman, S., van Campenhoudt, O., Gütlich, P.: The two-step spin conversion in a supramolecular triple helicate dinuclear iron(II) complex studied by Mössbauer spectroscopy. Eur. J. Inorg. Chem. 3333 (2006)
8. Šalitroš, I., Madhu, N. T. , Boča, R., Pavlik, J., Ruben, M.: Room temperature spin transition iron compounds. Monatsch. Chem. **140**, 695 (2009)
9. Garcia, Y., van Koningsbruggen, P.J., Lapouyade, R., Rabardel, L., Kahn, O., Wieczorek, M., Bronisz, R., Ciunik, Z., Rudolf, M.F.: Synthesis and spin crossover characteristics of polynuclear 4-(2′-hydroxy-ethyl)-1,2,4-triazole Fe(II) molecular materials. C. R. Acad. Sci. Paris IIc, pp 523 (1998)
10. Dîrtu, M.M., Rotaru, A., Gillard, D., Linares, J., Codjovi, E., Tinant, B., Garcia, Y.: Prediction of the spin transition temperature in Fe^{II} one dimensional coordination polymers: an anion based database. Inorg. Chem. **48**, 7838–7852 (2009)
11. Dîrtu, M.M., Garcia, Y., Nica, M., Rotaru, A., Linares, J., Varret, F.: Iron(II) spin transition 1,2,4-triazole chain compounds with novel inorganic fluorinated counteranions. Polyhedron **26**, 2259 (2007)
12. Varnek, V.A., Kryuchkova, N.A., Bushuev, M.B.: Quantum chemical calculations of the isomer shift in iron(II) complexes of 1,2,4-triazoles with a $^1A_1 \Leftrightarrow {}^5T_2$ spin transition. J. Struct. Chem. **47**, 1177 (2006)

Hyperfine Interact (2012) 205:57–61
DOI 10.1007/s10751-011-0414-5

Neutral and anionic duality of 1,2,4-triazole α-amino acid scaffold in 1D coordination polymers

Anil D. Naik · Marinela M. Dîrtu · Yann Garcia

Published online: 26 October 2011

Abstract A tiny supramolecular synthon, 4H-1,2,4-triazol-4-yl acetic acid (HGlytrz) which is bifunctional by design having an electronic asymmetry and conformational flexibility has been introduced to synthesize iron(II) complexes. Having 1,2,4-triazole or carboxylic extremities on the same framework HGlytrz could display dual functionality by acting as a neutral as well as anionic ligand based on the possibility of deprotonation of carboxylic group. Four new iron(II) HGlytrz complexes with ClO_4^- (**1**), NO_3^- (**2**), BF_4^- (**3**) and $CF_3SO_3^-$ (**4**) anions were prepared. Formulation of their composition which is complicated due to ligand deprotonation is discussed. Unlike its ester protected counterpart ethyl-4H-1,2,4-triazol-4-yl-acetate (αGlytrz) which show hysteretic room temperature spin crossover, **1**–**4** remain in the high-spin state as revealed by ^{57}Mössbauer spectroscopy. Prospects of such 1D coordination polymers with dangling unbounded carboxylic entities in the realm of self-assembled monolayer (SAM) are discussed.

Keywords ^{57}Fe Mossbauer spectroscopy · Coordination polymers · Spin-transition · 1,2,4-triazole

1 Introduction

Tailor made bifunctional molecular fragments are greatly sought in the fabrication of wide range of functional materials. We recently synthesized several supramolecular 1,2,4-triazole synthons that were introduced in thermochromic spin crossover (SCO) materials [1, 2], inhibitors for antibiotics [3], modular approach in the design of metal-organic frameworks (MOFs) [4, 5] and logistics for non-linear optics [5]. Among them ethyl-4H-1,2,4-triazol-4-yl-acetate (αGlytrz) has emerged as a prospective

A. D. Naik · M. M. Dîrtu · Y. Garcia (✉)
Institute of Condensed Matter and Nanosciences, MOST – Inorganic Chemistry,
Université Catholique de Louvain, Place L. Pasteur 1, 1348, Louvain-la-Neuve, Belgium
e-mail: yann.garcia@uclouvain.be

scaffold for the design of SCO materials with $[Fe(\alpha Glytrz)_3](ClO_4)_2$ showing abrupt, complete hysteretic SCO operating around room temperature [1]. In continuation of this work we now investigate the iron(II) coordination chemistry of the hydrolyzed derivative of αGlytrz, 4H-1,2,4-triazol-4-yl acetic acid (HGlytrz). This latter molecule has an interesting topology wherein the two extremities are occupied by potentially coordinating groups of 1,2,4-triazole and carboxylic group [4]. We have shown earlier by X-ray crystallography of a series of 3d complexes how this ligand could act either as anionic or neutral ligand depending upon reaction conditions [3, 4]. In the present work four new iron(II) HGlytrz complexes were prepared with ClO_4^- (**1**), NO_3^- (**2**), BF_4^- (**3**) and $CF_3SO_3^-$ (**4**) counteranions. FTIR and ^{57}Fe Mössbauer spectroscopies provide complimentary information about ligand's ability to act either as neutral (HGlytrz) or anionic form (Glytrz). Complexes **1**,**3**,**4** are 1D coordination polymers (CP) with bridging *N*1, *N*2− 1,2,4-triazole with ligand acting as neutral with concurrent formation of a small amount of 1D CP with dual status of ligand. Interestingly, **2** is exclusively formed of a 1D CP with HGlytrz which opens up a new strategy to induce the formation of a linear chains with non-coordinated potentially anchoring carboxylic groups that could be expected to find broad scope in self-assembled monolayers (SAM) in thin film fabrications.

2 Experimental

Iron(II) complexes were isolated by reaction of the corresponding Fe^{II} salts, $[Fe(H_2O)_6](Anion)_2$ (anion = BF_4^-, ClO_4^-, $CF_3SO_3^-$) and $[Fe(H_2O)_6](NO_3)_2$ (prepared *in situ* [6]) with HGlytrz (1:3 stoichiometry) dissolved in methanol in a $N_{2(g)}$ atmosphere. The off-white powders thus obtained are highly sensitive to air and moisture and therefore stored under N_2 atmosphere/desiccator.

3 Results and discussion

SEM (scanning electron microscopy) images (Fig. 1b) reveals texture of the powders at the microscopic level. The texture is indefinable in **2** and **4** which is also evident from poor X-ray powder diffraction pattern (XRPD) (Fig. 2a). Comparatively **1** and **3** have distinct XRPD pattern which is apparent from SEM images on the bulk sample. In fact **3** show elongated needles of 60–80 nm thickness. Contrary to its ester analogue [1], **1**–**4** were not precipitated instantly during their syntheses thus increasing precipitation probability of more than one species in the bulk sample.

The strong υ(C=O) band in FTIR of ligand around 1730 cm^{-1} is still found as a strong band in **1**–**4** with shift in band position (up to 1744 cm^{-1}) except in **1** where the intensity is reduced comparatively. FTIR also supports the presence of anions with characteristic bands [$\upsilon(ClO_4^-)$ ~1050 cm^{-1} (**1**); $\upsilon(NO_3^-)$ ~1382 cm^{-1} (**2**); $\upsilon(BF_4^-)$ ~1060 cm^{-1} (**3**); $\upsilon(-SO_3^-)$ ~1259 cm^{-1} (**4**)]. This situation suggests that these complexes form 1D CPs with dangling carboxylic group which is still protonated thus acting as neutral ligand and coordinating iron ions through *N*1, *N*2 of 1,2,4-triazole units. In addition, except for **2**, there is a medium to strong band around 1630 cm^{-1} (1660 cm^{-1} in **1**) which is assigned to asymmetric stretching of $\upsilon(COO^-)$ and a medium band around 1250 cm^{-1} indicative of symmetric $\upsilon(COO^-)$

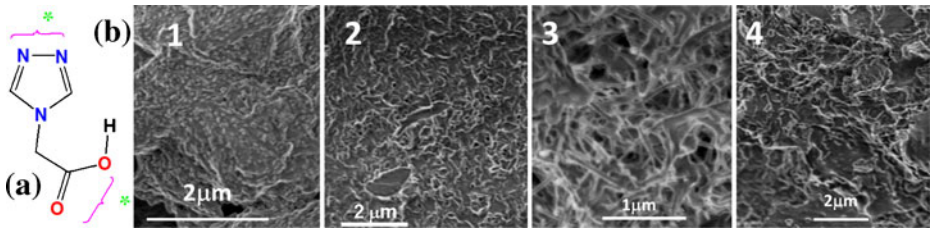

Fig. 1 **a** Molecular structure of HGlytrz with *indicating possible bifunctionality; **b** SEM images on **1**–**4**

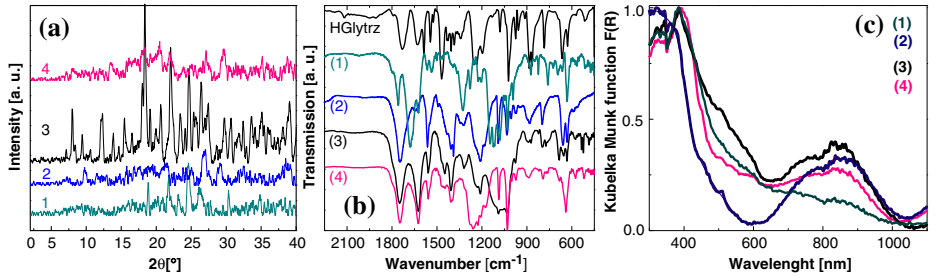

Fig. 2 **a** XRPD pattern for **1**–**4** at r.t. **b** FTIR for **1**–**4** expanded between 2200–500 cm^{-1} at r.t. **c** Diffuse reflectance spectra of **1**–**4** at r.t.

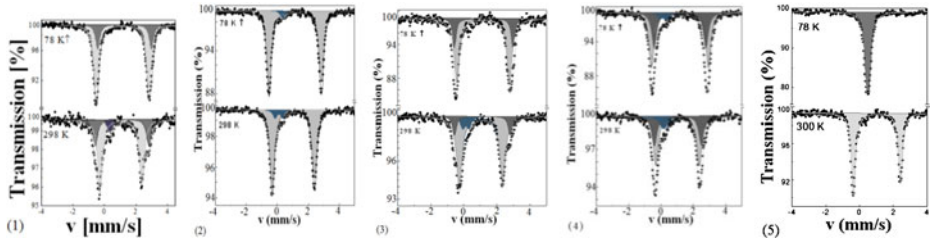

Fig. 3 ^{57}Fe Mössbauer spectra of **1**–**5** at 78 K and 298 K. *Grey*, *dark grey* and *blue gray* correspond to the HS(1), HS(2) and Fe^{III} impurities doublets, respectively

stretching based on our earlier reports [2–4]. This would indicate the presence of 1D chains with deprotonated ligands. Thus this observation leads to the conclusion that bulk samples of **1**, **3** and **4** have co-precipitation of two types of 1D CP with tentative composition: $[Fe(HGlytrz)_3](Anion)_2$ and $[Fe(HGlytrz)_2(Glytrz)]Anion$. Interestingly **2** which was prepared in aqueous methanol which does not show $\upsilon_{asym}(COO^-)$ exclusively forms 1D chain with neutral ligand of the composition $[Fe(HGlytrz)_3](NO_3)_2{\cdot}CH_3OH$ (**2**). The presence of a non-coordinated solvent molecule was confirmed by thermogravimetric analyses. Selected ^{57}Fe Mössbauer Spectra are shown in Fig. 3 and hyperfine parameters are grouped in Table 1.

As a consequence of these formulations, two types of high-spin (HS) sites would be expected for **1, 3, 4** which are indeed observed, hereafter denoted as HS1 and HS2 (Table 1). HS1 with isomer shift, δ^{HS1}, which is in the range of 1.05–1.13 mm/s

Table 1 Selected ^{57}Fe Mössbauer parameters in **1**–**5**

Compound	T (K)	δ (mm/s)	ΔE_Q (mm/s)	Γ/2 (mm/s)	%	Species
1	78	1.28(1)	3.41(2)	0.16(1)	25.7	HS1
		1.13(1)	3.36(1)	0.18(1)	74.3	HS2
	298	1.13(1)	3.39(2)	0.18(1)	25.4	HS1
		1.04(1)	2.66(1)	0.17(1)	67.3	HS2
		0.34(1)	–	0.2*	7.3	Fe^{III}
2	78	1.16(1)	3.38(1)	0.17(1)	97	HS
		0.33(1)	0.29(1)	0.10(1)	3	Fe^{III}
	298	1.04(1)	2.74(2)	0.18(1)	92	HS
		0.10(3)	0.49(1)	0.15(1)	8	Fe^{III}
3	78	1.20(1)	3.54(1)	0.12(1)	23.3	HS1
		1.17(1)	3.19(1)	0.18(1)	76.7	HS2
	298	1.12(1)	3.37(3)	0.14(1)	13.6	HS1
		1.04(1)	2.62(1)	0.20(1)	76.6	HS2
		0.13(3)	0.38(1)	0.16(1)	9.8	Fe^{III}
4	78	1.18(1)	3.20(2)	0.19(1)	38.4	HS1
		1.17(1)	3.51(1)	0.17(1)	54.1	HS2
		0.15(2)	0.43(1)	0.26(1)	7.5	Fe^{III}
	298	1.05(1)	2.91(1)	0.19(1)	33.6	HS1
		1.03(1)	2.69(3)	0.18(1)	54.2	HS2
		0.18(1)	–	0.32(1)	12.2	Fe^{III}
5[a]	298	1.03(1)	2.78(1)	0.15(1)	100	HS
	78	0.48(1)	0.20	0.16(1)	100	LS

δ: isomer shift (with respect to α-Fe at 298 K); ΔE_Q: quadrupole splitting; Γ/2: half width at half maximum;*Fixed parameter; [a][Fe(αGlytrz)$_3$](ClO$_4$)$_2$·MeOH [1]

and quadrupole splitting, ΔE_Q^{HS1} in the range 2.91 to 3.39 mm/s which is found in 15–30% in population. The situation is not very different at 77 K in terms of spin state change but the value of ΔE_Q value increases further. The relatively (compared to HS2, Table 1) higher value of ΔE_Q at 298 K indicates significant distortion at the iron centers which could be possible due to the strain created by supramolecular interactions that is established by the deprotonated ligand in **1**, **3** and **4**. The second HS signal (HS2) dominates the spectra (~54–76%, Table 1). The δ is in the range of 1.03 mm/s and ΔE_Q = 2.62–2.74 mm/s which is in the range of FeN_6 octahedra reported for the analogous complex **5** (Table 1) [1]. These results are in good agreement with our hypothesis about an admixture of two types of 1D chains in the bulk sample delineated from IR spectra of **1**, **3** and **4**. It has to be noted that in **2**, there is exclusively one type of HS species thus strongly supporting the interpretation from FTIR about the composition and coordination mode. The observed decrease in δ (Table 1) on warming from 77 K to 298 K in **1**–**4** is due to relativistic second order Doppler shift [6]. Due the fact that these complexes are highly susceptible to aerial oxidation, all complexes shows 8–12% of Fe^{III} species. Further supportive informations, on admixture of CP in **1**–**4**, were obtained from diffuse reflectance spectra (Fig. 2c). The broad band of $^5T_{2g} \rightarrow {}^5E_g$ around 800 nm clearly indicates the presence of more than one HS species. It has to be noted that even though the spectrum for **2** does not show multiple species, the band around 800 nm begin to split hinting the formation of other species when recorded in air atmosphere. The fact that self-assembly of HGlytz occurs in these CPs is highly desirable in the field

of self-assembled monolayers (SAM) where advantage of unbound carboxylic groups could be explored further in binding to a wide variety of substrate while maintaining the functional core intact [7].

Acknowledgements We gratefully acknowledge support from IAP INANOMAT, the FNRS (2.4508.08, 4.4507.10), a ARC grant of the Académie Universitaire Louvain and from the Groupe Francophone de Spectromètrie Mössbauer for supporting A. D. N. to attend GFSM 2011 (Strasbourg) and ICAME 2011 (Kobe).

References

1. Dîrtu, M.M., Naik, A.D., Marchand-Brynaert, J., Garcia, Y.: Room temperature hysteretic spin transition in 1D iron(II) coordination polymers. J. Phys. Conf. Ser. **217**, 012085 (2010)
2. Dîrtu, M.M., Schmit, F., Naik, A.D., Rotaru, A., Marchand-Brynaert, J., Garcia, Y.: Spin transition sensors based on β-amino-acid 1,2,4-triazole derivative. Int. J. Mol. Sci. **12**, 5339 (2011)
3. Naik, A.D., Beck, J., Dîrtu, M.M., Bebrone, C., Tinant, B., Robeyns, K., Marchand-Brynaert, J., Garcia, Y.: Zinc complexes with 1,2,4-triazole functionalized amino acid derivatives: Synthesis, structure and β lactamase assay. Inorg. Chim. Acta **368**, 21 (2011)
4. Naik, A.D., Dîrtu, M.M., Léonard, A., Tinant, B., Marchand-Brynaert, J., Su, B.L., Garcia, Y.: Engineering three-dimensional chains of porous nanoballs from a 1,2,4-triazole-carboxylate supramolecular synthon. Cryst. Growth Des. **10**, 1798 (2010)
5. Dîrtu, M.M., Neuhausen, C., Naik, A.D., Léonard, A., Robert, F., Marchand-Brynaert, J., Su, B.L., Garcia, Y.: Superlative scaffold of 1,2,4-triazole derivative of glycine steering linear chain to a chiral helicate. Crystal Growth Des. **11**, 1375 (2011)
6. Dîrtu, M.M., Rotaru, A., Gillard, D., Linares, J., Codjovi, E., Tinant, B., Garcia, Y.: Prediction of the spin transition temperature in Fe^{II} one dimensional coordination polymers: an anion based database. Inorg. Chem. **48**, 7838–7852 (2009)
7. Naik, A.D., Stappers, L., Snauwaert, J., Fransaer, J., Garcia, Y.: A biomembrane stencil for crystal growth and soft lithography of a thermochromic molecular sensor. Small **6**, 2842 (2010)

Hyperfine Interact (2012) 205:63–67
DOI 10.1007/s10751-011-0426-1

Gold-surface binding of molecular switches studied by Mössbauer spectroscopy

Patrick Homenya · Markus Messerschmidt · Muhammad Nawaz Tahir · Victor Martinez · Yajun Cheng · Jochen S. Gutmann · Michael Klein · Stefan Jung · Morris Wolff · Reza Saadat · Driss Nariaki · Roman Boča · Göstar Klingelhöfer · Wolfgang Tremel · Franz Renz

Published online: 11 November 2011

Abstract The nonanuclear coordination compound $[Mo^{IV}\{(CN)Fe^{III}(3\text{-methyl-saldptn})\}_8]Cl_4$ exhibits multiple spin transitions (3-methyl-saldptn = N,N′-bis(3″-methyl-2″-hydroxy-benzyliden)-1,7-diamino-4-azaheptane). This spin crossover cluster is bound via a self-assembled monolayer onto a two dimensional array gold surface. Mössbauer spectroscopy indicates that the thermally and optically induced spin crossover of the compound is maintained. Thereby, the foundation for its potential practical application (e.g. in the field of information storage) was laid.

Keywords Nonanuclear · Spin crossover · Au surface · Self-assembled monolayer · Mössbauer spectroscopy

P. Homenya (✉) · M. Klein · S. Jung · M. Wolff · R. Saadat · D. Nariaki · F. Renz
Institut für Anorganische Chemie, Leibniz Universität Hannover, Callinstr. 9, 30167 Hannover, Germany
e-mail: patrick.homenya@acd.uni-hannover.de

F. Renz
e-mail: franz.renz@acd.uni-hannover.de

M. Messerschmidt · M. Nawaz Tahir · Y. Cheng · G. Klingelhöfer · W. Tremel
Institut für Anorganische Chemie und Analytische Chemie, Johannes Gutenberg-Universität Mainz, Duesbergweg 10–14, 55099 Mainz, Germany

J. S. Gutmann
Max Planck-Institut für Polymerforschung, Ackermannweg 8, 55128 Mainz, Germany

V. Martinez
Institut de Ciencia Molecular, University of Valencia, Valencia, Spain

R. Boča
Institute of Inorganic Chemistry, Slovak Technical University (FCHPT), Bratislava, Slovakia

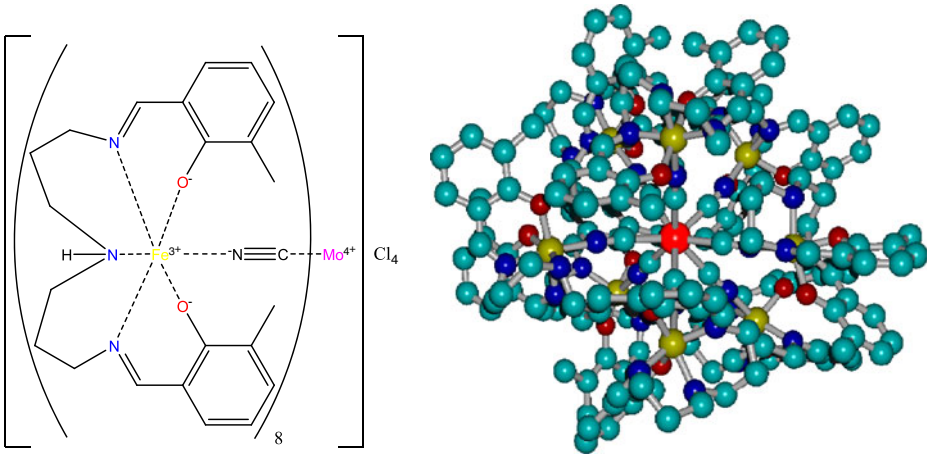

Fig. 1 Structural formula of $[Mo^{IV}\{(CN)Fe^{III}(3\text{-methyl-saldptn})\}_8]Cl_4$ **1** (*left*), Hyperchem 7 (MM+) calculated structure of the cation (*right*); hydrogen atoms are omitted for clarity

1 Introduction

The spin crossover is one of the most fascinating dynamic phenomena known in coordination chemistry. In this research area, switching between high spin and low spin states of a transition metal complex can be induced physically (e.g. by varying the temperature, applying pressure or through irradiation with light) or chemically (e.g. through solvate effects or pH influences) [1–4]. Recently, there has been interest in multinuclear systems in which an interplay between a spin crossover effect and magnetic exchange interactions occurs [5–8]. Among them is the star-shaped nonanuclear coordination compound $[Mo^{IV}\{(CN)Fe^{III}(3\text{-methyl-saldptn})\}_8]Cl_4$ **1** (3-methyl-saldptn = N,N′-bis(3″-methyl-2″-hydroxy-benzyliden)-1,7-diamino-4-azaheptane) (Fig. 1) [9–11].

Within **1** each iron center is potentially able to exhibit a thermally and optically induced spin crossover between the low-spin (LS; ^2T; S = 1/2) and the high-spin (HS; ^6A; S = 5/2) state [8–11]. Hence, **1** may contain between 8 and 40 unpaired electrons and offers a maximum of 8 potential spin transitions.

Many potential technical applications (e.g. in the field of information storage) require an individual addressing of these special molecular magnets, which is imaging, reading and eventually the manipulation of the molecules. In this instance, the concept of the self-assembled monolayers provides a suitable basis in order to obtain a monolayer of the spin crossover compound on various substrates [12].

In this case, a smooth gold surface was chosen due to its relatively inertness, the easy preparation, the well-defined order and since it offers the possibility of addressing the clusters individually by scanning probe microscopy (atomic force microscopy). Furthermore, an adsorption process onto a thin gold surface can be monitored by surface plasmon resonance spectroscopy [13].

The observation of the surface binding by surface plasmon resonance as well as the nanoscopic appearance of the individual nonanuclear complexes displayed by AFM and TEM imaging would exceed the extend of this article and will be published soon.

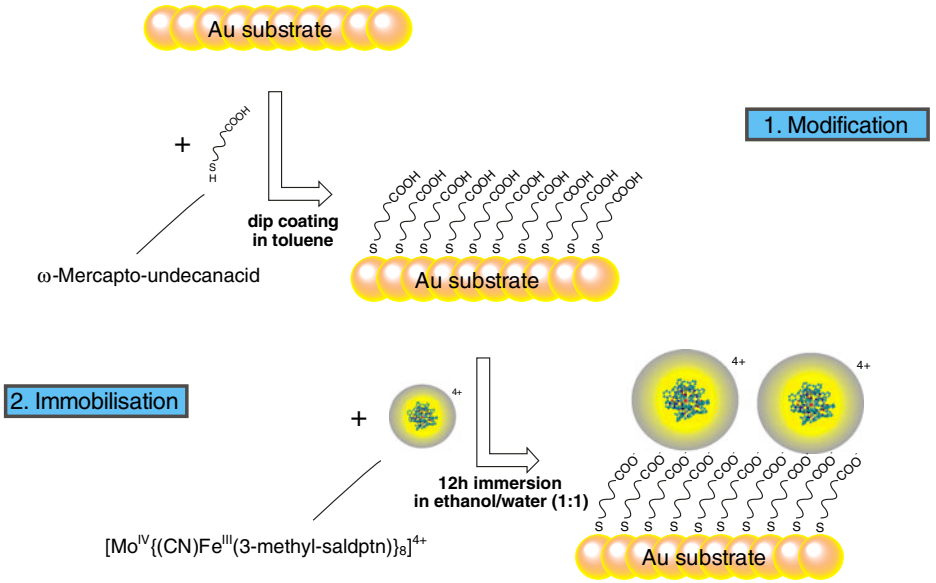

Fig. 2 Graphical representation of the immobilisation of $[Mo^{IV}\{(CN)Fe^{III}(3\text{-methyl-saldptn})\}_8]Cl_4$ **1** using a self-assembled monolayer

In this contribution the effect of the immobilisation on the nonanuclear spin crossover compound is demonstrated by direct comparison of bulk and surface Mössbauer spectroscopic measurements.

2 Experimental

2.1 Nonanuclear complex **1**

$[Mo^{IV}\{(CN)Fe^{III}(3\text{-methyl-saldptn})\}_8]Cl_4$ was synthesized as described in [12].

2.2 Immobilisation of $[Mo^{IV}\{(CN)Fe^{III}(3\text{-methyl-saldptn})\}_8]Cl_4$ onto a gold surface

The immobilisation results from electrostatic interactions between a modified and therefore negatively charged gold surface and the four-times positively charged complex (Fig. 2).

The gold surface is prepared by deposition of a 50 nm gold layer at a freshly cleaved mica slide. Onto this substrate a monolayer of ω-mercapto-undecane acid is deposited by a dip coating process in toluene. After cleaning the slides with 2-propanol, the clusters are bound ionically by a dip coating process as well: A solution of 10 mg $[Mo^{IV}\{(CN)Fe^{III}(3\text{-methyl-saldptn})\}_8]Cl_4$ dissolved in 20 mL of a ethanol/water mixture in a 1:1 ratio is prepared. The carboxylic acid modified gold surface is immersed in this solution for 12 h. Afterwards the slides are washed with 2-propanol three times. To remove the clusters from the surface an aqueous 0.1 molar $CaCl_2$ solution can be used.

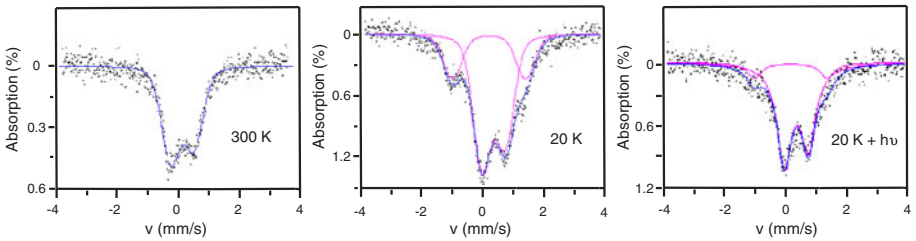

	300 K			20 K					
Surface bound	*Site 1*			*Site 1*			*Site 2*		
	Pop[%]	IS	QS	Pop[%]	IS	QS	Pop[%]	IS	QS
1	100	0.35	0.82	72	0.47	0.81	28	0.31	2.45
1 + hυ				85	0.47	0.80	14.8	0.28	2.45
Bulk material [11]	*Site 1*			*Site 1*			*Site 2*		
	Pop[%]	IS	QS	Pop[%]	IS	QS	Pop[%]	IS	QS
1	100	0.35	0.82	83	0.48	0.80	17	0.26	2.5

Fig. 3 Mössbauer spectra of immobilised $[Mo^{IV}\{(CN)Fe^{III}(3\text{-methyl-saldptn})\}_8]Cl_4$ clusters on Au(111) surfaces using a self-assembled monolayer

3 Results and discussion

Mössbauer measurements were performed in transmission and reflection geometry using a constant acceleration spectrometer and a helium bath cryostat. ^{57}Fe Mössbauer spectra were recorded between room temperature and 20 K using the 50 mCi source ^{57}Co(Rh). The RECOIL 1.03 Mössbauer Analysis Software was used to fit the experimental spectra [14]. Isomeric shift values are quoted relative to α-Fe at 293 K.

The measurements indicate that the spin crossover was maintained: Fig. 3 shows the temperature-dependent Mössbauer spectra of the nonanuclear compound **1** bound to a gold surface. As expected the measurements in reflection geometry show a less intensity in comparison to the bulk measurements [11]. In the Mössbauer spectrum at 300 K a quadrupole splitted doublet is observed which is slightly broadened due to relaxation, common for Fe(III) in its HS state (S = 5/2) [9, 10]. At 20 K the Mössbauer spectrum shows in addition to the Fe(III) in the HS state a second doublet which is characteristic for a Fe(III) in the LS state [9, 10]. A light irradiation (25 mW/cm^2, 514.5 nm green argon ion laser) at 20 K significantly alters the population of both states reversibly. Hence, the nonanuclear compound did not lose its thermal and optical "switchability" during the immobilisation to the gold surface. At 20 K the LS state is altered by ca. 11%, which is remarkably small with respect to a matrix and an anion exchange from chloride to carboxylate. **1** clearly exhibits after the immobilisation a thermally induced spin transition between HS and LS state. The area fraction of the respective doublets A(Fe^{III}-HS): A(Fe^{III}-LS) indicates that several Fe(III) centres switch. Therefore, there is a multiple electronic transition.

These results indicate that a surface bound cluster of **1** still bears the potential to act as a switch. Furthermore, those findings emphasize the possibility of fabricating

molecule based low-dimensional structures of spin crossover compounds by using self-assemled monolayers.

Acknowledgements Grant Agencies (Slovakia: VEGA 1/0052/11, VVCE 0004-07; Germany: Leibniz University, LNQE, ZFM; Uni Mainz, MWFZ; DAAD; DFG Re-1627; EU: Structural Funds, Interreg IIIA) are acknowledged for the financial support.

References

1. Gütlich, P., Goodwin, H.A.: Spin Crossover in Transition Metal Compounds I-III. Springer, Heidelberg (2004)
2. Renz, F.: Physical and chemical induced spin crossover. J. Phys.: Conf. Ser. **217**, 012022 (2010)
3. Kahn, O.: Molecular Magnetism. VCH, New York (1993)
4. Gütlich, P., Hauser, A., Spiering, H.: Thermisch und optisch schaltbare Eisen(II)-Komplexe. Angew. Chem. **106**, 2109–2141 (1994)
5. Brooker, S., Plieger, P.G., Moubaraki, B., Murray, K.S.: The first cobalt complex to exhibit both exchange coupling and spin crossover effects. Angew. Chem. Int. Ed. **38**, 408–410 (1999)
6. Real, J.A., Gaspar, A.B., Muñoz, M.C., Gütlich, P., Ksenofontov, V., Spiering, H.: Bipyrimidine-bridged dinuclear iron(II) spin crossover compounds. Top. Curr. Chem. **233**, 167–193 (2004)
7. Herchel, R., Boca, R., Gembicky, M., Kozisek, J., Renz, F.: Spin crossover in a tetranuclear Cr(III)-Fe(III)$_3$ complex. Inorg. Chem. **14**, 4103–4105 (2004)
8. Gaspar, A.B., Ksenofontov, V., Seredyuk, M., Gütlich, P.: Multifunctionality in spin crossover materials. Coord. Chem. Rev. **249**, 2661–2676 (2005)
9. Renz, F., Kerep, P.: The Nonanuclear [Mo(IV){(CN)Fe(III)(3-ethoxy-saldptn)}8]Cl4 complex compound exhibits multiple spin transitions observed by Mössbauer spectroscopy. Hyperfine Interact. **156**, 371–377 (2004)
10. Renz, F., Hill, D., Kerep, P., Klein, M., Müller-Seipel, R., Werner, F.: Effect of N-substitution in multinuclear complexes allows interplay between magnetic states and multistability investigated by Mossbauer spectroscopy. Hyperfine Interact. **168**, 1051–1056 (2006)
11. Tahir, M.N., Messerschmidt, M., Klein, M., Martinez, V., Theato, P., Metz, N., Hartmann, S., Kolb, U., Ksenofontov, V., Renz, F., Tremel, W.: Synthesis and immobilization of molecular switches onto titaniumdioxide nanowires. Polyhedron **28**, 1728–1733 (2009)
12. Schreiber, F.: Structure and growth of self-assembling monolayers. Prog. Surf. Sci. **65**, 151–256 (2000)
13. Gonzlez-Díaz, J.B., García-Martín, A., García-Martín, J.M., Cebollada, A., Armelles, G., Sepúlveda, B., Alaverdyan, Y., Käll, M.: Plasmonic Au/Co/Au nanosandwiches with enhanced magneto-optical activity. Small **4**, 202–205 (2008)
14. Lagarec, K., Rancourt, D.G.: Extended Voigt-based analytic lineshape method for determining N-dimensional correlated hyperfine parameter distributions in Mössbauer spectroscopy. Nucl. Instrum. Methods B **129**, 266–280 (1997)

Hyperfine Interact (2012) 205:69–73
DOI 10.1007/s10751-011-0402-9

Impact of ligand spacer and counter-anion in selected 1D iron(II) spin crossover coordination polymers

Marinela M. Dîrtu · France Schmit · Anil D. Naik · Aurelian Rotaru · Jacqueline Marchand-Brynaert · Yann Garcia

Received: 31 August 2011 / Accepted: 30 September 2011 / Published online: 13 October 2011

Abstract A new 1D coordination polymer $[Fe(\beta Alatrz)_3](ClO_4)_2 \bullet H_2O$ (1) with a neutral bidentate ligand, βAlatrz = 4H-1,2,4-triazol-4-yl-propionate, was prepared and its magnetic behavior was investigated by temperature dependent magnetic susceptibility measurements and ^{57}Fe Mössbauer spectroscopy. The temperature dependence of the high-spin molar fraction derived from ^{57}Fe Mössbauer spectroscopy recorded on cooling below room temperature reveals a gradual single step transition with $T_{1/2} = 173$ K between high-spin and low-spin states in agreement with magnetic susceptibility measurements. 1 presents striking reversible thermochromism from white, at room temperature, to pink on quench cooling to liquid nitrogen. The phase transition is of first order as deduced from differential scanning calorimetry, with $T_{1/2}$ matching the one determined by both SQUID and ^{57}Fe Mössbauer spectroscopy. A brief assessment has been made among closely related 1D coordination polymers to perceive the effect of ligand spacer length and anion effect on the spin crossover behavior of these new materials.

Keywords Coordination polymers · β-amino-acid · Spin-transition · 1,2,4-triazole · ^{57}Fe Mössbauer spectroscopy

M. M. Dîrtu · F. Schmit · A. D. Naik · J. Marchand-Brynaert · Y. Garcia (✉)
Institute of Condensed Matter and Nanosciences, Université Catholique de Louvain,
Place L. Pasteur 1, 1348 Louvain-la-Neuve, Belgium
e-mail: yann.garcia@uclouvain.be

A. Rotaru
Department of Electrical Engineering and Computer Science, "Stefan cel Mare" University,
University Street, No. 13, Suceava 720229 Romania

1 Introduction

The influx of a large number of contributions in the spin crossover (SCO) area significantly amplified the understanding of the phenomena, technological aspects and performances tuning, and revealed futuristic applications in the fabrication of molecular based sensors, memory devices, etc [1, 2]. In a typical Fe^{II} SCO compound the reversible electron transfer from a diamagnetic low-spin (LS, $^1A_{1g}$) state to a thermally populated paramagnetic high-spin (HS, $^5T_{2g}$) state is recognized as an entropy driven process and could be addressed thermally, optically, and electrically with a highly profound feedback [1, 2]. Derivatives of 4-substituted-1,2,4-triazole have long been an attractive scaffold in the design of such SCO compounds due to their diverse binding modes and bridging properties resulting in topologies varying from mononuclear complexes to high dimensional coordination polymers [1, 2, 4–7]. Recently we have introduced derivatives of α-amino acid (ethyl-4H-1,2,4-triazol-4-yl-acetate, **αGlytrz**) [3] and a β-amino acid (4H-1,2–4-triazol-4-yl-propionate, **βAlatrz**) [4] which differs by a carbon spacer (Fig. 1) and reported interesting magnetic sensors. In continuation of this work we have synthesized and investigated SCO properties of a new member: $[Fe(\beta\textbf{Alatrz})_3](ClO_4)_2{\cdot}H_2O$ (**1**) and made a brief comparison to its reported counterpart $[Fe(\beta\textbf{Alatrz})_3](CF_3SO_3)_2{\cdot}0.5H_2O$ (**2**) [4] having an anion of different geometry and one carbon less predecessor $[Fe(\alpha\textbf{Glytrz})_3](ClO_4)_2{\cdot}MeOH$ (**3**) [3].

2 Results and discussion

βAlatrz (Fig. 1a) was prepared according to the reported procedure [4]. A white powder was isolated from the reaction of **βAlatrz** and $[Fe(H_2O)_6](ClO_4)_2$ in a 3:1 ratio from methanol. Based on elemental and thermogravimetric analysis it was formulated as $[Fe(\beta\textbf{Alatrz})_3](ClO_4)_2{\cdot}H_2O$ (**1**). SEM image on bulk sample of 1 shows highly aggregated ∼2 μm diameter amorphous granules (Fig. 1c) that is confirmed by a poor X-ray powder diffraction (XRPD) pattern (Fig. 2a).

The carboxylic group of ester in **βAlatrz** shows two stretching vibrations corresponding to (C=O) and (C-O) at 1,728(s) and 1,205(s) cm^{-1}, respectively, which are almost unchanged (1,730 and 1,209 cm^{-1}) in **1** and ensures the stability of sensitive ester functional group. Inclusion of non coordinated perchlorate anion is confirmed by the strong characteristic band around 1,097 cm^{-1}. We conclude that **βAlatrz** bridges iron ions in a *N*1, *N*2-mode thus forming 1D chains which was also confirmed in **2** [4] and **3** [3]. The color of **1** is understood thanks to the diffuse reflectance spectrum (DRS) due to spin-allowed lowest energy d-d transition, $^5T_{2g} \rightarrow {}^5E_g$, for the HS sites (∼910 nm) and $^1A_{1g} \rightarrow {}^1T_{1g}$ and $^1A_{1g} \rightarrow {}^1T_{2g}$ d-d transitions of LS Fe^{II} sites at ∼450 nm (a weak bump) and ∼375 nm, respectively [8], suggesting coexistence of both spin states at room temperature (Fig. 2b). **1** presents a reversible thermochromism to dark pink upon cooling to $N_{2(l)}$ giving a good indication to the presence of SCO. From the magnetic susceptibility plot (Fig. 2c), it is found that $\chi_M T$ increases slightly from 0.12 cm^3 K mol^{-1} at 4 K to 0.38 cm^3 K mol^{-1} at 64 K, which is indicative of a small amount of HS Fe^{II} at low temperature. Between 64 K and 175 K $\chi_M T$ increases slowly and then more abruptly to reach a maximum of 2.98 cm^3 K mol^{-1} at 300 K, indicating an incomplete spin conversion. In the

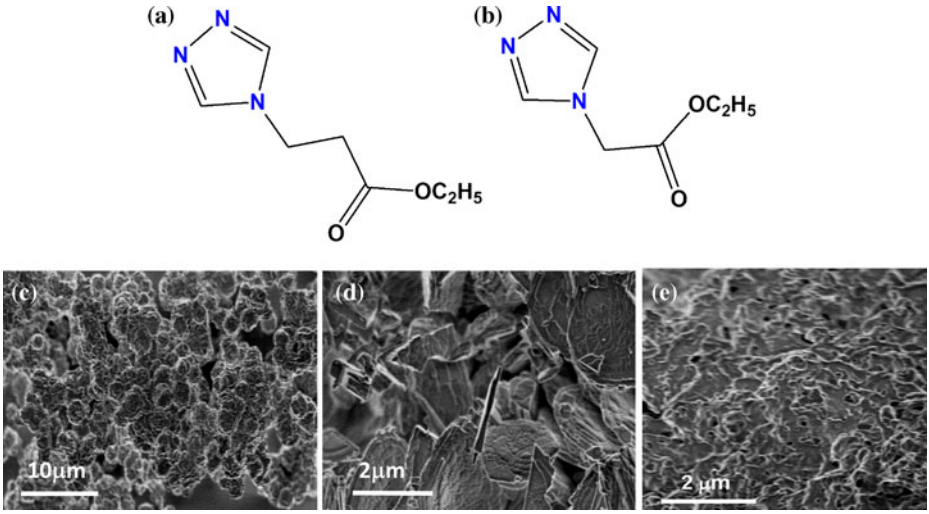

Fig. 1 Molecular structure of **βAlatrz** (**a**) and (**b**) **αGlytrz**. Comparison of texture of particles in bulk samples (**c**) **1** (**d**) **2** (**e**) **3**

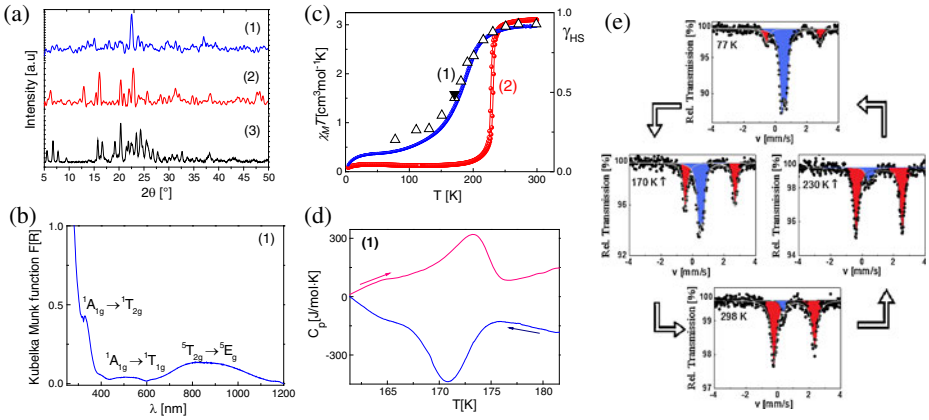

Fig. 2 (**a**) Comparative XRPD pattern for **1–3**. (**b**) DRS spectrum at r.t. for **1**. (**c**) Thermal variation of $\chi_M T$ in **1** and **2** and of γ_{HS} for **1** (triangles). (**d**) Heat capacity profiles for **1** derived from DSC at 10 K/min. The arrows indicate the cooling (←) and warming (→) modes, respectively. (**e**) Selected Mössbauer spectra for **1** showing LS and HS signals (in blue and red, respectively). The arrows indicate the followed thermal pathway

cooling mode the gradual character of the SCO is maintained with $T_{1/2} = 173$ K. Thermodynamic parameters for the SCO event in **1** was evaluated from differential scanning calorimetry (DSC) measurement. An endothermic peak was observed on warming at $T^{\uparrow}_{max} = 173$ K and an exothermic peak is recorded at $T^{\downarrow}_{max} = 171$ K, on cooling. The enthalpy $\Delta H^{HL} = 3.63$ kJ.mol^{-1} and entropy $\Delta S^{HL} = 21.1$ J.mol^{-1}K^{-1} taking into account the active SCO ions were derived.

Table 1 Selected ^{57}Fe Mossbauer parameters for **1**

T[K]	δ [mm/s]	ΔE_Q[mm/s]	$\Gamma/2$[mm/s]	Rel. area [%]	Species
77(1)	1.15(2)	3.40(1)	0.19(1)	20	HS
	0.54(1)	0.29(1)	0.15(1)	80	LS
130(1)	1.14(1)	3.21(2)	0.16(4)	27	HS
	0.54(7)	0.29(1)	0.16(1)	73	LS
170(1)	1.11(1)	3.14(2)	0.15(1)	47	HS
	0.54(1)	0.26(1)	0.13(1)	53	LS
190(1)	1.11(1)	3.06(1)	0.18(1)	69	HS
	0.54(1)	0.23(2)	0.14(1)	31	LS
215(1)	1.10(1)	2.97(1)	0.19(1)	83	HS
	0.43(1)	0.25(1)	0.18(1)	17	LS
250(1)	1.07(1)	2.81(1)	0.18(1)	92	HS
	0.25(2)	0.2*	0.15*	8	LS
298(1)	1.06(1)	2.56(1)	0.20(1)	93	HS
	0.51(1)	0.15*	0.15*	7	LS

δ: isomer shift (with respect to α-Fe at 298 K); ΔE_Q: quadrupole splitting; $\Gamma/2$: half width at half maximum, *fixed data

3 ^{57}Fe Mössbauer spectroscopy studies

Selected Mössbauer spectra are displayed in Fig. 2e and parameters are summarized in Table 1. At 77 K, the spectrum of **1** consists of two quadrupole doublets of different resonance area fractions. The major quadrupole doublet (80%) with isomer shift $\delta =$ 0.54(2) mm/s and quadrupole splitting, $\Delta E_Q = 0.29(2)$ mm/s corresponds to the LS state of Fe^{II}. The presence of a LS quadrupole splitting stems from a lattice contribution to the electric field gradient and therefore reveals a distorted character for the LS octahedron as expected for a constraint one within a 1D chain with a rigid linkage [7]. Another doublet, corresponding to HS Fe^{II} ions (20%), with $\delta = 1.14(1)$ mm/s and $\Delta E_Q = 3.15(2)$ mm/s confirms the incomplete nature of the ST at 77 K. Upon warming to 298 K, the area fraction of the HS doublet slowly increases until it reaches 93%, confirming a thermally induced LS $\rightarrow$ HS conversion. This conversion is incomplete, which is due to a small amount of LS species. Upon cooling back to 77 K, the HS and LS population follows a reverse trend. The temperature variation of δ^{HS}, of **1**, reveals a slight linear increase on cooling which is attributed to the second order Doppler shift. δ and ΔE_Q of both LS and HS species are typical of an $Fe^{II}N_6$ chain compound in which iron centers are bonded by triple *N*1,*N*2-triazole bridges [1].

A brief comparison of several aspects among **1–3** is necessary to understand the possible effect of texture of particles, ligand spacer and anion geometry on the observed variation of $T_{1/2}$ values and different SCO behavior. **1** with $T_{1/2} =$ 173 K is nearly 58 K lower than **2** ($T^{\downarrow}_{1/2}$ = 228 K and $T^{\uparrow}_{1/2} = 232$ K) which shows an abrupt but incomplete SCO [4] which is however lower than **3** by 38 K [3]. The later shows an abrupt, complete SCO with $T^{\downarrow}_{1/2}$ = 263 K and $T^{\uparrow}_{1/2}$ = 273 K [3]. Thus, with a similar anion but with one carbon less in the ligand spacer, the $T_{1/2}$ is considerably raised in **3** (by 38 K) which could be due to the compactness of molecular packing with smaller ligand scaffold, thereby strengthening cooperative and supramolecular interactions within the closer chains. Nevertheless, the important role of non coordinated solvent in **1** and **3** cannot be ignored. At the microscopic

level, it can be seen that **2**, which includes a linear type anion is highly crystalline with large hexagonal plates. In contrast, particles in **1** are highly aggregated and amorphous. In **3**, although XRPD is very different, SEM image shows undefined particles shape. These varied textures are expected to induce defects that ultimately could affect SCO behaviour. Thus **2** has shown more appealing SCO properties compared to **1** despite sharing the same framework and lattice solvent. Indeed this is modulated further by different secondary interactions brought by different geometry and electro-negativity of anions.

Acknowledgements We acknowledge financial support from IAP-VI (P6/17) INANOMAT, the Fonds National de la Recherche Scientifique (FNRS) (FRFC 2.4508.08, IISN 4.4507.10), the European Social Fund through Sectorial Operational Program Human Resources: PRiDE (No POSDRU/89/1.5/S/57083) and from a Concerted Research Action of the "Communauté Française de Belgique" allotted by the Académie Universitaire Louvain. We thank the Groupe Francophone de Spectromètrie Mössbauer (GFSM) for supporting A. D. N to attend ICAME 2011 (Kobe) and GFSM 2011 (Strasbourg). J. M. B. is a senior research associate of the F.R.S.-FNRS.

References

1. Gütlich, P., Garcia, Y., Goodwin, H.A.: Spin crossover phenomena in Fe(II) complexes. Chem. Soc. Rev. **29**, 419–427 (2000)
2. Bousseksou, A., Molnar, G., Salmon, L., Nicolazzi, W.: Molecular spin crossover phenomenon: recent achievements and prospects. Chem. Soc. Rev. **40**, 3313–3335 (2011)
3. Dîrtu, M.M., Naik, A.D., Marchand-Brynaert, J., Garcia, Y.: Room temperature hysteretic spin transition in 1D Iron(II) coordination polymers. J. Phys. Conf. Ser. **217**, 012085 (2010)
4. Dîrtu, M.M., Schmit, F., Naik, A.D., Rotaru, A., Marchand-Brynaert, J., Garcia, Y.: Spin transition sensors based on ß-amino-acid 1,2,4-triazole derivative. Int. J. Mol. Sci. **12**, 5339–5351 (2011)
5. Dîrtu, M.M., Rotaru, A., Gillard, D., Linares, J., Codjovi, E., Tinant, B., Garcia, Y.: Prediction of the spin transition temperature in Fe^{II} one-dimensional coordination polymers: an anion based database. Inorg. Chem. **48**, 7838–7852 (2009)
6. Dîrtu, M.M., Neuhausen, C., Naik, A.D., Rotaru, A., Spinu, L., Garcia, Y.: Insights into the origin of cooperative effects in the spin transition of $[Fe(NH_2trz)_3](NO_3)_2$: the role of supramolecular interactions evidenced in the crystal structure of $[Cu(NH_2trz)_3](NO_3)_2H_2O$. Inorg. Chem. **49**, 5723–5736 (2010)
7. Dîrtu, M.M., Garcia, Y., Nica, M., Rotaru, A., Linares, J., Varret, F.: Iron(II) spin transition 1,2,4-triazole chain compounds with novel inorganic fluorinated counteranions. Polyhedron **26**, 2259–2263 (2007)
8. Gütlich, P., Jung, J., Goodwin, H.A.: In: Coronado, E., Delhaès, P., Gatteschi, D., Miller, J.S. (eds.) Molecular Magnetism: From Molecular Assemblies to the Devices (1996)

Hyperfine Interact (2012) 205:75–79
DOI 10.1007/s10751-011-0412-7

Weak cooperativity in selected iron(II) 1D coordination polymers

Marinela M. Dîrtu · Damien Gillard · Anil D. Naik · Aurelian Rotaru · Yann Garcia

Published online: 16 November 2011

Abstract The spin crossover behaviour of a new class of Fe^{II} coordination polymers $[Fe(phtptrz)_3]I_2$ (**1**), $[Fe(phtptrz)_3](ReO_4)_2 \bullet CH_3OH$ (**2**) and $[Fe(phtptrz)_3]TaF_7 \bullet 6H_2O$ (**3**) based on a novel ligand 4-(3′-N-phtalimido-propyl)-1,2,4-triazole (phtptrz), were investigated by temperature dependent ^{57}Fe Mössbauer spectroscopy and magnetic susceptibility measurements. The adverse effect of bulky substituent on 1,2,4-triazole, favorable supramolecular interactions and influence of increasing anion size on spin crossover profile is discussed. **1** and **2** show thermally induced spin conversions of gradual and incomplete nature with associated thermochromism, and transition temperatures $T_{1/2} \sim 163$ K and 137 K, respectively. A spin state crossover is also identified for **3**.

Keywords ^{57}Fe Mössbauer spectroscopy · Coordination polymers · Spin-transition · 1,2,4-triazole

1 Introduction

Cooperativity factors which determine the importance in iron(II) spin crossover (SCO) materials performances have long been the subject matter of intensive research with targeted fascinating applications in sensor and memory devices [1, 2]. Abruptness, completeness and hysteresis width/shape of magnetic profiles are key elements to probe strength of cooperative interactions in SCO complexes which can be influenced by ligand design, anion geometry and charge, crystal defects, solvent

M. M. Dîrtu · D. Gillard · A. D. Naik · Y. Garcia (✉)
Institute of Condensed Matter and Nanosciences, MOST – Inorganic Chemistry,
Université Catholique de Louvain, Place L. Pasteur 1, 1348 Louvain-la-Neuve, Belgium
e-mail: ann.garcia@uclouvain.be

A. Rotaru
Department of Electrical Engineering and Computer Science, "Stefan cel Mare" University,
University Street, 13, Suceava 720229, Romania

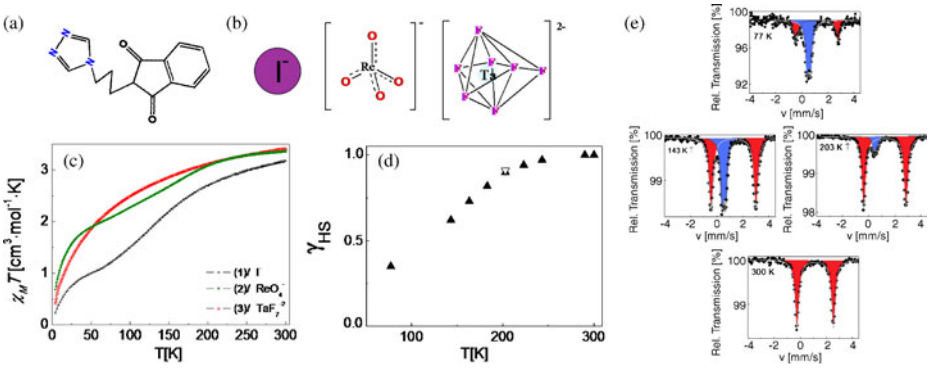

Fig. 1 **a** Molecular structure of phtptrz. **b** variation of anion geometry and charge. **c** $\chi_M T$ vs. T plot for **1–3**. **d** γ_{HS} vs. T curve on cooling and warming modes for **1**. **e** Selected ^{57}Fe Mössbauer spectra for **1**

occupancy etc. [3]. Self-assembled coordination polymers (CPs) represent a family of compounds where precisely organised molecular building blocks generate a long range cooperative phenomenon that has effective means of propagation through rigid covalent bonding and flexible supramolecular interactions [4]. Although this situation is usually set for small ligand modules, larger molecular fragments such as dendrimers [5] or extended alkyl chains [6] often show promising SCO profiles without cooperativity loss thus reviewing the selection criteria of ligand topology. We introduce in this context a new module for CPs: 4-(3′-N-phtalimido-propyl)-1,2,4-triazole (phtptrz) (Fig. 1a) where a bulky substituent is attached to *N*4 of 1,2,4-triazole via a multiple carbon spacer. This aromatic group, although bulkier, is a potential promoter of supramolecular interactions due to $\pi - \pi$ stacking and H-bonding interactions involving carbonyl groups. Further, influence of modifying anions geometry (spherical I^-, tetrahedral ReO_4^-, monocapped trigonal prism TaF_7^{2-}) and charge (monovalent and bivalent) is evidenced in the series of $[Fe(phtptrz)_3]I_2$ (**1**), $[Fe(phtptrz)_3](ReO_4)_2 \bullet CH_3OH$ (**2**) and $[Fe(phtptrz)_3]TaF_7 \bullet 6H_2O$ (**3**) whose spin switching properties are discussed herein.

2 Experimental

The phtptrz molecule was prepared according to ref [7]. Complexes were prepared as white powders by reacting phtptrz to $[Fe(H_2O)_6]^{2+}$ including a suitable anion (I^-, ReO_4^-, TaF_7^{-2}, Fig. 1b) in a 1:3 ratio in MeOH/H_2O following ref [8]. Spectroscopic, microanalysis and thermal analyses lead to the formulation of the new 1D coordination polymers **1–3**. Magnetic measurements were recorded on a SQUID device.

3 Results and discussion

Preliminary indications of SCO occurrence were obtained by a clear thermochromic response on quench cooling of the materials to $N_{2(l)}$. Indeed, white powders of **1** and **2**

Table 1 Comparison of ^{57}Fe Mössbauer parameters for **1**–**3**

Compound	T[K]	δ[mm/s]	ΔE_Q[mm/s]	$\Gamma/2$[mm/s]	$A_{HS}/A_{tot.}$	Spin state
1	300	1.13(1)	2.78(1)	0.18(1)	100	HS
	77	1.17(1)	3.25(1)	0.19(1)	35	HS
		0.55(1)	0.29(1)	0.16(1)	65	LS
2	300	1.09(1)	2.84(1)	0.22(1)	100	HS
	77	1.18(1)	3.21(1)	0.18(1)	75	HS
		0.51(1)	0.10(1)	0.19(1)	25	LS
3	300	1.09(1)	2.84(2)	0.18(1)	100	HS
	77	1.18(1)	3.36(1)	0.17(1)	75	HS
		0.31(1)	0.65(1)	0.23(1)	25	LS

δ: isomer shift (with respect to α-Fe at 300 K); ΔE_Q: quadrupole splitting; $\Gamma/2$: half width at half maximum; A_{HS}: Area of HS doublet; A_{tot}: total area

show reversible colour change to pink, contrary to **3**. Variable temperature magnetic susceptibility measurements for **1–3** were recorded over the temperature range 300–4 K (Fig. 1c). These SQUID measurements reveal a very smooth incomplete spin conversion for **1** and **2** with transition temperatures $T_{1/2} \sim 163$ K and 137 K, respectively. For **1** the room temperature $\chi_M T$ value of 3.18 cm^3 mol^{-1} K corresponds to high-spin (HS) Fe^{II} species. When cooled, this value gradually decreases to 1.1 cm^3 mol^{-1} K around 72 K after which the inflection becomes more gradual until 27 K, revealing an incomplete spin conversion. The subsequent drop of $\chi_M T$ at lower temperatures is attributed to zero-field splitting (ZFS) of remaining HS Fe^{II} species. This type of spin conversion is commonly observed for Fe^{II} complexes having a voluminous substituent on the *N*4 position of the triazole ring [9]. Complex **2** with ReO_4^- as counter anion has a similar magnetic profile; however, the decrease in $\chi_M T$ begins at a higher value, 3.42 cm^3 mol^{-1} K at 300 K, which is consistent with the HS state. It is followed by a slow decrease to 1.8 cm^3 mol^{-1} K at 40 K, after which ZFS causes a decrease in $\chi_M T$ product. In contrast, the magnetic curve of **3** does not apparently reflect any SCO process. As the temperature is lowered, the $\chi_M T$ value smoothly decreases until 50 K and drops rapidly below this temperature reaching a minimum at 4 K. Such a magnetic curve indicates very weak antiferromagnetic (AF) interactions between HS Fe^{II} ions. The best fit of the magnetic data with a Curie-Weiss law afforded a Weiss temperature $\theta = -55$ K, $g = 2.30(5)$ and by considering the number of nearest neighbours atoms ($z = 2$) [10], $J/k_B = -13(1)$ K was derived. The absence of maximum in the χ_M vs. T. plot confirms the weak AF coupling nature in **3**.

^{57}Fe Mössbauer spectroscopy further reveals variation of temperature dependent population of spin states in **1–3**. Selected Mossbauer spectra are shown in Fig. 1e and parameters are summarized in Table 1. In **1**, a quadrupole doublet (100% population) with isomer shift $\delta = 1.13(1)$ mm.s^{-1} and quadrupole splitting $\Delta E_Q = 2.78(1)$ mm.s^{-1} is identified at 300 K which is clearly indicative of HS Fe^{II} species. A slight asymmetry of the lines is observed which is attributed to a texture effect. On cooling, a spin conversion to the low-spin (LS) state is identified with appearance of a new signal depicted in blue at 203 K and 143 K. Indeed, at 77 K, another quadrupole doublet with $\delta^{LS} = 0.55(1)$ mm.s^{-1} and $\Delta E_Q^{LS} = 0.29(1)$ mm.s^{-1} is found, thus confirming the incomplete nature of the SCO process. For **2**, only 25% of HS

ions have switched to the LS state at 77 K whereas 65% have switched for **1**, in full agreement with SQUID data (Fig. 1c). Interestingly, δ^{HS}(77 K) for **1** and **2** are identical (Table 1) indicating absence of any appreciable change in the electronic distribution around each individual iron atoms. The absence of SCO is not confirmed for **3** as HS ions are detected at 300 K, whereas a mixture of LS/HS ions is probed at 77 K. Most interestingly, ΔE_Q^{LS}(77 K) is higher for **3** compared to **1**–**2** which indicate an important strained situation at the iron centers.

The trend in loss of SCO properties from **1** to **3** can be explained based on certain structural aspects. Although bulky substituent on the triazole ring with multiple carbon spacer of the ligand scaffold is not expected to give a favorable situation for cooperative SCO, as trinuclear species formation could have been expected [11], the affinity of $\pi - \pi$ stacking of aromatic groups and supramolecular interaction through carbonyl groups on the framework overcomes this barrier thus promoting the observed weakly cooperative SCO in **1** and **2**. This behaviour, which is also depicted in terms of variation of HS molar fraction derived by integration of the Mössbauer signals (Fig. 1d), indicates a cooperativity weakening which can be attributed too to a decrease of intermolecular contacts between chains. A clear influence of increasing anion size is consistent with a chain spacing [8]. The doubly charged voluminous anion in **3** considerably weakens cooperativity of the SCO system compared to singly charged anions [8], thereby leading to an almost HS material. Further incompleteness of SCO at lower temperature can also be attributed to steric factors that delay further growth of LS population. The progressive network shrinking during HS to LS conversion, on cooling, is thus halted due to network instability to further shrink that encounter steric clashes in the molecular packing with bulkier substitution, compared to 1D chains of the [Fe(4-amino-1,2,4-triazole)$_3$](anion)$_2$ series [4, 8].

Acknowledgements We acknowledge support from IAP INANOMAT, the Fonds National de la Recherche Scientifique (FNRS) (FRFC 2.4508.08, IISN 4.4507.10), the European Social Fund through Sectorial Operational Program Human Resources: PRiDE (No POSDRU/89/1.5/S/57083) and from a ARC Louvain. The Groupe Francophone de Spectrométrie Mössbauer is thanked for supporting A. D. N to attend ICAME 2011 (Kobe) and GFSM 2011 (Strasbourg).

References

1. Kahn, O., Kröber, J., Jay, C.: Spin transition molecular materials for displays and data recording. Adv. Mater. **4**, 718 (1992)
2. Garcia, Y., Ksenofontov, V., Gütlich, P.: Spin transition molecular materials: new sensors. Hyperfine Interact. **139/140**, 543 (2002)
3. Naik, A.D., Tinant, B., Muffler, K., Wolny, J.A., Schünemann, V., Garcia, Y.: Relevance of supramolecular interactions, texture and lattice occupancy in the designer iron(II) spin crossover complexes. J. Solid State Chem. **182**, 1365 (2009)
4. Garcia, Y., Niel, V., Muñoz, M.C., Real, J.A.: Spin crossover in 1D, 2D and 3D polymeric Fe(II) networks; spin crossover in transition metal compounds I. Top. Curr. Chem. **233**, 229 (2004)
5. Fujigaya, T., Jiang, D.-L., Aida, T.: Spin crossover dendrimers: generation number dependent cooperativity for thermal spin transition. J. Am. Chem. Soc. **127**, 5484 (2005)
6. Schlamp, S., Weber, B., Naik, A.D., Garcia, Y.: Cooperative spin transition in a lipid layer like system. Chem. Commun. **47**, 7152 (2011)
7. Boland, Y., Hertsens, P., Marchand-Brynaert, J., Garcia, Y.: New ditopic and tripodal 1,2,4-triazole-and tetrazole-based ligands for coordination chemistry. Synthesis **9**, 1504 (2006)
8. Dîrtu, M.M., Rotaru, A., Gillard, D., Linares, J., Codjovi, E., Tinant, B., Garcia, Y.: Prediction of the spin transition temperature in Fe^{II} one dimensional coordination polymers: an anion based database. Inorg. Chem. **48**, 7838–7852 (2009)

9. Wei, Y.L., Sonar, P., Grunert, M., Kusz, J., Schlüter, A.D., Gütlich, P.: Iron(II) spin transition complexes with dendritic ligands, Part II. Eur. J. Inorg. Chem. **25**, 3930 (2010)
10. Kahn, O.: Molecular Magnetism. Wiley (1993)
11. Garcia, Y., Guionneau, P., Bravic, G., Chasseau, D., Howard, J.A.K., Kahn, O., Ksenofontov, V., Reiman, S., Gütlich, P: Synthesis, crystal structure, magnetic properties and ^{57}Fe Mössbauer spectroscopy of the new trinuclear $[Fe_3(4\text{-}(2'\text{-hydroxy-ethyl})\text{-}1,2,4\text{-triazole})_6(H_2O)_6](CF_3SO_3)_6$ spin crossover compound. Eur. J. Inorg. Chem. 1531 (2000)

Hyperfine Interact (2012) 205:81–85
DOI 10.1007/s10751-011-0429-y

A Mössbauer spectroscopic study on the action of Ce in the catalyst for dehydrogenation of etylbenzene to styrene

Keyu Jiang · Qin Fan · Tong Chen · Changxi Miao · Zhenji Zhao · Xielong Yang

Published online: 11 November 2011

Abstract Two series of Fe-K catalysts for dehydrogenation of ethylbenzene to styrene were prepared with different amounts and different compounds of the additional element Ce. Mössbauer spectroscopy has been used to determine the Fe compound in the catalyst and to investigate the effect of Ce. The catalytic properties of the catalysts have also been measured. The results show that the element Ce in the catalyst is favorable to form the predecessor of the catalytic active phase, the compound $KFe_{11}O_{17}$ and that the optimal percentage of CeO_2 is 8%∼15% in the catalyst which is favorable to the formation of $KFe_{11}O_{17}$ and to get better catalytic properties.

Keywords Dehydrogenation of ethylbenzene · Mössbauer spectroscopy · Catalyst · Ce

1 Introduction

The most important catalyst used for dehydrogenation of ethylbenzene to styrene, is an iron-based catalyst. The main original material of the catalyst is ferric oxide (Fe_2O_3 or α-FeOOH) and potassium carbonate (K_2CO_3), in addition to other compounds of elements (Ce, Mg, Ti, Ca, et al). The amount of Ce compounds is more important than that of the compounds of other additional elements. In this work the present form of the Ce element in the catalyst and its catalytic function are investigated. On the other hand, in traditional catalysts the original compound of Ce is cerium nitrate. But this compound will be decomposed into nitrogen-oxides that

K. Jiang (✉) · Z. Zhao · X. Yang
Department of Physics, East China Normal University, Shanghai 200062, China
e-mail: keyujiang@126.com

Q. Fan · T. Chen · C. Miao
Shanghai Research Institute of Petrochemical Technology, SINOPEC, Shanghai 201208, China

could pollute our environment. So looking for a new substitute of cerium nitrate is also a focus of this work.

In our previous investigation using Mössbauer spectroscopy, it was determined that the fresh catalyst of potassium-promoted iron oxide contains a certain amount of potassium ferrite $KFe_{11}O_{17}$ with the spinel structure, which can be considered as the predecessor of the catalytic active phase [1]. It is also mentioned in other patents [2, 3]. In this work, Mössbauer spectroscopy was used to study the components of the products, especially to study the dependence between the formation of $KFe_{11}O_{17}$ and the amount of CeO_2 in the catalyst. Combining the Mössbauer spectroscopic results and the catalytic properties of the samples, the optimal amount of Ce could be determined and the best substitute of cerium nitrate could also be selected. This is useful information for manufacturing the industrial catalyst.

2 Experimental

To simplify the investigation, only 4 kinds of original materials, Fe_2O_3, K_2CO_3, MgO and Ce compounds were used for preparing samples. All raw materials are mixed together and shaped up, then calcinated at a certain temperature. Two series of samples with different amounts of Ce and different precursors of cerium (such as cerium oxalate, cerium nitrate and so on) were prepared.

^{57}Fe Mössbauer spectra were recorded at room temperature using a constant acceleration spectrometer with a 9.2×10^8Bq ^{57}Co(Pd) source in transmission geometry. Spectral parameters were obtained from computer fitting and the isomer shift was calculated with respect to an α-Fe foil of 25 μm thickness.

An isothermal stainless steel reactor with 2.5 cm inner diameter was used for measuring the catalytic activities in the laboratory. An amount of 100 ml of catalyst was placed in the reactor. The catalyst reacted under the following conditions: temperature 620°C, atmospheric pressure, liquid hourly space velocity (LHSV) 1.0 h^{-1} and steam to ethylbenzene ratio by weight 2:1. The reactive products were analyzed by gas spectrography.

3 Results and discussions

The presence of different iron compounds can be distinguished by their Mössbauer spectrum. We can see that in calcinated fresh catalyst the main compound of Fe-K is potassium ferrite $KFe_{11}O_{17}$, which has the spinel structure. It can be considered as the predecessor of the catalytic active phase [1, 4], which plays the important role in the dehydrogenation reaction of ethylbenzene. In the lattice of stoichiometric $KFe_{11}O_{17}$, there are four crystallographicaly identifiable Fe sites, namely, two octahedral sites (12k and 2a) and two tetrahedral sites. So the Mössbauer spectrum of the $KFe_{11}O_{17}$ can be resolved into four six-line hyperfine patterns assigned to these four sites. But in fact the sub-spectrum of the 2a octahedral site has a very small area and the hyperfine magnetic field H assigned to two tetrahedral sites is quite close. So we often fit the Mössbauer spectrum of potassium ferrite with four (or three) sub-spectra: $H = 48.4 \sim 48.9$ T is the contribution of Fe^{+3} on both tetrahedral sites, $H = 44.1 \sim 44.6$ T is that on an octahedral site, and other two (or one) smaller H

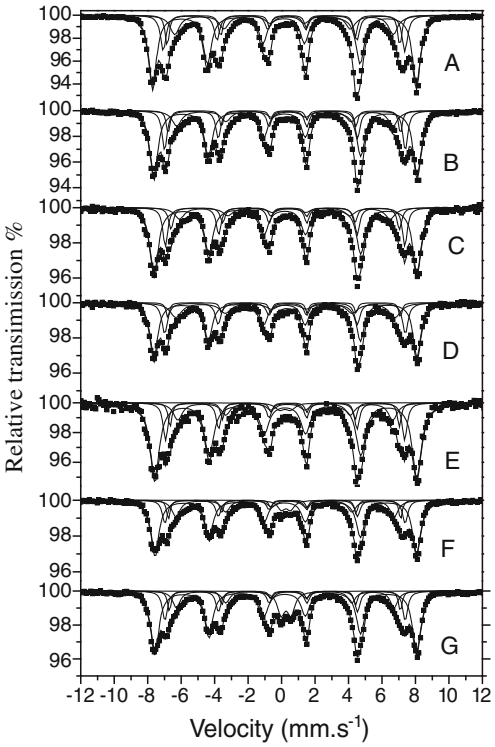

Fig. 1 Mössbauer spectra of sample A, B, C, D, E, F, G

Table 1 The parameters of Mössbauer spectra and catalytic activity of sample A∼G

Sample	A	B	C	D	E	F	G
Amount of Ce/%	0	2.5	8	10	15	20	30
Average width of peaks/mm·s^{-1}	0.263	0.266	0.275	0.281	0.270	0.255	0.244
Styrene yield/%	61.52	68.07	68.54	69.23	69.10	68.77	68.95

is that on the octahedral site with imperfect crystal lattice. Normally, the widths of Mössbauer peaks are noticeably broadened by interactions with the nearby excess potassium ions or other non-magnetic ions. It is found that the broader the peaks, the more disperse the catalyst. It is favorable to enhance the activity of catalyst [5].

In a first series of samples the amount of CeO_2 is 0%∼30%, and the amount of K, Mg (2% only) does not change. Figure 1 shows the Mössbauer spectra of 7 samples A∼G. In the Mössbauer spectra of all samples there are 4 sextets corresponding to $KFe_{11}O_{17}$. For sample E, F, G a doublet with small area (2%, 4%, 8%) also exists in the spectra. The doublet in the Mössbauer spectra assigned to Fe^{+3} in the catalyst also has contribution to the activity of the catalyst, because the samples F and G show better catalytic activity while their average widths are smaller (The sample L in Table 2 also proves this point). But not any cerium–iron compound can be detected in the Mössbauer spectra. X-ray diffraction results also prove that CeO_2 and Fe-K compound exist in the catalyst. However, different amounts of Ce give a different effect to the Fe-K compound in the catalyst, as shown in its Mössbauer parameters.

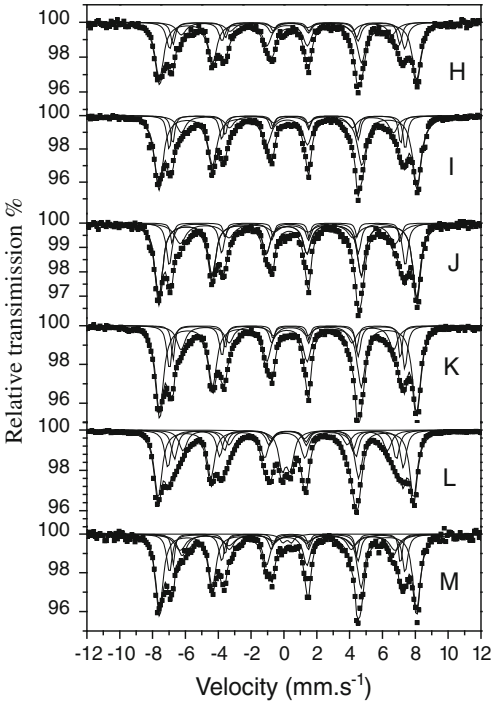

Fig. 2 Mössbauer spectra of sample H, I, J, K, L, M

Table 2 The parameters of Mössbauer spectra and catalytic activity of sample H~M

Sample	H	I	J	K	L	M
Compound of Ce	compound of Ce (new 1)	Cerium nitrate (condition a)	Cerium nitrate (condition b)	Compound of Ce (new 2)	Compound of Ce (new 3)	Compound of Ce (new 4)
Average width of peaks/ $mm{\cdot}s^{-1}$	0.291	0.285	0.281	0.267	0.260	0.255
Styrene yield/%	70.30	69.55	69.57	68.44	68.75	68.37

According to the percentage of each sub-spectrum area, the average width of the Mössbauer spectra peaks of the Fe-K compound was calculated and the result is shown in Table 1. From Table 1 the samples C, D and E have broader average width of Mössbauer spectra peaks and better catalytic and better catalytic property.

There are some reports [6, 7] about the study of the effect on the performance of this kind of Fe-K catalyst by different cerium salts. In our work, in order to look for a new substitute for cerium nitrate, a second series of samples H~M was prepared. Their original compound of Ce is different, but the real chemical formula of these Ce compounds cannot be disclosed because of commercial confidentiality. Samples I and J, which used the same raw material of cerium nitrate, were manufactured in different conditions.

The different original Ce compound also gives different effect to Fe-K compounds. Figure 2 shows the Mössbauer spectrum of 6 samples H~M. The calculated

average width of Mössbauer spectra peaks and their catalytic data are shown in Table 2. One kind of a new compound of Ce, sample H, that has broader average width of peaks and nice catalytic property, could become an optimal substitute of cerium nitrate in the future.

The Mössbauer parameters and the catalytic property of samples I and J, which use the same raw material of cerium nitrate, but different manufacturing conditions, show no obvious difference.

4 Conclusions

In conclusion, the above results prove that adding Ce into the Fe based catalyst is effective to form the predecessor of the catalytic active phase, compound $KFe_{11}O_{17}$, and also to improve the catalytic properties. The catalytic properties of the catalyst are optimal when the content of CeO_2 is 8%∼15%. In those cases the styrene yield could increase about 7% relative to the catalyst without Ce.

Acknowledgements The authors thank Dr. Jiang Dongmei for the Mössbauer measurements. The authors also wish to thank the Science and Technology Commission of Shanghai Municipality for the financial support of this project (No.10520706300).

References

1. Jiang, K.Y., Yang, J.X., Hu, B.Y., Yang, X.L., Mao, L.S., Yuan, Y.T., Zhang, G.L.: Hyperfine Interact. **111**, 45–49 (1998)
2. Watson, J.M., Crabbe, D.: Conrsen: JR.T.S. US4963343, 16 Oct 1990
3. Watson, J.M., Crabbe, D.: Conrsen: JR.T. S. US4975267, 4 Dec 1990
4. Jiang, K.Y., Fan, Q., Zhao, Z.J., et al.: Hyperfine Interact. **167**, 825–831 (2006)
5. Jiang, K.Y., Yang, X.L., Yuan, Y.T., et al.: Hyperfine Interact. **139/140**, 97–105 (2002)
6. Liao, S.J., Fan, Q., Miao, C.X., et al.: Chem. React. Eng. Tech. **24**(6), 493–497 (2008)
7. Xin, G.P.: Chem. Ind. Eng. Progr. **26**(8), 1192–1194 (2007)

Hyperfine Interact (2012) 205:87–90
DOI 10.1007/s10751-011-0440-3

Mössbauer study of C18N/Fe Langmuir-Blodgett layers

Erno Kuzmann · Judit Telegdi · Zoltán Németh · Attila Vértes · Lajos Nyikos

Published online: 10 November 2011

Abstract Langmuir-Blodgett (LB) films of octadecanoyl hydroxamic acid (C18N) complexed with Fe^{3+} ions have been prepared at various subphase pH values. The LB films consisting of different number of layers were investigated by ^{57}Fe conversion electron Mössbauer spectroscopy (CEM) at room temperature. The CEM detector contained a piece of α-iron, enriched with ^{57}Fe, using as an internal standard. The Mössbauer pattern of the C18N/Fe LB films is a doublet with parameters $\delta = 0.35$ mm/s and $\Delta = 0.74$ mm/s. A gradual increase of the relative occurrence of the doublet compared to the sextet of the internal standard was observed with the increasing number of layers, indicating the nearly uniform distribution of Fe among the LB layers.

Keywords Langmuir–Blodgett layer · ^{57}Fe CEM Mössbauer spectroscopy · Internal etalon · Octadecanoyl hydroxamic acid

1 Introduction

Amphiphilic molecules with small ionic head group and long hydrophobic chains are suitable for preparation of ultra thin, dense, protective Langmuir–Blodgett (LB) layers. These LB films on metal surfaces like copper could be applied as potential anticorrosive and bacterial adhesion preventing coatings [1]. In order to produce the most compact LB layer, the structure and behavior of amphiphiles in the molecular layer at the air–water interface should be very precisely monitored as the physical

E. Kuzmann · Z. Németh (✉) · A. Vértes
Institute of Chemistry, Eötvös Loránd University, Budapest, Hungary
e-mail: hentes@chem.elte.hu

J. Telegdi · L. Nyikos
Institute of Nanochemistry and Catalysis, Chemical Research Center, HAS, Budapest, Hungary

and chemical parameters of the subphase and the Langmuir monolayers influence the quality of LB films deposited onto solid supports [2, 3]. In order to incorporate counter ions into the LB film, salt of Fe^{3+} ions is dissolved in the aqueous subphase. At suitable pH value which influences the ionization of amphiphiles, the Fe^{3+} ions could form complex with the organic molecule. The aim of the present work was to study the incorporation and distribution of iron in the LB films of octadecanoyl hydroxamic acid (C18N) at various subphase pH values.

2 Experimental

6.5 mg Octadecanoyl hydroxamic acid (C18N) synthesized in our laboratory was dissolved in 10 ml of chloroform and used as stock solution. An aqueous solution of Fe^{3+} ions (chloride salt of Fe^{3+} ions at 5×10^{-5} M concentration) was used as a subphase at various pH values. For the Mössbauer study 90% ^{57}Fe enriched iron isotope was used. The pH was adjusted to the desired value by adding dilute solutions of NaOH or HCl. A proper amount of the stock solution was spread onto the aqueous subphase in a Langmuir trough (NIMA Technology Ltd., 611D) by micro syringe. After complete evaporation of the organic solvent (10 min) the compression was initiated at a speed of 200 cm^2 min^{-1}. Molecular area isotherms were obtained under continuous compression in the LB trough. Surface pressures were measured with a Wilhelmy plate balance.

^{57}Fe Mössbauer spectra of LB samples were recorded in reflection geometry with a conventional Mössbauer spectrometer (WISSEL) working in constant acceleration mode of conversion electron Mössbauer measurement using a RANGER-type CEM detector at room temperature. The CEM detector contained a piece of α-iron, enriched with ^{57}Fe, using as an internal standard. The γ-rays were provided by a 3×10^9 Bq ^{57}Co/Rh source.. Isomer shifts are given relative to α-iron. The Mössbauer spectra were analyzed by least-square fitting of Lorentzian lines by the help of the MOSSWINN code [4].

3 Results and discussion

The typical room temperature CEM spectrum of the C18N/Fe LB layers is a paramagnetic doublet with average isomer shift, $\delta = 0.35$ mm/s and quadrupole splitting, $\Delta = 0.74$ mm/s. These parameters reflect the occurrence of iron in valence state of Fe^{3+} in the LB layer. This result is confirmed by previous Mössbauer results, obtained also in transmission geometry, of LB layers [1].

Figure 1 shows room temperature CEM spectra of C18N/Fe LB films consisting of different number of layers. The envelop of the spectra was decomposed into a doublet and a sextet. The doublet corresponds to the iron microenvironment in the C18N/Fe LB layers. The sextet is the fingerprint of α-iron belonging to the internal etalon placed previously in the CEM detector in order to serve as a standard for the determination of the relative area of the doublet component at different layer numbers.

We have found a significant increase in the relative area of the doublet with the increasing number of LB layers (Fig. 1), in comparison with the relative area of the

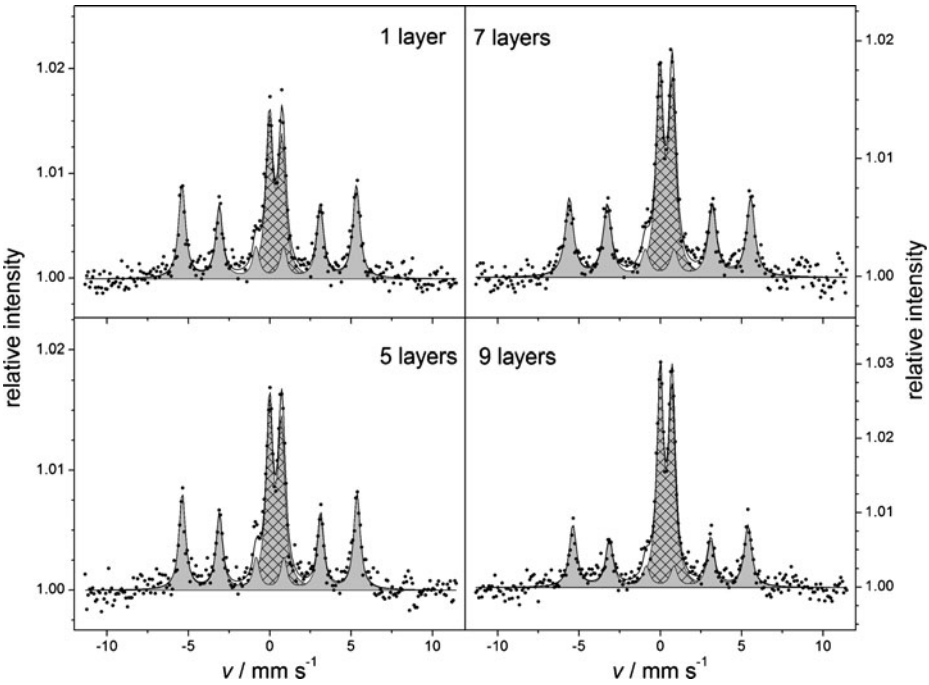

Fig. 1 ^{57}Fe CEM spectra of C18N/Fe Langmuir–Blodgett films consisting of different number of layers. The sextet is the fingerprint of α-Fe used as an internal standard built in the CEM detector

α-Fe used as an internal standard. This result gives information about the distribution of iron among the individual LB layers. Based on the spectrum evaluations, the calculation of iron distribution showed that each LB layer contains iron and the distribution of iron is nearly uniform among the LB layers.

Our result indicates a nearly uniform incorporation of iron into the LB nanolayers of amphiphiles with hydroxamic head groups, resulting an enhanced anticorrosion effect of the LB film [1], via the formation of more compact hydrophobic region of the layers kept together mainly by van der Waals forces and by the interaction of the head groups.

4 Conclusions

A nearly uniform distribution of iron in the Langmuir-Blodgett films of octadecanoyl hydroxamic acid (C18N) complexed with Fe^{3+} ions has been proven by the help of ^{57}Fe conversion electron Mössbauer spectroscopy using ^{57}Fe enriched α-iron as internal etalon built in the CEMS detector. The result of the Mössbauer spectroscopy gives an explanation for the increased anticorrosion and antifouling activity of the LB layers even with a very low iron concentration.

Acknowledgements The research was supported by grants of the Hungarian Science Foundation (OTKA K68135, K100424 and NN84307)

References

1. Telegdi, J., Szabó, T., Al-Taher, F., Pfeifer, E., Kuzmann, E., Vértes, A.: Mater. Corros. **61**, 1000–1007 (2010)
2. Telegdi, J., Rigó, T., Kálmán, E.: J. Electroanal. Chem. **582**, 191–201 (2005)
3. Al-Taher, F., Telegdi, J., Kálmán, E.: Colloids Surf. A Physicochem. Eng. Asp. **321**, 34–38 (2008)
4. Klencsár, Z., Kuzmann, E., Vértes, A.: J. Radioanal. Nucl. Chem. **210**(1), 105 (1996)

Hyperfine Interact (2012) 205:91–95
DOI 10.1007/s10751-011-0478-2

Effect of nanocrystallization on the electrical conduction of silver lithium phosphate glasses containing iron and vanadium

M. Y. Hassaan · M. M. El-Desoky · H. Masuda · S. Kubuki · T. Nishida

Published online: 29 November 2011

Abstract $xLi_2O\cdot(20\text{-}x)Ag_2O\cdot 20Fe_2O_3\cdot 60P_2O_5$ glasses (x = 0, 5, 10, 15 and 20 mol%) and $5Ag_2O\cdot 15Li_2O\cdot 5V_2O_5\cdot 15Fe_2O_3\cdot 60P_2O_5$ glass were prepared by melt-quenching of the reagent mixture at 1000 °C. Glass transition temperature (T_g) and crystallization temperature (T_c) of these samples were determined by differential thermal analysis (DTA). It proved that T_g increased with Li_2O content. XRD of as-quenched glasses confirmed their amorphous nature. XRD of samples heat treated for one hour at temperature near their T_c, indicated nanocrystals precipitated in the glassy matrix with an average particle size of 35 nm. Mössbauer results revealed that the relative fraction of Fe^{2+} was decreased with an increasing Li_2O content. The isomer shift values of Fe^{3+} lie in a range of 0.38–0.45 mm s^{-1}, while those for Fe^{2+} were 1.10–1.31 mm s^{-1}. Heat-treated sample of $5Ag_2O\cdot 15Li_2O\cdot 5V_2O_5\cdot 15Fe_2O_3\cdot 60P_2O_5$ glass exhibit an enhancement of the electrical conductivity by three orders of magnitude due to the 3d-electron (polaron) hopping from V^{4+} to V^{5+} in the "vanadate glass" units.

Keywords Vanadate glass · ^{57}Fe-Mössbauer spectroscopy · Electrical conductivity · Nano-crystallization

M. Y. Hassaan (✉)
Physics Department, Faculty of Science, Al-Azhar University, Nasr City, Cairo, Egypt
e-mail: myhassaan@yahoo.com

M. M. El-Desoky
Physics Department, Faculty of Science, Suez Canal University, Suez, Egypt

H. Masuda · S. Kubuki
Department of Chemistry, Graduate School of Science and Engineering,
Tokyo Metropolitan University, Hachioji 192-0397, Japan

T. Nishida
Department of Biological and Environmental Chemistry,
Faculty of Humanity-Oriented Science and Engineering,
Kinki University, Iizuka 820-8555, Japan

1 Introduction

The electrical conductivity of glass due to electronic conduction or mixed electronic–ionic conduction has been investigated extensively from the view points of their potential use as either electronic devices or electrolytes for rechargeable batteries [1]. Lithium or silver vanadate glasses containing other network-forming oxides (NWF) like P_2O_5 exhibit high mixed electronic–ionic conduction due to the transport of Li^+ or Ag^+ ions and the electronic conduction due to electron hopping between V^{4+} and V^{5+} [2]. Mixed electronic–ionic conduction can be utilized as a cathode material for secondary batteries [3, 4]. Improvement of the electrical conductivity of mixed electronic–ionic conducting amorphous materials after nanocrystallization has been observed in several glasses [3]. The main purpose of this work is to study the mixed ionic-electronic conduction of Ag_2O-LiO_2 phosphate glasses containing iron and vanadium, and also to study the effect of nanocrystallization on the enhancement of the conductivity.

2 Experimental

Reagent grade chemicals, Li_2CO_3, Ag_2O, V_2O_5, Fe_2O_3 and P_2O_5, were used for the sample preparation. After mixing a batch (10 g) in air, each mixture was melted at 1000°C for 30 min. By pressing the melt with copper blocks, bulk glass of 2 × 2 cm^2 size and 1 mm thickness was obtained with the composition of $xLi_2O\cdot(20\text{-}x)Ag_2O\cdot 20Fe_2O_3\cdot 60P_2O_5$ and $5Ag_2O\cdot 15Li_2O\cdot 5V_2O_5\cdot 15Fe_2O_3\cdot 60P_2O_5$ (denoted by ALVFP). Heat treatment of glass was carried out by heating in air for one hour near their crystallization temperature (T_c), which was determined by differential thermal analysis (DTA) together with glass transition temperature (T_g), and melting temperature (T_m) with Shimadzu DTA50. The structure of nanocrystalline particles was determined by X-ray diffractometry with RINT-TTR3. Mössbauer spectra were measured in a standard transmission geometry, using a source of ^{57}Co diffused in rhodium matrix. The calibration was performed using a natural iron foil. The dc conductivity (σ) was measured at temperatures between 393 and 633 K. Electrodes were attached with silver paste on both faces of the polished samples. A multimeter type Keithely 760 was used to collect the *I-V* data at room temperature.

3 Results and discussion

The DTA curve of LAVFP and the glass composition dependence of T_g, T_c and T_m are shown in Fig. 1. From Fig. 1 it is clear that T_g, T_c and T_m increase with an increasing lithium content. Generally, T_g shows a distinct increase when the coordination number of the network former increases, while a construction of nonbridging oxygen (NBO) causes a decrease of T_g. The continuous increase in the T_g suggests a continuing decrease in the coordination number of Fe^{3+} and Fe^{2+} ions and destruction of NBO atoms [3]. This indicates that the glass structure becomes more closed as a result of Li^+ substitution for Ag^+ with a larger ionic radius. T_g/T_m values determined for all the compositions in the present system fall in a range of 0.78

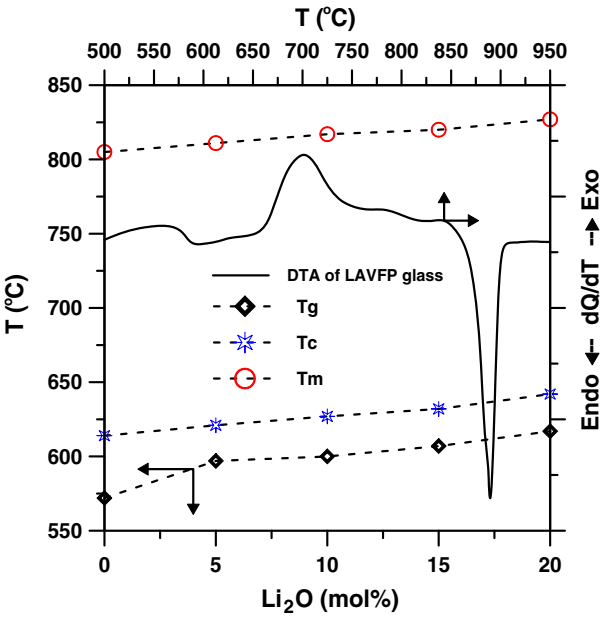

Fig. 1 DTA for LAFVP glass and composition dependence of glass transition temperature (T_g), crystallization temperature (T_c) and melting temperature (T_m)

~ 0.80, indicating high thermal stability because the T_g/T_m value of ideally stable glass is reported to be 0.67 [3].

XRD for as-quenched glass and heat-treated samples were measured. In case of as-quenched samples, only one halo peak is observed with no indication of crystalline particles. In case of the samples heat treated at temperature near their T_c for one hour shows a lot of peaks corresponding to nanocrystalline particles, superimposed on the halo peak. The XRD study indicates that annealing near their T_c triggers the precipitation of nanocrystalline particles in the glass matrix [3]. This reminds us that we can design and control the amount of nanocrystalline particles formed in the glass matrix by changing temperature and duration of isothermal annealing, and that we can enhance its physical properties like electrical conductivity, magnetic moment, coercive force, etc. Application of the Scherrer formula, to linewidth of the diffraction peaks yielded a mean diameter of *ca*. 35 nm for the nanocrystalline particles.

Mössbauer spectra of ALVFP glass before and after the heat treatment are shown in Fig. 2. Before heat treatment, they are composed of two doublets representing tetrahedral Fe^{2+} and Fe^{3+} (Fig. 2A). The absorption area for Fe^{2+} seems to decrease as the Ag_2O content is decreased due to the reducing effect of Ag_2O; see Fig. 2A and B. However, the values of isomer shift (δ, 1.10 $\sim$ 1.31 mm s^{-1} for Fe^{2+} and 0.38 $\sim$ 0.45 mm s^{-1} for Fe^{3+}) and quadrupole splitting (Δ, 2.21 $\sim$ 2.56 mm s^{-1} for Fe^{2+} and 0.49 $\sim$ 0.72 mm s^{-1} for Fe^{3+}) were nearly identical in all samples. The spectra of the heat-treated samples showed two doublets (Fig. 2B) with different parameters for the Fe^{2+} doublet. One doublet in heated samples is ascribed to Fe^{2+} ions with δ ranging from 0.94 to 1.36 mm s^{-1}. Absorption area and Δ for Fe^{2+} decreased as the Li_2O content was increased. The decrease of Δ reflects that the local symmetry around the iron nucleus was increased [5].

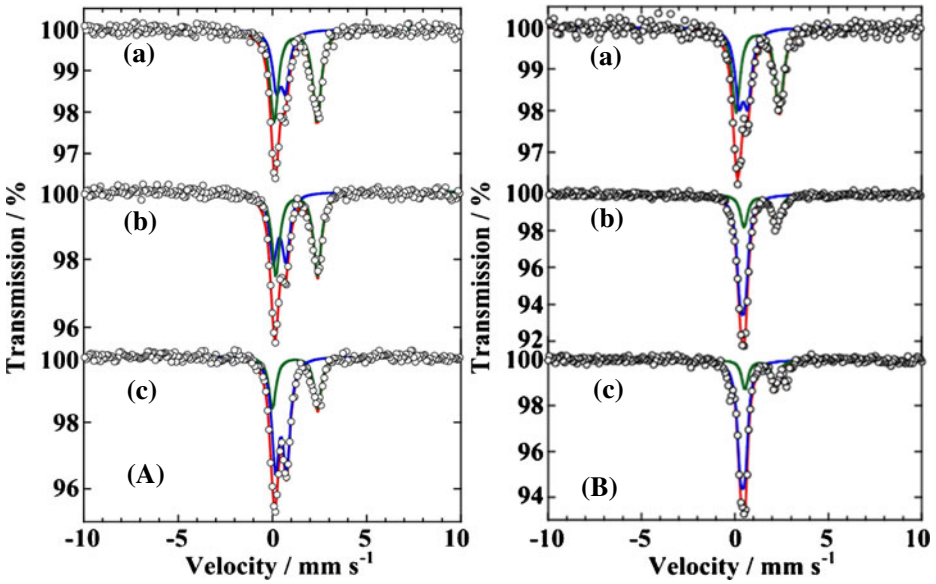

Fig. 2 Mössbauer spectra of LAVFP glasses with '*x*' of (**a**) 0, (**b**) 5 and (**c**) 10 mol%; (**A**) before and (**B**) after annealing

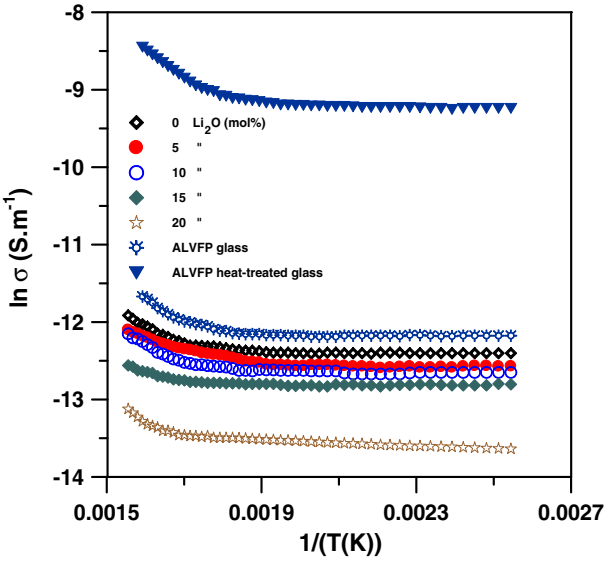

Fig. 3 Temperature dependence of dc conductivity (σ) as a function of Li_2O content for glasses, ALVFP glass and their heat-treated glass

Figure 3 shows that dc conductivity, σ, for ALFVP glass and heat-treated samples is decreased with an increasing Li_2O content that was changed from 0 to 20 mol%. Arrhenius type change of conductivity is given by:

$$\sigma = \sigma_o \exp(-W/kT), \quad (1)$$

where σ_o is a pre-exponential factor and W the activation energy. These Arrhenius plots are curved in a high temperature region as shown in Fig. 3. The value of W was estimated from the slope of the curve in a higher temperature region; 0.10–0.20 eV for heat-treated samples and 0.25 eV for heat-treated ALFVP, while 0.12–0.23 eV for as-quenched glasses and 0.33 eV for ALFVP glass. This means that an increase of Fe^{2+} causes a decrease of, W, and an increase of σ. It is clear from Fig. 3 that ALFVP samples obtained after annealing at T_c exhibit an enhancement of σ by three orders of magnitude. Similar results were obtained in other heat-treated samples. This is ascribed to the structural relaxation of "vanadate glass" units, involved with an increased probability of polaron hopping, as observed earlier in barium vanadate glasses [4, 5]. More discussion will be made elsewhere on the mechanism of Li^+- ion and Ag^+-ion conduction combined with the polaron hopping of "vanadate glass" units. The enhancement of electrical conductivity of heat-treated glasses can be attributed to (i) an increase in the concentration of Fe^{2+}–Fe^{3+} and V^{4+}–V^{5+} pairs and (ii) formation of, well-conducting regions along the glass-crystallites interfaces [2, 3].

4 Conclusion

The structure and conductivity of $xLi_2O{\cdot}(20\text{-}x)Ag_2O{\cdot}20Fe_2O_3{\cdot}60P_2O_5$ glasses (x = 0, 5, 10, 15 and 20 mol%) and $5Ag_2O{\cdot}15Li_2O{\cdot}5V_2O_5{\cdot}15Fe_2O_3{\cdot}60P_2O_5$ glass were investigated before and after isothermal annealing at a temperature near their T_c. Nanocrystallization involved with an increase in the electrical conductivity was observed by DTA, XRD, Mössbauer and dc conductivity measurements. It is possible to optimize the condition of heat treatment in order to realize the desired conductivity. XRD study of $10Li_2O{\cdot}10Ag_2O{\cdot}20Fe_2O_3{\cdot}60P_2O_5$ glass showed that heat treatment resulted in the precipitation of nanocrystals with an average particle size of 35 nm in the glassy matrix. Mössbauer results revealed that the fraction of Fe^{2+} decreased with an increasing Li_2O content. The isomer shift of Fe^{3+} lay in a range of 0.38–0.45 mm s^{-1}, while Fe^{2+} had an isomer shift of 1.10–1.31 mm s^{-1}. Heat-treated samples of $5Ag_2O{\cdot}15Li_2O{\cdot}5V_2O_5{\cdot}15Fe_2O_3{\cdot}60P_2O_5$ glass exhibited a marked enhancement of conductivity by three orders of magnitude due to the structural relaxation of "vanadate glass" units.

References

1. Duclot, M., Souquet, J.L.J.: Power Sources **97–98**, 610 (2001)
2. Garbarczyk, J.E., Wasiucionek, M., Jozwiak, P., Nowinski, J.L., Julien, C.M.: Solid State Ion. **180**, 531 (2009)
3. El-Desoky, M.M., Zayed, H.S.S., Ibrahim, F.A., Ragab, H.S.: Phys. B **404**, 4125 (2009)
4. Nishida, T., Yoshida Y., Takahashi, Y., Okada, S., Yamaki, J.: J. Radioanal. Nucl. Chem. **275**, 417 (2008)
5. Fukuda, K., Ikeda, A., Nishida, T.: Solid State Phenom. **90**, 215 (2003)

Hyperfine Interact (2012) 205:97–100
DOI 10.1007/s10751-011-0423-4

Formation and superparamagnetic behaviors of $LaFeO_3$ nanoparticles

Tatsuo Fujii · Ikkoh Matsusue · Makoto Nakanishi · Jun Takada

Published online: 26 October 2011

Abstract Formation of $LaFeO_3$ nanoparticles obtained from thermal decomposition of organometallic precursors was investigated as a function of the heat-treatment temperature. The precursors heat-treated below 300°C were amorphous, but above 350°C a single-phase of nanocrystalline $LaFeO_3$ was formed. The $LaFeO_3$ nanoparticles showed the superparamagnetic behavior in both magnetization and Mössbauer measurements. With increasing heat-treatment temperature, the crystallite size of $LaFeO_3$ nanoparticles was gradually increased. The quadrupole splitting and isomer shift of paramagnetic doublet pattern were affected by the growth of $LaFeO_3$ particles.

Keywords $LaFeO_3$ nanoparticles · Hot soap method · Superparamagnetism · Mössbauer spectroscopy

1 Introduction

Lanthanum orthoferrite, $LaFeO_3$, is one of the most common perovskite-type oxides and has been proposed for various applications such as solid oxide fuel cells, catalysts, chemical sensors, etc. [1, 2]. These properties should be enhanced by high surface area of fabricated $LaFeO_3$ particles. $LaFeO_3$ is known to be antiferromagnet with a Néel temperature T_N of 738 K [3]. However, antiferromagnetic nanoparticles often exhibit increasing net magnetization due to presence of uncompensated surface spins [4]. Recently we have reported that the $LaFeO_3$ nanoparticles exhibited considerable large magnetization at low temperature [5]. In this paper, we report the formation of $LaFeO_3$ nanoparticles obtained from thermal decomposition of organometallic

T. Fujii (✉) · I. Matsusue · M. Nakanishi · J. Takada
Department of Applied Chemistry, Faculty of Engineering,
Okayama University, Tsushima-naka 3-1-1, Okayama 700-8530, Japan
e-mail: tfujii@cc.okayama-u.ac.jp

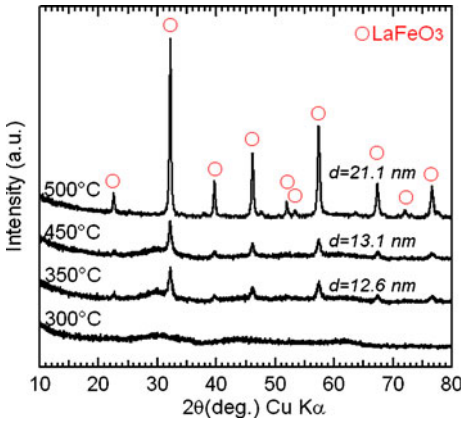

Fig. 1 XRD patterns of heat-treated samples at various temperatures. The crystallite size of $LaFeO_3$ nanoparticles evaluated from Scherrer's formula is indicated

precursors. Mössbauer spectra of $LaFeO_3$ nanoparticles were also discussed as a function of the heat-treatment temperature.

2 Experimental

Organometallic precursors for $LaFeO_3$ nanoparticles were synthesized by hot soap method. Equal amounts of iron acetylacetonate and lanthanum acetate were charged into a reaction flask with polyethylene glycol. Coordinating organic protective agents of oleic acid and oleylamine were injected into the reaction flask as well. Thereafter, the mixture was raised to 200°C and maintained for 3 h with stirring. By adding ethanol to the reaction mixture, organometallic precursors were precipitated and dried at 100°C for 1 h. For the thermal decomposition, the obtained precursors were heat-treated in air for 6 h at various temperatures between 300 and 600°C. Finally the samples were characterized by x-ray powder diffraction (XRD) with monochromatic Cu Kα, a vibrating sample magnetometer with high-sensitivity SQUID sensor and conventional transmission Mössbauer spectroscopy with a 925 MBq ^{57}Co/Rh source.

3 Results and discussion

Figure 1 shows the XRD patterns of heat-treated precursors at various temperatures. The sample heated at 300°C showed the diffuse XRD pattern with no crystalline phases. While at 350°C, broad XRD peaks attributed to the $LaFeO_3$ perovskite phase were observed. The average crystallite size estimated from the XRD peak broadening for $LaFeO_3$ particles prepared at 350°C was about 13 nm by using the Scherrer's equation. This value was fully consistent with the average grain size characterized by TEM observations. With increasing heat treatment temperature, the XRD peaks gradually became sharper and steeply intensified above 500°C because of the grain growth of the $LaFeO_3$ particles.

Room temperature Mössbauer spectra of the heat-treated samples prepared at various temperatures are shown in Fig. 2. The sample heated at 500°C, which had

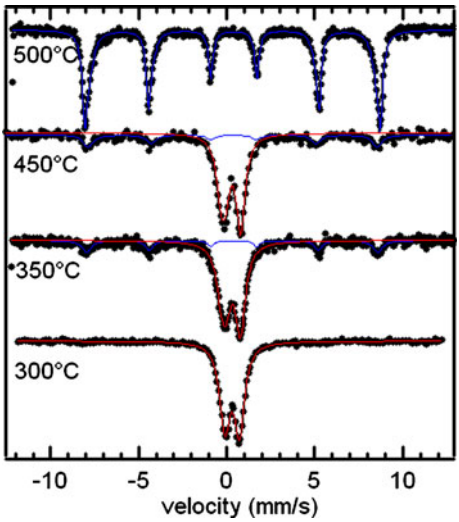

Fig. 2 Room temperature Mössbauer spectra of heat-treated samples at various temperatures. The solid lines indicate the fitted components

Table 1 Fitted Mössbauer parameters obtained from the spectra in Fig. 2

Heat temperature (°C)	Isomer shift (mm/s)	Quadupole splitting (mm/s)	Hyperfine filed (kOe)	Intensity (%)
500	0.376	–	513	100
450	0.364	–	508	23
	0.292	1.008	–	77
350	0.355	–	512	21
	0.313	0.924	–	79
300	0.327	0.824	–	100

a larger crystallite size, showed a clear sextet pattern due to antiferromagnetic ordering. However, paramagnetic doublet patterns were dominant for other samples heated at 350 and 450°C in spite of the formation of $LaFeO_3$. This behavior was attributed to superparamagnetism because of the fine crystallite size of $LaFeO_3$. The blocking temperature of about 30 K was confirmed by both magnetization and Mössbauer measurements [5]. Moreover, a large spontaneous magnetization of 7.8 emu/g was observed below the blocking temperature. The Mössbauer parameter of the doublet pattern indicated the systematic change depending on the heat-treatment temperature. The fitted parameters are listed in Table 1. The isomer shift gradually decreased while the quadrupole splitting gradually increased with increasing heat treatment temperature. This result suggested the formation of strong Fe-O bonds and ligand fields due to the crystallization of $LaFeO_3$ particles.

4 Conclusion

Nanocrystalline $LaFeO_3$ particles with an average diameter of 13 nm were prepared by thermal decomposition of organometallic precursors at 350°C. The obtained $LaFeO_3$ nanoparticles exhibited superparamagnetic behaviors. With increasing heat-

treatment temperature, the grain size of $LaFeO_3$ particles was gradually increased. The values of isomer shift and quadrupole splitting were changed systematically according to the crystallization of $LaFeO_3$ particles.

References

1. Nakayama, S.: $LaFeO_3$ perovskite-type oxide prepared by oxide-mixing, co-precipitation and complex synthesis methods. J. Mater. Sci. **36**, 5643–5648 (2001)
2. Popa, M., Calderon Moreno, J.M.: Lanthanum ferrite ferromagnetic nanocrystallites by a polymeric precursor route. J. Alloys Comp. **509**, 4108–4116 (2011)
3. Treves, D.: Studies on orthoferrites at the Weizmann Institute of Science. J. Appl. Phys. **36**, 1033–1039 (1965)
4. Kodama, R.H., Berkowitz, A.E.: Atomic-scale magnetic modeling of oxide nanoparticles. Phys. Rev. B **59**, 6321–6336 (1999)
5. Fujii, T., Matsusue, I., Nakatsuka, D., Nakanishi, M., Takada, J.: Synthesis and anomalous magnetic properties of $LaFeO_3$ nanoparticles by hot soap method. Mater. Chem. Phys. **129**, 805–809 (2011)

Hyperfine Interact (2012) 205:101–104
DOI 10.1007/s10751-011-0484-4

Structural and ^{57}Fe Mössbauer study of $EuCr_{1-x}Fe_xO_3$ nanocrystalline particles

H. M. Widatallah · T. M. H. Al-Shahumi · A. M. Gismelseed · Z. Klencsár · A. D. Al-Rawas · I. A. Al-Omari · M. E. Elzain · A. A. Yousif · M. Pekala

Received: 9 September 2011 / Accepted: 9 November 2011 / Published online: 8 December 2011

Abstract A structural and Mössbauer study of mechanosynthesized $EuCr_{1-x}Fe_xO_3$ nanocrystalline particles (~20–30 nm) is presented. The lattice parameters increase with increasing x-value leading to an increasingly distorted structure. The crystallite sizes range between 20 nm and 30 nm. Magnetic and ^{57}Fe Mössbauer measurements show the samples with $x < 0.7$ to be paramagnetic and those with $x \geq 0.7$ to be partially superparamagnetic at 298 K. The 78 K Mössbauer spectra of the samples with $x = 0.3$–1.0 are composed of well-resolved two sextets that are explicable in terms of the structural model that we recently have proposed for the $EuCrO_3$ nanoparticles according to which the transition metal ions and Eu^{3+} partly exchange their usual sites in the perovskite-related structure (Widatallah et al., J Phys D Appl Phys 44:265403, 2011). Consequently, the two sextets obtained at 78 K refer to Fe^{3+} ions at the usual B-octahedral site and the A-dodecahedral site usually occupied by Eu^{3+}.

Keywords Perovskite · Mössbauer spectroscopy · Milling · XRD · Magnetization

1 Introduction

$EuCrO_3$ and $EuFeO_3$ are useful materials in multiple fields of application that include, among others, solid oxide fuel cells, chemical sensing and optical

H. M. Widatallah (✉) · T. M. H. Al-Shahumi · A. M. Gismelseed · A. D. Al-Rawas · I. A. Al-Omari · M. E. Elzain · A. A. Yousif
Department of Physics, Sultan Qaboos University, P. O. Box 36, 123, Muscat, Oman
e-mail: hishammw@squ.edu.om

Z. Klencsár
Chemical Research Institute, Hungarian Academy of Sciences,
Pusztaszeri út 59-67, Budapest, 1025, Hungary

M. Pekala
Chemistry Department, University of Warsaw, 101, PL-02-089, Warsaw, Poland

communications [1–3]. The compounds crystallize in the space group *Pbnm* with four distorted perovskite units in the true crystallographic orthorhombic cell [1–4] where Eu^{3+} and the transition metal ions occupy the dodecahedral A- and octahedral B-sites, respectively. Both solids are anti-ferromagnetic with only weak ferromagnetism due to spin canting below ~181 K and ~662 K respectively [3, 5]. Rather than using the term Néel temperature (T_N) to refer to these temperatures [3] we shall follow Gibb [4, 5] in referring to them as Curie temperature (T_C). They actually signify the transition from the weak ferromagnetic state to the paramagnetic one. Previous studies on the $EuCrO_3$/ $EuFeO_3$ solid solutions were mainly performed on the $EuCr_{1-x}Fe_xO_3$ microcrystalline particles [2, 5]. Recently we have shown an unusual cationic site exchange to exist in $EuCrO_3$ nanocrystalline particles [1]. In the present study we report our preliminary studies on nanocrystalline $EuCr_{1-x}Fe_xO_3$ particles.

2 Experimental

Nanocrystalline $EuCr_{1-x}Fe_xO_3$ particles were prepared using mechanosynthesis starting from appropriate amounts of high purity Eu_2O_3, Cr_2O_3 and α-Fe_2O_3 in the 1: 1-*x*:*x* molar ratio ($x = 0.0, 0.1, 0.3, 0.5, 0.7, 0.9, 1.0$) using an identical milling and sintering regime to that reported by us recently [1]. X-ray powder diffraction (XRD) patterns were collected with a Philips PW1710 diffractometer using CuKα radiation ($\lambda = 1.5406$ Å). The thermal variation of the magnetization was recorded with a Faraday balance under a 1.5 T external magnetic field. ^{57}Fe Mössbauer spectra were recorded in the transmission mode at 298 K and 78 K using a 50 mCi ^{57}Co/Rh source. The isomer shifts are quoted relative to iron foil.

3 Results and discussion

Figure 1a shows the XRD patterns recorded from the pre-milled reactants' mixtures sintered (8 h) at the temperatures indicated. All patterns could be indexed to a single-phased perovskite-related $EuCr_{1-x}Fe_xO_3$ structure. The crystallite sizes were found to be in the range of 20–30 nm. Figure 1b shows the lattice parameters to generally increase with *x*. The increase in the *b* parameter becomes more pronounced at higher *x*. Consequently, a more distorted unit cell is to be expected at high x values. This unit cell expansion is expected as more of the larger Fe^{3+} ions (0.785 Å) replace the smaller Cr^{3+} ones (0.755 Å) [6]. Referring to our Rietveld refinement of the XRD pattern of the sample with $x = 0.0$ ($EuCrO_3$) [1], where the Eu^{3+} and Cr^{3+} ions were shown to partially exchange the A- and B-sites, a more pronounced site-exchange of Eu^{3+} and Fe^{3+} is anticipated in $EuCr_{1-x}Fe_xO_3$ nanoparticles on the basis of the higher ionic size of Fe^{3+}. Indeed initial analysis of ^{151}Eu data (not shown) suggests that a considerable amount of Eu^{3+} ions in the spectra of all samples exists at the transition metal B-sites. The T_C values were found to increase with increasing *x* from ~181 K, 172 K, 202 K, 425 K and 525 K for the $EuCr_{1-x}Fe_xO_3$ nanoparticles with $x = 0.0, 0.1, 0.3, 0.5$ and 0.7 respectively. The samples with $x = 0.9$ and 1.0 showed a similar T_C of ~625 K.

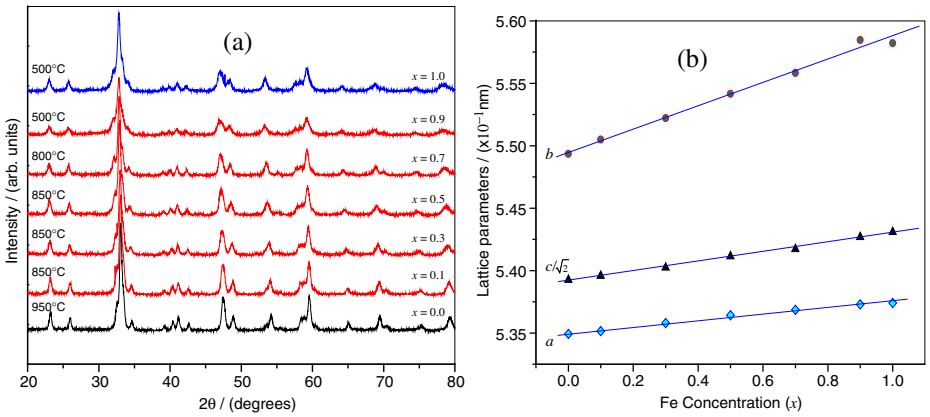

Fig. 1 **a** The XRD patterns of the $EuCr_{1-x}Fe_xO_3$ nanoparticles obtained at the temperatures indicated and **b** the variations with lattice parameters a, b and $c/\sqrt{2}$ with x

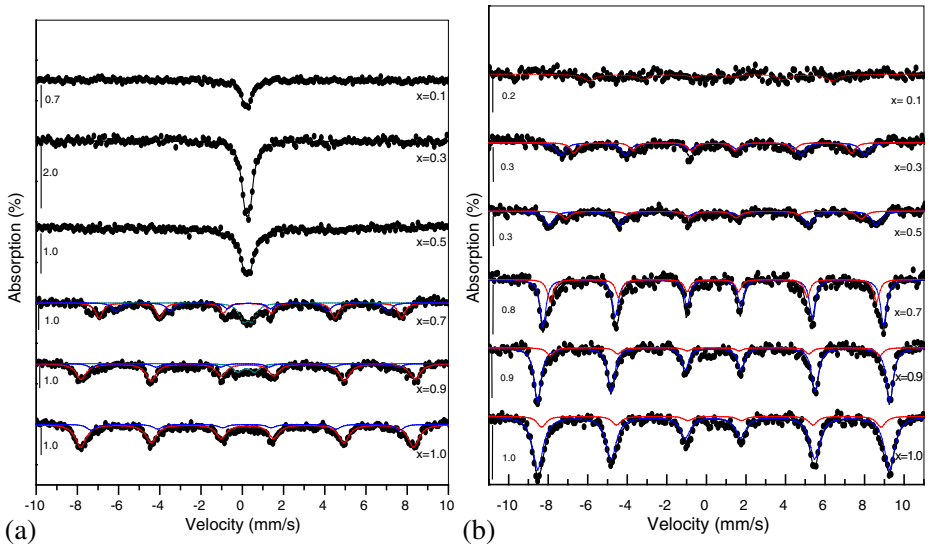

Fig. 2 The ^{57}Fe Mössbauer spectra recorded from the $EuCr_{1-x}Fe_xO_3$ nanoparticles at **a** 298 K, and **b** 78 K

The ^{57}Fe Mössbauer spectra recorded from the nanoparticles at 298 K and 78 K are given in Fig. 2a and b respectively. The fitted parameters are given in Table 1. In line with the magnetic measurements, the 298 K spectra of the particles with $x = 0.1$–0.5 depict paramagnetic doublets for $x = 0.1$ and 0.3 and a superparamagnetic doublet for $x = 0.5$ with very small quadrupole splitting that are presumably related to the distorted orthorhombic structure. For the samples with $x = 0.7$ and 0.9, where $T_C > 298$ K, the spectrum is composed of a broad magnetic six-line pattern superimposed on a central doublet. The latter is due to superparamagnetic particles whose volumes are smaller than the critical (blocking) volume required for depicting

Table 1 The ^{57}Fe Mössbauer parameters for the $EuCr_{1-x}Fe_xO_3$ nanoparticles at 298 K, and 78 K (between brackets and in italics)

X	Component	δ (mm/s)	ε (mm/s)	Δ(mm/s)	H_{eff}(T)	A(%) ±3
0.1	Doublet	0.34	0.22			100
	Doublet	0.36	0.22			100
0.3	Sextet I	*(0.46)*		*(−0.03)*	*(51.3)*	*(66)*
	Sextet II	*(0.47)*		*(0.03)*	*(46.4)*	*(34)*
	Doublet	0.36	0.30			100
0.5	Sextet I	*(0.47)*		*(−0.02)*	*(53.5)*	*(68)*
	Sextet II	*(0.45)*		*(0.03)*	*(51.2)*	*(32)*
	Doublet	0.37	0.43			23
0.7	Sextet I	0.40 *(0.47)*		0.04 *(−0.02)*	45.6 *(53.5)*	49 *(68)*
	Sextet II	0.48 *(0.45)*		0.04 *(0.03)*	41.1 *(51.2)*	28 *(32)*
	Doublet	0.31	0.79			12
0.9	Sextet 1	0.39 *(0.48)*		0.01 *(0.03)*	50.3 *(55.3)*	74 *(87)*
	Sextet II	0.27 *(0.51)*		−0.01 *(0.02)*	46.3 *(51.8)*	14 *(13)*
1.0	Sextet 1	0.36 *(0.47)*		−0.02 *(0.04)*	50.2 *(55.2)*	82 *(85)*
	Sextet II	0.38 *(0.46)*		−0.01 *(−0.09)*	46.5 *(53.3)*	18 *(15)*

δ: isomer shift, ε: quadrupole splitting, Δ: quadrupole shift, H_{eff}: magnetic hyperfine field, A: spectral area

the ferromagnetic nature. While the gradual increase in the quadrupole splitting values with x agrees with above XRD result that unit cell gets more distorted at higher x values, it also reflects an increasing cationic Eu-Fe site exchange. The magnetic part of the 298 K spectra, was fitted with two hyperfine-split sextets. These generally reflect Fe^{3+} in different environments. The gradual increase in the magnitude of H_{eff} for both sextets with increasing x clearly reflects enhanced exchange magnetic interactions. For the nanoparticles with $x = 1.0$, the 298 K spectrum is comprised of two sextets whose H_{eff} values are smaller than that reported for bulk $EuFeO_3$ (51.8 T) [5].

The Mössbauer spectrum recorded at 78 K, which is smaller than T_C for all samples, shows a very poorly resolved magnetic spectrum for the sample with $x = 0.1$. This is possibly due to the very small number of ^{57}Fe nuclei and the associated limited magnetic exchange interactions. Well resolved six-line magnetic patterns were attained for the rest of the samples ($x = 0.3 - -1.0$); each of which was fitted with two sextets (Table 1). We attribute the sextets with the higher magnetic fields in the above Mössbauer analysis with B-sites Fe^{3+} ions having a majority Fe^{3+} nearest cationic neighbors. The sextets with lower fields are associated with A-site Fe^{3+} as well as B-site Fe^{3+} with Eu^{3+} and/or Cr^{3+} nearest neighbors. A possibility that our initial analysis of ^{151}Eu Mössbauer data supports as indicated above.

References

1. Widatallah, H.M., Al-Harthi, S.H., Johnson, C., Klencsar, Z., Gismelseed, A.M., Moore, E.A., et al.: J. Phys. D Appl. Phys. **44**, 265403 (2011)
2. Niu, X., Du, W., Du, W.: Sens Actuat. B Chem. **99**, 399 (2004)
3. Tsushima, K., Takemura, I., Osaka, S.: Solid. State Commun. **7**, 71 (1969)
4. Gibb, T.C.: J. Chem. Soc. Dalton Trans. 2245 (1981)
5. Gibb, T.C.: J. Chem. Soc. Dalton Trans. 2031 (1983)
6. Winter, M.J.: www.webelements.com. University of Sheffield, UK (1995–2011)

Hyperfine Interact (2012) 205:105–109
DOI 10.1007/s10751-011-0504-4

Magnetic and Mössbauer studies of Fe and Co co-doped SnO_2

Shin Kono · Kiyoshi Nomura · Yasuhiro Yamada · Jun Okabayashi

Published online: 20 December 2011

Abstract 1–5% Fe and 1% Co co-doped SnO_2 samples were synthesized by sol-gel method. Their magnetization increased with increasing crystal size of rutile SnO_2. Their Mössbauer spectra contain a broad sextet, magnetic relaxation components, and paramagnetic doublet peaks for less than 3% Fe doping. The sextet of α-Fe_2O_3 was observed instead of magnetic relaxation peaks for Fe doping of above 4%. The broad sextet and relaxation components may be related to the magnetic properties of Fe and Co co-doped SnO_2.

Keywords Fe and Co co-doped SnO_2 · Diluted magnetic semiconductors · Mössbauer spectroscopy

1 Introduction

The wide-band-gap oxide semiconductor SnO_2 is a well-known transparent material that is used in gas sensors [1]. Since the discovery of Co-ion-doped TiO_2 in 2001 [2], transition metal (TM) doped oxide semiconductors with spin-related functionalities have been attracting attention for use as room-temperature diluted magnetic semiconductors. Fe-ion-doped SnO_2 [3–5] and Co-ion-doped SnO_2 [6] have been fabricated by sol-gel method [4–6] and pulsed laser deposition [3]. However, their

S. Kono · Y. Yamada
Department of Chemistry, Tokyo University of Science, 162-8601, Tokyo, Japan

K. Nomura (✉)
School of Engineering, The University of Tokyo, Hongo 7-3-1, Bunkyoku, 113-8656, Tokyo, Japan
e-mail: k-nomura@t-adm.t.u-tokyo.ac.jp

J. Okabayashi
Research Center for Spectrochemistry, The University of Tokyo, 113-0033, Tokyo, Japan

magnetic properties vary depending on the growth conditions. The presence of oxygen vacancies has been found to be essential for ferromagnetic ordering. Detailed investigations are needed to determine the ferromagnetism mechanism. Coey et al. proposed a model in which defect-induced magnetism occurs between TM ions via oxygen vacancies [7, 8]. The next step in studying SnO_2-based diluted magnetic semiconductors requires controlling the saturation magnetization (M_s) and coercive field (H_c) by the TM concentrations. With this goal in mind, we have focused on TM co-doped SnO_2. Nomura et al. have observed the enhanced magnetization by co-doping Co and Fe into SnO_2 and investigated the dependence of the magnetization on the Co concentration for 1% Fe-ion doping [9].

This study is to investigate the effect of the Fe-ion concentration on the magnetism of Fe and Co co-doped SnO_2.

2 Experimental

SnO_2 powders co-doped with 1–5% Fe and 1% Co were prepared by sol-gel method. $SnCl_2{\cdot}2H_2O$ and metallic Fe and Co were dissolved in citric acid, HCl, and ethylene glycol. These solutions were condensed at 80°C and calcined at 250°C for 2 h. The black shiny gels obtained were oxidized at 550°C in air for 0.5 h and then annealed at 550°C for 3.5 h after milling. The obtained powders became brownish white in color with increasing TM concentration.

The crystal structures were determined by x-ray diffraction (XRD) using Cu K_α x-rays. The magnetic properties at room temperature were measured using a vibrating sample magnetometer (VSM). X-ray absorption spectroscopy (XAS) was performed at BL-7A, Photon Factory, High-energy Accelerator Organization to investigate the valence states of the Co ions. ^{57}Fe Mössbauer spectra were obtained at room temperature in transmission geometry using a ^{57}Co (Cr) source and the Doppler velocity was calibrated using α-Fe.

3 Results and discussion

Almost all the XRD patterns obtained for SnO_2 doped with 1–5% Fe and 1% Co reveal rutile-type SnO_2 (lattice parameters: $a = 4.74$ Å, $c = 3.19$ Å). No XRD peaks corresponding to other phases (hematite) were detected. Figure 1a shows VSM results measured at room temperature. M_s increases with increasing Fe concentration, reaching a maximum at 4% Fe and 1% Co; when the Fe concentration is increased to 5% Fe, M_s decreases and H_c increases. This enhancement in M_s occurs only in Fe and Co co-doped samples; it was not observed in samples with single ions. Crystal sizes were estimated from the line width of (110) XRD peaks using the Scherrer's formula. The relationship between the crystal size and magnetization is plotted in Fig. 1b. M_s increases with increasing crystal size. The enhancement of M_s originates from the large crystal size.

Figure 2a shows Mössbauer spectra of 1–5% Fe and 1% Co co-doped SnO_2. The spectra were fitted by two kinds of doublets originated from quadrupole splitting (QS). Fe^{3+} ionic states are revealed by isomer shift value of 0.3 mm/s. The D1 and D2 components are defined as the small and large QS, respectively. The D1 (0.8 mm/s)

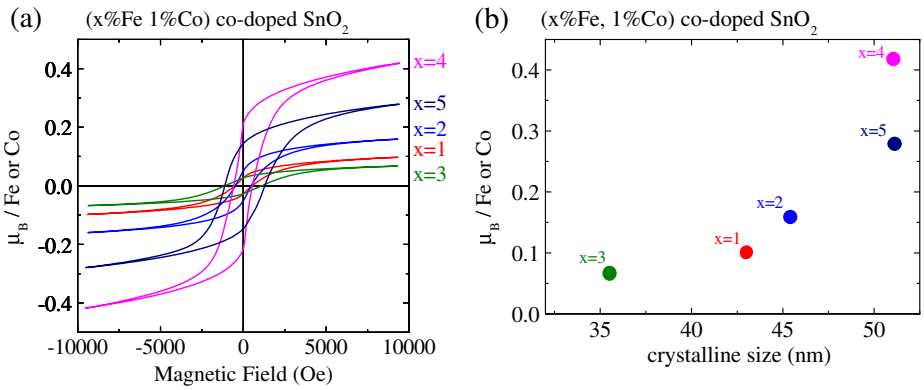

Fig. 1 **a** Magnetization curves obtained by VSM for x% Fe and 1% Co co-doped SnO_2. **b** Crystal sizes of SnO_2 estimated by XRD versus saturation magnetization by VSM

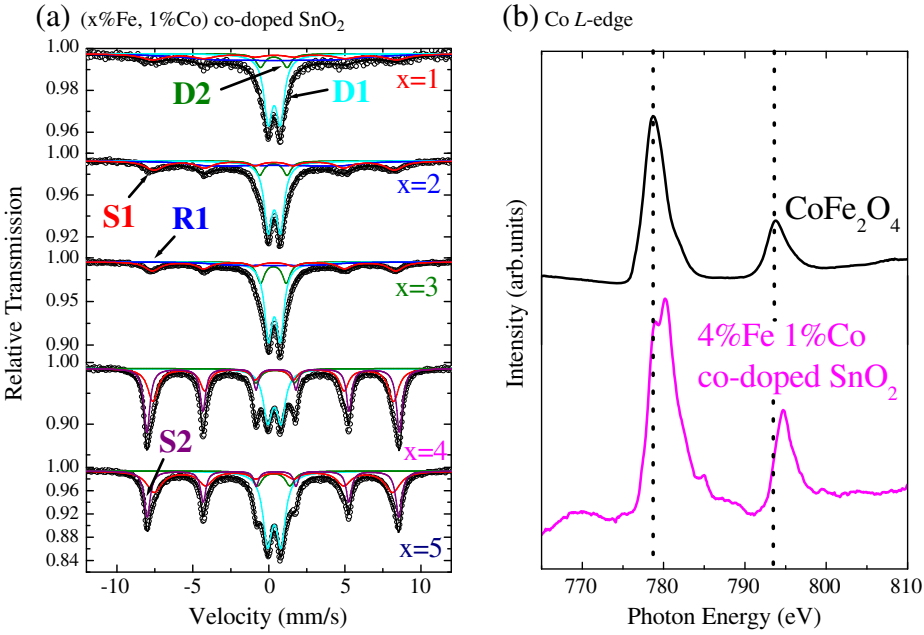

Fig. 2 **a** Mössbauer spectra of x% Fe and 1% Co co-doped SnO_2. **b** Co L-edge XAS 4%Fe and 1%Co co-doped SnO_2 and that of Co-ferrite

originates from Fe^{3+} ions substituted in the Sn site and that the D2 (1.8 mm/s) comes from Fe^{3+} ions near many defects (oxygen vacancies). The intensity ratio D2/D1 increases with increasing Fe concentration, which suggests that the amount of oxygen vacancies increases with increasing TM doping. A sextet component (S1) and a broad magnetic relaxation component (R1) are also observed in the Mössbauer spectra. The broad R1 component originates from spin fluctuations within the relaxation time of 10^{-7} s in Mössbauer effect. With increasing Fe concentration, S1 with a hyperfine

field of 49 T increases while R1 decreases. The spectral weights are considered to transfer from R1 to S1 components with increasing Fe concentration. On the other hand, a S2 component with a hyperfine field of 51 T appears, while the R1 component is greatly diminished. The Mössbauer parameters of the S2 component are quite similar to those of hematite [10], suggesting that α-Fe_2O_3 segregation occurs at more than 4% Fe and 1% Co co-doping. Since excess Fe ions contribute to nanoparticle formation, it is considered that α-Fe_2O_3 can be segregated over the solubility limit.

Figure 2b shows the XAS spectra of the Co L-edge region for Fe and Co co-doped SnO_2 and Co ferrite ($CoFe_2O_4$). Since $CoFe_2O_4$ is assumed to contain the Co^{2+} state, the line shapes of Fe and Co co-doped SnO_2 cannot be explained by only Co^{2+} states. The additional peaks observed at higher photon energies originate from Co^{3+} states [11]. All the samples have very similar XAS spectra. Therefore, Co^{2+}/Co^{3+} mixing states are dominant.

We discuss the relationship between the magnetization and Mössbauer spectra. First, R1 and S1 components are considered to be due to spin fluctuation and spin ordering of the doped Fe ions, respectively. The suppression of R1 with increasing Fe concentration may be related to the increase of the magnetic impurity phases or hematite. Therefore, the sample up to 3% Fe and 1% Co seems to be single phase. Second, co-doping enhances M_s so that it can be used to tune the magnetic properties. It may originate from the exchange interaction between Fe^{3+} and Co^{2+}/Co^{3+} ions via oxygen vacancies. Another possible cause is the formation of $CoFe_2O_4$. The Mössbauer spectrum of Co-ferrite ($CoFe_2O_4$) has been also fitted by two sextet peaks based on the assumption that there are two kinds of Fe sites in the spinel structure [12, 13]. For Fe-ion doping over the stoichiometric $CoFe_2O_4$, α-Fe_2O_3 compound may be segregated at doping higher than 4% Fe. The ferromagnetism mechanisms of enhanced M_s in the co-doping samples (less than 3% Fe doping) without the formation of precipitated compounds should be clarified further. Antiferromagnetic interaction between TM ions might be considered for more than 3% Fe doping. Defect-induced ferromagnetism models [7] have been proposed for single-ion doped cases. However, these models cannot explain the enhancement in M_s observed in co-doped samples. A double-exchange-like mechanism through carrier kinetics between Fe^{3+} (d^5) and Co^{2+} (d^7) electrons may give rise to the enhanced M_s.

4 Conclusion

Fe and Co co-doped SnO_2 synthesized by sol-gel method. Fe and Co co-doping was found to enhance the magnetization. Mössbauer spectra revealed that the magnetic relaxation and sextet components may result from diluted magnetism for less than 3% Fe doping. However, the magnetic enhancement for 4% Fe and 1% Co doping may be mainly due to Co ferrite formed with hematite precipitation.

References

1. Ghim, W.H.: Sci. Adv. Mater. **3**, 150 (2011)
2. Matsumoto, Y., Murakami, M., Shono, T., Hasegawa, T., Fukumura, T., Kawakami, M.P., Ahmet, P., Chikyow, T., Koshihara, S., Koinuma, H.: Science **291**, 854 (2001)

3. Coey, J.M., Douvalis, A.P., Fitzgerald, C.B., Venkatesan, M.: Appl. Phys. Lett. **84**, 1332 (2004)
4. Nomura, K., Barrero, C.A., Sakuma, J., Takeda, M.: Phys. Rev. B **75**, 184411 (2007)
5. Punnoose, A., Hays, J., Thurber, A., Engelhard, M.H., Kukkadapu, R.K., Wang, C., Shuthanandan, V., Thevuthasan, S.: Phys. Rev. B **72**, 054402 (2005)
6. Zuo, Y., Ge, S., Zhao, Y.X., Zhou, X., Xiao, Y., Zhang, L.: J. Appl. Phys. **104**, 023905 (2008)
7. Coey, J.M.D., Venkatesan, M., Fitzgerald, C.B.: Nat. Matters **4**, 173 (2005)
8. Coey, J.M.D., Stamenov, P., Gunning, R.D., Venkatesan, M., Paul, K.: New J. Phys. **12**, 053025 (2010)
9. Nomura, K., Okabayashi, J., Okamura, K., Yamada, Y.: J. Appl. Phys. **110**, 083901 (2011)
10. Kurihara, H., Yajima, T., Nomura, K.: J. Jpn. Soc. Powder. Powder. Metall. **56**, 116 (2009)
11. Mizokawa, T., Tjeng, L.H., Lin, H.J., Chen, C.T., Kitawaki, R., Terasaki, I., Lambert, S., Michel, C.: Phys. Rev. B **71**, 193107 (2005)
12. Kim, Y.I., Kim, D., Lee, C.S.: Physica B **337**, 42 (2003)
13. Ahmed, S.R., Ogale, S.B., Papaethymiou, G.C., Ramesh, R., Kofinas, P.: Appl. Phys. Lett. **80**, 1616 (2002)

Hyperfine Interact (2012) 205:111–115
DOI 10.1007/s10751-011-0447-9

Electron magnetic resonance and Mössbauer studies on iron doped SnO_2 nanoparticles

Maria Nicoleta Grecu · Serban Gr. Constantinescu · Daniela Ghica · Doina Tărăbăşanu-Mihaila · Lucian Diamandescu

Published online: 8 December 2011

Abstract Iron doped (0.25–7.5% molar) hydrothermal nano-SnO_2 was characterized by electron magnetic resonance (EMR) and Mössbauer spectroscopies. Only a small fraction of transition metal ions are in magnetic ordered state, contrary to the similar crystallographic compound TiO_2. Temperature dependences of spectra suggest that by increasing iron concentration, or annealing temperature, iron ions migrate to nanoparticles surfaces forming disordered iron oxides.

Keywords EMR · Mössbauer effect · SnO_2 nanoparticles · Paramagnetic defects

1 Introduction

Tin dioxide (SnO_2) is a semiconductor which combines good electrical conductivity with optical transparency, being very interesting for optoelectronic applications. Also, it has remarkable properties as an oxidation catalyst, or gas sensor. Recent discovery of room temperature ferromagnetism in Co-doped SnO_2 [1] has increased the interest in its study [2]. Numerous investigations have been performed on transition metal doped SnO_2 (V, Mn, Fe, Co, Rh, Ni, Cr) [3, 4]. In spite of this effort the data are often contradictory [4–6], and there is no clear model to explain the behaviour of transition metal ions and the existence or not of the ferromagnetic ordering. All studies have put in evidence the importance of the preparation route and of the thermal treatments. Therefore a study of local magnetic and structural properties of hydrothermal nano-SnO_2 doped with iron was performed with EMR and Mössbauer spectroscopy.

M. N. Grecu (✉) · S. Gr. Constantinescu · D. Ghica · D. Tărăbăşanu-Mihaila · L. Diamandescu
National Institute of Materials Physics, 077125 Magurele-Bucharest, Romania
e-mail: mgrecu@infim.ro

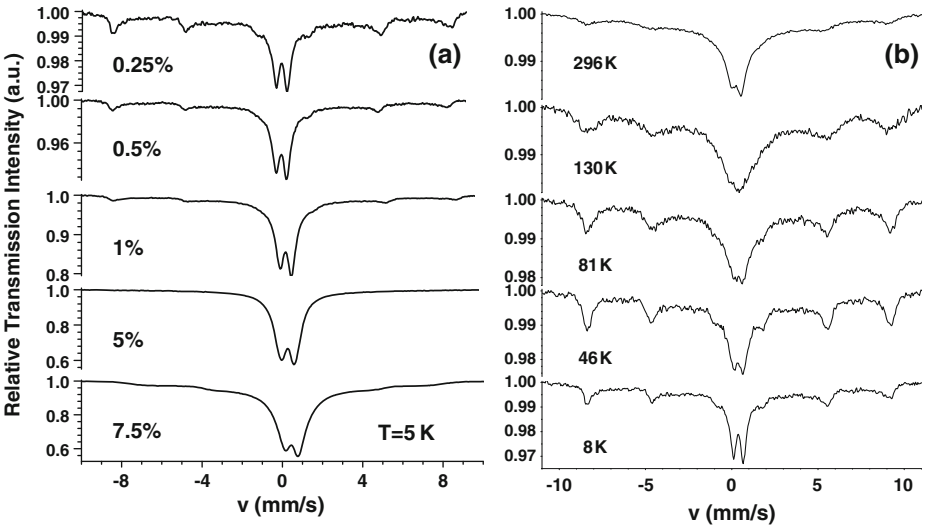

Fig. 1 ^{57}Fe Mössbauer spectra at 5 K vs. iron concentration (a), and the temperature dependence of spectra for the sample with 0.25% iron

2 Experimental

Iron doped SnO_2 nanoparticles, with different concentrations of ^{57}Fe (0.25%–7.5% mol α-Fe_2O_3), were synthesized by a hydrothermal route at 200°C as in [7, 8]. The analysis of X-ray diffraction patterns, performed with a Bruker D8 Advance diffractometer, revealed the formation of the rutile SnO_2 phase without any impurity under the limit of instrument sensitivity. The average crystallite sizes were 3–4 nm for all samples. The EMR spectra for as-prepared and annealed samples, one hour at 550°C in air and/or vacuum, were recorded at different temperatures (100–290 K) on X-band CMS 4800 and Q-band Bruker ELEXSYS-500 spectrometers. ^{57}Fe Mössbauer spectra in transmission geometry were obtained with AM50 Promeda and Wissel-SeeCo spectrometers, in the temperature range 5–298 K, using a ^{57}Co:Rh source. The χ^2 procedure was used for deconvolution of the spectra, with theoretical constrains of intensities, line widths Γ and positions of γ-line-resonances in magnetic and quadrupolar elementary patterns resonances.

3 Results and discussions

Mössbauer data In Fig. 1 the Mössbauer spectra are plotted for as-prepared samples with different ^{57}Fe concentrations (Fig. 1a) and at different temperatures for the sample with 0.25% iron (Fig. 1b). In Fig. 2 spectra for 1% Fe samples (initial and annealed) are shown by comparison.

Standard deconvolution of the spectra evidenced an increasing magnetic contribution with decreasing temperature and iron concentration (see Fig. 3). One remarks the almost symmetric doublet for the sample with 0.25% relative to the asymmetric one for Fe 7.5% at 5 K. It suggests no hidden magnetic patterns under the doublet

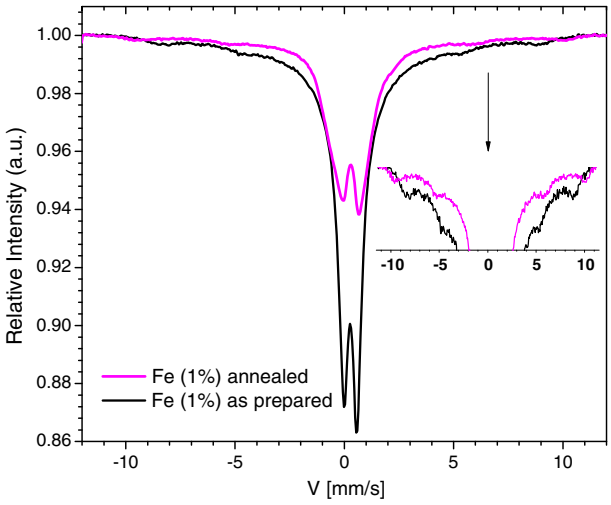

Fig. 2 Mössbauer spectra at RT for 1% ^{57}Fe sample, as prepared and annealed at 550°C

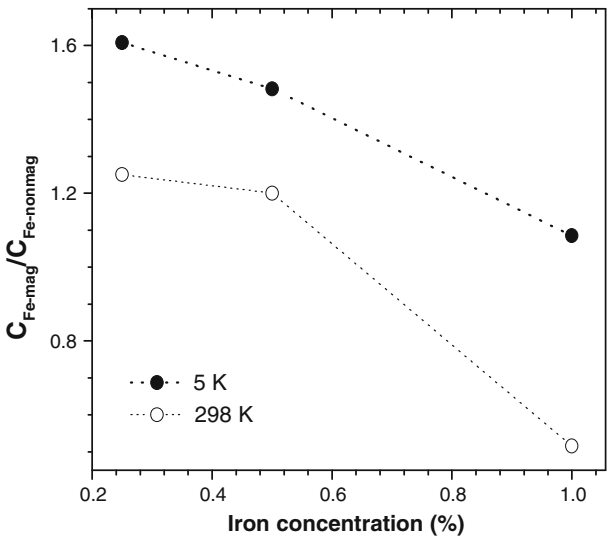

Fig. 3 Ratio of magnetic on nonmagnetic component of MS spectra at 5 and 298 K

for this sample and at this temperature. The doublet could correspond to iron substituting Sn ions. The broadening of doublet component could be explained by iron concentration dependence of grain size [7, 8]. The increasing of the magnetic contribution at low temperatures suggests a superparamagnetic transition; a multimodal distribution of the grain sizes is possible. The spectra of annealed samples at 550°C evidence apparently a smaller magnetic contribution relative to as-prepared sample (see Fig. 2), but under the doublet there is a hidden contribution. We have to note that in the spectrum of annealed sample, ferric ions are about 95–100% and the hyperfine magnetic field is more intense (60 ± 0.3 T) comparative to 53 ± 0.3 T in

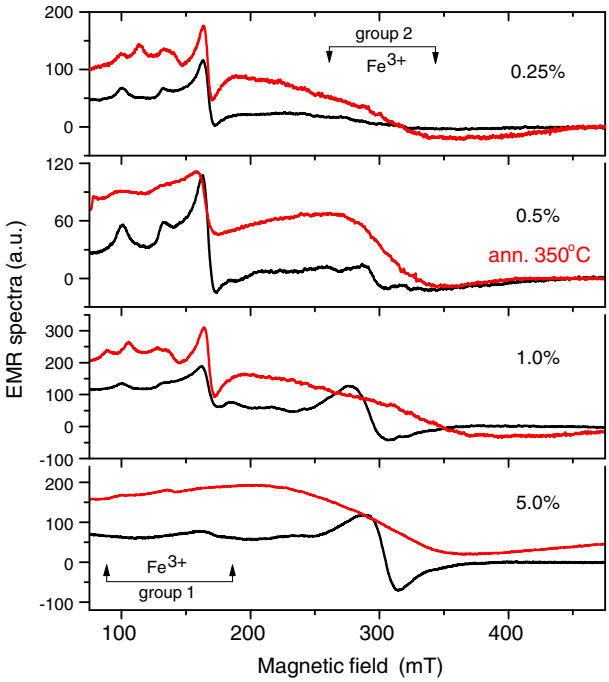

Fig. 4 X-band EMR spectra for as prepared samples (*black*) and annealed at 550°C (*red*)

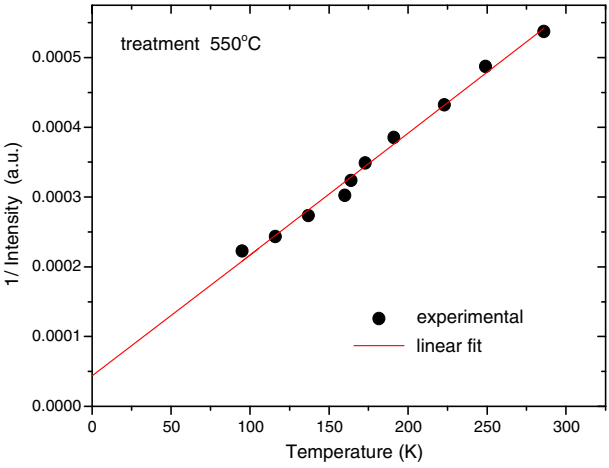

Fig. 5 Temperature dependence of spectral intensity for SnO_2:^{57}Fe (1%) ann. air 550°C

non-treated sample. It suggests a complex magnetic coupling between iron ions and defects [6].

EMR data Typical EMR spectra and their dependence of iron concentrations are given in Fig. 4. Three groups of resonance lines are observed: two important groups of Fe^{3+} ions lines were detected. At low fields ($g_{ef} \sim 4$–8) the lines were attributed to iron ions in low symmetry crystalline fields [5] and can be associated with paramagnetic ions in distorted crystalline positions.

They are responsible for the paramagnetic pattern (quadrupole doublet) observed in Mössbauer spectra. At higher ion concentrations these lines broaden due to dipole-dipole interactions. The other group of lines around $g_{ef} = 2.1–2.2$ presents the characteristics of weakly magnetic coupled ions (small shift towards lower fields and broadening at low temperatures). The air annealing 1h at 550°C (see Fig. 4, red lines) enhances and broadens very much these lines, suggesting that they come from iron distributed in the surface layer. The large broadening is a clear sign of the disorder in the nanoparticle surface. The double integral of spectra, proportional to EMR active iron ions concentration, has an antiferromagnetic temperature dependence (Fig. 5). There is also a third group of EMR lines, better observed in Q-band at higher fields ($g \leq 2.0$), in annealed samples. These lines are associated with the paramagnetic defects—hole ($g = 2.008$, line width 0.4 mT) or trapped electrons ($g = 1.994$; 1.997) in oxygen vacancy sites at the surface of SnO_2 nanoparticles.

4 Conclusions

Both EMR and Mössbauer investigations evidence the disordered distribution of iron ions in the bulk and on the surface of SnO_2 nanoparticles. A part of iron ions are magnetically coupled; they are sensitive to thermal treatment in air supporting the model of their distribution in the nanoparticle surface layer.

Acknowledgements We gratefully acknowledge financial suport from CNCSIS–UEFISCSU, Romanian project PNII–IDEI nr. 4/2010, code ID-106.

References

1. Ogale, S.B., et al. (15 auths): High temperature ferromagnetism with a giant magnetic moment in transparent Co-doped $SnO_{2-\delta}$. Phys. Rev. Lett. **91**, 077205–077209 (2003)
2. Batzill, M., Diebold, U.: The surface and materials science of tin oxide. Prog. Surf. Sci. **79**, 47154 (2005)
3. Wang, X.L, Dai, Z.X., Zeng, Z.: Search for ferromagnetism in SnO_2 doped with transition metals (V, Mn, Fe, Co). J. Phys. Condens. Matter **20**, 045214–045222 (2008)
4. Coey, J.M.D., Douvales, A.P., Fitzgerald, C.B., Venkatesan, M.: Ferromagnetism in Fe-doped SnO_2 thin films. Appl. Phys. Lett. **84**, 1332 (2004)
5. Punnoose, A., Reddy, K.M., Hays, J., Thurber, A., Andronenko, S., Misra, S.K.: Dopant spin states and magnetic interaction in transition metal (Fe^{+3}) doped semiconductor nanoparticles: an EMR and magnetometric study. Appl. Magn. Reson. **36**, 331–345 (2009)
6. Nomura, K., Barrero, C., Sakuma, J., Takeda, M.: Room-temperature ferromagnetism of sol-gel-synthesized $Sn^{57}_{1-x}Fe_xO_{2-\delta}$. Phys. Rev. B **75**, 184411–184413 (2007)
7. Constantinescu, S., Diamandescu, L., Bibicu, I., Tarabasanu-Mihaila, D., Feder, M.: Hyperfine Interactions and dynamics characteristics of ^{119}Sn in $xSnO_2$-(1-x)αFe_2O_3 nanoparticle-system. Hyperfine Interact. **184**, 83–89 (2008)
8. Diamandescu, L., Constantinescu, S., Bibicu, I., Tarabasanu-Mihaila, D., Feder, M., Vlaicu, M.: Mössbauer investigation of hyperfine interactions in diluted Fe—SnO_2 nanoparticles. J. Phys. Conf. Series. **217**, 012110–012113 (2010)

Hyperfine Interact (2012) 205:117–120
DOI 10.1007/s10751-011-0442-1

Mössbauer study of ε-$Al_xFe_{2-x}O_3$ nanomagnets

Kana Yamada · Marie Yoshikiyo · Asuka Namai · Shin-ichi Ohkoshi

Published online: 8 November 2011

Abstract A series of Al^{3+}-substituted ε-Fe_2O_3 nanomagnets, ε-$Al_xFe_{2-x}O_3$ ($x = 0$, 0.21, 0.40), with large coercive field values was studied by ^{57}Fe Mössbauer spectroscopy. The hyperfine field and absorption coefficient in the Mössbauer spectra changed with x. These behaviors can be explained by the selective replacement of Fe^{3+} ions with Al^{3+} ions. This is the first report on the Mössbauer spectra of metal-substituted ε-Fe_2O_3.

Keywords Mössbauer spectroscopy · ε-Fe_2O_3 · ε-$Al_xFe_{2-x}O_3$ · Nanomagnet

1 Introduction

Iron oxide, Fe_2O_3, has four polymorphs at normal pressure and temperature: α-, β-, γ-, and ε-phases [1]. Among these, α-Fe_2O_3 with a corundum structure (hematite) and γ-Fe_2O_3 with a spinel structure (maghemite) exist in nature, and various Mössbauer studies on these phases have been reported [1, 2]. In contrast, ε-Fe_2O_3 is very rare and preparation of a single phase of ε-Fe_2O_3 is difficult. Hence, Mössbauer studies of ε-Fe_2O_3 have been limited to mixed samples containing α- and γ-Fe_2O_3 [3]. However, our group successfully synthesized a single phase of ε-Fe_2O_3 in 2004 using a combination of reverse-micelle and sol-gel techniques, and observed an extremely large coercive field value of 20 kOe at room temperature [4–10].

ε-Fe_2O_3 has an orthorhombic crystal structure in the $Pna2_1$ space group (a = 5.102 Å, b = 8.781 Å, c = 9.466 Å) with four nonequivalent Fe^{3+} sites, i.e., distorted

K. Yamada · M. Yoshikiyo · A. Namai · S. Ohkoshi (✉)
Department of Chemistry, School of Science, The University of Tokyo,
7-3-1 Hongo, Bunkyo-ku, Tokyo 113-0033, Japan
e-mail: ohkoshi@chem.s.u-tokyo.ac.jp

S. Ohkoshi
CREST, JST, 5 Sanbancho, Chiyoda-ku, Tokyo 102-0075, Japan

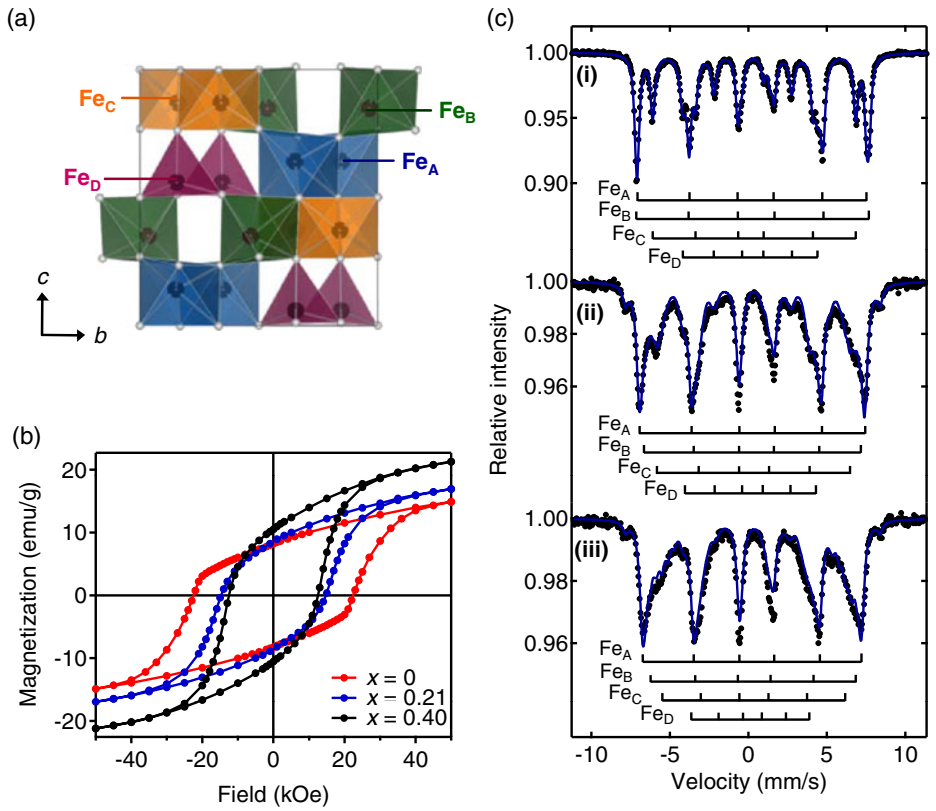

Fig. 1 **a** Crystal structure of ε-Fe_2O_3, **b** magnetization versus external magnetic field plots for ε-$Al_xFe_{2-x}O_3$ (x = 0, 0.21, 0.40) at room temperature, and **c** Mössbauer spectra of ε-$Al_xFe_{2-x}O_3$ at room temperature for x = (i) 0, (ii) 0.21, and (iii) 0.40. *Black dots* and *blue lines* represent the observed and fitted spectra, respectively

octahedral Fe_A and Fe_B sites, regular octahedral Fe_C site, and tetrahedral Fe_D site (Fig. 1a) [10]. In addition, we have synthesized metal-substituted ε-iron oxide (ε-$M_xFe_{2-x}O_3$, M = Al, Ga, In) [11–14]. Figure 1b shows the magnetic hysteresis loops of ε-$Al_xFe_{2-x}O_3$ [13]. ε-$Ga_xFe_{2-x}O_3$ and ε-$Al_xFe_{2-x}O_3$ show high-frequency millimeter wave absorption, while ε-$In_xFe_{2-x}O_3$ exhibits a phase transition between ferrimagnetism and antiferromagnetism [11–13, 15]. In this paper, we report ^{57}Fe Mössbauer spectra of Al^{3+}-substituted ε-Fe_2O_3.

2 Experimental section

A series of ε-$Al_xFe_{2-x}O_3$ ($x = 0, 0.21, 0.40$) spherical nanoparticles with average sizes of 24–54 nm were synthesized using the methods reported in our previous paper [13]. The ^{57}Fe Mössbauer spectra of ε-$Al_xFe_{2-x}O_3$ were measured at room temperature in a transmission geometry using a ^{57}Co/Rh source. The obtained spectra were analyzed with WinNormos software using the least squares method.

3 Results and discussion

Figure 1c(i) shows the Mössbauer spectrum of the sample for $x = 0$, which consists of four sextets with line area ratios of 3:2:1:1:2:3. These four sextets belong to the four Fe^{3+} (Fe_A, Fe_B, Fe_C, and Fe_D) sites in ε-Fe_2O_3. Least squares analysis indicates that the hyperfine field (HF) values of Fe_A, Fe_B, Fe_C, and Fe_D sites are 45.3, 46.0, 40.1, and 26.6 T, respectively. The isomer shift (IS) values of the Fe_A–Fe_D sites are 0.35, 0.39, 0.37, and 0.19 mm/s, respectively, while the quadrupole shift (QS) values are −0.23, −0.22, 0.00, and −0.17 mm/s, respectively. These observed Mössbauer parameters correspond to the previously reported values [1, 3, 6, 7, 15].

Figure 1c(ii) and (iii) show the Mössbauer spectra of the samples $x = 0.21$ and 0.40, respectively. In the case of magnetic materials, the HF value of an Fe^{3+} ion depends on the product of the number of nearest neighboring Fe^{3+} ions (Z) and the superexchange interaction between the center Fe^{3+} ion and the neighboring Fe^{3+} ions through O^{2-} ions (J_{ex}). Hence, when a magnetic Fe^{3+} ($S = 5/2$) is substituted by a diamagnetic Al^{3+} ($S = 0$), one sextet for each Fe^{3+} site is split into several sextets due to the appearance of reduced Z integers ($Z - 1$, $Z - 2$, ...). Thus, we analyzed the Mössbauer spectra for $x = 0.21$ and 0.40 using more than one sextet assuming that only Fe_D site is replaced by Al^{3+} ion, since Fe_D site is expected to be replaced by Al^{3+} ion on the basis of our previous knowledge. Consequently, the average HF values of the Fe_A, Fe_B, Fe_C, and Fe_D sites for the sample $x = 0.21$ are 44.6, 42.7, 37.5, and 26.0 T, the IS values are 0.38, 0.38, 0.34, and 0.19 mm/s, the QS values are −0.29, −0.25, −0.02, and −0.13 mm/s, and the relative absorption intensities are 1, 1, 1, and 0.4, respectively. For the sample $x = 0.40$, the HF values of Fe_A–Fe_D sites are 42.9, 39.4, 35.2, and 24.4 T, the IS values are 0.38, 0.33, 0.34, and 0.19 mm/s, the QS values are −0.30, −0.28, −0.02, and −0.13 mm/s, and the relative absorption intensities are 1, 1, 1, and 0.2, respectively. In these samples, α-Fe_2O_3 is contained as an impurity.

As the degree of Al^{3+} substitution increased, the HF values of the Fe_A–Fe_D sites gradually decreased, and the absorption intensity of the Fe_D site significantly decreased. These behaviors can be understood by considering that the Al^{3+} ion selectively replaces the Fe_D site. This interpretation corresponds to the results of the XRD patterns in our previous paper [13]. Al^{3+} ions predominantly substitute for the tetrahedral Fe_D site because Al^{3+} ions have difficulty replacing the octahedral Fe^{3+} sites due to the smaller ionic radius of octahedral Al^{3+} (0.535 Å) compared to that of Fe^{3+} (0.645 Å) [16]. Hence, Al^{3+} ions prefer to substitute for the smaller tetrahedral Fe^{3+} site.

Acknowledgements The present research was supported partly by CREST program of JST, a Grant-in-Aid for Young Scientists (S) from JSPS, a Grant for the Global COE Program "Chemistry Innovation through Cooperation of Science and Engineering", APSA from MEXT Japan, The Asahi Glass Foundation, Sekisui Integrated Research, and the Center for Nano Lithography & Analysis, The University of Tokyo, supported by MEXT Japan. A. N. is grateful to JSPS Research Fellowships for Young Scientists. We are grateful to Mr. T. Goto, Mr. T. Yoshida, and Mr. T. Miyazaki from DOWA Electronics Materials Co., Ltd., for the valuable discussions.

References

1. Cornell, R.M. , Schwertmann, U.: The Iron Oxide. VCH, Weinheim (1996)
2. Greenwood, N.N. , Gibb, T.C.: Mössbauer Spectroscopy. Chapman and Hall, London (1971)

3. Tronc, E., Chaneac, C., Jolivet, J.P.: J. Solid State Chem. **139**, 93 (1998)
4. Jin, J., Ohkoshi, S., Hashimoto, K.: Adv. Mater. **16**, 48 (2004)
5. Ohkoshi, S., Sakurai, S., Jin, J., Hashimoto, K.: J. Appl. Phys. **97**, 10K312 (2005)
6. Kurmoo, M., Rehspringer, J.-L., Hutlova, A., D'Orleans, C., Vilminot, S., Estournes, C., Niznansky, D.: Chem. Mater. **17**, 1106 (2005)
7. Gich, M., Frontera, C., Roig, A., Taboada, E., Molins, E., Rechenberg, H.R., Ardisson, J.D., Macedo, W.A.A., Ritter, C., Hardy, V., Sort, J., Skumryev, V., Nogues, J.: Chem. Mater. **18**, 3889 (2006)
8. Sakurai, S., Namai, A., Hashimoto, K., Ohkoshi, S.: J. Am. Chem. Soc. **131**, 18299 (2009)
9. Machala, L., Tucek, J., Zboril, R.: Chem. Mater. **23**, 3255 (2011)
10. Sakurai, S., Jin, J., Hashimoto, K., Ohkoshi, S.: J. Phys. Soc. Jpn. **74**, 1946 (2005)
11. Sakurai, S., Kuroki, S., Tokoro, H., Hashimoto, K., Ohkoshi, S.: Adv. Funct. Mater. **17**, 2278 (2007)
12. Ohkoshi, S., Kuroki, S., Sakurai, S., Matsumoto, K., Sato, K., Sasaki, S.: Angew. Chem. Int. Ed. **46**, 8392 (2007)
13. Namai, A., Sakurai, S., Nakajima, M., Suemoto, T., Matsumoto, K., Goto, M., Sasaki, S., Ohkoshi, S.: J. Am. Chem. Soc. **131**, 1170 (2009)
14. Ohkoshi, S., Namai, A., Sakurai, S.: J. Phys. Chem. C **113**, 11235 (2009)
15. Tucek, J., Zboril, R., Namai, A., Ohkoshi, S.: Chem. Mater. **22**, 6483 (2010)
16. Shannon, R.D.: Acta Crystallogr., A. **32**, 751 (1976)

Hyperfine Interact (2012) 205:121–124
DOI 10.1007/s10751-011-0502-6

Mössbauer spectroscopy of protein-passivated iron oxide nanoparticles

Heming Huang · Ramona Christmann · Roland Ulber · Volker Schünemann

Published online: 20 December 2011

Abstract Within this work we report a Mössbauer spectroscopic study of uncoated and bovine serum albumin (BSA-) passivated magnetic iron oxide particles. Electron microscopy confirms the successful preparation of the particles with sizes in the 10 to 30 nm range. The analysis of the Mössbauer spectra at high fields shows that only 20% of the iron is present in form of Fe_3O_4–nanoparticles. The majority (80%) of the iron is present as maghemite (γ–Fe_2O_3). Coating with BSA does not influence the particle morphology and does also not affect the magnetite to maghemite ratio.

Keywords Maghemite · Magnetite · Nanoparticles · Mössbauer spectroscopy · Bovine serum albumin

1 Introduction

Magnetic iron oxide nanoparticles have potential applications in thermal therapy, as magnetic carriers for medical drugs, as contrast agents in magnetic resonance imaging or as carriers for precious noble metals in reusable catalysts for liquid phase reactions. A major problem which has to be overcome is the lack of long-time stability of the magnetic carrier particles e.g. in catalytic applications. Therefore passivation of the particle surface is often performed by preparing metal nanoparticles with silica or polymer coatings. Recently the preparation of protein-passivated Fe_3O_4 nanoparticles with low toxicity and rapid heating properties for thermal therapy has been reported [1]. The preparation of the Fe_3O_4 nanoparticles has been done according to Massart's co-precipitation method [1, 2] and Bovine serum albumin (BSA) has been

H. Huang · R. Christmann · V. Schünemann (✉)
Department of Physics, University of Kaiserslautern, Erwin-Schrödinger-Str. 46, 67663 Kaiserslautern, Germany
e-mail: schuene@physik.uni-kl.de

R. Ulber
Institute of Bioprocess Engineering, University of Kaiserslautern, Erwin-Schrödinger-Str. 46, 67663 Kaiserslautern, Germany

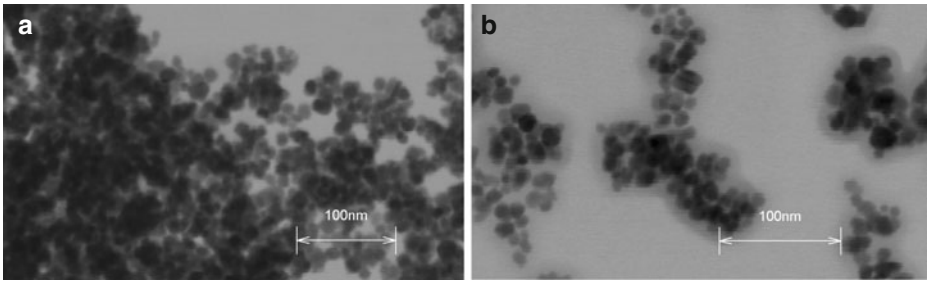

Fig. 1 Transmission electron micrographs of as prepared magnetic iron oxide particles according to Massart's method [1, 2] before (**a**) and after coating with BSA (**b**)

used as coating for the iron oxide particles. The protective BSA layer ensures not only high stability and low cytotoxicity, but also relatively easy biofunctionalization by means of attaching targeting molecules via the surface lysine groups of the protein [1]. Within this work we report a Mössbauer spectroscopic study of these BSA-passivated magnetic iron oxide particles, which has at least to our knowledge not been performed up to now.

2 Materials and methods

Bovine Serum Albumin (BSA) was purchased by Carl Roth GmbH. The magnetic iron oxide particles were prepared by coprecipitation of Fe(II) and Fe(III) chlorides according to Massart's method [2]. With maintaining a molar ratio of Fe^{2+}:Fe^{3+} = 1:2, 0.0575 g $FeCl_2 \cdot 4H_2O$ and 0.1575 g $FeCl_3 \cdot 6H_2O$ were dissolved in 10 ml milliQ water under nitrogen. After 10 min purging with nitrogen, 2.5 ml NH_4OH was added to the solution. The formed black solution was incubated at 90°C for 20 min and then cooled down to room temperature. The black precipitate was collected with a magnet and washed twice with water. The BSA-coated iron oxide nanoparticles were prepared using the iron oxide nanoparticles and 250 mg BSA, which was each added to 20 ml milliQ water [1]. The mixture was sonicated for 4 h. The particles were collected with a magnet and washed twice with water in order to remove excess BSA. Mössbauer spectra were measured in a closed cycle cryostat equipped with a superconducting magnet (Cryo Industries of America Inc.) and recorded using a conventional spectrometer in the constant-acceleration mode. Isomer shifts are given relative to α-Fe at room temperature. The spectra were analyzed by least-square fits using Lorentzian line shapes.

3 Results and discussion

Transmission electron micrographs of the as prepared magnetic iron oxide particles are shown in Fig. 1. Both, the uncoated iron oxide particles (Fig. 1a) and the BSA-passivated iron oxide particles (Fig. 1b) have a mean diameter of 12 nm. Obviously the BSA-coating does neither influence the size nor the morphology of the iron oxide particles.

Mössbauer spectra of the uncoated iron oxide nanoparticles obtained at 150 K in zero magnetic field as well in an external field of 5 T are displayed in Fig. 2a and b.

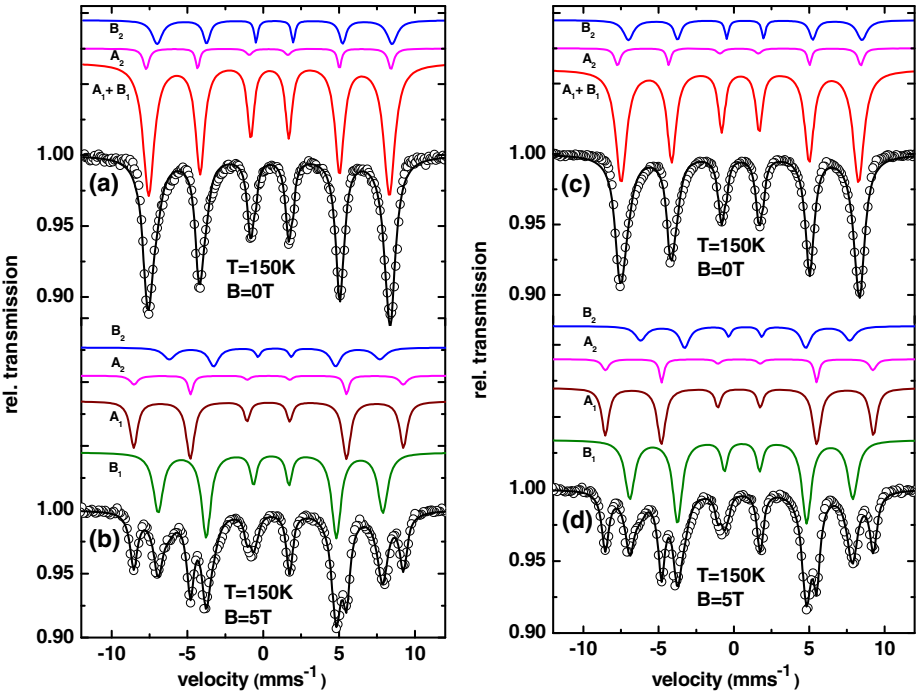

Fig. 2 (*left*) Mössbauer spectra of as prepared iron oxide particles obtained at 150 K in zero field (**a**) and in a field of 5 T perpendicular to the γ-ray (**b**). (*right*) Mössbauer spectra of BSA-passivated iron oxide particles obtained at 150 K in zero field (**c**) and in a field of 5 T perpendicular to the γ-ray (**d**). The *solid lines* represent the result of an analysis with symmetrical sextets (intensity ratio 3:2:1 for (a) and 3:4:1 for (b)) and parameters given in Table 1

The majority of the spectral area (~80%) in the high field spectrum consists of two sextets with opposite hyperfine fields (30% for component A_1 and 51% for component B_1). The ratio of both spectral areas A_1/B_1 equals about to 0.59, which is the ratio expected for the ferrimagnetic γ–Fe_2O_3 spinel with (AB_2O_4) structure, if one assumes that all Fe^{3+} vacancies are located on the octahedral B-lattice [3]. The isomer shift for A_1 $\left(\delta_{A_1} = 0.35\ \text{mms}^{-1}\right)$ and B_1 $\left(\delta_{B_1} = 0.51\ \text{mms}^{-1}\right)$ are both characteristic for Fe^{3+} ions. Therefore we conclude that component A_1 represents Fe^{3+} ions in the tetrahedral sublattice and component B_1 represents Fe^{3+} ions in the octahedral B lattice sites of ferrimagnetic γ–Fe_2O_3.

A minority of the spectral area (20%) with the components A_2 and B_2 show indeed characteristic Mössbauer parameters of Fe_3O_4. The isomer shift of component B_2 $\left(\delta_{B_1} = 0.75\ \text{mms}^{-1}\right)$ is characteristic for $Fe^{2.5+}$ – $Fe^{2.5+}$ ions in the octahedral B lattice sites of Fe_3O_4 at temperatures above the Verwey transition ($T_v \cong 110$ K) where electron hopping and spin pairing occurs. This is also consistent with the antiparallel alignment of the internal hyperfine field of B_2 with the external field. Component A_2 exhibits $\delta_{A_2} = 0.35\ \text{mms}^{-1}$ and its internal hyperfine-field aligns parallel with the external field, a behavior which is typical for Fe^{3+} ions of the tetrahedral A sublattice of magnetite [4].

Table 1 Mössbauer parameters of the uncoated and BSA coated magnetic iron oxide nanoparticles as obtained from the analysis of the spectra shown in Fig. 2

B(T)	Component	Rel. area(%)	$\delta(mms^{-1})$	$\Delta E_Q(mms^{-1})$	$\Gamma_{1,2,3}(mms^{-1})$	$B_{hf}(T)$
Uncoated magnetic iron oxide nanoparticles						
0	A_1+B_1	80.2	0.41	0	0.9,0.7,0.5	49.2
	A_2	6.6	0.35	0	0.5,0.3,0.5	50
	B_2	13.2	0.75	0	0.8,0.6,0.3	48
5	A_1	30.6	0.35	0	0.6,0.6,0.5	55.1
	B_1	51.1	0.51	0	0.8,0.7,0.5	45.9
	A_2	6.1	0.35	0	0.6,0.4,0.4	55
	B_2	12.2	0.75	0	1.0,0.8,0.4	43
BSA coated magnetic iron oxide nanoparticles						
0	A_1+B_1	80.2	0.42	0	0.9,0.7,0.5	48.8
	A_2	6.6	0.35	0	0.5,0.3,0.5	50
	B_2	13.2	0.75	0	0.8,0.6,0.3	48
5	A_1	29.9	0.35	0	0.6,0.6,0.5	55.2
	B_1	49.7	0.52	0	0.8,0.7,0.5	45.8
	A_2	6.8	0.35	0	0.6,0.4,0.5	55
	B_2	13.6	0.75	0	0.9,0.8,0.4	43

In conclusion this study shows univocally that the main phase of the particles prepared according to Massart's method is not Fe_3O_4 as in general believed but γ–Fe_2O_3. Coating with BSA does not influence the particle morphology and does also not affect the magnetite to maghemite ratio.

Acknowledgement This work has been supported by the research initiative NANOKAT.

References

1. Samanta, B., Yan, H., Fischer, N., Shi, J., Jerry, D.J., Rotello, V.: J. Mater. Chem. **18**, 1204 (2008)
2. Massart, R.: IEEE Trans. Magn. **17**, 1247 (1981)
3. Greenwood, N.N., Gibb, T.C.: Mössbauer Spectroscopy. Chapman and Hall Ltd, London (1971)
4. Vandenberghe, R.E., De Grave, E.: Mössbauer effect studies of oxidic spinels. In: Grandjean, F., Long, G.J., (eds.) Mössbauer Spectroscopy Applied to Inorganic Chemistry, vol. 3, p. 59. Plenum Press, New York (1984)

Hyperfine Interact (2012) 205:125–128
DOI 10.1007/s10751-011-0495-1

Surface crystallization of Co-containing NANOPERM-type alloys

Marcel Bruno Miglierini · Tomas Hatala · Jiri Frydrych · Klara Šafářová

Published online: 21 February 2012

Abstract Formation of crystalline phases is detected at different depths of the surface regions in $(Fe_{1-x}Co_x)_{76}Mo_8Cu_1B_{15}$ ($x = 0, 0.25$) alloy by CEMS and CXMS techniques. Magnetite is predominantly present on the wheel sides of the ribbons while the alloy is amorphous. During annealing, formation of bcc-Fe and bcc-Fe,Co starts earlier on the air sides of the $x = 0$ and $x = 0.25$, respectively.

Keywords Nanocrystalline alloy · Surface crystallization · CEMS · CXMS

1 Introduction

Magnetic properties of nanocrystalline alloys play an important role when employed in practical applications [1]. The improvement of magnetic parameters is often looked for by substitution of Fe with Co [2]. Consequently, both structure and magnetic arrangement of the alloy are affected. In this paper, we concentrate on the investigation of surface features of Co-substituted NANOPERM-type alloys.

2 Experimental details

Ribbons of $(Fe_{1-x}Co_x)_{76}Mo_8Cu_1B_{15}$ ($x = 0, 0.25$) metallic glass were prepared by rapid quenching (width 2 mm, thickness 23 μm) using iron enriched in ^{57}Fe to 50%.

M. B. Miglierini (✉) · T. Hatala
Institute of Nuclear and Physical Engineering, Slovak University of Technology, Ilkovičova 3, 812 19 Bratislava, Slovakia
e-mail: marcel.miglierini@stuba.sk

M. B. Miglierini · J. Frydrych · K. Šafářová
Regional Centre of Advanced Technologies and Materials, Departments of Experimental Physics and Physical Chemistry, Faculty of Science, Palacky University, 17. listopadu 12, 771 46 Olomouc, Czech Republic

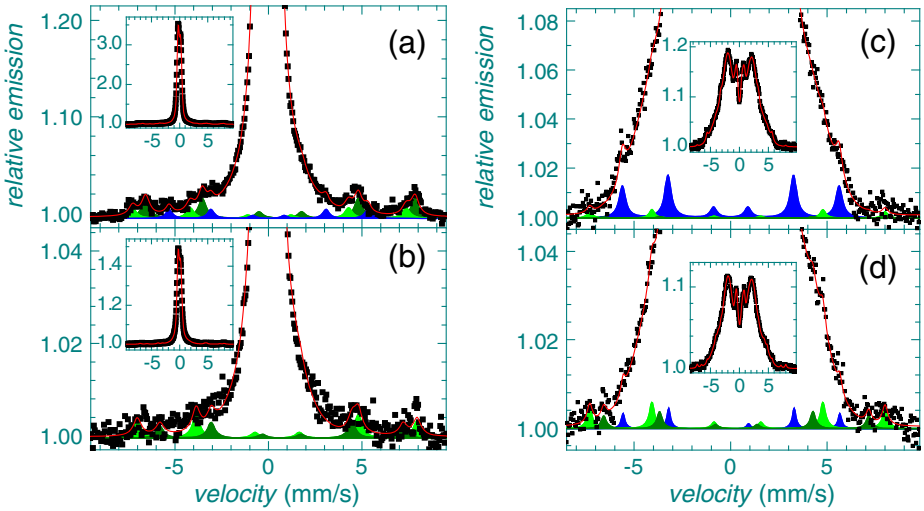

Fig. 1 Air sides of $(Fe_{1-x}Co_x)_{76}Mo_8Cu_1B_{15}$ alloy for $x = 0$ (**a**, **b**) and $x = 0.25$ (**c**, **d**) annealed at 370°C and recorded by CEMS (**a**, **c**) and CXMS (**b**, **d**) techniques. Crystalline components are given in colour: magnetite–*green*, bcc-Fe/Fe, Co–*blue*. Insets show spectra in full range

Both wheel and air surfaces were investigated by conversion electron Mössbauer spectrometry (CEMS) and by conversion X-ray Mössbauer spectrometry (CXMS) that provide information from the depths of about 200 nm and 1 μm, respectively. Evaluation of Mössbauer spectra was performed by the Confit software [3].

The acquisition of atomic force microscopy (AFM) surface topographic images and magnetic force microscopy (MFM) images was carried out by scanning probe microscope NTEGRA Aura in a map topography mode and in magnetic properties mode, respectively.

Samples were studied in the as-quenched (amorphous) state and after heat treatment in a vacuum furnace for 30 min which has eventually ensured formation of nanocrystalline grains with different amounts.

3 Results and discussion

Examples of CEMS and CXMS spectra recorded from air sides of the $(Fe_{1-x}Co_x)_{76}Mo_8Cu_1B_{15}$, $x = 0, 0.25$ ribbons annealed at 370°C are shown in Fig. 1. Broad spectral lines are assigned to the amorphous part of the alloy. They were reconstructed by distributions of quadrupole splitting and hyperfine magnetic fields that correspond to non-magnetic and magnetic regions, respectively. Presence of crystalline phases is indicated by magnetically split spectral components. According to the hyperfine field values they correspond to (disordered and/or substituted) magnetite, bcc-Fe ($x = 0$) and bcc-Fe,Co ($x = 0.25$) phases. The latter was fitted with up to four sextets of Lorentzian lines.

Relative areas of the crystalline phases derived from all spectra are plotted against temperature of annealing in Fig. 2. In $x = 0$, the formation of bcc-Fe starts earlier in

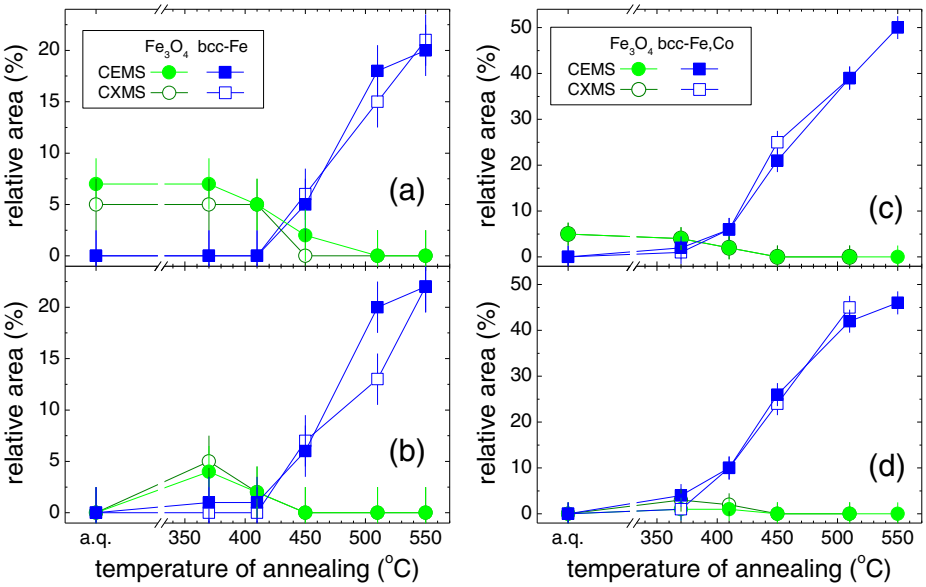

Fig. 2 Relative areas of crystalline phases (magnetite–*green*, bcc-Fe/Fe, Co–*blue*) derived from CEMS (*full symbols*) and CXMS (*opened symbols*) spectra and plotted against temperature of annealing (a.q.–as-quenched) for wheel (**a**, **c**) and air (**b**, **d**) sides of $(Fe_{1-x}Co_x)_{76}Mo_8Cu_1B_{15}$ alloy for $x = 0$ (**a**, **b**) and $x = 0.25$ (**c**, **d**)

the uppermost surface films (CEMS–Fig. 2b) on the air side which has faced the surrounding atmosphere (air) during the production of the ribbons. No bcc-Fe is detected on the wheel side (Fig. 2a) that was in direct contact with the rotating wheel and thus was exposed to better quenching conditions (more effective dissipation of heat). On the other hand, the amount of magnetite is higher at the wheel side but only in the samples that are still amorphous, i.e. below the temperature of annealing of 410°C. With the onset of crystallization traces of magnetite vanish. We can speculate that magnetite, as a corrosion product, might be formed owing to residual humidity that is trapped inside the surface pockets. These are fingerprints of the wheel's surface roughness into the quenching melt. That is why the wheel side of the ribbon is matt while the air side is shiny.

Addition of Co ($x = 0.25$) significantly alternates magnetic microstructure of this NANOPERM-type Mo-containing alloy which is demonstrated by notable magnetic splitting of the spectra in Fig. 1c and d. Surface crystallization is also different. Presence of bcc-FeCo nanocrystals is revealed already after moderate annealing at 370°C and evolves more rapidly on the air side. As in the previous case of $x = 0$, more abundant magnetite is detected on the wheel side but extends to deeper surface regions because CEMS and CXMS results are almost equal.

A tendency towards magnetic order in $x = 0.25$ is demonstrated by appearance of magnetic domains. They can be visualised by the help of MFM in Fig. 3b. A part of a domain is seen in which a tendency of an internal structure to develop occurs. Position of magnetic moments is different inside nanocrystalline grains the positions of which are documented by AFM in Fig. 3a.

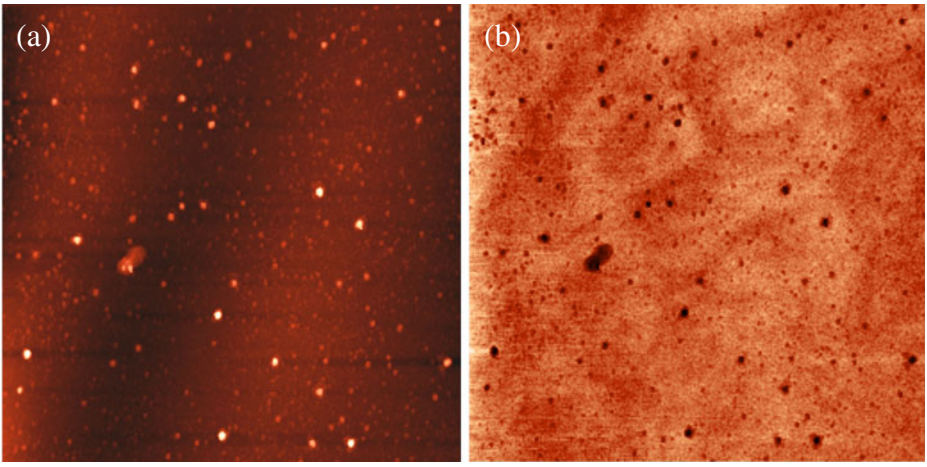

Fig. 3 AFM (**a**) and MFM (**b**) images taken from the air side of $(Fe_{0.75}Co_{0.25})_{76}Mo_8Cu_1B_{15}$ alloy annealed at 550°C. The displayed area is of 50 × 50 μm^2

4 Conclusion

After annealing at low enough temperatures when the alloys are still amorphous, presence of magnetite was revealed on both surfaces of the ribbons. Its content is higher at the immediate surface (CEMS) than in deeper regions (CXMS). With the onset of crystallization, only bcc-Fe and/or bcc-Fe,Co phases were identified.

Acknowledgements This work has been supported by research projects VEGA 1/0286/12, SK-PL-0013–09 and by the Operational Program Research and Development for Innovations–European Regional Development Fund (project CZ.1.05/2.1.00/03.0058 of the Ministry of Education, Youth and Sports of the Czech Republic).

References

1. McHenry, M.E., Laughlin, D.E.: Acta Mater. **48**, 223 (2000)
2. Willard, M.A., Laughlin, D.E., McHenry, M.E., et al.: J. Appl. Phys. **84**, 6773 (1998)
3. Žák, T., Jirásková, Y.: Surf. Interface Anal. **38**, 710 (2006)

Hyperfine Interact (2012) 205:129–133
DOI 10.1007/s10751-011-0496-0

Vibration DOS of ^{57}Fe and Zn doped rutile Sn(Sb) oxides

Kiyoshi Nomura · Alexandre Rykov · Zoltán Németh · Yoshitaka Yoda

Published online: 6 December 2011

Abstract Sn oxides co-doped with Zn, Sb and ^{57}Fe were prepared by sol-gel method, and especially the doping effect of non-magnetic Zn ions was studied. The bulk saturation magnetization is in accordance with the intensity of the magnetic component in Mössbauer spectra. The nuclear inelastic scattering (NIS) spectra of these compounds were measured in SPring 8. The vibration density of states (VDOS) of ^{57}Fe doped Sn(Sb) oxides showed that the softening peaks around 15–20 meV appeared by doping less than 10% Zn ions. The clusters of non-magnetic $ZnFe_2O_4$ may be most probably formed under the limit of XRD detections. The results suggest that the strengthening of ferromagnetism, which appears in the dilute Zn doping, may occur due to the spin arrangement of dilute Fe^{3+} through magnetic defects rather than the formation of magnetic iron oxides.

Keywords Vibration density of states (VDOS) · Mössbauer spectroscopy · Nuclear inelastic scattering · Diluted magnetic oxide semiconductors · Zn doping effect of Fe and Sb doped SnO_2

K. Nomura (✉) · A. Rykov · Z. Németh
School of Engineering, The University of Tokyo, Hongo 7–3–1,
Bukyo-ku, Tokyo 113–8656, Japan
e-mail: k-nomura@t-adm.t.u-tokyo.ac.jp

Z. Németh
Institute of Chemistry, Eötvös Loránd University,
Pázmány P. s. 1/A, 1117 Budapest, Hungary

Y. Yoda
Japan Synchrotron Radiation Research Institute,
Sayo, Hyogo 679–5198, Japan

1 Introduction

Transparent diluted magnetic oxide semiconductors (DMS), which show ferromagnetism at room temperature, are expected to be one of the most intriguing spintronics materials [1, 2]. Ferromagnetic behavior can occur as an impact of low concentration of doped magnetic atoms on wide gap semiconductors. The ferromagnetism is presumed to be induced either due to the spin arrangement of magnetic atoms through localized spins trapped in oxygen vacancies or due to formation of precipitated magnetic clusters. It is necessary to reveal how the dilute or clustered ferromagnetic atoms are involved into metal oxide semiconductor.

Recently, we have measured nuclear resonant inelastic scattering (NIS) spectra of metal oxides using synchrotron radiation, and revealed that NIS measurement is useful for determination of dilution or cluster formation of doped ions [3]. We also have conducted ^{119}Sn Mössbauer study of Fe doped SnO_2 under magnetic fields. ^{119}Sn Mössbauer spectra were influenced a little by magnetic fields [4]. The co-doping of SnO_2 with Sb and Fe ions were found to improve electrical conductivity and magnetism. Sb ions enhance the solubility of Fe ions in SnO_2, widening the possibilities of enhancing the physical properties of cassiterite based materials [5]. Zn doping effect of 20% Fe and 10% Sb doped SnO_2 were studied, as well [6]. In the present study, we determine local vibration density of state (VDOS) distribution of ^{57}Fe in various Fe and Sb doped Sn oxides.

2 Experimental

^{57}Fe and Sb doped $SnO_{2-\delta}$ co-doped with Zn (less than 30%) were obtained by sol-gel method. $SnCl_2{\cdot}2H_2O$, $SbCl_3$, ZnO, metallic ^{57}Fe and natural Fe were dissolved by using HCl or HNO_3 and citric acid. Each solution was mixed according to the nominal amounts of compounds, and completed with ethylene glycol. The proper amount of enriched ^{57}Fe was mixed into natural abundant Fe solution to adjust into about 2% ^{57}Fe content. These solutions were condensed at 80–90°C and decomposed at 250°C during 2 h. The xerogel was oxidized in air at 550°C for 1 h, and, after milling, the powders were finally annealed at 550°C for 1 h. Mössbauer spectra were measured by using ^{57}Co(Cr) and calibrated using α-Fe foil. ^{57}Fe NIS spectra were measured in SPring8, using BL09, of which the energy resolution was 2.5 meV. Phonon DOS distributions were calculated from NIS spectra.

3 Results and discussion

Figure 1 shows the experimental saturation magnetization of $Zn_xFe_ySb_zSn_{1-(x+y+z)}O_{2-\delta}$ plotted against n_c/n_i, where $n_c = 4 - 4 * (1 - x - y - z) - 5 * z - 3 * y - 2 * x$ is the number of charge carriers, and $n_i = y$ is the number of doped magnetic ions. In this case, it is assumed that there are no precipitated products and no defects of SnO_2 such as oxygen vacancy, that is $\delta = 0$. The deviation among saturation magnetizations may be produced due to defects. Around $n_c/n_i = 1$, large saturation magnetizations were obtained, and the saturation magnetizations decreased when n_c/n_i increased. This is in good accordance with the results of Behan

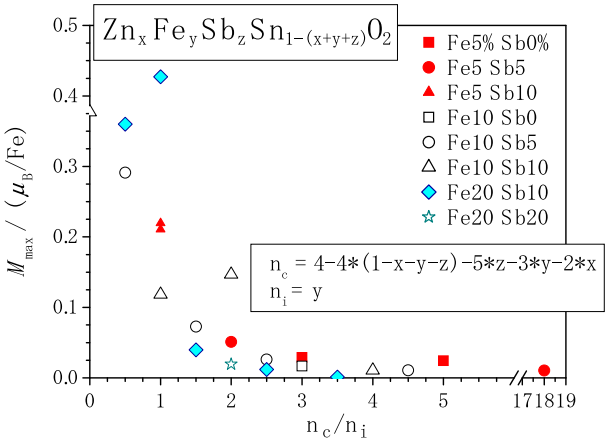

Fig. 1 Relationship between saturation magnetization and n_c/n_i of $Zn_xFe_ySb_zSn_{1-(x+y+z)}O_2$

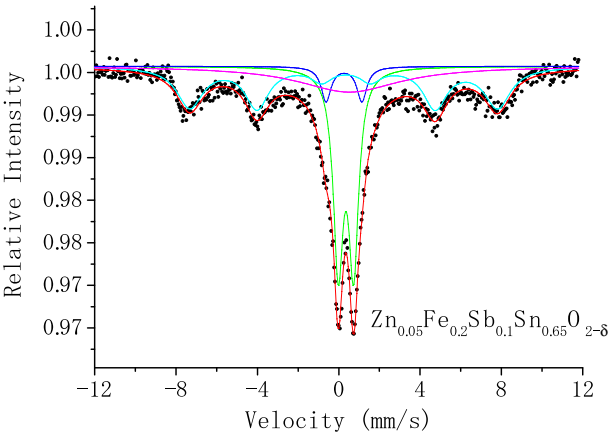

Fig. 2 Typical Mössbauer spectrum of $Zn_{0.05}Fe_{0.20}Sb_{0.10}Sn_{0.65}O_{2-\delta}$

et al., who has found the same tendency in Al and Mn/Co doped ZnO [7]. This behavior was explained by a standard DMS model, where the localized spins of the doping magnetic ions are interacting with band electrons. The bulk magnetization depends then strongly on the carrier density. In our samples, the relatively high dilute magnetism is expected to occur due to the increased solubility of charge carriers. It is confirmed from XRD patterns that the main rutile structure of 10% Sb and 20% Fe-doped tin oxide has been kept up to additionally 10% doping of non-magnetic Zn ions. Sb^{5+} plays a role of stabilization of rutile structure of SnO_2 and induction of carrier density. Zn oxides seem to be dissolved in SnO_2, and not well crystallized at Zn concentrations less than 10%. At more than 10% Zn concentration, the impurity of Zn compounds such as Zn_2SnO_4 and $Zn_{2.33}Sb_{0.67}O_4$ was clearly detected by XRD. At lower Zn concentrations, the impurity may be nano particles of paramagnetic $ZnFe_2O_4$. However, the magnetization increased with doping Zn from 1% to 7% [6].

Typical Mössbauer spectrum of $Zn_xFe_ySb_zSn_{1-(x+y+z)}O_{2-\delta}$ is shown in Fig. 2. The magnetic split components in Mössbauer spectra are related with the intensity of

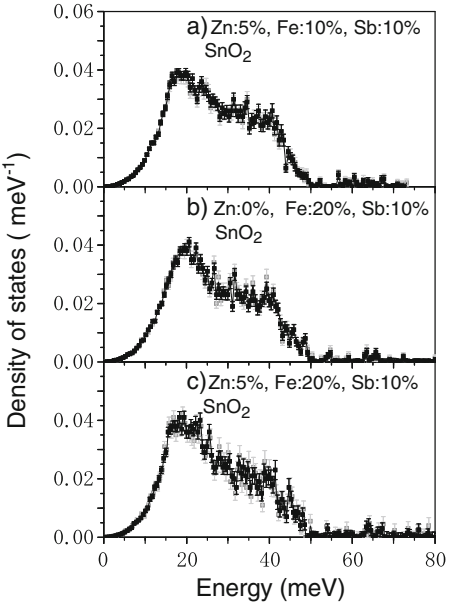

Fig. 3 ^{57}Fe VDOS of SnO_2 doped with **a** 5% Zn + 10% Fe + 10% Sb, **b** 20% Fe + 10% Sb and **c** 5% Zn + 20% Fe + 10% Sb. *Solid plots*: calculated from phonon creation peaks of NIS spectra. *Gray* plots: calculated from phonon annihilation peaks of NIS spectra

bulk magnetization in the range of less than 10% Zn doping rates. It is an interesting phenomenon that the magnetic exchange interaction increases with dilution of Fe ions by non-magnetic Zn ions. The results suggest that there are many defects produced at the interface between tin oxides and zinc oxides.

From the analysis of NIS spectra it is found that even ^{57}Fe VDOS of 20% Fe doped in SnO_2 (10% Sb) resembles ^{119}Sn VDOS of tin oxide itself and ^{57}Fe VDOS of light Fe doped SnO_2 although the distribution was a little expanded as shown in Fig. 3. When doping Zn into the Sn oxides, the VDOS distributions increased a little around 15–20 meV. The softening of VDOS is generally observed for nano iron oxide particles [8]. Supposing the formation of Fe products with Zn and Sb, $ZnFe_2O_4$ emerged as most possible candidate, which should be a non-magnetic nano particle. It is considered that the large saturation magnetization observed in the case of doping less than 10% Zn ions is supposed to be due to dilution of Fe^{3+} into rutile structure rather than formation of precipitated magnetic iron oxides, however, the cluster formation of magnetic iron oxides may not be excluded completely out. Therefore, magnetic components in Mössbauer spectra are considered to be due to spin arrangement of dispersed iron ions through the magnetic defects rather than to high-purity magnetic oxide clusters such as maghemite.

4 Conclusions

We have measured ^{57}Fe nuclear inelastic scattering of the Zn, Fe, and Sb doped SnO_2 compounds at BL09 of SPring8. We concluded the followings; high doping of 20% Fe in 10% Sb doped SnO_2 is possible. Zn doping may make many defects at the interface between SnO_2 and Zn compounds. VDOS analyzed from NIS spectra showed that the peaks appeared at low energy range in VDOS by doping Zn

ions, which suggests the formation of most possible $ZnFe_2O_4$ clusters, non-magnetic ferrite. The enhanced magnetism observed at the range of less than 10% Zn doping is considered to be due to spin arrangement of dispersed Fe^{3+} ions through magnetic defects rather than to precipitation of magnetic iron oxides.

Acknowledgement Authors express to thank Mr. S. Kono for help measuring NIS. Z. Nemeth is grateful to Matsumae International Foundation for supporting his studies at the University of Tokyo.

References

1. Sakuma, J., Nomura, K., Barrero, C.A., Takeda, M.: Thin Solid Films **515**, 8653–8655 (2007)
2. Nomura, K., Barrero, C.A., Sakuma, J., Takeda, M.: Phys. Rev. B **75**, 184411 (2007)
3. Rykov, A.I., Nomura, K., Sakuma, J., Barrero, C., Yoda, Y., Mitsui, T.: Phys. Rev. B **77**, 014302 (2008)
4. Nomura, K., Kuzmann, E., Barrero, C.A., Stichleutner, S., Homonnay, Z.: Hyperfine Interact. **184**, 57–62 (2008)
5. Nomura, K., Barrero, C.A., Kuwano, K., Yamada, Y., Saito, T., Kuzmann, E.: Hyperfine Interact. **191**, 25–32 (2009)
6. Németh, Z., Ito, Y., Nomura, K., Rykov, A., Yoda, Y.: submitted to Applied Physics A. (in preparation for publication)
7. Behan, A.J., Mokhtari, A., Blythe, H.J., Score, D., Xu, X-H., Neal, J.R., Fox, A.M., Gehring, G.A.: Phys. Rev. Lett. **100**, 047206 (2008)
8. Rüffer, R.C.R.: Physique **9**, 595–607 (2008)

Hyperfine Interact (2012) 205:135–138
DOI 10.1007/s10751-011-0550-y

Mössbauer study on the antiferromagnetic FeO synthesized under high pressure

Takuro Yoshikawa · Yasushi Kanke · Hideto Yanagihara · Eiji Kita · Yorihiko Tsunoda · Kiiti Siratori · Kay Kohn

Published online: 13 January 2012

Abstract Mössbauer study and magnetic measurements were carried out on the stoichiometric FeO, prepared with the high pressure (∼5.5GPa) synthesis technique. Well known defects (Koch-Cohen clusters) in FeO are detected even in the stoichiometric specimen, prepared at high temperatures.

Keywords FeO · High pressure synthesis · Mössbauer spectroscopy

1 Introduction

A series of 3d mono oxides, MO (M = Mn, Fe Co and Ni), have a simple NaCl crystalline structure and their electronic states have been investigated intensively for long time. In the case of FeO and CoO, one or two electrons exist in the degenerated $d\varepsilon$ orbitals due to the regular octahedral ligands. Co-existence of the spin-orbit interaction, because of only the partial quenching of the orbital angular momentum ($S = 2$ and $L = 1$), and the Jahn-Teller effect with both T_{2g} and E_g type of the lattice distortion bring about a complex situation [1, 2].

Difficulty in the sample preparation makes the experimental investigation of fundamental properties of FeO difficult. Stoichiometric compound cannot be synthesized at ambient pressure. Instead one obtains Fe_XO with $X \lesssim 0.96$. Lattice defects introduced by this non-stoichiometry are reported to form a cluster structure (Koch-Cohen cluster) [3].

T. Yoshikawa · H. Yanagihara · E. Kita (✉) · K. Siratori
Institute of Applied Physics, University of Tsukuba, Tsukuba, 305-8573, Japan
e-mail: kita@bk.tsukuba.ac.jp

Y. Kanke
National Institute of Materials Science, Tsukuba, Ibaraki, 305-0044, Japan

Y. Tsunoda · K. Kohn
School of Science and Engineering, Waseda University, Tokyo 169-8555, Japan

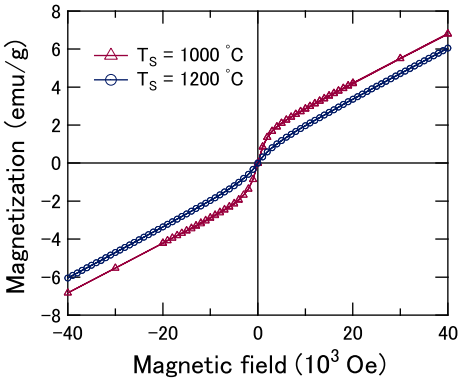

Fig. 1 Magnetization curves for the FeO samples prepared under high pressure and high temperature

It was reported that stoichiometric FeO can be achieved by disproportionation of Fe_XO at 225 °C [4]. However, formation of the ferromagnetic Fe_3O_4 is inevitable in this case and the magnetic investigation of FeO is impossible [5].

Synthesis of the stoichiometric FeO can be achieved by the preparation of the specimen under high pressure [6]. In this study, we performed Mössbauer and magnetic studies on the stoichiometric FeO prepared with the high pressure synthesis technique. It is disclosed that the Koch-Cohen cluster does exist even in this case, especially when the reaction temperature is high.

2 Experimental procedure

Samples were synthesized using a modified belt-type high pressure and high temperature apparatus installed in the National Institute of Materials Science (NIMS) [7]. The starting material was prepared by mixing α-Fe and Fe_2O_3 powder with the atomic ratio of Fe : O = 1 : 1, approximately 0.4 g in total, and was sealed in a Pt capsule. The capsule was heated up to $T_s = 1000$ °C and 1200 °C under 5.5 GPa for 1 h. Total composition of the specimen can be expected unchanged.

Powder X-ray diffraction of the synthesized samples revealed that they are in an NaCl type single phase and no trace of other compounds was detected. Magnetization measurements were carried out with a conventional SQUID magnetometer. Mössbauer spectra were recorded on a conventional constat acceleration spectrometer at room temperature. The velocity scale and isomer shift were calibrated relative to α-Fe at room temperature and line widths (FWHM) of 0.27 mm/s for the outer lines of α-Fe were obtained. Data were analyzed using a commercially available analysis program, MossWinn Ver.3.

3 Result and discussion

The magnetization curves recorded at room temperature are shown in Fig. 1. They are linear to the applied fields in a range between 10 kOe and 40 kOe. However, small amounts of ferromagnetic components are clearly seen in both magnetization curves. Assuming that the residual ferromagnetic parts are composed of α-Fe, the

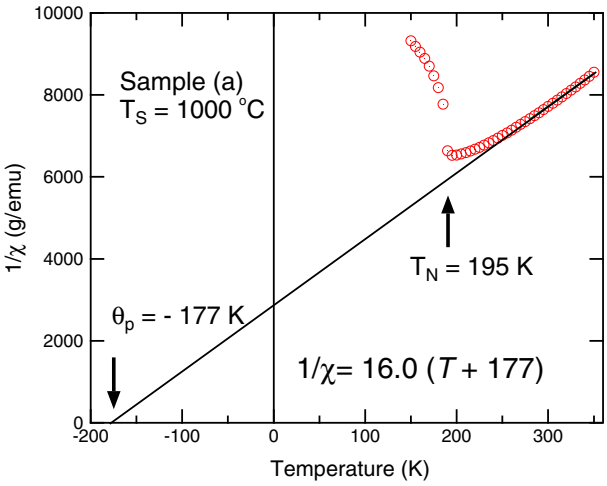

Fig. 2 Inverse susceptibility plotted against temperature for the $T_s = 1000$ °C sample

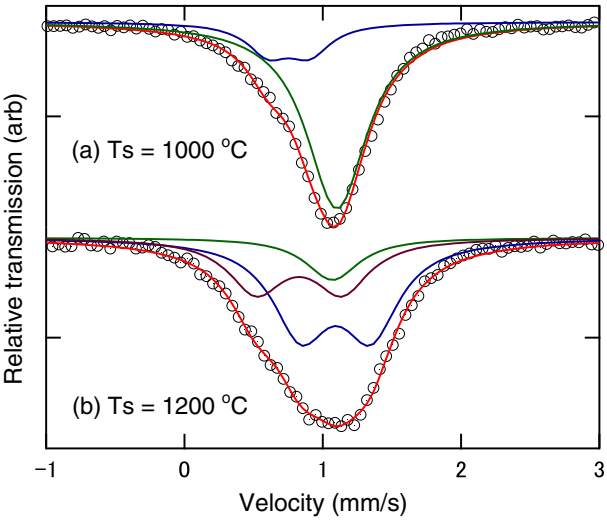

Fig. 3 Mössbauer spectra recorded at room temperature for FeO samples prepared under high pressure and high temperature. The reaction temperatures are (**a**) $T_s = 1000$ °C and (**b**) $T_s = 1200$ °C. Fitting parameters are summarized in Table 1

amounts are estimated to be 0.69 at % for the $T_s = 1000$ °C sample and 0.24 at % for the $T_s = 1200$ °C sample, respectively. From this result, higher reaction temperature may bring lower concentration of ferromagnetic components.

Paramagnetic susceptibilities can be deduced from the linear parts. Figure 2 shows the inverse susceptibility plotted against temperature for the $T_s = 1000$ °C sample. T_N was about 195 K and the paramagnetic Curie temperature, θ_p, was estimated as -177 K. According to the Curie constant, the effective magnetic moment, μ_{eff}, was determined as 5.68 μ_B. This amplitude fits to the case of angular momentum of $S = 2$ and $L = 1$, [1] though the temperature range of the measurement cannot be considered wide enough. It is noted that the ferromagnetic components in the samples were less temperature dependent.

Table 1 Mössbauer parameters for FeO spectra at 298 K

Sample	T_s (°C)	Site	IS[a] (mm/s)	QS (mm/s)	LW (mm/s)	Area (%)
(a)	1000	Fe^{2+}:A	1.088		0.536	82.0
		Fe^{2+}:B	0.755	0.297	0.370	18.0
(b)	1200	Fe^{2+}:A	1.070		0.469	12.5
		Fe^{2+}:B	1.094	0.507	0.496	56.0
		Fe^{2+}:C	0.828	0.620	0.481	31.5

[a]relative to Fe metal

Mössbauer spectra recorded at room temperature are shown in Fig. 3. The sharper spectrum was observed for the $T_s = 1000\,^{\circ}C$ sample, compared with that prepared at $T_s = 1200\,^{\circ}C$. The spectrum for the $T_s = 1000\,^{\circ}C$ sample can be fit to the combination of a major singlet, about 80 % of the absorption, and an additional minor doublet (Fig. 3a). No significant absorption due to magnetite was observed, in contrast to the previous reports [4, 5]. The singlet can be attributed to the Fe^{2+} ions in a cubic environment without defects and the doublet Fe^{2+} in defect sites. The isomer shift of the singlet is about 1.08 mm/s. This value is comparable to the isomer shift of $Fe_{0.861}O$ (1.05 mm/s) but larger than that reported for FeO containing small amount of Cr^{3+} ions [8].

On the other hand, the spectrum for the sample prepared at $T_s = 1200\,^{\circ}C$ is more complex and at least two kinds of Fe sites with lower symmetry are responsible for doublets in the spectrum. It is noted that the fitting is not unique and many models have been proposed [9]. This result suggests that the number of Fe defects are larger in the sample prepared at $T_s = 1200\,^{\circ}C$. We have to conclude that the stoichiometric FeO without lattice defect has not been synthesized yet. However, high pressure synthesis can produce specimens which have less defect sites than those produced under ambient pressure conditions. We expect that the stoichiometric FeO without defects can be synthesized in near future.

Acknowledgement Mössbauer study was carried out in Tandem Accelerator Complex, University of Tsukuba (UTTAC).

References

1. Kanamori, J.: Prog. Theor. Phys. **17**, 177 (1957)
2. Siratori, K., Kohn, K.: J. Phys. Soc. Jpn. **79**, 114720 (2010)
3. Koch, F., Cohen, J.B.: Acta Crystallogr. **B25**, 275 (1969)
4. Hentschel, B.F.: Z. Naturforsch. **25**, 1996 (1970)
5. Greanwood, N., Howe, A.: J. Chem. Soc. Dalton 116 (1972)
6. Katsura, T., Iwasaki, B., Kimura, S., Akimoto, S.: J. Chem. Phys. **47**, 4559 (1967)
7. Taniguchi, T., Akaishi, M., Kanke, Y., Yamaoka, S.: Rev. Sci. Instrum. **75**, 1959 (2004)
8. Shrotri, J.J., et al.: Hyperfine Interact. **28**, 733 (1986)
9. McCammon, C.A., Price, D.C.: Phys. Chem. Miner. **11**, 250 (1985)

Hyperfine Interact (2012) 205:139–147
DOI 10.1007/s10751-011-0411-8

Iron-sulfur clusters—new features in enzymes and synthetic models

Eckhard Bill

Published online: 8 November 2011

Abstract Mössbauer spectroscopy is very important for the characterization of iron sulfur clusters in biological and synthetic molecules. The electric and magnetic hyperfine parameters obtained for ^{57}Fe provide valuable information about the electronic structure of the different iron sites occurring in Fe:S clusters. Although known since more than four decades, research in this field is very active, revealing unexpected functions, structures and redox states. In this overview, new aspects of double exchange and vibronic coupling in a structurally well-characterized two-iron model compound are discussed, the electronic structure of extremely reduced clusters with all iron in ferrous or even in iron(I) state is elucidated, and an exciting new type of cubane cluster occurring in oxygen-insensitive hydrogenases is presented. The latter cluster involves structural changes during function and it supports more than one redox transition, which may be essential for oxygen protection of the enzymes.

Keywords Iron-sulfur cluster · FeS · Double exchange · Super-reduced · Low valent iron · Low coordination · Hydrogenases · Magnetic measurements · Applied field Mössbauer · Paramagnetic properties

1 Introduction

Iron sulfur proteins have been discovered in the 1960s during studies on photosynthetic and nitrogen-fixing bacteria and submitochondrial parts of mammalian cells [1]. They are distinguished by the presence of inorganic clusters of iron and sulfide (Fe:S clusters) with one to eight ferric or ferrous ions and about the same number of 'acid-labile' sulfides (S^{2-}). The clusters are covalently bound to the protein, mostly by coordination to cysteinate sulfur (S^{-}). They represent one of the most ubiquitous

E. Bill (✉)
Max-Planck Institute for Bioinorganic Chemistry, 45470 Mülheim/Ruhr, Germany
e-mail: bill@mpi-muelheim.mpg.de

and versatile prosthetic groups found in biological molecules, abundant in all present and ancient forms of life [1–4]. Even an inorganic origin or prelude of life with an iron- and sulfide-based primordial metabolism was proposed [5]. The appearance of Fe:S clusters, however, is not protein dependent, since vigorous research in bio-inspired inorganic chemistry has provided a large variety of synthetic monomeric to tetrameric, or oligomeric iron-sulfur clusters [6], many of which are accurate analogs of the natural systems.

Iron-sulfur clusters play various physiological roles, with more than 120 distinct types of iron-sulfur enzymes and proteins known [1, 4, 7]. This is possible partly because sulfur can occur in different oxidation states, and forms highly covalent bonds with little energy necessary to make and break bonds. Iron, of course is a 'fitting partner' with a large variety of electronic configurations and close-lying redox states [2]. The chemical versatility allows Fe:S clusters easily to accept, store and donate electrons, in some cases employing long transport chains like in the linear assembly of 8–9 clusters in compound 1 of the respiratory chain for aerobic cell metabolism. Beyond such simple electron transfer, Fe:S cluster can couple electron and proton transfer. Others have structural roles, or more remarkable, serve as sensors for H_2, O_2, NO, or the iron level in the cell. Some clusters are directly involved in catalytic steps, in which they bind and activate substrates at a unique iron site. Recently, the role of cluster formation and enzyme maturation for gene expression and genetic disorder has captured much attention [8], not least due to the medical implications [9, 10].

2 Common types of clusters and electronic structures

Iron in the most common Fe:S clusters has the formal oxidation state iron(II) or iron(III) with quasi-tetrahedral coordination environment; therefore it is high-spin throughout. Mononuclear, dinuclear and trinuclear clusters occur in two oxidations states, supporting the red/ox couples $[1Fe]^{3+}$/ $[1Fe]^{2+}$, $[2Fe–2S]^{2+}$/ $[2Fe–2S]^{1+}$, and $[3Fe–4S]^{1+}$/ $[3Fe–4S]^{0+}$, respectively (see Table 1). In the oxidized states, these clusters are all-ferric, whereas the reduced $[1Fe]^{2+}$ cluster is ferrous and the reduced $[2Fe–2S]^{1+}$ and $[3Fe–4S]^{0+}$ cluster have one ferrous ion each (mixed valences) [11]. Four-iron, [4Fe–4S], clusters occur in three oxidation state (3+, 2+, 1+), although in a particular protein never both redox pairs are supported (they function either as a so-called low-potential or a high-potential Fe:S protein). The clusters of higher nuclearity (four and more) are mixed-valent in all oxidation states and show valence delocalization, predominantly occurring in pairs of formal Fe(II)–Fe(III) ions. The underlying double-exchange mechanism [12–14] accomplishes a substantial contribution to the redox potential of the systems [15].

The Mössbauer parameters of Fe:S clusters are clearly distinct from those of other biological iron centers, like hemes and non-heme centers with 'hard' oxygen and nitrogen ligands. Particularly the isomer shifts are characteristically low, due to the short and covalent Fe-S bonds caused by four-coordination and high covalency of sulfur [21]. Table 1 summarized the basic Mössbauer parameters of Fe:S clusters with one to four iron sites, whereas comprehensive and detailed descriptions also of the highly interesting magnetic properties are found in recent reviews [11, 22–24], including those of the more specific eight-iron and composite clusters.

Table 1 Typical properties of most common Fe:S clusters

Type	Formal valences[a]	Spin	δ/mms^{-1}(4.2K)	$\lvert\Delta E_Q\rvert$/mms^{-1}	Ref.
$[1Fe]^{3+}$	III	5/2	0.32	0.5	[16]
$[1Fe]^{2+}$	II	2	0.70	3.25	[16]
$[2Fe–2S]^{2+}$	2xIII	0	0.27	0.6	[17]
$[2Fe–2S]^{1+}$	III,II[b]	$\frac{1}{2}$	0.35, 0.65	0.6, 2.7	[17]
$[3Fe–4S]^{1+}$	3xIII	$\frac{1}{2}$	0.27	0.63	[18]
$[3Fe–4S]^{0}$	{II/III}, III[c]	2	0.46, 0.32	1.47, 0.52	[14]
$[4Fe–4S]^{1+}$	{II/III}, 2xII[d]	$\frac{1}{2}$	0.5, 0.58	1.32, 1.89	[19]
$[4Fe–4S]^{2+}$	2x{II/III}	0	0.42	1.12[e]	[19]
$[4Fe–4S]^{3+}$	{II/III}, 2xIII	$\frac{1}{2}$	0.4, 0.29	1.03, 0.88[e]	[20]

[a]Mixed-valence pairs are indicated by brackets {–}

[b]Two subspectra for localized Fe(III) and Fe(II) sites

[c]Two distinct subspectra with intensity ratio 2:1

[d]Two subspectra with intensity ratio 1:1

[e]Average value from non-resolved subspectra

3 Exchange and double-exchange in a synthetic [2Fe–2S] compound

Synthetic analogues for biological [2Fe–2S] cores are well established in bioinorganic chemistry [6], although terminal ligands other than thiolates, like the histidine-nitrogens in so-called Rieske clusters, are still rare (see ref. in [25]). Mössbauer spectra of a Rieske-type model complex with an asymmetric set of ligands have been published only recently [26]. Most reported analogues of [2Fe–2S] sites have been synthesized exclusively in the all-ferric state, while the mixed valent $[2Fe–2S]^{1+}$ state could, if at all, only be accessed by electrochemical methods in solution [27]; Gibson and Beardwood generated the first such reduced [2Fe–2S] cluster [28]. Although neither the molecular structures nor the magnetic susceptibilities could be determined, the electronic structure could be studied in solution by EPR and Mössbauer spectroscopy. That compound was the first Fe:S dimer with partial valence delocalization and competing exchange and double exchange interaction [29]. Now we could investigate a similar complex with mixed valent $[2Fe–2S]^{1+}$ core, which was crystallized, so that metric details could be related with the electronic structure; and also magnetic susceptibilities could be measured with a powder sample [25].

Two distinct iron sites are found, but the isomer shifts and quadrupole splitting ($\delta = 0.47$ mm/s, $\Delta E_Q = 1.41$ mm/s, and $\delta = 0.69$ mm/s, $\Delta E_Q = 2.90$ mm/s) deviated from typical values known for ferric and ferrous ions (see also Table 1). Comparisons with suitable reference systems, as well as the empirical correlation [30] $\delta(x) = [1.43–0.40{\cdot}x]$ mm/s, found for δ and the oxidation number (x) of FeS_4 units, revealed a mixing coefficient of 20% for the electronic configurations $[Fe^{2+}–Fe^{3+}]$ ("A") and $[Fe^{3+}–Fe^{2+}]$ ("B") (i.e. $a^2 = 0.8$, $b^2 = 0.2$ for $\psi = a{\cdot}\psi\text{“}_A\text{”} + b{\cdot}\psi\text{“}_B\text{”}$). Magnetic susceptibility measurements reveal antiferromagnetic coupling of the iron sites. The effective coupling constant ($J_{eff} = -134$ cm^{-1}; for $H = -2JS_1S_2$), however, comprises the combined and competing effects of exchange interaction, intrinsic electron transfer (double exchange) [12–14] and charge localization [15] due to static and vibronic coupling to the environment [31–36].

The values of J_{eff} and a^2 can be rationalized by using a phenomenological model that describes the energies of the spin states of a mixed-valent iron dimer in terms of the exchange coupling constant J, a double exchange parameter B to account for delocalization, and an effective energy difference Δ_{AB} of the configurations "A" and "B" that summarizes the charge-localizing contributions from static site differences as well as vibronic coupling. The eigenvalues of the double-exchange Hamiltonian are given as [14, 15, 29, 37]:

$$E_{\pm}(S) = -JS(S+1) \pm 1/2\sqrt{\Delta_{AB}^2 + B^2(2S+1)^2} \quad (1)$$

where the subscripts (±) denote the 'gerade' and 'ungerade' solutions, the splitting of which corresponds to the energy of the intervalence band, $\Delta_{\mathrm{iv}} = |E_+(S) - E_-(S)|$ for spin $S = 1/2$ here, whereas the effective coupling constant is given by the energy difference of the ground state doublet and the excited quartet, $J_{\mathrm{eff}} = 1/3|E_-(1/2) - E_-(3/2)|$. Unfortunately, the intervalence band cannot be directly detected neither here nor for other $[2\mathrm{Fe–2S}]^{1+}$ clusters, presumably because of unfavorably low energy.

The mixing coefficient a^2 can be given in closed form as a function of Δ_{AB}/J and B/J [29]. However, with the input of only two experimental variables, J_{eff} and a^2, the equations cannot be readily solved. Hence we adopted $B = 700\ \mathrm{cm}^{-1}$ for the double exchange parameter, as determined by DFT calculations [38], which enabled us to obtain from equation (1) the true exchange interaction $J = -341\ \mathrm{cm}^{-1}$, and the double-exchange splitting $\Delta_{\mathrm{AB}} = 1{,}050\ \mathrm{cm}^{-1}$. The J value is remarkably large, but it is consistent with the result of ligand-K-edge XAS [39, 40] and DFT [38] investigations. Moreover, the set of parameters predicts for the intervalence band an energy of $\Delta_{\mathrm{iv}} = 1{,}750\ \mathrm{cm}^{-1}$, or $\lambda_{\mathrm{iv}} = 5{,}714$ nm. Apparently such transitions are difficult to detect, but in particular the result rules out previous tentative assignments of bands around 540 nm. The corresponding large splitting of 'gerade' und 'ungerade' total spin states, S_+ and S_-, would not be consistent with the observed $S = 1/2$ ground state of $[2\mathrm{Fe–2S}]^{1+}$ clusters. In summary, the data resolve a long-lasting debate in Fe:S cluster chemistry.

4 Super-reduced Fe:S clusters

In the known Fe:S clusters, the iron ions are in the +2 and +3 oxidation states, even in synthetic systems, which provide a much broader range of supporting ligands than amino-acid residues in biology. Clusters in which all the iron ions are in the Fe^{2+} state are rare, with the only known biological examples being the Fe protein [41–44] and the [8Fe–7S] P-cluster [3, 45, 46] of nitrogenase, and the super-reduced activator component of the enzyme system 2-hydroxyglutaryl-CoA dehydratase [47]. The all-ferrous state, $[4\mathrm{Fe–4S}]^0$, of the four-iron cluster in the activator protein was established by the Mössbauer parameters, $\delta = 0.65$ mm/s and $\Delta E_{\mathrm{Q}} = 1.51$–$2.19$ mm/s, which are typical of $\mathrm{Fe(II)S_4}$ sites. Parallel-mode electron paramagnetic resonance (EPR) spectra showed sharp signals at $g = 16$ and 12, indicating an integer-spin system. EPR spectra and magnetic Mössbauer spectra could be consistently simulated with total spin $S_{\mathrm{t}} = 4$ with weak zero-field splitting parameters $D = -0.66\ \mathrm{cm}^{-1}$ and $E/D = 0.17$. The putative consequences of the all-ferrous $[4\mathrm{Fe–4S}]^0$ state for the physiological role of the clusters are still under discussion [3, 47].

The so-called Rieske proteins from the bacterial and mitochondrial phosphorylation systems (for chemical energy storage) have a unique [2Fe–2S] cluster in which one of the two Fe atoms is coordinated by two histidine rather than two cysteine residues. The all-ferrous state $[2Fe–2S]^0$ was produced in solution by chemical reduction with a europium salt (Eu^{II}DTPA), and has been characterized by protein-film voltammetry and UV– spectroscopy. We have measured EPR and Mössbauer spectra to explore the electronic structure of iron [48]. The two ferrous ions are both high spin ($S_{Fe} = 2$, $\delta = 0.70$ mm/s, $\Delta E_Q = 2.76$ mm/s for 2-Cys-coordination, $\delta = 0.81$ mm/s, $\Delta E_Q = 2.32$ mm/s for 2-His-coordination). They are antiferromagnetically coupled ($-J > 30$ cm^{-1}) to give a diamagnetic ($S = 0$) ground state, as could be inferred from applied-field Mössbauer spectra. The ability of the Rieske cluster to exist in three oxidation states (2+, 1+, and 0) without an accompanying coupled reaction, such as a conformational change or protonation, is highly unusual. A combination of experimental data and calculations based on density functional theory suggested strongly that a proton binds to one of the cluster μ_2-sulfides, which demonstrates the coupling of electron and proton transfer in these systems [48].

There are no reports of iron-sulfide systems in which the iron ions could be reduced to the Fe^{1+} level. However, that oxidation state has been suggested for some sites of the FeMoco cluster of nitrogenase to explain certain intermediates. Recently the first example of an iron(I)-sulfide compound has been isolated [49], which suggests that iron(I) is in fact feasible in biological iron sulfide chemistry. The compound is a di-iron complex with two terminal β-diketiminate ligands (N-coordinating) and an S^{2-} bridge, i.e. the iron site are three-coordinated. The zero-field Mössbauer spectrum is a symmetric doublet with parameters $\delta = 0.67$ mm/s, $\Delta E_Q = 2.17$ mm/s [49]. The values are distinctly different from those of the starting compound with three-coordinate Fe(II) site ($\delta = 0.86$ mm/s, $\Delta E_Q = 0.58$ mm/s), and they resemble those of other three coordinate (non-sulfido) Fe(I) complexes like LFe(I)(HCCPh) ($\delta = 0.50$ mm/s, $\Delta E_Q = 2.05$ mm/s) [50]. The iron ions are antiferromagnetically coupled ($J = -122$ cm^{-1}, $S_{Fe} = 3/2$), showing the usual temperature dependence of the effective moments as expected from the Heisenberg Hamiltonian. Apparently the exchange interaction supersedes the effects of spin-orbit coupling observed for the only known other mononuclear three-coordinate Fe(I) system [50].

5 Unusual four-iron cluster in an O_2-tolerant [NiFe]-hydrogenase

The microorganism *Aquifex aeolicus* (lat. water maker) is a hyperthermophilic Knallgas bacterium with optimum growth at 85°C [51]. It has three distinct [NiFe] hydrogenases, among which Hydrogenase I (Hase I) is an integral part of a respiration pathway for the reduction of O_2 to water by using hydrogen [51, 52]. According to its function, the enzyme exhibits enhanced tolerance for dioxygen, as compared to 'normal' [NiFe] hydrogenases [53, 54]. This is a highly interesting feature with respect to research projects aiming at the connection of the energy-harvesting photosystem of green plant and the energy conversion catalyzed by hydrogenases (hydrogenases can operate in both directions, i.e. use or produce hydrogen).

Hase I consists of two subunits; the large subunit contains the catalytic [NiFe] site and the small subunit has three iron-sulfur clusters as electron relais system [51].

According to the amino-acid residues available for cluster binding, spectroscopic data, redox titration experiments and upcoming structural data obtained from single-crystal X-ray diffraction data, there are a [3Fe–4S], a 'normal' [4Fe–4S] and an unusual "[4Fe–4S]" cluster. The latter is located proximal to the [NiFe] center and appears to have a very unusual coordination with six cysteine residues [52].

Surprisingly, the three Fe:S clusters mediate four redox transitions. Analyses of the electrochemical results, in combination with EPR spectroscopy, show that the proximal "[4Fe–4S]" cluster is associated with two single-electron steps in a very small potential range, which has never been observed so far for any biological system. A proof that this fourth oxidation is in fact localized on the cluster and not related to a ligand oxidation could be obtained from Mössbauer spectroscopy. The system is at the resolution limit of Mössbauer spectroscopy as it contains twelve individual iron sites, the contributions of which are partially overlapping. However, not all of them must be disentangled because Fe:S cluster exhibit valence and charge delocalization so that many iron sites are similar even when they have different formal valences. The key feature for a successful interpretation of such data is the fact that specific coordination at some individual sites, particularly of the so-called proximal cluster, results in distorted charge distribution, as can be seen by unusual Mössbauer parameters.

The Mössbauer analysis was focused on the extreme redox states, which are the hydrogen-reduced and a chemically super-oxidized one; only under these conditions the samples are homogenous. In other preparations, superpositions of different redox states are expected according to the individual redox potentials of the clusters, as found by EPR titration experiments [52, 55]. The zero-field Mössbauer spectra of *H_2-reduced* samples are asymmetric quadrupole spectra, which can be fitted as expected for full reduction of the three clusters, except that one quadrupole doublet (accounting for 1/12 intensity) sticks out because of an extraordinarily large quadrupole splitting. Based on global simulations of applied-field spectra that were done to assign particularly the magnetic hyperfine tensors, this iron site can be best described as a $Fe^{2.5+}$ site of the proximal "[4Fe–4S]" cluster, which has an unusually distorted coordination. Another iron of that cluster appears to show predominant localized Fe(II) character ($\delta = 0.72$ mm/s). Particularly the signs of the A-tensors were helpful in this program, since they reveal the local spin orientation. We treated the proximal cluster in analogy with the coupling known for ferrous and ferric site in cubane Fe:S clusters [54].

The Mössbauer spectra of *super-oxidized* Hase I also show a unique subspectrum with large quadrupole splitting (2.42 mm/s). The data set could be consistently fitted by adopting one oxidized $[3Fe–4S]^{1+}$ cluster ($S = 1/2$, medial), one oxidized classical $[4Fe–4S]^{2+}$ cluster ($S = 0$, distal), the unusual (proximal) four-iron cluster ($S = 1/2$) and the low-spin Fe ($S = 0$, [NiFe] site). Applied-field analyses, however, indicate that the unusual coordination may have changed the face of the cuboid proximal cluster. Details of the interpretation shall be worked out [56] in conjunction with the upcoming crystal structure of Hase I.

In summary, the unprecedented plasticity of the proximal cluster of Hase I appears to be related to the two extra cysteins in its near environment. Structural data and Mössbauer spectra show that both these cysteins are involved in cluster coordination, forming a very unusual coordination sphere. This new type of cluster appears to occur in several oxygen tolerant [NiFe] hydrogenases, as is reported in two recent

molecular structure studies [57, 58]. Its extraordinary properties suggest a role for sequestering reactive oxygen species in order to endow oxygen tolerance to the system.

Acknowledgements The Mössbauer study of the Hydrogenase 1 was performed in very close collaboration with Prof. Wolfgang Lubitz and Dr. Maria E. Pandelia from the MPI for Bioinorganic Chemistry in Mülheim, Germay. I am extraordinary thankful for this interesting and fruitful common project. The Hase 1 samples were originally prepared by M.T. Giudici-Orticoni, Pascale Tron, Christophe Legér, Vincent Fourmond, and Wolfgang Nitschke from Laboratoire de Bioeìnergeìtique et Ingeìnierie des Proteìines, Mediterranean Institute of Microbiology, 13402 Marseille Cedex 20, France, which I highly appreciate. Other work with the groups of Judy Hirst, Oxford (England), Wolfgang Buckel, Marburg (Germany), Franc Meyer, Göttingen (Germany), and Patrick L. Holland, Rochester (USA), is also gratefully acknowledged. Work published with these groups is fully cited in the text. Last-not-least I thank the excellent technicians at the MPI, Andreas Göbels, Bernd Mienert, and Frank Reikowsky, for extremely helpful assistance. Financial support was coming from the Max-Planck Society.

References

1. Beinert, H., Holm, R.H., Münck, E.: Iron-sulfur clusters: nature's modular, multipurpose structures. Science **277**, 653–659 (1997)
2. Beinert, H.: Iron-sulfur proteins: ancient structures, still full of surprises. J. Biol. Inorg. Chem. **5**(1), 2–15 (2000)
3. Rees, D.C.: Great metallclusters in enzymology. Ann. Rev. Biochem. **71**, 221–246 (2002)
4. Rees, D.C., Howard, J.B.: The interface between the biological and inorganic worlds: iron-sulfur metalloclusters. Science **300**(5621), 929–931 (2003). doi:10.1126/science.1083075
5. Huber, C., Wächtershäuser, G.: Activated acetic acid by carbon fixation on (Fe,Ni)S under primordial conditions. Science **276**(5310), 245–247 (1997). doi:10.1126/science.276.5310.245
6. Rao, V.P., Holm, R.H.: Synthetic analogues of the active sites of iron-sulfur proteins. Chem. Rev. **104**(2), 527–560 (2003). doi:10.1021/cr020615+
7. Johnson, D.C., Dean, D.R., Smith, A.D., Johnson, M.K.: Structure, function, and formation of biological iron-sulfur clusters. Ann. Rev. Biochem. **74**(1), 247–281 (2005). doi:10.1146/annurev.biochem.74.082803.133518
8. Dos Santos, P.C., Dean, D.R.: Bioinorganic chemistry—electrons in Fe-S protein assembly. Nat. Chem. Biol. **6**(10), 700–701 (2010). doi:10.1038/nchembio.438
9. Lill, R.: Function and biogenesis of iron-sulphur proteins. Nature **460**(7257), 831–838 (2009)
10. Sheftel, A., Stehling, O., Lill, R.: Iron-sulfur proteins in health and disease. Trends Endocrinol. Metab. **21**(5), 302–314 (2010)
11. Solomon, E.I., Xie, X., Dey, A.: Mixed valent sites in biological electron transfer. Chem. Soc. Rev. **37**(4), 623–638 (2008)
12. Zener, C.: Interaction between the d-shells in the transition metals. 2. Ferromagnetic compounds of manganese with Perovskite structure. Phys. Rev. **82**(3), 403–405 (1951)
13. Anderson, P.W., Hasegawa, H.: Considerations on double exchange. Phys. Rev. **100**(2), 675–681 (1955)
14. Papaefthymiou, V., Girerd, J.-J., Moura, I., Moura, J.J.G., Münck, E.: Mössbauer study of D. gigas ferredoxin II and spin coupling model for the Fe3S4 cluster with valence delocalization. J. Am. Chem. Soc. **109**(15), 4703–4710 (1987)
15. Noodleman, L., Case, D.A., Mouesca, J.M., Lamotte, B.: Valence electron delocalization in polynuclear iron-sulfur clusters. J. Biol. Inorg. Chem. **1**(2), 177–182 (1996)
16. Schulz, C.E., Debrunner, P.G.: Rubredoxin. J. Phys. Coll. **37**(C6), 153–158 (1976)
17. Münck, E., Debrunner, P.G., Tsibris, J.C.M., Gunsalus, I.C.: Mössbauer parameters of putidaredoxin and its selenium analog. Biochemistry **11**(5), 855–863 (1972)
18. Kent, T.A., Huynh, B.h., Münck, E.: Iron-sulfur proteins: spin-coupling model for three-iron cluster. Proc. Natl. Acad. Sci. U. S. A. **77**(11), 6574–6576 (1980)

19. Middleton, P., Dickson, D.P.E., Johnson, C.E., Rush, J.D.: Interpretation of the Mössbauer spectra of Four-Iron Ferredoxin from Bacillus stearothermophilis. Eur. J. Biochem. **88**, 135–141 (1978)
20. Middleton, P., Dickson, D.P.E., Charles, E.J., Rush, J.D.: Interpretation of the Mössbauer spectra of the high-potential iron protein from chromatium. Eur. J. Biochem. **104**(1), 289–296 (1980)
21. Gütlich, P., Bill, E., Trautwein, A.X.: Mössbauer spectroscopy and transition metal chemistry. Springer, Berlin Heidelberg (2011)
22. Cammack, R.: Iron-sulfur clusters in enzymes: themes and variations. In: Cammack, R. (ed.) Iron-Sulfur Proteins, vol. 38. Advances in Inorganic Chemistry, pp. 281–323. Academic Press, San Diego (1992)
23. Schünemann, V., Winkler, H.: Structure and dynamics of biomolecules studied by Mössbauer spectroscopy. Rep. Prog. Phys. **63**(3), 263–353 (2000)
24. Mouesca, J.-M., Lamotte, B.: Iron-sulfur clusters and their electronic and magnetic properties. Coord. Chem. Rev. **178–180**, 1573–1614 (1998)
25. Albers, A., Demeshko, S., Dechert, S., Bill, E., Bothe, E., Meyer, F.: The complete characterization of a reduced biomimetic [2Fe-2S] cluster. Angew. Chem. Int. Ed. **50**(39), 9191–9194 (2011)
26. Ballmann, J., Albers, A., Demeshko, S., Dechert, S., Bill, E., Bothe, E., Ryde, U., Meyer, F.: A synthetic analogue of rieske-type [2Fe-2S] clusters. Angew. Chem. Int. Ed. **47**(49), 9537–9541 (2008)
27. Mascharak, P.K., Papaefthymiou, G.C., Frankel, R.B., Holm, R.H.: Evidence for the localized iron(III)/iron(II) oxidation state configuration as an intrinsic property of [Fe2S2(SR)4]3- clusters. J. Am. Chem. Soc. **103**(20), 6110–6116 (1981). doi:10.1021/ja00410a021
28. Beardwood, P., Gibson, J.F.: Iron-sulfur dimers with benzimidazolate-thiolate, -phenolate or bis(benzimidazolate) terminal chelating ligands. Models for Rieske-type proteins. J. Chem. Soc. Dalton Trans. **16**, 2457–2466 (1992)
29. Ding, X.Q., Bill, E., Trautwein, A.X., Winkler, H., Kostikas, A., Papaefthymiou, V., Simpoulos, A., Beardwood, P., Gibson, J.F.: Exchange interactions, charge delocalization and spin relaxation in a mixed-valence diiron complex studied by Mössbauer-spectroscopy. J. Chem. Phys. **99**(9), 6421–6428 (1993)
30. Hoggins, J.T., Steinfink, H.: Empirical bonding relationships in metal-iron-sulfide compounds. Inorg. Chem. **15**(7), 1682–1685 (1976)
31. Piepho, S.B.: Vibronic coupling for calculations of Mixed-Valence Line-Shapes—the interdependence of vibronic and MO effects. J. Am. Chem. Soc. **110**(19), 6319–6326 (1988)
32. Piepho, S.B., Krausz, E.R., Schatz, P.N.: Vibronic coupling for calculation of mixed-valence absorption profiles. J. Am. Chem. Soc. **100**(10), 2996–3005 (1978)
33. Girerd, J.J.: Electron transfer between magnetic ions in mixed valence binuclear systems. J. Chem. Phys. **79**, 1766–1775 (1983)
34. Blondin, G., Girerd, J.-J.: Interplay of electron exchange and electron transfer in metal polynuclear complexes in proteins or chemical models. Chem. Rev. **90**, 1359 (1990)
35. Bominaar, E.L., Borshch, S.A., Girerd, J.-J.: Double-exchange and vibronic coupling in mixed-valence systems. Electronic structure of [Fe4S4]3+ clusters in high-potential iron protein and related models. J. Am. Chem. Soc. **116**, 5362–5372 (1994)
36. Bominaar, E.L., Hu, Z., Münck, E., Girerd, J.-J., Borshch, S.: Double exchange and vibronic coupling in mixed-valence systems. Elelctonic structure of exchange-coupled siroheme-[Fe4S4]2+ chromophore in oxidized *E. Coli* sulfite reductase. J. Am. Chem. Soc. **117**(26), 6976–6989 (1995)
37. Münck, E., Papaefthymiou, V., Surerus, K.K., Girerd, J.J.: Double exchange in reduced Fe3S3 clusters and novel clusters with MFe3S4 cores. Acs Symposium Series **372**, 302–325 (1988)
38. Orio, M., Mouesca, J.M.: Variation of average g values and effective exchange coupling constants among 2Fe-2S clusters: a density functional theory study of the impact of localization (trapping forces) versus delocalization (double-exchange) as competing factors. Inorg. Chem. **47**(12), 5394–5416 (2008). doi:10.1021/ic701730h
39. Anxolabehere-Mallart, E., Glaser, T., Frank, P., Aliverti, A., Zanetti, G., Hedman, B., Hodgson, K.O., Solomon, E.I.: Sulfur K-edge X-ray absorption spectroscopy of 2Fe-2S ferredoxin: covalency of the oxidized and reduced 2Fe forms and comparison to model complexes. J. Am. Chem. Soc. **123**(23), 5444–5452 (2001)
40. Glaser, T., Rose, K., Shadle, S.E., Hedman, B., Hodgson, K.O., Solomon, E.I.: S K-edge X-ray absorption studies of tetranuclear iron-sulfur clusters: μ-sulfide bonding and its contribution to electron delocalization. J. Am. Chem. Soc. **123**(3), 442–454 (2000). doi:10.1021/ja002183v

41. Angove, H.C., Yoo, S.J., Burgess, B.K., Münck, E.: Mössbauer and EPR evidence for an all-ferrous Fe4S4 cluster with S = 4 in the Fe protein of nitrogenase. J. Am. Chem. Soc. **119**(37), 8730–8731 (1997)
42. Musgrave, K.B., Angove, H.C., Burgess, B.K., Hedman, B., Hodgson, K.O.: All-ferrous titanium(III) citrate reduced Fe protein of nitrogenase: an XAS study of electronic and metrical structure. J. Am. Chem. Soc. **120**(21), 5325–5326 (1998)
43. Angove, H.C., Yoo, S.J., Münck, E., Burgess, B.K.: An all-ferrous state of the Fe protein of nitrogenase—interaction with nucleotides and electron transfer to the MoFe protein. J. Biol. Chem. **273**(41), 26330–26337 (1998)
44. Yoo, S.J., Angove, H.C., Burgess, B.K., Hendrich, M.P., Münck, E.: Mössbauer and integer-spin EPR studies and spin-coupling analysis of the 4Fe–4S (0) cluster of the Fe protein from Azotobacter vinelandii nitrogenase. J. Am. Chem. Soc. **121**(11), 2534–2545 (1999)
45. Angove, H.C., Yoo, S.J., Munck, E., Burgess, B.K.: Role(s) of the P-clusters in nitrogenase catalysis. J. Inorg. Biochem. **74**(1–4), 65–65 (1999)
46. Surerus, K.K., Hendrich, M.P., Christie, P.D., Rottgardt, D., Orme-Johnson, W.H., Münck, E.: Mössbauer and integer-spin EPR of the oxidized P-clusters of nitrogenase—P_{ox} is a non-Kramers system with a nearly degenerate ground doublet. J. Am. Chem. Soc. **114**(22), 8579–8590 (1992). doi:10.1021/ja00048a034
47. Hans, M., Buckel, W., Bill, E.: Spectroscopic evidence for an all-ferrous [4Fe–4S](0) cluster in the superreduced activator of 2-hydroxyglutaryl-CoA dehydratase from Acidaminococcus fermentans. J. Biol. Inorg. Chem. **13**(4), 563–574 (2008)
48. Leggate, E.J., Bill, E., Essigke, T., Ullmann, G.M., Hirst, J.: Formation and characterization of an all-ferrous Rieske cluster and stabilization of the [2Fe–2S]0 core by protonation. Proc. Natl. Acad. Sci. U. S. A. **101**(30), 10913–10918 (2004)
49. Clark, M.M., Stubbert, B.D., Brennessel, W.W., Bill, E., Holland, P.L.: Synthesis, structure, and spectroscopy of an iron(I)-sulfide complex. Inorg. Chem (2011, accepted)
50. Stoian, S.A., Yu, Y., Smith, J.M., Holland, P.L., Bominaar, E.L., Münck, E.: Mössbauer, electron paramagnetic resonance, and crystallographic characterization of a high-spin Fe(I) diketiminate complex with orbital degeneracy. Inorg. Chem. **44**(14), 4915–4922 (2005)
51. Brugna-Guiral, M., Tron, P., Nitschke, W., Stetter, K.O., Burlat, B., Guigliarelli, B., Bruschi, M., Giudici-Orticoni, M.T.: NiFe hydrogenases from the hyperthermophilic bacterium Aquifex aeolicus: properties, function, and phylogenetics. Extremophiles **7**(2), 145–157 (2003). doi:10.1007/s00792-002-0306-3
52. Pandelia, M.-E., Fourmond, V., Tron-Infossi, P., Lojou, E., Bertrand, P., Leger, C., Giudici-Orticoni, M.-T., Lubitz, W.: Membrane-bound hydrogenase I from the hyperthermophilic bacterium aquifex aeolicus: enzyme activation, redox intermediates and oxygen tolerance. J. Am. Chem. Soc. **132**(20), 6991–7004 (2010). doi:10.1021/ja910838d
53. Fontecilla-Camps, J.C., Volbeda, A., Cavazza, C., Nicolet, Y.: Structure/function relationships of NiFe- and FeFe-hydrogenases. Chem. Rev. **107**(10), 4273–4303 (2007). doi:10.1021/cr050195z
54. Surerus, K.K., Chen, M., Vanderzwaan, J.W., Rusnak, F.M., Kolk, M., Duin, E.C., Albracht, S.P.J., Münck, E.: Further characterization of the spin coupling observed in oxidized hydrogenase from chromatium-vinosum—a Mössbauer and multifrequency EPR study. Biochemistry **33**(16), 4980–4993 (1994)
55. Pandelia, M.-E., Nitschke, W., Infossi, P., Giudici-Orticoni, M.-T., Bill, E., Lubitz, W.: Characterization of a unique FeS cluster in the electron transfer chain of the oxygen tolerant NiFe hydrogenase from Aquifex aeolicus. Proc. Natl. Acad. Sci. **108**(15), 6097–6102 (2011). doi:10.1073/pnas.1100610108
56. Pandelia, M.-E., Nitschke, W., Infossi, P., Giudici-Orticoni, M.-T., Bill, E., Lubitz, W. (2012, to be published)
57. Shomura, Y., Yoon, K.-S., Nishihara, H., Higuchi, Y.: Structural basis for a [4Fe-3S] cluster in the oxygen-tolerant membrane-bound [NiFe]-hydrogenase. Nature advance online publication (2011). doi:http://www.nature.com/nature/journal/vaop/ncurrent/abs/nature10504.html#supplementary-information
58. Fritsch, J., Scheerer, P., Frielingsdorf, S., Kroschinsky, S., Friedrich, B., Lenz, O., Spahn, C.M.T.: The crystal structure of an oxygen-tolerant hydrogenase uncovers a novel iron-sulphur centre. Nature advance online publication (2011). doi:http://www.nature.com/nature/journal/vaop/ncurrent/abs/nature10505.html#supplementary-information

Hyperfine Interact (2012) 206:1–5
DOI 10.1007/s10751-011-0497-z

Cooperative spin transition and thermally quenched high-spin state in new polymorph of $[Fe(qsal)_2]I_3$

Kazuyuki Takahashi · Tetsuya Sato · Hatsumi Mori · Hiroyuki Tajima · Yasuaki Einaga · Osamu Sato

Published online: 3 December 2011

Abstract Novel polymorph of the ferric spin crossover complex, β-$[Fe(qsal)_2]I_3$ [qsalH = *N*-(8-quinolyl)salicylaldimine], has been prepared and characterized by magnetic susceptibilities and Mössbauer spectra. β polymorph exhibited a cooperative complete spin transition with a thermal hysteresis of 25 K and a tendency to be quenched in the high-spin (HS) state, which is contrastive to a gradual incomplete spin conversion in α polymorph.

Keywords Spin crossover · Ferric complex · Polymorph · Magnetic properties · Mössbauer spectra

1 Introduction

Polymorphism in spin crossover (SCO) compounds affords valuable information on the effects of the coordination geometries and intermolecular interactions upon their magnetic behaviors. Despite a number of examples of polymorphism in the Fe(II) SCO complexes, the polymorphic Fe(III) SCO complexes have been rarely reported [1, 2]. The family of the ferric SCO complexes, $[Fe(qsal)_2]X$ [X = counter anion],

K. Takahashi (✉)
Department of Chemistry, Graduate School of Science, Kobe University,
Kobe, Hyogo 657-8501, Japan
e-mail: ktaka@crystal.kobe-u.ac.jp

T. Sato · H. Mori · H. Tajima
Institute for Solid State Physics, University of Tokyo, Kashiwa, Chiba 277-8581, Japan

Y. Einaga
Department of Chemistry, Keio University, Yokohama, Kanagawa 223-8522, Japan

O. Sato
Institute for Materials Chemistry and Engineering, Kyushu University,
Kasuga, Fukuoka 816-8580, Japan

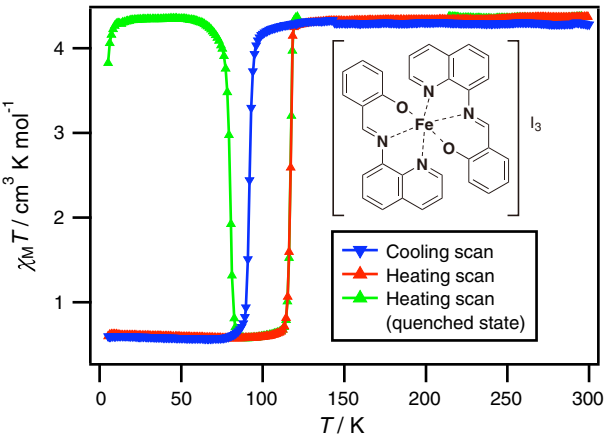

Fig. 1 The $\chi_M T$ versus T product for β-$[Fe(qsal)_2]I_3$ at scan speed with 1 K min^{-1}

was known as a versatile component for multifunctional SCO compounds [3–7]. Recently we have reported the crystal structures and gradual SCO behaviors under pressures for $[Fe(qsal)_2]I_3$ (Fig. 1) [8], which is hereafter designated as α-$[Fe(qsal)_2]I_3$. In the course of previous experiments, we have found another polymorph, β-$[Fe(qsal)_2]I_3$. In this paper we will report the temperature dependence of magnetic susceptibilities and Mössbauer spectra for β-$[Fe(qsal)_2]I_3$, which exhibited a cooperative spin transition with a wide thermal hysteresis of 25 K and a tendency to be quenched in the high-spin (HS) state.

2 Experimental

Preparation of β-$[Fe(qsal)_2]I_3$ Tetrabutylammonium triiodide ($TBA{\cdot}I_3$) (80 mg) was dissolved in 160 ml of methanol and filtered off. The solution was poured into the filtered solution of $[Fe(qsal)_2]NO_3$ (50 mg) in 100 ml of methanol. The precipitates appeared within a few hours and were filtered off. β-$[Fe(qsal)_2]I_3$ was obtained as very thin dark brown platelets concomitant with a small amount of tiny black crystalline aggregates of α-$[Fe(qsal)_2]I_3$ and large black rectangular parallelepipeds, which was a nonstoichiometric compound designated as $[Fe(qsal)_2]I_{2.75}$. All the measurements were performed on the sample separated under microscope. Anal. Calcd for $C_{32}H_{22}N_4O_2I_3$: C, 41.28; H, 2.38; N, 6.02. Found: C, 41.01; H, 2.66; N, 5.80%.

Magnetic susceptibility measurements Magnetic susceptibilities were measured on a Quantum Design MPMS SQUID magnetometer under 0.5 T in the temperature range of 2–300 K. Data were corrected for diamagnetic contributions estimated by Pascal constants.

Mössbauer spectra The Mössbauer spectra were measured on a constant acceleration spectrometer with a source of ^{57}Co/Rh in the transmission mode. The measurements at low temperature were performed with a closed-cycle helium refrigerator (Iwatani Co. Ltd.). The obtained Mössbauer spectra were fitted with symmetric Lorentzian doublets by a least squares fitting program.

3 Results and discussion

3.1 Preparation and characterization

β-$[Fe(qsal)_2]I_3$ was prepared by metathesis between $[Fe(qsal)_2](NO_3)$ and TBA·I_3 in methanol. Contamination by α-$[Fe(qsal)_2]I_3$ and $[Fe(qsal)_2]I_{2.75}$ sometimes occurred on more dilute or slower diffusion conditions. The composition for β-$[Fe(qsal)_2]I_3$ was confirmed by microanalyses. Powder XRD measurement for β-$[Fe(qsal)_2]I_3$ revealed that peak positions were different from the ones simulated from the crystal structure of α-$[Fe(qsal)_2]I_3$, clearly indicating that β-$[Fe(qsal)_2]I_3$ is a new polymorph of $[Fe(qsal)_2]I_3$.

3.2 Magnetic susceptibilities

The variable temperature magnetic susceptibilities were measured on a polycrystalline sample of β-$[Fe(qsal)_2]I_3$ at a scan speed of 1 K min^{-1}. The $\chi_M T$ versus T product is shown in Fig. 1. The $\chi_M T$ value at 300 K is 4.30 cm^3 K mol^{-1}, suggesting the $Fe(qsal)_2$ cation is almost in the HS state. On lowering the temperature, the $\chi_M T$ value abruptly decreased at around 95 K ($T_{1/2} \downarrow = 92$ K). The $\chi_M T$ value of 0.60 cm^3 K mol^{-1} at 5 K indicated the complex is almost in the low-spin (LS) state. On heating the sample, the $\chi_M T$ value discontinuously increased at around 110 K ($T_{1/2} \uparrow = 117$ K). Since the temperature dependences of $\chi_M T$ on repeating the cooling and heating scans were reproducible, β-$[Fe(qsal)_2]I_3$ is a novel SCO compound showing a wide thermal hysteresis loop of 25 K. It should be noted that the $\chi_M T$ values below the transition temperature depended on the cooling scan speeds. The faster the cooling speeds were, the higher the $\chi_M T$ values below the transition temperature were. When the room-temperature sample was inserted into an MPMS chamber setting the temperature of 5 K, the sample could be completely quenched in the HS state (Fig. 1, green triangles). On heating the quenched sample at a scan speed of 1 K min^{-1}, the quenched HS state was relaxed to the ground LS state at around 80 K. These magnetic behaviors were different from a gradual incomplete spin conversion without a thermal hysteresis in α-$[Fe(qsal)_2]I_3$ ($T_{1/2}$ = ca.240 K).

3.3 Mössbauer spectra

The Mössbauer spectra were measured on a polycrystalline sample of β-$[Fe(qsal)_2]I_3$. The spectrum at 293 K demonstrated one doublet (Fig. 2a), which was ascribed to the HS state (isomer shift (IS) = 0.232, quadrupole splitting (QS) = 0.616 mm s^{-1}). On cooling the sample without temperature control, the spectrum at 15 K consisted of one LS doublet (81.3%, IS = 0.062, QS = 2.861 mm s^{-1}) and one HS doublet (18.7%, IS = 0.331, QS = 0.595 mm s^{-1}) (Fig. 2b). Since the compound was easy to be trapped in the quenched HS state as described above, the spectrum at 15 K cooled after retaining the temperature of 80 K for a few hours was recorded again. Consequently, only one LS doublet spectrum was observed (IS = 0.075, QS = 2.878 mm s^{-1}) (Fig. 2c). This means that the former HS doublet is derived from the quenched HS state. On heating, the LS doublet (IS = 0.349, QS = 0.734 mm s^{-1}) was recovered at 130 K (Fig. 2d).

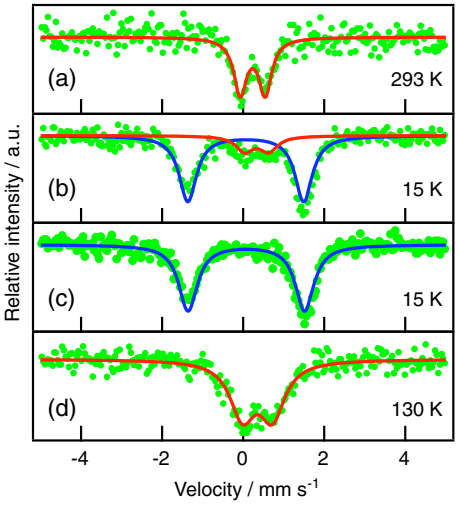

Fig. 2 Mössbauer spectra for β-[Fe(qsal)$_2$]I$_3$ at **a** 293 K, **b** 15 K after cooling without temperature control, **c** 15 K after annealing at 80 K, and **d** 130 K. *Green circles* indicate the observed spectra. *Blue* and *red lines* show the fitted curves for the high-spin and low-spin states, respectively

3.4 External treatments

When the crystals of β-[Fe(qsal)$_2$]I$_3$ were poured into pressure transmitting media such as Daphne 7373, Fluorinert, silicone oils, and water-ethanol, they broke into pieces and the spin transition disappeared. On the other hand, the magnetic behavior for α-[Fe(qsal)$_2$]I$_3$ have never changed in the pressure media [8]. Furthermore, grinding the crystals of β-[Fe(qsal)$_2$]I$_3$ also resulted in disappearance of the HS to LS conversion on lowering temperature. These observations indicate that the spin crossover behavior in β-[Fe(qsal)$_2$]I$_3$ is very sensitive to external treatments.

4 Conclusion

The temperature dependence of magnetic susceptibilities and Mössbauer spectra revealed that a new polymorphic ferric complex, β-[Fe(qsal)$_2$]I$_3$, exhibited a complete spin transition between the HS and LS states ($T_{1/2}\downarrow = 92$ K, $T_{1/2}\uparrow = 117$ K). This magnetic behavior was quite different from that of α-[Fe(qsal)$_2$]I$_3$ [8]. Furthermore, its magnetic behavior was quite sensitive to external treatments. These observations imply that a large structural change may accompany the spin transition in β-[Fe(qsal)$_2$]I$_3$. Since the comparison between the crystal structures of two polymorphs would provide the insight into a rational design for SCO compounds, the crystal structure analysis for β-[Fe(qsal)$_2$]I$_3$ is now in progress.

Acknowledgements This work was partly supported by a Grant-in-Aid for Scientific Research on Innovative Areas of Molecular Degrees of Freedom (No. 20110007), and a Grant-in-Aid for Young Scientists (B) (No. 19750107) from the Ministry of Education, Culture, Sports, Science, and Technology of Japan.

References

1. Faulmann, C., Szilágyi, P., Jacob, K., Chahine, J., Valade, L.: New J. Chem. **33**, 1268 (2009)
2. Collet, E., Boillot, M.-L., Hebert, J., Moisan, N., Servol, M., Lorenc, M., Toupet, L., Cointe, M., Tissot, A., Sainton, J.: Acta Crystallogr. **B65**, 474 (2009)
3. Takahashi, K., Cui, H.-B., Kobayashi, H., Einaga, Y., Sato, O.: Chem. Lett. **34**, 1240 (2005)
4. Takahashi, K., Cui, H.-B., Okano, Y., Kobayashi, H., Einaga, Y., Sato, O.: Inorg. Chem. **45**, 5739 (2006)
5. Takahashi, K., Cui, H.-B., Okano, Y., Kobayashi, H., Mori, H., Tajima, H., Einaga, Y., Sato, O.: J. Am. Chem. Soc. **130**, 6688 (2008)
6. Takahashi, K., Mori, H., Kobayashi, H., Sato, O.: Polyhedron **28**, 1776 (2009)
7. Neves, A., Dias, J., Vieira, B., Santos, I., Branco, M., Pereira, L., Waerenborgh, J., Almeida, M., Belo, D., da Gama, V.: CrystEngComm **11**, 2160 (2009)
8. Takahashi, K., Sato, T., Mori, H., Tajima, H., Sato, O.: Physica B **405**, S65 (2010)

Hyperfine Interact (2012) 206:7–11
DOI 10.1007/s10751-011-0436-z

^{57}Fe Mössbauer probe of spin crossover thin films on a bio-membrane

Anil D. Naik · Yann Garcia

Published online: 1 November 2011

Abstract An illustrious complex $[Fe(ptz)_6](BF_4)_2$ (ptz = 1-propyl-tetrazole) (**1**) which was produced in the form of submicron crystals and thin film on Allium cepa membrane was probed by ^{57}Fe Mossbauer spectroscopy in order to follow its intrinsic spin crossover. In addition to a weak signal that corresponds to neat SCO compound significant amount of other iron compounds are found that could have morphed from **1** due to specific host-guest interaction on the lipid-bilayer of bio-membrane. Further complimentary information about biogenic role of membrane, was obtained from variable temperature Mossbauer spectroscopy on a ∼5% enriched $[^{57}Fe(H_2O)_6](BF_4)_2$ salt on this membrane.

Keywords Spin crossover · 1-propyl-tetrazole · Thin films · Nanoparticles · Bio-membrane · Onion

1 Introduction

Currently there is an intensive research towards developing novel rational techniques for thin film deposition and nanoparticles synthesis of Fe^{II} spin crossover (SCO) materials that have foreseeable prospects in molecular electronics [1]. In an unique approach under green technology, we recently introduced an inner epidermis of onion bulb (*Allium cepa*) (Fig. 1a–c) as a novel support to grow single crystals (Fig. 1d) of desired size and for thin film processing of a SCO material [2]. This radical approach differs from the classical one using conventional supports like glass, quartz, Si-wafer etc. This hybrid functional material was also used as natural stencil in soft lithography, for the first time, to print nanodots (30–55 nm) on Si wafer [2]. As a proof of concept, we selected a thermochromic Fe^{II} complex,

A. D. Naik · Y. Garcia (✉)
Institute of Condensed Matter and Nanosciences, Université Catholique de Louvain, Place L. Pasteur 1, 1348 Louvain-la-Neuve, Belgium
e-mail: yann.garcia@uclouvain.be

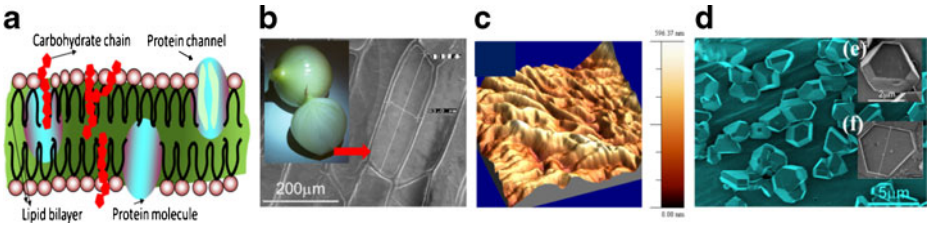

Fig. 1 **a** Model of membrane lipid-bilayer. **b** SEM image on onion membrane. **c** AFM image revealing surface inhomogeneity [2]. **d** SEM image showing dense crystal growth on **M1**. **e** SEM image on single metamorphosed crystal. **f** Neat hexagonal crystal grown on ITO support shown for comparison [6]

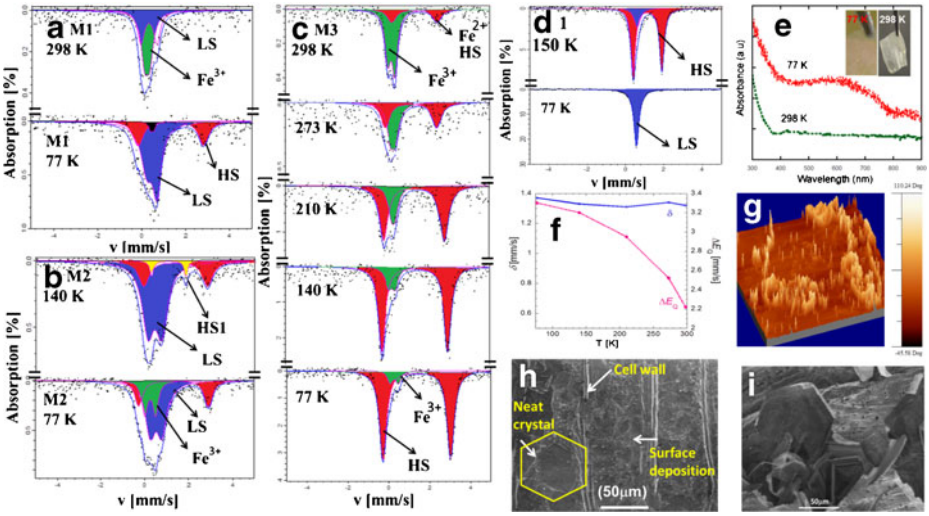

Fig. 2 **a**–**d** Selected ^{57}Fe Mossbauer spectra of **M1**, **M2**, **M3** and **1**. **e** Thermal SCO detected by Uv-vis [2], the inset showing thermochromism of the membrane. **f** Temperature variation of δ and ΔE_Q for **M3**. **g** AFM image of **M1**. Elevated bright areas indicate presence of crystals [2]. **h** SEM image on dip coated **M2**. **i** SEM image of **M3**

$[Fe(ptz)_6](BF_4)_2$ (**1**) (ptz = 1-propyl-tetrazole), whose thermally and light-induced spin transition has been very well documented [3–5]. Thin films (~25 nm thickness) and nanoparticles/crystals (<40 nm–3 μm) of **1** were successfully produced on the membrane and the SCO was confirmed by Uv-visible spectroscopy and visual thermochromism (Fig. 2e) [2]. Scanning electron micrographs (SEM) of membrane with deposited crystals (**M1**) shows drastic morphogenesis to truncated hexagonal bipyramid (Fig. 1e) as opposed to neat hexagonal crystals grown on glass/ITO plates (Fig. 1f) [6] whereas membrane with thin film (**M2**) leads to neat hexagonal crystals along with thin film deposition (Fig. 2h). In continuation of this work, and for the first time ^{57}Fe Mossbauer spectroscopy was explored not only to study intrinsic SCO on *Allium cepa* membrane but also to probe any possible metamorphosed iron complex entrapped in/over lipid-bilayer of the membrane (Fig. 1a) that could have escaped routine spectroscopic radar. The perspective of the present study not only assures

tremendous prospects in green chemistry under nanotechnology umbrella but is also expected to shed light on diverse important topics like transport mechanism across bio-membrane, bio-membranes in heavy metal retention from industrial effluents, iron uptake and trafficking in biological systems etc.

2 Experimental

1 was synthesized according to the reported procedure [3]. Details about *Allium cepa* membrane (Fig. 1b) processing, loading and characterization of **1** on membrane, SCO operation were earlier described [2]. Membrane (**M1**) with sub-micron sized crystals of **1** and membrane with thin film (**M2**) were selected for the present study [2]. A significant deposition has occurred on **M2** surface with large neat hexagonal crystals being evidenced (Fig. 2h). A 5% enriched sample of $[Fe(H_2O)_6](BF_4)_2$ (**2**) was dip coated on the membrane to produce **M3**. Several pieces of **M1**/**M2** were stacked together for Mössbauer measurements in order to improve signal to noise ratio.

3 ^{57}Fe Mossbauer spectroscopy

Hyperfine parameters for **M1-3**, **1** and **2** are summarized in Table 1 and selected spectra are shown in Fig. 2a–d. At 77 K, the Mössbauer spectrum of **M1** shows three resonance signals with different quadrupole splitting: (i) a major signal (68 %) with $\delta = 0.47(1)$ mm/s and $\Delta E_Q = 0.47(1)$ mm/s which stems from low-spin (LS) **1** species, with a distorted octahedron, after adhesion on the membrane support. This observation confirms the SCO occurrence that was precluded from the color change to pink on cooling (Fig. 2e). (ii) Another quadrupole doublet with $\delta^{HS} = 1.34(2)$ mm/s and $\Delta E_Q^{HS} = 2.97(1)$ mm/s (28 %), which corresponds to the co-deposited iron salt **2** with a smaller quadrupole splitting compared to the powder sample (Table 1) indicative of a more distorted octahedron, as expected on the biomembrane support. (iii) a minor doublet (4%) with $\delta = 0.48(3)$ mm/s and $\Delta E_Q = 0.16(1)$ mm/s which point out to LS octahedra of **1** that are less distorted compared to the major species (Fig. 2a). At 298 K, the HS signal is no longer detected as a major fraction of Fe^{III} and LS Fe^{II} species dominate the spectrum. This result is consistent with the ones obtained on **M3** at r. t. for which **2** is hardly observed whereas a major ferric fraction is detected (Fig. 2c) due to the overestimation of these species at r.t. [7]. The situation is slightly different for **M2** at 77 K with detection of Fe^{III} species as observed for **M3** (Fig. 2c), which was prepared under similar conditions, along with signals of LS **1** and of HS **2**. A 140 K, co-deposited complex **2** is still observed along with LS **1**, whereas a weak doublet with $\delta = 1.07$ mm/s and $\Delta E_Q = 1.57$ mm/s, is now detected. It corresponds to HS **1** [3], which expectedly disappear at 77 K where the HS to LS crossover is complete.

In both deposition methods (leading to **M1** and **M2**), the remote possibility of fractional internalization of sensor, which might not be seen in its original form through the semi-permeable membrane, for instance as Fe^{III} species, cannot be excluded [8]. The membrane permeability might also be subjected to any kind of adverse effect under the working acid pH of 3–4 [2] and may facilitate iron ions to

Table 1 ^{57}Fe Mossbauer parameters of **M1**, **M2**, **M3**, **1** and **2**

Code T(K)	Parameters			
	δ mm/s	ΔE_Q mm/s	$\Gamma/2$ mm/s	Rel. area, Spin, oxi. state
M1 298	0.30(1)	0.73(3)	0.18(1)	41, LS-Fe^{II}
	0.22(3)	0.24(1)	0.2(5)	59, Fe^{III}
M1 77	0.47(1)	0.47(1)	0.24(1)	68, LS **1**
	1.34(2)	2.97(1)	0.27(1)	28, **2**
	0.48(3)	0.16(1)	0.12(1)	4, LS **1**
M2 140	0.43(3)	0.63(1)	0.32(5)	71, LS-Fe^{II}
	1.39(1)	2.91(1)	0.29(1)	24, **2**
	1.07(1)	1.57(1)	0.11(1)	5, HS, **1**
M2 77	0.53(1)	0.54(5)	0.28(1)	56, LS **1**
	1.32(1)	3.19(3)	0.23(1)	23, **2**
	0.25(1)	0.49(1)	0.16(2)	21, Fe^{III}
1				
298 [3]	0.91	1.05	–	100, HS-Fe^{II}
150[a]	1.13(3)	1.49(1)	0.14(5)	83, HS-Fe^{II}
	0.59(2)	0	0.2[b]	17, LS-Fe^{II}
77[a]	0.56(2)	0	0.16(2)	100, LS-Fe^{II}
77 [3]	0.44	0	–	100, LS-Fe^{II}
2[c] 298	1.26(3)	1.30(1)	0.14(5)	100 HS-Fe^{II}
2[c] 77	1.38(4)	3.46(3)	0.18(6)	100 HS-Fe^{II}
M3 298	1.32(5)	2.22(1)	0.26(1)	28, HS-Fe^{II}
	0.18(1)	0.34(2)	0.16(1)	72, Fe^{III}
M3 273	1.14(1)	2.52(2)	0.26(1)	49, HS-Fe^{II}
	0.25(1)	0.26(1)	0.21(1)	51, Fe^{III}
M3 210	1.31(4)	2.95(8)	0.25(6)	75, HS-Fe^{II}
	0.30(7)	0.18(2)	0.2(1)	25, Fe^{III}
M3 140	1.33(1)	3.2(3)	0.20(2)	83, HS-Fe^{II}
	0.22(1)	0.32(1)	0.2(1)	17, Fe^{III}
M3 77	1.37(8)	3.30(1)	0.21(1)	91, HS-Fe^{II}
	0.26(6)	0.40(1)	0.16(7)	9, Fe^{III}

δ: isomer shift (with respect to α-Fe at 298 K); ΔE_Q: quadrupole splitting; $\Gamma/2$: half width at half maximum

[a] **1** recrystallized from MeOH
[b] Fixed data
[c] Powder sample [10]

traverse the membrane. In this context, it is interesting to note the presence of K^+ ions in metamorphosed nanocrystals on **M1** [2].

This intriguing possibility prompted us to investigate the possible biogenic role of *Allium cepa* membrane on **2**, proposed here as a reference material, by recording a series of Mössbauer spectra at selected temperatures (Table 1, Fig. 2c), which indeed reveals interesting features. Spectrum of **M3** at 77 K is dominated by a quadrupole doublet with $\delta = 1.37$ mm/s and $\Delta E_Q = 3.30$ mm/s that matches very well with powder sample of **2** (Table 1). There is also a small amount of Fe^{III} species which is due to iron oxidation. Indeed, the iron percentage in onion is too low (0.2 mg/100g of onion, 2%) to yield any inherent signal [9]. Subsequent spectra recorded upon warming up to 298 K indicate a decrease of

δ^{HS} and ΔE_Q^{HS} as expected (Fig. 2f). It has to be noted that even for the neat sample **2**, ΔE_Q (3.46 mm/s) at 77 K was drastically reduced to 1.30 mm/s at 298 K which is in agreement with a phase transition due to temperature dependent anion disorder [10]. The area fraction of Fe^{III} species in **M3** grew upon warming and dominates the r.t. spectrum which can be rationalized on the basis of the Debye temperature (θ_D) differences between ferrous and ferric ions [11] as HS ferric species tend to have a higher θ_D than HS ferrous species [7]. Having confirmed by Mössbauer spectroscopy that no disproportion of **1** occurs, as already shown by X-ray powder diffraction and Raman data [2], we were interested to learn if the crystal field of **1** could have been affected by the deposition. This hypothesis is confirmed, by comparing the spin state properties of **M1**/**M2** with the one of the powder sample of **1** which has a transition temperature $T_{1/2} \sim 135$ K, on warming from 77 K [4]. Thus, a LS state stabilization is observed as the SCO only starts at 140 K for **M2**. This situation may results from possible interactions with membrane organics, which may affect the immediate surrounding of the complex, thus modifying the crystal field, as much as non coordinated anions can do in a crystal lattice [1].

Acknowledgements We acknowledge financial support from IAP INANOMAT, FNRS (FRFC 2.4508.08, IISN 4.4507.10), ARC - Académie Universitaire Louvain, and from the Groupe Francophone de Spectrométrie Mössbauer (GFSM) for supporting A. D. N. to attend ICAME 2011 (Kobe) and GFSM 2011 (Strasbourg).

References

1. Gütlich, P., Garcia, Y., Goodwin, H.A.: Spin crossover phenomena in Fe(II) complexes. Chem. Soc. Rev. **29**, 419 (2000)
2. Naik, A.D., Stappers, L., Snauwaert, J., Fransaer, J., Garcia, Y.: A biomembrane stencil for crystal growth and soft lithography of a thermochromic molecular sensor. Small **24**, 2842 (2010)
3. Franke, P.L., Haasnoot, J.G., Zuur, A.P.: Tetrazoles as ligands. Part IV. Iron(II) complexes of monofunctional tetrazole ligands, showing high-spin-low-spin transitions. Inorg. Chim. Acta **59**, 5 (1982)
4. Müller, E.W., Ensling, J., Spiering, H., Gütlich, P.: High-spin ↔ low-spin transition in hexacoordinate complexes of iron(II) with monodentate 1-alkyltetrazole ligands: a variable-temperature. Mössbauer, magnetic susceptibility, and far-infrared study. Inorg. Chem. **22**, 2074 (1983)
5. Chong, C., Mishra, H., Boukheddaden, K., Denise, S., Collet, E., Ameline, J.-C., Naik, A.D., Garcia, Y., Varret, F.: Electronic and structural aspects of spin transitions observed by optical microscopy. The case of $[Fe(ptz)_6](BF_4)_2$. J. Phys. Chem. B **114**, 1975 (2010)
6. Chong, C., Berini, B., Boukheddaden, K., Codjovi, E., Linares, J., Garcia, Y., Naik, A.D., Varret, F.: Characterization of spin crossover crystal surface by AFM. Phys. Status Solidi A **207**, 1227 (2010)
7. Garcia, Y., Ksenofontov, V., Lapouyade, R., Naik, A.D., Robert, F., Gütlich, P.: Synthesis and magnetic properties of an iron 1,2-bisthienyl perfluorocyclopentene photochromic coordination compound. Opt. Mater. **33**, 942 (2011)
8. Schönherr, J.: Characterization of aqueous pores in plant cuticles and permeation of ionic solutes. J. Exp. Bot. **57**, 2471 (2006)
9. Bajaj, K.L., Kaur, G., Singh, J., Gill, S.P.S.: Chemical evaluation of some important varieties of onion (Allium cepa L.). Qual. Plant. Plant Foods, Hum. Nutr. **30**, 117 (1980)
10. Asch, L., Dezsi, I., Lohner, T., Molnar, B.: Mössbauer study of the phase transition in $Fe(BF_4)_2 \bullet 6H_2O$ and $Co(BF_4)_2 \bullet 6H_2O$. Chem. Phys. Lett. **39**, 177 (1976)
11. Gibb, T.C.; Greenwood, N.N.: Mössbauer Spectroscopy. Chapman and Hall Ltd., London (1971)

Hyperfine Interact (2012) 206:13–18
DOI 10.1007/s10751-011-0544-9

Mössbauer studies of frataxin role in iron-sulfur cluster assembly and dysfunction-related disease

Ricardo Garcia-Serres · Martin Clémancey · Jean-Louis Oddou · Annalisa Pastore · Emmanuel Lesuisse · Jean-Marc Latour

Published online: 29 December 2011

Abstract Friedreich ataxia is a disease that is associated with defects in the gene coding for a small protein frataxin. Several different roles have been proposed for the protein, including iron chaperoning and iron storage. Mössbauer spectroscopy was used to probe these hypotheses. Iron accumulation in mutant mitochondria unable to assemble iron sulfur clusters proved to be insensitive to overexpression of frataxin, ruling out its potential involvement as an iron storage protein similar to ferritin. Rather, it was found that frataxin negatively regulates iron sulfur cluster assembly.

Keywords Mössbauer spectroscopy · Frataxin · Iron sulfur cluster · Iron accumulation

1 Introduction

Friedreich ataxia (FRDA) is an autosomal recessive neurodegenerative disease with an occurrence of 1 in 40,000 in the caucasian population. This inherited disorder was

R. Garcia-Serres · J.-L. Oddou
Université Joseph Fourier, 38054 Grenoble Cedex 9, France

M. Clémancey
CNRS, UMR5249, Grenoble, France

A. Pastore
Medical Research Council National Institute for Medical Research, London, UK

E. Lesuisse
Laboratoire Mitochondries, Métaux et Stress oxydant,
Institut Jacques Monod, CNRS-Université Paris, Diderot, France

J.-M. Latour (✉)
CEA, iRTSV, LCBM, 38054 Grenoble Cedex 9, France
e-mail: jean-marc.latour@cea.fr

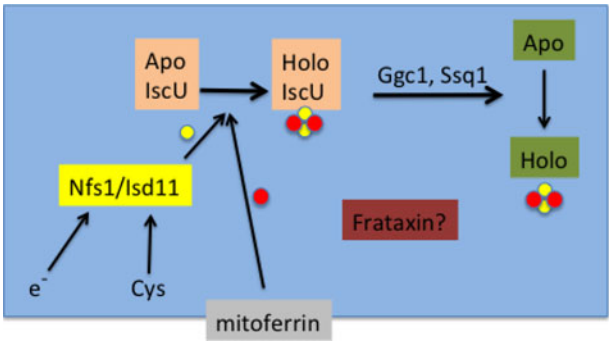

Fig. 1 Partner proteins involved in iron sulfur cluster biogenesis. Iron (●) is imported through mitoferrin, sulfide (●) from cysteine by Nfs1/Isd11

identified in 1843 by Friedreich. The most frequent symptom and disease cause of FRDA is hypertrophic cardiomyopathy that develops ca 25 years after onset of the disease, which occurs generally around age 14 [1]. Genetic studies in the mid-1990s have shown that the disease is associated with a deficiency in a specific protein that was coined frataxin (FXN). FXN is a small (14 kDa) mitochondrial protein highly conserved from bacteria (CyaY) to yeast (Yfh1) to humans (FXN). Its deficiency is associated with abnormalities of iron metabolism: decreased iron–sulfur cluster (ISC) biogenesis, accumulation of iron in mitochondria and depletion in the cytosol, enhanced cellular iron uptake, and impaired heme biosynthesis. It was recently shown that ISC biogenesis is the first defect, while iron accumulation occurs in a later stage of the disease [2]. Figure 1 illustratres the various processes and proteins involved and the proposed potential roles of FXN.

Several structures of FXN of prokaryote as well as eukaryote origins are available both in crystalline and in solution states [3]. They reveal that FXN comprises a β sheet and two α helices, and that one helix possesses a patch of negatively charged aspartate/gutamate residues, possibly involved in iron binding. Indeed it was shown that in excess of iron and oxidative conditions FXN oligomerizes and binds a high number of iron atoms that assemble to form an aggregate, a behavior reminiscent of that of the iron storage protein ferritin, which led some authors to propose that FXN is an iron storage protein involved in mitochondria protection against oxidative stress [4].

Mössbauer spectroscopy, which evidences iron whatever its chemical form and its spin state, is perfectly suited to trace it in cells, and studies of iron distribution in organelles have recently been developed as a tool to follow iron metabolism in native or stress conditions [5]. Mössbauer has also been extensively used to characterize ISC clusters in proteins and enzymes [6] and recently in the scaffold proteins involved in ISC biogenesis [7]. We took advantage of these available background informations to investigate two possible roles of FXN as (i) an iron storage protein or (ii) a regulator of ISC biogenesis.

2 Experimental section

^{57}Fe Mössbauer experiments were operated as already described [8, 9]. Analysis of the data was performed with the program WMOSS (WEB Research, Edina, MN).

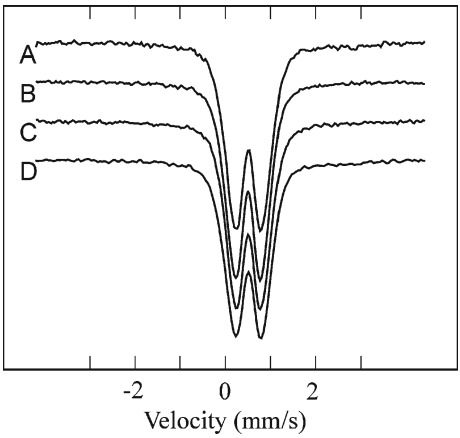

Fig. 2 Mössbauer spectra of mitochondria from different yeast strains: Δyfh1 **a**, Δssq1 **b**, Δggc1 **c**, Δggc1-YFH1 **d**. Spectra recorded at 78 K in zero applied magnetic field

Samples of mitochondria strains were prepared as described [10]. Sample preparation for kinetic analysis through Mössbauer spectroscopy was done under strict anaerobic conditions (within an inert atmosphere box with an oxygen content <2 ppm) by mixing the scaffold protein IscU, the desulfurase IscS, the reducing agent DTT, a $^{57}Fe^{2+}$ salt and cysteine in the ratio 1 mM/10 μM/5 mM/1.2 mM/5 mM. Two parallel experiments were performed, one in the absence and one in the presence of 50 mM of bacterial frataxin CyaY. The reaction was initiated by addition of cysteine and the samples were frozen at different times: 0, 5, 15, 30, 60 or 120 min. The expriments were run in triplicate with overlapping time domains to assess the reproducibility of the observations. In addition, control experiments were performed on mixtures lacking a component, and no Fe-S cluster formation was observed in any of these controls. All samples and controls for Mössbauer analyses were frozen in liquid nitrogen within the box and kept at that temperature until measurement.

3 Results

3.1 Iron accumulation in mitochodria

Iron accumulation is a regular symptom observed in FRDA patients. It is associated with a defect in frataxin and can be observed in mutant strains in which the protein is lacking (Δyfh1 strain). However it can be observed also in strains that possess FXN and assemble ISC but lack one of the ISC transporter chaperones (Δssq1 and Δggc1 strains), and are therefore unable to transfer ISC to their target proteins. Previous Mössbauer studies of yeast mitochodria Δyfh1 strain [10] had identified the aggregate form as polydisperse nanoparticles of iron phosphate. To assess whether iron accumulates always in the same chemical form we compared Δyfh1 to Δssq1 and Δggc1 strains. In addition, we studied Δggc1-YFH1, a particular strain lacking Ggc1 but overexpressing FXN, to evaluate if FXN can act as an iron storage protein.

Figure 2 illustrates the Mössbauer spectra of the strains under consideration in the present study. Consistent with previous observations [10], the 4.2 K Mössbauer spectrum of Δyfh1 mitochondria (Fig. 1a) displayed one slightly asymmetric quadrupole

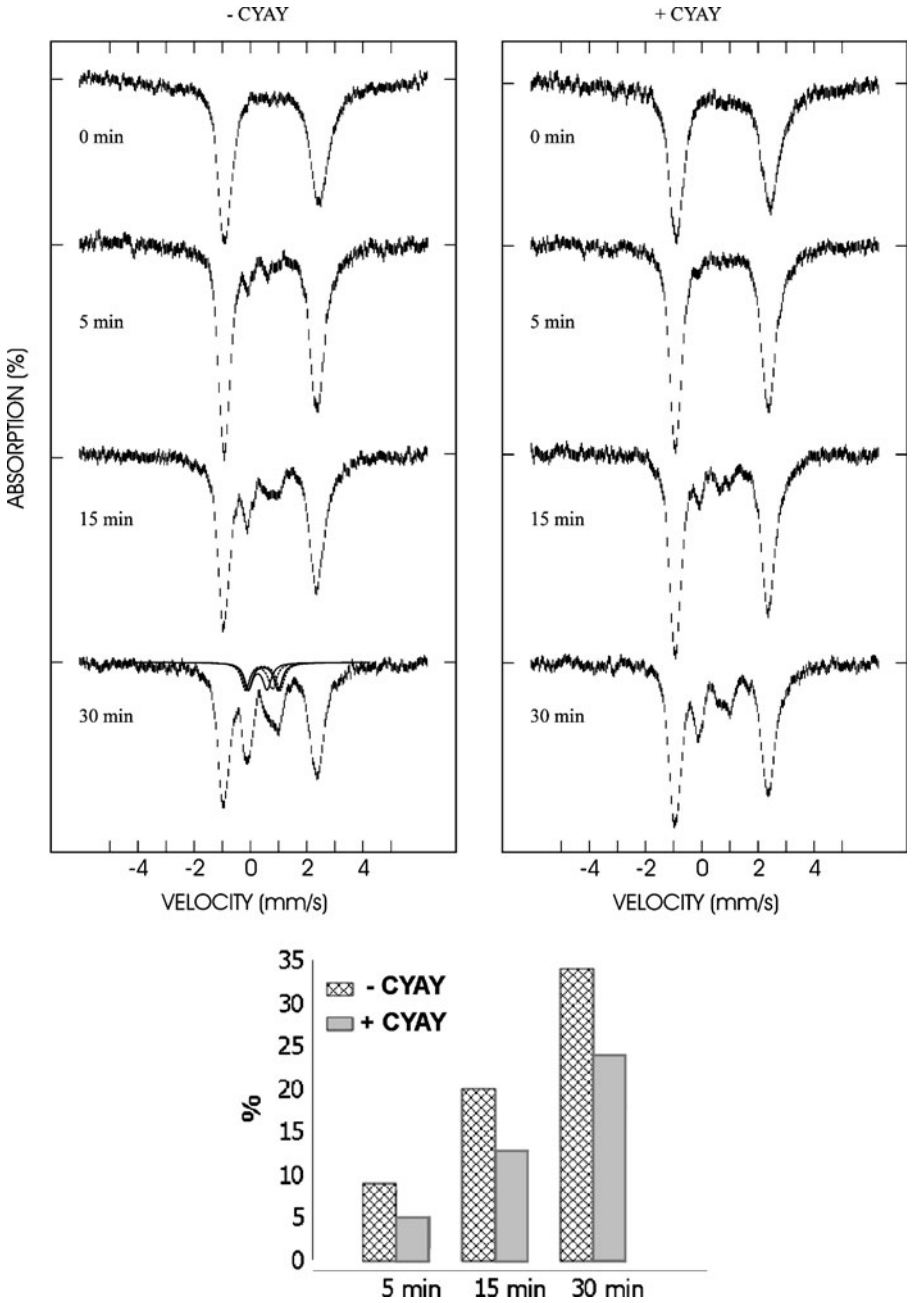

Fig. 3 (*top*) Monitoring of the FeS cluster assembly reaction through Mössbauer spectroscopy. The spectra were recorded in the absence (*left panel*) or in the presence (*right panel*) of CyaY. The spectra were recorded at 4.2 K and with a magnetic field of 60 mT applied parallel to the γ rays. The deconvolution into the two FeS clusters is shown on the spectrum recorded in absence of CyaY at 30 min. (*bottom*) Time dependence of the total cluster formation in absence and presence of CyaY

doublet with $\delta = 0.52(1)$ mm/s, $\Delta EQ = 0.63(2)$ mm/s and $\Gamma = 0.52/0.50(2)$ mm/s, typical of a high-spin ferric iron bound to oxygen/nitrogen in an octahedral arrangement. Spectra recorded in applied magnetic fields up to 7 T reflected a distribution of hyperfine fields, similar to those observed by Lindahl et al. in their study of mitochondria from Yah1p- and Atm1p-depleted cells [10]. The spectra of the strains Δssq1 and Δggc1 (Fig. 2b and c) are identical to that of Δyfh1 mitochondria indicating that iron aggregates are the same whatever the process leading to the aggregation. It is of interest that these aggregates differ strongly from those formed in the well known iron storage protein ferritin [11, 12]. Comparison of the two strains Δggc1 and Δggc1-YFH1 (Fig. 2c and d) again reveals no difference in the aggregates. This is an important observation with respect to the potential role of FXN as an iron storage protein. Indeed, its overexpression in conditions of potential iron availability does not bring any noticeable change in the iron distribution and thus does not support this role.

3.2 Iron sulfur cluster biogenesis

Very recent results have evidenced that ISC formation occurs within a complex involving the scaffold protein IscU, the cysteine desulfurase assembly IscS and Isd11 and FXN [2]. Biochemical and optical studies of ISC formation in a bacterial system have suggested that FXN could be a negative regulator of ISC synthesis [13] but an inverse effect was reported in a eukaryot [14].

In order to verify the effect of FXN on bacterial ISC formation and in particular its molecular aspects we used Mössbauer spectroscopy to monitor the respective formation of the [2Fe2S] and [4Fe4S] clusters upon cysteine addition to a mixture of a $^{57}Fe^{2+}$ salt, dithiothreitol, the scaffold protein IscU and the cysteine desulfurase IscS in the presence and in the absence of bacterial frataxin CyaY. The reaction mixture was prepared anaerobically and frozen at fixed time points after cysteine addition. Figure 3 top illustrates the respective Mössbauer spectra recorded at four reaction times: 0, 5, 15 and 30 min. The initial spectra (t = 0 min) consist of a broad doublet assigned to a tetrahedral ferrous thiolate. As the reaction proceeds, new components appear and grow in, which correspond to IscU bound $[2Fe2S]^{2+}$ and $[4Fe4S]^{2+}$ clusters [7], as shown by the deconvolution of the spectrum recorded after 30 min in absence of CyaY. Comparison of the spectra in absence vs presence of CyaY reveals two interesting features: (i) a higher amount of clusters is formed in absence than in presence of CyaY (Fig. 3 bottom), as previously reported [13], and (ii) the presence of CyaY does not bring any significant difference in the respective proportions of the two clusters. These observations thus (i) confirm that bacterial frataxin CyaY down-regulates ISC synthesis, and (ii) indicate that this regulation is a global effect and does not affect the reductive transformation of the $[2Fe2S]^{2+}$ clusters into $[4Fe4S]^{2+}$.

4 Conclusion

These studies illustrate the high potential of Mössbauer spectroscopy to monitor the transformation of iron species during biological processes. More specifically, in the present case, they support the potential role of frataxin as a regulator of

ISC biogenesis and disfavor its involvement as an iron storage protein. Work is in progress to precise the molecular aspects of frataxin regulatory activity.

References

1. Marmolino, D.: Friedreich's ataxia: past, present and future. Brain Res. Rev. **67**, 311–330(2011)
2. Schmucker, S., Puccio, H.: Understanding the molecular mechanisms of Friedreich's ataxia to develop therapeuticapproaches. Hum. Mol. Genet. **19**, R103–R110 (2010)
3. Bencze, K.Z., Kondapalli, K.C., Cook, J.D., McMahon, S.: The structure and function of frataxin. Crit. Rev. Biochem. Mol. Biol. **41**, 269–291 (2006)
4. Karlberg, T., Schagerlöf, U., Gakh, O., Park, S., Ryde, U., Lindahl, M., Leath, K., Garman, E., Isaya, G., Al-Karadaghi, S.: The structures of frataxin oligomers reveal the mechanism for the delivery and detoxification of iron. Structure **14**, 1535–1546 (2006)
5. Lindahl, P.A., Holmes-Hampton, G.P.: Biophysical probes of iron metabolism in cells and organelles. Curr. Opin. Chem. Biol. **15**, 342–346 (2011)
6. Beinert, H., Holm, R.H., Münck, E.: Iron-sulfur clusters: nature's modular, multipurpose structures. Science **277**, 653–659 (1997)
7. Agar, J.N., Krebs, C., Frazzon, J., Huynh, B.H., Dean, D.R., Johnson, M.K.: IscU as a scaffold for iron-sulfur cluster biosynthesis: sequential assembly of [2Fe-2S] and [4Fe-4S] clusters in IscU. Biochemistry **39**, 7856–7862 (2000)
8. Seguin, A., Sutak, R., Bulteau, A.-L., Garcia-Serres, R., Oddou, J.-L., Lefevre, S., Santos, R., Dancis, A., Camadro, J.-M., Latour, J.-M., Lesuisse, E.: Evidence that yeast frataxin is not an iron storage protein in vivo. Biochim. Biophys. Acta **1802**, 531–538 (2010)
9. Iannuzzi, C., Adinolfi, S., Howes, B.D., Garcia-Serres, R., Clémancey, M., Latour, J.-M., Smulevich, G., Pastore, A.: The role of CyaY in iron sulfur cluster assembly on the E. coli IscU scaffold protein. PLoS ONE **6**, e21992 (2011)
10. Lesuisse, E., Santos, R., Matzanke, B.F., Knight, S.A.B., Camadro, J.-M., Dancis, A.: Iron use for haeme synthesis is under control of the yeast frataxin homologue (Yfh1). Hum. Mol. Genet. **12**, 879–889 (2003)
11. Watt, G.D., Frankel, R.B., Papaefthymiou, G.C.: Reduction of mammalian ferritin. Proc. Natl. Acad. Sci. U. S. A. **82**, 3640–3643 (1985)
12. Yang, C.-Y., Meagher, A., Huynh, B.H., Sayers, D.E., Theil, E.C.: Bound to horse spleen Apoferritin: an x-ray absorption and Mössbauer spectroscopy study that shows that iron nuclei can form on the protein. Biochemistry **26**, 497–503 (1987)
13. Adinolfi, S., Iannuzzi, C., Prischi, F., Pastore, C., Iametti, S., Martin, S.R., Bonomi, F., Pastore, A.: Bacterial frataxin CyaY is the gatekeeper of iron-sulfurcluster formation catalyzed by IscS. Nat. Struct. Mol. Biol. **16**, 390–396 (2009)
14. Tsai, C.-L., Barondeau, D.P.: Human frataxin is an allosteric switch that activates the Fe-S cluster biosynthetic complex. Biochemistry **49**, 9132–9139 (2010)

Hyperfine Interact (2012) 206:19–22
DOI 10.1007/s10751-011-0493-3

Nuclear inelastic scattering of heme proteins: from iron ligand vibrations to low energy protein modes

Beate Moeser · Adam Janoschka · Juliusz A. Wolny · Igor Filipov · Aleksandr I. Chumakov · F. Ann Walker · Volker Schünemann

Published online: 9 December 2011

Abstract The binding of the signal molecule nitric oxide (NO) to the NO transporter protein Nitrophorin 2 (NP2) from the bloodsucking insect *Rhodnius prolixus* has been characterized by Mössbauer spectroscopy as well as nuclear forward scattering (NFS) and nuclear inelastic scattering (NIS). A striking feature of the vibrational spectrum obtained from NP2-NO is a vibration at 594 cm^{-1}. This mode is assigned to a Fe-NO stretching mode via simulation of the NIS data by density functional theory (DFT) coupled with molecular mechanics (MM) methods. At frequencies below 100 cm^{-1} collective motions like heme doming occur which could explain spectroscopic features observed by NIS at these low energies.

Keywords Proteins · Nitric oxide · Nuclear forward scattering · Nuclear inelastic scattering · Heme doming

Electronic supplementary material The online version of this article (doi:10.1007/s10751-011-0493-3) contains supplementary material, which is available to authorized users.

B. Moeser
University of Regensburg, Institute of Physical and Theoretical Chemistry, 93040 Regensburg, Germany

A. Janoschka · J. A. Wolny · V. Schünemann (✉)
Department of Physics, University of Kaiserslautern, Erwin-Schrödinger-Str. 46, 67663 Kaiserslautern, Germany
e-mail: schuene@physik.uni-kl.de

I. Filipov · F. A. Walker
Department of Chemistry, University of Arizona, Tucson AZ 85721-0041, USA

A. I. Chumakov
ESRF, 38043 Grenoble Cedex, France

1 Introduction

The heme proteins the nitrophorins (NP) are found in the salivary glands of the bloodsucking insect *Rhodnius prolixus*. In order to feed, the saliva containing the NPs is injected into the victim's tissues, and due to the dilution and pH change (from ~5.5 in the salivary glands to 7.35 in the tissues) the iron ligand nitric oxide (NO) is released. NO then causes dilation of the victim's capillaries and inhibition of platelet aggregation so that more blood flows to the insect [1]. In mammals the signal molecule NO, although highly toxic in high concentrations, is not only involved in vasodilation, but also in inflammatory processes. Therefore we were interested in the question whether the binding of this signal molecule to its transporter protein could be followed by nuclear inelastic scattering (NIS).

2 Materials and methods

The isoform nitrophorin 2 (NP2) was expressed in BL21(DE3) *E. coli* cells (Novagen). Details of the preparation can be found in [2]. Two samples were prepared with ~8 mM ^{57} Fe-enriched NP2: (i) NO-free (NP2) at pH 7.5 and (ii) NO-bound (NP2-NO) at pH 5.5 with NO added at a molar ratio of 1.5. The samples were transferred into a special sample holder which allows performing Mössbauer spectroscopy as well as NFS and NIS experiments on the same sample. Mössbauer spectra were measured in a He-bath cryostat (Oxford MD 306) and recorded using a conventional spectrometer in the constant-acceleration mode. Isomer shifts are given relative to α-Fe at room temperature. The spectra were analyzed by least-square fits using Lorentzian line shapes. NIS and NFS experiments were performed at ID 18 of the ESRF with an energy resolution of 16 cm^{-1}. Geometry optimizations and frequency calculations were performed with GAUSSIAN 03 [3]. As input for the calculations, the PDB entry 1T68 of NP2-NO was used. QM/MM calculations were performed on the whole protein by applying the method ONIOM [4]. The heme moiety and its ligands were treated with DFT (functional B3LYP with basis set CEP-31G) and the rest of the protein with the universal force field UFF. Normal mode analysis was performed on the optimized structures and NIS spectra were calculated according to [5].

3 Results and discussion

The Mössbauer spectrum of NP2 obtained at T = 77 K shows an asymmetric doublet with $\delta = 0.30$ mms^{-1} and $\Delta E_Q = 2.53$ mms^{-1} (Fig. 1a). These parameters are indicative of a ferric low spin heme iron with two axial ligands [6]. The asymmetry of the spectrum as well as the large line width is caused by paramagnetic relaxation effects [6]. Addition of NO to NP2 leads to a symmetric doublet with $\delta = -0.01$ mms^{-1} and $\Delta E_Q = 1.86$ mms^{-1} (Fig. 1b). These parameters are comparable to those of the NO complex of the isoform nitrophorin 4 ($\delta = 0.00$ mms^{-1} and $\Delta E_Q = 1.84$ mms^{-1} [7]). NFS measurements obtained during the NIS scans of NP2 and NP2-NO (see Fig. 1e,f) are shown in Fig. 1c and d. The spectra exhibit a beating structure which is caused by the presence of quadrupole interaction. The fact that the ΔE_Q-values obtained

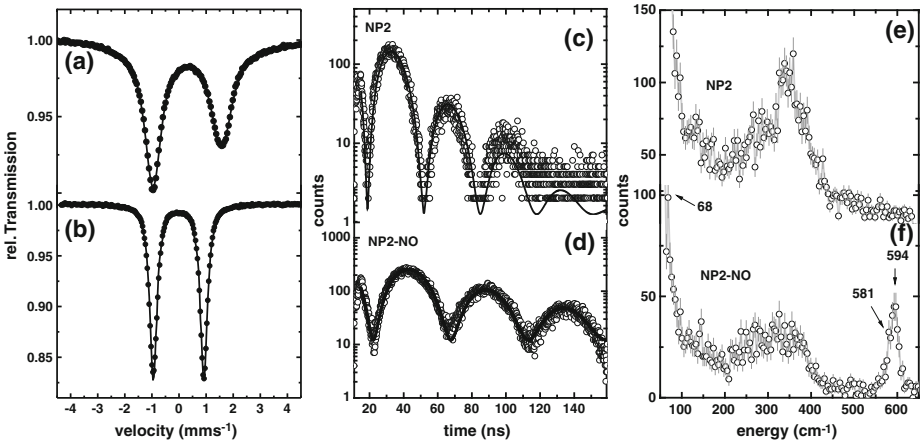

Fig. 1 **a** Mössbauer spectra of NP2 taken at T = 77 K. The *solid line* represents a Lorentzian fit with an asymmetric doublet yielding: $\delta = 0.30 \pm 0.01$ mms^{-1}, $\Delta E_Q = 2.53 \pm 0.01$ mms^{-1}, $\Gamma_1 = 0.86 \pm 0.01$ mms^{-1}, $\Gamma_2 = 1.11 \pm 0.01$ mms^{-1}. **b** Mössbauer spectrum of NP2-NO taken at T = 77 K. The *solid line* is a Lorentzian fit with $\delta = -0.01 \pm 0.01$ mms^{-1}, $\Delta E_Q = 1.86 \pm 0.01$ mms^{-1} and $\Gamma = 0.40 \pm 0.01$ mms^{-1}. **c** NFS spectrum of NP2 taken at T = 100 K. The *solid line* is a simulation using the software Motif [8] yielding $\Delta E_Q = 2.60 \pm 0.05$ mms^{-1} and $t_{eff} = 1.58 \pm 0.05$. **d** NFS spectrum of NP2-NO. The *solid line* has been calculated with $\Delta E_Q = 1.89 \pm 0.05$ mms^{-1} and $t_{eff} = 1.80 \pm 0.05$. Experimental NIS spectra of NP2 (**e**) and of NP2-NO (**f**) obtained at ID 18 of ESRF

from Mössbauer spectroscopy and from NFS (see caption of Fig. 1c,d) are very similar, indicates that no radiation damage had occurred during the NIS experiments. The comparison of the NIS data of NP2 (Fig. 1e) and of NP2-NO (Fig. 1f) shows

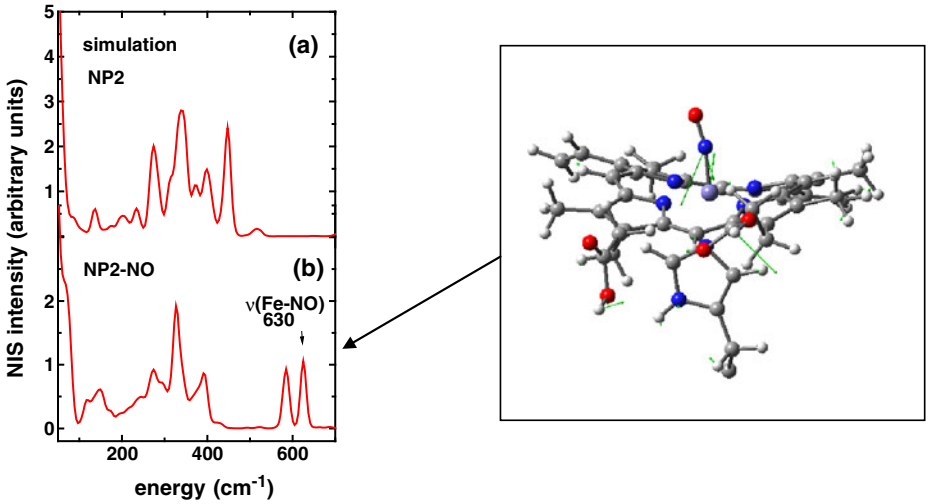

Fig. 2 Simulated NIS-spectra calculated by QM/MM calculations of the whole protein. The optimized heme structure of NP2-NO used for calculating the NIS data presented in Fig. 1e and f is shown in the inset. Only the parts of the molecules treated with DFT are displayed. The residual parts of the protein, which were taken into account by force field calculations, are not shown. The *arrows* describe atom movements of a protein mode with significant Fe-NO stretching character. The calculated energy of this mode is 630 cm^{-1}

that NO binding leads to an intense vibration at 594 cm^{-1}. Simulations of the NIS data are shown in Fig. 2. The simulated NIS spectrum of NP2 (Fig. 2a) has been calculated assuming NH_3 as an axial ligand distal to the heme (pdb entry 2EU7). Albeit the spectrum was calculated with a ferric low-spin heme iron as indicated by Mössbauer spectroscopy and NFS [6] (see Fig. 1a,c), the simulated NIS pattern of NP2 shows a band at 449 cm^{-1} with Fe-NH_3 stretch character which is not present in the experimental data (Fig. 1e). Therefore the sixth ligand is very likely not an NH_3, but another unknown small molecule from the protein expression and purification. In the energy region between 200 and 400 cm^{-1} a complex vibrational structure caused by in-plane as well as out-of-plane iron movements is observed.

Calculation of the NIS spectra of NP2-NO yields a mode at 630 cm^{-1} with strong Fe-NO stretching character (see Movie 1 in supplement) in good agreement with experiment. At energies below 100 cm^{-1} about 300 protein modes have been calculated. Among the most intense are 4 modes at 69, 70, 72 and 74 cm^{-1} all of which involve considerable heme doming (see Movie 2, supplement). It is also striking that the experimental NIS spectrum of NP2-NO has an intense band at 68 cm^{-1}. Based on the simulations presented this band can be assigned to protein modes involving strong heme doming character.

Acknowledgements This work has been supported by the German Federal Ministry of Education and Research under contract number 05 K10UKA, by the ESRF via experiment No. SC 2111 and by the research initiative NANOKAT.

References

1. Ribeiro, J.M.C., Hazzard, J.M.H., Nussenzveig, R.H., Champagne, D.E., Walker, F.A.: Science **260**, 539 (1993)
2. Moeser, B., Janoschka, A., Wolny, J., Paulsen, H., Filippov, I., Berry, R.E., Zhang, H., Chumakov, A.I., Walker, F.A., Schünemann, V.: (submitted to J. Am. Chem. Soc.)
3. Frisch, M.J., et al.: Gaussian 03, Revision E.01. Gaussian Inc., Wallingford, CT (2004)
4. Dapprich, S., Komáromi, I., Byun, S., Morokuma, K., Frisch, M.J.: J. Mol. Struct., Theochem **1–21**, 461 (1999)
5. Paulsen, H., Benda, R., Herta, C., Schünemann, V., Chumakov, A.I., Duelund, L., Winkler, H., Toftlund, H., Trautwein, A.X.: Phys. Rev. Lett. **86**, 1351 (2001)
6. Benda, R., Schünemann, V., Trautwein, A.X., Cai, S., Polam, J.R., Watson, C.T., Shokhireva, T.K., Walker, F.A.: J. Biol. Inorg. Chem. **8**, 787 (2003)
7. Wegner, P., Benda, R., Schünemann, V., Trautwein, A.X., Berry, R.E., Balfour, C.A., Wert, D., Walker, F.A.: How a blood sucking insect gets its meal: The ferriheme proteins Nitrophorin 2 and 4 studied by Mössbauer Spectroscopy. In: Thomas, M.F., Williams, J.M., Gibb, T.C. (eds.) Hyperfine Interactions (C), vol. 5. Proceedings of the International Conference on the Applications of the Mössbauer Effect (ICAME 2001), 2–7 Sept 2001, Oxford, U.K., p. 253. Kluwer Academic Publishers, Dordrecht (2002)
8. Shvyd'ko, R.H.: Hyperfine Interact. **125**, 173 (2000)

Hyperfine Interact (2012) 206:23–33
DOI 10.1007/s10751-011-0499-x

Manipulation of the heme electronic structure by external stimuli and ligand field

Yoshiki Ohgo · Masashi Takahashi · Kazuyuki Takahashi · Yukiko Namatame · Hisashi Konaka · Hatsumi Mori · Saburo Neya · Shinya Hayami · Daisuke Hashizume · Mikio Nakamura

Published online: 7 December 2011

Abstract This review describes the switching behaviors of the electronic structure, which were observed in iron(III) porphyrinoids, by the addition of external stimuli. The combined analysis by various methods, such as EPR, Mössbauer, SQUID, single crystal X-ray structure analysis, revealed a wide variety of electronic structures of the heme related complexes. This paper focuses in particular on the spin-crossover

Y. Ohgo (✉) · M. Nakamura
Department of Chemistry, School of Medicine, Toho University, Ota-ku,
Tokyo 143-8540, Japan
e-mail: yohgo@med.toho-u.ac.jp

Y. Ohgo
Toho University Advanced Medical Research Center, Ota-ku, Tokyo 143-8540, Japan

Y. Ohgo · M. Takahashi · M. Nakamura
Division of Chemistry, Graduate School of Science, Toho University, Funabashi,
Chiba 274-8510, Japan

K. Takahashi · H. Mori
Institute for Solid State Physics, The University of Tokyo, Kashiwa,
Chiba 277-8581, Japan

Y. Namatame · H. Konaka
Rigaku Corporation, Akishima, Tokyo 196-8666, Japan

S. Neya
Department of Physical Chemistry, Graduate School of Pharmaceutical Sciences,
Chuoh-Inohana, Chiba, Chiba 260-8675, Japan

S. Hayami
Department of Chemistry, Graduate School of Science and Technology,
Kumamoto University, Kurokami, Kumamoto 860-8555, Japan

D. Hashizume
Advanced Technology Support Division, RIKEN-Advanced Science Institute, Wako,
Saitama 351-0198, Japan

phenomenon in the solid state. An overview of spin-crossover phenomena found in iron(III) porphyrinoids between (i) $S = 5/2$ and $S = 1/2$, (ii) $S = 3/2$ and $S = 1/2$, (iii) $S = 5/2$ and $S = 3/2$, will be described.

Keywords Spin-crossover · Iron(III) · Porphyrin · Porphyrinoid · Electronic structure

Abbreviations

Axial Ligands	
3-ClPy	3-chloropyridine;
1-MeIm	1-methylimidazole;
HIm	imidazole;
DMAP	4-(N,N-dimethylamino)pyridine;
4-CNPy	4-cyanopyridine;
Py	pyridine;
THF	tetrahydrofuran
Porphyrin dianioins	
OEP	dianions of 2,3,7,8,12,13,17,18-octaethylporphyrin;
TPP	dianions of 5,10,15,20-tetraphenylporphyrin;
OETPP	dianions of 2,3,7,8,12,13,17,18-octaethyl-5,10,15,20-tetraphenylporphyrin;
OETArP	dianions of 2,3,7,8,12,13,17,18-octaethyl-5,10,15,20-tetraarylporphyrins

1 Introduction

In biological systems, only sophisticatedly controlled systems have survived during the long evolutional process. Hence, investigations to clarify the orbital interactions or the nature of the chemical bonds between metals and ligands in the metalloproteins are quite important not only for understanding their functional activation mechanisms, but also for the development of related catalysts or functional materials in a biomimetic way. In this way hemeproteins have attracted much attention because of their wide variety of functions in spite of the same or similar prosthetic groups at the active center. One of the reasons for these versatile functions is the tailor made cavity around each heme provided by the unique protein matrix. The protein matrix manipulates the environment, such as the axial ligand field, around the heme, and the heme deformation, which switches the electronic structure of the heme to regulate its functions.

Another attractive characteristic is that the heme iron(III) ion can adopt various spin states such as $S = 5/2$, 3/2, and 1/2. Of the three spin states, $S = 5/2$ and $S = 1/2$ systems are very common both in models and bio-systems. On the other hand,

Scheme 1 Spin-crossover triangle in iron(III) porphyrinoids

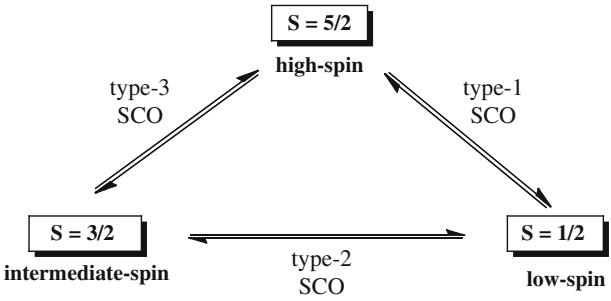

$S = 3/2$ systems are less common because of the difficulty in tuning the ligand-field to obtain such complexes.

In reality, complexes are not always existing as pure single state. Some complexes exhibit, however, a spin-crossover phenomenon caused by external stimuli such as temperature, pressure and photo irradiation. The phenomenon is quite important in biological systems because it is closely-linked to the functional tuning processes in enzymatic cycles catalyzed by heme proteins. There are three types of spin-crossover processes; the spin-crossover between $S = 5/2$ and $S = 1/2$(type-1), $S = 3/2$ and $S = 1/2$(type-2), and $S = 5/2$ and $S = 3/2$(type-3) (Scheme 1).

Among the heme related complexes, the type-1 spin-crossover was discovered by Beetlestone and co-workers back in 1964 [1]. This type-1 spin crossover between the $S = 5/2$ and $S = 1/2$ has been most extensively studied in six-coordinated complexes such as $[Fe(OEP)(3\text{-}ClPy)_2]^+$ [2], $[Fe(TPP)(N_3)_2]$ [3], and $[Fe(OEP)(N_3)(1\text{-}MeIm)]$ [4, 5], while the type-2 spin-crossover was only recently found by ourselves in 2001 [6, 7]. As for the type-3 spin-crossover, no example has ever been reported until recently. Actually, the mixed $S = 5/2, 3/2$ spin state is considered to be a quantum mechanical spin admixture rather than the thermal equilibrium between two different spin states [8, 9].

In the course of the study, we and others clarified that the non-planarity of the heme is one of the key-factors to control the functions in the model heme complexes [10, 11]. And the importance of the non-planarity of the heme, which was found in naturally occurring hemeproteins, is further emphasized by the findings of the conservation of the distortion modes in the same functional proteins from different species as reported by Shelnutt and co-workers [12]. Thus, the deformation modes of heme are closely connected to the heme electronic structure regulated by the d_π-p_π interactions among iron(III) d-orbitals, frontier orbitals of the porphyrin ring and axial ligands [13, 14].

In accordance with the above mentioned fascinating features of the heme, we established a system to manipulate these spin-crossover phenomena of the iron(III) heme by using the combination of heme deformation, axial ligand field, electronic nature of the peripheral substituents, and so on. Thus, "The Spin-crossover Triangle in Iron(III) Heme" has been completed [1–9, 15]. In this review, the authors describe an overview of the spin-crossover triangle of the iron(III) heme and the response of the heme electronic structure to the external stimuli.

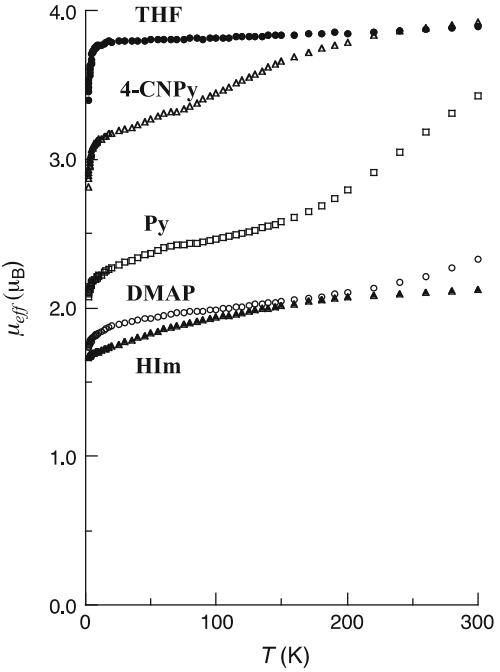

Figure 1 Temperature dependence of the effective magnetic moments of $[Fe(OETPP)L_2]^+$, where L are HIm(▲), DMAP(◯), Py(□), 4-CNPy(△), and THF(●), taken for microcrystalline samples by SQUID magnetometry

Table 1 Mössbauer parameters of a series of $[Fe(OETPP)L_2]^+$

Ligands		T/*K*	IS/*mm s*$^{-1}$	QS/*mm s*$^{-1}$	Spin state
THF		290	0.41	3.65	3/2
		80	0.50	3.50	3/2
4-CNPy	Site A	290	0.37	3.26	3/2
	Site A	80	0.57	3.03	3/2
	Site B	80	0.20	2.70	1/2
Py		290	0.32	2.76	3/2, 1/2
		80	0.25	2.29	1/2
DMAP		290	0.19	2.21	1/2
		80	0.26	2.31	1/2

Source: Ref. [6]

2 Spin-crossover between $S = 3/2$ and $S = 1/2$

2.1 SQUID magnetometry

Among the 6-coordinated porphyrin complexes, the combination of a highly saddled porphyrin, such as OETPP, with comparatively weak-field axial ligands produces spin-crossover complexes between $S = 3/2$ and $S = 1/2$ [6, 7].

Figure 1 shows the temperature dependence of the effective magnetic moments of a series of $[Fe(OETPP)L_2]^+$ complexes. The field strength of the axial ligands is in the order of HIm > DMAP > Py > 4-CNPy > THF. The results indicate that $[Fe(OETPP)(HIm)_2]^+$ and $[Fe(OETPP)(DMAP)_2]^+$ are in the low-spin state,

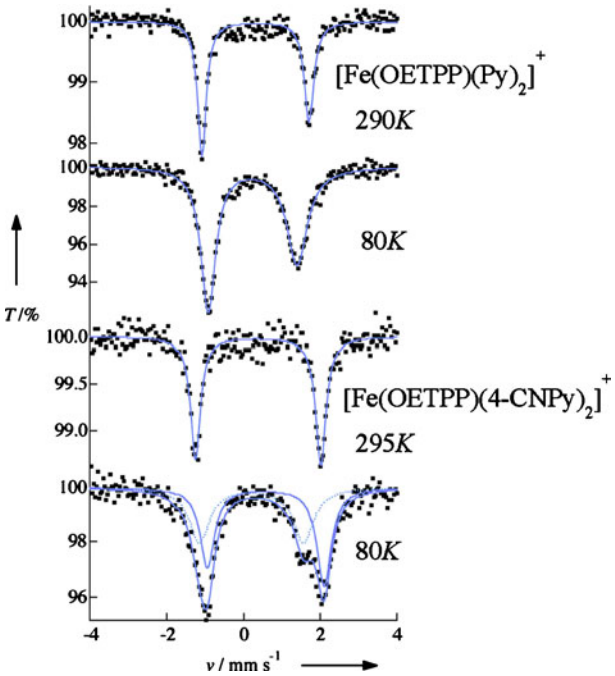

Figure 2 ^{57}Fe Mössbauer spectra of $[Fe(OETPP)(Py)_2]^+$ and $[Fe(OETPP)(4\text{-}CNPy)_2]^+$ at ambient temperature and 80 *K*. The Site A and Site B of $[Fe(OETPP)(4\text{-}CNPy)_2]^+$ at 80 K are expressed in *solid line* and *dotted line*, respectively

while the $[Fe(OETPP)(THF)_2]^+$ complex is in the quite pure intermediate-spin state over a wide range of temperatures. The complexes with comparatively weak-field ligands, $[Fe(OETPP)(4\text{-}CNPy)_2]^+$ and $[Fe(OETPP)(Py)_2]^+$, show the spin-crossover behavior between $S = 3/2$ and $S = 1/2$. While the $[Fe(OETPP)(Py)_2]^+$ complex exists as an exclusively low-spin species below 100 *K*, the fraction of the intermediate-spin species is gradually increasing when the temperature is raised from 100 *K* to 300 *K*. In a similar fashion, the $[Fe(OETPP)(4\text{-}CNPy)_2]^+$ complex exists as a thermal equilibrium mixture of the intermediate spin species and the low-spin species below 220 *K*. The complex, however, exists as an almost pure intermediate-spin species above 220 *K*.

2.2 Mössbauer spectra

Table 1 lists the Mössbauer parameters, IS(isomer shift) and QS(quadrupole splitting) measured at ambient temperature and 80 *K*, of a series of the $[Fe(OETPP)L_2]^+$ complexes. Also, ^{57}Fe Mössbauer spectra of $[Fe(OETPP)(Py)_2]^+$ and $[Fe(OETPP)(4\text{-}CNPy)_2]^+$ are shown in Fig. 2.

The IS and QS values for $[Fe(OETPP)(THF)_2]^+$ at both temperature indicate that the complex is in an almost pure intermediate spin state. Correspondingly, the IS and QS values for $[Fe(OETPP)(4\text{-}CNPy)_2]^+$, 0.37 and 3.26 $mm\ s^{-1}$, at ambient temperature suggest that the complex is in an intermediate spin state. In contrast, the IS and QS values for $[Fe(OETPP)(DMAP)_2]^+$ at ambient temperature indicate that the complex is in the $S = 1/2$ state. It is noteworthy that the Mössbauer parameters for $[Fe(OETPP)(Py)_2]^+$ at ambient temperature are between those of the

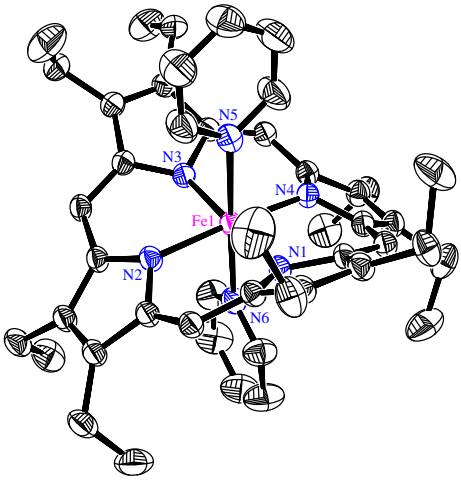

Figure 3 ORTEP diagrams of $[Fe(OETPP)(Py)_2]^+$. Thermal ellipsoids are drawn at the 30% probability level

$[Fe(OETPP)(THF)_2]^+$ and $[Fe(OETPP)(DMAP)_2]^+$, indicating that the complex exists as a thermal mixture of the intermediate spin species and the low spin species. The IS and QS values for $[Fe(OETPP)(DMAP)_2]^+$ at 80 *K*, 0.26 and 2.31 *mm* s^{-1}, indicate that the complex maintains its low spin state during the temperature change. On the other hand, when the temperature is lowered to 80 *K*, another newly produced doublet (Site B) is appearing in addition to the initial component (Site A) in the Mössbauer spectra of the $[Fe(OETPP)(4\text{-}CNPy)_2]^+$. The IS and QS values for Site A and Site B are, 0.57 and 3.03 *mm* s^{-1}, 0.20 and 2.70 *mm* s^{-1}, respectively. The result clearly indicates that the complexes are in a spin-crossover process between $S = 3/2$ and $S = 1/2$. On the contrary, for the $[Fe(OETPP)(Py)_2]^+$ complex, only one doublet is observed throughout the temperature range. The IS and QS values decrease to 0.25 and 2.27 *mm* s^{-1}, which indicates that the complex is in an almost low spin state at 80 *K*. So, the observed spin-crossover phenomena for both $[Fe(OETPP)(4\text{-}CNPy)_2]^+$ and $[Fe(OETPP)(Py)_2]^+$ are essentially similar, but there is a difference in the exchange speed in the thermal equilibrium process in the Mössbauer time scale, 10^{-7} s^{-1}.

2.3 Mechanistic aspect of the spin-crossover process

Crystallographic studies are extremely advantageous to clarify the mechanisms during the spin-crossover process. But, in general, it is quite difficult to observe the influence of a structural change in a spin-crossover process, since spin-crossover processes are often accompanied by a structural phase transition.

In the case of $[Fe(OETPP)(Py)_2]^+$, however, a temperature dependent X-ray structure analysis has been successfully carried out at 80, 180, and 298 *K* [7]. Due to a temperature change from 298 to 80 *K*, the volume of the unit cell shows a contraction of about 6.7%.

Figure 3 shows the molecular structure of $[Fe(OETPP)(Py)_2]^+$, which clearly exhibits a highly saddled structure. The maximum deviation from the mean $C_{20}N_4Fe$ plane is 1.312(3) Å for one of the β-pyrrole carbon atoms. The deviation of *meso* carbons from the mean porphyrin plane is 0.05 Å, which indicates that the complex

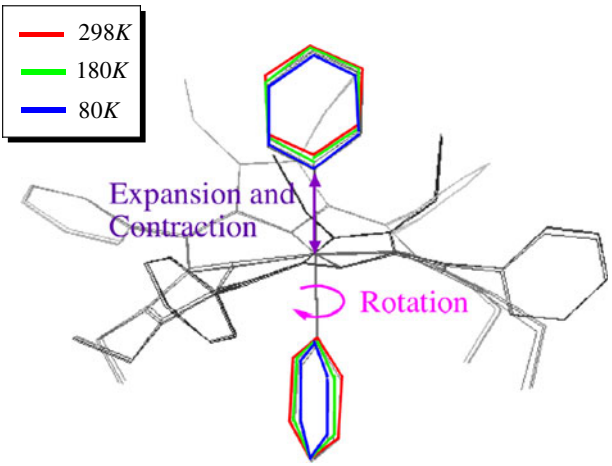

Figure 4 Temperature dependence of the structure in $[Fe(OETPP)(Py)_2]^+$

adopts a pure saddled deformation. A contraction of the axial bonds and the equatorial bonds is observed as the temperature is lowered. The average axial bond lengths, Fe-N_{ax}, at 298 *K*, 180 *K*, and 80 *K* are 2.201(3)Å, 2.041(4)Å, and 1.993(3)Å, respectively. Corresponding average equatorial bond lengths, Fe-N_p, are 1.985(3)Å, 1.954(3)Å, and 1.957(3)Å, respectively. The bond contraction between 298 and 180 *K* is much larger than that between 180 and 80 *K*; the bond contractions for the Fe-N_{ax} are 0.160 and 0.048 Å for each temperature range, respectively, while those for the Fe-N_p are 0.031 and <0.01 Å. Another notable change in structure is the rotation angle ϕ of the pyridine ligand; ϕ is defined as the dihedral angle between the coordinated pyridine plane and N_p-Fe-N_p. The pyridine ligands are placed almost along the diagonal N_p-Fe-N_p axes perpendicularly above and below the porphyrin; the average ϕ is fairly small, 2.4°, at 298 *K*. On cooling the crystal, the rotation angle increases from 2.4° to 6.0°, and then to 9.7°. The increase in the rotation angle can be ascribed to the contraction of the Fe-N_{ax} bond at lower temperature. Because of the bond contraction, the steric repulsion between the axial pyridine ligands and porphyrin ring should increase. Thus, the axial pyridine ligands rotate around the Fe-N_{ax} bond to minimize the steric repulsion. The mechanism of the spin-crossover process associated with the above-mentioned structural changes is explained as follows. As the temperature is lowered, the dynamics of the molecules, especially in the peripheral substituents, is restrained. Consequently, the molecules inside the crystal suffer chemical pressure from the neighboring molecules. As a result, the iron-nitrogen bonds are contracting especially in axial direction, since the complex is readily compressed in the axial direction due to the long Fe-N_{ax} bond. It should be noted that the crystallographic b-axis is almost coinciding with the Fe-N_{ax} bond, indicating a small tilt angle of about 15°. Hence, a larger contraction of the lattice constant is observed for the b-axis than for the a- and c- axes on cooling the crystal. These results clearly indicate that the contraction of the axial bonds is closely related to the mechanism of the spin-crossover between $S = 3/2$ and $S = 1/2$. Namely, the contraction of the axial bonds destabilizes the d_{z2} orbital and induces a spin transition from $S = 3/2$ to $S = 1/2$. The structural changes during the spin-crossover process between $S = 3/2$ and $S = 1/2$ are summarized in Fig. 4.

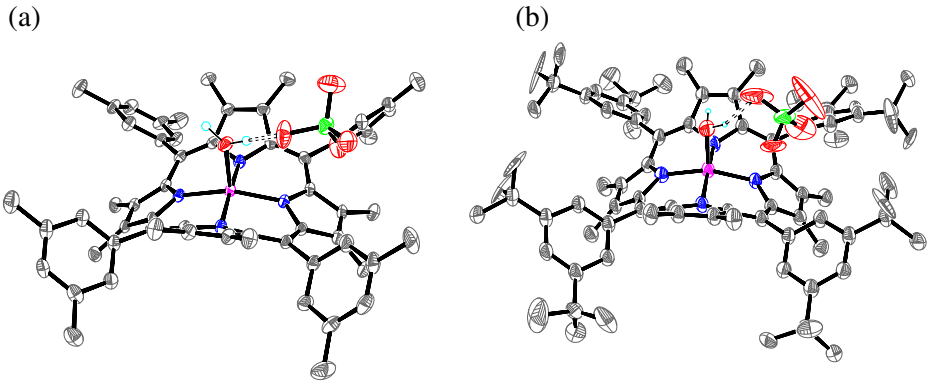

Figure 5 Molecular structures of $[Fe(OMTArP)(H_2O)]ClO_4$ **a** Ar = 3,5-Me_2Ph and **b** 3,5-^{t}Bu$_2$Ph. Ellipsoids are colored in *grey* (carbon), *blue* (nitrogen), *red* (oxygen), *green* (chlorine), *cyan* (hydrogen), and *magenta* (iron). Hydrogen bonds are shown as *dotted lines*

Table 2 Comparison of geometric parameters in 5-coordinated saddle shaped iron (III) porphyrin complexes

Complex	Fe-N_p[a)]	Fe-X_{ax}[b)]	ΔFe[c)]	N4 area[d)]	S[e)]	Ref
$[Fe(OMTArP)(H_2O)]^+$						
Ar=3,5-Me_2Ph	1.946(4)	2.084(4)	0.285(2)	7.45	3/2	[15]
Ar=3,5-^{t}Bu$_2$Ph	1.960(2)	2.056(2)	0.232(1)	7.59	3/2	[15]
Fe(OMTPP)Cl	2.034	2.247	0.464	7.87	5/2	[18]
Fe(OETPP)Cl	2.030	2.242	0.467	7.83	5/2	[18]
Fe(OETPP)ClO_4	1.963	2.059	0.262	7.59	3/2	[19]

a) Bond length (Å) between iron and pyrrole nitrogen. b) Bond length (Å) between iron and axial ligand. c) Out-of-plane deviation (Å) of iron (III) ion from the N_4 plane. d) The area (Å^2) of the plane consisting of the nitrogen atoms of the pyrrole rings. e) Spin state at ambient temperature

3 Spin-crossover between $S = 5/2$ and $S = 3/2$

A wide variety of research has been carried out on the spin transition in naturally occurring heme proteins because of its relevance to the important functional tuning process. While spin transitions between $S = 5/2$ and $S = 1/2$, and between $S = 3/2$ and $S = 1/2$ have been observed both in heme proteins and model heme complexes, the spin transition between $S = 5/2$ and $S = 3/2$ has never been observed before. In fact, the mixed $S = 5/2$ and $S = 3/2$ spin state is considered to be a quantum mechanical spin admixture caused by the spin-orbit coupling between $S = 3/2$ and $S = 5/2$ spin states [8, 9]. The structurally similar highly saddled mono aqua complexes, $[Fe(OMTArP)(H_2O)]ClO_4$, where Ar is 3,5-dimethylphenyl(3,5-Me_2Ph) and 3,5-bis(tert-butyl)phenyl(3,5-^{t}Bu$_2$Ph), however, exhibit the unprecedented example showing the spin transition between $S = 3/2$ and $S = 5/2$ spin states [15]. Shortly thereafter, several reports regarding spin-crossover between $S = 5/2$ and $S = 3/2$ have been published [16, 17].

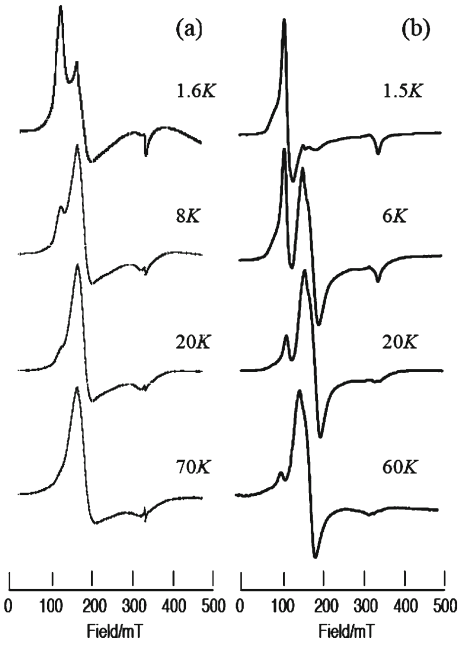

Figure 6 EPR spectra of $[Fe(OMTArP)(H_2O)]ClO_4$ **a** Ar = 3,5-Me_2Ph and **b** 3,5-$^{t}Bu_2$Ph taken in the solid at various temperatures

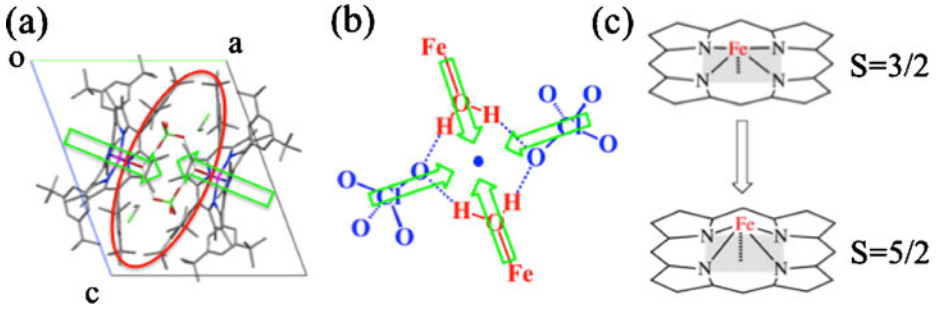

Figure 7 Structural change of $[Fe(OMTArP)(H_2O)]ClO_4$, where Ar = 3,5-$^{t}Bu_2$Ph, during the spin-crossover process between $S = 5/2$ and $S = 3/2$

3.1 X-ray structure analysis

Figure 5 shows the molecular structure of the 3,5-Me_2Ph and 3,5-$^{t}Bu_2$Ph complexes. The complexes adopt highly saddled deformations with deviations from the least-squares plane equal to 1.32–1.35 Å at the pyrrole-β carbons for both complexes. Table 2 shows the geometric parameters of these complexes together with some analogous complexes [15–17]. Significantly short Fe-N_p bond lengths and the extremely small distance of the iron from the N4 plane, ΔFe, observed in the $[Fe(OMTArP)(H_2O)]ClO_4$, which is comparable to those of $Fe(OETPP)ClO_4$, clearly indicate that these complexes are in the intermediate spin state.

3.2 EPR spectra

Temperature dependent EPR spectra of $[Fe(OMTArP)(H_2O)]ClO_4$, (a)Ar=3,5-Me_2Ph and (b) 3,5-^{t}Bu$_2$Ph, are given in Fig. 6.

Both complexes show similar temperature dependence of the spectra in the solid state. The EPR spectra at low temperature exhibit two types of signals, which are characteristic for high spin and intermediate spin species. The *g* values, determined by computer simulations of the observed spectra, are as follows: $[Fe(OMTArP)(H_2O)]ClO_4$ (a) Ar=3,5-Me_2Ph: 6.10, 5.90, 2.00 ($S = 5/2$), and 4.20, 3.80, 2.10 ($S = 3/2$); (b) 3,5-^{t}Bu$_2$Ph: 6.10, 5.90, 2.00 ($S = 5/2$), and 4.37, 3.77, 1.99 ($S = 3/2$). To our great surprise, the signal intensities for the intermediate-spin species increased, while those for the high-spin species decreased as the temperature was raised. Thus, both 3,5-Me_2Ph and 3,5-^{t}Bu$_2$Ph complexes exist exclusively as intermediate spin complexes above 70 *K*.

The phenomenon is observed reversibly during the temperature change. The temperature dependence of the EPR spectra clearly indicates that the complexes are in the spin-crossover process between $S = 5/2$ and $S = 3/2$. The van't Hoff plots yield ΔH° and ΔS° values corresponding to the equilibrium given in (1) to be 112 $J{\cdot}mol^{-1}$ and 52 $J{\cdot}mol^{-1}{\cdot}K^{-1}$ for the 3,5-Me_2Ph complex, and 100 $J{\cdot}mol^{-1}$ and *19* $J{\cdot}mol^{-1}{\cdot}K^{-1}$ for the 3,5-^{t}Bu$_2$Ph complex, respectively.

$$\text{High Spin} \underset{\rightleftharpoons}{\overset{K}{=\!=}} \text{Intermediate Spin} \tag{1}$$

3.3 Mechanistic implication

As for crystal packing, the 3,5-Me_2Ph complex has a one-dimensional hydrogen bonding channel along a-axis. Contrary, the 3,5-^{t}Bu$_2$Ph complex exists as a discrete dimeric structure connected by hydrogen bonding shown in Fig. 7a and b.

The mechanisms of this spin-crossover process can be explained in terms of the difference in the molecular structure and crystal structure between ambient temperature and low temperature. At ambient temperature, the axial ligand water molecule, the counter perchlorate anion and the crystal solvent are highly disordered because of the thermal motion. But at extremely low temperature, those dynamics should settle down. The resultant vacant space (red circle in the Fig. 7a) should be filled by the rearrangement of the molecules as shown in green allows in the Fig. 7a. These movements, which correspond to the contraction of the hydrogen bond network around the symmetry center, induce the extruding rearrangement of the iron from the N4 plane in Fig. 7b and c. The resulting large out of plane displacement of the iron(III) ion can stabilize the d_{x2-y2} orbital and induce the spin transition from $S = 3/2$ to $S = 5/2$.

Acknowledgements This work was supported by Research Promotion Grants from the Toho University Graduate School of Medicine (Nos. 05-21 and 06-01 to Y.O.) and by Grant- in-Aid for Scientific Research from the Ministry of Education, Culture, Sports, Science and Technology, Japan (No. 18655025, 20550068 and 23550083 to Y.O.). This work was also supported by the Research Center for Materials with Integrated Properties, Toho University and Advanced Medical Research Center, Toho University. We also thank the Instrument Center of Institute for Molecular Science (IMS), Japan Synchrotron Radiation Research Institute (RIKEN, JASRI, SPring-8), and Photon Factory, High Energy Accelerator Research Organization (PF, KEK). The authors are grateful to

Mr. Motoyasu Fujiwara and Mr. Tadashi Ueda of the IMS for the assistance with the EPR and SQUID measurements.

References

1. Beetlestone, J., George, P.: Biochemistry **3**, 707 (1964)
2. Scheidt, W.R., Geiger, D.K., Haller, K.J.: J. Am. Chem. Soc. **104**, 495 (1982)
3. Ellison, M.K., Narsi, H., Xia, Y.-M., Marchon, J.-C., Schulz, C.E., Debrunner, P.G., Scheidt, W.R.: Inorg. Chem. **36**, 4804 (1997)
4. Neya, S., Tsubaki, M., Hori, H., Yonetani, T., Funasaki, N.: Inorg. Chem. **40**, 1220 (2001)
5. Neya, S., Chang, C.K., Okuno, D., Hoshino, Y., Hata, M., Funasaki, N.: Inorg. Chem. **44**, 1193 (2005)
6. Ikeue, T., Ohgo, Y., Yamaguchi, T., Takahashi, M., Takeda, M., Nakamura, M.: Angew. Chem. Int. Ed. **40**, 2617 (2001)
7. Ohgo, Y., Ikeue, T., Nakamura, M.: Inorg. Chem. **41**, 1698 (2002)
8. Maltempo, M.M., Moss, T.H., Cusanovich, M.A.: Biochim. Biophys. Acta **342**, 290 (1974)
9. Maltempo, M.M.: J. Chem. Phys. **61**, 2540 (1974)
10. Nakamura, M., Ohgo, Y., Ikezaki, A.: Electronic and magnetic structures of iron porphyrin complexes. In: Kadish, K.M., Smith, K.M., Guilard, R. (eds.) Handbook of Porphyrin Science, vol. 7, pp. 1–146. World Scientific, Singapore (2010)
11. Walker, F.A.: Proton NMR and EPR spectroscopy of paramagnetic metalloporphyrins. In: Kadish, K.M., Smith, K.M., Guilard, R. (eds.) The Porphyrin Handbook, vol. 5, pp. 81–183. Academic Press, San Diego, CA (2000)
12. Hobbs, J.D., Shelnutt, J.A.: J. Protein. Chem. **14**, 19–25 (1995)
13. Cheng, R.-J., Chen, P.-Y., Lovell, T., Liu, T., Noodleman, L., Case, D.A.: J. Am. Chem. Soc. **125**, 6774 (2003)
14. Conradie, J., Ghosh, A.: J. Phys. Chem. B. **107**, 6486 (2003)
15. Ohgo, Y., Chiba, Y., Hashizume, D., Uekusa, H., Ozeki, T., Nakamura, M.: Chem. Commun. (18), 1935–1937 (2006). doi:10.1039/b601412g
16. Neya, S., Takahashi, A., Ode, H., Hoshino, T., Hata, M., Ikezaki, A., Ohgo, Y., Takahashi, M., Hiramatsu, H., Kitagawa, T., Furutani, Y., Kandori, H., Funasaki, N., Nakamura, M.: Eur. J. Inorg, Chem., **20**, 3188 (2007)
17. Neya, S., Takahashi, A., Ode, H., Hoshino, T., Ikezaki, A., Ohgo, Y., Takahashi, M., Hiramatsu, H., Kitagawa, T., Furutani, Y., Lórentz-Fonfría, V.A., Kandori, H., Teraoka, J., Funasaki, N., Nakamura, M.: Bull. Chem. Soc. Jpn. **81**, 136 (2008)
18. Cheng, R.-J., Chen, P.-Y., Gau, P.-R., Chen, C.-C., Peng, S.-M.: J. Am. Chem. Soc. **119**, 2563 (1997)
19. Barkigia, K.M., Renner, M.W., Fajer, J.: J. Porphyr. Phthalocya. **5**, 415 (2001)

Hyperfine Interact (2012) 206:35–46
DOI 10.1007/s10751-011-0418-1

How Mössbauer spectroscopy can improve Li-ion batteries

Pierre-Emmanuel Lippens · Mohammed El Khalifi · Mohamad Chamas · Alexis Perea · Moulay-Tahar Sougrati · Costana Ionica-Bousquet · Laurent Aldon · Josette Olivier-Fourcade · Jean-Claude Jumas

Published online: 7 December 2011

Abstract In the domain of Li-ion batteries, Mössbauer spectroscopy is mainly used for the characterization of electrode materials and the analysis of electrochemical reactions. Depending on the properties under investigation, different approaches are often considered, which are based on *ex situ, in situ* and *operando* measurements. The specific electrochemical cells and sample preparations used for such measurements are described in this paper. Applications to selected examples of cathode and anode materials are presented in order to show how Mössbauer spectroscopy, when associated with other techniques, provides essential information to understand the mechanisms and improves the performances of Li-ion batteries.

Keywords Mössbauer spectroscopy · In situ · Operando · Li-ion batteries · Electrode materials · $LiFePO_4$ · Tin · Intermetallics

1 Introduction

New energy productions are crucial not only for the preservation of environment but also for the development of our societies since fossil fuel reserves will dry up in a near future. The recent development of renewable and intermittent energies based on sunlight or wind and the growth of new needs such as clean vehicles or portable electronics require new electrical energy storage systems. Thus, there is a strong demand for electrochemical systems and Li-ion batteries are, at the present time, one of the most interesting systems in terms of performances. Most of the research works are focused on new materials in order to increase energy density, reduce aging phenomena, lower the cost and improve safety [1].

P.-E. Lippens (✉) · M. El Khalifi · M. Chamas · A. Perea · M.-T. Sougrati · C. Ionica-Bousquet · L. Aldon · J. Olivier-Fourcade · J.-C. Jumas
Institut Charles Gerhardt, UMR CNRS 5253, Equipe Agrégats Interface et Matériaux pour l'Energie, Université Montpellier 2, CC1502, 34095 Montpellier Cedex 5, France
e-mail: lippens@univ-montp2.fr

The energy density of a Li-ion cell increases with both the electrode potential difference and the specific capacity of the electrodes. Compared to the present materials, it is in principle possible, but rather difficult, to increase the specific capacity of the cathode while it is not possible to decrease the potential of the anode. Thus, the best way to increase the energy density is to look for high potential cathodes and high capacity anodes. In order to find new electrode materials and improve their performances it is important to understand the electrochemical reactions that take place during the charge-discharge cycles. This is not an easy task because the electrochemical cells are rather complex systems composed by composite electrodes, multicomponent electrolyte, current collectors, etc. Thus, it is essential to combine different techniques and perform *in situ* and *operando* measurements for a reliable analysis of such mechanisms.

X-ray diffraction (XRD) is certainly the most commonly used technique to study electrode materials. Such a technique provides useful information on mechanisms involving crystalline phases but is of poor interest when the materials are amorphous and/or nanostructured, which is often the case with Li-ion batteries. Thus, atomic scale characterization is important in this respect, especially with element sensitive techniques, in order to follow local changes due to reactions of the electrode materials with lithium or aging processes [2]. Since many new electrode materials contain iron or tin atoms, Mössbauer spectroscopy can be used for such characterizations [3–7]. Combined with other experimental tools such as XRD, X-ray photoemission spectroscopy (XPS), X-ray absorption spectroscopy (XAS) or magnetic measurements it is then possible to give a consistent description of the phenomena which can be furthermore compared to theoretical models.

In this paper, we will show from some selected examples how Mössbauer spectroscopy can improve the performances of electrode materials for Li-ion batteries. Specific electrochemical cells are presented and applications of Mössbauer spectroscopy to new and promising cathode materials: lithium metal phosphates and anode materials: tin based intermetallics are discussed.

2 Experimental method

Mössbauer measurements can be made *ex situ* on electrode materials extracted from the electrochemical cell, *in situ* on material in the cell and *operando* on material in the cell during charge-discharge cycles. The two latter modes provide the most useful information that is directly related to changes within the cell. *Operando* mode allows to continuously study the electrochemical reactions with lithium. For example, in galvanostatic mode a constant current is applied to the cell and the Mössbauer spectra are recorded during cycling. *In situ* mode has a more general meaning since it also includes studies of the electrode material in the cell at a given stage of lithiation as a function of time, temperature, etc.

Different types of cells have been proposed for *in situ* experiments with batteries. To our knowledge, the first *in situ* Mössbauer experiments were performed by Geronov et al. for the investigation of an iron electrode in alkaline solution [8], three years before the first XRD *in situ* measurements [9]. Two decades after the Geronov's cell, Dunlap et al. proposed an *in situ* cell based on commercial 2325 cell in order to study Li-ion batteries [10, 11]. A cylindrical cell was used by Wattiaux

et al. [12] and an aluminium-laminated polyethylene bag by Ariyoshi et al. [13]. In our group, we have performed Mössbauer experiments with three kinds of cells. In the past, we used Bellcore plastic Li-ion batteries [14] for tin based anodes [15–17]. Such a cell can be easily used with a Mössbauer experimental set-up but requires specific technology and a rather high amount of electrochemically active material compared to other cells. We use now two other kinds of cell depending on the main electrochemical mechanisms that take place in the electrode materials.

The first cell was initially developed for *in situ* XRD and XAS measurements in transmission or reflection geometry and a detailed description is given in Ref. [18]. The modified XRD-XAS cell can be easily used with powdered electrode materials if only a rather small pressure is required to maintain electrical contacts between particles. This is the case of insertion materials in which electrochemical mechanisms are governed by topotactic reactions and to a great extent when electrochemical reactions take place with small volume variations.

The second cell was adapted from a Swagelok-type cell which is commonly used for electrochemical tests of Li-ion batteries. Such a cell presents easily achieved proper installation, excellent gas-tight sealing and low cost. It can be easily used with powdered electrode materials even when electrochemical reactions take place with volume variations such as alloying or conversion reactions. The cell is made of the commercially available Swagelok tube union made of perfluoroalkoxy polymer and stainless steel tubes with extremities formed by PMMA γ-transparent windows. The anode is made of a thin lithium foil of high quality in contact with the stainless steel tube and the cathode is formed by powdered active material pressed against a beryllium foil used as a connector.

For *in situ* and *operando* measurements, the cells are placed between the γ-rays source and the detector. The measurements are usually performed under galvanostatic conditions with a Biologic SP-150 potentiostat. The Mössbauer data are recorded during several hours (depending on the Li rate and the required signal-to-noise ratio), saved and then the memory is cleaned and so on. Each spectrum is collected during the reaction of a small number of lithium, typically lower than 0.1 Li per active center (0.05 Li for $LiFePO_4$ and 0.1Li for $FeSn_2$). This means that Mössbauer data are collected continuously during the charge-discharge cycles, which justifies the use of "operando" term for such experiments. A conventional Mössbauer experimental set-up is used for such measurements [16].

3 Application to cathode materials

Commonly used cathode materials are lithium-metal oxides but there is an increasing interest for lithium metal phosphates with olivine structure like $LiFePO_4$ [19–22]. $LiFePO_4$ is inexpensive, environmentally friendly, safe, with good cycle life and high specific capacity compared to other cathode materials. In addition, the potential ($\sim$3.4 V v.s. Li^+/Li^0) can be increased by substituting another transition metal for Fe. However, $LiFePO_4$ is a wide band gap semiconductor and must be used as powdered nanoparticles with carbon coating for a good electrical percolation [23] although cation doping can also increase the electronic conductivity [24]. The performances also depend on intrinsic defects like Li/Fe antisites but also on impurities like iron oxides or iron phosphides that can be formed during the synthesis depending on the

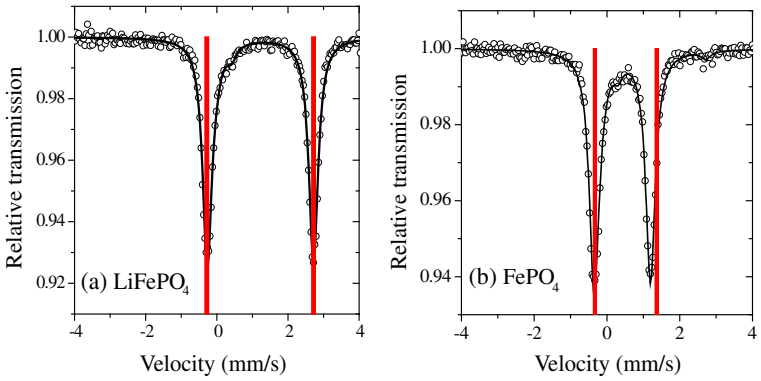

Fig. 1 ^{57}Fe Mössbauer spectra of $LiFePO_4$ (**a**) and $FePO_4$ (**b**); Comparison between experimental data at room temperature (*black circles*) and DFT calculations (*red vertical lines*)

experimental conditions. The characterization of the pristine material, the analysis of the charge-discharge mechanisms and the influence of defects can be studied by ^{57}Fe Mössbauer spectroscopy and we present here several applications of this technique.

At room temperature, the ^{57}Fe Mössbauer spectra of both $LiFePO_4$ and $FePO_4$ are formed by doublets. For $LiFePO_4$, the experimental values of the isomer shift and quadrupole splitting are $\delta = 1.22$ mm/s and $\Delta = 2.96$ mm/s, respectively. These values are close to those obtained by DFT calculations, taking into account both the spin polarization and the correlation of the Fe 3d electrons (Fig. 1a). This can be interpreted from the Fe^{2+} high spin configuration of the iron atoms in distorted octahedral environments formed by oxygen atoms. The charge (delithiation) leads to olivine $FePO_4$ with Mössbauer parameters $\delta = 0.45$ mm/s and $\Delta = 1.53$ mm/s close to the DFT values (Fig. 1b). Compared to $LiFePO_4$, the value of δ decreases because the extraction of one lithium is accompanied with the decrease of one Fe3d$\downarrow$ electron per Fe, changing high spin Fe^{2+} (in $LiFePO_4$) into high spin Fe^{3+} (in $FePO_4$). This affects the electronic structure near the Fermi level as shown by XPS and DFT calculations [25]. The observed decrease of Δ is also related to the decrease of one Fe 3d electron per Fe that strongly influences the Fe 3d electron density shape.

The reversible charge-discharge cycles have been studied by *operando* ^{57}Fe Mössbauer spectroscopy by different authors and interpreted as $LiFePO_4/FePO_4$ two-phase reactions [26, 27]. The substitution of Fe by Mn ($LiFe_{1-x}Mn_xPO_4$) increases the voltage from 3.4 V vs. Li^+/Li^0 to 4.1 V vs. Li^+/Li^0. Unfortunately, the full substitution ($x = 1$) leads to capacity fading that could be due to structural instability (the Jahn-Teller distortion around Mn^{3+} ions in $MnPO_4$) and low conductivity [28]. Better rate capabilities have been obtained with partial Fe/Mn substitution but the potential profile is formed by two plateaus at about 3.5 V and 4 V vs. Li^+/Li^0 due to the Fe^{3+}/Fe^{2+} and Mn^{3+}/Mn^{2+} redox reactions, respectively. A two dimensional phase diagram of $Li_yFe_xMn_{1-x}PO_4$ as a function of (x,y) ($0 \leq x,y \leq 1$) has been proposed by Yamada et al. [29]. We have obtained similar results and we briefly summarize here, as an example, the mechanism obtained for $Li_yFe_{0.75}Mn_{0.25}PO_4$ by *operando* ^{57}Fe Mössbauer spectroscopy with the XRD-XAS modified cell described above. The electrochemical curve shows the expected two plateaus although the potentials are different for the charge and the discharge because of polarization

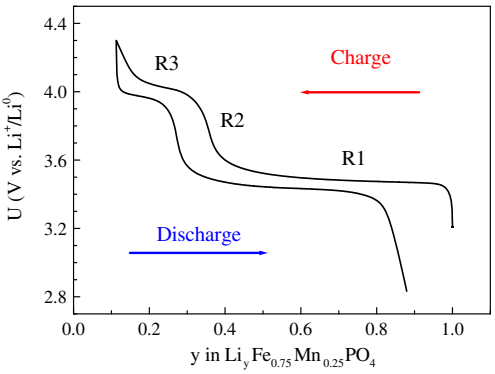

Fig. 2 Potential curve of the first charge-discharge cycle for $LiFe_{0.75}Mn_{0.25}PO_4$ in modified XRD-XAS cell at C/40. R1-R3 denote the three regions discussed in the text

effects (Fig. 2). Three regions can be defined by considering the transition between the two plateaus.

The three regions were unambiguously distinguished from *operando* XRD which clearly shows, for the charge, two-phase regions for $y \leq 0.25$ (Region R3) and $0.55 \leq y \leq 1$ (Region R1), and a single-phase region for $0.25 \leq y \leq 0.55$ (Region R2). The ^{57}Fe Mössbauer spectra obtained at room temperature for the first cycle are shown in Fig. 3.

The first spectrum ($y = 0$) is formed by a doublet ($\delta = 1.23$ mm/s and $\Delta = 2.95$ mm/s), similar to that of $LiFePO_4$, that can be assigned to high spin Fe^{2+}. At the end of the region R1 ($y = 0.55$), the spectrum can be fitted with two doublets that can be attributed to Fe^{2+} ($\delta = 1.28$ mm/s and $\Delta = 2.71$ mm/s) and Fe^{3+} ($\delta = 0.43$ mm/s and $\Delta = 1.1$ mm/s). Thus, a mixed valence phase was formed during the delithiation of $LiFe_{0.75}Mn_{0.25}PO_4$. All the intermediate spectra in R1 were fitted with these contributions and reaction in R1 can be written

$$\begin{aligned} LiFe^{2+}_{0.75}Mn^{2+}_{0.25}PO_4 \leftrightarrow\ & (1-y)\,Li + 2.22\,(y-0.55)\,LiFe^{2+}_{0.75}Mn^{2+}_{0.25}PO_4 \\ & +2.22\,(1-y)\,Li_{0.55}Fe^{2+}_{0.3}Fe^{3+}_{0.45}Mn^{2+}_{0.25}PO_4 \\ & \text{with } 0.55 \leq y \leq 1 \end{aligned} \tag{1}$$

The second region R2 ($0.25 \leq y \leq 0.55$) is characterized by a strong increase of the potential up to about 4.0 V. A systematic shift of the (200) diffraction peak at $2\theta \sim 29.5°$ of the phase $Li_{0.55}Fe^{2+}_{0.3}Fe^{3+}_{0.45}Mn^{2+}_{0.25}PO_4$ suggests a solid solution in this region. The relative contribution of Fe^{2+} to the Mössbauer spectra decreases whereas that of Fe^{3+} increases. The Mössbauer parameters do not change significantly except for the quadrupole splitting of Fe^{3+} that increases gradually (22%) with the oxidation of iron. This indicates significant lattice changes in agreement with XRD results. Thus, the extraction of lithium in region R2 changes the oxidation state from Fe^{2+} to Fe^{3+}, which also causes modifications of the Fe 3d electron density shape around Fe^{3+}, following the single-phase reaction:

$$\begin{aligned} Li_{0.55}Fe^{2+}_{0.3}Fe^{3+}_{0.45}Mn^{2+}_{0.25}PO_4 \leftrightarrow\ & (0.55-y)\,Li + Li_yFe^{2+}_{y-0.25}Fe^{3+}_{1-y}Mn^{2+}_{0.25}PO_4 \\ & \text{with } 0.25 \leq y \leq 0.55 \end{aligned} \tag{2}$$

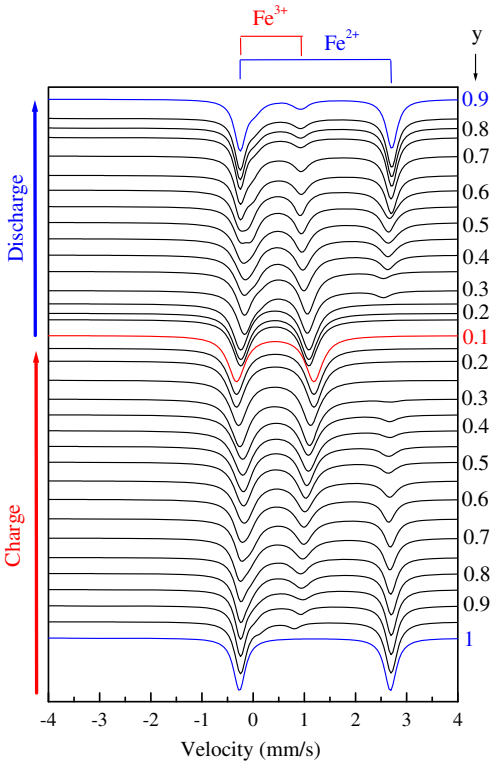

Fig. 3 ^{57}Fe Mössbauer spectra of $Li_yFe_{0.75}Mn_{0.25}PO_4$ (with $0.1 < y < 1$) in a modified XRD-XAS cell for *operando* measurements during the first cycle at C/40 and room temperature

Finally, the third region R3 ($0.1 \leq y \leq 0.25$) corresponds to the oxidation of Mn^{2+} into Mn^{3+} which occurs on the short potential plateau around 4.0 V. In this region, the first Mössbauer spectrum ($y = 0.25$) with Mössbauer parameters: $\delta = 0.41$ mm/s and $\Delta = 1.30$ mm/s can be assigned to $Li_{0.25}Fe^{3+}_{0.75}Mn^{2+}_{0.25}PO_4$ and the last one reflects the contribution of both this compound and the fully delithiated compound $Fe^{3+}_{0.75}Mn^{3+}_{0.25}PO_4$ ($\delta = 0.41$ mm/s and $\Delta = 1.52$ mm/s). The two-phase reaction in this region can be written

$$Li_{0.25}Fe^{3+}_{0.75}Mn^{2+}_{0.25}PO_4 \leftrightarrow (0.25 - y)\,Li + 4y\,Li_{0.25}Fe^{3+}_{0.75}Mn^{2+}_{0.25}PO_4 + 4(0.25 - y) \times Fe^{3+}_{0.75}Mn^{3+}_{0.25}PO_4 \text{ with } 0 \leq y \leq 0.25 \quad (3)$$

The overall mechanism is reversible and is also observed for the discharge. It strongly differs from the two-phase reaction in $LiFePO_4$.

Mössbauer spectroscopy is also widely used to characterize the pristine materials in order to optimize the electrochemical performances. As an example, an asymmetric broadening of the low velocity peak of the Mössbauer spectrum of $LiFePO_4$ is often observed, as shown for samples obtained in tube furnace under argon flow (Fig. 4). Such spectrum can be fitted with the main sub-spectrum due to $LiFePO_4$ (88%) and a two-component sub-spectrum that can be assigned to Fe_2P (12%). The latter compound must be considered as an impurity that decreases the specific capacity of the electrode. It is due to reducing synthesis conditions (Ar/H_2 flux) and forms a surface layer that must be as thin as possible [30].

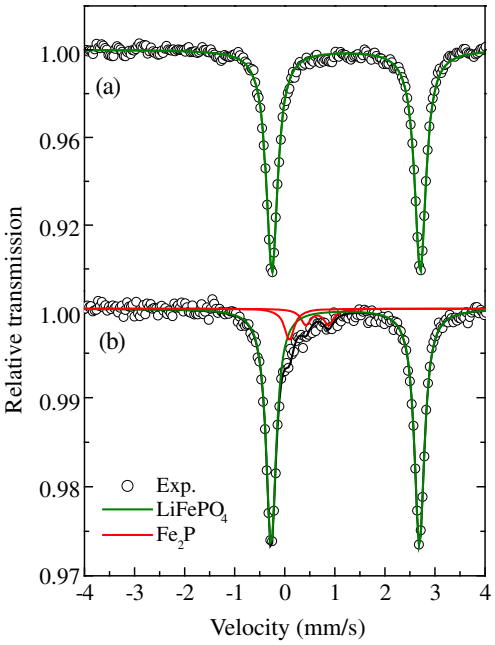

Fig. 4 ^{57}Fe Mössbauer spectra of two samples of $LiFePO_4$ obtained with different synthesis conditions: pure $LiFePO_4$ (**a**) and $LiFePO_4$ with Fe_2P impurity (**b**)

4 Application to anode materials

The most commercially used anodes for Li-ion batteries are made from carbon or titanates. The electrochemical reaction mechanisms are based on reversible insertion of Li ions in the host material and the energy density is limited by the small number of inserted Li. For example, only 1 Li per 6 C can be intercalated into graphite, which gives a specific capacity of 370 Ah/kg. In order to overcome this limitation, materials that reversibly react with lithium by alloying-dealloying processes or by conversion reactions have been proposed. Si and βSn are promising high capacity anode materials that form alloys with lithium and their theoretical specific capacities are 4200 Ah/kg and 990 Ah/kg, respectively. However, alloying reactions suffer for large volume variations leading to poor cycling performances. To minimize the structural instabilities, different strategies have been considered for βSn, such as nanosized tin [31], tin oxides [32], tin composite oxides (TCO) [33], metallic tin dispersed in a composite oxide [34–36] and tin-metal alloys. In the latter case, tin is associated with an electrochemically inactive metal that is expected to be extruded during the first discharge from the pristine materials in order to form metallic nanoparticles that buffer volume variations. Different metals have been considered including Cu [37], Ni [38–40], Co [41, 42], Fe [43–45] or Nb [46]. The case of Co is of particular interest and Sony commercialized in 2005 the Nexelion battery with a Co-Sn-C amorphous anode improving the capacity of the battery by 30% compared to other systems [47–51]. However, the replacement of Co by another metal such Fe might reduce the cost of the electrode materials and improve the environmental impact [52]. We present here some results for $FeSn_2$ which is the tin richest binary compound with Fe and has a maximum theoretical capacity of about 800 Ah/kg (for 4.4 Li/Sn).

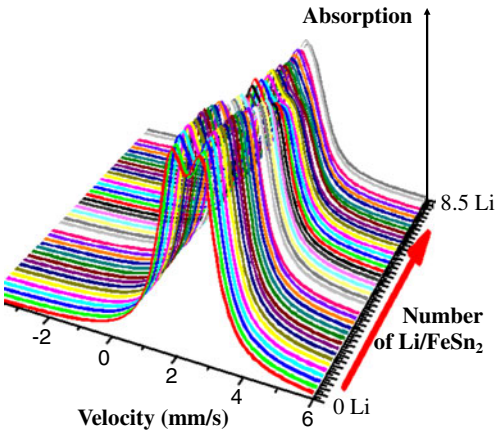

Fig. 5 ^{119}Sn Mössbauer spectra of nanostructured $FeSn_2$ in modified Swagelok cell for *operando* measurements during the first discharge at C/10 and room temperature

This compound is of particular interest since it can be easily nanostructured, which increases the specific surface area of the active material. It can be considered as a reference compound for transition metal-tin intermetallics as anode materials since the reaction mechanisms are very similar. And last but not least, it contains two Mössbauer isotopes ^{57}Fe and ^{119}Sn.

The electrochemical tests and the study of the mechanisms were performed with a composite electrode formed by nanostructured $FeSn_2$ (80 wt.%), polytetrafluoroethylene as binder (10 wt.%) and carbon black (SP) as conductive additive (10 wt.%). About 8 Li/$FeSn_2$ reacted with the electrode during the first discharge at a rate of C/10 [45]. ^{119}Sn Mössbauer *operando* measurements were performed with the modified Swagelok-type cell at room temperature (Fig. 5). The spectrum of the pristine material is formed by a doublet ($\delta = 2.2$ mm/s, $\Delta = 0.9$ mm/s) which is transformed into a single and slightly asymmetric peak at the end of the discharge [45]. The latter peak was fitted with two components ($\delta = 1.88$ mm/s, $\Delta = 0.2$ mm/s and $\delta = 1.96$ mm/s, $\Delta = 0.7$ mm/s) that can be attributed to Li_7Sn_2 nanoparticles [53, 54]. The composition of this Li-Sn alloy differs from the expected maximum composition ($Li_{22}Sn_5$) reducing the specific capacity of the electrode by about 20%. All the other spectra obtained during the discharge were successfully fitted by considering these two contributions.

The relative amounts of $FeSn_2$ and Li_7Sn_2 were evaluated from the relative subspectrum areas and the ratio of the Lamb-Mössbauer factors of these two materials (Fig. 6).

The observed linear variations indicate that the first discharge can be described by the conversion reaction

$$FeSn_2 + 7Li \rightarrow Fe + Li_7Sn_2 \quad (4)$$

Thus, nanostructured $FeSn_2$ is directly transformed into Li_7Sn_2 nanoparticles without the intermediate Li-Sn phases observed for βSn anode material [55].

The iron particles formed during the discharge were characterized from magnetic measurements for the fully lithiated electrode material. The variations of the magnetization as a function of the magnetic field, H, at different temperatures show change from ferromagnetic to superparamagnetic regime at about 20 K. The saturation

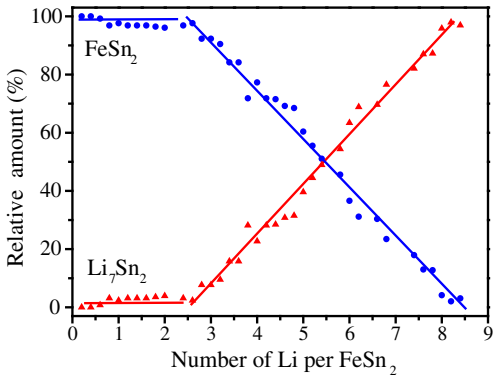

Fig. 6 Relative amounts of $FeSn_2$ (*blue circles*) and Li_7Sn_2 (*red triangles*) evaluated from *operando* ^{119}Sn Mössbauer measurements during the first discharge as a function of the number of Li per $FeSn_2$

magnetization at H = 5T and T = 5K is of about 220 Am^2/kg and is close to that of bulk α-Fe. This suggests that nanoparticles are coated with a non-magetic layer as expected for the surface electrolyte interphase (SEI) previously observed by XPS [39, 45]. In the superparamagnetic regime, the magnetization curves were fitted with a Langevin function in order to evaluate the iron nanoparticle diameter. The obtained value of about 3 nm is consistent with ZFC-FC measurements. Thus, the averaged iron nanoparticle size is constant during the first discharge.

The ^{119}Sn Mössbauer spectra are strongly modified if nanostructured $FeSn_2$ is replaced by $FeSn_2$ microparticles as active material in the pristine electrode. This is due to the size/cristallinity of the particles that allows observing transferred hyperfine field. The Mössbauer spectrum obtained at the end of the discharge is similar to that observed for nanostructured $FeSn_2$ and can also be assigned to Li_7Sn_2. The other spectra of the discharge can be fitted with these two contributions (Fig. 7).

Thus, the same basic reaction mechanism is obtained for the two types of $FeSn_2$ pristine materials: the first discharge transforms $FeSn_2$ into a nanocomposite Fe/Li_7Sn_2. This nanocomposite should be considered as the real starting electrode material. The behaviour of the battery on cycling depends on the first discharge which is a crucial restructuring step. For example, high rate cycling requires a first low rate discharge [56].

By combining ^{57}Fe and ^{119}Sn Mössbauer experiments, we have found that the following cycles consist in dealloying of Li_7Sn_2 leading to Li-rich Li_xSn alloys (on charge) followed by alloying of Li-rich Li_xSn alloys up to Li_7Sn_2 (on discharge). The iron nanoparticles did not react with Sn at the electrochemical regimes considered in our experiments (C/10–10C) and acted as a buffer to limit the volume variations as expected. However, a capacity fading generally occurs after 50 cycles because of the loss of electrical contacts during the charge-discharge cycles and the growth/coalescence of the particles, as shown by *in situ* Mössbauer experiments [45]. The capacity fading is observed for all the tin based intermetallics although it can be reduced by optimizing the electrode formulation or the material composition [48, 57, 58]. Although the reaction mechanisms are similar for the other transition metals, back reactions of tin with the metallic nanoparticles were often observed by Mössbauer spectroscopy during the charge. For example, Ni_3Sn_4 is reformed at the end of charge [39], while a complex Co-Sn-Li alloy is obtained with $CoSn_2$ pristine material [16]. Even in the case of $FeSn_2$, back reaction of Fe with Sn has been

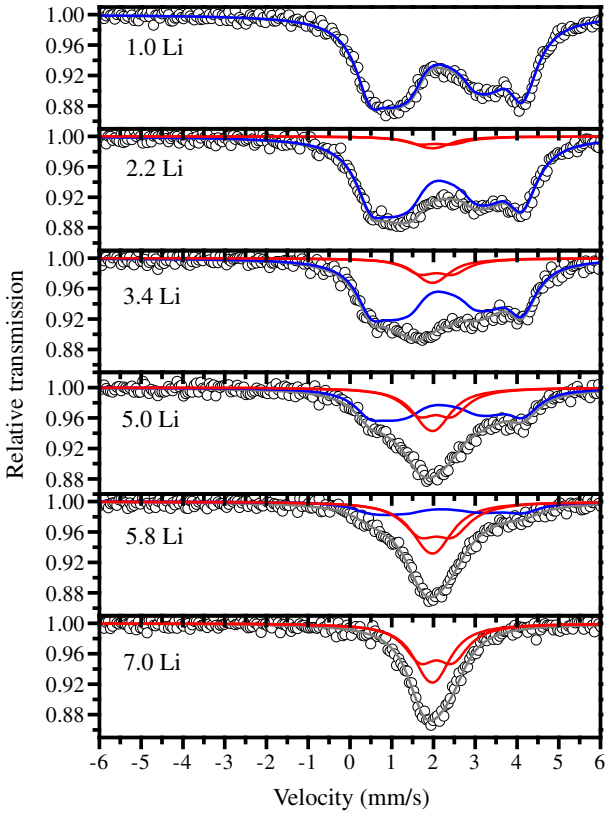

Fig. 7 Selected ^{119}Sn Mössbauer spectra of microsized $FeSn_2$ based electrode in modified Swagelok cell for *operando* measurements during the first discharge at C/10 and room temperature. The spectra were fitted with the contributions of $FeSn_2$ (*blue*) and Li_7Sn_2 (*red*)

observed, but at very low lithium rate [59]. Thus, both the nature of the metal and the electrochemical test conditions affect the charge process. However, it is still not clear whether cycling performances are improved with inactive metallic nanoparticles that buffer the volume variations of Li-Sn alloys or with metallic nanoparticles trapping Sn during the charge to avoid the formation of βSn or poorly lithiated Li-Sn alloys.

5 Conclusion

Mössbauer spectroscopy provides useful and detailed information on electrode materials for Li-ion batteries and electrochemical reaction mechanisms that is essential to improve the performances as energy density, cycling capability or safety. *In situ* and *operando* measurements are crucial for such characterizations since they allow continuous measurements during current flow and avoid extraction of the materials from the electrochemical cell. It is possible to follow redox reactions, changes in local electronic structure and local environments of the Mössbauer isotopes, formation of amorphous and nanocristalline phases during charge-discharge cycles, but also to detect impurities in the pristine materials or to analyse phase instability as a function of time due to aging phenomena.

However, Mössbauer spectroscopy must be combined with other techniques, including theoretical approaches, for the analysis of the complex mechanisms that take place within or at the surface of the electrode particles. At this condition, it will be possible to improve performances and find new electrode materials for the future energy storage systems.

Acknowledgement This work has been carried out in the framework of the European Research Institute ALISTORE. The authors would like to thank SAFT Company Bordeaux (contract 02988) for the financial support.

References

1. Tarascon, J.M.: Phil. Trans. Royal Soc. A **368**, 3227 (2010)
2. Naille, S., Dedryvère, R., Zitoun, D., Lippens, P.E.: J. Power Sources **189**, 814 (2009)
3. Lippens, P.E., Jumas, J.C. (Guest Ed.): It's all about the battery. Mössbauer Eff. Ref. Data J., **33**(2) (2010)
4. Jumas, J.-C., Womes, M., Lippens, P.E., Olivier-Fourcade, J.: Hyperfine Interact. **182**, 103 (2008)
5. Robert, F., Lippens, P.E., Olivier-Fourcade, J., Jumas, J.C., Morcrette, M.: J. Power Sources **146**, 492 (2005)
6. Aldon, L., Kubiak, P., Picard, A., Lippens, P.E., Jumas, J.C., Olivier-Fourcade, J.: Hyperfine Interact. **156**, 497 (2004)
7. Lippens, P.E., Jumas, J.C.: Nanocomposites, Ionic Conducting Materials and Structural Spectroscopies. Springer, Series: Electronic Materials: Science & Technology, Vol. 10, Knauth, Philippe; Schoonman, Joop (Eds.), ISBN: 978-0-387-33202-4, p. 247–272 (2008)
8. Geronov, Y., Tomov, T., Georgiev, S.: J. Appl. Electrochem. **5**, 351 (1975)
9. Chianelli, R.R., Scanlon, J.C., Rao, B.M.L.: J. Electrochem. Soc. **125**, 1563 (1978)
10. Mao, O., Dunlap, R.A., Courtney, I.A., Dahn, J.R.: J. Electrochem. Soc. **145**, 4195 (1998)
11. Dunlap, R.A., Obrovac, M.N., Li, J., Smith, A., Hatchard, T.D., Sanderson, R.J., Dahn, J.R.: Mössbauer Eff. Ref. Data J. **33**, 32 (2010)
12. Wattiaux, A., Fournès, L., Delmas, C.: Mössbauer Eff. Ref. Data J. **33**, 37 (2010)
13. Ariyoshi, K., Ohzuku, T.: Mössbauer Eff. Ref. Data J. **33**, 43 (2010)
14. Tarascon, J.M., Gozdz, A., Schmutz, C., Shokoohi, F., Warren, P.C.: Solid State Ionics **86**, 49 (1996)
15. Aldon, L., Ionica, C., Lippens, P.E., Morcrette, M., Larcher, D., Tarascon, J.M., Jumas, J.C.: Hyperfine Interact. **167**, 729 (2006)
16. Bousquet, C.M., Lippens, P.E., Aldon, L., Olivier-Fourcade, J., Jumas, J.C.: Chem. Mater. **18**, 6442 (2006)
17. Aboulaich, A., Robert, F., Lippens, P.E., Aldon, L., Olivier-Fourcade, J., Willmann, P., Jumas, J.C.: Hyperfine Interact. **167**, 733 (2006)
18. Leriche, J.B., Hamelet, S., Shu, J., Morcrette, M., Masquelier, C., Ouvrard, G., Zerrouki, M., Soudan, P., Belin, S., Elkaïm, E., Baudelet, F.: J. Electrochem. Soc. **157**, A606 (2010)
19. Pahdi, A.K., Nanjundaswami, K.S., Goodenough, J.B.: J. Electrochem. Soc. **144**, 1188 (1997)
20. Yamada, A., Chung, S.C., Hinokuma, K.: J. Electrochem Soc. **48**, A224 (2001)
21. Shiratsuchi, T., Okada, S., Yamaki, J.I., Yamashita, S., Nishida, T.: J. Power Sources **173**, 979 (2007)
22. Zhang, W.J.: J. Power Sources **196**, 2962 (2011)
23. Julien, C.M., Mauger, A., Zaghib, K.: J. Mater. Chem. **21**, 9955 (2011)
24. Wagemaker, M., Ellis, B.L., Luetzenkirchen-Hecht, D., Mulder, F.M., Nazar, L.F.: Chem. Mater. **20**, 6313 (2008)
25. Castro, L., Dedryvère, R., El Khalifi, M., Lippens, P.E., Bréger, J., Tessier, C., Gonbeau, D.: J. Phys. Chem C **114**, 17995 (2010)
26. Andersson, A.S., Kalska, B., Häggström, L., Thomas, J.O.: Solid State Ionics **130**, 41 (2000)
27. Aldon, L., Perea, A., Womes, M., Ionica-Bousquet, C.M., Jumas, J.-C.: J. Solid State Chem. **183**, 218 (2010)
28. Yamada, A., Hosoya, M., Chung, S.C., Kudo, Y., Hinokuma, K., Liu, K.Y., Nishi, Y.: J. Power Sources **119**, 232 (2003)
29. Yamada, A., Kudo, Y., Liu, K.Y.: J. Electrochem. Soc. **148**, A1153 (2001)

30. Rho, Y.H., Nazar, L., Perry, L., Ryan, D.: J. Electrochem. Soc. **154**, A283 (2007)
31. Wang, F., Zhao, M.S., Song, X.P.: J. Power Sources **175**, 558 (2008)
32. Chouvin, J., Olivier-Fourcade, J., Jumas, J.C., Simon, B., Biensan, P.H., Madrigal, F.J.F., Tirado, J.L., Vicente, C.P.: J. Electroanal. Chem. **494**, 136 (2000)
33. Idota, Y., Kubota, T., Matsufuji, A., Maekawa, Y., Miyasaka, T.: Science **276**, 1395 (1997)
34. Zheng, Y., Yang, J., Nuli, Y.N., Wang, J.L.: J. Power Sources **174**, 624 (2007)
35. Aboulaich, A., Mouyane, M., Robert, F., Lippens, P.E., Olivier-Fourcade, J., Willmann, P., Jumas, J.C.: J. Power Sources **174**, 1224 (2007)
36. Mouyane, M., Lippens, P.E., Womes, M., Ducourant, B., Willmann, P., Olivier-Fourcade, J.: Hyperfine Interact. **187**, 27 (2008)
37. Naille, S., Dedryvère, R., Leroy, S., Martinez, H., Lippens, P.E., Jumas, J.C., Gonbeau, D.: J. Power Sources **174**, 1086 (2007)
38. Naille, S., Lippens, P.E., Morato, F., Olivier-Fourcade, J.: Hyperfine Interact. **167**, 785 (2006)
39. Ehinon, K.K.D., Naille, S., Dedryvère, R., Lippens, P.E., Jumas, J.C., Gonbeau, D.: Chem. Mater. **20**, 5388 (2008)
40. Hassoun, J., Panero, S., Simon, P., Taberna, P.L., Scrosati, B.: Advanced Mat. **19**, 1632 (2007)
41. Alcantara, R., Rodriguez, I., Tirado, J.L.: Chem. Phys. Chem. **9**, 1171 (2008)
42. He, J., Zhao, H., Wang, J., Chen, J.: J. Alloys Compd. **508**, 629 (2010)
43. Mao, O., Dunlap, R.A., Dahn, J.R.: Solid State Ionics **118**, 99 (1999)
44. Nwokeke, U.G., Alcántara, R., Tirado, J.L., Stoyanova, R., Zhecheva, E.: J. Power Sources **196**, 6768 (2011)
45. Chamas, M., Lippens, P.E., Jumas, J.C., Boukerma, K., Dedryvère, R., Gonbeau, D., Hassoun, J., Panero, S., Scrosati, B.: J. Power Sources **196**, 7011 (2011)
46. Naille, S., Mouyane, M., El Amraoui, M., Lippens, P.-E., Jumas, J.-C., Olivier-Fourcade, J.: Hyperfine Interact. **187**, 19 (2008)
47. Sony, U.S. Patent 0053131
48. Ferguson, P.P., Martine, M.L., George, A.E., Dahn, J.R.: J. Power Sources **194**, 794 (2009)
49. Ferguson, P.P., Todd, A.D.W., Dahn, J.R.: Electrochem. Commun. **10**, 25 (2008)
50. Ortiz, G.F., Alcántara, R., Rodríguez, I., Tirado, J.L.: J. Electroanal. Chem. **605**, 98 (2007)
51. Hassoun, J., Panero, S., Mulas, G., Scrosati, B.: J. Power Sources **171**, 928 (2007)
52. Nwokeke, U.G., Chadwick, A.V., Alcántara, R., Alfredsson, M., Tirado, J.L.: J. Alloys Compd. **509**, 3074 (2011)
53. Robert, F., Lippens, P.E., Fourcade, R., Jumas, J.C., Morcrette, M., Tarascon, J.M.: Hyperfine Interact. **167**, 797 (2006)
54. Robert, F., Lippens, P.E., Olivier-Fourcade, J., Jumas, J-C., Gillot, F., Morcrette, M., Tarascon, J-M.: J. Solid State Chem. **180**, 339 (2007)
55. Lippens, P.E., Aldon, L., Ionica, C.M., Robert, F., Olivier-Fourcade, J., Jumas, J.C.: Characterization of Li insertion mechanisms in negative electrode materials for Li-ion batteries by Mössbauer spectroscopy and first-principles calculations. In: Knauth, P., Masquelier, C., Traversa, E., Wachsman, E.D. (eds.) Solid State Ionics 2004. Materials Research Society Symposium Proceedings, vol. 835, pp. 249–260. Materials Research Society, Warrendale (2005)
56. Chamas, M., Lippens, P-E., Jumas, J-C., Hassoun, J., Panero, S., Scrosati, B.: Electrochim. Acta **56**, 6732 (2011)
57. Sivasankaran, V., Marino, C., Chamas, M., Soudan, P., Guyomard, D., Jumas, J.C., Lippens, P.E., Monconduit, L., Lestriez, B.: J. Mater. Chem **21**, 5076 (2011)
58. Li, J., Le, D.B., Ferguson, P.P., Dahn, J.R.: Electrochim. Acta 55, 2991 (2010)
59. Dunlap, R.A., Mao, O., Dahn, J.R.: Phys. Rev. B **59**, 3494 (1999)

Hyperfine Interact (2012) 206:47–50
DOI 10.1007/s10751-011-0404-7

Chemical state of Fe in $LaNi_{1-x}Fe_xO_3$ and its effect on electrical conduction property

Takuya Hashimoto · Eiki Niwa · Chie Uematsu · Erina Miyashita · Takeshi Ohzeki · Katsumi Shozugawa · Motoyuki Matsuo

Published online: 26 October 2011

Abstract Mössbauer absorption spectra of single phase $LaNi_{1-x}Fe_xO_3$ ($0.2 \leq x \leq 1.0$) have been measured. Increase of quadrupole splitting with increasing x from 0.2 to 0.6 suggested successful substitution of Fe ion for Ni. Variation of isomer shift with x suggested valence of Fe approched 4+, i.e., concentration of itinerant hole on Fe increased with decrease of Fe content, showing agreement with increase of electrical conductivity with decreasing x from 1.0 to 0.4. It can be prospected that higher electrical conductivity might be obtained if sintering property of the specimens with x less than 0.4 is improved.

Keywords $LaNi_{1-x}Fe_xO_3$ · Solid oxide fuel cells · Electrical conductivity · Mössbauer spectroscopy · Chemical State of Fe

1 Introduction

$LaNi_{1-x}Fe_xO_3$ attracts much interest as a new cathode material for solid oxide fuel cells (SOFC). It has been reported that the specimen with $x=0.4$ is the most promising since it shows the highest electrical conductivity and stability among $LaNi_{1-x}Fe_xO_3$ [1, 2]. In order to clarify the origin of this high property of $LaNi_{0.6}Fe_{0.4}O_3$, the variation of chemical state of Fe on its content and its effect on the electrical conduction property of $LaNi_{1-x}Fe_xO_3$ should be analyzed. So far, the chemical state of Fe in $LaNi_{1-x}Fe_xO_3$ has been investigated by Mössbauer spectroscopy [3–7]. However, analyzed specimens by Goeta et al. [3] and Asai

T. Hashimoto (✉) · E. Niwa · C. Uematsu · E. Miyashita · T. Ohzeki
Department of Integrated Sciences in Physics and Biology, College of Humanities and Sciences, Nihon University, 3-25-40 Sakurajousui, Setagaya-ku, Tokyo 156–8550, Japan
e-mail: takuya@chs.nihon-u.ac.jp

K. Shozugawa · M. Matsuo
Department of Multidisciplinary Sciences, Graduate School of Arts and Sciences, The University of Tokyo, 3-8-1 Komaba, Meguro-ku, Tokyo 153–8902, Japan

and Sekikawa [4] were limited to ones with x smaller than 0.25. Marzec [5] and Świerczek et al. [6] reported Mössbauer spectra of $LaNi_{1-x}Fe_xO_3$. They succeeded in the observation of a magnetic phase transition at room temperature between antiferromagnetic and paramagnetic around $x = 0.7$. However, their measured specimen was limited within $0.6 \leq x \leq 1.0$ owing to the difficulty in single phase preparation of specimens with x less than 0.5 by their employed solid state reaction method, resulting in the failure to analyze the variation of the chemical state of Fe around $LaNi_{0.6}Fe_{0.4}O_3$. We succeeded in the preparation of single phase of $LaNi_{1-x}Fe_xO_3$ with $0.3 \leq x \leq 1.0$ by the optimization of preparation conditions of the solid state reaction method [7]. Mössbauer spectroscopy was performed on the specimens and not only a magnetic phase transition around $x = 0.7$ but also the paramagnetic properties in the specimens with $0.3 \leq x \leq 0.6$ at room temperature were observed. However, the chemical state of Fe was not discussed in the paper since single phase material with x less than 0.2 could not be prepared. Recently, we have succeeded in the preparation of single phase $LaNi_{1-x}Fe_xO_3$ regardless of Fe content employing a solution mixing process, the so-called Pechini method [2]. In this paper, Mössbauer spectroscopy has been carried out for specimens with $0.2 \leq x \leq 1.0$. Compositional variation of the chemical state of Fe has been investigated and its effect on electrical conduction property has been discussed.

2 Experimental

$LaNi_{1-x}Fe_xO_3$ ceramic specimens were prepared by solid state reaction of La_2O_3, NiO and Fe_2O_3 powders or by the Pechini method from acqueous solution of La_2O_3, $Ni(NO_3)_2{\cdot}6H_2O$ and $Fe(NO_3)_3{\cdot}9H_2O$. Detailed preparation conditions of solid state reaction and Pechini method are refered in [7] and [2], respectively. The perovskite phase without second phase was obtained for the specimens with $0.3 \leq x \leq 1.0$ and $0.0 \leq x \leq 1.0$ by solid state reaction and the Pechini method, respectively. For the specimens with $0.0 \leq x \leq 0.4$ and $0.6 \leq x \leq 1.0$, rhombohedral and orthorhombic distorted perovskite single phase were observed, respectively. For $LaNi_{0.5}Fe_{0.5}O_3$, mixture of the both phases were obtained at room temperature.

Mössbauer absorption spectra of the specimens were measured using 14.4 keV γ-ray from ^{57}Co/Rh foil at room temperature. Curve fitting using Lorentz functions was carried out on the spectra for the evaluation of isomer shift, quadrupole splitting and internal magnetic field by using an originally manufactured program. The isomer shift was expressed with respect to the centroid of the spectrum of α-Fe. The electrical conductivity at 500∼800°C in air was measured by the four probe method [2].

3 Results and discussion

Mössbauer spectra of the specimens with $0.3 \leq x \leq 1.0$ were reproduced with those reported in ref. [7]. A magnetic phase transition between antiferromaginetic and paramagnetic was also observed at $x = 0.7$. Figure 1(a) shows enlarged Mössbauer spectra of the specimens with $0.2 \leq x \leq 0.6$. Only doublet peaks were observed in the spectra, indicating paramagnetism in these specimens. The quadrupole splitting

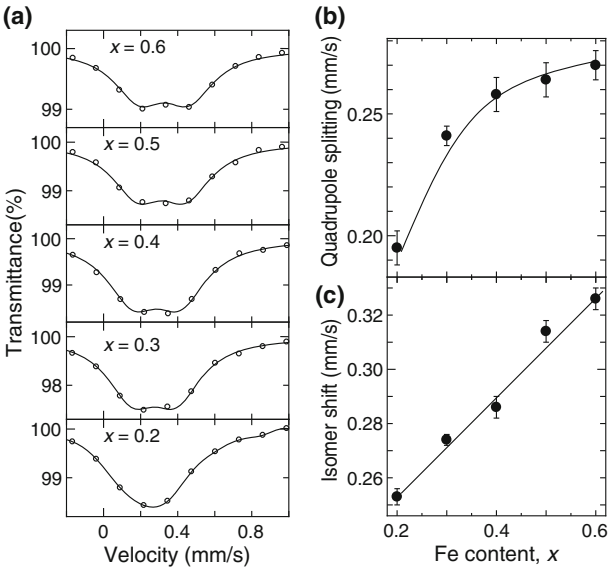

Fig. 1 Fig. 1 (**a**) Mössbauer spectra of $LaNi_{1-x}Fe_xO_3$ ($0.2 \leq x \leq 0.6$) at room temperature. (**b**) Quadrupole splitting and (**c**) isomer shift of $LaNi_{1-x}Fe_xO_3$ ($0.2 \leq x \leq 0.6$)

and isomer shift were evaluated and represented in Fig. 1(b) and (c) as a function of composition. With increasing Fe content from 0.2 to 0.6, not only Ni ions but also Fe ions appear as a second neighbor of the Fe ion, resulting in lower symmetry of the electrical field around the Fe ion. The increase of quadrupole splitting with increasing x can be ascribed to the lowering of the electrical field symmetry around the Fe ion, indicating successful substitution of Fe for Ni. From the isomer shift shown in Fig. 1(c), it can be concluded that the valence of Fe in the specimens is fundamentally 3+. The isomer shift decreased with decreasing Fe content, suggesting a slight increase of the valence of Fe, *i.e.* generation of itinerant hole on Fe orbital according to slightly shifting the following chemical equilibrium to the right side.

$$Fe^{3+} + Ni^{3+} \leftrightarrow Fe^{4+} + Ni^{2+}$$

It can be suggested that the chemical equilibrium shifts to the left side and that the concentration of itinerant holes decreases with increase of Fe up to 0.6. For Mössbauer spectra of the specimens with x larger than 0.8, sextet peaks were observed, indicating an interaction between electrons of Fe^{3+} resulting in antiferromagnetic properties and localized holes. From this evaluation of the chemical state of Fe, it was prospected that the electrical conductivity of $LaNi_{1-x}Fe_xO_3$ increased with decreasing Fe content, showing correspondence with the variation of the electrical conductivity on x from 1.0 to 0.4. However, the electrical conductivity of polycrystalline specimens decreased with decreasing Fe content from 0.4 to 0.1 [2]. We regard that the origin of the decrease of electrical conductivity should be the poor sintering property of the specimens with small x and that the electrical conductivity might increase if the sintering property is improved.

4 Conclusion

Mössbauer spectra revealed that the chemical state of Fe in $LaNi_{1-x}Fe_xO_3$ approached 4+ with decreasing Fe content, which indicated increase of concentration of itinerant hole. This showed agreement with the increase of electrical conductivity with decreasing x from 1.0 to 0.4. It can be probable that $LaNi_{1-x}Fe_xO_3$ with higher electrical conductivity can be prepared if the sintering property of specimens with x less than 0.4 is improved.

Acknowledgements This work was financially supported by a grant from the "Strategic Research Base Development" Program for Private Universities subsidized by MEXT (2009) and Nihon University Strategic Projects for Academic Research "Nanotechnology Excellence-Nanomaterial based Photonic and Quantum Technologies."

References

1. Chiba, R., Yoshimura, F., Sakurai, Y.: Solid State Ion. **124**, 281 (1999)
2. Niwa, E., Uematsu, C., Miyashita, E., Ohzeki, T., Hashimoto, T.: ECS Trans. **35**, 1935 (2011)
3. Goeta, A.E., Goya, G.F., Mercader, R.C., Punte, G., Falcón H., Carbonio, R.: Hyperfine Interact. **90**, 371 (1994)
4. Asai, K., Sekizawa, H.: J. Phys. Soc. Jpn. **49**, 90 (1980)
5. Marzec, J.: J. Power Sources **173**, 671 (2007)
6. Świerczek, K., Marzec, J., Pałubiak, D., Zając, W., Molenda, J.: Solid State Ion. **177**, 1811 (2006)
7. Ohzeki, T., Hashimoto, T., Shozugawa, K., Matsuo, M.: Solid State Ion. **181**, 1771 (2010)

Hyperfine Interact (2012) 206:51–61
DOI 10.1007/s10751-011-0410-9

Environmental applications: catalysts and removal or re-cycling of by products

Károly Lázár

Published online: 28 October 2011

Abstract Some applications of Mössbauer spectroscopy are presented with environmental implications. In particular, catalytic processes are discussed with examples for catalyst immobilisation, for removal of contaminants and for decomposition of harmful compounds. Examples are also presented for processes of recycling of end products.

Keywords Environmental applications · Catalysts · Recycling of by products

1 Introduction

Since the method of Mössbauer spectroscopy is unique and, among other advantages, a very sensitive analytical tool for a few elements, it can successfully be applied in certain environmental studies as well. There is a great number of publications related to environmental applications (studies of mineral processing, corrosion etc. [1, 2]).

Here a few examples are presented to illustrate the possibilities of further applications. The common feature in the discussed examples is that the Mössbauer method is a complementary one, other relevant informations are collected from other appropriate studies. The examples are selected from different applications, namely from the field of catalysis, from the removal of contaminants and from recycling of by-products.

2 Catalysts

Mössbauer spectroscopy may successfully contribute to study of catalysts [3]. Most of these studies are related to in situ characterization of solid supported catalysts. Three

K. Lázár (✉)
Institute of Isotopes, HAS, Budapest,
P.O.B. 77, 1525, Hungary
e-mail: lazar@iki.kfki.hu

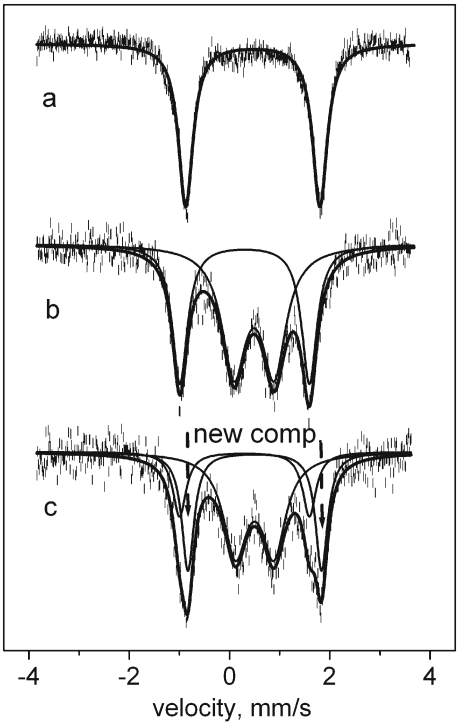

Fig. 1 Encapsulation of Fe-phtalocyanine to Y zeolite, 77 K Mössbauer spectra. **a** bare Fe-phthalocyanine complex, **b** Fe-phtalocyanine synthesized in Y zeolites, **c** Fe-phthalocyanine in hydroquinone/H_2O_2/acetic acid reaction mixture

examples are shown in the next paragraphs, namely for catalyst immobilisation, and for removal and conversion of harmful products. All of them have environmental implications.

2.1 Immobilisation - encapsulation of Fe-phthalocyanine catalytic centres into cages of Y zeolite

Immobilisation of catalysts has at least two significant advantages over non-immobilised homogeneous catalysts: i/ the separation of the catalyst is more easy for the immobilised solid phase catalysts after having the catalytic process finished, and ii/ the recycling and repeated usage is also facilitated for the immobilised substance.

Iron complexes can be used in homogeneous catalytic processes. Their activity and performance can be improved by encapsulating them into zeolite cages. On the other side, their synthesis becames more sophisticated – the complex molecule, coordinating the Fe^{2+} ion in its centre by four nitrogen atoms, should be built up stepwise inside the zeolite. Four phthalonitryle and one Fe^{2+} in the centre can form the required Fe-phthalocyanine complex in Y zeolite. Then, it can be used to catalyse a mild oxidation, e.g. in the hydroquinone + hydrogen peroxide => benzoquinone process in acetic media. Further experimental details and conditions are reported in [4].

The stages can be followed by Mössbauer spectra recorded at 77 K on frozen slurries containing the immobilised solid phase and the reaction mixture. The spectrum of pure iron phthalocyanine in acetic acid media is shown in Fig. 1a. The spectrum

of the complex encapsulated in the cages of Y zeolite (in H_2O_2/acetic acid media) is shown in Fig. 1b. The synthesis is not perfect, the doublet of bare Fe^{3+} ions also appears in the centrum of the spectrum as an additional component. In the third stage, a novel doublet with slightly increased isomer shift appears in the spectrum after addition of hydroquinone to the reaction slurry, demonstrating the coordination change taking place in the ligand sphere at a part of the central Fe^{2+} atoms of the complexes (Fig. 1c). This change illustrates that the close vicinity of iron is influenced by the process, ie. the immobilised Fe^{2+} takes part in the reaction. The same materials have also been tested in real catalytic conditions, they could be used several times in repeated reaction cycles with only minor decrease of the activity [5].

2.2 Removal of contaminants and decomposition of harmful compounds

2.2.1 Removal/conversion of harmful chlorinated hydrocarbons to reuseable compounds: hydrogen assisted dechlorination of dichloroethane on PtSn/SiO_2 catalyst

Possible toxic effects of the chlorinated hydrocarbons were revealed in the last decades and the usage of these compounds has been restricted as much as possible since then. The stocks and the recovered materials should be converted to more valuable products with the simultaneous removal of the chlorine from these compounds. An example is the conversion of dichloroethane (a favoured solvent used frequently earlier) to ethylene in the process:

$$CH_2Cl - CH_2Cl + H_2 = CH_2 = CH_2 + 2HCl.$$

Noble metal catalysts (e.g. Pt) can be used to promote the dechlorination, however they facilitate formation of saturated hydrocarbons (e.g. ethane instead of the more valuable ethylene). Addition of some amount of tin to Pt advantageously modifies the properties of the catalyst, by forming ethylene in high selectivity.

Addition of tin provides also a mean to track the changes taking place in the active phase of the catalyst by in situ ^{119}Sn Mössbauer spectroscopy. A series of spectra recorded at 77 K shows the interconversion of various tin-containing species during the activation and catalytic reaction recorded on a high dispersion PtSn/SiO_2 catalyst (1 wt% total metal content, Pt/Sn atomic ratio 1:2; Fig. 2). The processes taking place in the bimetallic phase can be interpreted by considering the linear dependence in the isomer shift of tin in the Pt-Sn bimetallic phase on the composition, it decreases from pure metallic tin (2.52 mm/s) as the Pt content inreases (Pt_3Sn , IS = 1.2 mm/s) [6].

The first spectrum is recorded on the SiO_2 catalyst support coimpregnated with solutions of H_2PtCl_6 and $SnCl_2$ and drying afterwards. The spectrum attests for the exclusive presence of Sn(IV) state (Fig. 2a). After a modest activation (in H_2 at 490 K) tin-rich and Pt-rich bimetallic phases are present (IS = 2.45 mm/s $\sim$ $PtSn_4$, and IS = 1.32, $\sim$ Pt_3Sn mm/s) besides doublets of Sn(IV) and Sn(II) (Fig. 2b). After a more expressed reduction in hydrogen (620 K) the Pt content increases both in the in the metallic components, the dominating phase is the $PtSn_2$ (IS = 2.16 mm/s, with two-third of the spectral area - Fig. 2c). After having the catalyst exposed to the reaction mixture (CH_2Cl-CH_2Cl, H_2, N_2; 1:5:25) at 470 K for 24 h, the earlier spectrum changes significantly. Namely, tin is depleted in the bimetallic phase, metallic

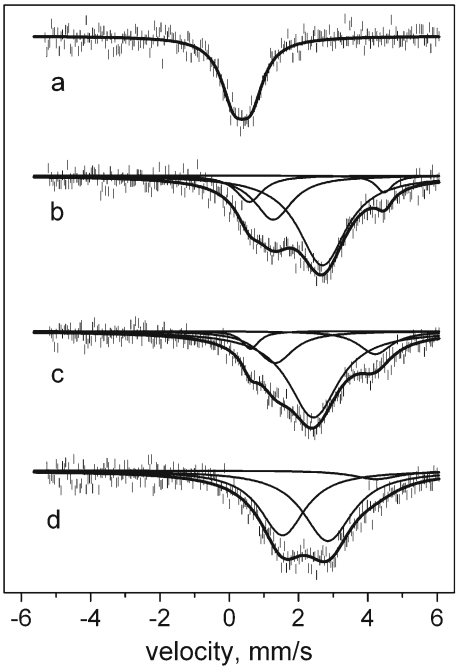

Fig. 2 Conversions of tin containing species in $PtSn/SiO_2$ catalysts during hydrogen assisted dechlorination of dichloromethane, sequential series of 77 K in situ Mössbauer spectra. **a** $PtSn/SiO_2$ as prepared with coimpregnation, **b** after modest activation in hydrogen at 490 K, **c** after more severe reduction in hydrogen at 650 K, **d** after 24 h exposure to $CH_2Cl\text{-}CH_2Cl/H_2/N_2$ reaction mixture at 470 K

tin is the most abundant component (IS = 2.53 mm/s,) besides a Pt-rich (IS = 1.22 mm/s) bimetallic component (Fig. 2d). This fourth spectrum demonstrates that the reaction mixture (in particular the chlorine in it) extracts tin from the bimetallic phase, providing a mean for chlorine-tin interaction. Further details and interpretations are described in [7].

In summary, this series of spectra illustrates how the various interconversions take place among Sn(IV) => tin-rich and tin-depleted PtSn bimetallic and metallic tin phases during the different stages of catalytic dechlorination reaction.

2.2.2 Low temperature oxidation of CO – $PtSn/SiO_2$ catalyst

Carbon monoxide is poisonous even in very low concentrations. With regard to industrial aspects it may be formed as a side product in several processes and its presence can be disadvantageous in various gas mixtures. For instance, hydrogen can be produced in large scale by combining methane reformation and water gas shift reaction. The product gas mixture ($CO_2 + H_2$) may still contain ca. 1% carbon monoxide, which is still a high contaminant level for the intended processes, e.g. for fuel cell applications. Thus, removal of carbon monoxide may have importance either as for removing a poisonous gas, or for improving efficiency of large scale processes.

One of the possibilities is the oxidation of carbon monoxide to carbon dioxide. A favoured catalyst is the supported $Pt\text{-}Sn/SiO_2$ for this process. The efficient catalysts may already operate at low temperatures, e.g. slightly above room temperature (~320 K).

Presence of tin allows to study these catalysts by in situ Mössbauer spectroscopy, too. A series of experiments was performed on a $Pt\text{-}Sn/SiO_2$ catalyst (Pt/Sn atomic

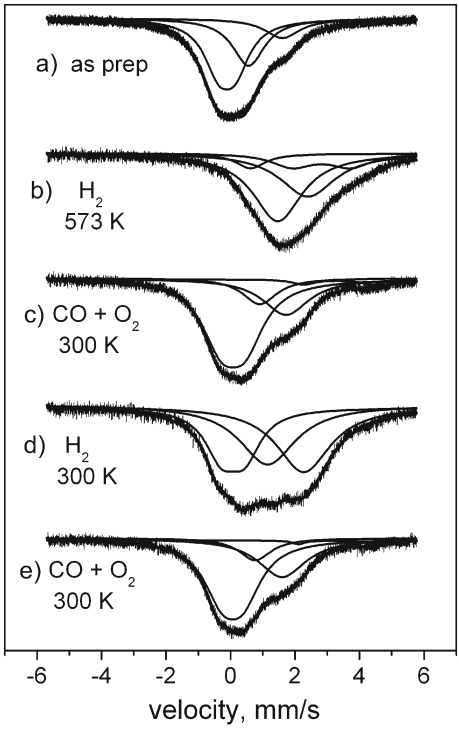

Fig. 3 Sequential series of 77 K Mössbauer spectra collected on $PtSn/SiO_2$ catalysts prepared by CSR method and used for low temperature oxidation of carbon monoxide. **a** after preparation, **b** after activation in hydrogen at 573 K, **c** after exposure to $CO + O_2$ mixture at 300 K, **d** after exposure to hydrogen at 300 K **e** after repeated exposure to $CO + O_2$

ratio = 3:2). The catalyst was prepared by a special method, by the procedure of the "controlled surface reaction" (CSR) in which tin was deposited on 3 % Pt/SiO_2 precursor by anchoring tin exclusively on the surface of high dispersion platinum particles from $^{119}Sn(CH_3)_4$ and decomposing the formed trimethyl compound afterwards. 77 K Mössbauer spectra collected in a series of measurements are shown in Fig. 3. At the start, after the CSR preparation, most of tin became oxidized to Sn^{4+} (Fig. 3a). Pt-Sn bimetallic phase can be developed by treating the catalyst in hydrogen at 573 K. As it was mentioned in the previouos example of hydrodechlorination, the isomer shift of tin in PtSn bimetallic phase allows the distinction between different PtSn components. The hydrogen treatment results in the formation of a Pt rich ($\sim Pt_3Sn$) and a tin rich ($\sim PtSn_2$) major components (isomer shifts 1.37, and 2.41 mm/s, respectively, Fig. 3b). Treatment in $CO + O_2$ mixture at room temperature decomposes most of the bimetallic components by oxidizing tin to Sn^{4+}, stable Pt:Sn = 1:1 bimetallic component remains only in 25% of the spectral area (Fig. 3c). The effect of the next treatment in hydrogen at room tempearature is very demonstrative, the presence of the previous bimetallic Pt rich ($\sim Pt_3Sn$) and tin rich ($\sim PtSn_2$) components is restored for c.a. 2/3rd portion of tin (Fig. 3d). The process is reversible, repetition the $CO + O_2$ treatment results in the restoration of the previous state shown in Fig. 3c (Fig. 3e). The fact that the Sn^0 (in bimetallic particles) $\Leftrightarrow$ Sn^{4+} process is reversible at room temperature depending on the reactant gases, is convincingly demonstrated and shows the high ability of tin for conversions.

It is worth mentioning that ^{119}Sn spectra were also recorded at room temperature. The temperature dependence of the intensity of the components could be estimated from the comparison of the 77 K and 300 K spectra. From this dependence the recoilless fraction and the strengths of bond of the components could also be proposed. From these considerations we have concluded that the reversibly formed Sn^{4+} component is not bonded to the oxide support, instead, it is still on the surface of metallic particles [8].

Parallel catalytic studies showed that the studied ^{119}Sn-Pt/SiO_2 system is a very effective low temperature catalyst for CO oxidation. Effective oxidation of even traces of carbon monoxide was accomplished at rather low temperature (~320 K). Cycles of oxidation/reduction were performed at this temperature, and the catalyst was stable, it maintained its activity during several cycles [9].

2.2.3 N_2O decomposition – FeZSM-5 catalyst

The removal of greenhouse gases is also of environmental importance. One ot these gases is dinitrogen oxide, N_2O. For its decomposition iron containing microporous zeolites were proven very effective (Fe-ZSM5, Fe-FER etc.). The mechanism of the decomposition is not known in all detail, various explanations were proposed [10]. Among the steps, one is the possible formation of very active, atomic oxygen attached to extra-framework iron ions in the zeolite cages (this oxygen was called "alpha-oxygen"). Surprisingly, it was also demonstrated that the stabilization of the reactive alpha-oxygen can be provided by ferrous, Fe^{2+} extra-framework ions [11, 12]. Thus, curiously, in spite of beeing exposed to active oxygen, these ferrous ions are not oxidised to ferric, Fe^{3+} state.

Studying this reaction, we demonstrated experimentally the existence of the extra-framework Fe^{2+} ions in this reaction by in-situ Mössbauer spectra recorded under reaction conditions. First, Fe-ZSM-5 was synthesized (Si/Fe = 200), using enriched ^{57}Fe. Fe^{3+} ions were incorporated into the framework as the appearance of the paramagnetic relaxation attest in the spectrum recorded at 77 K (Fig. 4a). The phenomenon was detected on beta-zeolites as early as 1990 [13], and later as well [14]. In the next step, Fe^{2+} ions were introduced to the extra-framework positions of the zeolite by ion exchange with $FeCl_2$ (Si/Fe = 50). The resulting 77 K spectrum is the sum of the previous spectrum and the quadrupole doublet of the Fe^{2+} ions located in extra-framework sites (Fig. 4b).

In the following stage a spectrum was recorded at reaction conditions (at 620 K, in N_2O, during 6 h treatment). Surprisingly, the presence of Fe^{2+} persists, in spite of the ambient strong oxidizing atmosphere imposed by the N_2O (Fig. 4c). Parallel temperature programmed decompositon measurement was also performed on the same sample, it proved that the maximal rate of the N_2O decomposition is at ca. 600 K (i.e. the catalyst is active at the conditions of recording the Mössbauer spectrum) [15]. A 77 K spectrum was collected after the treatment in N_2O (Fig. 4d) and a subsequent spectrum after evacuation at 670 K (Fig. 4e). The comparison of the two later spectra shows that on a part of the extra-framework a reversible $Fe^{3+} \Leftrightarrow Fe^{2+}$ process may proceed. The final spectrum (Fig. 4e) is practically the same as the one recorded before the catalytic reaction (Fig. 4b), i.e. the catalyst has not been changed noticeably.

This presented example illustrates that the actual states of catalyts can be studied in environmentally important reactions by in situ Mössbauer spectroscopy, and

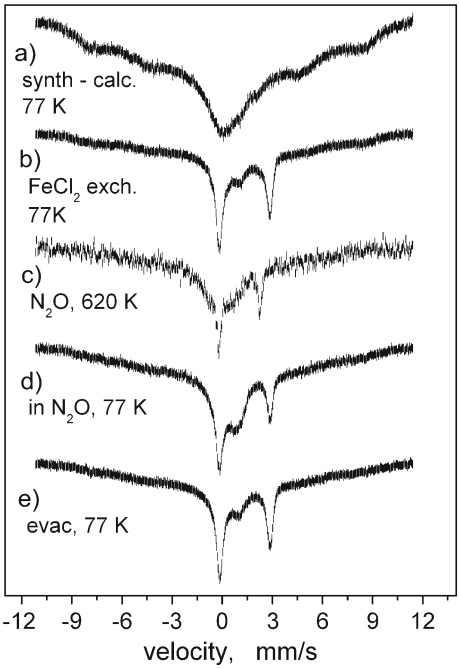

Fig. 4 Sequential in situ Mössbauer spectra collected on Fe-ZSM-5 samples in decomposition of N_2O. **a** 77 K spectrum of ^{57}Fe-ZSM-5, **b** ^{57}Fe-ZSM-5 ion exchanged with $FeCl_2$, 77 K, **c** spectrum recorded under reaction conditions – N_2O, 620 K, **d** after treatment of **c** in N_2O at 77 K, **e** after evacuation at 620 K, recorded at 77 K

conclusions can be drawn with regard to stabilisation of the catalytic centres in steady state conditions.

3 Removal of contaminants with additives

One important step at the purification of communal waste water is the removal of phosphates. Usually Al^{3+} and Fe^{3+} salts are added to the sewage then these salts hydrolyse and the formed phosphates precipitate. The phosphate removal takes place with Fe^{3+} ions (phosphates of Fe^{3+} precipitate, whereas Fe^{2+} phosphates are soluble). The direct addition of Fe^{3+} and Al^{3+} salts is not the best solution, since they should be given in 2–3 fold excess (compared to the stoichiometry with phosphates) and removal of surplus hydroxides is also needs care.

This process can be improved by applying an additive in which the iron component is stabilised in high dispersion. Namely, if $FeSO_4.7H_2O$ is mixed in a strong grinding with a natural zeolite (containing mostly clinoptilolite, Cp) then most of Fe^{2+} ions will be located inside the zeolite cages. The strong grinding is important – practically it is a mechanochemical process in which the crystal structure of the $FeSO_4.7H_2O$ is destructed (as was proven in parallel XRD studies [16]). It is also worth to remark that the process proceeds preferably with Fe^{2+} ions, Fe^{3+} ions incline to form oxyhydroxide oligomers and they do not migrate inside the cages. Additon of lime stone ($CaCO_3$) and lime cream ($Ca(OH)_2$) to the grinding mixture is also advantageous to promote the $Fe^{2+} => Fe^{3+}$ oxidation in the later stage at the usage, without these ingredients the mixture is ineffective.

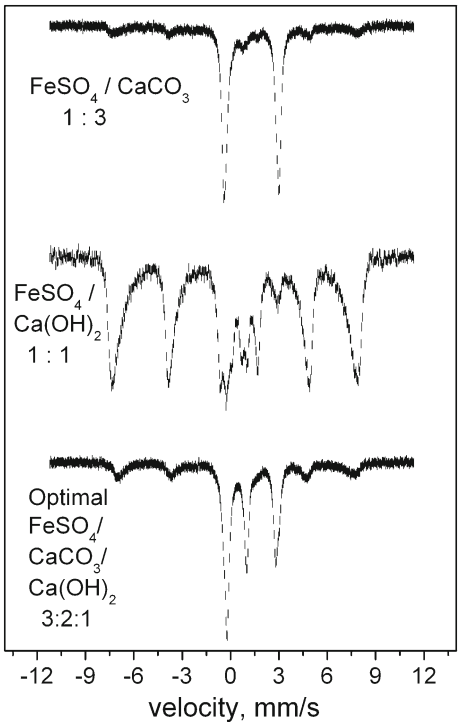

Fig. 5 77 K Mössbauer spectra of $FeSO_4$. $7H_2O$ + clinoptilolite + lime stone/lime cream mixtures used for removal of phosphorous from sewage water

Various natural zeolite (Cp), $FeSO_4$. $7H_2O$, lime stone and lime cream mixtures were prepared and evaluated for their efficiency for phosphate removal in laboratory scale experiments. The best compositons were tested in large scale processes, in a municipial sewage processing plant (3000 m^3/day capacity). The mixture prepared with optimal composition provided 99.5 % removal of phosphate (from 2×10^{-5} mol/L to 1×10^{-7} mol/L). Further details are reported in [16].

77 K Mössbauer spectra of various additive mixtures were recorded, three of them are shown in Fig. 5. Figure 5a shows the stabilisation of Fe^{2+} ions in the zeolite cages (the mixed components are $FeSO_4.7H_2O$ and $CaCO_3$ in 0.3 : 1.0 mole ratio (with ca. 50 wt % Cp), the predominant component in the spectrum is the doublet of Fe^{2+}. Addition of lime cream promotes the hydrolysis already at the mixing and grinding of components (Fig. 5b – $FeSO_4.7H_2O/Ca(OH)_2$ ~1:1, with ca. 40 wt % Cp). In this spectrum the sextet of Fe^{3+} oxyhydroxide is the dominant component. The optimal performance was achieved with a $FeSO_4.7H_2O/CaCO_3/Ca(OH)_2$ ~3:2:1 mixture (~40 wt % Cp), The corresponding 77 K Mössbauer spectrum is shown in Fig. 5c. The spectrum consists of the Fe^{2+} doublet originated from the exchanged Fe^{2+} ions and another doublet characterising the high dispersion Fe^{3+}, the contribution of the larger oxyhydroxides is only modest in the background magnetically split sextet.

Thus, Mössbauer spectra contribute to the understanding of the mechanism of the function of the additive. First, by the mechanical grinding the Fe^{2+} ions are introduced into the cages of clinoptilolite – they are stabilized there (the solid phase product can be stored, transported etc.). When this product is mixed with the aqueous sewage, the Fe^{2+} ions are released from the cages. The bare ions are oxidized in

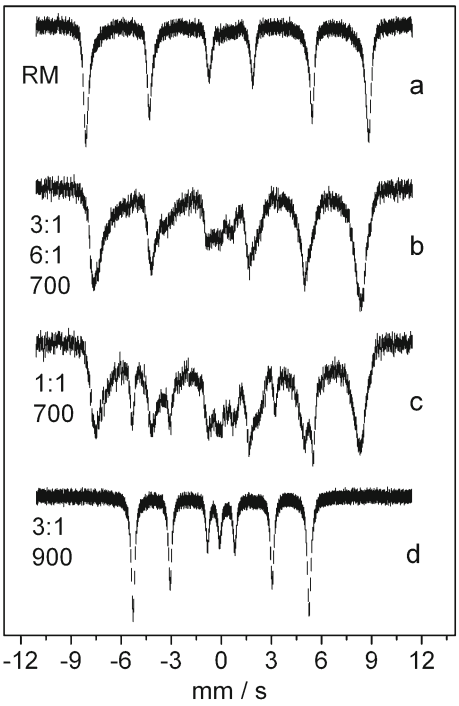

Fig. 6 Mössbauer spectra of mixtures of red-mud and petrol coke treated at various temperatures

the aqueos media to Fe^{3+}. In the next step they hydrolyze in a part and from the high dispersion oxyhydroxide and phosphate the precipitate may form. The $CaCO_3$ and $Ca(OH)_2$ components added earlier to the mixture provide the appropriate advantageous conditions for the oxidation of Fe^{2+} and for the hydrolysis.

4 Recycling of end-products: recovery of iron from red mud

The following example is related to the utilization of the residue of the aluminium production with Bayer process, in which the starting raw mineral, bauxite is digested with NaOH. The amount of processed bauxite is huge, for instance it is in the order of hundred thousand tons per year in Hungary. Thus, the amounts of by-products are also tremendous, their storage as harmful wastes is disadvantageous from environmental aspects.

One of the main residues of the aluminium production is the so called „red mud" which contains iron in high percentage. Typical main components in Hungarian samples are: Fe_2O_3 (35–44 wt%), Al_2O_3 (14–18 wt%), SiO_2 (12–14 wt%), Na_2O (7–11 wt%).

Various reducing agents can be used to recover iron from red mud by cost-saving methods. For instance, an appropriate option is petrol coke, which is also an end-product of a large scale process, namely that of the petroleum refining. Petrol coke (PC) has a strong reducing potential since its typical elemental composition is 91 wt% C, 4.5 wt% H, 4 wt% S.

In a series of wide-scale experiments red mud (RM) and petrol coke (PC) mixtures with various ratios of components were heated up to different temperatures (with a ramp of 5 deg/min to 770, 870, 970, and 1170 K), the processes were followed by differential thermal analysis and thermogravimetry and the products formed were analysed by XRD and Mössbauer spectroscopy [17].

Various iron containing components can be identified in the spectra as the reduction is in progress. For illustration a series of 77 K spectra is shown in Fig. 6. The first spectrum is recorded on the dried red mud (RM) sample (Fig. 6a). After heating to 970 K depending on the RM/PC ratio presence of magnetite – wüstite mixtures can be detected at RM/PC ratios 6:1 and 3:1 (Fig. 6b), whereas metallic iron also forms at RM/PC = 1 ratio in ca. 8% (Fig. 6c). By increasing the upper temperature of the heating to 1170 K, formation of metallic iron prevails at 3:1 and 1:1 RM/PC ratios as Fig. 6d attests. Further details of the experiments can be found in [17].

5 Conclusions

Selected examples of the application of the Mössbauer spectroscopy with environmental implications have been presented. The unique analitical features of the method can advantageously be utilized by combining them with informations obtained by other techniques.

Acknowledgements The help of S. Stichleutner in preparing some figures is thankfully acknowledged. The presentation of results was supported by the Hungarian National Research Grant (OTKA 81863).

References

1. Murad, E., Cashion, J.: Mössbauer Spectroscopy of Environmental Materials and their Industrial Utilization, Kluwer, Boston (2004)
2. Vértes, A., Czakó-Nagy, I.: Mössbauer spectroscopy and its application to corrosion studies. Electrochim. Acta **34**, 721–758 (1989)
3. Millet, J.-M.M.: Mössbauer specroscopy in heterogeneous catalysis. Adv. Catal. **51**, 309–350 (2007)
4. Lázár, K., M-Szeleczky, A., Notheisz, F., Zsigmond, Á.: Encaged iron phthalocyanine for oxygen transfer; Catalytic and Mössbauer spectroscopy study. Stud. Surf. Sci. Catal. **94**, 720–727 (1995)
5. Zsigmond, Á., Notheisz, F., Szegletes, Z.S., Bäckvall, J.E.: Aerobic oxidations on metal macrocycles encapsulated in zeolites. Stud. Surf. Sci. Catal. **94**, 728–735 (1995)
6. Charlton, J.S., Cordey-Hayes, M., Harris, I.R.: A study of the ^{119}Sn Mössbauer isomer shifts in some platinum-tin and gold-tin alloys. J. Less-Common Met. **20**, 105–112 (1970)
7. Rhodes, W.D., Margitfalvi, J.L., Borbáth, I., Lázár, K., Kovalchuk, V.I., d'Itri, J.L.: Hydrogen-assisted 1,2-dichloroethane dechlorination catalysed by Pt-Sn/SiO_2 catalysts of different preparations. J. Catal. **230**, 86–97 (2005)
8. Margitfalvi, J.L., Borbáth, I., Lázár, K., Tfirst, E., Szegedi, Á., Hegedűs, M., Gőbölös, S.: In situ characterization of Sn-Pt/SiO_2 catalysts used in low temperature oxidation of CO. J. Catal. **203**, 94–103 (2001)
9. Margitfalvi, J.L., Borbáth, I., Hegedûs, M., Tfirst, E., Gőbölös, S., Lázár, K.: Low-temperature CO oxidation over new types of Sn-Pt/SiO2 catalysts. J. Catal. **196**, 200–204 (2000)
10. Yakovlev, A.L., Zhidomirov, G.M., van Santen, R.A.: DFT calculations on N_2O decomposition by binuclear Fe complexes. J. Phys. Chem. B **105**, 12297–12302 (2001)
11. Dubkov, K.A., Ovanesyan, N.S., Shteinman, A.A., Starokon, E.V., Panov, G.I.: Evolution of iron states and formation of α-sites upon activation of FeZSM-5 zeolites. J. Catal. **207**, 341–352 (2002)

12. Taboada, J.B., Overweg, A.R., Koyman, P.J., Arends, I.W.C.E., Mul, G.: Following the evolution of iron from framework to extra-framework positions in isomorphously substituted [Fe,Al]MFI with ^{57}Fe Mössbauer spectroscopy. J. Catal. **231**, 56–66 (2005)
13. Kumar, R., Date, S.K., Bill, E., Trautwein, A.: Mössbauer spectroscopic study of ferrisilicate analog of zeolite BETA. Zeolites **11**, 211–213 (1991)
14. Schwarze, M., Sobalik, Z., Caspary, E.G., Niznansky, D.: Characterization of structure of Fe-species in Fe-ferrierite using Mössbauer spectroscopy. Czechoslov. J. Phys. (Suppl. E), **56**, E147–E155 (2006)
15. Lázár, K., Pozdnyakova, O., Wootsch, A., Fejes, P.: Iron ions in ZSM-5 zeolite: Fe^{3+} in framework, Fe^{2+} in extra-framework positions in catalytic N_2O decomposition. Hyperfine Interact. **167**, 779–784 (2006)
16. Kalló, D., Papp, J.: Wastewater treatment with natural clinoptilolite. Stud. Surf. Sci. Catal. **125**, 699–706 (1999)
17. Egyházy, T., Kovács, J., Fülöp, T., Solymár, K.: Utilisation of bauxite residue by modified metallurgical concept. In: Proceedings of the Institute of Environmental and Chemical Engineering, pp. 77–85. Pannon University, Travaux (2004)

Hyperfine Interact (2012) 206:63–66
DOI 10.1007/s10751-011-0551-x

Installation of an IR microscope at the nuclear resonance beamline ID18 of ESRF

Sergej Rackwitz · Juliusz A. Wolny · Kai Muffler · Hans-Jörg Krüger · Sabine Reh · Harald Kelm · Alexander I. Chumakov · Volker Schünemann

Published online: 20 January 2012

Abstract An IR microscope has been installed at the beamline ID18 at the ESRF in Grenoble, France in order to obtain nuclear inelastic scattering (NIS) data and IR spectra simultaneously. This setup combines the advantages of both spectroscopic methods. The applicability of the installed setup to the study of the spin crossover (SCO) phenomenon in polynuclear iron complexes has been shown.

Keywords Nuclear inelastic scattering · Density functional theory · Infrared spectroscopy · Spin crossover

1 Introduction

For the investigation of the vibrational properties of Mössbauer nuclei nuclear inelastic scattering (NIS), also called nuclear resonant vibrational spectroscopy (NRVS) has shown to be a powerful tool [1–3]. All vibrations with a contribution of a displacement of the Mössbauer nucleus parallel to the synchrotron beam can be detected. Due to the high brilliance of the synchrotron radiation of 3rd generation synchrotrons samples with micrometer dimensions can be used. The coupling of NIS with complementary techniques like IR- and Raman spectroscopy allows the assignment of the molecular modes, especially if the experimental data are compared

S. Rackwitz (✉) · J. A. Wolny · K. Muffler · V. Schünemann
Department of Physics, University of Kaiserslautern, Erwin-Schrödinger-Str. 46, 67663 Kaiserslautern, Germany
e-mail: rackwitz@physik.uni-kl.de

H. J. Krüger · S. Reh · H. Kelm
Department of Chemistry, University of Kaiserslautern, Erwin-Schrödinger-Str. 54, 67663 Kaiserslautern, Germany

A. I. Chumakov
ESRF, 38043 Grenoble Cedex, France

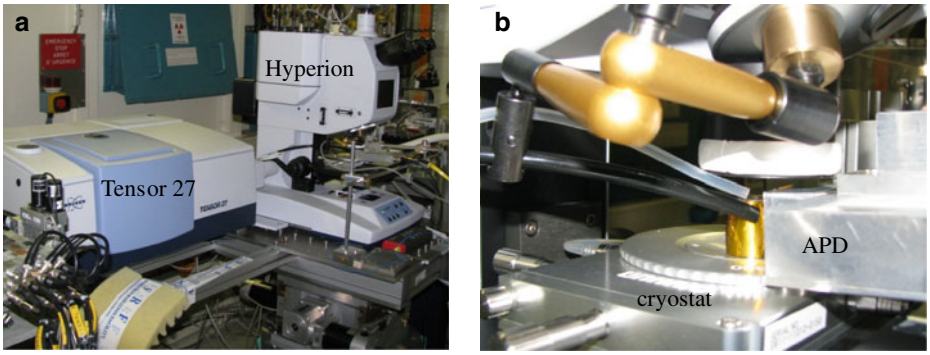

Fig. 1 **a** Installed setup of the IR microscope (Hyperion, Bruker AG) with the spectrometer (Tensor 27, Bruker AG) at ID18 of ESRF during beam time CH3079. **b** A closer look at the cryostat (Linkam station) and the avalanche photodiode (APD) for NIS detection. See also Fig. 2 for sample position within the cryostat

to simulations based on density functional theory (DFT) [4]. In this way a full understanding of the vibrational properties of the sample can be achieved. Here we report on the installation of an IR microscope at the beamline ID18 of the ESRF which enables combined NIS and Micro-IR investigations. The installation of a Raman microscope as a sample environment has been published in [5].

2 Materials and methods

The setup combines a Tensor 27 FTIR spectrometer and a confocal Hyperion microscope, both manufactured by Bruker AG. It allows taking IR data of sample areas down to $10 \times 10\ \mu m^2$ within the region of 550 to 7500 cm^{-1}. The IR microscope was mounted on a self-constructed aluminum table (see Fig. 1a) which was fixed on a z stage (Huber 5103.2; $20 \times 20\ cm^2$) mounted on a goniometer (Huber goniometer heads 5202). The spectrometer needed to be shifted back to clear the synchrotron beam path and is placed on the left side of the microscope. For an accurate adjustment of all spatial directions and angles the center of mass of the aluminum table was aligned with the center of the z-stage.

Since the FTIR spectrometer is shifted considerably from the center of the z-stage a 60 kg counter mass was installed. The total weight of this construction is about 200 kg. In order to allow simultaneous Micro-IR and NIS measurements at varying temperatures a minicryostat (see Fig. 1b) dedicated to optical microscopy was modified (see Fig. 2 for details).

The temperature controlled surface of the cryostat was lifted up by placing a copper block onto it. For temperature isolation a plexiglass tube including a window for the NIS beam encased the block. In addition a combination of Kapton and Mylar foils was put around the tube. On top a BaF_2 glass was fixed, which is transparent for infrared light. The so modified cryostat was successfully operated in the temperature range from ~160 K to 300 K.

The set-up was tested by investigating a single crystal of a dimeric Fe(II) complex $[\{Fe(L)\}_2(bbim)](ClO_4)_2 \cdot 2EtCN$ (L=N,N′-dimethyl-2,11-diaza[3.3](2,6) pyridine-

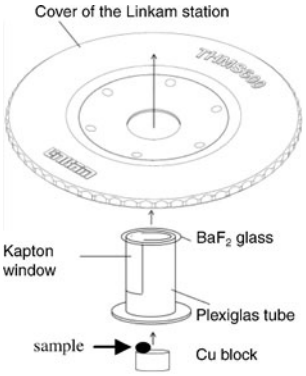

Fig. 2 Modified setup of the cryostat (Linkam station)

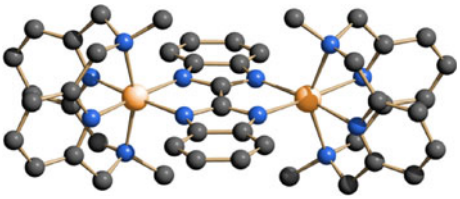

Fig. 3 X-ray structure of the dimeric Fe(II) complex $[\{Fe(II)(L)\}_2(bbim)]^{+2}$ investigated in this study obtained at 150 K. The iron atoms are depicted in orange, carbon is black and nitrogen is blue [6]

ophane; bbim = 2,2′-Bibenzimidazolate) (see Fig. 3). One iron of this complex undergoes an abrupt spin crossover (SCO) from high spin (HS; S = 2) to low spin (LS; S = 0) at 175 K, whereas the other iron stays in its HS state [6].

3 Results and discussion

Figure 4a shows experimental NIS data of $[\{Fe(L)\}_2(bbim)](ClO_4)_2{\cdot}2EtCN$ taken at 300 K. A DFT based simulation assuming both irons being in the HS state (Fig. 4b) reproduces the experimental data well. The broadening of the NIS data at 300 K is due to multi-phonon excitations which are not included in the simulations presented in this study [7, 8]. The simulation of the experimental NIS data obtained at 160 K (Fig. 4c) shows that only one iron site has switched to the LS state (Fig. 4d). The Fe-N modes in Fig. 4d within 185–220 cm^{-1} arise only from the HS iron of the HS-LS dimer, whereas the modes in between 380–610 cm^{-1} are those of the LS iron only. These LS modes have Fe-N stretching character whereas the modes within 270–300 cm^{-1} are Fe-N bending modes arising from both irons [4]. Figure 4e includes the IR data of the same sample, taken simultaneously. The most pronounced changes due to the spin crossover effect are observed within the energy region from 850 to 1050 cm^{-1}. According to our DFT analysis these modes include CH_2-N_{sp3} or aromatic ring stretching. Since these modes also have Fe-N stretching character they are sensitive to the spin state of the iron and serve as spin marker bands.

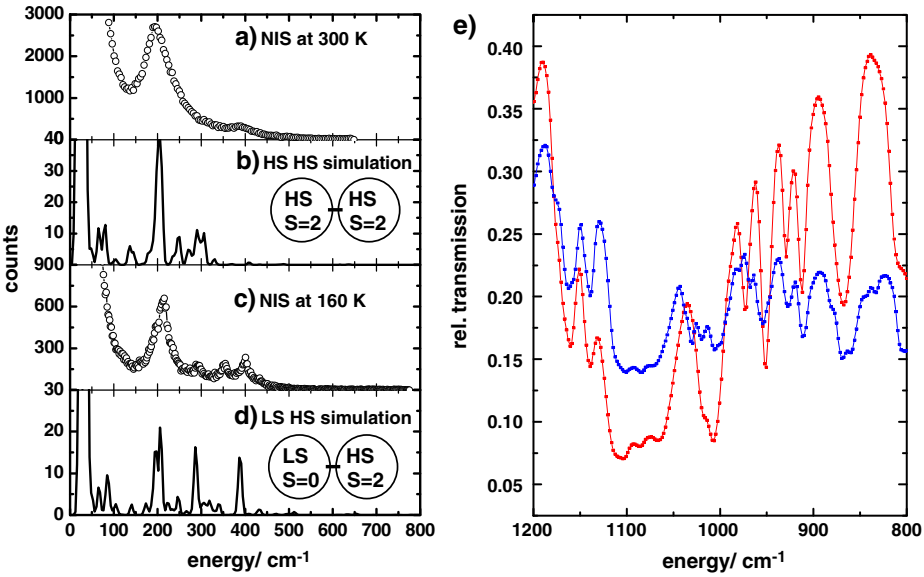

Fig. 4 Exp. (o) (**a** at 300 K, **c** at 160 K) and sim. (-) (**b** for HS-HS sim., **d** for LS-HS sim.) NIS spectra of $[\{Fe(L)\}_2(bbim)](ClO_4)_2 \cdot 2EtCN$ and **e** IR spectra of $[\{Fe(L)\}_2(bbim)](ClO_4)_2 \cdot 2EtCN$ taken at 300 K (*red*) and 160 K (*blue*)

Acknowledgements This work has been supported by the German Federal Ministry of Education and Research under contract number 05KS70K2 and 05K10UKA, by the DFG TRR-SFB-88 3MET and by the ESRF via experiment No. CH 3079.

References

1. Gerdau, E., de Waard, H. (eds): Nuclear resonant scattering of synchrotron radiation (Part A). Hyperfine Interact. **123/124** (1999); (Part B). Hyperfine Interact. **125** (2000)
2. Seto, M., Yoda, Y., Kikuta, S., Zhang, X.W., Ando, M.: Phys. Rev. Lett. **74**, 3828 (1995)
3. Sturhahn, W., Toellner, T.S., Alp, E.E., Zhang, X.W., Ando, M., Yoda, Y., Kikuta, S., Seto, M., Kimball, C.W., Dabrowski, B.: Phys. Rev. Lett. **74**, 3832 (1995)
4. Wolny, J.A., Rackwitz, S., Achterhold, K., Garcia, Y., Muffler, K., Naik, A.D., Schünemann, V.: Phys. Chem. Chem. Phys. **12**, 14782–14788 (2010)
5. Muffler, K., Wolny, J.A., Hersleth, H.P., Achterhold, K., Rüffer, R., Schünemann, V.: J. Phys.: Conference Series **217**, 012004 (2010)
6. Krüger, H.-J.: Coord. Chem. Rev. **253**, 2450–2459 (2009)
7. Kohn, V.G., Chumakov, A.I., Rüffer, R.: Phys. Rev. Lett. **92**, 243001 (2004)
8. Chumakov, A.I., Sturhahn, W.: Hyperfine Interact. **123/124**, 781–808 (1999)

Hyperfine Interact (2012) 206:67–70
DOI 10.1007/s10751-011-0434-1

^{149}Sm and ^{57}Fe nuclear resonant inelastic scattering of filled skutterudites $SmFe_4X_{12}$ (X: pnictogen)

Satoshi Tsutsui · Hisao Kobayashi · Yoshitaka Yoda · Hitoshi Sugawara · Chihiro Sekine · Takahiro Namiki · Ichimin Shirotani · Hideyuki Sato

Published online: 1 November 2011

Abstract ^{149}Sm and ^{57}Fe nuclear resonant inelastic scattering (NRIS) measurements were carried out on $SmFe_4P_{12}$, $SmFe_4As_{12}$ and $SmFe_4Sb_{12}$. A clear dip structure of the ^{57}Fe NRIS spectrum was found in $SmFe_4P_{12}$, which was not clearly observed for $SmFe_4As_{12}$ and $SmFe_4Sb_{12}$. On the other hand, the line width of the phonon excitation in the ^{149}Sm NRIS spectrum increases with increasing the ionic radius of the pnictogen. These findings imply that the hybridization between the Sm and Fe phonon modes is correlated to changes in the ionic radius of the pnictogen.

Keywords Filled skutterudite · Nuclear resonant inelastic scattering · Element-specific phonon spectrum

1 Introduction

Cage-structured compounds such as filled skutterudites and clathrates have attracted considerable interest owing to their strongly correlated electron systems and

S. Tsutsui (✉) · Y. Yoda
Japan Synchrotron Radiation Research Institute, SPring-8, Sayo, Hyogo 679-5197, Japan
e-mail: satoshi@spring8.or.jp

H. Kobayashi
Graduate School of Materials Science, University of Hyogo, Kamigori, Hyogo 678-1297, Japan

H. Sugawara
Graduate School of Science, Kobe University, Kobe, Hyogo 657-8501, Japan

C. Sekine · T. Namiki · I. Shirotani
Department of Electric and Electronic Engineering, Muroran Institute of Technology, Muroran, Hokkaido 050-8585, Japan

H. Sato
Department of Physics, Tokyo Metropolitan University, Hachioji, Tokyo 192-0937, Japan

application as thermoelectric materials. One of the key features of these compounds is the presence of a low-lying optical mode associated with the atoms inserted into the cage structure, which is called a guest mode. Since the phonon-glass-electron-crystal model was first proposed [1], the importance of guest modes for thermal insulation has been discussed [2–5]. In strongly correlated electron systems, on the other hand, superconductivity in β-pyrochlore compounds is an example of superconductivities correlated with low-lying guest modes [6].

Nuclear resonant inelastic scattering (NRIS) is a unique technique for investigating element-specific phonon spectra in materials. It can be applied to a limited number of elements including Mössbauer isotopes that can be excited by sunchrotron radiation X-rays. However, it is a useful tool for elucidating atomic dynamics in cage-structured compounds. In the present work, the atomic dynamics in filled skutterudites were investigated by performing ^{149}Sm and ^{57}Fe NRIS experiments.

2 Experimental procedure

NRIS measurements were carried out at BL09XU of SPring-8 in Japan. ^{57}Fe NRIS measurement of $SmFe_4P_{12}$ at 300 K was carried out with 3.5 meV resolution using a Si(5 1 1)-Si(9 7 5) nested-type high-resolution monochromator (HRM) and those of $SmFe_4As_{12}$ and $SmFe_4Sb_{12}$ at 300 K were carried out with 1.6 meV resolution using a Ge(4 2 2)-Si(9 7 5)-Si(9 7 5) HRM [7]. ^{149}Sm NRIS measurements of $SmFe_4P_{12}$ and $SmFe_4Sb_{12}$ at 25 K ($SmFe_4As_{12}$ at 9 K) were carried out with 1.5 meV resolution using a Si(4 4 0)-Si(16 8 8)-Ge(4 2 2) HRM (a Si(4 4 0)-Si(16 8 8) nested-type HRM) [7, 8].

3 Experimental results and discussion

The ^{149}Sm NRIS spectra of $SmFe_4X_{12}$ (X: P, As and Sb) are shown in Fig. 1a. All the spectra obtained exhibit relatively sharp excitation, suggesting the presence of a dispersionless mode similar to an Einstein mode. Similar spectra have already been reported for other filled skutterudites [4, 9]. The excitation energy decreases with increasing ionic radius of X, whereas the line width increases with increasing X ionic radius. With respect to the excitation energy, the present results indicate that the guest-free space is an important parameter. This was also suggested by the results of other experiments on filled skutterudites [10–12].

The ^{57}Fe NRIS spectra of $SmFe_4X_{12}$ at 300 K are shown in Fig. 1b. Unlike the ^{149}Sm NRIS spectra, the contribution of the Fe atoms to the acoustic modes was clearly observed in the ^{57}Fe spectra. As was reported Ref. [9], a dip structure was found in the ^{57}Fe NRIS spectrum of $SmFe_4P_{12}$ in spite of the inferior energy resolution of 3.5 meV. The energy at which the dip structure was found is in good agreement with that of Sm phonon excitation observed by ^{149}Sm NRIS, although the Sm phonon energy is slightly shifted, mainly due to the shirinkage of the unit cell volume with decreasing temperature [13]. The presence of the dip structure is evidence that the guest modes are hybridized with the acoustic modes. This was supported by the reasonable agreement between the energy of the dipstructure in the ^{57}Fe NRIS spectra and the Einstein temperature obtained by EXAFS experiments

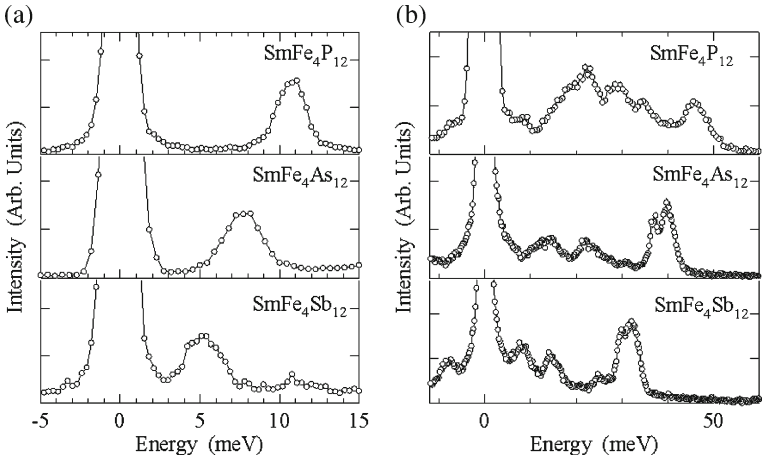

Fig. 1 **a** ^{149}Sm nuclear resonant inelastic scattering spectra of $SmFe_4P_{12}$ at 25 K, $SmFe_4As_{12}$ at 9 K and $SmFe_4Sb_{12}$ at 25 K. **b** ^{57}Fe nuclear resonant inelastic scattering spectra of $SmFe_4P_{12}$, $SmFe_4As_{12}$ and $SmFe_4Sb_{12}$ at 300 K

on the series of RFe_4P_{12} (R: rare-earth). On the other hand, the dip structure in the $SmFe_4As_{12}$ or $SmFe_4Sb_{12}$ spectrum was less clearly observed than that in the $SmFe_4P_{12}$ spectrum. The result for $SmFe_4Sb_{12}$ is very similar to that for $EuFe_4Sb_{12}$ [14, 15]. In addition, the X-ray absorption spectrum of $SmFe_4Sb_{12}$ ($EuFe_4Sb_{12}$) using the Sm (Eu) L_3-edge demonstrates that the Sm (Eu) is trivalent (divalent) [16, 17]. These findings imply that the Fe atomic dynamics are correlated to the X atoms in the series of $SmFe_4X_{12}$ compounds.

Hereafter, we discuss the X-dependence of the dip structure in the ^{57}Fe NRIS spectrum and the line width in the ^{149}Sm NRIS spectra of $SmFe_4X_{12}$ compounds. We interpret the dip structure and the line width in terms of the change in the hybridization between the Sm modes and acoustic modes including the Fe atoms. When the sum rule for NRIS measurements [18] is applied to the present results, the average force constants are 293 ± 10, 189 ± 2 and 156 ± 4 N / m for $SmFe_4P_{12}$, $SmFe_4As_{12}$ and $SmFe_4Sb_{12}$, respectively, at the Fe site. This infers that the cage consisting of Fe and X atoms is softened by changes in the atomic radius of X. This softening leads to strong hybridization between the Sm modes and acoustic modes, i.e., the contribution of the Fe atoms to the acoustic modes. Consequently, the line width in the Sm NRIS spectra, which reflects the density of states at the Sm site, is the broadened by the dispersion of the Sm modes as guest modes.

4 Summary

We carried out ^{149}Sm and ^{57}Fe NRIS measurements on the series of $SmFe_4X_{12}$. The X-dependence of the NRIS spectra is interpreted in terms of the X-dependence of the hybridization between Fe modes, which partially play the role of acoustic modes, with Sm modes as guest modes.

Acknowledgements The author ST appreciates T. Hasegawa, N. Ogita and M. Udagawa for their fruitful discussion. NRIS experiments were carried out under the approval of JASRI (Proposal Nos. 2004B0377-ND3b-np, 2005A370-ND3b-np, 2005B0041, 2007B1107, 2008A1054). This work was supported by Grants-in-Aid for Scientific Research on Priority Area "Skutterudite" (No. 18027017) and on Innovative Areas "Heavy Electrons" (No. 20102004 and 20102005) from MEXT, Japan and Grants-in-Aid for Young Scientists (No. 20740181) and the Scientific Research C (No. 22540345) from JSPS.

References

1. Slack, G.A.: In: Rowe D. (ed.) CRC handbook of thermoelectrics, p. 407. CRC press, Boca Raton (1995)
2. Keppens, V., et al.: Nature **395**, 876 (1998)
3. Hermann, R.P., et al.: Phys. Rev. Lett. **90**, 135505 (2003)
4. Long, G.J., et al.: Phys. Rev. B **71**, 140302 (2005)
5. Tsutsui, S., et al.: J. Phys. Soc. Jpn. **77**, 033601 (2008)
6. Nagao, Y., et al.: J. Phys. Soc. Jpn. **78**, 064702 (2009) and references therein
7. Yoda, Y., et al.: AIP Conf. Proc. **879**, 926 (2007)
8. Yoda, Y.: Private communication.
9. Tsutsui, S., et al.: Hyperfine Interact. **168**, 1073–1077 (2006)
10. Matsuhira, K., et al.: J. Phys. Soc. Jpn. **78**, 124601 (2009)
11. Mizumaki, M., et al.: J. Phys. Soc. Jpn. **80**, 074603 (2011)
12. Tsutsui, S, et al.: J. Phys.: Conf. Ser. **92**, 012171 (2007)
13. Tsutsui, S., et al.: J. Phys. Soc. Jpn. **77**(suppl. A) 257–259 (2008)
14. Tsutsui, S., et al.: J. Phys. Soc. Jpn. **76**, 065003 (2007)
15. Wille, H.-C., et al.: Phys. Rev. B **76**, 140301 (2007)
16. Mizumaki, M., et al.: Physica B **383**, 144 (2006)
17. Bauer, E.D., et al.: J. Phys. Cond. Mat. **16**, 5095 (2004)
18. Lipkin, H.J.: Phys. Rev. B **52**, 10073 (1995)

Hyperfine Interact (2012) 206:71–74
DOI 10.1007/s10751-011-0530-2

Study of interparticle interaction in conjugates of magnetic nanoparticles injected into mice

Raul R. Gabbasov · Valery M. Cherepanov · Michael A. Chuev · Michael A. Polikarpov · Vladislav Y. Panchenko

Published online: 24 December 2011

Abstract In this work the first fast stage of the biodegradation *in vivo* of magnetic ferrofluid was investigated. The appearance of a paramagnetic doublet was observed in Mössbauer spectra of mouse liver within 2 h after intravenous injection of the ferrofluid. It was shown that nanosized superparamagnetic particles were combined into groups in the initial magnetic beads of the ferrofluid and were connected inside each group by magnetic dipole interaction. It was found that the appearance of a paramagnetic doublet in the spectrum of mouse liver is caused by the decrease of the magneto-dipole interaction between the superparamagnetic nanoparticles.

Keywords Mössbauer spectroscopy · Magnetic nanoparticles · Biodegradation · Interparticle interaction

1 Introduction

Magnetic particles based on iron oxide magnetite Fe_3O_4 and maghemite γ-Fe_2O_3 are considered to be the most promising materials for targeted drug delivery. Their popularity is due to an assumption of their good bio-compatibility. Human organs contain a lot of endogenous iron, for example, in liver ferritin or in gem-containing proteins, such as blood hemoglobin. On the other hand, nanoparticles may have greater toxicity than iron in a molecular form. Therefore, a study of mechanisms of their natural degradation and removal is vital for the implementation of the method into clinical practice.

R. R. Gabbasov (✉) · V. M. Cherepanov · M. A. Polikarpov · V. Y. Panchenko
National Research Center "Kurchatov Institute", Moscow, 123182, Russia
e-mail: graul@list.ru

M. A. Chuev
Institute of Physics and Technology, Russian Academy of Sciences, Moscow, 117218, Russia

Mössbauer spectroscopy is one of the methods for the investigation of the metabolism of superparamagnetic particles *in vivo* [1, 2]. This method is insensitive to the majority of organic atoms (carbon, hydrogen, oxygen, nitrogen, etc.) and provides a means of segregation of spectral contributions from exogenous iron contained in particles and endogenous iron contained in ferritin or hemoglobin. Furthermore, Mössbauer spectroscopy regards a set of nanoparticles as a system of interacting single domain magnetic clusters and gives information about magnetic interactions between particles [3].

It was shown using the Mössbauer spectroscopy of mouse's organs [1, 2] that after the injection of magnetite nanoparticles in the form of ferrofluid into the tail vein of mice that they are accumulated mainly in their liver and spleen. The control measurements of mouse's organs without injection did not show a significant concentration of iron. In addition, the shape of the Mössbauer spectrum of the mouse liver after injection differs significantly from the original spectrum of the injected nanoparticles. In particular, along with the magnetically split component of the liver's spectrum, corresponding to the injected particles, an additional paramagnetic doublet was observed which is typical for non-magnetic forms of iron. It indicates a degradation processes of the injected particles in the mice body. The measurements showed that qualitative changing of the spectra occurs within a few hours after injection. Such rapid transformation cannot only be explained by the slow biodegradation processes only.

In [3] we observed a similar behavior of Mössbauer spectra of hematite nanoparticles. In that work samples of superparamagnetic particles were prepared by precipitation of a suspension of the powder in ethanol with small addition of ethanol-soluble glue. Samples demonstrated classical superparamagnetic behavior with temperature. But the blocking temperature of the superparamagnetic transition proved to be different for samples with different amounts of glue. This transformation was caused by changing of the magnetic interparticle interaction.

Similar processes can take place in a live body due to interaction of magnetic nanoparticles with the biochemical environment. This hypothesis can be tested in in vitro experiments on the destruction of intrinsic magnetic beads chemically or by heat and the dissolution of the resulting nanoparticles in analogy with [3].

2 Experiment

We used commercially available magnetite nanoparticles enclosed in magnetic beads and conjugated with a polysaccharide matrix in form of ferrofluid ARA250 produced by Chemicell GmbH (Germany) [4].

17 mg of ferrofluid was injected intravenously into a mouse. The mouse was sacrificed in 2 h after the injection of nanoparticles. The mouse liver was extracted and lyophilized. The Mössbauer spectrum of the mouse liver was measured on a conventional gamma-resonance spectrometer with a ^{57}Co (Rh) source at a temperature of 300 K (Fig. 1d). Another sample of ferrofluid was dried and 12 mg of dry powder was dissolved in ethanol with the addition of the binding polymer (ethanol dissolvable phenol-formaldehyde resin and polyvinyl butyral). In another experiment the polysaccharide has been removed by heating the sample to high temperature (400°C). Mössbauer spectra of the initial nanobeads, the nanobeads dissolved in

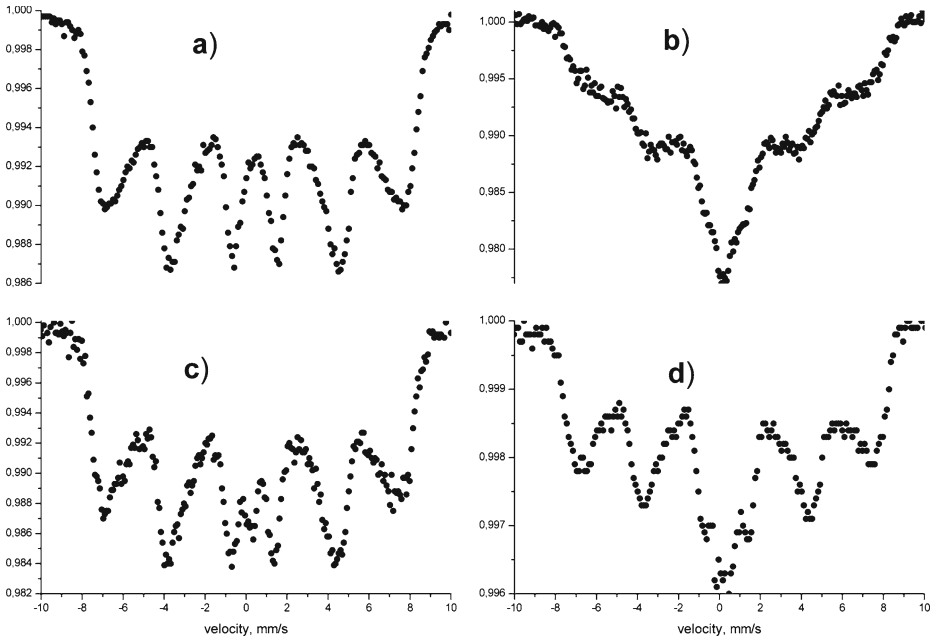

Fig. 1 Mössbauer spectra of ^{57}Fe nuclei in magnetite nanoparticles ARA250 in **a** initial bead, **b** the bead after its partial destruction in vitro in alcohol with addition of a the binding polymer, **c** the bead after its partial destruction by heating and **d** mice liver in 2 h after injection *in vivo* of the nanoparticles

ethanol with the polymer addition and the nanobeads after heat destruction were measured at temperature 300 K (Fig. 1a, b, and c).

3 Results and discussions

The Mössbauer spectrum of initial nanobeads (Fig. 1a) does not contain any sign of the paramagnetic doublet. In accordance with our assumption the superparamagnetic particles in the magnetic bead are divided into groups and connected inside each group by magnetic dipole interaction. After heating the sample of initial nanobeads at 400°C the polysaccharide matrix was destroyed and part of the particles left their magneto-coupled groups and have acquired superparamagnetic properties (Fig. 1c). After dissolving in ethanol the superparamagnetic particles separate as consequence of polysaccharide shell partial dissolution. In this case, the binding polymer prevents aggregation of the particles increasing the effective distance between them. In this case, the interaction between separated particles disappears also and the Mössbauer spectrum demonstrates a paramagnetic doublet (Fig. 1b).

In the case of biodegradation *in vivo*, magnetic beads demonstrate similar behavior: in a live body the polysaccharide shell of beads was destroyed, the superparamagnetic particles were separated and the interaction between them disappeared.

As a consequence, the generation of a paramagnetic doublet in the spectrum of the mouse liver was observed (Fig. 1d).

All these procedures give rise to the generation of the same paramagnetic doublet in the spectra. Hence, our assumption was proven experimentally.

Thus, the appearance of the paramagnetic doublet in the spectrum of mouse liver is a consequence of decreasing of magneto-dipole interaction.

Acknowledgement The study was supported by RFBR grants.

References

1. Nikitin, M.P., Gabbasov, R.R., et al: Magnetic nanoparticle degradation *in vivo* studied by Mössbauer spectroscopy. AIP Conf. Proc. **1311**, 401–407 (2010)
2. Chuev, M.A., Cherepanov, V.M, et al.: Interpretation of the Mössbauer spectra of the magnetic nanoparticles in mouse spleen. AIP Conf. Proc. **1311**, 322–328 (2010)
3. Polikarpov, M.A., et al.: Mössbauer spectra of hematite and magnetite magnetic nanoparticles in polymer composites. J. Phys. Conf. Ser. **217**, 012114 (2010)
4. Nanoparticles Chemicell fluidMAG-ARA http://www.chemicell.com

Hyperfine Interact (2012) 206:75–78
DOI 10.1007/s10751-011-0450-1

Mapping analyses of Fe-diffused mc-Si using Mössbauer microscope and photoluminescence

Kiyotaka Tanaka · Yuki Akiyama · Kazuo Hayakawa · Ken-ichi Yukihira · Yutaka Yoshida

Published online: 15 November 2011

Abstract ^{57}Fe-diffused multi-crystalline silicon (mc-Si) wafer was studied by both Mössbauer and photoluminescence (PL) microscopes. By observing the ^{57}Fe doped and non-doped areas separated with grain boundaries, substitutional and interstitial Fe impurities appear to influence differently on the PL intensities, which are closely related to the carrier trappings at the Fe.

Keywords ^{57}Fe-mapping · Fe doped mc-Si · Mössbauer microscope · Photoluminescence

1 Introduction

Multi-crystalline silicon (mc-Si) wafers are widely used for solar cells whose energy conversion efficiency is about 16 to 17%. This value could be improved up to 25%, if one could remove metallic impurities as well as crystal defects from the wafers. The lattice defects have been investigated by different evaluation techniques for semiconductors. One of the most successful methods appears to be photoluminescence (PL) spectroscopy and its imaging technique [1, 2]. Silicon solar cells are known to contain Fe impurities with concentrations between 10^{11} Fe/cm^3 and 10^{17} Fe/cm^3 which originate from raw materials and also from the crucible used for melting and solidification processes. The metallic impurities form deep levels in the silicon band gap, leading to a strong degradation of the solar cells due to carrier trappings at the impurities.

In this study, we combined a PL mapping technique with a "Mössbauer microscope", the latter of which has been developed in our group [3–6], and investigated space correlations between Fe and lattice defects in an Fe-diffused mc-Si wafer.

K. Tanaka (✉) · Y. Akiyama · K. Hayakawa · K. Yukihira · Y. Yoshida
Shizuoka Institute of Science and Technology, 2200–2 Toyosawa,
Fukuroi, Shizuoka 437–8555, Japan
e-mail: k-tanaka@ob.sist.ac.jp

Table 1 Experimental conditions of Mössbauer-microscope and PL intensity mappings

	Mössbauer-microscope map	PL intensity map
Beam type	γ−ray	DPSS laser
Energy	14.4 keV	2.33 eV (532 nm)
Spot size	250 μm	20 μm
Mapping area	6×6 mm^2	2×2 mm^2
Division	40	160
Mapping step	150 μm	12.5 μm

2 Experimental procedure

A ^{57}Fe layer with a thickness of 1.7 nm was deposited on the surface of a p-type mc-Si wafer (10^{16} B/cm^3) using electron-beam evaporation through an Al mask. Then, the wafer was annealed at 1000°C for one week in a vacuum of 10^{-4} Pa and Mössbauer transmission spectra were measured at room temperature. The experimental details were described in our previous paper [4]. Subsequently, the ^{57}Fe-diffused mc-Si was evaluated over the same area by both the microscopic techniques. In the Mössbauer microscope, the 14.4 keV-γ-rays were focused down to 250 μm by a multi-capillary X-ray lens. The internal conversion and Auger electrons due to ^{57}Fe Mössbauer effect were measured as functions of X-Y coordinates of the sample surface by a micro-channel plate (MCP) detector. Furthermore, PL spectra were measured at room temperature by a micro-PL spectrometer (Photon Design, MPL-800-SRD) using the 532 nm line as an excitation source. The PL intensities were plotted as functions of X-Y coordinates to form a mapping image. Since the peak wavelength in a PL spectrum corresponds to the band-gap energy of silicon, the mapping image provides a distribution of lattice defects where the intensity would be much lower than that of a perfect Si crystal. The measurement conditions for both techniques are summarized in Table 1.

3 Results and discussion

Figure 1 shows mapping images of the ^{57}Fe-diffused mc-Si wafer observed by (a) Mössbauer microscope and (b) PL intensity mapping, respectively. The former image was overlapped on a picture obtained by field emission scanning electron microscope (FE-SEM) to compare the Fe distribution with the microstructure of the sample. The mapping intensity of the Mössbauer image depended on the numbers of ^{57}Fe which distribute differently in different crystal grains near the surface. On the other hand, the latter image appeared to depend on the regions of the sample, which were separated not only by the grain boundaries (pointed out by white arrows), but also by the edge of the Al-mask for Fe deposition (black arrows). Such different regions were surrounded with a white broken line. Figure 1c shows a schematic drawing containing the two typical areas: (i) ^{57}Fe deposited regions separated by the grain boundary (white arrow) and (ii) ^{57}Fe deposited and not deposited regions due to the edge of the Al-mask (black arrow). The two areas (i) and (ii) in Fig. 1c correspond to the broken square areas marked in Fig. 1a and b, respectively.

In the area (i), the Mössbauer mapping intensities were rather high in the upper left area, corresponding dominantly to substitutional Fe which distributed with a Gausian diffusion profile down to about 100 nm from the surface [5]. When crossing

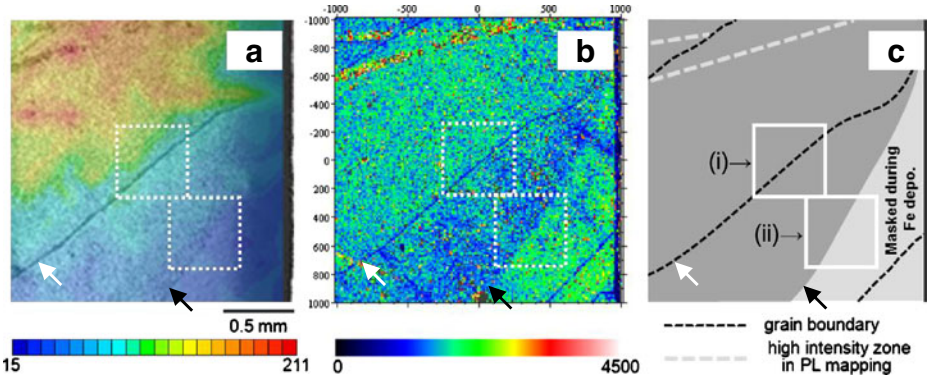

Fig. 1 2 × 2 mm^2-images observed in ^{57}Fe-diffused mc-Si: **a** composite of Mössbauer-microscope with FE-SEM, **b** PL intensity mapping, and **c** schematic drawing

the grain boundary from the upper left to the lower right region, the mapping intensity of substitutional Fe decreased abruptly at the boundary. On the other hand, relatively high PL intensities were found in the same region of the upper left, although this result apparently contradicted that observed by the Mössbauer microscope. A higer Fe concentration would lead to a lower PL intensity because of the carrier trappings at the Fe. However, substitutional Fe, which were distributing close to the surface, seem not to affect the PL intensity as strongly as in the case of interstitial Fe, the concentration of which was at least two orders of magnitude lower than that of substitutional Fe [5].

The area (ii) consisted of ^{57}Fe deposited and non-deposited regions at the upper left and the lower right of the square, respectively. The ^{57}Fe deposited region of the upper left showed a lower PL intensity, suggesting a considerable high concentration, although the Mössbauer intensity indicated a low Fe concentration. On the other hand, the PL intensity of the lower right region was considerably high, which was in accord with the fact that the region was masked during ^{57}Fe deposition. Generally, an Fe-doped Si contains interstitial Fe atoms distributing in the whole sample after the annealing at 1000°C. Accordingly, the PL intensity observed in the area (ii) reflect that interstitial Fe must exist in both the regions, but the concentrations of the interstitial Fe were different in these regions, yielding the low PL intensity in the upper left and the high intensity in the area (ii).

4 Summary

We have evaluated a ^{57}Fe-diffused mc-Si wafer by using both Mössbauer and PL microscopes. It was clear that the mapping intensities observed by the present investigations depend not only on the grain structure, but also on the Fe lattice sites and their distribution in the sample, which were produced during the annealing at 1000°C.

Acknowledgement This work was supported by a research grant from the Ministry of Education, Culture, Sports, Science &Technology in Japan for supporting strategic research projects of private university since 2010.

References

1. Tajima, M., Li, Z., Shimizu, R.: Photoluminescence mapping system applicable to 300 mm silicon-on-insulator wafers. Jpn. J. Appl. Phys. **41**, L1505 (2002)
2. Sugimoto, H., Inoue, M., Tajima, M., Ogura, A., Ohshita, Y.: Analysis of intra-grain defects in multicrystalline silicon wafers by photoluminescence mapping and spectroscopy. Jpn. J. Appl. Phys. **45**, L641 (2006)
3. Yoshida, Y., Horie, S., Niira, K., Fukui, K., Shirasawa, K.: In situ observation of iron atoms in multicrystalline silicon at 1273 and 300 K by Mössbauer spectroscopy. Physica B **376–377**, 227 (2006)
4. Yoshida, Y., Aoki, S., Sakata, K., Suzuki, Y., Adachi, M., Suzuki, K.: Iron impurities in multicrystalline silicon studied by Mössbauer spectroscopy. Physica B **401–402**, 119–122 (2007)
5. Yoshida, Y., Suzuki, K., Hayakawa, K., Yukihira, K., Soejima, H.: Mössbauer spectroscopic microscope. Hyperfine Interact. **188**, 121–126 (2009)
6. Yoshida, Y., Hayakawa, K., Yukihira, K., Ichino, M., Akiyama, Y., Kumabe, H., Soejima, H.: Development and applications of Mössbauer cameras. Hyperfine Interact. **198**, 23–29 (2010)

Hyperfine Interact (2012) 206:79–82
DOI 10.1007/s10751-011-0407-4

Development of system and technology for mössbauer spectroscopic microscope

Kazuo Hayakawa · Yuki Akiyama · Yoshinori Tsukamoto · Mikio Kurata · Kenichi Yukihira · Hiroyoshi Soejima · Yutaka Yoshida

Published online: 11 November 2011

Abstract We have been developing a "Mössbauer Spectroscopic Microscope (MSM)" which consists of a focusing lens for 14.4 keV γ-rays and a high precision X–Y stage. The measuring system both for electrons and γ-rays combined with a new Mössbauer driver, i.e., "a moving coil actuator with a liner encoder" enables us to measure the mapping images simultaneously corresponding to different spectral components. The system has a controlling system based on a LabVIEW program and a LIST mode data acquisition system (NIKI-GLASS/A3100). To investigate a correlation between the microstructure of a sample and ^{57}Fe atoms, a scanning electron microscope (APCO/Mini-EOC) is also installed to this system.

Keywords Mapping · Focusing γ-rays · Multi-capitally lens (MCX) · Fresnel zone plate (FZP) · LIST-mode data acquisition · Mössbauer spectroscopic microscope

1 Introduction

Material properties are known to depend strongly on the microstructures. A Mössbauer spectrum provides atomistic information at the nuclear probes through hyperfine interactions, but it gives only an average within an area irradiated by the γ-rays, i.e., typically 10 mmϕ in diameter. In order to control the fine structures of state-of-the-art microelectronic devices as well as steel products down to several 10 nm, there exist a strong interest in a mapping technique for bulk materials, providing the space resolution from 1 mm down to 10 nm. In the case of ^{57}Fe Mössbauer

K. Hayakawa · Y. Akiyama · Y. Tsukamoto · M. Kurata · K. Yukihira · Y. Yoshida (✉)
Shizuoka Institute of Science and Technology, Toyosawa 2200-2, Fukuroi-city,
Shizuoka 437-8555, Japan
e-mail: yoshida@ms.sist.ac.jp

H. Soejima
Shimadzu Corporation, Nishinokyo-Kuwabaracho 1, Nakagyou-ku, Kyoto 604-8511, Japan

Fig. 1 Main panel of the LabVIEW operating system for Mössbauer spectroscopic microscopy

spectroscopy, we have recently developed a microscopy [1–3] using a focusing lens for 14.4 keV-γ-rays, i.e., multi-capillary X-ray lens (MCX) [4]. The microscopy provides a space resolution of 200μm so far, and we are further challenging to achieve the resolution down to sub-micrometer range using a combination lens of MCX with a Fresnel Zone Plate (FZP) [3]. In this paper, we report mainly on: (1) a user operation system using LabVIEW program, (2) a LIST-mode data accumulation system and a controlling system of X–Y stage, (3) a new Mössbauer driver suitable for a constant velocity operation.

(1.) User operation system using LabVIEW program:

Figure 1 shows the main panel of the LabVIEW operating system developed on Windows 7-PC for the Mössbauer Spectroscopic Microscopy (MSM). The main panel contains several sub-panel buttons corresponding to the different operations, i.e., CCD/SEM operations, setting experimental parameters, setting mapping area, mapping measurement, displaying the results. In a typical operation, we firstly start observing a sample either by a CCD camera or by a Scanning Electron Microscopy (SEM, APCO/Mini-EOC). Secondary, we define the mapping area and the magnification by clicking the mouse on the display, yielding the control parameters for an X–Y stage controller which is connected to the main PC via RS232C. The accumulation time at each mapping point and the number of mapping step, which are typically 30 s and 80 $\times$ 80 points, respectively, will be given from the key board.

(2.) Measuring system

The measuring system consists of a LIST-mode data acquisition system (NIKI GLASS/A3100), a three-stage micro-channel-plate (MCP/HAMAMATSU) with a center hole for conversion and Auger electrons, a Si-PIN detector (AMP TEK) for 14.4 keV γ-rays, and the related standard modules (ORTEC) for the detector signals. The sample holder is fixed on an X-Y stage mounted in a vacuum chamber. The whole system configuration is shown in Fig. 2. A special program has been developed for the Mössbauer Spectroscopic Microscopy (MSM) to convert the three sets of the LIST-mode data as functions of time, into three sets of MCS data, i.e., a standard Mössbauer data as function of the Doppler velocity. These MCS data are read by the main LabVIEW program, and subsequently, the mapping data are produced by

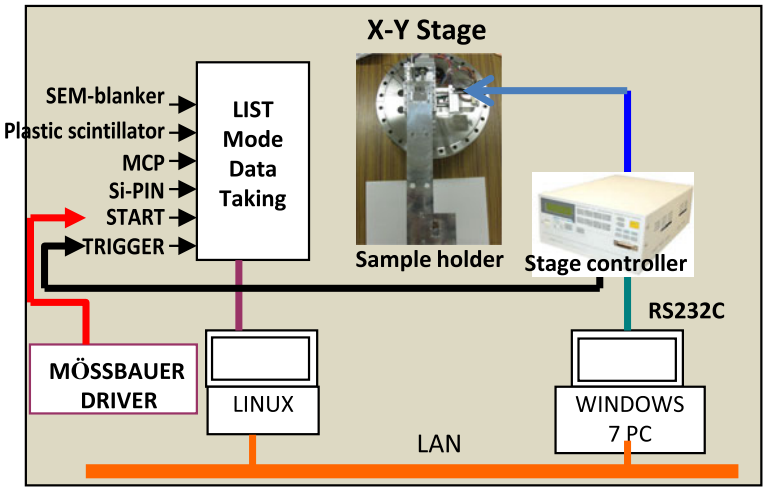

Fig. 2 System configuration: LIST-mode DATA taking system on LINUX PC and LabVIEW program on Windows PC, both of which are connected to X-Y stage controller and Mössbauer driver

summing up all data from a certain velocity range and are finally plotted as function of the position of the focused γ-ray spot.

This detection system is connected to a stage controller of X–Y stage (SIGMA TECH), which realizes the positioning of the X–Y stage within 10 nm. The LIST-mode system saves (1) three different inputs from the detectors every 5 ns as function of time, (2) a start pulse from the function generator for the Mössbauer driver, and (3) a trigger signal from the stage controller which will be sent to A3100 when the positioning of the stage is achieved after moving the position from one to the next mapping position. Furthermore, the LIST-mode module (A-3100) accepts different timing signals for coincidence measurements, i.e., one fast-timing signal from a plastic scintillator placed around the ^{57}Co source to measure 122 keV-γ-rays and another TTL signal from a function generator which produces a blanker pulse for the SEM electron beam.

The SEM can be operated from the operation sub-panel, which is presently developed by APCO. The acceleration voltage of SEM can be varied between −0.5 and −5.0 kV, and the resolution is expected to be 15 nm at−5.0 kV with a beam current of 0.2 nA. This electron gun can be also used to inject electrons into a sample, and a mapping image can be simultaneously measured to study an electron induced phenomena. In addition, we detect the characteristic X-rays and the electrons due to Mössbauer effect alternatively, producing different mapping images.

(3) A new Mössbauer driver.

We are trying to use “a moving coil actuator with a liner encoder (SMAC)” as a new Mössbauer driver, the price of which is much cheaper than those of conventional Mössbauer drivers. Figure 3 shows the velocity of the source (red) as well as the error signal (blue) as functions of time obtained in a test run. By counting the electrons and γ-rays at the different velocities alternatively it is possible to measure the mapping images simultaneously corresponding to the different Mössbauer spectral

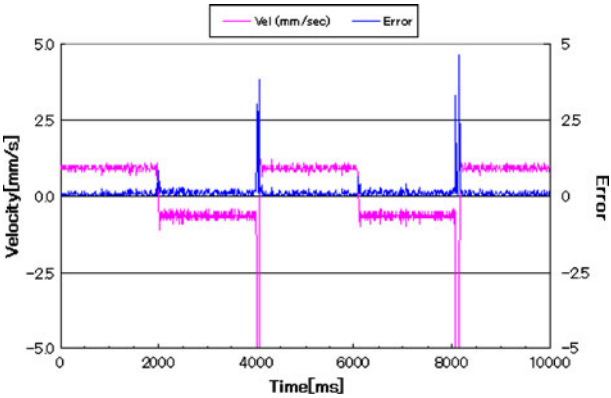

Fig. 3 The constant velocities of source are obtained alternatively at −0.63 and 0.93 mm/s, making us possible to measure the mapping images simultaneously corresponding to different spectral components

components. This actuator provides a positioning resolution of 1.0μm, enabling us to move the ^{57}Co source either with a constant velocity mode, or with a constant acceleration mode. The former mode enables us to control the velocity within about 3 %, as can be seen in Fig. 3, while the latter (not shown in Fig. 3) within 10% depending on the magnitude of the maximum velocity presently. To improve the resolution, we are planning to use a different actuator with a higher resolution of 0.1μm as the next step.

2 Summary

The system and technology of "Mössbauer Spectroscopic Microscope" has been shown in this paper. Mainly described are the operation system based on LabVIEW program, the measuring system with a LIST-mode module combined with the X-Y stage controller and the new Mössbauer driver using a moving coil actuator with a liner encoder. The Mössbauer Spectroscopic Microscope appears to be promising to open totally new applications in the spectroscopy even in a laboratory.

Acknowledgements This project has been supported since 2008 by Japan Science and Technology Agency in the project: The development of systems and technology for advanced measurement and analysis.

References

1. Yoshida, Y., Suzuki, K., Hayakawa, K., Yukihira, K., Soejima, H.: Mössbauer spectroscopic microscope. Hyperfine Interact. **188**, 121 (2009)
2. Yoshida, Y., Kamimura, T., Ichino, M., Hayakawa, K., Yukihira, K., Soejima, H.: Mössbauer spectroscopic microscope. J. Phys.: Conf. Ser. **217**, 012003 (2010)
3. Yoshida, Y., Hayakawa, K., Yukihira, K., Ichino, M., Akiyama, Y., Kumabe, H., Soejima, H.: Hyperfine Interact. **198**, 23 (2010)
4. Soejima, H.: Japan Patent 2014379 (1986); Japan Patent 2001797 (1988)

Hyperfine Interact (2012) 206:83–86
DOI 10.1007/s10751-011-0532-0

Upgrade of the nuclear resonant scattering beamline, BL09XU in SPring-8

Yoshitaka Yoda · Yasuhiko Imai · Hisao Kobayashi · Syunji Goto · Kunikazu Takeshita · Makoto Seto

Published online: 13 January 2012

Abstract An Upgrade of the nuclear resonant scattering beamline, BL09XU in SPring-8 has been conducted. A liquid nitrogen cooled high-heat load monochromator was installed and a 2nd experimental hutch was constructed. The instruments installed in the hutch allow for a variety of sample conditions. Newly developed high-resolution monochromators with better stability including the back scattering geometry monochromator have opened up the easy access to more isotopes and more precise measurements.

Keywords Nuclear resonant scattering · Synchrotron radiation · Mössbauer effect · X-ray beamline · High-resolution monochromator

1 Introduction

Nuclear resonant scattering (NRS) beamlines were constructed in the 3rd generation SR facilities after the first observation of NRS at DESY [1] and the first observation of the nuclear resonant inelastic scattering at TRISTAN-AR [2]. In SPring-8 the

Y. Yoda (✉) · Y. Imai · S. Goto · K. Takeshita
Japan Synchrotron Radiation Research Institute/SPring-8, Sayo-cho, Sayo-gun, Hyogo 679-5198, Japan
e-mail: yoda@spring8.or.jp

H. Kobayashi
Graduate School of Material Science, University of Hyogo, Kamigori-cho, Ako-gun, Hyogo 678-1297, Japan

M. Seto
Research Reactor Institute, Kyoto University, Kumatori-cho, Sennan-gun, Osaka 590-0494, Japan

Y. Yoda · Y. Imai · H. Kobayashi · M. Seto
CREST, Japan Science and Technology Agency, Saitama 332-0012, Japan

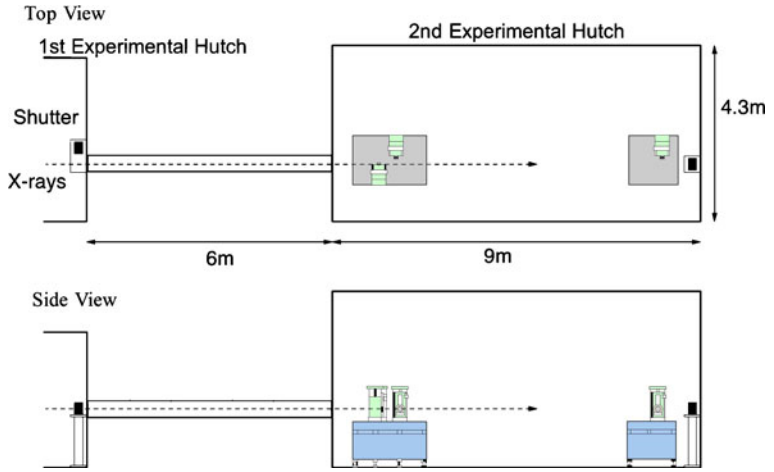

Fig. 1 Schematic view of the 2nd Experimental hutch at BL09XU, SPring-8. The goniometers are mounted on the two optical tables in the 2nd hutch. The first table is mainly used for the sample mounting and the second one is mainly used for the back scattering HRMs

nuclear resonant scattering beamline, BL09XU [3] was constructed in 1997 with one optics hutch for the high heat-load monochromator and one experimental hutch for the high- resolution monochromator (HRM) and the sample. We report the upgrade of BL09XU, which has been done after 2006.

2 2nd experimental hutch

The 2nd experimental hutch is designed to fulfill the following requirements. (1) The HRM and the sample should be separated for the energy stability of the HRM which requires the temperature stability. (2) The sample space for the big devices such as a super-conducting magnet, a laser heating device and an ultra-high vacuum chamber is needed. (3) The HRM for X-rays above 30 keV should be arranged using cryo-cooled back-scattering geometry because we have many attractive Mössbauer isotopes above 30 keV. (4) The space for the focusing optics is needed for the very small samples because the beam size is $\sim$1.0 mm $\times$ 0.6 mm in FWHM at the sample position without focusing. (5) It is better to keep the HRMs for different isotopes on the tables in the 1st experimental hutch to save time for changing the isotopes and improve the stability.

The hutch was constructed in the winter shutdown of 2006. It is 9 m long, 4.3 m wide and 4.3 m high. It is located 6 m downstream of the 1st experimental hutch as shown in Fig. 1. The temperature in the hutch is controlled within 0.1° by the air conditioner. Two optical tables are placed in the hutch. The Goniometers and sample stages can be arranged at any position on the tables by means of air pads. The first table is 1800 mm long and 1200 mm wide. It is mainly used for the sample mounting in the cryostat or in the diffraction geometry. The second table is 1200 mm long and 1200 mm wide. It is mainly used for the back scattering HRMs. The hutch is large enough to install the above mentioned big instruments. We also have enough

space for the focusing optics. The two experimental hutches are connected by the vacuum pipe with a 248 mm inner diameter. The 20 mm wide Kapton windows on both side of the vacuum pipe has vertical acceptance of 250 mm from 1400 mm to 1650 mm. The beam height from the high-heat load monochromator is 1430 mm. This big acceptance makes the setting easier and ensures the flexible design of the HRMs in the future.

3 Sample environment

A super-conducting magnet and a laser heating system have been installed for the experiments under multiple extreme conditions. Both the magnet and the laser heating system are placed behind the 1st optical table in the 2nd experimental hutch and removable from the beam path when it is not in use.

The super-conducting magnet was designed based on the Oxford Instruments SM4000. A diamond anvil cell (DAC) can be loaded inside to allow for the high-pressure experiments combined with high magnetic fields and low temperature. The highest magnetic field is 8 T (horizontal) and the lowest temperature is 1.5 K. This magnet can be used for the nuclear forward scattering experiment.

The laser heating system with DAC was prepared for the high pressure experiments combined with high temperature. It is similar to the system installed at the high-pressure research beamline BL10XU, SPring-8 [4]. The sample in the DAC is heated by the YAG laser from the top and the bottom. The sample can reach temperatures higher than 1500 K. Two avalanche photo diode detectors can be set near the sample for the nuclear inelastic scattering experiment. This system can also be used for the nuclear forward scattering experiment.

4 X-ray optics

A liquid nitrogen cooled monochromator [5] was installed as a high-heat load beamline monochromator in the spring of 2006 in place of the water-cooled diamond monochromator, which was installed in 2004.

The cryo-cooled back-scattering monochromator was installed at the end of the 2nd experimental hutch. The liquid helium continuous flow optical cryostat, which is based on the Oxford Instruments Optistat CF-V, is mounted on the goniometer with 2 axes of θ and φ. The temperature is controlled by the Cryo-con 32B temperature controller. The sapphire crystal is used close to $\pi/2$ Bragg angle [6] and the silicon crystal is used at the high Bragg angle [7]. In case of the backscattering geometry, the sample is located in the 1st experimental hutch. The offset from the direct beam is made by the double crystal Si 111 reflections arranged at the first table in the 2nd experimental hutch.

The optical table, 1800 mm long, was installed in the 1st experimental hutch for the HRMs. The nested in-line type HRMs [8] have been developed for ^{151}Eu and ^{149}Sm and ^{119}Sn in place of the 3 bounce type HRMs [9] and used for the user experiments [10–12]. The 3-bounce type HRM for ^{57}Fe with the resolution of 0.8 meV [13] has been developed and used for the user experiments [14]. These HRMs are arranged in the 1st experimental hutch and the samples are usually installed in the new 2nd

experimental hutch. Consequently the stability of the HRMs has improved and easier access to the different isotopes has been achieved.

5 Summary

The nuclear resonant scattering beamline, BL09XU in SPring-8 has successfully been upgraded. The installed instruments have been working well and allowed for the variety of sample conditions and wider selection of isotopes.

Acknowledgements The construction was supported by CREST project of JST headed by Seto and the hutch was dedicated to the CREST members until 2010. The development of the back scattering HRMs was carried out under the approval of JASRI (Proposal No. 2007B1581, 2008A1453, 2008B1429, 2009B2135).

References

1. Gerdau, E., et al.: Phys. Rev. Lett. **54**, 835 (1985)
2. Seto, M., et al.: Phys. Rev. Lett. **75**, 2216 (1995)
3. Yoda, Y., et al.: Nucl. Instrum. Methods A **467**, 715 (2001)
4. Ohishi, Y., et al.: High Press. Res. **28**, 163 (2008)
5. Mochizuki, T., et al.: Nucl. Instr. Methods A **467–468**, 647 (2001)
6. Imai, Y., et al.: Proc. SPIE **6705**, 670512 (2007)
7. Tsutsui, S., et al.: J. Phys. Soc Jpn. **76**, 065003 (2007)
8. Ishikawa, T.: Rev. Sci. Instrum. **63**, 1015 (1992)
9. Yoda, Y., et al.: AIP Conf. Proc. **879**, 926 (2007)
10. Saito, M., et al.: Appl. Phys. Express **2**, 026502 (2009)
11. Kamihara, Y., et al.: Phys. Rev. B **78**, 184512 (2008)
12. Suharyadi, E., et al.: J. Magn. Magn. Mater. **322**, 158 (2010)
13. Chumakov, A.I., et al.: Nucl. Instrum. Methods A **383**, 642 (1996)
14. Tinberg, E., et al.: J. Am. Chem. Soc. **132**, 18168 (2010)

Hyperfine Interact (2012) 206:87–90
DOI 10.1007/s10751-011-0444-z

Time-domain interferometry experiments using multi-line nuclear absorbers

Makina Saito · Makoto Seto · Shinji Kitao · Yasuhiro Kobayashi · Masayuki Kurokuzu · Yoshitaka Yoda

Published online: 23 November 2011

Abstract The microscopic slow dynamics in various samples has been studied by a time-domain interferometry (TDI) method using nuclear resonant scattering (NRS) of synchrotron radiation and an improvement of the efficiency of TDI is highly desired. To realize it, we developed the TDI method using α-Fe foils with multi-line Mössbauer spectra as nuclear absorbers. Compared to the conventional TDI method using single-line Mössbauer absorbers, the reduction of the measuring time is expected by a simulation study. The simulation study shows a comparatively large change on the multi-line TDI time spectra by the diffusion in a sample and indicates much improvement of the efficiency. We obtained time spectra of the multi-line TDI and the obtained quasi-elastic broadening values of NRS energy width obtained by fitting the time spectra were confirmed to be close to the values obtained by the conventional TDI and estimated standard deviations by the multi-line TDI were comparatively small as expected by the simulation study.

Keywords Nuclear resonant scattering · Time-domain interferometry method · Slow dynamics · Liquid crystal

The microscopic slow dynamics with a time scale of around 100 ns has attracted much interest in the various scientific areas. To study it, a time-domain interferometry (TDI) method using nuclear resonant scattering (NRS) of synchrotron radiation

M. Saito · M. Seto · S. Kitao · Y. Kobayashi · M. Kurokuzu
Research Reactor Institute, Kyoto University, Osaka 590-0494, Japan

M. Saito (✉) · M. Seto · S. Kitao · Y. Kobayashi · M. Kurokuzu · Y. Yoda
CREST, Japan Science and Technology Agency, Saitama 332-0012, Japan
e-mail: seto@post3.rri.kyoto-u.ac.jp

Y. Yoda
Japan Synchrotron Radiation Research Institute, Hyogo 679-5198, Japan

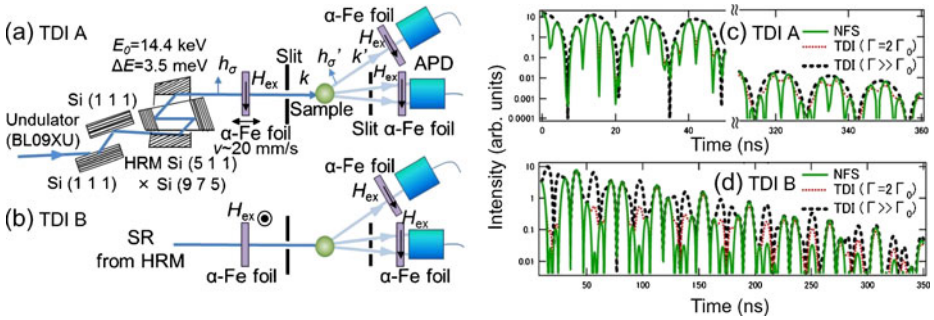

Fig. 1 Experimental setups of **a** TDI A and **b** TDI B, and the time spectra of **c** TDI A and **d** TDI B calculated under some conditions shown in the text

(SR) has been developed by using the ^{57}Fe first excited state, which has the natural energy-width Γ_0 of 4.6 neV [1]. After that, TDI method has been applied to study on for example, an ionic liquid [2]. In order to improve the efficiency, we used α-Fe foils having hyperfine splitting Mössbauer spectra as nuclear absorbers of TDI. Compared to the conventional TDI using single-line nuclear absorbers, the multi-line TDI method, whose set ups are shown in Fig. 1a and b (explained later), is expected to reduce a measuring time because intensity of nuclear forward scattering (NFS) from each nuclear absorber is shown by a simulation study to be increased by using thicker nuclear absorbers for the new TDI without a decrease of efficiency [3]. By considering the principal of TDI method, TDI time spectra changes from the time spectra calculated by the coherent sum of NRS electric fields from two absorbers to the time spectra calculated by the incoherent sum of them with increasing the degree of a diffusion in a sample due to the destroy of phase correlation of NRS by the diffusion in a sample as explained for the case of the conventional TDI [1]. Similar change could be confirmed for the case of the multi-line TDI: As shown in Fig. 2, calculated time spectra of TDI ($\Gamma = 2\Gamma_0$) relax from NFS time spectra (or TDI ($\Gamma << \Gamma_0$)) to the time spectra of TDI ($\Gamma >> \Gamma_0$), which is identical with the time spectra calculated by the incoherent sum of NRS from two absorbers, where Γ is the quasi-elastic broadening of the line width of NRS. The significant difference between NFS time spectra (or TDI ($\Gamma << \Gamma_0$)) and the time spectra of TDI ($\Gamma >> \Gamma_0$) of the multi-line TDI compared to the change of the conventional TDI is expected to cause much improvement of efficiency, which is numerically estimated by the simulation study [3]. Therefore, demonstrating this new TDI method is thought to be valuable and we report first multi-line TDI experiments in this paper.

The TDI experiments were performed at BL09XU of SPring-8 in Japan. Incident radiation with 3.5-meV energy-width at the nuclear resonant energy of the first excited state of ^{57}Fe was obtained by using a high-resolution monochromator (HRM) shown in Fig. 1. The sample used is a liquid crystal, 4-cyano-4′-octylbiphenyl (8CB). TDI measurements with two different experimental setups were attempted by changing the directions of the external magnetic field to α-Fe foils as follows: in the setups "A" shown in Fig. 1a, the external magnetic fields $\boldsymbol{H}_{ex}$, whose directions are parallel to the directions of the magnetic field vector of SR $\boldsymbol{h}_\sigma$ and perpendicular to the wave vectors of incident SR $\boldsymbol{k}$, were applied to upstream α-Fe foils, showing 2-line energy spectra in this condition. The upstream α-Fe was driven with a constant

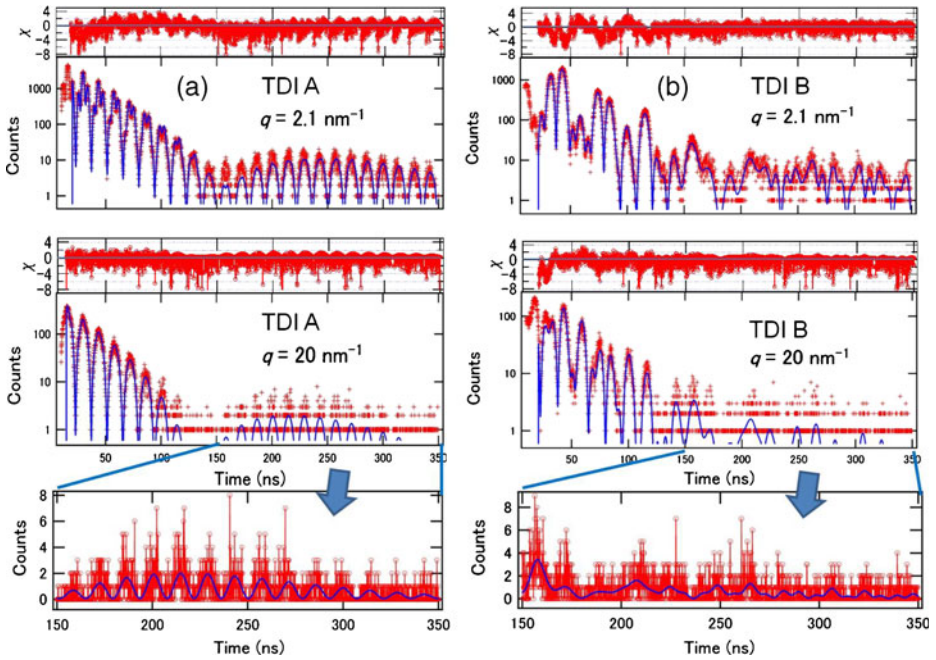

Fig. 2 Time spectra of **a** TDI A obtained at $q = 2.1$ and 20 nm^{-1} and **b** TDI B obtained at $q = 2.1$ and 20 nm^{-1}. Solid lines show fitting curves and χ (=(sim.-exp.)/sim.^0.5) of the fitting results are shown

speed of about 20 mm/s. The external magnetic fields were also applied to the downstream α-Fe foils in the same manner with respect to scattered $\boldsymbol{k}$' and $\boldsymbol{h}_\sigma$', and they were not driven. On the other hand, as shown in the setups "B" in Fig. 1b, $\boldsymbol{H}_{\rm ex}$ perpendicular to $\boldsymbol{k}$ and $\boldsymbol{h}_\sigma$ were applied to the upstream α-Fe foils, showing 4-line energy spectra, while the $\boldsymbol{H}_{\rm ex}$ perpendicular to $\boldsymbol{k}$' and parallel to $\boldsymbol{h}_\sigma$' were applied to the downstream α-Fe foils, showing 2-line energy spectra. Here, all α-Fe foils were not driven. Magnetic circuits composed by permanent magnet pieces were used to apply magnetic fields of about 0.2 T. Two sets of multi-element avalanche photo diode (APD) detectors were arranged at positions with a momentum transfer q of 2.1 and 20 nm^{-1}. Obtained TDI time spectra of setups "A" and "B" for 6 h at 299.8 K at each q are shown in Fig. 2a and b, respectively. In this temperature the 8CB is under smectic A phase. The expected changes shown in Fig. 1c and d could be confirmed in the obtained TDI time spectra shown in Fig. 2.

Obtained time spectra were fitted by MOTIF [4] modified to analyze TDI time spectra by taking account of the quasi-elastic broadening Γ of the line width of NRS from upstream α-Fe by 8CB as discussed following paper in detail [3], and all time spectra were successfully fitted by using a Lorentz function for the quasi-elastic broadening of NRS as shown in Fig. 2 [5]. The obtained Γ values at $q = 2.1$ and 20 nm^{-1} in the unit of Γ_0 are 0.379(25) and 6.29(51) for TDI A, and 0.340(5) and 6.53(37) for TDI B, respectively. The obtained Γ values by the multi-line TDI experiments were confirmed to be close to the values of 0.328(64) and 9(22) by the conventional TDI experiments with the same measuring time. There are deviations

to some extent in the fittings as shown in Fig. 2, which may cause systematic errors of obtained Γ values, though obtained Γ values by the new TDI are not concluded to be inconsistent (or consistent) each other. To fit the spectra better, for example checking of homogeneity of the absorbers may be necessary. Obtained comparatively small σ_Γ values of new TDI could be explained by the simulation study and relatively large σ_Γ value obtained by the conventional TDI at $q = 20\ \mathrm{nm}^{-1}$ could be explained by a low quality of the time spectra originating from the comparatively low NRS intensity of the conventional TDI (about 0.26 times compared to that of TDI B). In conclusion, we could obtain the time spectra of the multi-line TDI in the two experimental setups and the multi-line TDI method is expected to enable further study on microscopic dynamics in the near future by further developments.

Acknowledgements We thank Prof. S. Kishimoto for the development of APD detectors. These experiments were performed with the approval of the Japan Synchrotron Radiation Research Institute (Power User Priority Program No. 2011A0086) and partly supported by the grant-in-aid for Japan Society for the Promotion of Science Fellows.

References

1. Röhlsberger, R.: Nuclear condensed matter physics with synchrotron radiation, chap. 4, p. 260, and references therein. Springer, Berlin (2004)
2. Saito, M., Seto, M., Kitao, S., Kobayashi, Y., Higashitaniguchi, S., Kurokuzu, M., Sugiyama, M., Yoda Y.: Development of ^{151}Eu time-domain interferometry and its application for the study of slow dynamics in ionic liquid. Appl. Phys. Express **2**, 026502 (3 pp.) (2009)
3. Saito, M., Seto, M., Kitao, S., Kobayashi, S., Kurokuzu, M., Yoda, Y.: (2011, in preparation)
4. Shvyd'ko, Y.V.: Nuclear resonant forward scattering of x rays: time and space picture. Phys. Rev. B **59**, 9132–9143 (1999)
5. Benadda, M.D., Carru, J.C. Druon, C.: A measuring device for the determination of the electric permittivity of materials in the frequency range 0.1–3000 MHz. J. Phys., E J. Sci. Instrum. **15**, 132–136 (1982)

Hyperfine Interact (2012) 206:91–94
DOI 10.1007/s10751-012-0572-0

Co^{2+} interaction with *Azospirillum brasilense* Sp7 cells: a ^{57}Co emission Mössbauer spectroscopic study

Alexander A. Kamnev · Anna V. Tugarova · Borbála Biró · Krisztina Kovács · Zoltán Homonnay · Ernő Kuzmann · Attila Vértes

Published online: 4 February 2012

Abstract Preliminary ^{57}Co emission Mössbauer spectroscopic data were obtained for the soil bacterium *Azospirillum brasilense* Sp7 ($T = 80$ K) in frozen $^{57}Co^{2+}$-containing suspensions and in their dried residues. The Mössbauer parameters were compared with those for *A. brasilense* strain Sp245 differing from strain Sp7 by ecological behaviour. Live cells of both strains showed metabolic transformations of $^{57}Co^{2+}$ within an hour. Differences in the parameters observed for the two strains under similar conditions suggest dissimilarities in their metabolic response to Co^{2+}.

Keywords Cobalt(II) metabolism · *Azospirillum brasilense* · ^{57}Co emission Mössbauer spectroscopy

1 Introduction

Cobalt is a trace element with a wide variety of biological functions [1, 2], which at higher concentrations can become toxic [3]. Interaction of bacterial cells with cobalt ions, besides its scientific aspects [2–4], is also of ecological significance [5].

Presented at the International Conference on the Applications of the Mössbauer Effect, 25–30 September 2011, Kobe, Japan.

A. A. Kamnev · A. V. Tugarova
Institute of Biochemistry and Physiology of Plants and Microorganisms, Russian Academy of Sciences, 410049, Saratov, Russia

B. Bíró
Research Institute for Soil Science and Agricultural Chemistry, Hungarian Academy of Sciences, 1025, Budapest, Hungary

K. Kovács (✉) · Z. Homonnay · E. Kuzmann · A. Vértes
Institute of Chemistry, Eötvös Loránd University, P.O. Box 32, 1512, Budapest, Hungary
e-mail: kkriszti@chem.elte.hu

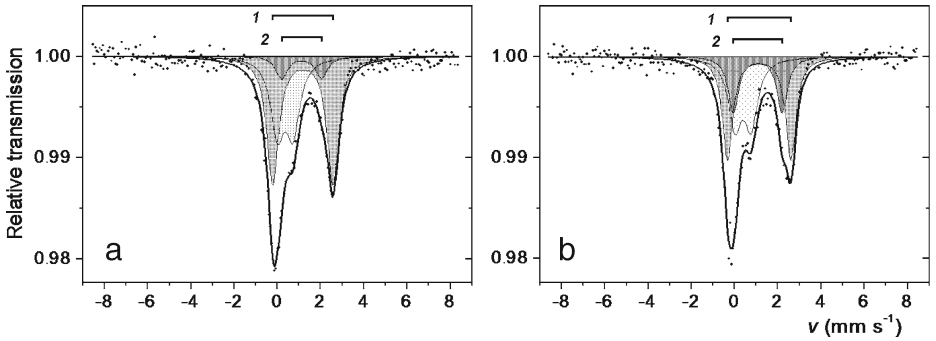

Fig. 1 Emission Mössbauer spectra of *A. brasilense* Sp7 live cells incubated with $^{57}CoCl_2$ (**a**) for 2 min or (**b**) for 1 h and rapidly frozen in liquid nitrogen (measured dried at $T = 80$ K). The positions of the two quadrupole doublets corresponding to daughter $^{57}Fe^{II}$ forms (dark-shaded, 1 and 2; see Table 1, samples "Live (2 min), *D*" and "Live (1 h), *D*") are shown above the spectra (the third light-shaded doublets correspond to daughter $^{57}Fe^{III}$ resulting from after-effects)

The bacterium *Azospirillum brasilense* has long been under study worldwide owing to its phytostimulating potential [6]. This species also represents a good model for studying its responses to ecological factors. Its strain Sp245 is a facultative endophyte (capable of penetrating into and colonising the plant root tissues), while strain Sp7 is an epiphyte (colonising the root surface only). Thus, the two strains of the same species occupy different ecological niches and can show differences in behaviour under similar conditions [4].

Emission (^{57}Co) Mössbauer spectroscopy is a sensitive and informative tool, which has scarcely been used in biology-related studies [2, 4, 7]. In this preliminary work, ^{57}Co emission Mössbauer spectra were measured for live and dead cells of *A. brasilense* strain Sp7 at $T = 80$ K in frozen $^{57}Co^{2+}$-containing aqueous suspensions and for their dried residues. The results are compared with similarly obtained data reported earlier for *A. brasilense* strain Sp245 [4].

2 Experimental

A. brasilense Sp7 cells were grown and prepared for ^{57}Co emission Mössbauer measurements as reported earlier [4]. Emission spectra were measured as in [4] for live and dead cells (hydrothermally treated at 90°C for 1 h) in frozen aqueous suspensions (1.4×10^9 cells ml^{-1}; 0.2 ml, 1.2 mCi $^{57}CoCl_2$, corresponding to 1.2×10^{-5} M $^{57}Co^{2+}$, which is weakly toxic to *A. brasilense* Sp7 [4]) and for their dried residues at $T = 80$ K and processed using the MOSSWINN program [8].

3 Results and discussion

Typical Mössbauer spectra are shown in Fig. 1. The main Mössbauer parameters calculated from the spectra are listed in Table 1. As for strain Sp245 [4], for Sp7 in all cases two quadrupole doublets of daughter high-spin $^{57}Fe^{II}$ components were found corresponding to two chemical forms of parent $^{57}Co^{II}$.

Table 1 Mössbauer parameters calculated from ^{57}Co emission spectra for live or dead cells of *A. brasilense* Sp7 (in brackets, the corresponding data are presented for *A. brasilense* strain Sp245 taken from [4]), incubated with $^{57}CoCl_2$ for specified periods of time and then rapidly frozen in liquid nitrogen (measured at $T = 80$ K), in aqueous suspension (*S*) or dried (*D*)

Samples of bacterial cells	Multiplet[a]	δ,[b] mm s^{-1}	ΔE,[c] mm s^{-1}	A,[d] %
Live (2 min), *S*	Doublet 1	1.10 (1.26)	2.59 (3.00)	56 (44)
	Doublet 2	0.89 (1.20)	2.00 (2.23)	19 (20)
Live (1 h), *S*	Doublet 1	1.16 (1.26)	2.84 (2.89)	35 (51)
	Doublet 2	1.02 (1.16)	2.18 (2.03)	31 (20)
Dead (1 h), *S*	Doublet 1	1.17 (1.24)	2.75 (3.00)	45 (44)
	Doublet 2	1.00 (1.17)	2.13 (2.18)	28 (27)
Live (2 min), *D*	Doublet 1	1.18 (1.24)	2.79 (3.08)	55 (19)
	Doublet 2	1.12 (1.14)	1.84 (2.35)	10 (23)
Live (1 h), *D*	Doublet 1	1.14 (1.22)	2.93 (2.84)	43 (38)
	Doublet 2	1.07 (1.00)	2.25 (2.03)	23 (8)
Dead (1 h), *D*	Doublet 1	1.17	2.78	57
	Doublet 2	1.04	1.95	7

[a]Main doublets corresponding to daughter $^{57}Fe^{II}$ forms stabilised after the $^{57}Co \rightarrow {}^{57}Fe$ nuclear transition (the residual $^{57}Fe^{III}$ forms resulting from after-effects had $\delta \sim 0.36$–0.39 mm s^{-1}, $\Delta E \sim 0.7$–1.0 mm s^{-1})

[b]Isomer shift (relative to α-Fe at room temperature)

[c]Quadrupole splitting

[d]Relative resonant absorption area

Errors: for δ, ± 0.02 mm s^{-1}; for ΔE, ± 0.05 mm s^{-1}; for A, ± 7 rel.%

Dead Sp7 cells, both in suspension (*S*) and dried (*D*; see Table 1), gave very close parameters; slight differences in ΔE and A for their doublets 2 may be attributed to changes in the $^{57}Co^{2+}$ microenvironment caused by drying. In suspensions (*S*), dead cells gave the parameters statistically indistinguishable from those for live cells frozen after 1 h, while for dried samples (*D*) the parameters for dead cells are much closer to those for live cells frozen after 2 min. This can logically be ascribed to possible gradual changes still occurring in the latter while drying.

Note that the contributions from after-effects (see e.g. the third narrow doublets in both spectra in Fig. 1) markedly increased upon drying for live cells frozen 2 min after their contact with $^{57}Co^{2+}$ (from 25% (*S*) to 35% (*D*); see the data in Table 1) and for dead cells (from 27% (*S*) to 36% (*D*)). These contributions, comprised by different yields of after-effects from each ^{57}Co microenvironment, depend on their electron-acceptor properties that may change upon drying which alters the hydration. This may account for changes in the areas of doublets 1 and 2 upon drying. For doublets 1 and 2 (*S* and *D*, 1 h) the δ and ΔE values are close, but their areas change oppositely on drying, assuming different hydration of the Co sites.

For live cells frozen 2 min and 1 h after their contact with $^{57}Co^{2+}$ (measured both as *S* and *D*), notable differences in Mössbauer parameters were found, reflecting metabolic transformations of $^{57}Co^{2+}$ occurring within an hour. (Similar metabolic changes were detected earlier in emission Mössbauer spectra for live cells of strain Sp245 [4].) Also, the increased contributions of doublets 2 in going from 2-min to 1-h samples suggest their relation to ongoing metabolic processes.

However, the Mössbauer parameters for strains Sp245 [4] and Sp7 (see Table 1), obtained under similar conditions, show significant differences both in δ and ΔE for

both quadrupole doublets 1 and 2. This suggests dissimilarities in their metabolic response to Co^{2+}, in line with the data obtained earlier using FTIR spectroscopy [4].

4 Conclusions

Using ^{57}Co emission Mössbauer spectroscopy, live cells of *A. brasilense* strain Sp7 were shown to metabolise $^{57}Co^{2+}$ within an hour, similarly to the data on strain Sp245 of this bacterium reported earlier. Thus, any changes in the Mössbauer parameters observed for live cells can be related to their metabolism, although after-effects have also to be considered.

The Mössbauer parameters for strain Sp7 (in frozen suspensions or dried) differed from those for Sp245 (reported earlier) under similar conditions, suggesting dissimilarities in their metabolic response to Co^{2+}, in line with the previous FTIR spectroscopic data.

Acknowledgements This work was supported by NATO (Project ESP.NR.NRCLG 982857), Hungarian Science Fund (OTKA Projects K68135, 100424, K71215, NN84307), and under the Agreements on Scientific Cooperation between the Russian and Hungarian Academies of Sciences for 2008–2010 (Projects 45, 46) and for 2011–2013 (Projects 28, 29).

References

1. Maret, W.: Metallomics **2**, 117–125 (2010)
2. Kamnev, A.A.: J. Mol. Struct. **744–747**, 161–167 (2005)
3. Ranquet, C., Ollagnier-de-Choudens, S., Loiseau, L., Barras, F., Fontecave, M.: J. Biol. Chem. **282**, 30442–30451 (2007)
4. Kamnev, A.A., Tugarova, A.V., Antonyuk, L.P., Tarantilis, P.A., Kulikov, L.A., Perfiliev, Yu.D., Polissiou, M.G., Gardiner, P.H.E.: Anal. Chim. Acta **573–574**, 445–452 (2006)
5. Christensen, T.H., Kjeldsen, P., Bjerg, P.L., Jensen, D.L., Christensen, J.B., Baun, A., Albrechtsen, H.-J., Heron, G.: Appl. Geochem. **16**, 659–718 (2001)
6. Bashan, Y., de-Bashan, L.E.: Adv. Agron. **108**, 77–136 (2010)
7. Nath, A.: J. Nucl. Radiochem. Sci. 11, A1–A3 (2010)
8. Klencsár, Z., Kuzmann, E., Vértes, A.: J. Radioanal. Nucl. Chem. **210**, 105–118 (1996)

Hyperfine Interact (2012) 206:95–100
DOI 10.1007/s10751-011-0491-5

Mössbauer studies of hemoglobin in erythrocytes exposed to neutron radiation

Katarzyna Niemiec · Magdalena Kaczmarska · Mateusz Buczkowski · Maria Fornal · Władysław Pohorecki · Krzysztof Matlak · Józef Korecki · Tomasz Grodzicki · Kvetoslava Burda

Published online: 29 November 2011

Abstract We studied radiation effects on the stability of various states of hemoglobin (Hb) in red blood cells (RBC) irradiated with a very low dose of neutron rays, 50 μGy. We investigated RBCs isolated from blood of healthy donors. Mössbauer spectroscopy was applied to monitor different forms of Hb. Our results show, for the first time, that oxyhemoglobin (OxyHb) and deoxyhemoglobin (DeoxyHb) are two Hb forms sensitive to such a low neutron radiation. Both Hbs change into a new Hb form (Hb_{irr}). Additionally, OxyHb transfers into $HbOH/H_2O$, which under our experimental conditions is resistant to the action of neutron rays.

Keywords Read blood cell · Neutrons · Mössbauer spectroscopy

1 Introduction

All living organisms are continuously exposed to an ionizing radiation. The average dose rate of the background radiation (radioelements in the soil, rocks, cosmic radiation or medical procedures) is around 2.5 mSv per year, i.e. 5 nSv/min at the

K. Niemiec · M. Kaczmarska · M. Buczkowski · K. Burda (✉)
Faculty of Physics and Computer Science, Department of Medical Physics and Biophysics,
AGH University, al. Mickiewicza 30, 30-059 Kraków, Poland
e-mail: kvetoslava.burda@fis.agh.edu.pl

M. Fornal · T. Grodzicki
Department of Internal Medicine and Gerontology, Collegium Medicum,
Jagiellonian University, Krakow, Poland

W. Pohorecki
Faculty of Energy and Fuels, AGH University, Krakow, Poland

K. Matlak · J. Korecki
Faculty of Physics and Computer Science, Department of Solid State Physics,
AGH University, Krakow, Poland

sea level. The primary effect of ionizing radiation is the production of free radicals and reactive oxygen species (ROS). All molecules in living organisms are potential targets.

Within the frame of this work we studied the influence of neutron radiation. The applied dose of 50 μGy is several orders of magnitude lower than those used in radioimmunotherapy (∼keV) or in prevention of posttransfusion-associated graft-versus-host disease (25–50 Gy) [1]. It is even three orders of magnitude lower than doses at which hormesis phenomena were reported (5–200 mGy). Moreover, the rate dose of the radiation (1.1 mGy/min) is only about 200 times higher than that one estimated for the background radiation. It is known, that neutrons can produce observable damage at lower absorbed doses than β- , γ- or X-radiation because they show higher relative biological effectiveness (RBE) which depends on the energy transfer (LET) being a function of the radiation type, energy and the properties of the target [2–4]. It was observed that μGy doses of ionizing radiation, independently of its type, may cause serious oxidative stress in living organisms. They may damage lipids and proteins, especially enriched in -SH groups [5, 6]. Therefore we wanted to check if there is a detectable influence of ionizing irradiation at an exposure time of a few minutes and at a very low dose rate of ionizing radiation on the hemoglobin (Hb) states in red blood cells (RBCs). We have chosen RBCs because they can serve as a good model system for studying the influence of ionizing radiation on the biomembranes of mammalian cells. Their structure is well known and mature RBCs have no nucleus or any other cellular organelles. We applied Mössbauer spectroscopy to follow different Hb states in untreated and irradiated RBCs. This method was shown to be a sensitive tool in the investigations of the valence and spin states of iron as well as properties of its binding sites [7–9].

2 Materials and methods

Erythrocytes were isolated from blood via centrifugation in phosphate buffer (pH 7.4) using a standard method [10]. The washed RBCs were suspended in the phosphate buffer at the cell concentration of $8{\cdot}10^{10}$ red cells / ml in a volume of about 1.5 ml. These samples were kept in a frozen state at −80°C before the measurement.

^{239}Pu-Be was our source of neutron radiation with two energetic maxima at 877 keV and 2.9 MeV. An average energy of the emitted neutrons was 4 ± 2MeV. Energy of the accompanying γ-rays was about 59 keV. The activity of this neutron source at the position of the sample was $1{,}36{\cdot}10^4$ Bq, what was equivalent to about 1.1 μGy/min or about 2 μSv/min [2].

In the Mössbauer experiments 50 mCi ^{57}Co(Rh) was a source of the 14.4 keV γ-radiation. The measurements were performed at 85 ± 0.1 K. Experimental data were fitted using Recoil Mössbauer Spectral Analysis Software [11].

3 Results and discussion

We studied the influence of a low dose of neutron radiation on the stability of Hb in RBCs isolated from two different representative healthy donors. The Mössbauer spectra of non-irradiated and irradiated samples are presented in Fig. 1A–D, respec-

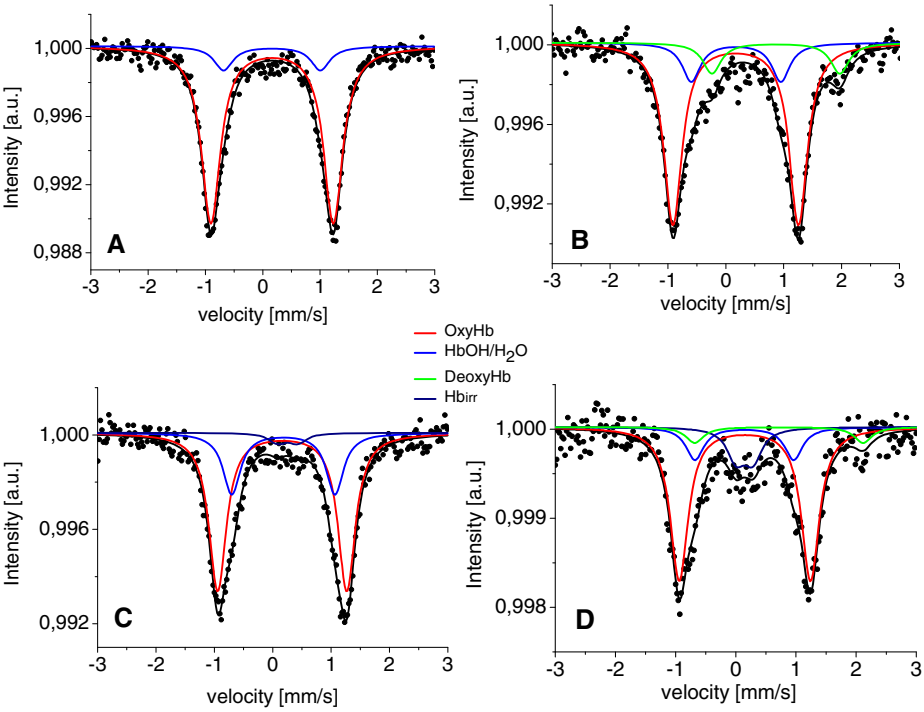

Fig. 1 Mössbauer spectra of non – irradiated (**A**, **B**) and irradiated (**C**, **D**) with 50 μGy neutron rays RBCs from healthy donors (**A**, **C** – sample 1; **B**, **D** – sample 2)

tively. Values of hyperfine parameters (IS – isomer shift, QS – quadrupole splitting) fitted to the experimental spectra obtained for both cases are collected in Table 1.

The Mössbauer spectra of untreated RBCs can be decomposed into two (sample 1) or three (sample 2) components characterized by different hyperfine parameters. The subspectrum with the largest QS of about 2.17 mm/s is characteristic for a diamagnetic state in oxygenated haemoglobin (OxyHb). At the moment, there are two models which may explain a diamagnetism of OxyHb: (i) the Pauling model suggesting an interaction between a low spin ferrous atom and singlet O_2 (a hydrophobic amino acids in the heme iron neighbourhood may help keep Fe^{2+} from becoming oxidized to Fe^{3+}) or (ii) the Weiss model assuming a strong antiferromagnetic coupling between a paramagnetic low spin ferric atom and a paramagnetic superoxide radical anion $O_2^{\cdot-}$ [7, 12–15]. Large quadrupole splitting comparable to that one observed for a high spin ferrous state results from a negative principal electric field gradient [7]. In OxyHb, the movement of the iron atom toward the porphyrin plane was caused by the contraction of the coordination bonds between iron and four nitrogens of the porphyrin.In consequence the proximal histidine (His) comes closer to the heme plane by about 0.5 Å. There is a hydrogen bond between distal His and the terminal oxygen atom of the coordinated molecular oxygen which stabilizes the Fe-OO angle about 120 degree as shown in ref. [16]. The doublet with QS $\sim$ 1.70 mm/s is assigned to deoxyhemoglobin in which the OH/H_2O molecule is the 6th ligand of the heme-iron ($HbOH/H_2O$). In this case the water molecule is

Table 1 Hyperfine parameters fitted to the Mössbauer spectra obtained for non-irradiated and irradiated RBCs isolated from healthy donors

Hyperfine parameters	Component 1 OxyHb	Component 2 $HbOH/H_2O$	Component 3 DeoxyHb	Component 4 Hb_{irr}
Sample 1 non-irradiated				
IS [mm/s]	0.16 ± 0.01	0.16 ± 0.04		
QS [mm/s]	2.14 ± 0.02	1.69 ± 0.15		
A [%]	88.0 ± 1.5	12.0 ± 1.5		
Sample 1 irradiated 45 min				
IS [mm/s]	0.16 ± 0.01	0.18 ± 0.02		0.25 ± 0.04
QS [mm/s]	2.21 ± 0.03	1.77 ± 0.07		0.35 ± 0.22
A [%]	69.0 ± 2.0	26.8 ± 2.0		4.2 ± 2.0
Sample 2 non-irradiated				
IS [mm/s]	0.17 ± 0.01	0.17 ± 0.04	0.87 ± 0.04	
QS [mm/s]	2.17 ± 0.02	1.55 ± 0.05	2.21 ± 0.08	
A [%]	72.3 ± 2.0	15.4 ± 2.0	12.3 ± 2.0	
Sample 2 irradiated 45 min				
IS [mm/s]	0.15 ± 0.01	0.14 ± 0.10	0.72 ± 0.17	0.14 ± 0.07
QS [mm/s]	2.18 ± 0.04	1.65 ± 0.21	2.80 ± 0.34	0.28 ± 0.12
A [%]	65.9 ± 2.0	14.3 ± 2.5	6.8 ± 2.5	13.3 ± 2.5

IS – isomer shift, QS – quadrupole splitting. The line width was 0.20 ± 0.02 mm/s

additionally bound to distal His via a hydrogen bridge [17]. One may consider the sixth Fe ligand as a hydroxide or water molecule depending on the delocalization of the hydrogen charge toward the His nitrogen or oxygen atom, respectively. In this case the heme-iron could be in a mixed valence state (Fe^{2+}/Fe^{3+}) having mixed spin states [7]. The third component with IS ∼ 0.9 mm/s and large QS comes from deoxygenated hemoglobin (DeoxyHb in sample 2) [7, 16]. In DeoxyHb the prophyrin is domed and the iron atom is displaced from the heme plane toward the proximal His. A second iron axial ligand is formed between Fe and distal His. In this case the heme iron is in a high spin state (S = 2). The large quadrupole splitting is due to the asymmetric charge distribution resulting from an extra electron in the xy plane [7, 16]. Irradiation of RBCs results in an occurrence of a new component with IS ∼ 0.20 mm/s and QS ∼ 0.30 mm/s. We call it Hb_{irr} and it can be assigned to five (six) -coordinated heme iron with CN(s)-group (low spin Fe^{3+} or high spin Fe^{3+} in a strong iron-ligand bonds with almost spherical electric field symmetry), which could be formed due to His imidazole ring radiolysis [18, 19]. However, the hyperfine parameters are also characteristic for a low spin ferrous state of the heme-iron bound to CO [7, 16]. Radiolysis of the protein-lipid matrix may cause the formation of carbon monoxide [19, 20]. The contribution of Hb_{irr} is low in the spectrum obtained for sample 1 (∼4%) and much higher in the case of sample 2 (∼13%). At the same time the content of OxyHb decreases in the spectra of both samples. Additionally, in the case of sample 1 the contribution of $HbOH/H_2O$ increases by ∼50% whereas in the case of sample 2 the content of this component remains unchanged but the DeoxyHb contribution decreases by ∼50%.

Our results show that there are two Hb forms sensitive to the neutron irradiation of RBCs at a very low dose of 50 μGy. OxyHb and DeoxyHb change into Hb_{irr}. Additionally, OxyHb may transfer into $HbOH/H_2O$, which is resistant to the action of neutrons under our experimental conditions.

4 Conclusions

Mössbauer spectroscopy allowed us to gain an insight into possible changes of Hb in the RBC irradiated with neutrons at a very low dose of 50 μGy. We observed that only two Hb forms (OxyHb and DeoxyHb), which are physiologically active in O_2 transport, are sensitive to this neutron radiation. Inactive $HbOH/H_2O$ seems to be resistant to such a low dose of neutron radiation.

Acknowledgements The study was approved by the Bioethics Committee of Jagiellonian University (KBET/11/B/2009). This work was partially supported by the Grant of Polish Ministry of Science and Education No. N-N-402-471337 and its grants for Scientific Research (AGH WFiIS). This work was carried out within the BIONAN group.

References

1. Treleaven, J., Gennery, A., Marsh, J., Norfolk, D., Page, D., Parker, A., Saran, F., Thurston, J., Webb, D.: Guidelines on the use of irradiated blood components prepared by the British Committee for Standards in Haematology blood transfusion task force. Br. J. Haematol. **152**(1), 35–51 (2011)
2. Blue, T.E., Gupta, N., Woollard, J.E.: A calculation of the energy dependence of the RBE of neutrons. Phys. Med. Biol. **38**, 1693–1712 (1993)
3. Chambers, D.B., Osborne, R.V., Garva, A.L.: Choosing an alpha radiation weigthing factor for doses to non-human biota. J. Environ. Radioact. **87**,1–14 (2006)
4. Raju, M.R., Eisen, Y., Carpenter, S., Inkert, W.C.: Radiobiology of a particles. III. Cell inactivation by a-particle traversals of the cell nucleus. Rad Result. **128**, 204–209 (1991)
5. Petkau, A., Chelack, W.S.: Radioprotective effect of superoxide dismutase on model phospholipid membranes. Biochim. Biophys. Acta **433**, 445–456 (1976)
6. Petkau, A., Chelack, W.S., Pleskach, S.D.: Protection of post-irradiated mice by superoxide dismutase. Int. J. Radiat. Biol. **29**, 297–299 (1976)
7. Lang, G., Marshall, W.: Mössbauer effect in some hemoglobin compounds. Proc. Phys. Soc. **87**, 3–34 (1966)
8. Burda, K., Hrynkiewicz, A., Kołoczek, H., Stanek, J., Strzałka, K.: Mixed valence state in iron-porphyrin aggregates. Biochim. Biophys. Acta **1244**, 345–350 (1995)
9. Kaczmarska, M., Kopyściańska, Z., Fornal, M., Grodzicki, T., Matlak, K., Korecki, J., Burda, K.: Influence of low doses of gamma rays on the stability of erythrocytes. Acta Biochim. Pol. **58** (2011, paper in press No 14610)
10. Burda, K, Lekki, J., Dubiel, S., Cieślak, J., Lekka, M, Stanek, J., Stachura, Z.: Molecular mechanism of hemolysis caused by organometallic compounds. Appl. Organomet. Chem. **10**, 148–154 (2002)
11. Rancourt, D.G., Ping, J.-Y.: Voigt-based methods for arbitrary-shape static hyperfine parameter distributions in Mössbauer spectroscopy. Nucl. Instrum. Methods B **58**, 85–87 (1991)
12. Pauling, L.: Nature of the iron-oxygen bond in oxyhaemoglobin. Nature **203**, 182–183 (1964)
13. Weiss, J.J.: Nature of the iron-oxygen bond in oxyhaemoglobin. Nature **202**, 83–84 (1964)
14. Collman, J.P., Gagne, R.R., Reed, Ch.A., Robinson, W.T., Rodley, G.A.: Structure of an Iron (II) dioxygen complex: a model for oxygen carrying hemeprotein. Proc. Natl. Acad. Sci. USA **71**, 1326–1329 (1974)
15. Suzdalev, J.P.: Gamma resonance spectroscopy of proteins in model systems (in Russian). Moscow, Nauka (1988)
16. Chen, H., Ikeda-Saiko, M., Shoik, S.: Nature of the Fe-O_2 bonding in oxy-myoglobin: effect of the protein. J. Am. Chem. Soc. **30**, 14778–14790 (2008)
17. Stryer, L., Kendrew, J.C., Watson, H.C.: The mode of attachment of the azide to sperm whale metmyoglobin. J. Mol. Biol. **8**, 96–104 (1964)

18. Rhynard, D., Lang, G., Spartalian, K., Yonetani, T.: Moessbauer studies of low-symmetry crystal fields in low-spin ferric heme complexes. J. Chem. Phys. **71**, 3715–3719 (1979), FEBS Lett. **186**, 158–162 (1985)
19. Oshtrakh, M.I., Semionkin, V.A.: Moessbauer effect study of gamma-irradiated human oxyhemoglobin. Radiat. Envir. Biophys. **30**, 33–44 (1991)
20. Prusakov, V.E., Stukan, R.A., Davidov, R.M., Gersonde, K.: Non-equilibrium state of a monomeric insect haemoglobin induced by γ-irradiation and detected by Moessbauer spectroscopy. FEBS Lett. **186**, 158–162 (1985)

Hyperfine Interact (2012) 206:101–104
DOI 10.1007/s10751-011-0428-z

Aspartic acid interaction with cobalt(II) in dilute aqueous solution: A ^{57}Co emission Mössbauer spectroscopic study

Alexander A. Kamnev · Anna V. Tugarova · Krisztina Kovács · Zoltan Homonnay · Erno Kuzmann · Attila Vértes

Published online: 11 November 2011

Abstract Emission (^{57}Co) Mössbauer spectra of the aspartic acid—$^{57}CoCl_2$ system were measured at $T = 80$ K in frozen aqueous solution and in the form of a dried residue of this solution. The Mössbauer spectra, besides a weak contribution from after-effects, showed two Fe^{2+}/Co^{2+} components which were ascribed to octahedrally and tetrahedrally coordinated $^{57}Co^{II}$ microenvironments in the Asp–cobalt(II) complex. This dual coordination mode may be due to the involvement of the second terminal carboxylic group of aspartic acid in the coordination sphere of Co.

Keywords Cobalt(II) complexes · Aspartic acid · ^{57}Co emission Mössbauer spectroscopy

Abbreviations

EMS Emission Mössbauer spectroscopy
Asp Aspartic acid

1 Introduction

Interaction of amino acids and oligopeptides with transition metal ions is of general interest as an approach to modelling metal binding within the active centres of

The material was originally presented at the International Conference on the Applications of the Mössbauer Effect (ICAME 2011), 25–30 September 2011, Kobe, Japan.

A. A. Kamnev · A. V. Tugarova
Institute of Biochemistry and Physiology of Plants and Microorganisms, Russian Academy of Sciences, 410049, Saratov, Russia

K. Kovács · Z. Homonnay (✉) · E. Kuzmann · A. Vértes
Institute of Chemistry, Eötvös Loránd University, P.O.Box 32, 1518, Budapest, Hungary
e-mail: homonnay@ludens.elte.hu

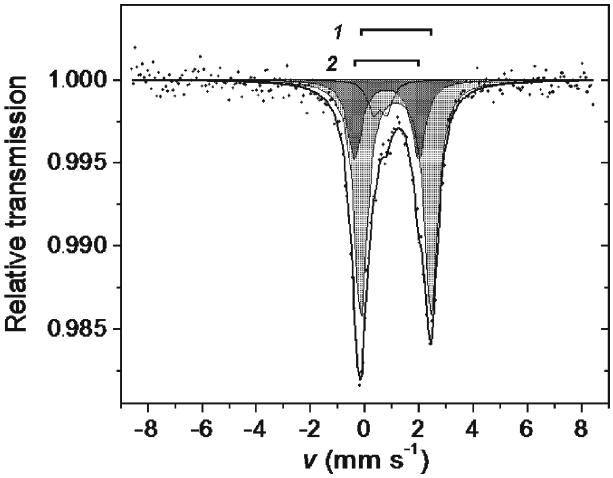

Fig. 1 Emission Mössbauer spectrum of aspartic acid (0.2 ml, 2 mM) incubated with 1.2 mCi $^{57}CoCl_2$ and then rapidly frozen in liquid nitrogen (dried solution; measured at $T = 80$ K). The positions of the two main doublets (1 and 2; shaded areas) corresponding to daughter $^{57}Fe^{II}$ forms (see Table 1, sample "Dried residue") are shown above the spectrum (the third weaker narrow doublet corresponds to daughter $^{57}Fe^{III}$ resulting from after-effects of the $^{57}Co \rightarrow {}^{57}Fe$ transition)

metalloenzymes, where usually a few amino acid residues form a specific cation-binding site [1, 2]. As for ^{57}Co emission Mössbauer spectroscopy (EMS), which has so far been rarely used in biological research [3–5], such studies are also necessary to form a database for a reliable interpretation of EMS data obtained for more complicated biological systems [4–6].

Aspartic acid (Asp; HOOC–CH(NH_2)–CH_2–COOH), an amino acid commonly present as a constituent in proteins [7], is also found, among other free amino acids, in plant root exudates [8]. K-Mg aspartate is a well-known medicine widely used in adjuvant therapy of heart diseases [9]. In addition, transition metal aspartates are used as a bioavailable form of mineral additives in feedstuff [10].

In this work, interaction of L-Asp with cobalt(II) ions in aqueous medium was studied using ^{57}Co EMS in frozen solution and for its dried residue.

2 Experimental

Emission Mössbauer spectra of the aspartic acid—$^{57}CoCl_2$ system (0.2 ml, 2 mM Asp, incubated with 4.5 MBq carrier-free $^{57}CoCl_2$ and then rapidly frozen in liquid nitrogen) were measured at $T = 80$ K in frozen aqueous solution. The air-dried residue of this solution was also measured at 80 K. Details of the measurement procedure were reported earlier [6]. The Mössbauer spectra were evaluated using the MOSSWINN program [11].

3 Results and discussion

A typical emission spectrum is shown in Fig. 1; the calculated Mössbauer parameters are listed in Table 1. For both the spectrum of the frozen aqueous solution and that of its dried residue, the best fit was achieved using three components, with two quadrupole doublets representing different high-spin daughter ferrous forms stabilised after the $^{57}Co \rightarrow {}^{57}Fe$ nuclear transition (see Table 1). The residual $^{57}Fe^{III}$,

Table 1 Mössbauer parameters calculated from ^{57}Co emission Mössbauer spectra for aspartic acid (0.2 ml, 2 mM) incubated with 1.2 mCi $^{57}CoCl_2$ and then rapidly frozen in liquid nitrogen (measured at $T = 80$ K, in frozen aqueous solution or dried)

Sample	Multiplet[a]	δ,[b] mm s^{-1}	Δ,[c] mm s^{-1}	Γ_{exp},[d] mm s^{-1}	A,[e] %
Frozen solution	Doublet 1	1.21(2)	2.82(3)	0.60(3)	72(7)
	Doublet 2	0.96(7)	2.3(1)	0.7(1)	19(8)
Dried residue	Doublet 1	1.15(1)	2.60(1)	0.59(2)	68(5)
	Doublet 2	0.80(3)	2.37(5)	0.63(7)	24(5)

[a]Main doublets corresponding to daughter $^{57}Fe^{II}$ forms stabilised after the $^{57}Co \rightarrow {}^{57}Fe$ nuclear transition (the residual $^{57}Fe^{III}$ forms result from after-effects). [b]Isomer shift (relative to α-Fe at room temperature). [c]Quadrupole splitting. [d]Full line width at half maximum. [e]Relative resonant absorption area. Calculated errors (in the last digits) are given in brackets.

which accounts for less than 10% of the spectral area in each spectrum, is due to after-effects [3, 5, 6]. Note that the resulting species under study using EMS may be described as an ^{57}Fe complex substituted for the 'parent' ^{57}Co binding site (retaining its geometry) [6]. In ^{57}Co emission Mössbauer spectra, lines are commonly broader than those in ^{57}Fe absorption experiments owing to special effects [5, 6, 12]. Thus the Γ_{exp} values obtained (see Table 1) are quite reasonable.

It should be noted that our earlier EMS data for other two amino acids, *o*-aminobenzoic (anthranilic) acid and tryptophan, showed one daughter $^{57}Fe^{II}$ component only in each case [6]. In the case of Asp, the presence of the second terminal carboxylic group (in addition to the typical carboxylic group with the neighbouring α-amino group) allows a dual coordination mode. Note that in the system studied, the Asp concentration (2 mM) was by ca. two orders of magnitude higher than that of $^{57}Co^{2+}$, allowing an equilibrium between the two complex forms in solution.

Thus, the parameters of doublet 1 (see Table 1) are typical for an octahedral coordination microenvironment of the parent high-spin $^{57}Co^{II}$ "inherited" by the daughter $^{57}Fe^{II}$. The significantly lower δ and Δ values for doublet 2 in both cases evidently represent tetrahedral coordination, which is relatively common for cobalt(II) complexes [1, 6].

4 Conclusions

^{57}Co emission Mössbauer spectra of the aqueous aspartic acid—$^{57}CoCl_2$ solution (both in frozen state and in dried form at $T = 80$ K) revealed two Co^{2+} components which can be ascribed to octahedral and tetrahedral $^{57}Co^{II}$ coordination in the Co^{II}-aspartic acid complex. This dual coordination mode can be interpreted as being due to the partial involvement of the additional terminal carboxylic group of aspartic acid in the coordination sphere of Co^{II}.

Acknowledgements This work was supported by NATO (Project ESP.NR.NRCLG 982857), Hungarian Science Fund (OTKA Projects K68135, 100424, K71215, NN84307), and under the Agreements on Scientific Cooperation between the Russian and Hungarian Academies of Sciences for 2008–2010 (Projects 45, 46) and for 2011–2013 (Projects 28, 29).

References

1. Holm, R.H., Kennepohl, P., Solomon, E.I.: Chem. Rev. **96**, 2239–2314 (1996)
2. Maret, W.: Metallomics **2**, 117–125 (2010)
3. Nagy D.L.: Hyperfine Interact. **83**, 3–19 (1994)
4. Nath A.: J. Nucl. Radiochem. Sci. **11**, A1–A3 (2010)
5. Kamnev, A.A.: J. Mol. Struct. **744–747**, 161–167 (2005)
6. Kamnev, A.A., Kulikov, L.A., Perfiliev, Y.D., Antonyuk, L.P., Kuzmann, E., Vértes, A.: Hyperfine Interact. **165**, 303–308 (2005)
7. Lee, T., Lin, Y.K.: Cryst. Growth Des. **10**, 1652–1660 (2010)
8. Simons, M., Permentier, H.P., de Weger, L.A., Wijffelman, C.A., Lugtenberg, B.J.J.: Mol. Plant-Microbe Interact. **10**, 102–106 (1997)
9. Iezhitsa, I.N., Spasov, A.A., Zhuravleva, N.V., Sinolitskii, M.K., Voronin, S.P.: Magnesium Res. **17**, 276–292 (2004)
10. Voronin, S.P., Golubov, I.I., Gumenyuk, A.P., Sinolitskii, M.K.: Bioavailable form of trace element additives to feed composites for animals and poultry. Patent of the Russian Federation No. 2411747, IPC A23K001/16 (2008)
11. Klencsár, Z., Kuzmann, E., Vértes, A.: J. Radioanal. Nucl. Chem. **210**, 105–118 (1996)
12. Perfiliev, Y.D., Rusakov, V.S., Kulikov, L.A., Kamnev, A.A., Alkhatib, K.: Hyperfine Interact. **167**, 881–885 (2006)

Hyperfine Interact (2012) 206:105–108
DOI 10.1007/s10751-011-0465-7

Mössbauer spectroscopy for characterizing biodegradation of magnetic nanoparticles in a living organism

Ilya Nikitich Mischenko · Michail Alexandrovich Chuev · Valeriy Mihailovich Cherepanov · Michail Alexeevich Polikarpov

Published online: 24 November 2011

Abstract We have developed a model for describing nanoparticles magnetic dynamics. This allows us to fit self-consistently the wide set of the experimental data, particularly, the evolution of Mössbauer spectral shape with temperature and external magnetic field as well as the magnetization curves for nanoparticles injected into mice. Thus, we reliably evaluate changes in characteristics of the nanoparticles and their chemical transformation to ferritin-like forms in mouse's organs as a function of time after injection of nanoparticles. Actually, the approach allows one to quantitatively characterize biodegradation and biotransformation of magnetic particles in a body.

Keywords Magnetic nanoparticles · Magnetic dynamics · Biodegradation

1 Introduction

Diverse shapes of the temperature- and field-dependent Mössbauer absorption spectra of magnetic nanoparticles (NP) obviously supplies one with a large amount of information about physical characteristics inherent to NP staying in different environment [1]. With that the longstanding ^{57}Fe Mössbauer spectroscopy is efficiently used to study spin states, electronic and dynamical properties of iron-containing proteins of animals and humans [2].

The main problem in interpreting the Mössbauer spectra of iron-containing NP injected into a living organism is to reliably decompose them into partial subspectra of exogenous iron atoms in NP and endogenous iron atoms [3]. The most adequate

I. N. Mischenko (✉) · M. A. Chuev · V. M. Cherepanov · M. A. Polikarpov
National Research Centre "Kurchatov Institute", 123182 Moscow, Russia
e-mail: IlyaMischenko@rambler.ru

M. A. Chuev
Institute of Physics and Technology, Russian Academy of Sciences, 117218 Moscow, Russia

model for describing the spectra is the multi-level relaxation model that takes into account their magnetic anisotropy and diffusion of uniform magnetization [4]. This model was efficiently used to fit the experimental spectra of an ensemble of magnetic NP at different temperatures, including NP injected into a living organism [3]. One more highly informative technique is based on measurements of the Mössbauer spectra of NP in a weak static magnetic field. A first-approximation theory for describing such spectra has been developed in the recent time [5, 6]. The theory can be extended within the multi-level relaxation model [4] on the basis of a model of magnetic dynamics developed in [5].

The main goal of this contribution is to demonstrate briefly the advantages of the theoretical approach to the self-consistent treatment of the temperature and field-dependent Mössbauer spectra for characterizing the biodegradation and biotransformation of magnetic NP in an organism by the example of behavior of NP injected into a mouse.

2 Samples

We have used commercially available ferrofluid "fluidMAG-ARA-250" (Chemicell Gmbh, Germany). The magnetic NP suspended in PBS were injected intravenously in tails of mice. At different time after the injection, the mice were sacrificed, organs extracted and lyophilized. The dried initial ferrofluid and lyophilized mouse's organs were then grinded and the powder samples were prepared for Mössbauer studies.

3 Relaxation model for describing the experimental data

The multi-level relaxation model for describing the Mössbauer spectra is based on the quantum-mechanical description of NP [4]. Calculations of the Mössbauer spectra within the model can be performed in terms of the stochastic approach according to which the absorption spectrum is described by the general expression [1, 4]:

$$\sigma(\omega) \propto -\mathrm{Im} \sum_{\alpha} |C_{\alpha}|^2 \langle W| \hat{A}_{\alpha}^{-1}(\omega) |1\rangle.$$

Here, $\alpha = (m_{\mathrm{e}}, m_{\mathrm{g}})$ specifies hyperfine transition with the nuclear spin projections m_{e} and m_{g} onto the $\mathbf{H}_{\mathrm{hf}}$ direction, C_{α} is the intensity of α-th transition, $\langle W|$ is the row vector of the equilibrium occupation probabilities of the stochastic states, $|1\rangle$ is a column vector with all components equal to unity. The operator $\hat{A}_{\alpha}(\omega)$ is defined by the diagonal matrix of hyperfine interaction and the relaxation matrix specified by the diffusion constant D [4].

The Mössbauer spectra of nanoparticles in a field can be described within a similar stochastic approach with operators of more general type [1, 6]:

$$\sigma(\omega) \propto -\mathrm{Im} \int \sin\Theta d\Theta \sum_{\eta} \mathrm{Sp}\left(\hat{V}_{\eta} \langle W| \hat{\mathbf{A}}^{-1}(\omega, \Theta) |1\rangle \hat{V}_{\eta}^{+}\right).$$

where Θ is the angle between the field direction and the particle's easy axis, $\hat{V}_{\eta}$ is the operator for the interaction of the gamma-quantum with a given polarization η and $\hat{\mathbf{A}}(\omega, \Theta)$ is a superoperator defined by the Liouville operators of hyperfine

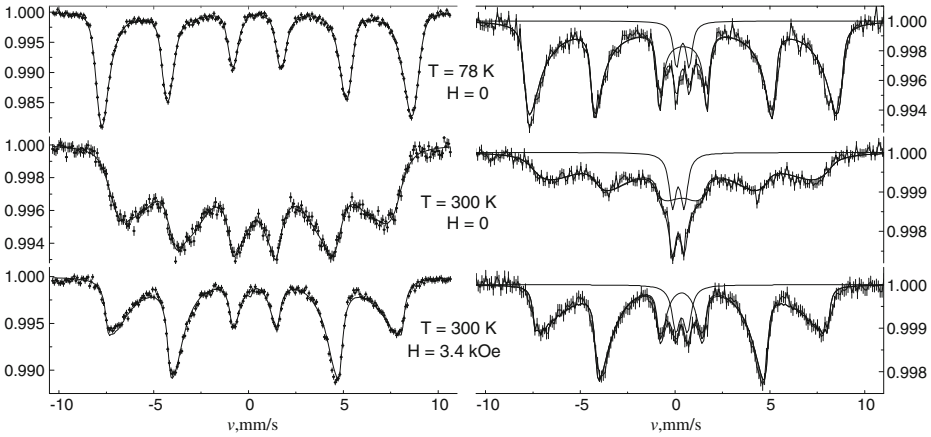

Fig. 1 ^{57}Fe Mössbauer spectra of initial NP (*left panel*) and a mouse liver 2 weeks after NP injection (*right panel*). Solid lines represent partial spectra of NP, calculated within the multi-level relaxation model, and ferritin-like contribution as well as the resulting spectra

interaction for each stochastic state and the relaxation matrix specified by the probabilities of transitions between the states [6].

4 Results

Using the formalism we have managed a least-squares fitting procedure to treat the set of experimental spectra (Fig. 1) and magnetization curves. This allows us to reliably characterize the sample with initial NP with estimates of: the average magnetic anisotropy energy $K\bar{V}/k_{\mathrm{B}} = 350 \pm 40\,\mathrm{K}$, the mean particle diameter $\bar{d} = 10.6 \pm 0.1\,\mathrm{nm}$, the Gaussian width of particle's size distribution $\sigma_d/\bar{d} = 0.21 \pm 0.03$, the critical field of magnetization reversal $H_{\mathrm{C}} = 1.62 \pm 0.08\,\mathrm{kOe}$, the ^{57}Fe concentration $n_{\mathrm{NP}} = (6.3 \pm 0.4) \cdot 10^{18}\ \mathrm{cm}^{-3}$, $D = 0.95 \pm 0.05$ mm/s and $H_{\mathrm{hf}} = 491.5 \pm 0.8$ kOe for $T = 300$ K.

An analogous fitting procedure has been applied to the spectra of the samples of mouse liver at different stages of biodegradation with an inclusion of additional variable parameters of a quadrupolar doublet, describing the contribution of ferritin-like proteins: the partial area, the isomer shift δ_{f}, and the quadrupolar splitting $2q$ [3]. The following principal physical parameters of the sample of mouse liver 2 weeks after NP injection have been evaluated: $K\bar{V}/k_{\mathrm{B}} = 50 \pm 20\,\mathrm{K}$, $\sigma_d/\bar{d} = 0.7 \pm 0.1$, $H_{\mathrm{C}} = 1.18 \pm 0.04$ kOe, $\delta_{\mathrm{f}} = 0.35 \pm 0.02$ mm/s and $2q = 0.60 \pm 0.03$ mm/s for $T = 300$ K.

Also, such an analysis allowed us to evaluate time evolution for NP and 'ferritin' concentrations: $n_{\mathrm{NP}} \cdot 10^{-18}\ (\mathrm{cm}^{-3}) = 5.8 \pm 0.5, 4.7 \pm 0.4, 2.1 \pm 0.3, 1.6 \pm 0.4$, and $n_{\mathrm{f}} \cdot 10^{-18}\ (\mathrm{cm}^{-3}) = 0.07 \pm 0.02, 0.08 \pm 0.01, 0.14 \pm 0.02, 0.63 \pm 0.04$ for the samples of mice sacrificed in 2 hours, 2 days, 2 weeks, 2 months after NP injection, respectively. These values were estimated from the partial spectral areas and recoilless fractions evaluated within the Debye model.

Thus, an analytical technique for characterizing the biodegradation and biotransformation of magnetic NP in an organism is developed and realized on the basis of self-consistent treatment of a minimal set of experimental data including three Mössbauer spectra taken at different temperatures and in a magnetic field as well as the magnetization curve for the sample studied.

Acknowledgement This work is supported by the Russian Foundation for Basic Research.

References

1. Chuev, M.A., Hesse, J.: Non-Equilibrium magnetism of single-domain particles for characterization of magnetic nanomaterials. In: Tamayo, K.B. (ed.) Magnetic Properties of Solids, pp. 1–104. Nova Science Publishers, New York (2009)
2. Papaefthymiou, G.C.: The Mössbauer and magnetic properties of ferritin cores. Biochim. Biophys. Acta **1800**, 886–897 (2010)
3. Chuev, M.A., Cherepanov, V.M., Deyev, S.M., Mischenko, I.N., Nikitin, M.P., Polikarpov, M.A., Panchenko, V.Y.: Interpretation of the Mössbauer spectra of the magnetic nanoparticles in mouse spleen. AIP Conf. Proc. **1311**, 322–328 (2010)
4. Jones, D.H., Srivastava, K.K.P.: Many-state relaxation model for the Mössbauer spectra of superparamagnets. Phys. Rev. **B34**, 7542–7548 (1986)
5. Chuev, M.A.: Mössbauer spectra of single-domain particles in a weak magnetic field. J. Phys.: Condens. Matter **20**(505201), 10(2008)
6. Chuev, M.A., Cherepanov, V.M., Polikarpov, M.A.: On the shape of the gamma-resonance spectra of slowly relaxing nanoparticles in a magnetic field. JETP Lett. **92**, 21–27 (2010)

Hyperfine Interact (2012) 206:109–114
DOI 10.1007/s10751-011-0451-0

Chemical proprieties of the iron-quinone complex in mutated reaction centers of Rb. sphaeroides

Agnieszka Hałas · Valerie Derrien · Pierre Sebban · Krzysztof Matlak · Józef Korecki · Jerzy Kruk · Květoslava Burda

Received: 1 September 2011 / Accepted: 27 October 2011 / Published online: 16 November 2011

Abstract We investigated type II bacterial photosynthetic reaction centers, which contain a quinone - iron complex (Q_A-Fe-Q_B) on their acceptor side. Under physiological conditions it was observed mainly in a reduced high spin state but its low spin ferrous states were also observed. Therefore, it was suggested that it might regulate the dynamical properties of the iron–quinone complex and the protonation and deprotonation events in its neighbourhood. In order to get insight into the molecular mechanism of the NHFe low spin state formation, we preformed Mössbauer studies of a wild type of *Rb. sphaeroides* and its two mutated forms. Our Mössbauer measurements show that the hydrophobicity of the Q_A binding site can be crucial for stabilization of the high spin ferrous state of NHFe.

Keywords Photosynthetic reaction center · Non-heme iron

International Conference on the Application of the Mössbauer Effect

A. Hałas · K. Burda
Faculty of Physics and Computer Science, Department of Medical Physics and Biophysics, AGH University, Kraków, Poland

V. Derrien · P. Sebban
Laboratoire de Chimie Physique, University of Paris XI, Orsay, France

K. Matlak · J. Korecki
Faculty of Physics and Computer Science, Department of Solid State Physics, AGH University, Kraków, Poland

J. Kruk
Faculty of Biochemistry, Biophysics and Biotechnology, Jagiellonian University, Kraków, Poland

K. Burda (✉)
Faculty of Physics and Computer Science, AGH University, al. Mickiewicza 30, 30–059 Kraków, Poland
e-mail: kvetoslava.burda@fis.agh.edu.pl

Abbreviations

Bacterial reaction center	BRC
Rhodobacter sphaeroides	*Rb. sphaeroides*
Rhodospirillum rubrum	*Rp. rubrum*
Quinone-iron complex	Q_A-Fe-Q_B
Non-heme iron	NHFe
Electron transfer	ET
Ubiquinone	UQ
Wild type	WT
Isomer shift	IS
Quadrupole splitting	QS

1 Introduction

The bacterial photosynthetic reaction center (BRC) is a membrane protein complex, which converts light energy into chemical free energy. BRC of *Rhodobacter sphaeroides (Rb.sphaeroides*), which belongs to purple bacteria, is considered as a model system to study the dynamical and structural proprieties of the photosynthetic reaction centers of type II. Each BRC is composed of three protein subunits L, M and H. The L and M proteins are connected on the acceptor side by the non-heme iron (NHFe) situated between the primary and secondary ubiquinone acceptor Q_A and Q_B, respectively. The ubiquinone is tightly bound to the Q_A site contrary to the one at the Q_B site. The Q_A ubiquinone, bound to the M subunit, is in a hydrophobic area whereas the Q_B ubiquinone, bound to the L subunit, is surrounded by charged and polar residues. The molecular mechanisms of the electron transfer between Q_A and Q_B ubiquinones have been a subject of challenging studies but the role of the NHFe, which is a very conservative component of RCs of the type II, in this process is still unknown [1, 2]. Especially the role of NHFe in stabilization of the Q_A and Q_B binding sites and in the primary electron transfer (ET) is not clear. A change of the NHFe valence state has never been detected in any system of type II [3]. But mixed spin states (low and high spin state) were observed in BRCs of *Rb. sphaeroides* and of *Rp. rubrum* [4, 5] and an exclusively low spin state in photosystem II of algae PSI^- mutant [6, 7]. We focused on studies of the NHFe valence and spin states in BRCs isolated form a wild type (WT) and two mutants of *Rb. sphaeroides* (see Fig. 1) [8, 9]. The double mutant, called later in this paper AA, has two point mutations near the Q_B acidic cluster: (L212Glu/L213Asp -> Ala/Ala). The triple mutant, called AATyr, has additionally a point mutation near the Q_A binding site (M249Ala->Tyr).

In our studies we applied Mössbauer spectroscopy to investigate the valence and spin state of the probing atom i.e. the isotope ^{57}Fe.

2 Materials and methods

The HIS tagged cells of *Rb.sphaeroides* (native and harbouring mutations) were grown in the medium deprived of natural iron and enriched with an iron isotope ^{57}Fe. The growing conditions and the BRC purification have previously been described

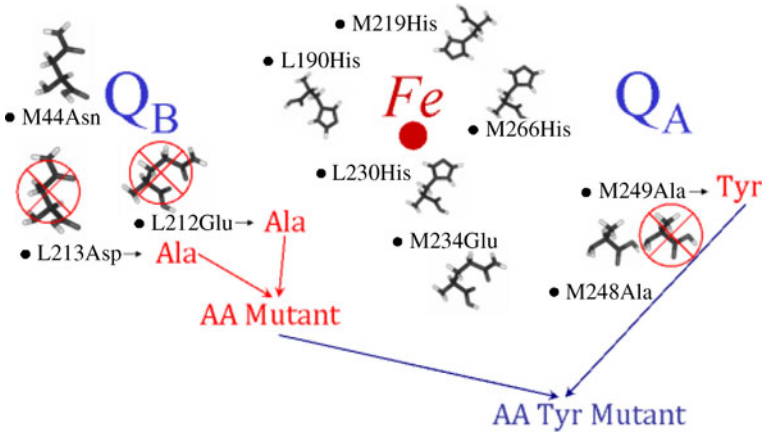

Fig. 1 The arrangement of amino acids at the proximity of the iron-quinone complex (Q_A-Fe-Q_B) in *Rb.sphaeroides*

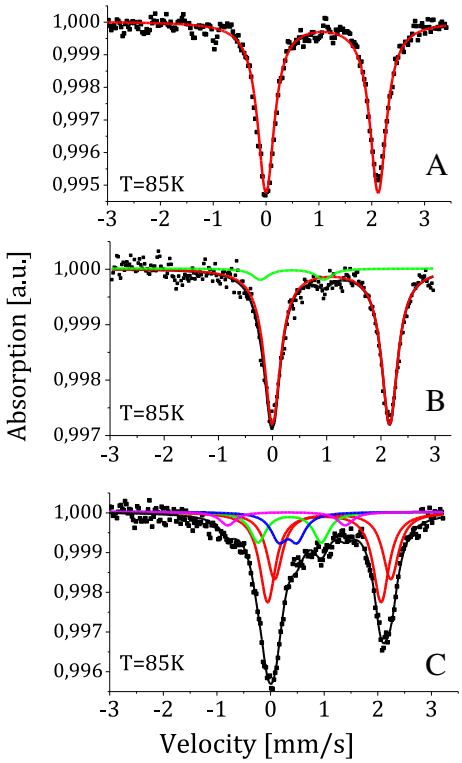

Fig. 2 Mössbauer spectra of WT (**a**), AA (**b**) and AATyr (**c**) BRC isolated from *Rb. sphaeroides*. The *solid lines* represent fits assuming symmetrical lorentzians. Different components are indicated by various colors. The spectra were measured at 85 K

in [9]. We used 900 nmol, 800 nmol and 1400 nmol in the WT, AA and AATyr BRCs, respectively. No differences were observed in the absorption spectra of the WT BRCs and its two mutated types (data not presented).The Mössbauer spectra were recorded in a home made cryostat using 50 mCi ^{57}Co/Rh and a proportional

Table 1 The hyperfine parameters of NHFe fitted to the Mössbauer spectra of WT, AA and AATyr BRCs

Hyperfine parameters	Component 1	Component 2	Component 3	Component 4	Component 5
WT					
IS [mm/s]	1,06 ± 0,01				
QS [mm/s]	2,12 ± 0,01				
A[%]	100 ± 2				
AA					
IS [mm/s]	1,08 ± 0,01		0,36 ± 0,10		
QS [mm/s]	2,16 ± 0,01		1,17 ± 0,20		
A[%]	93 ± 2		7 ± 1		
AA Tyr					
IS [mm/s]	1,15 ± 0,03	0,99 ± 0,03	0,25 ± 0,04	0,13 ± 0,05	0,17 ± 0,10
QS [mm/s]	2,12 ± 0,02	2,10 ± 0,03	0,98 ± 0,10	1,9 ± 0,1	0,44 ± 0,10
A[%]	38 ± 7	33 ± 6	10 ± 2	9 ± 1	10 ± 2

IS: isomeric shift, QS: quadrupole splitting. A: contribution in the spectrum. The line width in all cases was 0.18 ± 0.01 mm/s

counter to detect the radiation. The temperature stabilization was within 0.1 K. The isomer shifts are given vs. metallic Fe at room temperature. The recorded spectra were fitted using a Recoil program [10].

3 Results and discussion

In Fig. 2 we present Mössbauer spectra for BRCs of high purity obtained from wild type, AA and AATyr mutant of *Rb. sphaeroides.*

The hyperfine parameters of NHFe obtained from theoretical fits are given in Table 1.

The spectrum of WT BRCs is composed of a single doublet with hyperfine parameters characteristic for a high spin Fe^{2+} state [4, 11]. In the case of the AA mutant, the spectrum contains component of the high spin reduced state of the iron atom and a small contribution of a component, whose hyperfine parameters are more similar to those observed usually in the case of the reduced low spin state of the heme-iron in cytochromes [4, 12]. The AATyr spectrum is very different from those detected for WT and AA mutant BRCs. It requires five components to get a fit of good quality. The two components having isomer shift (IS) of about 1 mm/s are typical for a high spin ferrous state. Our estimation of this spectrum with a distribution of a quadrupole splitting (QS) showed that we can deconvolute this part of the spectrum using two sub-spectra. Component with IS = 0.13 mm/s and QS = 1.9 mm/s is more typical for iron in octahedral coordination, when one of the perpendicular ligands has a different character than the others. It is very often observed for heme - iron ligated with O_2 [13] but in our BRCs we have six-coordinated non-heme iron, what means that at least one of its ligands had to be modified in comparison to the state when NHFe occurs in a high Fe^{2+} state. The sub-spectrum with QS ≈ 1.0 mm/s is most probably related to the same NHFe state which is observed in the AA mutant but having a higher symmetry of the binding site. The sub-spectrum with the lowest quadrupole is related to the low spin ferrous state

of NHFe. Its hyperfine parameters do not change with the increasing temperature. A similar NHFe state was already observed in other photosynthetic systems of type II [4–7]. To understand the complexity of the AATyr spectra we performed measurements of the amount of ubiquinone binding at the Q_B site per reaction center using HPLC [14]. The ratio of ubiquinone Q_B per reaction center is 0.24, 0.77 for WT and AA, respectively, and no ubiquinone at this site was detected for AATyr BRCs. From those results, it turns out that the occupation of the Q_B site by UQ is not directly related to the state of NHFe. It was already shown in the reconstitution experiments, when independently of the amount of bound UQ at the Q_B site, only high spin ferrous state of NHFe was observed [11]. Therefore, we suggest that the presence of various states of NHFe in the case of AATyr BRCs is caused by the modification of the hydrophobicity in the vicinity of the Q_A binding site, whose differences between the double AA and triple AATyr mutant are confirmed (see Fig. 1).

4 Conclusion

The presented results suggest that the spin state of NHFe is not sensitive to the presence of the ubiquionone at the Q_B site but it is easily affected by the hydrogen network in the vicinity of the Q_A binding site. Especially, the hydrophobic character of the Q_A binding site is very important for the stabilization of the high spin ferrous state of NHFe, having been proved by the obtained Mössbauer spectra for the AATyr mutant in which M249Ala was substituted into a hydrophilic amino acid, tyrosine. The planned temperature dependent measurements will show if this modification of the acceptor site near the Q_A binding site may also influence the local flexibility of NHFe.

Acknowledgements This work was supported partially by grant No N N302 195035 (2008–2011) from Polish Ministry of Science and Higher Education. The groups cooperate within the BIONAN project. Project operated within the Foundation for Polish Science MPD Programme co-financed by the EU European Regional Development Fund. (A.H)

References

1. Kleinfeld, D., Okamura, M.Y., Feher, G.: Electron-transfer kinetics in photosynthethic reaction centers cooled to cryogenic temperatures in the charge-separated state: evidence for light-induced structural changes. Biochemistry **23**, 5780–5786 (1984)
2. Burda, K: Dynamics of electron transfer in photosystem II. Cell Biochem. Biophys. **47**(2), 271–284 (2007)
3. Hermes, S., Bremm, O., Garczarek, F., Derrien, V., Liebisch, P., Loja, P., Sebban, P., Gerwert, K., Haumann, M.: A time-resolved iron-specific x-ray absorption experiment yields no evidence for an Fe^{2+} to Fe^{3+} transition during Q_A^- to Q_B electron transfer in the photosynthetic reaction center. Biochemistry **45**(2), 353–359 (2006)
4. Orzechowska, A., Lipinska, M., Fiedor, J., Chumakov, A., Zajac, M., Slezak, T., Matlak, K., Strzalka, K., Korecki, J., Fiedor, L., Burda, K.: Coupling of collective motions of the protein

matrix to vibrations of the non-heme iron in bacterial photosynthetic reaction centers. Biochim. Biophys. Acta. Bioenerg. **1797**, 1696–1704 (2010)
5. Lipinska, M., Orzechowska, A., Fiedor, J., Chumakov, A.I., Slezak, T., Zajac,M., Matlak, K., Korecki, J., Hałas, A., Strzalka, K., Fiedor, L., Burda, K.: Influence of Cd^{2+} on the spin state of non-heme iron and on protein local motions in reactions centers from purple photosynthetic bacterium Rhodospirilium rubrum. J. Phys.: Conf. Ser. **217**, 012021(ICAME 2009) 135 (2010)
6. Burda, K., Kruk, J., Borgstädt, R., Stanek, J., Strzalka, K, Schmid, G.H., Kruse, O.: Low spin ferrous state of the non-heme iron in a Chlamydomonas reinhardtii PSI- mutant. FEBS Lett. **535**, 159–165 (2003)
7. Burda, K., Kruk, J., Strzałka, K., Stanek, J., Schmid G.H., Kruse, O.: Moessbauer studies of Cu(II) ions interaction with the non-heme iron and cytochrome b559 in a Chlamydomonas reinhardtii PSI minus mutant. Acta Physica Polonica A **109**, 237–247 (2006)
8. Tandori, J., Baciou, L., Alexov, E., Maroti, P., Schiffer, M., Hanson, D.K., Sebban, P.: Revealing the involvment of extended hydrogen-bond networks in the cooperative function between distant sites in bacterial centers. J. Biol. Chem. **276**, 45513–45515 (2001)
9. Sacquin-Mora, S., Sebban, P., Derrien, V., Frick, B., Lavery, R., Alba-Simionesco, C.: Probing the flexibility of the bacterial reaction center: the wild-type protein is more rigid than two site-specific mutants. Biochemistry **46**, 14960–14968 (2007)
10. Rancourt, D.G., Ping, J.-Y.: Voigt-based methods for arbitrary-shape static hyperfine parameter distributions in Mössbauer spectroscopy. Nucl. Instr. Methods B **58**, 85–97 (1991)
11. Debus, R.J., Feher, G., Okamura, M.Y.: Iron-depleted reaction centers from Rhodopseudomonas sphaeroides R-26. 1: characterization and reconstitution with Fe2+, Mn2+, Co2+, Ni2+, Cu2+, and Zn2+. Biochemistry **25**, 2276–2287 (1986)
12. Garbers, A., Reifarth, F., Kurreck, J., Renger, G., Parak, F.: Correlation between protein flexibility and electron transfer from Q_A^{-*} to Q_B in PSII membrane fragments from spinach. Biochemistry **37**, 11399–11404 (1998)
13. Lang, G., Marshall, W.: Mössbauer effect in some hemoglobin compounds. Proc. Phys. Soc. **87**, 3–34 (1966)
14. Kruk, J., Trebst, A.: Plastoquinol as a singlet oxygen scavenger in photosystem II. BBA Bioenergetics **1777**, 154–162 (2008)

Hyperfine Interact (2012) 206:115–118
DOI 10.1007/s10751-011-0521-3

Mössbauer effect of Ni-doped strontium ferrite

Naoki Miyajima · Kazuyuki Akasaka · Takeshi Waki · Yoshikazu Tabata · Yoshinori Kobayashi · Hiroyuki Nakamura

Received: 30 August 2011 / Accepted: 30 November 2011 / Published online: 20 December 2011

Abstract We applied ^{57}Fe Mössbauer spectroscopy to determine occupation sites of Ni atoms in the hexagonal M-type strontium ferrite. From spectral analyses of $Sr_{1-x}La_xFe_{11.6-x}Ni_xO_{19}$ with $x \leq 0.35$ at room temperature, we propose that Ni atoms occupy preferentially octahedral Fe ($12k$, $4f_2$ and $2a$) sites.

Keywords M-type hexagonal ferrite · Mössbauer effect · Site assignment

1 Introduction

The hexagonal magnetoplumbite-type (M-type) strontium ferrite is widely used as a permanent magnet owing to its excellent cost performance and high chemical stability. Thus, the improvement in its magnetic performance makes great impact on various fields. In $SrFe_{12}O_{19}$, the substitution of the transition-metal element Co is known to improve performance as a hard magnet [1, 2]. Since the Fe sublattice consists of five crystallographic sites (octahedral $12k$, $4f_2$, $2a$, tetrahedral $4f_1$, and bipyramidal $2b$), it is important to assign the sites occupied preferentially by Co atoms to know the function of Co and further to develop new advanced magnets in the next generation. For the sake, we have employed the Mössbauer measurements to confirm the Co occupation sites in $(Sr^{2+}\text{-}La^{3+})(Fe^{3+}\text{-}Co^{2+})_{12}O_{19}$, and obtained experimental results (Akasaka et al. unpublished manuscript) being thoroughly consistent with previous ones such as in [3], indicating that Co atoms occupy preferentially octahedral $4f_2$ (and possibly $2a$) site(s). This has been supported by Raman

N. Miyajima (✉) · K. Akasaka · T. Waki · Y. Tabata · H. Nakamura
Department of Materials Science and Engineering, Kyoto University, Kyoto 606-8501, Japan
e-mail: miyajima.naoki.7n@kyoto-u.ac.jp

Y. Kobayashi
Magnetic Materials Research Laboratory, NEOMAX Company, Hitachi Metals, Ltd.,
2-15-17 Egawa, Shimamoto-cho, Mishima-gun, Osaka 618-0013, Japan

spectroscopy [4]. However, this argument was found to be in discordance with the conclusion obtained recently from simultaneous analyses of neutron diffraction and extended X-ray absorption fine structure (EXAFS) spectra, which excludes $4f_2$ and $2b$ sites as possible Co occupation sites [5]. Furthermore, in previous studies, Co occupation at the $4f_1$ site has actually been suggested from neutron diffraction [6] and NMR measurements [3]. X-ray magnetic circular dichroism (XMCD) measurements also indicated that Fe atoms at the $4f_1$ site are replaced by Co [5]. This discrepancy may originate in the site assignment in Mössbauer analyses, for example, incorrect assignment between $4f_1$ and $4f_2$ sites with the same atomic fraction. However, a resent first-principle calculation (Ikeno and Tanaka, private communication) showed that sequences of calculated hyperfine parameters at the five different sites are completely consistent with the previous experimental assignment [7], excluding such a possibility of the incorrect assignment. Thus, as another approach to find out the origin of this discrepancy, we plan to check the consistency between Mössbauer and other experimental methods by measuring another system substituted by a different transition metal element. Here, we report a part of the study, Mössbauer results of Ni-doped strontium ferrites.

2 Experimental procedures

A series of powder samples were synthesized by solid state reaction by using powder materials $SrCO_3$, $La(OH)_3$, NiO, and Fe_2O_3. The raw materials were weighed in the nominal ratio in a chemical formula $Sr_{1-x}La_xFe_{11.6-x}Ni_xO_{19}$ ($x \leq 0.35$), mixed with a ball mill in water, dried at 432 K for 24 h in air, and calcined at 1523 K for 20 h in air. ^{57}Fe Mössbauer spectra were recorded with a conventional constant-acceleration-type spectrometer using a ^{57}Co(Rh) source at room temperature.

3 Results and discussion

Figure 1 shows the Mössbauer spectrum of $Sr_{0.8}La_{0.2}Fe_{11.4}Ni_{0.2}O_{19}$ at room temperature, as an example of experimental spectra. The spectrum was fitted assuming the presence of five different Fe sites. As a first step, possible emergence of Fe^{2+} atoms at the $2a$ site [8] was neglected. One may see relatively large discordance at some minor peaks, which is mainly ascribed to this simplification. In fact, the information only at room temperature may not be sufficient in this kind of analysis with a lot of fitting parameters. In the present case, we relied on the previous comprehensive analysis for the non-doped sample [3], used predetermined hyperfine parameters as initial values for the fitting, and confirmed that this method works well to discuss the Co occupation site in the Co-doped system.

Hyperfine parameters (isomer shift, quadrupole split and hyperfine field) obtained in the analysis are plotted against the Ni concentration, x, in Fig. 2. Concentration dependences of the parameters are not marked, and general trends are in agreement with those of Co-doped system (Akasaka et al. unpublished manuscript). Occupation ratios of Fe atoms for the Ni-doped system, which were estimated from integrated spectral intensities, are plotted in Fig. 3. Here we fixed the ratio of the $4f_1$ site to a constant value, four, because preliminary free-parameter fitting clearly

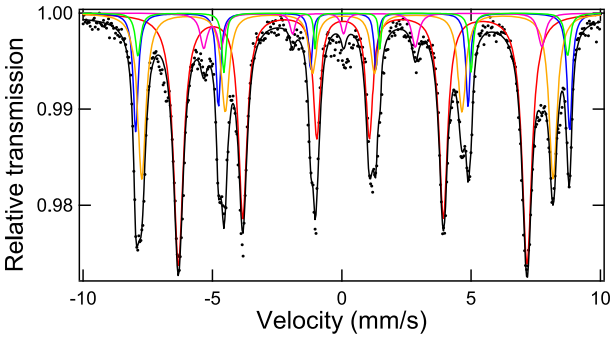

Fig. 1 Mössbauer spectrum of $Sr_{0.8}La_{0.2}Fe_{11.4}Ni_{0.2}O_{19}$ at room temperature fitted assuming the presence of five different Fe sites (*red*: 12*k*, *blue*: 4 f_2, *yellow*: 4 f_1, *green*: 2*a*, *purple*: 2*b*)

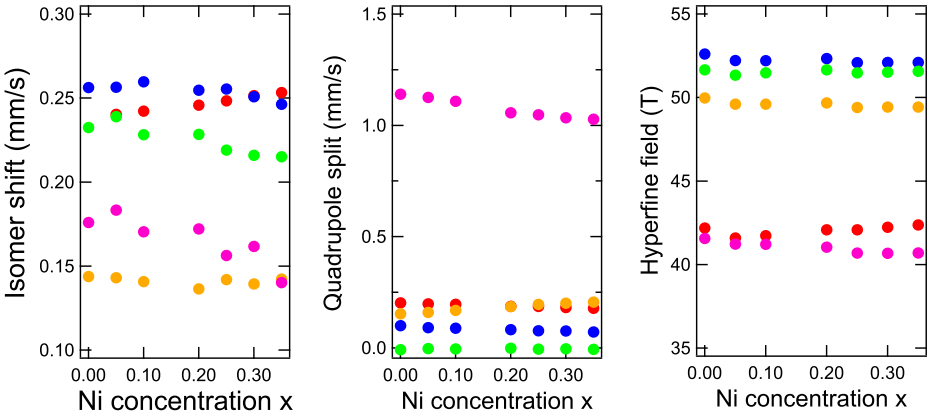

Fig. 2 Hyperfine parameters of $Sr_{1-x}La_xFe_{11.6-x}Ni_xO_{19}$ at room temperature plotted against the Ni concentration, *x*. See Fig. 1 for the symbol color

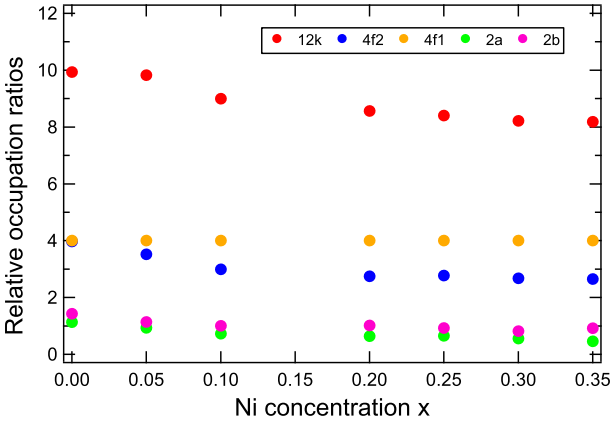

Fig. 3 Relative occupation ratios of Fe atoms in $Sr_{1-x}La_xFe_{11.6-x}Ni_xO_{19}$ plotted against the Ni concentration, *x*. The ratio of the 4 f_1 site was fixed to four

indicated that it does not decrease with x. Thus, relative values with respect to four for the $4f_1$ site are plotted for the other sites in the figure. The intensity ratio of $12k$, $4f_1$, $4f_2$, $2a$ and $2b$ for the non-doped sample is not 12 : 4 : 4 : 2 : 2, which is possibly ascribed to the anisotropic Debye-Waller factor depending on the site and/or the presence of some defects in the compounds. As seen in the figure, the intensities of $12k$, $4f_2$ (and possibly $2a$) sites decrease appreciably with the Ni substitution, suggesting Ni atoms occupy nearly randomly the octahedral sites.

In conclusion, Mössbauer experiments suggest that Ni atoms occupy octahedral $12k$, $4f_2$ (and possibly $2a$) sites in Ni-substituted M-type ferrites, $Sr_{1-x}La_xFe_{11.6-x}Ni_xO_{19}$ ($x \leq 0.35$). We are planning to make other experiments such as neutron diffraction and X-ray absorption fine structure measurements in order to cross-check with the present Mössbauer result and elucidate the origin of the discrepancy in the Co-doped sites.

Acknowledgements The authors are indebted to Prof. I. Tanaka and Dr. H. Ikeno for valuable discussion on first-principle calculations of hyperfine parameters, and to Prof. E. Matsubara for discussion on XAFS. This work was supported by "Kyoto Environmental Nanotechnology Cluster" as one of the projects in the Knowledge Cluster Initiative of the Ministry of Education, Culture, Sports, Science and Technology (MEXT), Japan.

References

1. Iida, K., Minachi, Y., Masuzawa, K., Kawakami, M., Nishio, H., Taguchi, H.: J. Magn. Soc. Japan **23**, 1093 (1999)
2. Ogata, Y., Takami, T., Kubota, Y.: J. Jpn. Soc. Powder Powder Metallurgy **50**, 636 (in Japanese) (2003)
3. Wiesinger, G., Müller, M., Grössinger, R., Pieper, M., Morel, A., Kools, F., Tenaud, P., Le Breton, J.M., Kreisel, J.: Phys. Status Solidi A **189**, 499 (2002)
4. Morel, A., Le, J.M., Breton, Kreisel, J., Wiesinger, G., Kools, F., Tenaud, P.: J. Magn. Magn. Mater. **242**–**245**, 1405 (2002)
5. Kobayashi, Y., Oda, E., Nishiuchi, T., Nakagawa, T.: J. Ceram. Soc. Jpn. **119**, 285 (2011)
6. Le Breton, J.M., Wiesinger, G., Tellez Blanco, C., Isnard, O., Teillet, J., Grössinger, R., Morel, A., Kools, F., Tenaud, P.: In: Proc. 8th Int. Conf. on Ferrites, Kyoto, p. 199 (2000)
7. Evans, B.J., Grandjean, F., Lilot, A.P., Vogel, R.H., Gerard, A.: J. Magn. Magn. Mater. **67**, 123 (1987)
8. Van Diepen, A.M., Lotgering, F.K.: J. Phys. Chem. Solids **35**, 1641 (1974)

Hyperfine Interact (2012) 206:119–124
DOI 10.1007/s10751-011-0480-8

An enthalpy of solution of platinum in iron studied by ^{57}Fe Mössbauer spectroscopy

Robert Konieczny · Rafał Idczak · Jakub Elsner · Jan Chojcan

Published online: 29 November 2011

Abstract The room temperature Mössbauer spectra of ^{57}Fe were measured for iron-based solid solutions $Fe_{1-x}Pt_x$ with x in the range $0.01 \leq x \leq 0.05$. The obtained data were analysed in terms of the binding energy E_b between two platinum atoms in the studied materials using the extended Hrynkiewicz–Królas idea. It was found that for $x < 0.05$ the energy is positive or Pt atoms interact repulsively. The extrapolated value of E_b for $x = 0$ was used for computation of the enthalpy H_{Fe-Pt} of solution of platinum in iron. The result $H_{Fe-Pt} = -0.62(16)$ eV/atom was compared with the corresponding values resulting from the semi-empirical Miedema's model of alloys and the proper data obtained with Calphad's calculations as well as theoretical computations on the basis of the modified embedded-atom model. The comparison shows that all mentioned values of H_{Fe-Pt} are in a qualitative agreement i.e. they are negative, and moreover our findings agree also quantitatively with the Miedema's model predictions.

Keywords Mössbauer spectroscopy · Enthalpy of solution · Binding energy · Iron alloys

1 Introduction

It has been proved that the ^{57}Fe Mössbauer spectroscopy is a useful tool for the study of interactions of impurity atoms dissolved in iron [1–5]. The technique is especially powerful when the impurity neighbours of the Mössbauer probe have a sufficiently large effect on the hyperfine field generated at the probe, to yield distinguishable components in the Mössbauer spectrum attributed to different configurations of the probe neighbours. Nevertheless, our present studies [6] show that the technique can

R. Konieczny (✉) · R. Idczak · J. Elsner · J. Chojcan
Institute of Experimental Physics, University of Wrocław, pl. M. Borna 9, 50-204 Wrocław, Poland
e-mail: robi@ifd.uni.wroc.pl

be also successfully applied to binary iron systems for which one observes unresolved Mössbauer spectra. The facts are worth noticing as the impurity interactions are simply related to the enthalpy of solution of the impurity elements in iron [7] and the enthalpy is widely used in developing and testing different models of binary alloys as well as methods for calculating the alloy parameters [8–12]. Moreover, the Mössbauer spectroscopy findings concerning the enthalpy in some cases can be useful to verify the corresponding experimental data derived from the calorimetric studies [13, 14]. The possibility is limited because the calorimetric investigations are performed in relatively high temperatures at which most of iron systems are in their high-temperature γ (fcc) phases whereas the Mössbauer studies provide information about enthalpy of solution in low-temperature α (bcc) phase. All the above encouraged us to use the ^{57}Fe Mössbauer spectroscopy for supplying the experimental enthalpy of solution of different elements in α-Fe.

In this paper we present results of the enthalpy investigations of the Fe-Pt system. For the system the shape of a spectrum is directly affected by atoms located in the first two coordination shells of the probing nuclei, but the Pt atoms have relatively small effect on the hyperfine field generated at the probe ^{57}Fe [15] and the spectrum measured is unresolved so simple study of annealed samples only does not give satisfied results. That is why to obtained proper data we performed the present studies such as previously for the Fe-Ni and Fe-Co systems [6].

2 Experimental and results

The samples of $Fe_{1-x}Pt_x$ alloys with x equal to 0.01, 0.02, 0.03, 0.04 and 0.05 were prepared by melting the Aldrich 99.999% pure iron and 99.9% pure platinum in an arc furnace filled with argon. The ingots were cold-rolled to the final thickness of about 0.02 mm and then the room temperature ^{57}Fe Mössbauer spectra were measured for the foils by means of a constant-acceleration POLON spectrometer of standard design. In the next step the samples were annealed in vacuum at 1270 K for 2 h. After that they were slowly cooled to room temperature during 6 h. Under these conditions, diffusion effectively stops at about 700 K [16], so the observed distributions of atoms in the annealed specimens should be the frozen-in state corresponding to 700 K (the 'freezing' temperature T_d). Spectra for these samples are presented in Fig. 1

All the obtained spectra were analysed in terms of three six-line patterns corresponding to different hyperfine fields B at ^{57}Fe nuclei generated by different numbers of Fe and Pt atoms located in the first two coordination shells of the probing nuclei. It was done under assumption that the influence of n Pt atoms on B as well as the corresponding isomer shift (IS) is additive and independent of the atom positions in the neighbourhood of the nuclear probe so the relationship between B, IS and n can be written as follows:

$$\begin{aligned} B(n) &= B + n\Delta B_{1,2} \\ IS(n) &= IS + n\Delta IS_{1,2} \end{aligned} \tag{1}$$

where $\Delta B_{1,2}$ ($\Delta IS_{1,2}$) stand for the changes of B (IS) with one Pt atom in the first or second coordination shell of the Mössbauer probe. At the same time the quadruple splitting (QS) of a subspectrum is a free parameter [17]. In most cases the above assumptions are enough to obtain reasonable results. However, platinum neighbours

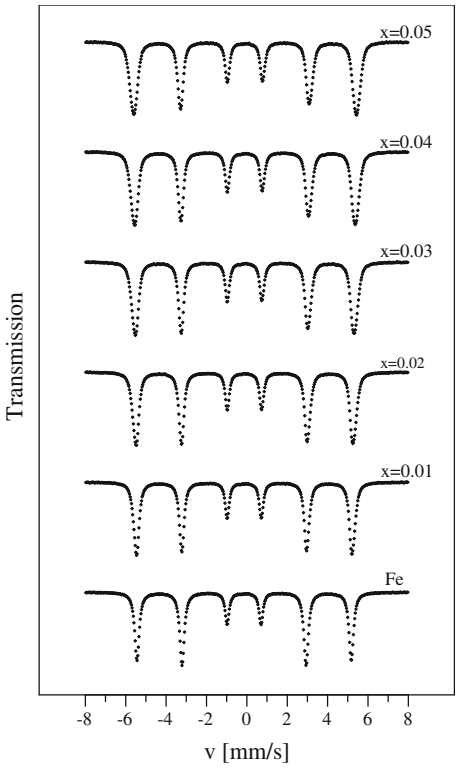

Fig. 1 The room temperature ^{57}Fe Mössbauer spectra for $Fe_{1-x}Pt_x$ alloys annealed in vacuum at 1,270 K for 2 h and slowly cooled to room temperature

Table 1 Some of the best-fit parameters of the assumed model of the ^{57}Fe Mössbauer spectrum measured for as-obtained samples of $Fe_{1-x}Pt_x$ alloys

x	B_0 [T]	$\Delta B_{1,2}$[T]	IS_0[mm/s] (relative to α-Fe)	$\Delta IS_{1,2}$[mm/s]
0.01	33.217(10)	0.9535(87)	0.0057(25)	0.0149(82)
0.02	33.346(11)	1.0220(52)	0.0130(26)	0.0146(49)
0.03	33.435(14)	0.9235(45)	0.0195(29)	0.0131(39)
0.04	33.579(19)	0.9500(45)	0.0291(32)	0.0110(36)
0.05	33.686(22)	0.9525(41)	0.0383(36)	0.0079(34)

The standard uncertainties for the parameters result from the variance of the fit

of the Mössbauer probe have a very small effect on the hyperfine field generated at the probe—see Fig. 1, so proper decomposition of the Mössbauer spectra to several components is impossible without additional assumptions on parameters of the components. The successful analysis of the experimental data was performed by taking into account two series of the spectra, measured for samples as-obtained in an arc furnace and after a certain heat treatment—see [6] for details. It is worth noticing that the fits obtained under these assumptions are quite good and the found values of the best-fit parameters (displayed in Table 1) are in quantitative agreement with corresponding data given in the literature; e.g. in Ref. [15]. The results were

Table 2 The binding energy E_b between a pair of Pt atoms in $Fe_{1-x}Pt_x$ alloys deduced from the ^{57}Fe Mössbauer spectra

x	c_1	c_2	$p(1)$	$p(2)$	E_b(eV)
0.01	0.1449(10)	–	0.1229	0.0081	–
0.02	0.2647(11)	0.01282(27)	0.2153	0.0286	0.069(13)
0.03	0.3715(17)	0.0521(14)	0.2827	0.0568	0.0272(77)
0.04	0.4155(18)	0.0944(14)	0.3294	0.0892	0.0141(49)
0.05	0.4434(20)	0.1683(15)	0.3593	0.1229	−0.0089(19)

The standard uncertainties for c_1 and c_2 result from the variance of the fit of the assumed model to the spectrum measured. The values of uncertainty for E_b were computed assuming that the uncertainty for the 'freezing' temperature T_d is 50 K

Table 3 The enthalpy H_{Fe-Pt} [eV/atom] of solution of platinum in iron

Miedema's model [11]	MEAM (γ-Fe) [18]	CALPHAD (γ-Fe) [19]	This work (α-Fe)
−0.585	−1.14	−1.18	−0.62(16)

used to determine parameters c_1 and c_2 for annealed samples (Table 2). Assuming that the Lamb-Mössbauer factor is independent of the configuration of atoms in the surroundings of the ^{57}Fe nucleus, the c parameters describe intensities of the components of a spectrum which are related to the existence of one and two Pt atoms in the two first coordination shells of ^{57}Fe.

Using the c_1 and c_2 values we calculated the binding energy E_b for pairs of Pt atoms in the studied materials (Table 2). The computations were performed, as in Refs. [1–6], on the basis of the modified Hrynkiewicz-Królas formula [1] for a $Fe_{1-x}D_x$ system

$$E_b = -kT_d \ln\left((1 + 2c_2/c_1)\,(c_2/c_1)\,(1 + 2p\,(2)\,/p\,(1))^{-1}\,(p\,(2)\,/p\,(1))^{-1}\right). \quad (2)$$

The E_b values are presented in Table 2.

In the next step we found the extrapolated value of E_b for $x = 0$ using $E_b(0.02)$ and $E_b(0.03)$. Finally, the $E_b(0)$ value was used for computation of enthalpy H_{Fe-Pt} of solution of platinum in iron. The calculations were performed on the basis of the Królas model [7] for the binding energy according to which:

$$H_{Fe-Pt} = -z \cdot E_b\,(0)\,/2, \quad (3)$$

where z is the coordination number of the crystalline lattice ($z = 8$ for α-Fe). The result is displayed in Table 3 together with proper value resulting from the Miedema's model of alloys [11] as well as with corresponding findings obtained with the modified embedded-atom model (MEAM) [18] and CALPHAD calculation [19] for γ (fcc) iron.

3 Conclusions

The positive values of the binding energy E_b between a pair of platinum atoms in the dilute iron-based Fe-Pt alloys speaks in favor of the suggestion that Pt atoms interact repulsively in iron matrix.

The enthalpy H_{Fe-Pt} of solution of platinum in iron determined from the ^{57}Fe Mössbauer spectra, −0.62(16) eV/atom, and the corresponding value of H_{Fe-Pt} resulting from the Miedema's model of alloys, −0.585 eV/atom, are practically the same or they are in a very good quantitative agreement. The result is interesting because the Mössbauer spectroscopy delivers information on the enthalpy of solution of platinum in the α (bcc) phase of Fe, being at about 700 K or in the ferromagnetic state whereas the semiempirical Miedema's model is based on calorimetric data which concern iron systems at relatively high temperatures at which they are paramagnetic. In other words the findings suggest that the experimental H_{Fe-Pt} value is practically independent of the magnetic order of iron and its temperature when the temperature exceeds 700 K.

The absolute values of H_{Fe-Pt} for γ (fcc) iron, resulting from the modified embedded-atom model (MEAM) [18] as well as calculations with the CALPHAD method [19] are about twice the value obtained by us for α-Fe. The difference is large enough to think that the unlike structure of the considered systems is not the only reason for that.

Acknowledgements This work was supported by the University of Wrocław under the grant 1466/M/IFD/11.

References

1. Chojcan, J.: Interaction between impurity atoms of 3d transition metals dissolved in iron. J. Alloys Compd. **264**, 50 (1998)
2. Chojcan, J.: A dilute-limit heat of solution of 3d transition metals in iron studied with ^{57}Fe Mössbauer spectroscopy. Hyperfine Interact. **156/157**, 523 (2004)
3. Chojcan, J.: Interactions between V atoms in iron-based Fe-V solid solutions. J. Alloys Comp. **350**, 62 (2003)
4. Chojcan, J., Ostrasz, A.: A dilute-limit heat of solution of aluminium in iron studied with ^{57}Fe Mössbauer spectroscopy. Acta Phys. Pol. A **114**, 1573 (2008)
5. Chojcan, J., Konieczny, R., Ostrasz, A., Idczak, R.: A dilute-limit heat of solution of molybdenum in iron studied with ^{57}Fe Mössbauer spectroscopy. Hyperfine Interact. **196**, 377 (2010)
6. Idczak, R., Konieczny, R., Konieczna, Ż, Chojcan, J.: An enthalpy of solution of cobalt and nickel in iron studiem with ^{57}Fe Mössbauer spectroscopy. Acta Phys. Polon. A **119**, 37 (2011)
7. Królas, K.: Correlation between impurity binding energies and heat of formation of alloys. Phys. Lett. A **85**, 107 (1981)
8. Bonny, G., Pasianot, R.C., Malerba, L., Caro, A., Olsson, P., Lavrentiev, M.Yu.: Numerical predictions of thermodynamic properties of iron-chromium alloys using semi-empirical cohesive models: the state of the art. J. Nucl. Mater. **385**, 268 (2009)
9. Boom, R., De Boer, F.R., Niessen, A.K., Miedema, A.R.: Enthalpies of formation of liquid and solid binary alloys based on 3d metals. Physica **115B**, 285 (1983)
10. Dursun, I.H., Güvenç, Z.B., Kasap, E.: A simple analytical EAM model for some bcc metals. Commun. Nonlinear Sci. Numer. Simulat. **15**, 1259 (2010)
11. Miedema, A.R.: Energy effects and charge transfer in metal physics, modeling in real space. Physica B **182**, 1 (1992)
12. Lejaeghere, K., Cottenier, S., Claessens, S., Waroquier, M., Van Speybroeck, V.: Assessment of a low-cost protocol for an ab inito based prediction of the mixing enthalpy at elevated temperatures: the Fe-Mo system. Phys. Rev. B **83**, 184201 (2011)
13. Hultgren, R., Desai, P.D., Hawkins, D.T., Gleiser, M., Kelley, K.K.: Selected Values of Thermodynamic Properties of Binary Alloys. American Society for Metals, Metals Park, Ohio (1973)
14. Swartzendruber, L.J., Itkin, V.P., Alcock, C.B.: In: Okamoto, H. (ed.) Phase diagrams of binary iron alloys. Materials Information Society, Materials Park, Ohio (1993)
15. Vincze, I., Campbell, I.A.: Mössbauer measurements in iron based alloys with transition metals. J. Phys. F **3**, 647 (1973)

16. Cranshaw, T.E.: A Mössbauer study of ^{119}Sn in alloys of iron with Si, Al, and Rh: interaction potentials and phase diagrams. J. Phys.: Condens. Matter **1**, 829 (1989)
17. Falepin, A., Cottenier, S., Comrie, C.M., Vantomme, A.: Interpreting Mössbauer spectra reflecting an infinite number of sites: an application to $Fe_{1-x}Si$ synthesized by pulsed laser annealing. Phys. Rev. B **74**, 184108 (2006)
18. Kim, J., Koo, Y., Lee, B.-J.: Modified embedded-atom method interatomic potential for the Fe–Pt alloy system. J. Mater. Res. **21**, 199 (2006)
19. Fredriksson, P., Sundman, B.: A thermodynamic assessment of the Fe–Pt system. Calphad **25**, 535 (2001)

Hyperfine Interact (2012) 206:125–129
DOI 10.1007/s10751-011-0462-x

Si/Al influence on $Fe_{70}Al_{30-x}Si_x$ alloys

E. Legarra · F. Plazaola · E. Apiñaniz

Published online: 22 November 2011

Abstract The main aim of this work is to study the influence of silicon/aluminium ratio in the structural and magnetic properties of ordered $Fe_{70}Al_{30-x}Si_x$ alloys by means of X-ray diffraction, Mössbauer spectroscopy and magnetic (SQUID) measurements.

Keywords Fe intermetallics · Mossbauer spectroscopy · Magnetic inhomogeneities

1 Introduction

Around the $Fe_{75}Al_{25}$ content, the phase diagram of Fe-Al alloys presents a transition from B2 to D03 structure (decreasing temperature). Within this range, the magnetic behaviour is complex, particularly around 30 at% Al. Indeed, with decreasing temperature the magnetic behaviour of $Fe_{70}Al_{30}$ goes from ferromagnetic through superparamagnetic-like behaviour to end in a spin-glass like state [1]. Small angle neutron scattering experiments in alloys around 30 at% Al show magnetic clusters that evolve with temperature [2, 3]. Si, like Al, is a non-magnetic element and it has only one p electron more than Al, so Si is a very appropriate adding element for studying the complex magnetic behaviour of Fe-Al alloys. It is also worth noting that Fe-Si and Fe-Al alloys have the same ordered (D03 and B2) structures [4]. The main

E. Legarra · F. Plazaola (✉)
Elektrizitatea eta Elektronika Saila, Euskal Herriko Unibertsitatea, UPV/EHU,
p. k. 644, 48080 Bilbao, Spain
e-mail: fernando.plazaola@ehu.es

E. Apiñaniz
Fisika Aplikatua I Saila, Euskal Herriko Unibertsitatea, UPV/EHU,
Urkixo zumarkalea z/g, 48013 Bilbao, Spain

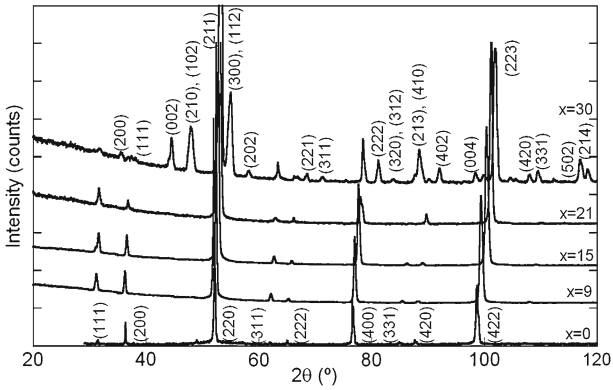

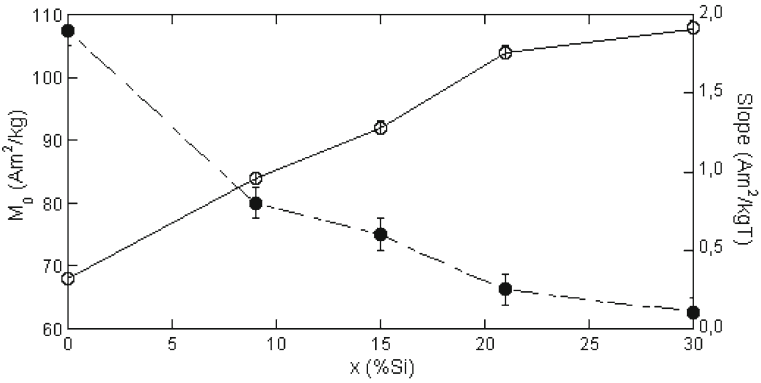

Fig. 1 XRD of $Fe_{70}Al_{30-x}Si_x$ alloys. x = 0–30 alloys show cubic phases. $D8_8$ is also present in x = 30

Fig. 2 M_0 (empty circles) and slope (filled circles) curves of $Fe_{70}Al_{30-x}Si_x$ alloys at RT (see text)

aim of this work is to study the influence of silicon/aluminium ratio in the structural and magnetic properties of ordered $Fe_{70}Al_{30-x}Si_x$ alloys.

2 Experimental

Induction melting obtained samples were powered by mechanical crushing. To obtain large domains of ordered structures, they were annealed at 1223 K, then cooled down to 1023 K and kept at this temperature for 3 h; after they were cooled down to 823 K and kept there for 1 week (in order to obtain great amount of D03 structure). The samples were studied by X-ray diffraction (XRD), magnetic measurements and Mössbauer spectroscopy. NORMOS program [5] was used to fit the spectra obtained in transmission geometry with ^{57}Co-Rh.

3 Results and discussion

In the XRD of $Fe_{70}Si_{30}$ (see Fig. 1) there is one structure that is not present in the other samples: the hexagonal $D8_8$, but even the minimum Al content makes this structure disappear. The long-range order parameter is very close to 1 and

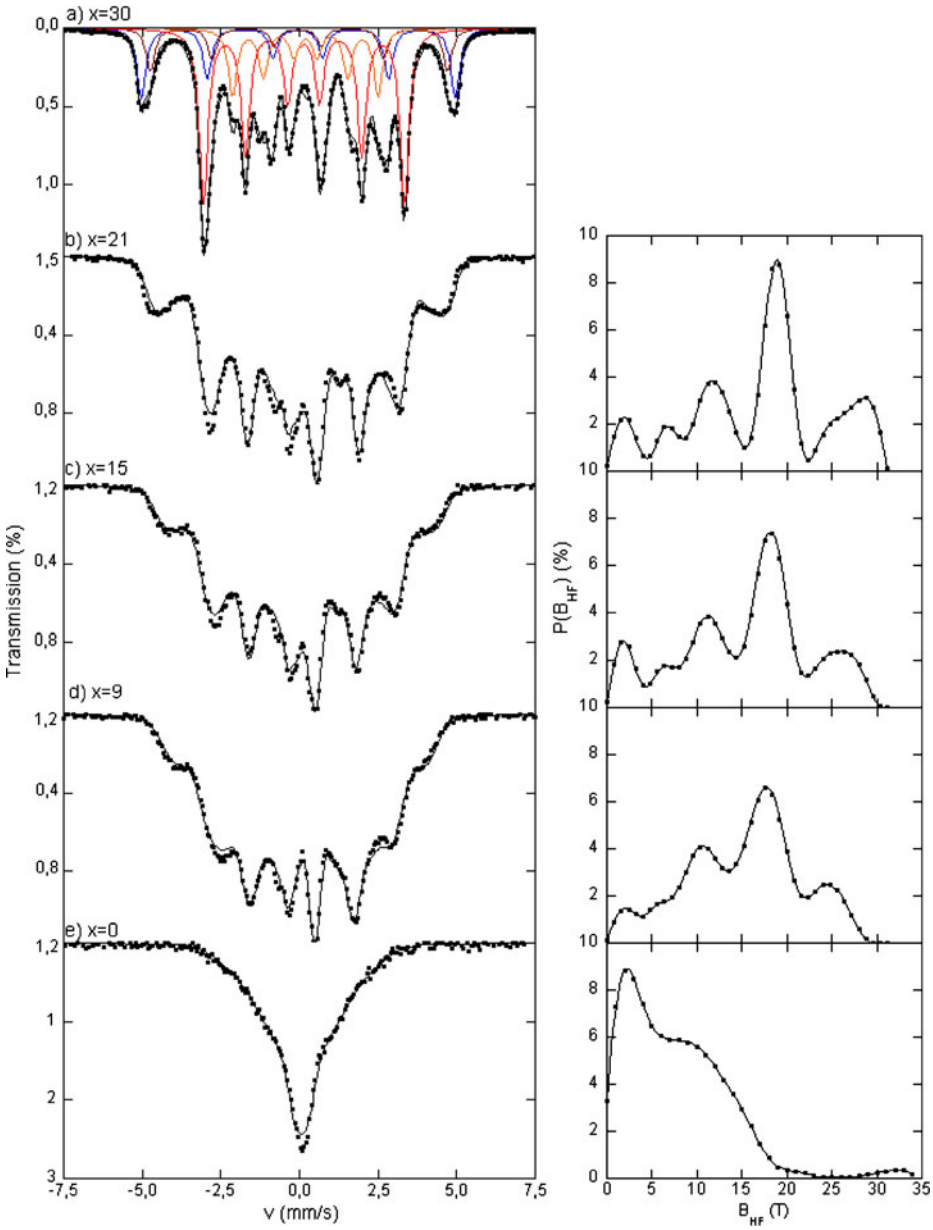

Fig. 3 Mössbauer spectra of $Fe_{70}Al_{30-x}Si_x$ alloys at RT and the corresponding P(Bhf)

the increase of Si/Al ratio makes the lattice parameter of D03 decrease linearly. However, by means of XRD it is very difficult to obtain the amount of D03 and B2 ordered structures because reflections are located at the same angles. Anyway, Fig. 1 shows a clear variation of the ratio of (111) and (200) peak intensities, indicating the presence of B2 structure in the samples with large Al content.

Figure 2 shows M_0, linear fit of the magnetization between 4T and 7T extrapolated to zero applied field, and its slope versus Si content. M_0 decreases with Al content, but the magnetization slope at high fields increases. The M(H) curve of $Fe_{70}Si_{30}$ alloy is the unique that saturates at high fields. It indicates that $Fe_{70}Si_{30}$ is the only alloy that is in a classical ferromagnetic state. The Mössbauer spectra of the binary alloys $Fe_{70}Si_{30}$ and $Fe_{70}Al_{30}$ are very different (see Fig. 3). The first one can be fitted using discrete sextets. Indeed, it has been fitted with two sextets corresponding $D8_8$ (Fe_5Si_3) structure and 4 to the D03 one. The fit of D03 structure indicates the amount of Fe in it is 73%, in good agreement with the fact that $D8_8$ structure needs an excess of Si atoms with respect to the nominal one.

However, the Mössbauer spectrum of $Fe_{70}Al_{30}$ sample, similar to the spectrum obtained by other authors [6, 7], can only be fitted by means of a continuous distribution of B_{hf} fields. Indeed, the fit by means of a hyperfine field distribution (see Fig. 3) shows that the larger contribution is centred at 2 T, and contributions of B_{hf} up to 20 T decrease monotonously. Even though, Mössbauer spectra of ternary alloys can be well fit with 4 discrete sextets (whose width increases in relation to $x = 30$ alloy) and one doublet, Fig. 3 shows the fit performed with a continuous distribution of B_{hf}. $P(B_{hf})$ indicates clearly that with Al content increase the B_{hf} of the observed bumps decreases, and they get wider and merge into two wide bumps located at 2T and 10T. Assuming that the width of each bump is only due to different Al/Si chemical configuration around Fe, one would expect the maximum width to occur at $x = 15$ (the minimum should be at $x = 0$ and $x = 30$). However, the width of the bumps increases with Al content and the maximum is observed in $x = 0$ alloy. Therefore, the change of the structural chemical surroundings of Fe positions by Al/Si substitution in these very ordered alloys is not the cause of the observed behaviour in Mössbauer spectra. Its origin must be on magnetic grounds. On the other hand, Fig. 2 shows that the introduction of Al produces a deviation from classical ferromagnetic behaviour, which increases with increasing Al content. So, these results clearly suggest the latter behaviours must be correlated. Moreover, Figs. 2 and 3 show that M_0 and the maximum B_{hf} decrease with Al content increase in the alloy.

4 Conclusions

Al addition makes $D8_8$ phase present in $Fe_{70}Si_{30}$ alloy disappear. Magnetic measurements and Mössbauer data show that Si addition to $x = 0$ alloy changes completely and monotonically the complex magnetism, related to magnetic inhomogeneities [2, 3], to a classic ferromagnetic behaviour. So, the influence of Si and Al in the magnetism of Fe in this alloy series is opposite.

Acknowledgements Acknowledgement is given to the Basque and the Spanish Governments under Grants IT-443–10 and MAT2009–14398.

References

1. Shull, R.D., Okamoto, H., Beck, P.A.: Solid State Commun. **20** 863 (1976)
2. Motoya, K., Shapiro, S.M., Muraoka, Y.: Phys. Rev. B **28** 6183 (1983)

3. Martin-Rodriguez, D., Plazaola, F., del Val, J.J., Garitaonandia, J.S., Cuello, G.J., Dewhurst, C.: J. Appl. Phys. **99**, 08H502 (2006)
4. Schmid, F., Binder, K.: J. Phys.: Condens. Matter **4**, 3569 (1992)
5. Brand, R.A., Lauer, J., Herlach, D.M.: J. Phys. F: Met. Phys. **13**, 675 (1983)
6. Takahashi, S., Onodera, H., Li, X.G., Miura, S.: J. Phys.: Condens. Matter **6**, 9235 (1997)
7. Schmool, D.S., Araujo, E., Amado, M.M., Feio, M.A., Rodriguez, D.M., Garitaonandia, J.J.S., Plazaola, F.: J. Magn. Magn. Mater. **1342**, 272–276 (2004)

Hyperfine Interact (2012) 206:131–134
DOI 10.1007/s10751-011-0492-4

Mössbauer study of mechanical deformation induced order-disorder transition in $Fe_{75}AlSi$ alloys

Estibaliz Legarra · Fernando Plazaola · Estibaliz Apiñaniz · Jose Angel Garcia · Jose Javier Saiz Garitaonandia

Published online: 29 November 2011

Abstract We study the influence of different Al/Si ratios on the magnetic and structural properties of mechanically disordered powder $Fe_{75}Al_{25-x}Si_x$ alloys. The results indicate that addition of Si to binary Fe-Al alloys makes the disordering more difficult. The study of the hyperfine fields indicates that there is an inversion of the behavior of the hyperfine field of the Fe atoms surrounded by 8 Fe atoms with disordering. The magnetic and hyperfine measurements indicate that the influence of Si is opposite to the one of Al in the magnetism of Fe atoms.

Keywords Fe based ternary alloys · Mössbauer spectroscopy · Mechanical deformation

1 Introduction

There is not much information about the influence of the mechanical deformation in the magnetism of Fe-Si alloys [1, 2]. However, there are many studies about the influence of the mechanical deformation in the magnetism of Fe-Al alloys, where the order-disorder transition induces a dramatic reinforcement of the magnetism of the samples [3]. The most common explanation to this phenomenon is related to changes in the nearest-neighbor configuration with the disordering, that is to say, to the disorder around Fe atoms. However, Hernando et al. [4], taking into account the

E. Legarra · F. Plazaola (✉) · J. A. Garcia · J. J. S. Garitaonandia
Zientzia eta Teknologia Fakultatea, Euskal Herriko Unibertsitatea, UPV/EHU, p. k. 644, 48080 Bilbao, Spain
e-mail: fernando.plazaola@ehu.es

E. Apiñaniz
Fisika Aplikatua I Saila, Euskal Herriko Unibertsitatea, UPV/EHU, Urkixo zumarkalea z/g, 48013 Bilbao, Spain

lattice parameter increase associated with the disorder of these alloys, suggested that the magnetic reinforcement was also related to changes in volume.

In this work we study systematically the influence of different Al/Si ratios on the magnetic and structural properties of mechanically disordered powder $Fe_{75}Al_{25-x}Si_x$ alloys by means of Mössbauer spectroscopy, X-ray diffraction and magnetic measurements.

2 Experimental

The samples have been obtained by means of induction melting. Afterwards, they were powdered and annealed to obtain large domains of ordered structures. The annealed samples were milled by means of a planetary ball mill Retsch PM4. The milling was made with a ball:powder rate of 10:1 and three balls of 10 mm diameter at 295 rpm. Jars and balls were of Chrome steel. We have used Co K_α radiation with a Broker-AXS Discover Bragg-Brentano difractometer and the Rietveld method to analyse the diffractograms. The Mössbauer spectroscopy has been performed in transmission geometry with a ^{57}Co-Rh source. The spectra were fitted with NORMOS Program [9]. Magnetic measurements were performed in a SQUID magnetometer (Quantum Design MPMS) at 300 K from 0–7 T.

3 Results and discussion

The main non-equivalent positions in ordered $Fe_{75}Al_{25-x}Si_x$ are the ones corresponding to Fe atoms surrounded by 8 Fe atoms (8Fe) and 4 Fe atoms (4Fe).

Figure 1 shows Mössbauer spectra of milled alloys for 1 and 5 milling hours. The spectra fit indicates that the disorder is very high (characterized by disordered A2 structure content, in which the binomial distribution gives population probabilities of around 10% to 8Fe and 4Fe environments) in all samples after 5 milling hours. However, after 1h of milling time $Fe_{75}Si_{25}$ alloy is not highly disordered, as subspectra related to the most populated 8Fe and 4Fe non-equivalent positions of stoiquiometric D03 structure are majority (only 28% of A2 structure). Nevertheless, the disorder of the alloy increases with Al content in the alloy. The content of A2 structure versus milling time (not shown) indicates that after 3h of milling time all the samples are highly disordered, but while the disorder of ternary alloys continues increasing towards 100% A2, the disorder on $Fe_{75}Si_{25}$ alloy saturates at 83%.

Figure 2 shows that the evolution of the saturation magnetization (M_s) with milling time and Si content in the alloy is similar to the one shown by $<B_{hf}>$, the mean hyperfine field. Their values decrease with milling time in the alloys with Si content higher or equal to 12.5at%, but increase in the alloys with Si content less or equal to 7.5at%. The behaviour observed clearly indicates that the introduction of Si in the binary $Fe_{75}Al_{25}$ alloy opposes the magnetic behaviour induced by Al in the magnetism of Fe in these alloys [3]. Indeed, for alloys with Si content below around 10 at% the magnetic behaviour of the completely disordered alloys is like the one found in alloys of the Fe rich side of the FeAl phase diagram, M_s and $<B_{hf}>$ increase

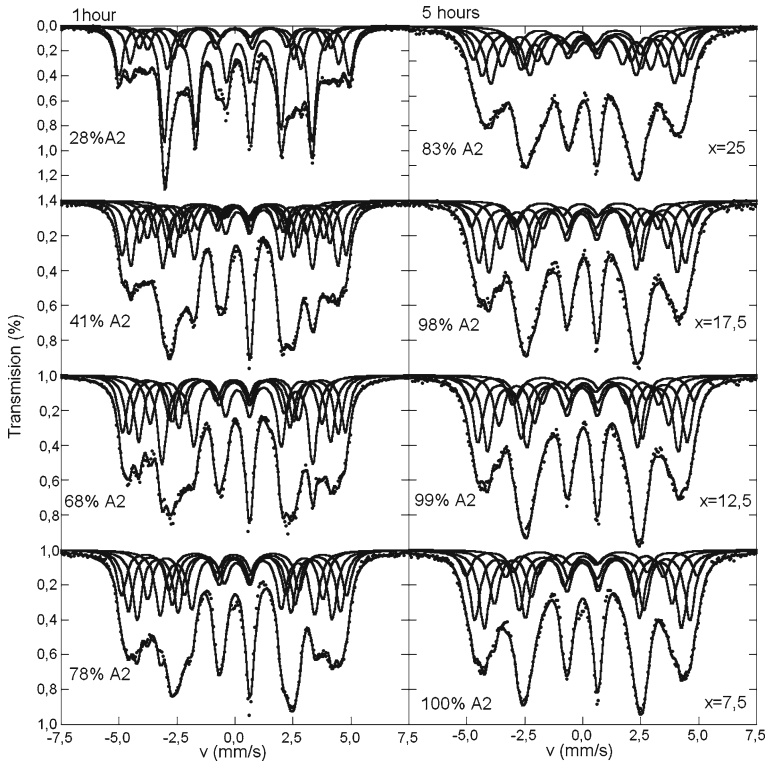

Fig. 1 Mössbauer spectra of 1 hour and 5 hours milled $Fe_{75}Al_{25-x}Si_x$ alloy series

with disorder [5]; however, in the case of alloys with a Si content above ~10 at% the behavior is the opposite: M_s and $<B_{hf}>$ decrease with disorder.

Figure 2 shows the evolution of B_{hf} with the disorder for 4Fe and 8Fe non-equivalent positions, B_{hf}(4Fe) and B_{hf}(8Fe), too. It is observed that the behaviour of B_{hf}(4Fe), the most populated in D03 structure, follows a relatively similar trend to the one found in $<B_{hf}>$, but in the case of the alloy x = 7.5 there is a small decrease of the B_{hf}(4Fe) in the first 2 hours of milling, and it increases afterwards. On the other hand, B_{hf}(8Fe) is very sensitive to the disorder introduced and it shows an inversion in the trend in respect to the one found in the ordered alloy (0 h). In the ordered alloys B_{hf}(4Fe) increases with Si decrease and this trend is maintained in the disordering. However, in the case of the ordered B_{hf}(8Fe) it increases with Si content in the alloy but this trend changes during milling time to show, in the completely disordered samples, the opposite behaviour. Therefore, after complete deformation of the alloy, both non-equivalent Fe positions show the same trend (opposite to that of the ordered alloys); that is to say, the B_{hf}(4Fe) and B_{hf}(8Fe) increase with Si content decrease. The inversion of the B_{hf} behaviour in the disordering process makes 8Fe non-equivalent position very sensitive to the degree of disordering in $Fe_{75}Al_{25-x}Si_x$ alloy system.

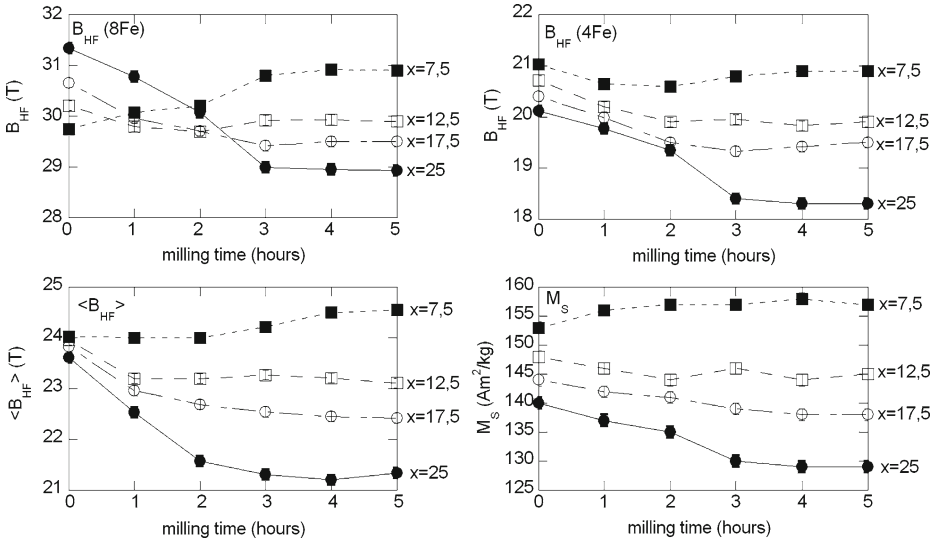

Fig. 2 B_{hf} versus milling time of 4Fe and 8Fe positions, $<B_{hf}>$ and M_S of $Fe_{75}Al_{25-x}Si_x$

4 Conclusions

The addition of Si to binary $Fe_{75}Al_{25}$ alloy makes the disordering more difficult. The hyperfine fields of $Fe_{75}Al_{25-x}Si_x$ alloy series indicate that there is a redistribution of non-ferrous atoms around Fe atoms with the disordering; indeed, there is an inversion of the behavior of the hyperfine field of non-equivalent positions of Fe atoms. The addition of Si to binary $Fe_{75}Al_{25}$ alloys opposes the magnetic behavior induced by Al in the magnetism of Fe in these alloys.

Acknowledgements Authors want to acknowledge the Basque Government and the Spanish CICYT under Grants IT-443-10 and MAT2009-14398.

References

1. Elsukov, E.P., Konygin, G.N., Barinov, V.A., Voronina, E.V.: J. Phys.: Condens. Matter **4**, 7597 (1992)
2. Lehlooh, A.F., Fallad, S.M., Mahmood, S.H.: Hyperfine Interact. **139/140**, 335 (2002)
3. Apiñaniz, E., Plazaola, F., Garitaonandia, J.S., Martín, D., Jiménez, J.A.: J. Appl. Phys. **93**, 7649 (2003)
4. Hernando, A., Amils, X., Nogues, J., Suriñach, S., Baro, M.D., Ibarra, M.R.: Phys. Rev. B **58**, 11864 (1998)
5. Zamora, L.E., Perez Alcaraz, G.A., Velez, G.Y., Betancur, J.D., Marco, J.F., Romero, J.J., Martinez, A., Palomares, F.J., Gonzalez, J.M.: Phys. Rev. B **79**, 094418 (2009)

Hyperfine Interact (2012) 206:135–139
DOI 10.1007/s10751-011-0481-7

An enthalpy of solution of rhenium in iron studied by ^{57}Fe Mössbauer spectroscopy

Robert Konieczny · Rafał Idczak · Weronika Szarypo · Jan Chojcan

Published online: 24 November 2011

Abstract The room temperature Mössbauer spectra of ^{57}Fe were measured for iron-based solid solutions $Fe_{1-x}Re_x$, with x in the range $0.01 \leq x \leq 0.05$. The obtained data were analysed in terms of the binding energy E_b between two rhenium atoms in the Fe-Re system. The extrapolated value of E_b for $x = 0$ was used for computation of enthalpy of solution of rhenium in iron. The result was compared with that resulting from the cellular atomic model of alloys by Miedema. The comparison shows that our findings are in a qualitative agreement with the Miedema's model predictions.

Keywords Mössbauer spectroscopy · Binding energy · Enthalpy of solution · Iron alloys

1 Introduction

The ^{57}Fe Mössbauer spectroscopy is a useful tool for the study of interactions of impurity atoms dissolved in iron [1–8]. At the same time from the findings concerning the impurity interactions one can easily derive the enthalpy of solution of the impurity elements in iron [9]. This considerably increases importance of the studies as the experimental values of the enthalpy play an essential role in developing and testing different models of binary alloys as well as methods for calculating the alloy parameters [10–16]. The main source of such experimental data is calorimetric study of the enthalpy of formation of binary systems [17]. Unfortunately, sometimes there are significant discrepancies in the data obtained by different authors. This is observed e.g. for the Fe-V alloys [18, 19]. Moreover, the calorimetric investigations are

R. Konieczny (✉) · R. Idczak · W. Szarypo · J. Chojcan
Institute of Experimental Physics, University of Wrocław,
pl. M. Borna 9, 50-204 Wrocław, Poland
e-mail: robi@ifd.uni.wroc.pl

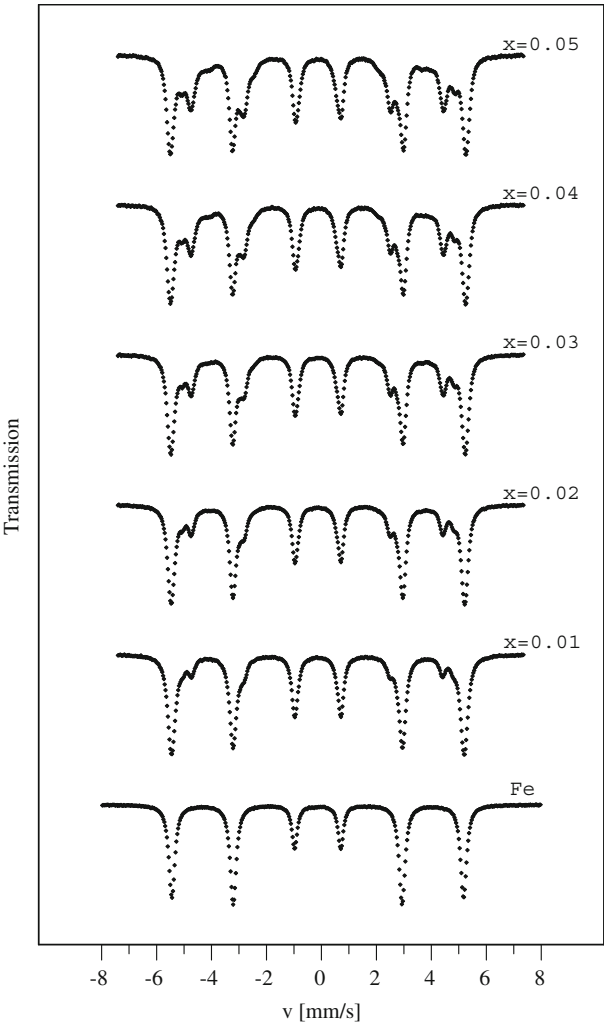

Fig. 1 The ^{57}Fe Mössbauer spectra for the $Fe_{1-x}Re_x$ alloys measured at room temperature after the annealing process at 1270 K

performed in relatively high temperatures at which some of iron systems are in their high-temperature γ (fcc) phases. Such situation exists for instance in the case of the Fe-Mn system. Consequently, there is no calorimetric data concerning the enthalpy of solution of Mn in the low-temperature α (bcc) phase of Fe. All the above encouraged us to use the ^{57}Fe Mossbauer spectroscopy for supplying the experimental enthalpy of solution of different elements in α-Fe. In our previous studies we collected the proper spectra for the Fe-V [1], Fe-Cr [2], Fe-Mn [3], Fe-Al [4], Fe-Ni [5], Fe-Co [5], and Fe-Mo [6] alloys.

In this work we have extended the investigations to the Fe-Re system. According to our knowledge there is no experimental data concerning the enthalpy of solution of Re in Fe. The value of the enthalpy can be simply predicted only on the basis of the semi-empirical cellular atomic model of alloys developed by Miedema [10].

Table 1 Some of the best-fit parameters of the assumed model of the ^{57}Fe Mössbauer spectrum measured for $Fe_{1-x}Re_x$ alloys

x	B_0 [T]	ΔB_1[T]	ΔB_2[T]	ΔIS_1[mm/s]	ΔIS_2 [mm/s]
0.01	33.197(15)	−4.710(10)	−2.396(28)	−0.0348(10)	0.0104(10)
0.02	33.296(16)	−4.7524(63)	−2.502(13)	−0.0344(10)	0.0119(11)
0.03	33.396(14)	−4.8039(58)	−2.561(11)	−0.0320(10)	0.0154(11)
0.04	33.474(17)	−4.8152(63)	−2.609(10)	−0.0318(12)	0.0170(14)
0.05	33.523(19)	−4.8260(64)	−2.6490(98)	−0.0328(11)	0.0222(27)

The standard uncertainties for the parameters result from the variance of the fit

2 Experimental and results

The samples of iron-rhenium alloys containing 1, 2, 3, 4 and 5 at. % of Re, were prepared by melting appropriate amounts of the Aldrich 99.999% pure iron and 99.99% pure rhenium in an arc furnace filled with argon. Resulting ingots were cold-rolled to the final thickness of about 0.05 mm and then the foils were annealed in vacuum at 1270 K for 2 h. After that they were slowly cooled to room temperature during 6 h. Under these conditions, diffusion effectively stops at about 700 K [20], so the observed distributions of atoms in the annealed samples should be the frozen-in state corresponding to 700 K (the 'freezing' temperature T_d). The room temperature measurements of the ^{57}Fe Mössbauer spectra for Fe-Re alloys were performed in transmission geometry by means of a constant-acceleration POLON spectrometer of standard design. The spectra measured are presented in Fig. 1.

They were analysed in terms of six six-line patterns corresponding to different hyperfine fields B at ^{57}Fe nuclei generated by different numbers of Fe and Re atoms located in the first two coordination shells of the probing nuclei. It was done under assumption that the influence of Re atoms on B as well as the corresponding isomer shift IS of a subspectrum, is additive and independent of the atom positions in the given coordination shell of the nuclear probe although it can be different for atoms located in unlike shells. In other words it was accepted that for each subspectrum the quantities B and IS are linear functions of the numbers n_1 and n_2 of Re atoms located, respectively, in the first and second coordination shells of ^{57}Fe and the functions can be written as follows:

$$\begin{aligned} B(n_1, n_2) &= B_0 + n_1 \Delta B_1 + n_2 \Delta B_2, \\ IS(n_1, n_2) &= IS_0 + n_1 \Delta IS_1 + n_2 \Delta IS_2, \end{aligned} \tag{1}$$

where ΔB_1 (ΔIS_1) and ΔB_2 (ΔIS_2) stand for the changes of B (IS) with one Re atom in the first and second coordination shell of the Mössbauer probe. At the same time the quadruple splitting QS of a subspectrum is a free parameter [21]. It is worth noticing that the fits obtained under these assumptions are quite good and the found values of the best-fit parameters (displayed in Table 1) are in a good agreement with corresponding data given in the literature; e.g. in Ref. [22] one can find that for the $Fe_{0.97}Re_{0.03}$ alloy $\Delta B_1 = -4.72(3)$ T, $\Delta B_2 = -2.25(7)$ T, $\Delta IS_1 = -0.035(5)$ mm/s.

As the main result of the analysis the values of parameters c_1 and c_2 of each spectrum were determined. Assuming that the Lamb-Mössbauer factor is independent of the configuration of atoms in the surroundings of the ^{57}Fe nucleus, the parameters are total intensities of those components of a spectrum which are related to the

Table 2 The binding energy E_b between a pair of Re atoms in $Fe_{1-x}Re_x$ alloys deduced from the ^{57}Fe Mössbauer spectra

x	c_1	c_2	p_1	p_2	E_b (eV)
0.01	0.1758(15)	–	0.1229	0.0081	–
0.02	0.2472(25)	0.0206(30)	0.2153	0.0286	0.033(10)
0.03	0.3084(27)	0.0464(33)	0.2827	0.0568	0.0219(55)
0.04	0.3329(28)	0.0898(33)	0.3294	0.0892	0.0003(31)
0.05	0.3417(25)	0.1246(31)	0.3593	0.1229	−0.0054

The standard uncertainties for c_1 and c_2 result from the variance of the fit of the assumed model to the spectrum measured. The values of uncertainty for E_b were computed assuming that the uncertainty for the 'freezing' temperature T_d is 50 K

Table 3 The enthalpy H_{Fe-Re} [eV/atom] of solution of rhenium in iron

Miedema's model [10]	This work (α-Fe)
−0.015	−0.22(13)

existence of one and two Re atoms in the two first coordination shells of nuclear probes ^{57}Fe, respectively.

$$c_1 = c\,(1,0) + c\,(0,1)\,,$$
$$c_2 = c\,(2,0) + c\,(1,1) + c\,(0,2)\,. \tag{2}$$

The results are listed in Table 2.

The c_1 and c_2 values were used to calculate the binding energy E_b for pairs of Re atoms in the studied materials (Table 2). The computations were performed on the basis of the modified Hrynkiewicz-Królas formula [7, 23]

$$E_b = -kT_d \cdot \ln\left[(1 + 2 \cdot c_2/c_1) \cdot (c_2/c_1) \cdot (1 + 2 \cdot p\,(2)\,/p\,(1))^{-1} \cdot (p\,(2)\,/p\,(1))^{-1}\right]. \tag{3}$$

In the next step we found the extrapolated value of E_b for $x = 0$ using $E_b(0.02)$ and $E_b(0.03)$. Finally, the $E_b(0)$ value was used for computation of the enthalpy of solution H_{Fe-Re} of Re in iron. The calculations were performed on the basis of the Królas model [9] for the binding energy according to which

$$H_{Fe-Re} = -z \cdot E_b\,(0)\,/2 \tag{4}$$

where z is the coordination number of the crystalline lattice ($z = 8$ for α−Fe). The result is displayed in Table 3 together with the value resulting from Miedema's model of alloys [10].

3 Conclusions

The positive value of the binding energy E_b between two rhenium atoms in the $Fe_{1-x}Re_x$ alloys with $x \leq 0.03$, speaks in favour of the suggestion that Re atoms interact repulsively in iron matrix. The value −0.22(13) eV/atom for the enthalpy of solution H_{Fe-Re} of rhenium in α-iron, determined from the ^{57}Fe Mössbauer spectra are in a qualitative agreement with that −0.015 eV/atom, resulting from the semi-empirical Miedema's model of alloys [10] which is based on hundreds calorimetric data

concerning the heat of formation for different binary systems. Both H_{Fe-Re} values mentioned above are negative but absolute values of them are essentially different.

Although till now, in the available literature, one cannot find proper theoretical calculations of H_{Fe-Re}, we hope that our experimental findings presented in this paper will stimulate such computations in future, just as it happened in the case of the Fe-Mo system [16].

Acknowledgement This work was supported by the University of Wroclaw under the grant 1010/S/IFD.

References

1. Chojcan, J.: Interactions between V atoms in iron-based Fe-V solid solutions. J. Alloys Comp. **350**, 62–67 (2003)
2. Chojcan, J.: Interactions between Cr atoms in iron. Phys. Status Solidi B **219**, 375–381 (2000)
3. Chojcan, J., Roztocka, G.: Interactions between Mn atoms in iron. Phys. Status Solidi B **204**, 829–833 (1997)
4. Chojcan, J., Ostrasz, A.: A dilute-limit heat of solution of aluminium in iron studied with ^{57}Fe Mössbauer spectroscopy. Acta Phys. Pol. A **114**, 1573–1578 (2008)
5. Idczak, R., Konieczny, R., Konieczna, Ż., Chojcan, J.: An enthalpy of solution of cobalt and nickel in iron studiem with ^{57}Fe Mössbauer spectroscopy. Acta Phys. Pol. A 119, 37 (2011)
6. Chojcan, J., Konieczny, R., Ostrasz, A., Idczak, R.: A dilute-limit heat of solution of molybdenum in iron studied with ^{57}Fe Mössbauer spectroscopy. Hyperfine Interact. **196**, 377 (2010)
7. Chojcan, J.: Interaction between impurity atoms of 3d transition metals dissolved in iron. J. Alloys Compd. **264**, 50 (1998)
8. Chojcan, J.: A dilute-limit heat of solution of 3d transition metals in iron studied with ^{57}Fe Mössbauer spectroscopy. Hyperfine Interact. **156/157**, 523–529 (2004)
9. Królas, K.: Correlation between impurity binding energies and heat of formation of alloys. Phys. Lett. A **85**, 107–110 (1981)
10. Miedema, A.R.: Energy effects and charge transfer in metal physics, modeling in real space. Physica B **182**, 1–17 (1992)
11. Bangwei, Z., Yifang, O.: Theoretical calculation of thermodynamic data for bcc binary alloys with the embedded-atom method. Phys. Rev. B **48**, 3022–3029 (1993)
12. Dursun, I.H., Güvenç, Z.B., Kasap, E.: A simple analytical EAM model for bcc metals. Commun. Nonlinear Sci. Numer. Simulat. **15**, 1259–1266 (2010)
13. Sluiter, M.H.F., Kawazoe Y.: Prediction of the mixing enthalpy of alloys. Europhys. Lett. **57**, 526–532 (2002)
14. Klaver, T.P.C., Drautz, R., Finnis, M.W.: Magnetism and thermodynamics of defect-free Fe-Cr alloys. Phys. Rev. B **74**, 094435 (2006)
15. Bonny, G., Pasianot, R.C., Malerba, L., Caro, A., Olsson, P., Lavrentiev, M.Yu.: Numerical predictions of thermodynamic properties of iron-chromium alloys using semi-empirical cohesive models: the state of the art. J. Nucl. Mater. **385**, 268–277 (2009)
16. Lejaeghere, K., Cottenier, S., Claessens, S., Waroquier, M., Van Speybroeck, V.: Assessment of a low-cost protocol for an ab inito based prediction of the mixing enthalpy at elevated temperatures: the Fe-Mo system. Phys. Rev. B **83**, 184201 (2011)
17. Hultgren, R., Desai, P.D., Hawkins, D.T., Gleiser, M., Kelley, K.K.: Selected Values of Thermodynamic Properties of Binary Alloys. American Society for Metals, Metals Park (OH) (1973)
18. Myles, K.M., Aldred, A.T.: J. Phys. Chem. **68**, 64 (1964)
19. Kubaschewski, O., Probst, H., Geiger, K.H.: Z. Phys. Chem. Neue Folge **104**, 23 (1977)
20. Cranshaw, T.E.: A Mössbauer study of ^{119}Sn in alloys of iron with Si, Al, and Rh: interaction potentials and phase diagrams. J. Phys. Condens. Matter **1**, 829–846 (1989)
21. Falepin, A., Cottenier, S., Comrie, C.M.: A. Vantomme, Interpreting Mössbauer spectra reflecting an infinite number of sites: an application to $Fe_{1-x}Si$ synthesized by pulsed laser annealing. Phys. Rev. B **74**, 184108 (2006)
22. Vincze, I., Campbell, I.A.: Mössbauer measurements in iron based alloys with transition metals. J. Phys. F **3**, 647–663 (1973)
23. Hrynkiewicz, A.Z., Królas, K.: Formation of two-impurity complex in dilute alloys observed through perturbed angular correlations of γ rays. Phys. Rev. B **28**, 1864–1869 (1983)

Hyperfine Interact (2012) 207:1–5
DOI 10.1007/s10751-011-0454-x

Study of the structural and magnetic properties of metallic iron-hematite particles for use in magnetorheological fluids

Diana Marcela Osorio Ospina · Irvin Jadway Castro Navas · German Antonio Pérez Alcázar · Jesus Anselmo Tabares

Published online: 23 November 2011

Abstract Magnetorheological (MR) fluids are new iron-based materials, whose applications include brakes, dampers, clutches, shock absorbers systems and polishing of optical surfaces (lens and mirrors). They are dependent on the size and shape of particles as the magnetic properties. Interested in the possibility of using iron-rich powders, commonly used in nondestructive testing, ranging in size from a few μm to about 200 μm and lower cost than those commercially used for MR fluids, a study of the structural and magnetic properties of iron-rich metallic particles by X-ray diffraction (XRD) and Mössbauer spectroscopy (MS) at room temperature has been done. Powders, as received, were separated into particle sizes smaller than 20 μm (sample A) and in the range of 20–38 μm (sample B) because these are the sizes generally required for applications in MR fluids. The particles whose sizes exceed the above values were ground in a high energy planetary mill for 3 h, using different values of rotational speed/time: 200 rpm for one hour, a pause of 10 s, 140 rpm for one hour, pause 10 s and then 175 rpm during the last hour. These powders were sieved to obtain particles smaller than 20 μm (sample C). According XRD results, in all samples, only α-Fe (lattice parameter a = 2,867(2) Å) and Fe_2O_3 (lattice parameter a = 5,037(1) Å and c = 13,755(8) Å) were present. The Mössbauer spectra were fitted with two sextets. The hyperfine parameters values allowed us to assign the highest relative area spectrum (sextet) corresponding to α-Fe and the second one to Fe_2O_3 in accord to the XRD results. Thus, the preparation method using mechanical milling for diminishing the size of the metallic particles allowed us to get particles with size and magnetic properties that could lead to potentially MR fluids applications.

Keywords X ray diffraction · Mössbauer spectroscopy · Magnetorheological fluid

D. M. Osorio Ospina · I. J. Castro Navas
Escuela de Ingeniería de Materiales, Universidad del Valle, AA 25360 Cali, Colombia

G. A. Pérez Alcázar · J. A. Tabares (✉)
Departamento de Física, Universidad del Valle, AA 25360 Cali, Colombia
e-mail: jesus_tabares_8@hotmail.com

1 Introduction

Magnetorheological (MR) fluids are iron based new materials. MR fluids are considered smart materials because the rheological property (viscosity) can be altered or changed by applying a magnetic field in order to perform a controlled function. According Kciuka and Turczyn [1], MR fluids consist of suspensions of micron sized (3 to 5 μm) magnetizable particles suspended in an adequate carrier liquid (mineral oil, synthetic oil, water or ethylene glycol). Additional stabilizers and surfactants are included to prevent gravitational settling, enhance lubricity and change initial viscosity. O'Grady et al. [2] state the feasibility of the use of particles with sizes in a wider range (1–100 μm) without appreciable loss of magnetic response, because in micrometric magnetic particles there are multidomains that under the action of a magnetic field can increase the net magnetic moment of the particles. Thus, a deep knowledge of particle sizes and their magnetic properties is mandatory when some kind of magnetic particles is intend to be used in MR fluid projects. In this work, a study of structural and magnetic properties of metallic iron-hematite particles, commonly used in non-destructive testing, whose sizes vary from a few microns to 200 μm, was performed by X-ray diffraction (XRD) and Mössbauer Spectroscopy (MS) at room temperature.

2 Experimental

Magnetic particles (Magnavis 8A Red, main sizes 180 μm) which are coloured by red pigments [2], commonly used in non-destructive testing, were selected to be used in this study in order to establish their viability for the preparation of MR fluids. Powders, as received, were separated by size particles scale less than 20 μm (sample A) and in the range from 20 μm to 38 μm (sample B), because these sizes are generally referred for their applications [3]. The particles that exceeded these were ground in a high energy planetary mill for around 3 h, using different rotation speed/time values: 200 rpm and one hour, 10 s pause, 140 rpm one hour, 10 s pause and 175 rpm in the last hour. The jars and balls are made of hardened stainless steel with a relation sample mass to balls mass of 1 to 15 using 30 g of powders. In the milling process atmospheric air was used. This powder was sieved in order to separate it in the same previous sizes ranges. The sample of ground and sieved powders with sizes less than 20 μm, was named sample C. The samples A and B present a red coloration but C sample exhibits a gray-brown colour. All Mössbauer spectra were obtained with the aid of a homemade autonomous Mössbauer spectrometer [4] operating in constant acceleration mode using a LND proportional counter (Xe-CO_2, 1520 Torr) with a 57Co (Rh) source at RT. Spectra were fitted with MOSFIT program and the isomer shifts are referred to α-Fe. The X-ray patterns of the samples were performed at RT using the Cu/Kα radiation (PanAnalytical Diffractmeter). To obtain the lattice parameters and phase proportion it was used the GSAS program, which consider Rietveld analysis to refine de XRD patterns [5]. The main crystallite size in the parallel ($\phi||$) and perpendicular ($\phi\perp$) directions to the incident X-rays were calculated too.

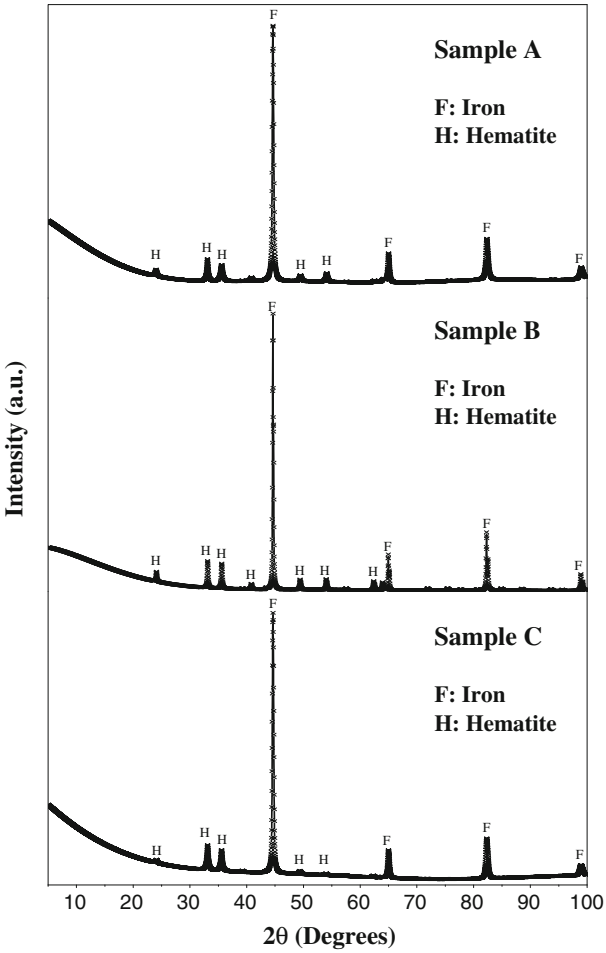

Fig. 1 XRD patterns of samples A, B, C. Note the peaks corresponding to metallic iron (F) and hematite (H) are the only ones present

3 Results and discussion

3.1 XRD

Figure 1 shows the X ray patterns of the samples according powder particles sizes: A (less than 20 μm), B (20 to 38 μm), and C (less than 20 μm after grinding and sieving). It is apparent that only the α-Fe (F) and Fe_2O_3 (H) peaks are present. According Rietveld fitting results for the mentioned samples, the lattice parameters correspond to α-Fe (a = 2,867(2) Å) and Fe_2O_3 (a = 5,037(1) Å and c = 13,755(8) Å). The weight fractions were 76.0% and 24.0%, (sample A), 68.7% and 31.3% (sample B), 68.5% and 31.5% (sample C) for α-Fe and Fe_2O_3, respectively. This clearly shows that the grinding process of particles with sizes larger than 38 μm can produce particles (sample C) with the same phases as those found in A and B, although apparently

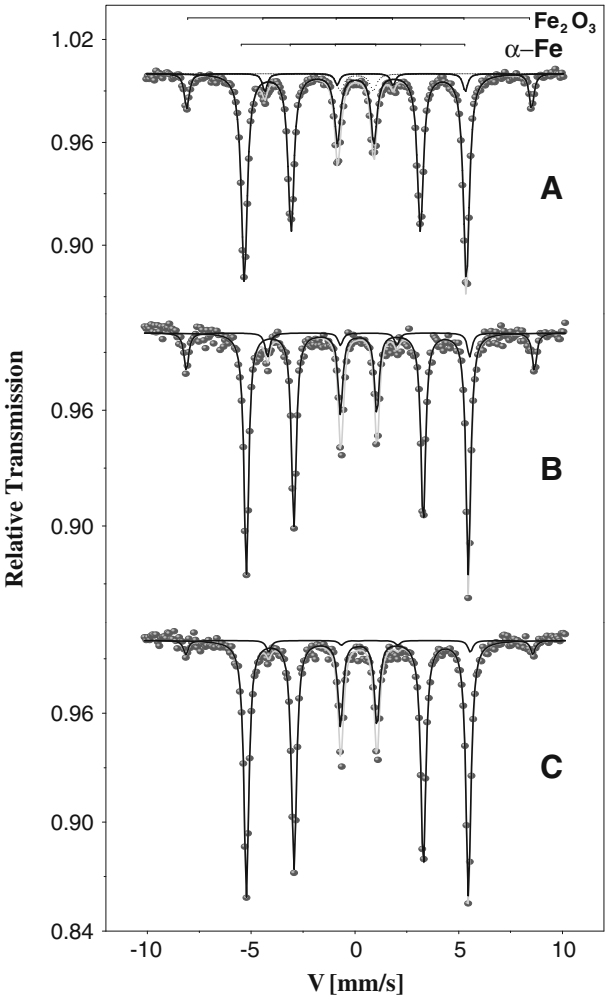

Fig. 2 Room temperature Mössbauer spectra. The hyperfine parameters correspond to metallic iron (α-Fe) and hematite (Fe_2O_3)

favors the increase of the Fe_2O_3 component compared with the same phase in sample A, where A and C are samples with the same range in particle size. This difference in the proportion of Fe_2O_3 is probably due to its recognized high fragility (an oxide of iron) compared to α-Fe [6]. There is a significant reduction in the crystallite size of the sample (C) compared with sample (A): a) from $\phi\perp = 77{,}7$ to 55,1 nm and $\phi|| = 71{,}0$ to 56,2 nm, for α-Fe, and b) from $\phi\perp = 79{,}3$ to 22,1 nm and $\phi|| = 84{,}9$ to 22,3 nm for Fe_2O_3. According the ratio $\phi_{(C)}/\phi_{(A)}$, there is a crystallite size reduction to ∼2/3 in α-Fe and to ∼1/3 in Fe_2O_3. It is characteristic of the grinding process that there is a decrease in particle size due to material fracture which is accompanied by a reduction in crystal size and a distortion in the crystalline lattice [7].

3.2 Mössbauer

Figure 2 shows the Mössbauer spectra obtained for the different samples A, B and C. All spectra were fitted with two sextets. The values of their Mössbauer parameters

correspond to the metallic iron (α-Fe) and hematite (Fe_2O_3). More precisely, in samples A and B, the relative areas are very similar, 90% and 10% for α-Fe and Fe_2O_3, respectively. In sample C the relative area of α-Fe increases to 96% with the corresponding decreasing in Fe_2O_3 relative area (4%). This effect could be related to removing of Fe_2O_3 of the surface of particles by milling, that is expected because the high fragility of iron oxides. This is consistent with the color variation experienced by the sample C compared to the original samples A and B. Thus, it is clear the Fe_2O_3 is on the surface of particles. It is not clear why is observed a decreasing in the relative area of Fe_2O_3 meanwhile in XRD results, the weight fraction (%) varies from 24.0% (A) to 32.4% (C). In summary, the results reveal that our milling process reduces the size of particles but do not induce changes in the structure or magnetic properties (hyperfine field) of the constituent particles [8] and occurs the removing of Fe_2O_3 from the particles surface.

4 Conclusions

XRD allowed us to determine two phases present in each sample, corresponding to α-Fe and Fe_2O_3, and quantify the weight fraction of them and the variation of the crystallite sizes. There were also identified by MS both α-Fe and Fe_2O_3, magnetic phases and their relative area determined, showing an increase of the α-Fe relative area in the ground sample, because removing of pigment, associated to Fe_2O_3 from the particles surface after grinding. Thus, the preparation method using mechanical milling for diminishing the size of the metallic particles allowed us to get particles with size and magnetic properties that could lead to potentially MR applications.

Acknowledgements This work was financially supported in part by "El Patrimonio Autónomo Fondo Nacional de Finaciamiento para la Ciencia, la Tecnologia y la Innovacion Francisco Jose de Caldas" under contract RC – No. 275–2011. Additionally, the authors are greatly indebted to the Vicerrectoria de Investigaciones and Magister in Physics Program, Universidad del Valle, Cali, Colombia for project funding.

References

1. Kciuka, M., Turczyn, R.: Properties and applications of magnetorheological fluids. JAMME **18**, 3–4 (2006)
2. Magnaflux: Magnetic particle inspection, particle #8A Red. Publishing Commercial web. http://www.magnaflux.com/Products/MagneticParticleInspection/MagnavisVisible/VisibleDryMethodProducts/Magnavis8ARed.aspx
3. O'Grady, K., Patel, V., Charles, S.W.: Magnetorheological Fluids, pp. 3–4. Taylor & Francis Group, LLC (2008)
4. Sanchez Asseff, A.J., Bohorquez, A., Pérez Alcázar, G.A., Pfannes, H.-D.: An autonomous programmable system for Mössbauer spectroscopy, accessed by a PC program. Hyperfine Interact. **110**, 135–141 (1997)
5. Larson, A.C., Von Dreele, R.B.: GSAS, General Structure Analysis System, pp. 88–748. Los Alamos National Laboratory report LAUR (2004)
6. Florez, J.M., Mazo-Zuluaga, J., Casanova, H., Restrepo J.: Rev. Col. de Física **38**(4), 1503–1506 (2006)
7. Cornell, R.M., Schwertmann, U.: The Iron Oxides: Structure-Properties-Reactions- Occurrence and Uses, p. 151. VCH (1996)
8. Sanchez, L.C., Arboleda, J.D., Saragovi, C., Zysler, R.D., Barrero, C.A.: Physica B **389**, 145–149 (2007)

Hyperfine Interact (2012) 207:7–12
DOI 10.1007/s10751-011-0448-8

A proof-of-principle experiment of EIT with gamma radiation in $FePSe_3$ single crystal

Hisakazu Muramatsu · S. Nakajo · K. Nakagami · K. Nagata · S. Mochizuki · H. Suzuki

Published online: 15 November 2011

Abstract From a series of Mössbauer measurements performed on a single crystal of $FePSe_3$, we have observed the effect of electromagnetically induced transparency (EIT) in a second nuclear system, after a first experiment using the mineral siderite $FeCO_3$. When the condition of nuclear level crossing was fulfilled, an obvious deficit in absorption was observed at the point of level crossing. This reduced absorption cannot be ascribed to saturation effects because of the specific geometry of the measurement. We conclude that the observed deficit in absorption is due to coherence and interference effects.

Keywords EIT · Electromagnetically induced transparency · Mössbauer effect · Level-crossing

1 Introduction

Electromagnetically induced transparency (EIT) has been demonstrated under several experimental conditions: in continuous wave and pulsed regimes for different wavelengths raging from optics to microwaves [1–8]. Interesting proposals have been discussed so far to obtain lasing for gamma rays by utilizing coherent effects, and the EIT effect via the level-crossing technique at the single-photon level has been theoretically predicted [9–12]. Some features of quantum optics related to inversion less amplification are translated to nuclear systems, but there are several differences between the nuclear and atomic systems (shorter wavelength, weaker

H. Muramatsu (✉) · S. Mochizuki · H. Suzuki
Department of Chemistry, Faculty of Education, Shinshu University, Nagano-shi, Nagano 380-8544, Japan
e-mail: hmurama@shinshu-u.ac.jp

S. Nakajo · K. Nakagami · K. Nagata
Graduate School of Education, Shinshu University, Nagano-shi, Nagano 380-8544, Japan

nuclear transitions, no coherent gamma-ray sources). Although there are some difficulties connected with nuclear systems, some ideas have been proposed that could be translated to nuclear radiation [13, 14], and they show that nuclear systems offer some advantages compared to the atomic ones because of the possibility of controlled nuclear level mixing phenomena.

We have already reported the first steps towards a proof-of-principle experiment, demonstrating EIT with gamma radiation for the Mössbauer effect in the mineral siderite $FeCO_3$ using the level-crossing technique [15–17]. We have tried to seek other candidates for absorbers possible to use in the same type of experiment. Recently, we have successfully synthesized small flakes of single crystal of $FePSe_3$. In the present paper we will report the second proof-of-principle experiment demonstrating EIT for the Mössbauer effect by using a single crystal of $FePSe_3$. Our attention will be focused on the problem whether $FePSe_3$ can be an appropriate absorber for EIT experiments or not.

2 Experimental

$FePSe_3$ was synthesized by solid phase reaction in a vacuum-shielded tube (Vycol glass tube) containing a mixture of stoichiometric amounts of high-purity elements, for 1 month. The reaction temperature to synthesize was set to be 840°, and the cooling rate was 40 degree/day. Single crystals of $FePSe_3$, shaped like thin foils, were obtained with a dimension of 3 mm × 3 mm. Since the direction of the hyperfine magnetic field is parallel to the principal axis of the electric field gradient (EFG), the *c* axis, all measurements were made with the gamma-ray parallel to the *c* axis, i.e. the direction perpendicular to the ab-plane. The single crystal sample was sandwiched in between two lead collimators with a window of 2 mm in diameter and mounted on a copper sample holder in a cryostat connected to a small He gas filled refrigerator (Cryo-Mini, Iwatani Plantec Co.) in such a way that the ab-plane faces the direction of the gamma-rays at a right angle. Mössbauer spectra were recorded in transmission geometry in the temperature range of 300 K to 16 K, using a single-line source of ^{57}Co (10 mCi) in a rhodium matrix and a conventional constant acceleration transducer. The calibration of the velocity scale for the spectrometer was carried out using an α-Fe foil.

3 Results and discussion

A strong temperature-dependent internal magnetic field parallel to the EFG-axis in the single crystal allows for crossings in the nuclear level structure of ^{57}Fe. Besides the magnetic hyperfine field, the Fe^{2+} nucleus in the crystal is subjected to a large axially symmetric EFG, which results in a well-resolved quadrupole doublet. (See Fig. 1a) Below the Néel temperature (106 K), Mössbauer spectra consist generally of six absorption lines due to its antiferromagnetic behavior. When dealing with a single crystal, however, depending on the orientation of the incident gamma ray with respect to the crystal c-axis, different selection rules apply. The source emits a statistical mixture of left- and right-circularly polarized photons, each allowing for a specific, angle-dependent, Δm transition. In case of the gamma photon being incident

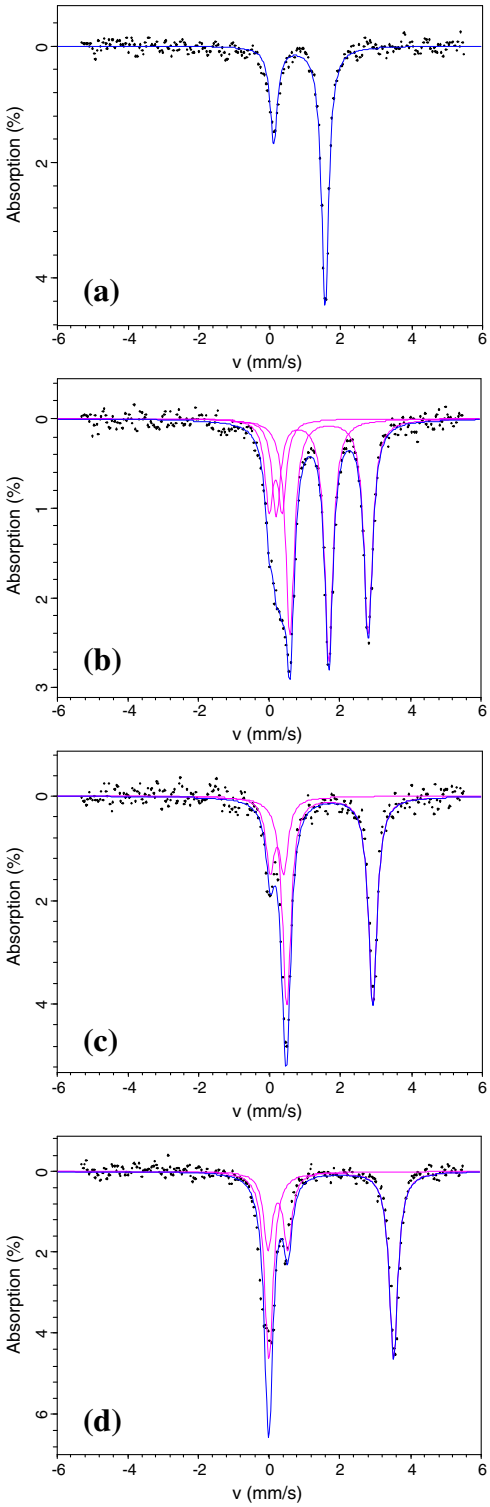

Fig. 1 Mössbauer spectra taken with $FePSe_3$ single crystal at various temperatures. **a** R.T., **b** 106 K, **c** 105 K, **d** 31 K

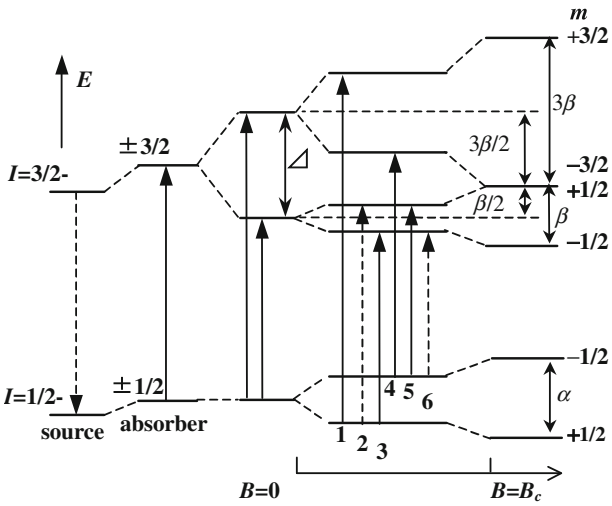

Fig. 2 Energy levels of the system as a function of the magnetic hyperfine field, B_{hf}

perpendicular to the crystal c-axis ($\theta = \pi/2$), each photon can coherently excite three transitions, and then six Mössbauer lines can be observed. On the other hand, when the gamma photon is incident along the crystal c-axis ($\theta = 0$), each photon can only excite one transition. In total, only four lines can be observed. We call this orientation the '*parallel geometry*' hereafter. In the actual measurements, since Mössbauer spectra of the $FePSe_3$ single crystal were taken in parallel geometry, the observed spectra consist of a paramagnetic quadrupole doublet at higher temperatures and four magnetically split lines below the Néel temperature due to its antiferromagnetic behavior. In the present spectral analyses, we decomposed the spectrum into two pairs of doublets. Each doublet (we call it a *component*) has 6 parameters in total, that is, Center Shift (C.S.), Splitting (distance between the two lines in each doublet), Linewidth (w_+), Area (A), Area Ratio (A_-/A_+), and Linewidth Ratio (w_-/w_+). The components are defined as follows; for example, component-1 consists of (+3/2, +1/2) and (−3/2, −1/2) transitions while (+3/2, +1/2) and (−3/2, −1/2) transition are designated to transition 1 and 4, respectively. The component-2, consisting of (+1/2, +1/2) and (−1/2, −1/2) transitions, that is $\Delta m = 0$ transition, vanishes in the present geometry.

As we have already experienced in our previous work, we encountered a curious behavior of the parameters obtained from an analysis under the condition that all parameters were allowed to be free except that Area Ratio (A_-/A_+) and Linewidth Ratio (w_-/w_+) are fixed to be equal to 1 ('*equal intensity and equal width*'). So, in the next step, we have fixed some parameters in such a way that the center-shift value is set to be the expected value from the extrapolation of the higher temperature region and the values of splitting are nearly equal to the expected ones from the shape of the temperature dependence for the hyperfine field (B_{hf}). From the theoretical considerations, some relations between each splitting of two pairs of doublets shown in Fig. 2 were taken into account when some parameters were fixed in the analyses. In this way we could get a set of parameters for the final fitted spectrum.

In Fig. 1 are shown Mössbauer spectra taken with a $FePSe_3$ single crystal absorber at various temperatures. It should be noted that there coexist paramagnetic and

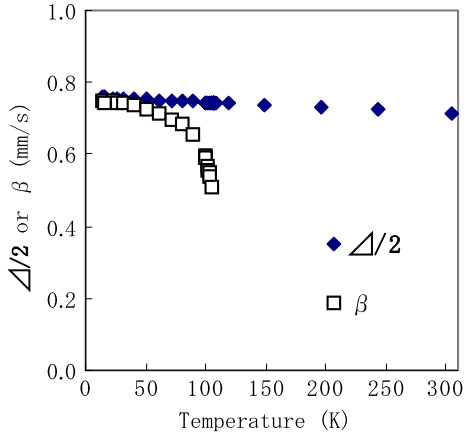

Fig. 3 Temperature dependence of magnetic hyperfine field and one half of the quadrupole splitting

antiferromagnetic phases around the temperature of the phase transition (around 106 K), as shown in Fig. 1b.

As is easily seen from Fig. 2, at the crossing temperature, β should be equal to one half of the quadrupole splitting ($\Delta/2$). As shown in Fig. 3, from the analysis of a series of Mössbauer spectra taken at various temperatures, the values of $\Delta/2$ closely approach β values around 30 K, and then we determine that below 30 K the states $|I = 3/2,\ m = -3/2\rangle$ and $|I = 3/2,\ m = 1/2\rangle$ cross and are mixed, and two lines, 4(−1/2, −3/2) and 5(−1/2, 1/2), merge into one single line. A typical spectrum at this level-crossing region is depicted in Fig. 1d. In this spectrum an obvious deficit in absorption was observed at colliding peaks around 0 mm/s, and this might be explained as an interference of the two transition amplitudes corresponding to the two lines having the same energy.

We have to rule out other possible causes for this reduction in absorption in order to confirm that we have observed EIT. If two absorption lines overlap and a thick absorber is used, the total intensity of the coinciding lines is in general not necessarily the sum of the intensities of the two partner lines due to saturation effects. This is, however, not the case, as is mentioned below. The single line source, ^{57}CoRh, emitted photons having a well-defined circular polarization, either $\sigma = +1$, or $\sigma = -1$, each occurring statistically with the same probability. In general, each photon can induce different Δmtransitions according to the transformation of the photon wavefunction when rotating from the propagation axis to the axis of the hyperfine fields. In the perpendicular geometry, since each photon, whatever its circular polarization, can induce three possible transitions, $\Delta m = 1$, $\Delta m = 0$ and $\Delta m = -1$, some correction for the effective thickness and the total intensity at the sum peaks would be required. In the parallel geometry, only the transitions $\Delta m = \sigma$ are possible and hence, for a particular photon, only one transition can be induced, either $\Delta m = 1$ or $\Delta m = -1$, depending statistically on the circular polarization. Therefore, the effective thicknesses of such a transition and its doublet partner are exactly equal, and the intensity of the sum peak is consequently expected to be the sum of the intensities of the two partners. Therefore, we conclude that the observed deficit in absorption is due to coherence and interference effects.

References

1. Tittonen, I., et al.: Phys. Rev. B **47**, 7840 (1993)
2. Vagizov, F.G.: Hyperfine Interact. **61**, 1359 (1990)
3. Lippmaa, M., et al.: Phys. Rev. B **52**, 10268 (1995)
4. Shvydko, Y.V., et al.: Phys. Rev. Lett. **77**, 3232 (1996)
5. Shvydko, Y.V., et al.: Phys. Rev. Lett. **52**, R711 (1995)
6. Olariu, S., et al.: Europhys. Lett. **37**, 177 (1997)
7. Olariu, S., et al.: Phys. Rev. B **50**, 616 (1994)
8. Kocharovskaya, O., et al.: Phys. Rev. Lett. **82**, 3593 (1999)
9. Coussement, R., et al.: Phys. Rev. Lett. **71**, 1824 (1993)
10. Kocharovskaya, O., et al.: Laser Phys. **9**, 745 (1999)
11. Kolesov, R., et al.: Opt. Commun. **179**, 537 (2000)
12. Shakhmuratov, R., et al.: Opt. Commun. **179**, 525 (2000)
13. Coussement, R., Put, P., Schevenneels, G., Hardeman, F.: Hyperfine Interact. **23**, 273 (1985)
14. Put, P., Coussement, R., Schevenneels, G., Hardeman, F., Berkes, I., Hlimi, B., Marest, G., Sau J., Sayouty, E.H.: Phys. Lett. A **103**, 151 (1984)
15. Coussement, R., et al.: Phys. Rev. Lett. **89**(10), 107601 (2002)
16. Odeurs, J., et al.: Hyperfine Interact. **143**, 97 (2002)
17. Gheysen, S., et al.: J. Mod. Opt. **51**, 2589 (2004)

Hyperfine Interact (2012) 207:13–17
DOI 10.1007/s10751-011-0453-y

Solvation of gold and rare earths by tributyl phosphate

Frank Matthew Gagliardi · John D. Cashion

Published online: 29 November 2011

Abstract Frozen solution samples were made from gold chloride and $KAu(CN)_2$ solvated with TBP/xylene. The ^{197}Au Mössbauer parameters were similar to those same species as frozen solutions or adsorbed onto activated carbon. Solvated samples from EuO dissolved in HCl or H_2SO_4 and frozen gave characteristic Eu(III) spectra. All the spectra were consistent with bonding to the TBP being through hydronium ions or water molecules.

Keywords Solvation · Gold · Europium · Tributyl phosphate · Bonding

1 Introduction

The technique of solvent extraction is commonly used in many industrial processes and separates compounds based on their relative solubilities in two different immiscible liquids. When metals are extracted by solvation, the coordinated water molecules around the metal ion are replaced partially or completely by the extractant, thus forming an organically soluble species. The phosphate ester tri-n-butyl phosphate (TBP) is used in many metal extraction processes, including the PUREX process for uranium extraction as $UO_2(TBP)_2(NO_3)_2$. TBP initiates association with the solute through the donor electron pair on the P = O part of the molecule and works better from nitrate or chloride solutions than from sulphate or phosphate solutions. However, in spite of the widespread data on its uses, much less is known about the mechanisms by which it bonds to particular metal complexes. The extraction systems can be complex and the extracted species are not easily defined.

Our principal aim was to study the extraction of gold from chloride solution, which is an environmentally more attractive system than using cyanide. However, the gold chloride species are easily reduced to the metal, for example in carbon–in-pulp

F. M. Gagliardi · J. D. Cashion (✉)
School of Physics, Bld 27, Monash University, Melbourne, Vic 3800, Australia
e-mail: john.cashion@monash.edu

processes. We have shown that when using some forms of polyurethane foam as the adsorbent [1, 2], this reduction can be avoided. Polyurethane foams can be loaded with suitable extractants, such as TBP, to improve the adsorption. TBP can also be adsorbed onto carriers such as nanoparticulate magnetite to enable magnetically assisted chemical separation.

2 Sample preparation

The gold chloride systems were prepared by first dissolving metallic gold in aqua regia and then diluting it to a pH of −0.9. TBP is miscible in most common organic solvents and xylene was chosen as a suitable carrier for the TBP. Two different concentrations of 10% and 50% TBP in xylene were prepared. The TBP/xylene mixture was added to the acid solution, shaken for approximately 5 min and then centrifuged. An aliquot of approximately 0.45 ml of the organic phase was then frozen quickly (>15 K/s) by pipetting into a cylindrical teflon absorber holder held onto a copper block below the surface of liquid nitrogen. Rapid cooling at >10 K/s prevents crystallization and the viscosity of the liquid increases until a metastable glass phase is formed which will have the same composition as the liquid and should have a similar structure. The gold cyanide sample was prepared similarly by dissolving commercial $KAu(CN)_2$ in water, mixing it with the TBP/xylene, centrifuged, and frozen quickly.

The rare earths are also amenable to extraction with TBP and were selected as possibly providing complementary bonding information to that from the gold. The rare earth samples were prepared by dissolving EuO and Gd_2O_3 in HCl or H_2SO_4 acids of various strengths. In each case, the metal-containing samples were added to the TBP/xylene, centrifuged, and an appropriate amount for the Mössbauer experiments frozen into teflon absorber holders.

3 Results

The ^{197}Au spectrum, taken at 5 K, of gold from chloride solution extracted into 50% TBP in xylene is shown in Fig. 1a and the fitted parameters are IS = 1.09(2) mm/s (w.r.t. Pt), QS = 1.59(3) mm/s and FWHM = 2.02 mm/s. The spectrum from 10% TBP in xylene appears to be the same within error, but as the dip is reduced proportional to the fraction of TBP, the spectrum is not as well defined. The spectrum of the gold cyanide sample, also taken at 5 K, showed the characteristic broad splitting and Gol'danskii-Karyagin effect of the $Au(CN)_2^-$ ion (Fig. 1b) with parameters IS = 3.17(4) mm/s , QS = 10.4(1) mm/s, FWHM = 1.92 mm/s and area ratio $A_+/A_- = 0.89$.

The ^{151}Eu spectra at 78 K each showed a typical broadened single line for the unresolved quadrupole splitting, with an effective isomer shift (IS_{eff}) of 0.8 mm/s and FWHM of 3.4 mm/s for the sulphuric acid sample and IS_{eff} of 0.3 mm/s and FWHM of 3.0 mm/s for the hydrochloric acid sample. Although the original oxide was Eu(II), the IS_{eff} values are clearly Eu(III). ^{155}Gd spectra taken at 4.2 K of several different samples did not show any measurable absorption. This was unfortunate, since Gd^{3+} is an S-state ion whose IS and QS values usually allow for a good interpretation in terms of the bonding.

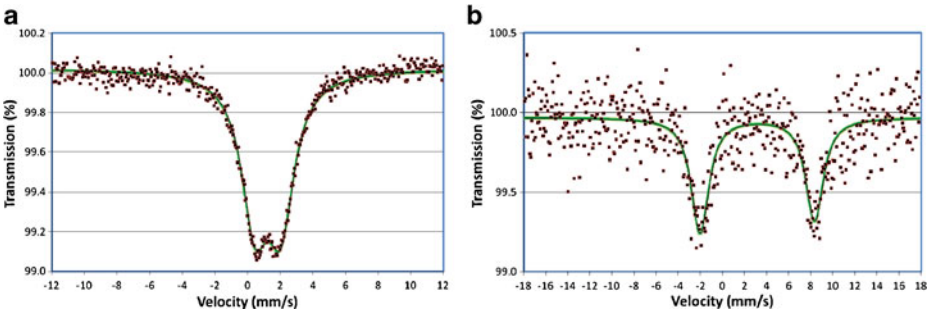

Fig. 1 ^{197}Au Mössbauer spectra of **a** frozen TBP/xylene/$[AuCl_4]^-$ and **b** frozen TBP/xylene/$Au(CN)_2^-$ complexes, both taken at 5 K

4 Discussion

TBP itself is not basic enough to take a proton out of the aqueous phase. Water, a stronger base than TBP, can acquire protons from the aqueous phase to form the hydronium ion, H_3O^+. TBP extracts hydronium ions or partially hydrated hydronium ions out of the aqueous phase [3]. Each TBP molecule is hydrogen bonded to one of the hydrogen atoms of the hydronium ion or of a water molecule. The overall positive charge of the hydronium ion attracts the negatively charged gold species, $[AuCl_4]^-$. This results in species of the form [4]

$$3\text{TBP}.y\text{H}_2\text{O}.\text{H}_3\text{O}^+ \ldots \text{AuCl}_4^- \qquad \text{with } 0 \le y \le 3.$$

The IS and QS agree with the parameters of the $[AuCl_4]^-$ species adsorbed onto polyurethane foams observed by Cashion et al. [1, 2] which had IS = 1.06–1.09 mm/s and QS = 1.58–1.63 mm/s.

Wan and Miller [5] reported no shift in the infrared spectrum of $Au(CN)_2^-$ with alkyl phosphorous esters and concluded that the extracted species are in the form of an ion pair

$$\text{M}^+ \ldots \text{Au}\,(\text{CN})_2^- \cdot \text{mRPO} \cdot \text{nH}_2\text{O}.$$

The linear N-C-Au-C-N molecule has negatively charged ends which are attracted to the hydronium ions as described above. One notable feature of Mössbauer spectra of the $Au(CN)_2^-$ ion is that all crystalline or frozen solution samples produce a strong Gol'danskii-Karyagin effect [6], while samples adsorbed onto activated carbon or polyurethane foams do not [6, 7]. This is because, in the former case, the bonding of the molecule is only at the negatively charged nitrogen ends, allowing the gold atom to vibrate more strongly perpendicular to the molecule. For the adsorbed molecules the additional bonding at the gold atom limits the perpendicular vibration. The presence of a Gol'danskii-Karyagin effect in the frozen $Au(CN)_2^-$—TBP complex is consistent with the other frozen solution samples and shows that the $Au(CN)_2^-$ ion is only bonded to the complex at either one or both ends.

Comparison of the parameters with those from the prior samples just described [6, 7] and discussed in ref. [8], shows that the IS is the same as for crystalline $KAu(CN)_2^-$ and smaller than that for the adsorbed species, implying that there is negligible bonding at the gold atom in agreement with the previous paragraph. The

QS is slightly larger than that of the crystalline species, suggesting a slight change in the length of the molecule.

The parameters of the Eu-Cl sample were almost identical to those obtained for frozen $EuCl_3$ solutions [9] inferring close association with water. $Eu(NO_3)_3$ complexed with TBP has been shown [10] to have 3 TBP molecules with one water molecule in low $[HNO_3]$ and no water molecules at high $[HNO_3]$. Ma et al. [11] evaluated the efficiency of TBP for extracting trivalent rare earths from $HNO_3/LiNO_3$ solutions and showed that it reached a local maximum at Eu before dropping by a factor of 1.5 to Gd. Since TBP extracts divalent actinide and rare earth ions more efficiently than trivalent ones, it is probable that the absence of a Gd absorption was due to a reduced extraction compared to the Eu sample, rather than to the much higher energy gamma rays (86.5 keV, compared to 21.6 keV) and consequent reduced recoilless fraction.

5 Conclusions

Solutions of gold chloride and $KAu(CN)_2$ were added to a TBP/xylene mixture and the solvated species frozen rapidly. The $[AuCl_4]^-$ species showed Mössbauer parameters very similar to those obtained following adsorption onto activated carbon. The $Au(CN)_2^-$ species showed a strong Gol'danskii-Karyagin effect which, together with the IS, indicated that there was no bonding at the gold atom. These spectra, and those from Eu(III) complexes, were consistent with bonding to the TBP being through hydronium ions or water molecules.

Acknowledgements We are pleased to acknowledge the support of the Australian Research Council and the Australian Institute of Nuclear Science and Engineering, and a Monash Graduate Scholarship for FMG. We also thank W H Jay for helpful discussions.

References

1. Cashion, J.D., Brown, L.J., Jay, W.H.: Mössbauer spectroscopy applied to mineralogy and minerals extraction. In: Resourcing the 21st Century, Australas. Inst. Mining Metall., pp. 285–289. Carlton (1997)
2. Cashion, J.D., Brown, L.J.: Gold mineralogy and extraction. Hyperfine Interact. **111**, 271–280 (1998)
3. Conocchioli, T.J., Tocher, M.I., Diamond, R.M.: The extraction of acids by basic organic solvents, V. J. Phys. Chem. **69**, 1106–1113 (1965)
4. Tocher, M.I., Whitney, D.C., Diamond R.M.: The extraction of acids by basic organic solvents, IV. J. Phys. Chem. **68**, 368–374 (1964)
5. Wan, R.I., Miller, J.D.: Research and development activities for the recovery of gold from alkaline cyanide solutions. In: Arbiter, N., Han, K.N. (eds.) Gold—Advances in Precious Metals Recovery, pp. 143–190. Gordon & Breach, London (1990)
6. McGrath, A.C., Hall, J.S., Cashion, J.D.: Effect of environment on dicyanoaurate ions—crystalline frozen solution and carbon-adsorbed species. Hyperfine Interact. **46**, 673–679 (1989)
7. Jay, W.H., Cashion, J.D., Brown, L.J.: Mössbauer study of gold adsorption on polyurethane foams. Hyperfine Interact. **71**, 1399–1402 (1992)
8. Murad, E., Cashion, J.D.: Mössbauer Spectroscopy of Environmental Materials and their Industrial Utilization, pp. 347. Kluwer, Boston (2004)

9. Greenwood, N.N., Turner, G.E., Vértes, A.: A Mössbauer and spectrophotometric study of aquochloroeuropium(III) complexes. Inorg. Nucl. Chem. Lett. **7**, 389–393 (1966)
10. Zhang, P., Kimura, T.: Complexation of Eu(III) with dibutyl phosphate and tributyl phosphate. Solv. Extr. Ion Exch. **24**, 149–163 (2007)
11. Ma, E., Wang, G.L., Yan, X.M., Yuan, C.Y.: Studies on the extraction and coordination of rare earths with β-ketophosphonates. In: Xu, G.X., Xiao, J.M. (eds.) New Frontiers in Rare Earth Science and Applications, vol. 1, pp. 488–492. Science Press, Beijing (1985)

Hyperfine Interact (2012) 207:19–23
DOI 10.1007/s10751-011-0472-8

^{57}Fe conversion electron Mössbauer study of oxidized iron-nickel alloy pins

Junko Nishimura · Kiyoshi Nomura

Published online: 6 December 2011

Abstract Iron-nickel alloy pins were pretreated at 700°C and 500°C for 30 min in H_2, and additionally heat-treated at 600°C for 30 min in N_2 atmosphere, respectively. The oxide layers of these samples were compared with that of a non-preheated sample. Thin iron oxide layers on all samples were observed by scanning electron microscopy (SEM), X-ray diffraction (XRD) and ^{57}Fe conversion electron Mössbauer (CEM) spectrometry. The iron products of Fe_3O_4 and γ-Fe_2O_3 were determined among various heated samples.

Keywords Iron-nickel alloy · Oxidation layers · Mössbauer spectrometry · Fe_3O_4 · Gamma-Fe_2O_3

1 Introduction

It is required in industry to realize glass-to-metal sealing contacts in microelectronic packages. Iron-nickel alloy is useful as the thermal expansion curve is accordant with that of hard borosilicate glass between 0–350°C [1]. But since iron-nickel alloy is not adhesive to the glass, hermetic sealing is realized by bonding of molten glass with an oxide films on the iron-nickel alloy [2, 3]. When glass contacts with oxides on iron-nickel alloy in the wetting process, it is reported that the oxides are dissolved into glass to form the reaction product Fe_2SiO_4 [4]. It is believed that especially

J. Nishimura (✉)
Department of Engineering, NEOMAX KAGOSHIMA Co., Ltd, 50-8, Midori-machi, Izumi City, Kagoshima, 899-0201, Japan
e-mail: NISHIMURA.JK@neomax.co.jp

K. Nomura
Department of Applied Chemistry, School of Engineering, The University of Tokyo, Hongo 7-3-1, Bunkyo-ku, Tokyo, 113-8656, Japan
e-mail: k-nomura@t-adm.t.u-tokyo.ac.jp

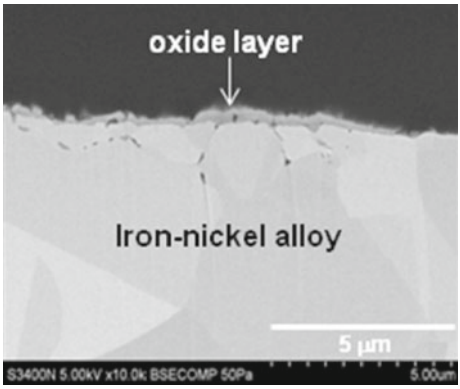

Fig. 1 Cross-section SEM image of sample C after heat-treatment

Fe^{2+} compounds contribute to glass-metal adhesion. When the iron-nickel alloy is heat-treated before contacting to glass, it is important to get sufficiently thick oxide layers containing Fe^{2+} for high bonding strength sealing. The purpose of this paper is to characterize the oxidized surface of iron-nickel alloy pins by conversion electron Mössbauer (CEM) spectrometry, scanning electron microscopes (SEM), and X-ray diffractions (XRD).

2 Experimental

Iron-nickel alloy pins used in this study were 0.4 mm in length and 0.2 mm in diameter and the composition of the alloy is essentially 42 mass% nickel balanced with iron. The iron-nickel alloy pin samples A, B and C, were obtained by the following treatment. Iron-nickel alloy pins A and B were preheated at 700°C and 500°C for 30 min in H_2 atmosphere, respectively, to reduce the oxides on the surface, and sample C was not preheated. All samples (A, B and C) were then additionally heat-treated at 600°C for 30 min in N_2 atmosphere in order to form the uniform oxide surface.

The crystalline oxides on the samples were measured by XRD, and the cross-section of the samples was studied by SEM. ^{57}Fe CEM spectra were measured at room temperatures by a backscattering type of He-CH_4 gas flow counter, and calibrated by using an α-Fe foil, and fitted with Mosswinn Software.

3 Results and discussion

Figure 1 shows the cross-sectional SEM image after sample C was heat-treated at 600°C in N_2 atmosphere. Thick oxide layers were observed around grains especially on uneven surfaces. It is found by SEM that the oxide layer was grown up to 2 μm in thickness.

The XRD pattern of sample C is shown in Fig. 2. The detailed pattern of the oxide layer shows the trace diffraction peaks of hematite (α-Fe_2O_3) and magnetite (Fe_3O_4) phases in addition to the diffraction peaks of Fe and Ni alloy, taenaite (Metallic Fe, Ni) phase. The taenaite phase is the original phase of Fe and Ni alloy. However, it

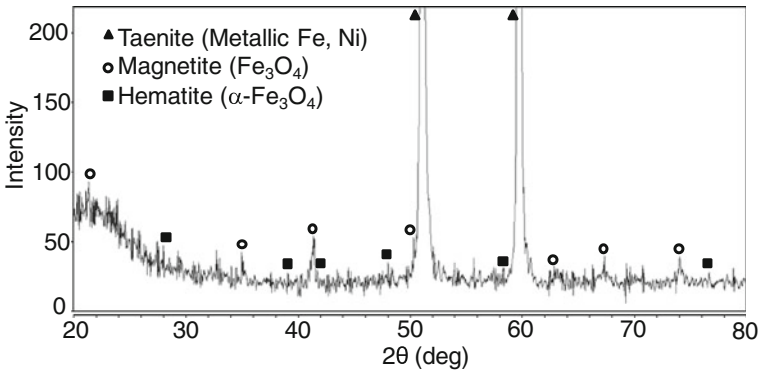

Fig. 2 XRD pattern of sample C after heat-treatment

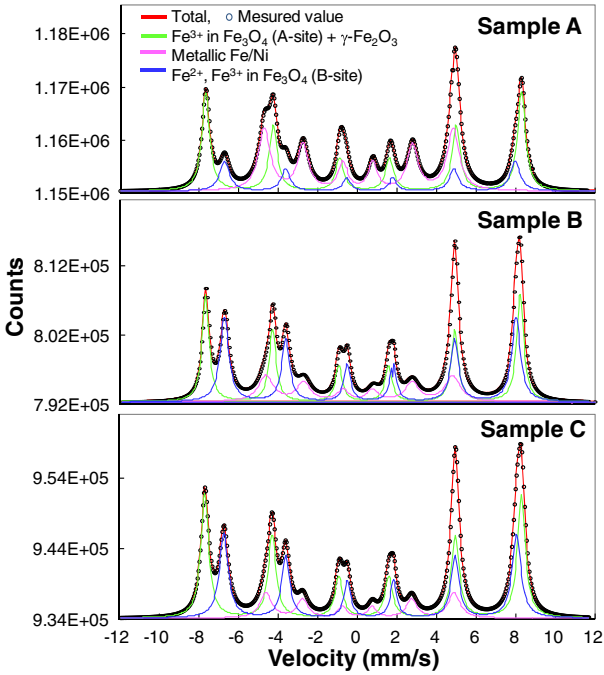

Fig. 3 ^{57}Fe Mössbauer spectra of heat-treated samples A, B and C

is difficult to compare the quantity of produced hematite and magnetite in samples A, B and C by XRD peaks.

Room temperature CEM spectra are deconvoluted into three sextets as shown in Fig. 3. The analyzed Mössbauer parameters are listed in Table 1. The hyperfine fields of three sextets are about 29T, 46T, and 49T, respectively. The sextet with $B_{hf} = 29T$ corresponds to the metallic state because the isomer shift, IS, is close to 0 mm/s. It is considered to be due to the substrate alloy. The second sextet with $B_{hf} = 46T$ shows the mixed valence states of Fe^{3+} and Fe^{2+} because of the IS = 0.66 mm/s. This comes from $Fe^{+2.5}$ in B site of magnetite (Fe_3O_4). The third sextet with $B_{hf} = 49.5T$ shows

Table 1 Mössbauer parameters of sample A, B and C

Fe states	Parameter	Sample A	Sample B	Sample C
Fe^{3+} in Fe_3O_4(A-site)+γ-Fe_2O_3 or	Area (%)	43.3%	48.4%	40.0%
$(Fe^{3+})_A[Fe_{1-3x}{}^{2+}Fe_{1+2x}{}^{3+}\square_x]_BO_4$	δ (mm/s)	0.34	0.31	0.31
	B_{HF} (T)	49.5	49.5	49.3
	Δ (mm/s)	−0.05	−0.03	−0.04
	Γ (mm/s)	0.48	0.48	0.42
Metallic Fe/Ni alloy	Area (%)	40.6%	14.6%	20.6%
	δ (mm/s)	0.04	0.07	0.07
	B_{HF} (T)	29.6	29.4	29.3
	Δ (mm/s)	0.05	0.15	0.08
	Γ (mm/s)	0.72	0.7	0.91
Fe^{2+}, Fe^{3+} in Fe_3O_4(B-site)	Area (%)	16.1%	37.0%	39.4%
	δ (mm/s)	0.62	0.66	0.66
	B_{HF} (T)	45.6	45.7	45.7
	Δ (mm/s)	0.01	−0.01	0.01
	Γ (mm/s)	0.59	0.54	0.53

the valence state of Fe^{3+} because of the IS = 0.34 mm/s. The third sextet originates from two Fe^{3+} species, the A site of Fe_3O_4 and maghemite (γ-Fe_2O_3) because it is hard to distinguish both sextets of γ-Fe_2O_3 and A site of Fe_3O_4. The doublet of FeO was not detected, and the sextet of hematite with $B_{hf} = 51T$ was not clearly observed although the trace peaks were recognized in XRD patterns.

The area intensity ratio of A-site and B-site of Fe_3O_4 was assumed to be 1/2. As a result, we derive that the sample A, B and C contain 24.4%, 55.5% and 59.1% of Fe_3O_4, respectively.

On the other hand, the component of γ-Fe_2O_3 estimated in this study may be one of magnetite components if the magnetite does not have the constant intensity ratio of 1/2 for A site/ B site, that is magnetite with oxygen defects [6]. In this case, the formula can be written as $(Fe^{3+})_A[Fe_{1-3x}{}^{2+}Fe_{1+2x}{}^{3+}\square_x]_BO_4$ ($0 < x < 0.33$). However, in order to estimate the iron states, the area intensity ratio of γ-Fe_2O_3 was calculated by subtracting the area intensity ratio of 1/2 of B-site from the area intensity ratio of the sextet with the largest magnetic field. As the results, the sample A, B and C contain 35.2%, 29.9% and 20.3% of γ-Fe_2O_3, respectively.

In the wetting process, a chemical reaction occurs between oxides and SiO_2 in the glass drop as follows [4]: $2Fe_3O_4 + 3SiO_2 = 3Fe_2SiO_4 + O_2$. A sufficient thickness of oxide on the metal surface is required for sealing with high bonding strength [5]. If magnetite with large contents of Fe^{2+} were effective for contact between glass and alloy, it would be not necessary to preheat in H_2 atmosphere before heating at 600°C in N_2 atmosphere.

4 Summary

In order to study thin iron oxide layers on Fe-Ni alloy, we have prepared samples by preheating in H_2 at 700°C and 500°C and heat-treatments at 600°C in N_2 atmosphere, and characterized by SEM, XRD, and CEMS. It is found that the iron oxide layers produced on Fe-Ni alloy consist of Fe_3O_4 and γ-Fe_2O_3, but not FeO and α-Fe_2O_3. The product ratios of Fe_3O_4 and γ-Fe_2O_3 were estimated by CEMS. It is concluded

that preheating in H_2 atmosphere is not necessary, and that only heating at 600°C in N_2 atmosphere is practically useful for glass-metal contact because of the large amount of Fe_3O_4 produced.

References

1. Buckley, R.G.: Electr. Prod. **8**, 15–17 (1979)
2. Luo, D., et al.: J. Univ. Sci. Technol. Beijing **5**, 267–271 (2008)
3. Macey, C., et al.: Appl. Surf. Sci. **21**, 139–150 (1985)
4. Luo, D., et al.: J. Alloys Compd. **477**, 407–413 (2009)
5. Chanmuang, C., et al.: Mater. Sci. Eng. A **474**, 218–224 (2008)
6. Vandenberghe, R.E., et al.: Hyperfine Interact. **126**, 247–259 (2000)

Hyperfine Interact (2012) 207:25–28
DOI 10.1007/s10751-011-0467-5

Iron-containing microphases in multiwalled carbon nanotubes

Alexey V. Sobolev · Nikolai B. Cherkasov · Igor A. Presniakov · Serguei V. Savilov

Published online: 7 December 2011

Abstract The phase composition of carbon nanotubes (CNTs) with encapsulated iron atoms was examined by ^{57}Fe Mössbauer spectroscopy. It was shown that iron atoms were stabilized in thermodynamically stable iron carbide and oxide phases and phases that are not usual under synthesis conditions (γ-Fe and γ-Fe_2O_3).

Keywords Multiwalled carbon nanotubes · Mössbauer spectroscopy

1 Introduction

The interest of researchers specializing in various areas of material sciences in carbon nanotubes (CNT) has increased in recent years primarily because of a wide range of their application in different technologies. A fairly high surface area of these materials and their thermal stability allow nanotubes to be used as carriers of various catalysts, and the possibility of chemical modification of their surfaces enables to create new hybrid materials [1].

2 Experimental

The synthesis of iron-containing multiwalled carbon nanotubes was performed on an injection unit following the procedure described in [2].

A. V. Sobolev (✉) · N. B. Cherkasov · I. A. Presniakov · S. V. Savilov
Chemistry Department, Lomonosov Moscow State University, Moscow, 119991, Russia
e-mail: salex12@rambler.ru
URL: http://www.chem.msu.ru/rus/radio/03.html

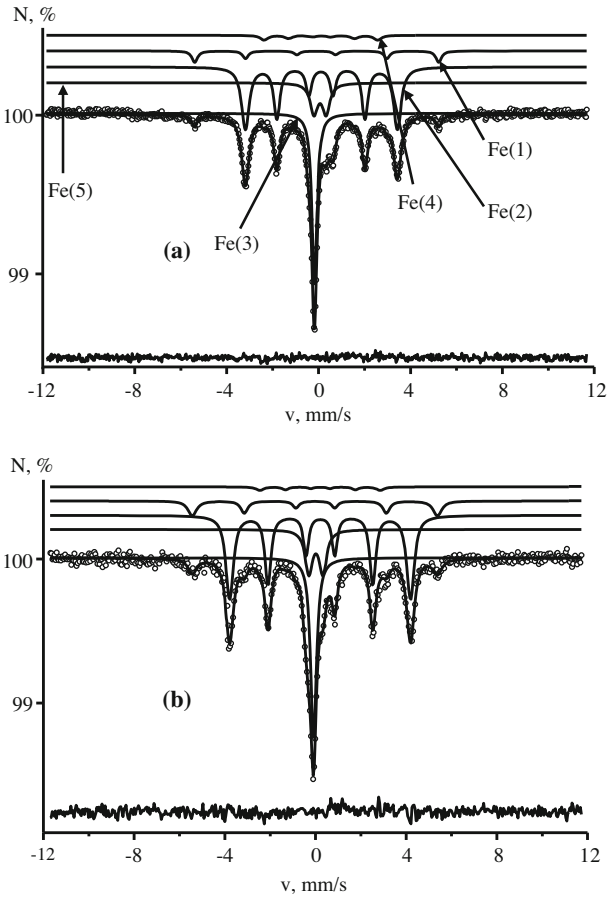

Fig. 1 ^{57}Fe Mössbauer spectra of the Fe-CNT sample at 293 K (**a**) and 77 K (**b**)

3 Results and discussion

The ^{57}Fe Mössbauer spectrum of CNT measured at T = 293 K was best fitted as a superposition of three magnetic subspectra Fe(1), Fe(2), and Fe(4) one paramagnetic quadruple doublet Fe(5) and singlet line Fe(3) (Fig. 1a). The hyperfine parameters of subspectra and its composition are listed in Table 1. The situation with two paramagnetic subspectra Fe(3) and Fe(5) is unambiguous. The isomer shift ($\delta(5)$) and quadrupole spitting ($\Delta(5)$) of the Fe(5) doublet can correspond either to $Fe_{1-x}C_x$ superparamagnetic particles [3] or to the iron–graphite complex already mentioned above [4]. The high quadruple splitting value for Fe(5) component is evidence of a substantial distortion of the local environment of iron atoms, and broadened linewidth ($\Gamma(5) \approx 0.40$ mm/s) shows that its nearest environment is nonuniform. The isomer shift of the Fe(3) subspectrum can be assigned either to the face-centered γ-Fe polymorph, which becomes magnetically ordered only at low temperatures [3], or to small α-Fe phase particles in the superparamagnetic state (d $\sim$ 60 Å) [5]. To solve the problem of the origin of the Fe(3) singlet component, we measured the Mössbauer spectrum at 77 K. The model interpretation of the spectrum (Fig. 1b)

Table 1 Hyperfine parameters of the ^{57}Fe Mössbauer spectra of the Fe-CNT sample

T, K	Component	δ, mm/s	ε, mm/s	H, kOe	Γ, mm/s	S, %	Phase
293	Fe(1)	0.00(1)	0.01(1)	332(1)	0.29(2)	7.1(4)	α–Fe
	Fe(2)	0.20(1)	0.01(1)	207(1)	0.40(1)	52.8(5)	Fe_3C
	Fe(3)	−0.09(1)	0	0	0.26(1)	23.7(1)	γ–Fe
	Fe(4)	0.20(1)	−0.01(2)	155(2)	0.40(1)	4.2(4)	Fe_3C_{1+x}
	Fe(5)	0.15(1)	0.27(1)	0	0.39(1)	12.3(6)	Fe-gr.
77	Fe(1)	0.08(1)	−0.01	338(1)	0.46(1)	10.5(9)	α–Fe
	Fe(2)	0.31(1)	−0.01(1)	250(1)	0.40(1)	52.0(8)	Fe_3C
	Fe(3)	0.01(1)	0	0	0.32(1)	22.1(9)	γ–Fe
	Fe(4)	0.34(2)	−0.1(1)	166(5)	0.40(1)	2.1(6)	Fe_3C_{1+x}
	Fe(5)	0.20(2)	0.31(1)	0	0.40(1)	13.3(8)	Fe-gr.

showed that the relative contributions (S(i)) of all the partial components including the Fe(3) singlet line remained almost unchanged within the temperature dependence accuracy to the λ-Mössbauer factors (Table 1). This result allows us to exclude the possibility of the formation of small α-Fe particles, i.e. the Fe(3) singlet component should be assigned to γ-Fe particles. This conclusion is favored by Fe(5) singlet line broadening observed in the low temperature spectrum ($\Gamma_3(300\ \mathrm{K}) = 0.26\ \mathrm{mm/s} \rightarrow \Gamma_3(77\ \mathrm{K}) = 0.32\ \mathrm{mm/s}$), which can be caused by the beginning of magnetic ordering of γ-Fe particles [3]. The temperature of the appearance of the line broadening at $T \approx 85 \pm 5$ K, obtained from recent temperature dependence of Γ_3 ($77 \div 300$ K), is very close to the Neel temperature ($T_N = 90$ K) of polycrystalline γ-Fe particles [3], which shows that γ-iron particles are not amorphous or superparamagnetic. Unexpectedly, the γ-Fe phase, which is thermodynamically unstable at $T < 1011$ K [6], is characterized by a substantial relative contribution of $S_3 \approx 24\%$ (Table 1). Conversely, the relative contribution of the Fe(1) component corresponding to the thermodynamically stable α-Fe phase comprises only several percent ($S_1 = 7$–10%). There can be several reasons for the stabilization of a significant amount of the γ-Fe phase unstable at low temperatures in Fe-CNT samples. The kinetic factor is a high rate of cooling of the products of CNT-Fe synthesis, which can cause "freezing" of the γ-iron phase formed at high temperatures. A similar explanation was suggested in a study of multiwalled CNTs grown on an inert oxidized silicon substrate preliminarily covered by an iron-containing catalyst performed using conversion electron Mössbauer spectroscopy [7, 8]. It was shown that metastable γ-Fe particles with Fe_3C carbide coating were largely localized at nanotube tails, where the rate of product cooling was maximum. The thermodynamic factor is related to different specific volumes of two iron polymorphs, $V_{\gamma\text{–Fe}} < V_{\alpha\text{–Fe}}$ [9]. According to this inequality, the γ-Fe $\rightarrow$ α-Fe low temperature phase transition should be accompanied by an increase in the specific volume of the system. It follows that, when iron particles are closely packed in a small volume inside nanotubes, reversible γ-Fe $\leftrightarrow$ α-Fe transition equilibrium remains strongly shifted to the left even at low temperatures.

4 Conclusions

In the Fe-CNT samples obtained, iron-containing particles are stabilized in the form of three phases magnetically ordered and two paramagnetic at $T = 293$ K phases.

Over the whole temperature range studied, magnetically ordered α-Fe and Fe_3C particles do not exhibit superparamagnetic behavior. The temperature dependence of Γ_1 of α-Fe component amounting to its area (S_1) reveals a small part of α-Fe to be the only phase in amorphous or nanoscaled.

Acknowledgement This work was financially supported by the Russian Foundation for Basic Research (project no. 09-03-00840a).

References

1. Serp, P., Corrias, M., Kalck, P.: Appl. Catal. A: Gen. **253**, 337 (2003)
2. Savilov, S.V., Zosimov, G.A., Lunin, V.V.: RF Patent No. 2310601 (2007)
3. Prados, C., Crespo, P., Conzalez, J.M., et al.: Phys. Rev. B **65**, 113405 (2002)
4. Novakova, A.A., Yu, T., Kiseleva, Il'ina, Yu.V., et al.: Al'tern. Energ. Ekol. **3**, 37 (2004)
5. Morup, S., Knudsen, J.E.: J. Phys. C **18**, 2943 (1985)
6. Bodker, F., Morup, S., Linderoth, S.: Phys. Rev. Lett. **72**, 282 (1994)
7. Ruskov, T., Asenov, S., Spirov, I., et al.: J. Appl. Phys. **96**, 7514 (2004)
8. Ruskov, T. Spirov, I., Ritschel, M., et al.: J. Appl. Phys. **100**, 084326 (2006)
9. Matter, P.H., Wang, E., Millet, J.-M.M., et al.: J. Phys. Chem. **111**, 1444 (2007)

Hyperfine Interact (2012) 207:29–32
DOI 10.1007/s10751-011-0479-1

Magnetic iron-containing nanoparticles on the surface of multiwalled carbon nanotubes

Alexey V. Sobolev · Serguei V. Savilov · Nikolai B. Cherkasov · Igor A. Presniakov · Anton S. Ivanov

Published online: 2 March 2012

Abstract Based on the temperature dependence of the hyperfine parameters of the ^{57}Fe nuclei, the qualitative and quantitative phase composition of nanocrystalline iron oxides on the surface and on the tails of the "classic" multiwalled carbon nanotubes (CNT) was investigated. From the observed temperature dependence it was shown that the contribution of the nonmagnetic iron-containing phase is caused by small size nanoparticles on the CNTs surface.

Keywords Multiwalled carbon nanotubes · Mössbauer spectroscopy · Iron oxides

1 Introduction

The application of micro- and nanometer magnetic materials based on complex metal oxides is currently one of the most important areas of modern physics and chemistry of materials and electronics. In addition, a special interest in the study of oxide particles of such size on the surface of an inert carrying base is aroused due to the possibility of the application of such objects in catalytic processes [1]. One of such systems is maghemite, which is oxide γ-Fe_2O_3 with spinel structure.

2 Experimental

The synthesis of iron-containing CNTs was performed on an injection unit following the procedure described in [2]. A mixture of acetylacetonate Fe(II) in benzene and ethanol solution was used as a precursor and nitrogen gas was used as purge gas. The synthesis temperature was 900–950 K.

A. V. Sobolev (✉) · S. V. Savilov · N. B. Cherkasov · I. A. Presniakov · A. S. Ivanov
Chemistry Department, Lomonosov Moscow State University, 119991 Moscow, Russia
e-mail: salex12@rambler.ru
URL: http://www.chem.msu.ru/rus/radio/03.html

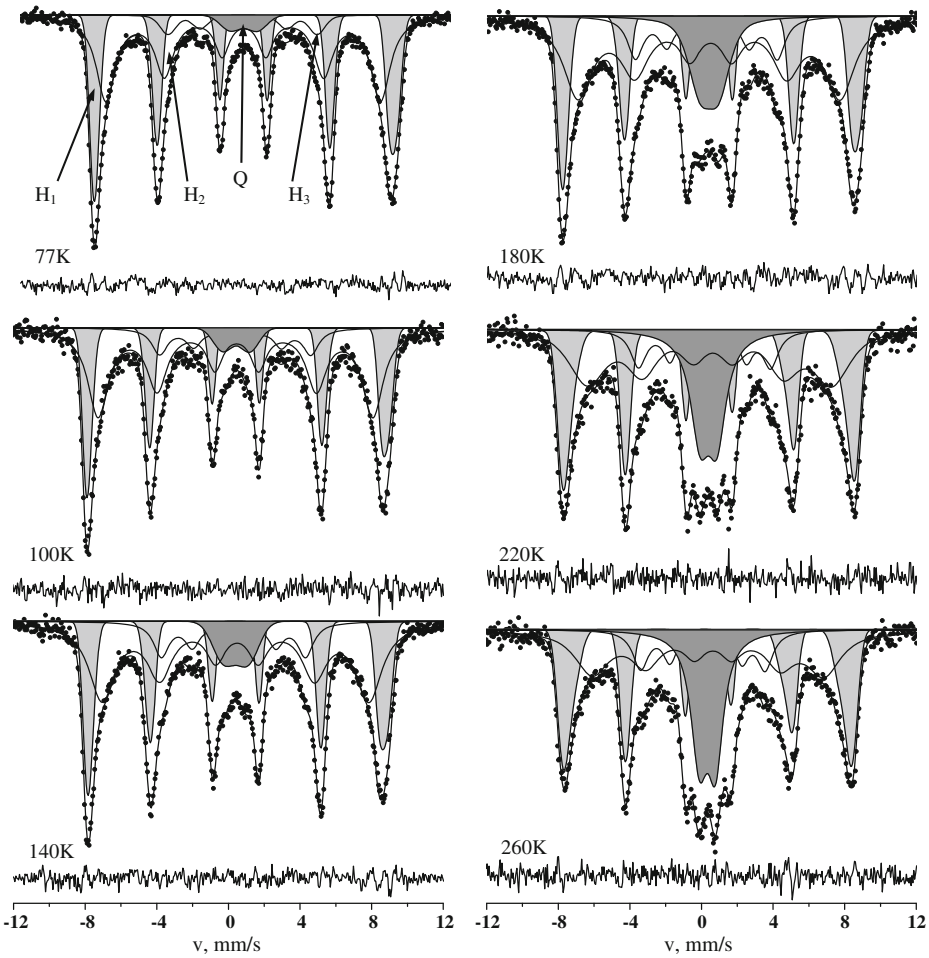

Fig. 1 ^{57}Fe Mössbauer spectra of carbon nanotubes at different temperatures

3 Results and discussion

^{57}Fe Mössbauer spectra of the obtained samples of CNTs, measured over a wide temperature range (Fig. 1), represent a complex magnetic structure consisting of several magnetic subsystems. According to electron microscopy, the particle size varies in the range 5–40 nm, so the analysis of an experimental Mössbauer spectra of these particles which is often carried out by introducing a distribution function of hyperfine magnetic fields or by computing with a model of a superposition of discrete subspectra, does not allow a satisfactory fit. In the analysis of such distributions, it is possible to establish maximum and average hyperfine magnetic fields on the ^{57}Fe nuclei. However, in the case of multiphase nanosystems there can be a loss of quantitative and qualitative information about the composition of the samples when introducing a distribution function $P(\mathrm{H})$, especially when there are significantly different values of isomer shifts (δ), quadrupole shifts (ε) of Zeeman sextets involved.

Therefore, the Mössbauer spectra were analysed in the framework of the superposition of three magnetic subspectra (H_1, H_2, H_3) and a quadruple doublet (Q). The magnetic subspectrum corresponding to hyperfine field H_1 was fitted as a quasidistribution of hyperfine magnetic fields $P(H)$ with their parameters corresponding to iron oxide γ-Fe_2O_3. During the fitting procedure of this component relations were imposed on the ratio of the partial sextets in this component, in accordance with the population of the cationic positions in the structure of γ-Fe_2O_3 being equal to 2:1 [3], as well as on the difference in isomer shift ($\Delta\delta$), which was set to 0.13 mm/s for this compound [3]. The analysis of the dependence of the average hyperfine field ($<H>$) on temperature, as well as the average linewidth ($<\Gamma>$) for this component is consistent with the data of electron microscopy and indirectly confirms the assumption of a fairly wide size distribution of iron oxide nanoparticles γ-Fe_2O_3. From the analysis of the temperature dependence of the isomer shift the temperature coefficient of the isomer shift $d\delta/dT = -(6.4 \pm 0.5) \cdot 10^{-4}\,\mathrm{mm \cdot s^{-1} \cdot K^{-1}}$ was determined for the ^{57}Fe nuclei in this subspectra.

The second magnetic component H_2 of the spectrum, with a large area, represents a strongly broadened Zeeman sextet with the hyperfine parameters (δ, ε) which correspond to Fe^{3+} cations being in an oxygen environment [3]. An accurate identification of this phase in this case is difficult, however, considering the very significant decrease in the amount of this component with increasing temperature. Since the carbon nanotubes on the surface of iron particles are on the average smaller in comparison with iron-containing nanocrystallites at the CNTs tails, we can assume that the features of the formation of nanoparticles of iron oxides in various parts of the tubes are different in terms of synthesis conditions.

Finally, the third magnetic component H_3 hyperfine parameters correspond to the Fe_3C compound [4], but the temperature change of the hyperfine magnetic field of this component as well as in the case of H_1 and H_2 is quite different from "classic" Brillouin-type systems. Such behavior of the hyperfine magnetic field for all magnetic subspectra indirectly confirms the nanocrystalline nature of all of the particles of iron-containing phases.

In addition, it should be noted that the spectrum has no relaxation component represented by a magnetic sextet, which is characterized in the simplest case of superferromagnetism by a flip time (τ) of the magnetic moment and has an activation character ($\tau = \tau_0 \exp(|K_e|\,V/kT)$) [5]. Although the appearance in the spectra of nanoparticles of such a relaxation component is expected, however, in the case of our broad distribution of particle sizes, the amount of such a component may be negligible in comparison with the magnetic and paramagnetic components.

4 Conclusion

Thus, on the basis of studies we have shown that nanocrystalline particles of γ-Fe_2O_3 with a wide size in distribution are formed on the surface of CNTs. It is established that these particles are mainly localized at the tails of the nanotubes. Also the presence of polycrystalline phase Fe_3C was shown, which subspectrum contribution is practically independent from temperature changes. It was shown that the main phase transfer from magnetic ordered phase into a non-magnetic components is reflected in the decrease of the H_2 component contribution in the overall spectrum.

Using this dependence it can be concluded that small (20 nm) (H_2 component) iron oxide particles, comparable to γ-Fe_2O_3, are located on the CNTs surface.

Acknowledgements This work was financially supported by the Russian Foundation for Basic Research (project no. 09-03-00840a).

References

1. Serp, P., Corrias, M., Kalck, P.: Appl. Catal. A Gen. **253**, 337 (2003)
2. Savilov, S.V., Zosimov, G.A., Lunin, V.V.: RF Patent No. 2310601 (2007)
3. da Costa, G.M., De Grave, E., Vandenberghe, R.E.: Hyperfine. Interact. **117**, 207 (1998)
4. Bauer-Grosse, E., Le Caer, G., Fournes, L.: Hyperfine. Interact. **27**, 297 (1986)
5. Predoi, Â., Kuncser, V., Filoti, G.: Rom. Rep. Phys. **56**, 373 (2004)

Hyperfine Interact (2012) 207:33–36
DOI 10.1007/s10751-011-0489-z

Mössbauer spectroscopy: analysis and predictions for Li-ion batteries

Josette Olivier-Fourcade · Costana Mihaela Ionica-Bousquet · Pierre-Emmanuel Lippens · Jean-Claude Jumas

Published online: 15 December 2011

Abstract Due to their high storage capacity Sn-based materials are of considerable interest as negative electrode for Li-ion batteries. However the strong volume change occurring during the alloy formation strongly limits the electrochemical performances (cycle and time life). Analysis by Mössbauer spectroscopy using model compounds (Sn, Sn-Li and transition metal-Sn alloys) shows that the volume expansion is related to the structural change from a Sn based network to a Li based network. Two types of materials are proposed here to overcome this problem: tin dispersion in an electrochemically inactive oxide matrix with buffer role to absorb volume changes or tin alloying with an inactive transition metal to minimize the volume expansion. The use of Mössbauer spectroscopy (*in situ operando* mode) allows a dynamic approach which is essential to understand the fundamental causes of ageing on cycling and to define then the key issues to be solved for material's application.

Keywords Negative electrode materials · Lithium insertion mechanism · Sn-based composites · *In situ operando* Mössbauer

1 Introduction

Sn-based materials are of considerable interest as negative electrode for Li-ion batteries because they can store more than twice as much lithium amount as that of graphite does. Metallic tin can react with lithium to form a variety of Li-rich alloys (Li_7Sn_2 or $Li_{22}Sn_5$) with high capacity storage (847 up to 994 Ah/kg). However the drastic volume change occurring during the alloy formation strongly limits their electrochemical performances. Several approaches to solve theses problems have

J. Olivier-Fourcade · C. M. Ionica-Bousquet · P.-E. Lippens · J.-C. Jumas (✉)
Institut Charles Gerhardt Montpellier (UMR 5253), Université Montpellier II,
CC1502, Place E. Bataillon, 34095 Montpellier cedex 5, France
e-mail: jumas@univ-montp2.fr

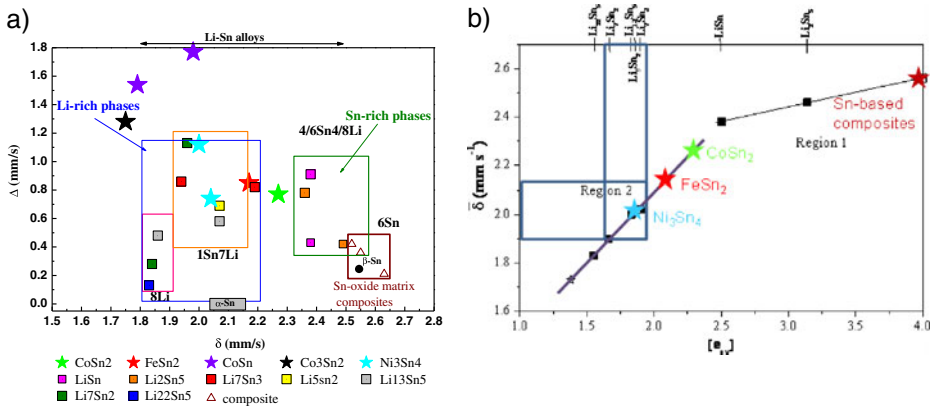

Fig. 1 **a**) .$\Delta - \delta$ correlation diagram for the different tin sites of Sn-based materials and (**b**) Isomer shift average value as a function of electronic density

been recently analyzed [1] and among the different possibilities the use of Sn-based composite materials or multi-element metallic materials seems to be the most favorable.

In this paper we present how Mössbauer Spectroscopy (MS) can be used to analyze and to predict the electrochemical behavior of such materials from correlation diagrams established for model compounds (Sn, Sn-Li and transition metal-Sn alloys). Two examples ($Sn^0/Sn^{II}B_xP_yO_z/BPO_4$ composites and M_xSn_y intermetallics) will illustrate the capabilities of MS to identify the mechanisms governing the electrochemical reactions.

2 Correlation diagrams

Figure 1 shows correlation diagrams obtained from the Mössbauer data of some reference compounds [2]. From the $\Delta - \delta$ diagram (Fig. 1a) two main domains are identified: Sn-rich phases ($\delta > 2.30\ mms^{-1}$) with continuous networks based on Sn-Sn bonds of covalo-metallic character and Li-rich phases ($1.80 < \delta < 2.20\ mms^{-1}$) with networks based on Li^+ close packing. The analysis of these data shows that during alloying the volume expansion is linked to the structural change corresponding to the transition from a Sn based network to a Li based network. This diagram allows identifying the nature and composition of the Li-Sn alloys formed during cycling [2].

The $\bar{\delta} - [e_{av}]$ diagram (Fig. 1b), drawn from the data of the Li-Sn system, allows the determination of the averaged Hume-Rothery electronic density $[e_{av}]$ for any Sn-based material by considering its $\bar{\delta}$ and the analysis of reaction mechanisms as described by Naille et al. [2].

3 $Sn^0/Sn^{II}B_xP_yO_z/BPO_4$ composite

Recently a new approach to avoid the large volume expansion during the lithiation process has been proposed with Sn particles embedded in an oxide matrix. The

$Sn/0.2BPO_4$ composite obtained by carbothermal synthesis [3] exhibits a complex structure that can be described by $Sn^0/Sn^{II}B_xP_yO_z/BPO_4$ involving metallic Sn^0 ($\delta = 2.53$ mms^{-1}, $\Delta = 0.36$ mms^{-1}) and an oxidized species $Sn^{II}B_xP_yO_z$ ($\delta = 3.31$ mms^{-1}, $\Delta = 1.63$ mms^{-1}) acting as a link between the Sn^0 and BPO_4 particles. This composite material exhibits a reversible capacity of 600 Ah/kg and the lithium insertion/extraction mechanism was characterized by *in situ operando* MS. At the beginning of the first discharge we observe the $Sn^{II} \rightarrow Sn^0$ reduction and then a progressive Li-Sn alloying reaction. At the end of the first discharge a mixture of Li-rich alloys (Li_7Sn_3, Li_5Sn_2 and $Li_{13}Sn_5$) can be evidenced with a $\bar{\delta} \sim 1.97$ mms^{-1}. During the first charge only a part of lithium can be removed leading to LiSn as final composition characterized by a $\bar{\delta} \sim 2.35$ mms^{-1}. The proposed mechanism for Sn/BPO_4 composite materials consists in two steps: i) reduction of Sn^{II} forming the interface with active species leading to a restructuration of the composite and ii) formation of Li_xSn alloys (up to Li_7Sn_3). During the discharge the conversion of the Sn-Sn network ($\bar{\delta} = 2.53$ mms^{-1}) to a Li-Li network ($\bar{\delta} \sim 1.97$ mms^{-1}) induces an important structural change responsible for the volume expansion.

4 M_xSn_y intermetallics (M = Fe, Ni)

$FeSn_2$ ($\delta = 2.18$ mms^{-1}, $\Delta = 0.83$ mms^{-1}) [4] and Ni_3Sn_4 ($\delta = 1.95$ mms^{-1}, $\Delta = 0.63$ mms^{-1}and $\delta = 1.98$ mms^{-1}, $\Delta = 1.37$ mms^{-1}) [5] are located in the same domain as that of the Li-rich phases (Fig. 1a) and present comparable [e_{av}] (Fig. 1b). In both cases the first electrochemical cycle leads to the formation of a Li_7Sn_2/M^0 nanostructured composite. Ageing is then linked to the reversibility of the reaction which initially depends on the nature of M. For Ni_3Sn_4 we observe a good reversibility because there is no coalescence of Ni^0 particles during cycling [5]. For $FeSn_2$ as shown by ^{57}Fe MS we observe an agglomeration of the Fe^0 particles during cycling and the reversibility doesn't exceed 50 cycles [4]. We can notice that Ni_3Sn_4 is located (Fig. 1b) with the first Li_xSn alloys rich in lithium ($2.33 < \times < 2.60$). This domain where Sn-based intermetallic compounds and Li_xSn alloys present comparable values of [e_{av}] seems to be very favourable to good electrochemical performances. In this way it is possible to predict the electrochemical behavior of Sn-based materials from their Mössbauer data by using the diagram shown on Fig. 1b.

5 Conclusions

In the field of new Sn-based materials as negative electrode for Li-ion batteries, MS has allowed us to establish correlation diagrams ($\delta - \Delta$ or $\bar{\delta} - [e_{av}]$) that make easier the analysis of the reaction mechanisms and in some cases that predict their electrochemical behavior. Thanks to MS a better understanding of Sn-based composites and intermetallics has been obtained and the combination of these two approaches, currently underway, is a promising way of creating new high-performance materials. In this context MS has a bright future [6].

Acknowledgements The authors would like to thank ALISTORE-ERI (FR 3104CNRS), ANR ANECDOTE, CNES, SAFT and Languedoc Roussillon Region for financial supports.

References

1. Larcher, D., Beattie, S., Morcrette, M., Edström, K., Jumas, J.-C., Tarascon, J.M.: Recent findings and prospects in the field of pure metals as negative electrodes for Li-ion batteries. J. Mater. Chem. **17**, 3759–3772 (2007)
2. Naille, S., Jumas, J.-C., Lippens, P.-E., Olivier-Fourcade, J.: ^{119}Sn Mössbauer parameters as predictive tool for future Sn-based negative electrode materials. J. Power Sources **189**, 814–817 (2009)
3. Mouyane, M., Ruiz, J.-M., Artus, M., Cassaignon, S., Jolivet, J.-P., Caillon, G., Jordy C., Driesen, K., Scoyer, J., Stievano, L., Olivier-Fourcade, J., Jumas, J.-C.: Carbothermal synthesis of Sn-based composites as negative electrode for lithium-ion batteries. J. Power Sources **196**, 6863–6869 (2011)
4. Chamas, M., Lippens, P.-E., Jumas, J.-C., Boukerma, K., Dedryvère, R., Gonbeau, D., Hassoun, J., Panero, S., Scrosati, B.: Comparison between microparticles and nanostructured particles of $FeSn_2$ as anode materials for Li-ion batteries. J. Power Sources **196**, 7011–7015 (2011)
5. Ehinon, K.K.D., Naille, S., Dedryvère, R., Lippens, P.-E., Jumas, J.-C., Gonbeau, D.: Ni_3Sn_4 electrodes for Li-ion batteries: Li-Sn alloying process and electrode/electrolyte interface phenomena. Chem. Mater. **20**, 5388–5398 (2008)
6. Lippens, P.-E., Jumas, J.-C.: It's all about the battery… Mössbauer Eff. Ref. Data J. **33**(2), 31–54 (2010)

Hyperfine Interact (2012) 207:37–40
DOI 10.1007/s10751-011-0469-3

Mössbauer Spectroscopy: an elegant tool for the active sites identification and quantification in Pt-Sn-In based naphta reforming catalysts

Ali Jahel · Sylvie Lacombe · Priscilla Avenier · Josette Olivier-Fourcade · Jean-Claude Jumas

Published online: 29 November 2011

Abstract Trimetallic PtSnIn/Al_2O_3-Cl catalysts have been synthesized by successive impregnations (SI) of metals and characterized by ^{119}Sn Mössbauer Spectroscopy (MS). Various Sn-species have been identified thanks to the use of a Δ (Quadrupole Splitting) – δ (Isomer shift) diagram. ^{119}Sn MS results show that addition of different amounts of In (0.11 to 0.55 wt.%) lead to the formation of $Pt_xSn(O)$ oxo-metallic phases. As the In loading increases these $Pt_xSn(O)$ oxo-metallic phases are richer in Pt. The preferential formation of a given Sn phase in these catalysts is directly related to the preparation method.

Keywords Naphtha-reforming catalysts · Pt-Sn-In Mössbauer Spectroscopy · $Pt_xSn(O)$ oxo-metallic phases

1 Introduction

Alumina supported Pt-Sn heterogeneous catalysts are widely employed in the catalytic naphtha reforming industry [1]. Trimetallic catalysts are considered to be superior to their bimetallic counterparts in terms of stability and resistance to deactivation by coke. However, little information about these materials can be found in the literature. Few examples exist on the promotion of Pt-Sn systems by another metal such as indium [2].

^{119}Sn Mössbauer Spectroscopy (MS) is a powerful tool to fully classify Sn species as a function of their hyperfine parameters in these systems [3, 4] as shown on Fig. 1.

A. Jahel · S. Lacombe · P. Avenier
IFP Energies nouvelles, Rond-point de l'échangeur de Solaize, BP 3, 69360 Solaize, France

J. Olivier-Fourcade · J.-C. Jumas (✉)
Institut Charles Gerhardt Montpellier (UMR 5253), Université Montpellier II, CC1502, Place E. Bataillon, 34095 Montpellier cedex 5, France
e-mail: jumas@univ-montp2.fr

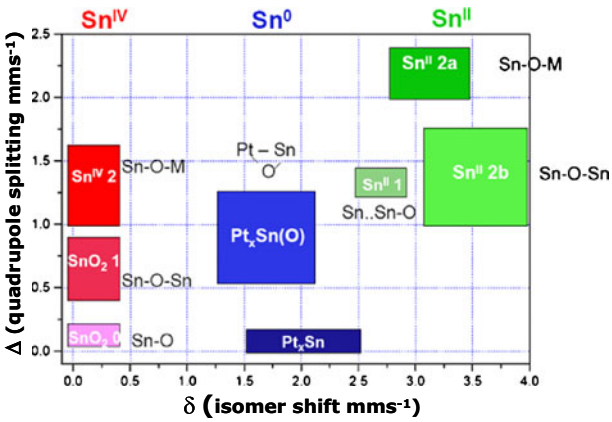

Fig. 1 Classification of the Sn species [3] observed on Sn-based catalysts and of model compounds as a function of their Mössbauer parameters

Using this diagram we have previously shown that the presence of In in Pt/Al_2O_3SnIn-Cl catalysts obtained by co-precipitation of Sn and In with the alumina precursor following a sol-gel method (CP samples) favours the formation of Pt_xSn alloys [5, 6]. In the absence of indium, a Sn^0 unalloyed phase was rather identified. The consequent activity and selectivity differences have been interpreted on the basis of these results [5]. In this paper we present an ^{119}Sn Mössbauer characterization for PtSnIn based catalysts obtained by successive impregnations (SI) of metals.

2 Preparation of catalysts by SI and characterization by ^{119}Sn MS

The calcined γ-alumina support was first impregnated with In using the proper amount of $In(NO_3)_3$, $5H_2O$ to yield 0.10, 0.30, 0.40 and 0.55 wt.% of In relative to support's mass. After this, each of the obtained supports was impregnated with $SnCl_2$, $2H_2O$ (0.30 wt.% of support's mass). Finally the obtained bimetallic supports were impregnated with H_2PtCl_6 (0.30 wt.% of support's mass). The chlorine content of the catalysts was adjusted to approximately 1 wt.% by injecting distilled water to the catalyst at 520° in dry air flow.

^{119}Sn Mössbauer spectra were recorded at room temperature in the transmission mode on a standard spectrometer using a $Ca^{119m}SnO_3$ source of 370 MBq nominal activity. All isomer shifts are given with respect to the room temperature spectrum of $BaSnO_3$. All catalysts were characterized in the reduced form (500°C, 2 h in 1 l/h/g H_2 stream). The reduction was performed in special-U shaped reduction cells adapted for MS measurements. Once reduction was completed, the cell was neutralized and sealed under vacuum.

3 Results and discussion

The different Sn species (Table 1) have been identified using the diagram reported on Fig. 1. Ratios with which Sn species are formed have been estimated from the contributions of their sub-spectra corrected using their different *f* factors (Lamb

Table 1 ^{119}Sn hyperfine parameters δ (mms^{-1}), Δ (mms^{-1}) of species and their corrected contribution CC (%) to spectra of reduced SI samples recorded at room temperature

Sample	δ	Δ	FWHM[a]	CC [b]	Attribution	Absorption (%)
$PtSnIn_{0.11}Al_2O_3$-Cl	0.36(0)	1.48(6)	0.88(2)	4	Sn^{IV} 2	0.88
	3.10(3)	2.17(3)	0.88(6)	26	Sn^{II} 2a	
	3.86(2)	1.32(2)	0.88(3)	50	Sn^{II} 2b	
	1.95(6)	1.48(6)	0.88(2)	20	$Pt_xSn(O)$	
$PtSnIn_{0.31}Al_2O_3$-Cl	0.02(0)	0.68(1)	1.07(2)	8	SnO_2 1	0.63
	3.15(3)	2.49(4)	1.07(3)	36	Sn^{II} 2a	
	3.55(3)	1.18(4)	1.07(7)	40	Sn^{II} 2b	
	1.46(0)	1.35(3)	1.07(2)	16	$Pt_xSn(O)$	
$PtSnIn_{0.41}Al_2O_3$-Cl	−0.20(0)	0.30(1)	1.01(2)	4	SnO_2 1	0.59
	3.26(5)	2.34(5)	1.01(1)	36	Sn^{II} 2a	
	3.61(5)	1.14(6)	1.01(5)	43	Sn^{II} 2b	
	1.25(9)	1.08(9)	1.01(2)	17	$Pt_xSn(O)$	
$PtSnIn_{0.55}Al_2O_3$-Cl	3.16(5)	2.08(6)	1.07(6)	44	Sn^{II} 2a	0.74
	3.73(7)	1.34(9)	1.07(2)	34	Sn^{II} 2b	
	1.05(6)	1.28(7)	1.07(2)	22	$Pt_xSn(O)$	

[a] Full Width at Half Maximum, [b] Corrected Contribution (quantitative)

Mössbauer factors). Experimentally these *f* factors have been determined as 0.55 (SnO_2 1 and Sn^{IV} 2), 0.18 (Sn^0/alloys), 0.34 ($Pt_xSn(O)$), 0.35 (Sn^{II} 2a) and 0.31 (Sn^{II} 2b) [7].

At 0.11 wt% In, the obtained spectrum is composed of 4-subspectra: an unreduced "Sn^{IV} 2" oxide, the two "Sn^{II} 2a" and "Sn^{II} 2b" oxides and a metallic Sn phase ($\delta = 1.95$ mms^{-1} and $\Delta = 1.48$ mms^{-1}). The hyperfine parameters of this phase thus lie at the lower limit of isomer shifts of Sn-rich Pt_xSn alloys (Fig. 1), but its relatively high quadrupole splitting indicates that this phase is rather an oxo-metallic $Pt_xSn(O)$ phase. Higher In loadings (0.31, 0.41 and 0.55 wt%) also lead to a comparable formation of these oxo-metallic phases (16, 17 and 22% respectively). More importantly, the isomer shift of the formed $Pt_xSn(O)$ phase in trimetallic catalysts decreases when the In content increases. The Pt and Sn relative atomic concentrations in these formed $Pt_xSn(O)$ phases can be estimated starting from the isomer shift at which the phase is observed in the spectrum and following the same rule applied for Pt_xSn alloys, i.e. phases with lower isomer shifts are richer in Pt and those with higher isomer shifts are richer in Sn [3]. This implies that in trimetallic catalysts, as the In loading increases, less Sn is engaged in the observed $Pt_xSn(O)$ phase. Such a decrease in the Sn atomic concentration is in accordance with the substitution of Sn by the added In, which is also an evidence of the close Pt-In proximity in these catalysts. The effect of indium in the ternary PtSnIn based system is therefore qualitatively understood as a function of its introduction method, its loading, and the introduction method of the other elements, *i.e.* Pt and Sn. The CP catalysts have surprisingly higher Sn^0/Pt ratios compared to SI catalysts, where the elements were initially thought to be closer to Pt due to the preparation method. This is attributed to the presence of Pt_xSn alloys in CP catalysts only and to the replacement of Sn in $Pt_xSn(O)$ by surface indium in SI catalysts. The interpretation

of activity and selectivity differences for the two differently prepared PtSnIn systems is mostly based on these Sn^0/Pt ratios [7].

4 Conclusions

This study represents a solid basis for the profound understanding of complex metallic interactions that exist in PtSnIn based systems. MS is an elegant analytical tool which provides valuable complementary information to other techniques such as EXAFS and XPS. Thanks to MS it has been shown that the preferential formation of a given Sn phase in these catalysts is directly related to the preparation method, as well as the presence (or not) of other promoters.

Acknowledgements Authors are thankful to the Languedoc Roussillon Region for the financial support to X-rays and gamma-rays platform (Contracts n° 2006 Q-086 and 2008 – 094192).

References

1. Antos, G.J., Aitani, A.M.: Catalytic Naphtha Reforming, 2nd edn. Marcel Dekker, New York (2004)
2. Bocanegra, S.A., Castro, A.A., Scelza, O.A., de Miguel S.R.: Characterization and catalytic behavior in the n-butane dehydrogenation of trimetallic InPtSn/$MgAl_2O_4$ catalysts. Appl. Catal. Gen. **333**(1), 49–56 (2007)
3. Olivier-Fourcade, J., Womes, M., Jumas, J.-C., Le Peltier, F., Morin, S., Didillon, B.: Investigation of redox properties of different PtSn/Al_2O_3 catalysts. Chem. Phys. Chem. **5**, 1734–1744 (2004)
4. Womes, M., Le Peltier, F., Morin, S., Didillon, B., Olivier-Fourcade, J., Jumas, J.-C.: Study of the reaction mechanisms between Sn-(n-$C_4H_9)_4$ and alumina surface sites—application to the controlled preparation of PtSn/Al_2O_3 catalysts. J. Mol. Catal. A: Chem. **266**, 55–64 (2007)
5. Jahel, A., Avenier, P., Lacombe, S., Olivier-Fourcade, J., Jumas, J.-C.: Effect of indium in trimetallic Pt/Al_2O_3SnIn-Cl naphtha-reforming catalysts. J. Catal. **272**, 275–286 (2010)
6. Jahel, A., Avenier, P., Lacombe, S., Olivier-Fourcade, J., Jumas, J.-C.: Investigation by Mössbauer spectroscopy of Sn redox transformations during H_2/O_2 titration on Pt/Al_2O_3Sn-Cl and Pt/Al_2O_3SnIn-Cl naphtha reforming catalysts. J. Phys.: Conf. Ser. **217**, 011245 (2010)
7. Jahel, A.: Study of the indium addition to the Pt-Sn/Al_2O_3-Cl ystem used in catalytic naphta reforming. PhD thesis, Montpellier (2010)

Hyperfine Interact (2012) 207:41–44
DOI 10.1007/s10751-011-0425-2

A Mössbauer study of the magneto-structural coupling effect in $SrFe_2As_2$ and SrFeAsF

Zhiwei Li · Xiaoming Ma · Hua Pang · Fashen Li

Published online: 1 November 2011

Abstract In the present paper, we report a comparison study of $SrFe_2As_2$ and SrFeAsF using Mössbauer spectroscopy. The temperature dependence of the magnetic hyperfine field is fitted with a modified Bean–Rodbell model. The results give much smaller magnetic moment and magneto-structural coupling effect for SrFeAsF, which may be understood as due to different inter-layer properties of the two compounds.

Keywords Mössbauer spectroscopy · Iron based superconductors · Magneto-structural coupling effect

1 Introduction

The surprising discovery of superconductivity by Hideo Hosono and co-workers in fluorine-doped LaFeAsO with transition temperature as high as 26 K [1] has stimulated worldwide efforts to study this new family of superconductors [2]. Among many discovered iron-based superconductors, the 122-type $AeFe_2As_2$ (Ae = Ba, Sr, Ca, Eu) and the 1111-type ReFeAsO (Re = La, Ce, Pr, Nd, etc.) families are the most studied materials [2]. And it has been shown that magnetism and structural tuning may play important roles in the pairing mechanism of these superconductors [3, 4]. There is also an interesting interplay between the crystal structure and magnetism

This work was supported by the National Natural Science Foundation of China under Grants No. 10975066.

Z. Li · X. Ma · H. Pang (✉) · F. Li
Institute of Applied Magnetics, Key Lab for Magnetism and Magnetic Materials of the Ministry of Education, Lanzhou University, Lanzhou 730000, Gansu, People's Republic of China
e-mail: hpang@lzu.edu.cn

Z. Li
e-mail: z.w.lee@live.cn

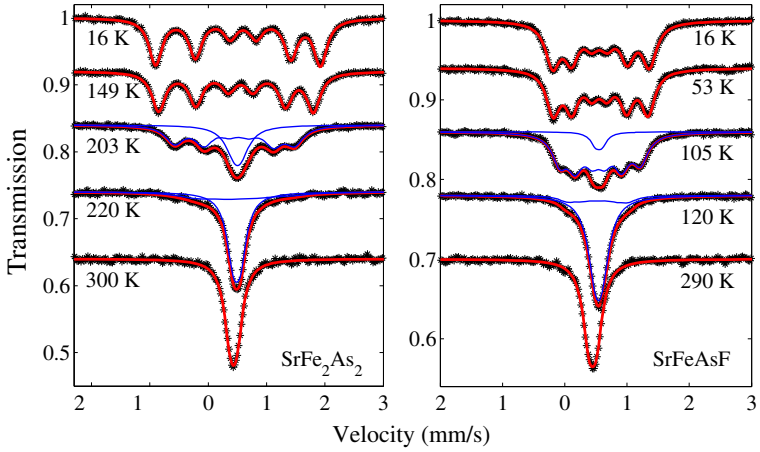

Fig. 1 Mössbauer spectra taken at indicated temperatures of the $SrFe_2As_2$ and SrFeAsF compounds

degrees of freedom [5]. However, a clear understanding of the relationship between magnetism and structural tuning is far from reached.

Mössbauer spectroscopy has been proved to be a useful tool to probe the local magnetic field at the iron nucleus of these materials [6, 7]. A comparison study of the 122-type and 1111-type families may yield valuable information about the magneto-structural coupling effect (MSCE). Therefore, in the present work, $SrFe_2As_2$ and SrFeAsF compounds are prepared and studied through Mössbauer spectroscopy. The result suggests that the MSCE for $SrFe_2As_2$ is stronger than that for the SrFeAsF compound, which may be due to the different properties of Sr and SrF inter-layers for $SrFe_2As_2$ and SrFeAsF, respectively.

2 Experimental

Polycrystalline $SrFe_2As_2$ and SrFeAsF compounds were prepared using conventional solid-state reaction method similar to previous reports [8, 9]. Phase purity were checked by X-ray powder diffraction (XRPD) on a Philips X'pert diffractometer with Cu K_α radiation. The lattice constants were found to be $a = 3.925$ Å, $c = 12.365$ Å for $SrFe_2As_2$ and $a = 4.002$ Å, $c = 8.970$ Å for SrFeAsF, which are in good agreement with previously reported values [8, 9]. Transmission Mössbauer spectra at temperatures between 16 K and 300 K were recorded using a conventional constant acceleration spectrometer with a γ-ray source of 25 mCi ^{57}Co in palladium matrix.

3 Results and discussion

Mössbauer spectra (MS) at selected temperatures are shown in Fig. 1. As can be seen, the spectra for both $SrFe_2As_2$ and SrFeAsF compounds can be well fitted by only one doublet/(sextet) above/(below) the transition region, indicating that there is no Fe containing impurity phase in our sample, coincidence with the XRPD results.

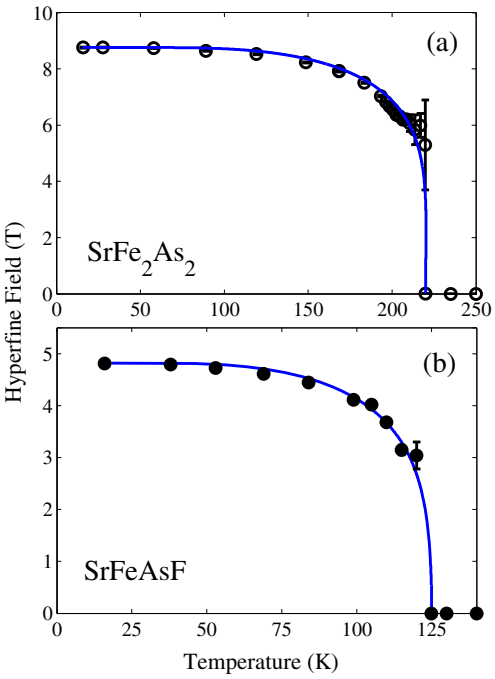

Fig. 2 Temperature dependence of the hyperfine field, $B_{hf}(T)$, extracted from least-squares fits of the Mössbauer spectra. The *blue solid lines* are theoretical fits to the data (see text)

At temperatures in the transition region the MS are fitted with the superposition of a doublet and a sextet. This means that the spin density wave (SDW) develops below or about onset of the magnetism and rapidly reaches quasi-rectangular form upon lowering of the sample temperature [6].

The variation of the HF with temperature is shown in Fig. 2. To investigate the MSCE, we fit the temperature dependence of the HF with a modified Bean–Rodbell model. To include MSCE, we rewrite the Gibbs free energy per unit volume as [7, 10] $G = -\frac{1}{2}Nk_BT_Nm^2 + \frac{1}{2}B\varepsilon^2 + \lambda\varepsilon m^2 - TNk_B\left[\ln 2 - \frac{1}{2}\ln\left(1-m^2\right) - m\tanh^{-1}m\right]$, where m is the sublattice magnetization, ε the strain, T_N the Néel temperature, B the elastic modulus, k_B the Boltzmann constant, and λ is the coupling coefficient. Following the same procedure as done by Bean and Rodbell, first minimizing the total energy with respect to ε and then with respect to m one can obtain the implicit dependence of m on T as [10] $T/T_N = \left(m/\tanh^{-1}m\right)\left(1+\eta m^2/3\right)$, where $\eta = 6\lambda^2/T_NBNk_B$ is a fitting parameter, which involves the magneto-structural coupling coefficient and elastic modulus and controls the order of the magnetic phase transition with $\eta < 1$ for a second order phase transition and $\eta > 1$ for a first order phase transition. Obviously, a larger λ will lead to a larger η, which will creates a larger energy barrier in the free-energy landscape when $\eta > 1$ [7]. This should leads to a sharper magnetic transition as shown in Fig. 2 for $SrFe_2As_2$.

The fitted results are also plotted in Fig. 2 (solid curve). The zero temperature HF is found to be 8.76 T and 4.82 T for $SrFe_2As_2$ and SrFeAsF, respectively. And T_N is determined to be 220 K for $SrFe_2As_2$ and 125 K for SrFeAsF, which are in good agreement with reported values [8, 9]. The structural factor η is found to be 1.09 and 0.8 for $SrFe_2As_2$ and SrFeAsF, respectively, indicating stronger MSCE for

$SrFe_2As_2$ than SrFeAsF. The only difference for the two compounds is the non-superconducting layers, namely Sr layer and F-Sr-F layer for $SrFe_2As_2$ and SrFeAsF, respectively. From the XRPD results one can obtain that a larger F-Sr-F layer leads to a larger distance along the *c*-direction between the FeAs plane for the SrFeAsF, which should reduce the effective interactions between the FeAs layers. Moreover, due to different properties of Sr and F-Sr-F inter-layers for $SrFe_2As_2$ and SrFeAsF, the crystal field for the two compounds should be different. This could lead to a completely different electronic structure for the two compounds, which may lead to the observed different magnetic moments and MSCE.

4 Conclusions

In summary, our Mössbauer results show that $SrFe_2As_2$ have a much larger magnetic moment than SrFeAsF. And the antiferromagnetic phase transition is sharper for $SrFe_2As_2$, indicating a stronger magneto-structural coupling effect than that in SrFeAsF, which might due to different inter-layer properties of the two compounds.

References

1. Kamihara, Y., Watanabe, T., Hirano, M., Hosono, H.: J. Am. Chem. Soc. **130**, 3296 (2008)
2. Paglione, J., Greene, R.L.: Nat. Phys. **6**, 645 (2010)
3. Lumsden, M.D., Christianson, A.D., J. Phys.: Condens. Matter **22**, 203203 (2010)
4. Lee, C.H., Lyo, A., Eisaki, H., Kito, H., Fernandez-Diaz, M.T., Ito, T., Kihou, K., Matsuhata, H., Braden, M., Yamada, K.: J. Phys. Soc. Jpn. **77**, 083704 (2008)
5. Egami, T., Fine, B.V., Singh, D.J., Parshall, D., Cruz, C., Dai, P.: Physica C **470**, S294 (2010)
6. Blachowski, A., Ruebenbauer, K., Zukrowski, J., Rogacki, K., Bukowski, Z., Karpinski, J.: Phys. Rev. B **83**, 134410 (2011)
7. Li, Z.W., Ma, X.M., Pang, H., Li, F.S., J. Phys.: Condens. Matter **23**, 255701 (2011)
8. Tegel, M., Rotter, M., Weiβ, V., Schappacher, F.M., Pöttgen, R., Johrendt, D., J. Phys.: Condens. Matter **20**, 452201 (2008)
9. Han, F., Zhu, X., Mu, G., Cheng, P., Wen, H.H.: Phys. Rev. B **78**, 180503(R) (2008)
10. Bean, C.P., Rodbell, D.S.: Phys. Rev. **126**, 104 (1962)

Hyperfine Interact (2012) 207:45–48
DOI 10.1007/s10751-012-0561-3

A Mössbauer study of $Ba(Fe_{1-x}Mn_x)_2As_2$ single crystals

Xiaoming Ma · Zhiwei Li · Jiangwei Bai · Hua Pang · Fashen Li

Published online: 2 February 2012

Abstract Single crystals of $Ba(Fe_{1-x}Mn_x)_2As_2$ (x = 0, 0.016, 0.064) have been prepared and studied by ^{57}Fe Mössbauer spectroscopy in the temperature range from 30 K to room temperature. The Mössbauer spectra show a change in the spectral shape with the change of Mn concentrations. It is found that both the hyperfine field and the magnetic phase transition temperature decrease with the increasing of Mn concentrations.

Keywords Magnetic phase transition · Mössbauer spectroscopy · $Ba(Fe_{1-x}Mn_x)_2As_2$

1 Introduction

Recently, systematic studies of underdoped $BaFe_2As_2$ have revealed interesting results regarding the relationship between structure, magnetism and superconductivity. With the decreasing of temperature, the $BaFe_2As_2$ parent compound undergoes simultaneous structural and magnetic phase transitions from a paramagnetic tetragonal phase to an orthorhombic antiferromagnetic phase at 140 K [1]. The structural/magnetic phase transition appears to split into two distinct phase transitions, both of which are suppressed with increasing electron doping (Co or Ni) at Fe site, and superconductivity arises for an appreciable range of doping [2, 3]. On the contrary, hole doping by Cr or Mn at the Fe site does not induce superconductivity, although the structural and magnetic phase transition are also suppressed [4, 5].

This work is supported by the National Natural Science Foundation of China under Grants No. 10975066 and 10774061.

X. M. Ma · Z. W. Li · J. W. Bai · H. Pang (✉) · F. S. Li
Lanzhou University, Lanzhou 730000, China
e-mail: hpang@lzu.edu.cn

X. M. Ma
e-mail: maxm2009@lzu.edu.cn

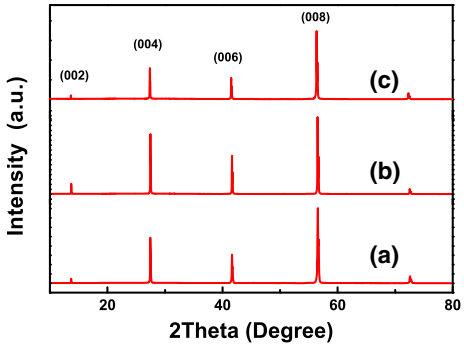

Fig. 1 XRD patterns of the prepared single crystals of $Ba(Fe_{1-x}Mn_x)_2As_2$: **a** x = 0, **b** 0.016, **c** 0.064

Given the strong coupling between structure, magnetism and superconductivity, the magnetic and structural properties of the hole doped $BaFe_2As_2$ compounds also require further investigations.

In addition, in iron-based superconductors magnetism, as well as superconductivity, is confined to Fe-As layers. Further investigations have shown that in Ba-122 iron pnictide, the Fe sublattice shows a spin density wave (SDW) magnetic order [1, 6]. Therefore, the ^{57}Fe Mössbauer spectroscopy has a natural advantage in studying the hyperfine fields at the Fe nuclei and the related magnetic properties of Fe atoms. There have been some reports about the observation of the SDW magnetic order using Mössbauer spectroscopy [6–9]. In this paper, we present Mössbauer study of powdered single crystals of $Ba(Fe_{1-x}Mn_x)_2As_2$ with x = 0, 0.016, 0.064.

2 Experimental details

Single crystals of $Ba(Fe_{1-x}Mn_x)_2As_2$ (x = 0, 0.016, 0.064) were grown out of a FeAs self-flux using conventional high-temperature solution growth techniques [2]. The prepared samples were well-formed plates with typical size of 5 × 5 × 0.2 mm^3 and the actual Mn concentrations were determined by the atomic absorption spectroscopy. The X-ray diffraction results, as shown in Fig. 1, suggest that the crystallographic c-axis is perpendicular to the plane of the plate. Transmission Mössbauer spectroscopy studies were performed using a conventional constant acceleration drive with a ^{57}Co:Pd source. The absorbers were prepared in powder form (10 mg of natural Fe/cm^2). The velocity calibration was performed with sodium nitroprusside powder at room temperature (RT) and all isomer shifts were quoted relative to the α-Fe foil at RT.

3 Results and discussion

Mössbauer spectra of $Ba(Fe_{1-x}Mn_x)_2As_2$ (x = 0, 0.016, 0.064) single crystals at temperatures between 30 K and RT are shown in Fig. 2. At RT, the spectra are single absorption lines with a little asymmetry, indicating a small amount of a foreign FeAs phase [10]. The content of the FeAs phase is too small to be reasonably fitted, so the spectra were fitted with single lines. As can be seen, at temperatures below the

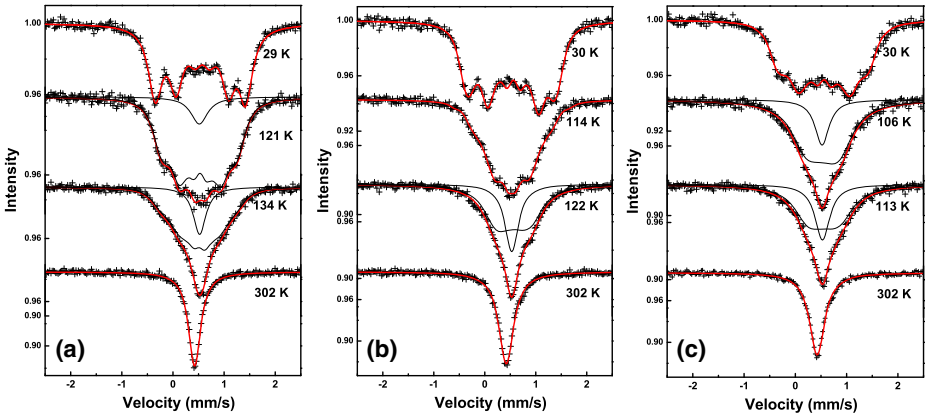

Fig. 2 ^{57}Fe Mössbauer spectra of the single crystals of $Ba(Fe_{1-x}Mn_x)_2As_2$ obtained at indicated temperatures: **a** $BaFe_2As_2$; **b** $Ba(Fe_{0.984}Mn_{0.016})_2As_2$; **c** $Ba(Fe_{0.936}Mn_{0.064})_2As_2$

Table 1 Selected hyperfine parameters as obtained for $Ba(Fe_{1-x}Mn_x)_2As_2$

x	Temperature (K)	IS (mm/s)	HF (T)	2ε (mm/s)
0	29	0.56	5.24	−0.05
	RT	0.42	–	–
0.016	30	0.54	4.79	−0.04
	RT	0.42	–	–
0.064	30	0.55	4.49	−0.03
	RT	0.43	–	–

IS is the isomer shift, HF is the average hyperfine field and 2ε is the quadrupole shift

SDW transition point, the spectra are not typical sextets and it is impossible to fit the data with only one sextet. Therefore, the spectra were fitted assuming a distribution of hyperfine fields. The hyperfine parameters at selected temperatures are listed in Table 1.

As shown in Table 1, the isomer shift (IS) values for all samples are around 0.42 mm/s at RT, which is typical for the $Th_2Cr_2Si_2$-type compounds. The almost identical IS values may be due to the small doping level of the samples or the fact that doping at iron site by similar atoms, such as Co, Ni, has little effect on IS [8]. The hyperfine fields of $Ba(Fe_{1-x}Mn_x)_2As_2$ exhibit strong dependence on the Mn concentrations. First, the hyperfine field drops from 5.24 T for $BaFe_2As_2$ to 4.79 T and 4.49 T for $x = 0.016$ and $x = 0.064$ around 30 K, respectively. Second, as shown in Fig. 2a, the spectrum of the parent compound changes from a singlet pattern to a complex pattern with magnetic splitting around 134 K, and the transition temperature is similar to the reported results [1, 10]. However, for the Mn-containing samples, the magnetic transitions are suppressed to lower temperatures with the increasing of Mn concentrations: 122 K for $x = 0.016$ and 113 K for $x = 0.064$. Third, as shown in Fig. 2, the linewidths of the spectra obtained around 30 K increase obviously for the doped compounds, which has also been observed in $Ba(Fe_{1-x}Ni_x)_2As_2$ system [9]. The broadening of the linewidth suggests a distribution of the local magnetic environment, which may be caused by the coexistence of commensurate and incommensurate SDWs [9, 11] and/or inhomogeneous Mn substitutions.

4 Conclusion

In conclusion, Mössbauer studies of single crystals of $Ba(Fe_{1-x}Mn_x)_2As_2$ have been performed. Our results show that Mn-substitution changes the shape of the spectra significantly and both the hyperfine field and the SDW transition temperature decrease with the increase of the Mn concentrations in the range of $0 < x < 0.064$.

References

1. Rotter, M., et al.: Spin-density-wave anomaly at 140 K in the ternary iron arsenide $BaFe_2As_2$. Phys. Rev. B **78**, 020503 (2008)
2. Chu, J.H., et al.: Determination of the phase diagram of the electron-doped superconductor $Ba(Fe_{1-x}Co_x)_2As_2$. Phys. Rev. B **79**, 014506 (2009)
3. Sefat, A.S., et al.: Structure and anisotropic properties of $BaFe_{2-x}Ni_xAs_2$ (x = 0, 1, and 2) single crystals. Phys. Rev. B **79**, 094508 (2009)
4. Kim, M.G., et al.: Antiferromagnetic ordering in the absence of structural distortion in $Ba(Fe_{1-x}Mn_x)_2As_2$. Phys. Rev. B **82**, 220503 (2010)
5. Marty, K., et al.: Competing magnetic ground states in nonsuperconducting $Ba(Fe_{1-x}Cr_x)_2As_2$ as seen via neutron diffraction. Phys. Rev. B **83**, 060509 (2011)
6. Olariu, A., et al.: Incommensurate spin density wave versus local magnetic inhomogeneities in $Ba(Fe_{1-x}Ni_x)_2As_2$: a ^{57}Fe Mössbauer spectroscopy study. arXiv:1106 1332 (2011)
7. Blachowski, A., et al.: Shape of spin density wave versus temperatures in AFe_2As_2 (A = Ca, Ba, Eu): a Mössbauer study. Phys. Rev. B **83**, 134410 (2011)
8. Airat, K., et al.: Mössbauer studies of the superconducting cobalt/nickel-doped $BaFe_2As_2$. Whither go the injected electron(s)? J. Phys., Condens. Matter **23**, 202201 (2011)
9. Israel, N., et al.: Mössbauer studies of $Ba(Fe_{1-x}Ni_x)_2As_2$. J. Phys., Condens. Matter **22**, 355701 (2010)
10. Inowik I., et al. Mössbauer spectroscopy determination of iron foreign phases in the superconcucting systems; $RAsFeO_{1-x}$, $RAsFeO_{1-x}F_x$, and $Sr_{1-x}K_xFe_2As_2$. J. Supercond. Novel Magnetism **21**, 297 (2008)
11. Klauss, H.H., et al.: Commensurate spin DensityWave in LaFeAsO: a local probe study. Phys. Rev. Lett. **101**, 077005 (2008)

Hyperfine Interact (2012) 207:49–52
DOI 10.1007/s10751-011-0403-8

A CEMS search for precipitate formation in ^{57}Fe implanted ZnO

Krishanlal Bharuth-Ram · Hilary Masenda · Terence B. Doyle · Sebastian Geburt · Carsten Ronning · Harald Palle Gunnlaugsson

Published online: 8 November 2011

Abstract Conversion electron Mössbauer Spectroscopy measurements have been made on ZnO single crystals implanted with 60 keV ^{57}Fe to 4 and 8 at.% peak concentrations, and annealed up to 800°C. The spectra show quite strong changes with annealing, but no evidence of magnetic components, thus precluding the formation of large sized precipitates or secondary phases. Above an annealing temperature of 650°C, the dominant spectral component is a doublet with hyperfine parameters typical of Fe^{3+}, which is attributed to Fe^{3+} ions in nano-precipitates ∼5 nm in size.

Keywords ZnO · ^{57}Fe implanted · CEMS · Nano-precipitates

1 Introduction

The theoretical work of Dietl et al. [1] and Sato and Katayama-Yoshida [2], predicting room temperature ferromagnetism (RTFM) in p-type ZnO implanted with ≥5% Mn ions as well as other transition metal (TM) ions, spawned a flurry of experimental investigations on the search for RTFM in transition metal doped ZnO and other

K. Bharuth-Ram (✉) · T. B. Doyle
School of Physics, University of KwaZulu-Natal, Durban 4041, South Africa
e-mail: kbr@tlabs.ac.za

H. Masenda
School of Physics, University of the Witwatersrand, WITS, Johannesburg 2050, South Africa

T. B. Doyle
iThemba LABS, Somerset West 7129, Western Cape, South Africa

S. Geburt · C. Ronning
Institue of Solid State Physics, University of Jena, 07743 Jena, Germany

H. P. Gunnlaugsson
Department of Physics and Astronomy, Aarhus University, 8000 Aarhus, Denmark

metallic oxides. The experimental results however have been ambiguous and often contradictory regarding the magnetic properties of different $Zn_{1-x}TM_xO$ systems, and revisit of earlier measurements [3] and reviews [4, 5] have questioned whether the TM ions are uniformly distributed in the host matrix on the appropriate atom site or if clusters, precipitates or secondary phases are responsible for the observed magnetic effects.

An understanding of the behaviour of the incorporated TM atoms and their impact on the crystal structure of the host is essential if the desired magnetic properties are to be realised. In a recent study Schumm et al. [6] applied Raman scattering and XRD measurements to study impurity incorporation, induced defects and disorder in ZnO implanted with TM ions with a step-like profile with concentrations up to 16 at.%. Their results showed the presence of micro-precipitates, and additionally secondary phases in samples with $\geq$8 at. % Mn ions.

In this contribution we present results of our conversion electron Mössbauer spectroscopy (CEMS) investigations on ZnO implanted with ^{57}Fe ions with 60 keV energy and to peak concentrations of 4 at.% and 8 at.%.

2 Experimental details

Mass separated ^{57}Fe ions were implanted with 60 keV energy at room temperature into ZnO single crystal substrates commercially available from Crystec GmbH, Berlin. TRIM simulations gave a Gaussian implantation profile with a mean depth of about 30 nm and half-width (HWHM) of about 10 nm. The implantation fluence was chosen to give ^{57}Fe peak concentrations of 4 and 8 at.%. CEMS measurements were made at room temperature, on the as-implanted samples and after annealing the samples for 30 min in flowing N_2 at temperatures up to 800°C.

3 Results and discussion

Figure 1 presents the CEMS spectra of ZnO single crystals implanted with ^{57}Fe to peak concentrations of (a) 4 at.% (ZnO:Fe4) and (b) 8 at.% (ZnO:Fe8), respectively (corresponding to respective fluencies of 1.2×10^{16} ^{57}Fe/cm^2 and 2.4×10^{16} ^{57}Fe/cm^2), and annealed at the temperatures indicated. The set of spectra for each sample was analyzed in a simultaneous fit to the data obtained after the annealing at the different temperatures. The fit components and their assignments are listed in Table 1, where isomer shifts are given relative to α-Fe.

On implantation, the spectra of both samples show significant contributions (>50%) from Fe in defect sites in the ZnO lattice (Fe_D) plus an asymmetric doublet with isomer shift and quadrupole splitting consistent with Fe^{2+} on substitutional Zn sites in the wurtzite lattice. The spectra show dramatic changes with annealing, but no evidence of any magnetic component, thus ruling out the formation of large sized precipitates or secondary (ZnFeO) complexes.

After the annealing at 350°C, the Fe_D fraction reduces to 6% and 12%, respectively, for ZnO:Fe4 and ZnO:Fe8, and a second doublet with hyperfine parameters of Fe^{3+} appears. After annealing at $T_A \geq 650$°C, the spectra of both samples are dominated by a quadrupole doublet which accounts for >80% of the spectral area

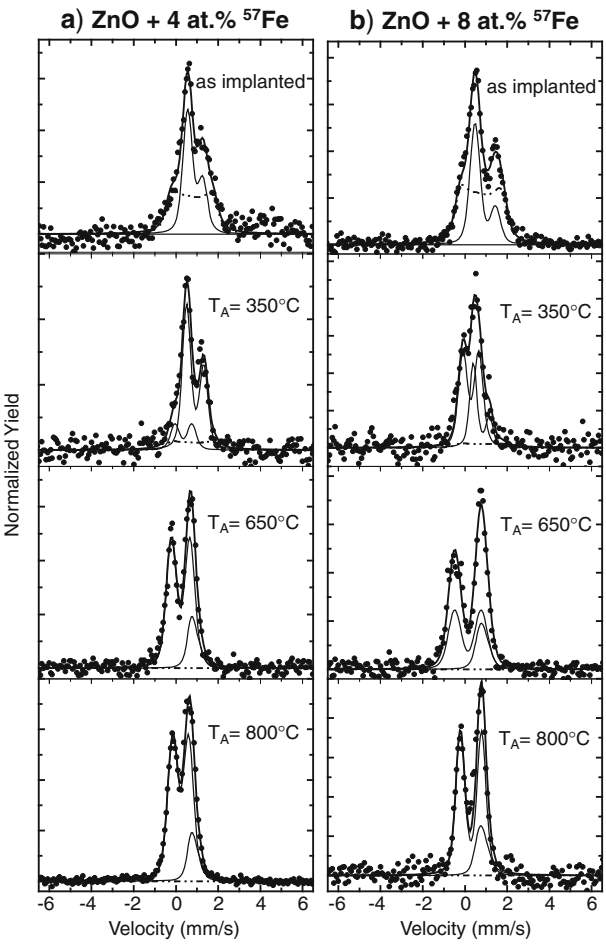

Fig. 1 CEMS spectra of ZnO single crystals implanted with **a**) 4 at.% and **b**) 8 at.% ^{57}Fe, observed after annealing at the temperatures indicated

at $T_A = 800°C$. The isomer shift and quadrupole splitting (ΔE_Q) of the doublet for ZnO:Fe4 (ZnO:Fe8) have values of 0.28 (0.22) mm/s and 1.00 (0.75) mm/s, which are typical of parameters for Fe^{3+}, but larger than the values for substitutional Fe^{3+} in ZnO [7]. As stated above, Schumm et al. [6] conducted Raman scattering and XRD measurements on ZnO samples implanted with TM ions at a range of energies to give a step-like profile with concentrations up to 16 at.% (total implantation fluencies up to $2.5 \times 10^{17}/cm^2$). Their results showed the presence of micro-precipitates, and additionally secondary phases in samples with $\geq$8 at.% Mn ions. In the present measurements the peak implantation fluence is an order of magnitude lower, and the absence of secondary phases is not unexpected. However, [6] also shows the presence of micro-precipitates even in the samples with lower TM ion concentrations. We therefore attribute the dominant doublet observed at $T_A \geq 650°C$ to nano-sized Fe^{3+} precipitates, the absence of any magnetic components in the spectra indicating that these are $\sim$5 nm in size.

Table 1 Hyperfine parameters (isomer shift δ, quadrupole splitting ΔE_Q) and Gaussian broadening σ of the components required to fit the spectra presented in Fig. 1

T_A		ZnO:Fe4			ZnO:Fe8		
		δ (mm/s)	ΔE_Q (mm/s)	σ (mm/s)	δ (mm/s)	ΔE_Q (mm/s)	σ (mm/s)
As-implanted	Fe^{2+}	0.96(2)	−0.97(2)	0.19	0.91(2)	−0.71(2)	0.18
	Fe_D	0.74(2)	1.33(3)	0.10	0.74(2)	1.33(2)	0.10
350°C	Fe^{2+}	0.78(2)	−0.77(2)	0.12	0.91(2)	−0.81(2)	0.15
	Fe_D	0.74(4)	1.33(4)	0.10	0.74(4)	1.33(4)	0.10
	Fe^{3+}	0.28(2)	0.75(2)	0.18	0.35(2)	0.80(2)	0.17
650°C	Fe^{2+}	0.92(2)	−0.37(2)	0.19	0.91(2)	−0.35(2)	0.15
	Fe^{3+}	0.14(2)	1.25(2)	0.26	0.22(2)	0.87(2)	0.20
800°C	Fe^{2+}	0.90(2)	−0.37(2)	0.19	0.91(2)	−0.35(2)	0.15
	Fe^{3+}	0.28(2)	1.00(2)	0.17	0.22(2)	0.75(2)	0.20

4 Conclusions

We have conducted CEMS measurements on ZnO samples implanted with 4 and 8 at.% ^{57}Fe.

The spectra show quite dramatic changes with annealing, but no evidence of magnetic components. Above an annealing temperature of 650°C, the dominant spectral component is a doublet with hyperfine parameters typical of Fe^{3+}, which is attributed to Fe^{3+} ions in nanoclusters ∼5 nm in size.

Acknowledgement This study was undertaken within the National Research Foundation (South Africa)—Deutsche Forschungsgemeinschaft (Germany) (contract Ro1198/13-1) bi-lateral research program.

References

1. Dietl, T., Ohno, H., Matsukura, F., Cibert, J., Ferrant, D.: Science **287**, 1019 (2000)
2. Sato, K., Katayama-Yoshida, H.: Jpn. J. Appl. Phys., Part 2 **40**, L334 (2001)
3. Zhou, S., Potzger, K., Talut, G., Reuther, H., von Borany, J., Grötzschel, R. Skorupa, W., Helm, M., Fassbender, J.: J. Appl. Phys. **103**, 023903 (2008)
4. Pearton, S.J., Heo, W.H., Ivill, M., Norton, D.P., Steiner, T.: Semicond. Sci. Technol. **19**, R59–R74 (2004)
5. Coey, J.M.D., Chambers, S.A.: MRS Bull. **33**, 1053–1058 (2008)
6. Schumm, M., Koerdel, M., Müller, S., Ronning, C., Dynowska, E., Gołacki, Z., Szuszkiewicz, W., Geurts, J.: J. Appl. Phys. **105**, 083525 (2009)
7. Gunnlaugsson, H.P., et al.: App. Phys. Lett. **92**, 142501 (2010)

Hyperfine Interact (2012) 207:53–59
DOI 10.1007/s10751-011-0421-6

Unfolding the role of iron in Li-ion conversion electrode materials by ^{57}Fe Mössbauer spectroscopy

José L. Tirado · Pedro Lavela · Carlos Pérez Vicente · Bernardo León · Candela Vidal-Abarca

Published online: 28 October 2011

Abstract ^{57}Fe Mössbauer spectroscopy is particularly useful in the study of oxide and oxalate conversion anode materials for Li-ion batteries. After reduction in lithium test cells, all these materials showed Mössbauer spectra ascribable to iron atoms in two different environments with superparamagnetic relaxation. The spectra recorded at 12 K revealed the ferromagnetic character in agreement with particle sizes of ca. 5 nm. The two types of iron can be ascribed then to surface and core atoms. Core iron atoms play an important role to retain high faradic capacity values for a large number of cycles. These atoms are preserved from irreversible reactions with the electrolyte and hence they promote a high reversibility and rate capability.

Keywords Conversion anode materials · Lithium-ion batteries · ^{57}Fe Mössbauer spectroscopy

1 Introduction

The future of electrochemical energy storage devices in transport applications is dependent on the development of higher capacity systems. The future "superbatteries" may be found in new technologies such as lithium-air or lithium-sulfur [1]. However, the lithium-ion related concepts still have serious possibilities of improvement. For the negative electrode, a minimum requirement is doubling the capacity of the conventional graphite electrode, which for example could increase the travel distance of an EV on a single electric charge.

In lithium-ion batteries, lithium metal is replaced by different compounds in order to avoid the problems associated with the poor reconstruction of the surface of the

J. L. Tirado (✉) · P. Lavela · C. Pérez Vicente · B. León · C. Vidal-Abarca
Laboratorio de Química Inorgánica, Universidad de Córdoba, Edificio Marie Curie, Campus de Rabanales, 14071 Córdoba, Spain
e-mail: iq1ticoj@uco.es

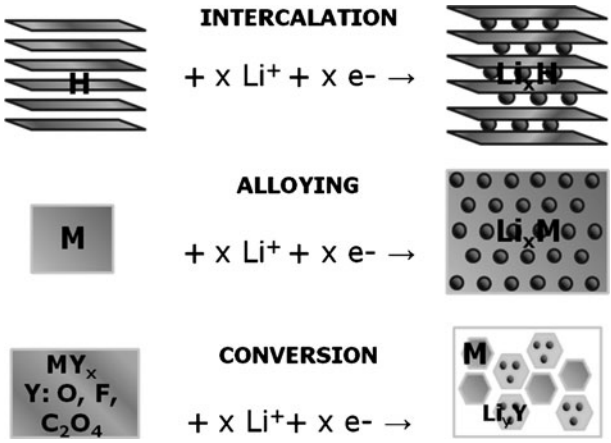

Fig. 1 Types of anode materials for Li-ion battery

lithium electrode on cycling. In general, the complete Li-ion battery can be written as: A/Electrolyte/C, where A and C are the anode and cathode, respectively, provided that C has a higher potential than A vs. Li/Li^+. When studying electrode materials for Li-ion batteries, it is common to use lithium test cells such as Li/Electrolyte/A or Li/Electrolyte/C, in which both A and C act as cathodes vs. lithium. However, they still can be referred to as A, (potential) anode material (for lithium-ion batteries), and C, (potential) cathode material (for lithium-ion batteries). The known active materials having relatively low potential vs. Li/Li^+, and thus being interesting for the anode (A) of Li-ion batteries, have different chemistries (Fig. 1). Among intercalation compounds, graphite and titanium oxides are currently exploited materials in commercial products. However, even for the promising graphene, capacities never double that of graphite on prolonged cycling [2]. Alloying materials such as tin and silicon may show capacities more than twice that of graphite, but the problems associated to the colossal volume changes associated to lithium addition-extraction damage their cycling properties [3]. Finally, vast group of materials that are known to participate in reversible conversion reactions with lithium were more recently studied [4].

Initially, the unexpected reversibility of the conversion process was reported for binary first-row transition metal oxides, while subsequently it was extended to mixed oxides [5–12]. More recently, we were able to extend the reversible conversion to transition metal oxysalts, such as oxalates and carbonates, in which new mechanisms of charge storage such as double layer capacitive effects were detected [13–17]. Other researchers have extended this group of compounds to metal formates [18].

^{57}Fe Mössbauer spectroscopy is a powerful tool to deepen in the mechanism of reaction during cell charge and discharge of both conversion oxides and oxysalts containing iron. The possibilities of application that will be discussed below include confirmation of the reduction to metallic state to avoid confusion with side processes such as SEI formation or double-layer charge storage, study of the environment(s) of atoms in the reduced electrode, maximum re-oxidation achievable and changes in particle size-magnetic ordering on cycling, which may unveil the origin of capacity retention-fading.

2 Experimental

Different synthesis procedures can be used to obtain mixed oxides with highly homogeneous composition and controlled particle size. Here, MFe_2O_4 oxides were alternatively prepared by a reverse micelles procedures with Span 80 as a surfactant [19] and by using citrate precursors [20]. The synthesis of dihydrate transition metal oxalates $MC_2O_4{\cdot}2H_2O$ was carried out by the reverse micelles method, using isooctane as the oil phase, and cetyltrimethylammonium bromide surfactant and hexanol co-surfactant [13].The resulting hydrated oxysalts were thermally decomposed at 200°C under vacuum to produce the dehydrated forms MC_2O_4.

The electrochemical tests were carried out in two-electrode Swagelok-type lithium test cells were used. The electrodes were prepared by blending the powdered active material (60%) with carbon black (30%) and poly vinylidene fluoride (10%) dissolved in N-methyl-pyrrolidone. The weight of active material in the electrodes for cycling experiments was about 3 mg, and the electrode was 9 mm in diameter. The slurry was cast onto a Cu foil and vacuum-dried at 120°C. As the negative electrode, a lithium foil was used. The electrolyte was a solution of ethylene carbonate-diethyl carbonate in 1:1 weight proportion, including 1 M $LiPF_6$, supported by a porous glass-paper disk. The cells were assembled/disassembled in an Ar-filled glovebox (H_2O, $O_2 < 1$ ppm). Charge/discharge experiments were interrupted at selected voltages and the electrodes removed without relaxation period for spectroscopic and diffraction examination.

^{57}Fe Mössbauer spectra were recorded in transmission mode by using an EG&G constant acceleration spectrometer and a ^{57}Co (Rh matrix) (10 mCi) γ source. The velocity scale was calibrated from the magnetic sextet of a high-purity iron foil absorber. Experimental data were fitted to Lorentzian lines by using a least-squares-based method. The quality of the fit was controlled by the classical $\chi 2$ test. All isomer shifts are given relative to the centre of the α-Fe spectrum at room temperature. The measurements at low temperatures were carried with a CRYOGENICS cryostat coupled to a CRYO.CON temperature controller.

3 Results and discussion

A typical conversion reaction in oxide materials is:

$$MO_x + 2xLi^+ + 2xe^- \rightarrow Li_2O + M \quad (1)$$

The theoretical capacities for mixed oxides are collected in Table 1. All the values are noticeably above the theoretical capacity of graphite (ca. 372 $mAhg^{-1}$). Several iron-containing oxides such as MFe_2O_4 (M: Co, Ni) and $Co_{3-x}Fe_xO_4$ ($x = 1, 3$) ($0 \leq x \leq 1$) were shown to be potential candidates for the negative electrode of future Li-ion batteries. In both cases, the electrochemical reaction with lithium results in the formation of transition metals in their reduced state, together with lithium oxide. Lithium extraction allows the reoxidation of iron [7, 10, 19, 20].

For polycrystalline $NiFe_2O_4$ and $CoFe_2O_4$ samples, the ^{57}Fe Mössbauer showed a ferrimagnetic character [19, 20]. After reduction in lithium test cells to ca. 0 V vs. Li/Li^+, the electrode material showed Mössbauer spectra ascribable to iron atoms in two different environments (Fig. 2, Table 2). Both types of atoms show

Table 1 Theoretical capacities and references of the experimental study for different mixed-oxide conversion electrodes

Compound	Full-conversion theoretical capacity (mA h g^{-1})	Reference
Ni_5MgMnO_8	857	[5]
$NiCo_2O_4$	891	[6]
$NiFe_2O_4$	915	[7]
$ZnFe_2O_4$	889	[8]
$LiCoO_2$	822	[9]
$CoFe_2O_4$	914	[10]
$CuFe_2O_4$	896	[11]
$MnCo_2O_4$	906	[12]

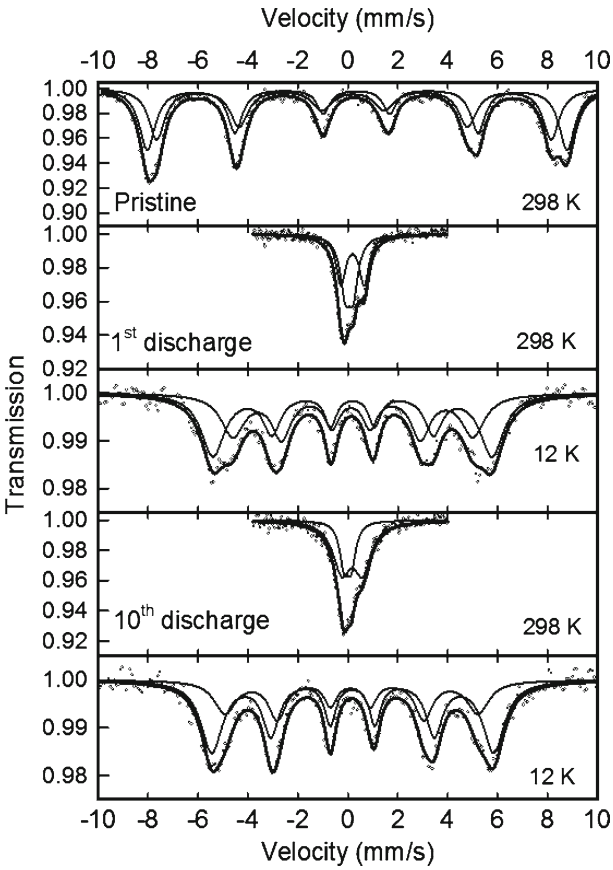

Fig. 2 ^{57}Fe Mössbauer spectra of $NiFe_2O_4$ and discharged electrodes recorded at 298 and 12 K, after 1 and 10 discharges

superparamagnetic relaxation. The spectra recorded at 12 K showed a recovery of the ferromagnetic character (Fig. 2). The reduced blocking temperature implies an enhanced diminution of particle size to ca. 5 nm, in agreement with electron microscopy observations (Fig. 3). The two types of iron can be ascribed then to surface and core atoms. Core iron atoms play an important role to retain high faradic capacity values for a large number of cycles. These atoms are preserved from

Table 2 Hyperfine parameters of pristine and electrochemically reacted electrodes recorded at room temperature

IS isomer shift, *QS* quadrupolar splitting, *LW* line width

Sample	IS	QS	LW	%
FeC_2O_4	1.181_4	1.621_8	0.414_{10}	
reduced	0.00_4	0.68_6	0.5_{10}	37
FeC_2O_4	0.22_3	0.87_3	0.51_4	63
reduced	0.05_1	0.33_1	0.39_3	44
$NiFe_2O_4$	0.17_1	0.92_2	0.51_3	56
reduced	0.04_1	0.00_2	0.61_7	17
$CoFe_2O_4$	0.04_1	0.65_3	0.61_2	83
reoxidized	0.28_2	0.99_3	0.49_6	57
$CoFe_2O_4$	0.25_1	0.49_3	0.49_3	43

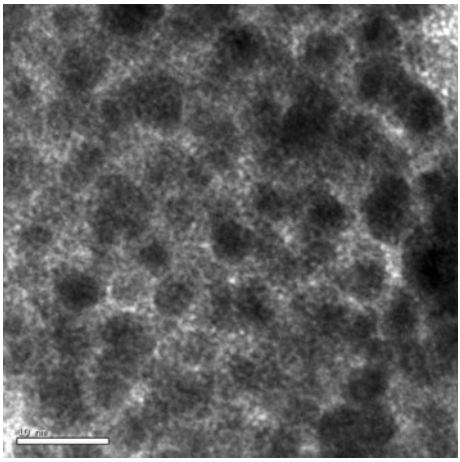

Fig. 3 TEM image of $CoFe_2O_4$ electrode after electrochemical reaction with lithium

irreversible reactions with the electrolyte and hence they promote a high reversibility and rate capability.

After re-oxidation in the cycled electrodes, Fe^{3+} is the main iron contribution, independently from the starting oxidation state of iron in these compounds, which could be interpreted by assuming the existence of Fe^{3+} oxides as well as non-oxidized iron in the solid to compensate for the available anions. Moreover, the two different types of iron atom (core and surface, Table 2) are still observable as quadrupolar doublets indicative of superparamagnetic nanoparticles, although their isomer shift is larger than in the reduced electrodes (Table 2). The size of the particles decreases on further cycling.

A typical conversion reaction of divalent metal oxalates is:

$$MC_2O_4 + 2Li^+ + 2e^- \rightarrow M + Li_2C_2O_4 \quad (2)$$

As compared with transition metal oxides, and irrespective of their different composition, the electrochemical reaction with lithium results in the formation of transition metals in their reduced state, in this case together with lithium oxalate. Lithium extraction allows the reoxidation of iron [13–15].

The RT ^{57}Fe Mössbauer spectra of iron-containing oxalates contain basically a single quadrupole splitted signal (Table 2). The spectrum recorded at 12 K (Fig. 4)

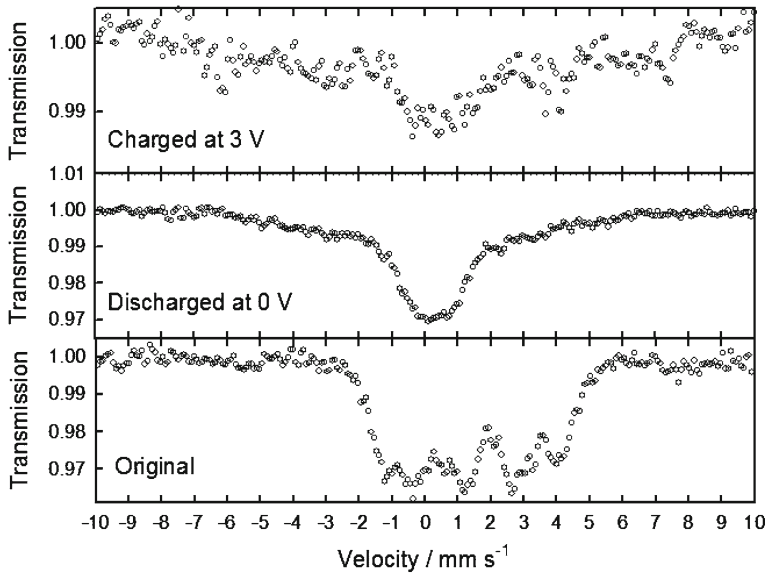

Fig. 4 ^{57}Fe Mössbauer spectra of FeC_2O_4 and used electrodes recorded at 12 K

reveals a poorly resolved cooperative magnetism. The limitations in the recording temperature did not allow discriminating the magnetic components, in agreement with its Néel temperature (11.7 K) [21]. After reduction in lithium test cells to ca. 0 V vs. Li/Li$^+$, the oxalate materials showed Mössbauer spectra ascribable to iron atoms in two different environments [13]. The spectra recorded at 12 K (Fig. 4) does not show the corresponding magnetic sextets. This phenomenon implies a significantly lower lattice coherence length than in the case of oxides. In fact the lower values prevent from direct observation by common electron microscopy techniques. Finally, the recharged electrodes recorded at 12 K reveal the reoxidation to Fe^{3+} with an incipient ferromagnetic component. Summarizing, as compared with oxides, the superparamagnetic state is observable at lower temperatures in the case of iron oxalate. This phenomenon is a consequence of smaller particles, which in turn may condition a significant contribution of the capacitive charge storage mechanism, as recently reported form the $Fe_xCo_{1-x}C_2O_4$ solid solutions [15].

4 Conclusions

Mössbauer spectroscopy has become an irreplaceable tool in the study of different conversion anode materials for Li-ion batteries. Relevant information is obtained on the changes in oxidation state and chemical environment of iron, which are commonly present in various electroactive species. Particularly, the nature of nanocrystalline or amorphous solids involved in the electrochemical reactions, which are reluctant to be characterized by conventional x-ray diffraction methods, can be easily unfolded by Mössbauer spectroscopy. The use of Mössbauer spectroscopy leads to a better understanding of the reaction mechanism, which finally allows an optimized

use of the electrode material. Notorious examples come from the study of nanodispersed materials, which provide large capacities, and improved cyclability.

Acknowledgements The authors are indebted to ERI ALISTORE, MICINN (MAT2008–05880) and Junta de Andalucía (FQM288 and Contract FQM-6017).

References

1. Scrosati, B.: Nature **473**, 448 (2011)
2. Bhardwaj, T., Antic, A., Pavan, B., Barone, V., Fahlman, B.D.: J. Am. Chem. Soc. **132**, 12556 (2010)
3. Besenhard, J.O., Yang, J., Winter, M.: J. Power Sources **68**, 87 (1997)
4. Poizot, P., Laruelle, S., Grugeon, S., Dupont, L., Tarascon, J.M.: Nature **407**, 496 (2000)
5. Alcántara, R., Jaraba, M., Lavela, P., Tirado, J.L.: J. Solid State Chem. **166**, 330 (2002)
6. Alcántara, R., Jaraba, M., Lavela, P., Tirado, J.L.: Chem. Mater. **14**, 2847 (2002)
7. Alcántara, R., Jaraba, M., Lavela, P., Tirado, J.L., Jumas, J.C., Olivier-Fourcade, J.: Electrochem. Commun. **5**, 16 (2003)
8. NuLi, Y.-N., Chu, Y.-Q., Qin, Q.-Z.: J. Electrochem. Soc. **151**, A1077 (2004)
9. Chadwick, A.V., Savin, S.L.P., Alcántara, R., Fernández Lisbona, D., Lavela, P., Ortiz, G.F., Tirado, J.L.: ChemPhysChem. **7**, 1086 (2006)
10. Lavela, P., Tirado, J.L.: J. Power Sources **172**, 379 (2007)
11. Bomio, M., Lavela, P., Tirado, J.L.: ChemPhysChem. **8**, 1999 (2007)
12. Lavela, P., Tirado, J.L., Vidal-Abarca, C.: Electrochim. Acta **52**, 7986 (2007)
13. Aragón, M.J., León, B., Pérez Vicente, C., Tirado, J.L.: Inorg. Chem. **47**, 10366 (2008)
14. Aragón, M.J., León, B., Pérez Vicente, C., Tirado, J.L., Chadwick, A.V., Berko, A., Beh, S.Y.: Chem. Mater. **21**, 1834 (2009)
15. Aragón, M.J., León, B., Serrano, T., Pérez Vicente, C., Tirado, J.L.: J. Mater. Chem. **21**, 10102 (2011)
16. Aragón, M.J., Pérez-Vicente, C., Tirado, J.L.: Electrochem. Commun. **9**, 1744 (2007)
17. Aragón, M.J., León, B., Pérez Vicente, C., Tirado, J.L.: J. Power Sources **196**, 2863 (2011)
18. Saravanan, K., Nagarathinam, M., Balaya, P., Vittal, J.J.: J. Mater. Chem. **20**, 8329 (2010)
19. Vidal-Abarca, C., Lavela, P., Tirado, J. L. : J. Phys. Chem. C, **114**, 12828 (2010)
20. Vidal-Abarca, C., Lavela, P., Tirado, J. L. : Solid State Ionics **181**, 616 (2010)
21. Simizu, S., Chen, J.Y., Friedberg, S.A., Martinez, J., Shirane, G.: J. Appl. Phys. **61**, 3420 (1987)

Hyperfine Interact (2012) 207:61–65
DOI 10.1007/s10751-011-0433-2

Electrical conductivity and local structure of barium manganese iron vanadate glass

Shiro Kubuki · Hitomi Masuda · Kazuhiko Akiyama · Isao Furumoto · Tetsuaki Nishida

Received: 23 August 2011 / Accepted: 18 October 2011 / Published online: 28 October 2011

Abstract Local structure and electrical conductivity of semiconducting $20BaO{\cdot}10Fe_2O_3 \cdot x\,MnO_2 \cdot (70-x)V_2O_5$ glass ($x = 0-30$), abbreviated as xBFMV, were investigated by means of ^{57}Fe-Mössbauer spectroscopy, differential thermal analysis (DTA) and DC four-probe method. Mössbauer spectrum of these vanadate glasses consists of a doublet with an identical isomer shift (δ) of 0.38±0.01 mm s^{-1}, indicating that distorted FeO_4 tetrahedra constitute the structural units with distorted VO_4 tetrahedra and VO_5 pyramids. Quadrupole splitting (Δ) gradually increases from 0.70±0.02 to 0.87±0.02 mm s^{-1} with an increase in the MnO_2 content, indicating an increased local distortion of $Fe^{III}O_4$ tetrahedra. DTA study of these glasses showed a gradual increase of glass transition temperature (T_g) from 329±5 to 411±5°C, showing an improved thermal durability. 'T_g vs. Δ plot' yielded a straight line with a large slope of 707°C(K)/mm s^{-1}, proving that Fe^{III} played a role of network former (NWF). An isothermal annealing of 10BFMV glass at 500°C for 1000 min resulted in a marked increase in the electrical conductivity (σ) from (4.5±3.9) × 10^{-7} to (1.4±0.3) × 10^{-2} S cm^{-1} and a decrease in the activation energy for the electrical conduction (E_a) from 0.33 ± 0.07 to 0.11±0.01 eV, while Δ of Fe^{III} decreased from 0.76±0.02 to 0.49±0.02 mm s^{-1}. These results suggest that decrease

S. Kubuki (✉) · H. Masuda · K. Akiyama
Department of Chemistry, Graduate School of Science and Engineering,
Tokyo Metropolitan University, Minami-Osawa 1-1,
Hachi-Oji, Tokyo 192-0397, Japan
e-mail: kubuki@tmu.ac.jp

I. Furumoto · T. Nishida
Major in Advanced Materials, Graduate School of Advanced Science and Engineering,
Kinki University, Kayanomori 11-6, Iizuka, Fukuoka 820-8555, Japan

T. Nishida
Department of Biological and Environmental Chemistry,
Faculty of Humanity-Oriented Science and Engineering,
Kinki University, Kayanomori 11-6, Iizuka,
Fukuoka 820-8555, Japan

in the distortion of $Fe^{III}O_4$ tetrahedra involved with the structural relaxation causes an increase in the probability of electron hopping from V^{IV} or V^{III} to V^{V}.

Keywords Barium manganese iron vanadate glass · ^{57}Fe-Mössbauer spectroscopy · Electrical conductivity · Structural relaxation

1 Introduction

Vanadate glass is known to be a semiconductor with an electrical conductivity (σ) of 10^{-7}–10^{-5} S cm^{-1}. The electrical conduction is known to be caused by polaron hopping from V^{IV} or V^{III} to V^{V} [1]. A drastic increase in σ was discovered in annealed barium iron vanadate glass [2] having a registered trademark of '*NTA glass*™' in Japan. Nishida reported a large charge-discharge capacity of 150 mAh g^{-1} in lithium-ion battery (LIB) in which cathode active material of annealed vanadate glass, Li_2O-Fe_2O_3-V_2O_5-P_2O_5, was used successfully [3]. This result indicates that vanadate glass could be a good candidate for the cathode active material of LIB. In the present study, substitution of manganese for vanadium was investigated in barium iron vanadate glass, BaO-Fe_2O_3-V_2O_5, in order to investigate the relationship between the local structure and the conductivity.

2 Experimental

Vanadate glasses with a composition of $20BaO{\cdot}10Fe_2O_3 \cdot x MnO_2{\cdot}(70\text{-}x)V_2O_5$, abbreviated as *x*BFMV, were prepared by a conventional melt-quenching method. Weighed amounts of $BaCO_3$, Fe_2O_3, MnO_2 and V_2O_5 of reagent grade were well mixed in a mortar and melted at 1200°C for 1 h in an electric muffle furnace. Homogeneous dark brown glass samples could be prepared when '*x*' was equal to or less than 30. Enriched isotope of $^{57}Fe_2O_3$ (^{57}Fe = 95.54 %) was used for some sample preparation. Isothermal annealing was carried out at 500°C for 1000 min. Mössbauer measurement was performed by a constant acceleration method with a source of ^{57}Co(Rh) and a reference of α-Fe foil for isomer shift (δ). DTA was conducted from RT to 500°C under a heating rate of 10°C min^{-1} by using 10 mg of finely pulverized glass sample. α-Al_2O_3 was used as a reference of the temperature. Values of σ were measured at temperatures ranging from 30 to 125°C by dc-four probe method under the electric current from −1.0 to 1.0 mA.

3 Results and discussion

Mössbauer spectra of 10BFMV glass measured before and after isothermal annealing at 500°C for 1000 min, are shown in Fig. 1. When '*x*' was increased from 0 to10, 20 and 30, consistent δ value of 0.38±0.01 mm s^{-1} were observed, while quadrupole splitting (Δ) increased from 0.70 to 0.76, 0.79 and 0.87±0.02 mm s^{-1}. These results indicate that Fe^{III} atoms form distorted $Fe^{III}O_4$ tetrahedra, and that they became more distorted when MnO_2 was substituted for V_2O_5. In annealed samples, a marked decrease in Δ was observed like 0.52 ($x = 0$), 0.49 ($x = 10$) and 0.43±0.02 mm s^{-1} ($x = 20$), showing a largely decreased local distortion of FeO_4

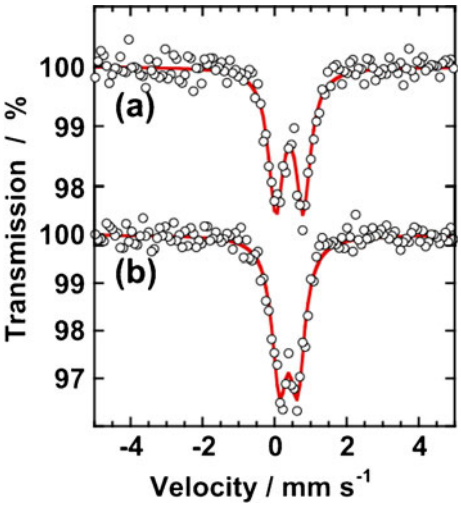

Fig. 1 Mössbauer spectra of $20BaO{\cdot}10Fe_2O_3{\cdot}10\,MnO_2{\cdot}60\,V_2O_5$ glass of (**a**) before and (**b**) after isothermal annealing conducted at 500°C for 1000 min

tetrahedra involved in the structural relaxation. In case of annealed sample with x of 30, Δ of 0.54±0.02 mm s^{-1} was observed, which is slightly larger than other annealed samples. This can be explained by the difference in the ionic radius of Mn^{IV} (39 pm) that is much smaller than that of V^{IV} (53 pm) [4]. It is considered that oxygen atoms constituting the network will be intensively attracted to Mn^{IV} in both as-quenched glass and annealed samples. Large Δ of 0.87±0.02 mm s^{-1} obtained for as-quenched glass sample supports this idea. We can describe that chemical property of "vanadate glass" is predominantly observed when MnO_2 content is equal to or less than 20 mol%.

DTA curves of xBFMV glass are depicted in Fig. 2. A gradual increase in glass transition temperature (T_g) was observed from 329 to 347, 372 and 411±5°C, while that in crystallization temperature (T_c) from 378 to 400, 429 and 465±5°C. A linear relationship found between T_g and Δ of Fe^{III} was termed 'T_g-Δ rule' [5], *i.e.*:

$$T_g = a\Delta + b \tag{1}$$

where a and b are slope and intercept of the straight line, respectively. According to the 'T_g-Δ rule' [5], large 'a' value of 680°C(K)/mm s^{-1} is generally obtained when Fe^{III} is located at tetrahedral site as network former (NWF), whereas 'a' becomes only 35°C(K)/mm s^{-1} when Fe^{III} is located at octahedral site as network modifier (NWM). In the present study, a large 'a' of 707°C(K)/mm s^{-1} was obtained, indicating that Fe^{III} atoms occupy tetrahedral site as NWF.

A slight decrease in σ value from (2.5±1.2) × 10^{-6} to (4.7±3.8) × 10^{-7}, (4.2±0.3) × 10^{-7} and (2.3±1.0) × 10^{-7} S cm^{-1} was observed when the 'x' value of xBFMV glass increased from 0 to 10, 20, and 30. These results will be due to decrease in number of carriers (V^{IV}or V^{III}) when MnO_2 was substituted for V_2O_5. In the case of 10BFMV glass, a marked increase in σ was observed from (4.7±3.8) × 10^{-7} to (1.4±0.3) × 10^{-2} S cm^{-1} after the annealing. According to the small polaron hopping theory [1], temperature dependence of σ is expressed by:

$$\sigma T = \sigma_0 \exp(-E_a/kT), \tag{2}$$

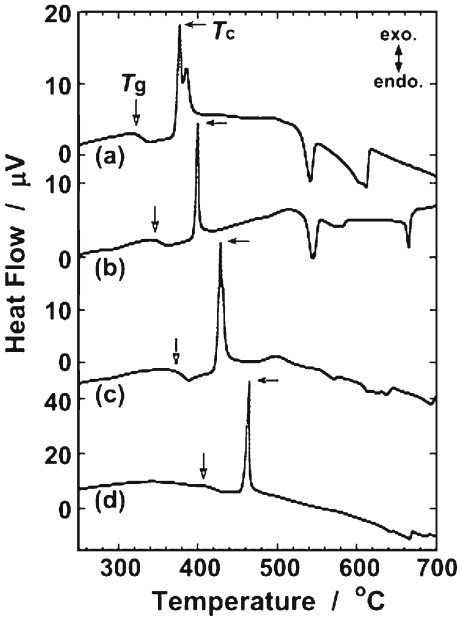

Fig. 2 DTA curves of $20BaO{\cdot}10Fe_2O_3 \cdot xMnO_2 \cdot (70-x)V_2O_5$ glasses with 'x' of (**a**) 0, (**b**) 10, (**c**) 20 and (**d**) 30, recorded at a heating rate of 10°C/min

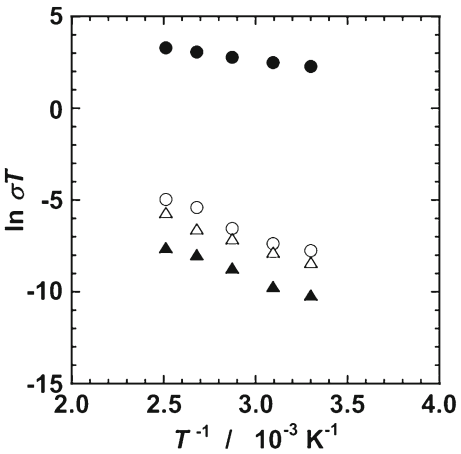

Fig. 3 $\ln \sigma T$ *vs.* $1/T$ plot of $20BaO{\cdot}10Fe_2O_3 \cdot xMnO_2 \cdot (70-x)V_2O_5$ glasses with x of 10 (circle) and 30 (triangle) measured before annealing (open symbols) and after isothermal annealing conducted at 500°C for 1000 min(closed symbols)

where E_a and k are activation energy for electric conduction and Boltzmann constant, respectively. As shown in Fig. 3, a drastic decrease in the E_a from 0.33±0.07 to 0.11±0.01 eV was observed after the annealing of 10BFMV glass. On the other hand, a constant E_a value of 0.29±0.06 eV was obtained in the case of 30BFMV glass. It is interesting that the decrease in the local distortion of $Fe^{III}O_4$ tetrahedra and a marked increase in the conductivity are clearly observed when 'x' is 10 or less, *i.e.*, the distortion of network involved with an increase in σ is intrinsic the vanadate glass.

4 Summary

Structure of *x*BFMV glass with *x* of 0, 10, 20 and 30 was investigated by means of ^{57}Fe-Mössbauer and DTA. Fe^{III} atoms are incorporated in the glass matrix to form distorted FeO_4 tetrahedra, and play a role of NWF at the substitutional sites of VO_4 tetrahedra by sharing corner oxygen atoms with each other. Electrical conductivity of 10BFMV glass increased from 4.7×10^{-7} to 1.4×10^{-2} S cm^{-1} after isothermal annealing conducted at 500°C for 1000 min. Increase in the conductivity is ascribed to a decrease in the distortion of VO_4 and FeO_4 units constituting the glass network, accompanied by a decrease in the activation energy for the electron hopping (E_a) from 0.33 to 0.11 eV, and an increased probability of polaron (3d-electron) hopping from V^{IV} or V^{III} to V^{IV}.

Acknowledgement One of the authors (SK) expresses his gratitude for the financial support by Grant-in-Aid for Scientific Research (C) (KAKENHI, No. 23550229).

References

1. Mott, N.F.: Electrons in disordered structures. Adv. Phys. **16**(61), 49–144 (1967)
2. Nishida, T.: Japanese Patent No. 3854985 (2006)
3. Nishida, T., Yoshida Y., Takahashi, Y., Okada, S., Yamaki, J.: Mössbauer study of $LiFeVPO_x$ as a new cathode material for lithium-ion battery. J. Radioanal. Nucl. Chem. **275**, 417–422 (2008)
4. Evans, H.T., Jr.: Ionic radii in crystals, properties of solids (Sec. 12). In: Lide, D.R., Frederikse, H.P.R. (eds.) CRC Handbook of Chemistry and Physics, 74th Edition, pp. 12–8, 12–9. CRC press, Florida (1993)
5. Homonnay, Z., Musić, S., Nishida, T., Kopelev, N.S., Vertés, A.: Mössbauer effect in inorganic glasses. In: Vértes, A., Homonnay, Z. (eds.) Mössbauer Spectroscopy of Sophisticated Oxides, pp. 27–87. Akademiai Kiado, Budapest (1997)

Hyperfine Interact (2012) 207:67–71
DOI 10.1007/s10751-011-0419-0

^{155}Gd Mössbauer spectroscopic and powder X-ray diffraction study of CeO_2–$GdO_{1.5}$ solid solution

Akio Nakamura · Kazutaka Imai · Naoto Igawa · Yoshihiro Okamoto · Etsuji Yamamoto · Shirou Matsukawa · Masashi Takahashi

Published online: 28 October 2011

Abstract Powder X-ray diffractometry and ^{155}Gd-Mössbauer spectroscopy have been applied to $Ce_{1-y}Gd_yO_{2-y/2}$ ($0 \leq y \leq 1.0$) prepared at 1,450°C. The former shows that this system forms a complete solid solution being the disordered defect-fluorite type in the $0 \leq y \leq 0.3$ range and the ordered C-type in the $0.3 < y \leq 1.0$ range. Its marked positive non-Vegardianity was consistently interpreted as a generalized Vegard-law behaviour of this distortion-dilated solid solution having Gd^{3+}—oxygen vacancy associative nature. The latter also clarifies that in the ordered C-type phase with decreasing y the 8b-site ^{155}Gd-Mössbauer intensity steadily diminishes and vanishes at $y \sim 0.50$, indicating that the more distorted minor 8b Gd^{3+} in C-type $GdO_{1.5}$ is being preferentially replaced with Ce^{4+}.

Keywords CeO_2-$GdO_{1.5}$ solid solution · X-ray diffractometry · ^{155}Gd-Mössbauer spectroscopy · Non-Vegardian lattice parameter behaviour · Non-random local structure

1 Introduction

A variety of grossly oxygen-vacancy (V_O) type $M_{1-y}Ln_yO_{2-y/2}$ solid solutions (ss) are formed between fluorite(F)-type MO_2 (M^{4+} =Zr, Hf, Ce, Th, U, etc.) and its V_O-

A. Nakamura (✉) · E. Yamamoto
Advanced Science Research Center, Japan Atomic Energy Agency,
Tokai, Naka, Ibaraki 319–1195, Japan
e-mail: nakamura.akio@jaea.go.jp

N. Igawa · Y. Okamoto
Quantum Beam Science Directorate, Japan Atomic Energy Agency,
Tokai, Naka, Ibaraki 319–1195, Japan

K. Imai · S. Matsukawa · M. Takahashi
Department of Chemistry, Toho University, Funabashi, Chiba 274–8510, Japan

ordered superstructure of C-type lanthanide (Ln) sesquioxide $LnO_{1.5}$ (Ln^{3+} =La-Lu, Sc, Y). These so-called defect-fluorite (DF) oxides have been the object of enormous research efforts due to their importance in nuclear, electrochemical and ceramic etc areas. Yet, much remains elusive even today as to their exact nature of complex local structure and its correlations with their key properties such as oxide-ion conductivity (σ(ion)), radiation tolerance and thermal stability, etc. To serve this purpose we have been engaged in their comprehensive coupled Ln (^{151}Eu and ^{155}Gd)-Mössbauer and powder X-ray diffraction (XRD) studies [1–8]. We report here results of one such coupled ^{155}Gd Mössbauer and XRD study of $Ce_{1-y}Gd_yO_{2-y/2}$ ($0 < y \leq 1.0$). Even in this one, which is one of the most thoroughly studied ceria solid solutions, the reported phase and structure data are often mutually discrepant, needing a more intensive further study over the whole $0 \leq y \leq 1.0$ range.

2 Experimental

Samples with various Gd content (y) in $\Delta y = 0.05$ interval over the entire $0 \leq y \leq 1.0$ range were prepared as follows; the nitrate mixture solution with a given Gd/Ce ratio was dried at 70°C, calcined at 800°C, and after pelletizing finally heated twice at 1,450°C for 12 h with intermediate grinding. These samples are ground into fine powders and are used for the XRD and ^{155}Gd-Mössbauer measurements. The former was made with a powder X-ray diffractometer (JEOL JDX3530K) using Cu K_α radiation in $10° \leq 2\theta \leq 110°$ range (0.02° step in 1∼2 sec). As detailed in previous papers [4–7], the latter was made at 12 K inside a cryostat using a ^{155}Eu/$^{154}SmPd_3$ source and a Mössbauer Doppler-velocity calibrator (Wissel MVC-450). The ^{155}Gd Mössbauer spectra of almost all the samples with the same ∼150 mg Gd/cm^2 were computer-fitted to a quadrupole-split five-line spectrum for 86.5 keV γ-ray ($I_g = 3/2$, $I_e = 5/2$, $\eta = 0$) using a Lorentz approximation. The value of isomer shift (δ) is referred to the ^{155}Eu/$^{154}SmPd_3$ source.

3 Results and discussion

Figure 1a shows the present XRD lattice parameter (a_0(ss)) data [8] with those of Bevan et al [9] and reveals two important features of phase and a_0(ss) behaviour of this system:

1. This system, when prepared at a relatively low temperature of 1,450°C (<1,500°C), forms a complete solid solution, being the disordered DF-type in the $0 \leq y \leq 0.30$ range and the ordered C-type in the much wider $0.30 < y \leq 1.0$ range. In contrast, the hitherto most representative Bevan et al's data for samples prepared at a higher 1,600°C show the existence of a clear miscibility gap ($0.52 < y < 0.73$) between conversely the wider DF-type phase in the lower $0 \leq y \leq 0.52$ range and the much narrower ordered C-type phase in the higher $0.73 \leq y \leq 1.0$ range. The present data thus indicate that by adopting a relatively low temperature heating (1,450 < 1,500°C) one can prepare the complete solid solution of this system wherein the ordered C-type is the major phase.
2. In reference to there-drawn conventional Vegard-law (VL) baseline (a_0(VL)), this system is markedly positively non-Vegardian; $\Delta a_0(ss) = a_0(ss) - a_0(VL) >> 0$.

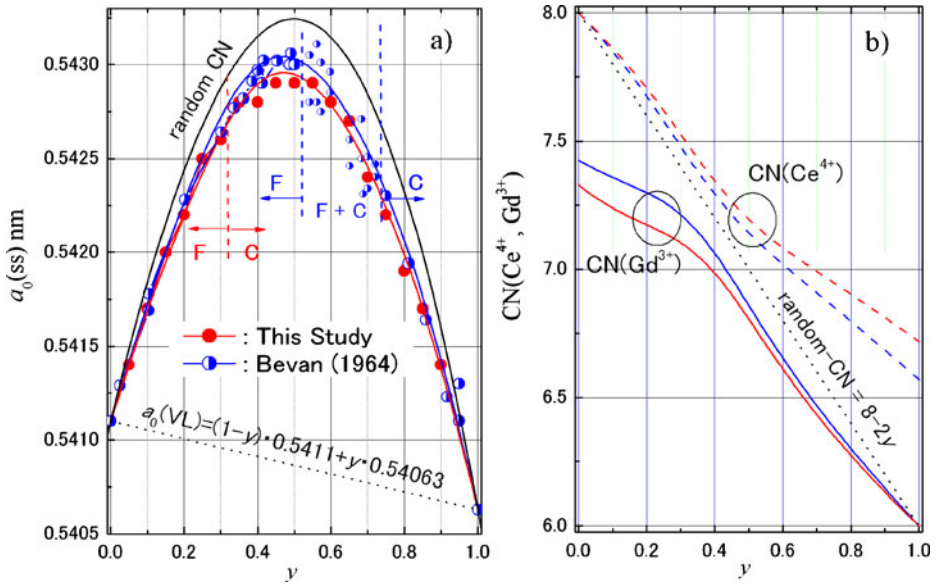

Fig. 1 a_0(ss)(exp) vs. y plot and the model curve of the $Ce_{1-y}Gd_yO_{2-y/2}$ (**a**) (left) and its random and non-random oxygen CN(Gd^{3+}, Ce^{4+}) model curves (**b**) (right)

Recently the author proposed a generalized Vegard-law (VL) a_0(ss) model [2] which can give a quantitative account for such marked non-Vegardianity of ceria solid solutions. The model allows to extract quantitative non-random oxygen coordination number data around the cations (CN(Ce^{4+}, Ln^{3+})) from the a_0(ss) analysis, by employing the systematized Shannon's ionic-radii r_C(Ce^{4+}, Ln^{3+}) expressions as a function of oxygen CN to give the average cation radius of the system; $r_C(\mathrm{av})=(1\text{-}y)\cdot r_C(Ce^{4+}) + y\cdot r_C(Ln^{3+})$. As $r_C(Ce^{4+})$ and $r_C(Ln^{3+})$ have mutually different CN dependence, the random→non-random CN change of the system produces the corresponding change of r_C and $a_0(\mathrm{ss})(=(1\text{-}y)\cdot f_F(r_C) + y\cdot f_C(r_C))$ in a fully coupled unified manner (where $f_F(r_C) = a_0(\mathrm{F})$ and $f_C(r_C) = a_0(\mathrm{C})/2$ are lattice-parameter functionals of F-type MO_2 and C-type $LnO_{1.5}$, respectively, as a function of r_C; see [2] for details). Applying this generalized VL to total six CeO_2-$LnO_{1.5}$s (Ln^{3+} =Y. Gd. Eu, Sm, Nd and La), the author clarified that with increasing $r_C(Ln^{3+})$ these systems steadily shift from the dopant(Ln^{3+})-V_O associative to the host(Ce^{4+})-V_O associative, the switchover occurring at the Ln^{3+} ~Sm-Nd. Bevan et al's data were used there for the analysis of this system.

Now that our new a_0(ss) data have also become available, we have re-analyzed both sets of a_0(ss) data more deliberately with the model and have drawn the respective most reasonable a_0(ss) model curves in Fig. 1a and non-random CN(Ce^{4+}, Gd^{3+}) curves in Fig. 1b. Though the difference between these two sets of a_0(ss) data appears small, in reference to the generalized-VL a_0(random-CN) model curve in Fig. 1a having the random CN(Gd^{3+})=CN(Ce^{4+}) =8–2y curve in Fig. 1b, the more negatively generalized non-Vegardian nature of our samples prepared at the lower

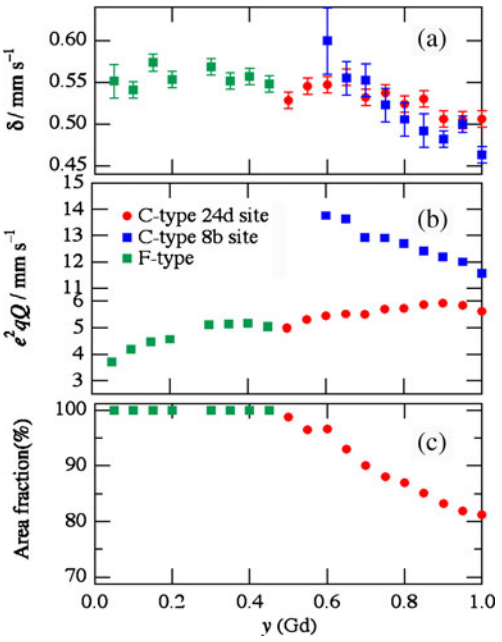

Fig. 2 ^{155}Gd-Mössbauer δ (**a**), QS (**b**) and 24-d site area fraction data (**c**) vs. y plots of the $Ce_{1-y}Gd_yO_{2-y/2}$

1,450°C than Bevan et al's samples prepared at the higher 1,600°C (i.e. a_0(this study)< a_0(Bevan)< a_0(random-CN)) in Fig. 1a and the corresponding more Gd^{3+}-V_O associative nature of our samples than Bevan et al's (i.e. CN(Gd^{3+})(this study)< CN(Gd^{3+})(Bevan)< CN(Gd^{3+})(random)=8–2y) in Fig. 1b seem clear enough. This thus provides a first direct a_0 evidence for this system that the system is becoming more non-random with decreasing the preparation temperature.

The ^{155}Gd-Mössbauer results are summarized in Fig. 2a, b and c as δ, quadrupole splitting (QS) and 24d-site absorption area fraction (%) vs. y plots, respectively: In Fig. 2a the δ value exhibits a steady increase with decreasing $y = 1.0 \rightarrow 0.50$ in the ordered C-type phase, suggesting the increase in ionic character of the Gd^{3+}-O^{2-} bond with increasing oxygen-CN of the system (Fig. 1b). As is well known, in the ideal C-type structure of $GdO_{1.5}$ (CN = 6 at $y = 1.0$) two O^{2-}s out of eight around the Gd^{3+} are regularly missing either face- or body-diagonally for the three-fourth (3/4) 24d or the one-fourth (1/4) 8b Gd site, respectively, giving apparent two-doublet ^{155}Gd spectra composed of the more distorted minor 8b doublet and the less distorted major 24d doublet in 1:3 ratio, as seen in Fig. 2b and c. Their most notable and obvious trend is the sharp diminishment of the minor 8b-site $^{155}Gd^{3+}$-Mössbauer intensity with decreasing y in Fig. 2c and its final disappearance at $y \sim 0.50$ fairly before the XRD macroscopic order-disorder (C→DF) phase change is observed at $y \sim 0.30$ in Fig. 1a. The QS data in Fig. 2b even indicate that the local distortion around this vanishing 8b Gd^{3+} is being increasingly enhanced with decreasing y. These data thus clearly demonstrate that with decreasing y the more distorted minor 8b Gd^{3+} site in C-type $GdO_{1.5}$ at $y = 1.0$ is being preferentially replaced with the Ce^{4+}, and therefore below $y \sim 0.50$ basically the major 24d-site based Gd^{3+} local structure only persists in the disordered DF phase. The CN(Ce^{4+}, Ln^{3+}) data in

Fig. 1b indicate that when y decreases from 1 to zero (=0) and the CN(average)=8–2y increases from 6 to 8, the CN(Ce^{4+}) increases from ~6.6–6.7 at $y \sim 1.0$ to ~7.2 at $y \sim 0.50$ and finally to 8 at $y = 0$, always maintaining the Gd^{3+}-V_O associative nature (CN(Gd^{4+}) <CN(Ce^{4+})) over the entire $0 \leq y \leq 1.0$ range. Accordingly, one can reasonably guess that in the ordered C-type solid solution the minor 8b site preferentially replaced with the Ce^{4+} should be more oxygen rich than the major 24d site, i.e. CN(8b)> CN(24d)> 6 as whole, thereby driving the locally less oxygen-rich 8b Gd^{3+}-O^{2-} configuration to the increasingly more-distorted metastable or even unstable vanishing state.

4 Conclusion

The $Ce_{1-y}Gd_yO_{2-y/2}$ solid solution ($0 \leq y \leq 1.0$) prepared at 1,450°C has been studied with powder X-ray diffractometry and ^{155}Gd-Mössbauer spectroscopy. Contrary to our conventional knowledge of this system, the XRD results show that the relatively low-temperature (1,450°C) heating can lead to the formation of its complete solid solution wherein the ordered C-type is the major solid solution phase ($0.3 < y \leq 1.0$). Its marked positive non-Vegardianity could also be consistently analyzed with the proposed lattice-parameter model [2, 3] as a generalized Vegard-law behaviour of this distortion-dilated non-random solid solution having dopant (Gd^{3+})—oxygen vacancy (V_O) associative non-randomness. The^{155}Gd-Mössbauer results further clarified that in the ordered C-type phase with decreasing y the 8b-site ^{155}Gd-Mössbauer intensity sharply diminishes and finally disappears at $y \sim 0.50$, evidencing that the more distorted minor 8b Gd^{3+} site in C-type $GdO_{1.5}$ at $y = 1.0$ is being preferentially replaced with Ce^{4+}.

References

1. Nakamura, A., Masaki, N., Otobe, H., Hinatsu, Y., Wang, J., Takeda, M.: Pure Appl. Chem. **79**, 1691 (2007)
2. Nakamura, A.: Solid State Ion. **181**, 1543 (2010)
3. Nakamura, A.: Solid State Ion. **181**, 1631 (2010)
4. Wang, J., Takeda, M., Shishido, T.: J. Nucl. Mater. **340**, 52 (2005)
5. Wang, J., Otobe, H., Nakamura, A., Takeda, M.: J. Solid State Chem. **176**, 105 (2003)
6. Wang, J., Takeda, M., Nakamura, A: J. Nucl. Mater. **340**, 33 (2005)
7. Nakamura, A., Otobe, H., Wang, J., Takeda, M.: J. Phys. Chem. Solids **66**, 35 (2005)
8. Imai, K.: MS thesis, Toho University (2010)
9. Bevan, D.J.M., Baker, W.W., Martin, R.L., Park, T.C.: Proc. 4th Conf. on Rare Earth Research, Phoenix, AZ, p. 411 (1964)

Hyperfine Interact (2012) 207:73–79
DOI 10.1007/s10751-011-0431-4

Mössbauer study of FINEMET type nanocrystalline ribbons irradiated with swift heavy ions

Ernő Kuzmann · Sándor Stichleutner · András Sápi · Lajos Károly Varga · Károly Havancsák · Vlamidir Skuratov · Zoltán Homonnay · Attila Vértes

Published online: 15 November 2011

Abstract As-quenched and stress field annealed FINEMET ribbons were irradiated with 246 MeV energy Kr, 470 MeV energy Xe and 720 MeV energy Bi ions and investigated by ^{57}Fe Mössbauer spectroscopy and XRD methods. The change in relative areas of the 2nd and 5th lines in the Mössbauer spectra indicated significant changes in the magnetic anisotropy of both as-quenched and stress annealed FINEMET due to irradiation with swift heavy ions. Differences were observed between the effect of irradiations with various ions having different energy and fluence. The effect of irradiation on the magnetic orientation in FINEMET was explained in terms of radiation induced defects. The swift heavy ion irradiation can be applied to produce FINEMET ribbons with more favorable soft magnetic properties for technological applications.

Keywords FINEMET · Heavy ion irradiation · Mössbauer spectroscopy · Induced magnetic anisotropy · Nanocrystalline ribbon

E. Kuzmann (✉) · S. Stichleutner · A. Sápi · Z. Homonnay · A. Vértes
Institute of Chemistry, Eötvös University, Budapest, Hungary
e-mail: kuzmann@ludens.elte.hu

S. Stichleutner
Institute of Isotopes, HAS, Budapest, Hungary

L. K. Varga
Research Institute for Solid State Physics and Optics,
HAS, Budapest, Hungary

K. Havancsák
Department of Materials Physics,
Eötvös University, Budapest, Hungary

V. Skuratov
Joint Institute for Nuclear Research, Dubna, Russia

1 Introduction

Soft magnetic nanocrystalline alloys are subject of research interest since the discovery of $Fe_{73.5}Si_{13.5}Nb_3B_9Cu_1$ FINEMET composition in 1988 by Y. Yoshizawa, S. Oguma and K. Yamauchi [1]. Nanocrystalline FINEMET shows excellent soft magnetic properties of high permeability ($\sim 10^5$ at 1 kHz), large magnetization ($\sim$1.2 T), low magnetostriction ($\sim 2 \times 10^{-6}$), low coercivity ($\sim$1 A/m) and low power loss (< 5 J/m^3 per cycle at 100 kHz and $B_p = 0.1$ T). This is achieved by the ultrafine grain structure of the Fe-Si phase embedded in an amorphous matrix produced by annealing melt-spun amorphous ribbons above the crystallization temperature. An improvement of the magnetic properties can be achieved by inducing a transversal magnetic anisotropy via stress annealing [2]. Another excellent method to alter the magnetic anisotropy in amorphous and nanocrystalline ribbons is the introduction of a large number of defects by the help of swift heavy ion irradiation [3]. In the case of as-quenched amorphous FINEMET, irradiation induced changes in the direction of magnetisation have already been shown due to 593 MeV Au ion irradiation [4]. Earlier investigations [4–22] on FINEMET involved Mössbauer spectroscopy, too.

The aim of the present work was to investigate the radiation effect of different swift heavy ions on as-quenched amorphous and stress annealed nanocrystalline FINEMET samples. For this goal we studied the change in magnetic anisotropy via the change in relative areas of the 2nd and 5th lines in Mössbauer spectra of both as-quenched and stress annealed FINEMET upon irradiation with various swift heavy ions, and checked the phase composition and crystal structure by XRD.

2 Experimental

$Fe_{73.5}Si_{13.5}Nb_3B_9Cu_1$ FINEMET ribbons were rapidly quenched and subsequently stress annealed at 550°C for 1 h under different tensile stresses between 0–124 MPa.

The irradiation of the samples was carried out with 246 MeV energy $^{86}Kr^{8+}$ ions (10^{13} and 10^{14} ion·cm^{-2}), 470 MeV energy $^{132}Xe^{35+}$ ions (10^{13} ion·cm^{-2}) as well as 720 MeV energy $^{209}Bi^{51+}$ ions (5×10^{11} ion·cm^{-2}) at room temperature, at a current density of 0.5 μA cm^{-2} and at a vacuum of about 10^{-3} Pa at the U-400 cyclotron of the Flerov Laboratory of Nuclear Reactions, JINR, Dubna, Russia.

Powder X-ray diffractograms of the samples were measured by a computer controlled DRON-2 X-ray diffractometer using CoKα radiation and a β filter. The evaluation of the XRD patterns was made by the EXRAY code.

The ^{57}Fe Mössbauer spectra of the FINEMET samples were taken at 295K temperature using conventional spectrometer (WISSEL) in transmission geometry. The magnetic anisotropy was characterized by measuring the relative ratio of 2nd and 5th lines of sextets, determining the angle θ between the directions of magnetic moment and γ-ray from the formula

$$\frac{A_{2,5}}{A_{1,6}} = \frac{4\sin^2\theta}{3(1+\cos^2\theta)}$$

at the relative ratio of $A_{1,6}/A_{3,4} = 3$.

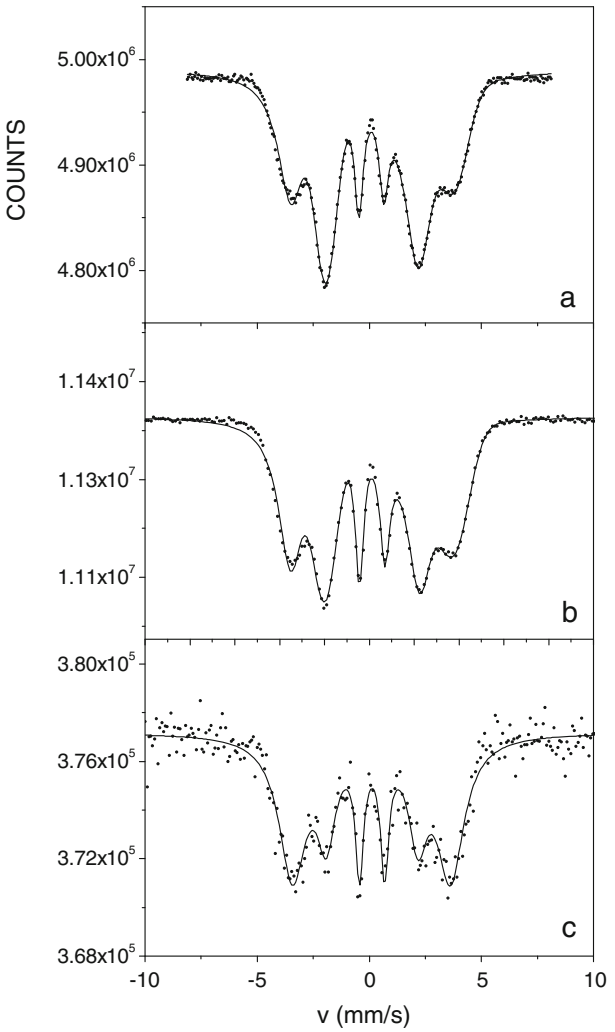

Fig. 1 ^{57}Fe Mössbauer spectra of as-quenched FINEMET (**a**) and irradiated with 720 MeV Bi (**b**) and 470 MeV Xe (**c**) ions

Table 1 Data for average direction of magnetic moment in non-irradiated and swift heavy ion irradiated as-quenched FINEMET

Sample	State	Ion/energy	Ratio $A_{2,5}/A_{3,4}$	Angle θ
basic1	amorphous	Non-irradiated	4.0	90
basic1	amorphous	Bi/720 MeV	2.42	60.25
basic1	amorphous	Xe/470 MeV	1.35	45.26

3 Results and discussion

No changes were observed in the position, width and relative intensity of lines in the X-ray diffractograms of neither as-quenched irradiated nor stress annealed irradiated samples compared to those of corresponding non-irradiated ones. The XRD results

Table 2 Site assignment of the spectral components of stress annealed FINEMET

Sign	Site assignment
Am	Amorphous phase
A4	Fe having 4 nearest Fe neighbors in sublattice A
A5	Fe having 5 nearest Fe neighbors in sublattice A
A6	Fe having 6 nearest Fe neighbors in sublattice A
D, A8, A7	Fe in sublattice B and Fe having 7 or 8 nearest Fe neighbors in sublattice A

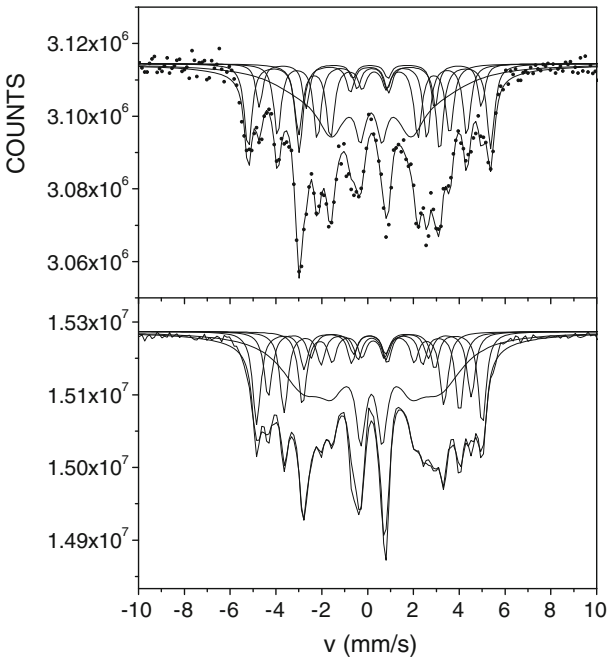

Fig. 2 ^{57}Fe Mössbauer spectra of stress annealed (20 MPa, 550°C 1 h) FINEMET non-irradiated (*top*) and irradiated with 246 MeV energy Kr ions with a dose of 10^{14} ion/cm^2 (*bottom*)

of irradiated FINEMET show no changes in crystallinity, phase composition and texture of samples due to swift heavy ion irradiation.

The spectrum of non-radiated sample (Fig. 1a) is a typical pattern of as-quenched sample and shows a magnetically split spectrum with broad lines. This spectrum is characteristic for amorphous alloys. The average isomer shift $\delta = 0.1$ mm/s and hyperfine field $B = 21$ T are in good agreement with those observed previously for the as-quenched FINEMET [4]. The relative area of $A_{2,5}/A_{3,4} = 4$. This indicates that the magnetic moments are parallel with the plane of the amorphous ribbon. The spectra of irradiated samples (Fig. 1b and c) reflect significant changes in the magnetic anisotropy via the decrease in relative areas of the 2nd and 5th lines due to the effect of the irradiation with various heavy ions (Table 1). This evidently shows that swift heavy ion irradiations induce considerable change in magnetic anisotropy in amorphous as-quenched FINEMET. The observed changes are similar to those obtained in the case of Au ions by Miglierini et al. [4].

The Mössbauer spectra of all stress field annealed samples were decomposed into 5 sextets similarly as in the case of previous works for the annealed FINEMET [20,

Table 3 Effect of stress annealing and swift heavy ion irradiations on the change of orientation of magnetization

20 MPa	Non-irradiated	Bi, 720 MeV 5×10^{11} ion/cm^2	Xe, 470 MeV 10^{13} ion/cm^2	Kr, 246 MeV 10^{14} ion/cm^2
$A_{2,5}/A_{3,4}$	3.13	1.83	1.17	1.18
angle, θ	69.5	52.4	42.3	42.5
124 MPa	Non-irradiated	Bi	Xe	Kr
$A_{2,5}/A_{3,4}$	2.7	1.5	1.16	1.17
angle, θ	63.8	47.6	42.2	42.3

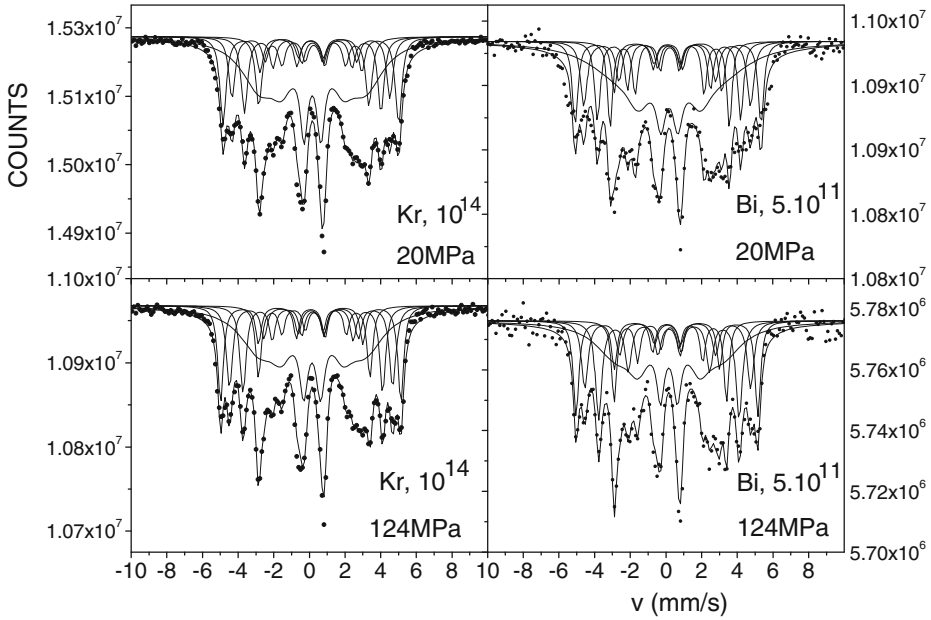

Fig. 3 ^{57}Fe Mössbauer spectra of stress annealed FINEMET ribbons irradiated with swift heavy ions, (**a**) Kr, 20 MPa, (**b**) Kr, 124 MPa, (**c**) Bi, 20 MPa and (**d**) Bi, 124 MPa

21]. The site assignment of the components is given in Table 2. In the case of the non-irradiated sample (Fig. 2, top) we have found an effect of the stress field on the magnetic anisotropy which is illustrated in Table 3. The magnetic anisotropy (the deviation of average direction of moment from the plane – note that for the sample annealed without stress field $A_{2,5}/A_{3,4} = 4$ and angle $\theta = 90°$) changes with increasing stress field.

The spectrum in Fig. 2, bottom illustrates well that swift heavy ion irradiation induces considerable changes of magnetic anisotropy not only in the amorphous phase but in the Fe-Si nanocrystallites as well. The data obtained from the Mössbauer spectra for the change of magnetic anisotropy due to the irradiation of different heavy ions in stress annealed FINEMET are shown in Table 3. The effect of the swift heavy ion irradiation on the change of orientation of magnetization is much larger than the effect of stress annealing. The comparison of Mössbauer spectra in Fig. 3

Table 4 Stopping power (dE/dx) calculations for different ions with different energies in 20 μm thick FINEMET performed with the SRIM 2008 code (dE/dx is given in keV/μm units)

Ion	Ion energy, MeV	dE/dx electronic	dE/dx Nuclear	Projected range,μm	Vacancy/Ion
Kr	246.00	2.087×10^4	34.72	15.16	34332
Xe	470.00	3.548×10^4	61.84	18.22	66516
Bi	720.00	5.076×10^4	143.4	20.40	104130

shows that the lower dose Bi irradiation has a smaller and stress annealing dependent effect on the orientation change of the magnetization than that in the case of higher dose Kr irradiation. The effect of radiation induced change in magnetic anisotropy dominates at the applied Kr and Xe irradiation, resulting in a saturation effect when the effect of stress annealing is smeared out.

Our findings can be associated with the defects produced by irradiation because of the corresponding changes in the orientation of spins depending on the direction of stresses occurring around these defects. On the other hand, some contribution from the spin reorientation around the stress centers formed during the inhomogeneous solidification process (mainly in the case of as-quenched amorphous alloy) as a consequence of mixing of atoms due to irradiation has to be taken into consideration [3, 4].

Our calculations with the SRIM 2008 code [23] (Table 4) are consistent with the differences of the observed effect of the irradiation with different energy, mass and dose of heavy ions related, first of all, to the number of defects created.

4 Conclusion

Significant changes in the magnetic anisotropy were found via the decrease in relative areas of the 2nd and 5th lines in Mössbauer spectra of both as-quenched and stress annealed FINEMET ribbons due to the effect of the irradiation with various swift heavy ions. Comparing the effect of stress annealing and swift heavy ion irradiation on the change of orientation of magnetization we have found that the effect of the irradiation is significantly higher. The swift heavy ion irradiation can be applied to produce FINEMET ribbons with more favorable soft magnetic properties for technological applications.

Acknowledgements The research was supported by grants of the Hungarian Science Foundation (OTKA K68135 and K100424) and by the Hungarian Academy of Sciences under project no.EAI-2009/003-10030.

References

1. Yoshizawa, Y., Oguma, S., Yamauchi, K.: J. Appl. Phys. **64**, 6044 (1988)
2. Kane, S.N., Alves, F., Gupta, A., Gupta, P., Varga, L.K.: Hyperfine Interact. **191**, 377–383 (2009)
3. Kuzmann, I.N.: Spirov, J. Nucl. Mater. **137**, 22 (1985)
4. Miglierini, M., Lancok, A., Pavlovic, M.: Hyperfine Interact. **189**, 45–52 (2009)
5. Herzer, G.: IEEE Trans. Mag. **26**, 1397 (1990)
6. Hono, K., Inoue, A., Sakurai, T.: Appl. Phys. Lett. **58**, 2180 (1991)
7. Zemèik, T., Jirásková, Y., Závéta, K., Eckert, D., Schneider, J., Mattern, N., Hesske, D.: Mater. Lett. **10**, 313 (1991)

8. Hampel, G., Pundt, A., J., Hesse: J. Phys.: Condens. Matter. **4**, 3195–3214 (1992)
9. Jiang, J., Zemèik, T., Aubertin, F., Gonser, U.: J. Mater. Sci. Lett. **10**, 763 (1991)
10. Rixecker, G., Schaaf, P., Gonser, U.: J. Phys.: Condens. Matter **4**, 10295 (1992)
11. Cserei, A., Jiang, J., Aubertin, F., Gonser, U.: J. Mat. Sci. **29**, 1213 (1994)
12. Miglierini, M.: J. Phys.: Condens. Matter. **6**, 1431 (1994)
13. Gupta, A., Bhagat, N., Principi, G.: J. Phys.: Condens. Matter. **7**, 2237 (1995)
14. Hofmann, B., Kronmüller, H.: Nanostruct. Mater. **6**, 961–964 (1995)
15. Zhang, Y., Hono, K., Inoue, A., Sakurai, T.: Appl. Phys. Lett. **69**, 2128 (1996)
16. Ayers, J.D., Harris, V.G., Sprague, J.A., Elam, W.T., Jones, H.N.: Nanostruct. Mater. **9**, 391 (1997)
17. Kane, S.N., Bhagat, N., Gupta, A., Varga, L.K.: J. Mag. Mag. Mat. **167**, 241–244 (1997)
18. Zhu, J., Clavaguera-Mora, M.T., Howells, W.S.: J. Appl. Phys. **84**, 6565 (1998)
19. Yoshizawa, Y., Metastable, J.: Nanocrystalline Mater. **1**, 51–62 (1999)
20. Boreggo, J.M., Conde, A., Pena-Rodríguez, V.A., Greneche, J.M.: Hyp. Int. **131**, 67–82 (2000)
21. Varga, L.K., Gercsi, Zs., Kovács, Gy., Kákay, A., Mazaleyrat, F.: J. Mag. Mag. Mat. **254**, 477 (2003)
22. Dubey, R., Gupta, A., Sharma, P., Darowski, N., Schumacher, G.: J. Magn. Magn. Mat. **310**, 2491–2493 (2007)
23. Ziegler, J.F., Biersack, J.P., Littmark, U.: The Stopping and Range of Ions in Solids. Pergamon Press, New York (1985)

Hyperfine Interact (2012) 207:81–88
DOI 10.1007/s10751-011-0420-7

Electronic spin transition of iron in the Earth's lower mantle

Jung-Fu Lin · Andrea Wheat

Published online: 1 November 2011

Abstract Silicate perovskite and ferropericlase are thought to be the primary constituents of the lower mantle, whereas silicate post-perovskite is more likely found in the lowermost mantle. Because these minerals contain certain amounts of iron, their properties and, consequently, those of the deep mantle, are strongly influenced by iron's spin and valence states. A high-spin to low-spin crossover in ferropericlase has been observed to occur in the middle part of the lower-mantle conditions. Recent Mössbauer results consistently show that Fe^{2+} predominantly exhibits extremely high quadrupole splittings in perovskite and post-perovskite, whereas a high-spin to low-spin transition of Fe^{3+} in the octahedral site occurs at high pressures. These results provide a new venue for discussion of the effects of the spin and valence states of iron on the physical and chemical properties of the lower mantle.

Keywords Spin transition · Lower mantle · Mössbauer spectroscopy · Diamond anvil cell

1 Introduction

Earth's lower mantle, the most voluminous layer of the planet, is subjected to extreme pressure-temperature (*P-T*) conditions of 23–136 GPa and approximately 1,600–3,500 K. The lower mantle, as described in terms of a pyrolitic compositional model, is mainly comprised of ferropericlase ((Mg,Fe)O; Fp; ∼33% by volume), aluminous silicate perovskite (Al-(Mg,Fe)SiO_3; ∼62% by volume; hereafter called perovskite or Pv), and ∼5% calcium silicate Pv ($CaSiO_3$, abbreviated CaPv) [1] (Figs. 1 and 2). Recent studies show that Pv transforms into silicate post-perovskite (PPv) within the D" layer, just above the core-mantle region. The implications of

J.-F. Lin (✉) · A. Wheat
Department of Geological Sciences, Jackson School of Geosciences,
The University of Texas at Austin, 1 University Station, Austin TX 78712, USA
e-mail: afu@jsg.utexas.edu

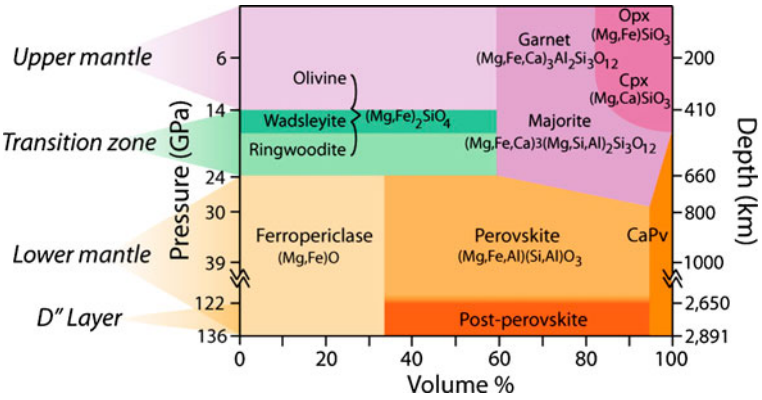

Fig. 1 Approximate mineral distribution within Earth's interior as a function of depth, pressure and volume%. Mineral abbreviation: Opx and cpx, orthopyroxene and clinopyroxene, respectively; CaPv, calcium silicate perovskite

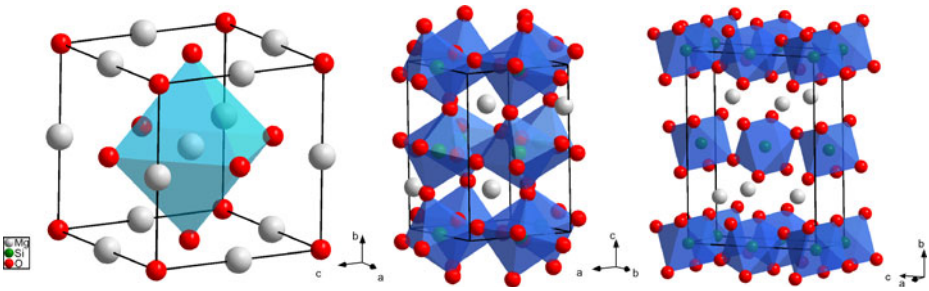

Fig. 2 Crystal structures of lower-mantle ferropericlase (*left*), silicate perovskite (*middle*), and silicate post-perovskite (*right*). Cubic ferropericlase is in the rock salt structure ($Fm\bar{3}m$); orthorhombic perovskite is in the *Pbnm* space group; orthorhombic post-perovskite is in the *Cmcm* space group

these minerals' physical and chemical properties are needed to explain the seismic, geochemical, geodynamic, and geomagnetic observations of the lower mantle. As the most abundant 3*d* transition metal in Earth's interior, iron affects many of the chemical and physical properties of the lower-mantle minerals [1]. Amongst the majority of these, iron exists mainly as ferrous iron (Fe^{2+}), with approximately 20% concentrated in Fp, whereas Pv and PPv, with approximately 10% total iron, can contain very high amounts of ferric iron (Fe^{3+}) [1].

Due to its partially filled 3*d*-electron orbitals, iron's electronic valence and spin states in the host phases can cause a dynamic range of physical and chemical properties of the lower mantle [1]. Previous studies have shown that Fe spin transitions and variations in Fe valence states can cause changes in density, elastic properties, electrical conductivity and radiative thermal conductivity of the lower-mantle minerals. Here, literature data on the spin and valence states of iron in Fp, Pv, and PPv at relevant *P*-*T* conditions have been evaluated. Focus is placed on the use of the hyperfine parameters, quadrupole splittings (QS) and chemical shifts (CS), seen in Mössbauer spectroscopic analyses including synchrotron Mössbauer

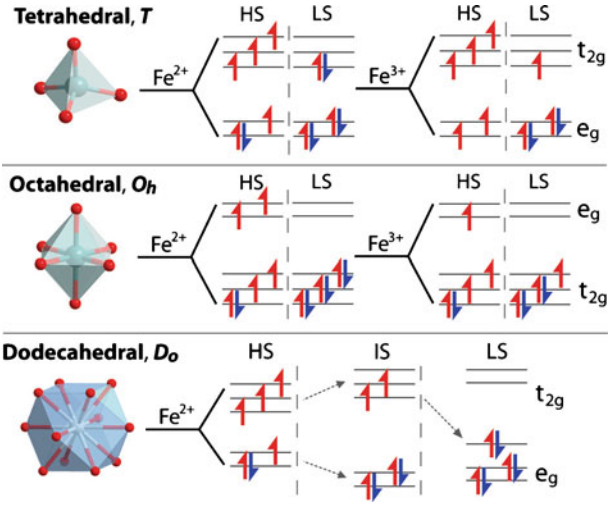

Fig. 3 Crystal field splitting diagrams for iron in tetrahedral, octahedral, and dodecahedral sites in the lower-mantle minerals. Iron is shown as a (2+) or (3+) cation in high-spin, intermediate-spin (dodecahedral site), and low-spin electronic configurations. The crystal field splitting energy (CFSE) can be altered by pressure, temperature, and/or composition. The energy of the e_g orbitals (those which are oriented towards the ligands) is heightened by increased repulsion due to shortened e_g orbital-ligand distance during pressure-induced unit cell distortion, resulting in an overall larger CFSE. When the CFSE surpasses the spin-pairing energy, the spin-pairing transition of 3*d* electrons is more favorable than jumping the energy gap to achieve aligned spins. For example, the low-spin state with all six 3*d* electrons paired ($S = 0$) in Fe^{2+} occurs at high pressures in the lower-mantle ferropericlase

spectroscopy (SMS), because these results act as site-specific fingerprints, assisting in the assignment of the valence and spin states of iron in the lower-mantle minerals.

2 Electronic spin transition of Fe^{2+} in Fp

Ferropericlase has a cubic rock-salt structure and forms a solid solution between periclase (MgO) and wüstite (FeO). A high-spin (HS) to low-spin (LS) transition of Fe^{2+} in the octahedral site occurs when the crystal field splitting energy exceeds the Hund's-rule exchange energy, causing the material to become low-spin and diamagnetic [1–4]. The measured values of QS, ~0.8 mm/s, and CS, ~1.2 mm/s, from Mössbauer spectra of Fp under ambient conditions are consistent with predominant high-spin Fe^{2+} in the octahedral coordination (Fig. 3) [5]. The concentration of the high-spin Fe^{3+} in ferropericlase, however, is typically very low (e.g., under the detection limit of the MS technique). At room temperature, the QS of the high-spin Fe^{2+} increases with pressure up to ~30 GPa, plateaus until ~60 GPa, and disappears with further pressure increase [5]. The CS of the high-spin state decreases with pressure increase; a noticeable drop of the CS occurs at approximately 60 GPa. The simultaneous disappearance of the QS and the drop of the CS at approximately 60 GPa are consistent with a spin transition of iron in Fp [5]. The ratio of the high-spin to low-spin states of iron in Fp, as a function of pressure, can be derived from the

modeling of the SMS spectra with changes in the QS and CS values. Depending on experimental conditions, a narrower to broader width of the spin transition has been reported [1, 5]. Although (Mg,Fe)O has always been regarded as a fully disordered solid solution system without noticeable short-range order at ambient conditions, recent Mössbauer analyses have demonstrated broadening of the high-spin Fe^{2+} quantum beats associated with significant changes in the short-range order, which deviates from the behavior of the homogeneous solid solution in Fp. These studies have indicated that the Fe^{2+} ions can form localized clusters in nearest-neighboring environments under high pressures. The short-range ordering of Fe^{2+} ions can cause an extension of the width of the spin crossover in (Mg,Fe)O at high pressures.

The electron shell of the high-spin Fe^{2+} ions in the octahedral coordination is spherically asymmetric with $S = 2$ and $t^3_{2g\uparrow} e^2_{g\uparrow} t^1_{2g\downarrow}$, whereas Fe^{2+} ions in the low-spin state are more spherically symmetric with $S = 0$ and $t^3_{2g\uparrow} t^3_{2g\downarrow}$ (the arrows indicate spin up or spin down whereas the superscripted numbers represent the number of the occupied electrons). The spin crossover arises from the condition in which the thermal energy at high P-T is sufficient to overcome the energy difference between the high-spin state and low-spin state [4]. Therefore, the local 3*d* electronic structures of the iron ions in Fp are strongly temperature dependent [4]. Most importantly, recent results show that the electronic spin-pairing transition of iron in Fp occurs over a very narrow range of pressure at room temperature but turns to a spin crossover with an extended transition pressure at the lower-mantle temperatures [4].

3 Spin and valence states of iron in Pv

Perovskite, with 5–10 mol% of Fe and Al, is the most abundant silicate mineral in the lower mantle, and exists at 660 km depth to several hundred kilometers above the core-mantle boundary. Iron in Pv exists in both Fe^{2+} and Fe^{3+} states and can occupy one of two crystallographic sites, the large dodecahedral Mg site (the A site) and the small octahedral Si site (the B site) [6–11] (Fig. 2). Current consensus on the site occupancy is that Fe^{2+} mainly occupies the A site whereas Fe^{3+} can occupy both the A and B sites [6–11]. Several studies have further shown that Fe^{2+} may self-disproportionate into Fe metal and Fe^{3+}, creating Fe^{3+}-enriched Pv. That is, the significant amount of Fe^{3+} in Pv is not a result of the oxidation state of the lower mantle, which is expected to be relatively reducing, but due to the crystal chemistry of Pv at high pressure. The Fe^{3+} content in Pv is also found to vary with the amount of the Al^{3+} likely through charge-coupled substitution with the Si^{4+} in the octahedral site [4, 6]. The Fe^{3+} content in Pv is approximately 20% without the presence of Al and 50–75% with the presence of Al^{3+}.

The reported spin transitions in Pv are much more complex than those in Fp, likely due to the low-symmetry oxygen ligand field and multiple site occupancies. These studies have shown that both Fe^{2+} and Fe^{3+} exist in the high-spin state in both of the A and B sites under ambient conditions [6–11]. Mössbauer analyses show that the high-spin Fe^{2+} exhibits a QS value of ~1.6 to 2.2 mm/s and a CS of ~1 mm/s in the A site. Interpretations of the high-pressure Mössbauer analyses have been quite different, although their main results on the QS values were similar—both experimental and theoretical studies have reported extremely high QS values

of Fe^{2+} (as high as ~4.4 mm/s) at high pressures [6–11] . The relative area of the high-QS doublet (3.4–4.4 mm/s) increases with pressure at the expense of the low-QS doublet (1.6–2.2 mm/s), indicating that the transition involves Fe^{2+} in the A site [7, 8]. The high-QS doublet becomes the dominant spectral feature in the high-pressure Mössbauer spectra at above approximately 30 GPa. Particularly, the new quadrupole doublet with the extremely high QS appears to have a very narrow linewidth and high CS (~1.1 mm/s) [7]. Together with X-ray emission spectroscopic (XES) analyses for the total spin momentum of iron in Pv, the occurrence of the Fe^{2+} site with the extremely high QS, very narrow linewidth, and relatively high CS has been assigned to be an intermediate-spin Fe^{2+} with a total spin momentum of one ($S = 1$) in the A site [7]. That is, a high-spin to an intermediate-spin crossover occurs in Pv at around 30 GPa, and Fe^{2+} remains stable in the intermediate-spin state at above 30 GPa in the lower mantle. At higher pressures, the intensity of the high QS component in the SMS spectra of PPv decreases, whereas the intensity of a new component with very low QS of less than 0.5 mm/s and a CS of ~0 mm/s increases. This new component was assigned to the low-spin Fe^{2+} occurring at 120 GPa and high temperatures.

However, it has been realized that the occurrence of the intermediate-spin state is very rare in geological materials and that high QS in iron does not necessarily imply the occurrence of the intermediate-spin state. For example, iron in almandine garnet is in the high-spin state with a QS of ~3.5 mm/s under ambient conditions. Theoretical calculations have been performed to interpret the spin states and the extremely high QS values of Fe^{2+} in Pv. Although not always in agreement with each other, these calculations show that the intermediate-spin state is not stable over all lower-mantle pressures, irrespective of the exchange-correlation functions used in the calculations [9]. The high-spin Fe^{2+} with QS of 2.3–2.5 mm/s is more stable at relatively low pressures, while the high-spin Fe^{2+} with QS of 3.3–3.6 mm/s is more favorable at higher pressure [9]. Based on these calculations, the extremely high QS site is a result of the iron atomic-site change, in which Fe ions move away from the central positions in the A site, rather than a spin-pairing transition.

For Fe^{3+} in Pv, it has been shown both experimentally and theoretically that Fe^{3+} enters into both A and B sites, suggesting a charge-coupled substitution mechanism [8, 10]. High-spin Fe^{3+} is known to exhibit very low QS compared to Fe^{2+} because all five 3*d* electrons are unpaired and form relatively spherical orbitals. Theoretical calculations further suggest that the Fe^{3+} in the A site has an even lower QS value than the B site Fe^{3+} [10]. Combined SMS and XES results for Fe^{3+}-containing Pv suggest that the low-spin population in the B site gradually increases to 100% with pressure up to 50–60 GPa, whereas Fe^{3+} in the A site remains high-spin to at least 136 GPa, consistent with recent theoretical calculations [8, 10]. SMS analyses further suggest that A site Fe^{3+} remains in the high-spin state in Al-bearing Pv, in which Fe^{3+} is expected to predominantly exist in the A site [8]. Therefore, these results indicate that the Fe^{3+} in the octahedral B site undergoes a high-spin to low-spin transition in Pv.

The QS of the Fe^{2+} in the A site and the Fe^{3+} in the B site exhibit exactly the opposite trends across the high-spin to the low-spin transition, and can be understood through their orbital occupancies. The low-spin Fe^{2+} in the A site located near the center of the site forms a 3*d* charge density with a cubic-like shape that barely contributes to the effective electric field gradient, leading to a very small QS [8, 10]. The high-spin Fe^{3+} also has a small QS (a small effective electric field gradient) in the

A and B sites because of an almost spherically-shaped electron charge distribution [8, 10]. However, the 3*d* orbitals of the low-spin Fe^{3+} contribute more significantly to the effective electric field gradients and lead to a larger QS.

4 Spin and valence states of iron in PPv

Post-perovskite is expected to be the most abundant phase in the Earth's core-mantle boundary region. Deciphering the spin and valence states of iron in PPv at relevant *P-T* conditions provides new insight into the properties of the region, including seismic discontinuities, rheology and plasticity, dynamic evolution and formation of superplumes, thermal gradients, core-mantle heat flux, and chemistry [11]. The PPv phase is found to be stable in the $CaIrO_3$-type structure (*Cmcm*). However, a number of kinked structures, formed by sliding the {010} planes of the Pv structure with variation in the stacking sequence of SiO_6 octahedral layers, have also been reported. Thus far, the presence of the kinked PPv phase has been found to increase the amount of Fe^{3+} in the sample. Experimental SMS results show Fe^{2+} likely exists in the bipolar-prismatic site and exhibits extremely high QS of 3.8–4.5 mm/s and relatively high CS in PPv [11]. Complementary high *P-T* XES studies, which are sensitive to the total spin momentum of iron, suggest that iron predominantly exists in the intermediate-spin Fe^{2+} state with $S = 1$ in the $CaIrO_3$-typed PPv at relevant *P-T* conditions of the lowermost mantle [11]. Since the intermediate-spin Fe^{2+} in PPv is found to be stable at 25 mol% and 40 mol% Fe, it is conceivable that the intermediate-spin Fe^{2+} is stable over a wide range of Fe content in PPv relevant to the D" region, where Fe-enrichment may be expected [11]. Similar to the discussion for Fe^{2+} in Pv, however, theoretical calculations suggest that Fe^{2+} in PPv is in the high-spin state at all mantle pressures, although theoretical QS values of the Fe^{2+} and Fe^{3+} remain to be computed.

SMS results on Fe^{3+}-rich PPv show that Fe^{3+} exists in two different sites, one site with a high QS of ~2 mm/s and another with a low QS of 0.3 mm/s, similar to the Fe^{3+} in Pv [12]. The low QS site is assigned to be the high-spin Fe^{3+} in the bipolar-prismatic site, whereas the high QS site with QS of ~2 mm/s is assigned as the low-spin Fe^{3+} in the octahedral site [12]. Based on the hyperfine parameters associated with the site assignments, the Fe^{3+} in the octahedral site undergoes a high-spin to low-spin transition at high pressures, causing the QS to increase from the high-spin state to the low-spin state [12]. In this mixed spin-state scenario, Fe^{3+} enters the site through charge-coupled substitution, as also suggested by theoretical calculations. Because the ionic radius of the low-spin Fe^{3+} is smaller than that of the high-spin Fe^{3+}, the low-spin Fe^{3+} is more stable in the smaller octahedral site of PPv.

The notable difference between the Mössbauer parameters of the Pv and PPv phases is that the QS of the low-spin Fe^{3+} site is much smaller in PPv. The smaller QS of the low-spin site in PPv can be explained by a less distorted octahedral site, since distortion from a cubic environment around the iron nucleus results in an increased QS value. Since PPv is the high-pressure polymorph of Pv, the QS of Fe^{2+} in PPv could be similar or related to that of Fe^{2+} in Pv as both phases exhibit extremely high QS values of around 4 mm/s. The calculated QS of Fe^{2+} in Pv is 3.3–3.6 mm/s at lower mantle pressures, consistent with the QS values for Fe^{2+} from SMS analyses in PPv [7–12].

5 Conclusions

The disappearance of the QS and drop in the CS of the octahedrally-coordinated Fe^{2+} in ferropericlase indicates the high-spin to low-spin transition at high pressures. The spin transition of iron in ferropericlase turns into a wide spin crossover at lower-mantle temperatures. Iron exists in the Fe^{2+} and Fe^{3+} states in both perovskite and post-perovskite. Both Fe^{2+} and Fe^{3+} exist in the high-spin state in perovskite under ambient conditions. Most recent studies have observed extremely high QS values of the Fe^{2+}, as high as ~4.4 mm/s, in perovskite under high pressures. The relative area of the high-QS doublet increases with pressure at the expense of the low-QS doublet, and has been assigned as an intermediate-spin Fe^{2+} in the A site, occurring at approximately 30 GPa. However, recent theoretical calculations support the notion that the extremely QS site is a result of the atomic-site change rather than a high-spin to intermediate-spin transition. At higher pressures, a new doublet component was assigned to the low-spin Fe^{2+} occurring at 120 GPa and high temperatures. Recent studies on Fe^{3+}-containing perovskite suggest that Fe^{3+} in the octahedral B site undergoes a spin-pairing transition in perovskite, whereas Fe^{3+} in the A site remains high-spin to at least 136 GPa.

Fe^{2+} likely exists in the bipolar-prismatic site with an extremely high QS of 3.8–4.5 mm/s in post-perovskite, which has been assigned to the intermediate-spin Fe^{2+} state with $S = 1$. However, theoretical calculations have found the intermediate-spin state unstable at lower-mantle pressures. Fe^{3+} exists in two different sites, the high-spin Fe^{3+} in the bipolar-prismatic site and the low-spin Fe^{3+} in the octahedral site. These site assignments indicate that the Fe^{3+} in the octahedral site undergoes a high-spin to low-spin transition at high pressures through charge-coupled substitution.

Acknowledgements This work was supported by NSF Earth Sciences (EAR-0838221). We thank J. Yang for her assistance in making Figs. 2 and 3. A.W. is supported by NSF-EAR Research Experience for Undergraduates (REU) Program.

References

1. Lin, J.F., Tsuchiya, T.: Spin transition of iron in the Earth's lower mantle. Phys. Earth Planet. Inter. **170**, 248–259 (2008)
2. Badro, J., Fiquet, G., Guyot, F., Rueff, J.P., Struzhkin, V.V., Vankó, G., Monaco, G.: Iron partitioning in Earth's mantle: toward a deep lower mantle discontinuity. Science **300**, 789–791 (2003)
3. Lin, J.F., Struzhkin, V.V., Jacobsen, S.D., Hu, M., Chow, P., Kung, J., Liu, H., Mao, H.K., Hemley, R.J.: Spin transition of iron in magnesiowüstite in Earth's lower mantle. Nature **436**, 377–380 (2005)
4. Lin, J.F., Vankó, G., Jacobsen, S.D., Iota-Herbei, V., Struzhkin, V.V., Prakapenka, V.B., Kuznetsov, A., Yoo, C.S.: Spin transition zone in Earth's lower mantle. Science **317**, 1740–1743 (2007)
5. Lin, J.F., Gavriliuk, A.G., Struzhkin, V.V., Jacobsen, S.D., Sturhahn, W., Hu, M., Chow, P., Yoo, C.S.: Pressure-induced electronic spin transition of iron in magnesiowüstite-(Mg,Fe)O. Phys. Rev. B **73**, 113107 (2006)
6. Li, J., Struzhkin, V., Mao, H., Shu, J., Hemley, R., Fei, Y., Mysen, B., Dera, P., Prakapenka, V., Shen, G.: Electronic spin state of iron in lower mantle perovskite. Proc. Natl. Acad. Sci. **101**, 14027–14030 (2004)
7. McCammon, C., Kantor, I., Narygina, O., Rouquette, J., Ponkratz, U., Sergueev, I., Mezouar, M., Prakapenka, V.B., Dubrovinsky, L.: Stable intermediate-spin ferrous iron in lower mantle perovskite. Nature Geosci. **1**, 684–687 (2008)

8. Catalli, K., Shim, S.H., Prakapenka, V.B., Zhao, J., Sturhahn, W., Chow, P., Xiao, Y., Liu, H., Cynn, H., Evans, W.J.: Spin state of ferric iron in $MgSiO_3$ perovskite and its effect on elastic properties. Earth Planet. Sci. Lett. **289**, 68–75 (2010)
9. Hsu, H., Umemoto, K., Blaha, P., Wentzcovitch, R.M.: Spin states and hyperfine interactions of iron in $(Mg,Fe)SiO_3$ perovskite under pressure. Earth Planet. Sci. Lett. **294**, 19–26 (2010)
10. Hsu, H., Blaha, P., Cococcioni, M., Wentzcovitch, R.M.: Spin-state crossover and hyperfine interactions of ferric iron in $MgSiO_3$ perovskite. Phys. Rev. Lett. **106**, 118501 (2011)
11. Lin, J.F., Watson, H.C., Vankó, G., Alp, E.E., Prakapenka, V.B., Dera, P., Struzhkin, V.V., Kubo, A., Zhao, J., McCammon, C., Evans, W.J.: Intermediate-spin ferrous iron in lowermost mantle post-perovskite and perovskite. Nature Geosci. **1**, 688–691 (2008)
12. Catalli, K., Shim, S.H., Prakapenka, V.B., Zhao, J., Sturhahn, W.: X-ray diffraction and Mössbauer spectroscopy of Fe^{3+}-bearing Mg-silicate post-perovskite at 128–138 GPa. Am. Mineral. **95**, 418–421 (2010)

Hyperfine Interact (2012) 207:89–95
DOI 10.1007/s10751-011-0463-9

Evidence for a weakening 'dead zone' in Tokyo Bay over the past 30 years

Katsumi Shozugawa · Naoki Hara · Yutaka Kanai · Motoyuki Matsuo

Published online: 29 November 2011

Abstract Weakened hypoxia in the past 30 years at a dredged area in Tokyo Bay was proven by the existence of amorphous hematite (α-Fe2O3) in sediments. The chemical states of iron in sediments can become a proxy for the scale of anoxia at the time of sedimentation. In 2009, we collected core sediments from a dredged area off Makuhari in Tokyo Bay that is very strongly anoxic in the summer. Every layer of the sediments was analysed by ^{57}Fe Mössbauer spectroscopy and excess 210Pb dating, and amorphous hematite was identified in the sediments from the 1976–1979, 1986–1989 and 2006–2009 layers. Using an estimate based on the Eh-pH diagram optimized for the sedimental environment, the existence of hematite in the dredged area proves that the scale of hypoxia/anoxia is decreasing, and these results agree well with the observed dissolved oxygen level of the seawater mass.

Keywords ^{57}Fe Mössbauer spectroscopy · Sediments · Hypoxia · Hematite

1 Introduction

'Seas of death' (dead zones) with little dissolved oxygen (DO) in the bottom water mass have expanded since the 1960s on sea coasts all over the world and have greatly influenced ecosystems and inshore fisheries [1]. This study suggests that the chemical

K. Shozugawa (✉) · N. Hara · M. Matsuo
Graduate School of Arts and Sciences, The University of Tokyo,
3–8–1 Komaba, Meguro, Tokyo 153–8902, Japan
e-mail: cshozu@mail.ecc.u-tokyo.ac.jp

Y. Kanai
National Institute of Advanced Industrial Science and Technology,
1–1–1 Higashi, Tsukuba, Ibaraki 305–8567, Japan

states of iron in sediments are a proxy for redox conditions, including hypoxia. Because iron is one of the most abundant elements included in sediments, its various chemical states on an Eh-pH diagram have been clarified [2], and iron is expected to have taken the chemical state corresponding to the redox status of seawater.

Moreover, to estimate the scale of past hypoxia/anoxia, it is necessary to study areas where more strongly anoxic water has occurred in the summers. At the seabed in Tokyo Bay, vast dredged trenches have been formed sporadically along the coasts by reclamation of the foreshore since the 1970s [3]. Although the water depth of the coastal Tokyo Bay is between 5 and 10 metres, the water depth of some dredged trenches reaches 30 metres. In particular, the dredged trench off Makuhari has the maximum area and depth, and strong hypoxia has been observed there due to the stagnation of water currents [3]. Therefore, this area is suitable for an estimation of past hypoxia/anoxia. In this study, sediment cores were collected from the Makuhari dredged trench, and the relationship between chemical states of iron according to sedimentation age and DO at sedimentation were analysed by using ^{57}Fe Mössbauer spectroscopy and excess ^{210}Pb dating.

2 Experimental

The Mössbauer spectra were measured with an Austin Science S-600 spectrometer using a 1.11 GBq ^{57}Co/Rh source at room temperature. The Doppler velocity was set to $\pm$10.0 mm·sec^{-1} maximum. Gamma rays at 14.4 keV were collected from each sample for two or three days. Curves were fitted to the resulting spectra using a personal computer, assuming that the spectra were composed of peaks with Lorentzian line shapes. The half-widths and peak areas of each quadrupole doublet were constrained to be equal. Isomer shifts were expressed with respect to the centroid of the spectrum of metallic iron foil. The excess ^{210}Pb method was used for the age determination of the sediments [4].

3 Results and discussion

In the dredged trench, the seabed is muddy and some methane exhaust (φ *ca.* 10 cm) appears on the surface (point A, depth: 26 m). In contrast, the non-dredged seabed (point B, depth: 8 m) is sandy, and no methane exhaust is visible. Both cores were cut in the vertical direction every 3 cm immediately after sampling. In order to prevent oxidation by the air, all samples were put into clean and impenetrable bags, and various measurements such as ^{57}Fe Mössbauer measurements were started from the day of sampling.

Figure 1 shows the DO in the bottom water at point A and at an observatory (non-dredged) near the Tokyo light beacon. Seawater above the dredged trench had the following features: 1) vertical circulation tended to be weak in summer, and 2) horizontal currents are the same as in other areas. That is, the Makuhari dredged trench underwent a localized event suggesting rapid DO consumption such as that by microbial respiration.

^{57}Fe Mössbauer spectra at 0–3 cm and 3–6 cm in depth at point A are shown in Fig. 2, and the parameters for all sediment layers are given in Table 1. The spectrum

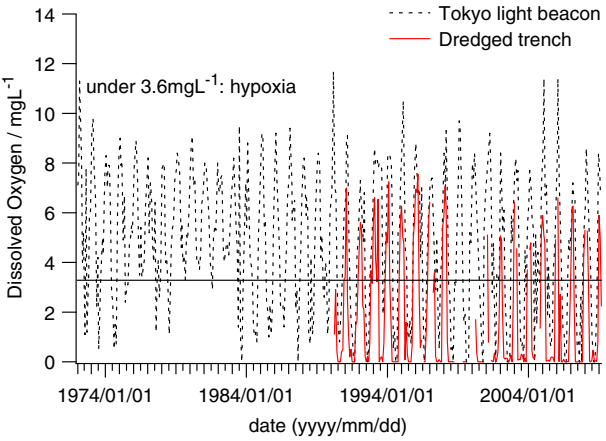

Fig. 1 Variation in DO over decades in the dredged area and at the Tokyo beacon

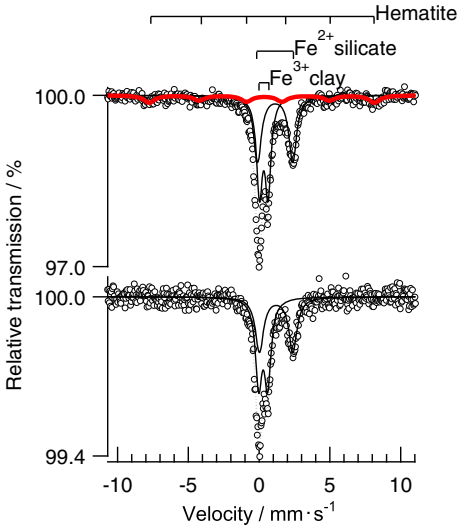

Fig. 2 ^{57}Fe Mössbauer spectra of sediments from dredged trench: spectra of the 0–3 cm layer (*top*) and the 3–6 cm layer (*bottom*)

of surface sediment (0–3 cm) in Fig. 2 includes three species. Two kinds of doublet peaks at the centre of the spectrum are Fe^{3+}h.s. (δ 0.3 mm·s^{-1}, Δ 0.6 mm·s^{-1}) and Fe^{2+}h.s. (δ 1.1 mm·s^{-1}, Δ 2.4 mm·s^{-1}), which can be tentatively identified as clay minerals and silicate minerals, respectively. A value likely to be associated with hematite, which shows a sextet component, also appears. Hematite has distinctive features such as a δ value of +0.3 mm·s^{-1}, Δ of −0.2 mm·s^{-1} and hyperfine field H of 50 T. Hematite was observed only at point A at depths of 0–3 cm, 24–27 cm and 36–39 cm. However, at point B, hematite was observed in the samples at all layers. Hematite was not detected by x-ray diffraction (XRD, D8 Advance, Bruker) measurement in any layers, suggesting the presence of amorphous hematite in the sediments.

Hematite, which has a sextet component, is also the major chemical species, the generation conditions of which must be considered. The Eh-pH diagram for hematite

Table 1 ^{57}Fe Mössbauer parameters of all sediment layers

Sampling site	Layers / cm	Sedimentation age	Species	Area / %	I.S.(δ)/mm·s^{-1}	Q.S.(Δ)/mm·s^{-1}	H.W./mm·s^{-1}	H.I. / T
Dredged trench (Point A)	0–3	2007.7	Clay (Fe^{3+} h.s.)	43.24	0.328(5)	0.604(9)	0.496(12)	
			Silicate (Fe^{2+} h.s.)	40.53	1.135(8)	2.487(15)	0.656(24)	
			Hematite	16.23	0.279(40)	−0.176(78)	0.940(160)	49.27(30)
	3–6	2005.2	Clay (Fe^{3+} h.s.)	54.96	0.287(17)	0.632(35)	0.561(24)	
			Silicate (Fe^{2+} h.s.)	45.04	1.207(28)	2.365(57)	0.696(42)	
	6–9	2002.7	Fe3+ h.s.	100	0.284(28)	0.675(46)	0.502(72)	
	9–12	2000.2	Clay (Fe^{3+} h.s.)	72.67	0.296(26)	0.583(51)	0.695(54)	
			Silicate (Fe^{2+} h.s.)	27.33	1.204(33)	2.457(67)	0.445(65)	
	12–15	1997.7	Clay (Fe^{3+} h.s.)	53.75	0.322(25)	0.548(40)	0.555(61)	
			Silicate (Fe^{2+} h.s.)	46.25	1.148(35)	2.461(68)	0.663(79)	
	15–18	1995.2	Clay (Fe^{3+} h.s.)	59.34	0.327(5)	0.579(9)	0.403(14)	
			Silicate (Fe^{2+} h.s.)	40.66	1.111(14)	2.553(27)	0.598(40)	
	18–21	1992.7	Clay (Fe^{3+} h.s.)	55.62	0.287(269)	0.586(529)	0.613(68)	
			Silicate (Fe^{2+} h.s.)	44.38	1.182(349)	2.396(696)	0.629(73)	
	21–24	1990.2	Clay (Fe^{3+} h.s.)	73.12	0.308(18)	0.545(29)	0.404(47)	
			Silicate (Fe^{2+} h.s.)	26.88	1.219(21)	2.759(42)	0.253(61)	
	24–27	1987.7	Clay (Fe^{3+} h.s.)	53.23	0.307(6)	0.622(10)	0.473(13)	
			Silicate (Fe^{2+} h.s.)	43.00	1.101(14)	2.450(26)	0.727(37)	
			Hematite	3.76	0.346(55)	−0.200(10)	0.331(13)	50.02(30)
	27–30	1985.2	Clay (Fe^{3+} h.s.)	59.39	0.257(131)	0.494(226)	0.611(125)	
			Silicate (Fe^{2+} h.s.)	40.61	1.147(250)	2.261(491)	0.752(195)	

	30–33	1982.7	Clay (Fe^{3+} h.s.)	64.22	0.307(9)	0.595(17)	0.578(24)	
			Silicate (Fe^{2+} h.s.)	35.78	1.163(13)	2.312(74)	0.570(70)	
	33–36	1980.1	Clay (Fe^{3+} h.s.)	59.10	0.325(7)	0.605(13)	0.493(18)	
			Silicate (Fe^{2+} h.s.)	40.90	1.124(15)	2.490(30)	0.648(39)	
	36–39	1977.6	Clay (Fe^{3+} h.s.)	47.78	0.324(4)	0.587(8)	0.486(11)	
			Silicate (Fe^{2+} h.s.)	34.68	1.141(8)	2.491(16)	0.591(26)	
			Hematite	17.54	0.342(55)	−0.199(108)	1.094(205)	49.34(45)
Non-dredged trench (Point B)	0–3	–	Clay (Fe^{3+} h.s.)	39.33	0.337(3)	0.590(6)	0.441(8)	
			Silicate (Fe^{2+} h.s.)	36.40	1.131(5)	2.458(10)	0.573(18)	
			Hematite	24.27	0.372(32)	−0.219(62)	1.139(120)	48.92(25)
	3–6	–	Clay (Fe^{3+} h.s.)	39.53	0.325(5)	0.613(9)	0.397(11)	
			Silicate (Fe^{2+} h.s.)	43.97	1.144(9)	2.457(18)	0.635(28)	
			Hematite	16.50	0.373(45)	−0.191(90)	0.852(179)	50.36(36)
	6–9	–	Clay (Fe^{3+} h.s.)	44.97	0.320(2)	0.587(3)	0.349(4)	
			Silicate (Fe^{2+} h.s.)	37.12	1.112(3)	2.533(6)	0.468(13)	
			Hematite	17.92	0.395(40)	−0.308(79)	1.067(153)	48.84(31)

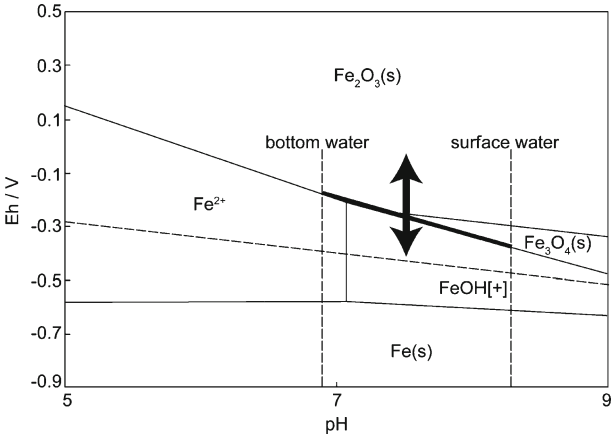

Fig. 3 Eh-pH diagram of iron optimized at sampling sites

generation at point A is shown in Fig. 3. The conditions for hematite generation at points A and B, indicated by the arrows in the figure, occur when the environment exceeds an Fe_2O_3−FeOH[+] boundary. For Eh in the seawater to become suitable for hematite generation, that is, to exceed the Fe_2O_3−FeOH[+] boundary in the diagram, it is reasonable to assume that the amount of DO increases. Theoretically, if the amount of DO is low in all the seawater, the Eh in the seawater will not be less than at least −200 mV. Since hematite was generated at all depths at non-dredged point B, which is a short distance from point A (ca. 500 m), the possibility that the iron concentration in the supplied seawater was low around point A becomes very small.

The radiation dose of excess ^{210}Pb at point A indicated that the sedimentation rate is 1.2 cm·year^{-1} (core average, MAR), and there was obviously no disturbance over the core. As the sedimentation rate in the inner part of Tokyo Bay was within 0.60 to 1.56 cm·year^{-1}, this was a reasonable value.

The sedimentation age of the core bottom layer (36–39 cm) at point A can be calculated from the slope as being around 1976 to 1979. Since the sedimentation age of the bottom occurs after the dredging, the core at point A is accumulated after the dredging. The sedimentation age of the layers in which the hematite was measured corresponds to the years 1976–1979, 1986–1989 and 2006–2009. Therefore, at those times, the Eh was clearly sufficient to generate hematite. As shown in Fig. 1, the DO in 1976–1979 and 1986–1989 did not fall to 0 mg·L^{-1} in summer, suggesting that the high Eh in seawater persisted through each year. Although the DO data for 2006–2009 are inconclusive, it is possible that the surface hematite that was oxidized by the air was observed. However, in the layers representing at least two of the time periods, proof of weakened hypoxia was clearly recorded in the sediment. Therefore, the agreement between the quality of hematite in sediment and past DO representing hypoxia has been confirmed. Since this method is very simple, it serves as a good index by which the scale of past hypoxia can be evaluated in other dead zones.

Acknowledgement This work was supported by a Grant-in-Aid for Young Scientists Start-up (20810007).

References

1. Diaz, R.J., Rosenberg, R.: Science **321**, 926–929 (2008)
2. Bale, C.W., Chartrand, P., Degtrev, S.A., Eriksson, G., Hack, K., Ben Mahfoud, R., Melancon, J., Pelton, A.D., and Petersen, S.: FactSage thermochemical software and databases. Calphad **26**, 189–228 (2002)
3. Sasaki, J., Kawamoto, S., Yoshimoto Y., Ishii, M. Kakino, J.: J. Coastal Res. **56**, 890–894 (2009)
4. Kanai, Y.: Appl. Radiat. Isot. **69**, 455–462 (2011)

Hyperfine Interact (2012) 207:97–105
DOI 10.1007/s10751-011-0437-y

In-situ Mössbauer spectroscopy with MIMOS II

Iris Fleischer · Göstar Klingelhöfer · Richard V. Morris · Christian Schröder · Daniel Rodionov · Paulo A. de Souza · the MIMOS II team

Published online: 1 November 2011

Abstract The miniaturized Mössbauer spectrometer MIMOS II was developed for the exploration of planetary surfaces. Two MIMOS II instruments were successfully deployed on the martian surface as payload elements of the NASA Mars Exploration Rover (MER) mission and have returned data since landing in January 2004. Mössbauer spectroscopy has made significant contributions to the success of the MER mission, in particular identification of iron-bearing minerals formed through aqueous weathering processes. As a field-portable instrument and with backscattering geometry, MIMOS II provides an opportunity for non-destructive in-situ investigations for a range of applications. For example, the instrument has been used for analyses of archaeological artifacts, for air pollution studies and for in-field monitoring of green rust formation. A MER-type MIMOS II instrument is part of the payload of the Russian Phobos-Grunt mission, scheduled for launch in November 2011, with the aim of exploring the composition of the martian moon Phobos. An advanced version of the instrument, MIMOS IIA, that incorporates capability for elemental analyses, is currently under development.

I. Fleischer (✉) · G. Klingelhöfer · D. Rodionov
Institute of Inorganic and Analytical Chemistry, Johannes Gutenberg University of Mainz, Mainz, Germany
e-mail: fleischi@uni-mainz.de

R. V. Morris
NASA Johnson Space Center, Houston, TX, USA

C. Schröder
University of Bayreuth and University of Tübingen, Tübingen, Germany

D. Rodionov
Space Research Institute IKI, Moscow, Russia

P. A. de Souza
Tasmanian ICT Centre, Hobart, Australia

Keywords Miniaturized Mössbauer spectrometer · MIMOS II · Mars Exploration Rover mission · In-situ Mössbauer spectroscopy · Non-destructive analysis

Abbreviations

MIMOS II	Miniaturized Mössbauer spectrometer
NASA	National Aeronautics and Space Administration
MER	Mars Exploration Rover
IDD	Instrument Deployment Device
MI	Microscopic Imager
RAT	Rock Abrasion Tool
APXS	Alpha Particle X-ray Spectrometer
npOx	Nanophase ferric oxide
XRD	X-Ray Diffraction
XRF	X-Ray Fluorescence
SDD	Silicon Drift Detector

1 Introduction

MIMOS II, the miniaturized Mössbauer spectrometer, was developed for the mineralogical exploration of solid planetary surfaces. The instrument consists of a sensor head measuring 50 × 50 × 90 mm and an electronics board.

Two instruments have successfully been employed on the martian surface since January 2004 as payload elements of the two NASA Mars Exploration Rovers (MER) Spirit and Opportunity [1, 2]. On Mars, MIMOS II has proven its ability to work at temperatures as low as 200 K and at an atmospheric pressure of ∼7 mbar. The backscattering instrument geometry does not require any sample preparation, which is a great advantage for measurements on the surface of another planet, and enables non-destructive analyses of terrestrial samples. As a field-portable instrument, MIMOS II has also been employed in a range of field studies. This paper provides a review of results from both extraterrestrial and terrestrial applications of MIMOS II instrumentation.

2 MER Mössbauer results

The twin Mars Exploration Rovers Spirit and Opportunity are equipped with a suite of analytical instruments, including a panoramic camera, a miniature thermal emission spectrometer and four contact instruments mounted on an Instrument Deployment Device (IDD), comprising a Microscopic Imager (MI), a Rock Abrasion Tool (RAT), an Alpha-Particle- X-ray spectrometer (APXS) and the miniaturized Mössbauer spectrometer MIMOS II. Figure 1 shows the instrument mounted on Opportunity's IDD, as imaged by the rover's panoramic camera.

The primary scientific objective of the MER mission was to search for traces of past water activity at two sites on the martian surface, Gusev crater and Meridiani Planum [2]. Whenever possible, observations of a surface target were carried out by several instruments, and evidence for aqueous alteration was found at both landing

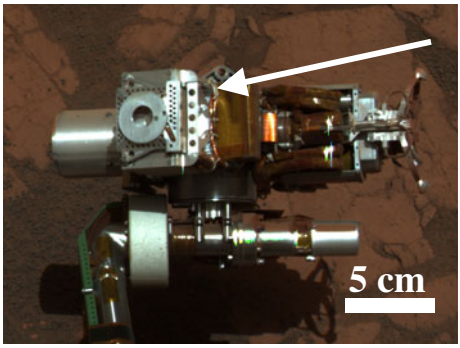

Fig. 1 MIMOS II (arrow) on Opportunity's IDD. Image courtesy of NASA/JPL/Pancam

sites. Based on Mössbauer spectra obtained with MIMOS II, iron-bearing minerals were identified at both landing sites that are also known from terrestrial settings and form only under aqueous conditions.

Originally planned as a 90-sol mission (a sol is a martian day), Spirit's journey continued through March 2010, and Opportunity's investigations continue to the present day, more than seven years after landing. To date, ~150 Mössbauer spectra have been recorded on separate surface targets at each landing site. Because of diurnal temperature variations on Mars, spectra are stored in up to 13 separate temperature windows 10 K wide, covering the range from below 180 K to above 290 K.

2.1 Results from Gusev crater

Gusev crater was chosen as the landing site for MER Spirit because its morphology implies the former presence of a lake and lacustrine sediments [3]. During its 90-sol primary mission, however, Spirit traversed a basaltic plain. The first Mössbauer spectrum on the martian surface was obtained on soil and revealed its basaltic signature dominated by olivine and pyroxene. The rocks on the plain were found to be basaltic. In some cases, thin surface coatings containing iron oxides were observed to cover the rocks, thus providing evidence for at least a low degree of oxidation [4, 5]. An example spectrum is shown in Fig. 2a.

On sol 156, Spirit started investigating the Columbia Hills. Instead of the relatively fresh, olivine-rich rocks on the plains, the rover encountered pervasively weathered rocks [6, 7]. With MIMOS II, hematite (α-Fe_2O_3) and goethite (α-FeOOH) were detected in outcrop rocks [8]. An example spectrum is shown in Fig. 2b. Goethite also occurs in terrestrial settings, where it normally forms only under aqueous conditions. Its presence is thus evidence that the rocks of the Columbia Hills came into contact with water [7, 8]. The combination of data from MIMOS II and other MER instruments revealed the presence of carbonate assemblages that probably precipitated from carbonate-rich solutions under hydrothermal conditions [9].

On sol 744, after crossing the summit of Husband Hill, Spirit reached Home Plate, a circular, layered plateau in the inner basin of the Columbia Hills ~90 m in diameter and 2–3 m high that likely originated from a hydrovolcanic explosion and deposition of pyroclastic material [10]. MIMOS II Mössbauer spectra reveal that Home Plate rocks are rich in magnetite. At the west side, rocks contain significant amounts of

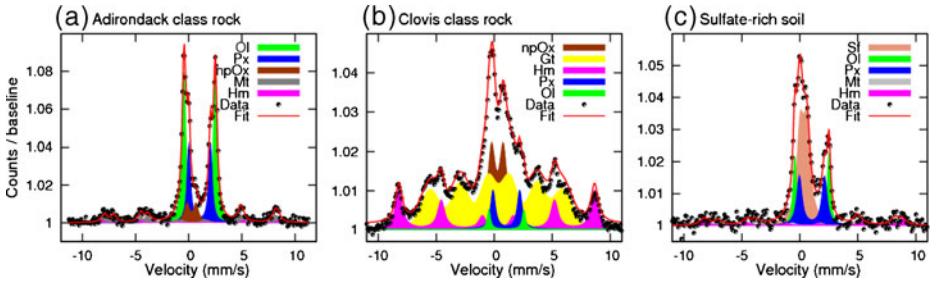

Fig. 2 Mössbauer spectra obtained at Gusev crater. **a** weakly-weathered Adirondack-class basaltic rock, **b** pervasively weathered Clovis class rock, **c** sulfate-rich soil. Legend: *Ol* olivine, *Px* pyroxene, *npOx* nanophase ferric oxide, *Mt* magnetite, *Hm* hematite, *Gt* goethite, *Sf* ferric sulfate

olivine and nanophase ferric oxide (npOx), while high abundances of pyroxene and little olivine are present at the east side [11]. This compositional transition may have originated from a combination of high and low temperature alteration processes [12].

Spirit spent its third martian winter on the northern slope of Home Plate and subsequently explored a small valley to the west. After a drive on sol 1871, the rover broke through a thin crust and became embedded in a deposit of mixed sulfate-rich and basaltic soil. An extensive investigation was initiated of freshly exposed, bright material. In agreement with high sulfur contents detected with the APXS, Mössbauer spectra revealed the presence of ferric sulfates (Fig. 2c). These, together with the nature of the crust, point to the occurrence of dissolution and precipitation processes just beneath the surface [13].

Communication with Spirit was lost at the onset of it's fourth martian winter in March 2010. Attempts to re-establish communication were terminated in May 2011, officially completing Spirit's mission.

2.2 Results from Meridiani Planum

Opportunity's landing site at Meridiani Planum was chosen because hematite indicative for aqueous processes had been detected from orbit [14]. Opportunity landed in ~20 m diameter Eagle crater, where the rover investigated an exposure of bright sedimentary outcrop rocks in the wall of the crater. With Opportunity's Mössbauer spectrometer, jarosite ($(K,Na)Fe_3^{3+}(SO_4)_2(OH)_6$) and hematite were detected in the outcrop matrix. An example spectrum is shown in Fig. 3a. The presence of jarosite is clear evidence for past water activity under acidic conditions at Meridiani Planum [15]. Hematite was also found to be the main constituent of mm-sized spherules (Fig. 3b) that have formed as sedimentary concretions (the so-called blueberries) within the outcrop rock and are weathering out by eolian erosion [16–18]. The hematite in both outcrop and spherules is characterized by two populations whose Mössbauer parameters exhibit different temperature-dependent behaviors [19]. The presence of different hematite populations implies more than one hematite-forming process or episode [17, 20].

The soil at Meridiani Planum was found to be practically identical to the soil at Gusev crater. The similarity of soils from these two locations on opposite sides of the planet indicates that martian soil is a globally distributed component [21]. To

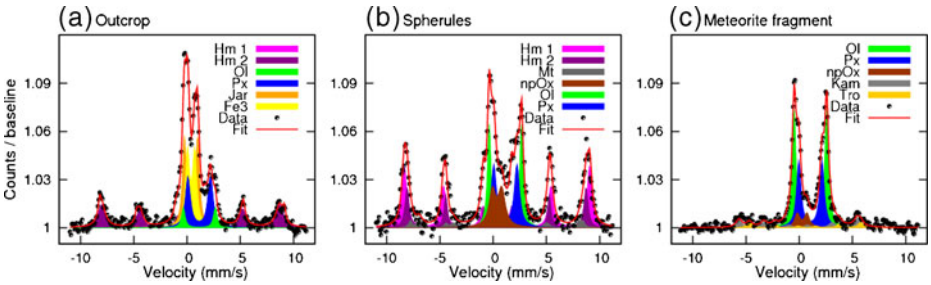

Fig. 3 Mössbauer spectra obtained at Meridiani Planum. **a** outcrop matrix, **b** hematite-rich spherules, **c** dark rock (meteorite fragment). Legend: *Hm* hematite, *Ol* olivine, *Px* pyroxene, *Jar* jarosite, *Fe3* unassigned ferric phase, *Mt* magnetite, *npOx* nanophase ferric oxide, *Kam* kamacite, *Tro* troilite

the present day, Opportunity has traversed more than 33 km. Along its traverse, the rover has investigated outcrop exposures on the plains and stratigraphic sections in the inner walls of a number of craters, the largest being Victoria with a diameter of ~800 m [22, 23]. For all investigated outcrop targets, the chemical and mineralogical compositions remain strikingly similar. Mössbauer spectra exhibit only minor variations, mostly with respect to the relative abundance of Fe-bearing phases [24]. Occasionally, Opportunity encountered dark rocks with no apparent connection to the ubiquitous bright outcrop. Typically, these rocks have dimensions of several centimeters and clusters are observed preferentially near craters. Based on their chemical and mineralogical composition derived from APXS and Mössbauer spectra, these "cobbles" can be distinguished into two groups interpreted as meteorite fragments and impact-breccias composed of local outcrop rock and basaltic sand [25, 26]. An example spectrum obtained on a meteorite fragment is shown in Fig. 3c. Opportunity also encountered six iron meteorites, whose weathering states provide information about the climate at Meridiani Planum since their impact [27–29].

Opportunity recently arrived at the rim of ~20 km diameter Endeavour crater, where the rover will investigate putative phyllosilicate-rich deposits that have been detected from orbit [30].

3 Mars analog studies

In support of the interpretation of the MER data set, terrestrial Mars analog sites were investigated. Recent field campaigns were focused on the investigation of sulfate- and oxide-rich mineral assemblages at Rio Tinto and Jaroso Ravine, Spain; two analog sites for Meridiani Planum [31, 32]. Studies were carried out with a combination of instruments, including MIMOS II, a Raman spectrometer [33] and the portable "Terra" XRD/XRF instrument [34].

The water of Rio Tinto exhibits a deep red color and a nearly constant acidic pH value of ~2.3 along its approximately 100 km long course. Sulfate minerals mainly form from aqueous alteration of the iron-rich sulfide minerals of the Iberian Pyrite Belt and precipitate from the river during dry, hot seasons [35]. Bedrock and evaporative precipitates were investigated in-situ at four different sampling sites

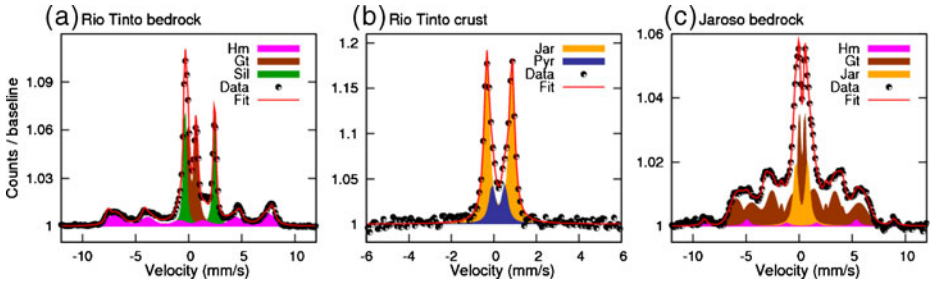

Fig. 4 Mössbauer spectra from Mars analog sites. **a** Rio Tinto river bedrock, **b** jarosite-bearing crust on Rio Tinto river bedrock, **c** assemblage of jarosite, goethite and hematite from Jaroso Ravine. Legend: *Hm* hematite, *Gt* goethite, *Sil* silicate, *Jar* jarosite, *Pyr* pyrite

during two field campaigns in 2008 and 2009. In addition to in-situ measurements, representative samples from all sampling sites were analyzed in detail after the field trip with laboratory instrumental setups.

The river bedrock was found to be constituted of conglomeratic, cemented materials with clast sizes in the range up to ~3 cm. The surface of the rocks is often covered with a dark crust, presumably from the influence of the acidic water. Mössbauer spectra reveal the presence of superparamagnetic goethite as the primary phase, with minor amounts of hematite and silicates from some clasts. An example spectrum is shown in Fig. 4 a. Portions of the river bedrock were covered with a red crust containing jarosite ($KFe_3(SO_4)_2(OH)_6$) [31]. An example spectrum is shown in Fig. 4b.

Sulfate minerals generally precipitate close to the stream margin. Precipitates with popcorn-like texture a few centimeters in diameter are very common, usually colored white or yellow, sometimes mixed with small amounts of red or grey. From the combination of Mössbauer spectroscopy and XRD, ferric sulfates were detected in these samples, including ferricopiapite ($Fe_5^{3+}O(SO_4)_6OH{\cdot}20H_2O$), coquimbite ($Fe_2(SO_4)_3{\cdot}9H_2O$), and rhomboclase ($(H_5O_2)^+Fe^{3+}(SO_4)_2{\cdot}2H_2O$). Crusts ~5 mm thick and several centimeters in diameter occur with a variety of colors including white and different shades of green and blue. They were found to contain the ferrous sulfates melanterite ($Fe^{2+}SO_4{\cdot}7H_2O$) and rozenite ($Fe^{2+}SO_4{\cdot}4H_2O$).

Jaroso Ravine, located within the Jaroso Hydrothermal System in south-eastern Spain, is the type locality of jarosite and a Mars analog site where mineral associations and formation processes can be studied in situ. With MIMOS II, jarosite was detected in association with goethite and hematite, in accordance with previous findings [36, 37]. An example spectrum is shown in Fig. 4c.

4 Terrestrial applications

As a field-portable instrument, MIMOS II has been employed in archaeological and environmental studies and in industrial applications. For the investigation of rare or precious materials such as archaeological artifacts, the backscattering geometry of MIMOS II enables non-destructive measurements.

On a Lekythos vase (500 B.C.), Mössbauer spectra were obtained on unpainted parts of the surface and on patterns painted with black and red color. The unpainted surface can be associated with poorly crystalline iron oxides, presumably produced during the firing process. Spectra obtained on black colored parts exhibit a sextet signature corresponding to well crystalline hematite. Spectra recorded on red colored parts were found to be practically identical to those from the unpainted surface, suggesting similar compositions [38].

In-situ analyses of ancient rock paintings were performed at Santana do Riacho, Minas Gerais, Brazil. For these measurements, MIMOS II was mounted on a tripod and put into contact with the painting on the wall. In total, six individual spots were investigated, which were separated by a few meters and exhibited distinctly different colors. The dominating Fe-oxide pigments were found to be hematite (red) and goethite (yellow/ochre), with an additional superparamagnetic Fe-oxide phase [39].

A sample of an ochre wall painting from a tomb in the district of Xunyi, Shaanxi, China, was investigated both at room temperature and at 200 K. Hematite and goethite were found to be present in the paint [40].

The investigation of ancient metallic artifacts yields information on their original composition, processing, and corrosion state. A Celtic helmet knob (discovered close to Aldrans, Tirol, Austria) was found to contain metallic iron, magnetite and superparamagnetic iron oxides. The higher concentration of magnetite on the surface compared to the interior suggests that magnetite stems from a corrosion process. The Mössbauer spectra, together with ashes and a patina on the artifact, indicate that the object may have been burnt as a sacrifice [41].

For another example, a roman mask and metallic fragments were found in excavations at “Villa von Allmend”, Saarland, Germany. Mössbauer spectra were obtained to determine whether a fragment was part of the mask or of another object. Significant amounts of wüstite ($Fe_{1-x}O$) were detected in the mask, along with magnetite, goethite and maghemite or hematite. The composition of the unidentified fragment was found to be clearly different: wüstite was not detected at all and magnetite, goethite, hematite and maghemite were identified with abundances different from those in the mask. Therefore, the fragment is not associated with the mask [41].

Air pollution studies were carried out in the metropolitan region of Vitória, Espirito Santo, Brazil. MIMOS II was installed in an airborne particle sampler. The accumulated particles were found to consist of hematite as the predominant phase, with goethite, pyrite, iron-bearing silicates, an ultrafine ferric phase and magnetite as subordinate phases. These minerals were found to originate from industrial plants producing iron-ore pellets (hematite), from handling and storing coal (pyrite), from steelwork plants (magnetite), from civil constructions (silicates), from industrial emissions and from strongly weathered tropical soils (ultrafine ferric phases). Hematite, goethite and silicates were also detected in soil [42].

A special experimental setup was developed for in-field monitoring of hydromorphic soils and the formation and transformation of the green-rust mineral fougerite, $[Fe^{2+}_{1-x}Mg_yFe^{3+}_x(OH)_{2+2y}]^{x+}[xA, mH_2O]^{x-}$, where x is the ratio Fe^{3+}/Fe_{tot} [e.g. 43]. Bore-hole investigations were carried out with MIMOS II placed inside a plexiglas tube. After programming instrument positions at several depths and acquisition intervals, the setup can work autonomously for several weeks [44]. Mössbauer spectra obtained during a field campaign in Fougères, France, are characteristic for fougerite. Variations in the Fe^{3+}/Fe_{tot} ratio were observed, providing evidence for fast redox transformations at well-defined points in the soil [43].

5 Conclusions and outlook

The miniaturized Mössbauer spectrometer MIMOS II has successfully been utilized in a wide range of extraterrestrial and terrestrial applications. Within the Mars Exploration Rover mission, two instruments contributed to the mission goal of searching for traces of past water activity by identifying minerals that are characteristic for aqueous weathering processes both at Gusev crater and at Meridiani Planum.

For MIMOS II as a field-portable instrument, a range of terrestrial applications has opened up. Investigations of rare and precious archaeological artifacts benefit from the possibility of performing non-destructive investigations. MIMOS II has been used to decipher the mineralogical composition of pigments used to paint pottery as well as on rock paintings. The original composition, corrosion state and treatment of metallic objects could be analyzed, and unassigned fragments could be compared to those objects based on their Mössbauer spectra. In autonomous, in-field setups, MIMOS II was successfully employed to trace sources of air pollution and to monitor transformations of the green-rust mineral fougerite.

A MER-type MIMOS II instrument is part of the payload of the Russian Phobos Grunt mission. Scheduled for launch in November 2011, the aim of this mission is to investigate the surface of the martian moon Phobos and return samples to Earth. Determining the surface mineralogical composition of Phobos will also shed light on the origin of the martian moons [45].

MIMOS IIA, an advanced version of the MIMOS II instrument, is equipped with a Silicon Drift Detector (SDD) system, which provides higher energy resolution that enables acquisition of X-ray fluorescence spectra suitable for elemental analysis in addition to Mössbauer spectra and will also decrease required integration times significantly [46]. A MIMOS IIA instrument was successfully tested during a field campaign at Mauna Kea, Hawaii [47], and it will surely open up new fields of application for in-situ Mössbauer spectroscopy.

Acknowledgements Development of the MIMOS II Mössbauer spectrometer was funded by the German Space Agency under contract 50QM99022 and supported by the Technical University of Darmstadt and the University of Mainz. C. Henrich is acknowledged for providing Fig. 4c. The support of the Russian space agency is acknowledged. We thank the reviewer of this manuscript for providing helpful comments.

References

1. Klingelhöfer, G., et al.: J. Geophys. Res. **108**(E12) 8067 (2003)
2. Squyres, S.W., et al.: J. Geophys. Res. **108**(E12), 8062 (2003)
3. Squyres, S.W., et al.: Science **305**, 794–799 (2004)
4. Morris, R.V., et al.: Science **305**, 833–836 (2004)
5. Haskin, L.A., et al.: Nature **436**, 66–69 (2005). doi:10.1038/nature03640
6. Squyres, S.W., et al.: J. Geophys. Res. Planet **111**, E02S11 (2006)
7. Morris, R.V., et al.: J. Geophys. Res. Planet **111**, E02S13 (2006)
8. Klingelhöfer, G., et al.: Hyperfine Interact. **166**, 549–554 (2005)
9. Morris, R.V., et al.: Science **329**, 421–423 (2010)
10. Squyres, S.W., et al.: Science **316**, 738–742 (2007)
11. Schröder, C., et al.: Lunar Planet. Sci. **39**, 2153 (2008)
12. Schmidt, M.E., et al.: Earth Planet. Sci. Lett. **281**, 258–266 (2009)
13. Arvidson, R.E., et al.: J. Geophys. Res. Planet **115**, E00F03 (2010)
14. Christensen, P.R., et al.: J. Geophys. Res. **105**(E4), 9623–9642 (2000)

15. Klingelhöfer, G., et al.: Science, **306**, 1740–1745 (2004)
16. Morris, R.V., et al.: Earth Planet. Sci. Lett. **240**, 168–178 (2005)
17. McLennan, S., et al.: Earth Planet. Sci. Lett. **240**, 95–121 (2005)
18. Golden, D.C., et al.: Am. Mineral. **93**, 1201–1214 (2008)
19. Fleischer, I., et al.: J. Geophys. Res. Planet **115**, E00F06 (2010)
20. Morris, R.V., et al.: Earth Planet. Sci. Lett. **240**, 168–178 (2005)
21. Yen, A., et al.: Nature **436**, 49–54 (2005)
22. Squyres, S.W., et al.: J. Geophys. Res. Planet **111**, E12S12 (2006)
23. Squyres, S.W., et al.: Science **324**, 1058–1061 (2009)
24. Morris, R.V., et al.: J. Geophys. Res. Planet **111**, E12S15 (2006)
25. Fleischer, I., et al.: J. Geophys. Res. Planet **115**, E00F05 (2010)
26. Schröder, C., et al.: J. Geophys. Res. Planet **115**, E00F09 (2010)
27. Ashley, J.W., et al.: J. Geophys. Res. Planet **116**, E00F20 (2011)
28. Fleischer, I., et al.: Meteorit. Planet Sci. **46**(1), 21–34 (2011)
29. Schröder, C., et al.: J. Geophys. Res. Planet **113**, E06S22 (2008)
30. Wray, J.J., et al.: Geophys. Res. Lett. **36**, L21201 (2009)
31. Fleischer, I., et al.: J. Phys.: Conf. Ser. **217**, 012062 (2010)
32. Klingelhöfer, G., et al.: Lunar Planet. Sci. **41**, 2736 (2010)
33. Rull, F., et al.: Lunar Planet. Sci. **39**, 1616 (2008)
34. Blake, D., et al.: Lunar Planet. Sci. **40**, 1484 (2009)
35. Fernandez-Remolar, C., et al.: Earth Planet Sci. Lett. **240**, 149–167 (2005)
36. Rull, F., et al.: EPSC Abs. **5**, EPSC2010-845 (2010)
37. Martinez-Frias, J., et al.: Earth Planets Space **56**, v–viii (2004)
38. de Souza, P.A., et al.: Hyperfine Interact. **151/152**, 125–130 (2003)
39. Klingelhöfer, G., et al.: Hyperfine Interact. **C5**, 423–426 (2002)
40. Klingelhöfer, G., et al.: Hyperfine Interact. **144/145**, 371–379 (2002)
41. de Souza, P.A.: Dissertation, University of Mainz, Germany (2004)
42. de Souza, P.A., et al.: J. Radioanal. Nucl. Chem. **246**(1), 85–89 (2000)
43. Feder, F., et al.: Geochim. Cosmochim. Acta **69**, 4463–4483 (2005)
44. Rodionov, D., et al.: Hyperfine Interact. **167**(1) 869–873 (2006)
45. Rodionov, D., et al.: Sol. Syst. Res. **44**(5), 362–370 (2010)
46. Blumers, M., et al.: Nucl. Instrum. Methods A **624**(2), 277–281 (2010)
47. Klingelhöfer, G., et al.: Lunar Planet. Sci. **42**, 2810 (2011)

Hyperfine Interact (2012) 207:107–108
DOI 10.1007/s10751-011-0508-0

Solving puzzles of glasses with nuclear resonance scattering

Aleksandr I. Chumakov

Published online: 7 December 2011

Abstract We compare the atomic motions in a glass and in a relevant crystal using nuclear inelastic scattering, a technique that determines the exact number of vibrational states. The results show that around the boson peak, the number of states in a glass is exactly the same as the number of sound wave states in the crystal around the transverse acoustic (TA) van Hove singularity. Furthermore, increasing pressure causes the transformation of the boson peak of the glass towards the TA singularity of the crystal. Once corrected for the difference in the elastic medium, the boson peak matches the TA singularity in energy and height. This suggests the identical nature of the two features.

Keywords Boson peak · Glass dynamics · Phonons · Nuclear inelastic scattering

Glasses are remarkably different from crystals at low temperature. They accumulate more heat and conduct less. This anomaly is related to a particular ensemble of atomic motions called the "boson peak", whose nature has remained unknown for more than 50 years.

Before the 1960s, a glass was thought to be an ideal elastic medium, where atomic motions are determined by sound waves according to the Debye model. According to C. Kittel's textbook, "the point was so obvious that it did not encourage experimental investigation" [1]. This state of blissful ignorance ended when measurements of specific heat and thermal conductivity revealed tremendous deviations from the Debye behaviour [2]. A little later these deviations were attributed to the boson peak—a universal feature in the density of vibrational states (DOS) for all glasses. Since then, the vibrations of atoms in glasses have remained a point of controversy. Dozens of theoretical models and hundreds of experimental results did not provide a

A. I. Chumakov (✉)
European Synchrotron Radiation Facility, BP220 Grenoble, 38043 France
e-mail: chumakov@esrf.fr

unified picture of how disorder in atomic positions makes glasses thermodynamically so different from ordered crystals.

Because of the lengthy research period, the boson peak has been called the last puzzle of solid state physics. Driven by the distinction from crystalline properties, the majority of theoretical models explained the boson peak by embracing features beyond sound waves.

We compared the atomic motions in a glass and a crystal using nuclear inelastic scattering, a technique that determines the exact number of vibrational states. The results show that around the boson peak, the number of states in a glass is exactly the same as the number of sound wave states in the crystal around the transverse acoustic (TA) van Hove singularity [3]. Thus, the glass has no additional modes in excess of the sound waves in the crystal.

The equivalence of the boson peak and the TA singularity in the absolute number of states suggests that the vibrational states of the boson peak belong to acoustic branches. Indeed, an alternative attribution of the boson peak to additional modes would face a problem to explain the ~35% deficit of acoustic states in the glass.

Application of pressure causes the transformation of the reduced DOS of the glass towards the reduced DOS of the crystal: The boson peak decreases in height and shifts to higher energy, moving towards the TA singularity [3]. Measurements of density and sound velocity suggest that the transformation is caused by a gradual stiffening of the elastic medium. Once corrected for the difference in the elastic medium (re-plotted in the Debye energy units), the boson peak matches the transverse acoustic singularity in height and energy [3].

These observations unambiguously identify the boson peak with sound waves. They lead to the conclusion that the anomaly in the heat capacity of glasses comes not from the additional modes, but from conventional sound waves, which, however, have lower frequencies in glasses due to structural disorder. Unexpectedly, but in accordance with the general theory of knowledge, the sound-wave nature of glass anomalies revealed here is a return to the earliest ideas, but with a new level of understanding.

References

1. Kittel, C.: Introduction to Solid State Physics. Wiley, New York (1967)
2. Phillips, W.A. (ed.): Amorphous Solids—Low Temperature Properties. Topics in Current Physics, vol. 24. Springer, Berlin (1981)
3. Chumakov, A.I., Monaco, G., Monaco, A., Crichton, W.A., Bosak, A., Rüffer, R., Meyer, A., Kargl, F., Comez, L., Fioretto, D., Giefers, H., Roitsch, S., Wortmann, G., Manghnani, M.H., Hushur, A., Williams, Q., Balogh, J., Parliński, K., Jochym, P., Piekarz, P.: Phys. Rev. Lett. **106**, 225501 (2011)

Hyperfine Interact (2012) 207:109–112
DOI 10.1007/s10751-011-0522-2

A comparison of crystalline and quasicrystalline Al-Mn-Fe compounds

Kamran Ali · Michael Reissner · Walter Steiner · Michael Feuerbacher

Published online: 18 December 2011

Abstract New complex metallic alloys of the Taylor phase Al_3Mn with 8, 10 and 12% Fe substitution are investigated by ^{57}Fe Mössbauer spectroscopy. Two groups of subspectra, with different hyperfine parameters are obtained, and are allocated to Fe sites with only Al nearest neighbors and Fe sites with both Al and Mn in the first shell. No difference between crystalline and quasicrystalline compounds is found indicating that long range periodicity plays a minor role.

Keywords Taylor phase · Spin glass · Complex metallic alloy

1 Introduction

We report on Taylor phase compounds on the Al-rich side of the Al-Mn phase diagram around 70% Al with Fe substitution up to 12 at%. These compounds are so-called 'Complex Metallic Alloys', with extreme large numbers of atoms in the unit cell. It was shown that the physical properties of such crystals are mainly determined by the existence of typical substructures, with length scales, which can substantially differ from the lattice constants [1]. A further important characteristic is inherent disorder, caused by partly or mixed occupancy of lattice sites and the occurrence of building blocks in different orientations inside the unit cell. By slightly different heat treatment a decagonal quasicrystal with nearly the same composition could be produced, which gives the possibility to investigate the similarity of both crystalline and quasicrystalline compounds on the very local basis of Mössbauer spectroscopy.

K. Ali · M. Reissner (✉) · W. Steiner
Institute of Solid State Physics, Vienna University of Technology, Vienna, Austria
e-mail: reissner@ifp.tuwien.ac.at

M. Feuerbacher
Institute of Microstructure Research, Forschungszentrum Jülich, Jülich, Germany

2 Experimental

Samples of the orthorhombic Taylor phase Al_3Mn (*Pnma*) with 8, 10, and 12% Fe substitution were produced by levitation induction melting in a water-cooled copper crucible under argon atmosphere followed by thermal annealing for 164 h at 1010°C [2]. For 10% Fe also a sample with decagonal structure could be synthesized. EDX-analysis gave the following compositions: $Al_{69}Mn_{23}Fe_8$, $Al_{70}Mn_{20}Fe_{10}$, and $Al_{68}Mn_{20}Fe_{12}$ for the crystalline and $Al_{71}Mn_{19}Fe_{10}$ for the quasicrystalline compound. Dc magnetic measurements were performed by QD-PPMS-9T-VSM and ^{57}Fe Mössbauer spectra were recorded with a standard constant acceleration spectrometer in transmission geometry between 4.3 K and room temperature. For analysis the full Hamiltonian including electrostatic and magnetic hyperfine interaction is solved [3]. Sample thickness was taken into account after [4].

3 Results

From magnetic measurements spin glass behavior is found for all samples with freezing temperature around 30 K, increasing with Fe concentration. Details of the magnetic measurements are given in [5, 6].

Mössbauer spectra above the freezing temperature are broadened, asymmetric doublets (Fig. 1). They can be fitted by only two subspectra with intensity ratio around 30:70 and line width around 50% larger than the experimental resolution. Quadrupole splitting $eQV_{zz}/4 = 0.15(0.34)$ mm/s, 0.16(0.34) mm/s, and 0.15(0.32) mm/s as well as center shift CS(rel.^{57}Fe$\underline{\text{Rh}}$) = 0.092(0.069) mm/s, 0.083(0.051) mm/s, and 0.093(0.071) mm/s for the majority(minority) component are obtained at 294 K for the Taylor phases with $x = 8$, 10, and 12% Fe, respectively. Same values are determined for the decagonal compound. In fitting the spectra by two discrete subspectra instead of distributions, the assumption of a fixed relation between quadrupole splitting and center shift could be avoided. This is surely not the only possibility to fit the data, but gains on reliability as the obtained hyperfine parameters change smoothly with concentration.

Below the freezing temperature the spectra are more complex (Fig. 1). To fit them, both subspectra were divided into three, where the sum of relative area of these three spectra is in fair agreement with that from the high temperature fits. An increase in number of subspectra does not improve the quality of the fit. For each group quadrupole splitting and center shift scatter only within measuring accuracy. Obtained mean hyperfine fields increase slightly with Fe concentration (8.1, 8.1, and 8.4 T for 8, 10, and 12% Fe). This is the same trend as found for the effective magnetic moment [6]. An analysis in terms of hyperfine field distributions gives large contributions at zero field for all samples. Within statistics of the recorded spectra no difference between crystalline and quasicrystalline samples is found (Fig. 1).

4 Discussion

In view of the complex structure—the unit cell of the T-phase consists of 156 atoms with ten different Mn sites—the two groups of subspectra have to be interpreted

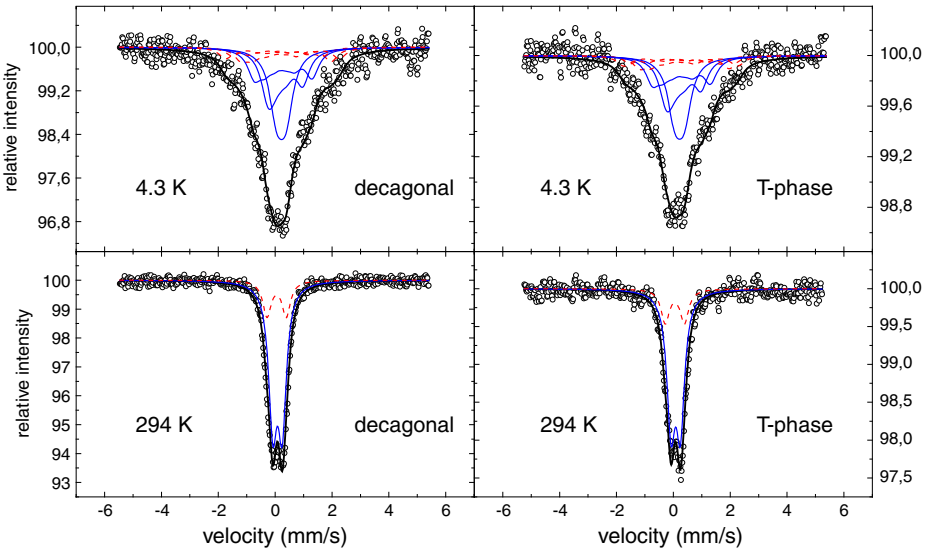

Fig. 1 Comparison of Mössbauer spectra for quasicrystalline (*left*) and crystalline (*right*) Al_3Mn with 10% Fe substitution for temperatures below and above the freezing temperature. The two groups of subspectra are indicated by *solid* and *dashed lines*

to be representatives of two characteristically different groups of crystallographic sites. If one defines the first Mn neighbor shell by the radius following from the sum of the metallic bonds of Al and Mn, one gets, using the occupation numbers given by [7], one Mn-site with only Al atoms in the first shell and a second site with two Mn atoms just at the border of this shell. For all other Mn sites Mn atoms are present in this shell, much closer to the central atom. This consideration defines two groups of Fe-environments for which different hyperfine parameters can be expected. According to our structural investigation and taking into account the concentrations obtained by EDX it was assumed that i) Fe replaces only Mn, ii) that deviations in Al concentration from the ideal $Al_3(Mn,Fe)$ composition changes only the occupation numbers of mixed Al/Mn sites and iii) that substitution is random. With these assumptions a ratio of the two groups of Fe environments very similar to the intensity ratio obtained for the two groups of subspectra is obtained.

The small difference in center shift for the two groups of Fe environments and the fact that the weighted mean quadrupole splitting and center shift are very similar to the ones obtained for samples with comparable Al concentration but other 3d-elements instead of Mn, like Pd [8], Cu [9] or Ni [10] indicates, that not the Mn-Fe interaction, but the Al(s,p)-Fe(3d) hybridization determines the charge density at the Fe nucleus. Within the investigated concentration interval changes in Fe concentration have only minor influence on the hyperfine parameters. The large contribution with zero field obtained in the hyperfine field distribution of all samples at temperatures below the freezing temperature might be allocated to Fe embedded on those Mn sites, which carry no moment [11]. As the hyperfine parameters for the decagonal sample are within experimental resolution identical with the ones of the crystalline compounds, it can be concluded that for the electronic exchange

interaction those length scales, which are determined by the very similar building blocks forming the T-Al_3Mn phase and the decagonal compound, are dominant. The presence of long range periodic atomic order is of less importance.

Acknowledgements Work performed within the EU Network of Excellence "Complex Metallic Alloys"

References

1. Urban, K., Feuerbacher, M.: J. Non-Cryst. Solids **334–335**, 143 (2004)
2. Balanetskyy, S., Meisterernst, G., Heggen, M., Feuerbacher, M.: Intermetallics **16**, 71 (2008)
3. Kündig, W.: Nucl. Instrum. Methods **48**, 219 (1967)
4. Mørup, S., Both, E.: Nucl. Instrum. Methods **124**, 445 (1975)
5. Ali, K., Reissner, M., Feuerbacher, M., Steiner, W.: Journal of Physics: Conference Series **200**, 032002 (2010)
6. Ali, K., Reissner, M., Feuerbacher, M., Steiner, W.: Solid compounds of transition elements. In: Bolet, J.L., Chevalier, B., Fruchart, D. (eds.) Book Series: Solid State Phenomena, vol. 170, p. 127 (2011)
7. Hiraga, K., Kaneko, M., Matsuo Y., Hashimoto S.: Phila. Mag. B **67**, 193 (1993)
8. Lawther, D.W., Dunlap, R.A.: J. Non-Cryst. Solids **153–154**, 49 (1993)
9. Brand, R.A., Pelloth, J., Hippert, F., Calvayrac, Y.: J.Phys.: Condens. Matter **11**, 7523 (1999)
10. Dunlap, R.A.: Phys. Mag. B **67**, 69 (1993)
11. Hafner, J., Krajči, M.: Phys. Rev. B **57**, 2849 (1998)

Hyperfine Interact (2012) 207:113–120
DOI 10.1007/s10751-011-0430-5

^{237}Np Mössbauer studies on actinide superconductors and related materials

Eric Colineau · Piotr Gaczyński · Jean-Christophe Griveau · Rachel Eloirdi · Roberto Caciuffo

Published online: 26 October 2011

Abstract Actinide materials play a special role in condensed matter physics, spanning behaviours of itinerant *d*-electron and localized *4f*-electron materials. This duality of the *5f* electrons confer to actinide-based intermetallic compounds a broad variety of physical properties such as magnetic or multipolar ordering, heavy fermion behaviour, quantum criticality, unconventional superconductivity... ^{237}Np Mössbauer spectroscopy is a unique microscopic tool for gaining information on the electronic and magnetic properties of Np systems.

Keywords Mössbauer spectroscopy · Neptunium · Actinides · Superconductivity

1 Introduction

Superconductivity was first reported in 1942 for uranium metal (α-U) [1] and in 1958 for U compounds [2]: UCo, U_6Mn, U_6Fe, and U_6Co, with critical temperatures T_c, of 1.7, 2.3, 3.9, and 2.3 K, respectively. A new class of U superconductors emerged in the early 1980's with the discovery of U heavy fermion (HF) superconductors (SC): UBe_{13} ($T_c = 0.85$ K) [3], UPt_3 ($T_c = 0.53$ K) [4], URu_2Si_2 ($T_c = 1.5$ K) [5] or UPd_2Al_3 ($T_c = 1.9$ K) [6]... Furthermore, in most of these systems, the SC phases coexist with antiferromagnetic (AF) correlations which have characteristic temperatures, usually the Néel temperature T_N, that are typically one order of magnitude larger

Work presented at ICAME-2011.

E. Colineau (✉) · P. Gaczyński · J.-C. Griveau · R. Eloirdi · R. Caciuffo
European Commission, Joint Research Centre, Institute for Transuranium Elements,
Postfach 2340, 76125 Karlsruhe, Germany
e-mail: eric.colineau@ec.europa.eu
URL: http://itu.jrc.ec.europa.eu

than the corresponding SC critical temperatures T_c. SC was even shown to co-exist with ferromagnetism in e.g. UGe_2 ($T_c \approx 0.8$ K, $T_C \approx 30$ K at p ≈ 1.2 GPa) [7] and URhGe ($T_c = 0.25$ K, $T_C = 9.5$ K) [8]. HF-SC still remain a major challenge for condensed matter physics. The existence of HF-SC and its coexistence or proximity with magnetic order suggests that the conventional mechanism of phonon-mediated SC is inappropriate and that alternative mechanisms, like spin fluctuations, should be considered for Cooper pairing.

Beside the large number of U superconductors, it is worth noticing the lack of transuranium superconductors: neither Np nor Pu metals are SC and, until a decade ago, no Np or Pu-based SC was reported (with the exception of Np Chevrel phases $Np_{1+x}Mo_6Se_8$ ($T_c = 5.6$ K) [9], where $5f$ electrons are thought not to be SC). The recent discovery of $5f$ electrons HF-SC in $PuCoGa_5$ [10], $PuRhGa_5$ [11] and $NpPd_5Al_2$ [12] has therefore been a major advance. Furthermore, their critical temperatures—$T_c \approx 18.5$, 8.7 and 4.9 K, respectively—are the highest of all f-electron systems.

Mössbauer effect can be observed in a number of actinide isotopes, however only the 60 keV electric dipole (E1) transition of the ^{237}Np isotope is suitable for systematic investigations, combining reasonable experimental constraints and exploitable output parameters [13]. Indeed, the excellent Mössbauer resonance of the ^{237}Np nucleus makes it a unique microscopic tool for gaining information on the electronic and magnetic properties of Np systems [14]. One consequence, however, of the rather high energy of the ^{237}Np Mössbauer transition, is the experimental limitation to fairly low temperatures, where the Lamb-Mössbauer factor is large enough to observe a sizeable effect.

In this paper, we review ^{237}Np Mössbauer spectroscopy (MoS) studies of the Np analogues of selected actinide superconductors: U heavy fermions, Pu "1:1:5" and the only Np-based SC known so far, $NpPd_5Al_2$.

2 Neptunium analogues of uranium heavy fermion superconductors

2.1 $AnBe_{13}$

UBe_{13}, one of the rare U-based HF-SC that does not show any AF ordering in the normal state, has a cubic crystal structure, a critical temperature $T_c = 0.85$ K, and a huge Sommerfeld coefficient of the specific heat $\gamma \approx 1{,}100$ mJ mole^{-1} K^{-2} [3].

Its isostructural homologue $NpBe_{13}$ also displays a huge quasi-particle mass enhancement $\gamma \approx 900$ mJ mole^{-1} K^{-2}, but orders AF at 3.4 K and is not SC down to 0.080 K [15]. ^{237}Np Mössbauer measurements have shown that the low-temperature properties were sensitive to Be content: samples with excess Be were not magnetic, whereas optimal samples had $T_N \approx 4.9$ K [16]. In the ordered state, the fit of the Mössbauer spectra requires two sites with different hyperfine fields ($B_{hf} = 241$ and 208 T) corresponding to Np ordered moments of 1.12 and 0.97 μ_B, respectively [17], and an intensity ratio ~2:1. These boundary conditions provided by MoS then allowed combined neutron diffraction experiments to determine the complex, modulated magnetic structure of $NpBe_{13}$ with wave vector $\mathbf{q} = (1/3,0,0)$, moments perpendicular to the propagation direction, and two sublattices with moments perpendicular to each other. The wave vector of the structure gave new information

on where to search for magnetic correlations in UBe_{13} [18]. However, subsequent investigations have revealed AF short-range magnetic correlations in UBe_{13} situated at $\mathbf{q} = (0.5,0.5,0)$ [19].

2.2 $AnRu_2Si_2$

URu_2Si_2 is a HF-SC with $T_c = 1.5$ K and $\gamma \approx 180$ mJ mole^{-1} K^{-2} that has a mysterious ground state below $T_0 = 17.5$ K [5] with a dipolar moment $m_U = 0.03\ \mu_B$. The order parameter has not been identified yet, and the phase has been called "hidden order" (HO). With pressure, the ground state switches from the HO phase to an AF phase ($m_U = 0.4\ \mu_B$), whereas SC is suppressed [20]. The application of high magnetic fields restores the HO phase [21].

It is worth noticing that ^{238}U MoS measurements have been performed on URu_2Si_2 [22]. However, this rotational electric dipole (E2) transition leads to a vanishing isomer shift $\delta_{IS} \rightarrow 0$ and broad line width that severely limit the access to hyperfine interactions and the information gained. It is nonetheless worthwhile noticing that the hyperfine magnetic field observed at the U site is one order of magnitude higher than expected for such a small magnetic moment.

Combined ^{237}Np MoS and neutron diffraction have shown that the $NpRu_2Si_2$ counterpart (tetragonal, like URu_2Si_2) is ordering at $T_N = 27.5$ K into an incommensurate structure ($\mathbf{q} = (0,0,0.86)$) with a maximum moment $m_{Np} = 1.5\ \mu_B$ aligned along the **c**-axis, and partial squaring at low temperatures [23]. The sizeable quadrupolar interaction ($e^2qQ \approx -66$ mm/s) contributes to make the Mössbauer pattern asymmetric and complex.

The intermediate systems $(U_{1-x}Np_x)Ru_2Si_2$ have also been studied and no SC has been detected by electrical resistivity measurements down to 1.5 K for all samples [24]. ^{237}Np MoS have revealed very similar patterns for all concentrations from $x = 0.9$ down to 0.05: δ_{IS}, e^2qQ and B_{hf} are nearly insensitive to x. It is also worth mentioning the rapid squaring of the Np moments modulation as x decreases: already for $x = 0.9$, only two distinct hyperfine fieds are observed and the main site represents 94% of the total intensity [25]. Finally, resonant x-ray magnetic scattering [26] have measured the ratio of the U and Np magnetic moments for $x = 0.1$ and $x = 0.5$ and, using m_{Np} from Mössbauer experiments, estimated $m_U \approx 0.4\ \mu_B$. This value corresponds to the moment observed in the AF phase of the pure URu_2Si_2 under pressure [27], although doping with Np might be considered as applying a "negative pressure" since it increases the lattice parameters. However, the substitution of U by Np introduces a strong molecular field at the U sites as a result of the large moment of 1.5 μ_B carried by Np. This molecular field acts on the U moment of 0.02 μ_B to increase it by one order of magnitude. Figure 1a shows the ^{237}Np Mössbauer spectra obtained for $x = 0.05$. Due to the very low amount of Np in this alloy, the spectrum required a full month recording and still displayed poor statistics, but the clear hyperfine magnetic splitting shows that the magnetic moment carried by Np is still $\approx$1.5 μ_B at such a low Np concentration.

2.3 $AnPd_2Al_3$

The largest ordered magnetic moment ($m_U = 0.85\ \mu_B$) in U HF-SC was observed in UPd_2Al_3 ($T_N = 14$ K; $T_c = 2$ K, $\gamma \approx 140$ mJ mole^{-1} K^{-2}) [28]. ^{238}U Mössbauer was

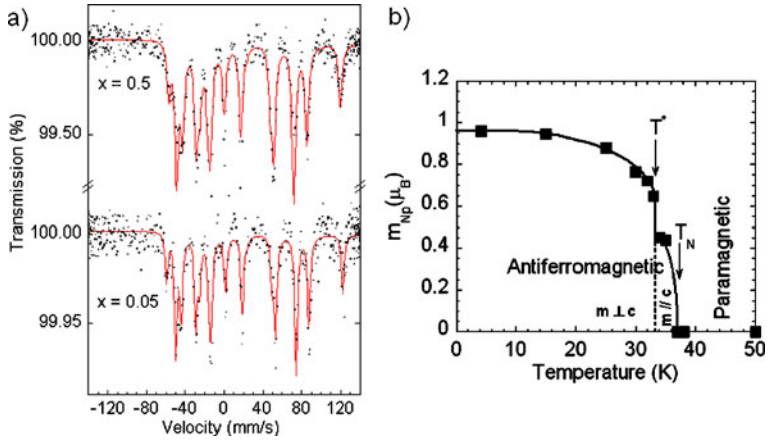

Fig. 1 **a** ^{237}Np Mössbauer spectra recorded at $T = 4.2$ K of $(U_{1-x}Np_x)Ru_2Si_2$ for $x = 0.05$ and $x = 0.5$. Notice the weak effect (∼0.1%) for $x = 0.05$, one order of magnitude smaller than for $x = 0.5$ (∼1%), scaling with Np concentration. Both patterns are similar and display similar hyperfine parameters. The fit assumes a single magnetic site (single value of B_{hf}). **b** Temperature dependence of the magnetic moment in $NpRhGa_5$ inferred from ^{237}Np MoS. The lines are guides for the eyes. The two magnetic transitions and the corresponding direction of the magnetic moments are indicated

also performed in this compound, but the magnetic transition is barely detectable (the line width increases from 50 mm/s to 60 mm/s at T_N) [22]. The hexagonal isostructural $NpPd_2Al_3$ parent compound is not SC down to 1.2 K [29]. ^{237}Np Mössbauer show that $NpPd_2Al_3$ orders at 38 K into a modulated magnetic structure with a maximum moment $m_{Np} = 1.67\ \mu_B$ [30]. Measurements on $(U_{1-x}Np_x)Pd_2Al_3$ solid solutions reveal that δ_{IS} and e^2qQ are insensitive to x, but m_{Np} and T_N are much affected by chemical substitution: as x increases T_N first decreases from 14 K down to 4.5 K, and finally increases dramatically up to 38 K [25]. Electrical resistivity measurements [31] indicate the collapse of superconductivity when Np is substituted to U: for $x = 0.005$, the critital temperature is significantly reduced ($T_c = 1.5$ K) and for $x = 0.01$ it is no more observed (down to 1.2 K).

2.4 AnRhGe

In the wake of UGe_2 [7] and $ZrZn_2$ [32], URhGe displays the intriguing coexistence of ferromagnetism (($T_C = 9.5$ K), and superconductivity ($T_c = 0.25$ K)—for the first time at ambient pressure in a f-electrons system [8]. URhGe crystallizes into an orthorhombic structure and has strongly correlated $5f$ electrons ($\gamma \approx 160$ mJ mole^{-1} K^{-2}).

On the contrary, no SC was observed down to $T = 1.8$ K in NpRhGe, but it orders AF at $T_N \approx 21.5$ K [33]. In the paramagnetic state, ^{237}Np Mössbauer spectra consist of a broad line, revealing a weak quadrupolar interaction. At 4.2 K, the spectrum can be analysed in terms of a unique set of hyperfine parameters, but the line broadening as well as the enhanced intensity of internal lines and reduced intensity of external lines are typical of relaxation effects. The value of the B_{hf} corresponds to an ordered

magnetic moment $m_{Np} = 1.14\ \mu_B$ and its Brillouin-like ($J = 1/2$) thermal variation suggests that the ground state of the Np ion is a magnetic doublet [34].

3 Neptunium analogues of Plutonium superconductors

3.1 $AnCoGa_5$

The first Pu-based superconductor, $PuCoGa_5$, with a critical temperature $T_c \approx 18.5$ K and a critical field $B_c \sim 74$ T, is unique among 5 *f* systems and has been proposed as a bridge between two classes of spin-fluctuation-mediated SC: the known HF-SC and the high-T_c copper oxides [10].

Its Np counterpart $NpCoGa_5$ was found to order AF at $T_N = 46.5$ K [35]. The value of the magnetic moment inferred from the Mössbauer B_{hf}, amounts to $m_{Np} = 0.84\ \mu_B$ at 4.2 K. Its variation with temperature follows a $J = 1/2$ Brillouin behavior, indicating that the ground state is a doublet, in agreement with the magnetic entropy released at T_N ($\sim$R ln2). The fact that e^2qQ measured in the ordered and paramagnetic states are about the same suggests that the Np moments are aligned along the c-axis which is the main component of the electric field gradient in the paramagnetic state (tetragonal symmetry). The value and direction of the ordered moment were later confirmed by neutron diffraction and the wave vector $\mathbf{q} = (0,0,1/2)$ determined [36].

3.2 $AnRhGa_5$

$PuRhGa_5$ is a SC with smaller critical parameters ($T_c \approx 8.7$ K and $B_c \sim 21$ T) than its Co analogue [11].

In analogy, $NpRhGa_5$ is an AF with lower T_N (37 K) [37] than $NpCoGa_5$. However, the magnetic phase diagram of $NpRhGa_5$ is more complex: it undergoes a second magnetic transition at $T^* = 32$ K, attributed to a reorientation of the magnetic moments from the c-axis to the basal plane, as evidenced by ^{237}Np MoS (Fig. 1b).

4 Neptunium superconductor

4.1 $NpPd_5Al_2$

Recently, SC involving 5 *f* electrons was observed for the first time in a Np compound, the paramagnetic HF $NpPd_5Al_2$ ($T_c = 4.9$ K and $\gamma = 200$ mJ mole^{-1} K^{-2}) with tetragonal symmetry [12]. This system thus represents a unique opportunity for the ^{237}Np Mössbauer resonance. No magnetic hyperfine splitting is observed indicating that the Np ions do not carry any magnetic ordered moments [38]. δ_{IS} (-11.1 mm/s vs $NpAl_2$) is close to the value expected for ionic Np^{4+}, but attributed rather to Np^{3+} (configuration $5f^4$), considering the influence of conduction electrons. The spectra recorded in the superconducting state are very similar to those taken in the normal state. However, a small increase in both δ_{IS} and e^2qQ is observed below T_c, indicating

Table 1 ^{237}Np hyperfine parameters inferred from MoS

Compound	δ_{IS} (mm/s)	e^2qQ (mm/s)	B_{hf} (T)	T_N/T_c (K)	Reference
$NpBe_{13}$	3.1	0	241/208	5 (AF)	[18]
$NpRu_2Si_2$	0.5	64	321/258/69	27.5 (AF)	[23]
$NpPd_2Al_3$	10.0	47	360/316/121	38 (AF)	[30]
NpRhGe	−2, 5	9	245	21 (AF)	[34]
$NpCoGa_5$	6.8	3.5	180	47 (AF)	[35]
$NpRhGa_5$	9.4	13.4	206	37 (AF)	[37]
$NpPd_5Al_2$	−11.1	22.0	0	5 (SC)	[38]

B_{hf} is given at 4.2 K, δ_{IS} and e^2qQ are given in the paramagnetic state
δ_{IS} is given versus the standard absorber $NpAl_2$

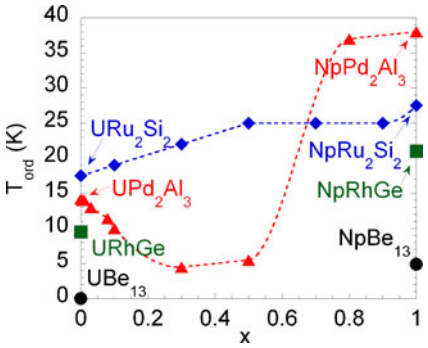

Fig. 2 Ordering temperature of U HF superconductors and their Np homologues. Data are also shown for $(U_{1-x}Np_x)Ru_2Si_2$ and $(U_{1-x}Np_x)Pd_2Al_3$ intermediate systems, as a function of the Np concentration x

that both the electronic density at the Np nuclei and the electric field gradient due to the 5*f* electrons are affected by the formation of Cooper pairs.

5 Summary

The hyperfine parameters inferred from ^{237}Np MoS in all reviewed compounds are summarized in Table 1. From the δ_{IS} values, it can be seen that all systems display the electronic configuration $5f^4$ corresponding to $J = 4$. The expected ordered moment for the free Np^{3+}ion would be 2.75 μ_B (intermediate coupling), i.e. $B_{hf} = 591$ T. Kondo effect and crystal field effects have been invoked to explain the reduced values of the magnetic moments in these compounds (see e.g. [35] and [38]).

It is clear from Fig. 2 that the Np systems show much larger ordering temperatures than their U counterparts. This is in agreement with the general trend observed in actinide intermetallics, attributed to the shorter spatial extension of 5*f* orbitals in Np compared to U and, consequently, the weaker hybridization/delocalization of 5*f* electrons in Np.

The x-dependence of the ordering temperature in $(U_{1-x}Np_x)Pd_2Al_3$ is unusual, with a minimum for $x = 0.3$ (see Fig. 2). Interestingly, UPd_2Al_3 and $NpPd_2Al_3$ have different easy axis ($\mathbf{m}_U \perp \mathbf{c}$ and $\mathbf{m}_{Np} \parallel \mathbf{c}$) and, from $x = 0.3$ to $x = 0$, the magnetic moment carried by Np is continuously rotating from the **c**-axis to the basal plane

[26]. Magnetic frustration may then explain the T_{ord} minimum observed at $x = 0.3$. The T_{ord} variation of $(U_{1-x}Np_x)Ru_2Si_2$ appears smooth and almost linear, although it should be noticed that for $x = 0$, the AF order vanishes and is replaced by the so-called "hidden order".

References

1. Aschermann, G., Justi, E.: Phys. Z. **43**, 207 (1942)
2. Chandrasekhar, B.S., Hulm, J.K.: J. Phys. Chem. Solids **7**, 259 (1958)
3. Ott, H.R., Rudiger, H., Fisk, Z., Smith, J.L.: Phys. Rev. Lett. **50**, 1595 (1983)
4. Stewart, G.R., Fisk, Z., Willis, J.O., Smith, J.L.: Phys. Rev. Lett. **52**, 679 (1984)
5. Schlabitz, W., Baumann, J., Pollit, B., Rauchschwalbe, U., Mayer, H.M., Ahleim, U., Bredl, C.D.: Z. Phys. B **62**, 177 (1986)
6. Geibel, C., Schank, C., Thies, S., Kitazawa, H., Bredl, C.D., Böhm, A., Rau, M., Grauel, A., Caspary, R., Helfrich, R., Ahleim, U., Weber, G., Steglich, F.: Z. Phys. B **84**, 1 (1991)
7. Saxena, S.S., Agarwal, P., Ahilan, K., Grosche, F.M., Haselwimmer, R.K.W., Steiner, M.J., Pugh, E., Walker, I.R., Julian, S.R., Monthoux, P., Lonzarich, G.G., Huxley, A., Sheikin, I., Braithwaite, D., Flouquet, J.: Nature **406**, 587 (2000)
8. Aoki, D., Huxley, A., Ressouche, E., Braithwaite, D., Flouquet, J., Brison, J.-P., Lhotel, E., Paulsen, C.: Nature **413**, 613 (2001)
9. Damien, D., de Novion, C.H., Gal, J.: Solid State Commun. **38**, 437 (1981)
10. Sarrao, J.L., Morales, L.A., Thompson, J.D., Scott, B.L., Stewart, G.R., Wastin, F., Rebizant, J., Boulet, P., Colineau, E., Lander, G.H.: Nature **420**, 297 (2002)
11. Wastin, F., Boulet, P., Rebizant, J., Colineau, E., Lander, G.H.: J. Phys.: Condens. Matter **15**, S2279 (2003)
12. Aoki, D., Haga, Y., Matsuda, T.D., Tateiwa, N., Ikeda, S., Homma, Y., Sakai, H., Shiokawa, Y., Yamamoto, E., Nakamura, A., Settai, R., Onuki, Y.: J. Phys. Soc. Jpn. **76**, 063701 (2007)
13. Kalvius, G.M.: J. Nucl. Mater. **166**, 5 (1989)
14. Sanchez, J.P., Colineau, E., Vulliet, P., Tomala, K.: J. Alloys Compd. **275**, 154 (1998)
15. Stewart, G.R., Fisk, Z., Smith, J.L., Willis, J.O., Wire, M.S.: Phys. Rev. B **30**, 1249 (1984)
16. Gal, J., Litterst, F.J., Potzel, W., Moser, J., Potzel, U., Kalvius, G.M., Fredo, S., Tapuchi, S.: Phys. Rev. B **36**, 2457 (1987)
17. Dunlap, B.D., Lander, G.H.: Phys. Rev. Lett. **33**, 1046 (1974)
18. Hiess, A., Bonnet, M., Burlet, P., Ressouche, E., Sanchez, J.P., Waerenborgh, J.C., Zwirner, S., Wastin, F., Rebizant, J., Lander, G.H, Smith, J.L.: Phys. Rev. Lett. **77**, 3917 (1996)
19. Coad, S., Hiess, A., McMorrow, D.F., Lander, G.H., Aeppli, G., Fisk, Z., Stewart, G.R., Hayden, S.M., Mook, H.A.: Physica B: Condensed Matter **764**, 276–278 (2000)
20. Hassinger, E., Knebel, G., Izawa, K., Lejay, P., Salce, B., Flouquet, J.: Phys. Rev. B **77**, 115117 (2008)
21. Aoki, D., Bourdarot, F., Hassinger, E., Knebel, G., Miyake, A., Raymond, S., Taufour, V., Flouquet, J.: J. Phys.: Condens. Matter **22**, 164205 (2010)
22. Tsutsui, S., Nakada, M., Nasu, S., Haga, Y., Honma, T., Yamamoto, E., Ohkuni, H., Onuki, Y.: Hyperfine Interact. **126**, 335 (2000)
23. Bogé, M., Bonnisseau, D., Burlet, P., Fournier, J.M., Pleska, E., Quézel, S., Rebizant, J., Rossat-Mignod, J., Spirlet, J.C., Wulff, M.: J. Nucl. Mater. **166**, 77 (1989)
24. Wastin, F., Bednarczyk, E., Rebizant, J., Zwirner, S., Lander, G.H.: J. Alloys Compd. **262–263**, 124 (1997)
25. Zwirner, S., Waerenborgh, J.C., Wastin, F., Rebizant, J., Spirlet, J.C., Potzel, W., Kalvius, G.M.: Physica B **80**, 230–232 (1997)
26. Lidström, E., Mannix, D., Hiess, A., Rebizant, J., Wastin, F., Lander, G.H., Marri, I., Carra, P., Vettier, C., Longfield, M.J.: Phys. Rev. B **61**, 1375 (2000)
27. Amitsuka, H., Sato, M., Metoki, N., Yokoyama, M., Kuwahara, K., Sakakibara, T., Morimoto, H., Kawarazaki, S., Miyako, Y., Mydosh, J.A.: Phys. Rev. Lett. **83**, 5114 (1999)
28. Dalichaouch, Y., de Andrade, M.C., Maple, M.B.: Phys. Rev. B **46**, 8671 (1992)
29. Seret, A., Wastin, F., Waerenborgh, J.C., Zwirner, S., Spirlet, J.C., Rebizant, J.: Physica B **206**& **207**, 525 (1995)

30. Zwirner, S., Spirlet, J.C., Rebizant, J., Potzel, W., Kalvius, G.M., Geibel, C., Steglich, F.: Physica B **681**, 186–188 (1993)
31. Wastin, F., Bednarczyk, E., Rebizant, J.: J. Alloys Compd. **437**, 271–273 (1998)
32. Pfleiderer, C., Uhlarz, M., Hayden, S.M., Vollmer, R., von Löhneysen, H., Bernhoeft, N.R., Lonzarichk, G.G.: Nature **412**, 58 (2001)
33. Boulet, P., Colineau, E., Wastin, F., Rebizant, J.: J. Magn. Magn. Mater. **272–276**, e327 (2004)
34. Colineau, E., Sanchez, J.-P., Wastin, F., Javorský, P., Riffaud, E., Homma, Y., Boulet, P., Rebizant, J.: J. Phys.: Condens. Matter **20**, 255234 (2008)
35. Colineau, E., Javorský, P., Boulet, P., Wastin, F., Griveau, J.-C., Rebizant, J., Sanchez, J.-P., Stewart, G.R.: Phys. Rev. B **69**, 184411 (2004)
36. Metoki, N., Kaneko, K., Colineau, E., Javorský, P., Aoki, D., Homma, Y., Boulet, P., Wastin, F., Shiokawa, Y., Bernhoeft, N., Yamamoto, E., Ônuki, Y., Rebizant, J., Lander, G.H.: Phys. Rev. B **72**, 014460 (2005)
37. Colineau, E., Wastin, F., Boulet, P., Javorský, P., Rebizant, J., Sanchez, J.-P.: J. Alloys Compd. **386**, 57–62 (2005)
38. Gofryk, K., Griveau, J.-C., Colineau, E., Sanchez, J.-P., Rebizant, J., Caciuffo, R.: Phys. Rev. B **79**, 134525 (2009)

Hyperfine Interact (2012) 207:121–125
DOI 10.1007/s10751-011-0416-3

^{155}Gd Mössbauer investigation of the magnetic order and spin-reorientation in $Gd_3Ag_4Sn_4$

C. J. Voyer · D. H. Ryan · J. M. Cadogan

Published online: 27 October 2011

Abstract In a recent study of the magnetic order in $Gd_3Ag_4Sn_4$ by neutron powder diffraction and ^{119}Sn Mössbauer Spectroscopy we showed that both the Gd(2d) and Gd(4e) sublattices order antiferromagnetically at 28.8(2) K. We also demonstrated that the 'magnetic event' around 8 K is in fact a 'plane to axis' spin-reorientation of the Gd magnetic structure. Here, we extend our study with ^{155}Gd Mössbauer Spectroscopy. The initial magnetic ordering at 30(2) K is clear for both sites and substantial changes in the hyperfine fields are observed at 8 K when the magnetic structure reorients.

Keywords Magnetic order · Spin-reorientation · Mössbauer Spectroscopy

1 Introduction

The $R_3T_4X_4$ family (R = rare earth, T = Cu, Ag, Au, Mn, Pd, and X = Si, Ge, Sn) crystallize in the orthorhombic $Gd_3Cu_4Ge_4$-type structure (space group *Immm*, #71) [1] in which the R atoms occupy two crystallographic sites (4e and 2d), the transition metal (T) occupies the 8n site and X occupies the 4f and 4h sites. In general, the R moments order antiferromagnetically, often with quite different moment values, and with distinct magnetic structures adopted by the two R sublattices. We refer the reader to our recent review of the magnetism of the $R_3T_4X_4$ compounds [2] for further details.

C. J. Voyer · D. H. Ryan
Department of Physics, McGill University, Montreal, QC H3A2T8, Canada

J. M. Cadogan (✉)
Department of Physics and Astronomy, University of Manitoba,
Winnipeg, MB R3T2N2, Canada
e-mail: cadogan@physics.umanitoba.ca

The magnetism of $Gd_3Ag_4Sn_4$ was first studied by Mazzone et al. [3] who observed magnetic 'events' at 22 K and 8 K in ac-susceptibility measurements. The 22 K 'event' was quite broad and could be suppressed by an applied field of 1 T. Magnetization data obtained at 5 K suggested a purely antiferromagnetic ordering of the Gd sublattices at a Néel temperature of 8 K.

In a previous paper [4] we used ^{119}Sn Mössbauer spectroscopy to show that the magnetic ordering temperature of $Gd_3Ag_4Sn_4$ is in fact 28.8(2) K. The sudden changes in the temperature dependences of the transferred hyperfine fields at the two Sn sites, evident in the ^{119}Sn spectra were interpreted in terms of the 8 K 'event' observed by Mazzone et al. [3] being a spin-reorientation of the Gd magnetic order, rather than a magnetic ordering of one of the Gd sublattices.

We subsequently determined the magnetic structures of the two Gd sublattices in $Gd_3Ag_4Sn_4$ by neutron powder diffraction [5]. We confirmed that the onset of long-range magnetic ordering is in accord with our ^{119}Sn Mössbauer results. At 2.8 K the Gd(4e) sublattice is antiferromagnetically ordered along the crystal *c*-axis, commensurate with the crystal lattice. The Gd(2d) sublattice is also ordered along the *c*-axis but its magnetic structure is incommensurate. Finally, our neutron diffraction work showed that the magnetic order of the Gd(4e) sublattice does indeed undergo a 90° reorientation from planar to axial on cooling. It is conceivable that magnetic exchange is sufficient to keep the two Gd sublattices collinear. Thus, the Gd(2d) would also undergo a 90° reorientation from planar to axial. This would be fully consistent with our ^{119}Sn Mössbauer work but we were unable to provide definitive proof of this suggestion on the basis of neutron diffraction.

Here, we present the results of our ^{155}Gd Mössbauer study of the local magnetism of the two Gd sites in $Gd_3Ag_4Sn_4$. Our ^{155}Gd results confirm the nature of the spin-reorientation of the magnetic order described above.

2 Experimental methods

The $Gd_3Ag_4Sn_4$ sample used in this study was the same sample used in our previous neutron diffraction [5] and ^{119}Sn Mössbauer [4] work and a detailed description of the sample preparation and characterisation can be found in our previous paper [5]. About 450 mg of powder and a 50 mCi $^{155}SmPd_3$ source were mounted vertically in a conventional cold-source spectrometer operated in sine-mode. The 86.55 keV ^{155}Gd Mössbauer $\gamma-$photons were isolated from the various x-rays emitted by the source using a high-purity Ge detector. The spectrometer's drive system was calibrated using a laser interferometer and velocities were cross-checked against ^{57}Co**Rh**/$\alpha-$Fe at room temperature. The ^{155}Gd Mössbauer spectra were fitted using a non-linear least-squares minimisation routine with line positions and intensities derived from an exact solution to the full Hamiltonian [6].

3 Results and discussion

Figure 1 shows the ^{155}Gd Mössbauer spectra of $Gd_3Ag_4Sn_4$ obtained between 30 K (above T_N) and 1.9 K. At 30 K the spectrum showed no signs of a magnetic hyperfine field at either site, as expected from our ^{119}Sn Mössbauer work [4], and

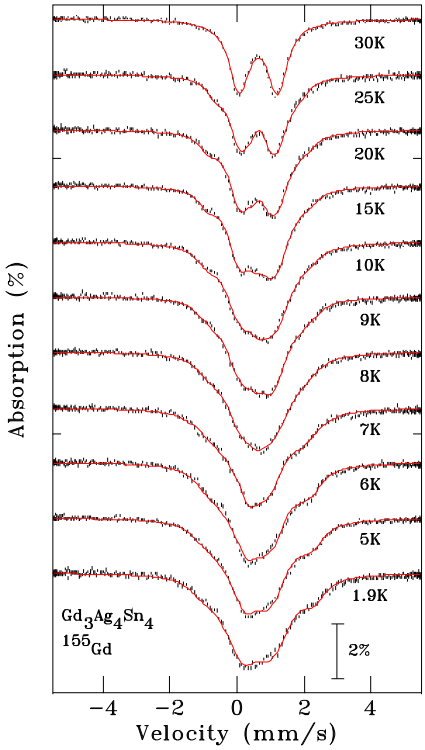

Fig. 1 ^{155}Gd Mössbauer spectra of $Gd_3Ag_4Sn_4$ showing the evolution of magnetic splitting upon cooling. The *solid lines* are fits to a full Hamiltonian solution as described in the text

we obtained values of 2.22(3) mm/s and 2.85(6) mm/s for the magnitude of the quadrupole splitting parameter eQ_gV_{zz} at the Gd(2d) and Gd(4e) sites, respectively. These values were then fixed for the magnetic spectra. The point symmetries of the Gd(2d) and Gd(4e) sites are *mmm* and *2 mm*, respectively, which require only that the principal axes of the electric field gradient (EFG) tensors at the two Gd sites lie along crystallographic axes, but do not permit an assignment of those axes. Furthermore, the strong line overlap at 1.9 K apparent in Fig. 1 made an independent determination of the asymmetry parameters (η) unreliable, we were therefore guided by the ^{170}Yb study of isostructural $Yb_3Cu_4Ge_4$ by Dhar et al. [7], who showed that the EFG at the Yb(2d) site "has a strong non-axial character" whereas that at the Yb(4e) site "has an axial character". Following a search over possible choices of η and the angle ϑ between eQ_gV_{zz} and B_{hf}, we found that $\eta(2d) = 1$ and $\eta(4e) = 0$ provided a self-consistent description of the magnetic spectra over the temperature range covered here (Fig. 1).

A clear magnetic splitting develops on cooling through T_N, and a fit to the temperature dependence of the hyperfine fields at the two Gd sites (B_{hf}^{2d} and B_{hf}^{4e}) yields an average Néel temperature of $T_N = 30(2)$ K (Fig. 2). We also show the angle between the hyperfine field and the principal axis of the EFG. Both Gd sites order together at T_N and the effects of the spin-reorientation at ~8 K are clear. Above 8 K, the Gd(2d) site orders with its hyperfine field perpendicular to its local EFG z-axis whereas the Gd(4e) site orders at 20° from its local EFG z-axis. Below the

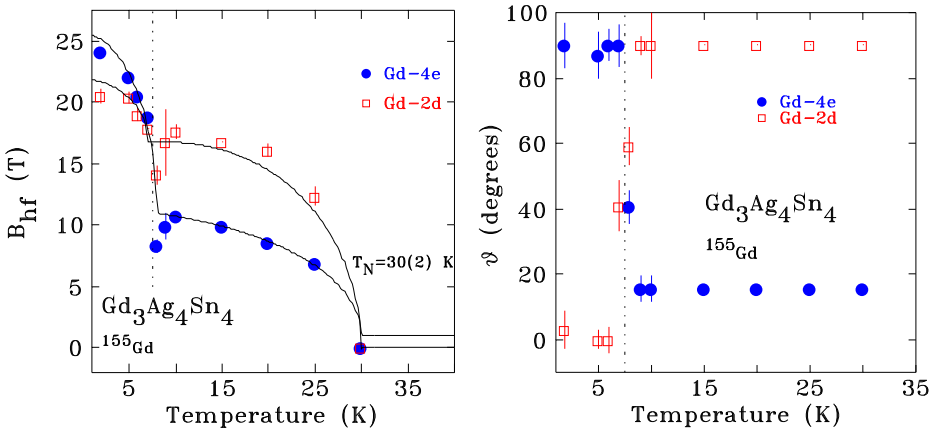

Fig. 2 Temperature dependences of the ^{155}Gd hyperfine magnetic fields (*left*) and the angle ϑ between the hyperfine field and the local EFG z-axis (*right*) at the two Gd sites

spin-reorientation transition, B_{hf}^{2d} is parallel to the local local EFG z-axis and B_{hf}^{4e} is perpendicular to it.

4 Conclusions

We have used ^{155}Gd Mössbauer spectroscopy to investigate the magnetic spin-reorientation in $Gd_3Ag_4Sn_4$. Our results confirm those in our previous neutron diffraction study. The magnetic ordering temperature derived from ^{155}Gd Mössbauer is 30(2) K, consistent with our earlier value of 28.8(2) K derived from ^{119}Sn Mössbauer data [4]. Our neutron diffraction data suggested that the magnetic 'event' previously observed at ~8 K is, in fact, a 'plane to axis' spin-reorientation of the Gd magnetic structure upon cooling. This conclusion is consistent with our previous ^{119}Sn Mössbauer spectroscopy work and is further confirmed here by ^{155}Gd Mössbauer spectroscopy.

Acknowledgements J. M. Cadogan acknowledges support from the Canada Research Chairs programme. Financial support for various stages of this work was provided by the Natural Sciences and Engineering Research Council of Canada and Fonds Québécois de la Recherche sur la Nature et les Technologies. We gratefully acknowledge the assistance of Raghu Rao and Robert Speranzini in arranging for the activation of the ^{155}Gd Mössbauer source in the National Research Universal (NRU) research reactor, which is operated by Atomic Energy of Canada, Ltd., at Chalk River, Ontario.

References

1. Rieger, W.: Die kristallstruktur von $Gd_6Cu_8Ge_8$ und isotypen phasen. Monatsch. Chem. **101**, 449–462 (1970)
2. Ryan, D.H., Cadogan, J.M., Voyer, C.J., Napoletano, M., Riani, P., Cranswick, L.M.D.: Using neutron diffraction and Mössbauer spectroscopy to study magnetic ordering in the $R_3T_4Sn_4$ family of compounds. Mod. Phys. Lett. B **24**, 1–28 (2010)

3. Mazzone, D., Riani, P., Napoletano, M., Canepa, F.: The magnetism of $Sm_3Ag_4Sn_4$ and $Gd_3Ag_4Sn_4$. J. Alloys Compd. **387**, 15–19 (2005)
4. Voyer, C.J., Ryan, D.H., Napoletano, M., Riani, P.: Magnetic ordering in $Gd_3Cu_4Sn_4$ and $Gd_3Ag_4Sn_4$ studied using ^{119}Sn Mössbauer spectroscopy. J. Phys. Condens. Matter **19**(156209), 10 (2007)
5. Cadogan, J.M., Ryan, D.H., Napoletano, M., Riani, P., Cranswick, L.M.D.: Neutron powder diffraction determination of the magnetic structure of $Gd_3Ag_4Sn_4$. J. Phys. Condens. Matter **21**(124201), 8 (2009)
6. Voyer, C.J., Ryan, D.H.: A complete solution to the Mössbauer problem, all in one place. Hyperfine Interact. **170**, 91–104 (2006)
7. Dhar, S.K., Singh, S., Bonville, P., Mazumdar, C., Manfrinetti, P., Palenzona, A.: Magnetic behaviour of $Yb_3Cu_4Ge_4$ and $Gd_3Cu_4Ge_4$. Physica B **312–313**, 846–847 (2002)

Hyperfine Interact (2012) 207:127–131
DOI 10.1007/s10751-011-0475-5

Study of the structure and electronic state of thiolate-protected gold clusters by means of ^{197}Au Mössbauer spectroscopy

Norimichi Kojima · Kazuhiro Ikeda · Yasuhiro Kobayashi · Tatsuya Tsukuda · Yuichi Negishi · Genta Harada · Tadashi Sugawara · Makoto Seto

Published online: 7 December 2011

Abstract We have investigated the structures and electronic states of a series of glutathionate-protected Au clusters, $Au_n(SG)_m$ with $n = 10 - \sim 55$, using ^{197}Au Mössbauer spectroscopy, which allows us to probe the local environment of the constituent Au atoms via isomer shift (*IS*) and quadrupole splitting (*QS*). The spectral profile abruptly changes on going from $Au_{22}(SG)_{17}$ to $Au_{25}(SG)_{18}$, then it smoothly changes to that of $Au_{\sim 55}(SG)_m$. However, the spectral profile dramatically changes on going from $Au_{\sim 55}(SG)_m$ to the dodecanethiolate-protected Au cluster with average diameter of 2 nm. The ^{197}Au Mössbauer spectra of glutathionate-protected Au clusters and dodecanethiolate-protected Au clusters were successfully analyzed on the basis of the structure and electronic state of $Au_{25}(SG)_{18}$.

Keywords Gold cluster · ^{197}Au Mössbauer spectroscopy · Nanomaterial

1 Introduction

In the last decade, small Au clusters composed of less than 100 atoms protected by organic ligands have attracted much attention as a prototypical system for fundamental studies on quantum size effect and as a building block of nano-scale

N. Kojima (✉) · K. Ikeda · G. Harada · T. Sugawara
Graduate School of Arts and Sciences, The University of Tokyo, Tokyo, 153-8902, Japan
e-mail: cnori@mail.ecc.u-tokyo.ac.jp

Y. Kobayashi · M. Seto
Research Reactor Institute, Kyoto University, Osaka, 590-0949, Japan

T. Tsukuda
Catalysis Research Center, Hokkaido University, Hokkaido, 001-0021, Japan

Y. Negishi
Department of Applied Chemistry, Faculty of Science, Tokyo University of Science, Tokyo, 162-8601, Japan

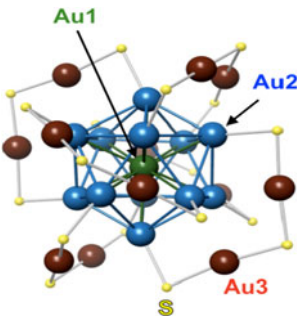

Fig. 1 Core structure of $Au_{25}(SR)_{18}$ [6, 7]. Large and small balls represent Au and S atoms, respectively. R group is omitted for simplicity

devices [1]. In connection with organic ligands, thiolates (RS) have extensively been used [2]. Among small Au clusters, the Au-thiolate compound composed of 25 Au atoms and 18 thiolates ($Au_{25}(SR)_{18}$) has been studied most extensively as a prototype system of stable $Au_n(SR)_m$ clusters [3]. In 2007, we proposed the structure of $Au_{25}(SG)_{18}$ by ^{197}Au Mössbauer spectroscopy [4], based on the "core-in-cage" model theoretically predicted by Iwasa and Nobusada; the Au_7 core is caged by two –[Au–S(R)–]$_3$ and one –[Au–S(R)–]$_{12}$ cyclic oligomers [5]. Since then, the geometrical structure of $Au_{25}(SC_2H_4Ph)_{18}$ was determined by single crystal X ray diffraction [6] and by theoretical calculation [7]. According to the structural analysis, $Au_{25}(SR)_{18}$ is composed of an icosahedral Au_{13} core whose surface is protected by six staples, –S(R)–[Au–S(R)–]$_2$, as shown in Fig. 1. Based on the structure of $Au_{25}(SC_2H_4Ph)_{18}$, we re-analyzed the ^{197}Au Mössbauer spectrum of $Au_{25}(SG)_{18}^{-}$ [8]. In this paper, we have analyzed the ^{197}Au Mössbauer spectra of $Au_n(SG)_m$ ($n = 10 - \sim 55$) and dodecanethiolate-protected Au clusters with the average diameters of 2 nm and 4 nm (here after, described as Au clusters of 2 nm and 4 nm) on the basis of the structure and electronic state of $Au_{25}(SG)_{18}$.

2 Experimental

The $Au_n(SG)_m$ samples with (n, m) = (10, 10), (15, 13), (18, 14), (22, 16), (22, 17), (25, 18), (29, 20), (33, 22), (39, 24), (45, 28), and ($\sim$55, m) [9] were fractionated from nearly monodisperse Au:SG clusters ($d_{av} \sim 1$ nm) using polyacrylamide gel electrophoresis (PAGE) [3(a), 10]. In order to obtain the ^{197}Au Mössbauer spectra with sufficient S/N ratio, each cluster was accumulated up to 50–100 mg by repeating the elaborative PAGE procedure [4]. The dodecanethiolate-protected Au clusters of 2 nm and 4 nm were prepared by the direct chemisorption method and the ligand-exchange method, respectively [11]. The distribution of particle size and the diameter of dodecanethiolate-protected Au clusters were analyzed by small-angle X-ray scattering as well as transmission electron microscopy [11].

^{197}Au Mössbauer spectra were measured at the Research Reactor Institute of Kyoto University. The γ-ray source (77.3 keV), ^{197}Pt, was generated by neutron irradiation of a 98%-enriched ^{196}Pt metal foil. The γ-ray source and samples were cooled down to 16 K. The *IS* value of Au foil was referenced to 0 mm/s. The spectra were calibrated by using the six lines of a body-centered cubic iron foil (α-Fe). Mössbauer spectra were fitted with a MossWinn 3.0 program [12].

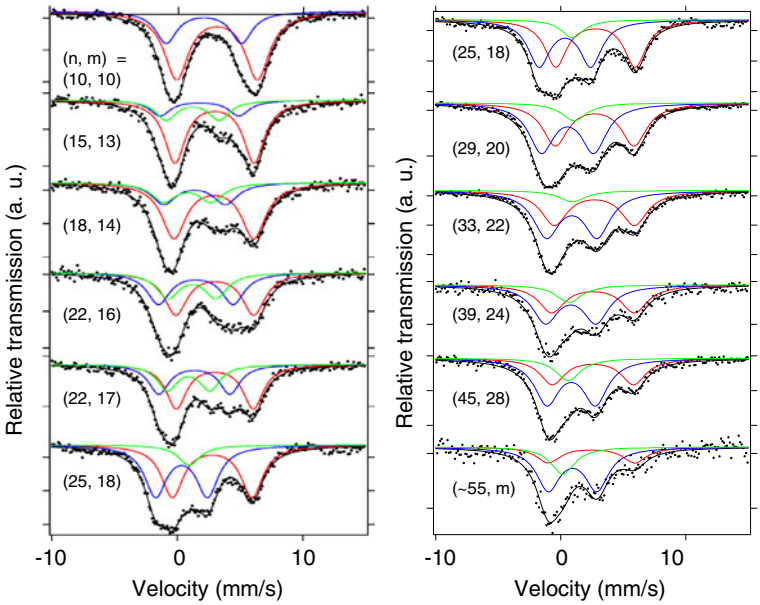

Fig. 2 ^{197}Au Mössbauer spectra of $Au_n(SG)_m$ ($n = 10 - \sim 55$)

3 Results and discussion

The ^{197}Au Mössbauer spectra of $Au_n(SG)_m$ with (n, m) = (10, 10), (15, 13), (18, 14), (22, 16), (22, 17), (25, 18), (29, 20), (33, 22), (39, 24), (45, 28), and (~55, m) are shown in Fig. 2. These spectra were analyzed based on the structure of $Au_{25}(SR)_{18}$ ($SR = SC_2H_4Ph$). As shown in Fig. 1, the Au atoms in $Au_{25}(SR)_{18}$ are classified into three sites from the viewpoint of chemical environment; a single central Au atom of the core (**Au1**, green ball in Fig. 1), twelve Au atoms at the core surface each of which are bound by a single thiolate (**Au2**, blue ball in Fig. 1), twelve Au atoms on the outermost layer which are bound by two thiolates (**Au3**, red ball in Fig. 1). These three sites should exhibit different isomer shift (*IS*) and quadrupole splitting (*QS*) values due to the difference in electronic structures of each site. On the basis of symmetry considerations, the **Au1** and **Au2**/**Au3** atoms presumably produce singlet ($QS = 0$) and doublet peaks, respectively. Therefore, the spectrum was fitted by the superposition of a singlet Lorentzian and two sets of doublet Lorentzians while assuming identical FWHM values for all the components. The ^{197}Au Mössbauer spectrum of $Au_{25}(SR)_{18}$ in Fig. 2 is the best fitting result taking account the structure. The doublet (**c3**) with the largest *IS* (2.78 mm/s) and *QS* (6.35 mm/s) is assigned to the twelve Au atoms (**Au3**) on the outermost layer coordinated by two thiolates. These Mössbauer parameters, *IS* and *QS*, are typical of Au(I) coordinated by two sulfur atoms [13]. The second doublet (**c2**) with $IS = 0.34$ mm/s and $QS = 4.14$ mm/s is assigned to the twelve Au atoms at the core surface, each of which bound by a single thiolate (**Au2**). The singlet (**c1**) with $IS = 0.94$ mm/s and $QS = 0.00$ mm/s is assigned to the central Au atom of the core (**Au1**). This assignment is consistent with the structure of $Au_{25}(SR)_{18}$.

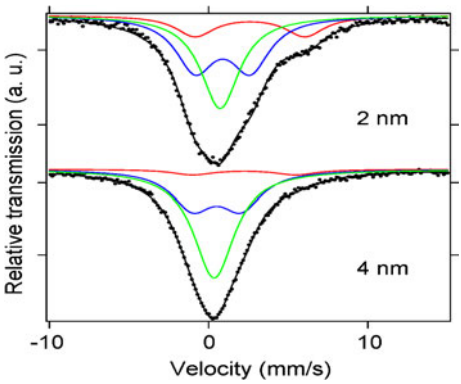

Fig. 3 ^{197}Au Mössbauer spectra for dodecanethiolate-protected Au clusters of 2 nm and 4 nm

As shown in Fig. 2, the ^{197}Au Mössbauer spectra of a series of $Au_n(SG)_m$ evolve drastically as a function of the core size. Asymmetric doublet profile of the $Au_{10}(SG)_{10}$ spectrum could be fitted by a superposition of two sets of doublets. The *IS* and *QS* values obtained are 3.06 and 6.68 mm/s, respectively, for the major component and 2.48 and 5.71 mm/s for the minor component. According to the correlation between the *IS* and *QS* values established for various kinds of Au(I) and Au(III) compounds, these Au atoms fall in a category of Au(I) atoms directly coordinated by two SG ligands [13]. The spectra of $Au_n(SG)_m$ ($15 \leq n \leq 22$) were fitted by three sets of doublets. Two components are assigned to Au(I) coordinated by two SG ligands since the *IS* and *QS* values are smoothly correlated to those of $Au_{10}(SG)_{10}$. The third component having the smallest *IS* and *QS* values is assigned to Au(I) coordinated by a single SG ligand which is smoothly correlated to those of the **Au2** atoms coordinated by a single SG ligand. The spectral profile abruptly changes on going from $Au_{22}(SG)_{16}$ to $Au_{25}(SG)_{18}$, in which a core Au atom (**Au1**) comes out.

On the other hand, on going from $Au_{25}(SG)_{18}$ to $Au{\sim}_{55}(SG)_m$, the spectral profile smoothly converges to that of $Au{\sim}_{55}(SG)_m$. In these Au clusters, the spectrum was fitted by the superposition of a singlet Lorentzian due to core Au atoms and two sets of doublet Lorentzians due to Au atoms coordinated by a single SG ligand and two SG ligands. With increasing *n*, the ratio of **Au2** atoms to **Au3** atoms increases. However, the spectral profile dramatically changes on going from $Au{\sim}_{55}(SG)_m$ (the average diameter is estimated at about 1.4 nm) to the dodecanethiolate-protected Au cluster of 2 nm.

Figure 3 shows the ^{197}Au Mössbauer spectra for the dodecanethiolate-protected Au clusters of 2 nm and 4 nm. These spectra are also fitted by the superposition of a singlet Lorentzian and two sets of doublet Lorentzians. These components correspond to those of $Au_{25}(SG)_{18}$, **c1**, **c2**, and **c3**. The Mössbauer parameters (*IS*, *QS*, area) of **c1**, **c2**, and **c3** for the Au cluster of 2 nm are estimated at (0.73 mm/s, 0.0 mm/s, 39.00%), (0.88 mm/s, 3.47 mm/s, 43.70%), (2.60 mm/s, 6.90 mm/s, 17.30%), respectively. In the case of the Au cluster of 4 nm, on the other hand, those of **c1**, **c2**, and **c3** are estimated at (0.35 mm/s, 0.0 mm/s, 56.80%), (0.51 mm/s, 3.07 mm/s, 37.70%), (2.23 mm/s, 6.51 mm/s, 5.60%), respectively. In the case of dodecanethiolate-protected Au cluster of 4 nm, the Au core atoms free from dodecanethiole are dominant.

4 Conclusion

We have investigated the structures and electronic states of a series of glutathionate-protected Au clusters, $Au_n(SG)_m$ with $n = 10 - Au\sim_{55}(SG)_m$ and dodecanethiolate-protected Au clusters of 2 nm and 4 nm using ^{197}Au Mössbauer spectroscopy, which allows us to probe local environment of the constituent Au atoms via isomer shift (*IS*) and quadrupole splitting (*QS*) and area. The spectral profile of ^{197}Au Mössbauer spectrum abruptly changes on going from $Au_{22}(SG)_{17}$ to $Au_{25}(SG)_{18}$, then it smoothly changes to that of $Au\sim_{55}(SG)_m$. However, the profile dramatically changes on going from $Au\sim_{55}(SG)_m$ to the dodecanethiolate-protected Au cluster of 2 nm. The ^{197}Au Mössbauer spectra of $Au_n(SG)_m$ and dodecanethiolate-protected Au clusters of 2 nm and 4 nm were successfully analyzed on the basis of the structure and electronic state of $Au_{25}(SG)_{18}$.

Acknowledgement We wish to thank Prof. K. Nobusada for valuable discussions on the theoretically predicted structure of $Au_{25}(SG)_{18}$.

References

1. Clusters and Colloids; Schmid, G. (ed.) VCH: Weinhiem, Germany (1994). (b) Daniel, M.-C., Astruc, D.: Chem. Rev. **104**, 293 (2004)
2. Schaff, T.G., Whetten, R.L.: J. Phys. Chem. **B104**, 2630 (2009). (b) Price, R.C., Whetten, R.L.: J. Am. Chem. Soc. **127**, 13750 (2005). (c) Tsunoyama, H., Negishi, Y., Tsukuda, T.: J. Am. Chem. Soc. **128**, 6036 (2006)
3. Negishi, Y., Nobusada, K., Tsukuda, T.: J. Am. Chem. Soc. **127**, 5261 (2005). (b) Shichibu, Y., Negishi, Y., Tsunoyama, H., Kanehara, M., Teranishi, T., Tsukuda, T.: Small **3**, 835 (2007). (c) Jin, R., Qian, H., Wu, Z., Zhu, Y., Zhu, M., Mohanty, A., Garg, N.: J. Phys. Chem. Lett. **1**, 2903 (2010). (d) Parker, J.F., Fields-Zinna, C.A., Murray, R.W.: Acc. Chem. Res. **43**, 1289 (2010)
4. Ikeda, K., Kobayashi, Y., Negishi, Y., Seto, M., Iwasa, T., Nobusada, K., Tsukuda, T., Kojima, N.: J. Am. Chem. Soc. **129**, 7230 (2007)
5. Iwasa, T., Nobusada, K.: J. Phys. Chem. C **111**, 45 (2007)
6. Heaven, M.W., Dass, A., White, P.S., Holt, K.M., Murray, R.W.: J. Am. Chem. Soc. **130**, 3754 (2008). (b) Zhu, M., Lanni, E., Garg, N., Bier, M.E., Jin, R.: J. Am. Chem. Soc. **130**, 1138 (2008)
7. Akola, J., Walter, M., Whetten, R.L., Häkkinen, H., Grönbeck, H.: J. Am. Chem. Soc. **130**, 3756 (2008)
8. Tsukuda, T., Negishi, Y., Kobayashi, Y., Kojima, N.: Chem. Lett. **40**, 1292 (2011)
9. The $Au_{55}(SG)_m$ has not completely been isolated. Therefore, $Au_n(SG)_m$ with the distribution of Au atoms around $n = 55$ represents $Au\sim_{55}(SG)_m$
10. Kimura, K., Sugimoto, N., Sato, S., Yao, H., Negishi, Y., Tsukuda, T. J. Phys. Chem. C **113**, 14076 (2009)
11. Nagao, O., Harada, G., Sugawara, T., Sasaki, A., Ito, Y.: Jpn. J. Appl. Phys. **43**, 7742 (2004)
12. MossWin 3.0 Dr. Zoltan Klencsar, http://www.netx.hu/mosswinn/index.html
13. Mössbauer Handbooks: ^{197}Au Mössbauer spectroscopy, Mössbauer Effect Data Center, The University of North Carolina, U.S.A. (1993)

Hyperfine Interact (2012) 207:133–137
DOI 10.1007/s10751-011-0485-3

The hyperfine properties of a hydrogenated Fe/V superlattice

M. Elzain · M. Al-Barwani · A. Gismelseed · A. Al-Rawas · A. Yousif · H. Widatallah · K. Bouziane · I. Al-Omari

Published online: 8 December 2011

Abstract We study the effect of hydrogen on the electronic, magnetic and hyperfine structures of an iron-vanadium superlattice consisting of three Fe monolayers and nine V monolayers. The contact charge density (ρ), the contact hyperfine field (B_{hf}) and the electronic field gradient (EFG) at the Fe sites for different H locations and H fillings are calculated using the first principle full-potential linear-augmented-plane-wave (FP-LAPW) method. It is found that sizeable changes in the hyperfine properties are obtained only when H is in the interface region.

Keywords Hyperfine properties · Hydrogenated iron-vanadium · Superlattice

1 Introduction

Iron-vanadium superlattices constitute a benchmark for the various studies carried out on magnetic nanostructures. Due to the slight mismatch between the Fe and V lattice constants, the superlattices have tetragonal structures. The *c*/*a* ratio was found to depend on the thicknesses of Fe and V layers [1]. The quality of the Fe-V interface of dc sputtered samples was studied by Andersson et al. [2] using conversion electron Mössbauer spectroscopy (CEMS) and x-ray diffraction. Sharp interfaces were found for growth temperatures of 330°C or less. Large V induced magnetic moments for the trilayer V/Fe/V were obtained by Clavero et al. using a diverse assortment of experimental techniques [3]. From CEMS measurements by Nordström et al. [4], iron layers of thickness less than five monolayers were reported to be non-magnetic. Kalska et al., using CEMS, also reported differences in the degree of flatness between Fe on V and V on Fe interfaces [5].

M. Elzain (✉) · M. Al-Barwani · A. Gismelseed · A. Al-Rawas · A. Yousif · H. Widatallah · K. Bouziane · I. Al-Omari
Department of Physics, College of Science, Sultan Qaboos University, Box 36, Al Khod 123, Muscat, Oman
e-mail: elzain@squ.edu.om

Introduction of H into Fe/V superlattices strongly distort the local lattice structure as determined through extended x-ray absorption fine structure, where variations up to around 7% of the local *c* parameter were reported [6]. Moreover, a hydrogen depletion zone of 1–2 monolayers in the V layer was reported [7]. The magnetic properties of Fe/V superlattices can be reversibly tuned by hydrogenation [8]. For a two-monolayer Fe superlattice, it was found that the Fe atoms in the pristine sample possess a magnetic moment of 1.7 μ_B, while for the hydrogenated samples the Fe atoms with neighboring V-H complexes possess moments in the range 2.1–2.2 μ_B [8]. The average magnetic moment per Fe atom was found to increase with increasing H content [9]. To our knowledge, there are no Mössbauer data on hydrogenated Fe/V superlattices.

The effect of H on the IEC and magnetic moment of a superlattice composed of three Fe layers and five V layers was studied by Ostanin et al. [10] using the full-potential linear-muffin-tin orbitals. The disappearance of the antiferromagnetic interlayer exchange coupling (IEC) for large H concentration was attributed to the decrease of the density of states at the Fermi level.

We used the FP-LAPW method as implemented in the WIEN2k package [11] to calculate the hyperfine properties at the interface and inner Fe sites in Fe_3V_9 superlattice versus the H location and H content. It is found that sizeable changes in the hyperfine properties are obtained only when H is in the interface region. The technical details of the calculation are found in [12] by Elzain and Al-Barwani.

2 Results and discussion

Figure 1 shows the unit cell along the BCC <001> direction used to calculate the magnetic and hyperfine properties of the hydrogenated Fe/V superlattice Fe_3V_9. We have performed calculations with H atoms at both Oz octahedral and tetrahedral interstitial sites. This paper shows the results with the H atoms at the Oz octahedral sites (Fig. 1). The H atoms are indexed by numbers from −1 to 5 with H at the interface Fe monolayer being indexed 0. Hydrogen atoms with index 5 lie at the centre of the V layer, while those with indices 1 and −1 lie at the V interface monolayer and the Fe interior monolayer respectively. The lattice parameters were relaxed to give the energy minimum. Ferromagnetic interlayer configurations were found to be energetically stable in all the present cases. In Table 1 we show the magnetic hyperfine fields (B_{hf}) at the interface and the central Fe monolayers together with the local Fe moments for different H locations. As seen from the table the values of B_{hf} for H locations farther from the interface remain almost the same as that of the H free case Fe_3V_9. The magnitudes of B_{hf} at both Fe sites for H at positions 1 and 0 at the interface are larger than that of Fe_3V_9. The corresponding local magnetic moments within the muffin-tin radii show almost similar trends. However, we find that the ratios of B_{hf} to the local moments of Fe at the two sites are different. It is clear that the effect of H on the magnetic hyperfine fields is felt only when the H atoms are located at the interface.

The isomer shifts at the interface and central Fe atoms relative to α-Fe are shown in Table 2. In general the values of the isomer shifts for H position far from the interface are small. Comparing the values of the isomer shifts to that of H free case (Fe_3V_9), sizeable changes are observed only when H is at the interface or inside

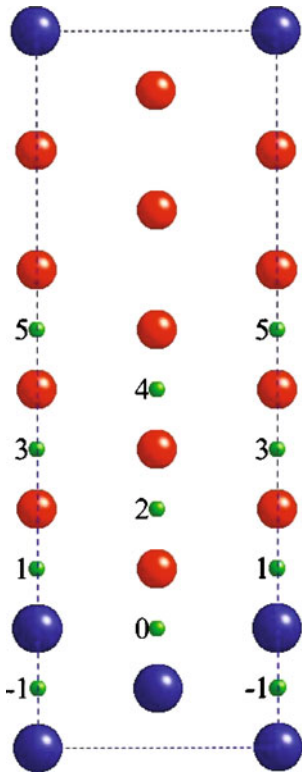

Fig. 1 Fig. 1 The unit cell of the Fe_3V_9 superlattice. Dark (*blue*) large balls represent Fe and light (*red*) large balls represent V. The small (*green*) balls represent H at the (Oz) octahedral interstitial sites. The indices give the hydrogen locations within the superlattice

Table 1 The first and second rows: the contact hyperfine fields (in Tesla) and the third and fourth rows: the local magnetic moments (in Bohr Magnetons) at the interface Fe (0), the interior Fe (−1) for different H locations

	Fe_3V_9	−1	0	1	2	3	4	5
Fe (0)	−17.5	−14.1	−22.0	−21.4	−17.5	−18.1	−18.3	−18.0
Fe (−1)	−22.0	−28.5	−25.8	−24.4	−22.0	−22.9	−23.0	−22.4
Fe (0)	1.57	1.57	2.03	1.86	1.63	1.63	1.59	1.54
Fe (−1)	2.55	2.59	2.42	2.54	2.58	2.54	2.56	2.55

the Fe layer. We found that the changes in the contact charge densities of Fe at the interface and the central sites follow the same trends as the change in atomic volumes at the same sites. This confirms our earlier conclusion that changes in the properties of Fe/V superlattices are attributed to volume effect [12].

The quadrupole splittings shown also in Table 2 are in general large at the Fe interface atom and relatively small for the central Fe atom. From these results one concludes that the effect of H outside the interface region can not be detected by the Mössbauer measurement.

We now consider the effect of H filling of the Oz sites starting from the center of the V layer and proceeding towards the interface. In Table 3 we show the magnetic hyperfine field, the isomer shift and the quadrupole splitting at the interface and the central Fe atoms versus the ratio of the number of H atoms to the number of V atoms

Table 2 The isomer (top) and quadrupole (bottom) splitting in mm/s at the interface Fe(0) and the central Fe(−1) atoms respectively for different H locations

	Fe_3V_9	−1	0	1	2	3	4	5
Fe (0)	−0.08	0.02	0.37	0.10	−0.07	−0.05	−0.04	−0.06
Fe (−1)	0.01	0.43	0.16	0.07	0.03	0.03	0.05	0.04
Fe (0)	−0.40	−0.40	−1.24	0.09	−0.33	−0.60	−0.32	−0.41
Fe (−1)	−0.05	−0.79	−0.09	0.09	−0.12	−0.05	−0.07	−0.06

Table 3 The respective magnetic hyperfine field (in Tesla, top), the isomer shift (in mm/s, middle) and the quadrupole splitting (in mm/s, bottom) at the interface Fe(0) and the central Fe(−1) atoms versus the fraction of H at the Oz sites

H/V	0	1/9	2/9	3/9	4/9	5/9
Fe (0)	−17.5	−18.0	−18.6	−18.9	−18.7	−18.5
Fe (−1)	−22.1	−22.4	−22.9	−22.9	−23.1	−23.6
Fe (0)	−0.08	−0.06	−0.05	−0.04	−0.04	−0.06
Fe (−1)	0.01	0.04	0.04	0.05	0.05	0.04
Fe (0)	−0.40	−0.41	−0.36	−0.34	−0.52	−0.59
Fe (−1)	−0.05	−0.06	−0.06	−0.10	−0.05	−0.05

in the unit cell. We note that the isomer shift does not practically change with H contents, while the magnitude of the magnetic hyperfine field at central monolayer slightly increases. The magnitude of the quadrupole splitting decreases at first and then increases as H contents increases.

As a result of these findings, when H is introduced in Fe/V superlattices there will be minor changes in the magnetic hyperfine fields and the quadrupole splitting at the Fe sites in the interface region if H is restricted to region outside the interface. This is in contrast with increase in the average magnetic moment with H contents observed experimentally [9] and confirmed theoretically [12]. However, the presence of H in the interface region will be reflected in large changes in all hyperfine parameters. Henceforth, Mössbauer measurements could be used to detect the absence or presence of H in the interface region.

In conclusion, the magnetic hyperfine fields, isomer shifts and quadrupole splittings at the interface and the central Fe sites in a Fe_3V_9 flat interface superlattice were calculated for different H locations and different H fillings. It is found that significant changes in the hyperfine parameters are detectable only when H resides in the interface region. This could be used to confirm the presence or absence of a depletion region in Fe/V superlattices.

References

1. Björck, M., Pärnaste, M., Marcellini, M., Andersson, G., Hjörvarsson, B.: J. Magn. Magn. Mater. **313**, 230 (2007)
2. Andersson, G., Nordström, E., Wäppling, R.: Eurphys. Lett. **60**, 731 (2002)
3. Clavero, C., Skuza, J.R., Choi, Y., Haskel, D., Sanchez-Hanke, C., Loloee, R., Zhernenkov, M.: Phys. Rev. B **80**, 024418 (2009)
4. Nordström, E., Kalska, B., Häggström, L., Blomqvist, P., Wäppling, R.: Hyperfine Interact. **141/142**, 465 (2002)
5. Kalska, B., Blomqvist, P., Häggström, L., Wäppling, R.: Europhys. Lett. **53**, 395 (2001)

6. Pálsson, G.K., Kapaklis, V., Dura, J.A., Jacob, J., Jayanetti, S., Rennie, A.R., Hjörvarsson, B.: Phys. Rev. B **82**, 245424 (2010)
7. Andersson, G., Hjörvarsson, B., Isberg, P.: Phys. Rev B **55**, 1774 (1997)
8. Remhof, A., Nowak, G., Zabel, H., Björck, M., Pärnaste, M., Hjörvarsson, B., Uzdin, V.: Europhys. Lett. **79**, 37003 (2007)
9. Labergerie, D., Westerholt, K., Zabel, H., Hjörvarsson, B.: J. Magn. Magn. Mater. **225**, 373 (2001)
10. Ostanin, S., Uzdin, V.M., Demangeat, C., Wills, J.M., Alouani, M., Dreyssé, H.: Phys. Rev. B **61**, 4870 (2000)
11. Blaha, P., Schwarz, K., Madsen, G.K.H., Kvasnicka, D., Luitz, J.: In: Schwarz, K. (ed.) WIEN2k: An Augmented Plane Wave + Local Orbitals Program for Calculating Crystal Properties. Technische Universitat Wien, Vienna, Austria (2009)
12. Elzain, M., Al-Barwani, M.: Mod. Phys. Lett. B **25**, 2239 (2011)

Hyperfine Interact (2012) 207:139–143
DOI 10.1007/s10751-011-0406-5

Study on the ferromagnetic state in iron mixed-valence complexes, $A[Fe^{II}Fe^{III}(dto)_3]$ ($A = (n\text{-}C_nH_{2n+1})_4N$; $dto = C_2S_2O_2$) by means of Mössbauer spectroscopy

Yuki Ono · Atsushi Okazawa · Masaya Enomoto · Norimichi Kojima

Published online: 28 October 2011

Abstract We have investigated the ferromagnetic states for $(n\text{-}C_nH_{2n+1})_4N[Fe^{II}Fe^{III}(dto)_3]$ ($n = 3$–6; $dto = C_2O_2S_2$) by means of ^{57}Fe Mössbauer spectroscopy. The major component of the spin configuration in the ferromagnetic states for $n = 3$ and 4 is the low-temperature phase (LTP) with the Fe^{III} ($S = 5/2$) and Fe^{II} ($S = 0$) states. The high-temperature phase (HTP) of $n = 4$ remains by more than 20%, which is consistent with two ferromagnetic transitions ($T_C = 7$ & 13 K). Moreover, it was revealed that the Mössbauer spectra in the ferromagnetic states for $n = 5$ and 6 correspond to the HTP consisting of the Fe^{II} ($S = 2$) and Fe^{III} ($S = 1/2$) states.

Keywords Mixed-valence complex · Dithiooxalato · Ferromagnetism · Mössbauer spectroscopy

1 Introduction

The mixed-valence iron complex $(n\text{-}C_3H_7)_4N[Fe^{II}Fe^{III}(dto)_3]$ ($dto = C_2O_2S_2$) is an intriguing material showing a new type of first-order phase transition around 120 K, where the thermally induced charge transfer between the Fe^{II} and Fe^{III} sites occurs

Electronic supplementary material The online version of this article (doi:10.1007/s10751-011-0406-5) contains supplementary material, which is available to authorized users.

Y. Ono · A. Okazawa · N. Kojima (✉)
Graduate School of Arts and Sciences, The University of Tokyo, Tokyo 153-8902, Japan
e-mail: cnori@mail.ecc.u-tokyo.ac.jp

A. Okazawa
e-mail: cokazawa@mail.ecc.u-tokyo.ac.jp

M. Enomoto
Department of Chemistry, Faculty of Science Division I, Tokyo University of Science, Tokyo 162-8601, Japan

reversibly [1]. The complex has a two-dimensional honeycomb network structure and the $(n\text{-}C_3H_7)_4N$ cations are intercalated between $[Fe^{II}Fe^{III}(dto)_3]_\infty$ layers [2]. The spin states of the iron sites change between $Fe^{III}S_6$ ($S = 1/2$)-$Fe^{II}O_6$ ($S = 2$) and $Fe^{II}S_6$ ($S = 0$)-$Fe^{III}O_6$ ($S = 5/2$) corresponding to the high-temperature phase (HTP) and low-temperature phase (LTP), respectively, due to the charge transfer phase transition (CTPT). The CTPT also occurs in $(n\text{-}C_4H_9)_4N[Fe^{II}Fe^{III}(dto)_3]$, while the CTPT does not occur in $(n\text{-}C_nH_{2n+1})_4N[Fe^{II}Fe^{III}(dto)_3]$ (n = 5 and 6) [3, 4]. Moreover, $(n\text{-}C_nH_{2n+1})_4N[Fe^{II}Fe^{III}(dto)_3]$ (n = 3–6) show the ferromagnetic phase transitions [3]. The Curie temperatures, T_C, for n = 3 and 4 are 7 K and 7 & 13 K, respectively, while those for n = 5 and 6 are 19.5 K and 22 K, respectively [3]. In this paper, we report the detailed analysis of the Mössbauer spectra in the ferromagnetic states of $(n\text{-}C_nH_{2n+1})_4N[Fe^{II}Fe^{III}(dto)_3]$ (n = 3–6).

2 Experimental

$(n\text{-}C_nH_{2n+1})_4N[Fe^{II}Fe^{III}(dto)_3]$ were prepared according to a similar way of the previous report [3] at the synthesis temperature of 10°C. For ^{57}Fe Mössbauer measurement, ^{57}Co in Rh was used as a Mössbauer source. The spectra were calibrated by the six lines of α-Fe, the center of which was taken as zero isomer shift. Mössbauer spectra have been fitted with a MossWinn 3.0 program [5]. The model was calculated by solving the exact Hamiltonian for mixed magnetic and quadrupole interaction with arbitrary relative orientation, where the following parameters are included; the isomer shift δ, the internal magnetic field H_n, the quadrupole splitting ΔE_Q, the angle θ between the principle axis of the electric field gradient (EFG) and the magnetization direction, the line width Γ, and the component V_{zz} of the EFG. The V_{zz} has the unit: 10^{21} V/m^2. The asymmetry parameter η of the EFG is herein zero.

3 Results and discussion

The parameters of the Mössbauer spectra in the ferromagnetic states for n = 3–6 are listed in Table 1.

The Mössbauer spectra of n = 3 at 4.2 K are shown in Fig. 1a and the fitting parameters are listed in Table S1 given in Online Resource. Mainly, a central doublet ($\delta = 0.43$ mm/s, $\Delta E_Q = 0.39$ mm/s) and a sextet with a large hyperfine field ($H_n =$ 447 kOe) from -8 to 8 mm/s were observed. The former can be assigned to the non-magnetic state of Fe^{II} ($S = 0$) and the latter is typical of the magnetically ordered state of Fe^{III} ($S = 5/2$). The Mössbauer parameters are similar to those in the ferromagnetic state of the LTP for $(SP)[Fe^{II}Fe^{III}(dto)_3]$ (SP = spiropyran) [6]. The sextets of the Fe^{II} ($S = 2$) and Fe^{III} ($S = 1/2$) sites, which correspond to the HTP, are also required to fit the spectra with ca. 15%. The θ value was estimated by the following equation for axial symmetry; $\Delta\varepsilon_1 - \Delta\varepsilon_2 = -1/2eV_{zz}\left(3\cos^2\theta - 1\right)$ (Fig. 1a). On the assumption of positive and negative V_{zz}, θ are estimated at 90° and 40°, respectively. Here, θ can be recognized as 90°, because the principal axis of V_{zz} lies along the D_3 axis of the $[Fe^{II}Fe^{III}(dto)_3]_\infty$ layer and H_n lies in

Table 1 The selected Mössbauer spectral hyperfine parameters in the ferromagnetic ordered states at 4 or 4.5 K for (n-$C_nH_{2n+1})_4N[Fe^{II}Fe^{III}(dto)_3]$ (n = 3–6)

		n = 3			n = 4			n = 5			n = 6		
		δ[a]	ΔE_Q[b]	H_n[c]	δ	ΔE_Q	H_n	δ	ΔE_Q	H_n	δ	ΔE_Q	H_n
LTP	Fe^{II} ($S = 0$)	0.43	0.39	–	0.46	0.46	–	–	–	–	–	–	–
	Fe^{III} ($S = 5/2$)	0.55[d]	0.90[d]	448	0.55[d]	0.95[d]	448	–	–	–	–	–	–
HTP	Fe^{II} ($S = 2$)	1.26[d]	1.41[d]	102	1.26[d]	1.41[d]	100	1.24	1.84	73	1.26[d]	1.37[d]	99
	Fe^{III} ($S = 1/2$)	0.33[d]	0.55[d]	234	0.33[d]	0.51[d]	241	0.40[d]	0.73[d]	246	0.42[d]	0.71[d]	248

[a] Isomer shift (mm/s)
[b] Quadrupole splitting (mm/s)
[c] Internal magnetic field (kOe)
[d] Parameter constrained to the given value

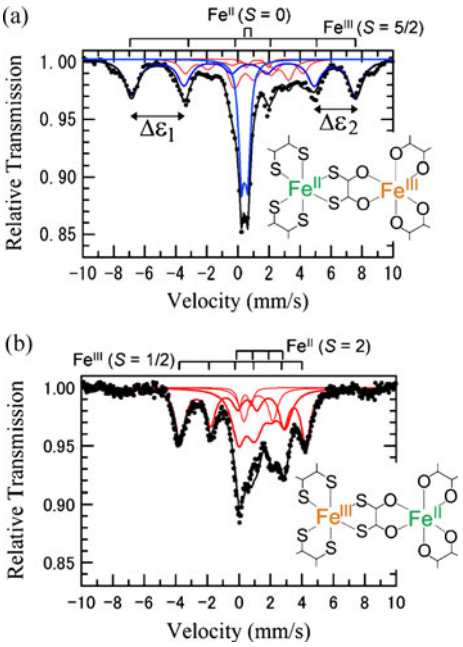

Fig. 1 Magnetically ordered Mössbauer spectra of **a** $(n\text{-}C_3H_7)_4N[Fe^{II}Fe^{III}(dto)_3]$ at 4.2 K and **b** $(n\text{-}C_5H_{11})_4N[Fe^{II}Fe^{III}(dto)_3]$ at 4 K

the $[Fe^{II}Fe^{III}(dto)_3]_\infty$ layer according to the anisotropic magnetization measurement [7].

We measured ^{57}Fe Mössbauer spectroscopy for n = 4 between 25 and 4.5 K (Fig. S1 and Table S2). The spectrum in the ferromagnetic state at 4.5 K for n = 4 is mainly similar to that for n = 3. The central doublet (δ = 0.45 mm/s, ΔE_Q = 0.46 mm/s) of the Fe^{II} ($S = 0$) site and the sextet ($H_n = 448$) of the Fe^{III} ($S = 5/2$) site of the LTP were mainly observed. For n = 4, it should be note that two ferromagnetic transitions coexist with $T_C = 7$ and $T_C = 13$ K in the magnetic measurements [3]. Broad components of the spectra, which are not observed in n = 3, appeared above $T_C = 7$ K, indicating the development of the magnetic ordering in the HTP. The H_n values at 4.5 K corresponding to the Fe^{II} ($S = 2$) and Fe^{III} ($S = 1/2$) sites are estimated at 100 kOe and 241 kOe, respectively (see below). The component of the HTP for n = 4 are about 30%, therefore not only the LTP but also the HTP of n = 4 show the ferromagnetic phase transitions.

The Mössbauer spectra in the ferromagnetic states for n = 5 and 6 (Fig. S2, Table S3 and S4) considerably differ from those for n = 3 and 4. Figure 1b shows the spectrum for n = 5 at 4 K. In the cases of n = 5 and 6, the CTPT do not occur, therefore the spin configuration can be assigned to the Fe^{II} ($S = 2$) and the Fe^{III} ($S = 1/2$) corresponding to the HTP. The Mössbauer spectra were reasonably fitted with two sextets of the magnetically ordered HTP and additionally two doublets derived from their residual paramagnetic components (below ca. 10%). The sextets of the Fe^{III} ($S = 1/2$) sites have large H_n of 246 kOe (n = 5) and 248 kOe (n = 6) at 4 K. The Fe^{II} ($S = 2$) sites, on the other hand, have relatively small H_n of 73 kOe (n = 5) and 99 kOe (n = 6).

4 Conclusion

^{57}Fe Mössbauer spectroscopy is the most powerful tool to investigate the spin configurations in the magnetically ordered states for (n-$C_nH_{2n+1})_4N[Fe^{II}Fe^{III}(dto)_3]$. The Fe^{III} ($S = 5/2$) and Fe^{II} ($S = 0$) states dominate below the ferromagnetic transition temperatures for $n = 3$ and 4. In the case of $n = 4$, the ^{57}Fe Mossbauer spectra revealed the development of the magnetic ordering in the HTP. This is consistent with the result of the magnetic measurements. For $n = 5$ and 6, the spin configurations in the ferromagnetic states were assigned to the Fe^{III} ($S = 1/2$) and Fe^{II} ($S = 2$) states.

Acknowledgements This work was supported by a Grant-in-Aid for Scientific Research from the Ministry of Educational Science, Sports and Culture, Japan.

References

1. Kojima, N., Aoki, W., Itoi, M., Ono, Y., Seto, M., Kobayashi, Y., Maeda, Yu.: Solid State Commun. **120**, 165 (2001)
2. Itoi, M., Taira, A., Enomoto, M., Matsushita, N., Kojima, N., Kobayshi, Y., Asai, K., Koyama, K., Nakano, T., Uwatoko, Y., Yamaura, J.: Solid State Commun. **130**, 415 (2004)
3. Itoi, M., Ono, Y., Kojima, N., Kato, K., Osaka, K., Takata, M.: Eur. J. Inorg. Chem. **2006**, 1198 (2006)
4. Kojima, N., Ono, Y., Kobayashi, Y., Seto, M.: Hyperfine Interact. **175**, 156–157 (2004)
5. Klencsár, Z., Kuzmann, E., Vértes, A.: J. Radioanal. Nucl. Chem. **210**, 105 (1996)
6. Kida, N., Hikita, M., Kashima, I., Enomoto, M., Itoi, M., Kojima, N.: Polyhedron **28**, 1694 (2004)
7. Itoi, M., Enomoto, M., Kojima, N.: J. Magn. Magn. Mater. **272**, 1093 (2004)

Hyperfine Interact (2012) 208:1–6
DOI 10.1007/s10751-011-0458-6

Atomic short-range order in iron based Fe-Mo alloys studied by ^{57}Fe Mössbauer spectroscopy

Rafał Idczak · Robert Konieczny · Jan Chojcan

Published online: 18 November 2011

Abstract The room temperature Mössbauer spectra of ^{57}Fe were measured for iron-based solid solutions $Fe_{1-x}Mo_x$ with x in the range $0.01 \leq x \leq 0.05$. The obtained spectra gave clear evidence that after annealing process the distribution of impurity atoms in the first and the second coordination spheres of ^{57}Fe nuclei is not random and it cannot be described by the binomial distribution. Quantitatively, the findings are presented with the short-range order parameters.

Keywords Mössbauer spectroscopy · Short-range order · Iron alloys · International conference · Applications · Mössbauer effect

1 Introduction

Magnetic and thermodynamic properties of alloys depend, in general, on local fluctuations in composition. These fluctuations can be quantitatively described in terms of atomic short-range order (SRO) parameters α_i, introduced by Cowley [1].

$$\alpha_i = 1 - \frac{P_i\,(BA)}{x_B} \tag{1}$$

where P_i (BA) denotes the probability of finding an atom of type B in the ith nearest neighbour shell when centred on an atom of type A and x_B is a fraction of atoms B in the alloy. It is clear that the SRO parameter yields the same result when evaluated on a representative A or B atom. Physically, the parameter measures the deviation at short range from the random state, with values from 1-1/x_B to 1; 0 corresponds to the random state.

R. Idczak (✉) · R. Konieczny · J. Chojcan
Institute of Experimental Physics, University of Wrocław,
pl. M. Borna 9, 50-204 Wrocław, Poland
e-mail: ridczak@ifd.uni.wroc.pl

In the last years, there was much interest of theoretical [2, 3] and experimental [4–8] determination of SRO parameters in Fe-based binary alloys. Our work concerns determination of such parameters in $Fe_{1-x}Mo_x$ alloys, with x in the range $0.01 \leq x \leq 0.05$, using ^{57}Fe Mössbauer spectroscopy. We performed three series of measurements. The first for samples just after preparation by melting and being frozen-in high temperature state, second for samples after annealing at 1270 K for 2 h and third for samples after additional annealing at 1270 K for the next 2 h. Differences of SRO parameters derived from these three different series of data should show how the annealing process of $Fe_{1-x}Mo_x$ alloys influences, the distribution of Mo atoms in the nearest neighbour spheres of the ^{57}Fe Mössbauer probe and what is the type of interaction between Mo and Fe atoms (predominance of Fe-Fe and Mo-Mo or Fe-Mo bonds).

2 Experimental and results

The samples of iron-molybdenum alloys containing 1, 2, 3, 4 and 5 at. % of Mo, were prepared by melting appropriate amounts of the Aldrich 99.999% pure iron and 99.97% pure molybdenum in an arc furnace filled with argon. The ingots were cold-rolled to the final thickness of about 0.05 mm and then the room temperature ^{57}Fe Mössbauer spectra were measured for the foils by means a constant-acceleration POLON spectrometer of standard design. In the next step the samples were annealed in vacuum at 1270 K for 2h. After that they were slowly cooled to room temperature during 6h. Under these conditions, diffusion effectively stops at about 700 K [9], so the observed distributions of atoms in the annealed specimens should be the frozen-in state corresponding to 700 K. In the last step we repeated the annealing process at 1270 K for the next 2 h. The final concentrations of elements in the $Fe_{1-x}Mo_x$ specimens were estimated taking into account the weight losses during the melting process and assuming that they were due to evaporation of molybdenum only. The values of x estimated this way are: 0.00970(40), 0.01989(15), 0.02965(42), 0.0389(12) and 0.0491(11), where in brackets the maximal uncertainty of x is given.

Spectra for samples as-obtained and after the second annealing process are presented in Figs. 1 and 2. They were analysed in terms of six six-line patterns corresponding to different hyperfine fields B at ^{57}Fe nuclei generated by different numbers of Fe and Mo atoms located in the first two coordination shells of the probing nuclei. It was done under assumption that the influence of Mo atoms on B as well as the corresponding isomer shift IS of a subspectrum, is additive and independent of the atom positions in the given coordination shell of the nuclear probe although it can be different for atoms located in unlike shells. In other words it was accepted that for each subspectrum the quantities B and IS are linear functions of the numbers n_1 and n_2 of Mo atoms located, respectively, in the first and the second coordination shells of ^{57}Fe and the functions can be written as follows:

$$\begin{aligned} B(n_1, n_2) &= B_0 + n_1 \Delta B_1 + n_2 \Delta B_2, \\ IS(n_1, n_2) &= IS_0 + n_1 \Delta IS_1 + n_2 \Delta IS_2, \end{aligned} \tag{2}$$

where ΔB_1 (ΔIS_1) and ΔB_2 (ΔIS_2) stand for the changes of B (IS) with one Mo atom located in the first and the second coordination shells of the Mössbauer probe. At the same time the quadruple splitting QS of a subspectrum is a free parameter

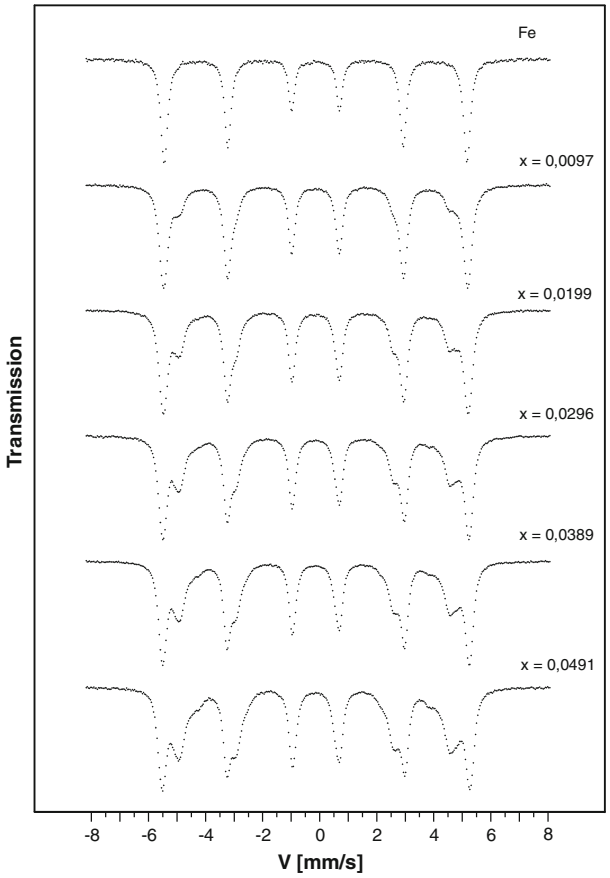

Fig. 1 The ^{57}Fe Mössbauer spectra for the $Fe_{1-x}Mo_x$ alloys measured at room temperature after melting process in an arc furnace

[10]. More details concerning sample preparations and method of analysing of the obtained spectra, including the values of B and IS parameters, can be found in our previous paper [11].

In disordered iron-based alloys, the probability $P(n_1, n_2)$ of local configuration of impurity atoms in the first and the second coordination spheres of ^{57}Fe nucleus is described by the binomial distribution:

$$P(n_1, n_2) = \frac{N_1!}{n_1!\,(N_1 - n_1)!} \frac{N_2!}{n_2!\,(N_2 - n_2)!} x^{n_1+n_2} (1-x)^{N_1+N_2-n_1-n_2} \tag{3}$$

where N_1 and N_2 denotes the coordination numbers of the first and the second sphere, x is the concentration of impurity atoms and n_1, n_2 stands for the numbers of impurity atoms in the first and the second coordination spheres. In the case of $Fe_{1-x}Mo_x$ alloys with the x range $0.01 \leq x \leq 0.05$ where atoms are distributed in the b.c.c. lattice, so $N_1 = 8$ and $N_2 = 6$. In the real alloys the distribution of impurity atoms is generally different than statistically predicted by (3). This deviation from the random state can be quantitatively described by SRO parameters. The Mössbauer spectroscopy is a very useful tool for determination of the parameters because the hyperfine field B and isomer shift IS depend on the number of impurity atoms in the

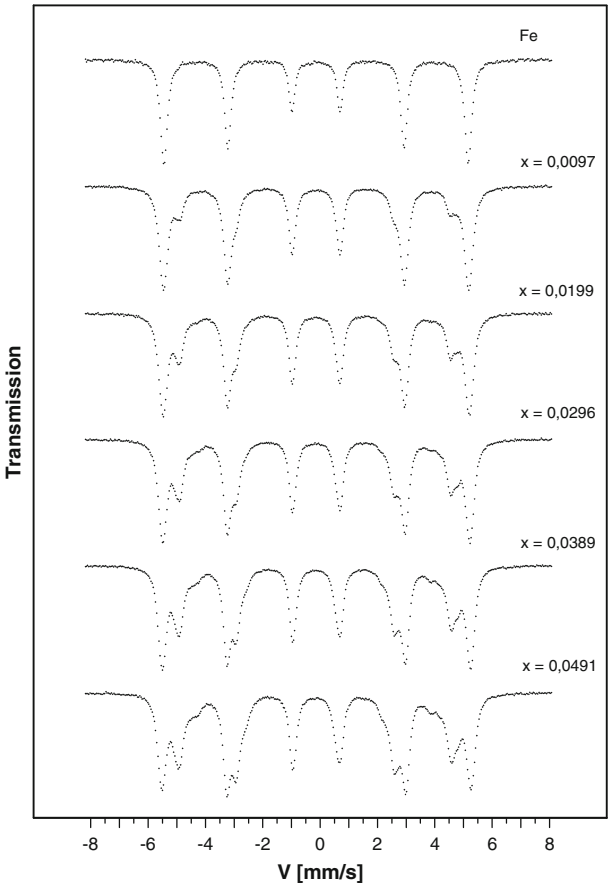

Fig. 2 The ^{57}Fe Mössbauer spectra for the $Fe_{1-x}Mo_x$ alloys measured at room temperature after the second the annealing process at 1270 K

vicinity of ^{57}Fe probe. The SRO parameters for systems with b.c.c. lattice have the following form:

$$\alpha_1 = 1 - \frac{\langle n_1 \rangle}{8x}, \alpha_2 = 1 - \frac{\langle n_2 \rangle}{6x} \tag{4}$$

where:

$$\langle n_1 \rangle = \sum_{n_1=1}^{8} n_1 P_{\exp}(n_1, n_2), \langle n_2 \rangle = \sum_{n_2=1}^{6} n_2 P_{\exp}(n_1, n_2) \tag{5}$$

$< n_1 >$ and $< n_2 >$ are the average numbers of non-iron Mo atoms in the first and the second coordination spheres of an iron atom and $P_{\exp}(n_1, n_2)$ denotes the probability of the configuration (n_1, n_2) of non-iron Mo atoms obtained from the analysis of the experimental Mössbauer spectra.

The SRO parameters α_1 and α_2 for $Fe_{1-x}Mo_x$ alloys calculated from (4) are presented in Figs. 3 and 4. In the samples before annealing process parameters α_1 and α_2, on average, are close to 0 and this provides that the distribution of Mo atoms in these samples is almost random. Situation significantly changes for the annealed samples, i.e. α_1 essentially decreases and α_2 increases on annealing. This indicates

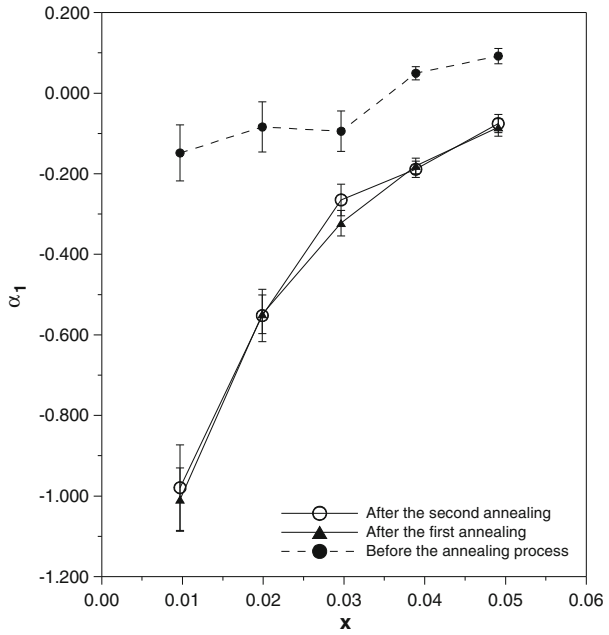

Fig. 3 The SRO parameter α_1 parameters as a function of fraction x of Mo atoms in the $Fe_{1-x}Mo_x$ alloys

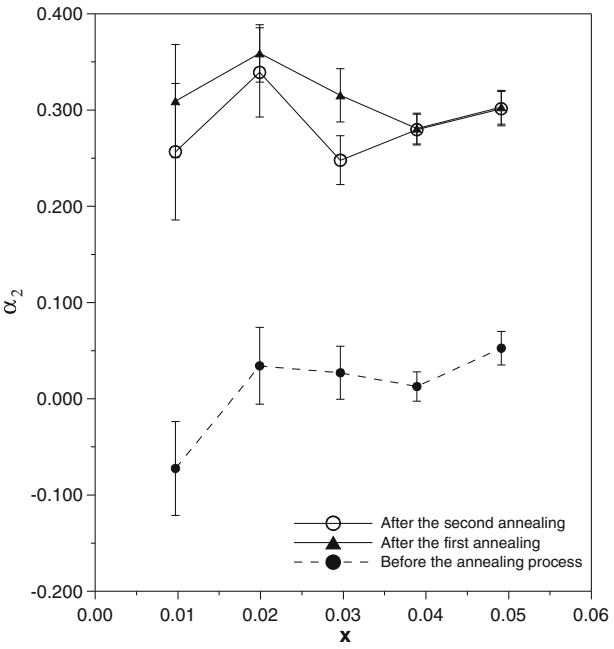

Fig. 4 The SRO parameter α_2 parameters as a function of fraction x of Mo atoms in the $Fe_{1-x}Mo_x$ alloys

that in the first coordination shell of ^{57}Fe probe, the Mo atoms are more abundant and in the second one they are rarer than it is expected for the random case. In terms of interactions it means that the interaction between Fe and Mo atoms is

attractive (predominance of Fe-Mo bonds) and this is in agreement with findings of our previous work [11]. Worth mentioning is the fact, that the values of parameters α_1 and α_2 in samples after the first and the second annealing processes are practically the same. This may indicate that the first annealing process at 1270 K for 2 h was sufficient to obtain the equilibrium state of $Fe_{1-x}Mo_x$ alloys.

3 Conclusions

The Mössbauer study of SRO parameters for $Fe_{1-x}Mo_x$ alloys reveals that the parameters depend on the heat treatment of the investigated specimens. For the samples as-obtained i.e. before annealing process, the SRO parameters α_1 and α_2 are nearly equal to 0. This suggests that the distribution of Mo atoms in the first two coordination shells of ^{57}Fe probe is almost random in the as-obtained specimens. On the other hand for the samples after one and two annealing processes at 1270 K during 2 h, one observes ordering-type correlations (the predominance of Mo-Fe bonds) manifested as increasing of α_1 and decreasing of α_2 parameter, caused by attractive interaction between Fe and Mo atoms.

Acknowledgement This work was supported by the University of Wrocław under the grants 1463/M/IFD/11 and 1010/S/IFD.

References

1. Cowley, J.M.: An approximate theory of order in alloys. Phys. Rev. **77**, 669–675 (1950)
2. Erhart, P., Caro, A., Serrano de Caro, M., Sadigh, B.: Short-range order and precipitation in Fe-rich Fe-Cr alloys: Atomistic off-lattice Monte Carlo simulations. Phys. Rev. B **77**, 134206 (2008)
3. Bonny, G., Erhart, P., Caro, A., Pasianot, R.C., Malerba, L., Caro, M.: The influence of short range order on the thermodynamics of Fe–Cr alloys. Model. Simul. Mater. Sci. Eng. **17**, 025006 (2009)
4. Whitte, G.L., Campbell, S.J.: Local atomic order in AuFe. Phys. Rev. B **30**, 5364–5366 (1984)
5. Yoshida, Y., Langmayr, F., Fratzl, P., Vogl, G.: Short-range order in Au-Fe alloys studied by high-temperature Mössbauer spectroscopy. Phys. Rev. B **39**, 6395–6402 (1989)
6. Chen, H., Anderson, J., Ohshima, K., Okajima, H., Harada, J.: Atomic short-range-order structure in Au-Fe alloys. Phys. Rev. B **42**, 2342–2346 (1990)
7. Jartych, J.E.: Local atomic order in nanocrystalline Fe-based alloys obtained by mechanical alloying. J. Magn. Magn. Mater. **265**, 176–188 (2003)
8. Cieślak, J., Dubiel, J.M.: Mössbauer-effect study of local atomic order in bcc $Fe_{100-x}Ti_x$ alloys with $x \leq 12$. J. Alloys Comp. **387**, 36–43 (2005)
9. Cranshaw, T.E.: A mössbauer study of ^{119}Sn in alloys of iron with Si, Al and Rh: interaction potentials and phase diagrams. J. Phys., Condens. Matter **1**, 829–846 (1989)
10. Falepin, A., Cottenier, S., Comrie, C.M., Vantomme A.: Interpreting Mössbauer spectra reflecting an infinite number of sites: an application to Fe1-xSi synthesized by pulsed laser annealing. Phys. Rev. B **74**, 184108 (2006)
11. Chojcan J., Konieczny R., Ostrasz A., Idczak R.: A dilute-limit heat of solution of molybdenum in iron studied with ^{57}Fe Mössbauer spectroscopy. Hyperfine Interact. **196**, 377–383 (2010)

Hyperfine Interact (2012) 208:7–11
DOI 10.1007/s10751-011-0506-2

Electronic property of $SrFe_2As_2$ under high pressure studied by ^{57}Fe Mössbauer spectroscopy

Shugo Ikeda · Kazuki Yoshida · Hisao Kobayashi

Published online: 9 March 2012

Abstract We have studied the electronic state of Fe atoms in $SrFe_2As_2$ under pressure at room temperature by ^{57}Fe Mössbauer spectroscopy using a single crystalline sample. A center shift $\delta_{c.s.}$ and an electric quadrupole interaction parameter $e^2qQ/2$ show the discontinuous increase and decrease at around 7 GPa,respectively, implying the pressure-induced structural phase transition. Furthermore, $\delta_{c.s.}$ deviates from the linear pressure dependence above 4 GPa without any anomaly in the pressure dependence of $e^2qQ/2$. The anomaly corresponds to a change of the pressure dependence of lattice parameter ratio c/a, where volume of the unit cell decreases monotonously with increasing pressure.

Keywords $SrFe_2As_2$ · Mössbauer spectroscopy · High pressure

1 Introduction

After the discovery of superconductivity in F-doped LaFeAsO with FeAs layers [1], various Fe-based materials show superconductivity. $SrFe_2As_2$ has a $ThCr_2Si_2$-type tetragonal structure with FeAs layers and physical properties are similar to those in LaFeAsO [2–4]. With replacing LaO by Sr^{2+}, the crystal structure is much simpler

S. Ikeda (✉) · H. Kobayashi · K. Yoshida
Graduate School of Material Science, University of Hyogo, 3-2-1 Koto, Hyogo 678-1297, Japan
e-mail: s.ikeda@sci.u-hyogo.ac.jp

S. Ikeda · H. Kobayashi
JST, CREST, Kawaguchi, Saitama 332-0012, Japan

S. Ikeda · H. Kobayashi
JST, TRIP, Chiyoda, Tokyo 102-0075, Japan

than that of LaFeAsO. $SrFe_2As_2$ shows a spin density wave (SDW) transition at $T_{SDW} = 200$ K with a structure change [3, 4]. The SDW transition is suppressed by pressure and then superconductivity appears around 4∼7 GPa [2, 3]. There is a correlation between magnetism, structure and superconductivity in this system. The ^{57}Fe Mössbauer spectroscopy is a local probe that is extremely sensitive to the electronic state and the local structure of Fe atoms in a compound. Thus, the purpose of this study has been to investigate the electronic state of Fe atoms in $SrFe_2As_2$ under pressure by ^{57}Fe Mössbauer spectroscopy.

2 Experimental procedure

Single crystals of $SrFe_2As_2$ enriched with 97 at.% ^{57}Fe were grown by a Sn flux method. The T_{SDW} value was estimated to be 200.4 K by the temperature dependence of the magnetic susceptibility. This value is very good agreement with the previous results [3, 4].

In the previous ^{57}Fe Mössbauer experiments on powder samples, asymmetric Mössbauer spectra were observed in AFe_2As_2 (A : Ca, Sr, Ba, and Eu) below T_{SDW}. Recent our ^{57}Fe Mössbauer experiment using the single crystal samples indicates that the origin of the asymmetry in the spectra using powder samples comes from an imperfect powder condition [5]. Thus, we have measured the ^{57}Fe Mössbauer spectra using the single crystal sample under pressure at room temperature to obtain the center shift $\delta_{c.s.}$ and the electric quadrupole interaction parameter $e^2qQ/2$, precisely. A clamp-type diamond anvil cell (DAC) was used to apply pressure with Daphne7474 as a pressure-transmitting medium to be ensured the hydrostatic condition. The DAC was mounted on a translation stage with the sample at a distance of approximately 3 mm from a ^{57}Co(Rh) point source [6]. The direction of the incident γ-ray was parallel to the [001] axis in the samples. The velocity scale was calibrated with a standard α-Fe foil.

3 Results and discussion

Typical ^{57}Fe Mössbauer spectra at some selected pressures are shown in Fig. 1. As can been seen, a single like absorption peak is observed and the position of the absorption peak decreases with increasing pressure. Since the $FeAs_4$ tetrahedron is not regular in $SrFe_2As_2$ with the tetragonal structure [2], two absorption peaks should be observed in the spectrum. Thus, these results indicate that the electrical quadrupole interaction is small in $SrFe_2As_2$. The principle z-axis of the diagonalized electric-field-gradient (EFG) tensor is along the [001] axis and the asymmetrical parameter of EFG tensor is zero because of the $\bar{4}m2$ local symmetry at the Fe site in $SrFe_2As_2$ with the tetragonal structure. The intensity ratio of two absorption peaks depends on the angle between the direction of the incident γ-ray and the principle z-axis of EFG tensor using a single crystalline sample. In the present experimental condition where the incident γ-ray is parallel to the [001] direction, the intensity ratio is 3. The solid lines in Fig. 1 represent the best fitting curves by this analysis.

Figure 2 shows the pressure dependences of the refined $\delta_{c.s.}$ and $e^2qQ/2$. The value of $\delta_{c.s.}$ decreases up to about 6 GPa with increasing pressure and shows a distinct

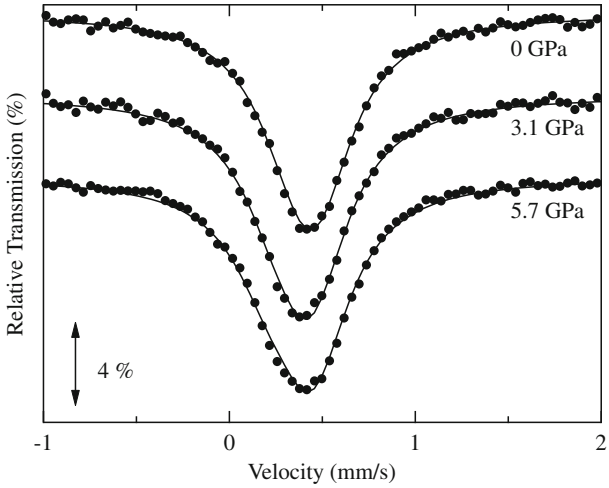

Fig. 1 Typical ^{57}Fe Mössbauer spectra at some selected pressures and room temperatures. The *solid lines* represent the results of fitting

anomaly at 6.8 GPa, as seen in Fig. 2a. Furthermore, $\delta_{\mathrm{c.s.}}$ decreases linearly above 7 GPa with increasing pressure. As shown in Fig. 2b, $e^2qQ/2$ increases monotonously up to about 6 GPa and has a lack of pressure dependence above 7 GPa within our experimental accuracy. These results strongly suggest that the electronic state of Fe atoms in $SrFe_2As_2$ changes discontinuously at around 7 GPa.

We obtain a good fit of the linear form below 3 GPa,

$$\delta_{\mathrm{c.s}} = 0.395(2) - 0.0159(9)\ P\ \ \mathrm{mm/s}. \tag{1}$$

In the pressure range between 4 and 6 GPa, $\delta_{\mathrm{c.s.}}$ deviates from (1) and shows the smaller pressure dependence than that below 3 GPa. Above 7 GPa, we also obtain a good fit of the linear form,

$$\delta_{\mathrm{c.s}} = 0.385(7) - 0.0045(8)\ P\ \ \mathrm{mm/s}. \tag{2}$$

The obtained coefficient of P above 7 GPa is 3.5 times smaller than that below 3 GPa. The anomalies in the pressure dependence of $\delta_{\mathrm{c.s}}$ reveal that the electronic state of Fe atoms in $SrFe_2As_2$ changes at around 4 and 7 GPa. Meanwhile, the pressure dependence of $e^2qQ/2$ indicates the anomaly only at around 7 GPa, as seen in Fig. 2b.

Recently it was found by the high-pressure x-ray diffraction measurements at room temperature [7] that the phase transition from the tetragonal to a collapsed tetragonal structure occurs at 10 GPa with large volume reduction. Below 10 GPa, the pressure dependence of lattice parameter ratio c/a changes at around 5 GPa, where volume of the unit cell decreases monotonously with increasing pressure. Accordingly, the anomalies in the pressure dependence of $\delta_{\mathrm{c.s}}$ and $e^2qQ/2$ at 7 GPa most likely correspond to the pressure-induced structural phase transition at 10 GPa. The difference of the critical pressure between both experiments is caused by non-hydrostatic pressure conditions in the high-pressure x-ray diffraction measurements because they did not used pressure-transmitted medium. The deviation from the

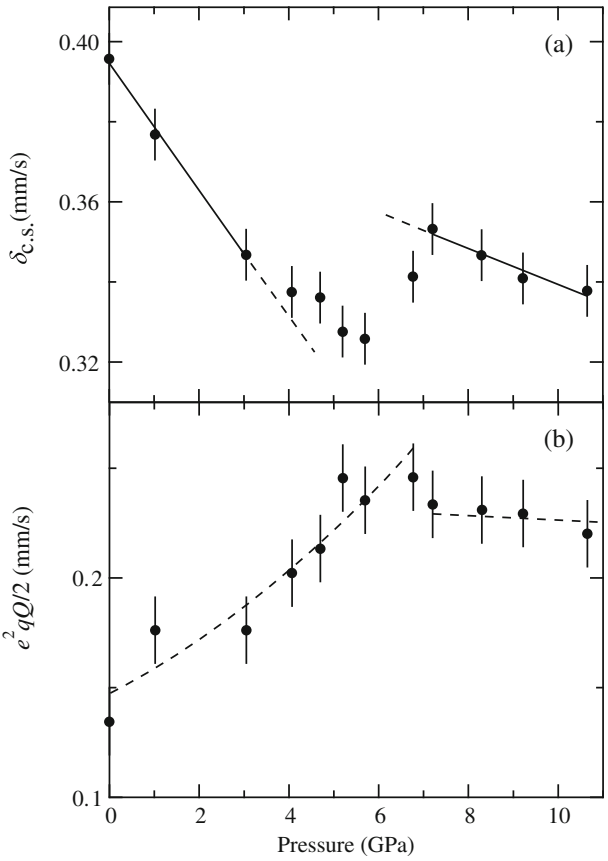

Fig. 2 Pressure dependences of the refined **a** center shift $\delta_{c.s.}$ and **b** electric quadrupole interaction parameter $e^2qQ/2$ in $SrFe_2As_2$ at room temperature. The *solid lines* represent the results of fitting. The *broken lines* are guides to the eye

linear relation between $\delta_{c.s}$ and P around 4 GPa correlates with the change of the pressure dependence of c/a. Since we did not observed any anomaly in the pressure dependence of $e^2qQ/2$ around 4 GPa, the volume of the $FeAs_4$ tetrahedron decreases monotonously around 4 GPa with increasing pressure.

4 Summary

We have measured the ^{57}Fe Mössbauer spectra of $SrFe_2As_2$ under high pressure at room temperature using the single crystalline sample. The pressure dependences of $\delta_{c.s}$ and $e^2qQ/2$ show the anomalies at 7 GPa, which correspond to the pressure-induced structural phase transition. The change of the pressure dependence of $\delta_{c.s}$ around 4 GPa correlates with that of the pressure dependence of c/a in the tetragonal structure. It is noted that the pressure range from 4 to 7 GPa almost coincides with that where the superconductivity appears in $SrFe_2As_2$ at low temperature [3, 4]. In order to investigate this relation, it is necessary to measure the temperature dependence of ^{57}Fe Mössbauer spectra in $SrFe_2As_2$ under high pressure.

References

1. Kamihara, Y., et al.: J. Am. Chem. Soc. **130**, 3296 (2008)
2. Tegel, M., et al.: J. Phys. Condens. Matter **20**, 452201 (2008)
3. Kotegawa, H., et al.: J. Phys. Soc. Jpn. **78**(8), 083702 (2009)
4. Matsubayashi, K., et al.: J. Phys. Soc. Jpn. **78**(7), 073706 (2009)
5. Ikeda, S., et al.: J. Phys. Soc. Jpn. **81**, 033703 (2012)
6. Kobayashi, H., et al.: J. Phys. Condens. Matter. **9**, 515 (1997)
7. Uhoya, W.O., et al.: J. Phys. Condens. Matter **23**, 122201 (2011)

Hyperfine Interact (2012) 208:13–18
DOI 10.1007/s10751-012-0573-z

Characterization of mineral phases of agricultural soil samples of Colombian coffee using Mössbauer spectroscopy and X-ray diffraction

Humberto Bustos Rodríguez · Dagoberto Oyola Lozano · Yebrayl Antonio Rojas Martínez · Marlene Rivera Pinilla · German Antonio Pérez Alcázar

Published online: 3 February 2012

Abstract Soil chemical analysis, X-ray diffraction (XRD) and Mössbauer spectrometry (MS) of ^{57}Fe were used to characterize mineral phases of samples taken from the productive layer (horizon A) of agricultural coffee soil from Tolima (Colombia). Chemical analysis shows the chemical and textural parameters of samples from two different regions of Tolima, i.e., Ibagué and Santa Isabel. By XRD phases like illite (I), andesine (A) and quartz (Q) in both samples were identified. The quantity of these phases is different for the two samples. The MS spectra taken at room temperature were adjusted by using five doublets, three of them associated to Fe^{+3} type sites and the other two to Fe^{+2} type sites. According to their isomer shift and quadrupole splitting the presence of phases like illite (detected by DRX), nontronite and biotite (not detected by XRD) can be postulated.

Keywords X-ray diffraction · Mössbauer spectrometry

1 Introduction

Numerous studies of soils [1–12] have been made in many countries by using the combination of the X ray diffraction (XRD) and Mössbauer spectrometry (MS) (even Mössbauer analyses of Martian soil [13] have been reported). Coffee is the most important agricultural product of Colombia. From the historical point of view, coffee has been very important for the country, not only by being the basis of a

H. Bustos Rodríguez (✉) · D. O. Lozano · Y. A. R. Martínez · M. R. Pinilla
Universidad del Tolima, Grupo Ciencia de Materiales y Tecnología en Plasma,
A.A.546, Ibagué, Colombia
e-mail: hbustos@ut.edu.co

G. A. P. Alcázar
Universidad del Valle, Grupo Metalurgia Física y Teoría de las Transiciones de Fase,
A.A.25360, Cali, Colombia

Table 1 Chemical parameters of two samples from topsoil cultivation of coffee taken from Tolima (Colombia)

Sample	pH	CIC[a]	0M %	P[b]	Ca[a]	Mg[a]	Na[a]	K[a]	Fe[b]	Cu[b]	Zn[b]	Mn[b]	B[b]	S[b]	Al[a]
1911-Ibague	6,1	20,9	3,2	15,7	6,4	2,2	0,2	0,18	16,8	1,6	2,1	24	1,1	24,8	0
1673-Santa Isabel	7,3	16	6,1	59	4	2,9	0,2	0,27	10,4	0,1	2,4	8,8	0,9	58	0

OM organic matter

[a]meq. $(100\ g)^{-1}$

[b]mg. Kg^{-1}

The methodology basically quantifies the available iron in the soil for plant nutrition, namely the Iron (Fe^{+2}). The aluminum content is zero, since this element is of no importance in agricultural soils when the pH of these is greater than 5.6

production known worldwide, but because it has played a key role in the formation of the cultural and social structure of Colombia.

In this work we report on a study of the chemical, structural and hyperfine properties of coffee agricultural soils collected from two regions of Tolima Department (Colombia), in the municipalities of Ibague (sample 1911) and Santa Isabel (sample 1673), the last one catalogued as the mildest coffee of Colombia. The chemical analysis was performed by using procedures established by ICA (Colombian Agricultural Institute) [14].

2 Experimental procedure

The samples were collected, prepared and chemically analyzed according to procedures established by ICA (Colombian Agricultural Institute). They were collected from the productive layer (horizon A) and were obtained from 0 to 20 cm depth. The physical-chemical analysis was performed in the laboratory of soils (LASEREX) of the University of Tolima, Colombia. The samples were measured in a transmission Mössbauer spectrometer using a Co-57/Rh source in the Materials Science Laboratory of the University of Tolima, Colombia. The spectra were fitted by using the MOSFIT program [15] and pure α-Fe was used for calibration. The XRD analysis to establish the structure and the lattice parameters were performed at room temperature for all samples using the Panalytical X-Pert diffractometer of the University of Valle, Colombia with the Cu-Kα radiation, and the patterns were refined using the Maud program [16].

3 Results and discussion

The physical-chemical analysis yielded texture parameters (percentage of clay, silt and sand) and chemical parameters such as pH, the percentage of organic matter and elements contents, particularly P, Ca, Mg, Na, K, Fe, Cu, Zn, Mn, B and S. The methodology basically quantifies the available iron in the soil for plant nutrition, namely the ferrous iron. The aluminum content is zero, since this element is of no importance in agricultural soils when the pH of these is greater than 5.6. The pH and CEC (Cation Exchange Capacity) chemical parameters, obtained by physical-chemical analysis (Table 1) indicate more acidity in the productive layer of the Santa

Table 2 Texture parameters of two samples from topsoil cultivation of coffee taken from Tolima (Colombia)

Sample	Sandy (%)	Silt (%)	Clay (%)
1911-Ibague	12,5	18	69,5
1673-Santa Isabel	10,5	20	69,5

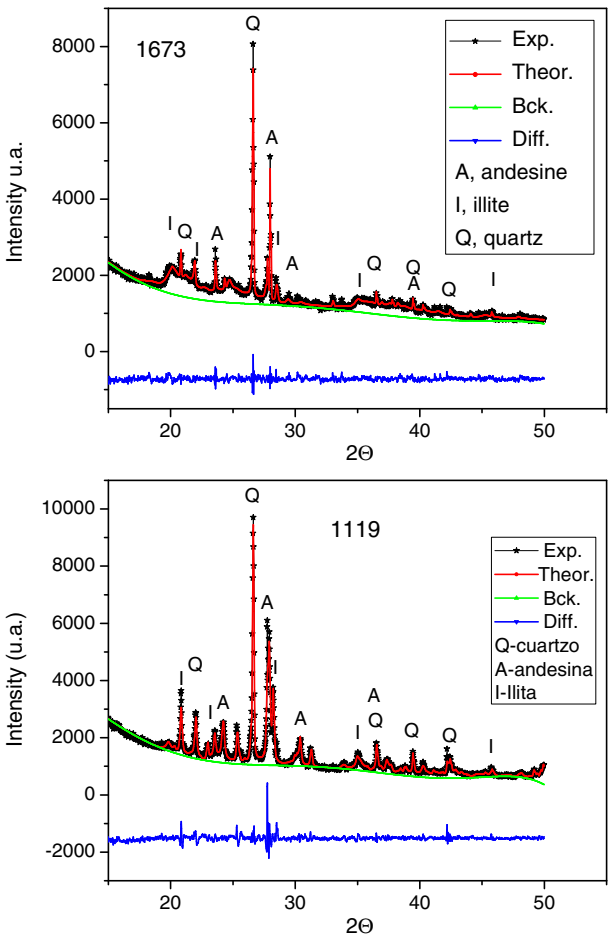

Fig. 1 X-ray patterns of samples taken from the productive layer (horizon A) of agricultural coffee soil-grown from Tolima (Colombia)

Isabel region (sample 1673) and a greater ability to retain nutrients in the productive layer in the Ibague region (sample 1911). Also, a higher content of iron (Fe^{+2}) is found in the productive layer of the Ibague region. Table 2, presents the texture parameters. It can be noted that the two productive layers have an equal content of clay, a higher content of sand for the Ibagué region and a higher content of silt for the Santa Isabel region.

X-rays diffraction patterns of the samples are shown in Fig. 1. The refinement of the XRD patterns showed the presence of quartz (Q), andesine (A) and illite (I) phases. The quantitative analysis shows that sample 1119 contains (in wt. %):

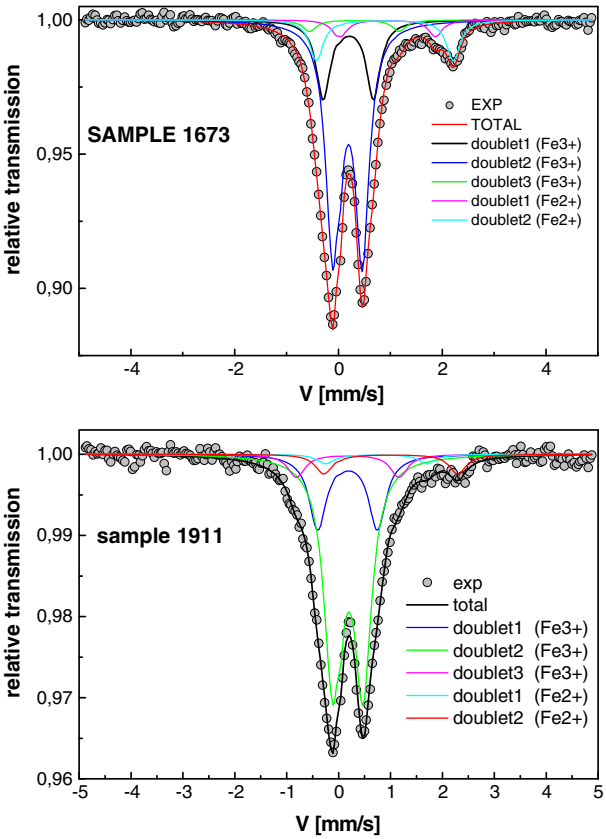

Fig. 2 Mössbauer spectra of samples taken from the productive layer (horizon A) of agricultural coffee soil-grown from Tolima (Colombia)

Table 3 Hyperfine parameters obtained for mineral samples

Sample	Doublet	IS (mms^{-1}) ±0.050	QS (mms^{-1}) ±0.050	Area (%)
1911-Ibague	1 (Fe3+)	0,397	1,110	21
	2 (Fe3+)	0,404	0,543	64
	3 (Fe3+)	0,398	1,938	6
	4 (Fe2+)	0,950	1,913	3
	5 (Fe2+)	1,231	2,543	6
1673- Santa Isabel	1 (Fe3+)	0.416	0.931	21
	2 (Fe3+)	0.400	0.528	61
	3 (Fe3+)	0.530	1.687	3
	4 (Fe2+)	1.160	1.830	4
	5 (Fe2+)	1.120	2.600	11

8.384 ± 0.011 of Q, 69.360 ± 0.002 of A, and 22.256 ± 0.005 of I. Sample 1673 contains: 32.823 ± 0.002 of Q, 57.583 ± 0.002 of A, and 9.595 ± 0.002 for I. In both samples andesine is the majority phase.

Figure 2 shows the room temperature Mössbauer spectra of the samples. Both spectra were fitted with five paramagnetic doublets. By using the MOSFIT adjustment program the hyperfine parameters (Table 3) of these sites were calculated. For

fitting the spectra three Fe^{+3} sites and two Fe^{+2} sites were required. From the isomer shift and quadrupole splitting parameters, the possible presence of illite (I), biotite (B) and nontronite (N) can be postulated. Illite was detected by XRD, but biotite and nontronite were not, showing that these two phases are present with a wt. % lest that 2%.

4 Conclusions

In the sample of Santa Isabel region (mildest coffee), a minor presence of iron (Fe^{+2}) has been determined by physic-chemical analysis and using Mössbauer spectrometry it was found that there are equal numbers of sites of iron (three sites of Fe^{+3} and two sites of Fe^{+2}). By comparing the hyperfine parameters with the values given in the Mössbauer Mineral Handbook [17] we propose illite, biotite and nontronite as possible iron phases present in the soils.

Acknowledgements The authors would like to thank to the Central Committee of Research of the University of Tolima, for the financial support given. Similarly, the authors thank Dr. Friedrich Wagner from the Physics Department of Technical University of Munich, Germany, for his valuable scientific advice.

References

1. Tanejaa, S.P., Rajb, D.: Mössbauer and X-ray studies of soils. Nucl. Instrum. Methods Phys. Res., B Beam Interact. Mater. Atoms **76**(1–4), 233–235 (1993)
2. Cerón Loayza, M.L.: Estudio mineralógico de suelos agrícolas por espectroscopia Mössbauer. Tesis de Maestría. UNBA (2001)
3. Mijovilovich, A.E.: Estudio Mössbauer de óxidos e hidróxidos de Fe: Aplicación al estudio de suelos. Doctoral Tesis. UNBA (1997)
4. Mijovilovich, A.E., Morras, H., Causevic, H., Saragovi, C.: Mössbauer study of the mineralogy in two different Argentine soils. Hyperfine Interact. **122**, 83–95 (1999)
5. Gunnlaugsson, H.P., Rasmussen, H., Madsen, M.B., Nørnberg, P.: New analysis of the Mössbauer spectra of olivine basalt rocks from Gusev crater on Mars. Planet. Space Sci. **57**, 640–645 (2009)
6. Hidalgo, C., Etchevers, J.D., Martínez-Richa, A., Yee-Madeira, H., Calderon, H.A., Vera-Graziano, R., Matus, F.: Mineralogical characterization of the fine fraction (< 2 μm) of degraded volcanic soils and tepetates in Mexico. Appl. Clay Sci. **49**, 348–358 (2010)
7. Kirwan, L.J., Deeney, F.A., Croke, G.M., Hodnett, K.: Characterization of various Jamaican bauxite ores by quantitative Rietveld X-ray powder diffraction and 57Fe Mössbauer spectroscopy. Int. J. Miner. Process. **91**, 14–18 (2009)
8. Bustos Rodríguez, H.: Estudio de propiedades electrónicas y estructurales de muestras minerales de menas auríferas colombianas, mediante el uso de microscopia óptica, espectrometría Mössbauer, difracción de rayos-x, SIMS y LAM-ICP-MS. Ph.D. Physical Sciences Tesis, Universidad del Valle (2006)
9. Bustos Rodríguez, H., Rojas Martínez, Y., Oyola Lozano, D., Pérez Alcázar, G.A., Fajardo, M., Mojica, J., Molano, J.C.: Hyperfine Interact. **161**, 61–68 (2005)
10. Bustos Rodríguez, H., Oyola Lozano, D., Rojas Martínez, Y.A., Pérez Alcázar, G.A., Balogh, A.G.: Invisible gold in Colombian auriferous soils. Hyperfine Interact. **166**, 605–611 (2005)
11. Bustos Rodríguez, H., Oyola Lozano, D., Rojas Martínez, Y.A., Pérez Alcázar, G.A., Flege, S., Balogh, A.G., Cabri, L.J., Tubrett, M.: Mineralogical analysis of auriferous ores from the El Diamante mine, Colombia. Hyperfine Interact. **175**, 195–206 (2007)
12. Ipus, J.J., Mojica, J., Pérez Alcázar, G.A.: Caracterización de arcillas colombianas por espectroscopia Mössbauer y difracción de rayos-x. Rev. Colomb. Fís. **37**(1), 187–190 (2005)

13. Gunnlaugsson, H.P., Rasmussen, H., Madsen, M.B., Nørnberg, P.: New analysis of the Mössbauer spectra of olivine basalt rocks from Gusev crater on Mars. Planet. Space Sci. **57**, 640–645 (2009)
14. ICA, Fertilizantes en diversos cultivos, Centro Experimental Tibaitata, octubre (1981)
15. Larson, A.C., Von Dreele, R.B.: General Structure Analysis System (GSAS). Los Alamos National Laboratory Report LAUR 86–748 (2004)
16. Varret, F., Teillet, J.: Unpublished MOSFIT program (1976)
17. Stevens, J.G., Khasanov, A.M., Miller, J.W., Pollak, H., Li, Z.: Mössbauer mineral handbook. Mössbauer Effect Data Center (2002)

Hyperfine Interact (2012) 208:19–23
DOI 10.1007/s10751-011-0471-9

Orbital order in layered manganites probed with ^{57}Fe Mössbauer spectroscopy

Yutaka Ueda · Kiyoshi Nomura · Alexandre I. Rykov

Published online: 29 November 2011

Abstract In mixed-valence manganites, the doped iron species play the roles of simultaneous probes and ruiners for the orbital order occurring in the Mn-O electronic subsystem. We investigated the Mn^{3+}-based undoped system $RBaMn_2O_{5.5}$ and the half-doped systems $RBaMn_2O_6$, and $RBaMn_2O_5$ substituting a tiny portion of Mn^{3+} sites with Fe^{3+}. Single-site Mössbauer spectra were observed at room temperature in the charge-orbitally ordered state, i.e., below T_{COO}, for R=Y, Sm, Gd. Size of the rare earth ion strongly influences the quadrupole splitting in $RBaMn_2O_6$, but not in $RBaMn_2O_5$.

Keywords Mixed valence · Fe-doped manganites · A-site ordered perovskites · Mössbauer spectra · Effect of rare-earth ionic size on quadrupole splitting

1 Introduction

Charge and orbital order (COO) in manganites can melt under magnetic field, so that the material becomes metallic. Under application of very high magnetic fields the drop in resistance is colossal, however, smaller magnetic fields are sufficient to melt the less stable COO in manganites doped with Fe. In high-T_c (high-T_{COO})

Y. Ueda · A. I. Rykov
Institute for Solid State Physics, The University of Tokyo, 5-1-5 Kashiwanoha, Kashiwa, 277-8581, Chiba, Japan

K. Nomura · A. I. Rykov
Graduate School of Engineering, The University of Tokyo, Hongo 7-3-1, 113-8656, Tokyo, Japan

A. I. Rykov (✉)
Mössbauer Effect Data Center, Dalian Institute of Chemical Physics, Chinese Academy of Sciences, 457 Zhongshan Road, Dalian 116023, China
e-mail: rykov@dicp.ac.cn

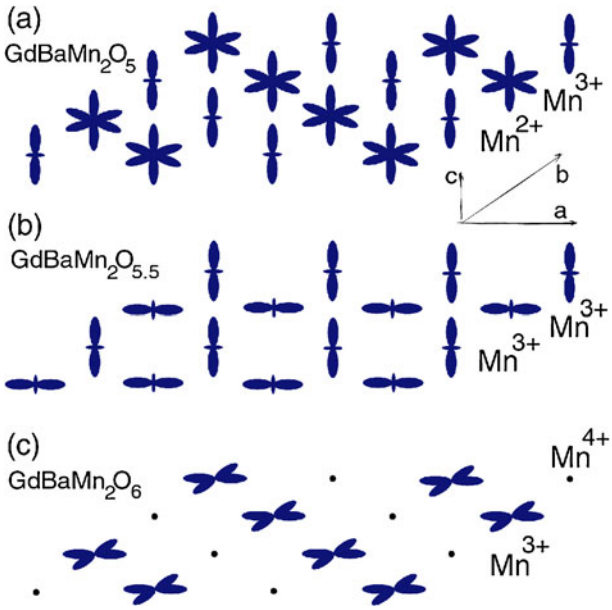

Fig. 1 Orbital order within one layer of $GdBaMn_2O_{5+y}$ (y = 0, 0.5 and 1). Filled states of the orbital e_g-doublet are depicted

manganites, Fe doping at the level of 2% suppresses the value of T_{COO} by 40 or 50 K [1]. The value of T_{COO} monotonically decreases with increasing atomic size of rare earth, but remains above room temperature for such low doping levels as 2% of Fe (cf. T_{COO} = 450 K and T_{COO} = 350 K in $YBaMn_{1.96}Fe_{0.04}O_6$ and in $SmBaMn_{1.96}Fe_{0.04}O_6$, respectively). Thin films of such materials as $SmBaMn_2O_6$ are expected to show the gigantic and ultrafast responses arising from COO melting that makes these materials very attractive for correlated electron device technologies [2].

In the structure of the layered mixed-valence manganites $RBaMn_2O_{5+y}$ the large-size cations R^{3+} and Ba^{2+} form the separate layers alternating along c-axis with MnO_{1+y} layers. For the oxygen content (5+y) values of 5, 5.5 or 6 all the MnO_{1+y} layers are identical to each other. Each layer accommodates the charge and orbital order between Mn^{2+} and Mn^{3+} (y = 0), Mn^{3+} and Mn^{3+} (y = 0.5) and Mn^{3+} and Mn^{4+} (y = 1) shown in Fig. 1.

2 Experimental

Non-conventional multistep gas-heat-treatment procedures were used to synthesize these ^{57}Fe-doped powdered samples for R=La, Pr, Nd, Sm, Gd, Y. Integer-valued and half-integer-valued oxygen contents (y = 0, y = 0.5 and y = 1) in $RBaMn_2O_{5+y}$ are well-defined and isolated. They are stabilized owing to the orbital ordering of three different types shown in Fig. 1. However, easy sample annealing in reducing or oxidizing gas atmospheres may not lead to these orbitally ordered states. A-site disordered perovskites would result with no superstructure. Instead, in the A-site of the parent perovskite structure, the large-size cation R^{3+} and Ba^{2+} layered arrangement must be formed beforehand. The layered R-Ba superstructure becomes a crucial prerequisite for the orbital order of the Mn-O network. The layer-growing

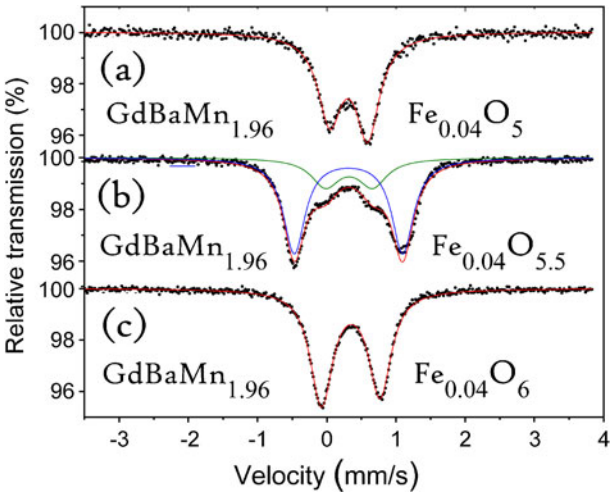

Fig. 2 Room-temperature Mössbauer spectra in $GdBaMn_2O_{5+y}$ ($y = 0$, 0.5 and 1). Isomer shifts of the main doublet are 0.316(2), 0.313(2) and 0.345(1) mm/s relative α-Fe and quadrupole splittings are 0.547(3), 1.567(3), and 0.850(3) mm/s for $y = 0$, 0.5 and 1, respectively

treatment in the clean reducing 6 N Ar atmosphere at 1,350°C was always necessary to obtain the A-site ordered deoxygenated structures ($y = 0$) at the first synthesizing step [3–5]. Subsequently, oxygenating and reducing treatments in layer-preserving regimes at low temperature (~500°C) allowed varying only the oxygen contents and related orbital arrangements within Mn-O layers.

3 Results and Discussion

When a small amount of manganese is substituted with iron we observe that all Fe ions take the form of Fe^{3+}. All the Fe^{3+} ions reside in the sites of Mn^{3+}. This is not surprising because the Mn^{3+} and Fe^{3+} ions are very similar in size. In contrast, the site of Mn^{4+} is too small for Fe^{3+} and the site of Mn^{2+} is too large for Fe^{3+}.

Against the similarity of ionic sizes and charges, the orbital properties of the Mn^{3+} and Fe^{3+} ions are very different. The Jahn-Teller (JT) ion Mn^{3+} tends to sit in a low-symmetry environment. The symmetry degrades when only one of e_g orbitals is half-filled. However, for Fe^{3+} ion both of the e_g orbitals are half-filled, so that the semi-closed d-shell of Fe^{3+} is spherically symmetric. Unlike to the JT ions, such as Mn^{3+} or Cu^{2+}, the ion Fe^{3+} have no valence contribution to the electric field gradient (EFG) at the place of ^{57}Fe nuclei. Therefore, when Fe^{3+} is placed at the octahedral site of Mn^{3+} the observed quadrupole splitting reproduces faithfully the distortion of octahedral environment of Mn^{3+}.

In agreement with the number of the non-equivalent structural positions for Mn^{3+} the Mössbauer spectra are single-site in oxygen-depleted (O_5) and oxygen-saturated (O_6) samples, but show two doublets for the intermediate oxygen content (Fig. 2). In the latter case, the major doublet comes from the site with the in-plane orientation of the principal component of EFG. The minor subspectrum for $y = 0.5$, as well as the spectra for $y = 0$ and $y = 1$ come from sites with out-of-plane orientation of the main component of EFG ($V_{ZZ} \perp MnO_{1+y}$ planes).

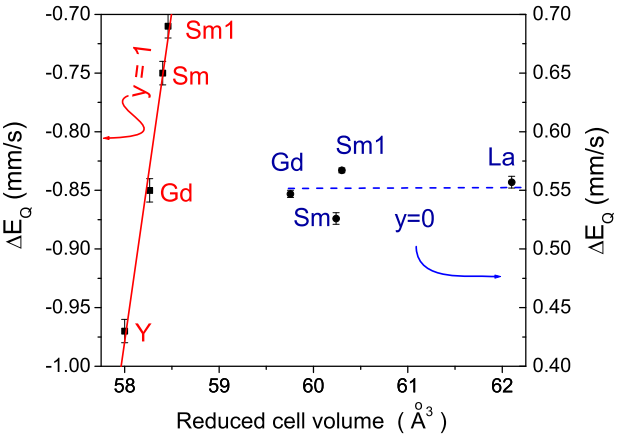

Fig. 3 Dependence of the room-temperature quadrupole splitting on the volume of reduced (perovskite-like) cell in $RBaMn_2O_{5+y}$ (y = 0 and 1). The symbol Sm1 denotes the compounds $Sm_{0.9}Nd_{0.1}BaMn_{1.96}Fe_{0.04}O_5$ and $Sm_{0.9}Nd_{0.1}BaMn_{1.96}Fe_{0.04}O_6$

The 5-fold and 6-fold coordinations adopted by the Fe^{3+} ions are pyramidal in (a) and (b, minor doublet) and octahedral in (b, major doublet) and (c). Basically, they are the same as for Mn^{3+}. However, due to the difference of the orbital configurations of the Fe^{3+} and Mn^{3+} ions there appears some difference between the FeO_5 and MnO_5 pyramids [5]. Exact locations of the dopant Fe^{3+} and host Mn^{3+} inside of the pyramid do not coincide. The isotropic dopant ion Fe^{3+} is shifted towards the apex to equalize the fifth out-of-plane Fe-O distance with the four in-plane distances. In absence of such a shift we must expect much larger quadrupole splitting than observed.

Filling the in-plane orbital of the e_g-doublet in $RBaMn_2O_6$ (Fig. 1, c) induces in MnO_6 octahedra the strong vertical contraction that is reflected in the value of quadrupole splitting. The contraction is enhanced with smaller size of the rare earth R. Therefore, the absolute value of quadrupole splitting ΔE_Q increases when the volume of the reduced cell (perovskite-like cell) decreases (left-hand linear dependence in Fig. 3). On the other hand, in $RBaMn_2O_5$, where the thickness of the MnO_2 layer is determined mainly by the spherically symmetric ion Mn^{2+}, the value of ΔE_Q is roughly independent of the size of rare-earth ion R^{3+} (right-hand line in Fig. 3).

Asymmetry between the doublet line intensities arises mainly from platy habitus of layered crystals whose main surfaces are perpendicular to V_{ZZ}. The out-of-plane and in-plane 3d-orbitals are the half-filled orbitals of Mn^{3+} in the O_5 and O_6 cases, where $V_{ZZ} > 0$ and $V_{ZZ} < 0$, respectively. The opposite signs of V_{ZZ} results in opposite doublet asymmetries in Fig. 2 (a) and (c) owing to platy habits of microcrystals aligned in the plane of Mössbauer absorber. Additionally, a smaller asymmetry contribution exists owing to vibrational anisotropy. The total asymmetry is somewhat enhanced by this effect (Goldanskii–Karyagin) in O_6, but weakened in O_5 case [1, 6].

The orientation of V_{ZZ} along the vertical axis of the tetragonal P4/mmm modification [5] is obviously dictated for all R (except Y) in $RBaMn_2O_6$ by the axial site symmetry. The signs of V_{ZZ} are always confirmed by the ionic point charge model. Applying the ionic model to FeO_5 pyramid (y = 0), one expects the positive sign of V_{ZZ} as observed. For the octahedron (y = 1), strongly compressed along

vertical direction, the ionic model gives $V_{ZZ} < 0$. Although $YBaMn_2O_6$ undergoes monoclinic distortion at T_{COO}, this relatively small distortion has no effect on quadrupole splitting. As shown by linear fit in Fig. 3 and by our structure refinements, the vertical compression of octahedron increases quickly with decreasing the volume of perovkite cell; this strong compression continues to determine the value of quadrupole splitting even in presence of additional monoclinic distortion.

The fact that only one Mn^{3+} site exists in the cases of O_5 and O_6 Mössbauer spectra shows that the charge-ordered domains are configured under control of the frozen disorder of Fe. Random distribution of the Fe dopants tends to break down the ordered domains; however, the charge order would be reconstructed, centering all Mn^{3+} sites at Fe^{3+} ions. In contrast, two distinct Mn^{3+} sites exist in the $O_{5.5}$ phases synthesized at 1,450°C [5]. On cooling the iron dopants fall out preferentially into the octahedral sites of $GdBaMn_2O_{5.5}$, so that the population of pyramidal Fe species (inner doublet area) is found to be 4 times smaller.

References

1. Rykov, A.I., Ueda, Y., Nomura, K., Seto, M.: Phys. Rev. B **79**, 224114 (2009)
2. Ogimoto, Y., Nakamura, M., Harada, N., Ogawa, N., Miyano, K.: Math. Sci. Eng. B **173**, 51–56 (2010)
3. Millange, F., Caignaert, V., Domenges, B., Raveau, B.: Chem. Mater. **10**, 1974 (1998)
4. Nakajima, T., Kageyama, H., Ueda, Y.: J. Phys. Chem. Solids **63**, 913 (2002)
5. Rykov, A.I., Ueda, Y., Nomura, K.: J. Solid State Chem. **182**, 2157–2166 (2009)
6. Rykov, A.I., Seto, M., Ueda, Y., Nomura, K.: J. Appl. Crystallogr. **42**, 496–501 (2009)

Hyperfine Interact (2012) 208:25–28
DOI 10.1007/s10751-011-0432-3

^{151}Eu Mössbauer measurements of $CuLa_{1-x}Eu_xO_2$ with luminescent property

Fumito Fujishiro · Takuya Hashimoto · Masashi Takahashi

Received: 31 August 2011 / Accepted: 16 October 2011 / Published online: 26 October 2011

Abstract An increase of the asymmetric ratio of photoluminescence lines from $CuLa_{1-x}Eu_xO_2$ was observed under 100 K, suggesting a lower site symmetry for the Eu cation. Mössbauer spectra of $CuLa_{0.8}Eu_{0.2}O_2$ measured at 77 K revealed that the valence of Eu is trivalent and that the crystal structure of $CuLa_{1-x}Eu_x$ O_2 might contain a EuO_6 octahedron with lower symmetry. The thermodynamic stability of the valence of Cu and Eu was calculated, showing agreement with Mössbauer spectra.

Keywords $CuLa_{1-x}Eu_xO_2$ · ^{151}Eu Mössbauer spectra · Photoluminescence · Thermodynamic calculation

1 Introduction

Polycrystalline $CuLa_{1-x}Eu_xO_2$ shows orange photoluminescence (PL) at room temperature, which is different from PL observed for usual Eu^{3+} or Eu^{2+} containing materials. The valence of Eu in $CuLa_{1-x}Eu_xO_2$ at room temperature has been clarified to be trivalent from Mössbauer spectroscopy and the origin of the orange PL has been identified as PL lines due to magnetic transitions ($^5D_0$ - $^7F_{0,1}$ transitions) of Eu^{3+} [1].

F. Fujishiro (✉)
Department of Physics, College of Humanities and Sciences, Nihon University, Tokyo, Japan
e-mail: fujishiro@phys.chs.nihon-u.ac.jp

T. Hashimoto
Department of Integrated Sciences in Physics and Biology, College of Humanities and Sciences, Nihon University, Tokyo, Japan

M. Takahashi
Department of Chemistry, Faculty of Sciences, Toho University, Funabashi, Chiba, Japan

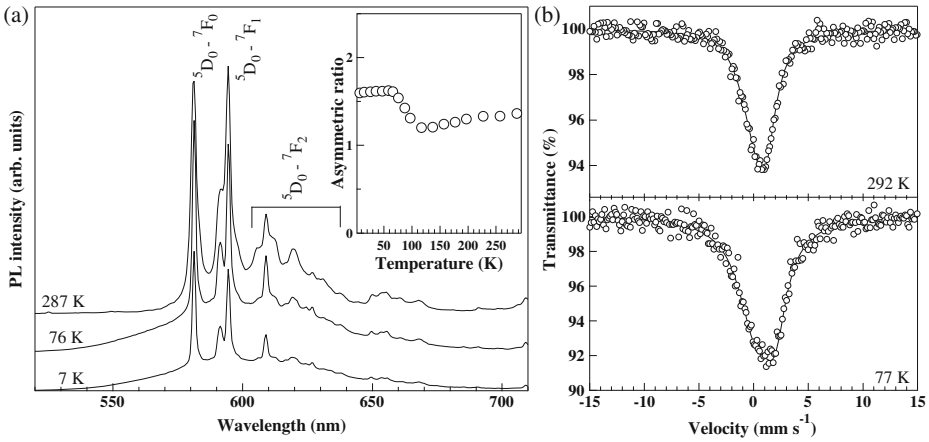

Fig. 1 **a** Photoluminescence spectra of $CuLa_{0.98}Eu_{0.02}O_2$ at 7 K, 76 K and 287 K. The asymmetric ratio is shown in the inset. **b** Mössbauer spectra of $CuLa_{0.8}Eu_{0.2}O_2$ at 292 K and 77 K

In usual Eu^{3+} containing materials, Eu^{3+} is substituted into a site without inversion symmetry due to its large ionic radius, showing a red luminescence due to an electric dipole transition ($^5D_0$ - $^7F_2$ transition). However, for $CuLa_{1-x}Eu_xO_2$, since the Eu^{3+} substitution site is the La^{3+} site in the LaO_6 octahedron with inversion symmetry, which forbids the $^5D_0$ - $^7F_2$ transition, orange PL due to the $^5D_0$ - $^7F_{0,1}$ transition was observed to be more dominant than that due to the $^5D_0$ - $^7F_2$ transition [1]. Therefore, the relative PL intensity of the $^5D_0$ - $^7F_2$ transition to the $^5D_0$ - $^7F_1$ one, which is called the asymmetric ratio, gives a measure of the degree of distortion from the inversion symmetry of the local environment of Eu^{3+} in the matrix [2]. Sharp PL lines due to the dipole transitions of $CuLa_{0.98}Eu_{0.02}O_2$ with little variation as a function of temperature between 7 K and room temperature have been observed, except for an asymmetric ratio enhancement with decreasing temperature below 100 K. This suggests that the valence of Eu would be maintained at this temperature range but that the local environment of the Eu cation might be changed. In this study, in order to analyse the valence and the local environment of the Eu cation by temperature directly, Mössbauer spectroscopy at 77 K and 292 K has been measured on $CuLa_{1-x}Eu_xO_2$. Also a thermodynamic calculation of the valence of Cu and Eu cations was performed to confirm the valence of Eu in $CuLa_{1-x}Eu_xO_2$ evaluated with Mössbauer spectroscopy.

2 Experimental

Single phase $CuLa_{1-x}Eu_xO_2$ was prepared by the solid state reaction method with sintering 1273 K for 12 h under N_2 gas flow [1]. ^{151}Eu Mössbauer spectra were measured at 77 and 292 K using γ-rays from a $^{151}Sm/SmF_3$ light source. The isomer shift was calculated with respect to that of EuF_3 as a standard. PL spectra were measured with excitation laser light of the UV line from a continuous wave He-Cd laser (325 nm) at temperatures between 7 K and 287 K.

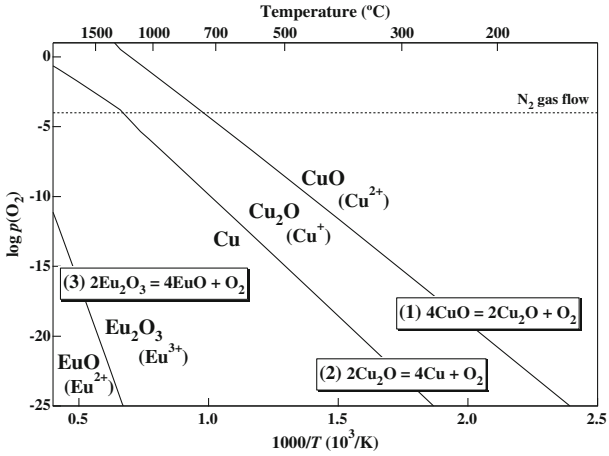

Fig. 2 Ellingham diagram for copper oxides and eurpium oxide. The *dotted line* represents log $p(O_2)$ under N_2 gas flow

3 Results and discussion

Figure 1a shows PL spectra of $CuLa_{0.98}Eu_{0.02}O_2$ at 7 K, 76 K and 287 K. As shown in the inset, the asymmetry ratio increased abruptly at 100 K with decreasing temperature, suggesting that the octahedron in which the Eu cation was substituting for La would distort in this temperature range.

Mössbauer spectra of $CuLa_{0.8}Eu_{0.2}O_2$ at 292 K and 77 K are shown in Fig. 1b. Isomer shifts are 0.62 mm s^{-1} at 292 K and 0.68 mm s^{-1} at 77 K, which can be indexed as absorption for trivalent Eu [3]. The absorption of Eu^{2+} that should be observed around 13 mm s^{-1} [4] was not observed, indicating that the valence of Eu cation was trivalent both at 292 K and 77 K. Although it is difficult to determine the accurate quadrupole coupling constants (e^2qQ) and asymmetric parameter (η) due to rather large linewidth for the $I = 5/2$ to 7/2 transitions of ^{151}Eu, the e^2qQ and η values at 292 K are estimated to be 7.5 mm s^{-1} and 0.47, respectively. At 77 K, these values increased to 8.7 mm s^{-1} and 0.54, suggesting that the crystal structure of $CuLa_{1-x}Eu_xO_2$ might contain a distorted octahedron at low temperature, in agreement with the increase of the asymmetric ratio of the PL spectra.

Trivalent Eu in $CuLa_{1-x}Eu_xO_2$ detected with Mössbauer spectroscopy and suggested in the PL spectra also showed correspondence with a thermodynamic calculation. Figure 2 shows coexistence lines of Cu_2O/CuO [5], Cu/Cu_2O and EuO/Eu_2O_3 calculated using program MALT-2 [6]. For the preparation of $CuLa_{1-x}Eu_xO_2$, sintering was performed at 1273 K under N_2 gas flow with oxygen partial pressure, $p(O_2)$, of about 10^{-4} atm. It has been revealed that monovalent Cu and trivalent Eu were thermodynamically stable in sintering conditions, which corresponds to the observed Mössbauer spectroscopy results.

4 Conclusion

Mössbauer spectra of $CuLa_{0.8}Eu_{0.2}O_2$ at 77 K revealed that the valence of Eu is trivalent and suggested that the crystal structure of $CuLa_{1-x}Eu_xO_2$ might contain a lower symmetry site for Eu^{3+} in the octahedron, which accounts for the increase

of the asymmetric ratio of PL spectra. A thermodynamic calculation elucidated the stability of Cu^{+} and Eu^{3+} under the preparation conditions, in agreement with the Mössbauer spectroscopy results.

Acknowledgements We would like to thank Prof. M. Matsuo (Department of Multidisciplinary Sciences, Graduate School of Arts and Sciences, The University of Tokyo) for useful discussions. We are also grateful to Prof. S. Mochizuki (College of Humanities and Sciences, Nihon University) for performing PL measurements. This work was financially supported by a grant from the "Strategic Research Base Development" Program for Private Universities Subsidized by MEXT (2009).

References

1. Fujishiro, F., Murakami, M., Hashimoto, T., Takahashi, M.: Orange luminescence of Eu^{3+}-doped $CuLaO_2$ delafossite oxide. J. Ceram. Soc. Jpn. **118**, 1217–1220 (2010)
2. Nogami, M., Enomoto, T. Hayakawa, T.: Enhanced fluoresscence of Eu^{3+} induced by energy transfer from nanosized SnO_2 crystals in glass. J. Lumin. **97**, 147–152 (2002)
3. Tanabe, S., Hirao, K., Soga, N.: Mössbauer spectroscopy of ^{151}Eu in oxide crystals and glasses. J. Non-Cryst. Solids **113**, 178–184 (1989)
4. Gerth, G., Kienle, P., Luchner, K.: Chemical effects on the isomer shift in ^{151}Eu. Phys. Lett. **27A**, 557–558 (1968)
5. Hashimoto, T., Koinuma, H., Kishio, K.: Thermodynamic estimation of oxidation ability of various gases used for the preparation of superconducting films at high vacuum. Jpn. J. Appl. Phys. **30**, 1685–1686 (1991)
6. Yokokawa, H., Yamauchi, S., Matsumoto, T.: Thermodynamic database MALT for windows with gem and CHD. Calphad **26**, 155–166 (2002)

Hyperfine Interact (2012) 208:29–32
DOI 10.1007/s10751-011-0483-5

Observation of the charge order in perovskite manganite $Pr_{0.5}Ca_{0.5}MnO_3$ by Mössbauer quadrupole effect

Shin Nakamura · Akio Fuwa · Yorihiko Tsunoda

Published online: 23 November 2011

Abstract The charge order in a perovskite manganite $Pr_{0.5}Ca_{0.5}MnO_3$ was investigated by Mössbauer spectroscopy. The quadrupole splitting and the absorption line width jump to an increase when lowering the temperature below 230 K (T_{co}), which is indicative of a phase transition to a monoclinic structure due to the charge ordering, or due to a local Jahn-Teller effect due to the presence of Mn^{3+} ions. The intensity ratio of the doublet lines also changes at T_{co}. Local and dynamical Jahn-Teller effect (polarons) with a relaxation time of 10^{-8} s is present even in the metallic state.

Keywords Perovskite manganite · $Pr_{0.5}Ca_{0.5}MnO_3$ · Charge order · ^{57}Fe Mössbauer spectroscopy · Quadrupole effect

1 Introduction

The half-doped perovskite manganite $Pr_{0.5}Ca_{0.5}MnO_3$ has an orthorhombic structure (*Pnma*) with lattice constants $a = 5.403$ Å, $b = 7.612$ Å, $c = 5.395$ Å at room temperature [1]. The material shows a metal-to-insulator (MI) transition at 230 K (T_{co}) due to the Mn^{3+}-Mn^{4+} charge and orbital ordering [2, 3]. Upon a further decrease in temperature, the material turns into a CE type antiferromagnet with $T_N = 180$ K. Goff and Attfield [4] proposed that the charge ordered structure has a monoclinic symmetry ($P2_1/m$) with lattice constants $a = 10.8700$ Å, $b = 7.488923$ Å,

S. Nakamura (✉)
Department of Science and Engineering, Teikyo University, Utsunomiya 320-8551, Japan
e-mail: shin@koala.mse.teikyo-u.ac.jp

S. Nakamura
Advanced Research Institute of Science and Engineering, Waseda University, Shinjuku-ku, Tokyo 169-8555, Japan

A. Fuwa · Y. Tsunoda
Faculty of Science and Engineering, Waseda University, Shinjuku-ku, Tokyo 169-8555, Japan

$c = 5.3499$ Å, and $\beta = 90.069°$ at 10 K. The structure contains three independent Mn sites, Mn1, Mn2a, and Mn2b, occupied by Mn^{4+}, Mn^{3+}, and Mn^{3+} ions respectively. The phenomenon has been intensively investigated mostly by diffraction, transport and static magnetic measurements, while measurements concerning its dynamic property and local structure have not been conducted so much. Mössbauer spectroscopy is a microscopic and dynamic probe with observation time of 10^{-8} s. Especially the quadrupole interaction is very sensitive to the local structure around the ions of interest. In this research, we have applied Mössbauer spectroscopy in order to investigate the change in local structure around Mn ions caused by the charge ordering in $Pr_{0.5}Ca_{0.5}MnO_3$.

2 Experiments

A single crystal of $Pr_{0.5}Ca_{0.5}MnO_3$ with 0.5% ^{57}Fe substituting for Mn was prepared by the FZ method in oxygen atmosphere. The resistivity measurement confirmed that the specimen still exhibits the MI transition around 230 K. A (121) plane disk with 6.2 mm diameter and 70 μm thickness was used as absorber. The ^{57}Fe Mössbauer spectroscopy was conducted in conventional transmission geometry by using ^{57}Co-in-Rh (25 mCi) as the γ ray source. The Doppler velocity scale was calibrated with respect to Fe-metal. Lorentzian line shapes were assumed for the analysis.

3 Results and discussions

In Fig. 1, the spectra around T_{co} are shown. The spectrum consists of an asymmetric doublet with intensity ratio $I_2/I_1 = 0.90$ at 298 K. The isomer shift (IS) and quadrupole splitting (QS) at 298 K are 0.36 mm/s and 0.14 mm/s, respectively, indicating that the substituting ^{57}Fe ions are in 3+ state and correctly occupy octahedral Mn sites. Using the structure parameters [1] and assuming a point charge model for the electric potential of i-element $V^{(i)}$, the electric field gradient (EFG) tensor can be calculated by the summation over lattice, $V_{pq} = \sum_i \left(\partial^2 V^{(i)}/\partial p \partial q\right)$. Here (p, q) denote (x, y, z). Diagonalizing the 3×3 matrix yields $QS_{cal} = 0.10$ mm/s and $(I_1/I_2)_{cal} = 0.93$ (with $\eta = 0.8$, $\theta = 73°$, and $\varphi = 18°$), both of which coincide well with the observations. Below 230 K, a broadening of the spectrum and an increase of the QS are seen. It is not clear whether the spectrum is composed of three subspectra corresponding to Mn1, Mn2a, and Mn2b sites, but here we analyze it to be one doublet. The spectra at 150 K, 79 K, and 4.2 K are clearly split by a magnetic hyperfine field, which is well consistent with the antiferromagnetic nature of this material. Unfortunately we cannot determine $e^2qQ/2$ in the magnetically ordered state, since we do not have information about the directions of the EFG axes. Hereafter we concentrate on the parameters in the paramagnetic region.

The IS increases almost linearly with decreasing temperature and no change is seen at 230 K. This indicates that the substituting Fe^{3+} ions remain in the 3+ state through T_{co}. The temperature dependencies of the QS and the absorption line width (W) are shown in Fig. 2. The QS is almost constant above 230 K, but jumps to an increase below 230 K. The QS value reaches 0.33 mm/s at 180 K. By using the structure parameters at 10 K [4], the QS_{cal} at Mn1, Mn2a, and Mn2b sites are

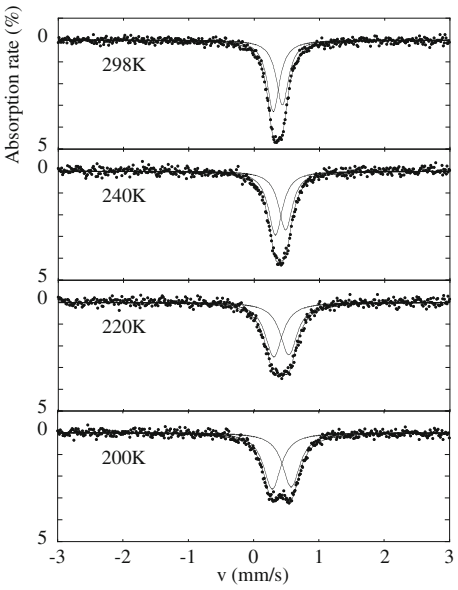

Fig. 1 Mössbauer spectra of ^{57}Fe-substituted $Pr_{0.5}Ca_{0.5}MnO_3$ specimen around the charge order temperature

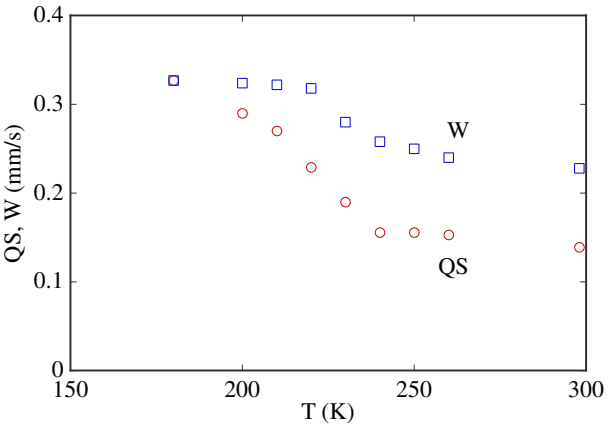

Fig. 2 Temperature dependence of the quadrupole splitting (QS) and the line width (W)

calculated to be 1.97, −0.92 and 0.89 mm/s, respectively. The observed value is not as large as expected, presumably because of the higher measurement temperature, but its increasing nature through T_{co} is just consistent. The W also shows a similar temperature variation. These observations are indicative of a phase transition to a monoclinic structure due to the charge ordering, or to a local Jahn-Teller (JT) effect due to the presence of Mn^{3+} ions. As shown in Fig. 3, the intensity ratio I_2/I_1 also changes to about 0.95 below 230 K. This suggests a change in the EFG axes, which is another plausible consequence of the charge order phase transition.

It is noted in Fig. 2 that W gradually increases with decreasing temperature even in the metallic state (above 230 K). This is abnormal in the sense of usual lattice vibrations. We assume that this is due to the local and dynamical JT effect, or polarons, with a relaxation time of about 10^{-8} s. The presence of such dynamical polarons in

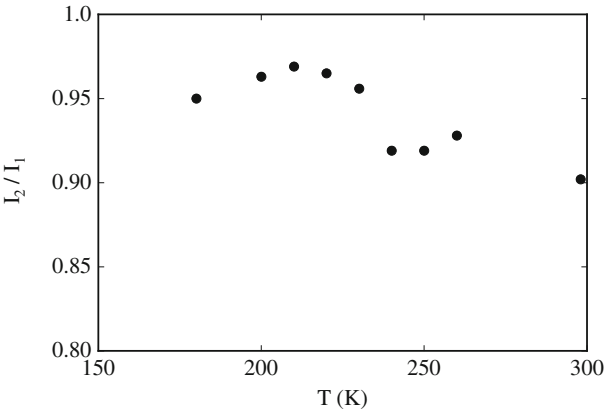

Fig. 3 Temperature dependence of the intensity ratio of doublet lines (I_2/I_1)

the perovskite manganites [5] is considered to be the cause of the high resistivity (10^{-2} Ωcm) in the metallic state.

References

1. Jirák, Z., Krupicka, S., Simsa, Z., Dlouhá, M., Vratislav, S.: J. Magn. & Magn. Mater. **53**, 153 (1985)
2. Tomika, Y., Asamitsu, A., Kuwahara, H., Moritomo, Y., Tokura, Y.: Phys. Rev. **B53**, R1689 (1996)
3. Kajimoto, R., Yoshizawa, H., Tomioka, Y., Tokura, Y.: Phys. Rev. **B63** 212407 (2001)
4. Goff, R.J. , Attfield, J.P. : Phys. Rev. **B70** R140404 (2004)
5. Wakabayashi, N., Shimomura, S., Dai, P., Fernandez-Baca, J.A., Tomioka, Y., Tokura, Y.: Appl. Phys. **A74** S1782 (2002)

Hyperfine Interact (2012) 208:33–37
DOI 10.1007/s10751-011-0529-8

The structural and magnetic behaviour of the $MgFe_{2-x}Cr_xO_4$ spinel ferrite

Abbasher Mahmoud Gismelseed · K. A. Mohammed · M. E. Elzain · H. M. Widatallah · A. D. Al-Rawas · A. A. Yousif

Published online: 5 January 2012

Abstract The crystal structure and magnetic properties of the spinel system $MgFe_{2-x}Cr_xO_4$ (with x = 0, 0.2, 0.4, 0.6, 0.8, 1.0) have been investigated by means of X-ray diffraction (XRD), and Mössbauer spectroscopy. The XRD patterns showed the samples were single-phase cubic spinels. The 295 K Mössbauer spectra of the studied samples showed a continuous collapse of the internal magnetic field for both tetrahedral (A) and octahedral [B] sites with increasing Cr contents. Their 78 K Mössbauer spectra showed an ordered magnetic structure for both sites with the internal magnetic fields decreasing with increasing Cr contents. The continuous decrease in the internal magnetic field is interpreted in terms of the weakening of A-B exchange interaction. The cation distribution at tetrahedral (A) and octahedral [B] sites and its effect on Mössbauer parameters is studied. Mg^{2+} ions are found to occupy both sites A and B, while Cr^{3+} ions occupy site B only.

Keywords Spinel ferrite · Mossbauer spectra · Superexchange interaction · Chromites

1 Introduction

The spinel ferrites are ferrimagnetic oxides with their magnetic cations forming two sublattices, namely the tetrahedral (A) and the octahedral [B] crystallographic sites. The structure of the ideal spinel consists of a cubic close-packed array of anions, with one eighth of the tetrahedral and one half of the octahedral interstices occupied by cations, so that the cation to anion ratio is 3:4 [1].The structural and magnetic environments of these two sites are quite different and are very sensitive to the

A. M. Gismelseed (✉) · K. A. Mohammed · M. E. Elzain · H. M. Widatallah · A. D. Al-Rawas · A. A. Yousif
Department of Physics, College of Science, Sultan Qaboos University, P.O.Box 36, Code 123, Al-khoud, Oman
e-mail: abbasher@squ.edu.om

Table 1 Mössbauer hyperfine parameters at 295 K and 78 K (between parentheses), the cation distribution and the lattice constants of $MgFe_{2-x}Cr_xO_4$. The isomer shift δ (±0.02), quadrupole splitting ΔE_Q (±0.01), and linewidth Γ_3 (±0.01) are in mm/s

x	Site	δ	ΔE_Q	Γ_3	A(%)	Cation distribution	Lattice constant (a)
0.0	A	0.27 (0.35)	0.01 (−0.01)	0.52 (0.54)	49	$(Mg_{0.01}Fe_{0.99})$	8.3924
	B	0.34 (0.43)	0.06 (0.01)	0.56 (0.57)	51	$[Mg_{0.99}Fe_{1.01}Cr_{0.0}]$	
0.2	A	0.25 (0.34)	−0.01 (−0.01)	0.46 (0.47)	55	$(Mg_{0.01}Fe_{0.99})$	8.3896
	B	0.32 (0.43)	0.01 (0.01)	0.44 (0.45)	45	$[Mg_{0.99}Fe_{0.81}Cr_{02}]$	
0.4	A	0.26 (0.36)	−0.01 (0.01)	0.50 (0.52)	62	$(Mg_{0.01}Fe_{0.99})$	8.3806
	B	0.30 (0.41)	0.01 (−0.01)	0.50 (0.52)	38	$[Mg_{0.99}Fe_{0.61}Cr_{0.4}]$	
0.6	A	0.27 (0.36)	−0.01 (−0.01)	0.58 (0.52)	62	$(Mg_{0.13}Fe_{0.87})$	8.3731
	B	0.29 (0.41)	0.01 (0.01)	0.55 (0.52)	38	$[Mg_{0.87}Fe_{0.53}Cr_{06}]$	
0.8	A	0.28 (0.35)	0.01 (0.01)	0.60 (0.55)	59	$(Mg_{0.29}Fe_{0.71})$	8.3666
	B	0.31 (0.39)	−0.04 (0.01)	0.62 (0.52)	41	$[Mg_{0.71}Fe_{0.49}Cr_{0.8}]$	
1.0	A	0.30 (0.37)	0.57 (−0.01)	0.30 (0.78)	67	$(Mg_{0.33}Fe_{0.67})$	8.3624
	B	0.11 (0.38)	0.01 (−0.01)	3.60 (0.54)	33	$[Mg_{0.67}Fe_{0.33}Cr_{1.0}]$	

chemical compositions, preparation sintering temperature and sintering time. Also the type and the amount of cations substitution have very strong effect on the properties. That means it is possible to change the relative strengths of the exchange interactions in spinels by changing the type of the magnetic ions as well as by selective substitution of non-magnetic atoms on the tetrahedral and octahedral sites which lead to interesting spin configurations.

It was reported that substitution of magnetic ion Cr^{3+} in many ideal/mixed spinel ferrites affected the magnetic properties markedly similar to that of non-magnetic substitution [2, 3]. The preference of Cr^{3+} ions for octahedral sites is due to the favourable fit of the charge distribution of these ions in the crystal field of the octahedral sites [4]. In this work the spinel system $MgFe_{2-x}Cr_xO_4$ (with x = 0, 0.2, 0.4, 0.6, 0.8, 1.0) have been prepared, and investigated by means of X-ray diffraction (XRD), and Mössbauer techniques to elucidate the site occupancy of the cations in the system.

2 Experimental

A series of Mg- ferrite substituted by Cr, $MgFe_{2-x}Cr_xO_4$ (with x = 0, 0.2, 0.4, 0.6, 0.8, 1.0) were prepared using the conventional double sintering technique, as described in [5]. XRD data were recorded on a Philips diffractometer (model pw 1820), using Cu-Kα radiation. Mössbauer spectra were obtained at 295 K and 78 K on a powdered sample using a constant acceleration Mössbauer spectrometer with 50 mCi ^{57}Co in Rh source. The low temperature measurement was performed using a liquid nitrogen flow cryostat. The spectrometer was calibrated with α-Fe foil spectrum at 295 K. The measured data were analyzed using a non-linear least-square fitting program assuming Lorentzian lines.

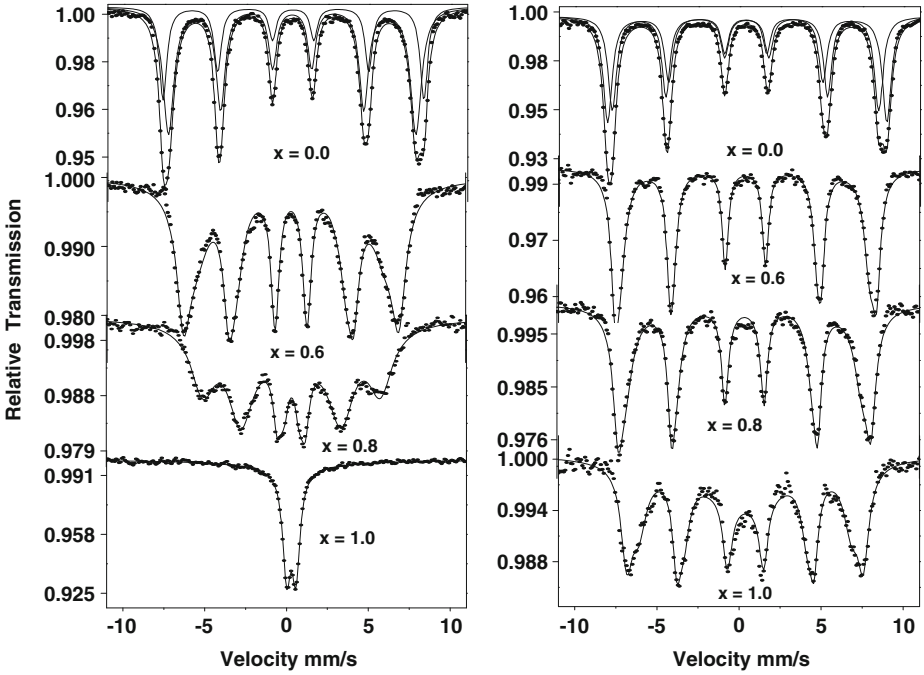

Fig. 1 295 K and 78 K Mössbauer spectra of $MgFe_{2-x}Cr_xO_4$

3 Results and discussion

The observed diffraction patterns of the studied samples confirmed the formation of single-phase cubic spinel, with no additional phases from other materials. The calculated lattice parameters are in close agreement with the earlier values reported in the literature [3]. The systematic decrease in the lattice parameter with increasing chromium substitution as shown in Table 1 is attributed to the ionic radius of six-fold-coordinated Cr^{3+} being smaller (0.64 Å) than that of Mg^{2+} (0.66 Å) and six-fold-coordinated high-spin Fe^{3+} (0.67 Å) [6].

The Mössbauer measurements at 295 K and 78 K of the studied system are illustrated in Fig. 1. The 295 K measurements show magnetic components for $x \leq 0.6$ and then relaxed spectra with a continuous collapse of the internal magnetic field for both tetrahedral (A) and octahedral [B] sites with increasing Cr contents above those contents; while at 78 K the Mössbauer measurements of all the samples exhibit a magnetic behavior. The magnetic components of the spectra were fitted assuming a superposition of two magnetic sextets assigned to Fe ions at the A- and B-sites according to their magnetic fields H_A and H_B. The larger magnetic fields assigned to the B-site is mainly due to the greater covalence and consequently greater degree of spin delocalization at the A-sites [7]. A summary of the hyperfine interaction parameters is presented in Table 1. As seen in the table the isomer shifts of the two sites for both measured temperatures show no sizeable change with Cr^{3+} content. This is indicative that the s-electron density at the nucleus of the Fe^{3+} cation

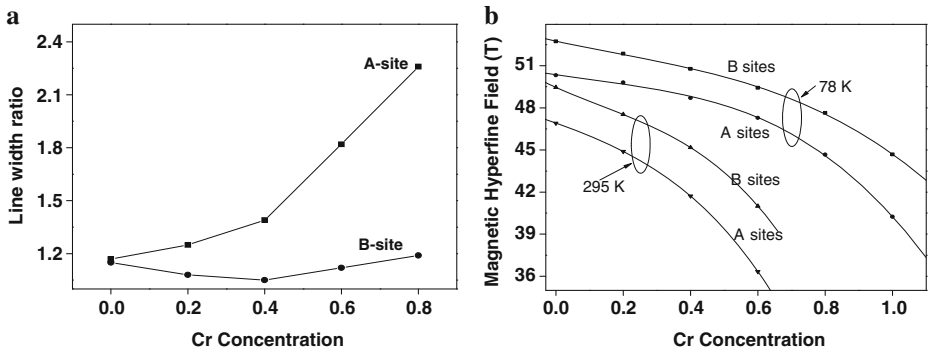

Fig. 2 **a** Variation of the ratios $(\Gamma 1/\Gamma 3)_A$ and $(\Gamma 1/\Gamma 3)_B$. **b** Variation of the magnetic hyperfine fields with Cr content measured at 295 K and 78 K

in either sub-lattice remains largely unaffected by the increasing number of Cr^{3+} ionic nearest neighbours [7]. Figure 2a shows the variation of the measured line width ratios $(\Gamma 1/\Gamma 3)_A$ and $(\Gamma 1/\Gamma 3)_B$ of the tetrahedral and octahedral sites. Such variation is in fact, expected due to a distribution of the hyperfine fields at the A-site caused principally by a random distribution of Cr^{3+}, Fe^{3+} and fraction of Mg^{2+} ions at the B-site, since the Fe^{3+} A-sites would feel different configurations of cations occupying the twelve nearest neighbours B-sites. The distribution of Fe ions over the A- and B-sites is proportional to the relative area of A- and B- Mössbauer subspectra. In the light of site preferences for each cation of the series the cation distribution in Table 1 is determined using $(Mg_{1-\gamma}Fe_{\gamma})[Mg_{\gamma}Fe_{1-x-\gamma}Cr_x]$ where γ is the inversion parameter which reflects the fraction of A-sites occupied by Fe^{3+} [3].

The effective hyperfine magnetic field measured by the Mossbauer effect at 295 and 78 K for the two sublattices as a function of Cr concentration is shown in Fig. 2b. These effective fields consist of three field contributions: i) the core field which results from the polarization of s electrons by the magnetic moments of the d electrons ii) the dipolar field which is produced by the surrounding magnetic ions and depends on the cation distribution among the two sublattices and finally iii) the supertransferred field originally arising from the magnetic moments of the nearest neighbour cations; i.e. from the intrasublattice interactions J_{AA}, J_{BB} and intersublattice interaction J_{AB} [8]. Within the range $0 < x < 0.4$ the substitution of the Fe^{3+} (5 μB) with Cr^{3+} (3 μB) at the B-site causes a reduction in the number of the active bonds FeA-O-FeB that A-site iron ions experience and hence to reduction in the corresponding hyperfine magnetic field at the A-sites Fe nuclei. Furthermore, since the substitution within this range would not affect the Fe^{3+} ions concentration at A-sites, a direct reduction in the hyperfine magnetic field at the B-site iron nuclei is not expected. But the decrease at the A-sites magnetic moment weakens the J_{AB} interaction and indirectly causes a reduction in the magnetic field at B-sites iron nuclei. Moreover, the continuation in the reduction of the hyperfine magnetic field at the two sites for $x \geq 0.6$ is attributed to the distribution of the Mg^{2+} (with zero moment) among the two sublattices together with continuous reduction of Fe^{3+}. Such reduction in the hyperfine magnetic field could be taken as an indication of the weakening the ferrimagnetic behaviour of the system with increasing Cr content that leads to decrease in Currie temperature as seen in the 295 K spectra.

References

1. Navrotsky, A., Kleppa, O.J.: J. Inorg. Nucl. Chem. **29**, 2701 (1967)
2. Lee, S.H., Yoon, S.J., Lee, G.J., Kim, H.S., Yo, C.H., Ahn, K., Lee, D.H., Kim, K.H.: Mater. Chem. Phys. **61**, 147 (1999)
3. Gismelseed, A.M., Yousif, A.A.: Physica B **370**, 215–222 (2005)
4. Siddique, M., Butt, N.M., Shafi, M., Abbas, T., Misbah-ul-Islam, J.: J. Radioanal. Nucl. Chem. **258**, 525 (2003)
5. Gismelseed, A.M., Mohammed, K.A., Widatallah, H.M., Al-Rawas, A.D., Elzain, M.E., Yousif, A.A.: J. Phys. Conf. Ser. **217**, 012138 (2010)
6. Krauz, W, Nolze, G.: J. Appl. Crystallogr. **29**, 301–303 (1996)
7. Attia, S.M.: Egypt. J. Solids **29**, 329 (2006)
8. Ata-Allah S.S., Fayek, M.K., Refai, H.S., Mostafa, M.F.: J. Solid State Chem. **149**, 434 (2000)

Hyperfine Interact (2012) 208:39–42
DOI 10.1007/s10751-011-0445-y

Magnetic properties of $Nb_{1-x}Hf_xFe_2$

Stephen J. Harker · Glen A. Stewart · Hiroshi Okimoto · Katsuhiko Nishimura · Wayne D. Hutchison

Published online: 15 November 2011

Abstract ^{57}Fe-Mössbauer spectroscopy for the $Nb_{1-x}Hf_xFe_2$ intermetallic series reveals the presence of local Fe 6h-site moments well above the magnetic transition temperatures determined from bulk magnetisation measurements. The techniques combine to demonstrate that the system orders antiferromagnetically at $x = 0.4$ with a remarkable change to strong ferromagnetic character between $x = 0.7$ and 0.8. Low temperature spin glass behaviour is observed for $x = 0.45$ to 0.79.

Keywords Mössbauer spectroscopy · Intermetallics · Spin glass · Laves phase

1 Introduction

The intermetallic series $Nb_{1-x}Hf_xFe_2$ ($0 < x < 0.8$) forms with the hexagonal C14 Laves phase structure with space group $P6_3/mmc$ and exhibits an unusual range of magnetic properties. Stoichiometric $NbFe_2$ is a weak itinerant antiferromagnet with a spin-density-wave transition at $T_{sdw} \approx 10$ K [1]. More recently, considerable interest has been directed at the existence of ferromagnetic quantum criticality for a small excess of Nb ([2] and references therein). In its unannealed form, $HfFe_2$ exhibits a minor C14 phase component (the preferred phase is cubic C15) that orders ferromagnetically at $T_C \approx 427$ K [3, 4]. With increasing Hf concentration, the magnetic ordering temperature is expected to increase fairly smoothly between these

S. J. Harker · G. A. Stewart · W. D. Hutchison (✉)
School of Physical, Environmental and Mathematical Sciences, The University of New South Wales, Australian Defence Force Academy, Canberra, ACT 2600, Australia
e-mail: w.hutchison@adfa.edu.au

H. Okimoto · K. Nishimura
Graduate School of Science and Engineering, University of Toyama, Toyama, 930–8555, Japan

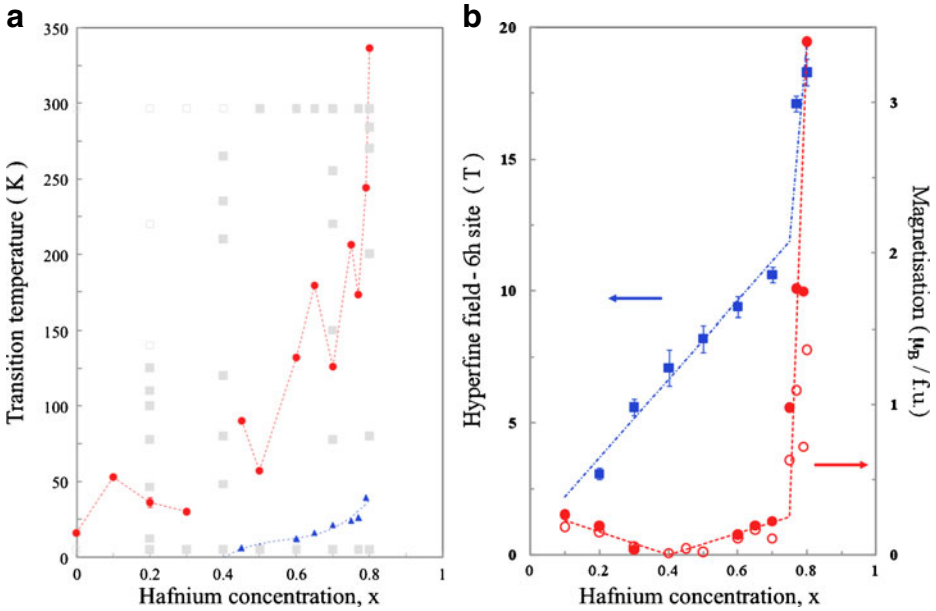

Fig. 1 **a** Bulk magnetic phase transition temperatures (*circles*) and spin glass transitions (*triangles*) for $Nb_{1-x}Hf_xFe_2$ are compared with ordered (*solid squares*) and paramagnetic (*open squares*) magnetic behaviour as indicated by ^{57}Fe-Mössbauer spectroscopy. **b** The low temperature (T = 5 K) magnetic behaviour of $Nb_{1-x}Hf_xFe_2$ is represented by the magnetisation observed for an applied field of 0.1 T (*open circles*), the saturation magnetisation (*solid circles*), and the magnetic hyperfine field (B_{hf}) at the Fe 6h-site. *Broken lines* are a guide to the eye

two end values. However, it is difficult to be precise about ordering temperatures and magnetic structure from the magnetisation measurements alone. The m ain thrust of this work is the use of ^{57}Fe-Mössbauer spectroscopy to monitor the magnetism at the atomic level via the magnetic hyperfine fields (B_{hf}) acting at the 2a- and 6h-Fe sites. To this end, Mössbauer spectra have been recorded as a function of temperature and hafnium concentration ($0 < x < 0.8$), and our analysis is presented in conjunction with new bulk magnetisation data.

2 Experimental details

Single-phase, polycrystalline samples of $Nb_{1-x}Hf_xFe_2$ were synthesised from high purity elemental constituents via argon arc melting. Ingots were then wrapped in Ta foil and sealed in evacuated quartz tubes for annealing at 1000°C for one week. Bulk magnetisation measurements were performed on a Quantum Design MPMS magnetometer capable of measuring down to 2 K in applied fields up to 7 T. The ^{57}Fe-Mössbauer spectra were recorded using a liquid helium bath cryostat and a 20 mCi ^{57}Co:Rh source mounted externally on a sinusoidal motion drive. They were analysed using a full Hamiltonian model [5]. However, the parameters eta, theta and phi were fixed to zero, thus amounting to coaxial magnetic and electric quadrupole hyperfine interactions. The 6h and 2a component sub-spectra intensities were

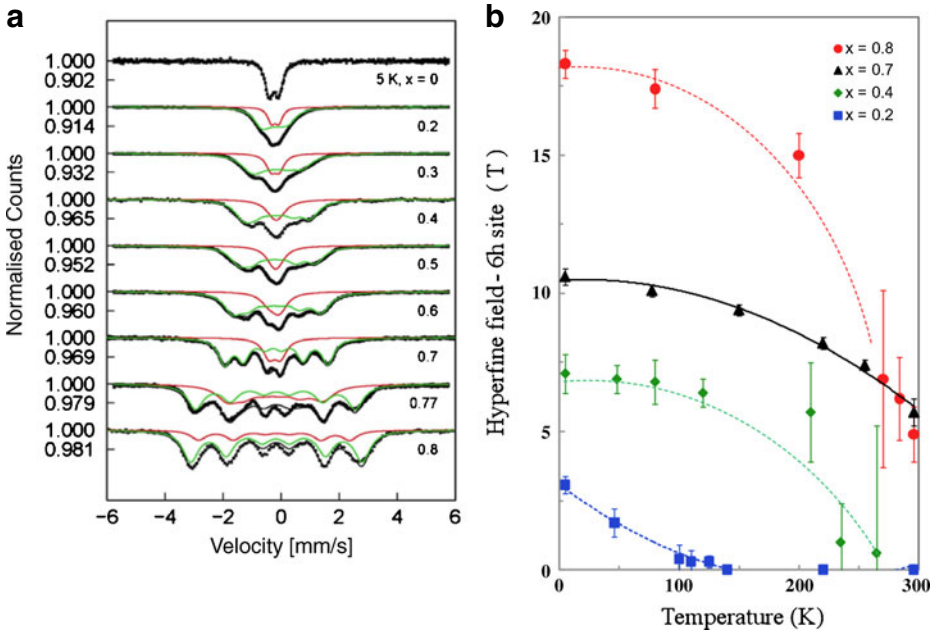

Fig. 2 **a** ^{57}Fe-Mössbauer spectra recorded at 5 K for $Nb_{1-x}Hf_xFe_2$ with the indicated hafnium concentrations, x. The sub-spectra correspond to the 6h- and 2a-sites (*green* and *red*, respectively). **b** Magnetic hyperfine field (B_{hf}) fitted to the 6h-site sub-spectrum as a function of temperature for $x = 0.2$, 0.4, 0.7 and 0.8

maintained at the expected ratio of 3:1 for the two Fe sites in this structure. The B_{hf} value was fixed to zero for spectra above the magnetic transition temperature and allowed to vary for temperatures below the transition. In some spectra overlapping peaks made it necessary to carefully choose starting parameters to achieve consistent fits.

3 Results

Low field (0.1 T) bulk magnetisation data for the $Nb_{1-x}Hf_xFe_2$ intermetallics generally indicate a single magnetic phase transition. The transition temperatures estimated, via extrapolation of M^2 *v's* T plots to the temperature axis, are plotted in Fig. 1a as a function of x (solid circles). Based on Arrott plots, the nature of the magnetic order was determined as being ferrimagnetic with decreasing saturation magnetisation in the range $x = 0.2$ to 0.3, antiferromagnetic for $x = 0.4$, and ferrimagnetic with increasing magnetisation for $x = 0.45$ to 0.7. There is a remarkable change to strong ferromagnetic character between $x = 0.7$ and 0.8. Estimated values of the saturation magnetisation are shown in Fig. 1b (solid circles). In addition, a comparison of field cooled and zero field cooled M data indicates an additional low temperature spin glass-like phase for $0.45 < x < 0.8$. These latter transition temperatures are indicated by triangles in Fig. 1a.

The ^{57}Fe-Mössbauer spectra were recorded for 5 K and 296 K, and also as a function of temperature for selected hafnium concentrations. Except for the strongly

ferromagnetic compounds ($0.7 < x < 0.8$) B_{hf} is zero at the higher symmetry 2a-site, so that the 6h-site B_{hf} is the more useful probe of local Fe magnetism. The full set of 5 K spectra is shown in Fig. 2a and the corresponding fitted 6h-site B_{hf} (solid squares in Fig. 1b) are observed to increase almost linearly over $0.2 < x < 0.7$. This supports the argument for antiferromagnetic order at $x = 0.4$ (as opposed to an array of negligible local moments). The temperature dependence of B_{hf} is fitted for $x = 0.2$, 0.4, 0.7 and 0.8 (Fig. 2b) and the distribution of non-zero B_{hf} values (solid squares in Fig. 1a) indicates that the magnetic transition temperatures derived from Mössbauer spectroscopy are generally higher than those derived from bulk magnetisation measurements. This is puzzling, given that the bulk magnetic data offer no indication for higher temperature antiferromagnetic behaviour.

4 Discussion

In apparent contradiction of the bulk magnetic data, the low temperature 6h-site B_{hf} for the $Nb_{1-x}Hf_xFe_2$ series increases monotonically while the saturation magnetisation exhibits a minimum at $x = 0.4$. Furthermore the Mössbauer data indicate generally higher transition temperatures. The former is consistent with the existence of an antiferromagnetic phase while the latter needs to be explored further. In addition, the magnetisation data reveal spin glass behaviour at low temperatures in the region $x = 0.45$ to 0.79, which may be partly responsible for the suppression of the bulk moment through this region.

Acknowledgements This work was carried out under the umbrella of the Agreement for Academic Exchange between UNSW, Canberra and The University of Toyama.

References

1. Yamada, Y., Nakamura, H., Kitaoka, Y., Asayama, K., Koga, K., Sakata, A., Murakami, T.: J. Phys. Soc. Jpn. **59**, 2967 (1990)
2. Neal, B.P., Ylvisaker, E.R., Pickett, W.E.: Phys. Rev. B **84**, 085133(1–7) (2011)
3. Ikeda, K.: Z. Metallkd **68**, 195 (1977)
4. Belosevic-Cavor, J., Cekic, B., Novakovic, N., Ivanovic, N., Manasijevic, M.: Mat. Sci. Forum **89**, 453–454 (2004)
5. Pollard, R.J., McCann, V.H., Ward, J.B.: J. Phys. C **15**, 6807 (1982)

Hyperfine Interact (2012) 208:43–48
DOI 10.1007/s10751-011-0408-3

$DyNi_2Mn$—magnetisation and Mössbauer spectroscopy

Jian Li Wang · Stewart James Campbell · Shane Joseph Kennedy · Shi Xue Dou · Guang Heng Wu

Published online: 16 October 2011

Abstract The physical properties of $DyNi_2Mn$ doped with ^{57}Fe have been investigated by X-ray diffraction, magnetisation (10–300 K) and ^{57}Fe Mössbauer spectroscopy measurements (5–300 K). $DyNi_2Mn(^{57}Fe)$ crystallizes in the $MgCu_2$-type cubic structure ($Fd^{-}3m$ space group). The ordering temperature is found to be $T_C = 99(2)$ K, much higher than those of $DyNi_2$ (∼22 K) and $DyMn_2$ (∼35 K). Analyses of isothermal M–H curves and the related Arrott plots confirm that the magnetic phase transition at T_C is second order. The magnetic entropy change around T_C is 4.0 J/kg K for a magnetic field change of 0 T to 5 T. The spectra above T_C exhibit features consistent with quadrupolar effects while below T_C the spectra exhibit magnetic hyperfine splitting. The Debye temperature for $DyNi_2Mn$ has been determined as $\theta_D = 200(20)$ K from a fit to the variable temperature isomer shift IS(T).

Keywords Phase transition · Mössbauer spectroscopy · Magnetic entropy change

J. L. Wang · S. J. Campbell (✉)
School of Physical, Environmental and Mathematical Sciences,
The University of New South Wales,
Canberra, ACT 2600, Australia
e-mail: stewart.campbell@adfa.edu.au

J. L. Wang · S. J. Kennedy
Bragg Institute, ANSTO, Lucas Heights, NSW 2234, Australia

J. L. Wang · S. X. Dou
Institute for Superconductivity and Electronic Materials,
University of Wollongong, Wollongong, NSW 2522, Australia

G. H. Wu
Institute of Physics, Chinese Academy of Science,
Beijing 100190, People's Republic of China

1 Introduction

RNi_2Mn compounds have been found to exhibit the $MgCu_2$-type structure even though the ratio of rare earth atoms to transition metal atoms is 1:3 [1–4]. Rietveld refinements of x-ray and neutron diffraction patterns of RNi_2Mn compounds, demonstrated that Mn atoms occupy two inequivalent crystal sites: the 8a and 16d [1, 2, 4, 5]. As part of our systematic investigation of the magnetic properties of this novel RNi_2Mn system, here we present a detailed investigation of the critical magnetic behavior of $DyNi_2Mn(^{57}Fe)$ around the magnetic transition temperature by DC magnetisation (10–300 K) and ^{57}Fe Mössbauer spectroscopy measurements.

2 Experimental

An ingot of $DyNi_2Mn$ doped with ~0.5 wt% ^{57}Fe, was prepared by standard argon arc-melting the mixtures of starting elements (purities >= 99.9%). X-ray diffraction (Cu-K_α radiation; $\lambda = 1.5418$ Å) confirmed that $DyNi_2Mn(^{57}Fe)$ exhibits the $MgCu_2$ structure (space group Fd-3m). The lattice constant, $a = 7.154(3)$ Å, is slightly larger than that of $DyNi_2Mn$ ($a = 7.140$ Å) reported in [1, 2, 4]; this variation may be linked with the actual Mn content as discussed in [4]. DC magnetization measurements were carried out over the temperature range 10–340 K in a SQUID magnetometer ($\mu_0 H =$ 0–5 T). The ^{57}Fe Mössbauer spectra were obtained between 5 K and 300 K using a standard constant-acceleration spectrometer and a ^{57}Co**Rh** source. The spectrometer was calibrated at room temperature with an α-iron foil.

3 Results and discussion

The Curie temperature $T_C \sim 99 \pm 2$ K derived from the magnetization data is slightly higher than the published value of $T_C = 94$ K for pure $DyNi_2Mn$ but significantly higher than the values for $DyNi_2$ ($T_C \sim 22$ K) and $DyMn_2$ ($T_C \sim 35$ K) [1, 2]. Figure 1a and b show the M versus H and related Arrott plots of M^2 versus H/M around Curie temperature. The positive slopes of the Arrott plots (Fig. 1b) indicate that the phase transition around T_C is second order [4, 6].

The critical properties of a second-order magnetic phase transition can be described by critical exponents β, δ and γ derived from magnetization measurements around the transition temperature (e.g. [7]). According to the conventional static scaling law, the exponents can be expressed by the following equations. Below T_C, the temperature dependence of the spontaneous magnetization $M_S(T)$ is governed by the equation:

$$M_S(T) = M_0 \left| (T - T_C) / T_C \right|^{-\beta}. \tag{1}$$

The initial susceptibility above T_C is given by

$$\chi_0^{-1}(T) = (h_0 / M_0)(T - T_C / T_C)^{\gamma}, \tag{2}$$

while at T_C, M and H are related by

$$M = D H^{1/\delta}, \tag{3}$$

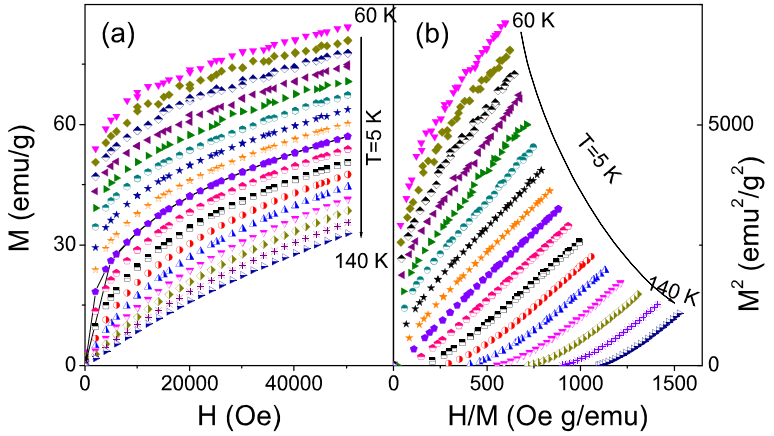

Fig. 1 **a** Magnetization as a function of applied DC field (H = 0–50 kOe) around T_C. **b** Arrott-plots of M^2 as a function of H/M for the magnetization data of Fig. 1a. The positive slopes indicate that the transition at T_C is second-order

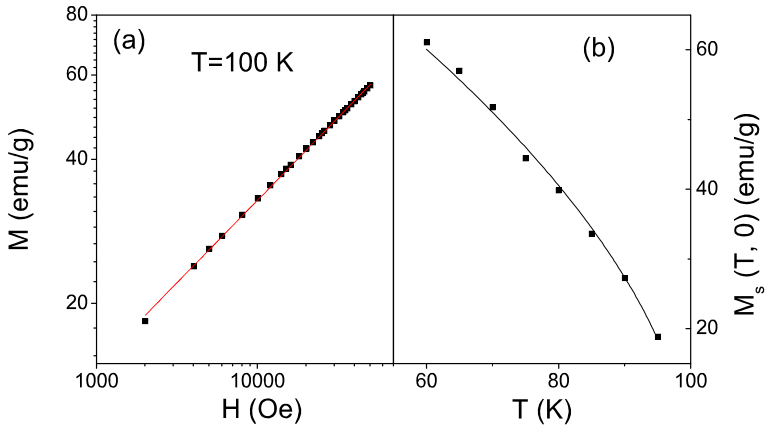

Fig. 2 **a** Critical isotherm at T = 100 K on a double-logarithmic scale. The line represents the fit of M vs H resulting in $\delta = 2.90 \pm 0.02$ based on the power relation $M \sim H^{1/\delta}$. **b** Spontaneous magnetization M_s (T, 0) vs T. The line represent the fit of M_s(T, 0) vs T based on equation (1) leading to $T_C = 99.4$ K and $\beta = 0.57 \pm 0.04$

where M_0, h_0/M_0, and D are the critical amplitudes. As shown in Fig. 2a, the high-field magnetization data at $T_C = 99(2)$ K, is described well by a straight line of slope $1/\delta$, leading to the fitted value $\delta = 2.90 \pm 0.02$. Following standard procedure, the limiting M_S(T, 0) values at H = 0 have been determined from the intercept to the y-axis of Fig. 1b by extrapolating the Arrott plots. Figure 2b shows a graph of M_S(T, 0) as a function of T. A fit of the M_S(T, 0) versus T curve to (1) results in the value $\beta = 0.57 \pm 0.04$ (full line in Fig. 2b). Applying the Widon scaling relation $\delta = 1 + \gamma/\beta$, to the δ and β values determined above, leads to $\gamma = 1.08 \pm 0.06$. The mean field interaction model for long range ordering has theoretical critical exponents of $\beta = 0.5$, $\gamma = 1.0$ and $\delta = 3.0$ with theoretical values based on the three

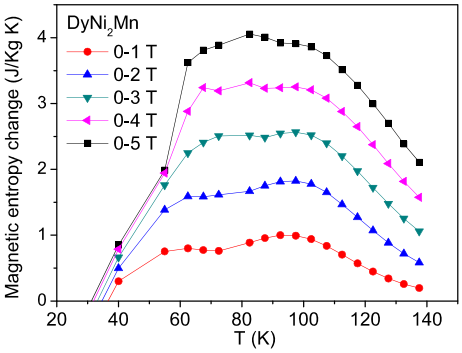

Fig. 3 Temperature dependence of the isothermal magnetic entropy change $-\Delta S_M(T, \mathrm{H})$ as measured in magnetic fields up to 5 T and derived from magnetic data in Fig. 1a

dimensional Heisenberg model for short range interactions of $\beta = 0.365$, $\gamma = 1.386$ and $\delta = 4.80$ [8]. The δ, β, γ values derived for $DyNi_2Mn(^{57}Fe)$ indicate that long range interactions dominate the critical behavior around T_C, similar to the behavior detected for $TbNi_2Mn$ [4].

The isothermal entropy change $-\Delta S_M$ associated with a change in magnetic field ΔH from H = 0 to value H, has been derived from the Maxwell relation (e.g. [4, 6]) $\Delta S_M(T, H) = \mu_0 \int_0^H \left(\frac{\partial M}{\partial T}\right)_H dH$. Figure 3 shows the dependence of the magnetic entropy $-\Delta S_M$ on temperature and external field. The curves exhibit a broad peak around T_C (typical for a second order phase transition [4, 6]) with maximum values around 80 K of $-\Delta S_M \sim 2.5$ J/kg K and 4.0 J/kg K for $\Delta\mu_0$H = 0–3 T and 0–5 T, respectively. The extended plateau of the $-\Delta S_M$ versus T curve may lead to a large relative cooling power where the RCP is used as an indicator of the cooling efficiency of a magnetocaloric material. For $DyNi_2Mn(^{57}Fe)$, the RCP for the field changes of 0–1 T, 0–2 T, 0–3 T, 0–4 T and 0–5 T are 72.6 J/kg, 146.4 J/kg, 169.3 J/kg, 280.2 J/kg and 333.3 J/kg, respectively.

The Mössbauer spectra were analysed as described previously [4, 6] (typical spectra and fits with sub-spectral components are shown in Fig. 4a). The 150 K and 300 K spectra exhibit quadrupolar effects consistent with a paramagnetic state as expected above $T_C \sim 100$ K with the 5 K spectrum exhibiting features characteristic of magnetically split sub-spectra consistent with the onset of magnetic hyperfine interactions below T_C. Given that the Mn atoms enter both the 8a and 16d sites in RNi_2Mn compounds [1, 2, 4, 6], it is expected that the dopant ^{57}Fe atoms would also enter the 8a and 16d sites. The paramagnetic spectra are described well using two sub-spectra consistent with ^{57}Fe atoms located at the 8a and 16d sites. While the spectra for magnetically split spectra would also be expected to be fitted using two sub-sextets to represent ^{57}Fe atoms in the 8a and 16d sites, it was found that at least three sub-sextets are needed to provide optimal fits for the spectra below the magnetic ordering temperature T_C [4, 6] (similar behavior has been found for RMn_2 compounds (R = Tb, Dy, Ho) where two sub-spectra rather than a single sub-spectrum are required [9–11]). The observed average hyperfine field values of Fig. 4b result from contributions to the exchange interactions present in the Dy and transition metal (Ni, Mn) sublattices and correspondingly reflect the magnetic order in the Dy and (Ni, Mn) sublattices.

As shown in Fig. 4b, the Debye temperature of $DyNi_2Mn(^{57}Fe)$ has been determined from the temperature dependence of the isomer shift IS(T)

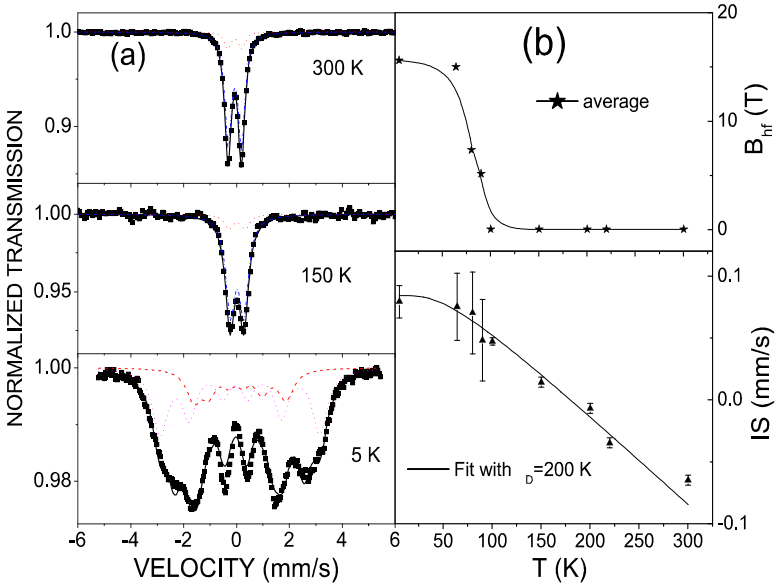

Fig. 4 **a** ^{57}Fe Mössbauer spectra of DyNi$_2$Mn(^{57}Fe) at T = 5 K, 150 K and 300 K. The fits to the spectra are described in the text (see also [4, 6]). **b** Variation of average magnetic field B_{hf} and isomer shift IS(T) with temperature

(IS(T) = IS_0(T) + IS_{SODS}(T) [12, 13]). IS_0(T) represents the temperature dependence of the charge density at the probe nucleus which is generally weakly temperature dependent while IS_{SODS}(T), the so-called second-order Doppler shift, can be described in terms of the Debye model for the phonon spectrum by $IS_{SODS}(T) = -\frac{3kT}{2mc}\left[\frac{3\theta_D}{8T} + 3\left(\frac{T}{\theta_D}\right)^3 \int_0^{\tau} \frac{x^3}{e^x - 1} dx\right]$ (m is the mass of the ^{57}Fe nucleus, k Boltzmann's constant, c the velocity of light, and $\tau = \theta_D/T$ the reduced temperature). The Debye temperature has been derived to be $\theta_D = 200 \pm 20$ K on fitting the mean isomer shift data to the above equation.

References

1. Wang, J.L., Tang, C.C., Wu, G.H., Liu, Q.L., Tang, N., Wang, W.Q., Wang, W.H., Yang, F.M., Liang, J.K., de Boer, F.R., Buschow, K.H.J.: Solid State Commun. **121**, 615 (2002)
2. Wang, J.L., Marquina, C., Ibarra, M.R., Wu, G.H.: Phys. Rev. B **73**, 94436 (2006)
3. Jackson, D.D., McCall, S.K., Weir, S.T., Karki, A.B., Young, D.P., Qiu, W., Vohra, Y.K.: Phys. Rev. B **75**, 224422 (2007)
4. Wang, J.L., Campbell, S.J., Kennedy, S.J., Zeng, R., Dou, S.X., Wu, G.H.: J. Phys.: Condens. Matter. **23**, 206002 (2011)
5. Mushnikov, N.V., Gaviko, V.S., Park, J., Pirogov, A.N.: Phys. Rev. B **79**, 184419 (2009)
6. Wang, J.L., Campbell, S.J., Zeng, R., Dou, S.X., Kennedy, S.J.: J. Appl. Phys. **109**, 07E304 (2011)
7. Padmanabhan, B., Bhat, H.L., Elizabeth, S., Rößler, S., Rößler, U.K., Dörr, K., Müller, K.H.: Phys. Rev. B **75**, 024419 (2007) and references therein

8. Kaul, S.N.: J. Magn. Magn. Mater. **53**, 5 (1985)
9. Marzec, J., Przewoźnik, J., Żukrowski, J., Krop, K.: J. Magn. Magn. Mater. **157/158**, 413 (1996)
10. Stoch, P., Pszczoła, J., Dąbrowski, L., Suwalski, J., Pańta, A.: J. Alloys Compd. **337**, 33 (2002)
11. Oddou, J.L., Jeandey, C., Ballou, R., Deportes, J., Ouladdiaf, B.: Solid State Commum. **85**, 419 (1993)
12. Long, G.J., Hautot, D., Grandjean, F., Morelli, D.T., Meisner, G.P.: Phys. Rev. B **60**, 7410 (1999)
13. Wang, J.L., Campbell, S.J., Tegus, O., Marquina, C., Ibarra, M.R., Phys. Rev. B **75**, 174423 (2007)

Hyperfine Interact (2012) 208:49–52
DOI 10.1007/s10751-011-0486-2

Mössbauer study on Y-type hexaferrite $Ba_2Mg_2Fe_{12}O_{22}$

Shin Nakamura · Yorihiko Tsunoda · Akio Fuwa

Published online: 8 December 2011

Abstract Mössbauer study on a Y-type hexaferrite $Ba_2Mg_2Fe_{12}O_{22}$ has been conducted by using a single crystal specimen. The spins are in the *c*-plane down to 60 K. For $18h_{VI}$ site Fe, the quadrupole shifts and the outermost line width change around 195 K, where the transition from ferrimagnetic to proper screw spin structure takes place. Below 50 K, the spin reorientation transition to a longitudinal conical structure was also recognized. At 16 K, the spins incline about 15° from the *c*-plane.

Keywords Y-type hexaferrite · $Ba_2Mg_2Fe_{12}O_{22}$ · Magnetic transition · ^{57}Fe Mössbauer spectroscopy · Quadrupole shift

1 Introduction

A Y-type hexaferrite $Ba_2Mg_2Fe_{12}O_{22}$ has a hexagonal structure ($R\bar{3}m$) with the lattice constants of $a = 5.880$Å and $c = 43.515$Å at room temperature. The Fe^{3+} ions and Mg^{2+} ions equally occupy six crystallographic sites: two tetrahedral sites ($6c_{IV}$ and $6c^*_{IV}$) and four octahedral sites ($3a_{VI}$, $3b_{VI}$, $6c_{VI}$, and $18h_{VI}$) [1, 2]. The material is a ferrimagnet with the Curie temperature of 553K. The Fe^{3+} spins are in the *c*-plane, i.e. along [1 $\bar{1}$ 0] direction. Below 195K, the spins form a proper screw structure with the propagation vector along the *c*-axis. The turn angle of the helix is about 70° at 9 K [2]. It was found recently that a spin reorientation transition to a

S. Nakamura (✉)
Department of Science and Engineering, Teikyo University, Utsunomiya 320-8551, Japan
e-mail: shin@koala.mse.teikyo-u.ac.jp

S. Nakamura
Advanced Research Institute of Science and Engineering, Waseda University,
Shinjuku-ku, Tokyo 169-8555, Japan

Y. Tsunoda · A. Fuwa
Faculty of Science and Engineering, Waseda University, Shinjuku-ku, Tokyo 169-8555, Japan

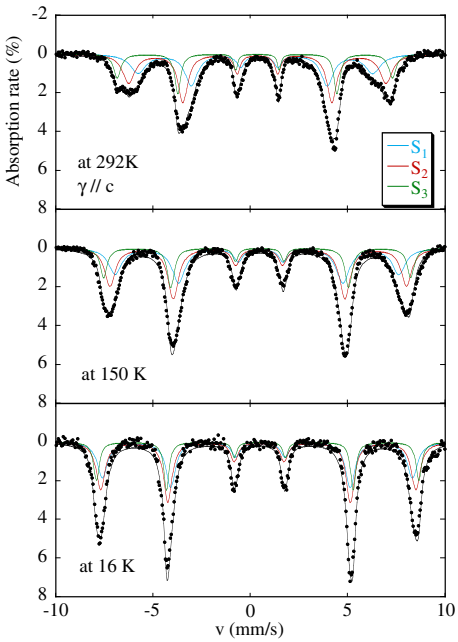

Fig. 1 Mössbauer Spectrum of single crystal $Ba_2Mg_2Fe_{12}O_{22}$ at 292, 150, and 16 K

longitudinal conical structure takes place below 50 K [3]. The spins incline about 10–20° from the *c*-plane. The magnetoelectric behavior, or multiferroic behavior, was also found, and thus the interests on this material have been revived. The Mössbauer spectroscopic studies on this material, however, have not been conducted so much [4, 5]. This is presumably because of its complex spectrum originated from the six crystallographic Fe sites. Moreover, in the ferrimagnetic region, Fe ions on $18h_{VI}$ site (site symmetry *.m*) decompose into three types, since there are three different electric field gradient (EFG) axes with respect to the spin direction $[1\,\bar{1}\,0]$. Here in this paper, we report the detailed Mössbauer spectrum of $Ba_2Mg_2Fe_{12}O_{22}$ by using a single crystal specimen.

2 Experiments

The single crystal of $Ba_2Mg_2Fe_{12}O_{22}$ was prepared by the flux method [1, 2]. The *c*-plane platelet with about 6 mm × 4 mm × 40 μm size was used as absorber. The ^{57}Fe Mössbauer spectroscopy was conducted in conventional transmission geometry by using ^{57}Co-in-Rh (25 mCi) as the γ ray source. The incident γ ray direction was parallel to the *c*-axis. Doppler velocity scale was calibrated with respect to Fe-metal. Lorentzian line shapes were assumed for the spectrum analysis.

3 Results and discussions

The paramagnetic spectrum at 583 K apparently consists of an asymmetric broad doublet. At this point we cannot analyze as a superposition of the sex doublets, but

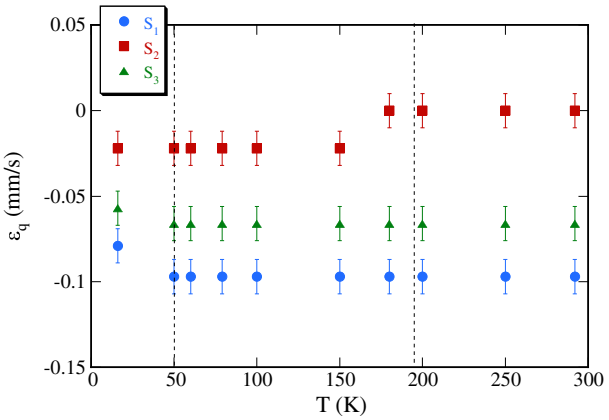

Fig. 2 Temperature dependence of the quadrupole shift (ε_q) for the three subspectra

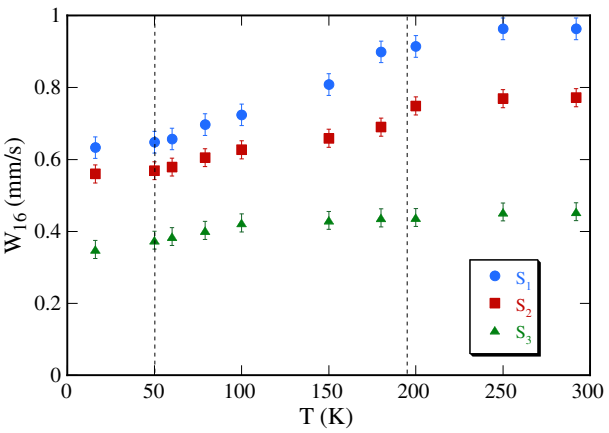

Fig. 3 Temperature dependence of the outermost line width (W_{16}) for the three subspectra

we tentatively obtain the average quadrupole splitting (QS) of about 0.43 mm/s. In Fig. 1, the magnetically ordered spectrum at 292, 150, and 16 K are shown. Considering the strength of magnetic interaction (or magnitude of hyperfine field) [2, 4, 5] and the site symmetry, we classified the six types of Fe^{3+} into three groups: from the inner one, termed S_1 ($6c_{IV}$, $6c_{VI}$, $3b_{VI}$), S_2 ($18h_{VI}$), and S_3 ($6c^*_{IV}$, $3a_{VI}$) for convenience. The intensity ratio should be S_1:S_2:S_3 = 1.67:2:1. The absorption line intensity ratios are 3:4:1:1:4:3 above 60 K, which indicates that the spins are in the c-plane. The isomer shifts (IS) are 0.36, 0.36, and 0.29 mm/s for S_1, S_2, and S_3, respectively, indicating that all Fe ions are in 3+ state. The hyperfine fields (H_{hf}) are 374.5, 410.5, and 439.1 kOe, respectively. The quadrupole shifts (ε_q) are −0.10, 0.00, and −0.07 mm/s, respectively. For S_1 and S_3, where all the constituent sites have three-fold axial symmetry, the principal axis of EFG (z-axis) is in the c-direction and thus approximately $-4\varepsilon_q = e^2qQ/2 = QS$. The observed ε_q values for S_1 and S_3 seem to be in accordance with this relation. On the other hand for S_2, it is not valid, because the constituent $18h_{VI}$ site does not have any axial symmetry. In the ferrimagnetic region, S_2 is actually composed of three subspectra having different ε_q's, which apparently results in $\varepsilon_q = 0.00$ in the analysis. At 16 K, IS 's are 0.44,

0.42, and 0.43 mm/s for S_1, S_2, and S_3, respectively, and H_{hf}'s are 494.8, 503.0, and 514.5 kOe, respectively. The intensities of 2–5 lines decrease below 50 K. The line intensity ratio is about 3:3.5:1:1:3.5:3 at 16 K, which indicates that the spins are no longer in the *c*-plane but incline about 15° from the *c*-plane. This corresponds well to the longitudinal conical spin structure below 50K.

In Fig. 2, the temperature dependences of ε_q are shown. That of S_2 changes from 0.00 to −0.022 mm/s below 195K. At the same time the outermost line width W_{16} (FWHM) of S_2 becomes sharper as shown in Fig. 3. These features can be explained by calculating ε_q of $18h_{VI}$ by using the crystal structure parameters [1]. The three *z*-axes (calculated) are directed about ±10° from the *c*-plane. Above 195K, the angles between the *z*-axes and $[1\,\bar{1}\,0]$ give three ε_q^{cal} of 0.189, −0.026, and −0.082mm/s. The average of the three is 0.027mm/s. Since the moment rotates in the *c*-plane below 195K, the angular factors are averaged, which gives unique ε_q^{cal} of −0.012mm/s. Although the values are slightly different from the analyzed ones, its changing nature through 195K is consistent. On the other hand for S_1 and S_3, no changes in ε_q occur around 195K, since the spins are still in the *c*-plane. Below 50K, the magnitudes of ε_q for these two decrease, which correspond to the longitudinal conical spin structure. From the angular factor, we can estimate that the spins of S_1 and S_3 incline about 14° and 12°, respectively, from the *c*-plane. The values are in good agreement with that estimated by the 2–5 line intensity.

References

1. Momozawa, N., Yamaguchi, Y., Mita, M.: J. Phys. Soc. Jpn. **55**, 1350 (1986)
2. Momozawa, N., Nagano, Y., Utsumi, S., Abe, M., Yamaguchi, Y.: J. Phys. Soc. Jpn. **70**, 2724 (2001)
3. Ishiwata, S., Taguchi, Y., Murakawa, H., Onose, Y., Tokura, Y.: Science **319**, 1643 (2008)
4. Albanese, G., Carbucicchio, M., Deriu, A., Asti, G., Rinaldi, S.: Appl. Phys. **7**, 227 (1975)
5. Deriu, A., Licci, F., Rinaldi, S., Besagni, T.: J. Magn. Magn. Mater. **22**, 257 (1981)

Hyperfine Interact (2012) 208:53–57
DOI 10.1007/s10751-011-0443-0

Mössbauer study of giant hard magnetic $K_2Fe_3(OH)_2(SO_4)_3(H_2O)_2$

Kiyoshi Nomura · Tadashi Sugano · Serge Vilminot · Mohamedally Kurmoo · Ernő Kuzmann

Published online: 10 November 2011

Abstract $K_2Fe_3(OH)_2(SO_4)_3(H_2O)_2$ was prepared by hydrothermal synthesis. The crystal structure is the isomorphous phase of $K_2Co_3(OH)_2(SO_4)_3(H_2O)_2$. Mössbauer spectra of $K_2Fe_3(OH)_2(SO_4)_3(H_2O)_2$ were measured at low temperatures between room temperature and 14 K, and the hyperfine interactions were analyzed. The Neel temperature is 39 K. Two paramagnetic Fe^{2+} species were observed in the Mössbauer spectrum at room temperature, and Mössbauer spectra measured below 38 K were decomposed into four magnetic subspectra. From the temperature dependence, it is found that the local electron density at each site is largely deviating at low temperatures, which may induce the giant coercivity.

Keywords Magnetic material · Hard magnet · Potassium iron compound · Mössbauer spectra

K. Nomura (✉)
School of Engineering, The University of Toyo, Hongo 7-3-1, Bunkyo-ku,
Tokyo 113-8656, Japan
e-mail: k-nomura@t-adm.t.u-tokyo.ac.jp

T. Sugano
Meiji Gakuin University, Totsuka-ku, Yokohama 244-8539, Japan

S. Vilminot
Institut de Pysique et Chimie des Materiaux de Strasbourg, 67034 Strasbourg, France

M. Kurmoo
Universite de Strasbourg, 67070 Strasbourg, France

E. Kuzmann
Eotvos University, Pazmany P.s. 1/A, 1117 Budapest, Hungary

Table 1 Lattice constant of $K_2Fe_3(OH)_2(SO_4)_3(H_2O)_2$, compared with $K_2Co_3(OH)_2(SO_4)_3(H_2O)_2$

Space group: $Cmc2_1$	a/Å	b/Å	c/Å	V/Å^3
Fe compound	17.9118(5)	7.6591(2)	9.8570(3)	1352.26(6)
Co compound	17.9496(9)	7.5576(4)	9.7594(6)	1323.93(12)

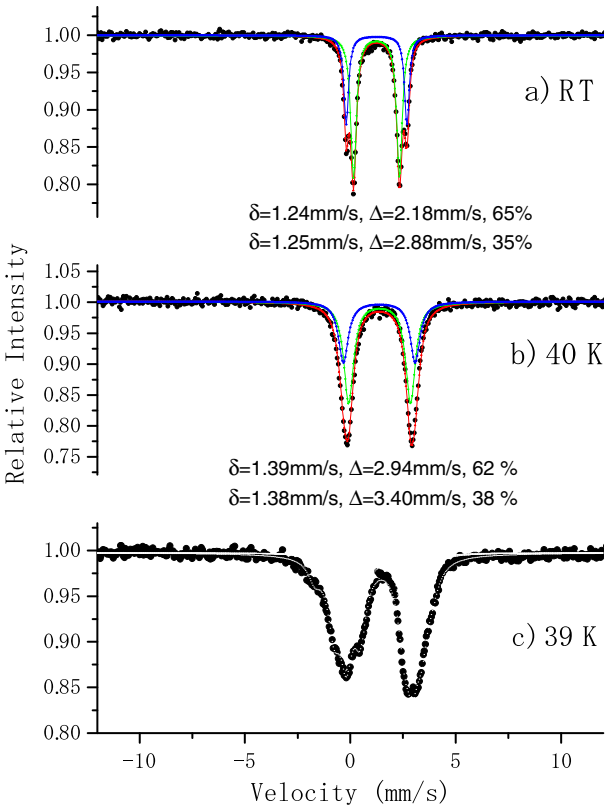

Fig. 1 Mössbauer spectra of $K_2Fe_3(OH)_2(SO_4)_3$ $(H_2O)_2$ at room temperature, 40 K and 39 K

1 Introduction

A method for controlling coercivity in synthesizing magnetic materials is not well known though it is said that the anisotropy energy of the crystal increases magnetic coercivity. The anisotropic magnetic moments of transition metal ions such as Fe^{2+}, Co^{2+}, and Mn^{3+} are large enough, but it is difficult to control the magnetic moments in crystals. It was reported that monocrystalline $K_2Co_3(OH)_2(SO_4)_3(H_2O)_2$ is a ferrimagnetic material with large coercive fields (H//a; 50 kOe, H//b; 25 kOe at 1.8 K). Its Neel temperature is 30 K [1]. As oxides with high coercivity, it is known that ε-Fe_2O_3 [2] shows a high coercive field of 22 kOe at room temperature [3]. The coercive field of $K_2Fe_3(OH)_2(SO_4)_3(H_2O)_2$ is 40 kOe at 4 K, and the Neel temperature is about 39 K. In order to clarify the local magnetic properties of this compound, we have studied the temperature dependence of the Mössbauer spectra, and determined the magnetic hyperfine fields at the iron atoms occupying each site.

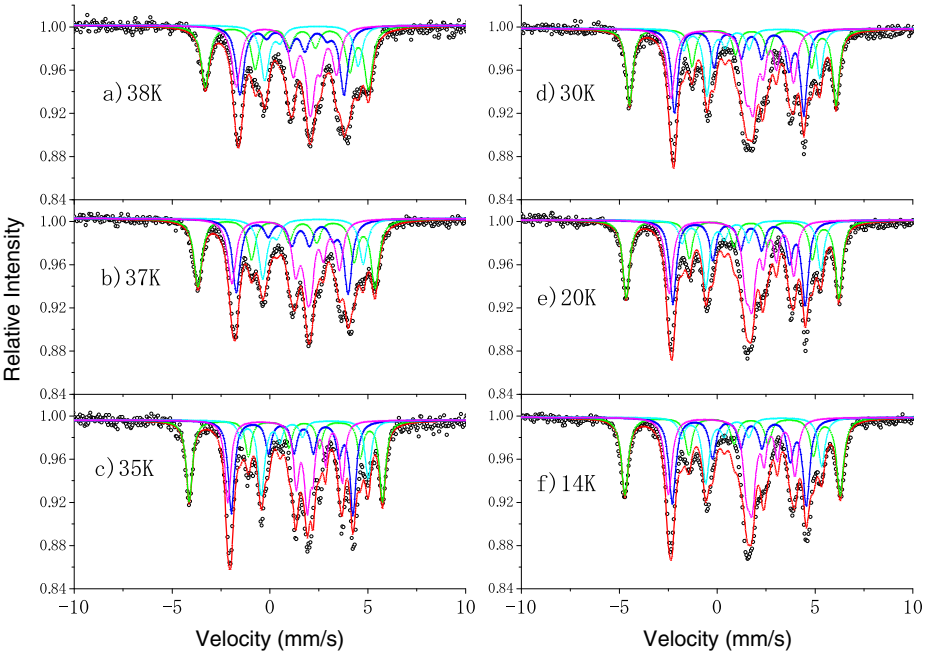

Fig. 2 Mössbauer spectra of $K_2Fe_3(OH)_2(SO_4)_3$ $(H_2O)_2$, measured at **a**) 38 K, **b**) 37 K, **c**) 35 K, **d**) 30 K, **e**) 20 K, and **f**) 14 K

2 Experimental

A powder sample was synthesized in an autoclave for 48 h at the temperature of 200°C by mixing iron sulphate, potassium sulphate, and potassium hydroxide with the molar ratio at 2:1:1. The crystal structure of $K_2Fe_3(OH)_2(SO_4)_3(H_2O)_2$ was determined being isomorphous with that of the Co system by X-ray diffraction [1] as shown in Table 1.

Mössbauer spectra were measured by using $^{57}Co(Cr)$ and a constant acceleration mode, and the Doppler velocity was calibrated using the data of an α-Fe foil at room temperature. Low temperature Mössbauer spectra were measured using a mini cryostat (Iwatani Co.). Mosswinn software was used for the analysis of the Mössbauer spectra.

3 Results and discussion

Two doublets of paramagnetic Fe^{2+} (isomer shift, $\delta = 1.24 \pm 0.01$ mm/s, quadrupole splitting, $\Delta = 2.18 \pm 0.02$ mm/s, line width, $\Gamma = 0.30 \pm 0.01$ mm/s, Area relative intensity $= 65 \pm 1\%$; $\delta = 1.25 \pm 0.01$ mm/s, $\Delta = 2.88 \pm 0.02$ mm/s, $\Gamma = 0.30 \pm 0.01$ mm/s, Area int. $= 35 \pm 1\%$) were observed in the room temperature Mössbauer spectrum as shown in Fig. 1. At 40 K, the isomer shift and quadrupole splitting of both doublets increased a little, and the difference between the two doublets became small. The electronic density at the two iron sites is not different, but the

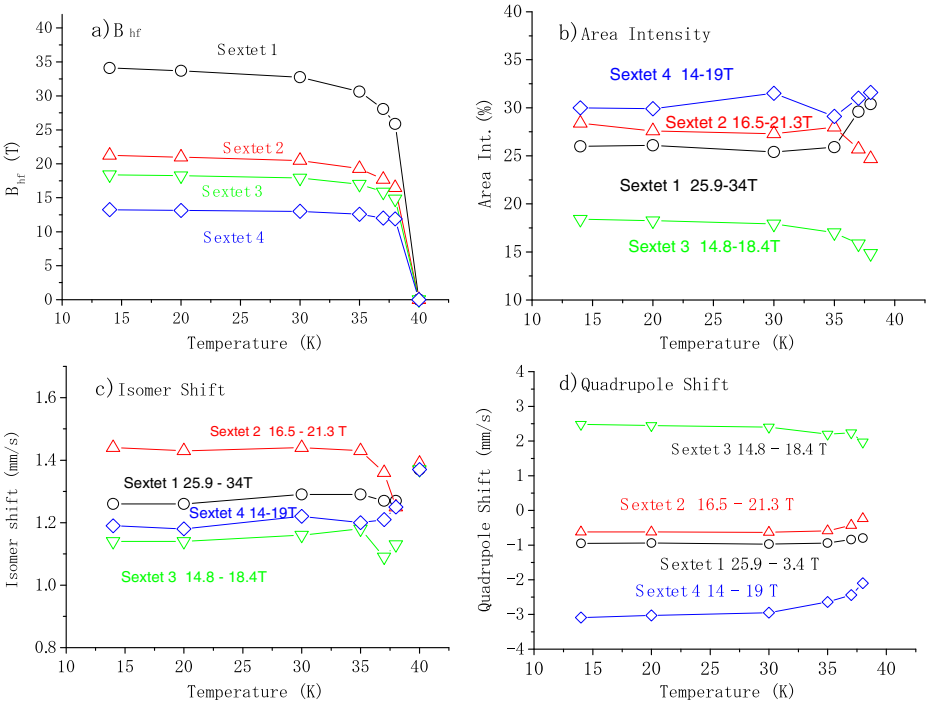

Fig. 3 Temperature dependence on **a** internal magnetic fields, **b** area intensity, **c** isomer shifts, and **d** quadrupole shifts of $K_2Fe_3(OH)_2(SO_4)_3(H_2O)_2$. The errors were estimated as follows; **a** B_{hf} ≦0.1 T, **b** Area Intensity ≦0.5%, **c** Isomer shift ≦0.01 mm/s, **d** Quadrupole shift ≦0.02 mm/s

electric field gradient around Fe^{2+} is strongy affected at low temperatures. At 39 K, magnetic ordering began to occur, but it was hard to analyze the Mössbauer spectrum precisely. Mössbauer spectra measured below 38 K were clearly developed into four magnetic sextets as shown in Fig. 2. The analysed Mössbauer parameters are shown in Fig. 3. Four magnetic sextets show $B_{hf} = 34.0$ T, 21.3 T, 19.0 T, and 18.4 T at 14 K (Fig. 3a). The magnetic sextets with high magnetic field order are named as sextet 1, 2, 3 and 4. The area intensity ratios are shown in Fig. 3b). Considering the sites occupied by Fe^{2+} in the crystalline structure, there are two sites with 1: 2 ratios, in which the directions of magnetic moments are anti-parallel with respect to each other [1]. The site occupation ratio is reflected in the Mössbauer spectra measured above 40 K. This shows ferrimagnetism at the lower temperatures, but four different Fe sites were observed at the lower temperatures. It might arise from the distorted crystallites because the large synthesized polycrystals were crushed in order to make uniform thickness of absorbers for the measurement of the Mössbauer spectra. The powder may contain amounts of small crystals with oriented planes. The area intensity ratio of the sextet lines was not always 3:2:1:1:2:3 as for a random orientation of magnetic moments. When analysing Mössbauer spectra, the area intensity of second and fifth peaks was not fixed.

The isomer shifts of the four magnetic sextets are between 1.15 mm/s and 1.45 mm/s below 35 K, which mean completely Fe^{2+} states. The deviating isomer

shifts and area intensities observed at 37 and 38 K may be due to fitting errors because of overlapping sub-spectra. The isomer shift values of the four sextets are very different from those of the two doublets (1.38 mm/s) at 40 K. This means that a charge disproportion of each site may occur at lower temperatures as shown in Fig. 3c. One quadrupole shift value of a sextet increased while the quadrupole shift values of the other three sextets decreased when lowering the measurement temperature (Fig. 3d). Moreover, the quadrupole shifts of the magnetic components were somewhat enhanced when lowering the temperature, which may suggest a crystalline distortion. These Mössbauer results may support that the compounds have large coercive fields.

4 Conclusion

$K_2Fe_3(OH)_2(SO_4)_3(H_2O)_2$ was prepared by hydrothermal synthesis as an isomorphous phase of $K_2Co_3(OH)_2(SO_4)_3(H_2O)_2$. Mössbauer spectra of $K_2Fe_3(OH)_2(SO_4)_3(H_2O)_2$ were measured at low temperatures between room temperature and 14 K. Two paramagnetic Fe^{2+} species were observed in the Mössbauer spectra above 40 K, and Mössbauer spectra measured below 38 K were decomposed into four magnetic subspectra. From the temperature dependence of isomer shifts, quadrupole shifts and magnetic fields, it is found that the local electron density at each site is largely deviating at low temperatures, which may induce the giant coercivity.

References

1. Vilminot, S., et al.: Chem. Mater. **22**, 4090–4096 (2010)
2. Tronc, E., et al.: J. Solid State Chem. **139**, 93–104 (1998)
3. Tuèek, J., et al.: Chem. Mater. **22**, 6483–6505 (2010)

Hyperfine Interact (2012) 208:59–63
DOI 10.1007/s10751-011-0415-4

Doping-induced valence change in $Yb_5Ge_{4-x}(Sb, Ga)_x$: ($x \leq 1$)

D. H. Ryan · N. R. Lee-Hone · J. M. Cadogan · K. Ahn · V. K. Pecharsky · K. A. Gschneidner Jr.

Published online: 26 October 2011

Abstract Following our earlier observation that the ytterbium valence distribution in $Yb_5Ge_{4-x}Si_x$ was independent of x, we use ^{170}Yb Mössbauer spectroscopy to follow the Yb valence distribution in Sb and Ga doped Yb_5Ge_4. The crystal structure does not change for either dopant and the Yb valence, while affected, proves quite resistant to change, with only one third of the electrons added or removed by the dopants leading to $Yb^{3+} \leftrightarrow Yb^{2+}$ conversion.

Keywords Lanthanide · Valence · Mössbauer spectroscopy

1 Introduction

The R_5X_4 (R = Y, La–Lu; X = Si, Ge, Sn) compounds became the subject of intense investigation after the discovery of a giant magnetocaloric effect in $Gd_5Si_2Ge_2$ [1]. Systematic phase relationship and structural data have been obtained for most of

D. H. Ryan · N. R. Lee-Hone
Department of Physics, McGill University, Montreal, QC, H3A2T8, Canada

J. M. Cadogan (✉)
Department of Physics and Astronomy, University of Manitoba, Winnipeg, MB, R3T2N2, Canada
e-mail: cadogan@physics.umanitoba.ca

K. Ahn · V. K. Pecharsky · K. A. Gschneidner Jr.
Ames Laboratory of the U.S. Department of Energy, Iowa State University, Ames, IA 50011-3020, USA

K. Ahn · V. K. Pecharsky · K. A. Gschneidner Jr.
Department of Materials Science and Engineering, Iowa State University, Ames, IA 50011-2300, USA

the $R_5Ge_{4-x}Si_x$ systems and two key parameters have been identified which affect the balance between the magnetic and structural energies in the R_5X_4 phases. The first is the ratio of the ionic radius of the rare earth, r_R, to the weighted average radius of the metalloid elements, r_X [2] and the second is the valence electron concentration [3]. As the ratio r_R/r_X decreases, the crystal structures of most R_5X_4 compounds change in the sequence: tetragonal $Zr_5Si_4 \rightarrow$ orthorhombic $Gd_5Si_4 \rightarrow$ monoclinic $Gd_5Si_2Ge_2 \rightarrow$ orthorhombic Sm_5Ge_4 [2]. The Yb_5X_4 compounds are of particular interest because Yb can occur in two valence states: Yb^{2+} (r_R = 1.94 Å) and Yb^{3+} (r_R = 1.74 Å). This allows us to explore the effects of both the valence electron concentration and the relative metallic radii (r_R/r_X). Surprisingly, $Yb_5Ge_{4-x}Si_x$ adopts the orthorhombic Gd_5Si_4-type (*Pnma* #62) structure, with a constant Yb^{2+}:Yb^{3+} population ratio of 1.09(4) for all x [4]. In this paper, we investigate the effects of Sb and Ga doping in Yb_5Ge_4. Sb and Ga have respectively one more and one less electron in their outer shell than Ge, allowing us to drive $Yb^{3+} \leftrightarrow Yb^{2+}$ interconversion directly, while the very different metallic radii of Sb (1.59 Å) and Ga (1.41 Å), both larger that that of Ge (1.37 Å), could drive the Yb valence towards the larger Yb^{2+}, effectively maintaining an approximately constant r_R/r_X ratio.

2 Experimental methods

The samples used in this study ($Yb_5Ge_{4-x}Sb_x$ (x = 0.5, 0.75, 1), $Yb_5Ge_{4-x}Ga_x$ (x = 0.5, 1) and Yb_5Ge_4) were prepared at the Ames Laboratory by induction melting stoichiometric mixtures of the pure elements following the standard procedure described elsewhere [5]. X-ray powder diffraction was used to verify the structure and phase composition of the materials. All of the materials were found to crystallize in the orthorhombic Gd_5Si_4-type *Pnma* structure. A second phase (11:10) is present in the Sb doped samples, amounting to ~5–15 mol % of the materials.

^{170}Yb Mössbauer spectroscopy was used to determine the relative proportions of Yb^{2+} and Yb^{3+}. A 20mCi ^{170}Tm source was prepared by neutron activation of ~20 mg of Tm as a 10 wt% alloy in aluminium. The source and sample were mounted vertically in a helium flow cryostat and the drive was operated in sine mode. The 84.25 keV Mössbauer γ-photons were isolated from the various x-rays emitted by the source using a high-purity Ge detector. The spectrometer's drive velocity was calibrated with a laser interferometer and velocities were cross-checked against ^{57}Co**Rh**/α-Fe at room temperature. All spectra were obtained at 5 K (except for Yb_5Ge_4 which was part of the earlier study [4] and was taken at 8 K) and fitted using a nonlinear least-squares minimization routine with line positions and intensities derived from an exact solution to the full Hamiltonian [6].

3 Results and discussion

The 84.25 keV $2^+ \rightarrow 0^+$ transition in ^{170}Yb involves a rotational change at almost constant nuclear volume, so the isomer shift is essentially independent of valence. However, the electric field gradients (EFG) associated with the two valence

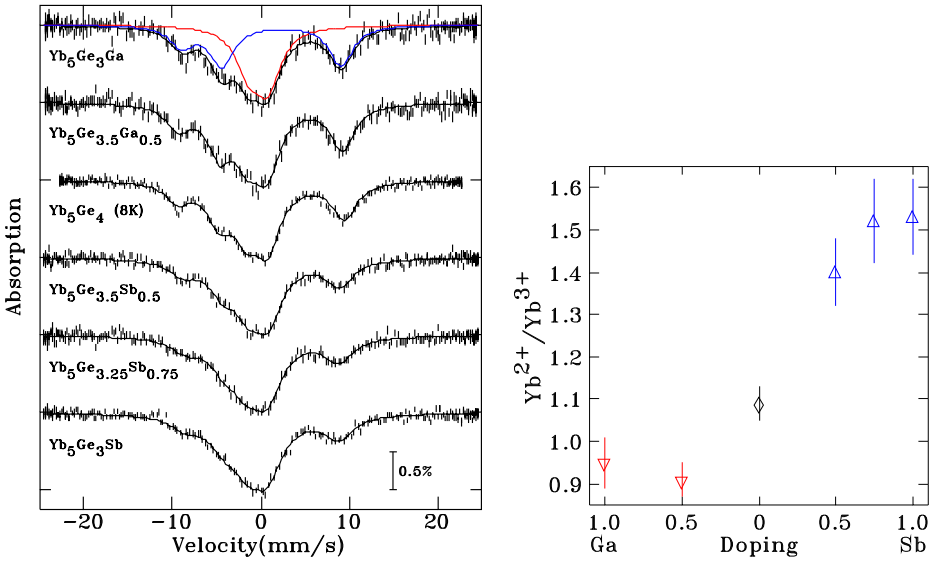

Fig. 1 (*Left*) ^{170}Yb Mössbauer spectra of $Yb_5Ge_{4-x}(Sb, Ga)_x$: ($x \leq 1$), obtained at 5 K (except for Yb_5Ge_4, taken at 8 K). The *solid lines* are fits to a full Hamiltonian solution as described in the text. For the top spectrum (Yb_5GaGe_3) we also show the two components Yb^{2+} (*red*) and Yb^{3+} (*blue*). (*Right*) Dopant dependence of the Yb^{2+}:Yb^{3+} area ratio, deduced from fits to the ^{170}Yb Mössbauer spectra

states are quite different. Yb^{2+} has a nonmagnetic, closed shell $4f^{14}$ electronic configuration, leaving only a small contribution to the EFG from the lattice, whereas Yb^{3+} has a $4f^{13}$ configuration which results in a significant 4f contribution to the EFG. The ^{170}Yb Mössbauer spectra of the studied compounds are shown in the left panel of Fig. 1. Each spectrum consists of two paramagnetic components, corresponding to the two valence states of Yb. As with $Yb_5Ge_{4-x}Si_x$ [4], it was not possible to resolve the contributions from the three ytterbium sites, and only a valence separation was possible. The right panel of Fig. 1 shows the Yb^{2+}:Yb^{3+} subspectral area ratio plotted against the dopant content. Doping with Sb strongly increases the Yb^{2+}:Yb^{3+} ratio, whereas Ga doping produces a smaller decrease. This difference in the strength of the doping effects may derive from the larger size of the dopants supporting (in the case of Sb) or competing with (in the case of Ga) the valence shift. One way to separate out the effects of dopant size (r_X) is to combine our data with those from $Yb_5Ge_{4-x}Si_x$ [4] in the left panel of Fig. 2, where it is clear that doping with the larger Ga actually leads to a cell volume *decrease* while the increase with Sb doping is slower than expected. Both departures from the trend established by $Yb_5Ge_{4-x}Si_x$ are due to $Yb^{3+} \leftrightarrow Yb^{2+}$ conversion.

Finally, in the right panel of Fig. 2 we show the total valence electron count, per formula unit, as a function of dopant (Ga = 3; Ge = 4; Sb = 5 with the Yb value derived from the measured Yb^{2+}:Yb^{3+} ratio). No valence conversion would give a slope of unity, while full dopant-induced conversion would yield zero slope. The

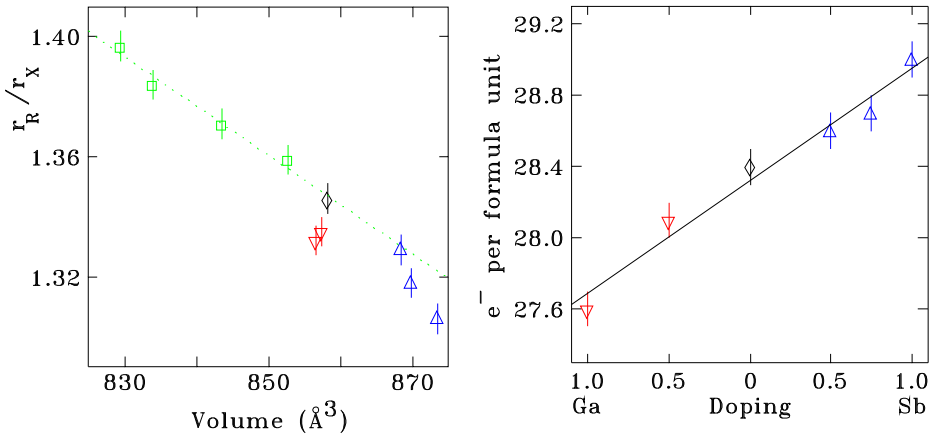

Fig. 2 (*Left*) Cell volume dependence of the atomic radii ratio (r_R/r_X). □ (*green*) and the *dashed line* show the trend for $Yb_5Ge_{4-x}Si_x$ [4]. ▽ (*red*) and △ (*blue*) show data for gallium and antimony doping respectively. (*Right*) Dopant dependence of the weighted valence electron count

fitted slope of 0.63(6) indicates that the Yb valence distribution is rather robust, with only about *one-third* of the valence electrons donated by the dopants actually leading to $Yb^{3+} \leftrightarrow Yb^{2+}$ valence conversion, with the other two-thirds entering the conduction band.

In order to obtain more information on the relative importance of dopant size and valence, we plan to investigate the effects of In (over-sized acceptor) and As (size-matched donor) doping in this system.

4 Conclusions

We have examined the effect of Ga and Sb doping on the Yb^{2+}:Yb^{3+} population ratio in the $Yb_5(Ge, Ga, Sb)_4$ system by ^{170}Yb Mössbauer spectroscopy. Sb doping has a large effect on the Yb valence ratio, due to the combined effects of the increased atom size and the increase in valence electron concentration. In the case of Ga doping, the competing effects of the increased atom size and the reduced electron valence concentration lead to significantly smaller changes in the Yb^{2+}:Yb^{3+} ratio. Finally, the crystallographic cell volume increases with Sb doping, and decreases with Ga doping, an effect which is explained in part by the change in average weighted volume of the Yb ions, due to the change in the Yb^{2+}:Yb^{3+} ratio.

Acknowledgements JMC acknowledges support from the Canada Research Chairs programme. Financial support for various stages of this work was provided by the Natural Sciences and Engineering Research Council of Canada and Fonds Québécois de la Recherche sur la Nature et les Technologies. Source activation was by M. Butler at the McMaster Nuclear Reactor (MNR), Hamilton, Ontario. Work at Ames Laboratory is supported by the U.S. Department of Energy, Office of Basic Energy Sciences, Division of Materials Sciences and Engineering under Contract No. DE-AC02-07CH11358 with Iowa State University.

References

1. Pecharsky, V.K., Gschneidner, K.A. Jr.: Giant magnetocaloric effect in $Gd_5Si_2Ge_2$. Phys. Rev. Lett. **78**, 4494-7 (1997)
2. Pecharsky, A.O., Pecharsky, V.K., Gschneidner, K.A. Jr.: Phase relationships and low temperature heat capacities of alloys in the Y_5Si_4-Y_5Ge_4 pseudobinary system. J. Alloys Compd. **379**, 127 (2004)
3. Choe, W., Pecharsky, V.K., Pecharsky, A.O., Gschneidner, K.A. Jr., Young, V.G., Miller, G.J.: Making and breaking covalent bonds across the magnetic transition in the giant magnetocaloric material $Gd_5(Si_2Ge_2)$. Phys. Rev. Lett. **84**, 4617 (2000)
4. Voyer, C.J., Ryan, D.H., Ahn, K., Gschneidner, K.A. Jr., Pecharsky, V.K.: Valence and magnetic ordering in the $Yb_5Si_xGe_{4-x}$ pseudobinary system. Phys. Rev. B **73**, 174422 (2006)
5. Ahn, K., Tsokol, A.O., Mozharivskyj, Y., Gschneidner, K.A. Jr., Pecharsky, V.K.: Phase relationships and structural, magnetic and thermodynamic properties of the Yb_5Si_4–Yb_5Ge_4 pseudobinary system. Phys. Rev. B **72**, 054404 (2005)
6. Voyer, C.J., Ryan, D.H.: A complete solution to the Mössbauer problem, all in one place. Hyperfine Interact. **170**, 91–104 (2006)

Hyperfine Interact (2012) 208:65–69
DOI 10.1007/s10751-011-0503-5

Dilute magnetic properties of Fe doped Al_2O_3 powders prepared by sol-gel method

Kiyoshi Nomura · Ryosuke Kinoshita · Isao Sakamoto · Jun Okabayashi · Yasuhiro Yamada

Published online: 4 January 2012

Abstract Aluminium oxides doped with 1% ^{57}Fe were prepared by sol-gel method, and annealed for 3 hours at various temperatures between 550°C and 1100°C. Amorphous phases were obtained below 1000°C, and crystalline α–Al_2O_3 was formed at 1100°C. Although Al_2O_3 itself shows diamagnetism, the light doping of Fe ions into aluminium oxide induced a very weak ferromagnetism, but the ferromagnetism disappeared by longer annealing. Mössbauer spectra were composed of paramagnetic Fe^{2+} and Fe^{3+} species for samples heated below 750°C, and of paramagnetic Fe^{3+} above 850°C, in addition to a magnetic sextet and relaxation peaks of Fe^{3+}. The magnetic and quadrupole interactions of the sextet and the relaxation peaks and the density functional calculations suggest that the lightly doped Fe^{3+} ions are substituted at Al sites in the Al_2O_3 lattice.

Keywords Dilute magnetism · Fe doping · Amorphous and crystalline aluminium oxide · Mössbauer spectra · Nano-materials

K. Nomura (✉)
School of Engineering, the University of Tokyo, 7-3-1, Hongo, Bunkyo-ku, Tokyo, 113-8656, Japan
e-mail: k-nomura@t-adm.t.u-tokyo.ac.jp

R. Kinoshita · I. Sakamoto
Department of Electric Engineering, Hosei University, Koganei, Tokyo 184-8584, Japan

J. Okabayashi
School of Science, the University of Tokyo, 7-3-1, Hongo, Bunkyo-ku, Tokyo, 113-0033, Japan

Y. Yamada
Department of Chemistry, Tokyo University of Science, Kagurazaka, Shinjyuku-ku, Tokyo, 162-8601, Japan

1 Introduction

Ferromagnetic phenomena have been observed at room temperature (RT) by doping diluted magnetic impurities into semiconductors and insulators with a large band gap [1–3]. We found that $Y_3Al_5O_{12}$(YAG) doped with <1% Fe ions shows RT ferromagnetism, and we have analyzed the hyperfine structures by Mössbauer spectrometry [4]. Dilute ferromagnetic insulators (DMI) are also useful for spin transfer electronics as well as dilute magnetic semiconductors (DMS). Tunnel magnetic resistance is observed when Al_2O_3 is implanted with Fe ions, Co ions, and/or Au ions in vacuum [5, 6]. The single crystal Al_2O_3 plates, implanted with ^{57}Fe and Au ions, were characterized by conversion electron Mössbauer spectroscopy [6]. In this case, the implanted irons exist as metallic clusters and as Fe^{2+} ions. Al_2O_3 is a transparent insulator with a band gap of 6–8 eV, and the crystalline structure is the same corundum as α–Fe_2O_3. In this paper, in order to investigate the magnetism of particles of 1% Fe doped Al_2O_3, and to confirm the hyperfine structure produced by doping dilute Fe ions, we have studied sol-gel synthesized Fe doped alumina, heated at various temperatures.

2 Experimental

In order to prepare nominal compositions such as $Al_{1.98}Fe_{0.02}O_3$, citric acid solutions of Al ions and ^{57}Fe ions were mixed with ethylene glycol. The solutions were condensed at about 80°C to form a colloidal gel. After the gel was heated at 350°C for 2 hours to form xerogel, the xerogel was heated at various temperatures from 550°C to 1100°C for 3 hours, respectively. The colour of the powders prepared changed from dark brown to white with increasing heating temperature. These samples were analysed by X-ray diffractions (XRD: Cu target), vibrational sample magnetometry (VSM), and Mössbauer spectrometry. Mössbauer spectra were measured by using a ^{57}Co(Cr) source and the Doppler velocity was calibrated by using an α–Fe foil. Mosswinn program was used for the analysis of the Mössbauer spectra.

3 Results and discussion

XRD patterns of prepared samples are shown in Fig. 1. Amorphous structures were obtained below 1000°C although crystalline α–Al_2O_3 was partly included at 1000°C, and full crystalline α–Al_2O_3 was obtained at 1100°C. The lattice parameter of α–Al_2O_3 doped with 1% Fe increased by $a = 0.006$ nm from α–Al_2O_3 because the ionic radius of Fe^{3+} (0.064 nm) is larger than that of Al^{3+}(0.051 nm). The crystallite size was about 45 nm at 1100°C. The light doping of Fe ions into alumina induced ferromagnetism although the alumina itself without magnetic ions showed diamagnetism. With increasing heating temperature, the saturation magnetization decreased up to 750°C and increased again above 950°C as shown in Fig. 2. The sample heated at 1100°C showed saturation magnetization of 0.0031 μ_B/Fe a.u. and coercivity of 285 Oe. The weak ferromagnetism was observed for all 1% Fe doped alumina heated for 3 hours.

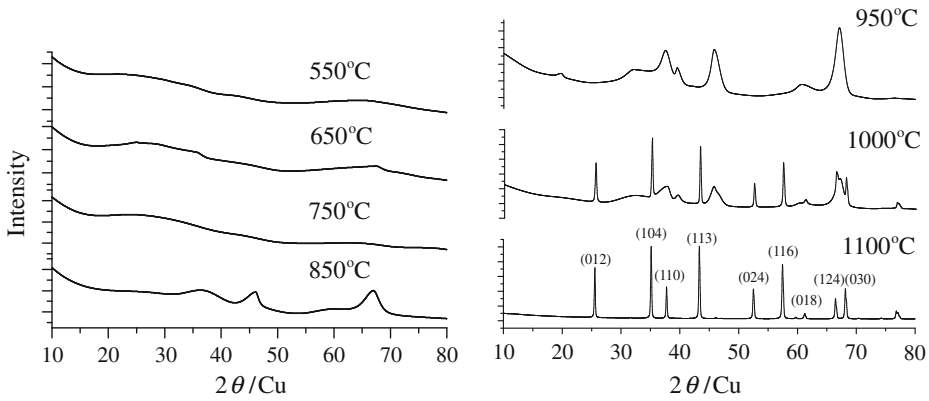

Fig. 1 XRD patterns of alumina doped with 1% ^{57}Fe, prepared by sol-gel method and annealed for 3 hours at various temperatures

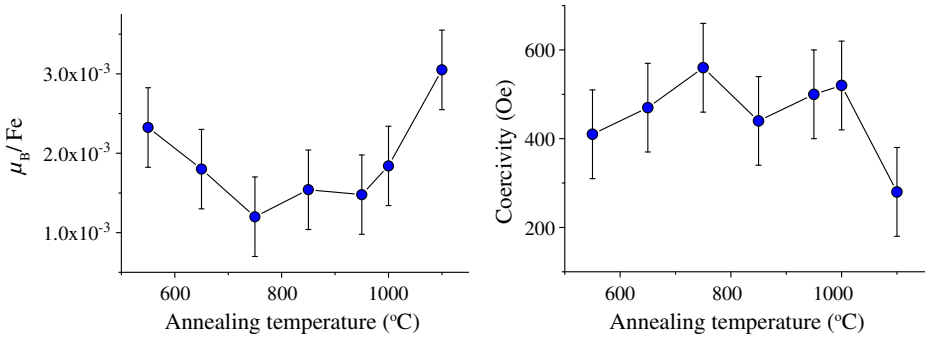

Fig. 2 Saturation magnetization and coercivity of alumina doped with 1% ^{57}Fe, prepared by sol-gel method and annealed for 3 hours at various temperatures

The Mössbauer spectra, as shown in Fig. 3, are decomposed into doublets, sextet, and broad magnetic peaks. For the sample heated below 750°C, the spectra are composed of two doublets, D1 (isomer shift (IS) = 0.51–0.86 mm/s, quadrupole splitting (QS) = 1.01–1.44 mm/s), and D2 (IS = 0.91–1.07 mm/s, QS = 1.93–2.2 mm/s). The former shows the mixed valence states of Fe^{2+} and Fe^{3+} and the latter is clearly assigned to Fe^{2+} ions. Above the heating temperature of 850°C, one doublet with IS = 0.32–0.38 mm/s and QS = 0.76–1.3 mm/s is clearly observed, which comes from the Fe^{3+} species. The isomer shifts of the broad magnetic peaks are visually observed to be close to nearly zero Doppler velocity. Metallic iron states should not exist in these samples, and the peaks were analysed by using the Blume-Tjon magnetic relaxation method. As a result, Mössbauer parameters of the magnetic relaxation peaks (IS = 0.028–0.45 mm/s, $\tau = 10^{-8.4}$–10^{-9} s, $V_{zz} = (0.17–3.02) \times 10^{21}$ V/m^2) were obtained, assuming an inner magnetic field, $B_{hf} = 50.4$ T, and asymmetry parameter, $\eta = 0.5$. The iron states in the relaxation peaks are clearly due to Fe^{3+} from the isomer shifts. The parameters of the contained magnetic sextet were IS = 0.23–0.36 mm/s, B_{hf} = 48.8–50.6 T, and QS (or 2ε) = 0.04–0.28 mm/s. With

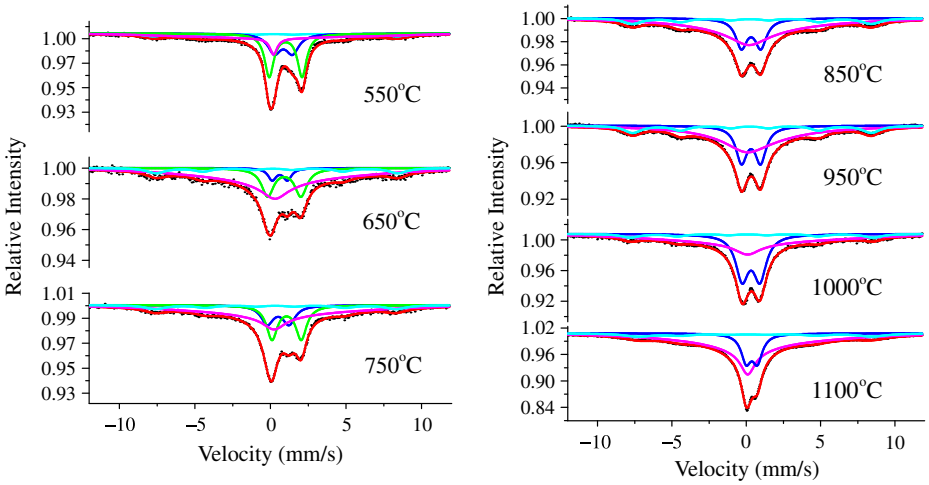

Fig. 3 Annealing temperature dependence on Mössbauer spectra of alumina doped with 1% ^{57}Fe

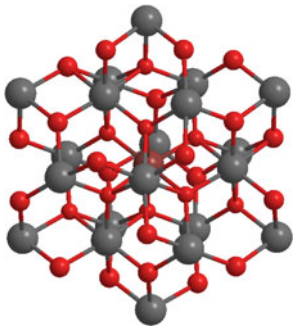

Fig. 4 The cluster of $Fe@Al_{20}O_{30}$ used for density functional calculation. *Brown*, *black*, and *red* balls indicate Fe, Al, and O atoms, respectively

increasing temperature, the doublet of paramagnetic Fe^{2+} decreased, and the doublet of Fe^{3+} increased. Above 850°C all Fe species were more oxidized into Fe^{3+} species, and the QS values of the doublets became small. The QS values of all magnetic sextets and the V_{zz} of relaxation peaks were positive.

Density functional calculations were performed using ORCA program package [7, 8] in order to estimate Mössbauer parameters of the Fe atom in substitutional position of Al in Al_2O_3 lattice. It was assumed that a Fe atom was located in the centre of a $Al_{20}O_{30}$ cluster (Fig. 4). Calculated Mulliken atomic charge and spin density of the Fe atom were 3.15 electrons and 4.25 electrons /a.u.^{3}, respectively. The calculated Mössbauer parameters of Fe in $Al_{20}O_{30}$ cluster were $\eta = 0.513$, QS = +0.102 mm/s, and $\rho(0) = 11816.5475$ /a.u.^{3}, which are in good agreement with the observed parameters. It was found that Fe atoms in Al_2O_3 have positive QS value.

The magnetic sextet with positive QS value and the relaxation peaks with positive V_{zz} suggest that Fe ions are incorporated into Al atom sites of alumina. Magnetic relaxation peaks varied with annealing temperatures. However, Mössbauer spectra of 5% Fe doped alimina showed a sextet (51T) with negative QS value (−0.2 mm/s)

in addition to a doublet, not including broadened peaks. It is found clearly from the negative QS value that a cluster of hematite (α–Fe_2O_3) is precipitated from Al_2O_3. There is no solid solution of Al and Fe oxides in the case of higher doping of Fe ions into Al_2O_3. The magnetic hysteresis of 1% Fe doped alumina disappeared also by further annealing for 6 hours, and the Mössbauer spectrum after longer annealing became similar to that before the treatment although the intensity ratios of the components were a little different. It is not clear what the origin of magnetically broadened patterns is; it might be due to antiferromagnetic order or might not be. It is considered that defects or a deformed surface of nano grains might induce very weak ferromagnetic order even if the materials were antiferromagnetic. It has been reported that lattice defects and deformations might be the most likely sources of weak ferromagnetism in Hf oxides [9] and YAG doped with dilute Fe ions [4].

4 Conclusion

Aluminium oxides doped with 1 % ^{57}Fe were prepared by the sol-gel method, and annealed for 3 hours at various temperatures. The Fe species were oxidized more at the higher annealing temperatures. The light doping of Fe ions into aluminium oxides induced a weak ferromagnetism at room temperature although the longer annealing lost the ferromagnetic hysteresis. Both the magnetic and quadrupole interactions of the sextet and relaxation peaks and the density functional calculations suggest that the Fe species are substitutional at Al atom sites in aluminium oxides in the case of light doping. However, higher doping of Fe ions at high temperatures induces precipitation of hematite clusters in the Al_2O_3 lattice.

References

1. Matsumoto, Y., Murakami, M., Shono, T., Hasegawa, T., Fukumura, T., Kawasaki, M., Ahmet, P., Chikyow, T., Koshihara, S., Koinuma, H.: Science **291**, 854 (2001)
2. Yun, F., Morkoc, H.: Mater. Sci. Mater. Electron. **16**, 555 (2005)
3. Nomura, K., Barrero, C.A., Sakuma, J., Takeda, M.: Phys. Rev. B **75**, 184411 (2007)
4. Nemeth, Z., Nomura, K., Ito, Y.: Phys. Chem. C **113**, 20044 (2009)
5. Hayashi, N., Sakamoto, I., Wakabayashi, H., Toriyama, T., Honda, S.: J. Appl. Phys. **94**, 2597 (2003)
6. Kinoshita, R., Sakamoto, I., Hayashi, N., Nomura, K., Honda, S., Ishida, T., Iio, S., Tashiro, H., Toriyama, T.: Jpn. J. Appl. Phys. **50**, 01BE01 (2011)
7. Romelt, M., Ye, S., Neese, F.: Inorg. Chem. **48**, 784 (2009)
8. Petrenko T., Sturhahn, W., Neese, F.: Hyperfine Interact. **175**, 165 (2008)
9. Coey, J.M.D., Venkatesan, M., Stamenov, P., Fitzgerald, C.B., Dorneles, L.S.: Phys. Rev. B **72**, 024450 (2005)

Hyperfine Interact (2012) 208:71–74
DOI 10.1007/s10751-011-0438-x

Mössbauer study of ^{119}Sn in ^{119}In* implanted 3C-SiC

Hilary Masenda · Krishanlal Bharuth-Ram · Deena Naidoo · Haraldur Páll Gunnlaugsson · Torben Esmann Mølholt · Haflidi Petur Gislason · Karl Johnston · Roberto Mantovan · Rainer Sielemann · Guido Langouche · Sveinn Olafson · Gerd Weyer · the ISOLDE Collaboration

Published online: 11 November 2011

Abstract ^{119}Sn Mössbauer measurements have been made on a 3C-SiC single crystal implanted with 60 keV precursor radioactive ^{119}In* ions at ISOLDE/CERN. Spectra collected at sample temperatures of 300–670 K have been analysed in terms of two single lines and a quadrupole split doublet, which based on their isomer shifts are assigned respectively to Sn ions located on substitutional Si sites (Sn_{Si}) and interstitial sites (Sn_I) and in defect complexes near substitutional sites. The substitutional Sn_{Si} fraction increases from 25% at room temperature to 60% at 680 K.

H. Masenda · D. Naidoo
School of Physics, University of the Witwatersrand, WITS 2050, Johannesburg, South Africa

K. Bharuth-Ram (✉)
School of Physics, University of KwaZulu-Natal, Durban 4041, South Africa
e-mail: kbr@saao.ac.za

H. P. Gunnlaugsson · G. Weyer
Institute of Physics and Astronomy, Aarhus University, 8000 Aarhus, Denmark

T. E. Mølholt · H. P. Gislason · S. Olafson
Science Institute, University of Iceland, Dunhaga 3, IS-107 Reykjavík, Iceland

K. Johnston
PH Division, ISOLDE/CERN, 1211 Geneva 23, Switzerland

R. Mantovan
Laboratorio MDM, IMM- CNR, 20041 Agrate Brianza (MB), Italy

R. Sielemann
Helmholtz-Zentrum-Berlin, 14109 Berlin, Germany

G. Langouche
Instituut voor Kern-en Stralings fysika, University of Leuven, 3001 Leuven, Belgium

Keywords ^{119}In implantation · SiC · ^{119}Sn-Mössbauer spectroscopy

PACS 76.80.+y · 75.30.Hx · 75.47.Lx · 75.50.Pp

1 Introduction

The physical properties of SiC such as its wide band gap and its radiation hardness is expected to lead to enhanced performance in a wide variety of applications, in particular in conditions where conventional silicon-based devices cannot function. However planar surface devices are difficult to realize by doping during epitaxial growth [1]. As an alternative, ion implantation offers accurate control of both the dopant profile and depth, thus making possible the fabrication of planar SiC devices with tailored doped areas. Ion implantation of Sb^+ ions into Si, however, was found to produce considerable displacement of the lattice atoms, which increased with implantation and resulted in the formation of an amorphised layer at a dose of $\sim 10^{14}$ /cm^2 [2].

The present ^{119}Sn Mössbauer spectroscopy (MS) measurements were therefore aimed at investigating the lattice location of the implanted ions and the defect complexes they form in SiC implanted with extremely low dose ^{119}In* ions. In earlier ^{119}Sn-Mössbauer studies on SiC [3–5], the structure of the defects and their annealing characteristics have been investigated on samples implanted with radioactive precursor $^{119}In^+$, $^{119m}Sn^+$, $^{119}Sb^+$ and $^{119m}Te^+$, and were observed to display strong dependence on the chemical nature of the implanted impurities. The investigations on ^{119}In* implanted SiC, however, were conducted only with implantation at 300 K, and instrumental problems yielded spectra with rather broad lines. The present measurements are an extension of the MS study on ^{119}In* implanted SiC.

2 Experimental details

Radioactive ^{119}In* ions, produced at ISOLDE/CERN by 1.4 GeV proton-induced fission in a UC_2 target and elemental selective laser ionization, were implanted with 60 keV energy at an angle of 30° into a 3C-SiC single crystal sample held at 300–670 K in an implantation chamber. The maximum implantation fluence was 10^{12} ions/cm^2. ^{119}In* ($t_{1/2}$ = 140 s) decays to the ^{119}Sn 780 keV excited state, which in turn decays through the 23.8 keV Mössbauer state. Mössbauer emission spectra were collected with a resonance detector, equipped with a ^{119}Sn-enriched $CaSnO_3$ electrode, mounted outside the chamber on a conventional constant-acceleration drive system at 90° to the beam direction.

3 Results and discussion

Mössbauer spectra, measured at the temperatures indicated, are shown in Fig. 1. They have been analysed in a simultaneous fitting procedure with two single lines, S1 and S2, and a quadrupole split doublet component, D1, with Voigt profiles of Lorentzian line-width (FWHM) Γ = 0.67 mm/s and Gaussian broadening σ. The temperature dependence of the line positions were assumed to follow a second order

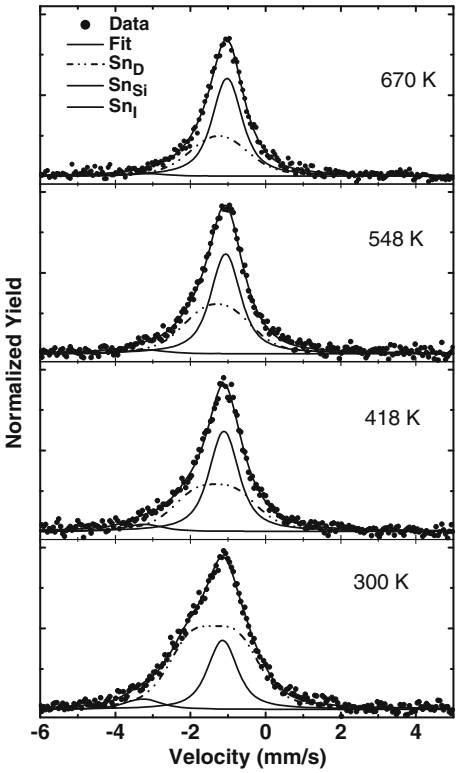

Fig. 1 Mössbauer spectra of ^{119}Sn in 3C-SiC observed at the temperatures indicated

Table 1 Isomer shift (δ), quadrupole splitting (ΔE_Q) and Gaussian broadening (σ) of the spectral components determined from the spectra shown in Fig. 1

	$D1(Sn_D)$	$S1(Sn_{Si})$	$S2(Sn_i)$
δ (mm/s)	1.49(2)	1.27(3)	3.40(5)
ΔE_Q (mm/s)	1.18(5)		
σ (mm/s)	0.47	0.21	0.32

Doppler shift; the quadrupole splitting of the doublet was set as a free parameter, but, within errors, was found to follow a $T^{3/2}$ dependence. The line broadening and the hyperfine parameters extracted from the fits to the spectra are listed in Table 1, where the isomer shifts are given relative to $Ca^{119}SnO_3$.

For assignment of the spectral components in terms the lattice location of the Sn ions, we compare our results with those summarised in [4]. The spectra of all the SiC samples implanted with the different pre-cursor isotopes shows a dominant line with isomer shift $< \delta >= 1.30(2)$ mm/s, and which combined channelling and Mössbauer studies [6] show to be due to Sn ions in Si sites. The isomer shift value is in excellent agreement with our result for line S1. In addition, the parameters of the quadrupole split component D1 determined in the present study are consistent with those of line "3" in ref. [3] where it is attributed to ^{119}Sn atoms on Si sites but in a defect complex with a neighbouring vacancy.

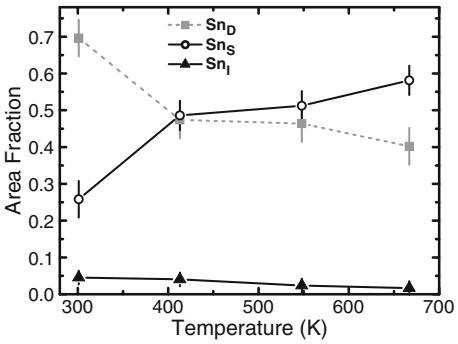

Fig. 2 Temperature dependence of area fractions of the spectral components

The isomer shift of the weak line S2 is quite large (3.4(1) mm/s), but within the range (3–4 mm/s) reported for interstitial type Sn defects in group IV semiconductors [6]. Accordingly, components S1, S2 and D1 are assigned respectively to Sn ions at substitutional Si sites (Sn_{Si}), interstitial sites (Sn_I) and in defect complexes around substitutionally located Sn (Sn_D). They are referred to in Fig. 1 by their assigned identities.

The temperature dependence of the area fractions of the spectral components is presented in Fig. 2. Strong annealing of lattice defect is evident in the temperature range 300–420 K, while there is tendency of a second stage above 550 K with the Sn_{Si} fraction increasing to 60% at 670 K.

4 Conclusions

We have conducted ^{119}Sn Mössbauer measurements on a 3C-SiC single crystal sample following the implantation of ^{119}In* at temperatures between 300 K and 670 K. The spectra have been decomposed into two single lines and a quadrupole split doublet which, after comparison with earlier MS and channelling studies, are assigned to Sn ions at substitutional Si sites (Sn_{Si}), interstitial sites (Sn_I), and in defect complexes around substitutionally located Sn (Sn_D).

There is clear evidence of an annealing stage of lattice damage in the temperature range 300–420 K; above 420 K the damage component continues to decrease with suggestion of a second annealing stage above 550 K. The substitutional Sn_{Si} fraction increases from 25% at room temperature to 60% at 670 K.

Acknowledgements This work was supported by the NRF (South Africa), RII3-EURONS, the Cariplo Foundation, the German BMBF and the Icelandic Research Fund.

References

1. Negoro, Y., Katsumoto, K., Kimoto, T., Matsunami, H.: J. Appl. Phys. **96**, 224–228 (2004)
2. Hart, R.R., Dunlap, H.L., Marsh, O.J.: Radiat. Eff Defects S **9**, 261–266 (1971)
3. Petersen, J.W., Weyer, G., Loft Nielsen, H., Damgaard, S., Choyke, W.J., Andreasen, H.: Hyperfine Interact. **23**, 17–42 (1985)
4. Weyer, G., Nylandsted-Larsen, A., Holm, N.E., Nielsen, H.L.: Phys. Rev. **B21**, 4939–4947 (1980)
5. Weyer, G., Damgaard, S., Petersen, J.W., Heinemeier, J.: Hyperfine Interact. **7**, 4292–4300 (1980)
6. Petersen, J.W., Andersen, J.U., Damgaard, S.: Hyperfine Interact. **9/10**, 989–993 (1981)

Hyperfine Interact (2012) 208:75–78
DOI 10.1007/s10751-011-0427-0

Reclassification of CK chondrites confirmed by elemental analysis and Fe-Mössbauer spectroscopy

Shiro Kubuki · Jun Iwanuma · Kazuhiko Akiyama · Miki Isa · Naoki Shirai · Mitsuru Ebihara · Tetsuaki Nishida

Published online: 1 November 2011

Abstract Twenty CK chondrites collected in the Antarctica Continent were characterized by inductively-coupled plasma mass spectrometry (ICP-MS), prompt gamma ray analysis (PGA), instrumental neutron activation analysis (INAA), X-ray diffractometry (XRD) and ^{57}Fe-Mössbauer spectroscopy. As a result of elemental analysis, it was revealed that 18.2∼26.4 mass% of iron was included in the each chondrite. Mössbauer spectrum of LEW86258, classified as a typical CK chondrite, was found to be composed of two paramagnetic doublets and two magnetic sextets. Mössbauer spectra were assigned to the absorption due to forsterite ($Mg_{1.36}Fe_{0.64}SiO_4$) and magnetite (Fe_3O_4), as also confirmed by XRD. XRD study of LAP03834, reclassified from CK to R chondrite, revealed the presence of crystalline phase due to forsterite. These results indicate that LAP03834 and related chondrites, *i.e.*, MET01149, LAP03923 and MAC02453, should be reclassified as R or LL chondrite.

Keywords CK Chondrite · ^{57}Fe-Mössbauer spectroscopy · X-ray diffractometry

1 Introduction

Chondrites are defined as stone meteorites mainly composed of silicates with spherical particles called chondrules, providing us information about the earlier stage of the

S. Kubuki (✉) · J. Iwanuma · K. Akiyama · M. Isa · N. Shirai · M. Ebihara
Department of Chemistry, Graduate School of Science and Engineering,
Tokyo Metropolitan University, Minami-Osawa 1-1,
Hachi-Oji, Tokyo 192-0397, Japan
e-mail: kubuki@tmu.ac.jp

T. Nishida
Department of Biological and Environmental Chemistry,
Faculty of Humanity-Oriented Science and Engineering,
Kinki University, Kayanomori 11-6, Iizuka, Fukuoka 820-8555, Japan

Solar System formation. Chondrites are now classified into fifteen groups, depending on the chemical composition and mineralogy [1]. They are petrologically classified into seven groups of group 1 to 7, depending on the degree of aqueous alteration and thermal metamorphism. CK chondrites are characterized by 1 mm diameter and 15% of modal abundances of chondrules. However, classification of CK chondrites is known to be relatively difficult because of less availability of the samples [2]. In order to investigate the relationship between the chemical composition and the structure of CK chondrites collected in the Antarctica Continent, measurements of neutron activation analyses (PGA and INAA), inductively coupled plasma-mass spectrometry (ICP-MS), X-ray diffractometry (XRD), and ^{57}Fe-Mössbauer spectroscopy were carried out.

2 Experimental

Antarctic CK chondrites tentatively classified as CK3 (LAP03834, MET01149), CK4 (ALH85002, DAV92300, EET99430, LAR04318, LEW86258, PCA91470), CK4/5 (PCA 82500), CK5 (EET83311, EET87507, EET90015, LAP03784, LAP3923, LAR06874, MAC02453, RBT03522), CK5/6 (EET87860) and CK6 (LAR06872, LEW87009) were loaned by the Meteorite Working Group (NASA / Johnson Space Center, USA). Several hundred mg of powdered samples were irradiated with neutron at JRR-3 and JRR-4 of Japan Atomic Energy Agency. JB-1 and Allende were used as the standard materials. Elemental abundances were determined by PGA and INAA by using JRR-3 and JRR-4 reactors of Japan Atomic Energy Research Institute, respectively. The detailed procedures of PGA and INAA are given in [3]. Mössbauer spectra were recorded by a constant acceleration method with a source of ^{57}Co(Rh) and a reference of α-Fe foil. Mosswinn 3.0i XP was used for the spectral analysis. XRD pattern was recorded from $2\Theta = 10$ to 80° at 0.02° intervals at a scanning rate of 5° min^{-1}. Cu-K$_\alpha$ X-rays ($\lambda = 0.1541$ nm) were used for XRD study, generated under the tube voltage and the current of 50 kV and 300 mA, respectively. Crystalline phases were identified with a standard compiled by the International Center for Diffraction Data (ICDD).

3 Results and discussion

As a result of elemental analysis, Fe/Mn abundance ratios of LAP03834, MET01149, LAP 03923 and MAC02453 were calculated to be 94.0, 111.9, 66.3 and 70.5, respectively. These values are much lower than that of typical CK chondrite, *i.e.*, *ca.* 200. Hence, we suggest that LAP03834 and MET01149 should be classified as R chondrite, having Fe/Mn ratio of around 100, while LAP 03923 and MAC02453 as LL chondrite with the Fe/Mn ratio of *ca.* 70 [4].

Mössbauer spectrum illustrated in Fig. 1a is typical of CK chondrite containing about 20% of magnetite. Mössbauer spectrum of LAP03834 is composed of two paramagnetic doublets with isomer shift (δ) values of 1.17 ($\pm$0.01) and 1.40 ($\pm$0.01) mm s^{-1}, as illustrated in Fig. 1b. The former δ value is attributed to octahedral Fe^{II}, and the latter to dodecahedral one [5]. A similar spectrum was obtained for

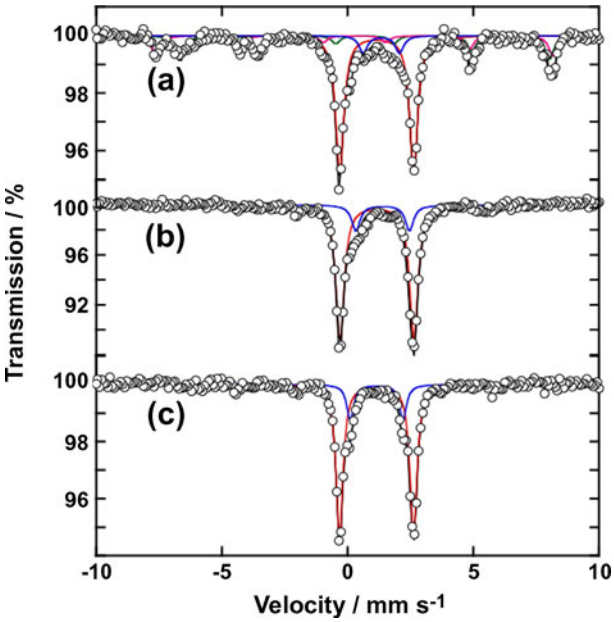

Fig. 1 Mössbauer spectra of **a** LEW86258 (typical CK chondrite), **b** LAP03834 (R chondrite reclassified from CK3), and **c** LAP03923 (LL chondrite reclassified from CK5)

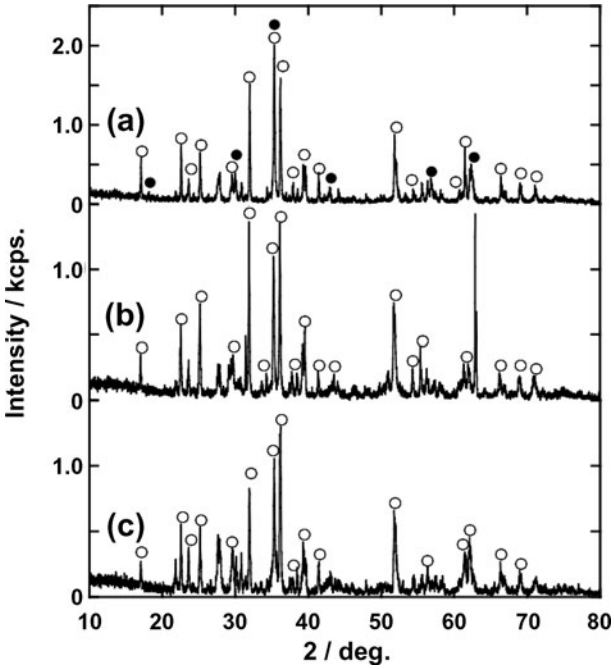

Fig. 2 XRD patterns of **a** LEW86258 (typical CK chondrite), **b** LAP03834 (R chondrite reclassified from CK3), and **c** LAP03923 (LL chondrite reclassified from CK5). Open and solid circles denote forsterite and magnetite, respectively

LAP03923 (Fig. 1c). It is noteworthy that all CK chondrite contain two magnetic components as shown in Fig. 1a, while reclassified four chondrites, *i.e.*, LAP03834, MET01149, LAP03923 and MAC02453 show no magnetic components.

XRD patterns of LEW86258 (typical CK chondrite), LAP03834 (R chondrite reclassified from CK3), and LAP03923 (LL chondrite reclassified from CK5) are shown in Fig. 2. The XRD pattern of CK chondrite (Fig. 2a) shows intense peaks at 2Θ of 35.2, 36.3 and 31.9° due to forsterite $Mg_{1.36}Fe_{0.64}SiO_4$ and also at 35.4, 30.2 and 62.4° due to magnetite Fe_3O_4. It is noted that XRD patterns of LAP03834 (Fig. 2b) and LAP03923 (Fig. 2c) showed no peaks due to magnetite phase. Similar results were observed for MET01149 and MAC02453, indicating that the mineral compositions of these four chondrites are clearly different from that of CK chondrite, as confirmed from the Mössbauer spectra. We can conclude that these chondrites should be distinguished from others on the basis of the difference in the crystalline phase and chemical environment, as respectively detected by XRD and ^{57}Fe-Mössbauer spectroscopy.

4 Summary

Twenty CK chondrites collected in the Antarctica Continent were characterized by elemental analysis, X-ray diffractometry (XRD) and ^{57}Fe-Mössbauer spectroscopy. Mössbauer spectrum of LAP03834, previously classified as a member of CK chondrite, consists of two paramagnetic doublets due to Fe^{II} with δ values of 1.17 ± 0.01 and 1.40 ± 0.01 mm s^{-1}. Forsterite phase ($Mg_{1.36}$ $Fe_{0.64}SiO_4$) was confirmed from the XRD study. Similar results were obtained for MET01149, LAP03923 and MAC02453, indicating that the mineral compositions of these four chondrites are quite different from that of typical CK chondrite which generally has magnetite phase (Fe_3O_4). LAP03834 and MET01149 could be classified as R chondrite, while LAP 03923 and MAC02453 as LL chondrite.

References

1. Weisberg, M.K., McCoy, T.J., Krot, A.N.: Systematics and evaluation of meteorite classification in meteorites and the early Solar System II. In: Lauretta, D.S., McSween Jr. H.Y., Binzel, R.P. (eds.) University of Arizona Press, pp. 19–52 (2006)
2. The Meteoritical Bulletin Database. http://www.lpi.usra.edu/meteor/metbull.php
3. Isa, M.: Chemical characteristics for CK carbonaceous chondrite meteorite group. Master's thesis, Tokyo Metropolitan University, pp. 11–13 (2011)
4. Isa, M., Shirai, N., Ebihara, M., Kubuki, S., Yamaguchi, A.: Chemical characteristics for CK carbonaceous chondrite. In: Abstract Book of 42th Lunar and Planetary Science Conference. http://www.lpi.usra.edu/meetings/lpsc2011/pdf/1876.pdf (2011)
5. Dyar, M.D., Schaefer, M.W.: Mössbauer spectroscopy on the surface of Mars: constrains and expectations. Earth Planet. Sci. Lett. **218**, 243–259 (2004)

Hyperfine Interact (2012) 208:79–84
DOI 10.1007/s10751-011-0490-6

Mössbauer, TEM/SAED and XRD investigation on waste dumps of the Valea lui Stan gold mines

Serban_Grigore Constantinescu · Sorin S. Udubasa · Gheorghe Udubasa · Victor Kuncser · Nicoleta Popescu-Pogrion · Ionel Mercioniu · Marcel Feder

Published online: 1 December 2011

Abstract The complementary investigation techniques, Mössbauer spectroscopy, transmission electron microscopy with selected area electron diffraction (TEM/SAED), X-ray diffraction (XRD) have been used to investigate the fate of the Valea lui Stan, Romania, gold-ore nanoscale-minerals during the long time of residence in the waste dumps. The preliminary investigations showed such waste dumps to contain significant amount of metals which cannot be identified by conventional methods. An intense research activity started up in order to evaluate the possibilities to recycle Valea lui Stan waste dumps and to recover metals by chemical or phytoextraction procedures. The waste dumps naturally show different mineral constituents with clay minerals as major phases, observed by XRD-technique. Although the waste dumps materials have whitish-yellowish colours, MÖSSBAUER technique evidences the presence of the finely dispersed iron bearing minerals. The authors are focusing to inspect and analyze Fe-compounds in the samples collected from Valea lui Stan's waste dumps in order to identify the magnetic phases by Mössbauer technique.

Keywords Mössbauer · TEM/SED · XRD · Waste dump · Iron oxides

1 Introduction

The geological structure of Valea lui Stan area (South Carpathians, Romania) is extremely complicated involving several metamorphic groups of Precambrian age

S. Constantinescu (✉) · V. Kuncser · N. Popescu-Pogrion · I. Mercioniu · M. Feder
National Institute of Materials Physics, Bucharest-Magurele, P.O.Box MG-07, Bucharest, Romania
e-mail: sconst@infim.ro

S. S. Udubasa · G. Udubasa
Fac. of Geology & Geophysics, University of Bucharest, Bucharest, Romania

and sedimentary formations of Permian and Cretaceous ages. The dominant rocks are micaschists, orthoclase-bearing gneisses, amphibolites, migmatites, limestones and scarcely developed ultramafics. The sedimentary formations are represented mainly by conglomerates. The ores are shear-zone related and display a typical association of Au-As-Cu [1, 2]. Arsenopyrite, pyrite, pyrrhotite, etc. are the major gold bearing sulphides and Mössbauer investigations have pointed out the presence of iron minerals very finely dispersed, mainly at nanometric scale. A set of $k = 3$ samples VS-k has been selected from the waste dumps of Valea lui Stan for detailed investigations. The low temperature inspection of VS-k samples by Mössbauer technique evidenced the Fe-phases. The present work intends to inspect the iron phases in powdered VS samples by Mössbauer technique in $T \in [300\ K–4.2\ K]$, taking into account the iron (ferric/ferrous, magnetic/nonmagnetic) phases' powerful diagnose of this technique. The RT spectra of samples are similar, but the inspection at liquid nitrogen temperature (LNT) VS-3 sample (as collected from waste dump) evidenced the magnetic phases. So, the authors are focussing to inspect and analyze the magnetic phases of Fe-oxides in this sample and its magnetically separated sample, VS-3m.

2 Experimental aspects

Some 25 samples (weighting about 0.5 kg each) have been collected from the waste dump of the former gold mine at Valea lui Stan, near the town of Brezoi, South Carpathians. The samples VS (Valea lui Stan) −1, −2 and −3 were chosen as they showed the highest metals contents. All the samples are similar, being intensely altered during the 50 years of waste residence. The samples have been inspected and analysed by the following techniques: XRD (Bruker-D8 ADVANCE spectrometer), **TEM/SAED** (JEOL-JEM 200Cx transmission electron microscope) and **MÖSSBAUER** (standard AM50 Promeda and Wissel-SeeCo) spectrometers in transmission geometry, using a ^{57}Co: Rh source and the velocity range up ±12 mm/s. The Mössbauer spectra have been obtained in the temperature range from 4.5 K (LHeT – liquid helium temperature) up to 300 K (RT – room temperature).

3 Results and discussion

The XRD (see Fig. 1a) patterns of all VS-samples are similar as concerns the presence of magnetic phases. The VS-samples showed to be the most complex. The analysis of them by Rietveld fit procedure evidenced silicate phases (>58%–100%) containing SiO_2 (∼10%–30% quartz) and micas (∼25%–52%, muscovite, biotite, etc.), hydrous ferric oxides, iron hydroxides and/or hydrated ferric sulphate (∼14%–40%) and other phases (∼6% for VS-1 up to 42% for VS-3). One can remark the contribution of phases with assumed amount of Fe (44% up to 90% for VS-3 and VS-2 respectively). On the other hand, TEM/SAED did not find trace amounts of hydrated ferric sulphate and the preliminary EDX techniques evidences low traces (3–4% ±1.7) of S.

The analysis of TEM/SAED images evidenced the main phase of SiO_2 with ferric oxides (see Fig. 1b). The observed iron-oxides phases are hematite, maghemite and

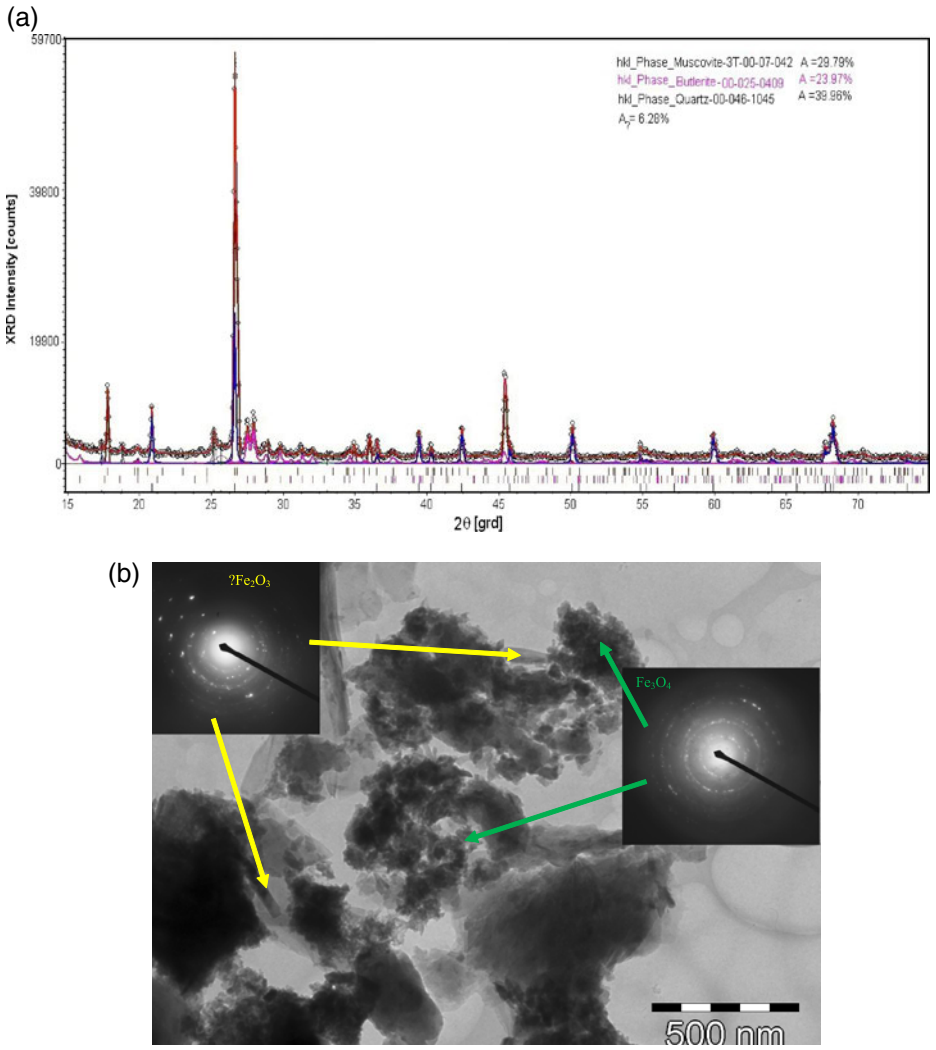

Fig. 1 The XRD patterns of VS-1 samples with the determined areas of the phase components, using the Rietveld fit procedure; (**b**) TEM/SAED images of VS-3 sample

magnetite. In Fig. 2 Mössbauer spectra of samples VS-3 (Fig. 2a, 2c1) and VS-3m (Fig. 2b, 2c2) obtained at different temperatures are plotted. The analysis of spectra was carried out using standard fit and magnetic field distribution procedures. The presence of two elementary quadrupolar patterns is easy distinguished in the spectra, for T > LNT for all VS samples. VS-3 and VS-3m hyperfine parameters are Δ_Q [mm/s] = 2.67, 0.72, δ_{Fe} [mm/s] = 1.13, 0.70, weights w[%] = 31, 66, and Δ_Q[mm/s] = 1.60, 0.60, δ_{Fe} [mm/s] = 0.57 and 0.37, w[%] = 7, 23, respectively. It is expected that the difference between the ferric nonmagnetic phases of the two samples, is due to the magnetically separation of VS-3m samples from as extracted VS-3 sample. The lack of magnetic patterns in VS-3 RT spectra could be explained by phases with

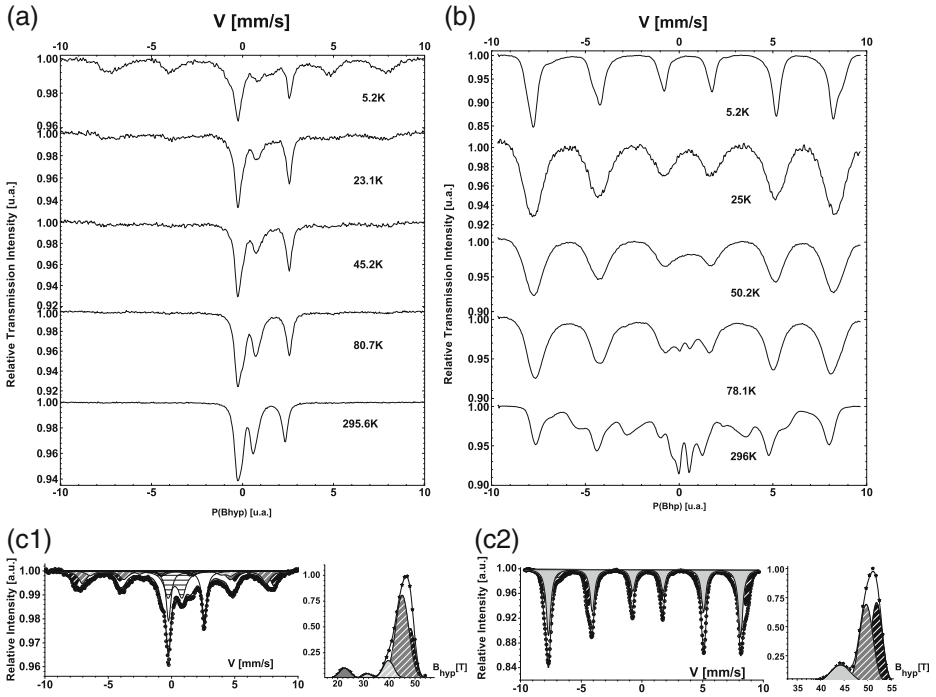

Fig. 2 The experimental Mössbauer spectra of the sample VS-3 (**a**) and VS-3m (**b**) for T ∈ 296K-5K, and the fit of LHeT magnetic field distribution (**c1**) and (**c2**) respectively

magnetic transitions below RT or/and the low concentration of the magnetic phases in the as extracted VS-3 global sample. The magnetic and nonmagnetic patterns of VS-3m RT spectrum, are revealing a bimodal magnetic field distribution in the ranges B[T] ∈ (20–39);(39–52), with probabilities, P_1(B,RT) > P_2(B,RT). All these suggest the presence of ferric nonmagnetic /magnetic phases in VS-3m and VS-3 and the presence of a ferrous phase at least in VS-3. The values of the VS-3 quadrupolar elementary patterns could indicate the muscovite phases containing Fe^{2+} and Fe^{3+}, [3]. The deconvolution of VS-3 LHeT spectra show magnetic phases only at T < LNT, but the nonmagnetic ones is still exists. The hyperfine parameters values of nonmagnetic and magnetic phases are in the Table 1.

One can remark the large values of half linewidths (Γ [mm/s] ∈ [0.65–0.77) of Fe^{3+} elementary magnetic patterns, which could suggest more magnetic phases. The values of B suggest a mixture of Fe^{3+}-oxides, -hydroxides with cation substitution (probably Mn, Co, Ti, more surely Al), [4–6] and even trace of copper iron sulphides. The VS-3m paramagnetic phases are less and less intense under at T ≤ LNT and at LHeT only a spectrum of elementary magnetic phases remained, the bimodal magnetic field distribution becomes B[T] ∈ [40–50];[45–55], P_1(B, LHeT) < P_2(B, LHeT).

The deconvolution of spectra reveals five magnetic elementary patterns (see Table 1) suggesting for the first four patterns the mixture of hematite with maghemite phases with the most probably Al—cation substitution. The bimodal magnetic fields

Table 1 The Mössbauer hyperfine parameters for LHeT

VS-3 sample				VS-3m sample			
w[%]	δ_{Fe} [mm/s]	ε_Q /* Δ_Q [mm/s]	B [T]	w [%]	δ_{Fe} [mm/s]	ε_Q /Δ_Q [mm/s]	B [T]
25	0.2	0.02	48.71	18	0.49	0.07	52.07
3	0.46	0.03	45.12	20	0.45	−0.08	51.86
18	0.44	0.3	34.50	44	0.48	−0.13	49.68
23	1.29	2.81	–	12	0.35	0.00	48.58
21	0.41	2.26	–	6	0.62	0.12	44.84
9	0.38	1.10	–	–			
±2	±0.04	±0.08	±0.31	±2	±0.03	±0.06	±0.52

and the temperature dependences of VS-3m spectra could be explained by the presence of the bimodal distribution of the grain sizes D suggesting a superparamagnetic transition. One could consider the limit between two sorts of particles is under 15 nm, taking into account the low T (<LNT) under which the paramagnetic pattern disappears. That is true for VS-sample, but it is possible both a magnetic ordering phase transition of some VS-3 constituent compounds and a hidden super paramagnetic transition of an invisible magnetic pattern at RT.

4 Conclusions

The aim of this paper is to present the results of complex investigations carried out on the waste dump material which are resulting from Valea lui Stan's mining of gold ore, hosted by metamorphic rocks. The main results by applying the above mentioned structural techniques consist in identification of several minerals not known in the primary ores of Valea lui Stan gold deposit, such as maghemite associated with other mineral grains (gold, silver etc.) at the nanometric scale. The native gold forms spheroidal grains up to 50 nm in size either isolated or as coalescent coral-like aggregates, included in different minerals. These analytical procedures were followed by experiments concerning metal uptake by plants, as a contribution to decontamination of old mining areas. In addition, gold recovery by plants has been partly successful. Such data will be published elsewhere.

Acknowledgements The financial support of the Ministry of Education, Research and Innovation of Romania through the PNCD-II project No. 31-081/2007-2010 is gratefully acknowledged.

References

1. Udubasa, S.S., Popescu-Pogrion, N., Popescu, I.V., Constantinescu, S., Udubasa, G.: Mineralogical and structural fingerprint methods of nanominerals' identification. J. Sci. Arts **2**(9), 323–331 (2009)
2. Udubasa, S.S., Constantinescu, S., Grecu, M.N., Popescu-Pogrion, N., Udubasa, G., Popescu, G.C., Tolea, F., Popescu, I.V.: Structural (EM, XRD, NGR, ESR) investigations on some sulphides from Costesti, Valea lui Stan and Jidostita gold ores (Southern Carpathians, Romania). Rom. J. Phys. **52**(1–2), 93–104 (2007)

3. Finch, J., Gainsford, A.R., Tennant, W.C.: Polarized optical absorption and ^{57}Fe Mössbauer study of pegmatitic muscovite. In: Stevens, J.G., Khasanov, A.M., Miller, J.W., Pollak, H., Li, Z. (eds.) Mössbauer mineral handbook. Am. Mineral. **67**, 59–68 (1982)
4. Cornell, R.M., Schwertzmann, U.: The iron oxides: structure, properties, reactrions, occurences, uses. Wiley-VCH, Verlag GmbH & Co KGaA Weinheim, ISBN: 3-527-30274-3 (2003)
5. Murad, E.: Properties and behavior of iron oxides as determined by mössbauer spectroscopy. In: Stucki, J.W., et al. (eds.) Iron in soils and clay minerals, issue C12, pp. 309–350. D. Reidel Publishing Company, Dordvecht, NED and Boston, MA (1988)
6. Murad, E., Cashion, J.: Mössbauer spectroscopy of environmental materials and their industrial utilization. Kluwer Academic (2004)

Hyperfine Interact (2012) 208:85–89
DOI 10.1007/s10751-012-0579-6

Mössbauer study of dissimilatory reduction of iron contained in glauconite by alkaliphilic bacteria

Nataliya I. Chistyakova · Vyacheslav S. Rusakov · Alexey A. Shapkin · Tatyana N. Zhilina · Darya G. Zavarzina

Published online: 14 February 2012

Abstract ^{57}Fe Mössbauer investigations of glauconite and new solid phases formed during the process of the bacterial growth in alkaline environment were carried out at room temperature, 78 K and 4.8 K. The magnetically ordered phase formed during bioleaching of glauconite by *G. ferrihydriticus* in pure culture or in combination with *Cl. alkalicellulosi* represented as a mixture of off-stoichiometric magnetite and maghemite. In case of combined binary bacterium culture growth the relative content of magnetically ordered phase was more than for the *G. ferrihydriticus* growth.

Keywords Mössbauer spectrometry · Glauconite · Alkaliphilic bacterium · Iron reducing bacterium

1 Introduction

Soda deposits are formed at the final stages of continental CO_2-weathering. It could occur under alkaline conditions either chemically or stimulated biotically. There are two main groups of alkaliphilic microbial agents that act in anaerobic conditions on the water-rock contact: a) fermentative hydrolytic decomposers of particulate organic matter, e.g. cellulose, capable to produce organic acids as the products of metabolism; b) respiratory anaerobes, utilizing dissolved compounds with external electron acceptors. The aim of our work was to study the interactions between representatives of this two group of alkaliphilic anaerobes and glauconite $[K_{<1}(Fe^{3+}, Fe^{2+}, Al, Mg)_{2-3}[Si_3(Si, Al)O_{10}] [OH]_2 \cdot nH_2O]$ by Mössbauer spectroscopy.

N. I. Chistyakova (✉) · V. S. Rusakov · A. A. Shapkin
Faculty of Physics, M.V. Lomonosov Moscow State University,
Leninskie gory, 119991 Moscow, Russia
e-mail: nchistyakova@yandex.ru

T. N. Zhilina · D. G. Zavarzina
Winogradsky Institute of Microbiology, Russian Academy of Sciences,
Prospect 60-letiya Oktyabrya 7/2, 117312 Moscow, Russia

2 Experimental

Two alkaliphilic anaerobic bacteria were used in the work. Bacteria *Clostridium alkalicellulosi* (strain Z-7026) [1] was isolated from the sediments of soda lake Verhnee Beloe (Buryatia, Russian Federation), it is hydrolitic decomposer. The growth conditions are: pH 8.0–10.2 (pH_{opt} 9.0); T = 18 − 39°C (T_{opt} 35°C). NaCl 0–30 g/l ($NaCl_{opt}$ 10 − 20 g/l). This strain is able to fermenting cellulose producing lactate, acetate, ethanol, formate and H_2.. Bacteria *Geoalkalibacter ferrihydriticus* (strain Z-0531) [2] was isolated from the sediments of soda lake Khadyn (Tuva, Russian Federation), it is respiratory anaerobe. The growth conditions are: pH 7.8–10.0 (pH_{opt} 8.6); T = 18 − 39°C (T_{opt}35°C). NaCl 0–50 g/l ($NaCl_{opt}$0 g/l). The strain Z-0531 utilizes acetate, formate, lactate, ethanol, H_2 with ferrihydrite as an electron acceptor. Siderite [$FeCO_3$] and/or magnetite [Fe_3O_4] are the main reduced solid products [2, 3].

For the experiment 70 ml of carbonate buffered anaerobic medium (total mineralization 15 g/l, pH 9.5) in 120 ml flasks with 200 mg of micas were used. Microcellulose (MCC) (10% w/v) either acetate (2 g/l) were added as substrates. Time of exposition was 165 days at 35°C.

^{57}Fe Mössbauer investigations of solid phase samples obtained during the process of the bacterium growth were carried out at room temperature, 78 K and 4.8 K. The program SpectrRelax from MSTools Complex was used for spectra processing.

3 Results and discussion

Mössbauer spectra of initial glauconite, glauconite in cultivation medium in sterile conditions, solid phases obtained as a result of biotic alkalinolysis of glauconite by *Cl. alkalicellulosi with MCC*,*G. ferrihydriticus* with acetate and combined alkalinolysis of glauconite by binary culture of *Cl. alkalicellulosi* and *G. ferrihydriticus* with MCC as organic substrate are shown in Fig. 1. Spectra were recorded at room temperature and at 78 K. Room temperature spectra were paramagnetic type spectra. In (d) and (e) spectra small intensity sextet with broaden lines was observed.

There are some different models for glauconite spectrum fitting [4–6] (four-doublet or three-doublet models) due to the different possible distribution of ferric and ferrous atoms in different position M1 and M2 of glauconite. The octahedral sheet of glauconite contains three structurally-independent positions: one trans-octahedron (M1) and two cis-octahedra (M2) differing in positions of the OH groups. However according to X-ray and oblique-texture electron diffractions, and EXAFS spectroscopy [7] only the *cis*-sites are occupied by cations. Therefore the presence of more than one quadrupole doublets in the spectra is not due to the occupation of both types of positions but such factors as charge and type of neighboring octahedral cations, distribution of Al and Si in tetrahedral.

Room temperature Mössbauer spectrum of initial glauconite (Fig. 1a) was satisfactory fitted by a superposition of four quadrupole doublets corresponding to ferric and ferrous ions: $\delta_1 = 0.36 \pm 0.01$ mm/s, $\Delta_1 = 0.47 \pm 0.01$ mm/s; $\delta_2 = 0.49 \pm 0.04$ mm/s, $\Delta_2 = 1.37 \pm 0.06$ mm/s; $\delta_3 = 1.16 \pm 0.02$ mm/s, $\Delta_3 = 1.73 \pm 0.03$ mm/s; $\delta_4 = 1.15 \pm 0.01$ mm/s, $\Delta_4 = 2.74 \pm 0.02$ mm/s. For 78 K spectrum two quadrupole shift distributions were extracted – one for Fe^{3+} atoms and one for Fe^{2+}. Comparison

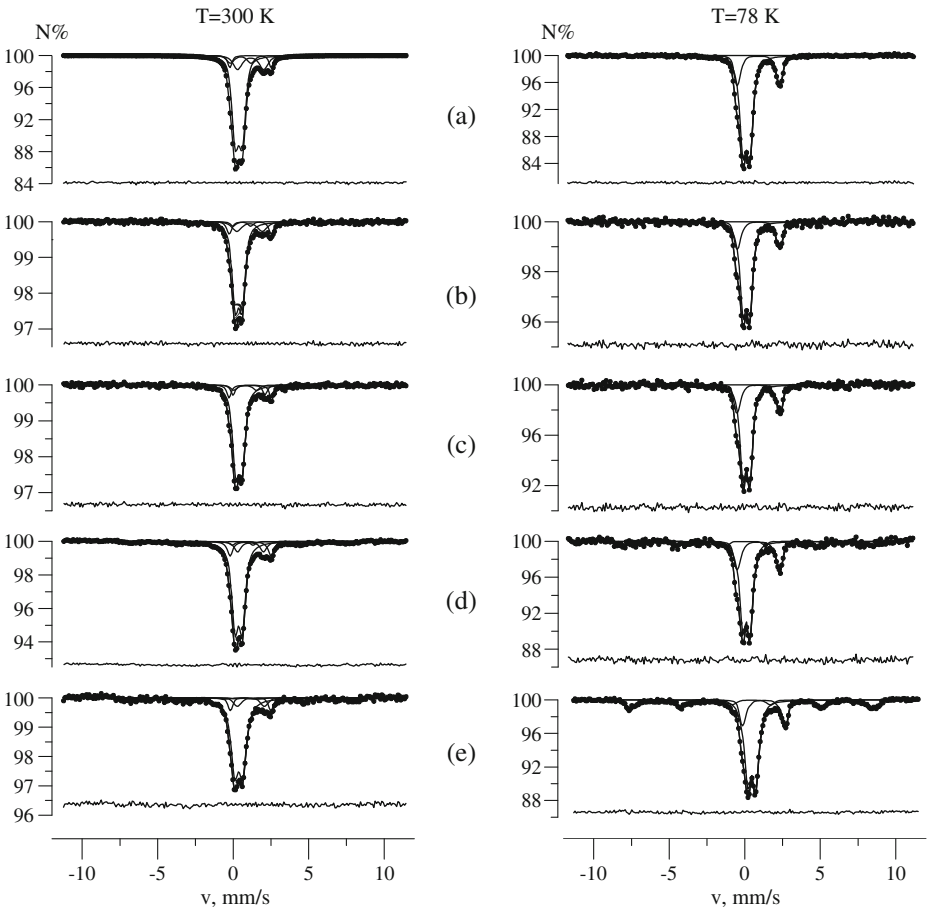

Fig. 1 Mössbauer spectra recorded at room temperature and at 78 K of initial glauconite (**a**), initial glauconite in cultivation medium in sterile conditions (**b**), solid phases obtained during the growth of *Cl. alkalicellulosi* with MCC and glauconite (**c**), *G. ferrihydriticus* with acetate and glauconite (**d**), binary culture of *Cl. alkalicellulosi* and *G. ferrihydriticus* with MCC and glauconite (**e**)

of (a) and (b) spectra in Fig. 1 showed that these spectra did not virtually differ. So a cultivation medium in sterile conditions did not significantly affect on initial glauconite. Similar results were observed when comparing (a) and (c) spectra. Thus *Cl. alkalicellulosi* did not reduce Fe^{3+} during its biotic alkalinolysis of glauconite. In the samples obtained as a result of *G. ferrihydriticus* growth with acetate and glauconite (Fig. 1d) the formation of magnetically ordered phase (about 5%) was observed. In 78 K spectrum the relative intensity of sextet reached 15%. In case of combined growth of *Cl. alkalicellulosi* and *G. ferrihydriticus* (Fig. 1e) the relative intensity of sextet increased and for 78 K spectrum was 22%. Thereby the content of synthesized magnetically ordered phase was more in case of combined binary bacterium culture growth. The increase in Fe^{2+} atoms content in solid phases obtained as a result of *G. ferrihydriticus* (d) and binary culture growth (e) occurred due to a decrease of Fe^{3+} atoms content and besides this decrease observed for

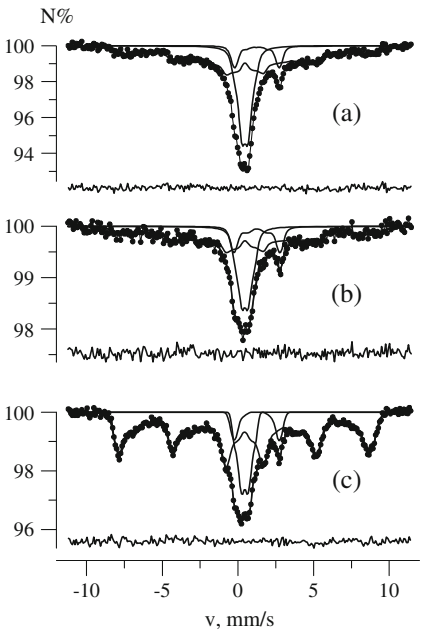

Fig. 2 Mössbauer spectra recorded at 4.8 K of initial glauconite (**a**), initial glauconite in cultivation medium in sterile conditions (**b**), binary culture of *Cl. alkalicellulosi* and *G. ferrihydriticus* with MCC as organic substrate and glauconite (**c**)

the position which corresponded to second doublet with larger quadrupole splitting. Moreover the intensity of the third doublet which corresponded to Fe^{2+} atoms also decreased.

Mössbauer investigations were carried out at 4.8 K (Fig. 2) to determine the magnetically ordered phase formed during binary culture growth. In 4.8 K spectrum of glauconite sextet with relative intensity $59 \pm 3\%$ appeared. The hyperfine magnetic field corresponding to maximum distribution was 491 ± 17 kOe which correlated with data obtained in [8]. These measurements also showed that spectra of initial glauconite and glauconite in cultivation medium did not virtually differ. In case of binary culture growth the intensity of sextet significantly increased. The difference between intensities of two sextets in (b) and (c) spectra which was equal to the relative intensity of the magnetically ordered phase was $19 \pm 3\%$ that corresponded to the results obtained at 78 K. The model fitting of the spectrum (c) showed the presence of Fe^{2+} atoms in magnetically ordered phase. The analysis of hyperfine parameters of this sextet made us conclude that magnetically ordered phase was a mixture of off-stoichiometric magnetite (Fe_3O_4) and maghemite (γ-Fe_2O_3).

4 Conclusions

Biotic alkalinolysis of glauconite by *G. ferrihydriticus* in pure culture or in combination with *Cl. alkalicellulosi* leaded to formation of new magnetically ordered phase containing magnetite and maghemite. While *Cl. alkalicellulosi* was inactive in enchancing weathering, binary combination of *G. ferrihydriticus* resulted in predominant synthesis of magnetically ordered phase.

Acknowledgements This study was supported in part by the Program "Origin and Evolution of Biosphere" of the Presidium of the Russian Academy of Sciences and the Foundation for Support of Russian Science.

References

1. Zhilina, T.N., Kevbrin, V.V., Tourova, T.P., Lysenko, A.M., Kostrikina, N.A., Zavarzin, G.A.: Clostridium alkalicellum sp.nov., an Obligately Alkaliphilic Cellulolytic Bacterium from a Soda Lake in the Baikal Region. Mikrobiol. **74**, 642–653 (2005) (in Russian)
2. Zavarzina, D.G., Kolganova, T.V, Boulygina, E.S., Kostrikina, N.A, Tourova, T.P., Zavarzin, G.A.: *Geoalkalibacter ferrihydriticus* gen. nov. sp. nov., the First Alkaliphilic Representative of the Family *Geobacteracea*, Isolated from a Soda Lake. Microbiol. **75**, 673–68 (2006)
3. Chystyakova, N.I., Rusakov, V.S., Shapkin, A.A., et al.: Investigations of iron minerals formed by dissimilatory alkaliphilic bacterium with ^{57}Fe Mössbauer spectroscopy. AIP Conf. Proc. **1258**, 68–74 (2010)
4. Rolf, R.M., Kimball, C.W., Odom, I.E.: Mössbauer characteristics of Cambrian glauconite, central U.S.A. Clays Clay Miner. **25**, 131–137 (1977)
5. Govaert, A., de Grave, E., Quartier, H., Chambaere, D., Robbrecht G.: Mössbauer analysis of glauconites of different belgian finding places. J. Phys. **40**(2), 442–444 (1979)
6. Ali, A. M., Hsia, Y., Liu, R., Zhang, J., Duan, W., Chen, L.: A Mössbauer study of evolution of glauconite from Chinese seas. Spectrosc. Lett. **34**(6), 701–708 (2001)
7. Drits, V.A., McCarty, D., Zviagina, B.B.: Crystal-chemical factors responsible for the distribution of octahedral cations over trans- and cis-sites in dioctahedral 2:1 layer silicates. Clays Clay Miner. **54**(2), 131–152 (2006)
8. Longworth, G., Townsend, M.G., Ross, C.A.M.: Mössbauer spectra of several magnetic sheet silicates in external magnetic field. Hyperfine Interact. **28**, 451–454 (1986)

Hyperfine Interact (2012) 208:91–94
DOI 10.1007/s10751-011-0417-2

Mössbauer study of the Ordinary-Chondrite meteorite Thylacine Hole–001

J. M. Cadogan · E. J. Devlin

Published online: 26 October 2011

Abstract The Thylacine Hole–001 meteorite was recovered from the Nullarbor Desert (Australia) in 1977 and is an Ordinary Chondrite, Group H4/5br, which has undergone moderate to severe (B/C) weathering. We have characterised the Fe-bearing phases in Thylacine Hole–001 by ^{57}Fe Mössbauer Spectroscopy at 300 K, 100 K, 50 K and 4 K. The spectrum at 300 K is dominated by the paramagnetic doublets of Olivine, Pyroxene and a Ferric component which is most likely nanoparticulate Goethite. Magnetically split sextets due to Maghemite or Magnetite are also present, consistent with the relatively advanced terrrestrial age of 28,500 yrs The nanoparticulate Goethite component shows a blocked, magnetically split sextet at low temperatures. We also observe the effects of magnetic ordering of the Olivine and Pyroxene below 50 K.

Keywords Meteorite · Mössbauer spectroscopy

1 Introduction

The Ordinary Chondrites account for about 87% of all known meteorites recovered on Earth and are well suited to study by ^{57}Fe Mössbauer Spectroscopy as they contain significant amounts of Fe (as Fe^0 and Fe^{2+}), bound up mainly in silicates (Olivine, Pyroxene), Fe(Ni) metal (Kamacite, Taenite) and sulphides (FeS Troilite). In this paper, we use ^{57}Fe Mössbauer spectroscopy carried out over the temperature range

J. M. Cadogan (✉)
Department of Physics and Astronomy, University of Manitoba, Winnipeg, MB R3T 2N2, Canada
e-mail: cadogan@physics.umanitoba.ca

E. J. Devlin
Institute of Materials Science, NCSR Demokritos, Aghia Paraskevi 153 10, Athens, Greece

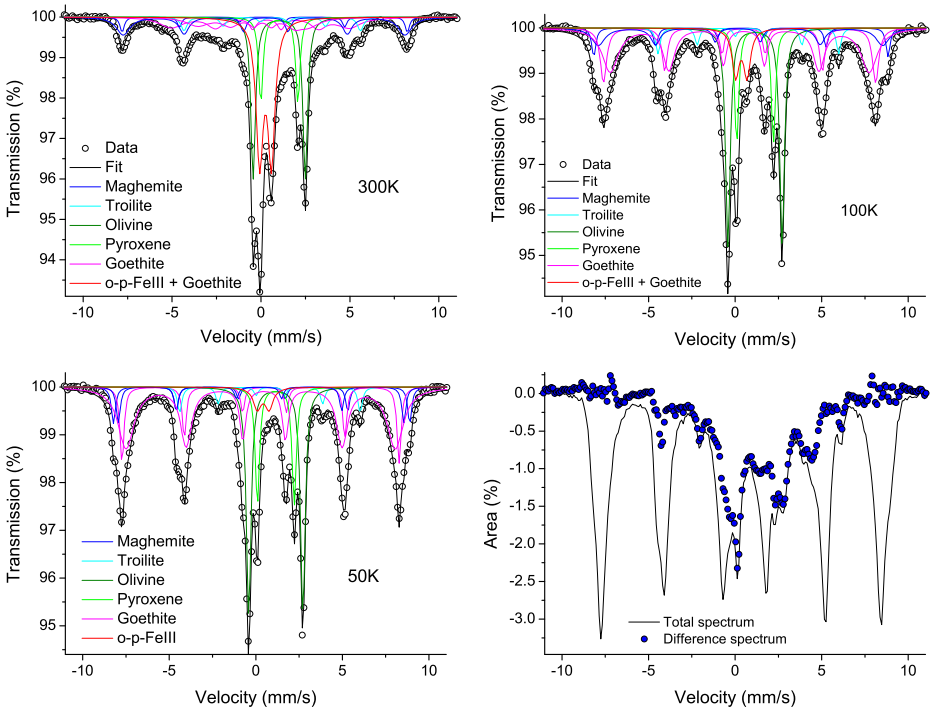

Fig. 1 The ^{57}Fe Mössbauer spectra of Thylacine Hole–001, collected at 300 K, 100 K, 50 K and 4 K. In the case of the 4 K spectrum, we show the full experimental spectrum as a *black*, *continuous line*, and the residual spectrum, after stripping the well-split magnetic components due to Maghemite and Goethite, as *blue dots*

4–300 K to study the Thylacine Hole–001 meteorite which was found in 1977 in the Nullarbor Desert region of Australia at the coordinates
31° 35′ S, 127° 36′ E [1]. Thylacine Hole–001 is classified as a brecciated H4/5 ordinary chondrite 'find' with medium to severe weathering (weathering grade B/C). Chemical analysis gave a Fayalite ($[Mg,Fe]_2SiO_4$) content of 19.7 mol.% and a Ferrosilite ($[Mg,Fe]_2(SiO_3)_2$) content of 17.6 mol.% [2]. Its 'terrestrial age' has been estimated at greater than 28,500 yrs [3]. The aim of this study is to quantify the relative amounts of Fe^{2+}/Fe^0 and Fe^{3+} present in this weathered meteorite to provide data crucial to the investigation of terrestrial weathering processes.

2 Experimental Methods

A small sample of the Thylacine Hole–001 meteorite was provided by Prof. A. Bevan of the Western Australia Museum and is representative of the bulk of the meteorite. Its catalogue number is WAM13428. The Mössbauer sample was prepared by grinding a portion of the meteorite and the absorber had an area density of about 300 mg cm^{-2}. ^{57}Fe Mössbauer spectroscopy was carried out at 300 K, 100 K, 50 K and 4.2 K in transmission mode with a ^{57}Co**Rh** source. All Mössbauer spectra were least-

Table 1 ^{57}Fe Mössbauer parameters for Thylacine Hole–001 (at 300 K)

Component	I.S. (mm/s)	Q.S. (mm/s)	B_{hf} (T)	Area (%)	Assignment
Doublet 1	1.13(2)	2.94(3)	0	20(2)	Olivine $(Mg,Fe)_2SiO_4$
Doublet 2	1.14(2)	2.08(3)	0	10(2)	Pyroxene $(Mg,Fe)SiO_3$
Doublet 3	0.36(2)	0.66(3)	0	26(2)	o-p-Fe^{3+}
Sextet 1	0.80(2)	−0.12(4)	30.9(3)	4(2)	Troilite (FeS)
Sextet 2	0.33(2)	−0.10(3)	49.4(2)	13(2)	Maghemite (γ-Fe_2O_3)
Sextet 3	0.24(2)	0.16(3)	50.0(2)	3(2)	Maghemite (γ-Fe_2O_3)
Sextet 4	0.26(2)	−0.38(3)	31.2(3)	13(2)	Goethite (α-FeOOH)
Sextet 5	0.36(2)	−0.54(3)	19.4(3)	10(2)	n-Goethite (α-FeOOH)

squares fitted using the WMOSS program and all isomer shifts are quoted relative to the α-Fe calibration spectrum.

3 Results and Discussion

The Mössbauer spectra of Thylacine Hole–001 are shown in Fig. 1 and in Table 1 we give the hyperfine parameters for the various spectral components determined at 300 K. The spectrum is dominated by the quadrupole doublets of Olivine (20(2)% area), Pyroxene (10(2)%) and paramagnetic Fe^{3+} (26(2)%), most likely in an octahedral coordination (denoted here as o-p-Fe^{3+}). The Olivine quadrupole splitting of 2.94(3) mm/s allows us to estimate the Olivine composition to be around 30(10) mol%Fa., using the data of Menzies et al. [4]. The rather large o-p-Fe^{3+} content is consistent with the advanced terrestrial age of this meteorite.

The presence of antiferromagnetic Troilite is readily distinguished from other possible magnetic phases with hyperfine fields in the range 30–33 T, such as Kamacite and Taenite, by its large positive isomer shift, indicative of the Fe^{2+} in Troilite. The identification of the magnetic components with hyperfine fields around 49–51 T is not straightforward and we have ascribed them to Maghemite, although one cannot completely rule out the possibility of some form of substituted Magnetite.

The most significant change observed upon cooling to 100 K is the decrease in the sub-spectral area associated with the o-p-Fe^{3+} doublet, from 26(2)% to 7(2)%. This reduction is accompanied by an increase in the area of the magnetically split component with a hyperfine field of 46.6(2) T, which we have ascribed to nanoparticulate Goethite. These data place the blocking temperature of the n-Goethite between 300 K and 100 K. Some Goethite particles are blocked at 300 K. In Tables 2 and 3 we give the hyperfine parameters for the various spectral components, determined at 100 K and 50 K, respectively.

A comparison of the spectra acquired at 50 K and 4 K shows the disappearance of the sharp paramagnetic doublets associated with Olivine and Pyroxene, indicating that these two components order magnetically below 50 K. The magnetic ordering of both Olivine and Pyroxene has been reported in [5, 6] and a ^{57}Fe Mössbauer study of ordering in Olivine has been published by de Oliveira et al. [5]. The magnetically split spectra are quite complex and to illustrate this effect we show in Fig. 1 the residual absorption in the 4 K spectrum, after stripping the well-split components due to Maghemite and Goethite.

Table 2 ^{57}Fe Mössbauer parameters for Thylacine Hole–001 (at 100 K)

Component	I.S. (mm/s)	Q.S. (mm/s)	B_{hf} (T)	Area (%)	Assignment
Doublet 1	1.25(2)	3.12(3)	0	21(2)	Olivine $(Mg,Fe)_2SiO_4$
Doublet 2	1.26(2)	2.12(3)	0	10(2)	Pyroxene $(Mg,Fe)SiO_3$
Doublet 3	0.46(2)	0.66(3)	0	7(2)	o-p-Fe^{3+}
Sextet 1	0.90(2)	−0.06(4)	32.5(3)	5(2)	Troilite (FeS)
Sextet 2	0.34(2)	0.14(3)	51.2(3)	9(2)	Maghemite (γ-Fe_2O_3)
Sextet 3	0.44(2)	0.00(3)	53.0(2)	5(2)	Maghemite (γ-Fe_2O_3)
Sextet 4	0.48(2)	−0.22(3)	49.0(2)	14(2)	Goethite (α-FeOOH)
Sextet 5	0.49(2)	−0.24(3)	46.6(2)	29(2)	n-Goethite (α-FeOOH)

Table 3 ^{57}Fe Mössbauer parameters for Thylacine Hole–001 (at 50 K)

Component	I.S. (mm/s)	Q.S. (mm/s)	B_{hf} (T)	Area (%)	Assignment
Doublet 1	1.26(2)	3.12(3)	0	21(2)	Olivine $(Mg,Fe)_2SiO_4$
Doublet 2	1.26(2)	2.12(3)	0	10(2)	Pyroxene $(Mg,Fe)SiO_3$
Doublet 3	0.53(2)	0.68(3)	0	3(2)	o-p-Fe^{3+}
Sextet 1	0.93(2)	−0.02(4)	32.5(3)	4(2)	Troilite (FeS)
Sextet 2	0.35(2)	0.12(3)	51.4(3)	6(2)	Maghemite (γ-Fe_2O_3)
Sextet 3	0.45(2)	0.02(3)	53.3(2)	6(2)	Maghemite (γ-Fe_2O_3)
Sextet 4	0.50(2)	−0.24(3)	49.9(2)	12(2)	Goethite (α-FeOOH)
Sextet 5	0.49(2)	−0.20(3)	48.5(2)	38(2)	n-Goethite (α-FeOOH)

4 Conclusions

We have identified the Fe-bearing phases in the ordinary chondrite meteorite Thylacine Hole–001 by ^{57}Fe Mössbauer spectroscopy. The principal components are Olivine, Pyroxene, Maghemite, n-Goethite and Troilite. We have also observed the effects of magnetic ordering of the Olivine and Pyroxene phases below 50 K.

Acknowledgements JMC is grateful for support from the Canada Research Chairs programme. Financial support for parts of this work was provided by NSERC (Canada). We are grateful to the Western Australia Museum for providing the Thylacine Hole–001 sample. Finally, JMC acknowledges many useful discussions with P.A. Bland.

References

1. Wlotzka, F.: The Meteoritical Bulletin, No. 77: 1994 November. Meteoritics **29**, 891–897 (1994)
2. Bevan, A.W.R., Binns, R.A.: Meteorites from the Nullarbor Region, Western Australia: 1. A review of past recoveries and a procedure for naming new finds. Meteoritics **24**, 127–133 (1989)
3. Bland, P.A., Bevan, A.W.R., Jull, A.J.T.: Ancient meteorite finds and the Earth's surface environment. Quat. Res. **53**, 131–142 (2000)
4. Menzies, O.N., Bland, P.A., Berry, F.J.: An ^{57}Fe Mössbauer study of the Olivine solid solution series: Implications for meteorite classification and deconvolution of unequilibrated chondrite spectra. Lunar Planet. Sci. **XXXII**, 1622–1623 (2001)
5. de Oliveira, J.C.P., da Costa, M.I. Jr.: Schreiner W.H. and Vasquez A.: Magnetic properties of some iron-poor natural Olivines. J. Magn. Magn. Mater. **98**, 239–244 (1991)
6. Wiedenmann, A., Regnard, J.R.: Neutron diffraction study of the magnetic ordering in Pyroxenes $Fe_xM_{1-x}O_3$. Solid State Commun. **57**, 499–504 (1986)

Hyperfine Interact (2012) 208:95–98
DOI 10.1007/s10751-011-0520-4

^{57}Fe Mössbauer analysis of the Upper Triassic-Lower Jurassic deep-sea chert: Paleo-redox history across the Triassic-Jurassic boundary and the Toarcian oceanic anoxic event

Tomohiko Sato · Yukio Isozaki · Katsumi Shozugawa · Kimiko Seimiya · Motoyuki Matsuo

Published online: 14 December 2011

Abstract We investigated the paleo-redox change across the Triassic-Jurassic (T-J) boundary (∼200 Ma) and the Early Toarcian oceanic anoxic event (T-OAE; ∼183 Ma) recorded in the Upper Triassic to Lower Jurassic pelagic deep-sea cherts in the Inuyama area, Central Japan. The present ^{57}Fe Mössbauer spectroscopic analysis for these cherts identified five iron species, i.e., hematite (α-Fe_2O_3), pyrite (FeS_2), paramagnetic Fe^{3+}, and two paramagnetic Fe^{2+} with different quadrupole splittings. The occurrence of hematite and pyrite in deep-sea cherts essentially indicates primary oxidizing and reducing depositional conditions, respectively. The results confirmed that oxidizing conditions persisted in deep-sea across the T-J boundary. In contrast, across the T-OAE, deep-sea environment shifted to reducing conditions. The first appearance of the gray pyrite-bearing chert marked the onset of the deep-sea oxygen-depletion in the middle Pliensbachian, i.e., clearly before the shallow-sea T-OAE.

Keywords Mössbauer spectroscopy · Iron · Deep-sea chert · Redox · Toarcian

1 Introduction

Pelagic deep-sea cherts in ancient accretionary complexes are useful to reconstruct oceanic paleo-environments, because pre-Jurassic deep-sea floors have been lost from the Earth's surface by the oceanic subduction. Accessory iron-bearing minerals in deep-sea cherts, such as hematite and pyrite, have been used as redox indicators

T. Sato (✉) · Y. Isozaki
Department of Earth Science and Astronomy, Graduate School of Arts and Sciences, The University of Tokyo, 3–8–1 Komaba, Meguro, Tokyo 153–8902, Japan
e-mail: tomohiko@ea.c.u-tokyo.ac.jp

K. Shozugawa · K. Seimiya · M. Matsuo
Department of Chemistry, Graduate School of Arts and Sciences, The University of Tokyo, 3–8–1 Komaba, Meguro, Tokyo 153–8902, Japan

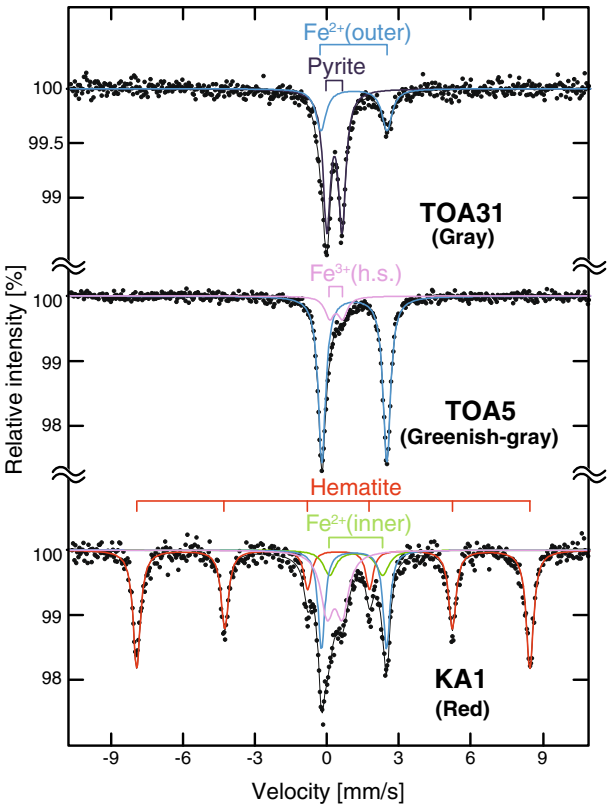

Fig. 1 Mössbauer spectra of the analyzed cherts at Katsuyama, Central Japan. KA1, TOA5, and TOA31 are representative of *red*, *greenish-gray*, and *gray* cherts, respectively

for ancient deep-sea environments, as in the case of the Permian-Triassic boundary Superanoxia [1, 2]. In order to analyze paleo-redox history across the Triassic-Jurassic (T-J) boundary (~200 Ma) and the Early Toarcian Oceanic Anoxic Event (T-OAE; ~183 Ma), this study examined the Mössbauer spectra of the Upper Triassic to Lower Jurassic deep-sea cherts in the Inuyama area, Central Japan.

2 Sample and method

The Upper Triassic to Lower Jurassic pelagic deep-sea cherts at the Katsuyama section in Inuyama record the Triassic-Jurassic boundary and the T-OAE intervals [3–5]. The T-J boundary lies in the red cherts, whereas the T-OAE interval lies in organic-rich black cherts above the grayish cherts. Chert samples were prepared following the same procedure as previous studies [2, 6]. Mössbauer spectra were measured with an Austin Science S-600 Mössbauer spectrometer using a 1.11 GBq ^{57}Co/Rh source at room temperature (293 K). Mössbauer spectra were fitted by a least-square method with restrictions of intensity and half width of peaks. All doublets were treated as symmetric. Peak positions of pyrite were constrained as in previous studies [2, 6]. The presence of pyrite crystals was also checked under the microscope.

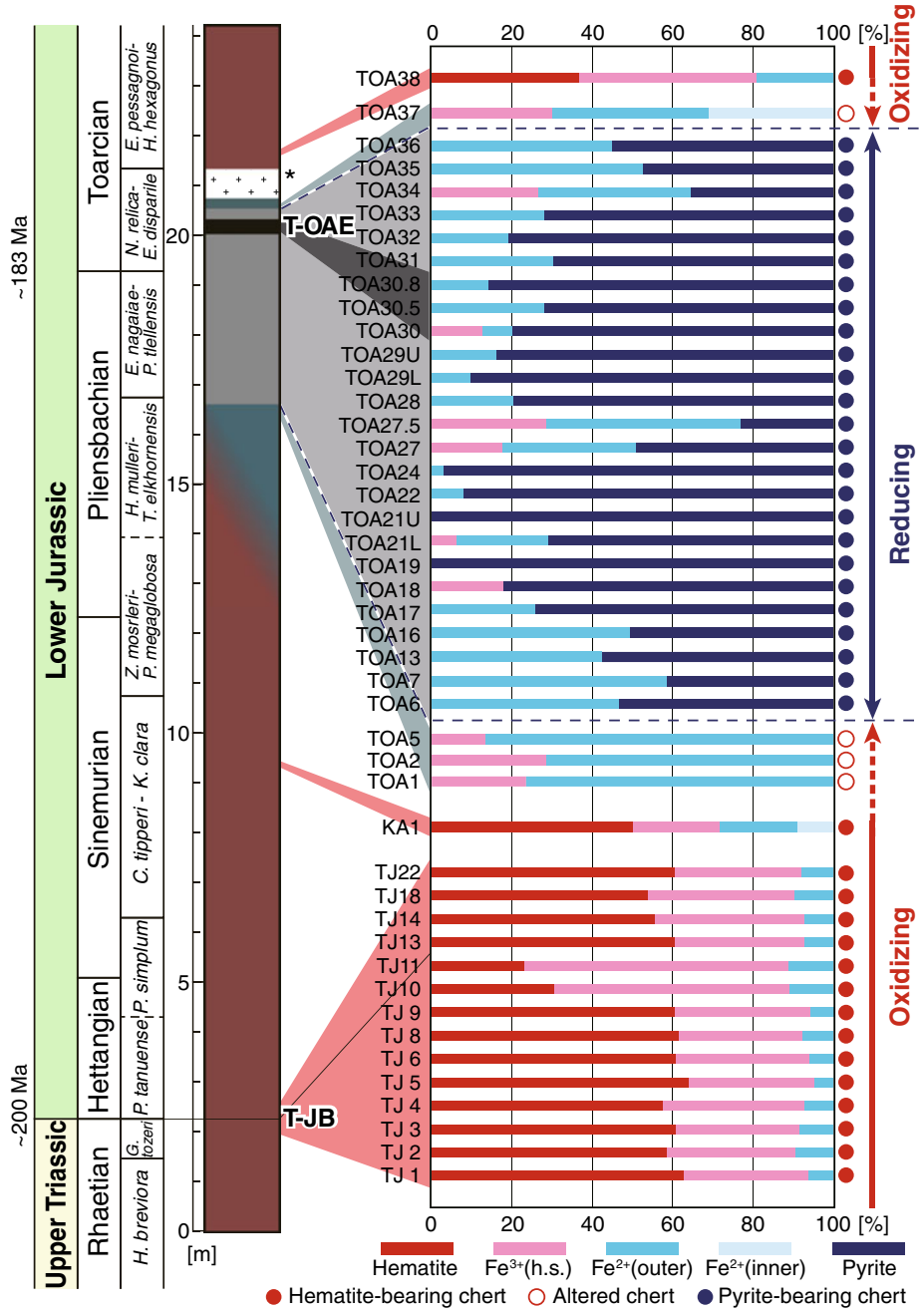

Fig. 2 Stratigraphic column showing the color and the iron-species composition of the Upper Triassic to Lower Jurassic pelagic deep-sea cherts at Katsuyama, Central Japan. * shows white massive chert. Radiolarian assemblage-zones are from [4, 5]

3 Results and discussion

The Mössbauer analysis for 45 chert samples identified five iron species from the analyzed deep-sea cherts (Fig. 1); hematite (α-Fe_2O_3), pyrite (FeS_2), paramagnetic Fe^{3+}(high spin; h.s.), and two types of paramagnetic Fe^{2+}(h.s.), i.e., Fe^{2+}(outer) with larger quadrupole splitting (QS) and Fe^{2+}(inner) with smaller QS. Red cherts contain hematite, Fe^{3+}(h.s.), Fe^{2+}(outer), and occasionally Fe^{2+}(inner), suggesting their primary deposition in oxidizing conditions. The grayish colored cherts are classified into two groups; i.e. ones with pyrite, Fe^{2+}(outer), and occasionally Fe^{3+}(h.s.), and the others mainly with Fe^{2+}(outer) and some Fe^{3+}(h.s.) without pyrite. The former group with framboidal pyrites was likely deposited primarily under reducing conditions, whereas the latter group without pyrite was likely altered from primary hematite-bearing red cherts [6]. Fe^{3+}(h.s.) and Fe^{2+}(outer) are likely included in clay minerals such as illite or chlorite. Fe^{2+}(inner) may be contained in siderite ($FeCO_3$)-like amorphous mineral that is derived from hematite by the post-depositional alteration.

4 Paleo-redox history

Figure 2 shows the secular change of paleo-redox in the studied Upper Triassic to Lower Jurassic deep-sea cherts. As for the T-J boundary, consistent occurrence of the red hematite-bearing cherts (TJ1–22) suggests that the deep-sea environment remained in oxidizing condition across the T-J boundary. In contrast, the mid-Pliensbachian to Toarcian interval (~4 m thick) consists of the framboidal pyrite-bearing gray cherts (TOA6–36), suggesting their deposition under reducing conditions. In addition, organic-rich black cherts (TOA30–30.8) corresponding to the shallow-sea T-OAE occur in the middle of this interval. The greenish-gray cherts (TOA1–5, 37), immediately below and above the reducing interval, contain mainly Fe^{2+}(outer) without pyrite nor hematite. They represent altered parts from the primary hematite-bearing cherts, in accordance with a recent study [6]. The onset of the reducing condition in deep-sea is marked by the first appearance of the gray pyrite-bearing chert (TOA6), lying ~3.5 m below the T-OAE black cherts (TOA30–30.8), at the *Hsuum mulleri-Trillus elkhornensis* (Radiolaria) Zone [4, 5], i.e. in the Lower Pliensbachian. This indicates that the deep-sea environment changed from oxidizing to reducing clearly before the shallow-sea T-OAE, and persisted in the reducing condition much longer than the shallow-sea environment.

References

1. Isozaki, Y.: Science **276**, 235–238 (1997)
2. Matsuo, M., Kubo, K., Isozaki, Y.: Hyperfine Interact. (C) **5**, 435–438 (2003)
3. Hori, R.S.: Bull. Geol. Surv. Japan **44**, 555–570 (1993)
4. Hori, R.S.: Mar. Micropaleontol. **30**, 159–169 (1997)
5. Gröcke, D.R., Hori, R.S., Trabucho-Alexandre, J., Kemp, D.B., Schwark, L.: Solid Earth Discuss. **3**, 385–410 (2011)
6. Sato, T., Isozaki, Y., Shozugawa, K., Matsuo, M.: J. Asian Earth Sci. **42**, 1403–1410 (2011)

Hyperfine Interact (2012) 208:99–104
DOI 10.1007/s10751-011-0474-6

Mössbauer investigations of synthetic valleriite

Nataliya I. Chistyakova · Vyacheslav S. Rusakov · Tatyana V. Gubaidulina · Alexey M. Gapochka · Andrey Yu. Bychkov

Published online: 29 November 2011

Abstract Samples obtained as a result of the valleriite synthesis process under different conditions (temperature and proportion Cu:Fe:Mg in the initial mixture) were investigated by ^{57}Fe Mössbauer spectroscopy with attraction data of X-ray diffraction. Parameters of hyperfine interactions for valleriite were determined and crystal chemical identification of ^{57}Fe subspectra was carried out. It was found that valleriite was formed in samples synthesized at 150°C and 180°C and not formed in samples synthesized at 250°C.

Keywords ^{57}Fe Mössbauer spectroscopy · Valleriite

1 Introduction

Valleriite belong to incommensurable and modulated mixed-layer minerals. Valleriite is hydroxide-sulfides with mixed layered crystal structure. Common chemical formula of valleriite $CuFeS_2 \cdot \{n[Mg,Fe(OH)_2] + m(Al,Fe)(OH)_3\}$, where $1.3 \leq n \leq 1.6$ and $0 \leq m \leq 0.3$. In valleriite structure double sulfide layers with iron and copper cations presented in tetrahedral sites are situated between hydroxide brucite-like layers. Sulfide layers of valleriite are constructed of tetrahedra lying on their bases, at that all tetrahedral positions are filled in with statistically distributed iron and copper atoms. In the general case in brucite-like layers of valleriite divalent and trivalent cations are located in positions with octahedral environment of OH-groups [1].

N. I. Chistyakova (✉) · V. S. Rusakov · T. V. Gubaidulina · A. M. Gapochka
Faculty of Physics, M.V. Lomonosov Moscow State University,
Moscow, Russia
e-mail: nchistyakova@yandex.ru

A. Yu. Bychkov
Faculty of Geology, M.V. Lomonosov Moscow State University,
Moscow, Russia

2 Experimental

The objects for our investigation were four series of samples obtained as a result of the valleriite synthesis process under different conditions: temperature of synthesis and proportion Cu:Fe:Mg in the initial mixture. An sulphate aqueous solution was prepared by mixing 1 M H_2SO_4, $FeSO_4$, $CuSO_4$ and $MgSO_4$ solution in different proportions Cu:Fe:Mg. Then, sulphides quantitatively precipitated by addition of Na_2S solution produced by saturation of NaOH with gaseous H_2S. This reaction produces amorphous iron and copper sulphides. Then phases were placed with its supernatant solution in steel autoclave with Teflon liner at 150°C (exp. №3), 180°C (exp. №1 and 2) and 250°C (exp. №4) for 30 days. After the recrystallization sulphide precipitate was washed with distilled water and acetone and dried. Experiment №2 differs from experiment №1 by excess of sulfide sulfur Na_2S.

The produced crystal phases up to 10 micron size were studied by electron microscope. X-ray powder diffraction patterns of the sulphides were taken with a universal X-ray diffractometer (DRON-UM1) that measures the X-ray intensity distribution for oriented and powder samples using Co-Kα radiation with Fe filter (V = 35 kV, A = 25 mA). Measurements were made automatically with step 0.02° at speed of 4°/min. X-ray spectra were processed by the internal software XRAY and the Pcpdf 2003 database for the analysis of diffraction powder patterns.

The ^{57}Fe Mössbauer study was carried out at room temperature on the spectrometer operated in constant acceleration mode and equipped with a ^{57}Co-source into Rh-matrix. The calibration was accomplished relatively α-Fe. The program SpectrRelax from MSTools Complex was used for spectrum model fitting [2].

3 Results and discussion

Samples obtained as a result of the valleriite synthesis process at temperatures equal to 150°C, 180°C and 250°C and different proportions Cu:Fe:Mg in initial mixture were investigated by ^{57}Fe Mössbauer spectroscopy. X-Ray powder diffraction data are in a good agreement with data obtained in [3] for synthetic valleriite. It was found that all investigated samples are multiphase. We note that valleriite phase was not detected in samples synthesized at 250°C. The ^{57}Fe Mössbauer spectra of investigated samples are present on Figs. 1, 2 and 3.

In all experimental Mössbauer spectra of samples synthesized at 150°C and 180°C quadrupole doublets with values of Mössbauer line shift $\delta = 0.39 \div 0.54$ mm/s and quadrupole shift $\varepsilon = 0.46 \div 0.56$ mm/s were obtained (shaded subspectra on Figs. 1, 2, 3). The subspectrum with the parameter values corresponds to Fe^{2+} cations located in the positions of a tetrahedral environment of sulfur atoms [4]. Since it is known that sulfide layers of valleriite are constructed of tetrahedra, at that all positions are filled in with statistically distributed iron and copper atoms, we can assume that this quadrupole doublet corresponds to Fe atoms in sulfide layers of valleriite. Besides, subspectra with similar values of hyperfine parameters were obtained earlier in Mössbauer spectra of natural valleriite from North Korea and Sweden [5, 6]. In [7] analogue quadrupole doublets with $\delta = 0.42 \div 0.48$ mm/s and quadrupole splitting $\Delta = 2\varepsilon = 0.81 \div 1.28$ mm/s also were detected in Mössbauer spectra of natural valleriite and were interpreted as subspectra of sulfide layers of

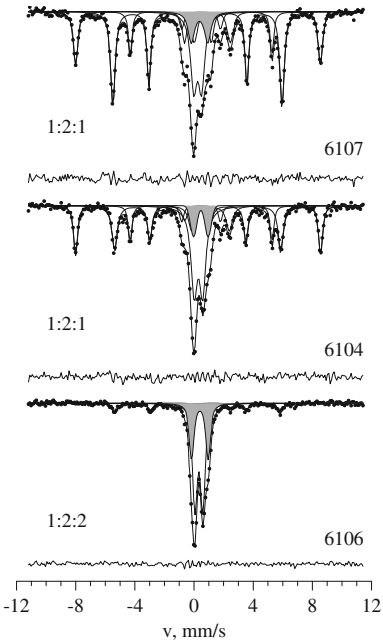

Fig. 1 The ^{57}Fe Mössbauer spectra of samples synthesized at different proportion Cu:Fe:Mg and t = 180°C (exp. №1)

valleriite. Mössbauer spectra of valleriite in [8] were processed by four quadrupole doublets. The doublet with similar parameters $\delta = 0.42 \div 0.42$ mm/s and $\Delta = 1.12 \div 1.32$ mm/s was attributed to Fe^{2+} atoms and doublets with $\delta = 0.24 \div 0.41$ mm/s and $\Delta = 0.74 \div 0.89$ mm/s – to Fe^{3+} in sulfide layer respectively. The fourth doublet with $\delta = 0.22 \div 0.28$ mm/s and $\Delta = 0.30 \div 0.28$ mm/s corresponded to Fe^{3+} in the hydroxide lattice.

In all spectra of investigated samples (Figs. 1, 2, 3) central quadrupole doublets with average values of hyperfine parameters $\delta \approx 0.30$ mm/s and $\varepsilon \approx 0.30$ mm/s and low-intensity quadrupole doublets with parameters $\delta \approx 1.1$ mm/s and $\varepsilon \approx 1.2$ mm/s were detected. These subspectra respectively correspond to tri- and divalent iron cations located in octahedral environment of oxygen atoms [4]. Since hydroxide brucite-like layers of valleriite may contain both Fe^{3+} and Fe^{2+} atoms, detected doublets can be attributed to valleriite brucite-like layers. On the other hand in accordance with [8] the first doublet can also be consistent with tetrahedrally coordinated Fe^{3+} atoms in sulfide layers. Moreover relative intensities of quadrupole doublets corresponding to divalent Fe cations are much lower than relative intensities of quadrupole doublets corresponding to trivalent Fe cations. But it should be noted that according to [9] parameters of hyperfine interactions of ^{57}Fe nuclei in pyrite FeS_2 are the values $\delta \approx 0.30$ mm/s and $\varepsilon \approx 0.30$ mm/s. Therefore central quadrupole doublet in experimental spectra may correspond to sulfide phase, which is not related to valleriite.

The model fitting and analysis of measured experimental spectra showed that all synthesized samples contained considerable (relatively the total iron content in the sample) amounts of chalcopyrite $CuFeS_2$. Zeeman sextet with parameters $\delta \approx 0.24$ mm/s and hyperfine magnetic field on ^{57}Fe nuclei $H_n \approx 350$ kOe in Mössbauer

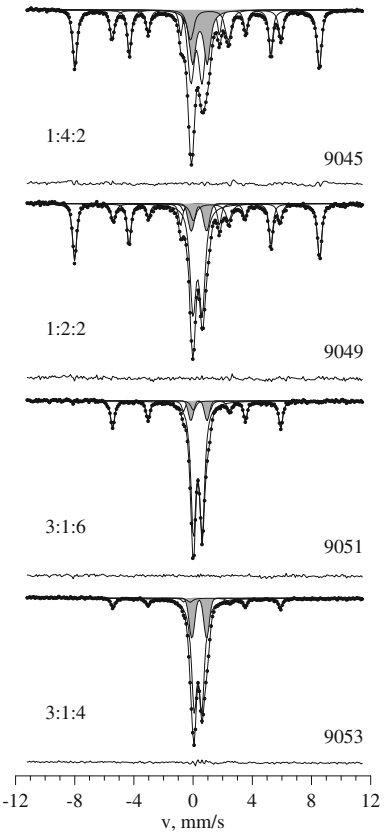

Fig. 2 The ^{57}Fe Mössbauer spectra of samples synthesized at different proportion Cu:Fe:Mg and t = 180°C (exp. №2)

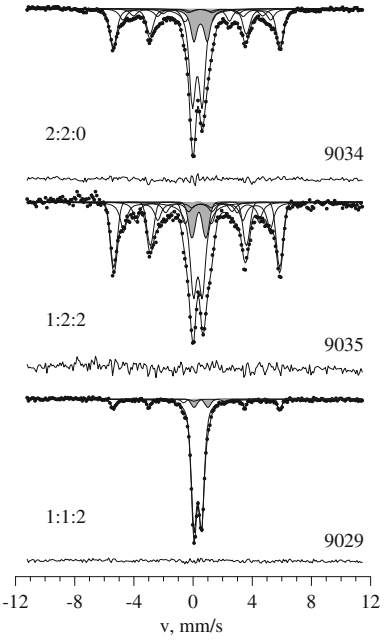

Fig. 3 The ^{57}Fe Mössbauer spectra of samples synthesized at different proportion Cu:Fe:Mg and t = 150°C (exp. №3)

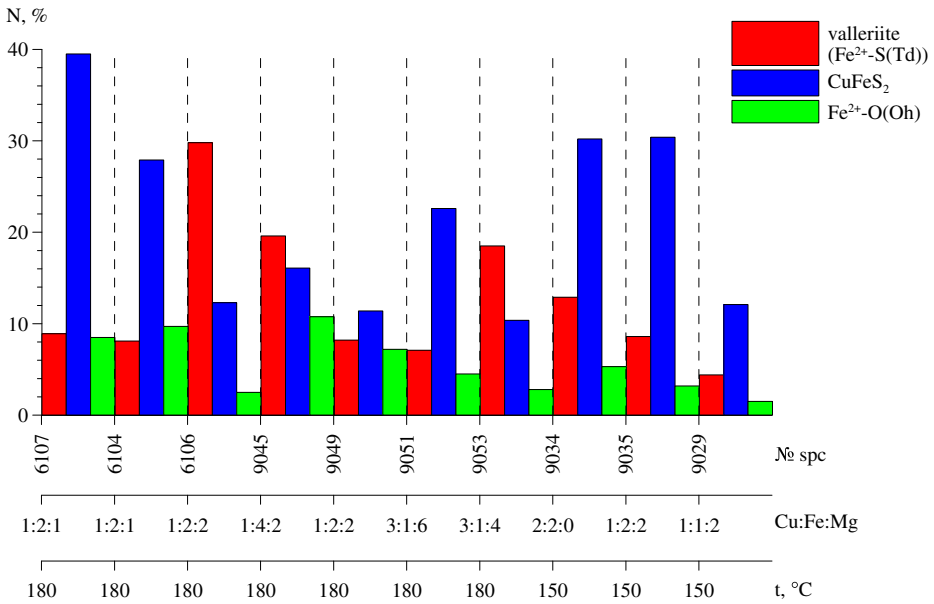

Fig. 4 Relative intensities of obtained subspectra of ^{57}Fe atoms in different phases depending on Cu:Fe:Mg proportion in initial mixture and synthesis temperature. The estimation of statistical errors of relative intensities is about 1–2%

spectra (Figs. 1, 2, 3) is related to ^{57}Fe atoms in chalcopyrite. Besides, in samples 6104, 6107, 9045 and 9049 hematite was detected. In samples 9034 and 9035 admixture of magnetically ordered phase with values of hyperfine magnetic fields H_n about 245 kOe and 310 kOe were exhibited.

The diagram, which shows relative intensities of detected subspectra corresponding to sulfide layers of valleriite, chalcopyrite and Fe^{2+} cations in octahedral environment of oxygen atoms is presented on Fig. 4. The most relative amount of valleriite formed in samples 6106, 9045 and 9053 synthesized at 180°C and with following proportions Cu:Fe:Mg in initial mixture 1:2:2, 1:4:2, 3:1:4. The comparison of two samples synthesized with equal proportions Cu:Fe:Mg = 1:2:2 but at different temperatures 180°C and 150°C (samples 6106 and 9035) shows (Fig. 4) that relative content of valleriite in samples 6106 significantly exceeds relative content of valleriite in sample 9035, i.e. in sample which was synthesized at higher temperature (180°C). Samples 6106 and 9049 were synthesized at equal temperature (180°C) and proportion Cu:Fe:Mg = 1:2:2. However the relative content of phases is different in these samples (Fig. 4). Apparently this is due to exess of Na_2S in synthesis process of sample 9049 as compared with sample 6106.

4 Conclusions

It was found that valleriite was formed at synthesis temperatures 150°C and 180°C and not formed at higher temperature (250°C). Most relative amount of valleriite

was contained in samples synthesized at 180°C and with proportions Cu:Fe:Mg in initial mixture equal to 1:2:2, 1:4:2, 3:1:4.

It was shown that hyperfine parameters values of subspectra corresponding to the sulfide layers of valleriite are $\delta = 0.39 \div 0.54$ mm/s and $\varepsilon = 0.46 \div 0.56$ mm/s. In Mössbauer spectra of samples synthesized at 150°C and 180°C quadrupole doublets with parameters $\delta \approx 1.1$ mm/s and $\varepsilon \approx 1.2$ mm/s were detected and these subspectra could correspond to iron positions in the hydroxide layers of valleriite.

References

1. Organova, N.I.: Crystal Chemistry of Incommensurable and Modulated Mixed-layer Minerals. Nauka, Moscow (1989)
2. Rusakov, V.S.: Mössbauer Spectroscopy of Locally Inhomogeneous Systems Institute of Nuclear Physics. National Nuclear Center of the Republic of Kazakhstan, Almaty (2000)
3. Iiishi, K., Tomisaka, T., Kato, T., Takeno, S.: Am. Mineral. **55**, 2107 (1970)
4. Reiff, W.M.: Mixed oxidation states and averaged electronic environments in iron compounds. In: Gruverman, I.J., Seidel, C.W. (eds.) Mössbauer Effect Methodology, vol. 8. L. Plenum Press, NY (1973)
5. Chistyakova, N.I., Gubaidulina, T.V., Rusakov, V.S.: Czechoslov. J. Phys. **56**(Suppl.E), E123 (2006)
6. Gubaidulina, T.V., Chistyakova, N.I., Rusakov, V.S.: Bull. Russ. Acad. Sci. Phys. **71**(9), 1269 (2007)
7. Shan, Q., Zhengmin C., Yanjing, C.: Chin. Sci. Bull. **41**, 1982 (1996)
8. Waanders, F.B., Pollak, H., Lachmann, G.: S. Afr. J. Sci. **95**(9), 387 (1999)
9. Vaughan, D., Craig, J.: Mineral Chemistry of Metal Sulfides. Cambridge University Press, Cambridge, London-New York-Melbourne (1978)

Hyperfine Interact (2012) 208:105–110
DOI 10.1007/s10751-011-0439-9

Mössbauer studies of subfossil oak

Uwe van Bürck · Friedrich E. Wagner · Anton Lerf

Published online: 8 November 2011

Abstract Subfossil oak wood found in a dried-up bog in Bavaria, Germany, was studied by Mössbauer spectroscopy. The bog oaks contain substantial amounts of iron taken up from the bog waters and presumably forming complexes with the tanning agents in the oak wood. The iron is mainly Fe^{3+} and much of this exhibits an uncommonly large quadrupole splitting of up to 1.6 mm/s that can tentatively be explained by the formation of oxo-bridged iron dimers. Only rarely, mainly in the dense wood of the roots of bog oaks, was divalent iron found. When the wood was ground to a powder the divalent iron oxidized to Fe^{3+} within hours. This suggests that iron is taken up from the bog water as Fe^{2+} and oxidizes only when the wood emerges from the water and comes into contact with air.

Keywords Mössbauer spectroscopy · Subfossil oak · Oak wood · Bog wood · Tannin · Polyphenols

1 Introduction

Wood may be preserved for thousands of years when buried under wet and anaerobic conditions in swamps, bogs, riverbeds or elsewhere below the groundwater table [1–3]. Oak wood in particular is often found exceptionally well preserved, presumably due to its high content of tanning agents. After slow drying to prevent cracking, such subfossil oak wood is highly appreciated for its hardness and durability, as well

U. van Bürck · F. E. Wagner (✉)
Physics Department E15, Technical University of Munich, 85747 Garching, Germany
e-mail: fwagner@tum.de

A. Lerf
Walther Meissner Institute, Bavarian Academy of Sciences, 85747 Garching, Germany

as for its appealing dark colour. It is used for making furniture and veneers, sculptures, musical instruments, tobacco pipes and various ornaments. Its popular name is bogwood or bog oak. Subfossil oaks are also the basis of the European dendrochronological oak tree calendar [4–8].

Subfossil oak wood often is rich in iron taken up from the groundwater. Its dark colour, which ranges from brown over brownish green to deeply black, results largely from reactions of the iron with the tanning agents in the oak wood. These reactions may be similar to those made use of in the production of ferro-gallic inks [9–13].

The iron content is often high enough for measuring Mössbauer spectra. We here report on a Mössbauer investigation of subfossil oak wood from a dried up bog in southern Germany. Besides being of interest in its own right, such studies may also shed light on other fields of iron-tannin chemistry, like the preservation of old manuscripts from iron-gall ink corrosion [11], or the development of rust converters and anti-corrosion agents for steel on the basis of tannic acids [14–16].

2 Samples and experiments

The subfossil oak samples investigated in the course of our studies are of central European provenance, either from bogs or from the flood plains of rivers, and were either directly collected in the nature or obtained from wood sculptors, veneer factories, or other sources. In this paper we discuss only specimens from a bog dried up for agricultural use, called the Donaumoos, which is situated south of the Danube near the towns of Neuburg and Ingolstadt in Bavaria, Germany. After drainage was started in the late 18th century, the water level slowly fell and the bog oaks dried slowly and are now often found in the course of building activities.

Usually, the outer parts of trunks of bog oak are strongly weathered, while in the interior hard solid and often nearly black wood is found. Usually solid samples from the interior with air dried densities between 0.8 and 0.9 g/cm^3 and thicknesses between 5 and 15 mm were taken for Mössbauer spectroscopy. The Mössbauer measurements were performed with sources of ^{57}Co in Rh. For measurements at 4.2 K, a liquid He bath cryostat was used in which the source was also cooled to 4.2 K. Measurements at 160 K were taken with only liquid nitrogen in the cryostat. All samples were measured within a small (4 mm/s) and a large (11 or 15 mm/s) velocity range to get the inner part with good resolution as well as the magnetically broadened part of the spectra. The spectra of the same sample were fitted simultaneously with suitable superpositions of Lorentzian lines.

3 Results

The Mössbauer spectra of most samples exhibit only ferric iron (Fig. 1 and Table 1). The RT spectra exhibit two ferric quadrupole doublets, one with splittings of about 0.8 mm/s and the other with rather large splittings of 1.3 to 1.6 mm/s. The relative intensity of the two components changes from sample to sample. At 4.2 K a substantial fraction of the iron splits magnetically into a sextet with broadened lines and mean hyperfine fields of 53 to 55 T and a broad, structureless magnetic background. The sextet component exhibits nearly no electric quadrupole shift. It is

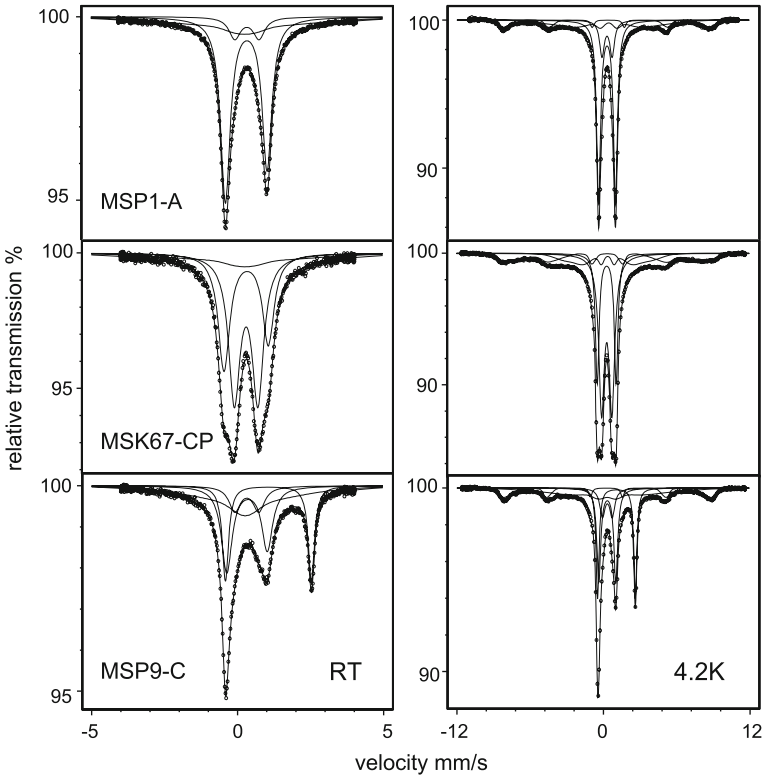

Fig. 1 Mössbauer spectra of some bog oak samples taken at ambient temperature (RT) and at 4.2 K. The corresponding Mössbauer parameters are compiled in Table 1

attributed to ferric iron exhibiting slow paramagnetic relaxations, an interpretation that is supported by the observation of the broad structureless background. Such a broad structureless component was also observed at 160 K and even at RT in the spectra taken with a large maximum velocity. It is attributed to magnetic relaxation phenomena in the regime intermediate between slow and fast relaxation. In the spectra shown in Fig. 1 the broad magnetic components were approximated by static Gaussian distributions of magnetic hyperfine fields.

At RT the quadrupole doublet with the larger quadrupole splitting in all cases shows a pronounced asymmetry, the line at negative velocity being considerably stronger than that at positive velocity (Fig. 1). At 4.2 K this asymmetry is practically absent, which suggests that it is due to an anisotropy of the Lamb-Mössbauer factor rather than to texture. The absence of texture was also established by measurements with a $1 \times 1 \times 1$ cm^3 cube of wood through which the γ rays were passed in a radial, tangential and axial direction, which revealed no differences in the doublet asymmetry. The doublet with the smaller quadrupole splitting did not show any noticeable asymmetry. The asymmetry must thus be considered as typical for the bonding situation of the iron giving rise to the large quadrupole interaction.

Ferrous iron was observed only in a few cases, most prominently in a sample of very dense wood from the roots of a bog oak (Fig. 1). When this wood was ground

Table 1 Isomer shifts (IS) relative to the ^{57}Co:Rh source having the same temperature as the absorber, electric quadrupole splittings (QS), FWHM linewidths (W) and relative areas (A_{rel}) for the quadrupole doublets observed in some bog oak specimens at RT and 4.2 K

Sample	T (K)	IS (mm/s)	QS (mm/s)	W (mm/s)	A_{rel} (%)
MSP1-A	298	0.31(1)	1.42(1)	0.40(2)	66.2(5)
		0.33(1)	0.83(1)	0.48(2)	10.2(3)
	4.2	0.29(1)	1.38(1)	0.39(2)	56.9(4)
		0.29(1)	0.83(1)	0.46(2)	13.1(3)
MSK67-CP	298	0.29(1)	1.52(1)	0.48(2)	36.2(7)
		0.30(1)	0.81(1)	0.48(3)	50.0(5)
	4.2	0.28(1)	1.54(1)	0.54(2)	24.9(3)
		0.28(1)	0.84(1)	0.36(3)	44.6(3)
MSP9-C	298	0.32(1)	1.38(1)	0.44(2)	33.2(14)
		0.32(1)	0.82(3)	0.58(3)	11.8(8)
		1.05(1)	2.94(3)	0.26(1)	24.5(3)
	4.2	0.31(1)	1.39(1)	0.38(1)	27.6(8)
		0.31(1)	0.80(2)	0.51(2)	10.9(8)
		1.06(1)	3.09(1)	0.29(1)	25.2(2)

The A_{rel} values do not add up to 100%, the balance being the components exhibiting broadening or magnetic splitting attributable to slow paramagnetic relaxation

to a powder, the ferrous iron oxidised to ferric iron within hours. When the sample that yielded the spectrum shown in Fig. 1 was re-measured after 5 years during which it was kept in a closed vessel in a nitrogen atmosphere, the intensity of the Fe^{2+} component had diminished by about 30 %. A similar sample kept in air for 5 years did no longer show any Fe^{2+}. These observations support the notion that the iron is deposited in the wood from the bog waters as Fe^{2+} and oxidises only after the wood falls dry and is exposed to air. In the very dense wood of roots the air apparently penetrates slowly enough for Fe^{2+} still to be found.

The total area under the spectra is about 3 times larger at 4.2 K than at RT, indicating a strong temperature dependence of the f-factors. This apparently affects all components in roughly the same way, since the relative intensities do not change much (Table 1). The iron contents of the samples can be estimated from the intensities at 4.2 K assuming that there the mean f-factor is the same as that of hematite, which was used for calibration. One of the highest iron contents was found in sample MSP9-C with 1.3 wt. %.

4 Discussion

In bog waters, the conditions are anaerobic, i.e., reducing, the pH is rather acidic and the iron is dissolved as Fe^{2+}. When iron penetrates into the waterlogged wood, it is expected to react with the polyphenols of the tannic substances, of which oak wood is particularly rich. While the iron is still divalent, it presumably forms monomeric complexes by binding to phenolic OH groups. This is presumably the iron we saw in the root of a bog oak. When a waterlogged tree falls dry, oxygen will penetrate into the wood and the iron will oxidise. One would then expect to observe ferric compounds like those obtained in the laboratory in reactions between iron and tannic substances. In such studies [14–16] ferric compounds with QS $\approx$ 0.8 mm/s have been

observed, which may explain the component with the small quadrupole splittings in bog oaks (Table 1). However, quadrupole splittings of more than about 1.2 mm/s were not observed in the products of such reactions. This raises the question what gives rise to the component with the large quadrupole splitting in bog oak.

Possibly, under oxidising conditions and when the pH rises, there is a tendency for forming small particles of oxyhydroxides [17]. On the way towards these, dimers like $[(H_2O)_4FeO_2Fe(H_2O)_4]^{4+}$, $[(H_2O)_4Fe(OH)_2Fe(H_2O)_4]^{6+}$ or $[(H_2O)_5FeOFe(H_2O)_5]^{5+}$ may form. At still higher pH values, these species would further polymerise and form iron oxyhydroxides. In the presence of polyphenols, this process may be hindered by complexation of the iron with polyphenols instead of water, and the polymerization process may stop at the stage of dimers or other rather small oxo-clusters. Rather large ferric quadrupole splittings have, indeed, been observed in a number of oxo-bridged dimers [18–21], which renders such clusters probable candidates for the component with the large quadrupole splitting in bogwood.

The reason for the large electric field gradients (EFG) in such dimers is the strong covalency of the bonds with the bridging oxygen due to the short iron-oxygen distances [22]. This is expected to give rise to a negative EFG. The strong axial bonds in oxo complexes may also cause an anisotropy of the f-factor, which should be larger along the molecular axis and hence the axis of the EFG than perpendicular to it. The asymmetry of the quadrupole doublets observed in the Mössbauer spectra of bog oak is in agreement with this and a negative value of the EFG, which supports the presence of clusters of the kind described.

The slowly relaxing ferric component in the Mössbauer spectra could not be clearly identified. The iron that yields the sextet pattern at 4.2 K may, in fact, become the heavily broadened component at 160 K and at RT and thus never appear in the spectra as a quadrupole doublet.

Acknowledgements We thank the collector of bogwood and artist, B. Th. Zimmermann of Pöttmes, for making many of the studied bog oak specimens available to us.

References

1. Schreiber, Ch., Wagenführ, R.: Holztechnologie **17**, 133 (1976)
2. Schulze-Drewitz, G.: Holztechnologie **3**, 266 (1962)
3. Bednar, H., Fengel, D.: Holz Roh–Werkst. **32**, 99 (1974)
4. Pilcher, J.R., Hillam, J., Baillie, M.G.L., Pearson, G.W.: New Phytol. **79**, 713 (1977)
5. Becker, B.: Radiocarbon **35**, 201 (1993)
6. Leuschner, H.H., Sass-Klaassen, U., Jansma, E., Baillie, M.G.L., Spurk, M.: Holocene **12**, 695 (2002)
7. Friedrich, M., Remmele, S., Kromer, B., Hofmann, J., Spurk, M., Kaiser, K.F., Orcel, Ch., Küppers, M.: Radiocarbon **46**, 1111 (2004)
8. Haneca, K., Čufar, K., Beekman, H.: J. Archaeol. Sci. **36**, 1 (2009)
9. Neevel, J.G.: Restaurator **16**, 193 (1995)
10. Danon, J., Darbour, M., Flieder, F., Genand-Riondet, N., Imbert, P., Jehanno, G., Roussel, Y.: In: Proceedings of the Indian National Academy of Sciences (Physical Sciences): International Conference on the Applications of the Mössbauer Effect, Jaipur, India 1981, p. 841
11. Banik, G.: In: Banik, G. (ed.) Tinterfraßschäden und ihre Ursachen. Kohlhammer, Struttgart (1999)
12. Rouchon-Quillet, V., Remazeilles, C., Bernard, J., Wattiaux, A., Fournes, L.: Appl. Phys. A **79**, 389 (2004)

13. Wagner, B., Bulska, E., Stahl, B., Heck, M., Ortner, H.M.: Anal. Chim. Acta **527**, 195 (2004)
14. Jaén, J.A., Araúz, E.Y., Iglesias, J., Delgado, Y.: Hyperfine Interact. **148/149**, 199 (2003)
15. Jaén, J.A., González, L., Vargas, A., Olave, G.: Hyperfine Interact. **148/149**, 227 (2003)
16. Gust, J., Suwalski, J.: Corrosion **50**, 355 (1994)
17. Jolivet, J.-P., Chanéac, C., Tronc, E.: Chem. Commun. 481 (2004)
18. Kurtz, D.M.: Chem. Rev. **90** 585, (1990)
19. Murray, K.S.: Coord. Chem. Rev. **12**, 1 (1974)
20. Bauminger, E.R., Harrison, P.M., Nowik, I., Treffry, A.: Biochem. **28**, 5486 (1989)
21. Schugar, H.J., Rossman, G.R., Barraclough, C.G., Gray, H.B.: J. Am. Chem. Soc. **94**, 2683 (1972)
22. Gütlich, P., Bill, E., Trautwein, A.X.: Mössbauer Spectroscopy and Transition Metal Chemistry. Springer, Heidelberg, p. 100 (2011)

Hyperfine Interact (2012) 208:111–116
DOI 10.1007/s10751-011-0409-2

The stabilization of archaeological iron objects: Mössbauer and XRD studies

Ursula Wagner · Thibault Demoulin · Rupert Gebhard · Werner Häusler · Cristina Mazzola · Ina Meissner · Friedrich E. Wagner

Published online: 15 November 2011

Abstract Archaeological iron objects that were buried in the ground for long times often corrode rapidly once they have been excavated. We have used Mössbauer spectroscopy and X-ray diffraction to elucidate some specific problems of the corrosion of such objects and gain insights that may help to improve the methods of conservation.

Keywords Mössbauer spectroscopy · Archaeology · Iron objects · Corrosion · Conservation

1 Introduction

Archaeological iron objects that were buried in the ground for centuries or millennia often corrode rapidly once they have been excavated and come into contact with air. Their conservation poses severe problems, both for objects on exhibition in museums and for objects stored elsewhere. A variety of treatments and manners of storage have been proposed for the conservation of such objects [1, 2], but they do not always yield satisfactory results.

^{57}Fe Mössbauer spectroscopy has been used widely in studies of iron corrosion (e.g., [3–6]), and the corrosion processes of archaeological artefacts both during

U. Wagner · W. Häusler · F. E. Wagner (✉)
Physik-Department E15, Technische Universität München,
85747 Garching, Germany
e-mail: fwagner@tum.de

T. Demoulin · R. Gebhard · C. Mazzola · I. Meissner
Archäologische Staatssammlung München,
Lerchenfeldstrasse 2, 80535 München, Germany

burial and after excavation have been investigated (e.g., [7–11]). The identification of the various iron oxide and oxyhydroxide phases formed during burial, after excavation and after various conservation treatments is an important application of Mössbauer spectroscopy. The oxides observed as corrosion products are mainly goethite, akaganéite, maghemite and hematite. Akaganéite ($FeO_{0.833}(OH)_{1.167}Cl_{0.167}$ according to Ståhl et al. [12]) in contact with the metallic surface is deemed to be particularly obnoxious [1], because it may release chloride ions and thus promote corrosion, though free chloride may often rather be the real culprit [12].

We have used Mössbauer spectroscopy and X-ray diffraction to elucidate specific questions arising in the analysis and conservation of archaeological iron artefacts from the heydays of the Celtic Culture in Central Europe (300–15 BC), e.g., nails, tools and weapons, many of them from the Celtic oppidum of Manching in Bavaria, Germany. Some objects had already been restored and subjected to conservation treatments decades ago, and with varying success. Their study allows an assessment of the long-time behaviour of restored material. In this paper we will report on some of the results obtained in this context.

2 Sensor for the efficiency of sealing methods for excavated objects

Since iron often begins to corrode rapidly on contact with air right after excavation, it is essential to protect the artefacts already at the site of excavation, for instance by sealing them into appropriate plastic foils. Mixtures of iron powder and ferrous chloride ($FeCl_2{\cdot}4H_2O$) have been suggested [13] as sensors to test such sealing methods. We have used 1:1 mixtures by mass of iron powder (grain size ca. 5 μm) and $FeCl_2{\cdot}4H_2O$ for this purpose. Experiments with such mixtures sealed into different plastic foils with or without drying agents and/or oxygen scavengers were performed as well as experiments in containers with controlled humidity and temperature. The reaction products were analyzed by Mössbauer spectroscopy and XRD.

At high humidity a complete reaction to akaganéite (called akaganéite M in the following) occurred, with no metallic iron or iron chloride left, as both the Mössbauer spectrum (Fig. 1) and the XRD pattern (Fig. 2) show. From the 1:1 mixing ratio of Fe and $FeCl_2{\cdot}4H_2O$, a Fe:Cl ratio of 1:0.278 results, which is higher than the ratio of 1:0.167 found by Ståhl et al. [12] for akaganéite. The mixing ratio of Fe and $FeCl_2{\cdot}4H_2O$ could, in fact, be varied between 1:0.6 and 1:1.2 and still a virtually complete reaction to akaganeite occurred, indicating that the akaganéite forms with widely different chlorine contents, either in its structure or adhering to the surface of crystallites. The RT Mössbauer spectrum of akaganéite M (Fig. 1) is different from that of akaganéite made by slow precipitation from a hydrous solution of $FeCl_3$ according to Schwertmann and Cornell [14] (akaganéite S, Fig. 1). While the latter is still all paramagnetic at 298 K, the former is largely magnetically ordered, though with a broad distribution of hyperfine fields around the mean value of 24 T, indicating that the ordering temperature is not far above ambient temperature. At 4.2 K the spectra of both akaganéites are virtually identical. The XRD patterns of the two akaganéites are also different: Akaganéite M exhibits a more pronounced monoclinic distortion than akaganéite S, which results in some of its diffraction peaks to split into two (Fig. 2). The different distortions may depend on the Cl content of the akaganéite.

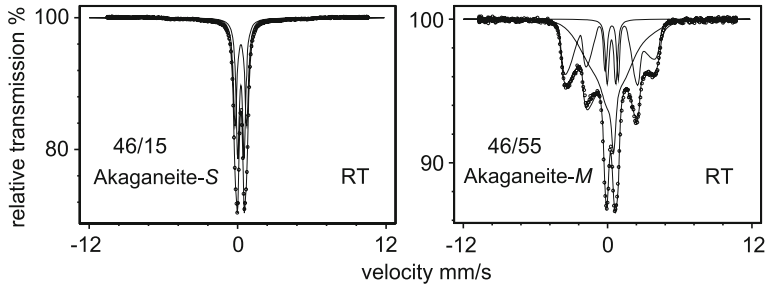

Fig. 1 ^{57}Fe Mössbauer spectra recorded at 298 K of akaganéite S (*left*) and of akaganéite M (*right*)

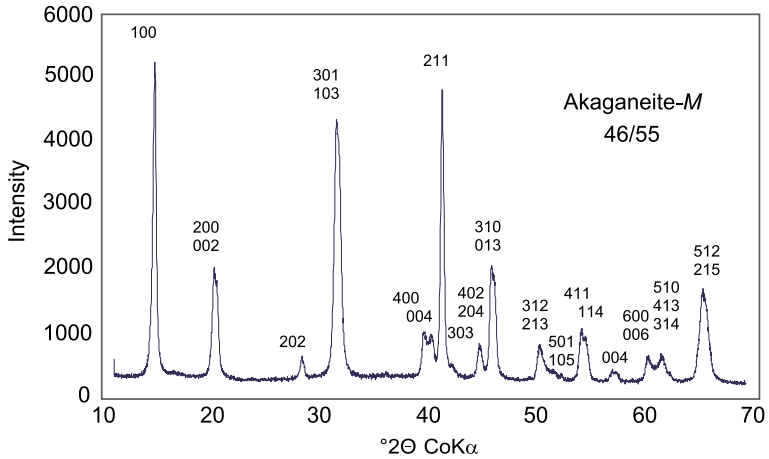

Fig. 2 X-ray diffraction pattern of akaganéite M made by the solid state reaction of a 1:1 mixture by mass of iron powder and $FeCl_2 \cdot 4H_2O$

3 Removal of akaganéite from iron objects by leaching methods

Akaganéite or free chloride ions present in the corrosion layer close to the metallic iron are believed to promote further corrosion [11]. It is therefore a major goal in the conservation of iron artefacts to remove chloride and akaganéite. For this, desalination by leaching in water or in solutions of NaOH or NaOH/Na_2SO_3 mixtures is often used [1]. The conversion of akaganéite into chlorine-free compounds can be monitored by Mössbauer spectroscopy. It turned out that solutions containing both NaOH and Na_2SO_3 are quite effective in converting akaganéite into goethite and hematite already at ambient temperature, while pure water or NaOH solutions do not affect the akaganéite (Fig. 3), though they may remove free chloride [15].

4 Studies on Celtic nails

As examples of corrosion studies on archaeological artefacts we report on two rather well preserved Celtic nails from the oppidum of Manching. Nail 46/43 was excavated

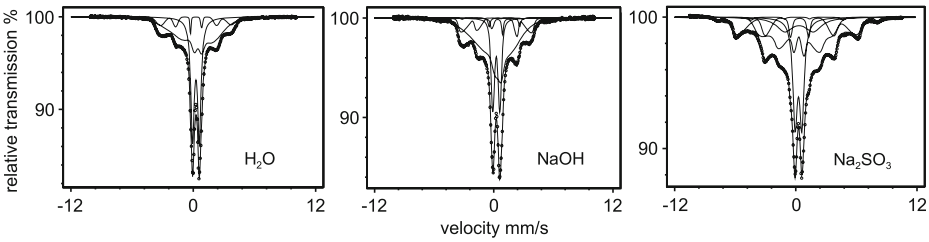

Fig. 3 Mössbauer spectra recorded at 298 K of akaganéite M after 7 days leaching in pure H_2O at 55°C, in a 4 g/l solution of NaOH at 55°C and in a solution of 6.3 g/l Na_2SO_3 plus 4 g/l NaOH at 25°C

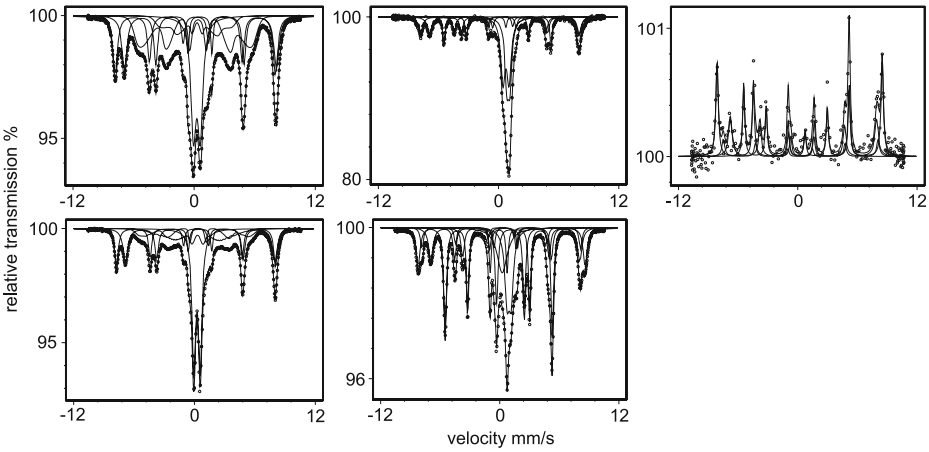

Fig. 4 RT Mössbauer spectra of the Celtic nails 46/43 (*upper row*) and 46/155 (*bottom row*). The spectra of samples from the corrosion layer are shown on the left. For the spectra in the middle these samples were reduced for 1 h with charcoal in a closed vessel at 900°C. On the right the CEMS spectrum of the thin oxide film formed by the same treatment on a freshly cut section through the metallic part of nail 46/43 is shown

in 1964 and then cleaned and covered with epoxy resin. It had developed a new corrosion layer under the epoxy film. Nail 46/155 was excavated in 1999 and hence stored untreated. Figure 4 shows that the Mössbauer spectra of the corrosion layers of both nails are very similar and show mainly magnetite and fine-grained goethite. The epoxy cover may have slowed corrosion, but did not affect the nature of the corrosion products. Small amounts of akaganéite are difficult to detect by Mössbauer spectroscopy in the presence of goethite. XRD is clearly superior in this respect and showed the presence of small amounts of akaganéite in both corrosion layers.

Thermal treatments of corroded iron artefacts may destroy akaganéite and drive off chloride. In agreement with previous observations [12, 16–18] we observed, by both XRD and Mössbauer spectroscopy, that akaganéite M and akaganéite S both convert into hematite when heated to about 400°C, though there are differences in the detailed behaviour.

Thermal treatments in reducing atmospheres above about 700°C convert the corrosion layers into mixtures of metallic iron, magnetite, wüstite and hematite. The

metallic surface becomes covered by a thin film of magnetite, wüstite and hematite that may prevent further oxidation. A Celtic nail treated at 850°C in a N_2+5% H_2 gas mixture 15 years ago and kept in air ever since shows no signs of new corrosion. The disadvantage of high temperature heat treatments is, however, that they will wipe out the microstructure of the metal that bears information on the production of the iron artefacts [1].

Figure 4 shows the effect of heat treatments on the two studied Celtic nails. When the nails were reduced with charcoal in a closed vessel at 900°C, the corrosion products were converted into magnetite, wüstite and metallic iron, though with different relative amounts that were also found to depend on the time of reduction: After 2 h more metallic iron was found than after only 1 h. A thin film consisting of hematite and magnetite formed on the surface of the metallic iron, as is shown by the CEMS spectrum of Fig. 4, which reveals 41% hematite, 33% magnetite and 26% metallic iron, the latter probably representing the iron substrate seen through the thin surface coating. Such surface coatings provide a good protection against further corrosion [3].

5 Conclusions

The aim of the present paper is to show that Mössbauer spectroscopy can be used in various ways to study questions related to the conservation of archaeological iron artefacts. In the future, more and more systematic work is expected to contribute to the solution of some of the pending problems of iron conservation.

Acknowledgements Support from the Federal Cultural Foundation and the Cultural Foundation of the German States (KUR program) is gratefully acknowledged.

References

1. Scott, D.A., Eggert, G.: Iron and Steel in Art: Corrosion, Colorants, Conservation. Archetype Publications, London (2009)
2. Dillmann, P., Béranger, G., Piccardo, P., Matthiesen, H. (eds.): Corrosion of Metallic Heritage Artefacts: Investigation, Conservation and Prediction for Long-Term Behaviour. Woodhead Publishing Inc., Cambridge (2007)
3. Meisel, W., Gütlich, P.: Werkst. Korros. **32**, 296 (1981)
4. Singh, A.K., Ericsson, T., Häggström, L., Gullman, J.: Corros. Sci. **25**, 931 (1985)
5. Cook, D.C.: Corros. Sci. **47**, 2550 (2005)
6. Cook, D.C.: Hyp. Interact. **153**, 61 (2004)
7. Long, G.J., Hautot, D., Grandjean, F., Vandormael, D., Leighley, H.P., Jr.: Hyp. Interact. **155**, 1 (2004)
8. Cook, D.C., Peterson, C.E.: AIP Conf. Proc. **765**, 91 (2005)
9. Fonseca, M.P.C., Bastos, I.N., Cayutero, A., Baggio Saitovitch, E.M.: Corr. Sci. **49**, 1949 (2007)
10. Novakova, A.A., Gendler, T.S., Manyurova, N.D., Turishcheva, R.A.: Corr. Sci. **39**, 1585 (1997)
11. Selwyn, L.S., Sirois, P.J., Argyropoulos, V.: Stud. Conserv. **44**, 217 (1999)
12. Ståhl, K., Nielsen, K., Jiang, J., Lebech, B., Hanson, J.C., Norby, P., van Lanschot, J.: Corr. Sci. **45**, 2563 (2003)

13. Turgoose, S.: Stud. Conserv. **27**, 97 (1982)
14. Schwertmann, U., Cornell, R.M.: Iron Oxides in the Laboratory. VHC, Weinheim, Germany (1991)
15. Reguer, S., Mirambet, F., Dooryhee, E., Hodeau, J.-L., Dillmann, P., Lagarde, P.: Corr. Sci. **51**, 2795 (2009)
16. Meroño, M.D., Morales, J., Tirado, J.L.: Thermochim. Acta **92**, 525 (1985)
17. Post, J.E., Heaney, P.J., Von Dreele, R.B., Hanson, J.C.: Am. Mineralogist. **88**, 782 (2003)
18. Gonzalez-Calbet, J.M., Franco, M.A.A.: Thermochim. Acta **58**, 45 (1982)

Hyperfine Interact (2012) 208:117–121
DOI 10.1007/s10751-011-0405-6

Temperature dependence of the quadrupole splitting of olivine and pyroxene from the Plains of Gusev Crater on Mars

David G. Agresti

Published online: 1 November 2011

Abstract In the present work, we report application of simultaneous fitting procedures to Mössbauer data acquired on the Plains of Gusev Crater by the MIMOS II spectrometer on board the Mars Exploration Rover Spirit. Based on a quantitative measure of spectrum quality, the 34 best of the ∼126 spectra acquired on the Plains are grouped together for a single simultaneous fit with a common least-squares criterion. Fitted values for the quadrupole splitting (QS) of olivine (Ol) from 200 K to 260 K are shown to lie between reported trend lines for Fo50 and Fo30 olivine, with a temperature gradient of $(-11.2 \pm 1.2) \times 10^{-4}$ mm/s/K, a nearly five-fold improvement in precision over the previously reported value, enabling extrapolation to QS(Ol) = (2.93 ± 0.01) mm/s at 295 K. QS of pyroxene fit as a single doublet exhibits a temperature gradient of $(-7.3 \pm 2.3) \times 10^{-4}$ mm/s/K.

Keywords Mössbauer · Mars-mineralogy · Simultaneous fitting · Olivine · Pyroxene

1 Introduction

After reaching Mars in 2004, the Mars Exploration Rover Spirit (MER-A) traversed the Plains of Gusev Crater for approximately 150 martian days (sols), where its MIMOS II Mössbauer (MB) spectrometer [1] acquired spectra in 10-K wide temperature intervals. Iron mineralogy was determined by fitting individual MB spectra of rock and soil targets, typically summed over temperature [2]. Unequivocal temperature dependence was reported only for the quadrupole splitting (QS) of olivine (Ol), for which a gradient of $-(9.7 \pm 5.0) \times 10^{-4}$ mm/s/K was derived (see Fig. 5 of [2]).

D. G. Agresti (✉)
Department of Physics, University of Alabama at Birmingham,
Birmingham, AL 35294, USA
e-mail: agresti@uab.edu

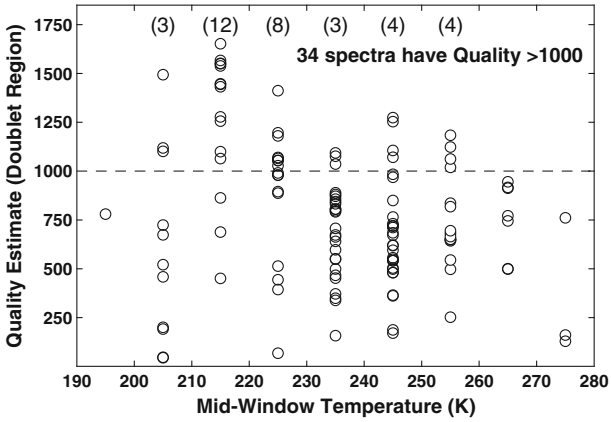

Fig. 1 Quality estimates for the "doublet region" of the ∼126 Mössbauer spectra taken on different sols at different temperatures during MER's traverse of the Plains of Gusev Crater. The number of spectra (sols) in each temperature interval is shown in parentheses at the top of the figure

In an ongoing effort [3–5], we have been fitting MER MB spectra simultaneously (simfitting) in order to enhance their information yield. Initially we derived a value for the QS(Ol) gradient of a single target with improved precision [3]. Later we demonstrated the presence of two distinct phases in Meridiani hematite [4, 5]. In this report the focus is on the doublet components of the ∼126 Plains spectra.

2 Data in the simfit set

To optimize simfitting, the quality of each of the ∼126 Plains spectra was defined as $Quality = \Sigma_i(\mathrm{S/N})_i$, the sum over channels of signal-to-noise, $\mathrm{S/N}_i = (Y_i - B)/\sqrt{Y_i}$, where Y_i = counts and B = baseline. The spectra were calibrated with *MERView* [6], fold-summed, and velocity referenced to α-Fe. For the *Quality* calculation, only velocities within the interval, (−2.5, 3.75) mm/s, the "doublet region," were included in the sum. The results are displayed in Fig. 1. Only the 34 spectra with *Quality* > 1,000 were fit simultaneously, using the MER-data fitting program, *MERFit* [3].

3 The spectral model

For the simft, each spectrum was modeled as a superposition of three doublets for Ol, pyroxene (Px), and nanophase oxide (npOx), and three sextets for magnetite (Mt1, Mt2) and hematite (Hm) (as in [2]). An example spectrum, together with its simfit model, is shown in Fig. 2. Because the sextets are weak in the doublet region (Mt < 2% and Hm < 1% total area), only their areas were varied in the simfit, while Area(Mt1)/Area(Mt2) was held to 1.54 [3]; other sextet values, listed in [2, 3], were held fixed during the simfit. Subspectral area ratios (doublets and sextets) were held equal for a given target, independent of temperature (fixed composition). For each doublet, width and center shift (CS) were the same for all spectra (i.e. independent of temperature), while QS was held equal for spectra at the same temperature.

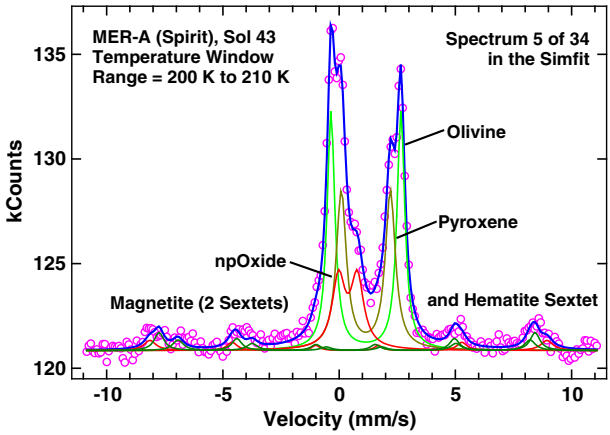

Fig. 2 Example spectrum showing the three doublets and three sextets used in the fit. The *open circles* are the fold-summed counts and the solid blue line is the fit spectrum

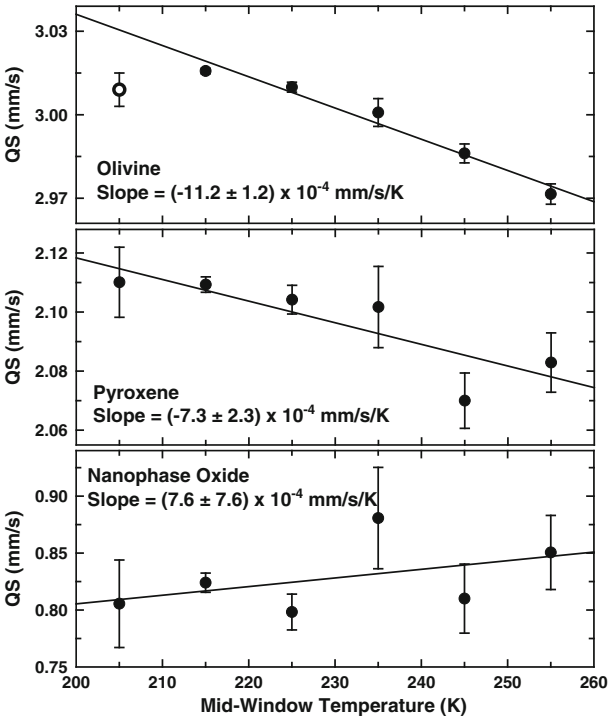

Fig. 3 Simfit values for quadrupole splitting (QS) in olivine, pyroxene, and nanophase oxide at each temperature, with computed error bars based on the linear fit and relative spectrum quality. The apparent outlier value for olivine at 205 K was not used in the linear fit

For MER MB spectra, it is expected that CS will not depend on temperature (see e.g. [2]) because sample and reference α-Fe foil are at the same temperature; however, an initial simfit did show such dependence for CS(Ol) and CS(Px). Following this, laboratory spectra [7] were fit for CS (relative to α-Fe at 295 K) and [CS–CS(α-Fe)] was computed for several olivines and pyroxenes at several temperatures. In each case, this difference varied <0.01 mm/s over the range from 200 K to 295 K.

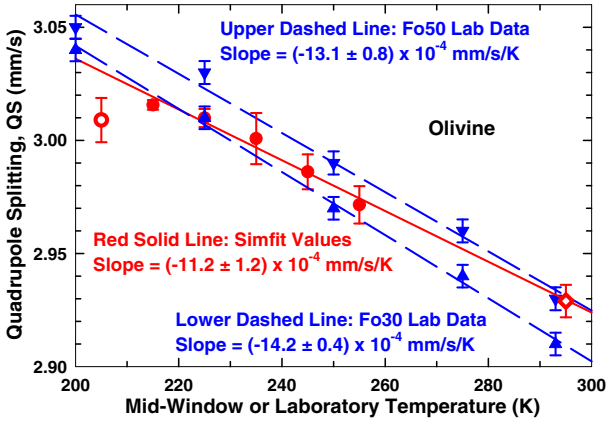

Fig. 4 A comparison of simfit QS values (*red filled circles*) with laboratory data (*up and down blue triangles*) for two synthetic olivines, Fo50 and Fo30 [8]. The *open red filled circle* at the left was not used in the linear fit. The *open red diamond* at the lower right is the extrapolation of the fitted line to a value of (2.93 ± 0.01) mm/s at 295 K

4 The results

The QS variation with temperature for Ol, Px, and npOx is shown in Fig. 3. For Ol, the precision in the gradient is improved by a factor of nearly 5. For Px, a gradient is observed with reasonable precision. No such gradient can be claimed for npOx.

5 Conclusions

Simfitted QS(Ol) from MER data may be compared with laboratory measurements using a rather throrough study of synthetic olivines from near forsterite (Fo) to fayalite (Fa) [8]. This work lists QS values for one-doublet fits of spectra acquired from 293 K to 200 K and below. In Fig. 4 we see that the MER QS(Ol) simfit values are well bracketed between the QS trend lines for Fo_{50} and Fo_{30}. This result, derived from MER-MB data alone, is consistent with a previous estimate of Fo_{42} – Fo_{49} for olivine of 4 Plains rocks (see Table 3 of [9]).

A comparison of the simfit QS(Px) temperature trend with laboratory data was not successful, perhaps because the pyroxene spectra of [7] are poorly fit with a single doublet, especially at lower temperatures. A two-doublet model (M1, M2 sites) for pyroxene will be tried. No explanation is at hand for the temperature dependence of CS(Ol) and CS(Px), when they are allowed to vary with temperature in the simfit.

Acknowledgements Thanks to Darby Dyar for permission to use unpublished spectra available at her Mt. Holyoke web site. Thanks to Iris Fleischer for pointing out Ref. [9] to the author. Development of *MERFit* was supported by NASA grant NNX06AD93G.

References

1. Klingelhöfer, G., et al.: Athena MIMOS II Mössbauer spectrometer investigation. J. Geophys. Res. **108**(E12), 8067 (2003). doi:10.1029/2003JE002138
2. Morris, R.V., et al.: Mössbauer mineralogy of rock, soil, and dust at Gusev crater, Mars: Spirit's journey through weakly altered olivine basalt on the plains and pervasively altered basalt in the Columbia Hills. J. Geophys. Res. **111**, E02S13 (2006). doi:10.1029/2005JE002584

3. Agresti, D.G., Gerakines, P.A.: Simultaneous fitting of Mars Mössbauer data. Hyperfine Interact. **188**, 113–120 (2009). doi:10.1007/s10751-008-9896-1
4. Agresti, D.G., Fleischer, I., Klingelhöfer, G., Morris, R.V.: On simfitting MER Mössbauer data to characterize Martian hematite. J. Phys. Conf. Ser. **217**, 012063 (2010). doi:10.1088/1742-6596/217/012063
5. Fleischer, I., Agresti, D.G., Klingelhöfer, G., Morris, R.V.: Distinct hematite populations from simultaneous fitting of Mössbauer spectra from Meridiani Planum, Mars. J. Geophys. Res. **115**, E00F06 (2010). doi:10.1029/2010JE003622
6. Agresti, D.G., Dyar, M.D., Schaefer, M.W.: Velocity scales for Mars Mössbauer data. Hyperfine Interact. **170**, 67–74 (2006). doi:10.1007/s10751-006-9472-5.
7. http://www.mtholyoke.edu/courses/mdyar/database/. Data used with permission. Accessed 24 Oct 2011
8. Sklute, E.C.: Mössbauer spectroscopy of synthetic olivine across the Mg-Fe solid solution. On the web at http://www.mtholyoke.edu/courses/mdyar/theses/Eli_Sklute_2006.pdf. Accessed 24 Oct 2011
9. McSween, H.Y., et al.: Mineralogy of volcanic rocks in Gusev Crater, Mars: Reconciling Mössbauer, Alpha Particle X-Ray Spectrometer, and Miniature Thermal Emission Spectrometer spectra. J. Geophys. Res. **113**, E06S04 (2008). doi:10.1029/2007JE0022970

Hyperfine Interact (2012) 208:123–131
DOI 10.1007/s10751-012-0563-1

Current status of iron-based superconductors

Yoichi Kamihara

Published online: 20 January 2012

Abstract Current status of iron-based superconductors is summarized. Although short range magnetic ordering and magnetic phase separation of Fe are controversial, (long range) magnetic and electronic phase diagrams of iron based superconductors can be classified into two-type. Antiferromagnetic ordering of itinerant Fe does not coexist with superconducting phase of $SmFeAsO_{1-x}F_x$. The very large H_{c2} of iron-based superconductors attract us to attempts at applications.

Keywords Iron-based superconductors · Applications · ^{57}Fe Mössbauer effect · Critical magnetic field · Superconducting critical current density

1 Iron-based superconductors

Although iron and iron-based compounds are representative ferromagnetic and/or ferrimagnetic materials, a considerable number of iron-based compounds have been reported as exhibiting superconductivity. Figure 1 shows superconductors containing itinerant Fe 3d electrons which had been reported before 2005. Intermetallic compounds [U_6Fe, Th_7Fe, Zr_2Fe, $R_2Fe_3Si_5$ (R = Sc, Y, Lu, and Tm)] and rare-earth filled skutterudites [$LnFe_4P_{12}$ (Ln = La, Y)], whose superconducting transition temperatures ranged from 1.8 to 7 K, show Pauli paramagnetic behavior in the

Y. Kamihara (✉)
Department of Applied Physics and Physico-Informatics, Faculty of Science and Technology, Keio University, 3-14-1 Hiyoshi, Yokohama, 223-8522, Japan
e-mail: kamihara_yoichi@appi.keio.ac.jp

Y. Kamihara
TRIP, Japan Science and Technology Agency, Sanban-cho bldg, 5, Sanban-cho, Chiyoda, Tokyo, 102-0075, Japan

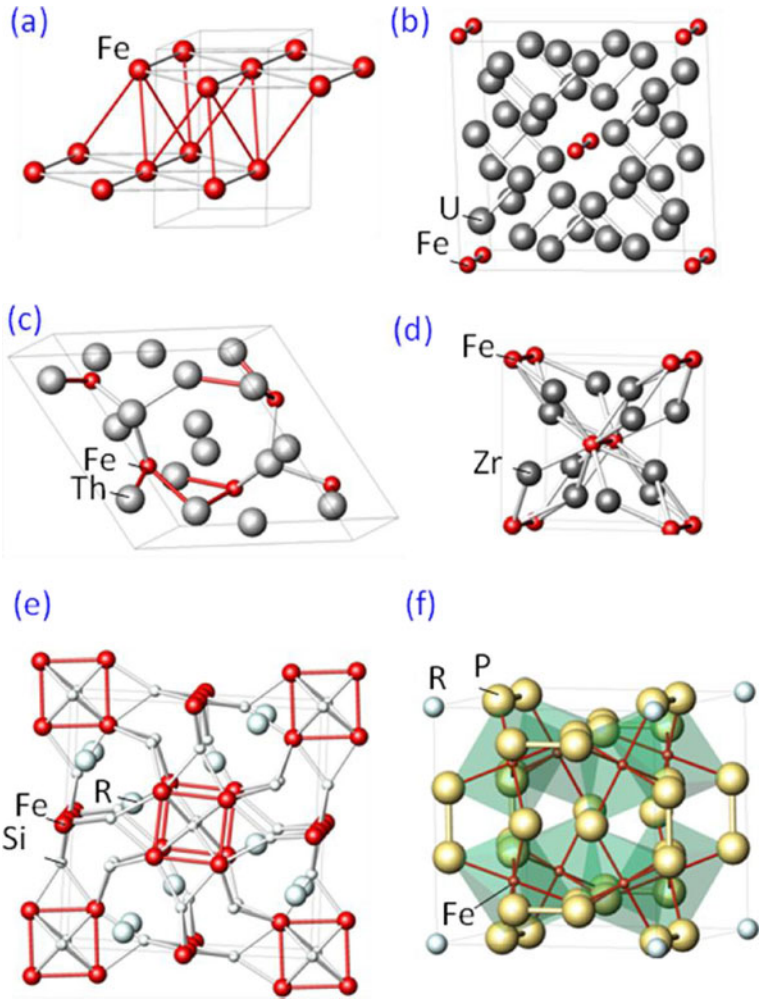

Fig. 1 Crystallographic structures of iron based superconductors. (**a**) ε-Fe [1], (**b**) U_6Fe [2], (**c**) Th_7Fe [3], (**d**) Zr_2Fe [4], (**e**) $R_2Fe_3Si_5$ (R = Sc, Y, Tm, and Lu) [5–9], (**f**) RFe_4P_{12} (R = La, Y) [10, 11]

normal conducting states, indicating that the magnetic moments of the iron are quenched. The quench of the magnetic moment is also observed in a high-pressure phase of elementary iron (ε-iron), which shows superconducting transition at ~2 K [1].

Since the first discovery of an iron-based superconductor, $LnFePnO_{1-x}F_x$ (Ln: Rare earth ions, Pn: Pnicogen ions) [12, 13] many researchers focus on this material as a candidate for a new high-T_c superconductor. After the first report, series of iron-based superconducting materials have been reported. Figure 2 shows crystallographic phases of iron-based high-T_c superconducting materials. These superconducting materials contain iron: a typical Mössbauer nuclide. T_c of iron-based superconductors reached at 55 K in F-doped SmFeAsO [33].

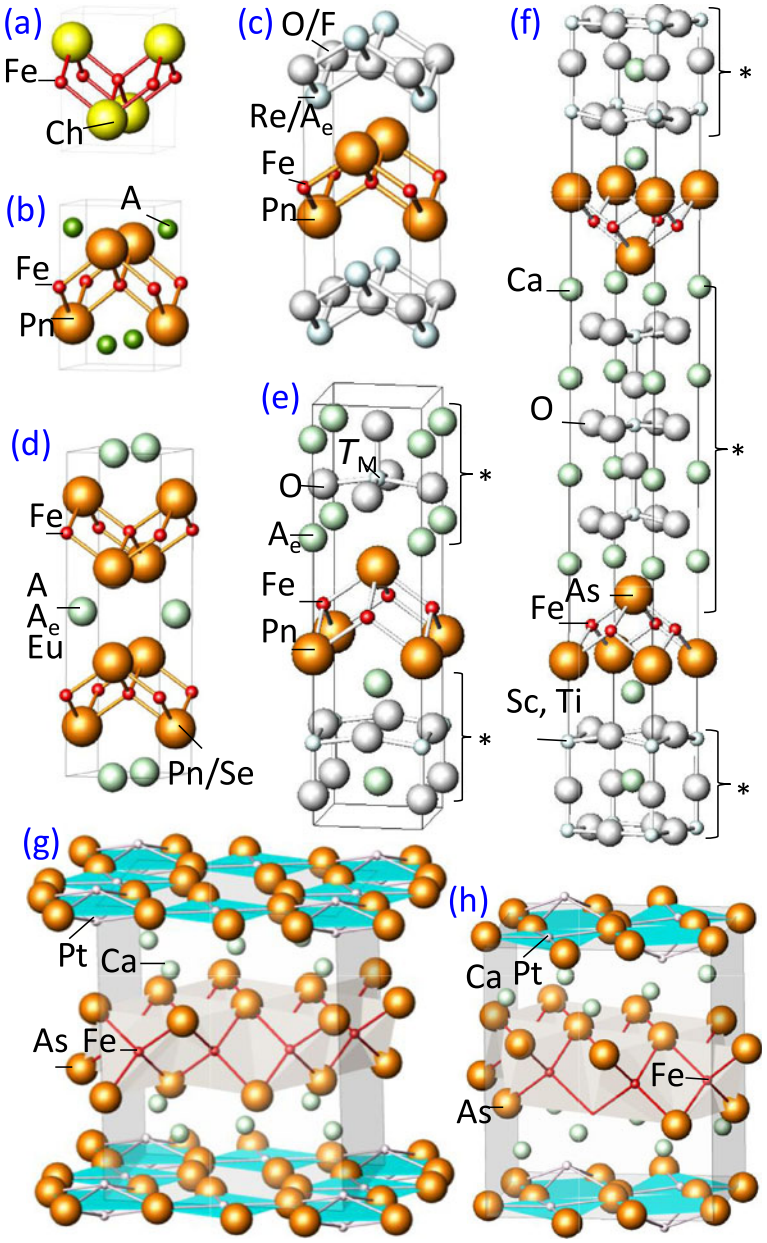

Fig. 2 Crystallographic structures of iron-based high T_c superconductors [14, 15]. (**a**) FeCh (Ch: S, Se, Te), 11-type [16], (**b**) AFePn (A: Li, Na, Pn = P, As), 111-type [17–19], (**c**) ReFePnO (Re: rare earth ions) / AeFePnF (Ae: Alkaline earth ion), 1111-type [12, 13, 20], (**d**) AFe_2Pn_2, $AeFe_2Pn_2$, $EuFe_2Pn_2$, AFe_2Se_2, 122-type [21–24], (**e**) $Ae_2TMFePnO_3$ (TM = Mg, Al, Ti, V), 21113-type [25–28], (**f**) $Ae_4TM_3Fe_2As_2O_8$ [29], * denotes homologus structures. (**g**) (**h**) Ce-Fe-Pt-As [30–32]

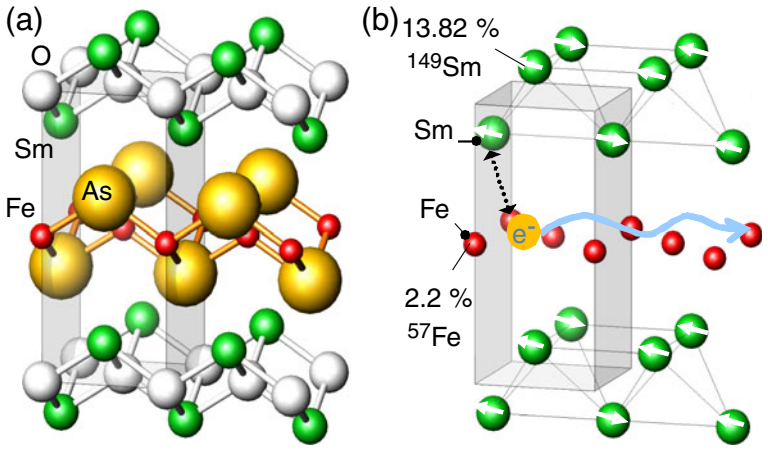

Fig. 3 Crystal structure (**a**) and schematic electrical conduction (**b**) of SmFeAsO

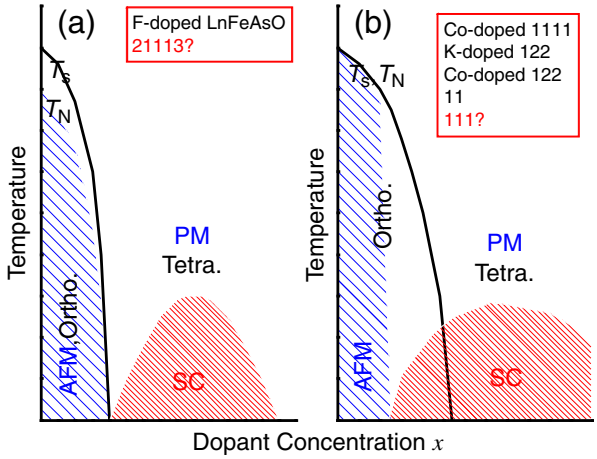

Fig. 4 Magnetic and electronic phase diagrams for Iron-based high-T_c superconductors

2 Magnetic and electronic phase diagram for iron-based high-T_c superconductors

Details for coexistence or not-coexistence of magnetic and superconducting phases were important issues for iron-based superconductors in 2008–2010 [34, 35]. In general, it is very difficult to measure element-specific magnetic moments in a compound containing plural magnetic element using DC magnetization measurement, heat capacity, and μ-SR measurement. In contrast, Mössbauer spectroscopy (MS) and nuclear resonant forward-scattering (NRFS) provide us information on the magnetic hyperfine field at nuclei position. MS and NRFS are also effective to distinguish main phase's magnetic ordering from impurity's magnetic ordering using isomer shift values like Knight shifts values in nuclear magnetic resonance (NMR). MS and NRFS are very good element-specific magnetic measurement methods. Indeed, magnetic properties of $SmFeAsO_{1-x}F_x$ are demonstrated by using ^{57}Fe MS and ^{149}Sm NRFS [36].

Table 1 Superconducting transition temperatures (T_c), superconducting transport-, intergrain-, intragrain-critical current densities (J_c), and upper superconducting critical fields (H_{c2}) for iron-based high-T_c superconductors

Chemical composition	Shape	T_c (K)	J_c (A/cm^2)			$\mu_0 H_{c2}$ (T)	Remarks	Refs.
			Transport	Intergrain	Intragrain			
LaFePO	Poly	2–5.4	–	–	–	0.01–0.1	–	[12, 43]
$LaFePO_{0.94}F_{0.06}$	Poly	6.1	–	1.3×10^4	1.3×10^4	~1	1.83 K	[44]
LaFePO	Single	6.6	–	–	–	4	2 K, H$\|\|ab$	[45]
$LaFePO_{1-d}$	Single	7.8	–	–	–	–	–	[45]
$LaFeAsO_{1-x}F_x$	Poly	26	–	–	–	–	–	[13]
	Poly	25	–	–	–	60$\perp ab$, 40//ab	0 K	[46]
	Single	11.5	–	–	–	–	–	[47]
	Wire	20	–	–	1.0×10^3	–	5 K	[48]
	Film(Poly)	24	1.0×10^3	–	–	120	2 K	[49]
$NdFeAsO_{1-x}F_x$	Film	45	–	–	–	–	PLD	[50]
	Single	37	–	–	1.0×10^5	–	5 K	[51]
	Single	46	–	–	–	200–300	0 K	[52]
	Poly	47	–	2.1×10^3	6.7×10^6	–	5 K	[53]
$SmFeAsO_{1-x}F_x$	Film	56.2	1.0×10^6	–	–	–	MBE	[54]
	Single	54	2.0×10^6	–	–	200–300	0 K	[55]
	Poly	52	–	–	1.1×10^5	–	5 K	[56]
	Wire	43	4.0×10^3	–	–	–	4.2 K	[57]
	Tape	43	2.7×10^3	–	–	–	4.2 K	[58]
$SmFeAsO_{1-d}$	Poly	53	–	4.0×10^3	7.3×10^6	–	2 K	[53]
$Ba_{1-x}K_xFe_2As_2$	Film	36.9	–	–	–	–	MBE	[59]
	Single	37	–	–	2.5×10^6	–	5 K	[60]
	Single	35.9	–	–	4.7×10^6	–	2 K	[61]
	Single	28.2	–	–	–	70	0 K	[62]
	Poly	35	–	2.0×10^4	2.0×10^6	–	5 K	[63]
	Wire	35	1.0×10^4	–	–	–	4.2 K	[64]

Table 1 (continued)

Chemical composition	Shape	T_c (K)	J_c (A/cm^2)			$\mu_0 H_{c2}$ (T)	Remarks	Refs.
			Transport	Intergrain	Intragrain			
$Sr_{0.6}K_{0.4}Fe_2As_2$	Wire	35	2.5×10^4	–	–	–	4.2 K	[65]
$BaFe_{2-x}Co_xAs_2$	Single	22	–	–	2.6×10^5	–	5 K	[66, 67]
	Single	22	–	–	–	50⊥*ab*, 55//*ab*	0 K	[68]
	Film	22.15	4.5×10^6	–	–	–	4.2 K	[69]
	Film	22	4.0×10^6	–	–	–	4 K	[70]
	Film on tape	21.3	3.5×10^6	–	–	–	2 K	[71]
$SrFe_{2-x}Co_xAs_2$	Film	17.1	–	–	–	47	0 K	[72]
	Film	17.6	5.0×10^5	–	–	–	4.5 K	[73]
$FeSe_{1+x}$	Poly	9	–	–	–	~16.3	0 K	[16]
	Single	9.8	–	–	2.2×10^4	–	1.8 K	[74]
	Film	6	–	–	–	–	–	[75]
	Wire	11	3.8×10^2	–	–	–	–	[76]
$FeSe_{0.25}Te_{0.75}$	Poly	13.7	–	–	–	40–50	1.4 K	[77]
$FeSe_{0.5}Te_{0.5}$	Film	16	5.9×10^4	–	–	–	4.5 K, 10 T	[78]
	Film	20.2	–	–	–	–	–	[79]
	Wire	10.5	2.3×10^2	–	–	–	4.2 K	[80]

Poly: polycrystalline sample, Single: single crystals, Wire: superconducting wires, Film: poly- and/or single crystalline thin film, Tape: superconducting tape, Film on tape: epitaxial thin film on a metallic tape, Transport J_c: J_c measured from voltage drop measuring method, Intergrain J_c: J_c between grain boundary, Intragrain J_c: J_c in grain boundary. T_cs in this table are onset of the magnetic shielding effects or T_c middle read from figures in cited references. When J_c, H_{c2} are extrapolated values, "0 K" are shown in remarks. MBE: Molecular beam epitaxy

Figure 3 shows crystallographic structure of SmFeAsO. Polycrystalline $SmFeAsO_{1-x}F_x$ samples were synthesized using two-step solid state reaction described elsewhere [36]. Purity of samples was checked by X-ray diffraction patterns using Cu K-α radiation. Resistivity and magnetization measurements, as well as by ^{57}Fe MS and ^{149}Sm NRFS spectroscopy, at various temperatures were performed to define superconducting, magnetic ordering temperatures. A magnetic phase diagram we have proposed is closer to that by Hess et al. [34] (Fig. 4a); that is long-range AF ordering of Fe (a static magnetism) does not persist in the superconducting regime. Such a relation between spin dynamics and SC is a common feature among $LnFeAsO_{1-x}F_x$ (Ln = La, Ce, Pr, Nd, and Sm). Our results indicate that the relation between the long range magnetic ordering and T_c of $LnFeAsO_{1-x}F_x$ shows similar topology to that of copper-based high-T_c superconductors. If short range magnetic ordering [37, 38] and magnetic phase separation [39, 40] of Fe are excluded, macroscopic magnetic and electronic phase diagrams of iron based superconductors can be classified into two-type demonstrated in Fig. 4. Present issues are microscopic, short-range-ordered, magnetic properties on a nanometer-range in iron-based high-T_c superconductors [41, 42].

3 Researches for applications of iron-based superconductors

Iron-based high T_c superconductors demonstrate very large upper critical magnetic fields (H_{c2}) which reach same extent compared with copper-based superconductors [81]. These attractive characteristics of iron-based superconductors triggered research into new iron-based superconductors as well as several attempts at applications. Table 1 shows transport critical current densities (J_c), and H_{c2} for several iron-based high-T_c superconductors.

4 Summary

Considerable number of iron-based high-T_c superconductors has been reported. If short range magnetic ordering and magnetic phase separation of Fe are excluded, magnetic and electronic phase diagrams of iron based superconductors can be classified into two-type. Present issues between magnetism and superconductivity of iron-based superconductors are microscopic, short-range ordered, magnetic properties on a nanometer range. The very large H_{c2} of iron-based superconductors triggered research into several attempts at applications.

References

1. Shimizu, K., et al.: Nature **412**, 316 (2001)
2. Chandrasekhar, B.S., Hulm, J.K.: J. Phys. Chem. Solids **7**, 259 (1958)
3. Matthias, B.T., et al.: J. Phys. Chem. Solids **19**, 130 (1961)
4. Havinga, E.E., et al.: J. Less-Common Met. **27**, 169 (1972)
5. Braun, H.F.: Phys. Lett. **A75**, 386 (1980)
6. Vining, C.B., et al.: Phys. Rev. **B27**, 2800 (1983)
7. Braun, H.F.: Phys. Lett. **A85**, 372 (1981)
8. Vining C.B., Shelton, R.N.: Solid State Commun. **54**, 53 (1985)

9. Schmidt, H., et al.: Phys. Rev. **B53**, 12389 (1996)
10. Meisner, G.P.: Physica, B + C **108**, 763 (1981)
11. Shirotani, I., et al.: J. Phys.: Condens. Matter **15**, S2201 (2003)
12. Kamihara, Y., et al.: J. Am. Chem. Soc. **128**, 10012 (2006)
13. Kamihara, Y., et al.: J. Am. Chem. Soc. **130**, 3296 (2008)
14. Kamihara, Y., Hosono, H.: Denshi Zairyo **49**, 18 (2010) (Japanese)
15. Kamihara, Y., Hosono, H.: Rev. High Press. Sci. Technol. **19**, 97 (2009) (Japanese)
16. Hsu, F.C., et al.: Proc. Natl. Acad. Sci. U. S. A. **105**, 14262 (2008)
17. Picher, M.J., et al.: Chem. Commun. (Cambridge) **45**, 5918 (2008)
18. Tapp, J.H. et al.: Phys. Rev. **B78**, 060505 (2008)
19. Deng, Z., et al.: Europhys. Lett. **87**, 37004 (2009)
20. Matsuishi, S., et al.: J. Am. Chem. Soc. **130**, 14428 (2008)
21. Rotter, M., et al.: Phys. Rev. Lett. **101**, 020503 (2008)
22. Rotter, M., et al.: Angew. Chem. Int. Ed. **47**, 7949 (2008)
23. Jeevan, H.S., et al.: Phys. Rev. B **78**, 092406 (2008)
24. Guo, J., et al.: Phys. Rev. B **82**, 180520 (2010)
25. Ogino, H., et al.: Supercond. Sci. Technol. **22**, 75008 (2008)
26. Zhu, X., et al.: Phys. Rev. B **79**, 220512 (2009)
27. Sato, S., et al.: Supercond. Sci. Technol. **23**, 45001 (2010)
28. Shirage, P.M., et al.: Appl. Phys. Lett. **97**, 172506 (2010)
29. Ogino, H., et al.: Appl. Phys. Express **3**, 063103 (2010)
30. Kakiya, S., et al.: J. Phys. Soc. Jpn. **80**, 093704 (2011)
31. Ni, N., et al.: Proc. Natl. Acad. Sci. **108**, E1019 (2011)
32. Löhnert, C., et al.: Angew. Chem. Int. Ed. **50**, 9195 (2011)
33. Ren, Z.A., et al.: Chin. Phys. Lett. **25**, 2215 (2008)
34. Hess, C.A., et al.: Europhys. Lett. **87**, 17005 (2009)
35. Drew, A.J., et al.: Nat. Mater. **8**, 310 (2009)
36. Kamihara, Y., et al.: New J. Phys. **12**, 033005 (2010)
37. Kitagawa, K., et al.: Phys. Rev. Lett. **103**, 257002 (2009)
38. Goko, T., et al.: Phys. Rev. B **80**, 024508 (2009)
39. Takeshita, S., et al.: J. Phys. Soc. Jpn. **77**, 103703 (2008)
40. Takeshita, S., et al.: Phys. Rev. Lett. **103**, 027002 (2009)
41. Shiroka, T., et al.: Phys. Rev. B **84**, 195123 (2011)
42. Luetkens, H., et al.: Nat. Mater. **8**, 305 (2009)
43. Kamihara, Y., et al.: Phys. Rev. B **77**, 214515 (2008)
44. Tsuchiya, Y., et al.: Physica C **470**, S300 (2010)
45. Hamlin, J.J., et al.: J. Phys., Condens. Matter **20**, 365220 (2008)
46. Hunte, F., et al.: Nature (London) **453**, 903 (2008)
47. Yan, J.Q., et al.: Appl. Phys. Lett. **95**, 222504 (2009)
48. Gao, Z., et al.: Supercond. Sci. Technol. **21**, 105024 (2008)
49. Haindl, S., et al.: Phys. Rev. Lett. **104**, 077001 (2010)
50. Kawaguchi, T., et al.: Appl. Phys. Lett. **97**, 042509 (2010)
51. van der Beek, C.J., et al.: Phys. Rev. B **81**, 174517 (2010)
52. Jaroszynski, J., et al.: Phys. Rev. B **78**, 174523 (2008)
53. Yamamoto, A., et al.: Supercond. Sci. Technol. **21**, 095008 (2008)
54. Ueda, S., et al.: Appl. Phys. Lett. **99**, 232505 (2011)
55. Moll, P.J.W., et al.: Nat. Mater. **9**, 628 (2010)
56. Tamegai, T., et al.: Physica **C469**, 915 (2009)
57. Fujioka, M., et al.: Appl. Phys. Express **4**, 063102 (2011)
58. Ma, Y., et al.: IEEE Trans. Appl. Supercond. **21**, 2878 (2010)
59. Takeda, S., et al.: Appl. Phys. Express **3**, 093101 (2010)
60. Wang, C., et al.: Supercond. Sci. Technol. **24**, 065002 (2011)
61. Yang, H., et al.: Appl. Phys. Lett. **93**, 142506 (2008)
62. Yuan, H.Q., et al.: Nature **457**, 565 (2009)
63. Wang, C., et al.: Appl. Phys. Lett. **98**, 042508 (2011)
64. Togano, K., et al.: Appl. Phys. Express **4**, 043101 (2011)
65. Gao, Z., et al.: Appl. Phys. Lett. **99**, 242506 (2011)
66. Sefat, A. S., et al.: Phys. Rev. Lett. **101**, 117004 (2008)
67. Prozorov, R., et al.: Phys. Rev. **B78**, 224506 (2008)
68. Kano, M., et al.: J. Phys. Soc. Jpn. **78**, 084719 (2009)

69. Lee, S., et al.: Nat. Mater. **9**, 397 (2010)
70. Katase, T., et al.: Appl. Phys. Express **3**, 063101 (2010)
71. Katase, T., et al.: Appl. Phys. Lett. **98**, 242510 (2011)
72. Baily, S.A., et al.: Phys. Rev. Lett. **102**, 117004 (2009)
73. Maiorov, B., et al.: Supercond. Sci. Technol. **22**, 125011 (2009)
74. Lei, H., et al.: Phys. Rev. B **84**, 014520 (2011)
75. Wang, M.J., et al.: Phys. Rev. Lett. **103**, 117002 (2009)
76. Ozaki, T., et al.: J. Appl. Phys. **111**, 013912 (2012)
77. Kida, T., et al.: J. Phys. Soc. Jpn. **78**, 113701 (2009)
78. Tsukada, I., et al.: Appl. Phys. Express **4**, 053101 (2011)
79. Bellingeri, E., et al.: Appl. Phys. Lett. **96**, 102512 (2010)
80. Ozaki, T., et al.: Supercond. Sci. Technol. **24**, 105002 (2011)
81. Sekitani, T., et al.: Physica B: Condens. Matter **346–347**, 319 (2004)

Hyperfine Interact (2012) 208:133–136
DOI 10.1007/s10751-011-0482-6

A ^{57}Fe Mössbauer study on the FeSe and Fe(Se,Te) superconductors: discontinuities in the hyperfine parameters at T_c

Johan Kaarle Mikael Lindén · Eeva-Leena Rautama · Maarit Karppinen · Hisao Yamauchi

Published online: 29 November 2011

Abstract Polycrystalline samples of $FeSe_{0.82}$ and $FeSe_{0.5}Te_{0.5}$ were synthesized using a solid-state reaction route. Bulk superconductivity was confirmed using SQUID magnetometry. The onset of T_c was at 8.0 K for $FeSe_{0.82}$ and 12.5 K for $FeSe_{0.5}Te_{0.5}$. Paramagnetic ^{57}Fe Mössbauer spectra were recorded at temperatures between 5.4 and 320 K in transmission geometry. All spectra exhibited simple quadrupole splitting. For $FeSe_{0.5}Te_{0.5}$ a small drop in the quadrupole splitting was observed about T_c upon cooling. Additionally, for both samples the isomer shift and the total absorption started to drop around T_c, indicating a softening of the lattice. The drop is estimated to correspond to at least 60 K from the original Debye temperatures.

Keywords ^{57}Fe Mössbauer spectroscopy · Chalcogenide superconductivity · Iron-based superconductors

1 Introduction

The Fe-based chalcogenide superconductors isostructural with β-FeSe have attracted a lot of attention during the last few years, due to their simple structure and yet relatively high critical temperatures [1]. No generally accepted theory for the mechanism behind the superconductivity in neither cuprates nor the Fe-based compounds has been put forth, although magnetic fluctuations are believed to play a key role in both categories of materials. The presence of Fe as a natural constituent in the latter category offers the possibility of monitoring the hyperfine interactions using

J. K. M. Lindén (✉)
Physics Department, Åbo Akademi University, 20500 Turku, Finland
e-mail: jlinden@abo.fi

E.-L. Rautama · M. Karppinen · H. Yamauchi
Department of Chemistry, Aalto University School of Science and Technology, 00076 Aalto, Finland

^{57}Fe Mössbauer spectroscopy. In measurements done thus far it has been found that Fe adopts the divalent low-spin ($S = 0$) state [2]. Therefore no magnetic signal is expected to be seen in the Mössbauer spectra, although presence of magnetic spin-density waves has been detected in several experiments [3, 4]. Recently we reported signs of lattice softening around T_c for both LiFeAs and $FeSe_{0.5}Te_{0.5}$ [5, 6]. A possible connection between the antiferromagnetic fluctuations and the lattice softening was recently suggested [7].

2 Experimental

The iron chalcogenide samples were prepared using a vacuum solid state reaction route. Samples with stoichiometries corresponding to $FeSe_{0.5}Te_{0.5}$ and $FeSe_{0.82}$ were manufactured. Stoichiometric quantities of high-purity iron, tellurium and selenium were mixed, sealed in evacuated fused quartz tubes and sintered for 20 h at 600°C followed by furnace cooling to room temperature. After regrinding and pelletizing the samples at 280 MPa a resintering at 650°C for 20 h followed.

The samples were characterized using ^{57}Fe transmission Mössbauer spectroscopy, powder X-ray diffraction (XRD) and SQUID magnetometry. The Mössbauer spectra were measured at selected temperatures between 5.4 and 320 K using a maximum Doppler velocity of ∼3 mm/s. Some measurements were done with ∼10 mm/s to check the presence of magnetic impurities. Sample thickness was ∼14 mg/cm^2. The low-velocity spectra were fitted using a paramagnetic component with isomer shift δ, line width Γ, peak intensity, and quadrupole coupling constant eQV_{zz} as fit parameters. Magnetic lines (when present) were fixed according to the 10-mm/s spectra. Results for the $FeSe_{0.5}Te_{0.5}$ sample were reported earlier [6]. However, more detailed results in which texture effects in the absorber have been included are presented here.

3 Results

The XRD pattern for $FeSe_{0.82}$ exhibited β-FeSe as the main phase together with δ-FeSe/Fe_7Se_8 (24 % according to Mössbauer data, *vide infra*), traces of elemental Se (∼3%, XRD) and Fe_3O_4 (3%, Mössbauer) as impurities. The $FeSe_{0.5}Te_{0.5}$ sample is isostructural with β-FeSe and a similar pattern as for $FeSe_{0.82}$ was obtained, with peaks shifted due to the Te substitution. Traces of Fe_3O_4 (4–5% Mössbauer & XRD) and (Te-substituted) Fe_7Se_8 (∼3% or less, XRD) were also detected. Superconductivity transitions were observed at 8 K and 12.5 K for the $FeSe_{0.82}$ and $FeSe_{0.5}Te_{0.5}$ samples, respectively, using a SQUID magnetometer recording in zero-field-cooling mode. Remeasurements in field-cooling mode (10 Oe) confirmed that the superconductivity was of bulk type, with a superconducting volume fraction of 15% for $FeSe_{0.5}Te_{0.5}$ and roughly 5% for $FeSe_{0.82}$, where the latter estimate was hampered by magnetic signals from δ-FeSe/Fe_7Se_8 and Fe_3O_4. The Verwey transition of the latter was also observed in the SQUID data. All ^{57}Fe Mössbauer spectra revealed the presence of a quadrupole-split ($|eQV_{zz}| \approx 0.6$ mm/s) paramagnetic doublet assigned to the β-FeSe type main phase observable down to 5 K, Fig. 1. For $FeSe_{0.82}$ small amounts of paramagnetic hexagonal FeSe and magnetically ordered

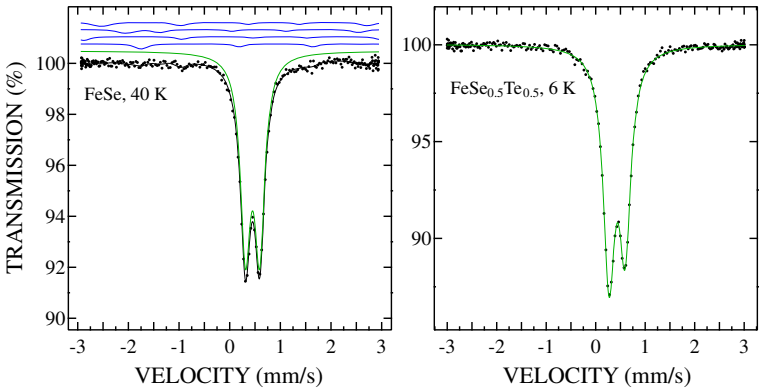

Fig. 1 Typical ^{57}Fe Mössbauer spectra of $FeSe_{0.82}$ and $FeSe_{0.5}Te_{0.5}$. Components used in the fittings are: main phase (*green*) and Fe_7Se_8 (*blue*)

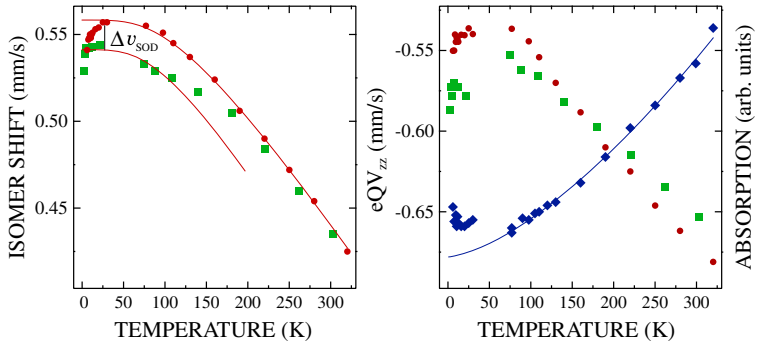

Fig. 2 *Left panel* Isomer shift vs. temperature for $FeSe_{0.82}$ (*green squares*) and $FeSe_{0.5}Te_{0.5}$ fitted with the Debye model [9] (*red bullets*). A softening around T_c is evident for both phases. *Right panel* Quadrupole coupling constant eQV_{zz} vs. temperature for $FeSe_{0.5}Te_{0.5}$ (*blue diamonds*) fitted with a power law, see text. Total Mössbauer absorption for $FeSe_{0.82}$ (*green squares*) and $FeSe_{0.5}Te_{0.5}$ (*red bullets*). A softening around T_c is evident

Fe_7Se_8 are observed, Fig. 1, whereas for $FeSe_{0.5}Te_{0.5}$ almost no impurities are seen in the low-velocity Mössbauer spectra. Spectra recorded with a Doppler velocity of 10 mm/s revealed presence of Fe_3O_4. Most of the impurity line-intensity is outside the velocity region used in the low-velocity measurements. The isomer shift of the main phase (~0.45 mm/s) is compatible with low-spin Fe^{2+}. At T_c both the isomer shift and total absorption (Fig. 2) drop, suggesting softening of the lattice. Similar results were previously reported for LiFeAs [3]. For $FeSe_{0.5}Te_{0.5}$ the estimated drop in the Debye temperature was estimated from the second-order Doppler shift (v_{SOD}) at $\theta_D \approx 60$ K [4].

The asymmetric doublet of the Mössbauer spectra of $FeSe_{0.5}Te_{0.5}$ was previously analyzed using a symmetric doublet of the main phase and a singlet due to an impurity phase [6]. However, as reported recently the absorber texturizes easily, [8] and accordingly a magic-angle measurement resulted in a symmetric doublet also in our case. The negative sign of eQV_{zz} was readily confirmed using the spectra of the

textured sample, but most importantly from the almost pure single-component data a very clear temperature dependence for eQV_{zz} could be extracted, Fig. 2. A clear drop in the absolute value of eQV_{zz} is evident about T_c. Analysis of the data reveals a typical $(1 - aT^{3/2})$ temperature dependence for the data above ~70 K, with a fitted to $3.5 \cdot 10^{-5}$ $K^{-3/2}$, in accord with previous results [8, 10]. For $FeSe_{0.82}$ a similar jump at T_c for eQV_{zz} is most probably present, but less clear due weaker statistics.

4 Conclusions

^{57}Fe Mössbauer investigations of $FeSe_{0.82}$ and $FeSe_{0.5}Te_{0.5}$ revealed a paramagnetic doublet down to ~5 K corresponding to Fe in the divalent $S = 0$ state. A lattice softening is evident in both the isomer shift and total absorption around T_c for both phases. The drop in Debye temperature is estimated at ~60 K. The quadrupole coupling constant exhibits also a jump around T_c.

Acknowledgement Mr. S. Fröjdö is acknowledged for his contribution to the sample synthesis.

References

1. Hsu, F.C., Luo, J.Y., Yeh, K.W., Chen, T.K., Huang, T.W., Wu, P.M., Lee, Y.C., Huang, Y.L., Chu, Y.Y., Yan, D.C., Wu, M.K.: Proc. Natl. Acad. Sci. USA **105**, 14262 (2008)
2. Kitao, S., Kobayashi, Y., Higashitaniguchi, S., Saito, M., Kamihara, Y., Hirano, M., Mitsui, T., Hosono, H., Seto, M.: J. Phys. Soc. Jpn. **77**, 103706 (2008)
3. Christianson, A.D., Goremychkin, E.A., Osborn, R., Rosenkranz, S., Lumsden, M.D., Malliakas, C.D., Todorov, I.S., Claus, H., Chung, D.Y., Kanatzidis, M.G., R.I Bewley, Guidi, T.: Nature **456**, 930 (2008)
4. Iikubo, S., Fujita, M., Niitaka, S., Takagi, H.: J. Phys. Soc. Jpn. **78**, 103704 (2009)
5. Gao, W.B., Lindén, J., Wang, X.C., Jin, C.Q., Tohyama, T., Karppinen, M., Yamauchi, H.: Solid State Commun. **150**, 1525 (2010)
6. Lindén, J., Libäck, J.-P., Karppinen, M., Rautama, E.-L., Yamauchi, H.: Solid State Commun. **151**, 130 (2011)
7. Yildirim, T.: Physica C **469**, 425 (2009)
8. Szymański, K., Olszewski, W., Dobrzyński, L., Satuła, D., Gawryluk, D.J., Berkowski, M., Puźniak R., Wiśniewski, A.: Supercond. Sci. Technol. **24**, 105010 (2011)
9. Nasu, S., Murakami, Y.: Phys. Stat. Sol. (b) **46**, 711 (1971)
10. Lodge, K.W.: J. Phys. F: Met. Phys. **9**, 2035 (1979)

Hyperfine Interact (2012) 208:137–147
DOI 10.1007/s10751-011-0511-5

Concluding remarks to ICAME2011

S. J. Campbell

Published online: 13 December 2011

Abstract An overview of the main aspects of ICAME2011 – tutorial lectures, oral and poster presentations, evening sessions - is presented along with a brief outline of several of the scientific highlights. Among other topics considered are the involvements of young scientists and female scientists, and operation of the oral and poster sessions. Despite the most challenging combinations of circumstances in the lead up to ICAME2011 that resulted in the change of venue at an advanced stage from Tokyo to Kobe, the Committee organised a high quality conference with many positive outcomes for the future. The Mössbauer community acknowledges and appreciates these efforts greatly.

Keywords Concluding remarks · International conference on the applications of the Mössbauer effect · ICAME2011

1 Introductory comments

ICAME2011, the 31st in the series of International Conferences on the Applications of the Mössbauer Effect, was held at the International Conference Center, Kobe, Japan from 25–30 September 2011. Consistent with its normal cycle and sequence, IBAME, the International Board on the Applications of the Mössbauer Effect, at its meetings during ICAME2007 in India, awarded the 2011 conference to Japan, a decision confirmed by IBAME at ICAME2009 in Austria. Having planned for almost 5 years for ICAME2011 to be held in Tokyo, the well documented tragic events of 11 March 2011 forced the Organising Committee to relocate the meeting from Tokyo to Kobe. As such the Mössbauer community acknowledges the significant

S. J. Campbell (✉)
School of Physical, Environmental and Mathematical Sciences,
The University of New South Wales, Canberra ACT 2600, Australia
e-mail: Stewart.Campbell@adfa.edu.au

extra loads and efforts required of the ICAME2011 organisers and wish to express their appreciation to the Organising Committee for their extraordinary efforts.

ICAME2011 was also shaped by the sad news reported in the days leading up to the conference, of the death of Rudolph L Mössbauer on 14 September 2011. A special tribute was paid to Professor Mössbauer at the Opening Ceremony by Dénes Nagy, Chairperson of IBAME, with Yutaka Yoshida, Chairperson of the Organising Committee, dedicating the conference to the memory of Professor Mössbauer.

At the outset I would like to thank the Organisers for the invitation and honour of presenting these "Concluding Remarks" to ICAME2011. Research based on the Mössbauer effect has been an integral part of my research activities since initial measurements carried out over 40 years ago as part of my PhD studies at Monash University. Since then I have been fortunate to have attended 12 ICAME conferences and several meetings in the ISIAME and Seeheim Mössbauer Workshop series. In accepting the responsibility of appraising ICAME2011, apart from attending all talks and sessions, as far as possible my aims were to adopt a 'clean sheet' attitude to ensure a fresh approach in my responses to the many facets of the conference. While this resulted in six busy days at ICAME2011, it emphasised my appreciation of the diverse and exciting range of science that can be undertaken using our incisive microscopic technique in low energy nuclear physics.

A conference comprises many aspects. Central to a successful meeting is of course the quality of the science presented and related publications. In addition to the standard oral and poster presentations over the 5 days of ICAME2011, the organisers arranged tutorial lectures for the day preceding the Opening, as well as evening sessions and innovative short five minute oral presentations. A brief appraisal of these key components together with other important issues such as the smooth operation of sessions (role of chairpersons, administrative and computer support and so on), is presented.

While science is mostly carried out in a cooperative manner by like-minded and friendly people, none the less science is a competitive affair with issues such as priority, funding, promotions and fame potentially involved. Research flourishes and develops progressively by the Scientific Method, a well established iterative process of experiment, systematic data collection and analysis, modelling, theory and feedback that we all understand and adopt. In outlining my observations and providing this feedback, I therefore offer a semi-quantitative assessment of ICAME2011 as we move forward with our enduring biennial series of international Mössbauer conferences.

2 The opening ceremony; statistics

As already indicated, the five day ICAME2011 meeting got underway with the strong awareness of all in attendance of the horrors that had led to the need to move from Tokyo to Kobe. This was captured by Conference Chairperson Yutaka Yoshida in his opening remarks: "So many things happen for this conference."; "11 March 2011: We were nearly ready, five years in preparation"; "Thank organising colleagues for their extraordinary efforts in organising this conference". As mentioned above, the Opening Ceremony was further tinged by news of the passing of our revered

Table 1 Breakdown by country of the 183 delegates at ICAME2011

Country	Delegates
Australia	3
Austria	3
Belgium	4
Canada	1
China	8
Columbia	2
Croatia	3
Czech Republic	5
Egypt	1
Finland	1
France	11
Germany	17
Hungary	6
Japan	80
Mexico	1
Oman	6
Peru	1
Poland	7
Portugal	1
Romania	2
Russia	7
Slovakia	1
South Africa	2
Spain	4
USA	6
TOTAL	183

colleague Rudolph L Mössbauer who, as we all know, was awarded a share of the 1961 Nobel Prize in Physics for his discovery and explanation of the effect that bears his name. A very fine overview and laudation of Professor Mossbauer's career was presented by Professor Nagy with Professor Yoshida dedicating the conference to the memory of Rudolph L Mössbauer. Further insightful words were provided by Honorary ICAME2011 Member Professor Teruya Shinjo who, drawing on his own experiences from international research collaborations, exhorted young Japanese colleagues to: "Attend Future ICAME Conferences; make good scientific results leading to attendance at future ICAME meetings, and to enjoy international friendships."

These introductory statements proved important to the conference as the way was now cleared to proceed in a focused manner on the key scientific aspects of ICAME2011. In particular, it allowed the aims of the conference as stated by Professor Yoshida - "Create a new generation of Mössbauer spectroscopists"; "Create strong bonds" - to be fully engaged by delegates. With a 50% decrease in visitor numbers to Japan during 2011, the attendance at ICAME2011 of 183 participants, comprising 33 invited; 118 registered and 32 students, was a very positive outcome for the organisers. As shown in Table 1, representatives of 25 countries attended the meeting with Japan, 80, and Germany, 17, having the largest contingents followed by France, China and Poland with 11, 8 and 7 delegates respectively.

3 Conference sessions – impressions

3.1 Tutorial lectures

In common with the practice at recent conferences, proceedings started the day before the official opening with a set of tutorial lectures aimed at students and junior researchers. The organisers had identified a gap in the Mössbauer literature with the six invited lecturers asked to target not just research students and early career researchers, but also to direct their oral and written presentations at the level of final year Bachelor studies which would also suit those in industry. A total of 34 students and delegates attended the set of lectures presented by six experienced and capable lecturers in the picturesque setting of the Sorakuen Gardens, Kobe. As requested, lecturers addressed the fundamentals of their topic with exemplary clarity and (mostly) avoided the common trap of overloading their slides. The fact that lecturers took time to *explain* their topic was appreciated by students.

Lecturers were required to prepare their presentations in written form with the aim of preparing a textbook comprising six chapters – General Principles; Chemical Applications; Earth Sciences; Fe-based Nanostructures; Magnetic Multilayers and Interfaces; Ion Implantation – to be published by Springer [1].

While it was not possible for Professor Philipp Gütlich to present his lecture, in keeping with the aim of ICAME2011, he prepared a special message for the next generation. Among his many insightful words, he drew out the importance of Mössbauer spectroscopy in introducing students to a wide range of fundamental aspects in science, concluding that "I consider it therefore highly recommendable, even necessary, that Mössbauer spectroscopy and relevant neighbouring fields are always part of the education in physics and chemistry." [2].

3.2 Oral and poster presentations

The conference programme was based around the nine topics deemed more or less standard for the series (see proceedings contents) along with the newer topic of Materials Research for the Global Environment, as well as Data Base and Hot Topics. Altogether around 75 talks were presented with 1 keynote lecture and 17 oral sessions (14 regular sessions of invited and contributed talks and 3 sessions of short oral presentations), together with 2 evening sessions and the opening and closing ceremonies. The poster sessions were busy affairs with 192 presentations in the 3 sessions, each of which lasted around 1.5 h.

Having attended all talks and inspected the numerous posters, the diversity and applicability of the Mössbauer effect in science continues to amaze and impress. On the one hand we reach for the stars (or at least planet Mars and meteorites fallen to Earth) to explore their mineralogy and to search for life, while on the other we plumb the depths to examine the quality of sea beds. In between these extremes we apply our incisive microscopic technique in an increasingly impressive myriad range of significant issues in science. I wonder if Professor Mössbauer, even in the enthusiastic state surrounding the award of his Nobel Prize in 1961, would have foreseen the potential for application of his discovery to the role of frataxin in iron-sulfur assembly and dysfunction-related disease, or delineation of the magnetic properties of Ni under very high pressure?

Table 2 Scientific highlights within my spheres of interest: (a) Highlights I; (b) Highlights II; (c) Highlights III

Presenter; Reference [3]	Title	Topic
(a) Highlights I		
A I Chumakov [I-14]	Solving puzzles of glasses with nuclear resonant scattering	Dynamics (T 4)
W Keune	Applications of Mössbauer spectroscopy in magnetism	Keynote
Jung-Fu Lin [I-12]	Electronic spin transition of iron in earth's lower mantle	Earth science, mineralogy and archaeology (T 9)
R Röhlsberger [I-1]	The collective lamb shift in nuclear γ–Ray superradiance	Advances in experimental techniques and methodology (T 2)
(b) Highlights II		
E Bill [I-5]	Iron-sulfur clusters – new features in hydrogenases and synthetic models	Chemical applications (T 6)
Pierre-Emmanuel Lippens [I-9]	How Mössbauer spectroscopy can improve Li-Ion batteries	Materials research for the environment (T 1)
E Colineau [I-16]	^{237}Np Mössbauer studies on actinide superconductors and related materials	Solid state physics (T 8)
J Tucek [I-17]	Zero valent iron nanoparticles and nanometric polymorphs of Fe(III) Oxide – from solid state synthesis to their applications	Nanomaterials (T 7)
Y Kamihara [I-18]	Iron based superconductors veiled probing internal magnetic fields of elements	Hot topics
Hans-Henning Klauss [I-19]	Competing order in iron Pnictidde superconductors	Hot topics
(c) Highlights III		
H Akai [I-3]	Theory of hyperfine interactions – reality of first-principle approaches	Theories of hyperfine interactions (T 3)
W M Reiff [I-6]	'High Spin Iron (II) – Mega-Gauss Internal Hyperfine Fields; Approach to Free Ion Magnetic Behaviour'	Chemical applications (T 6)
J-M Latour [I-7]	Mössbauer studies of Frataxin role in Iron-Sulfur assembly and dysfunction-related disease	Biological and medical applications (T 5)
I Fleischer [I-13]	In-Situ Mössbauer spectroscopy with MIMOS II	Earth science, mineralogy and archaeology (T 9)
J L Tirado [I-11]	Unfolding the role of iron in Li-Ion conversion electrode materials by ^{57}Fe Mössbauer spectroscopy	Materials science and industrial applications (T 10)

3.3 Scientific highlights

In attempting to indicate some of the many scientific highlights from the oral presentations that particularly caught my attention (Table 2), I was influenced most

by the key factors of good science and quality of presentation. This latter point includes many aspects such as: clear statements on the significance and context of the problem; the experimental and/or theoretical approaches; and the speaker's ability to explain the issues and outcomes as they develop. More technical aspects include the clarity and density of information contained in slides, the pace and styles of delivery, and of course the ability of the speaker to maintain interest and stick to time. This was epitomised for me in the talk by A I Chumakov who coaxed delegates through the intricacies of the long standing apparent dilemma of the boson peak in glasses while in parallel drawing out comparisons with a deep mystery in Russian history. All was finally revealed in the multi-facetted investigation with the boson peak shown by nuclear resonant inelastic scattering to be equivalent to the transverse acoustic van Hove singularity of the corresponding crystalline phase.

In addition to the talks listed in Table 2, I was also taken with the following high quality contributed talks (code as in the programme and abstract booklet [3]): Energy Domain Synchrotron Radiation ^{57}Fe Mössbauer Spectroscopy (T Mitsui, O-1; V Potapkin, O-2); Spectral Analysis (K Szymański, O-3); SF-HAXIESST Investigated by Mössbauer Spectroscopy (F Renz, O-5); Spin Crossover Thin Films (Y Garcia, O-6); Heme Proteins (V Schünemann, O-7); Weakening 'Dead Zone' in Tokyo Bay (K Shozugawa, O-19); Ni under very high pressure by NFS (I Sergueev, O-23); ^{155}Gd Mössbauer of Rare Earths (J M Cadogan, O-24); Multiferroic Thin Films (J Juraszek, O-30).

3.4 Evening sessions; short oral presentations

The evening session, in which five of the community's senior statespersons presented aspects of their many decades of research in applications of the Mössbauer effect, proved very successful. "The Golden Oldies" as I like to think of them, provided an interesting range of topics: 50 years of Mössbauer Spectroscopy: What Now? (C E Johnson); Diffusion Studies with the New X-Ray Sources (G Vogl); Redox Topotactic Reactions (J-M R Genin); Personal Recollections of R L Mössbauer (F E Wagner) and, 45 Years: From Antimony Mössbauer Spectroscopy to Nano Systems (J G Stevens). All speakers gave very fine talks in which their commitment, quality and passion shone through.

A Special Lecture - Fukushima Accident: What Happened? - was presented by M Baba of Tohoku University on the second evening of the conference. Professor Baba gave an excellent, didactic talk of great interest to the scientific audience. The consequences of the events of 11 March 2011 and beyond will continue to be felt for many years and our thoughts have been, and continue to be with the Japanese people.

The sessions of Short Oral Presentations, in which speakers were allowed only 5 min with no questions also proved successful. While such approaches have been used in other forums this was the first time they had been adopted at ICAME. These short talks were intended mainly for the younger scientists to encourage and help create the new Mössbauer generation. While most speakers presented 5 or 6 slides, several misjudged and tried to cram in as many as 10 slides. This led to serious overrun of time, generally to little avail in their intent to communicate their scientific message.

Table 3 Poster awards for young scientists at ICAME2011

Presenter; Reference [3]	Title	Topic
1. Kana Yamada [P7–24]	Mössbauer study of metal substituted ε-Fe_2O_3	Nanomaterials (T 7)
2. Mamoru Yasuike [P6–11]	Orientation of hyperfine magnetic fields of α–Iron films produced by Laser Deposition	Chemical applications (T 6)
3. Hajime Kamebuchi [P6–15]	Study on the spin crossover transition and glass transition for Fe(II) complex film, [Fe(II)(H-triazole)$_3$]@Nafion, by means of Mössbauer spectroscopy	Chemical applications (T 6)
4. Tomohiko Sato [P9–10]	^{57}Fe Mössbauer analysis of the upper Triassic-Lower Jurassic Deep-sea Chert: paleo-redox history across the Triassic-Jurassic boundary and the Toarcian Oceanic anoxic event	Earth science, mineralogy and archaeology (T 9)
5. Benedikt Klobes [P2–10]	Nuclear resonance scattering on Te Oxides	Advances in experimental techniques and methodology (T 2)
6. Alexis Perea [P10–20]	New ^{57}Fe Mössbauer investigations on $LiFe_{1-x}Mn_xPO_4$ (x = 0; 0.25; 0.5; 0.75) materials for Li-ion batteries	Materials science and industrial applications (T 10)
7. Raul R. Gabbasov [P5–7]	Breaking of interparticle interaction in conjugates of magnetic nanoparticles injected into the mice	Biological and medical applications (T 5)
8. Sergej Rackwitz [P2–1]	Installation of an IR microscope at the nuclear resonance Beam Line ID18 of ESRF	Advances in experimental techniques and methodology (T 2)
9. Hilary Masenda [P8–43]	Mössbauer study of ^{119}Sn in 3C-SiC following ^{119}In* implantation	Solid state physics (T 8)
10. Takashi Nagatomo [P6–19]	In-Beam Mössbauer spectroscopy of ^{57}Mn Implanted into Lithium Hydride	Solid State Physics (T 8)

3.5 Posters

The posters were of a consistently high quality and standard. Members of IBAME were charged with the difficult task of assessing the posters presented by young scientists for awards announced at the Closing Ceremony (Table 3). In the event P7–24 presented by Kana Yamada was preferred by a clear majority with P6–11 and P6–15 selected ahead of the other highly-rated posters as in Table 3.

The appointment of chairpersons for each poster session was good; this places responsibility squarely on the poster presenter to ensure they are present during the

time allocated for their session. On the other hand, the relatively short time of around 1.5 h allowed per session, combined with the fact that all posters were displayed for the entire conference, meant that delegates were less able to focus entirely on posters associated with a given session. I prefer to see posters displayed only for the day of their session as this allows their focused appraisal.

3.6 Talks; posters – some observations

With few exceptions, the overall quality of talks was high and speakers are to be congratulated. Over the course of 4.5 days the relatively large number of talks (about 75) created problems, particularly on the first two days when sessions continued to around 8.30–9.00 pm. About 20 talks were presented each day with as many as 10 talks following directly after each other. Educational experience tells us that attention spans do not allow the audience to concentrate for such extended periods and breaks - even if only of a mini-nature for recommended stretch breaks - should have been incorporated. Timing was helped both by the introduction of a 'Speakers Corner' adjacent to the lectern so time loss was kept to the minimum, and by the excellent computer technical support.

Given that posters are the presentation medium for most delegates, fewer talks would allow more time for appreciation of posters. With about 60 posters per session at ICAME2011, this corresponds to around 2 min per poster. Even if, say, 10–20 posters are of direct interest, this still only allows about 10–5 min per poster to digest the content and interact with the presenter.

The number of co-authors and collaborators seems to be increasing steadily; this probably reflects the increasing tendency towards consolidated use of specialised equipment and access to large facilities. Despite the sophistication and complexity of scientific problems tackled, fundamental issues endure. For example it is important to provide information about spectral analysis and sub-spectra, the quality of experimental apparatus, drive systems and so on.

3.7 Session chairpersons

The role of chairperson is very important - they help to keep the programme to schedule while assisting delegates to get the most out of sessions. Introduction of the impressive brass bell operated by a member of the support team proved a big help – its loud clang kept the speakers informed of timing, stirred those members of the audience who needed stirring, and allowed the chairperson to focus on the session. At the same time the chairperson has to pay attention to the audience; for example, on occasions the chairperson lost track of who the next questioner was, to the frustration of those concerned.

4 General impressions

4.1 Delegates

There appeared to be a fairly wide age distribution with young and not so young well represented among the 183 delegates (Table 1; Fig. 1). While it was pleasing to have

Fig. 1 (*Upper*) Young scientists and 'young at heart' scientists. (*Lower*) Female scientists should be encouraged and supported whenever possible

many female delegates, less pleasing was to find that of over 75 talks only 4 were presented by female speakers - an invited talk, a contributed talk and two short oral presentations. While many factors affect the work and intentions of a Programme Committee, it is important to ensure that, consistent with standards, young scientists and female scientists are encouraged and supported as much as possible.

4.2 Additional activities

International conferences are generally busy affairs and ICAME2011 was no exception. For example, many delegates were also involved in two IBAME meetings. The extensive list of agenda items underlines the efforts IBAME members, particularly the executive comprising Dénes Nagy (Hungary), Jean-Marc Greneche (France) and Michael Reissner (Austria), make on behalf of the community. Similarly many colleagues appreciated the meeting and discussions with Tao Zhang and Junhu Wang as they outlined the plans they and their team at the Mössbauer Effect Data Center, Dalian, China are developing in collaboration with the community. The Mössbauer community is well served by these two important bodies and they deserve our full support.

4.3 Social

To help offset the busy conference schedule, delegates were able to take part in an outing during the traditional break on Wednesday afternoon. Likewise Thursday evening saw a splendid banquet during which delegates were regaled by the wonderful concert provided by the trio of Mrs Itsuko Yoshida (piano), Mrs Naoko Kimura (violin) and Mr Masao Kimura (cello). For those delegates able to stay in Kobe on Friday afternoon after the closing ceremony, there was the opportunity for a very interesting visit to the SPring-8 synchrotron.

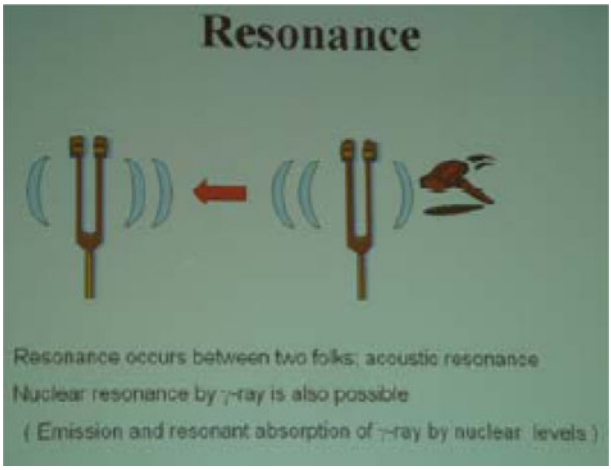

Fig. 2 Resonance between forks and resonance between folk in the Mössbauer community (after S Nasu, [1])

Fig. 3 Transfer of the mighty ICAME gavel, and with it the responsibility, from ICAME2011 in Japan to ICAME2013 in Croatia (*left* to *right*: Yutaka Yoshida, Chairperson ICAME2011, Dénes Nagy, Chairperson IBAME, Mira Ristić, Organising Committee ICAME2013, Mrs Itsuko Yoshida)

5 Appraisal

From the outset the organisers set themselves several challenges and targets - short publication time for ICAME2011 proceedings; publication of tutorial lectures as a book; short oral presentations and special evening sessions. Particularly impressive is the on-line publication of the 123 accepted papers on the Hyperfine Interactions web site by late November/early December 2011. Due to the organisers' efforts and with the support of the authors, referees and publisher, they have achieved these aims and contributed positively to the continuing development of the Mössbauer community.

Given the full schedule of talks and relatively short time available for posters perhaps two options should be considered for the future – either reduce the number of oral presentations or have parallel sessions. Introduction of two parallel sessions between the morning break and lunch on the second and fourth days of the conference would, for example, allow the programme committee greater flexibility. As

indicated above, a further recommendation is to increase participation of female scientists, consistent with maintaining standards (e.g. http://plato.stanford.edu/entries/affirmative-action/).

The commitment of the organisers to their tasks was evident at all stages. To Chairperson Yutaka Yoshida, Co-chairperson Tesuaki Nishida and all members of the organising committees: you have overcome significant hurdles and adversities in organising ICAME2011; you have done a very good job in ensuring smooth operation of all facets of the meeting while attaining high standards. We congratulate you on your efforts and the success of ICAME2011.

In the best traditions of science - which as we know is a friendly, cooperative but ultimately competitive environment - the following rating is proposed. In academic and research circles we assess student performance, review grant proposals, referee manuscripts and peer promotion applications and so on. Adopting the academic ranges of: pass (50–64); credit (65–74); distinction (75–84) and high distinction (85–100), my assessment is that ICAME2011 sits comfortably in the high distinction range – well done and congratulations.

6 Epilogue

As noted above, the tutorial lecturers explained the fundamentals of their topics clearly. Typical is the approach taken by Honorary ICAME2011 Member Professor Sabu Nasu in his discussion of resonance. In demonstrating the principle of resonance using tuning forks, Prof Nasu's slide (Fig. 2) also draws out well the resonance between folk, an aspect which underpins the enduring success of the Mössbauer community as we look towards ICAME2013 in Croatia (Fig. 3).

These concluding remarks are dedicated to the Japanese people who have been, and continue to be, affected by the natural disasters of 11 March 2011 and by subsequent events.

I would like to thank Professor Yutaka Yoshida and all members of the Organising Committee for their cooperation and for providing information about delegate numbers and poster awards at ICAME2011. My attendance at ICAME2011 was supported by Discovery Project DP110102386 from the Australian Research Council [4].

References

1. Yoshida, Y., Langouche, G. (eds): Tutorials on Mössbauer Spectroscopy (ICAME2011). Springer, Kobe, Japan (2011)
2. Abstract Booklet Tutorial Lectures. In: The 31st international Conference on the Applications of the Mössbauer Effect (ICAME2011, 25–30 September 2011, Kobe, Japan)
3. Yoshida, Y., Nishida, T., Programme and Abstract Booklet: The 31st International Conference on the Applications of the Mössbauer Effect (ICAME2011, 25–30 September 2011, Kobe, Japan)
4. Wang, J.L., Campbell, S.J., Kennedy, S.J., Dou, S.X., Wu, G.H.: Hyperfine Interact (Proc ICAME2011). doi:10.1007/s10751–011–0408–3